V CONGRESSO
GRUPPO NAZIONALE DI BIOINGEGNERIA (GNB 2016)

20-22 Giugno 2016

Università degli Studi di Napoli "Federico II"

ABSTRACT eBOOK

ISBN
978-88-941906-0-1

Napoli, 20 - 22 Giugno 2016

Università degli Studi di Napoli Federico II

Facoltà di Ingegneria

TOPICS

- Bioimmagini
- Bioinformatica
- Biologia computazionale
- System biology
- Biologia sintetica
- Biomateriali
- Biomeccanica del movimento umano
- Biomeccanica strutturale
- Biorobotica
- Controllo motorio e sensoriale
- Dispositivi, sistemi e tecnologie diagnostiche e terapeutiche
- Elaborazione di dati e segnali biomedici
- Informatica medica
- Ingegneria clinica
- Ingegneria della riabilitazione
- Ingegneria tissutale e medicina rigenerativa
- Modellistica matematica
- Neuroinformatica
- Neuroingegneria
- Tecnologie assistive
- Tecnologie nano, micro e indossabili
- Telemedicina

Gruppo Nazionale di Bioingegneria

Comitato di Presidenza

Paolo NETTI - *Università degli studi di Napoli "Federico II"*
Mario CESARELLI - *Università degli studi di Napoli "Federico II"*
Pierluca MAFFETTONE - *Università degli studi di Napoli "Federico II"*
Gaetano MANFREDI - *Università degli studi di Napoli "Federico II"*

Comitato Scientifico Nazionale

Emanuele BIONDI *Politecnico di Milano*
Angelo CAPPELLO *Università degli studi di Bologna*
Mario CESARELLI *Università degli studi di Napoli Federico II*
Mauro URSINO *Università degli studi di Bologna*
Luca CRISTOFOLINI *Università degli studi di Bologna*
Lorenzo CHIARI *Università degli studi di Bologna*
Nicola LOPOMO *Università degli studi di Brescia*
Annalisa BONFIGLIO *Università degli studi di Cagliari*
Francesco AMATO *Università degli studi di Catanzaro*
Andrea CORVI *Università degli studi di Firenze*
Claudia MANFREDI *Università degli studi di Firenze*
Roberto RAITERI *Università degli studi di Genova*
Giulio SANDINI *Università degli studi di Genova*
Silvio BICCIATO *Università degli studi di Modena e Reggio Emilia*
Giovanni SPARACINO *Università degli studi di Padova*
Claudio COBELLI *Università degli studi di Padova*
Arturo NATALI *Università degli studi di Padova*
Paolo NETTI *Università degli studi di Napoli Federico II*
Gianna TOFFOLO *Università degli studi di Padova*
Paolo MAGNI *Università degli studi di Pavia*
Riccardo BELLAZZI *Università degli studi di Pavia*
Giovanni MAGENES *Università degli studi di Pavia*
Arti AHLUWALIA *Università degli studi di Pisa*
Luigi LANDINI *Università degli studi di Pisa*
Beniamino FIORE *Politecnico di Milano*
Manuela RAIMONDI *Politecnico di Milano*
Andrea ALIVERTI *Politecnico di Milano*
Pasquale VENA *Politecnico di Milano*
Sergio CERUTTI *Politecnico di Milano*
Maria Laura COSTANTINO *Politecnico di Milano*
Riccardo PIETRABISSA *Politecnico di Milano*
Giuseppe BASELLI *Politecnico di Milano*
Alberto AUDENINO *Politecnico di Torino*
Marco KNAFLITZ *Politecnico di Torino*
Aurelio CAPPOZZO *Roma "Foro Italico"*
Silvia CONFORTO *Università degli studi Roma Tre*
Ugo DELLA CROCE *Università degli studi di Sassari*
Christian CIPRIANI *Scuola Superiore Sant'Anna*
Paolo DARIO Scuola *Superiore Sant'Anna*
Arianna MENCIASSI *Scuola Superiore Sant'Anna*
Silvestro MICERA *Scuola Superiore Sant'Anna*
Agostino ACCARDO *Università degli studi di Trieste*
Eugenio GUGLIELMELLI *"Campus Bio-Medico" di Roma*
Febo CINCOTTI *Università degli Studi di Roma "La Sapienza"*

Comitato Organizzatore Locale

Paolo BIFULCO
Filippo CAUSA
Diego DI BERNARDO
Francesco GENTILE

Il Quinto Congresso del Gruppo Nazionale di Bioingegneria (GNB 2016) è stato promosso e organizzato dal Dipartimento di Ingegneria Chimica, dei Materiali e della Produzione Industriale e dal Dipartimento di Ingegneria elettrica e delle Tecnologie dell'Informazione dell'Università degli Studi di Napoli Federico II. Si svolge nei giorni 20-22 giugno 2016, presso la sede della scuola politecnica e delle scienze di base dell'Università degli Studi di Napoli "Federico II" in Piazzale Vincenzo Tecchio, 80.

L'evento, giunto alla sua V edizione, rappresenta il principale momento di incontro dei bioingegneri italiani, comunità scientifica particolarmente attiva e pienamente inserita nel contesto della ricerca internazionale. Il Congresso fornisce una panoramica delle attività più recenti nel campo della Bioingegneria in Italia ed ha lo scopo di coinvolgere tutte le componenti della comunità scientifica, in particolare i giovani: gli studenti, sempre più numerosi nei corsi di laurea delle varie sedi universitarie, i dottorandi, i dottori di ricerca e i giovani ricercatori, che hanno scelto di scommettere su un settore fortemente innovativo con grandi potenzialitù di crescita e di traino per l'economia dell'intero paese.

La struttura del Congresso è organizzata in sessioni plenarie. Ogni sessione prevede una Lettura Magistrale, tenuta da nove eminenti personalità italiane e straniere. Comprende inoltre una tavola rotonda dal titolo: "*Sbocchi occupazionali del bioingegnere*" a cui partecipano diversi rappresentanti del mondo accademico, industriale e finanziario.

Il convegno contempla numerose presentazioni poster, da tenersi nel corso delle sessioni tematiche. Infine, durante il congresso le presentazioni derivanti dai poster più interessanti sono state invitate a presentare i contributi in sessione plenaria e, cinque di queste, insignite del "Premio Giovani Ricercatori".

In concomitanza con il Congresso, nel pomeriggio di mercoledì 22 giugno, a proseguimento della sessione mattutina del GNB, si svolge inoltre il meeting annuale del Capitolo Italiano della Società Europea di Biomeccanica (ESB-ITA) (http://www.esb- ita.it/home.html).

L'adesione complessiva a GNB 2016, è stata molto soddisfacente, con un totale di circa 270 iscrizioni. Una particolare attenzione è stata rivolta a favorire la partecipazione di studenti e di personale non strutturato, quali i dottorandi, i dottori di ricerca, gli assegnisti, che rappresentano circa l'80% delle iscrizioni totali.

Complessivamente, i contributi liberi sottoposti sono stati 231, a testimonianza della vitalità, dell'elevato livello di maturità e della vastità di temi di ricerca che rende la Bioingegneria uno tra i settori scientifici più multidisciplinari e dinamici. Ugualmente molto positiva la Call per i Premi per Giovani ricercatori.

Un doveroso ringraziamento va quindi a tutti coloro che hanno contribuito con l'invio delle sottomissioni. Solo l'ineluttabile limitazione costituita dalla disponibilità di tempo e dal numero dei Premi ha impedito di premiare un numero più elevato di giovani ricercatori.
Per tutti i lavori presentati, la selezione è stata accurata e impegnativa. Per questo esprimiamo tutta la nostra gratitudine e il nostro sentito ringraziamento ai membri del Comitato Scientifico e a tutti i colleghi che ci hanno aiutato nella revisione dei lavori.

Porgiamo un ringraziamento particolare all'Università degli Studi di Napoli "Federico II" e al suo Rettore, che hanno sponsorizzato il Convegno grazie alla disponibilità delle Aule e dei cortili della ex-facoltà di Ingegneria, permettendoci sia di avere una sede indimenticabile per il Congresso mantenendo basse le quote di iscrizione.

Infine, un ringraziamento ai più giovani colleghi del Comitato organizzatore locale, che hanno in maniera determinante collaborato per l'organizzazione e la buona riuscita di questo Congresso.

A concludere la nostra introduzione, un semplice sguardo ai temi delle sessioni scientifiche, qui sotto riportati, rende conto della vastità e modernità dei temi trattati nel corso del V Congresso del Gruppo Nazionale di Bioingegneria:

Sessione 1: Bioimmagini; Elaborazione di dati e segnali biomedici
Sessione 2: Biomeccanica del movimento umano; Biomeccanica strutturale; Biorobotica; Controllo motorio e sensoriale; Ingegneria della riabilitazione
Sessione 3: Biomateriali
Sessione 4: Ingegneria tissutale e medicina rigenerativa; Dispositivi, sistemi e tecnologie diagnostiche e terapeutiche; Tecnologie nano, micro e indossabili; Informatica medica; Telemedicina; Ingegneria clinica
Sessione 5: Modellistica matematica; Biologia computazionale; Biologia sintetica; System Biology; Neuroinformatica; Neuroingegneria; Bioinformatica

Queste sessioni raggruppano in realtà un ampio ventaglio di argomenti in cui potevano essere incasellate le sottomissioni e riassumono assai efficacemente la sempre maggiore penetrazione della Bioingegneria nel campo della gestione della salute, nel senso più estensivo del termine. Bioingegneria che è ormai una componente fondamentale non della ricerca, ma anche dell'intero l'ambito sanitario e assistenziale, incluse le molteplici applicazioni industriali che ad esso si accompagnano.

L'augurio è quindi quello che questo Congresso, e i prossimi, rappresentino non soltanto un ulteriore momento di crescita culturale della nostra Comunità, ma anche un'occasione di riflessione strategica sulle direzioni di sviluppo della Bioingegneria, che molto può dare al futuro del nostro paese.

Il Comitato Organizzatore - V Congresso GNB 2016

SPONSORS

We make it visible.

ABSTRACT
INVITED SPEAKERS

The future of biomedical engineering and robotics in the fourth industrial revolution

M.C. Carrozza
The Biorobotics Institute, Scuola Superiore Sant'Anna, Pisa, Italy

The objective of this analysis is to introduce and then critically describe the process of the so called 'fourth industrial revolution' by pointing out the different aspects and implications. I am not daring to apply an historical methodology because my background prevent me to enter in this field, but I want only to describe what we are living, spending an effort to anticipate what is going on and try to watch from different perspectives, industrial, social and scientific, in order to encourage the scientific and academic community to react and prepare for the changes that we are living at present time.

A. Science and society

Science, research, industrial development and social innovation are strictly interdependent, and in this framework, my vision for the future is that sustainable progress of humanity must be the ultimate mission of science. This is well depicted in the objectives of HORIZON 2020 where excellence in science, industrial leadership and social innovation are the main pillars for the research, training and development programs.

Nowadays, there is a bridge of social expectation that is linking science and politics, mainly related to the strong demand for science to address the challenges of the society, and for government to develop science or evidence based laws and policies. Stakeholders, governments and citizens are expecting that scientists solve the main problems of the society, this produced some awareness in scientists which is demonstrated very recently in a 2015 Nature issue, where the cover and some editorials are expressing the position that a strong interdisciplinary effort is necessary for identifying, segmenting and solving problems that affect humanity. After years of separation of the different disciplines in academia and science, now scientists are realizing that it is not possible to address global problems as clean energy production, urbanization, migration, starvation, antibiotics resistance or climate change without an holistic approach: social challenges requires comprehensive methods and knowledge, which must include human sciences, ethical issues and sustainability.

In this framework the importance of the inherently interdisciplinary science as it is biomedical engineering is more and more evident because it is producing a cultural approach appropriate to address the problems of the society.

B. Industrial Revolutions

In order to prepare to address the social innovation and moreover the societal challenges in general, I must go back to industrial revolutions and their schematic methodology to describe human progress because it is useful to describe what we are living and how science is now becoming crucial to understand what is happening and the transformation of the society.

In modern history, it is universally accepted that the process of change from an agrarian, handicraft economy to one dominated by industry and machine manufacturing is named Industrial Revolution. This process began in Britain, with the First Industrial Revolution in the 18th century, and then diffused in other parts of the world.

According to historians of economy, the first industrial revolution was related to technological developments such as the invention of machines to do the work of hand tools; the use of steam, and of other kinds of power, in place of the muscles of human beings and of animals; and the adoption of the organization of the factory system…

The second and third industrial revolutions followed the first and where characterized by different technological innovations which produced substantial and fundamental breakthroughs in producing goods and services.

The second industrial revolution, is dated in the middle of 19th century and was characterized by the emergence of chemical and steel industries, and the development of Germany as industrial power in parallel to UK, where the first revolution was centered. The third industrial revolution was the revolution of microelectronics, sensors, and mechatronics, ultimately producing miniaturization of devices and systems, embedded intelligence and robotics and automation for mass production.

C. Robotics and Biomedical Engineering

The integration of robotics with artificial intelligence, deep learning and high speed connection will revolutionize the society because devices will be connected to internet, and will become physically powerful, intelligent and adaptive. Large amount of data will be available with small latency and cloud robotics will enable us to share information, data, intelligence activities and brains. It will be possible to extend virtual and physical modeling of systems, to predict the outcome of phenomena and to model evolution of systems in action.

Robots were originally designed for manufacturing plants,

and nowadays mass production is not possible without robots but now they are indispensable in special environments as space for exploration, oceans for underwater activities or hospitals in surgical rooms. In particular, as it was predicted in science fiction, now deep space exploration is based on robotics, and robots will be essential for space science progress.

The next step will be for robots to enter in our everyday life: in the streets with self-driving cars, or 'at our place' in doing cleaning, entertainment or service activities. Therefore robotics is becoming 'social'.

In order to achieve these goals, engineers must address several issues, related to human-robot interaction, to safety, to sentience and adaptability. The problem of safe, secure and effective interaction between human being and robot, cannot be faced without addressing legal and ethical issues.

The road map is already in place, with time and application those issues will be studied and investigated, and robots will share life and environments with humans, supporting their physical and cognitive activities.

In this framework, I think that a novel role for biomedical engineering will be opened up, mainly because of the 'humanization' of technology, that will be more and more wearable and implantable in the human body, but also because of the fusion of bionics and robotics, that will produce more integration between natural and artificial, natural control from the user, and ultimately bioartificial organs where the boundary between artificial and natural will be undefined. The mission of biomedical engineering will be to 'humanize technology' in order to support human being and to avoid to 'robotize humans'.

Moreover, one of the most fascinating questions to answer in robotics will be originated by the integration of robotics with bionics and prosthetics, when robotics will enter into the human body with different levels of integration, to support human movements, physical interaction with the environment but also cognitive activities. Wearable robotics is expected to revolutionize the society in the next decade.

II. Conclusion

What are the implications of this transformation of technology? Which areas of science will be involved in the evolution of robotics? Biomedical engineering will be at the intersection between natural and artificial, with the ultimate goal of supporting human life, preventing diseases with personalized tools, and producing better recovery and rehabilitation.

What are the main milestones to be accomplished in the journey of robots from manufacturing plants, to the civil society and ultimately into the human body?

Real time detection of brain activity: research, development and applications in neurorehabilitation

F. Cincotti[1,2]

[1] *Dept. of Computer, Control, and Management Engineering "Antonio Ruberti", Sapienza University of Rome, Italy*
[2] *Neuroelectrical Imaging and BCI Laboratory, IRCCS Fondazione Santa Lucia, Rome, Italy*

I. Introduction

Brain-Computer Interfaces (BCIs) measure voluntary or task-related modulations of brain activity, translate them into control signals and, ultimately, into actions that have an effect on the environment, bypassing the natural efferent channels of the Central Nervous System (CNS).

Several types of BCIs exist, differing by: (i) the physical measurements of the CNS activity (electromagnetic, metabolic); (ii) the level of invasiveness required by the measurement; (iii) the features extracted from the input signal (spiking rates, evoked potentials, electroencephalographic (EEG) rhythms, etc.); (iv) the type of cognitive processing underlying the CNS activity modulation; (v) the nature of the output signal (continuous regression vs, discrete classification); (vi) the intended application (e.g. replacing, restoring or improving a lost function; supplementing or enhancing a natural function).

In this presentation, focus will be on non-invasive EEG-based systems and their clinical applications, reviewing recent advancements of the research field and discussing crucial issues to foster translation outside research laboratories.

I. BCIs to Replace Communication and Improve Motor Functions

Communication and control of the external environment can be restored in severely disabled people through direct brain-computer interaction, bypassing the impaired neuromuscular channels. In these applications, BCIs are designed to replace a lost function (e.g., speaking, writing, acting on appliances) in persons with severe diseases and little or no chance of recovery. Often BCIs are wrongly designed and assumed to provide a complete solution to communication needs of a user with severe motor disabilities. In fact an Assistive Device (AD) needs to be accessed by all possible residual communication channels of the user. Using BCIs as an additive (rather than alternative) access to the AD has been proposed and validated as an aid for communication and environmental control for users with Amyotrophyc Lateral Sclerosis (ALS) [1].

The rationale of using BCI systems to support the rehabilitation process after an insult to the CNS (e.g. a stroke) is their potential to monitor altered brain activity and guide it back to a physiological condition, along with the assumption that this recovery of brain activity leads to restoration of function. In fact, several randomized controlled trials demonstrated the efficacy of BCI-supported rehabilitation in stroke patients (see e.g. [1] for an approach to motor rehabilitation of the upper limb in subacute phase).

II. Industrial Takeup

Currently, most BCI-related commercial products target the research and development market. While applications designed for the general population (e.g. gaming interfaces, workload/vigilance monitors, biometric sensors, etc.) are attractive due to the large market size, health-oriented market applications are a promising opportunity for BCI products to enter the market, due to their peculiar opportunities to cover for the cost of the product. The aging population determines an increased need of effective tools supporting neuro-rehabilitation e.g. after a cerebrovascular accident. Other applications, including support to communication, despite their high potential impact on the users' Quality of Life, impose a difficult trade-off between technological value and affordability. Other forms of incentives for industries targeting this latter market are thus required.

III. Conclusion

Near-future research and innovation pathways in the clinical application of BCIs critically depends on (i) technical improvements, (ii) interactions with nearby disciplines (clinical and neuroscientific), and (iii) ability to identify a profitable market for companies wishing to take up research results. Interventions should always be designed taking into account relevant rehabilitation and neurophysiological principles, and clinical trials must be carried out according to current standards to provide solid evidence of efficacy and thus foster the integration of BCI-based intervention in the rehabilitation program of patients.

Acknowledgement

This work was partially supported by Sapienza University of Rome (grant C26A15N8LZ)

References

[1] Schettini, F., Riccio, A., Simione, L., Liberati, G., Caruso, M., Frasca, V., Calabrese, B., Mecella, M., Pizzimenti, A., Inghilleri, M., Mattia, D., Cincotti, F., 2015. Assistive Device with Conventional, Alternative, and BCI Inputs to Enhance Interaction with the Environment for People with ALS: A Feasibility and Usability Study. Arch. Phys. Med. Rehabil., 96(3):S46–53. doi:10.1016/j.apmr.2014.05.027

[2] F. Pichiorri, G. Morone, M. Petti, J. Toppi, I. Pisotta, M. Molinari, S. Paolucci, M. Inghilleri, L. Astolfi, F. Cincotti, and D. Mattia, "Brain-

computer interface boosts motor imagery practice during stroke recovery," Ann. Neurol., Feb. 2015. doi:10.1002/ana.24390

Locomotion at microscopic scales: some case studies on biological and bio-inspired motility

A. De Simone[1]

[1] *SISSA-International School for Advanced Studies, Via Bonomea 265, 34136 Trieste, ITALY; email: desimone@sissa.it*

I. Cell motility as a paradigm for locomotion at the micro-meter scale

Motility of cells, whose typical size is in the tens of micro-meters, is at the root of many fundamental processes in Biology. These include the immune system response, the establishment of connections in the nervous system network, metastatic tumor cells crawling to invade nearby tissues, and sperm cells successfully swimming their way by beating a flagellum until they reach and fertilize an egg cell. The detailed understanding of the mechanical processes enabling biological locomotion at the micro-meter scale is still a challenge.

In addition, motile cells can be regarded as micro-meter-scale, self-sufficient machines capable of executing controlled motion. They are able to generate bio-compatible forces over distances that are biologically meaningful; their structure has been optimized by evolution and natural selection. Learning the mechanical details of how cells move may guide the future design of bio-inspired, motile microscopic devices capable of navigating inside the human body for diagnostic or therapeutic purposes [1]-[3]. While the idea of building artificial devices emulating the capabilities of motile cells is quite natural, much remains to be done for this to be practical.

In recent years, we have been studying the mechanical bases of cellular motility by swimming and crawling [4]-[5]. In the context of swimming motility, our research has paid special attention on the connections between low Reynolds number swimming and Geometric Control Theory, and on the geometric structure of the underlying equations of motion [4]-[6]. The goal of our emphasis on conceptual principles has been the attempt to extract, from the study of the biological template, the "secrets" for successful design of engineered bio-inspired constructs. As a concrete example of our approach, we report on recent progress on reverse engineering of the euglenoid movement [7]-[8].

II. Reverse engineering the euglenoid movement: from unicellular swimmers to bio-inspired robots

Euglenids are unicellular aquatic organisms capable of moving either by beating a flagellum or by executing dramatic shape changes. These are accomplished thanks to a complex structure underlying the plasma membrane, made of interlocking proteinaceous strips, microtubules, and motor proteins.

We discuss the mechanisms by which the sliding of pellicle strips leads to shape control and locomotion, which have been studied by means of both theory (through the mechanics of active surfaces and its coupling to computational fluid dynamics for the surrounding fluid) and experiments. Moreover, we have implemented them into a new concept of surfaces with programmable shape, obtained by assembling 3d-printed strips in a construct mimicking the biological template.

We show that the subtle balance between constraints and flexibility leads to a wide variety of shapes that can be obtained with relatively simple controls. This suggests that euglenids exploit the passive resistance of body parts to reduce the complexity of controlling their shape. This is in close analogy to the notion of *morphological computation,* which has been advocated for the design of soft robots inspired by biological systems.

Acknowledgement

We gratefully acknowledge the financial support from the European Research Council through the ERC Advanced Grant 340685-MicroMotility.

References

[1] R. Dreyfus et al.: Microscopic artificial swimmers. Nature 437, 862-865 (2005).

[2] J.Feng, S.K. Cho: Mini and Micro Propulsion for Medical Swimmers. Micromachines 5, 97-113 (2014).

[3] F. Alouges, A. DeSimone, L. Giraldi, M. Zoppello: Can magnetic multilayers propel artificial microswimmers mimicking sperm cells? Soft Robotics 2, 117–128 (2015).

[4] F. Alouges, A. DeSimone, A. Lefebvre: Optimal strokes for low Reynolds number swimmers: an example. J. Nonlinear Science 18, 277–302 (2008).

[5] A. DeSimone, A. Tatone: Crawling motility through the analysis of model locomotors: two case studies. Eur. Phys. J. E 35, article no. 85 (2012).

[6] F. Alouges, A. DeSimone, L. Heltai, A. Lefebvre, B. Merlet: Optimally swimming Stokesian robots. Discrete Cont. Dyn. Systems B 18, 1189–1215 (2013).

[7] M.Arroyo, L. Heltai, D. Milan, A. DeSimone: Reverse engineering the euglenoid movement. Proc. National Academy of Sciences USA 109, 17874–17879 (2012).

[8] M. Arroyo, A. DeSimone: Shape control of active surfaces inspired by the movement of euglenids. J. Mech. Phys. Solids 62, 99–112 (2014).

From movement analysis to computer assisted surgery, a forty years long path toward new technologies

G. Ferrigno[1]

[1] *Neuroengineering and Medical Robotics Lab – Dept of Electronics, Information and Bioengin. – Politecnico di Milano*

A. Automated motion analysis technologies

About forty years ago, the first attempts to automated motion analysis started. Several researchers, aiming at movement kinematics and dynamics detailed analysis, contributed with different approaches ranging from polarized light to lateral effect photodiodes [1] leading to the first optical commercial systems in the middle of '80s. Efforts were put mainly in the increase of the spatial resolution (accuracy is another story) and sampling rate. Maturity was reached with the solid state cameras, CCD and CMOS. Further to the spatial and temporal resolution (which reach more than 1 mega pixel and hundreds of Hertz nowadays) other aspects have been faced. One for all is the camera calibration problem, borrowed from close range stereophotogrammetry and computer vision. Motion analysis cameras are indeed non metric. This opens a problem to be solved for making the triangulation possible, which is needed for the computation of the 3D coordinate of the markers used as body landmarks (see figure 1). The motion capture, which needs high accuracy in order to correctly compute kinematic and dynamic variables, is indeed still based on markers highlighting selected positions of the body as bony prominences or joints, although new easy, but much less accurate approaches as Kinect cameras are nowadays available. Camera calibration in its more complete form include the estimate of 11 parameters for the camera model plus other few (usually 2-4) for correcting lens optical distortions (see for example [2]):

$$p = \begin{bmatrix} x \\ y \\ 1 \end{bmatrix} = \begin{bmatrix} 1 & 0 & \Delta x(p,q) \\ 0 & 1 & \Delta y(p,q) \\ 0 & 0 & 1 \end{bmatrix} \begin{bmatrix} 1 & s & x_c \\ 0 & 1+m & y_c \\ 0 & 0 & 1 \end{bmatrix} \begin{bmatrix} c & 0 & 0 \\ 0 & c & 0 \\ 0 & 0 & 1 \end{bmatrix} R\left[I_3 \mid -P_0\right] \begin{bmatrix} X \\ Y \\ Z \\ 1 \end{bmatrix} \quad (1)$$

Complete system calibration requires shooting control points with known or unknown (preferred solution) position, but with some geometrical relationship among them (wands with three aligned markers are a typical choice).

B. Computer assisted surgery (CAS) and Navigation

It came then easy to extend the use of motion capture systems to computer aided surgery in order to locate body parts (tissues, organs, bones) both in patient's images and in the real world, making it possible to see the relative position of surgical tools wrt structures identified in the planning phase (Figure 2). Figure 3 is a classical CAS iconic description due to Russel Taylor (JHU) 2009.

The optical localizer of navigation systems consists of two cameras or three linear optical arrays pre-calibrated and coming into a rigid support so that factory calibration is not disrupted during their lifetime. Alternative approaches as ultrasonic transducers and electro-magnetic systems have been developed, but are still little used.

C. CRAS

The step from CAS to Computer and Robot Assisted surgery (CRAS) is straightforward. A PUMA 200 was used for the first robotic neurosurgery intervention [3] This breakthrough stemmed from the momentum of the development of CT-guided stereotactic devices in the late 1970's at the Memorial Medical Center at Long Beach, but was soon discontinued due to safety concerns about the robot arm (54 kg weight with 0.5 m/s movements) that was only designed to operate when separated by a physical barrier (fence) from people. The issue of the co-presence of robot and humans in the Operating Room (OR) is still an issue nowadays and is tackled with lightweight devices, "body" sensors, joint sensors, modulation of the stiffness, environmental surveillance cameras, etc. Though many robots used for surgery do not foresee an external navigation system, those, which are not tele-operated, need the steps of registration of patient data with the real patient body and with the robot base in the operating room. Such registrations can be done by laser scan (Rosa) or intraoperative imaging systems (Neuromate), although the use of a navigation system would be easier. More recent research approaches make wide use of navigation also for robotic surgery [4], see Fig 4.

D. References

[1] Woltring HJ, Marsolais EB (1980) Optoelectric (Selspot) gait measurement in two- and three-dimensional space--a preliminary report. Bull Prosthet Res. 10-34:46-52.

[2] Zhang Z. (2000) A Flexible New Technique for Camera Calibration, IEEE Trans. on Patt. An. and Machine Intel. PAMI, Vol. 22, No. 11, pp. 1330-1334.

[3] Y.S. Kwoh, I.S. Reed, J.Y. Chen, H. Shao, T.K. Truong and E.A. Jonckheere (1985) A new computerized tomographic aided robotics stereotactic system. Robot Age, Vol. 7, pp. 17-21

[4] Faria, C., Erlhagen, W., Rito, M. , De Momi, E. , Ferrigno, G., Bicho, E. (2015) Review of robotic technology for stereotactic neurosurgery. IEEE Reviews in Biomedical Engineering, Volume 8, 2015, Pages 125-137

Open Research Challenges in Rehabilitation Robotics

E. Guglielmelli[1]
[1] *Research Unit of Biomedical Robotics and Biomicrosystems*
Campus Bio-Medico University of Rome, Italy

Rehabilitation robotics emerged as a novel application area in the healthcare domain for robotics and automation technology in the late '90s, when the first trials on human subjects were carried out.

After more than 20 years since that time, this technology is still gaining increasing popularity for attracting research interests, clinical developments and industrial exploitation of cumulative findings on efficacy of robot-mediated therapy of a variety of muscoloskeletal disorders and neuromotor diseases.

Nevertheless, effectiveness and cost-effectiveness of those solutions which were used for implementing significant clinical applications are in many cases still quite weak or questionable, when structured techniques, such as systematic review and meta-analyises, for such evaluations are applied.

Starting from a critical overview of the main current scientific and technological limitations of the achievements to-date, this talk will present and discuss some of main open research challenges, covering both the area of functional recovery and of functional substitution.

Examples and case-studies being carried out at the Research Unit of Biomedical Robotics and Biomicrosystems of the Campus Bio-Medico University of Rome on some of these research challenges, such as non-anthropomorphic wearable machines, bio-cooperative controllers and intuitive human-machine interfaces, restoration of sensory feedback and learning capabilities (e.g. via neural interfaces), tele-rehabilitation and more, will be briefly introduced to support the proposed research roadmap for the next evolutions of rehabilitation robotics.

Finally, the talk will discuss the main reasons why, when observed from a genuine clinical perspective, the trajectory of rehabilitation technology appears far from reaching its maturity yet. To this aim, a recent, yet preliminary, Health Technology Assessment (HTA) study of rehabilitation robots, with a specific focus on solutions for the lower limb therapy, will be presented in order to outline the key importance of improving the quality of translational research and clinical trials on rehabilitation robotics technology so to fully demonstrate its cost-effectiveness and sustainability, and to pave the way for a massive development and deployment to the healthcare arena of these innovative solutions, which has the potential to generate a dramatic social and economic impact.

A multiscale biomechanical study to investigate the influence of mechanical loading in additive manufacturing scaffolds

D. Lacroix[1]
[1]*Department of Mechanical Engineering, University of Sheffield, United Kingdom*

Tissue engineering has become a new promising field of research with high prospects of being able to generate any kind of tissues at will. However, after more than ten years of research little is still known on the exact mechanisms of interactions between cells, biomaterials and external stimuli. One of the important processes affecting cell behavior is mechanotransduction, i.e. how the mechanical loading applied on the body is translated onto the cells. In order to better understand this load transfer computational models are being developed. Based on some mechanoregulation laws, the migration, proliferation and differentiation of cells can be predicted. In this study the simulation of cell seeding in a tissue engineering scaffold will be presented. It is shown how the macroscopic external loading applied onto the scaffold is of a different magnitude than the microscopic loading transduced at the scale level. A new methodology to simulate cell seeding enables to predict cell distribution within a scaffold and to optimize cell seeding as a function of cell density, pore shape and pore size. A single cell finite element model will also be presented to show the contribution of each component of the cytosleleton structure. In conclusion computational models are useful to optimize the cell seeding process depending on the type of scaffold chosen and in calculating the local mechanical stimuli affecting cells while it is practically impossible to measure it experimentally. It is believed that such approach will provide in the future a rationale for the consistent design of tissue engineering scaffolds.

Biological-basis for Designing Biomaterials for the Injured and Degenerated Host

A. Pandit

[1] *SFI Centre for Research in Medical Devices (CÚRAM), National University of Ireland, Galway*

Biomaterials are no longer considered innate structures and using functionalisation strategies to modulate a desired response whether it is a host or implant is currently an important focus in current research paradigms. Fundamentally, a thorough understanding the host response will enable us to design proper functionalisation strategies. The input from the host response needs to be weighed in depending on the host disease condition. In addition biomaterials themselves provide immense therapeutic benefits which needs to be accounted for when using functionalisaton strategies. Using functionalisation strategies such as enzymatic and hyperbranched linking systems, we have been able to link biomolecules to different structural moieties. The programmed assembly of biomolecules into higher-order self-organized systems is central to innumerable biological processes and development of the next generation of functionalized scaffolds. Recent design efforts have utilized a devolopmental biology approach toward both understanding and engineering supramolecular protein assemblies. Structural moieties have taken a variety of different forms such as nanofibers and nanoparticulate. This approach has resulted in functionalisation of micro and nanoparticles with biomolecules that include designed peptide motifs, growth factors and a multitude of gene vector systems. In addition, nature itself has abundant structural complexity that can be harnessed for targetted clinical applications. This talk will elucidate some of these ongoing strategies in our laboratory.

ACKNOWLEDGEMENT

Science Foundation Ireland (SFI) Grant Number 13/RC/2073

Geometric control of cell reprogramming

M.T. Raimondi[1]

[1] *Dept. of Chemistry, Materials and Chemical Engineering "Giulio Natta", Politecnico di Milano, Milano, Italy*

Many therapeutic applications of stem cells require accurate control of their differentiation. To this purpose there is a major ongoing effort in the development of advanced culture substrates to be used as "synthetic niches" for the cells, mimicking the native ones. The goal of the project NICHOID is to use a synthetic niche cell culture model to test my revolutionary hypothesis that in stem cell differentiation, nuclear import of gene-regulating transcription factors is controlled by the stretch of the nuclear pore complexes. If verified, this idea could lead to a breakthrough in biomimetic approaches to engineering stem cell differentiation.

The NICHOID team (Fig. 1) investigates this question specifically in mesenchymal stem cells (MSC), because they are adherent and highly mechano-sensitive to architectural cues of the microenvironment. To verify my hypothesis we will use a combined experimental-computational model of mechanotransduction. We will a) scale-up an existing three-dimensional synthetic niche culture substrate, fabricated by two-photon laser polymerization (Fig. 2), b) characterize the effect of tridimensionality on the differentiation fate of MSC cultured in the niches, c) develop a multiphysics/multiscale computational model of nuclear import of transcription factors within differentially-spread cultured cells, and d) integrate the numerical predictions with experimentally-measured import of fluorescently-labelled transcription factors.

Ground-breaking nature of the research and its potential impact

The use of two-photon laser micro/nanofabrication technologies for controlling the geometry of the synthetic cell niches is very innovative and could highly impact the field of cell culture technology. Two-photon laser polymerization is the only existing microfabrication technology allowing the control of fully-3D arbitrary microarchitectures with a resolution down to 100 nm. This allows fabricating architectural features of the cell adhesion substrate (such as micro-trusses, micro-pillars etc.) at a scale able to condition the adhesion configuration of single cells. For this reason, it holds a huge potential in the field of cell bioengineering. For example, it could allow the fabrication on an industrial scale of niche-patterned culture substrates integrated in standard multi-well culture plates.

Synthetic niches hold the potential to become the culture tool to control the long-term maintenance of multipotency or to promote lineage-specific differentiation of therapeutic cells. For example, MSC from patients could be expanded in the niches with a high efficiency while maintaining their multipotency, and used for therapies. Alternatively, expanded cells could be further maintained in culture until the formation of aggregates, which could be harvested and delivered repeatedly, while cells with higher "stemness" are maintained in culture within the niche substrate.

A new research field that could be impacted by the ground-breaking nature of the synthetic niche model, is fate control of Induced Pluripotency Stem (iPS) cells. Despite the high potential of iPS to revolutionise medicine, to date there exist very few successful re-differentiation protocols towards mature phenotypes for these cells. Neurobiology is the only field where stable differentiation protocols are present. This project could produce the knowledge and a technology to direct the differentiation of iPS to lineages other than neural and potentially bring iPS to an application in the clinical field.

The synthetic niche substrate could be a valid model to study niche-dependent stem cell types, other than MSC. For example, hematopoietic stem cells would be highly useful to model leukaemia-related pathologies and to test therapeutic candidates in vitro, but these cells alter their functionality when separated from the supporting cells of their native bone marrow niche. The artificial niche substrate, conveniently seeded with supporting cells, could provide an adequate culture model for hematopoietic stem cells, and for other stem cell types with similar limitations as well.

The mechanobiological model object of the NICHOID project could also be used to study the nuclear mechanosensing responses in pathological states. If my central hypothesis will be verified, unconventional cell properties correlating the nuclear membrane structure to its permeability (including structural proteins of the cytoskeleton, of the nucleus, of the nuclear membrane, and of the nuclear pore complexes) could become crucial new targets in cancer research. Also, culture of cancer cells on the synthetic niche substrate could induce different cell spreading states reproducing physical cues of tumour regulation provided by the perivascular niche. The mechanobiological model to be developed within this project can be used to set up an unconventional "physical" model for the metastatic niche of cancer cells, to explore their switch from dormancy to metastatic growth, as a function of the mechanical environment.

ACKNOWLEDGEMENT

This project has received funding from the European Research Council (ERC) under the European Union's Horizon 2020 research and innovation programme (grant agreement No 646990 - NICHOID).

Fig. 1. The research team of the NICHOID project. From left to right: Michele Nava (bioengineer), Manuela T. Raimondi (bioengineer), Barbara Bonandrini (cell biologist), Emanuela Jacchetti (biophysicist), Marta Tunesi (bioengineer), Lucia Boeri (molecular biologist) and Alberto Garcia Gonzalez (computational mechanist).

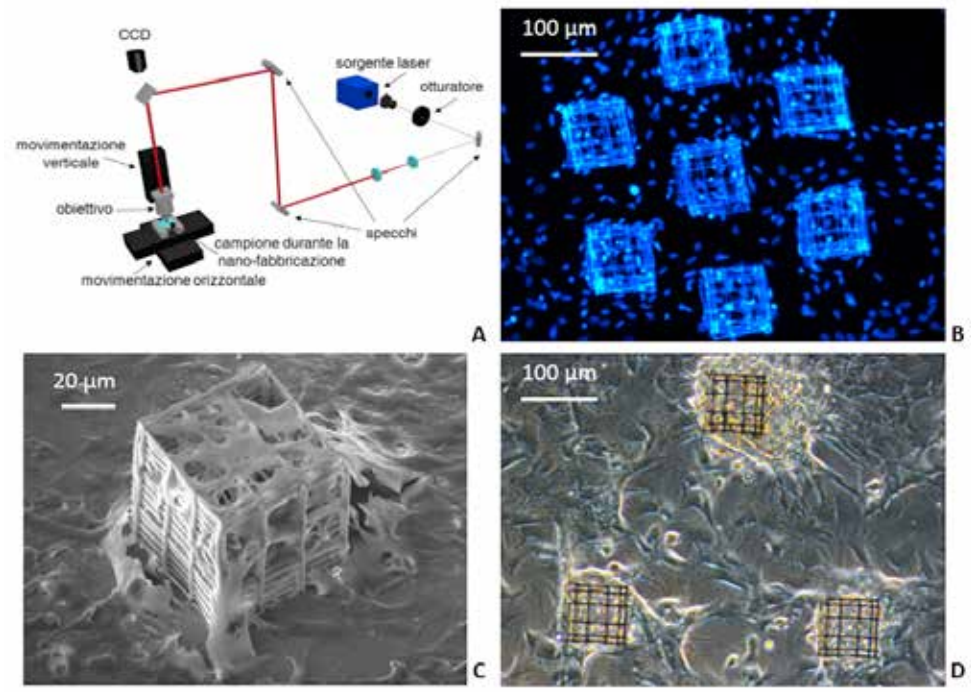

Fig. 2. A. Set-up for nanofabrication by two-photon laser polymerization. B. Nuclei of MSC cultured on the synthetic niche substrate. C. Individual "nichoid" populated by cells. D. Individual MSC colonies forming in the nichoids.

The use of animal-specific modelling to reduce, refine, and replace animal experimentation

M. Viceconti[1]

[1] *Dept. of Mechanical Engineering and Insigneo Institute for in silico Medicine, University of Sheffield*

I. INTRODUCTION

Animal experimentation plays an essential role in biological research, as it enables the direct investigation of fundamental mechanisms that would be difficult or impossible to explore *in vitro*. Animal experimentation is also used in the pre-clinical assessment of the safety and efficacy of new interventions, whether pharmaceuticals or medical devices. While the uses frequently involve the same methods and protocols there is a fundamental difference, that is frequently neglected.

In fundamental research animals are reference organisms; what we observe is true for that particular species. In the pre-clinical assessment of biomedical products, the animal experiment is a *model* of what would happen if the product was used on humans. This is a foundational difference: in the latter case there is no inherent truth content in what we observe in the animal; case by case we must demonstrate that such animal model is *predictive* of what would happen in humans under the same conditions.

Another important requirement that applies to any scientific experiment, and thus also to animal experimentation, is reproducibility. As biology become progressively more and more quantitative, the concept of reproducibility becomes more and more stringent, and the need for reproducible quantitative observations in animal experimentation becomes a paramount.

Last, the growing ethical concern associated to animal experimentation makes it indispensable to critically revise any animal experimentation to see where it is possible to reduce, refine (in the sense of reduce the associated suffering), and even replace it.

In this context we critically revised a well-established murine protocol for the pre-clinical evaluation of bone drugs. The protocol involves 14 weeks female C57BL/6J (BL6) mice; the animals are ovariectomised (OVX) under the expectation that this will produce a systemic hormonal alternation similar to that causing post-menopausal osteoporosis; a sham operation is performed on the control animals (SHAM), under the expectation that this would normalise the response with respect to the effects of surgery. Starting from four weeks after surgery some of the OVX animals are treated with the drug being tested, typically for another four weeks (OVX-INT). All animals are then culled, a long bone (typically the tibia) dissected, and from that a 1-2 mm^3 of cancellous bone are harvested from an epiphysis of each mouse. Tissue specimens are then analysed with micro-Computed Tomography (microCT), and the resulting images analysed with a 3D histomorphometry program, that provides quantifications such as Bone Volume Fraction (BV/TV), trabecular thickness, etc. These measurements are averaged across each intervention group, and then compared between groups. Normally one would expect to find higher values of BV/TV in the SHAM group, lower in the OVX group, and if the intervention works, higher in the OVX-INT group. Typically, between 10 to 50 mice are included in each group, to achieve statistical significance, due to the considerable inter-subject variability.

II. MATERIALS AND METHODS

We replicated a study to investigate the effect of Parathyroid hormone (PTH). 30 14-weeks female C57BL/6J (BL6) mice were randomly divided in five groups; to the three standard groups described above (SHAM, OVX, OVX-PTH) we added a fourth where the animals were not operated, left wild type (WT), and fifth where these WT animals were treated (WT-PTH). Using and *in vivo* microCT system (Scanco Viva-80), we examined the whole tibia of each animal once per week form the age of 14 weeks, to that of 22 weeks. On each microCT we performed a quantification of the Bone Mineral Content (BMC) over 40 anatomical compartments, sot map the BMC changes in each animal over time and across the whole tibia.

III. RESULTS

BMC quantifications over the 40 anatomical compartments were found much more reproducible than the conventional BV/TV quantifications. Power calculations suggest that this new method could reduce of 60% the number of animals involved in each study. The accurate and reproducible mapping of BMC over time and anatomical space made possible to show that the SHAM procedure produces changes in BMC over time and space that are not significantly different from those observed in WT mice; similarly, the only significant difference between SHAM and OVX was found in the most proximal region, below the growth plate. WT+PTH data showed for the first time how the PTH produce its anabolic effect, first affecting the most proximal regions near the growth plate, and then over time producing an increase in BMC also in the most distal regions.

IV. CONCLUSION

An accurate and reproducible quantification of BMC over space and time showed that SHAM surgery is, in this particular animal model, unnecessary; it also questioned the efficacy of OVX to provide a credible model for osteoporosis as observed in humans.

ABSTRACT
GNB

BIOIMMAGINI

High Frequency Ultrasound-guided procedures for the three *Rs* concept application.

L. Auletta[1], A. Greco[2–4], S. Albanese[2,3], P. Mirabelli[1], A. Zannetti[4], C. D'Alterio[5], G. Di Maro[1], F. M. Orlandella[1], G. Salvatore[1,3,6], A. Soricelli[1,6] and M. Salvatore[1]

[1] *IRCCS SDN, Napoli, Italy.*
[2] *Department of Advanced Biomedical Science, University of Napoli Federico II, Napoli, Italy.*
[3] *CEINGE Biotecnologie Avanzate, Napoli, Italy.*
[4] *Institute of Biostructures and Bioimaging, CNR, Napoli, Italy.*
[5] *National Cancer Institute, "Fondazione G. Pascale" IRCCS, Napoli, Italy.*
[6] *Department of Motor Science and Wellness, University Parthenope, Napoli, Italy.*

***Abstract*—The aim of this study was to generate a novel orthotopic mouse model of human follicular thyroid carcinoma using a High Frequency Ultrasound-guided injection system. Since the "three Rs" concept is gaining much more importance in all experimental animal models, our effort was targeted to reduce the number of animals needed in each experiment without lowering the statistical power of the recorded data. Preclinical imaging is an invaluable aid in this perspective, allowing longitudinal studies and to reduce the number of animals necessary to gain scientific results. On the other hand, instruments implementation, both on the hardware and software point of view, need to be as fast as researchers' demands. We describes the development of a HFUS-guided orthotopic injection procedure of Thyroid Carcinoma cells in the murine thyroid, in place of the much more invasive surgical technique.**

***Keywords*—HFUS, mouse models, technological progress, three *Rs*.**

I. Introduction

Thyroid carcinoma is the most common endocrine malignancy, with an increasing incidence worldwide [1]–[3]. In recent years, considerable efforts have been made to develop genetically engineered, xenograft and orthotopic mouse models of thyroid carcinoma in order to study the drugs effectiveness [3]–[5]. Orthotopic tumor models are more cumbersome to develop, but they allow cell growth directly in the organ of origin and can recapitulate metastatic behavior with sufficient penetrance and reproducibility [6]–[11].

High-frequency ultrasound (HFUS) is widely employed as a non-invasive method for imaging anatomic structures in mouse models of disease [12]–[15]. HFUS has the ability to detect structures as small as 30 lm, which is a property that has been exploited for thyroid visualization and analysis in mice [16].

The three *Rs* concept is gaining importance in all animals' experimental models. In this perspective our efforts are aimed to reduce both the number of animals and the discomfort level felt by the animals. Hence, this work describes the development of a HFUS-guided orthotopic injection procedure of different Thyroid Carcinoma cell lines in the murine thyroid, in place of the much more invasive surgical orthotopic injection.

II. Materials and Methods

The animal protocols used in this work were evaluated and approved by the Animal Use and Ethic Committee (OPBA) of CEINGE, Biotecnologie Avanzate (Naples, Italy; Protocol 15/2/14_n 3). All of the procedures described here were performed under general anesthesia with isoflurane in oxygen (induction phase: isoflurane 4% in oxygen 0.8 L/min; maintenance phase: isoflurane 2% in oxygen 0.8 L/min).

HFUS equipment, specifically Vevo 2100 (VisualSonics Inc., Toronto, Canada), with a multifrequency (22–55 MHz) probe (MicroScan® MS550D, VisualSonics Inc.) was used in all procedures. Each mouse (n = 20) was positioned in dorsal recumbency on the handling table of the Vevo imaging station (Vevo Integrated Rail System III; VisualSonics Inc.), and a thick pad of warm gel was placed over the ventral aspect of the neck to provide a coupling medium for the transducer.

Once the thyroid gland was identified in the transverse plane, the syringe, which was mounted on the injection mount of the Vevo Rail System, was slowly advanced until the needle tip entered the field of view, and its position was adjusted using the micro-manipulation mechanical controller. The needle was further advanced using the micromanipulation controls until the tip was within the thyroidal parenchyma; at this point, the cells were gently injected. Mice were left to recover from anesthesia.

III. Discussion

Having a reliable and reproducible animal model of thyroid cancer is an important step in the testing and development of novel therapeutics. Transgenic models are valid systems for preclinical tests to evaluate the feasibility, efficacy, and safety of new therapies against thyroid cancer, but one obstacle is the high costs related to transgenic mice compared with orthotopic models [17]. Furthermore, the development of new drugs often requires a high number of animals for testing [18]. Orthotopic models of thyroid cancer are an important tool in developing novel therapeutics because they more closely reflect the biological and morphological

features of cancer growth and metastasis in humans, and they will better predict potential clinical activity [6], [11].

Considering the "three *Rs*" concept, and the growing empathy and ethical doubts of the public opinion on experimental animals, researchers are directing their efforts in experimental designs and settings able to minimize the number of animals in each experimental procedure. In this perspective, preclinical imaging procedures allow longitudinal studies, which consent an excellent statistical power lowering the number of animals needed for each experiment, without the necessity to execute hystology at different time points.

In conclusion, we have shown that it is possible to induce an orthotopic model of thyroid cancer. This was possible thanks to the advancement of technology and to the efforts of researchers aimed at finding less invasive methods that optimize scientific results. Collaboration between physicists, engineers, chemists, biologists and veterinary doctors is paramount to accelerate and direct the hardware, software and technological implementations. Further investigations will be done to evaluate the reproducibility and repeatability of our methods and to translate it to other animal models of human cancer.

ACKNOWLEDGEMENT

This work was supported by grants from RRC-2014-2354542 Ricerca Corrente and GR-2010–2314003 Italian Ministry of Health. Part of the procedures and data reported in this abstract have been already published on "Thyroid" 2016;26(4):552-8.

REFERENCES

[1] National Cancer Institute 2015 SEER cancer statistics review, 1975–2012. Available at: http://seer.cancer.gov/csr/1975_2012/ (accessed September 2015).

[2] Y. Ito, Y. E. Nikiforov, M. Schlumberger and R. Vigneri "Increasing incidence of thyroid cancer: controversies explored", Nat Rev Endocrinol 2013, *9*, pp. 178–84.

[3] L. S. Kirschner, Z. Qamri, S. Kari and A. Ashtekar "Mouse models of thyroid cancer: a 2015 update", Mol Cell Endocrinol 2016, *421*, pp. 18–27.

[4] P. Pallante, R. Visone, C. M. Croce and A. Fusco "Deregulation of microRNA expression in follicular cell-derived human thyroid carcinomas. Endocr Relat Cancer 2010, *17*, pp. F91–F104.

[5] S. Kim, Y.-W. Park, B. A. Schiff, D. D. Doan, Y. Yazici, S. A. Jasser, M. Younes, M. Mandal, B. N. Bekele and J. N. Myers "An orthotopic model of anaplastic thyroid carcinoma in athymic nude mice", Clin Cancer Res 2005, *11*, pp. 1713–21.

[6] C. Nucera, M. A. Nehs, M. Mekel, X. Zhang, R. Hodin, J. Lawler, V. Nose and S. Parangi "A novel orthotopic mouse model of human anaplastic thyroid carcinoma", Thyroid 2009,*19*, pp. 1077–84.

[7] J. J. Killion, R. Radinsky and I. J. Fidler "Orthotopic models are necessary to predict therapy of transplantable tumors in mice", Cancer Metastasis Rev 1998, *17*, pp. 279–84.

[8] B. A. Teicher "Tumor models for efficacy determination", Mol Cancer Ther 2006, 5, pp. 2435–43.

[9] S. Kim "Animal models of cancer in the head and neck region", Clin Exp Otorhinolar 2009, 2, pp. 55–60.

[10] S. Song, D. Chang, Y. Cui, J. Hu, M. Gong, K. Ma, F. Ding, Z.-H. Liu and T.-Y. Wang "New orthotopic implantation model of human esophageal squamous cell carcinoma in athymic nude mice", Thorac Cancer 2014, *5*, 417–24.

[11] Z. A. Antonello and C. Nucera "Orthotopic mouse models for the preclinical and translational study of targeted therapies against metastatic human thyroid carcinoma with BRAF V600E or wild-type BRAF", Oncogene 2014, 33, 5397–404.

[12] S. Horie, R. Chen, L. Li, S. Mori and T. Kodama "Contrast enhanced high-frequency ultrasound imaging of early stage liver metastasis in a preclinical mouse model", Cancer Lett 2013, 339, 208–13.

[13] A. Bhan, A. Sirker, J. Zhang, A. Protti, N. Catibog, W. Driver, R. Botnar, M. J. Monaghan and A. M. Shah "High-frequency speckle tracking echocardiography in the assessment of left ventricular function and remodeling after murine myocardial infarction", Am J Physiol Heart Circ Physiol 2014, 306, H1371–83.

[14] E. L. Walk, S. McLaughlin, J. Coad and S. A. Weed "Use of high frequency ultrasound to monitor cervical lymph node alterations in mice", PLoS One 2014, *9*, e100185.

[15] A. Greco, A. R. D. Coda, S. Albanese, M. Ragucci, R. Liuzzi, Auletta L., S. Gargiulo, F. Lamagna, M. Salvatore and M. Mancini "High-frequency ultrasound for the study of early mouse embryonic cardiovascular system", Reprod Sci 2015, 22, pp. 1649–55.

[16] M. Mancini, E. Vergara, G. Salvatore, A. Greco, G. Troncone, A. Affuso, R. Liuzzi, P. Salerno, M. Scotto di Santolo, M. Santoro, A. Brunetti and M. Salvatore "Morphological ultrasound microimaging of thyroid in living mice", Endocrinology 2009, 150, pp. 4810–5.

[17] C. Schmutzle, C. Hoang-Vu, B. Ruger and J. Kohrle "Human thyroid carcinoma cell lines show different retinoic acid receptor repertoires and retinoid responses", Eur J Endocrinol 2004, 150, 547–56.

[18] X.-G. Zhu and S.-Y. Cheng "Modeling thyroid cancer in the mouse", Horm Metab Res 2009, 41, 488–499.

Fig. 1. HFUS-guided injection. Real time HFUS image of the FTC cells injection in the right thyroid lobe. On the left, the oblique hyperechoic line is the needle in the ultrasonographic field of view. On the right a dimension scale in millimeters.

Visual-like classification of lung tumour heterogeneity in DCE-CT sequences

S. Baiocco[1], D. Barone[2], G. Gavelli[2] and A. Bevilacqua[1,3]
[1] *Advanced Research Centre on Electronic Systems(ARCES), University of Bologna, Bologna, Italy*
[2] *Radiology Unit, IRCCS - Istituto Scientifico Romagnolo per lo Studio e la Cura dei Tumori (IRST), Meldola (FC), Italy*
[3] *Dept. of Computer Science and Engineering (DISI), University of Bologna, Bologna, Italy*

***Abstract*—Visual analysis still represents the gold-standard for CT image interpretation, conveying crucial information regarding the diagnosis and prognosis of lung cancer.**

This work presents the first automatic approach to quantify and classify the lung tumour heterogeneity based on dynamic contrast enhanced-CT (DCE-CT) image sequences, so as it is performed through visual analysis by expert.

***Keywords*—Image processing, heterogeneity, quantitative imaging, oncology.**

I. Introduction

In the oncologic field, tumour heterogeneity involves multiple levels, ranging from genetic to phenotypic variations [1], the latter being often investigated through medical imaging devices, CT included [2]. Visual assessment with CT modalities represents the basis for the analysis of tumour heterogeneity [3], which is an important prognostic factor, strongly associated with tumour malignancy [4].

The upgrade of CT technology, both in terms of number of detectors and gantry rotation speed, made these devices also suitable for functional analyses [5]. Dynamic contrast enhanced-CT (DCE-CT) yields functional maps [6] whose heterogeneity degree is primarily evaluated through visual assessment [7].

This work, the first in DCE-CT, presents an automatic methodological approach to classify the intra-tumour spatial (morphological) heterogeneity present in NSCLC lesions as performed by expert radiologists through visual analysis. In the age of personalized medicine, a non-invasive and automatic method to assess tumour heterogeneity can yield a clinical benefit.

II. Materials and Methods

A. DCE-CT protocol and image acquisition

37 datasets referring to 13 patients with NSCLC (age range 36-81 years) were considered. Each patient underwent axial DCE-CT, performed on a 256-slice CT system. This study was approved by the medical ethics committee.

An initial low-dose, unenhanced full-body CT scan is performed to identify the target lesions. For each lesion, regions of interest (ROIs) are manually outlined by the radiologists in those slices where the clinical features are considered as being the most representative ones (the so-called "reference" slices).

Then, soon after administering 50 mL of contrast agent at 5 mL/s, the same volume section (55 mm of z-coverage, 11 slices) is repeatedly scanned over time for 25 s at 0.8 Hz (80 kV, 250 mA) and the voxel-based tissue time-concentration curves (TCCs) signals (in Hounsfield Units, HU) of the reference slices are generated. In practice, the TCC of each voxel is represented by the collection of 20 attenuation values of the discrete temporal signal representing the dynamic evolution of the tracer in that voxel.

B. Heterogeneity taxonomy

At present, there is not any ground truth reported in the literature as a visual reference for the morphological heterogeneity degrees of lung tumour tissues. The evaluation of the heterogeneity is still left to the subjectivity of radiologist's assessment.

Nevertheless, assessing the heterogeneity in an objective manner represents the first step of any subsequent automatic image analysis procedure. To this purpose, a proper heterogeneity taxonomy was defined in agreement by two 25-year experienced readers, based on a 3-point scale:

- homogeneous pattern (Type 1), where the lesion tissue does not present heterogeneous regions;
- micro-inhomogeneous pattern (Type 2), where regions with different point densities are homogeneously distributed over the entire lesion;
- macro-inhomogeneous pattern (Type 3), characterised by the presence of one or more homogeneous regions, markedly different from the background (generally represented by low-density necrotic regions).

C. Spatio-temporal indexes

The two indexes we conceived are computed on the DCE-CT sequences for each reference slice by studying, for each ROI, the TCCs group properties within local windows $W(x,y)$ of size $w \times w$, centred on the slice coordinate (x,y), whose values in the image domain are denoted by Ω_W.

Let $\sigma(\Omega_W(m))$ be the *spatial* standard deviation of the TCC values assumed in $W(x,y)$, at the generic time sample t_m. The following indexes have been analysed on the whole sequence of the reference slice:

- MS, the *temporal* mean value of $\sigma(\Omega_W(m))$ values; MS was conceived to provide an estimate of temporal persistence of local spatial homogeneity;
- SS, the *temporal* standard deviation of $\sigma(\Omega_W(m))$ values; SS quantifies the temporal stability of local texture.

D. Single-feature analysis

MS and SS represent the first two feature considered for heterogeneity analysis. As regards MS, low values point out regions that keep locally homogeneous over time, while high values highlight voxels belonging to a heterogeneous tissue, characterised by a constant or a variable enhancement. Instead, SS shows low values when the local spatial

distribution of the contrast agent has a time steady dispersion, that is the TCCs' family is characterised by a temporal coherence of spatial properties of tissue, whether it is homogeneous or heterogeneous one. High SS values may occur when voxels belonging to different structures fall into the same window *W*, for instance, in case of a not negligible motion, or when the local enhancement changes dynamically, as in presence of blood vessels.

The outcome of each index was also represented by means of colorimetric maps as shown in Fig. 1.

E. Multi-feature analysis

The joint behaviour of the single indexes was explored by 2D feature analysis, implemented through unsupervised classification. *k*-means clustering algorithm was used to find out $k=4$ groups of voxels, with similar SS and MS behaviour. As shown in Fig. 2 (left), results are also given using a colorimetric cluster mask, CM, representing the third feature.

III. Assessment of results

A. Generation of ground truth

For each examination, two experienced radiologists visually scored the most representative slices using the heterogeneity degree previously defined. After that, they detected and outlined the heterogeneity regions represented by anatomical structures and physics-based artefacts too.

Usually, vessels and bronchi are well identifiable, as reported at left in Fig. 1 e Fig. 3, while detecting artefacts and necrotic regions is much harder and, even when succeeding, both boundaries and extent are detected with poor accuracy.

B. Visual analysis

A similar analysis was performed for the colour maps of the indexes we conceived. In this case, the regions on the maps which appear spatially semantically coherent were manually bounded and outlined, while for the colour masks, resulting from the clustering of the spatio-temporal indexes, the regions with uniform colours were directly considered.

Then, each map and each mask was assigned a visual score with the same 3-point scale previously used.

At the beginning, we hypothesised to perform an automatic matching between manual and computed ROIs. However, because of the uncertainty in delineating necrotic regions and artefacts, the matching of these regions was performed visually, by considering a "hit" when the ROIs of ground truth and those of features at least partially overlap.

IV. Results

In order to assess the performance of SS, MS and CM, a multiple binary classification test according to the *one-vs.-all* strategy was carried out. The capability of a single feature to discriminate one class from the remaining ones is assessed through using the well-known 2×2 contingency table and analysed in terms of sensitivity (SE) and specificity (SP).

SS results extremely specific for the three types of heterogeneity, producing the best results for Type 1 (SP=93%) and Type 3 (SP=90%), and also resulting highly sensitive (SE≥75%). In particular, in terms of sensitivity it produces the best results for Type 2 (SE=86%).

MS is highly specific for Type 2, but it is not sensitive enough. On the contrary, it produces good results in terms of sensitivity and specificity, for Type 1, while it results quite specific, but not sensitive enough, for Type 3.

CM returns the same good results as MS for Type 1. As regards Type 3, it results less specific than the other features and more sensitive than MS, showing in this case the same result as SS. As for Type 2, it shows the highest specificity values among these features (SP=97%), but it results to be poorly sensitive, similarly to MS and differently from SS.

Therefore, MS is a useful index, which can be used as a support to reinforce the results of SS through the construction of CM. Meanwhile, SS alone appears to be effective in recognising these three types of heterogeneities, even the most indefinite micro-inhomogeneous tissue.

V. Conclusion

As expected Type 1, because of its intrinsic homogeneity, is simpler to be identified by all the features. Type 2 is better identified by SS, which results more sensitive to highlight different structural inhomogeneities, showing high values when the local range of HUs is not preserved over time. In addition, MS and CM fail to detect the heterogeneity belonging to this type, which is identified with the greatest uncertainty even by the radiologists themselves. As far as Type 3 is concerned, it is better identified by SS and CM.

Usually, bronchi, blood vessels and haemorrhages are perfectly reproduced by the colorimetric maps of all features, while the hypodense necrotic regions outlined by radiologists have a weak correspondence with our feature's regions. Nonetheless, it is worth noting that the extent of these regions cannot be clearly outlined even by radiologists (Fig. 4).

This is the first work using sequences of DCE-CT to assess the morphological heterogeneity of lung tumours. The indices computed on the TCC signals proved to be effective to describe and measure the heterogeneity features visually detected by radiologists. Indeed, the approach developed permits an automatic classification of heterogeneities, with a high certainty degree (minimum $SP \geq 0.90$) for all types, with a good sensitivity (minimum $SE \geq 0.75$).

The main advantages of our approach include the introduction of objectivity in a crucial visual assessment task to assist radiologists in daily clinical activities and the possibility to exploit heterogeneity information within an automatic software pipeline.

References

[1] P. Lambin, *et al*., "Radiomics: extracting more information from medical images using advanced feature analysis.", *Eur. J. Cancer*, (2012) 48(4):441-446.

[2] C. Yip, *et al*., "Primary esophageal cancer: heterogeneity as potential prognostic biomarker in patients treated with definitive chemotherapy and radiation therapy.", *Radiology*, (2014) 270(1):141-148.

[3] B. Ganeshan, and K. A. Miles, "Quantifying tumour heterogeneity with CT.", *Cancer Imaging*, (2013) 13(1):140–149.

[4] F. Ng, *et al*.,"Assessment of tumor heterogeneity by CT texture analysis: can the largest cross-sectional area be used as an alternative to whole tumor analysis?.", *Eur. J. Radiol*., (2013) 82(2):342-348.

[5] A. Bevilacqua, D. Barone, S. Malavasi, and G. Gavelli, "Quantitative assessment of effects of motion compensation for liver and lung tumors in CT perfusion.", *Acad. Radiol.*, (2014) 21(11):1416-1426.

[6] R. García-Figueiras, *et al*., "CT perfusion in oncologic imaging: a useful tool?", *Am. J. Roentgenol*., (2013) 200(1):8-19.

[7] X. Yang, and M. V. Knopp., "Quantifying tumor vascular heterogeneity with dynamic contrast-enhanced magnetic resonance imaging: a review.", *Biomed Res. Int*., (2011) 2011.

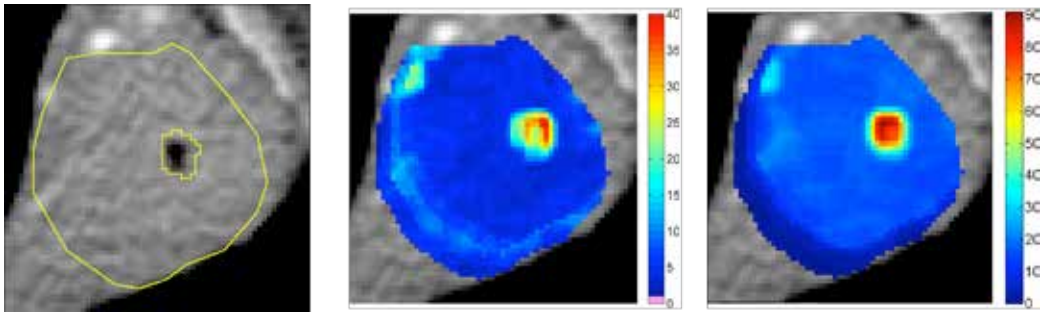

Fig. 1. Ground truth (left), colorimetric maps of SS (middle) and MS (right).

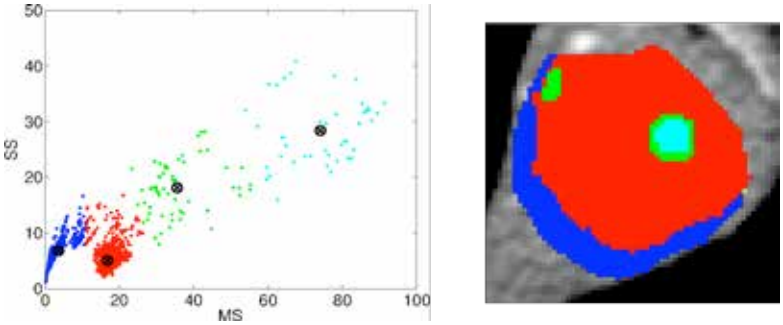

Fig. 2. MS–SS scatter plot (left) and its respective clusters mask (right). Data have been partitioned into four clusters, mapped by the red, blue, green and cyan colours, respectively.

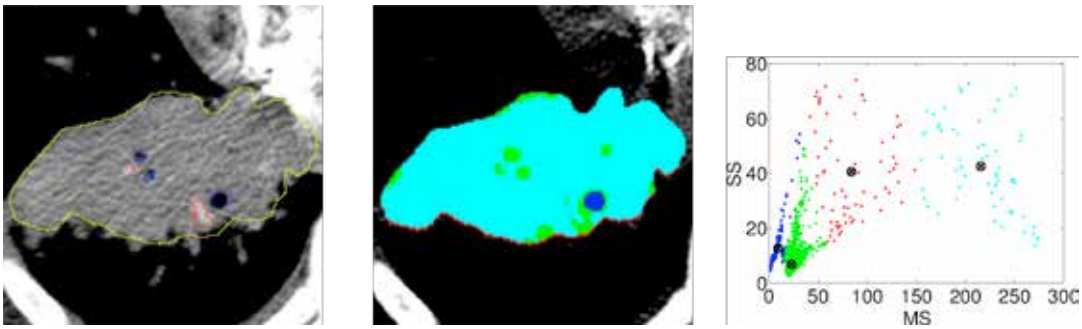

Fig. 3. Ground truth (left), colour mask of CM (middle), MS-SS scatter plot (right).

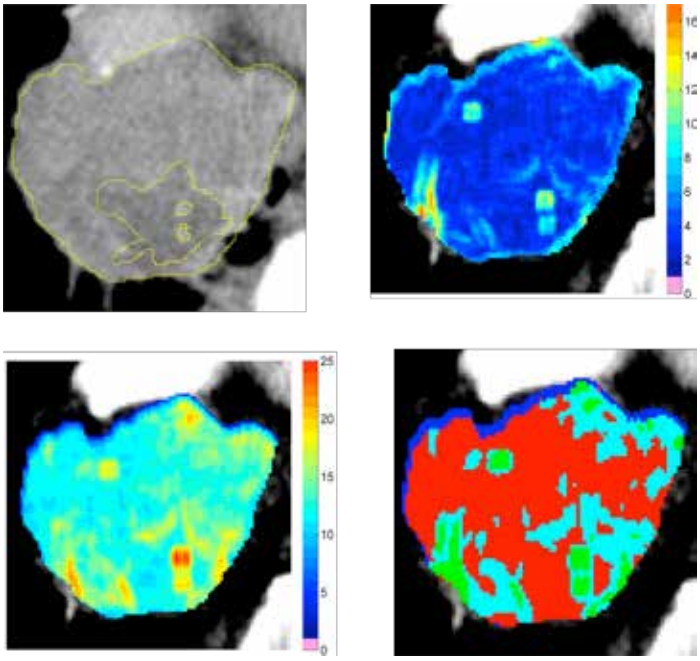

Fig. 4. Ground truth (top left), colorimetric map of SS (top right), colorimetric map of MS (bottom left), colour mask of CM (bottom right).

Tracing single neurons from mice cerebellum clarified tissue

A. L. Callara[1], C. Magliaro[2], V. Positano[3], N. Vanello[1], and A. Ahluwalia[2]
[1] *Dipartimento di Ingegneria dell'Informazione, Università di Pisa, IT*
[2] *Research Centre "E. Piaggio", University of Pisa, IT*
[3] *Fondazione CNR Regione Toscana 'G. Monasterio', Pisa, IT*

***Abstract*—Imaging neural structures in their native 3D arrangement may help our understanding of brain, since several studies available in the literature confirm the close relationship between cerebral architecture and function.**

To this end, a new workflow is designed to obtain faithful information on the 3D structure of neurons from L7GFP mice brain slices treated with CLARITY2 protocol. CLARITY-treated tissues are optically transparent and compatible with most of the classical microscopy techniques. A Smart Region Growing algorithm based on local features of the image intensity value histogram was then developed. The algorithm was tested on confocal datasets of Purkinje cells (PCs) from L7GFP clarified mice cerebellum. Single PCs were identified and isolated within their 3D environment. Preliminary results on neural morphology, such as the planar development of such cells are in agreement with previous knowledge available in the literature. The validation of the algorithm is then discussed.

***Keywords*—CLARITY, confocal imaging, 3D segmentation.**

I. Introduction

NEURONAL morphology and connectivity are the drivers of higher level brain function. Thus targeted investigations on neuronal morphometry might help unravel the link between cell morphology and neurologic diseases [1]. To unravel the neuronal structure-function relationship, it is necessary to study intact neurons within their native three-dimensional environment. Although confocal microscopy can be used to image tissues in 3D, light scattering and absorption limit the usefulness of this approach. Recently, optical clearing methods have been developed to overcome these limiting factors. The recently reported CLARITY method [2] is one of the most suitable approaches to generate transparent tissues, while preserving native structure. Moreover, CLARITY-treated tissues are compatible with classic fluorescence microscopy techniques. However, even when dealing with clarified tissues, 3D neuronal segmentation still represents a formidable challenge. Datasets, algorithms and algorithm-validation remain open issues within the context of 3D tracing.

Here, we propose an approach to isolate single neurons in their native environment from single photon confocal datasets from tissues treated with the CLARITY method. This approach is based on a region growing procedure that takes into account both local properties of signal intensity. Tissue treatment, image acquisition, image pre-processing and 3D neuron segmentation are described to define a workflow for 3D feature extraction. Preliminary results of the algorithm applied on confocal datasets of Purkinje cells (PCs) from L7GFP clarified mice cerebellum are reported.

II. Theoretical background

A. Confocal image acquisition characteristics and limitation

Two different sources of signal variability can be found in single photon confocal microscopy images. The first is related to light attenuation across the sample, and results in different image intensity at different depths in the sample (Fig. 1). In fact, the light emitted from the target falls off through the sample according to the Lambert-Beer's law (1).

$$I(z) = I_0 e^{-k_\lambda z} \quad (1)$$

Where I_0 is the initial light intensity, k_λ is the attenuation coefficient at the specific wavelength λ and z is the thickness of the specimen [3].

Another source of signal variability is related to the non-uniform distribution of fluorescent cells throughout the sample, which adds in-plane differences to the signal (Fig. 2).

B. Region growing approaches for neuron segmentation

Region growing algorithms are simple region-based image segmentation methods. These methods are used to separate regions with similar characteristics within images following two fundamental principles: the selection of a seed and the definition of a homogeneity predicate. The basic idea is to grow a region starting from a "seed" pixel or voxel and labeling each neighbor pixel of a Region of Interest according to similarity criteria. The process is iterated until there are no more labelable pixels. The homogeneity criterion can be based on similarity or discontinuity measures. The robustness of seed-based techniques is general affected by the signal intensity and presence of noise. However, these approaches are computationally efficient, thus encouraging researchers to develop techniques to overcome the above mentioned difficulties [4]. When it is necessary to handle images with intensity inhomogeneity, as those coming from confocal imaging, region growing schemes based on local features of the histogram represent a robust approach to segmentation. These methods are based on model fitting procedures which describe local image intensities with Gaussian distributions with different means and variances [5].

III. Methods

A. Tissue treatment and image acquisition

L7GFP mice were obtained from the laboratory of Farmacologia e Tossicologia, Facoltà di Medicina, University of Pisa, Italy. The experiments were conducted in conformity with the European Communities Council Directive of 24 November 1986 (86/609/EEC and 2010/63/UE) and in

agreement with the Italian DM26/14. Experiments were approved by the Italian Ministry of Health and Ethical Committee of the University of Pisa. Murine brain was treated according to the CLARITY2 protocol [6]. Mice cerebellum was cut into 1 mm thick slices with a LEICA VT1200S Vibratome. Hydrogel-embedded slices were kept in the CLARITY clearing solution at 37 °C for 5 days to be clarified. Image stacks from clarified slices were acquired using a Nikon A1 confocal microscope. Acquisition settings are shown in Table 1.

B. Image pre-processing

Confocal image stacks were filtered with a 3x3x3 pixel sized median filter in order to reduce noise and spikes. Then, an interpolation to cubic voxels was performed. All pre-processing steps were implemented within Matlab [7].

C. Smart region growing algorithm (SmRG algorithm)

Confocal datasets from fluorescent specimens are characterised by a great spatial variability in terms of pixel intensity. One approach for facing this issue is the use of a locally adaptive thresholding for the segmentation of neural structures. In this work, a local histogram-based region growing algorithm was developed. The background and neuronal tissue-related signals show a bimodal intensity distribution. Specifically, the background signal is characterized by a unimodal distribution with lower signal intensity with respect to neuronal tissue. The intensity distribution of neuronal tissue signal shows a higher dispersion with respect to the background distribution. Moreover, the samples we analyzed showed a quite flat signal distribution characterized by a low peak. For this reason, the use of model fitting procedures as Gaussian mixture models is not feasible. We propose to determine a local threshold to distinguish background and neuronal tissues looking at the derivative of the intensity histogram. Specifically, a histogram-knee is defined as the first minimum of the histogram, after the first histogram peak. The histogram-knee is estimated locally on a 16x16x16 pixel^3 sub-volume. The histogram-knee separates the two classes of pixels within the image, neuron and background, and therefore represents the homogeneity predicate for the region growing procedure. If a pixel lies on the left of the knee it will considered as a background pixel, while if it does not it will belong to the neuron pixels. The region growing process starts by selecting a pixel belonging to a particular soma. A cubic sub-volume is centered around the selected initial seed and the histogram-knee calculation is done. At this point the 26 neighbor pixels of the seed are classified as background or neuronal tissue. This procedure is repeated for each new pixel belonging to the neuronal tissue if a condition of distance is met. Specifically, the knee value is calculated if the distance from the pixel of the last knee-estimation is bigger than 5 pixels (3μm). The region growing process ends when there are no more pixels which satisfy the previous conditions. The entire work-flow of the PCs tracing in described in Fig. 4.

IV. Results and Discussion

A. PCs tracing

Confocal datasets of CLARITY-treated L7GFP mice cerebellum were analyzed in order to isolate single PCs. The proposed approach allowed the isolation of single neurons, although in some cases two or more neurons were merged.

Interestingly, the segmented PCs showed a planar distribution of the dendritic tree as described in the literature [1].

An objective validation of the proposed approach is still lacking. Specifically, it was not possible to validate our results against other standard tools as the Vaa3d and Tree2Tree that have been suggested as a ground truth for neuron segmentation. In fact, the latter approaches did not provide acceptable results on our CLARITY-treated tissues. Other approaches will be pursued in the future such as those based on manual segmentation by experts, although this operation cannot be easily performed given the high dendrites density. In this work, we checked the segmentation quality at the soma's level. The radii of different somas, from the original and segmented images, were estimated with a Matlab command implementing the Hough's transform. No statistically significant differences were found between the two sets of radii (Fig. 5).

V. Conclusion

The aim of this work was to define an innovative method to study neuron morphology in their native 3D arrangement. The use of tissue clearing techniques was integrated with image processing algorithms to trace single Purkinje neurons from 3D confocal image stacks of clarified mice cerebellum. In order to study the morphology of single PCs from the acquired images, a Smart-Region-Growing algorithm based on local features of the histogram was developed within the Matlab environment. Preliminary results showed that the SmRG algorithm can isolate single neurons with their characteristic planar structure. Future developments will pursue an objective validation of the algorithm.

The approach described here may be helpful for the study of those neurologic diseases which involve neurons at the morphologic level, such as Parkinson's, Alzheimer and Autism [8]. This should be possible analysing morphological features from segmented neurons.

References

[1] Dunn, E. M., Schilling, K. & Mugnaini, E. Development and fine structure of murine Purkinje cells in dissociated cerebellar cultures: dendritic differentiation, synaptic maturation, and formation of cell-class specific features. Anat. Embryol. (Berl). 197, 31–50

[2] Chung, K. & Deisseroth, K. CLARITY for mapping the nervous system. Nat. Methods 10, 508–13 (2013).

[3] Guan, Y. Q., Cai, Y. Y., Zhang, X., Lee, Y. T. & Opas, M. Adaptive correction technique for 3D reconstruction of fluorescence microscopy images. Microsc. Res. Tech. 71, 146–157 (2008).

[4] Mukherjee, S., Condron, B. & Acton, S. T. Chasing the neurome: segmentation and comparison of neurons. (2013)

[5] Wang, L., He, L., Mishra, A. & Li, C. Active contours driven by local Gaussian distribution fitting energy. Signal Processing 89, 2435–2447 (2009).

[6] Poguzhelskaya, E., Artamonov, D., Bolshakova, A., Vlasova, O. & Bezprozvanny, I. Simplified method to perform CLARITY imaging. Mol. Neurodegener. 9, 19 (2014).

[7] MATLAB 8.1, The MathWorks, Inc., Natick, Massachusetts, United States.

[8] Becker, E. B. E. & Stoodley, C. J. Autism spectrum disorder and the cerebellum. International Review of Neurobiology 113, (Elsevier Inc., 2013).

TABLE I
CONFOCAL ACQUISITION SETTINGS

Parameter	*Value*	*Units*
Magnitude	40x	
Grid	512x512	pixel
Pixel Size	0.62	µm/pixel
Laser Power	4.84	pW
Emission wavelength	488	nm
Excitation wavelength	502	nm
z-Step	1.2	µm

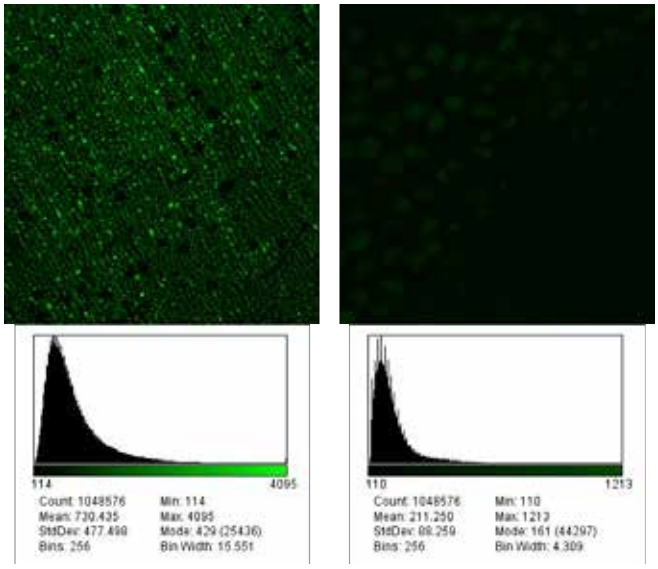

Fig. 1. Example of intensity variability. Confocal image and relative histogram for z = 0 (left) and z = 100um (right).

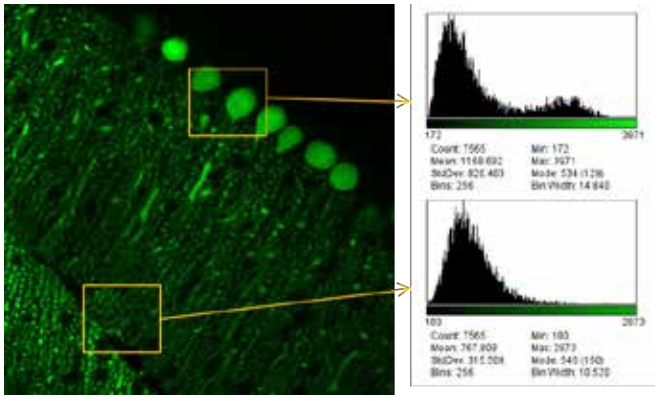

Fig. 2. In-plane signal differences due to biological variability.

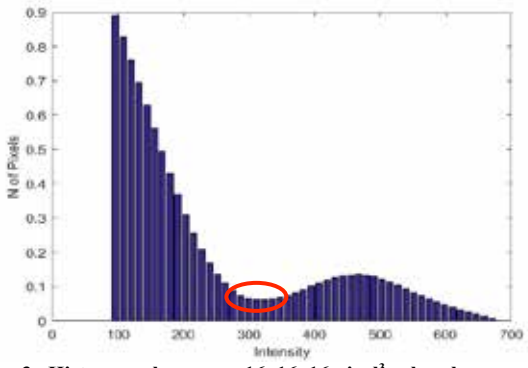

Fig. 3. Histogram-knee on a 16x16x16 pixel^3 sub-volume.

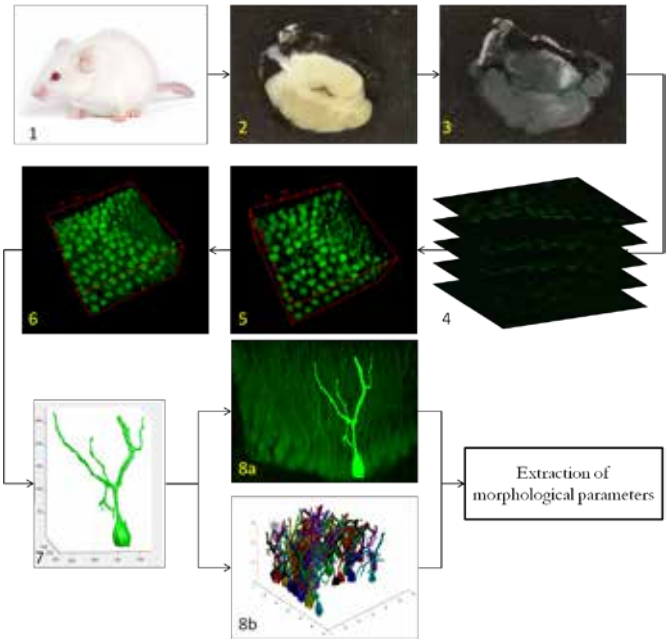

Fig. 4. Workflow. Mice (1) are treated in order to obtain cerebellum hydrogel-embedded slices (2). Slices are clarified (3). At the 5th day of clarification confocal stacks are acquired (4). 3D reconstruction of stacks (5) and pre-processing steps are applied (6). The SmRG algorithm is run (7) and a visual check of segmented structures is done both in ImageJ (8a) and in Matlab (8b). Morphological parameters are extracted.

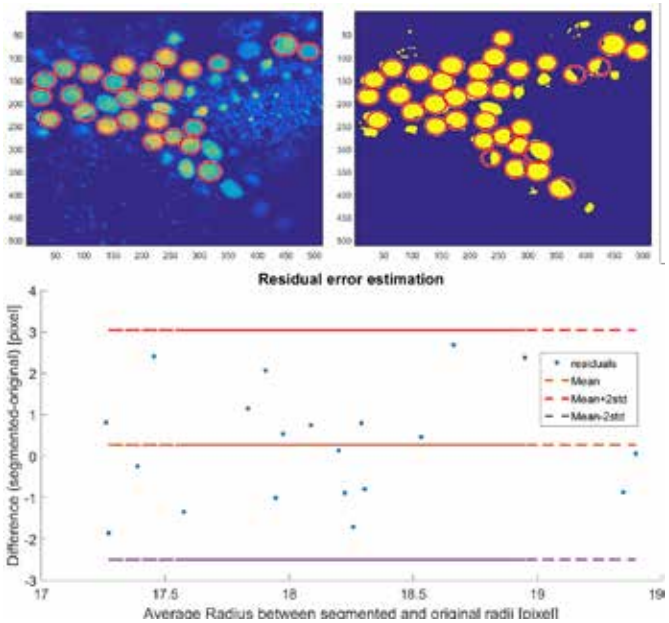

Fig. 5. Residual error estimation for n = 20 somas. The residuals are the difference between soma radii in the original image and soma radii in the segmented image. Maximum percentage error = 14%.

Predicting cognitive performance in MCI patients with small vessel disease using diffusion MRI

S. Ciulli[1,2,3], E. Salvadori[4], R. Valenti[4], A. Poggesi[4], D. Inzitari[4], M. Mascalchi[1], N. Toschi[3,5,6], L. Pantoni[4] and S. Diciotti[7]

[1] *Department of Clinical and Experimental Biomedical Sciences, University of Florence, Florence, Italy*
[2] *School of computer science and electronic engineering, University of Essex, Colchester, UK*
[3] *Medical Physics Section, Department of Biomedicine and Prevention, University of Rome "Tor Vergata", Rome, Italy*
[4] *Department NEUROFARBA, University of Florence, Florence, Italy*
[5] *Department of Radiology, Athinoula A. Martinos Center for Biomedical Imaging, Boston, MA, USA*
[6] *Harvard Medical School, Boston, MA, USA*
[7] *Department of Electrical, Electronic, and Information Engineering "Guglielmo Marconi", University of Bologna, Italy*

***Abstract*—Mild cognitive impairment (MCI) often occurs in patients with cerebral small vessel disease (SVD) and diffuse hyperintensities of cerebral white matter (WM) in T2-weighted magnetic resonance images. In MCI due to SVD, a major aspect of cognitive impairment lies in the impairment of executive functions. In this context, the Stroop test is often employed in probing executive functioning. Since MCI due to SVD has been hypothesized to result from WM tract damage, it can be characterized through diffusion tensor imaging (DTI), an MRI technique which permits in-vivo portrayal of WM tracts. In this work, we present a machine learning scheme tailored to predicting changes in executive functions (as measured by Stroop test) in patients with MCI and SVD. To this end, we employ data from 43 MCI patients with SVD and create a set of input features by averaging mean diffusivity (MD), fractional anisotropy (FA) and mode of anisotropy (MO) maps within 50 regions of interest (ROIs) located in WM. We then train a C-SVM classifier while simultaneously optimizing the C parameter in a 10-folds nested cross-validation loop, and achieve a prediction of impaired performance with high sensitivity (82.6%), specificity (90.0%) and accuracy (86.0%). In summary, we demonstrate how machine learning techniques can be employed in predicting impaired cognitive performance in MCI patients with SVD using MRI data alone, and that combining multiple DTI-related indexes can provide further improved classification performance.**

***Keywords*—Stroop test, MCI, DTI, machine learning.**

I. Introduction

MILD cognitive impairment (MCI) is a transitional state between normal ageing and dementia and is thought to anticipate dementia. Pre-dementia stages are also know to occur in cerebrovascular diseases, and cerebral small vessel disease (SVD) is widely recognized as one major cause of cognitive impairment [1]. Within the elderly population, MCI is common condition in patients with diffuse hyperintensities of cerebral white matter (WM) [visible in T2-weighted magnetic resonance (MR) images] and SVD [2]. In MCI due to SVD, cognitive impairment typically includes executive functions, which supervise the organization and execution of complex behavior, such as response inhibition (selective attention) [3]. The Stroop test is one of the most popular and widely employed second-level test sensitive to executive functioning [4]. It measures an aspect of executive control named interference resolution, which in turn involves selective attention [5].

In the context of SVD, the manifestation of MCI has been hypothesized to be due to WM tracts damage, which can result in a so-called disconnection syndrome [6]. Diffusion tensor imaging (DTI) is a well-established MR technique for in-vivo characterization of directional and overall diffusivity of water molecules in WM tracts, and is commonly employed to investigate microstructural modifications and their relation to neurophysiological mechanisms at the base of various neurodegenerative disorders [9]. In this context, machine learning techniques have been recently shown to be promising tools in neuroimaging data analysis [8].

In this study, we propose a machine learning scheme aimed at predicting, on a single-patient basis, the impairment in executive functions (evaluated by means of the Stroop test) in patients with MCI and SVD. For this purpose, we employ DTI-derived features as well as the baseline neuropsychological data from 43 MCI patients with SVD recruited in the RehAtt study [9], whose purpose is the rehabilitation of attention in patients with MCI and subcortical vascular changes.

II. Materials and Methods

A. Subjects

This study was conducted on forty-four elderly MCI patients with SVD which were recruited as part of the RehAtt trial. Each patient underwent extensive clinical, functional and neuropsychological assessment as well as MRI examination. One subject was excluded after MRI examination (see Section II-C). All further analyses were performed on the remaining 43 patients.

B. Neuropsychological assessment

All RehAtt participants were evaluated through a complete neuropsychological battery including several tests measuring executive functions [6], such as the Stroop test [5]. Raw Stroop test scores correspond to the time required to complete the task, which means lower scores are indicative of better performance.

After the evaluation, Stroop test scores were converted to equivalent scores (ES) by means of a quartile-based, nonparametric norming method. This methodology allows to convert age and education adjusted scores into an ordinal 5-point scale (ranging from 0 to 4) [9].

C. MRI Image Acquisition

All subjects underwent MR examinations on a 1.5 T system including diffusion weighted images, as detailed in

[9]. One patient was excluded after MR examination due to a technical problem during diffusion weighted acquisition.

D. Classification tasks

Since a dichotomic predictive classification between normal and impaired cognitive performance would have an important impact for clinical purposes, we categorized the distribution of the Stroop test performance (reformulated in terms of ES), hence exploring the task of classifying ES 0 (20 patients) vs. 1234 (23 patients).

E. Image processing

Diffusion weighted images were processed as described in [10] through dedicated software packages in order to compute the following DTI-derived indexes: mean diffusivity (MD), fractional anisotropy (FA) and mode of anisotropy (MO). These maps were then transformed into MNI152 standard space for subsequent processing.

F. Features vectors

Three input feature vectors were created by locally averaging MD, FA and MO maps within 50 regions of interest (ROIs) defined by the ICBM-DTI-81 atlas (see Fig. 1). In order to explore the differences in discrimination power between different DTI-derived features and their combinations, feature vectors composed of MD, FA, MO, as well as all possible combinations of two and three indexes were fed into the classifiers (see Table I).

G. Machine learning scheme

As base classifier we chose the particular type of kernel method machines known as support vector machines (SVMs), which have shown high classification abilities in neuroimaging applications to several neurological diseases [8]. We employed a typical SVM classifier (C-SVM) with a linear kernel (which is the internal product between pairs of feature vectors). Employing a linear kernel has the major advantage of allowing a direct interpretation of the trained model with also a reduced model overfit.

In this study, we trained the SVM classifiers while simultaneously optimizing the C parameter of C-SVM, by varying its value according to $C = 2^k$ with $k = \{-10, -9, \dots, 10\}$, in a 10-folds nested cross-validation (CV) loop [9]. Performance was quantified in terms of sensitivity, specificity and accuracy computed on the test set of the outer CV.

III. Results

Detailed results for all tests are reported in Table I. The best result in terms of sensitivity, specificity and accuracy was observed with the combination of MD and MO features (sensitivity 82.6%, specificity 90.0% and accuracy 86.0%).

TABLE I
CLASSIFICATION RESULTS (STROOP ES 0 VS. 1234): SENSITIVITY AND SPECIFICITY ARE REFERRED TO THE IDENTIFICATION OF STROOP ES 0 GROUP SUBJECTS

Feature vectors	*Sensitivity (%)*	*Specificity (%)*	*Accuracy (%)*
MD	69.6	60.0	65.1
FA	78.3	10.0	46.5
MO	65.2	55.0	60.5
MD + FA	78.3	25.0	53.5
MD + MO	82.6	90.0	86.0
FA + MO	82.6	55.0	69.8
MD + FA + MO	82.6	70.0	76.7

IV. Discussion and Conclusion

We have demonstrated the abilities of a machine learning scheme in predicting impaired performance in the Stroop test score in MCI patients with SVD using DTI data. In particular, we have shown that that MD and MO values WM are truly predictive of executive functions. FA values did not appear do contribute significantly in the considered classification task. This is in agreement with current literature in which FA presented lower and less extensive correlations with executive functions [10]. Finally, we have shown that, while each single-index set of features (apart from FA) provides satisfactory discriminatory ability, combining multiple DTI-related indexes can improve classification performance.

Acknowledgement

This work was supported by Tuscany Region (Italy) and Italian Health Ministry (Bando Ricerca Finalizzata 2010, Grant number RF-2010-2321706, PI Leonardo Pantoni).

References

[1] A. Zhou and J. Jia, "Different cognitive profiles between mild cognitive impairment due to cerebral small vessel disease and mild cognitive impairment of alzheimer's disease origin", *Journal of the International Neuropsychological Society*: JINS, vol. 15, pp. 898–905, 2009.

[2] L. Pantoni, A. M. Basile, G. Pracucci, K. Asplund, J. Bogousslavsky, *et al.*, "Impact of age-related cerebral white matter changes on the transition to disability – the LADIS study: rationale, design and methodology" *Neuroepidemiology*, vol. 24, pp. 51–62, 2005.

[3] E. Salvadori, A. Poggesi, G. Pracucci, D. Inzitari, and L. Pantoni, "Development and psychometric properties of a neuropsychological battery for mild cognitive impairment with small vessel disease: The VMCI-Tuscany study", *J Alzheimers Dis*, vol. 43, pp. 1313–1323, 2015.

[4] V. Hachinski, C. Iadecola, R. C. Petersen, M. M. Breteler, D. L. Nyenhuis, *et al.*, "National institute of neurological disorders and stroke-canadian stroke network vascular cognitive impairment harmonization standards", *Stroke*, vol. 37, pp. 2220–2241, 2006.

[5] C. M. MacLeod, "Half a century of research on the Stroop-T effect: An integrative review", *Psychological Bulletin*, vol. 109, pp. 163-203, Mar. 1991.

[6] M. Catani and D. ffytche, "The rises and falls of disconnection syndromes", *Brain*, vol. 128, pp. 2224–2239, 2005.

[7] J. Goveas, L. O'Dwyer, M. Mascalchi, M. Cosottini, S. Diciotti, *et al.*, "Diffusion-MRI in neurodegenerative disorders", *Magn Reson Imaging*, vol. 33, pp. 853–876, 2015.

[8] G. Orrù, W. Pettersson-Yeo, A. Marquand, G. Sartori, and A. Mechelli, "Using support vector machine to identify imaging biomarkers of neurological and psychiatric disease: a critical review" *Neurosci Biobehav Rev*, vol. 36, pp. 1140–1152, 2012.

[9] S. Ciulli, L. Citi, E. Salvadori, R. Valenti, A. Poggesi, *et al.*, "Prediction of impaired performance in Trail Making Test in MCI patients with small vessel disease using DTI data", *IEEE Journal of Biomedical and Health Informatics*, in press.

[10] M. O'Sullivan, D. K. Jones, P. E. Summers, R. G. Morris, S. C. Williams, and H. S. Markus, "Evidence for cortical "disconnection" as a mechanism of age-related cognitive decline," *Neurology*, vol. 57, pp. 632–638, 2001.

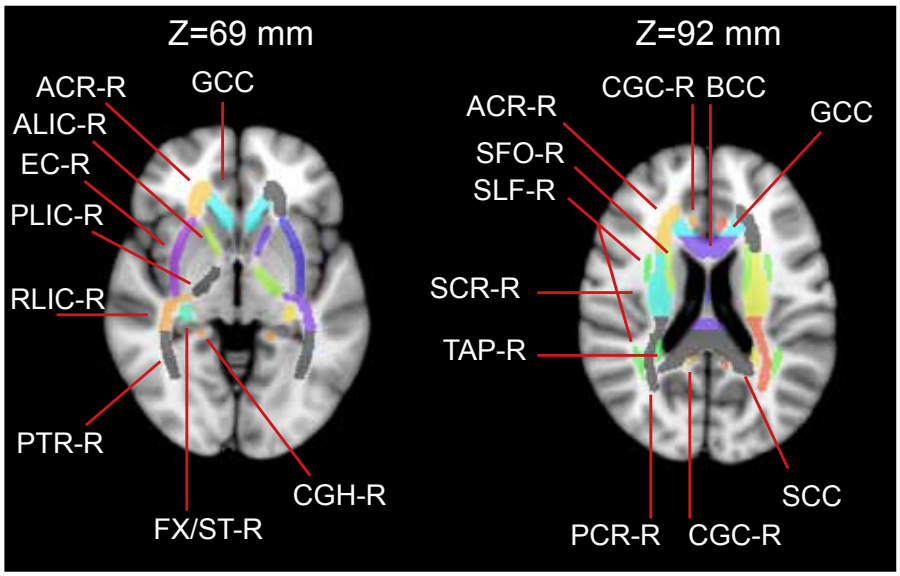

Fig. 1. Two axial views, at Z = 69 mm and Z = 92 mm (MNI coordinates), of the WM atlas ICBM-DTI-81, showing a subset of the 50 ROIs, overlaid on the MNI152 T1-weighted standard space. Bilateral ROIs are labeled on the right ("-R") side only.

Development of digital phantoms in CT imaging for simulation of pulmonary emphysema

S. Diciotti[1], A. Nobis[1,2], S. Ciulli[2,3,4], N. Landini[2], M. Mascalchi[2], N. Sverzellati[5], B. Innocenti[6]

[1] *Department of Electrical, Electronic, and Information Engineering "Guglielmo Marconi", University of Bologna, Cesena, Italy*
[2] *Department of Clinical and Experimental Biomedical Sciences, University of Florence, Florence, Italy*
[3] *School of Computer Science and Electronic Engineering, University of Essex, Colchester, UK*
[4] *Medical Physics Section, Department of Biomedicine and Prevention, University of Rome "Tor Vergata", Rome, Italy*
[5] *Section of Radiology, Department of Surgical Sciences, University of Parma, Parma, Italy*
[5] *BEAMS department, École polytechnique de Bruxelles, ULB Université Libre de Bruxelles, Bruxelles, Belgium*

***Abstract*— In this study we propose a set of digital phantoms of lung parenchyma simulating pulmonary emphysema in CT imaging using a 2-D finite element (FE) model based on a grid of beam elements. We generated 40 models using 4 different configurations of parameters with 10 randomizations for each configuration, mimicking several pathological conditions. Results showed that low-attenuation areas (LAA) images obtained from our model output simulate real LAA images as well as the LAA cluster size distribution of subjects with different emphysema grade. The digital phantoms may be efficiently used to test quantitative indexes of emphysema and to design realistic physical phantoms of LAA images in CT imaging.**

***Keywords*—digital phantoms, finite element analysis, emphysema, simulation.**

I. Introduction

COMPUTED tomography (CT) is a well-established imaging tool for the in vivo assessment of pulmonary emphysema, which appears as lung regions with low attenuation areas (LAA). Nowadays, several quantitative measurements of emphysema extent are adopted in clinical research [1]. Among them, the relative area (*RA*), defined as the percentage of the lung with density values below a given threshold, is one of the most common. Also, previous studies have shown that the cumulative distribution function of LAA clusters size in CT scans follows a power law characterized by an exponent *D*, which has been supposed to measure the complexity of the terminal airspace geometry [2].

Histopathologic measurements may provide a gold standard for the evaluation of both accuracy and precision of these indexes, but they suffer from unavailability of both large and public data sets. Numerical models of the lung parenchyma may fill this gap by evaluating the same model of lung parenchyma and generating standard reference images (*digital phantoms*) in different conditions (e.g., simulating mild, moderate or severe grade of emphysema, at varying inspiratory/expiratory level, different noise level, etc.) and with the possibility to be shared within the scientific community. Also, they may improve the understanding of the mechanisms of origin and progression of the disease and, in principle, paving the way through patient-specific models.

To this end, Mishima *et al.* [2] introduced a 2-D elastic spring network model for simulating lung parenchyma, by minimizing the potential energy using a simulated annealing algorithm. They found that neighboring smaller LAA clusters tend to coalesce and form larger clusters due to the fracture, under tension, of the weak elastic fibers separating them [2].

In the present study, we have developed an innovative 2-D finite element (FE) model, extending the spring network model proposed by Mishima *et al.,* for the simulation of LAA images in CT that enables the quantification of pulmonary emphysema related to smoking. The FE model of lung parenchyma simulates formation of emphysema and it has been set with 4 parameters configurations and 10 randomizations each one for simulating different grades of emphysema. A preliminary version of this work has been previously reported [3].

II. Materials and Methods

A. A 2-D finite element model of lung parenchyma

We developed a 2-D FE model of lung parenchyma constituted by a 2-D square grid of $L \times M$ nodes connected by identical elements. Each element represents an alveolar wall through a 2-node linear beam element. The model simulates the mechanisms of origin and development of emphysema related to smoking. According to the approach adopted by Mishima *et al.* [2], the model simulates emphysema of various grade through two parameters, N and S_{max}. The walls rupture caused by inflammation have been simulated by the removal of N nodes, randomly placed along the model grid (seed nodes), as well as all elements connecting these seed nodes to their neighbors [2]. Lung tissue strain occurring in normal breathing activity may lead to alveolar walls rupture, previously weakened by chemical activities due to inflammation. Also the local chemical activity and the related mechanical breakdown of alveolar walls have been simulated. Such process has been implemented by removing S additional nodes starting from the seed node along random walks (with S randomly chosen from a uniform distribution within $[0, S_{max}]$). All elements connected to these additional nodes have also been removed [2]. Once the 2-D structure of the model has been defined, a specific displacement has been applied to the external boundary of the model to pre-strain the tissue simulating an inspiratory condition. The border displacement has been chosen to achieve a strain of 0.20 in both horizontal and vertical directions, comparable with the usual range of strains of normal lung. A force-based model has demonstrated to well simulate a power law distribution

typical of the cluster size distribution [4]. Therefore, our model included simulation of mechanical breakdown by removing over-stressed elements (≥ 0.70 of the maximum von Mises element stress). A new equilibrium configuration of the grid was found, and the entire procedure of the element cutting was repeated three times.

An example of the model output before cutting over-stressed elements is shown in Fig. 1. It can be noticed that the iterative application of a threshold for cutting over-stressed elements generates the coalescence of clusters (Fig. 2).

B. Generation of the simulated LAA image from FE output

In order to generate a 2-D simulated LAA image derived from the node positions of the FE output, a square grid of the same size of the model grid has been overlaid on the FE output space. So, the original position of the model grid nodes were mapped onto the center of each image grid cell (Fig. 1 b) [3].

C. In vivo data set for FE model parameter setting

Even if the model is not patient-specific, we are interested in showing that our model may produce LAA images similar to those observed *in vivo*. For this purpose, we selected four subjects with variable emphysema grade, from mild (score 1) to severe (score 4), from a dataset of subjects belonging to the *ITALUNG* lung cancer screening trial employed and described in a previous study [5]. The *ITALUNG* study was approved by the local ethics committee. For each subject, one representative slice was selected for experimentally determining a set of parameters which produce similar simulated LAA images. Details of CT acquisition and reconstruction parameters have been described previously [5].

D. Choice of N and S_{max} parameters

We chose a grid size of $L \times M$=200×200 nodes. Four different couples of N and S_{max} parameters were chosen so that *RA* and *D* fell within the range of values observed in the subjects with various grade of emphysema (model 1: N=200, S_{max}=10, model 2: N =300; S_{max}=15, model 3: N =450; S_{max}=20, model 4: N =800; S_{max}=25). For each couple of N and S_{max}, 10 seed randomizations, and therefore 10 different FE models with the same parameters, were generated.

E. Comparison of cumulative functions between in vivo and simulated data

For each selected slice of subjects with emphysema we compared the cumulative function of the LAA size distribution with that of our simulated LAA of the corresponding model. A direct overlay between the simulated and *in vivo* cumulative functions is hampered by the arbitrary spatial scale of the models geometry. A proper spatial scale of the model was introduced intersecting the regression lines of cumulative functions of both simulated and *in vivo* LAA at the average spatial scale [(maximal + minimal)/2] in the real LAA image. This condition enables the selection of a spatial scale for the model output and to overlay the cumulative distribution of the models output in the same plot.

In order to also simulate the CT noise, N_n random voxels have been added to the simulated LAA images; N_n has been chosen empirically (N_n= 200, 300, 600 and 500 for models 1, 2, 3 and 4, respectively).

III. Results

In Fig. 3 the cumulative functions of cluster size have been shown for both *in vivo* data and the corresponding model. It is worth to note that the cumulative functions are quite overlapped and that the regression lines show very similar slopes (i.e. *D*).

The selected CT slices as well as a region of interest and its LAA image (using -950 HU threshold in real data) are shown in Fig. 4 along with the corresponding model output (in the first randomization). It can be noticed that the simulated LAA images - having similar *RA* and *D* indexes also visually resemble the distribution of the *in-vivo* LAA image. Indeed, even though LAA clusters have different locations and size each other, the cumulative distribution function of cluster size is highly similar.

IV. Conclusions

The model is able to generate a set of digital phantoms of LAA images that may be used to test quantitative indexes of emphysema and to design realistic physical phantoms of LAA images in CT imaging. This quantification is fundamental for assessment of novel treatments to reduce emphysema progression, including new drugs, surgery and devices.

Acknowledgement

This work was supported by the Italian Ministry of Health, by Tuscany Region (Italy) and by Ente Cassa di Risparmio di Firenze.

References

[1] B. C. Stoel and J. Stolk. "Optimization and standardization of lung densitometry in the assessment of pulmonary emphysema," *Invest Radiol*, vol. 39, pp. 681–688, 2004.

[2] M. Mishima, T. Hirai, H. Itoh, Y. Nakano, H. Sakai, *et al.* "Complexity of terminal airspace geometry assessed by lung computed tomography in normal subjects and patients with chronic obstructive pulmonary disease," *Proc Natl Acad Sci*, vol. 96, pp. 8829–8834, 1999.

[3] Diciotti S, Nobis A, Ciulli S, Landini N, Mascalchi M, *et al*. "Development and analysis of a finite element model to simulate pulmonary emphysema in CT imaging," In *Proceedings of the 37th Annual International Conference of the IEEE EMB Society*, 2015, pp. 6370-6373.

[4] B. Suki, K.R. Lutchen, and E.P. Ingenito. "On the progressive nature of emphysema roles of proteases, inflammation, and mechanical forces," *Am J Respir Crit Care Med*, vol. 168, pp. 516–521, 2003.

[5] M. Mascalchi, N. Sverzellati, M. Falchini, G. Favilli, S. Lombardo, L. Macconi, E. Paci, A. Lopes Pegna, F. Falaschi, M. Zompatori, and S. Diciotti. "Changes in volume-corrected whole-lung density in smokers and former smokers during the ITALUNG screening trial," *J Thorac Imaging*, vol. 27, pp. 255–262, 2012.

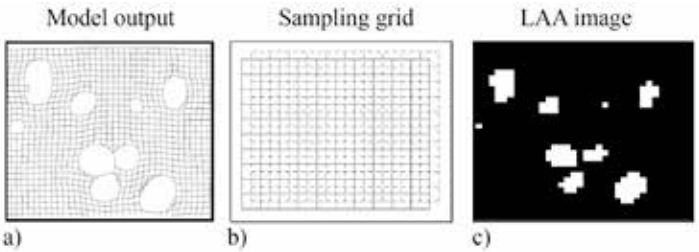

Figure 1: An example of the model grid is shown in a). The sampling grid is represented in b) whereas the corresponding model output showing simulated LAA clusters before cutting over-stressed elements, is depicted in c).

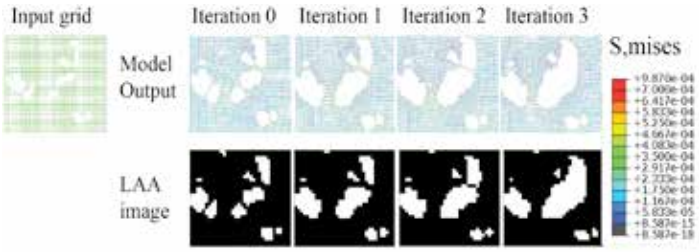

Figure 2: On the left, an example of the input grid of the model is shown. The model output corresponding to the input grip (iteration #0) is shown as well as the model output after each of the 3 iterations. The Von Mises stress distribution is overlaid in color. The corresponding LAA images are plotted below the model output. It is worth to note that clusters coalesce into bigger clusters as elements have been removed.

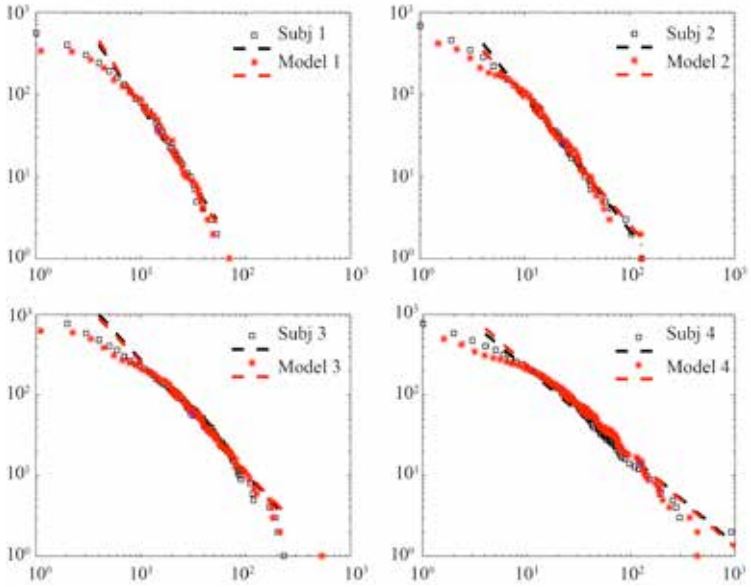

Fig. 3. Cumulative distribution functions of cluster size for the selected CT slice of each subject as well as that of the corresponding model (first randomization). It can be noticed that, for each subject, the two distribution substantially overlap. Dashed lines shows regression lines. RA-950=4.5%, D=1.89 for subject 1 (RA=5.9%, D=1.95 for model 1); RA-950=9.2%, D=0.99 for subject 2 (RA=11.6%, D=0.95 for model 2); RA-950=16.0%, D=1.41 for subject 3 (RA=20.9%, D=1.36 for model 3); RA-950=28.7%, D=1.09 for subject 4 (RA=33.7%, D=1.13 for model 4).

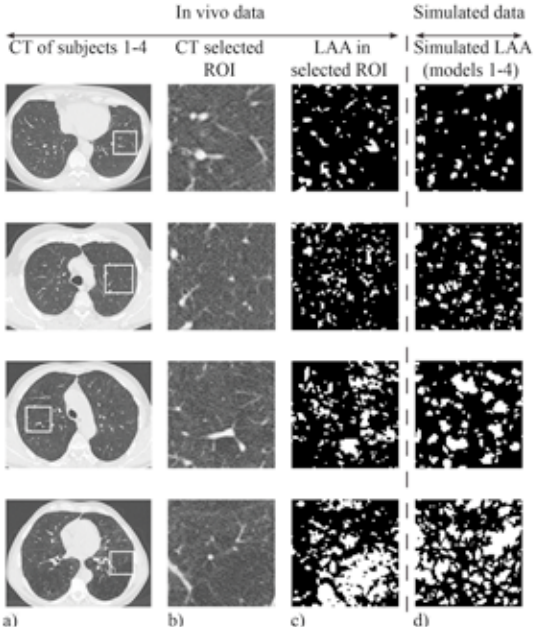

Fig. 4. Each row shows the images of a specific subject (subjects 1 and 2 with mild emphysema (score 1), subject 3 with mild to moderate emphysema (score 1-2) and subject 4 with moderate to severe emphysema (score 2-4)). Column (a): the selected CT slice with superimposed a 73x73 voxels region of interest (ROI); column (b): the CT image extracted within the ROI; column (c): LAA image obtained thresholding the CT slice at -950 HU; column (d): ROI of simulated LAA obtained with the four sets of parameters.

Image Processing of Ultra-terabyte Microscopic 3D Images

L. Acciai[1], P. Afferni[1], A. Bria[2], M. Guarrasi[3], G. Iannello[1], H. Peng[4], P. Soda[1]
[1] *Department of Engineering, University Campus Bio-Medico of Rome*
[2] *Department of Electrical and Information Engineering, University of Cassino and Southern Lazio*
[3] *CINECA – Interuniversity consortium*
[4] *Allen Institute for Brain Science*

***Abstract*—State-of-the-art microscopes can generate 3D images of terabyte size at high throughput. Processing and manipulation of these images require new software tools to perform a number of functions from stitching to visualization, to analysis. We present here our experiences in developing such tools applied to the processing of 3D images of whole mouse brains for neuroscience applications.**

***Keywords*—Ultra-terabyte image processing, 3D, light sheet microscopy, brain science.**

I. Introduction

CHARACTERIZING the cytoarchitecture of mammalian central nervous system on a brain-wide scale is becoming a compelling need in neuroscience. For example, realistic modeling of brain activity requires the definition of quantitative features of large neuronal populations in the whole brain. Quantitative anatomical maps will also be crucial to classify the cytoarchtitectonic abnormalities associated with neuronal pathologies in a high reproducible and reliable manner.

Light Sheet Microscopy (LSM) [1,2], coupled with chemical clearing procedures to render brain transparent [3] has recently gained a growing interest because it is the only method currently allowing the acquisition of a significant number of samples with full 3D resolution in a reasonable time. LSM produces very large datasets that require new tools to be managed and analysed. Although some work has been done to deal with the terabyte-sized images produced by the first generation of these new instruments [4,5,6], continuous and quick progress made by both LSM and clearing techniques is now producing images that may reach ultra terabyte dimensions, and even larger datasets could be produced in the near future.

The management of these huge datasets consists in a pipeline that include storage, stitching, co-registration among different acquisitions of the same sample, atlas mapping, visualization, extraction of meaningful information, which is currently the bottleneck for very large datasets. At the Computer Systems and Bioinformatics Lab of the university Campus Bio-Medico, in collaboration with the European Laboratory for Non-linear Spectroscopy (LENS), the University of Florence and the Allen Institute for Brain Science, we have been committed since many years in developing software components to build such a pipeline and make it available to neuroscience community [4,5,7,8].

In this abstract we summarize our recent results in this respect, and present ongoing work to both improve existing tools and enrich the pipeline with new functionalities.

II. Image Acquisition and Processing Steps

Due to the limited field of view of the light sheet-based microscopes, optical tomographs of macroscopic specimens (typically whole mouse brains) require many parallel image stacks (also referred to as tiles in the following) to cover the whole volume. Hence, multiple tiles, each composed by thousands of slices, are acquired using motorized stages. For volumes of approximately 1 cm^3 at submicrometer resolution and 16 bits color depth, the acquired data may easily exceed the teravoxel size. Tiles are therefore stored in lossless compressed format and typically each dataset may occupy from 1 to 3 terabyte on secondary storage.

Since tile positions provided by the stages are not sufficient to determine a reliable displacement between tiles, an overlapping region is introduced between tiles in order to make it possible the automatic combination of the stacks by means of a 3D-Stitching tool. Hence to extract useful biological information from images the following steps can be identified: (i) stitching (ii) co-registration among different acquisitions of the same sample, (iii) mapping the image to a mouse brain atlas in order to give full neuroscientific meaning to quantitative information extracted from the image (iv) image visualization and annotation, and (v) automatic analysis to extract meaningful biological information (i.e. cells segmentation, neurite tracing, etc.). We have not worked so far on co-registration of very large LSM images, whereas we have developed tools for all the other steps.

III. Developed Tools

A. Stitching

A stitcher capable to deal with terabyte-sized volumetric images was our first effort to provide useful tools. In 2012 we released the Terastitcher [4] that today is still the only tool really capable to deal with large images without the need of supercomputing facilities. Terastitcher was successfully used on images of up to 1 TB, but its first release had a number of limitations that prevented its use on larger images.

For this reasons we have introduced a number of improvements to make the Terastitcher capable of dealing with the images produced by LSMs which are continuously increasing in size. In particular, we introduced two main features specifically designed to deal with huge datasets. The first is the ability to run in parallel different instances of the

tool on different regions of the dataset, producing the same results than a sequential execution on the whole dataset. This strategy proved to be effective because on the one hand it required minimum changes in the code preserving its maintainability and independence of the underlying execution environment, and, on the other hand, it led to linear speedups on large datasets. A second very interesting feature was the ability to perform stitching-on-the-fly, that is the ability to leave the image in unstitched format after computing tile absolute position in the stitched image and perform stitching of any sub-volume on demand. Stitching-on-the-fly avoid the need to write the whole stitched image to non-volatile storage by default, but rather only to perform stitching either when it is really needed, or limited to the interesting portions of the image. Besides time, this approach enables also efficient use of secondary storage, which may become a critical issue when a single image reaches or exceeds tens of terabytes.

B. *Atlas mapping*

To provide LSM images with an annotated 3D reference space, we map images to existing mouse atlases such as Allen Brain Atlas (ABA), and Waxholm Space (WHS). Reference space pre-registered Nissl-stained or MRI volumes are typically made available together with the digital atlases to help in mapping new 3D images of specimens brains. Mapping LSM images, however, is a multimodality registration problem because the intensity profile of background fluorescence does not have a straightforward relationship with the intensity profile of the Nissl-stained or of the MRI volumes. One strategy to reduce complexity is to introduce an intermediary registration template with the same intensity profile as the specimen brains (i.e. LSM images). To avoid abnormalities possibly present in a single specimen, we create an unbiased template by averaging incrementally over many specimen brains and to this aim we are developing software tools to co-register multiple LSM images of different samples. Since atlas mapping of LSM images can be performed at reduced resolution comparable to the one of available digital atlases, this task does not require the use of high performance platforms

C. *Visualization and annotation*

Tools supporting true 3D visualization, annotation and analysis either do not scale well to the terabyte-size [9,10], or are limited owing to high expense of licenses (e.g. Amira(VSG), Imaris (Bitplane)) and infrastructures [11].

The open-source Vaa3D system [vaa3D] was specifically designed for exploring very large 3D data directly and efficiently without expensive virtual reality devices and/or parallel computing infrastructures. To this end, we developed Vaa3D-TeraFly, a plugin to extend the powerful 3D visualization and analysis capabilities of Vaa3D to images of potentially unlimited size [Bria2016]. When used with large volumetric images up to 2.5 Terabyte in size, Vaa3D-TeraFly exhibited real-time (subsecond) performance that scaled constantly on image size. Vaa3D-Terafly is based on a multi-resolution representation of the 3D image and supports three different formats. A flexible and specifically designed format, the BigDataViewer format [12] that is based in turn on the HDF5 standard, and the unstitched format, generated by the Terastitcher and mentioned in section III-A. Indeed the ability to navigate an unstitched image with Vaa3D-Terafly make even easier to perform a complete stitching only after having verified that it is worth the effort.

Vaa3D-Terafly has been implemented in C++ with Qt and OpenGL and it is freely and publicly available both as open-source and as binary package along with the main Vaa3D distribution.

D. *Automatic analysis*

When dealing with ultra-terabyte images, content analysis must necessarily be performed automatically, and operator intervention must be limited as much as possible and assisted by sophisticated tools.

While Vaa3D-Terafly provides effective solutions for what it is concerned with the latter issue, we also contributed to develop tools for automatically extract quantitative, biologically meaningful information from images.

In [Frasconi2014] the cell localization problem in LSM images has been solved combining semantic deconvolution by a supervised deep learning algorithm with a non-supervised mean shift-based method.

More recently we have tackled the neuron tracing problem and proposed algorithms for both cell segmentation and neuritis tracing [13,14].

REFERENCES

[1] H.U. Dodt, *et al*. "Ultramicroscopy: three-dimensional visualization of neuronal networks in the whole mouse brain, " *Nat Methods* 4, 331–336, 2007.

[2] L. Silvestri, *et al*. "Confocal light sheet microscopy: micron-scale neuroanatomy of the entire mouse brain," *Optics Express*, vol. 20, no. 18, pp. 20 582–20 598, 2012.

[3] K. Chung, *et al*. Structural and molecular interrogation of intact biological systems, *Nature* 497, 332–337, 2013.

[4] A. Bria and G. Iannello, "TeraStitcher - A tool for fast automatic 3Dstitching of teravoxel-sized microscopy images," *BMC Bioinformatics*, vol. 13, no. 1, p. 316, 2012.

[5] F. Amat, *et al*., "Efficient processing and analysis of large-scale light-sheet microscopy data, " Nat. Protocols, vol 10, no. 11, pp. 1679–1696, 2015.

[6] H. Peng, *et al*. "Extensible visualization and analysis for multidimensional images using Vaa3D," *Nat. Protocols*, vol. 9, no. 1, pp. 193–208, 2014.

[7] P. Frasconi, *et al*. "Large-scale automated identification of mouse brain cells in confocal light sheet microscopy images," *Bioinformatics*, vol. 30, no. 17, pp. i587–i593, 2014.

[8] A. Bria, *et al*. "TeraFly: real-time three-dimensional visualization and annotation of terabytes of multidimensional volumetric images," Nat. Methods, vol 13, no. 3, pp. 192–194, 2016

[9] J.L. Clendenon, *et al*. "Voxx: a pc-based, near real-time volume rendering system for biological microscopy," American Journal of Physiology - Cell Physiology, vol. 282, no. 1, pp. C213–C218, 2002.

[10] T. Pietzsch, *et al*. "Fiji: an open-source platform for biological- image analysis," Nat. Methods, vol. 9, no. 7, pp. 676–682, 2012.

[11] D.N. Williams, *et al*. "Ultrascale visualization of climate data," Computer, vol. 46, no. 9, pp. 68–76, 2013.

[12] T. Pietzsch, et al. "BigDataViewer: visualization and processing for large image data sets," Net. Methods, vol 12, no. 6, pp. 481–483, 2015.

[13] P. Soda, et al. "Computer-based automatic identification of neurons in gigavoxel-sized 3D human brain images," *Proc IEEE Eng Med Biol Soc., Milan*, pp. 7724-7727, 2015.

[14] L. Acciai et al., "Towards automated neuron tracing via global and local 3D image analysis," *Proc. IEEE Int. Symposium on Biomedical Imaging, Prague*, pp. 520-523, 2016.

CT Femur Alignment Before and After Total Hip Arthroplasty

L. Iuppariello[1], P. Bifulco[1], M. Fraldi[2], L. Esposito[2], P. Gargiulo[3] , M. Romano[4] and M Cesarelli[1]
[1] *Department of Electric Engineering and Information Technologies (DIETI), School of Engineering, University of Naples Federico II, via Claudio 21, 80125 Naples, Italy*
[2] *Department of Structures for Engineering and Architecture (DiSt), School of Engineering, University of Naples Federico II, via Claudio 21, 80125 Naples, Italy*
[3] *Department of Science – Vísindadeild Lndspitali (LSH), Biomedical Engineering Centre, Reykjavik University and Landspitali, Menntavegi 1, 101 – Reykjavik, Iceland*
[4]*DMSC, University "Magna Graecia", Catanzaro, Italy.*

***Abstract*--- Total hip arthroplasty is a widespread orthopaedic operation and consists of replace both the femoral head and the acetabulum. However, adaptation over time of a bone (bone remodelling) to the prosthesis, which changes physical demands of weight bearing, is not completely known. Computed Tomography can quantitatively assess local bone mineral density and the adaptation of a femur to the implanted prosthesis. Hence, bone remodelling can be monitored over time by means of cyclic CT scans (e.g. at 1 year, 2 year after the implantation). However, a femur of the same patient cannot be sliced exactly the same between two or more CT examinations (patient misalignment). Therefore 3D realignment of CT volumes is crucial in order to perform comparative studies. In addition CT images of a patient with a prosthesis result severely corrupted by the metallic artifact. This study proposes a 3D registration procedure to align CT volumes of femurs containing a prosthesis. Firstly CT images were processed to suppress the metallic artifact. After, a rough alignment (rigid and with 6 degrees of freedom) is performed by using three anatomic landmarks. This alignment in then refined by maximizing the similarity (of the HU values) of corresponding voxels between the two volumes. The whole procedure was tested using real pre-operative and post-operative (few day after) calibrated CT volumes. Analysis of the results show that the mean error tends to zero while the standard deviation scores about 150 HU.**

***Keywords* — Total Hip Arthroplasty, bone remodelling, metal artifact suppression, CT femur rigid registration.**

I. Introduction

Bone has the capability to adapt to changes in its mechanical loading through a process of remodelling, which is a lifelong process whereby old bone is replaced by new bone [1, 2]. For example, mechanical load forces in total hip arthroplasty (THA) continuously expose bone to remodelling processes according to Wolff's law, depending on implant size, geometry and stiffness of the prosthesis.

Conventional implants have shown a constant decrease of periprosthetic bone mineral density (BMD) in the proximal femur and a considerable periprosthetic bone resorption in the proximal femur due to stress shielding. Therefore, proximal load transfer to the trochanteric region should probably be aimed in modern implant designs.

It is important to avoid stress shielding and to reach a great mechanical compatibility of the steam with the bone, so that the physiological load transfer from the prosthetic head to the femur may be achieved [3, 4].

However, the modifications of bone mineral density and bone remodelling after THA surgery still remains unclear. Being able to measure the actual, local changes of BMD of a femur caused by the implanted prosthesis is of general importance in understanding the prosthesis-bone interaction and in planning THA surgery more appropriately by assessing fracture risk and implant stability [5, 6].

CT scans with Hounsfield unit (HU) quantification can assess very precisely local BMD and therefore bone quality. Unfortunately, CT images contacting the typical metallic implanted prosthesis are severely corrupted by artifact. This artifact significantly alters bone HUs and therefore the estimation of its BMD.

The aim of this preliminary study is to propose a 3D registration scheme to align pre-operative and post-operative CT volumes of patients undergoing THA surgery. Firstly, metallic artifact of post-operative CT were suppressed and then the pre-and post-operative femurs were precisely aligned.

II. Materials and Methods

A. Metallic artifact correction and femurs segmentation

Patient's pre-operative and post-operative (about few days after THA surgery) CT scan were acquired (pixel sizes were less than a millimetre while slice thickness wasone millimetre). HUs of the CT scanner were calibrated using a phantom enclosing different known materials [7].

First of all, a metal deletion technique was performed to get rid of the artifact caused by the prosthesis in the post-operative CT scans. The technique iteratively performs forward projection to replace detector measurements that involve metal. This produces a self-consistent set of projection data with the metal removed. First, each detector element is expanded until at least few photons are estimated. Next, the initial image is constructed by using linear interpolation. Because the forward-projected values do not exactly match the original projection data due to beam hardening, attenuation outside the reconstructed region, and other factors, a linear function was used to the forward-projected values to eliminate discontinuities. Finally, to further reduce streaking, rays passing near metal are replaced

with a weighted average of the experimental projection data and the forward-projected data, allowing a smoother transition. Figure 1 provides an example of the algorithm performance.

Once the metallic artifact was suppressed, the operated femur was segmented from both, pre-operative and post-operative, CT volumes. Firstly, bone tissues was roughly segmented by means of thresholding: voxel with HU values larger than 260 were preselected.

After, more sophisticated conditions were applied to separate the femur from the pelvis bone and isolated voxel contained by the muscle tissues. The segmented volumes were then smoothed by using 3D binary operators.

The procedures were developed in the Matlab R2015b® environment.

B. Femur alignment procedure

Although the patient was tried to be placed in the same position between the pre-operative and post-operative CT scanning, the resulting volumes obviously resulted not aligned.

The proposed procedure consists of two cascade stages. A rough 3D registration based on anatomic landmarks was followed by a finer 6 degrees of freedom rigid-global registration based on a HU similarity index.

In particular, three anatomic landmarks (a, b and c) were considered for each femur (see Fig. 2 as example):

a) the entrance of the arterial foramen in the femur shaft *(labelled "foramen" in Fig. 2)*;

b) the more posterior protuberance of the lesser trochanter *(labelled "pt" in Fig. 2)*;

c)the more posterior anterior protuberance of the greater trochanter *(labelled "gt" in Fig. 2)*.

These points were chosen as the most unambiguous and far between each other. More convenient landmarks on femur head and neck were not considered because not present in both volumes. The femur arterial foramen was clearly recognizable on the CT images and it constitutes an unequivocal reference point.

The transformation matrix defined by means the landmarks has been used to align the two pre-operative and post-operative DICOM volumes.

Then, starting from the 3D positioning obtained via the rough and ready alignment obtained through the landmarks, a finer adjustment is obtained by minimizing the HU differences in all the voxels belonging to the compact bone. This fine registration is based on the Mattes mutual information registration metric [8]. Both spatial transformations were assumed rigid and with six degrees of freedom. Finally, the aligned, post-operative femur was opportunely re-sampled (by means of linear interpolation) and a new DICOM volume was produced.

III. RESULTS

To quantitatively test the appropriateness of the whole procedure, the difference in HU of the corresponding voxels belonging to the pre-operative and the post-operative femur were computed. Whereas in few days the bone density of the femur has not changed at all, the expected result from the difference operation would be zero.

As example, Fig. 3 shows the histogram of the difference computed between aligned femurs (pre- and post-operative) of a subject of 71 years old who had implanted a cemented prosthesis. The distribution of the difference looks like a Gaussian with a mean of -55 HU and a standard deviation of 198 HU. Probably, the mean error is not zero because of the pre-processing adopted to suppress the large metal artifact caused by the high density material of the prosthesis. In general, the mean difference tends to zero, while the standard deviation scores about 150 HU.

The presented realignment procedure can be considered reliable within the limits highlighted by the analysis of the differences and can be used to test bone properties also using Finite Element Analysis [9].

REFERENCES

[1] Wolff J, Maquet P, Furlong R; 'The law of bone remodelling' Springer, 1986 126.

[2] Hadjidakis DJ, Androulakis II. Bone remodelling. Annals of the New York Academy of Sciences 2006; 1092 (Women's Health and Disease: Gynecologic, Endocrine, and Reproductive Issues):385-396.

[3] A. Braun, J. Papp, A. Reiter. The periprosthetic bone remodelling processing of vital bone reaction. Int. Orthop., 27 (SI) (2003), pp. 7–10.

[4] A. Herrera, V. Cnales, J. Anderson, C. Gracia-Arujo, A. Murcia-Mazon, A.J. Tonino. Seven to ten years follow up of an anatomic hip prosthesis. Clin. Orthop., 423 (2004), pp. 129–137.

[5] Rahmy AI, Gosens T, Blake GM, Tonino A, Fogelmann I. Periprosthetic bone remodelling of two types of uncemented femoral implant with proximal hydroxyapatite coating: a 3-year follow up study addressing the influence of prosthesis design and preoperative bone density on periprosthetic bone loss. Osteoporos Int. 2004;15:281–9.

[6] Brodner W, Bitzan P, Lomoschitz F, Krepler P, Jankovsky R, Lehr S, et al. Changesin bone mineral density in the proximal femur after cementless total hip arthroplasty. A five-year longitudinal study. J Bone Joint Surg Br. 2004;86:20–6.

[7] Steinarsdottir A, Þorbjornsson ES, Guðmundsson G, Gargiulo P. 2012. CT number calibration and dose assessment. Internal report. Reykjavik: Department of Science – Visindadeild Lndspitali (LSH) Biomedical Engineering Centre, Reykjavik University and Landspitali.

[8] Rahunathan, Smriti, D. Stredney, P. Schmalbrock, and B.D. Clymer. Image Registration Using Rigid Registration and Maximization of Mutual Information. Poster presented at: MMVR13. The 13th Annual Medicine Meets Virtual Reality Conference; 2005 January 26–29; Long Beach, CA.

[9] L. Esposito, P. Bifulco, P. Gargiulo & M. Fraldi. Singularity-free finite element model of bone through automated voxel-based reconstruction, Computer Methods in Biomechanics and Biomedical Engineering. 2016; 19 (3) : 257-262.

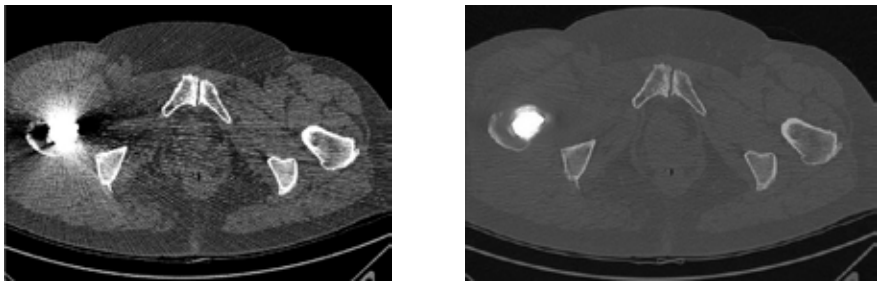

Figure 1: an example of an original CT slice including the prosthesis (on the left side) and the corrected imaged once suppressed the metal artefact (on the right side).

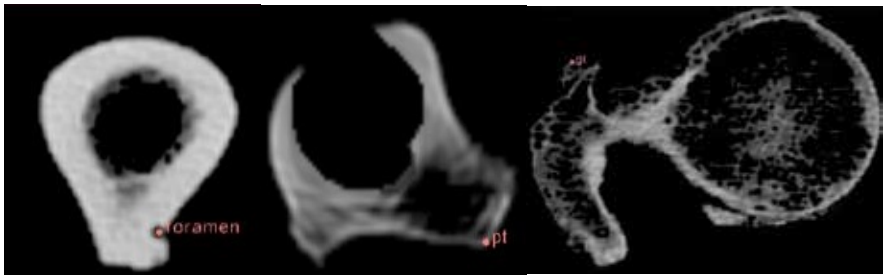

Figure 2: A representation of the three anatomic landmarks on different slices of a femur. On the left the landmark a) – arterial foramen; at the centre the landmark b) – lesser trochanter, on the right the landmark c) – greater trochanter.

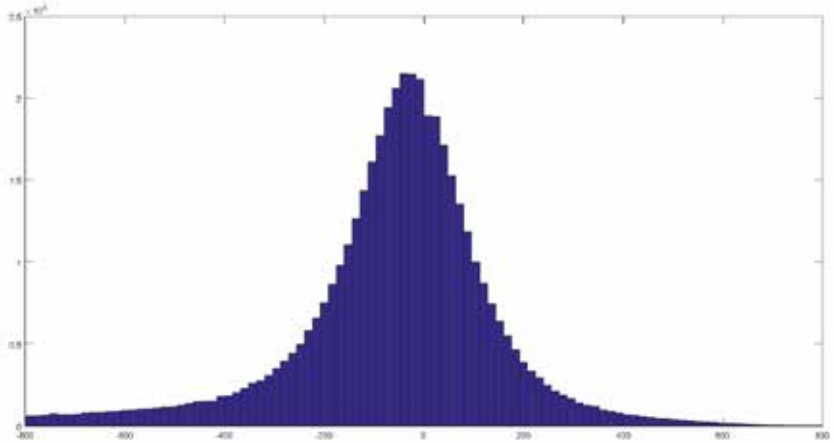

Figure 3: Histogram of the difference of HU values between a pre-operative and the corresponding post-operative femur computed on 4.4*10^5 voxels

Image enhancement in Digital Cytology: towards the design of a novel process

D. Giansanti[1], G. Maccioni[1], M. Pochini[2], A. Boschetto[2]and M.R. Giovagnoli[2]
[1] *Istituto Superiore di Sanità*
[2]*Università Sapienza*

***Abstract*—The study has the aim to propose a novel formalized approach to the heterogeneous aspects of the imaging in digital-cytology.**

A process of intervention has been proposed that involves three key-figures: the expert cytologist, the expert technician in biomedical laboratory, the ICT expert. This process comprises three issues focused on the imaging (sub-processes): (a) the focus emulation; (b) the visibility enhancement ; (c) the feature recognition. A properly designed electronic form has been customized to investigate the acceptance of the methodology.

A properly designed application of digital-cytology has been proposed based on Aperio to test the process. The process has been customized using the software Mathematica to design the three procedures of the sub-processes and has been successful-ly tested on two significant snapshots/case studies relevant to cervico-vaginal digital-cytology.

A process of intervention in the imaging has been designed and preliminary tested in digital-cytology. It allows the im-provement of information to analyze both for the expert cytol-ogist and technician of biomedical laboratory. It could be use-ful in tele-consulting, e-learning, in cooperative diagnosis and in the applications of image quality improvements..

***Keywords*— Digital Pathology, Image-enhancement, virtual microscopy**

.

I. Introduction

THE digital-pathology is playing an important role in the e-laboratory of cytology and has the chance both to change the work flows and optimize the job-work loads [1-2].

The digital-pathology comprises thus two branches:

– Digital-histology performed in the e-laboratory of histology;

– Digital-cytology performed in the e-laboratory of cytology [2].

Digital cytology still suffers with the following problems:

- -The visibility enhancement of details as in the case not exhaustive of the Chromatin, should be improved to better distinguish information in cancer diagnosis.
- It could be useful the emulation of the focus, furthermore it could save memory occupancy.

The image analysis and processing science [4-5] applied to medical imaging [4-5] could be of aid to overcame the listed problems. The objective of the study is the set-up and test of a process to face the above listed limitations. This implies (a) the focus to a specific application to produce images, (b) the design of the process based on specific tools using a dedicated software for the image enhancement and improving, (c) the design of a specific form to assess the advantage/improvement generated by the methodology in digital-cytology. The side ambitious objective is the set-up of a methodology which starting from a snapshot (usually with a memory occupancy of a few kbytes) from an e-slide (usually with an occupancy of Gbytes) enriches the infor-mation allowing a diagnostic intervention on several levels.

II. Methods

A. The Set-up of the Process

The process of intervention has been divided into three separate issues each one represented by the implementation of one sub-process aiming to overcome the limitations encountered in digital-cytology:

a) Visibility enhancement process (VE-P).

b) Feature recognition process (FR-P).

c) Emulation of focus function process (EFF-P).

These process can be also logically connected de-pending on a specific request of image analysis. In fact, the request can be heterogeneous embedding a combination of two or three actions. It could be, for example, required to emulate the focus to improve an image and then to apply a feature recognition in the focused image. It could be, for example, necessary to apply a 3D visualization to improve the diagnostic accuracy in the visibility enhancement and then to apply a feature recognition.

When you submit your final version, after your paper has been accepted, please use the same model, or modify the original version according to the instructions reported in this text.

A. E-slides

The e-slides used in the study have been scanned obtained by means of the Aperio (Aperio, USA) scanner have been positioned in a server at the URL http://www.dididtalslide.it. All the e-slides have been investigated at Zoom level = 40X.We used Image-scope which is compatible with the Windows OS platforms for the connection and extraction of the image-information arranged in snapshots from 3 e-slides relevant to cervico-vaginal cytology.

III. Results and Discussion

A Work-Group comprehending the key-figures in the e-laboratory of cytology i.e the ICT expert, the cytology expert and the technician of biomedical laboratory selected towards

the Network 27 snapshots significant for the study and recorded them in a digital-archive, indicating, according to the objective, the needed intervention among three chances (also selectable together), i.e visibility enhancement, feature recognition and emulation of the focus function. In conjunction with the choice of the snapshots the Work-Group has proposed a survey electronic form both to formalize and to assess the process of image improvement. As a tool for the design of the image-analysis and processing process we focused on Wolfram Matematica 9.0 (http://www.wolfram.com/mathematica/compare-mathematica/).

Unlike other systems, *Mathematica* applies intelligent automation in every part of the system, from algorithm selection to plot layout and user interface design. *Mathematica* requires no add-ons. It has built-in specialized functionality for many technical areas, from computational biology to wavelet analysis, all tightly integrated with the rest of the system.

The process of intervention has been implemented:

- The VE-P was focused to the 3D emulation has been found as a useful issue to face in digital-cytology in terms of *visualization enhancement* because of aid both to the cytologist and the technician in Biomedical Laboratory respectively in medical decision and or selection o the image. An Example of application of Mathematica is thus the 3D representation of the image. By converting the original image into a 2D array of luminance, i.e. grayscale image the resulting matrix organized numerical data may be displayed by a 3D plot .
- In order to perform the FR-P the following methodology has been developed in Wolfram Mathematica environment. The approach finds the matches between a sub-image called kernel and the original image. The advantage respect to other methods is that the kernel must not be designed as a numerical function but it is possible to use a part of the original image. The technician chooses a typical nucleus in the snapshot by clicking on it. This sub-image is used as kernel and the image correlation is calculated.
- The deconvolution methodology has been successfully applied to the snapshot to emulate the focus function and thus to set-up the EFF-P. We have assumed that the image undergrading is spatially invariant because the region is two orders smaller than original image. We chose a Gaussian matrix kernel for the so-called point spread function, considering that the degradation is due to the out-of-focus effect.

  Figure 1 and 2 show an example of image processing chosen from the collections. It enlightens that the Technician of the Biomedical Laboratory or the Cytology expert my interact with the software interface by changing parameters and explore different visualizations.

The compilation by a technician of biomedical (TLB) laboratory expert of the survey form after the application of the process of intervention and interaction with the interface gave an encouraging outcome in the case of the two different studies.

In fact some applicable parameters gave appreciable results such as for example:

- The high improvement of the *chromatin detail*
- The high improvement of both the *brightness and the sharpness*
- The *general improvement assessed in mean value*

IV. Conclusion

A study on the design of a process of intervention in digital-cytology as been proposed that faces:

(a) the focus emulation; (b) the visibility enhancement ; (c) the feature recognition. The process was tested on two case-studies. The study was tested on two case-studies. Generally the methodology could be useful in the e-laboratory of cytology for the image improving. In particular it could be of aid for the ICT expert directly supporting the professionals in the e-Laboratory of cytology and indirectly in telemedicine applications. The first immediate next step will be to deepen the investigation in all the extracted snaphots and to focus to specific case-studies to assess the improvement of the diagnostic accuracy using the proposed survey form [6-10].

The second immediate next step is the improving of the automation of the procedures in order to allow the use to the expert cytologist and technician in biomedical laboratory without the direct support of the ICT expert.

List of abbreviation

HTA Health Technology Assessment
ICT Information and Communication Technology
PC Personal Computer
TLB Technician in Biomedical Laboratory
VE-P Visibility enhancement process
FR-P Feature recognition process
EFF-P Emulation of focus function process

References

[1] Bondi A, Pierotti P, Crucitti P, Lega S. The virtual slide in the promotion of cytologic and hystologic quality in oncologic screenings. Ann Ist Super Sanita. 2010;46(2):144-50

[2] Giansanti D, Grigioni M, D'Avenio G, Morelli S, Maccioni G, Bondi A, Giovagnoli MR. Virtual microscopy and digital cytology: state of the art. Ann Ist Super Sanita. 2010;46(2):115-22

[3] Giansanti D, Castrichella L, Giovagnoli MR. The design of a health technology assessment system in telepathology. Telemed J E Health. 2008 Aug;14(6):570-5

[4] Russ J. C., The Image Processing Handbook Fifth Edition, CRC Press, (2006).

[5] Giansanti D, Boschetto A., Pochini M, Bottini L, Giovagnoli MR. Snapshots in digital cytology: a feasibility study based on the software tool mathematica focused on the image-enhancement and improving Patologica, Vol. 105, Oct, 2013 pp. 280.

[6] Demichelis F, Della Mea V, Forti S, Dalla Palma P, Feltrami CA. Digital storage of glass slides for quality assurance in histopathology and cytopathology. J Telemed Telecare 2002;8:138–142.

[7] Bondi A, Pierotti P, Crucitti P, Lega S. The virtual slide in the promotion of cytologic and hystologic quality in oncologic screenings. Ann Ist Super Sanita 2010;46:144–150.

[8] Giansanti D, Castrichella L, Giovagnoli MR. Telepathology requires specific training for the technician in the biomedical laboratory. Telemed J E Health 2008;14:801–807.

[9] Giansanti D. Pochini M. Giovagnoli MR Integration of tablet technologies in the e-laboratory of cytology: a health technology assessment. Telemed J E Health.2014 Oct;20(10):909-15.
[10] Giansanti D, Pochini M, Giovagnoli NR. How tablet technology is going to change cooperative diagnosis in the cytology e-laboratory Telemed J E Health 2013;19:991–993

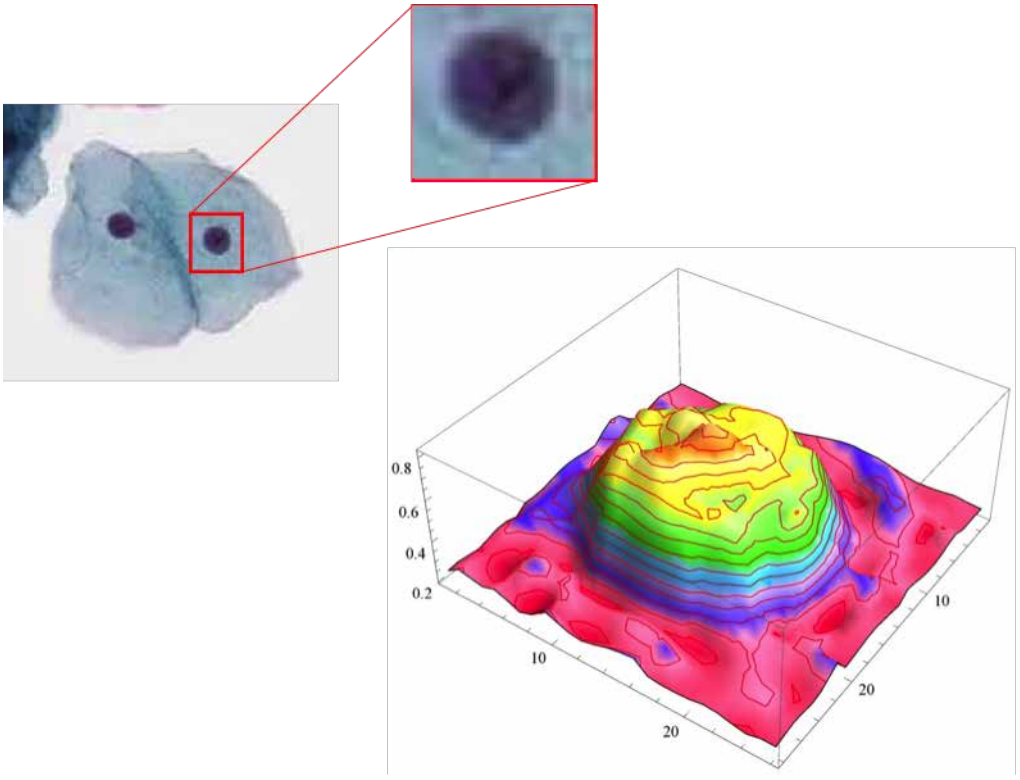

Fig. 1. Outcome of the case-study on the first snapshot: The visualization enhancement

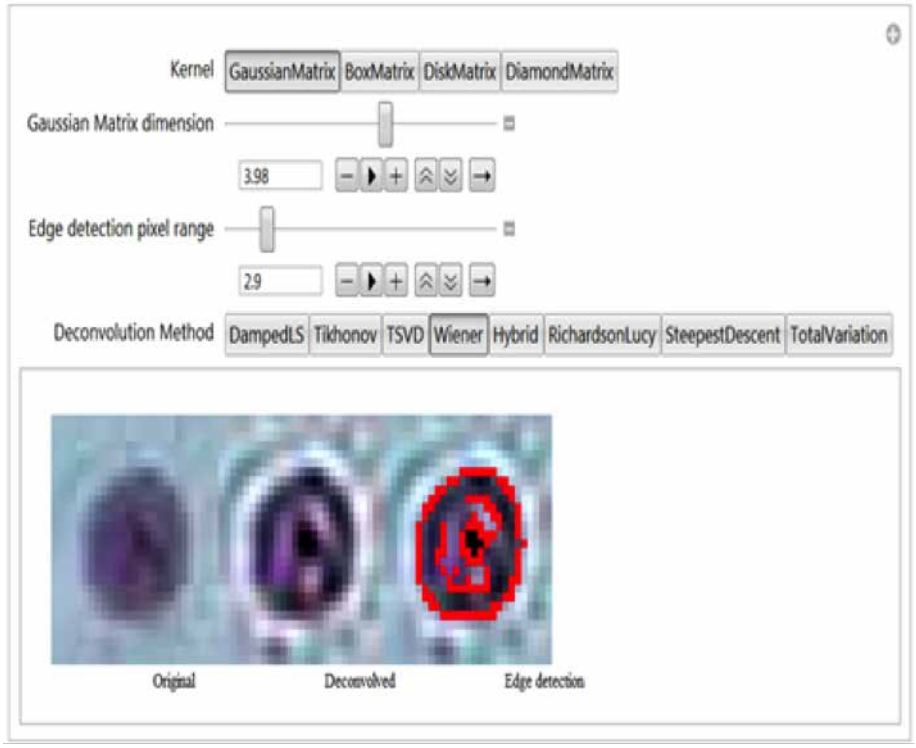

Fig. 2. Outcome of the case-study on the first snapshot: The Focus emulation

An automatic method to detect unreliable BF values on CT images of lung cancers

S. Malavasi[1,2] and A. Bevilacqua[2,3]

[1] Dept. of Electrical, Electronic and Information Engineering "Guglielmo Marconi" (DEI), University of Bologna, Italy
[2] Advanced Research Centre for Electronic Systems (ARCES), University of Bologna, Via Toffano 2/2, 40125 Bologna, Italy
[3] Dept. of Computer Science and Engineering (DISI), University of Bologna, Italy

***Abstract*— Computed Tomography perfusion (CTp) is an imaging technique widely applied in the study of the efficacy of the new anti-angiogenetic therapies. The presence of blood vessels, bronchi, and artefacts jeopardizes the computation of perfusion indexes and the visual analysis of perfusion maps. In this work, we propose an automatic method for the detection of those anatomical structures and artefacts responsible of unreliable perfusion values to be excluded from the analysis.**

***Keywords*— Quantitative imaging, error analysis, image processing, imaging artefacts, cancer.**

I. Introduction

Computed Tomography perfusion (CTp) is a widely available and non-invasive technique able to provide images with high spatio-temporal resolution [1]. The analysis of the tissue time-concentration curves (TCCs) that can be extracted from CTp images acquired before, during, and after the injection of a contrast agent, allows to obtain haemodynamic information of the investigated tissues that are largely used in oncology. In the recent years, some perfusion parameters, such as the blood flow (BF), have shown to be able to rapidly detect changes in the tumour's vascular structure, which could hint at possible anomalies in blood supply (i.e., tumour angiogenesis [2]). Hence, CTp is potentially able to monitor functional activities of tumours at their different stages [3], and predict treatment outcome or early therapeutic response of anti-angiogenetic therapies [4], before morphological changes become visible.

Currently, the reproducibility and the reliability of the functional results obtained with CTp, are still open issues and hamper the use of this technique in the clinical practice. The presence of artefacts inside images, mainly due to respiratory motion [5] or related to the acquisition phase (e.g., partial volume effect and beam hardening) [6], thwart the achievement of reliable TCCs, while the presence of vessels [7] and bronchi [8] jeopardize both the computation of local and global statistical perfusion indexes and the visual analysis of perfusion colorimetric maps. Commonly, only perfusion values out of the physiological range are considered as being unreliable and removed from the analysis by manually adjusting an appropriate window level [9]. Just recently, some steps forward have been taken to assess the reliability of the computed perfusion values [10] as well as to try improving their computation [11]. Anyway, these works do not associate fitting errors to their causes, if not to generic motion artefacts and, not at all, to anatomical structures.

This study presents a novel quantitative and automatic approach to detect those anatomical structures and those regions undergoing CTp reconstruction and acquisition artefacts, which could compromise the correct interpretation of CTp functional results and, ultimately, the clinical outcome.

II. Materials and Methods

A. CTp protocol and image acquisition

36 CTp examinations pertaining to 22 patients with a NSCLC having maximum transverse diameter greater than 2.5 cm in at least three sections were analysed. CT scans were performed on a 256-slice CT system (Brilliance iCT, Philips Medical Systems), with patient in the supine (feet first) position. An initial low-dose unenhanced full-body CT study was performed to identify target lesions at baseline conditions. Then, a 50-ml intravenous bolus of contrast agent (Iomeron, Bracco) was injected at 5 ml/s for axial cine contrast enhanced CT, followed by a single acquisition lasting 25 s (0.4 s rotation time, at 80 kV, 250 mA), yielding 20 scans of 11 slices each, with 55 mm of z-coverage, for a total amount of 220 images (512 x 512 pixel, 350 mm x 350 mm, 1.25 s temporal resolution).

B. Building perfusion maps

Two Regions of Interest (ROIs) were manually drawn by two expert radiologists for the aorta and for the tissue on a reference slice. The tissue ROI was then aligned on the remaining slices acquired at corresponding coach position in the x-y plane, as well as in the z direction, in order to compensate for the lesion movement. Time Concentration curves (TCCs) related to the voxels of the tissue ROI were then extracted and fitted according to the model described by the Hill's equation [12], by means of the Levenberg-Marquardt routine. The Hill's model is commonly used in pharmacodynamic models to describe non-linear drug dose–response and its four parameters shown in Eq. 1:

$$f_t(t) = E_0 + (E_{MAX} - E_0)\frac{t^{\alpha}}{(EC_{50})^{\alpha}+t^{\alpha}} \quad (1)$$

can be used to describe the diffusion of contrast agent inside tissues. E_0 and E_{max} represent the baseline and the saturation values, respectively, expressed in Hounsfield Units (HU), EC_{50} is the time instant of half-maximum response concentration of the curve and α is the non-linear parameter mostly affecting the slope of the curve. BF values are computed for each voxel according to the maximum slope method [13] during the first-pass phase (Eq.2):

$$BF = \frac{\frac{df_t(t)}{dt}\Big|_{max}}{f_a(t)|_{max}} \quad (2)$$

where $f_t(t)$ is the fitted TCC of the tissue and $f_a(t)$ is the TCC

of the arterial input. BF values are represented through the use of colorimetric maps. Voxels characterized by BF values strictly lower than 1 ml/min/100g, considered as being unlikely compliant with physiological values and rather ascribable to numerical errors, were excluded from the analysis and represented in the colour map with the pink colour. Fig. 1 shows an example of lung lesion visualized in a CTp slice, and its BF colorimetric map.

C. Automatic image segmentation

The fitting error μ_ε of each TCC is than computed as the mean absolute value of the distances between the TCC and the $f_t(t)$ in each acquisition time instant. The application of the triangle method (conceived to remove tails in unimodal distributions [14]) to the histogram of μ_ε pertaining to all the voxels of tissue ROI allows to find out a threshold value able to discriminate between "low" and "high" error values. Unreliable BF values pertaining to voxels with the highest error values were excluded from the analysis and highlighted in the pink colour in the BF colorimetric map. Fig. 2 shows an example of the μ_ε error colour map referring to lesion ID8 (a), its thresholded histogram (b) and the corresponding thresholded error (colour) mask (TEM) (c).

D. Manual annotation

In order to explore the capability of radiologists to identify unreliable perfusion values, we asked them to draw one ROI following the contour of each vessel, bronchus, or artefact visible on the reference slice of the CTp images inside the tissue ROI. These results were then compared with the TEM. A true positive value was assigned for each structure revealed by both radiologists and TEM, while a true negative value was assigned if nothing was manually and automatically detected inside the ROI. A false positive value was assigned in those cases where the structure highlighted by radiologists had not any influence on the reliability of the computed BF values. On the contrary, when a structure highlighted in the TEM was not identified by radiologists, but was recognized as being an artefact or an anatomical structure during a second later analysis of the CTp images, then a true negative value was assigned. Sensibility and specificity were finally computed for vessels, bronchi, and artefacts.

III. Results

Unreliable BF values highlighted inside TEM resulted to be structural aggregates, with spatial coherence (i.e. the same errors are shared by quite connected regions) and displaced in correspondence of anatomical structures or artefacts.

Medical doctors showed a very high specificity in detecting bronchi (100%) and blood vessels (100%). Fig. 3 shows an example of structures correctly detected by the Readers on the CTp image of a lung lesion and its corresponding TEM.

Things changed when facing artefacts. In two cases, the Readers pointed out the presence of artefacts that actually did not affect the reliability of the computed BF values, but that could have led to discard these two examinations. Even worst, there were 15 more cases where the Readers deeply underestimated the extension of the artefacts or missed the detection. In fact, without using TEM, medical doctors would have considered these data as being reliable, with possible risks of erroneous clinical considerations. Fig. 4 shows an example of ROI drawn by readers to delineate the beam-hardening artefact (a), whose extension has been underestimated, as one can see by looking at the red area shown in the TEM (b).

IV. Conclusion

This automatic method allows detecting those structures (i.e., vessels, bronchi, and artefacts) affecting the reliability of computed perfusion values, and determining their extension with a high precision. Its use becomes crucial in case of artefacts that can be perceived in a wrong way by human eyes and, hence, might lead medical doctors to wrong clinical consideration. This is yet more probable when the extension of these structures is underestimated or, even worst, not perceived. Our approach represents a fundamental step towards a more quantitative and standardize CTp imaging.

References

[1] Y. Ohno, et al., "Dynamic contrast-enhanced perfusion area detector CT for non-small cell lung cancer patients: Influence of mathematical models on early prediction capabilities for treatment response and recurrence after chemoradiotherapy", *Eur. J. Radiol.*, vol. 85, pp. 176-186, Jan. 2016.

[2] J.-B. Tylcza, et al., "Data-driven modeling and characterization of anti-angiogenic molecule effects on tumoral vascular density", *Biomed. Signal Proces.*, vol. 20, pp. 52–60, July 2015.

[3] G. Petralia, et al., "CT perfusion in solid-body tumours. Part I: technical issues", *Radiol. Med.*, vol. 115, pp. 843–857, Sept. 2010.

[4] N. Tacelli, et al., "Perfusion CT allows prediction of therapy response in non-small cell lung cancer treated with conventional and anti-angiogenic chemotherapy", *Eur. Radiol.*, vol. 23, pp. 2127–2136, Apr. 2013.

[5] T. Koh, et al., "Dynamic contrast-enhanced CT imaging of hepatocellular carcinoma in cirrhosis: feasibility of a prolonged dual-phase imaging protocol with tracer kinetics modelling", *Eur. Radiol.*, vol. 19, pp. 1184–1196, Jan. 2009.

[6] R. García-Figueiras, et al., "CT perfusion in oncologic imaging: a useful tool?", *Am. J. Roentgenol.*, vol. 200, pp. 8–19, Jan. 2013.

[7] C.S. Ng, et al., "Reproducibility of CT perfusion parameters in liver tumors and normal liver", *Radiology*, vol. 260, pp. 762–770, Sept. 2011.

[8] M. W. Huellner, et al., "Multiparametric PET/CT-perfusion does not add significant additional information for initial staging in lung cancer compared with standard PET/CT", *EJNMMI research*, vol. 4, pp. 1-13, Jan. 2014.

[9] K.A. Miles, et al., "Current status and guidelines for the assessment of tumour vascular support with dynamic contrast-enhanced computed tomography", *Eur. Radiol.*, vol. 22, pp. 1430–1441, July 2012.

[10] A. Bevilacqua, D. Barone, S. Malavasi, G. Gavelli, "Quantitative assessment of effects of motion compensation for liver and lung tumors in CT perfusion", *Acad. Rad.*, vol. 21 pp. 1416–1426, Nov. 2014.

[11] A. Gibaldi, D. Barone, G. Gavelli, S. Malavasi, A. Bevilacqua, "Effects of guided random sampling of TCCs on blood flow values in CT perfusion studies of lung tumors", *Acad. Rad.*, vol. 22, pp. 58–69, Jan. 2015.

[12] S. Goutelle, et al., "The Hill equation: a review of its capabilities in pharmacological modelling", *Fundam. Clin. Pharmacol.*, vol. 22, pp. 633–648, Nov. 2008.

[13] D. Ippolito, C. Capraro, A. Casiraghi, C. Cestari, S. Sironi, "Quantitative assessment of tumour associated neovascularisation in patients with liver cirrhosis and hepatocellular carcinoma: role of dynamic-CT perfusion imaging", *Eur. Radiol.*, vol. 22, pp. 803–811, Apr. 2012.

[14] G.W. Zack, W.E. Rogers, S.A. Latt, "Automatic measurement of sister chromatid exchange frequency", *J. Histochem. Cytochem.*, vol. 25, pp. 741–753, July 1977.

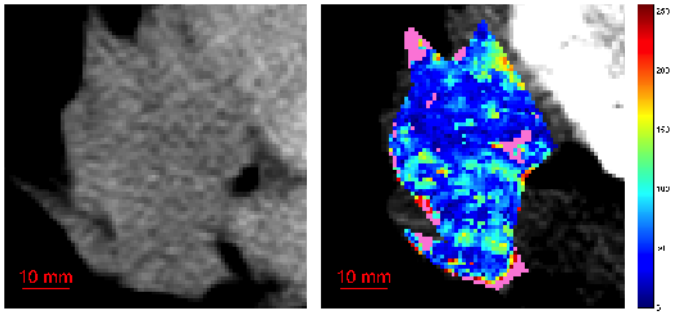

Fig. 1. CTp image of a lung lesion (a) and related BF colour map (b) with the pink voxels representing BF values unlikely compliant with the physiological range.

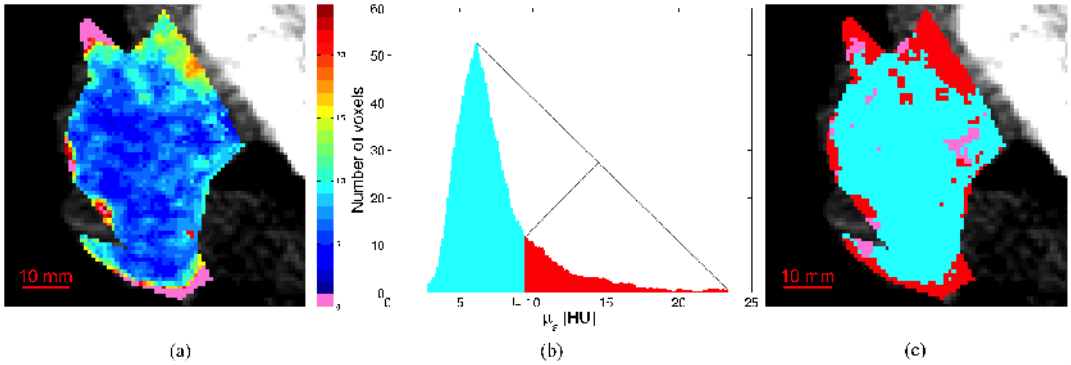

Fig. 2. Examples of the μ_ε colour map of a lung lesion (a), its thresholded histogram (b) and the corresponding thresholded colour mask (c) are shown. The red regions correspond to pixels whose fitting error was higher than the threshold T_T found out with the triangle method. Pink pixels correspond to zero-value perfusion voxels, while the cyan region is composed by the "survived" pixels, whose perfusion values can be correctly used.

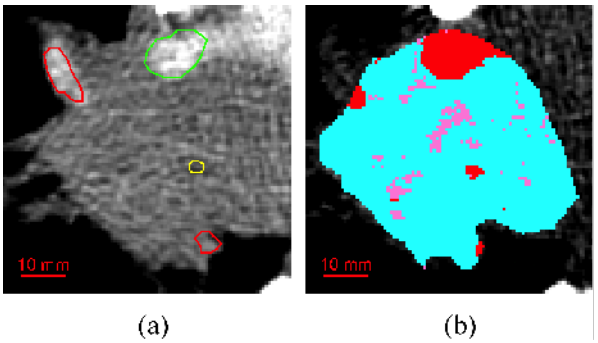

Fig 3. Two vessels (in red), one bronchus (in yellow), and one artefact from beam hardening (in green), manually contoured by the radiologists (a), with corresponding thresholded error mask (b).

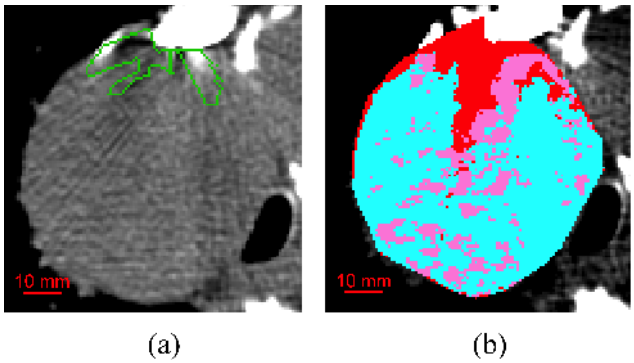

Fig. 4. A well-defined shape of an artefact (in green) drawn by the radiologists (a), that however fail in detecting its wide extent, highlighted in the error mask (b).

Quantifying complexity of the cerebral cortex in normal aging using fractal dimension

C. Marzi[1], S. Ciulli[2,3,4], and S. Diciotti[1]

[1] *Department of Electrical, Electronic, and Information Engineering "Guglielmo Marconi", University of Bologna, Cesena, Italy*
[2] *Department of Clinical and Experimental Biomedical Sciences, University of Florence, Florence, Italy*
[3] *School of Computer Science and Electronic Engineering, University of Essex, Colchester, UK*
[4] *Medical Physics Section, Department of Biomedicine and Prevention, University of Rome "Tor Vergata", Rome, Italy*

***Abstract*—The cerebral cortex manifests an inherent structural complexity of folding. The fractal geometry may describe the structural complexity of objects (such as the cerebral cortex) which show, in a proper range of spatial scales, *self-similarity*. In this study, we computed the fractal dimension of the cerebral cortex (imaged using T1-weighted sequences and segmented through *FreeSurfer* image analysis suite) using an automated selection of spatial scales in which the cerebral cortex manifests the highest self-similarity (in a statistical sense). We applied this procedure to a public dataset collected by the International Consortium for Brain Mapping (ICBM), composed of MRI examinations of 86 healthy subjects with age ranging from 19 to 85 years. The Pearson's correlation coefficient between fractal dimension of cerebral cortex and age was -0.72 ($p<0.001$). During normal aging, the fractal dimension of the cerebral cortex decreases hence reflecting the reduced complexity of cerebral folding. The fractal dimension has the potential to be used as a neuroimaging marker of complexity of the cerebral cortex and appears as a candidate marker able to assess cerebral changes in normal aging and possibly in various neurodegenerative disorders.**

***Keywords*—fractal dimension, aging, cerebral cortex, complexity.**

I. Introduction

THE cerebral cortex manifests an inherent structural complexity of folding. The fractal geometry enables to describe the structural complexity of objects which show, in a proper range of spatial scales, *self-similarity* (i.e. a geometrical property of objects composed of subunits and sub-subunits) that resemble the larger scale [1]. In this context, the fractal dimension D of an object is a measure of how much space it fills, taking into account its inherent highly detailed structure.

Previous studies have demonstrated that the cerebral cortex presents fractal properties, with self-similarity down to a spatial scale of 3 mm, which is approximately the human cortical thickness [2]. Still, Im *et al.* [3] found that the fractal dimension is a compact measure of shape complexity condensing cortical thickness, sulcal depth and folding area into a single numeric value. Within-subject reproducibility of the fractal dimension measure of different brain structures was also investigated [4].

In the present study, we aimed to 1) compute the fractal dimension of the cerebral cortex (imaged using T1-weighted sequences) using an automated selection of spatial scales in which the cerebral cortex manifests the highest self-similarity (in a statistical sense) and 2) assessing its potential use as a neuroimaging marker of natural aging in a large public dataset of healthy subjects.

II. Materials and Methods

A. Data set

For this study, we adopted the scans collected by the public *International Consortium for Brain Mapping* (ICBM) and belonging to the *1000 Functional Connectomes Project* (FCON 1000 Project). The dataset is composed of MRI examinations of 86 healthy subjects with age ranging from 19 to 85 years (41 men and 45 women, age 44.2±17.1 years, mean ± standard deviation). All subjects underwent high resolution T1-weighted imaging and resting state functional MRI on a 3-T scanner. In this study, only T1-weighted MR images were employed. They were acquired with a high resolution 3D sequence (Magnetization Prepared Rapid Gradient Echo, MPRAGE) with matrix size=256×256, slice thickness=1 mm and in-plane resolution of 1 mm.

B. Image segmentation

Completely automated cortical reconstruction of each subject's structural T1-weighted MRI scan was performed by employing the *FreeSurfer* image analysis suite (http://surfer.nmr.mgh.harvard.edu/) [5]. Briefly, this includes removal of non-brain tissue using a hybrid watershed/surface deformation procedure, automated Talairach transformation, segmentation of the subcortical white matter and deep gray matter volumetric structures, intensity normalization, tessellation of the gray/white matter boundary, automated topology correction [6] and surface deformation following intensity gradients to optimally place the gray/white and gray/cerebrospinal fluid borders at the location where the greatest shift in intensity defines the transition to the other tissue class. Once the cortical models are complete, a number of deformable procedures can be performed for further data processing and analysis including surface inflation, registration to a spherical atlas which is based on individual cortical folding patterns to match cortical geometry across subjects, parcellation of the cerebral cortex into units with respect to gyral and sulcal structure [7], and creation of a variety of surface based data including maps of curvature and sulcal depth. In the following, all post-processing procedures have been applied to the (bilateral) cerebral cortical reconstruction (Fig. 1).

C. Measurement of fractal dimension

The fractal dimension of cerebral cortex has been calculated through the box counting algorithm [8]: a grid containing 3-D cubes of side r has been superimposed on the

segmented cerebral cortex and the number of boxes (cubes) needed to fully cover the object has been counted. This procedure was repeated for various r values. In order to increase reproducibility, for each r, 20 uniformly distributed random offsets were applied on the grid origin and all the box counts (one for each offset) have been averaged to obtain a single $N(r)$ value [4]. We thus plotted $N(r)$ in a log-log plane and regressed it with a linear function having slope $-D$ using the coefficient of determination (adjusted for the number of data points) R^2_{adj}, as a goodness-of-fit indicator (Fig. 2). In the natural scale, this linear relationship in the log-log plane corresponds to a power law where D, the *fractal dimension,* is the exponent (with a negative sign) $N(r) = k\, r^{-D}$ and k is the prefactor [1].

In general, the range of spatial scales in which a structure manifests fractal properties is not known *a priori*. For this reason, in this study, we propose, for each subject, an automated selection of spatial scales based on the search of the range in which the linear regression shows the highest R^2_{adj}.

D. Experimental tests

The box counting algorithm was developed in C++ language by using the classes provided by the Insight Segmentation and Registration Toolkit (ITK) [9] for image processing algorithms, while the linear regression with automated selection of spatial scales was implemented in the Matlab environment (Mathworks, Natick, MA, USA). All computations have been performed on a Dell PowerEdge T620 workstation equipped with two 8-core Intel Xeon E5-2640 v2, for a total of 32 CPU threads, and 64 GB RAM, using the Oracle Grid Engine batch-queuing system. The processing time required approximately 9 hours of CPU time for *FreeSurfer* segmentation and about 5 minutes for the fractal dimension computation.

The box counting algorithm was executed using an exponential sampling of the spatial scales in the natural scale (which corresponds to a uniform sampling in the log-log plane) $r=2^k$ mm, with k={0, 1 , ..., 7}. The linear regression was carried out for each combination of minimal and maximal spatial scale taking into account the constrain that the data on which linear regression were calculated should contain a minimum number of data points (in this study we used a minimum number of 5 data points).

In order to assess the potential use of the fractal dimension as a neuroimaging marker of natural aging, we performed a linear regression analysis and computed the Pearson's correlation coefficient between fractal dimension measurements and age. Furthermore, we compared the fractal dimension measurements between men and women through a t-test (null-hypothesis of equal means). For all tests, a p-value <0.05 was considered statistically significant.

III. Results and Discussion

Table I shows the descriptive statistics of fractal dimension measurements of the cerebral cortex in 86 healthy subjects. The mean fractal dimension value of 2.495 (fractional) indicates that the cerebral cortex is a fractal structure and that it fills the space more than a surface and less than a volume structure. No significant difference in fractal dimension was found between men and women (p=0.97).

The minimal spatial scale at which the cerebral cortex manifested self-similarity was 1 (0) mm [median (interquartile range)] (range 1-2 mm). The maximal spatial scale was 32 (16) mm (range 16-64 mm). The coefficient of determination R^2_{adj} of linear regression was 0.999 ± 0.00006 (mean ± standard deviation) (range 0.9996-0.9998), thus proving an overall excellent fit within minimal and maximal scales.

Fig. 3 shows the linear regression between fractal dimension and age with a Pearson's correlation coefficient equal to -0.72 (p<0.001). During normal aging, the fractal dimension of the cerebral cortex decreases hence reflecting the reduced complexity of cerebral folding.

TABLE I
DESCRIPTIVE STATISTICS OF FRACTAL DIMENSION MEASUREMENTS OF CEREBRAL CORTEX

	Fractal dimension mean (standard deviation)
Men	2.496 (0.019)
Women	2.495 (0.027)
All	2.495 (0.024)

IV. Conclusions

Our approach allowed the automated selection of spatial scales in which the cerebral cortex of each subject manifests fractal properties, without the need of *a priori* or manual selection. The fractal dimension has the potential to be used as a neuroimaging marker of complexity changes of the cerebral cortex occurred during normal aging and appears as a candidate marker able to possibly assess changes due to various neurological disorders.

References

[1] B. B. Mandelbrot. *The Fractal Geometry of Nature*, W. H. Freeman and Company ed, 1983.

[2] V. G. Kiselev, K. R. Hahn and D. P. Auer. "Is the brain cortex a fractal?," *NeuroImage,* vol. 20, pp. 1765–1774, 2003.

[3] K. Im, J. Lee, U. Yoon, Y.Shin, S. Hong *et al* . "Fractal Dimension in Human Cortical Surface: Multiple Regression Analysis with Cortical Thickness, Sulcal Depth, and Folding Area," *Human Brain Mapping,* vol. 27, pp. 994-1003, 2006.

[4] J. Goñi, O. Sporns, H. Cheng, M. Aznárez-Sanado, Y. Wang *et al.* "Robust estimation of fractal measures for characterizing the structural complexity of the human brain: Optimization and reproducibility," *Neuroimage*, vol. 83, pp. 646-657, 2013.

[5] B. Fischl. "Freesurfer," *Neuroimage,* vol. 62, pp. 774–781, 2012.

[6] B. Fischl, A. Liu and A. M. Dale. "Automated manifold surgery: constructing geometrically accurate and topologically correct models of the human cerebral cortex," *IEEE Trans Med Imaging,* vol. 20, pp. 70-80, 2001.

[7] R. S. Desikan, F. Segonne, B. Fischl, B. T. Quinn, B. C. Dickerson, *et al.* "An automated labeling system for subdividing the human cerebral cortex on MRI scans into gyral based regions of interest," *Neuroimage* vol. 31, pp. 968-980, 2006.

[8] D. Russel, J. Hanson, E. Ott. "Dimension of strange attractors," *Phys. Rev. Lett.,* vol. 45, pp. 1175–1178, 1980.

[9] L. Ibanez, W. Schroeder, L. Ng and J. Cates. *The ITK software guide*, Kitware, 2003.

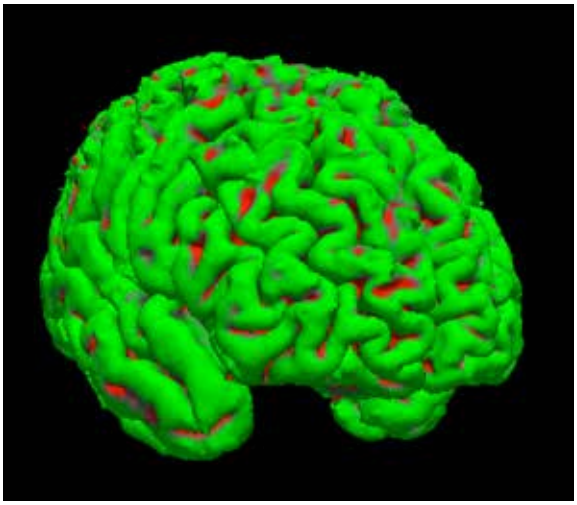

Fig. 1. An example of the 3-D segmentation of the cerebral cortex (subject code sub02382). The green regions are gyri and the red regions are sulci.

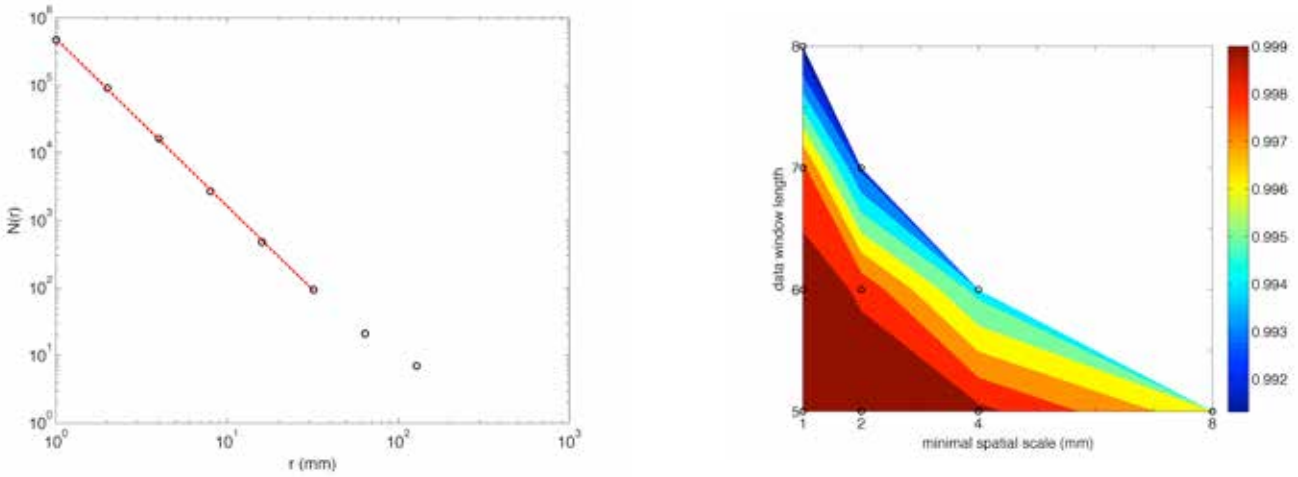

Fig. 2. In the left panel, the log-log plot of *N(r)* counts vs. cube side *r* corresponding to the 3-D segmentation shown in Fig. 1 is reported. The regression line which showed the highest R^2_{adj} (0.9997) is also superimposed. The contour plot showing R^2_{adj} as function of the minimal spatial scale and data window length is depicted in the right panel. Experimental data are indicated by circles. Highest R^2_{adj} was obtained with minimal scale of 1 mm and 6 data points.

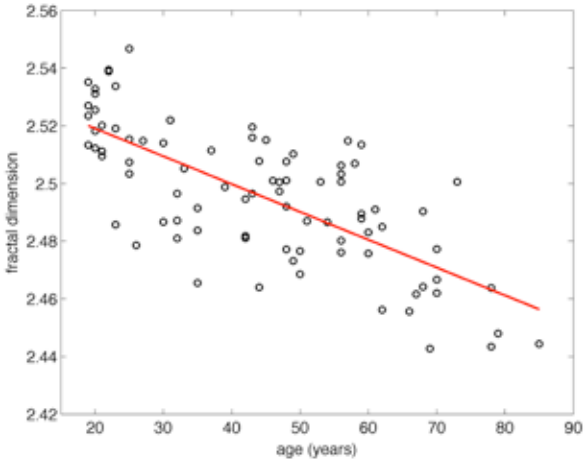

Fig. 3. Scatter plot showing age and fractal dimension measurements. The regression line is also superimposed (Pearson's correlation coefficient = -0.72, $p<0.001$).

Ultrasound plane-wave imaging using DMAS beamforming: first simulation results

G. Matrone[1], A. S. Savoia[2], G. Caliano[2], and G. Magenes[1]
[1] *Dipartimento di Ingegneria Industriale e dell'Informazione, Università degli Studi di Pavia, via Ferrata 1, Pavia, Italy*
[2] *Dipartimento di Ingegneria, Università degli Studi Roma Tre, via della Vasca Navale 84, Roma, Italy*

***Abstract*—Among the techniques aimed at improving the frame rate of medical ultrasound images, Plane-Wave Imaging (PWI) allows to achieve ultrafast imaging with frame rates up to 10 kHz. In PWI, in fact, a single plane wave transmission is used to acquire the image of the entire region of interest, as opposed to conventional B-mode imaging in which the image is acquired line by line. Unfortunately however, the use of an unfocused plane wave significantly reduces the achievable image quality.**

In this paper we present the first results obtained by applying Delay Multiply And Sum (DMAS) non-linear beamforming for the reconstruction of plane-wave images. This algorithm, originally conceived for microwave imaging, was recently proposed and adapted by the authors for use in ultrasound imaging, successfully achieving an improved image contrast resolution. By analysing the Point Spread Function (PSF) images and beampatterns, we thus show that DMAS allows to achieve significantly higher performances in PWI than conventional Delay and Sum (DAS), together with a high frame rate.

***Keywords*—DMAS beamforming, plane-wave imaging, ultrasound medical imaging.**

I. Introduction

B-MODE ultrasound images are conventionally acquired line by line, by transmitting and receiving each time a focused ultrasound beam along a certain scan direction, until all the region of interest has been covered. This actually limits the frame rate, as the time required to acquire a single frame is proportional to the number of scan lines and to the maximum depth to be investigated, and inversely related to the speed of sound in tissues (~1540 m/s). For example, if we consider a 10 cm image depth and 192 scan lines, the frame rate would be about 40 Hz. This parameter is particularly critical for example in cardiac applications, and even more in 3D/4D imaging, where the number of scan lines required to acquire the entire volume is in the order of thousands [1].

Ultrafast ultrasound imaging [2] is instead based on a different principle, i.e. on the transmission of plane waves, which makes it possible to achieve frame rates higher than 5000 Hz, leading to the development of several new valuable ultrasound imaging techniques [3]. Plane-Wave Imaging (PWI) in fact consists in transmitting/receiving a single plane (unfocused) wave front, which can be then post-processed and beamformed to reconstruct all the image lines in parallel. Hence, a single transmission is required to generate an image, with more than a 100-fold improvement of the frame rate.

The lack of a transmit focus however causes a worsening of image quality. For this reason, the use of coherent compounding has been proposed [1]: the coherent summation of several differently tilted plane-wave frames in fact allows to restore image contrast and resolution, unfortunately at the expense of the frame rate.

In a previous paper [4] we introduced the use of non-linear Delay Multiply And Sum (DMAS) beamforming (originally conceived for breast microwave imaging [5]) in ultrasound B-mode imaging, showing significant improvements in terms of contrast resolution compared to standard Delay And Sum (DAS) beamforming. Hence, this works aims to demonstrate that DMAS beamforming could be applied to PWI to improve image quality without affecting the high frame rate.

In this paper we present the first simulation results obtained by combining DMAS beamforming with PWI, and compare its performance to that of standard DAS by reconstructing the system Point Spread Function (PSF) images and beampatterns at different depths. The obtained results show that F-DMAS makes it possible to achieve a good contrast resolution, similarly to conventional B-mode imaging, but using only a single plane-wave, i.e. with a significantly higher frame rate.

II. Materials and methods

A. Plane-wave imaging

In a conventional focused linear scan, an active part of the transducer array (i.e. an active aperture) is used each time to transmit and receive a focused ultrasound wave. In this way a single scan line is acquired and, by shifting the aperture, all the image can be reconstructed line by line. Usually in reception the position of the focus is varied over time along the scan line, in order to implement dynamic focusing.

On the other hand, in PWI an unfocused plane wave is transmitted by all the array elements, and the whole image is acquired by means of a single transmit event. The backscattered signals are then collected by the array transducers and are synthetically focused a posteriori, in order to reconstruct the intensity values of each image scan line. Synthetic focusing is performed by considering the two-way travel times from the receive aperture elements to the focus; by varying the position of the focus along with time/depth, dynamic receive focusing is implemented.

B. Delay Multiply And Sum beamforming

In the improved DMAS version proposed by the authors, and called Filtered-DMAS (F-DMAS) [4], the re-aligned (i.e. focused) RF signals $s_n(t)$ are combinatorially coupled, multiplied and summed. Before multiplying the signal couples, the "signed" square root is applied to each signal sample in order to rescale their amplitude (so that the output signal would not be squared), while keeping the sign unaltered. The DMAS output signal $y(t)$ is thus computed as:

$$y(t) = \sum_{n=1}^{N-1} \sum_{m=n+1}^{N} sign(s_n(t)s_m(t)) \cdot \sqrt{|s_n(t)s_m(t)|} \quad (1)$$

Actually, this operation is very similar to the calculation of the aperture spatial autocorrelation function; hence, F-DMAS allows to achieve improved performances being based on a measure of backscattered signal spatial coherence.

Finally, a band-pass filter is applied to the beamformed signal *y(t)*, in order to attenuate the DC component, which originates in the spectrum after the multiplication stage, and to preserve only the second harmonics one.

By applying this procedure, each image line can be reconstructed; the lines are then used to build up the final image by performing envelope detection, normalization and logarithmic compression.

C. Simulation setup

Simulations were carried out in Matlab (The MathWorks, Natick, MA, USA) using the Field II simulator [6, 7]. The simulated scenario consisted of 5 reflecting point-scatterers at increasing depths (from 5 to 45 mm with a step of 10 mm) along the axial direction x=0 mm. A 192-element linear array operating at 5 MHz was modeled; the array pitch was 245 µm (elements width = 215 µm, height = 5 mm, kerf = 30 µm) and the fixed elevation focus was set at z=23.5 mm. The simulated excitation signal was a Gaussian-weighted, 2-cycle sinusoid at 5 MHz. 129 scan lines over the *xz* plane were considered. The sampling frequency was set to 100 MHz.

In the standard linear scan case, a 64-element active aperture was considered both in transmission and reception. The transmit focus was set at 23.5 mm and dynamic focusing was implemented in reception.

For PWI, all the array elements were used to transmit and receive the unfocused plane wave, and then synthetic receive dynamic focusing was applied a posteriori to reconstruct each image line, considering a 64-element receive aperture.

III. Results and Discussion

Fig. 1 shows the simulated PSFs at increasing depths, obtained when employing a classical linear scan or PWI with DAS and F-DMAS beamforming. In Fig. 2, the beampatterns (i.e. the lateral profiles of the maxima of the PSFs) at a depth of 5 mm, 25 mm and 45 mm are represented.

As expected, the use of an unfocused plane wave causes the beam side-lobe level to increase, as shown by Fig. 1a-b and by the gray dotted- and solid-line beampatterns in Fig. 2.

By applying F-DMAS to PWI instead, the contrast resolution significantly improves, and the beam profiles become similar or even better than those obtained with DAS in the conventional linear-scan case (cf. Fig. 1a-c). As a result, the PSF image obtained with PWI and F-DMAS (Fig. 1c) shows overall an even higher quality than that obtained in the classical focused line-by-line acquisition with DAS (Fig. 1a). Moreover, we should also point out that an edge-wave related artefact can be noticed in the proximity of each PSF in PWI images (Fig. 1b-c), which is however significantly less pronounced in the F-DMAS image.

The worsening of image quality in PWI is usually addressed by coherently compounding several tilted plane-wave frames, acquired by varying the transmit steering angle, at the expense of the frame rate (furthermore, this would also reduce the edge-wave related artifact which typically appears in single plane-wave images). The obtained results thus suggest that F-DMAS has the potential to improve the quality of plane-wave images without affecting the frame rate, or anyway limiting its reduction. This means that, in order to obtain the same performance of DAS with coherent compounding on N frames, F-DMAS is expected to require only $M < N$ frames.

Another aspect to be considered is that the use of an unfocused plane-wave reduces the spatial coherence of backscattered signals, which could partially influence the performance of F-DMAS beamformed images in a more realistic case. All these topics will thus be the object of in-depth future investigations.

IV. Conclusion

In this paper some preliminary results achieved by applying the F-DMAS beamforming algorithm to ultrasound PWI are presented. The PSF images clearly show that with F-DMAS the performance of PWI can be significantly improved compared to standard DAS beamforming, as F-DMAS allows to compensate for the reduction of resolution and contrast caused by the lack of focusing in transmission. Future developments of this work will involve the evaluation of F-DMAS in PWI with coherent compounding, both in a more complex simulated scenario and in experimental/*in vivo* trials.

Acknowledgement

This work has been partially funded by the National governments and the European Union through the ENIAC JU under grant agreement number 324257.

References

[1] G. Montaldo, M. Tanter, J. Bercoff, N. Benech, M. Fink, "Coherent plane-wave compounding for very high frame rate ultrasonography and transient elastography," in *IEEE Trans. Ultrason., Ferroelectr., Freq. Control*, vol. 56, no. 3, pp. 489-506, 2009.

[2] M. Tanter and M. Fink, "Ultrafast imaging in biomedical ultrasound," in *IEEE Trans. Ultrason., Ferroelectr., Freq. Control*, vol. 61, no. 1, pp. 102–119, 2014

[3] J. Bercoff, "Ultrafast Ultrasound Imaging", in *Ultrasound Imaging - Medical Applications*, Prof. Oleg Minin, Ed., InTech, [Online], 2011. Available: http://www.intechopen.com/books/ultrasound-imaging-medical-applications/ultrafast-ultrasound-imaging

[4] G. Matrone, A. S. Savoia, G. Caliano, G. Magenes, "The Delay Multiply and Sum beamforming algorithm in ultrasound B-mode medical imaging," in *IEEE Trans. Med. Imag.*, vol. 34, no. 4, pp. 940-949, 2015.

[5] H. B. Lim, N. T. Nhung, E. P. Li, and N. D. Thang, "Confocal Microwave Imaging for Breast Cancer Detection: Delay-Multiply-and-Sum Image Reconstruction Algorithm," in *IEEE Trans. Biomed. Eng.*, vol. 55, no. 6, pp. 1697-1704, 2008.

[6] J. A. Jensen, "Field: A Program for Simulating Ultrasound Systems," in *Med. Biol. Eng. Comput.*, vol. 34, pp. 351-353, 1996.

[7] J. A. Jensen and N. B. Svendsen, "Calculation of pressure fields from arbitrarily shaped, apodized, and excited ultrasound transducers," in *IEEE Trans. Ultrason., Ferroelect., Freq. Contr.*, vol. 39, no. 2, pp. 262-267, 1992.

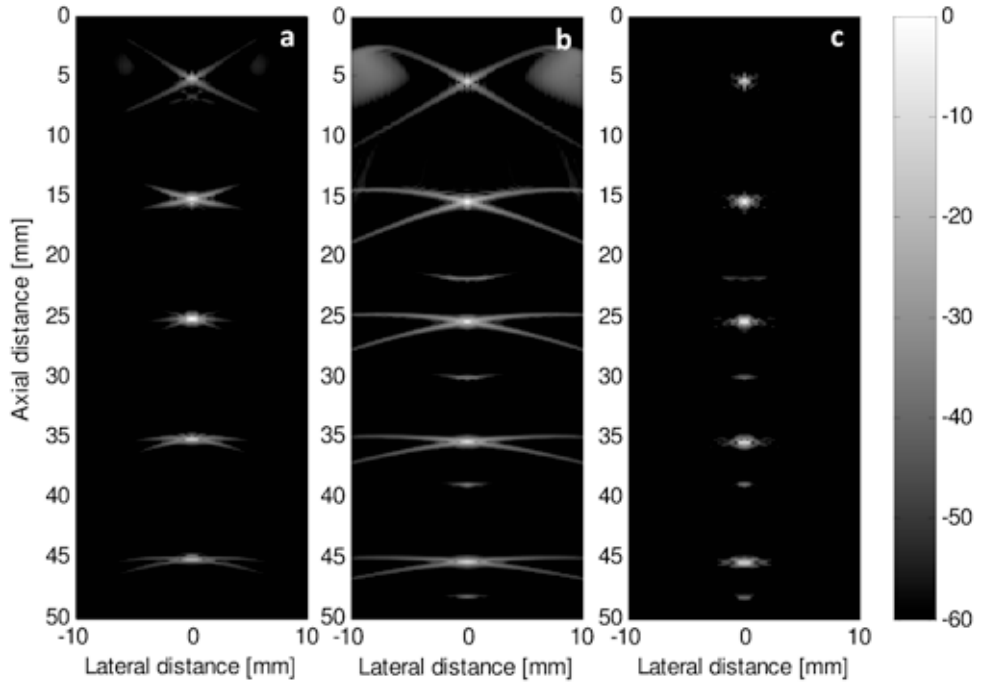

Fig. 1. Images of the PSF at 5-15-25-35-45 mm depth: a) standard B-mode linear scan with DAS beamforming; b) plane-wave image with DAS beamforming; c) plane-wave image with F-DMAS beamforming. Images are displayed over a 60 dB dynamic range (log scale).

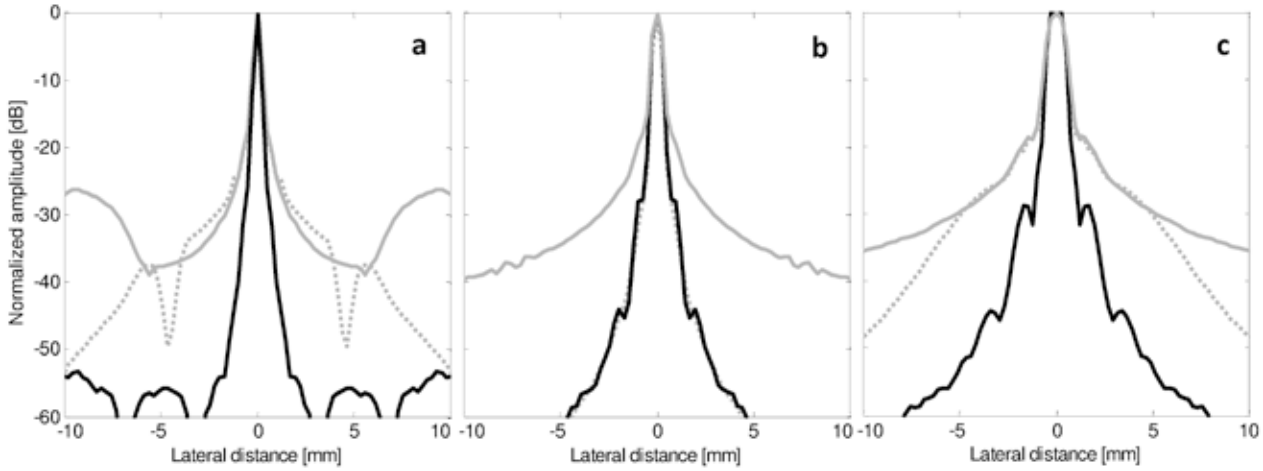

Fig. 2. Beampatterns at a) 5 mm, b) 25 mm and c) 45 mm depths. The dotted gray lines represent the beam profiles obtained with DAS beamforming in the case of a standard B-mode linear scan. The solid lines instead refer to PWI with DAS (gray line) or F-DMAS (black line) beamforming.

A Radiomic approach to soft tissues sarcoma

E. Montin[1], V.D.A. Corino[1], A. Messina[2] and L.T. Mainardi[1]
[1]*Politecnico di Milano / Dipartimento di Elettronica Informazione e Bioingegneria,Milan, Italy*
[2]*Istituto nazionale dei tumori di Milano / Dipartimento di radiodiagnostica per immagini unità 1, Milan, Italy*

***Abstract*—In this work we focused on the characterization of Radiomic features on Soft Tissues Sarcomas (STSs). These tumours have an intrinsic heterogeneity, which make their staging very difficult.**

Fourteen patients, with a known histological staging, were retrospectively analysed in order to characterize the *first-order statistic* features on the apparent diffusion coefficient (ADC) map obtained by diffusion weighted imaging acquisitions.

Globally, 34 features were calculated on ADC maps of 14 patients, seven patients of intermediate grade and seven patients of high grade. In order to select the most robust features, a Wilcoxon rank-sum test was performed on the null hypothesis of no differences in the two groups, of intermediate and high grade.

The results highlighted that 22 features had significant differences in the groups, making the radiomics of these rare tumours a possible methodology for the quantification and grading of STSs.

***Keywords*— Diffusion images, MRI, radiomics, sarcoma.**

I. Introduction

The emergence of Radiomics in oncological clinical field is growing more and more in the latest years. Radiomics extracts a large number of image characteristics, or features, in a non invasive way [1]. The assumption is that image features quantify crucial information regarding the entire tumour phenotype and thus they can highlight intraumour heterogeneity [1]**.**
Many studies reported that this heterogeneity could have profound implications in tumour staging and prognostic evaluation [2].

Soft tissue sarcomas (STSs) are rare and heterogeneous group of tumours that pose significant diagnostic and therapeutic challenges for clinical care and medical research [3]. Morphological studies and immunohistochemistry methods have demonstrated that most part of sarcomas originate from pluripotent mesenchymal cells, which are subjected to differentiation during the neoplastic transformation. Thus, the most recent classification is based on the differentiation line of the tumour [4]. Sarcomas are assigned a grade, low, intermediate, or high, based on the presence and frequency of certain cellular and subcellular characteristics associated with malignant biological behaviour. All STSs are surgically treated but histotype and grade might suggest a pre or post surgery combination of chemotherapy and radiation therapy [5].

Many works have underlined the potential use of diffusion weighted magnetic resonance imaging (DWI) techniques in the staging of STS, in particular, by means of the apparent diffusion coefficient (ADC) [6][7].
The aim of this work was to assess the capability of Radiomic features to characterize and/or differentiate STSs of different grades.

II. Material and methods

A. Study population ad Image acquisition

In this work we retrospectively analysed a subset of STSs patients from the Fondazione IRCCS- Istituto Nazionale dei Tumori of Milano (INT). These patients underwent to a DWI acquisition, performed on a 1.5 T Philips Achieva (Philips Medical system Achieva, Nederlands) available at the INT. The study was approved by the local ethics committee and all patients gave their written informed consent before being included.
We analysed 14 patients with a proven diagnosis of STS histological intermediate and high grade, 7 patients per group.
The DWI sequence was acquired axially by means of echo planar imaging (EPI) with TR 5400 ms, TE 78 ms with resolution 0.9, 0.9, 5 mm, without gap and the DWI b-values was set to: 50, 400, 800 and 1000 s/mm^2.

B. ADC maps creation

For each acquisition, we calculated the apparent diffusion coefficient (ADC) as the slope of the linear regression of the logarithm of the DWI exponential signal decay on the four b-values [8]. In such way, we obtained 14 ADC maps that constitute the basis for the computation of the Radiomic features. The ADC routine was developed in ITK 4.8 [9].

C. Features extraction

For each ADC map, we calculated, the so called first order statistic features [10] (FOS) on a region of interest (ROI) covering the full extent of the lesion.
In order to capture the entire heterogeneity of the tumour, an expert radiologist drew the ROIs on the DWI at the lower b-value, 50 s/mm^2.
In particular, we calculated 34 features: 12 computed on the gray level intensity of the ADC map and 22 on the histogram of the map.
The first 12 features were: energy, kurtosis, mean absolute deviation, maximum, mean, median, minimum, range, root mean square, skewness, standard deviation and variance [10] while the remaining 22, were: Shannon entropy, kurtosis, mean absolute deviation, maximum, mean, median, minimum, range, root mean squared, skewness, standard deviation, uniformity, variance, total frequency and 10 quantile of the histogram.
All the features were implemented in ITK 4.8 [9] and ROI were drawn by means of 3D Slicer.

D. Features reduction

Many studies use the Radiomic features to create a classification routine. However, the reliability of the classifier model might be compromised when the number of features is higher than the training dataset [11], thus, a reduction of the number of features is necessary. In the literature, this phenomenon is referred to as the curse of dimensionality [12].

In order to select the most robust features, a Wilcoxon rank-sum test was conducted on the 34 feature in the two groups, intermediate and high grade.

The test null hypothesis was no difference between the distribution of each feature in the two groups and we fixed the acceptance threshold at a p-value of 5%.

III. Results

Figure 1 reports two ADC maps of an intermediate (top panel) and high (bottom panel) grade STS. From the image, it is clear that intermediate grade lesion has a higher and less disperse ADC values in comparison to high grade.

By our analyses, we found that 22 features were statistically different in the two groups. Table 1 reports the mean values of each features in the two groups and the relative p-values.

Considering the features computed on the histogram of the map, 16/22 were significantly different in the two groups, while only 6/11 of the features are computed on the gray level intensity of the ADC map.

By a further analysis of Table 1, it is worth noting that the most significant features are in the histogram features group.

These two results are probably due to the fact that the heterogeneity of the STSs is better highlighted by the histogram features group.

Figure 2 shows an example of histogram of the ADC map for two patients, belonging to the intermediate and high grade groups. It can be noted that the histogram of the high grade is more spread out.

TABLE I

FEATURES VALUES IN THE INTERMEDIATE AND HIGH GRADE STSS

Features	*Intermediate G*	*High G*	*P-value*
S.Energy'	*1968686x10^9*	*97x10^9*	*0,26*
S.Kurtosis'	***6,87***	***3,10***	***0,03***
S.Mad'	*16426,16*	*434,97*	*0,71*
S.Max'	***245503,40***	***3298,29***	***0,05***
S.Mean'	***159847,44***	***1404,38***	***0,04***
S.Median'	***164021,16***	***1359,71***	***0,04***
S.Min'	*0,00*	*0,00*	*1,00*
S.Range'	***245503,40***	***3298,29***	***0,05***
S.RMS'	***161599,06***	***1506,09***	***0,04***
S.Skewness'	*-0,67*	*0,14*	*0,53*
S.STD'	*23609,62*	*535,80*	*0,80*
S.Variance'	*2071482807,14*	*293417,14*	*0,80*
H. Entropy'	***3,83***	***4,32***	***0,01***
H. Kurtosis'	***7,56***	***4,41***	***0,04***
H. Mad'	***0,0226***	***0,0202***	***0,03***
H. Max'	***0,14***	***0,09***	***0,04***
H. Mean'	*0,02*	*0,02*	*1,00*
H. Median'	*2*10^{-5}*	*5*10-5*	*0,13*
H. Min'	*0,00*	*0,00*	*1,00*
H. Range'	***0,14***	***0,09***	***0,04***
H. RMS'	***0,04***	***0,03***	***0,01***
H. Skewness'	***2,34***	***1,60***	***0,02***
H. STD'	***0,034***	***0,030***	***0,01***
H. Uniformity'	***0,09***	***0,06***	***0,01***
H. Variance'	***11*10^{-4}***	***7*10^{-4}***	***0,01***
H. Quantile 0.1'	***133824,06***	***783,65***	***0,02***
H. Quantile 0.2'	***145819,71***	***949,64***	***0,04***
H. Quantile 0.3'	***153549,32***	***1082,50***	***0,04***
H. Quantile 0.4'	***159145,90***	***1214,94***	***0,04***
H. Quantile 0.5'	***164001,52***	***1359,98***	***0,04***
H. Quantile 0.6'	***168141,54***	***1517,81***	***0,04***
H. Quantile 0.7'	*172362,03*	*1695,74*	*0,07*
H. Quantile 0.8'	*177016,59*	*1887,72*	*0,21*
H. Quantile 0.9'	*183321,89*	*2126,25*	*0,10*

In bold the significant features; *S:* signal, *H:* histogram.

IV. Conclusion

In this work we characterised a sub set of Radiomics features, on ADC maps of rare and heterogeneous STSs.

Many of the first order statistic features were significantly different between patients with intermediate and high grade STSs. In particular, we found that probably because of the intrinsic heterogeneity of the ADC of these lesions, the features calculated on the histogram of ADC maps seem to better discriminate between these two histological grades.

References

[1] C. Parmar, R. T. H. Leijenaar, P. Grossmann, E. Rios Velazquez, J. Bussink, D. Rietveld, M. M. Rietbergen, B. Haibe-Kains, P. Lambin, and H. J. W. L. Aerts, "Radiomic feature clusters and Prognostic Signatures specific for Lung and Head & Neck cancer," *Sci. Rep.*, vol. 5, p. 11044, 2015.

[2] R. Fisher, L. Pusztai, and C. Swanton, "Cancer heterogeneity: implications for targeted therapeutics.," *Br. J. Cancer*, vol. 108, no. 3, pp. 479–85, 2013.

[3] G. Demetri, R. Benjamin, E. Casper, T. DeLaney, and M. Heslin, "Soft Tissue Sarcoma: Clinical practice guidelines in oncology," *J. Cancer Res. Clin. Oncol.*, vol. 122, no. 7, pp. 381–382, Mar. 1996.

[4] N. Li, R. Yang, W. Zhang, H. Dorfman, P. Rao, and R. Gorlick, "Genetically transforming human mesenchymal stem cells to sarcomas: Changes in cellular phenotype and multilineage differentiation potential," *Cancer*, vol. 115, no. 20, pp. 4795–4806, 2009.

[5] X. Wang, M. A. Jacobs, and L. Fayad, "Therapeutic response in musculoskeletal soft tissue sarcomas: Evaluation by MRI," *NMR in Biomedicine*, vol. 24, no. 6. pp. 750–763, 2011.

[6] S. A. Khedr, M. A. Hassaan, N. M. Abdelrazek, and A. Y. Sakr, "Diagnostic impact of echo planar diffusion-weighted magnetic resonance imaging (DWI) in musculoskeletal neoplastic masses using apparent diffusion coefficient (ADC) mapping as a quantitative assessment tool," *Egypt. J. Radiol. Nucl. Med.*, vol. 43, no. 2, pp. 219–226, 2012.

[7] A. Surov, S. Nagata, A. A. A. Razek, S. H. Tirumani, A. Wienke, and T. Kahn, "Comparison of ADC values in different malignancies of the skeletal musculature: a multicentric analysis," *Skeletal Radiology*, 2015.

[8] D.-M. Koh and D. J. Collins, "Diffusion-weighted MRI in the body: applications and challenges in oncology.," *AJR. Am. J. Roentgenol.*, vol. 188, no. June, pp. 1622–1635, 2007.

[9] T. S. Yoo, M. J. Ackerman, W. E. Lorensen, W. Schroeder, V. Chalana, S. Aylward, D. Metaxas, and R. Whitaker, "Engineering and algorithm design for an image processing Api: a technical report on ITK--the Insight Toolkit.," *Stud. Health Technol. Inform.*, vol. 85, pp. 586–92, Jan. 2002.

[10] H. J. W. L. Aerts, E. R. Velazquez, R. T. H. Leijenaar, C. Parmar, P. Grossmann, S. Cavalho, J. Bussink, R. Monshouwer, B. Haibe-Kains, D. Rietveld, F. Hoebers, M. M. Rietbergen, C. R. Leemans, A. Dekker, J. Quackenbush, R. J. Gillies, and P. Lambin, "Decoding tumour phenotype by noninvasive imaging using a quantitative radiomics approach.," *Nat. Commun.*, vol. 5, p. 4006, 2014.

[11] a Janecek and W. Gansterer, "On the Relationship Between Feature Selection and Classification Accuracy.," *J. Mach. Learn. Res.*, vol. 4, pp. 90–105, 2008.

[12] W. B. Powell, *Approximate Dynamic Programming: Solving the Curses of Dimensionality: Second Edition*. 2011.

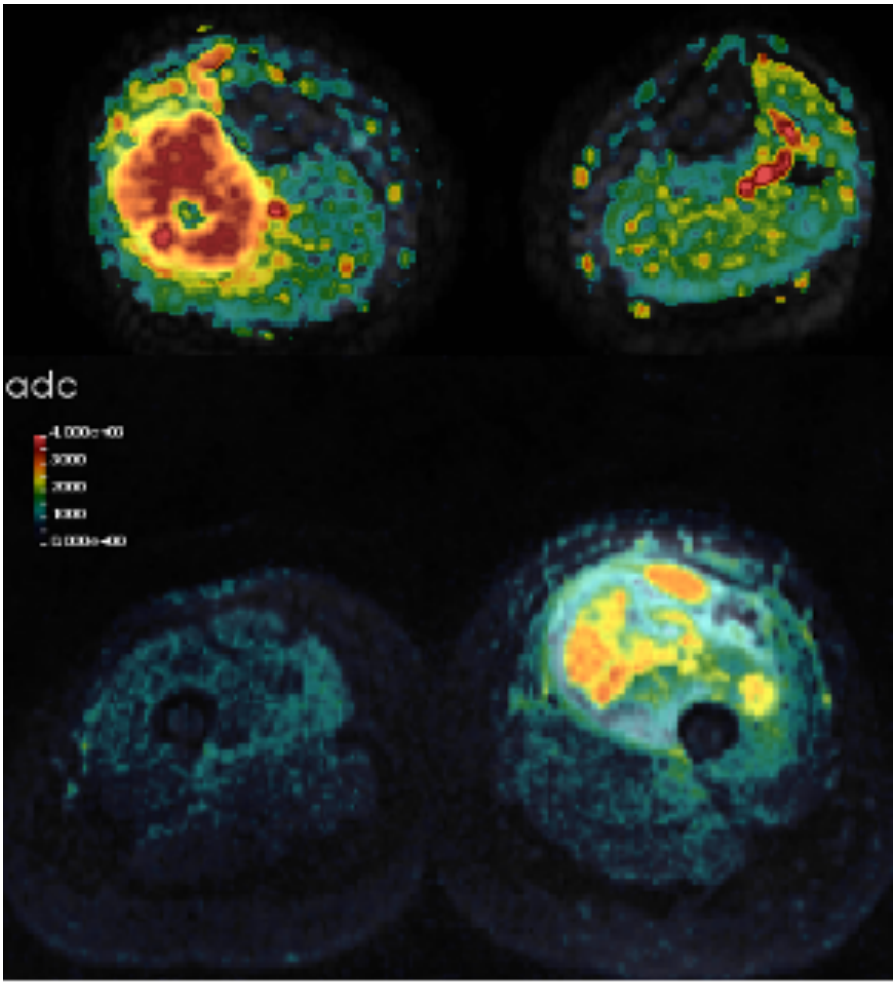

Figura 1 In figure is reported an example of an intermediate (top) and a high (bottom) grade STSs ADC map.

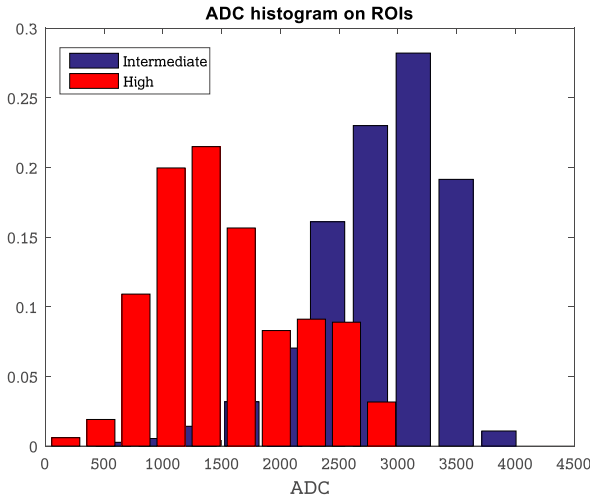

Figura 2: Histogram of intermediate(Blue) and high(red) grade STS of two representing patients

The added value of structured report in medical imaging. How to define standards for radiological and ultrasonographic investigations and the opinion of the Health Technology Assessment.

Manuela Stroili[1], Michele Bertolotto[2] and Elena Serena[2,2]
[1] *Department Health Technology Assessment, Medical Center Hospital "Ospedali Riuniti di Trieste",*
[2] *Department and Institut of Radiology, Medical Center Hospital and Residency in Radiodiagnostic, University of Triest*

***Abstract*— Structured reporting (SR) represents a relatively recent form of radiological report which aims to standardize both the format and the vocabulary used. The SR can improve communication between radiologists and patients and between radiologists and clinicians. The objective is creating first standards for building a structured report containing headings easy to interpret by the patients' referring physician and by the patients themselves.**

***Keywords*— Radiological structured report, HTA, health documentation, sonologist, bioimaging sciences.**

I. INTRODUCTION

Radiological investigations in healthcare are performed to obtain a diagnosis based on symptoms reported by the patients or their family or to confirm pathologies detected in screening programmes. After having studied and interpreted the images the radiologist writes his opinion in a document called medical report, which is delivered to the patient and physician for the purpose of seeking the best treatment as soon as possible.

II. THE PROBLEM OF THE CLARITY OF DIAGNOSIS

The report written by the radiologist is then handed off to other people that must understand it exactly and without doubts. It is essential to help decide drug therapy, invasive procedures, operability of patient and what type of surgical technique should be used for the best patient's outcome, either laparoscopic, robotic, or with an open approach. The greater the clarity of written text, the better the understanding by the patient, physician and surgeon. In many instances the radiology service delivers a CD with the images along with the paper's report that describes the diagnosis. However, understanding of the images contained within the CD requires a medical expertise and availability of technologies for their visualization. In a hospital, if the workflow allows, the radiologist tries to illustrate the imaging findings of inpatients to clinicians with a different expertise, such as surgeons, specialists in internal diseases, oncologists, radiation oncologist, etc. Possible therapeutic workflows are discussed with the aim to improve patients' survival with the best quality of life. This process cannot be used for outpatients. As a matter of fact, delivery of a CD cannot replace the discussion with an imaging expert, and the clarity of the medical report becomes the key instrument for image interpretation. Regardless of specialization, no guidelines are available in Europe for structured reporting of ultrasonographic and radiological investigations[1],[2],[5].

III. LOGICAL ANALYSIS, LANGUAGE AND WRITING

The first western theoreticians dealing with the identity of being and with use of language was Heraclitus of Ephesus (550-480 BC) who gave the name logos, a threefold law-harmony, Word-speech, thought-right reality. Heraclitus was probably the first to connect the form to content. Aristotle (384-322 BC Greece) introduced the logical analysis to draw formally correct conclusions, descending from the universal to the particular, and broke down into its simplest elements a reasoning, in our case to represent themselves in writing. In his book "Prior Analytics" (Logica) Aristotle exposes the leading laws: the principle of identity, for which A = A, and that of non-contradiction, whereby A ≠ not A, are not demonstrable but immediate to grasp [4].

A. The principle of Non-contradiction

The principle of non-contradiction asserts the falsity of every proposition implying that a certain proposition A and its negation, not A, are both true, at the same time and so. « It is impossible that the same attribute, at the same time, belongs and not belongs to the same item and under the same respect.» Aristotele, *Metafisica*. In a logical system a statement and its negation cannot stay together. Since all claims are true (including their negations) they would not be able to communicate a usable information. In mathematical logic a finite number of prerequisites brings to a final statement acting as conclusion [4].

B. The subjects of reasoning: the concepts

The concepts are essential for reasoning. Every concept is an institution of reality which can be represented through a definition. The concepts have two characteristics: 1. extension = capacity of a concept to refer to a number of things more or less wide; 2. understanding = number of

features specific to the definition of the concept. Usually the higher the extent the lower the ability of understanding [4].

IV. EXAMPLES OF CLASSIFICATION OF DIAGNOSIS IN INTERNATIONAL HEALTH

Since years, one of the purpose of health care is finding shared policies for naming the diagnosis of disease, conditions, health outcomes and suitable interventions to share knowledge, to carry on clinical trials, technological assessment, research and development.

A . The ICD-9-CM classification

All diseases and injuries related to patients discharged from hospitals are classified with the International Classification of Diseases, Tenth Revision, Clinical Modification (ICD-10-CM) based on definite criteria and on description in medical terms to detect the causes of morbidity and mortality.

B. International classifications DSM (diagnostic and statistical manual of mental disorders)

For psychiatric conditions DSM-5 exists, Diagnostic and Statistical Manual of Mental Disorders (DSM), approved by the Board of Trustees of the APA on December 1, 2012. Instead the ICF, upgradeable, it provides a unified and standard language for rehabilitation (WHO 2001), updating the international classification of impairments, disabilities and handicaps (ICIDH).

C. The DRG classification

For reimbursements to hospitals for acute diseases and for comparison among Hospitals the DRG classification system has been created of all patients discharged from hospitals (1982 USA Fetter-Yale University), also introduced in Italy. A DRG-grouper software assigns the DRG and MDC (Major Diagnostic Category) based on: main diagnosis at the time of hospital discharge, surgery, age, other diseases, if alive, died, discharged against doctor advice, transferred to another Department, sex and birth, weight. This system aggregates the 16,000 ICD9-CM system disease diagnoses in about 600 homogeneous groups.

D. The TNM classification for staging of cancers

The TNM system classifies malignant tumors on anatomical basis for defining their extension and allows staging of them. It is used internationally for subsequent diagnostic and therapeutic choices. The T Category describes the primary tumour and its extension; category N describes locoregional lymph nodes affected by cancer; category M describes the presence of distant metastases in target organs [4],[7].

V. SCORING SYSTEM DIAGNOSTIC RADIOLOGY

We present two examples of scoring system in Bioimaging.

A. PI-RADS Scoring System

The radiological scale PI-RADS [ESUR] is increasingly used for classification of prostate cancer based on MRI features. This system consists in assigning a score on a scale of 5 points where Score 1 indicates no disease and Score 5 a strong suspicion of cancer. Clinically significant disease is highly unlikely to be present for Score 1, and highly likely to be present for Score 5 [5].

B. BI-RADS Scoring System

In breast imaging based on mammography and ultrasound features the BI-RADS Scoring System is used to assign a diagnostic code associated with an increasing risk of cancer and with other clinical recommendations useful to the Surgeon [2].

VI. THE RADIOLOGICAL REPORT AND THE AUTONOMY OF THE RADIOLOGIST

The referring doctor has the problem to put an adequate diagnostic question. The radiologist and sonologist cannot perform a superficial imaging investigation and is therefore required to examine all images carefully.

VII. FIRST PROPOSE OF STRUCTURED REPORTING WITH DRAWING FOR MRI

After benchmarking with other University Health and literature searches we propose a first list of categories for Structured Reporting with Pictures in subsequent tables 1 and 2 [4],[6]. The Categories, represented in heading form, offer a remarkable and immediately grasped understanding to the reader, especially if they are not ambiguous or contradict each other. The drawing clarifies visually the localization of the lesions encountered and removes any doubt arising from the different terminology used by the reporting radiologists.

VIII. CONCLUSION

Structured Reporting can help radiologists to describe and summarize effectively information from Bioimages, and to promote a greater quality and consistency of reporting. Diagnostic features of pathologies observed are better described without ambiguity increasing the value of the report for the medical procedure. The effectiveness of the formulation of a clear diagnosis can prevent the need for repetition of imaging investigations and can improve the appropriateness in using technology with a reduction of expenses in public health.

REFERENCES

[1] Marcovici PA, Taylor GA. “Structured radiology reports are more complete and more effective than unstructured reports,” *Am J Roentgenol*, vol 203(6), pp. 1265-71., Dec 2014.

[2] American College of Radiology. *ACR Breast Imaging and Radiological Data System Birads.* 3rd ed. 2003. Reston, VA, USA.

[3] Kushner DC, Lucey LL. “Diagnostic radiology reporting and communication: the ACR guideline.” J Am Coll Radiol vol. 2, pp.15-21, 2005.

[4] M.Stroili, “Il Referto radiologico o ecografico strutturato con disegno.Il valore aggiunto della standardizzazione della forma della diagnosi per il chirurgo e l’internista nell’Health Technology Assessment” Poster Soc.Ital.And., Congresso triveneto ,Trieste, 2016.

[5] Barentsz, J. O., Richenberg, J., Clements, R., Choyke, P., Verma, S., Villeirs, G. ESUR prostate MR guidelines 2012. *European radiology*, vol. *22*(4), pp. 746-75, 2012.

[6] Radiology AOU Padua "Report RM" 2015.

[7] Sobin, L. H., and C. H. Wittekind. "UICC TNM classification of malignant tumors." 2012

TABLE 1 - ADMINISTRATIVE DATA AND PERSONAL DETAILS OF THE PATIENT IN STRUCTURED REPORT

Numering	The Report Categories	Description
1	Place and dispenser	Name of the city and the hospital or clinic where you made the exam
2	Finding responsible for delivery of the report and for communications with the patient	phone and e-mail address of the Secretariat of the Service
3	Numbering of report	number of unique exam report, with bar code and number
4	Pazient	master data with telephone and email of the patient and a family member and accompanying persons
5	The patient's clinical data	presence of anatomical-patologic report, blood tests and other exams

TABLE 2 - CLINICAL CATEGORIES OF STRUCTURED REPORT FOR STAGING PROSTATE CANCER IN RMI

Numering	The Report Categories	Description
1	Clinical question	clinical indication of the examination ex cancer staging
2	Equipment and Technique for examination	locating equipment and technique of examination
3	Dimension	brief description of the form with accurate measurements in mm and cm of the three principal axes: longitudinal, transverse and antero-posterior
4	Morfology	description of the structure (homogeneous, inhomogeneous, with identification of potential injuries measured in cm) and its relation with adjacent organs, by infiltration or compression
5	Lesions and Margins	description of form and size in mm/cm of any detected lesions, their home and their nature using scales of reference (ex: PI-RADS, BI-RADS) with scale legend after signing the scoresheet.
6	Prostate capsule	profile involvement by the newly-formed, traveling and for how many mm thick
7	Seminal vesicles	if infiltrated by tumor or tablets
8	Urinary tract (bladder and excretory pathways)	if infiltrated, tablets or mild tumour impression
9	Pelvic lymph nodes	the presence or absence of pathological lymph drainage valve and iliac stations
10	Pelvic skeletal structure	structural changes in the examined
11	Conclusion	clear summary of the findings
12	Score System	Reporting scale used with legend (es Pi-RADS, BI-RADS)
13	CD e Picture	Description of the area affected with anatomical localization of lesions and their relationship with the organs and glands are contiguous
14	Number of pages	Component pages in the report
15	Technical executor	Name and qualification of the technical executor
16	Radiologist	Name of radiologist
17	Physician's signature	Manual or digital signature of the radiologist

Feasibility of constrained spherical deconvolution and probabilistic tractography in the pediatric clinical setting

B. Toselli[1], D. Tortora[2], M. Severino[2], G. Morana[2], A. Rossi[2], and M. Fato[1]
[1]*DIBRIS, University of Genoa, Italy*
[2]*Neuroradiology Unit, Istituto Giannina Gaslini, Genoa, Italy*

Abstract— **Constrained spherical deconvolution (CSD) and probabilistic tractography allow the reconstruction of white matter tracts in the brain with higher precision compared to deterministic tractography algorithms. The optimal acquisition parameters required for CSD are not always suitable for children and neonates in the clinical setting. The aim of this work was to test the feasibility of probabilistic tractography with CSD on MR data with acquisition parameters commonly used for pediatric clinical MR studies.**

Keywords— **constrained spherical deconvolution, tractography, children, white matter fibers**

I. Introduction

DIFFUSION-WEIGHTED MR imaging (dMRI) has become the imaging method of choice to investigate the white matter (WM) microstructure *in vivo*. In particular, by combining the directional information and magnitude of anisotropic diffusion of the individual voxels, the trajectories of the WM bundles may be reconstructed and quantitative analysis of WM organization can be performed.

Based on the fiber orientations obtained from diffusion tensor imaging (DTI), the trajectories of a fiber pathway can be tracked using deterministic fiber tracking methods, including the FACT (Fiber Assignment by Continuous Tracking) method [1]. However, while these approaches are ideal for describing a single fiber population within a given voxel, they are limited in delineating the full dispersion of fiber pathways, parts of which pass through complex WM regions such as the centrum semiovale, where major WM tracts including the corticospinal tract, the superior longitudinal fasciculus, and the corpus callosum are known to intersect.

Constrained spherical deconvolution (CSD) and probabilistic tractography estimate, for each image voxel, the configuration of the fibers, called fiber orientation distribution (FOD), and reconstruct WM pathways by sampling this distribution at each step and following the obtained direction [2]. Making no assumptions on the fibers' configuration in each voxel, CSD allows the reconstruction of crossing tracts with higher precision.

The optimal acquisition scheme of the dMRI sequence for CSD was described by Tournier et al, and requires a strong magnetic field (3 Tesla), a high number of directions (at least 60), and high b-values (3000 ms) [2, 3]. This protocol requires a long acquisition time and is often not feasible in a clinical setting, especially in the pediatric age group.

The aim of this work was to test the feasibility of probabilistic tractography and CSD in a group of normal neonates and children studied with a clinical dMRI protocol on a 1.5 Tesla scanner.

II. Methodology

A. Subjects

Processing and analysis were conducted retrospectively on data previously acquired at the Istituto Giannina Gaslini in Genoa. We selected the dMRI studies of 10 neonates studied at term, and 3 children aged 5 to 9 years at the time of scan. All subjects underwent brain MR imaging for transient febrile convulsions or headaches. All were diagnosed as neurologically and developmentally normal by pediatric neurologists and had normal MR imaging findings. Parents signed an informed consent prior to image acquisition.

B. Image acquisition and pre-processing

Diffusion-weighted MR images were acquired with a 1.5 T MR unit (Philips Intera Achieva version 2.6; Best, the Netherlands), using a Reg DTI-high isoSENSE acquisition sequence commonly used in clinical practice. Acquisition parameters were as follows: 40 axial slices; slice thickness, 2 mm; acquisition matrix, 96 x 96 (in-plane resolution, 1.67 x 1.67 mm); TR/TE, 5156.53/78.414 ms. The signal was acquired along 34 non-collinear directions in the space, using a b-value of 800 s/mm^2. One measurement without diffusion weighting was also performed (b = 0 s/mm^2).

All brain MRI studies included a T1 or T2 anatomical sequence, with different acquisition parameters based on patient age; these sequences were used to assess the presence of brain lesions or malformations.

As a preprocessing step, all diffusion-weighted images were corrected for eddy currents using FSL tools [4].

C. Tractography

Fiber tracking was performed using the Mrtrix3 package (J-D Tournier, Brain Research Institute, Melbourne, Australia, https://github.com/MRtrix3/mrtrix3) [5] to reconstruct the WM tracts of interest. Each tract was delineated using a single-ROI or multi-ROI approach, depending on the tract of interest: during tractography, streamlines were seeded only from the given ROIs, with seeding points distributed uniformly inside the ROIs.

The spherical deconvolution method was used to estimate the FOD in each image voxel, while the streamlines were computed using the iFOD2 algorithm [6], which implements probabilistic tracking on the computed FODs. For each tract, 10,000 streamlines were generated, while the maximum

number of trials was set to 1 million. The parameters were set to the values which empirically proved to be the most appropriate for the data: in particular, the maximum streamline length was set to 200 mm, the maximum angle between tractography steps was 50°, and the minimum FA value (under which streamlines were terminated) was set to 0.3.

The same ROIs were used to perform tractography with a deterministic algorithm (FACT) using the Tensor_Det algorithm, which implements the traditional DTI methodology on the Mrtrix3 package. Parameters were left at the default values, which gave the best results for the data (maximum angle between steps, 9°; FA cutoff, 0.1; maximum length, 177 mm); for each tract, 10,000 streamlines were generated, with a maximum trial number of 1 million.

D.ROI placement and tract qualitative analysis

Three main white matter tracts were selected for this work: the cerebellar-thalamic tracts (CTT), corticopontocerebellar tract (CPCT), and corticospinal tracts (CST), reconstructed separately for the two hemispheres. The CPCT and the CST were reconstructed using a single seeding ROI, while two ROIs were defined for the CTT. ROIs were placed according to Catani [7]. Additional post-processing of the reconstructed tracts was not performed.

Visual assessment of the tracts was performed independently by two expert pediatric neuroradiologists (D.T. and M.S.) using a five point scale on which 1 point indicated unacceptable quality, 2 points indicated poor quality, 3 points indicated fair quality, 4 points indicated good quality, and 5 points indicated excellent quality [8]. The mean scores and standard deviations were reported for each tract and reconstructing techniques. The inter-observer agreement was evaluated with Cohen Kappa test.

III. Results

Visual assessment results and inter-reader agreement evaluation are reported in Table 1.

TABLE I
MEAN VISUAL ASSESSMENT SCORES

		Reader 1 (mean±SD)	Reader 2 (mean±SD)	K	p
CTT	FACT	2.31 ± 0.48	2.23 ± 0.44	.806	.003
	CSD	3.54 ± 0.52	3.62 ± 0.50	.843	.002
CPCT	FACT	2.31 ± 0.48	2.15 ± 0.38	.581	.021
	CSD	3.69 ± 0.48	3.69 ± 0.48	.639	.021
CST	FACT	2.38 ± 0.50	2.46 ± 0.52	.843	.002
	CSD	3.62 ± 0.50	3.54 ± 0.52	.843	.002

Visual assessment results and inter-reader agreement evaluation for the reconstructed tracts.

Figures show the results obtained with the two reconstructing techniques in a fully myelinated child (Fig. 1) and in an unmyelinated neonate (Fig. 2).

IV. Conclusion

This work demonstrates the feasibility of spherical deconvolution and probabilistic tractography in neonates and children studied on a 1.5 Tesla scanner with a clinical DTI protocol. Indeed, this study shows a 100% success rate for CSD fiber tractography reconstruction of afferent (CPCT) and efferent (CTT) cerebellar tracts and the CST. Moreover, CSD allowed reconstruction of WM tracts with better image quality compared to a deterministic approach, even in neonates with unmyelinated brains. To our knowledge, no previous study tested the feasibility of this technique in normal neonates and children. Fiori et al. recently reported preliminary data on 15 children with cerebellar atrophy/hypoplasia using a similar approach, showing the potential utility of quantitative analysis of scalars of the cerebellar WM tracts obtained with CSD [9]. Our data further confirm this initial experience, and lend support to the hypothesis that this technique may be viable in the clinical setting. Moreover, the present data expand the potential applications of CSD to larger patient populations, regarding both age and clinical conditions.

The main limitation of this study is the small sample size limiting the robustness of the statistical comparison. However, these convincing results encourage to perform further studies on a larger group of normal neonates and children, and to apply this technique to different pediatric brain diseases and malformations.

References

[1] S. Mori, B.J. Crain, V.P. Chacko, and P. Van Zijl, "Three□dimensional tracking of axonal projections in the brain by magnetic resonance imaging", Annals of neurology, vol. 45, pp. 265-269, 1999

[2] J.D. Tournier, F. Calamante, D.G. Gadian and A. Connelly, "Direct estimation of the fiber orientation density function from diffusion-weighted MRI data using spherical deconvolution", NeuroImage, vol. 23, pp. 1176-1185, 2004

[3] J.D. Tournier, F. Calamante and A. Connelly, "Determination of the appropriate b value and number of gradient directions for high-angular-resolution diffusion-weighted imaging", *NMR in Biomedicine*, vol. 26, pp. 1775-1786

[4] M. Jenkinson, C.F. Beckmann, T.E. Behrens, M.W. Woolrich and S.M. Smith, "FSL", *NeuroImage*, vol 62, pp. 782-790, 2012

[5] J.D. Tournier, F. Calamante and A. Connelly, "MRtrix: Diffusion tractography in crossing fiber regions", *International Journal of Imaging Systems and Technology,* vol. 22, pp. 53-66, 2012

[6] J.D. Tournier, F. Calamante and A. Connelly, "Improved probabilistic streamlines tractography by 2nd order integration over fibre orientation distributions", *Proceedings of the International Society for Magnetic Resonance in Medicine*, 2010, 1670

[7] M. Catani and M.T. De Schotten, M.T., "A diffusion tensor imaging tractography atlas for virtual in vivo dissections", *Cortex*, vol. 44, pp.1105-1132, 2008

[8] P. Beddy, R.D. Rangarajan, M. Kataoka, P. Moyle, M.J. Graves, and E. Sala, "T1-weighted fat-suppressed imaging of the pelvis with a dual-echo Dixon technique: initial clinical experience", *Radiology*, vol. 258, pp. 583-589, 2011

[9] S. Fiori, A. Poretti, K. Pannek, R. Del Punta, R. Pasquariello et al., "Diffusion tractography biomarkers of pediatric cerebellar hypoplasia/atrophy: preliminary results using constrained spherical deconvolution", *AJNR Am J Neuroradiol.*, 2015 [Epub ahead of print]

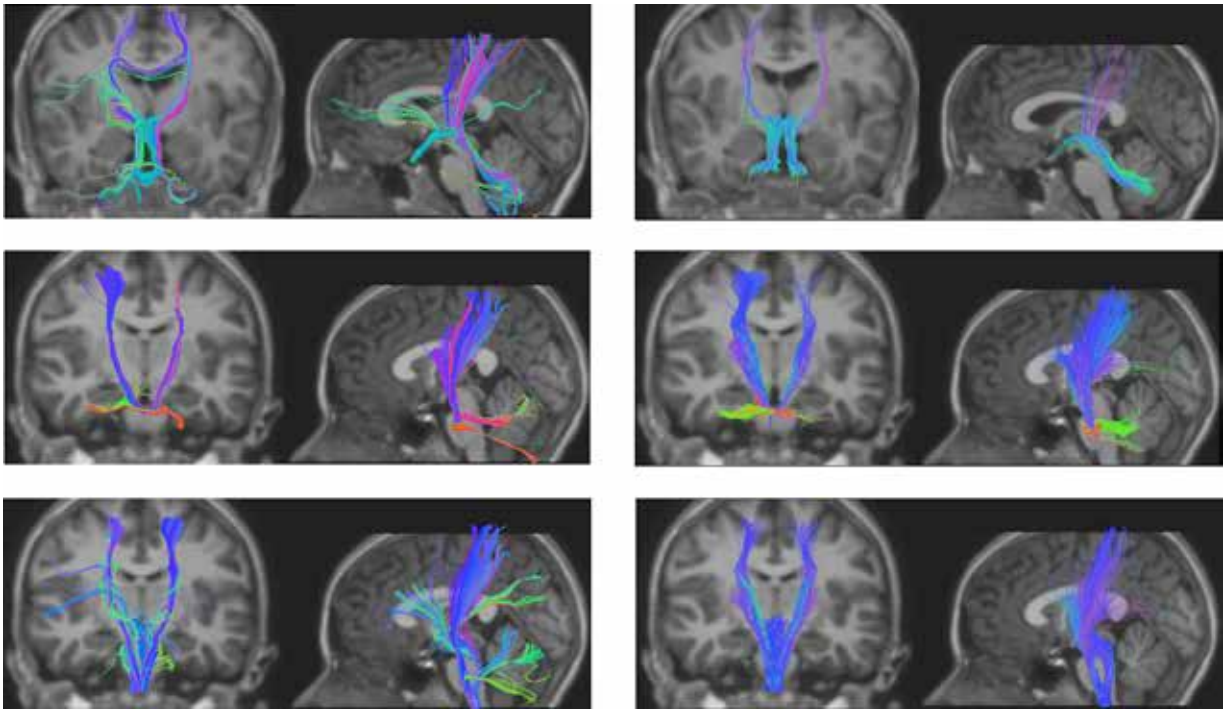

Figure 1. Comparison between deterministic (FACT) and probabilistic CSD tractography in a 9-year old child. The first column shows the reconstructed bundles for cerebellar-thalamic tracts (top row), corticopontocerebellar tracts (middle row) and corticospinal tract (bottom row) obtained with a traditional DTI deterministic tracking method (FACT), while the second column depicts the same reconstructed bundles obtained with probabilistic CSD tractography. Bundles are overlaid on coronal and sagittal T1-weighted images. Figures are representative of the global shape of the reconstructed bundles, irrespective of the cropping of the anatomic section.

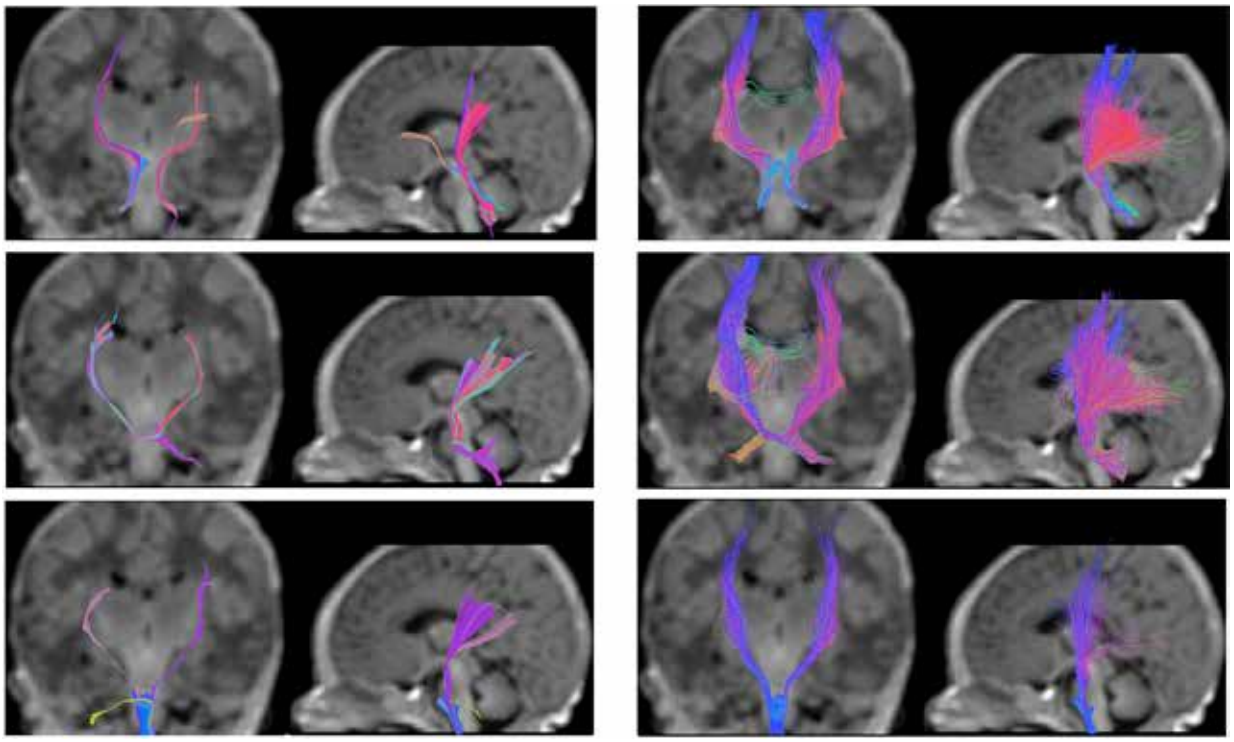

Figure 2. Comparison between deterministic (FACT) and probabilistic CSD tractography in a 3-day old neonate. The first column shows the reconstructed bundles for cerebellar-thalamic tracts (top row), corticopontocerebellar tracts (middle row) and corticospinal tract (bottom row) obtained with a traditional DTI deterministic tracking method (FACT), while the second column depicts the same reconstructed bundles obtained with probabilistic CSD tractography. Bundles are overlaid on coronal and sagittal T1-weighted images. Figures are representative of the global shape of the reconstructed bundles, irrespective of the cropping of the anatomic section.

BIOINFORMATICA

GeenaR: a flexible approach to pre-process, analyse and compare MALDI-ToF mass spectra

E. Del Prete[1,2], A. Facchiano[2], A. Profumo[3], C. Angelini[4], and P. Romano[3]
[1] *Dipartimento di Scienze, Università della Basilicata, Via dell'Ateneo Lucano 10, 85100, Potenza (Italy)*
[2] *Istituto di Scienze dell'Alimentazione, CNR, Via Roma 64, 83100 Avellino (Italy)*
[3] *IRCCS AOU San Martino IST, Largo Rosanna Benzi 10, 16132 Genova (Italy)*
[4] *Istituto per le Applicazioni del Calcolo, CNR, Via Pietro Castellino 111, 80131 Napoli (Italy)*

***Abstract*—Mass spectrometry is a set of technologies with many applications in characterizing biological samples. Due to the huge quantity of data, often biased and contaminated by different source of errors, and the amount of results that is possible to extract, an easy-to-learn and complete workflow is essential. GeenaR is a robust web tool for pre-processing, analysing, visualizing and comparing a set of MALDI-ToF mass spectra. It combines PHP, Perl and R languages and allows different levels of control over the parameters, in order to adapt the work to the needs and expertise of the users.**

***Keywords*—Mass Spectrometry, Proteomics, Statistical Analysis, Web tool**

I. Introduction

MASS spectrometry is, nowadays, one of the most important sources of biological data in proteomics [1][2][3]. This information is relevant for several applications, e.g., the identification of cancer biomarkers [4], the detection of food frauds [5], or the identification of doping substances in the fluids of athletes [6]. Matrix Assisted Laser Desorption Ionization - Time of Flight (MALDI-ToF) is one of the most used combined technology in mass spectrometry, because of the big volume of data which can be obtained in a short time, the high resolution and good accuracy and sensitivity [7].

Raw mass spectra are usually blurred with different kinds of disturbs (background noise, chemical noise, unnatural noise): thus, various pre-processing steps are compulsory in order to get clean mass spectra, in which the detection of the most important peaks is easier and more accurate [8]. Geena 2 [9] is a web tool, simple and intuitive to use for scientists from different research areas, with three levels of feature sets of increasing complexity, which are under the control of the user. Starting from its architecture, it is possible to integrate further tools in order to improve the analysis workflow with, e.g., the recognition of new data format, the implementation of new algorithms for the cleaning of the data, the graphical visualization and reporting of results, and the adoption of advanced statistics for the comparison of mass spectra.

The aim of this work is the extension of Geena 2 features, thus developing the GeenaR tool, with the aim of providing a wider range of statistical and visualization methods to the users, without making the use of the tool more difficult for researchers with little or no programming skills. To this aim, we will take advantage of the availability of several packages for mass spectrometry statistical analysis, written in R language [10], that are going to be integrated in the system.

II. Materials and Methods

A. Data type

A mass spectrum is an indented profile, with a trend and some typical peaks that characterize the source. The simplest format to describe a MALDI-ToF mass spectrum is a two-dimensional array, in which the first column represents the m/z values (mass over charge) and the second column represents the corresponding abundances, that is the abundance of the molecule having the given m/z value in the sample source. Spectrometers have, often, an embedded software for the representation of spectra as matrixes in various formats (txt, TSV, CSV). Other robust formats, recognized as standard in mass spectrometry, such as mzML (11), have been developed by the Human Proteome Organization Proteomics Standards Initiative (HUPO-PSI).

B. Workflow

The complete pipeline of GeenaR is shown in Fig.1. The main sections are three (preliminary, summary, analysis). Some features are already available in Geena 2, others under development thanks to the integration of the R environment. The details are described below.

MS Data Import. Mass spectra must be converted in a readable format, as already described in the previous paragraph. After the import step, the output format is in the text matrix format, thus mass spectrometry data are simple to read, both by users and by software, portable and re-usable.

MS Data Pre-Processing. After a check about the presence of a congruent number of data and about the monotonicity of the m/z values, different transformations over each mass spectrum are necessary. Briefly: isotopic peaks identification and joining, trimming, variance stabilization, smoothing, baseline correction, normalization [9][12].

Peak Detection. It is a crucial reduction step, because selected peaks represent the entire mass spectrum for the following evaluations. It is necessary to reconcile replicate spectra obtained from the same sample into a unique, representative spectrum. This can be done by aligning spectra over the m/z values and computing the average abundance for aligned peaks. For the selection of a reduced number of peaks, a threshold can be defined, either by interpolating some m/z values or by testing different SNRs (selected with an estimation algorithm).

Exploratory Data Analysis. Tidy mass spectra are shown in tabular and graphical forms, along with some basic

descriptive information, e.g., number of mass spectra for sample, number of peaks for mass spectrum, and so on. Particular attention is focused on the reporting step, in order to provide a log file containing the selected parameters and guarantee the reproducibility of the results.

Advanced Statistics. A feature matrix is a stricter representation of a mass spectrum extracted from the peaks list. Two mass spectra can then be compared by means of the corresponding feature matrices, in order to verify if they come from the same sample, using a spectrum similarity measure [13]. Furthermore, all feature matrices from several samples can be used to build a distance matrix and create a dendrogram for the selected mass spectra [14]. Finally, a variable selection method [15] can be applied to rank the peaks by importance, and a statistical validation can be carried out.

C. Algorithms overview

An original set of heuristic algorithms is already available in Geena 2. In short: the identification of isotopic peaks is performed by taking into account molecular weight of signals and the related trend of abundances; the normalization may be performed on the basis of a purposely included molecule; the peak selection may be performed by means of a threshold line, built by linearly interpolating values provided for given m/z values; the alignment is performed by selecting the nearest peaks, within a limited m/z difference, in the different mass spectra.

By means of some R packages [16], we aim at adding new statistical methods which are highly relevant for mass spectra analysis, like e.g., square root transformation for the variance stabilization, Savitsky-Golay filter for the smoothing, Statistics-sensitive Non-linear Iterative Peak-clipping (SNIP) algorithm for the baseline correction, Total Ion Current (TIC) method for the normalization, Local Weighted Scatterplot Smoothing (LOWESS) technique for the alignment, Median Absolute Deviation (MAD) method for the peak detection, cosine correlation as similarity measure, Linear Discriminant Analysis (LDA) method for the variable selection.

D. Development environment

GeenaR is written in PHP, Perl (from Geena 2) and R languages. In detail, we are incorporating the R packages *MALDIquant* and *MALDIquantForeign* [12] for mass spectra pre-processing and analysis, *OrgMassSpecR* [17] for mass spectra comparison, *dendextend* [18] and *pvclust* [19] for clustering, and *sda* [20] and *crossval* [21] for variable selection.

III. Discussion

Mass spectrum is an instant view of the proteome of a biological sample. The most important peaks of the spectrum may represent the complete mass spectrum, in order to perform advanced statistical analysis and characterize the sample. The analysis process must be simple, fast, complete and validated in order to support users having limited programming skills. Our flexible approach in GeenaR is simple, since all parameters are under the control of the users through a simple interface. The combination of PHP, Perl and R guarantees flexibility and high performance both in the analysis and in the output of results. The proposed pipeline is complete since it starts from the spectra generated by spectrometers, pre-process raw data, extract relevant information and execute advanced statistical analyses. The adoption of an extended statistical control supports in-silico validation of data, reproducibility of analyses and accuracy of results.

References

[1] H. Xuemei, A. Aslanian, and J. R. Yates, "Mass Spectrometry for proteomics," *Current opinion in chemical biology*, 12(5), pp. 483-490, 2008.

[2] M. Wagner, D. Naik, and A. Pothen, "Protocols for disease classification from mass spectrometry data," *Proteomics*, 3(9), pp. 1692-1698, 2003.

[3] L. Kall and O. Vitek, "Computational Mass Spectrometry–Based Proteomics," *PLoS Computational Biology*, 7(12), 2011.

[4] D.A. Prieto, D. J. Johann , B.R. Wei, X. Ye, K. C. Chan, et al., "Mass spectrometry in cancer biomarker research: a case for immunodepletion of abundant blood-derived proteins from clinical tissue specimens," *Biomarkers in medicine*, 8(2), pp. 269-286, 2014.

[5] M.F. Mazzeo, B. De Giulio, G. Guerriero, G. Garcia, A. Malorni, et al., "Fish authentication by MALDI-TOF Mass Spectrometry," *Journal of Agricultural and Food Chemistry*, 56(23), pp. 11071-11076, 2008.

[6] M. Thevis, and W. Schanzer, "Mass spectrometry in doping control analysis", *Current Organic Chemistry*, 9(9), pp. 825-848, 2008.

[7] R. J. Cotter, "Time-of-flight mass spectrometry: instrumentation and applications in biological research," *American Chemical Society*, Washington DC, 1997.

[8] K. R. Coombes, K. A. Baggerly, and J. S. Morris, "Pre-processing mass spectrometry data," *Fundamentals of Data Mining in Genomics and Proteomics*, Springer US, pp. 79-102, 2007.

[9] P. Romano, A. Profumo, M. Rocco, R. Mangerini, F. Ferri, and A. Facchiano, "Geena 2, improved automated analysis of MALDI/TOF mass spectra," *BMC Bionformatics*, 17(Suppl 4):61, pp. 247-269, 2016.

[10] R Core Team, "R: a language and environment for statistical computing," *R Foundation for Statistical Computing*, Vienna, Austria, 2014. URL: http://www.R-project.org/.

[11] E. W. Deutsch, "Mass spectrometer output file format mzML," *Methods in molecular biology (Clifton, NJ)*, 604, pp. 319–331, 2010.

[12] S. Gibb, and S. Strimmer, "MALDIquant: a versatile R package for the analysis of mass spectrometry data", *Bioinformatics*, 28(17), pp. 2270-2271, 2012.

[13] K. Seongho, and Z. Xiang, "Comparative analysis of mass spectral similarity measures on peak alignment for comprehensive two-dimensional gas chromatography mass spectrometry," *Computational and Mathematical Methods in Medicine*, vol. 2013, 2013.

[14] S. Sauer, A. Freiwald, T. Maier, M. Kube, R. Reinhardt, et al., "Classification and identification of bacteria by mass spectrometry and computational analysis," *PLoS ONE*, 3(7), 2008.

[15] M. Ahdesmaki, and K. Strimmer, "Feature selection in omics prediction problems using cat scores and false nondiscovery rate control", The Annals of Applied Statistics, 4(1), pp. 503-519, 2010.

[16] R. Gentleman, V. J. Carey, D. M. Bates, B. Bolstad, M. Dettling, et al., "Bioconductor: open software development for computational biology and bioinformatics", *Genome Biology*, 5, 2004. URL: https://www.bioconductor.org/.

[17] N. G. Dodder, and K. M. Mullen, "OrgMassSpecR: organic mass spectrometry," R package version 0.4-4, 2014. URL: http://CRAN.R-project.org/package=OrgMassSpecR.

[18] T. Galili, "dendextend: an R package for visualizing, adjusting, and comparing trees of hierarchical clustering," Bioinformatics, 31(22), pp. 1-3, 2015.

[19] R. Suzuki, and H. Shimodaira, "pvclust: hierarchical clustering with p-values via multiscale bootstrap resampling," R package version 2.0-0, 2015. URL: http://CRAN.R-project.org/package=pvclust.

[20] M. Ahdesmaki, V. Zuber, S. Gibb, and K. Strimmer, "sda: shrinkage discriminant analysis and CAT score variable selection," R package version 1.3.7, 2015. URL: http://CRAN.R-project.org/package=sda.

[21] K. Strimmer, "crossval: generic functions for cross validation," R package version 1.0.3, 2015. URL: http://CRAN.R-project.org/package=crossval

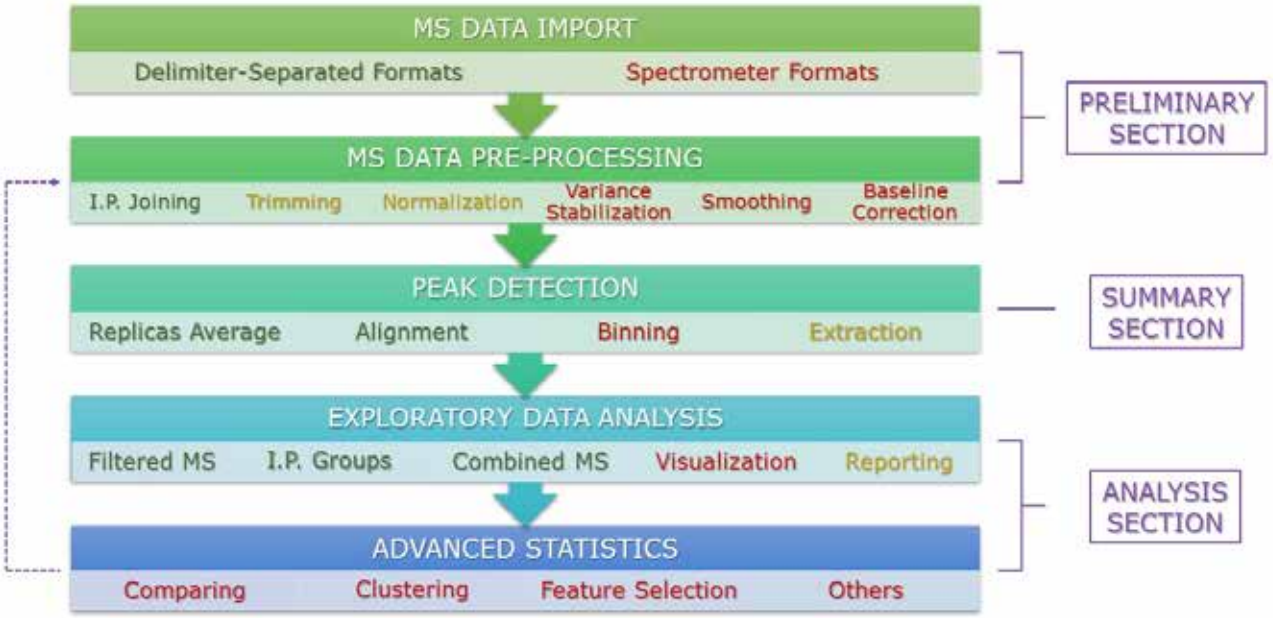

Figure 1: GeenaR analysis workflow. The pipeline is divided in three main section: preliminary, summary and analysis. Each section incorporates different tools highlighted with three distinct font colours: green denotes the tools already available in Geena 2; yellow denotes the tools available in Geena 2 and that will be extended in GeenaR by means of novel algorithms; red denotes the novel tools, currently under development and/or implementation, that will be included in GeenaR. The feedback arrow on the left represents a mass spectrometry data re-processing, useful in order to refine results after possible unexpected evidences.

Multiple variant callers and amplicon target resequencing in clinical bioinformatics

V.Favalli[1], M. Di Giovannantonio[1], E.Disabella[1], E.Arbustini[1].
[1] *Center for Inherited Cardiovascular Diseases, IRCCS Fondazione Policlinico San Matteo, Pavia, Italy*

***Abstract*—BRCA1/2 genetic testing in probands and family members with Hereditary Breast and Ovarian Cancer (HBOC) entered the clinical practice, in particular with introduction of Next Generation Sequencing (NGS). Guidelines for treatment and prevention management are based on presence or absence of pathogenic or probable pathogenic mutations. With the introduction of simpler preparation protocols, the focus critically shifts on analysis pipeline and interpretation. We implemented an amplicon target resequencing oriented pipeline for massive parallel sequencing of *BRCA1/2* genes.**

***Keywords*—Breast cancer, ovarian cancer, next generation sequencing, variant caller, amplicon resequencing.**

I. Introduction

In the past, *BRCA1* and *BRCA2* testing was performed on Sanger-based sequencing of the coding and flanking regions of the genes and was integrated by MLPA, exploring large gene rearrangements. In the last years, genetic testing moved from Sanger-based to next generation sequencing (NGS)-based technologies that have the major advantage of abating the time for testing. Sanger-based sequencing is now performed to confirm mutations identified by NGS and is used for cascade family screening once the mutation is identified in the probands. The assignment of a pathologic significance to missense mutations is based on consolidated evidences in existing public databases and segregation studies in families. Many missense variants are still classified as genetic variants of unknown significance (VUS). *In silico* analyses can support the interpretation of the significance of VUS but do not, by themselves, guarantee for a fully correct interpretation [1] Given the essential and unique role of pathologic mutations in *BRCA* genes for both preventive surgery and, more recently, for administering Olaparib in ovarian cancer in presence of *BRCA* mutation [2], the correct interpretation of variants is mandatory for providing patients with the most advance prevention and treatment options for HBOC syndrome. A wrong interpretation may negatively impact medical care: missing a pathologic missense mutation limits appropriate prevention and treatment strategies in both probands and carrier relatives; vice versa, wrong assignment of pathologic significance to a non pathologic VUS may induce wrong medical and surgical decisions.

In this context, the NGS analysis pipeline step of variant calling became crucial to delineate the genetic profile of the single patient. The study is focused on the problem of errors during variant calling, as both miscalling and not calling cases [3]. The aim of the study was to find the best case-specific pipeline for BRCA1/2 sequencing in terms of best balance between sensibility (not calling true positive) and sensitivity (report false positive as true).

We first chose two popular variant callers, Genome Analysis Tool Kit and Varscan2, and compared them with Miseq Reporter Illumina standard pipeline individually. The choice was driven by the idea to compare probabilistic, Bayesian statistics with a heuristic/statistic approach to call variants.

II. Materials and Methods

A. Data set

From Dec 2015 to March 2016, we analysed 56 samples from patients with breast/ovarian cancer positive history and suggestive family history.

Four samples were selected as reference set after complete sequencing using Sanger technique, and finding of six different variants (SNV in 2, Stop variant in 1, frameshift variant in 1).

Fifty-two samples were sequenced with NGS, analysed and variants identified were validated using Sanger technique.

B. Sequencing

TruSeq Custom Amplicon with specific design for BRCA1 and BRCA2 (AFP2) was used, according to Illumina preparation protocols. Mean coverage per amplicon was 600x, with mean quality score 40. All data was automatically analyzed by Miseq Reporter standard pipeline during run session, using AFP2 v2.0 manifest file.

C. Pipeline

Fastq files were extracted from Miseq machine. BWA-MEM aligner tool was used with reference sequence hg19.
Three variant calling methods was used: (1) Genome Analysis Tool Kit-3.5 (GATK,) [4], (2) Varscan 2.4.0 [5] and (3) Miseq Reporter standard pipeline. First data was pre-processed using IndelRealigner in GATK for all samples. We didn't use BaseRecalibrator (GATK) and MarkDuplicates (Picard) commands, by following the best practice procedures for amplicon protocol sequencing. All two variant caller performed the analysis with default parameters, in multisampling mode. The two vcf files obtained were used as input of the Intersect (Vcftool) command. The final vcf was composed by all variants obtained by GATK U Varscan2 (union-vcf).
Single vcf files, and union-vcf file were annotated with Variant Effect Predictor tool v86.
All methods were tested on Linux Ubuntu v 15.
Miseq Reporter vcf files were annotated using Illumina Variant Studio v2.2.

D. Performance measure of variant calling pipelines

To assess the performance of single variant caller VS union variant calling pipeline VS Miseq Reporter standard pipeline, we defined true positive (TP) variants called and Sanger validated; false positive (FP) variants called but not validated; false negative (FN) gold standard variants that were not called by a variant caller [6].

TABLE I
RESULTS OF VARIANT CALLERS

Variant caller	*Num of variants*	*TP*	*FN*	*FP*
GATK	149	100	2	49
Varscan2	188	119	3	69
Miseq Reporter	103	94	2	9
Union	170*	121	0	49

*Number of variants called and passed filters.

III. RESULTS

A. Single variant caller analysis

Results of single variant calling are reported in Table 1.

For GATK we used standard hard filtering [4]. For Varscan2 we used default filtering parameters [5].

Miseq Reporter did not call two variants, probably pathogenic, which were in the control set

GATK alone did not call two variants, one frameshift probable pathogenic, and one missense probable benign.

Varscan2 is the variant caller with the maximum number of false positive calls, and did not call three variants, 1 probable pathogenic e 2 benign.

All variant callers approach suffers the sequence composition of *BRCA 1 and 2*, rich of homopolymeric zones. Varscan2 denotes also the major difficulty in the starting and ending part of targets.

B. Union analysis and filtering

For GATK we used default parameters, for Varscan2 filtering parameters were restricted using --min-avg-qual equal to 20 and --min-coverage equal to 15.

After variant calling we filtered variants with quality by depth <6 and allele depth/read depth <20%.

The union of GATK and Varscan2 did not call false negative. The post calling filtering approach abated the number of false positive. The increase in number of samples analysed will open the possibility to deep the filtering approach and augment the sensitivity of the analysis.

IV. CONCLUSION

The variant calling phase of NGS analysis pipeline is crucial to avoid errors in correct genotyping. The evidence of a need of target based specific pipelines strategy is becoming stronger and stronger [7]. Our approach is a mixed variant calling strategy, turned to emphasize the qualities of every chosen variant caller. The sensibility of the approach was then balanced by the presence of a posteriori filtering step, specific of our experience on these genes.

Future development will be the implementation of a normalization tool for vcf files from different variant caller, selecting a standard pool of labels on which refine filtering parameters on specific target.

ACKNOWLEDGEMENT

All contents of this text are from continuous medical research on HBOC supported by the Italian Ministry of Health, Cariplo Foundation, Magica Onlus Charity, ADOS Charity.

REFERENCES

[1] Richards S, Aziz N, Bale S, Bick D, Das S, Gastier-Foster J, Grody WW, Hegde M, Lyon E, Spector E, Voelkerding K, Rehm HL, "ACMG Laboratory Quality Assurance Committee. Standards a guidelines for the interpretation of sequence variants: a joint consensus recommendation of the American College of Medical Genetics and Genomics and the Association for Molecular Pathology." *Genet Med,* vol 17, pp 405-24, May 2015.

[2] Frampton JE." Olaparib: a review of its use as maintenance therapy in patients with ovarian cancer." *Bio Drugs.*, vol 29, pp.143-50, Apr 2015**.**

[3] O'Rawe et al. "Low concordance of multiple variantcalling pipelines: practical implications for exome and genome sequencing.". *Genome Medicine*, vol 5, pp 28, 2013.

[4] McKenna A, Hanna M, Banks E, Sivachenko A, Cibulskis K, Kernytsky A, Garimella K, Altshuler D, Gabriel S, Daly M, DePristo MA, "The Genome Analysis Toolkit: a MapReduce framework for analyzing next-generation DNA sequencing data" . *GENOME RESEARCH,* vol 20, pp.1297-303, 2010.

[5] Koboldt, D., Zhang, Q., Larson, D., Shen, D., McLellan, M., Lin, L., Miller, C., Mardis, E., Ding, L., & Wilson, R. (2012). VarScan 2: Somatic mutation and copy number alteration discovery in cancer by exome sequencing *Genome Research* DOI: 10.1101/gr.129684.111 .

[6] Saito, T. & Rehmsmeier, M. The Precision-Recall Plot Is More Informative than the ROC Plot When Evaluating Binary Classifiers on Imbalanced Datasets. Plos One 10, e0118432, 2015.

[7] Hwang S, Kim E, Lee I, Marcotte EM. "Systematic comparison of variant calling pipelines using gold standard personal exome variants.". *Sci Rep*. vol 7. pp. 17875, Dec 2015.

Integrated network analysis for studying human lung squamous cell carcinoma

G. Fiscon[1,*], F. Conte[1,*], T. Colombo[1], L. Farina[2], and P. Paci[1]

[1] *Institute for Systems Analysis and Computer Science "A. Ruberti" (IASI) National Research Council (CNR) of Rome*

[2] *Department of Computer, Control and Management Engineering "A. Ruberti" (DIAG), Sapienza University of Rome*

** Equal contribution*

***Abstract*— We propose an integrated network-based approach to analyse the correlation network arising from large-scale gene expression data. Our approach represents a novel perspective to the problem of node classification by assigning roles to nodes on the basis of network topology together with the gene expression data. Our rationale is that the biological roles of nodes should be identifiable looking at local interactions of each node with respect to the global connectivity of the network. We applied our methodology to the RNA and microRNA-sequencing data of human lung squamous cell carcinoma in order to identify a small pool of genes that might have a key role in lung cancer development and progression.**

***Keywords*—network analysis, gene expression, lung cancer.**

I. Introduction

Lung carcinoma is one of the most frequently diagnosed cancers as well as the most common cause of cancer death worldwide (1.59 million deaths, 19.4% of the total in 2012). There were estimated to be 1.65 million new cases in 2015 in USA and lung cancer incidence is expected to increase in the future [1]. Thus, research groups of all over the world aim at improve the prevention, diagnosis, and treatment of this type of cancer. Thanks to next generation technologies, many open-access repositories offer researchers an ever-increasing collection of heterogeneous genomic data that have to be properly investigated from a global point of view. One of the largest public repositories of large-scale genomics data is The Cancer Genome Atlas (TCGA): a multi-dimensional catalogue of the key genomic changes associated with specific types of tumors. The study of oncogenic properties of tumor cells requires the combination of experimental data and computational approaches supporting better disease knowledge as well as diagnosis and prognosis. Among the computational methods, gene network analysis, taking into account relationships among genes, offers a powerful tool to identify key players that mark the shift from normal to cancer state.

We propose an integrated network analysis aiming to identify a small pool of genes (about hundreds) called "switch genes" that are involved in drastic changes of biological systems. Specifically, switch genes are characterized by a marked negative correlation with the expression profiles of their linked nodes in the network, but with the additional property of many significant negative correlations outside their communities. We set our procedure in [2], where we extracted switch genes by analysing the grapevine gene expression atlas [3]. They appear to be master regulator genes of transition from the immature to the mature growth phase of the grapevine developmental program.

In this work, we apply our approach on RNA- and microRNA- (miRNA) sequencing assays of human lung squamous cell carcinoma.

II. Methods

A. Dataset

The lung squamous cell carcinoma (lusc) dataset was obtained from TCGA repository (updated to December 2014). Data include: 1) 554 RNA-sequencing samples (of which, 503 are tumor and 51 normal samples) relative to 502 unique patients; 2) 525 miRNA-sequencing samples (of which, 480 are tumor and 45 normal samples) relative to 480 unique patients. Out of the whole set of patients, 38 have samples of cancer and matched normal tissues for both the RNA-sequencing (concerning protein-coding and non-coding RNAs abundance) and miRNA-sequencing.

B. *Differential Gene Expression Analysis*

We applied a pre-processing and filtering phase on data in order to remove genes whose expression did not change with statistical significance between the two conditions (matched normal and tumor). We selected 1683 RNAs and 18 miRNAs showing statistically significant differential expression based on False Discovery Rate (FDR) < 0.05.

C. *Network Analysis and identification of switch genes*

We built a co-expression network of differentially expressed RNAs and miRNAs based on the Pearson correlation between expression profiles of gene pairs. In this network, two nodes are connected if the absolute value of the Pearson correlation for their expression profiles is greater than a given threshold (0.75 or 85th percentile). The choice of this threshold should reflect a right balance between the number of edges and the number of connected components of the network: the number of edges should be as small as possible in order to have a manageable network (pointing towards a higher threshold) and the number of connected components should be as small as possible in order to preserve the integrity of the network (pointing towards a smaller threshold).

In order to detect the community structure of our network, we used the k-means clustering algorithm [4], which partitions *n* objects (here network nodes) into a predefined number *N* of clusters. The quality of clustering was evaluated by minimizing the Sum of the Squared Error (SSE), depending on the distance of each object to its closest centroid. A reasonable choice of the number of clusters is suggested by the position of an elbow in the SSE plot

computed as function of *N*. As distance measure, we used dist(x,y) = 1 – ρ(x,y), where ρ(x,y) is the Pearson correlation between expression profiles of nodes *x* and *y*. Table 1 lists cut-off values used throughout the analysis.

After finding the communities in the network, we classified nodes by computing the Average Pearson Correlation Coefficients (APCCs) between the expression profiles of a hub (i.e., nodes with more than 5 connections [5]) and each of its nearest neighbours. This classification of hubs was set in [5] where the authors studied protein-protein interactions (PPI) networks in yeast. They found a general bimodal distribution of the APCC corresponding to two classes of hubs that they named "party hubs" (with very high positive values of APCC) and "date hubs" (with moderate positive values of APCC). By applying this definition to the lusc correlation network, we found a trimodal distribution of APCC (Fig. 1 panel a), which allowed us to identify an additional class of hubs that we called "fight-club hubs", which display negative values of APCC.

Then, we combined expression data with the topological properties of nodes by using the cartographic representation of modular networks presented in [6] that assign a role to each node based on their inter-cluster and intra-cluster connectivity. This is reached by defining two statistics: the within-module degree *z* and the participation coefficient *P*,

$$z^i = \frac{k_i^{in} - \bar{k}_{C_i}}{\sigma_{C_i}} \qquad P = 1 - \left(\frac{k_i^{in}}{k_i}\right)^2$$

where k_i^{in} is the number of links of node *i* to nodes in its module C_i, k_i is the total degree of node *i*, and $\bar{k}_{C_i}$ and σ_{C_i} are the average and standard deviation of the total degree distribution of the nodes in the module C_i. According to *P* and *z* values, the plane is divided into seven regions (R1-R7), each defining a specific node role [6]. High *z* values correspond to nodes that are hubs within their module (local hubs), while high values of *P* identify nodes that interact mainly outside their community.

Finally, we coloured each node in the plane identified by *z* and *P* according to its APCC value thus defining what we called a heat cartography map. Our integrated network analysis allowed us to identify a special subclass of fight-club hubs falling in R4 region that we call "switch genes" (Fig. 1 panel b) and that are no local hubs and mainly interact outside their community.

TABLE 1
SUMMARY OF LUSC DATASET ANALYSIS

fold-change (FC) threshold	5.6
FDR threshold	0.05
Number RNAs DE	1683
Number miRNAs DE	18
Pearson Correlation threshold	0.75 (85th percentile)
Number of network nodes	1628
Number of clusters	3
Number of switch genes	274

III. RESULTS

We selected 1683 RNAs and 18 miRNAs statistically significant differentially expressed (FDR<0.05) in the analysis of TCGA lusc dataset and used them as input for our algorithm to explore switch genes associated with the tumor transformation. We unveiled 274 switch genes significantly up-regulated in tumor tissues that we proposed as good candidate biomarkers of lung carcinoma (Fig. 1 panel c).

Moreover, we studied the effect of targeted removal of date/party/fight-club hubs and switch genes on the lusc correlation network topology (Fig. 1 panel d). This analysis showed a critical contribution of switch genes and fight-club hubs in preserving the integrity of the network.

Finally, we investigated switch genes function by performing KEGG pathways [7] enrichment analysis by using the FIDEA server [8]. This analysis pointed out a strong association of switch genes in the regulation of cell cycle (Fig. 2 panels a-b). In particular, switch genes appear to be specifically involved in the G2 phase to mitosis transition (G2/M) of the cell cycle (Fig. 2 panel c). In fact, the list of switch genes encompasses Cyclins (e.g., Cyclin B) and Cyclin-dependent kinases (Cdk) that are crucial players of this checkpoint. Importantly, Cyclin B is a mitotic cyclin which binds to the cyclin kinase Cdk1, building the Mitosis Promoting Factor (MPF) complex. Its activity rises through the cell cycle until mitosis (G2/M transition), where it has a drastic fall due to degradation of cyclin B (Fig. 2 panel d).

IV. CONCLUSION

We proposed an integrated network analysis that allowed identifying putative key gene regulators of human lung squamous carcinoma. Specifically, we identified 274 switch genes that are significantly enriched in cell cycle annotation, supporting their crucial role in normal to cancer state transition. In the near future, we intend to extend our approach to the analysis of all tumours provided by TCGA.

ACKNOWLEDGEMENT

This work was supported by The Epigenomics Flagship Project (EPIGEN), funded by the Italian Ministry of Education, University and Research (MIUR), and the National Research Council (CNR).

REFERENCES

[1] Siegel RL, Miller KD, Jemal A "Cancer statistics, 2015." CA: a cancer journal for clinicians, 2015, 65: pp.5-29.

[2] Palumbo MC, Zenoni S, Fasoli M, Massonnet M, Farina L, Castiglione F, Pezzotti M, Paci P "Integrated network analysis identifies fight-club nodes as a class of hubs encompassing key putative switch genes that induce major transcriptome reprogramming during grapevine development". Plant Cell 2014, 26(12): pp.4617-4635

[3] Fasoli M, Dal Santo S, Zenoni S, Tornielli GB, Farina L, et al "The grapevine expression atlas reveals a deep transcriptome shift driving the entire plant into a maturation program". Plant Cell 2012, 24: pp.3489-505.

[4] Hartigan JA, Wong MA "Algorithm AS 136: A K-Means Clustering Algorithm" JR Stat Soc Ser C Appl Stat 1979, 28:pp.100–108.

[5] Han JD, Bertin N, Hao T, Goldberg DS, Berriz GF, Zhang LV, Dupuy D, Walhout AJ, Cusick ME, Roth FP, Vidal M "Evidence for dynamically organized modularity in the yeast protein-protein interaction network". Nature 2004, 430:pp.88-93.

[6] Guimera R, Amaral LAN "Functional cartography of complex metabolic networks". Nature 2005, 433:pp.895.

[7] Kanehisa, M, Sato Y, Kawashima M, Furumichi M, Tanabe M. "KEGG as a reference resource for gene and protein annotation". Nucleic Acids Res 2016, 44: pp. 457-462.

[8] D'Andrea D, Grassi L, Mazzapioda MG, Tramontano A "FIDEA: a server for the functional interpretation of differential expression analysis" Nucleic Acids Res 2013.

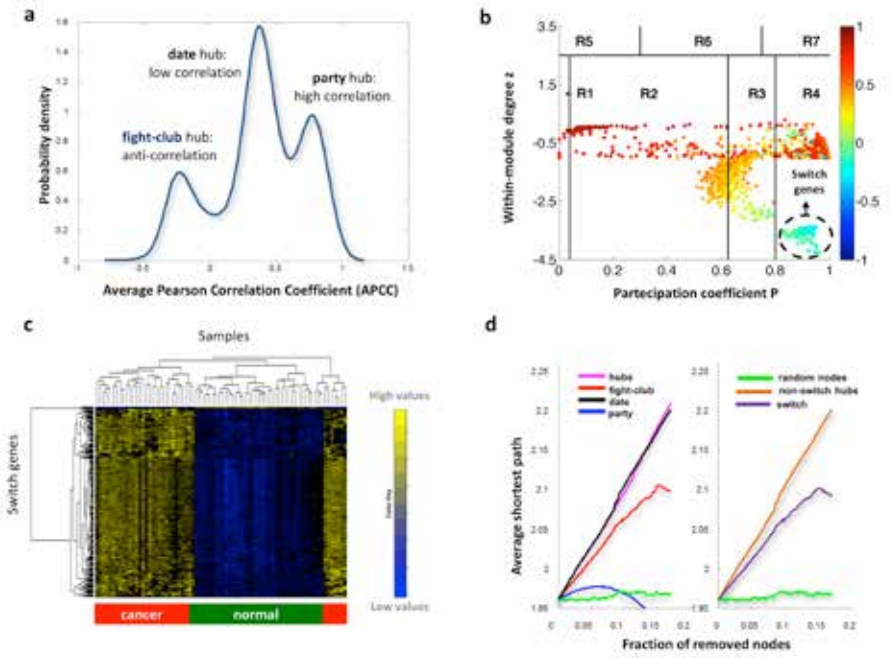

Fig. 1 Results of the lung squamous carcinoma network analysis. Panel a) depicts the APCC distribution for lusc correlation network, where the three peaks correspond to: 1) fight-club hubs, which are negatively correlated on average with their interaction partners; 2) date hubs, which show moderate co-expression; 3) party hubs, which are highly correlated with the expression of their interaction partners. The x-axis represents the APCC and the y-axis represents the estimated probability density of the APCC. Panel b) depicts the heat cartography map for lusc correlation network. The plane is divided into seven regions (R1-R7) defining the node roles and identified by two parameters (within-module degree *z*, participation coefficient *P*). Each node is colored according to its APCC value. Blue nodes are the fight-club hubs and among them those ones falling in the region R4 are the switch genes (i.e., genes are connected mainly outside their module, showing low *z* and high *P* values), highlighted by a dashed black circle. Panel c) depicts the dendrogram and heat map of switch genes, where the expression profiles are clustered according to rows (switch genes) and columns (samples) of the expression data matrix. The colors of the heat map refer to the z-score normalized expression levels in a blue (low) to yellow (high) scale. Panel d) depicts the robustness analysis for the lusc correlation network, where the x-axis represents the cumulative fraction of removed nodes, while the y-axis represents the average shortest path (i.e., the minimum number of consecutive links connecting two nodes). Each curve refers to the removal of different kinds of nodes, as indicated in the color legend.

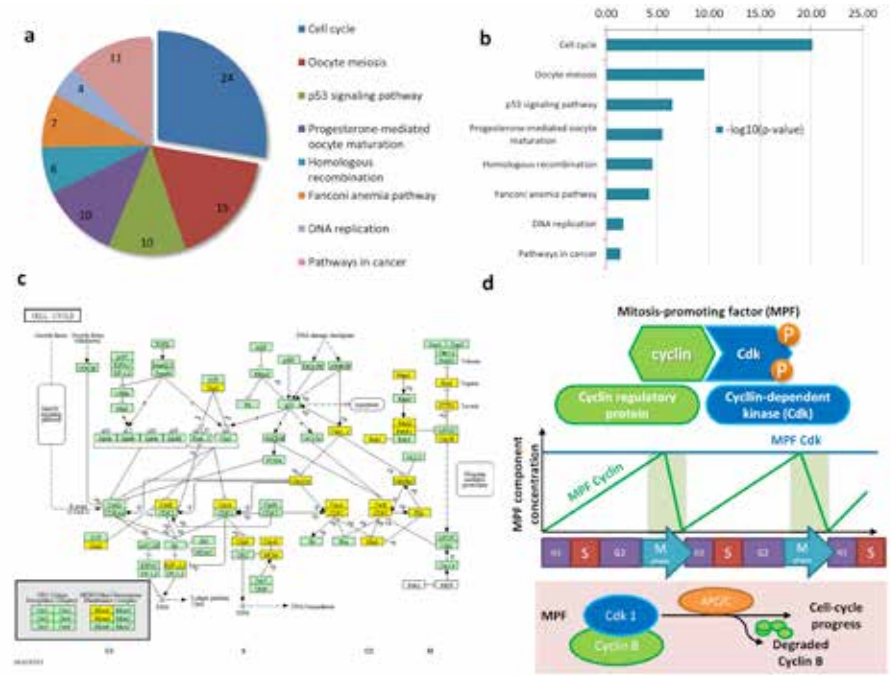

Fig. 2 Results of the KEGG pathways enrichment analysis for switch genes. Panel a) draws a pie chart of enriched KEGG pathways among switch genes. The number of switch genes annotated to each KEGG category is shown inside the cognate slice. Panel b) draws the histogram of top enriched KEGG pathways sorted by significance ($-\log_{10}$ of adjusted p-values). Only KEGG pathways with an adjusted p-value lower than 0.05 are shown. Panel c) draws the KEGG cell cycle pathway (hsa04110), where the 24 switch genes annotated for this category are highlighted in yellow. In particular, these include cyclins and cyclin-dependent kinases and result mostly involved in the G2/M phase of the cell cycle. Cyclin B is a mitotic cyclin which binds to the cyclin kinase Cdk1. This complex is called Maturation Promoting Factor or Mitosis Promoting Factor (MPF). Panel d) shows the activity of this complex that rises through the cell cycle until mitosis (G2/M transition), where it has a drastic fall due to degradation of cyclin B, while Cdk1 is constitutively present.

Molecular Modelling to Investigate Protein Misfolding and Aggregation in Neurodegenerative Spinocerebellar Ataxia

G. Grasso[1,3], M. A. Deriu[1], Jack A. Tuszynski[2], Andrea Danani[1], and U. Morbiducci[3]
[1] *Istituto Dalle Molle di studi sull'Intelligenza Artificiale (IDSIA), USI, SUPSI, Centro Galleria 2, Manno, Switzerland.*
[2] *Department of Physics, University of Alberta, Edmonton AB, Canada.*
[3] *Department of Mechanical and Aerospace Engineering, Politecnico di Torino, Corso Duca degli Abruzzi 24, Torino, Italy.*

***Abstract*— Abnormal aggregation of disease-specific proteins has been recognized as closely related to the onset of several neurodegenerative disorders. However, molecular reasons underneath the misfolding process and the protein aggregation pathway have not been entirely clarified yet. This is the case of the misfolding process of Ataxin-3, a poly-glutammine protein responsible for the neurodegenerative disease Spinocerebellar Ataxia Type 3. In this connection, computational approaches represent a powerful tool to describe molecular features of protein folding and protein-protein interactions with atomistic detail. An investigation focused on the JD dimerization mechanism will be presented here, suggesting possible aminoacids involved in the first step of Ataxin-3 aggregation. Moreover, enhanced sampling techniques, such as Metadynamics and Replica Exchange Molecular Dynamics, have been employed to characterize the thermodynamic stability and folding kinetics of Josephin Domain. Following experimental validation, these results can be considered as a basis for a future design of Ataxin-3 aggregation inhibitors that will require several key conformations identified in the present study as molecular targets for ligand binding.**

***Keywords*—Molecular Modelling, Neurodegenerative Disease, Spinocerebellar Ataxia, Molecular Dynamics.**

I. INTRODUCTION

The worldwide significant increase in the life expectancy has recently drawn the attention of the scientific community to pathologies of the elderly population, such as neurodegenerative diseases. In this connection, the polyglutamine (polyQ) disorders represent the most common form of inherited neurodegenerative disease. The main molecular feature characterizing all polyQ expansion diseases is related to an abnormal length of the glutamine tract in the codified protein, resulting from an unstable expansion of a cytosine–adenine–guanine (CAG) repeat in the causative gene. The present work is focused on the Ataxin 3 (At3), a 42 kDa intracellular protein responsible for the Spinocerebellar Ataxia type 3, also known as Machado Joseph Disease. Ataxin-3 consists of an N-terminal Josephin Domain (JD), and an unstructured flexible C-terminus, which contains the polyQ tract. Several experimental studies have indicated a double-step process for At3 fibrillogenesis, composed by an initial phase JD-mediated but polyQ-independent, followed by a polyQ-dependent step [1]. For these reasons, the JD have gained considerable scientific attention in the past. A first research line focused on investigating the protein residues involved in the JD's dimerization mechanism and, more in general, the aggregation pathway. As a second research line, a number of investigations have been carried out to describe the JD conformational states in solution. In detail, several JD models solved by NMR are available in literature (PDB entry 2JRI [2], 1YZB [3], 2AGA [4] and 2DOS [5]), demonstrating the existence of different structural conformations. Motivated by the still open debate in literature we have employed classical and enhanced Molecular Dynamics to shed light on i) JD dimerization mechanism and ii) JD conformational properties in solution. Our results suggest the JD aggregation as a multi-step process, characterized by an initial JD-JD binding mainly driven by Arg-101. Finally, we provide a thermodynamic and kinetic description of the JD transition pathway from the open-like to a closed-like conformation. Approaching this problem from an energetic point of view is of great importance especially in case of amyloidogenic proteins, given the intimate interconnection between the functional energy landscape and misfolding/aggregation risk.

II. MATERIALS AND METHODS

A. Classical Molecular Dynamics and Mode Analysis

Classical Molecular Dynamics was employed to study i) JD conformational properties in solution and ii) the JD dimerization mechanism. In addressing these issues, we set up two different molecular systems: i) the single JD in explicitly modelled water, the so-called JD^{Wat}, ii) two JDs in explicitly modelled water, the so-called JD-JD. Ten replicas of the molecular system, characterized by different JD-JD starting orientation, were generated and simulated for 150 ns. The 1YZB model [3] of JD was selected as the starting point for the present work. AMBER99-ILDN force-field [6]-[8] and water TIP3P model [9] were chosen to describe the system's topology. GROMACS 4.6 package was employed for all MD simulations and data analysis [10]. Alanine mutation simulations have been also carried out to verify the role of residues identified as mainly involved in JD protein-protein interaction. Principal Component Analysis (PCA) was applied to classical MD trajectories in case of JD^{Wat} simulation to elucidate large-scale and low-frequency modes, respectively, yielding collective motions leading to the JD conformational changes.

B. Metadynamics

The free energy landscape representing the JD folding pathway was investigated by means of Metadynamics [11]. The first eigenvector derived from the PCA was used as CV

for a well-tempered Metadynamics simulation of 500 ns starting from the open-like 1YZB model [12]. To perform Metadynamics simulations, a Gaussian width of 0.1 was used. Along the simulation, the initially prescribed Gaussian deposition rate value of 0.2 kJ/mol·ps was used and it gradually decreased on the basis of an adaptive scheme, with a bias factor of 20 [13]-[14]. The estimation of the free energy profile was performed by employing the reweighted-histogram procedure [15]-[16], taking into account three collective variables: the projection along the first PCA eigenvector, the JD's Radius of Gyration (RG), the hairpin angle and the alphaRMSD variable.

C. Replica Exchange Molecular Dynamics

Replica Exchange Molecular Dynamics (REMD) [17] was carried out to obtain a kinetic estimation of the JD monomer conformational transitions. In detail, 128 replicas were simulated for temperatures ranging from 300 K to 602 K. Temperatures are distributed following the exponential spacing law [18]-[19]. The resulting exchange probability was 0.35. The exchange attempt time interval was set to 2 ps. Each replica was simulated for 50 ns, obtaining a cumulative simulation time of 6.4 μs. In order to obtain a reliable estimate of the JD folding rates, the kinetic description developed by van der Spoel et al [20] was applied to the REMD trajectories.

III. RESULTS AND DISCUSSION

A. JD dimerization mechanism

The MD trajectories of the JD-JD system allow to identify residues mainly responsible for the dimerization process. In detail, the JD-JD residues' contact probability plot (**Fig. 1**) demonstrates that Arg101 is the residue most frequently involved in the JD-JD dimerization interface. This result is in close agreement with a very recent work [21] demonstrating Arg101/Arg103 as mainly responsible for JD interaction with hydrophobic/hydrophilic substrates. To carefully test this hypothesis, we run again the same set of ten JD-JD simulations by replacing the native Arg101/Arg103 residues with Alanine. The mutations have a strong effect on the JD-JD interaction propensity, providing a generalized reduction of the contact probability values.

B. JD Free energy landscape

The MD simulation of JD monomer in water environment was analyzed in order to study the JD conformational properties in solution. The RG calculated over the classical MD trajectories reveals the JD transition from half-open, characterized by RG of 1.7 nm, to a closed conformation, characterized by RG of 1.55 nm (**Fig. 2**a). To reduce the high-dimensionality of the MD trajectory and to identify the dominant molecular phenomena related to the JD closure, PCA was applied. The first eigenvector derived from the PCA was used as CV for a well-tempered Metadynamics simulation. Analyzing the free energy profiles reported in **Fig. 2**b, two energy wells of 36 kJ/mol and 4 kJ/mol, located at RG values of 1.55 nm and 1.78 nm, respectively, can be identified. Interestingly, the findings of our *in silico* study strongly suggest the closed conformation as the most likely for a Josephin Domain in solution, in agreement with models 2AGA [4].

C. JD Folding kinetics estimation

Analyzing the REMD trajectory at 310K, the JD conformational space can be divided into three main groups: open JD (O), closed JD (C) and intermediate state (I), containing both half-open and half-closed JD (**Fig. 3**). Analyzing the kinetics and thermodynamics results shown in **Fig. 3**, it is worth noticing that the closed JD arrangement represents the most energetically favorable configuration. In detail, transition between closed and intermediate states is characterize by deep energy barrier ($E_{C\text{-}I}$ = 36.7 kJ/mol), in close agreement with the computational results obtained by Metadynamics simulations (**Fig. 2**b). The corresponding rate constant is $\tau_{C\text{-}I}$=767.3 ns, explaining the reason behind the well established inability of the classical MD simulation in being able to explore the transition between closed and open JD (**Fig. 2**a) on a time scale of hundreds of nanoseconds [22]-[23]. Finally, the estimation of the average JD closed fraction at 310 K (fc=0.993), provides further evidence for the closed arrangement as the most likely for a JD monomer in water environment.

IV. CONCLUSION

In the present work, a MD approach has been employed to investigate JD protein-protein interactions and folding dynamics. A clear identification of the most likely JD-JD interacting sites is here provided. Moreover, a decisive evidence of the thermodynamic stability of the JD closed-like conformation is obtained by an extensive computational investigation concerning the JD folding pathway. Further studies will help in elucidating the interconnection between JD conformational properties and aggregation propensity. The above mentioned investigations might be a key to successfully design novel therapeutic strategies targeting SCA3.

REFERENCES

[1] Ellisdon, A.M. et al. (2006). J. Biol. Chem., 281, 16888–16896
[2] Nicastro, G. et al. To be Pubblished, 10.2210/pdb2jri/pdb
[3] Nicastro, G. et al. (2005). Proc. Natl. Acad. Sci. U. S. A., 102, 10493–10498
[4] Mao, Y. et al. (2005). Proc. Natl. Acad. Sci. U. S. A., 102, 12700–12705
[5] Satoh, T. et al. (2014). FEBS Lett., 588, 4422–4430
[6] Hornak, V. et al. (2006). Proteins Struct. Funct. Genet., 65, 712–725
[7] Lindorff-Larsen, K. et al. (2010). Proteins Struct. Funct. Bioinforma., 78, 1950–1958
[8] Lindorff-Larsen, K. et al. (2012). PLoS One, 7,
[9] Jorgensen, W.L. et al. (1983). J. Chem. Phys., 79, 926
[10] Hess, B. et al. (2008). J. Chem. Theory Comput., 4, 435–447
[11] Laio, A. et al. (2002). Proc. Natl. Acad. Sci. U. S. A., 99, 12562–12566
[12] Masino, L. et al. (2004). J. Mol. Biol., 344, 1021–1035
[13] Laio, A. et al. (2008). Reports Prog. Phys., 71, 126601
[14] Granata, D. et al. (2013). Proc. Natl. Acad. Sci. U. S. A., 110, 6817–6822
[15] Kumar, S. et al. (1992). J. Comput. Chem., 13, 1011–1021
[16] Bonomi, M. et al. (2009). J. Comput. Chem., 30, 1615–1621
[17] Sugita, Y. et al. (1999).141–151
[18] Denschlag, R. et al. (2009). Chem. Phys. Lett., 473, 193–195
[19] Lingenheil, M. et al. (2009). Chem. Phys. Lett., 478, 80–84
[20] van der Spoel, D. et al. (2006). Phys. Rev. Lett., 96, 238102
[21] Apicella, A. et al. (2013). PLoS One, 8, e58794
[22] Deriu, M.A. et al. (2016). PLOS Comput. Biol., 12, e1004699
[23] Deriu, M.A. et al. (2014). PLoS One, 9, e108677

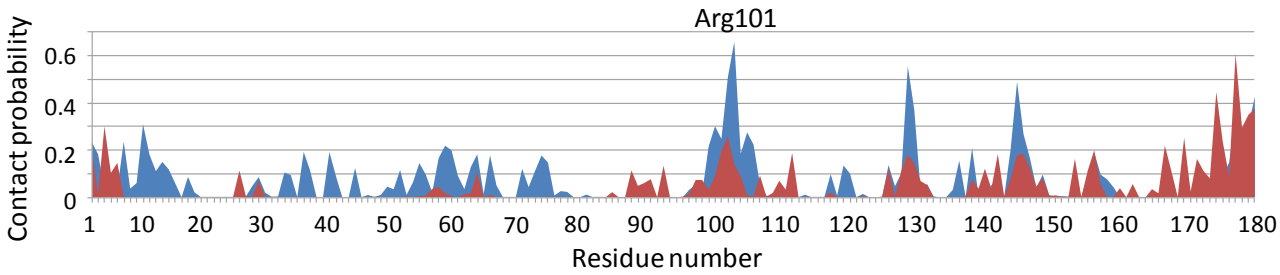

Fig. 1. The inter-monomer residue-residue distance is calculated for JD-JD (blue curve) by applying a distance cut-off of 0.28 nm. The last 50 ns of all simulations are considered for data sampling. Arg101 has been found to be the residue most frequently involved in the JD-JD dimerization interface. The same set of ten JD-JD simulations were performed by replacing the native Arg101/Arg103 residues with Alanine (red curve). The mutations have a strong effect on the JD-JD interaction propensity, providing a generalized reduction of the contact probability values.

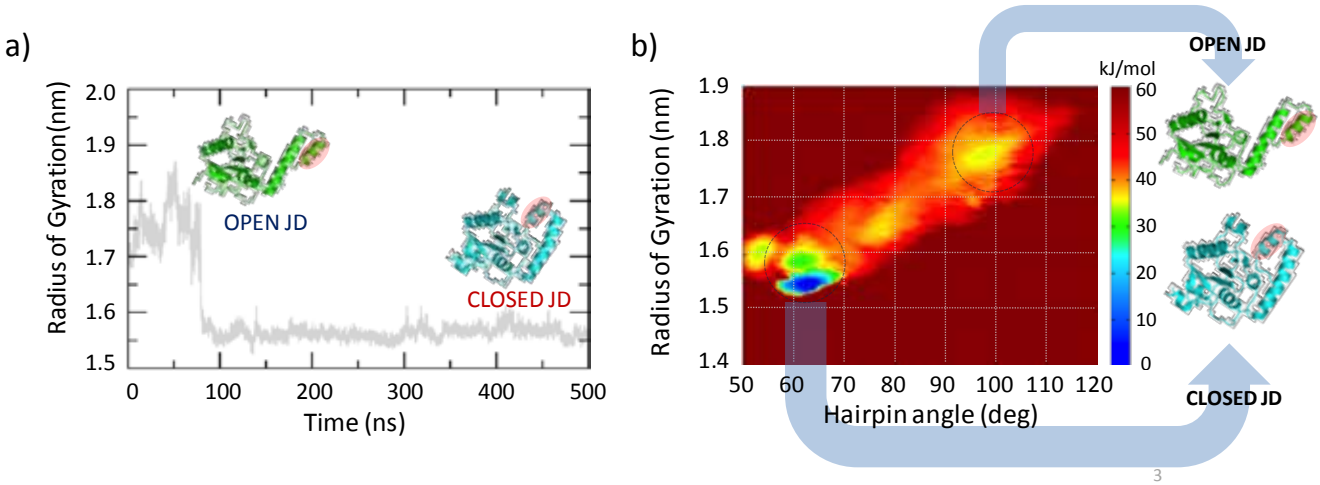

Fig. 2. a) The time evolution of the JD Radius of Gyration along the Classical MD simulation revels the JD transition from half-open to a closed conformation, characterized by RG lower of 1.55. b) 2D color map of the JD free energy landscape as function of JD Radius of Gyration and Hairpin angle, calculated by the reweighting histogram approach on the Metadynamics outcome. The visual inspection of the JD conformation corresponding to the free energy minima is also reported (right).

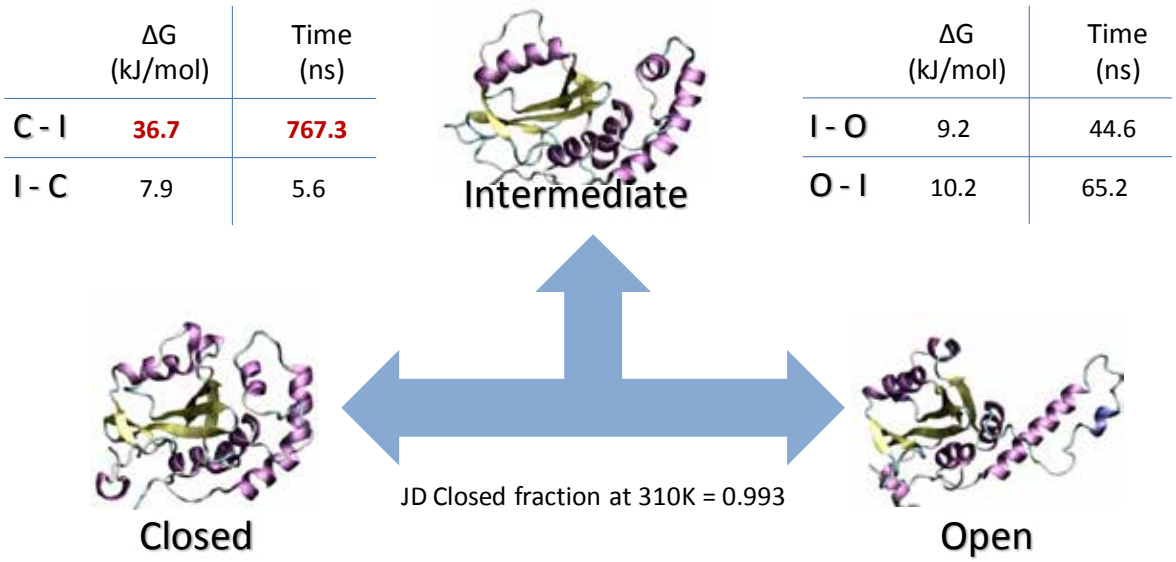

Fig. 3. Visual inspection of the JD conformational arrangements corresponding to closed (C), intermediate (I) and open (O) state together with the estimated forward and backward rate constants for folding together with the activation energies at 310K. Moreover, the estimation of the average JD closed fraction at 310 K (fc=0.993) is provided.

Identifying Functional Unknown Elements in Ribosomal RNA by Digital Signal Processing

N. Maggi[1], P. Arrigo[2], and C. Ruggiero[1]
[1] *Department of Informatics, Bioengineering, Robotics and Systems Engineering, University of Genoa*
[2] *CNR Institute of Macromolecular Studies (ISMAC), Genoa*

***Abstract*— The process of rRNA assembly in mammalian cells starts from the primary 47S transcript and, by a series of cleavages, leads to the production of three rRNAs: 18S, 28S and 5.8S. During this process, the non-coding flanking regions are removed. We have applied a digital signal processing analysis to one of this non-coding region (Internal Transcribed Spacer 1) to find out the presence of putative regulatory sites. The results show that known cleavage sites are detected and also encourage suggestions about other possible regions of interests that might play a role as regulatory site or recognition site.**

***Keywords*—DSP, Antinotch filters, ribosomal RNA.**

I. Introduction

RIBOSOMES are complex structures, which are present within all prokaryotic and eukaryotic cells in plants and animals. They play a major role in genetic translation for protein synthesis, linking amino acids together according to the order specified by messenger RNA (mRNA) molecules. Ribosomes are composed of two major components: the small subunit (SSU) which reads the RNA, and the large subunit (LSU) which joins amino acids together to form a polypeptide chain.

Ribosome biogenesis is a very complex process involving hundreds of molecular components. In eukaryotes, the process starts in the nucleolus where a precursor (47S pre-rRNA) is synthetized and processed into mature 18S, 5.8S, and 28S rRNAs in multiple steps [1]. In 47S precursor ribosomal RNA the 18S, 5.8S, and 28S rRNA sequences are flanked by the 5' and 3' ETS, ITS1 and ITS2. During the processing, these parts of the sequence are removed to lead to the formation of LSU (28S and 5.8S) and SSU (18S). Recent findings have highlighted the role of specific cleavage sites in this region that are mandatory for the biogenesis of ribosome [2].

Many methods have been used in order to detect the regulatory sites of nucleotide sequence. The two major classes of widely applied computational methods are based on descriptive statistical analysis of short nucleotide motifs called 'words' and on Hidden Markov Models. The search is often influenced by the incidence of relative small changes in primary sequences. The availability of reliable primary sequence databases allows to screen the distributional properties of nucleotide words not only on specific genomic sequences but also on the whole genomes. The major problem in the 'linguistic' analysis of nucleotide sequences is correlating a significant nucleotide motif with a specific biological function, such as recognition site for transcription factors or for restriction enzymes or for post-transcriptional and epigenetic regulation led by other nucleic acids [3]. Another difficulty related to the nucleotide word analysis is the lack of structural information about them, which limits the possibility to apply structural bioinformatics tools to predict protein – nucleic acid interactions. In the last decade the role of non-coding RNA has emerged as critical in the adaptation of gene expression to endogenous and exogenous stress. These regulatory RNAs are capable to interact as well as mRNAs as DNAs. However, both approaches focus on elements that are known, whereas recent findings in genomics have shown that functionally unknown elements are also present.

We propose a method based on a digital signal processing (DSP) analysis of ITS1 sequence using antinotch filters for the identification of embedded putative regulatory regions and/or of recognition sites.

II. Materials and Methods

A. Sequence extraction

Digital Signal Processing (DSP) has been widely applied in sequence analysis. Generally DSP is used for intron - exon discrimination and therefore for the identification of protein coding regions [4, 5]. We have applied a DSP technique to human ITS1 in order to identify and locate possible regions of interest which may be embedded in the sequence, even though ITS1 is a non-coding region. The sequence of the Human ribosomal DNA complete repeating unit can be found at the U.13369 entry in the NCBI nucleotide database (http://www.ncbi.nlm.nih.gov/nucleotide/). The ITS1 sequence is located between position 5528 and position 6622. This sequence is stored in NCBI database as a DNA. However, in ribosome biogenesis the whole DNA sequence is translated in a pre-rRNA sequence (47S) and is processed afterwords. For this reason, we have translated the sequence from NCBI database in the corresponding ITS1's mRNA sequence changing Timine bases with Uraciles.

B. Sequence coding

The application of DSP to a nucleotide sequence requires the transformation of the literal sequences in a numerical ones. Many methods have been proposed over the years [6], such as fixed mapping and physico-chemical property based mapping. In fixed mapping methods (Voss representation [7], tetrahedron method [8], integer representation [9] and complex representation [10]) the nucleosequences are transformed according to a series of arbitrary numerical sequences. Conversely, the latter methods (EIIP [11], atomic

number [12], paired numeric [13], DNA walk [14] and Z-curve representations [15]) use biophysical and biochemical properties of DNA/RNA biomolecules to map the sequences. These methods are more meaningful than fixed mapping because they seem to be more robust and, mostly, they generate a signal that carries some biological information.

Among these methods, we reckon that the Electro-Ionic Interaction Potential (EIIP) method is particularly promising because it is based on the average energy states of all valence electrons in each nucleotide. The EIIP for each nucleotide values are show in Table I.

TABLE I
ELECTRO ION INTERACTION PSEUDO POTENTIALS OF NUCLEOTIDES

Nucleotides	*EIIP values*
A	0.1260
G	0.0806
C	0.1340
U	0.0562

Using this transformation, we have encoded 4 input signals, (Ua(n), Ug(n), Uu(n), Uc(n)) one for each nucleobase, which has been pass through the filters described in section C.

C. Antinotch filter

An antinotch filter is a device that passes frequencies within a certain range and stops or attenuates frequencies outside that range (bandpass filter), providing high gain in the pass band region. An antinotch filter can be easily realized as an Infinite Impulse Response (IIR) filter and build from a second order allpass filter [16, 17]. The transfer function of the antinotch filter is

$$H(\mathrm{z}) = \frac{1}{2}\frac{(1-R^2)(1-z^{-2})}{(1-2R\cos\theta z^{-1}+R^2 z^{-2})} \qquad (1)$$

which has two poles at $Re^{\pm j\theta}$ and two zeros at ± 1. The stability condition of the filter is $R<1$. We have chosen $R=0.992$.

D. First order FIR filter

The four output from the antinotch filter have been filtered again through a Finite Impulse Response (FIR) filter with transfer function in Eq (2).

$$H_1(z) = 1 - \mathrm{e}^{j4\pi/3} z^{-1} \qquad (2)$$

This filter suppresses the frequency component at $\omega = 4\pi/3$.

To obtain the final outputs *Y*(*n*), the four output of the FIR filter have been combined according to Eq. (3).

$$Y(n) = \sum_{i\in F} |y_i(n)|^2, \qquad F = \{A,U,C,G\} \qquad (3)$$

III. RESULTS AND DISCUSSION

The signal obtained after filtering contains specific features of the human ITS1 sequence is shown in Fig. 2. The peaks may represent possible regions of interest in the sequence. Recent work [2] on pre-rRNA processing pathways in mammals (human and mouse), shows experimental findings about the known and putative cleavage sites in 47S pre-rRNA. Specifically, ITS1 seems to contain three different cleavage site. These sites have been called E, C, and 2 and they are located in the sequence respectively at position 5551, between positions 6162 and 6177, and 6469 and 6476. In addition, two other unnamed sites have been reported (position 6617 and 6622).

Taking into account these findings, it may be hypothesized that the peaks above may be related to the cleavage site E, C, 2 and to the one at the 5' end of ITS1. These findings would support the assumption that, the procedure highlights some other regions that could play a role as a regulatory sites or recognition sites for the binding of proteins / enzyme or small non-coding RNAs, such as mainly region 5800 – 6000 and possibly also region 6300 – 6400.

REFERENCES

[1] M. Fromont-Racine, B. Senger, C. Saveanu, and F. Fasiolo, "Ribosome assembly in eukaryotes," *Gene,* vol. 313, pp. 17-42, 2003.

[2] S.-T. Mullineux and D. L. J. Lafontaine, "Mapping the cleavage sites on mammalian pre-rRNAs: Where do we stand?," *Biochimie,* vol. 94, pp. 1521-1532, 2012.

[3] F. Giuliano, P. Arrigo, F. Scalia, P. P. Cardo, and G. Damiani, "Potentially functional regions of nucleic acids recognized by a Kohonen's self-organizing map," *Bioinformatics,* vol. 9, pp. 687-693, 1993.

[4] M. K. Hota and V. K. Srivastava, "Identification of protein coding regions using antinotch filters," *Digital Signal Processing,* vol. 22, pp. 869-877, 2012.

[5] S. S. Sahu and G. Panda, "Identification of Protein-Coding Regions in DNA Sequences Using A Time-Frequency Filtering Approach," *Genomics, Proteomics & Bioinformatics,* vol. 9, pp. 45-55, 2011.

[6] H. K. Kwan and S. B. Arniker, "Numerical representation of DNA sequences," pp. 307-310, 2009.

[7] R. F. Voss, "Evolution of long-range fractal correlations and 1/fnoise in DNA base sequences," *Physical Review Letters,* vol. 68, pp. 3805-3808, 1992.

[8] P. D. Cristea, "Conversion of nucleotides sequences into genomic signals," *Journal of Cellular and Molecular Medicine,* vol. 6, pp. 279-303, 2002.

[9] M. D. Kessler, P. D. Cristea, and G. J. Mueller, "Genetic signal representation and analysis," vol. 4623, pp. 77-84, 2002.

[10] D. Anastassiou, "Genomic signal processing," *IEEE Signal Processing Magazine,* vol. 18, pp. 8-20, 2001.

[11] D. Lalović and V. Veljković, "The global average DNA base composition of coding regions may be determined by the electron-ion interaction potential," *Biosystems,* vol. 23, pp. 311-316, 1990.

[12] R. B. Hoover, T. Holden, R. Subramaniam, R. Sullivan, E. Cheung, C. Schneider, *et al.*, "ATCG nucleotide fluctuation of Deinococcus radiodurans radiation genes," vol. 6694, pp. 669417-669417-10, 2007.

[13] M. Akhtar, J. Epps, and E. Ambikairajah, "Signal Processing in Sequence Analysis: Advances in Eukaryotic Gene Prediction," *IEEE Journal of Selected Topics in Signal Processing,* vol. 2, pp. 310-321, 2008.

[14] S. V. Buldyrev, N. V. Dokholyan, A. L. Goldberger, S. Havlin, C. K. Peng, H. E. Stanley, *et al.*, "Analysis of DNA sequences using methods of statistical physics," *Physica A: Statistical Mechanics and its Applications,* vol. 249, pp. 430-438, 1998.

[15] R. Zhang and C.-T. Zhang, "Z Curves, An Intutive Tool for Visualizing and Analyzing the DNA Sequences," *Journal of Biomolecular Structure and Dynamics,* vol. 11, pp. 767-782, 1994.

[16] P. Vaidyanathan and B.-J. Yoon, "Gene and exon prediction using allpass-based filters," in *Proc. IEEE Workshop on Gen. Sig. Proc and Stat*, 2002.

[17] P. P. Vaidyanathan and Y. Byang-Jun, "Digital filters for gene prediction applications," vol. 1, pp. 306-310, 2002.

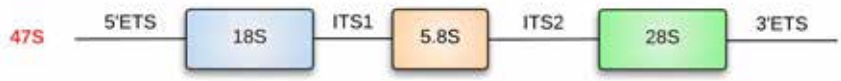

Figure 1 Composition of 47s RNA: 18S RNA forms the LSU

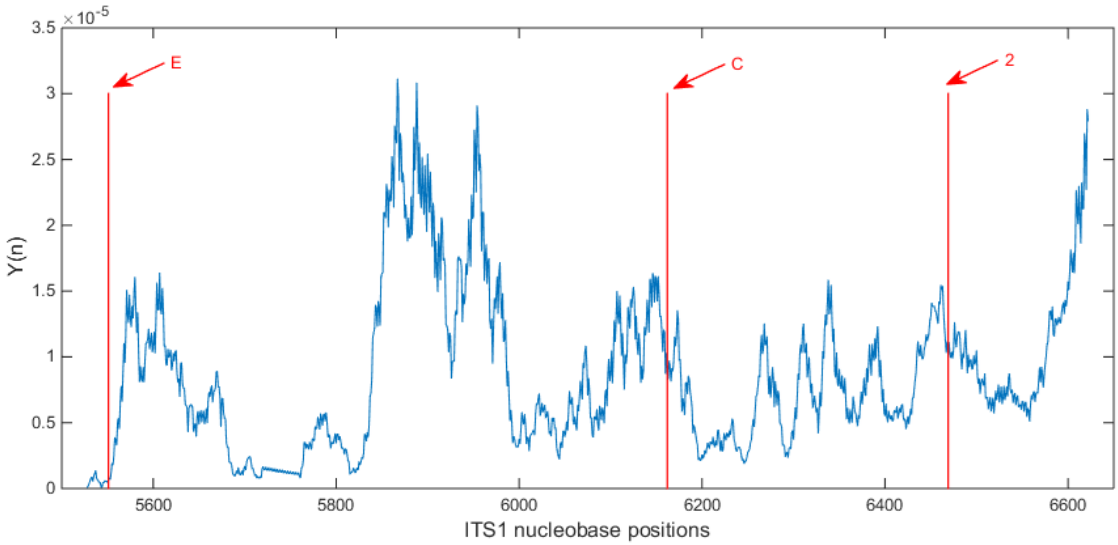

Figure 2. Output of genomic signal analisys process. In red positioning of cleavage site E, C, and 2 are reported

A Neural Network Approach to Human Posture Classification using RGB-D Camera

A. Manzi[1], F. Cavallo[1], and P. Dario[1]
[1] *The BioRobotics Institute, SSSA, Pisa, Italy*

***Abstract*—In this paper, we describe a human posture classifier based on a neural network approach. The neural network processes the human joints produced by a skeleton tracker using the depth streams of an RGB-D sensor. It is able to recognize standing, sitting and lying postures. Using only the depth streams of the sensor, the system can work in poor light conditions and also guarantees the privacy of the person. The neural network is trained with a dataset produced with the Kinect NUI tracker, but it is also tested with a different human tracker (NiTE/OpenNI). In particular, the aim of this work is to analyse the behaviour of the neural network even when the position of the extracted joints is not reliable and the provided skeleton is confused. Real-time tests, conceived to reproduce realistic and challenging situations for the tracker, have been carried out covering the whole operative range of the sensor.**

Experimental results have shown an accuracy of 99.6% using the NiTE tracker for the tests.

***Keywords*—human posture, depth camera, neural networks**

I. Introduction

In the recent years, the development of technologies strictly connected to humans increased exponentially. Nowadays, the advent of powerful mobile devices such as smart-phones and tablets are a reality, but in the near future smart home technologies will represent a huge market. Distributed environmental sensors, little robots, computers and wearable devices will share the home environment with us. These kinds of smart systems need to be aware of humans in order to effectively interacts with them to address several tasks such as behavioural and health monitoring. In the past, video surveillance systems have been proposed to address these issues, but some of their limitations include the light conditions and the lack of privacy.

The recent emergence of cheap depth sensors, so-called RGB-D sensors (e.g. Microsoft Kinect, Asus Xtion), has made it feasible and economically sound to capture in real-time not only colour images, but also depth maps with appropriate resolution and accuracy. A depth sensor can provide three-dimensional data structure as well as the 3D motion information of the subjects/objects in the scene, which has shown to be advantageous for human detection [1]. A monitoring system that uses only depth information is able to work in poor light conditions and provides privacy at the same time, which is a desirable feature for such kind of systems [2].

Several works about human postures detection with the RGB-D sensors exploit the use of skeleton tracking algorithms for rapidly transforming persons depth information to spatial joints that represent the human figure [3]-[4]. Unfortunately, when these methods are used for real world applications the output is not always stable and reliable. The reasons that reduce their performance depend on several factors. Among these, we have the distance between the person and the sensor (Fig. 1), the occlusions that occur when people interacts with environmental objects (Fig. 2) and also sideways poses that hides some parts of the user that are not visible to the sensor.

The aim of this work is to develop a system, based on depth cameras, which is able to classify three human postures, including standing, sitting, and lying positions that can work in real conditions. In order to do that, we need to deal with the aforementioned problems that afflict the skeleton tracker methods. Therefore, an artificial Neural Network (NN) model is adopted to rely on its generalization ability and its robustness against noisy and missed data. As opposed to other similar works [5]-[6], real-time tests, conceived to reproduce realistic and challenging situations for the tracker, covering the whole operative range of the sensor, have been carried out. During these experiments, the NN has been continuously fed with all the available joints generated by the skeleton tracker in order to analyse its robustness against unreliable and uncertain joints.

II. System

The proposed human posture detection relies on a skeleton tracker algorithm that is able to extract the joints of a person from the depth map. Two types of trackers have been used: Microsoft NUI (with the Kinect) and NiTE/OpenNI (using the Xtion Pro). These software tools are similar and provide the 3D position of the skeleton joints combined with an additional confidence value for each of them. This datum can assume three values: “tracked” when the algorithm is confident, “inferred” when it applies some heuristics to adjust the position, and “untracked” with uncertainty. Nevertheless, the “untracked” joints are anyway part of the whole skeleton and they have been used to analyse the robustness of the NN against noisy and uncertain values.

A. Dataset

The samples used to train the NN have been taken from the MSRDailyActivity3D dataset [7]. It is built with the Kinect NUI and contains 10 subjects performing various activities at the distance of about 2 m. For each frame of the video sequence, the position of 20 skeleton joints is stored in a text file. A total of 120 samples has been taken from these text files to build a set containing subjects in sitting, standing and lying position, equally subdivided.

B. NN Architecture

The structure of the NN has three layers, with 60 input neurons (3 coordinates for each 20 joints, as provided by the MSRDailyActivity3D dataset) and 3 output neurons, whose values range from 0 to 1 according to the posture. The neurons number of the hidden layer has been minimized using the cross-validation technique, in order to keep the amount of free variables, namely the associated weights, as small as possible [8], decreasing also the need of a large training set. As a result, an amount of 42 hidden units has been found as sufficient value. The sigmoid function and the iRPROP algorithm [9] have been used as activation function and learning phase respectively.

C. Training, Validation and Testing Sets

The dataset has been randomly divided into a training set, to adjust the weights of the NN, a validation set, to minimize the over-fitting, and a testing set to confirm the predictive power of the network. These sets are divided in 63, 21 and 36 samples respectively. Since the data are recorded at a fixed distance of about 2 m from the sensor, the joints have been normalized with the Euclidean norm to ensure depth invariant. The True Positive Rate (TPR) on the test set is 100%, since the data are free of excessive noise.

III. Real Time Tests

To understand the real performance of the network, real-time experiments have been set up both with the Kinect NUI and the NiTE tracker. Although these two software behave in a similar way, they have a significant difference. The first one represents the human skeleton with 20 joints, while the latter uses only 15 joints. Therefore, to work with our trained NN, the input is preprocessed to fill the missed joints with the closest available, as depicted in the Fig. 3.

A. Experimental Setup

The output of the NN is "standing", "sitting", and "lying" according to the value of the output neuron that is closest to 1. To analyze the results, the outputs are compared with the actual posture of the person, but the intermediate poses between postures (i.e. when the user is sitting down or standing up) are discarded. The experiment has been conducted in a real living room with a sofa. The sensors (Kinect and Xtion) have been placed at 1 m from the ground facing the sofa. A person, starting from the left, goes to the sofa, sits for a while, lies down, and then gets up again and goes away. The experiments have been carried out with 6 persons (3 male and 3 female) at 3 different distances (3.5, 2.5 and 1.5 m). This setup is intended to address the aforementioned human trackers problems about the distance and the melting issue between human and objects. All the tests run at 25 fps and the total number of analyzed frame are 5214.

B. Results

The NN output with the Kinect NUI proves to be extremely robust and reliable, achieving a 100% for all the three postures. The output with the NiTE skeleton tracker is less reliable and it is summarized with the confusion matrix of the Tab. I. We have to point out that these human trackers have been developed for natural interaction and gaming, and the players must stand in front of the sensor. Given that, the lying posture is expected to be the most challenging posture to classify. The TPR is 97.2% and it is worth to know that the actual lying posture can be misclassified only as sitting (FNR=2.8%), and that neither standing (also when the user is sideways) nor sitting is classified as lying. The overall accuracy for the three output is 99.6%.

TABLE I
CONFUSION MATRIX (NITE) ON 5214 FRAMES

	standing	*sitting*	*lying*	*accuracy*
standing	100%	0%	0%	100%
sitting	0%	100%	0%	99.5%
lying	0%	2.8%	97.2%	99.5%

II. Conclusion

The NN, trained with a Kinect dataset, demonstrates to well generalize also when it is fed with data produced by a different tracker (NiTE). Another important aspect to underline is that the misclassification for lying postures happens during postures transitions and that does not involve standing and sitting. The proposed system runs in real-time and, since it is based only on depth streams, it guarantees the privacy of the person and it is able to work also in poor light conditions.

These results make it feasible to develop solutions for smart environment involving depth cameras, such as falling event detectors. Smart homes of the future can have multiple depth cameras covering areas with high risk of fall, such for example bathroom and bedroom.

References

[1] J. Sung, C. Ponce, B. Selman and A. Saxena, "Human activity detection from rgbd images," CoRR, vol. Abs/1107.0169, 2011.
[2] X. Yu, "Approaches and principles of fall detection for elderly and patient," 10th Int. Conf. on e-health Networking Applications and Services. pp. 42-47, 2008.
[3] G. Chen, M. Giuliani, D. Clarke, A. Gaschler and A. Knoll, "Action recognition using ensemble weighted multi-instance learning," ICRA, 2014.
[4] M. Munaro, S. Ghidoni, D. T. Dizmen and E. Menegatti, "A Feature based Approach to People Re-Identification using Skeleton Key points," ICRA, 2014.
[5] O. Patsadu, C. Nukoolkit and B. Watanapa, "Human gesture recognition using Kinect camera," Computer Science and Software Engineering (JCSSE), 2012 International Joint Conference, 2012.
[6] T. Le, M. Nguyen and T. Nguyen, "Human posture recognition using human skeleton provided by Kinect," Computing, Management and Telecommunications (ComManTel), International Conference, 2013.
[7] J. Wang, Z. Liu, Y. Wu and J. Yuan, "Mining Actionlet Ensemble for Action Recognition with Depth Cameras," IEEE Conference on Computer Vision and Pattern Recognition (CVPR 2012), 2012.
[8] K. L. Priddy and P. E. Keller, "Artificial Neural Networks: An Introduction," SPIE Press, 2005.
[9] C. Igel and M. Husken. "Improving the Rprop Learning Algorithm," Second International Symposium on Neural Computation (NC 2000), pp. 115-121, ICSC Academic Press, 2000.

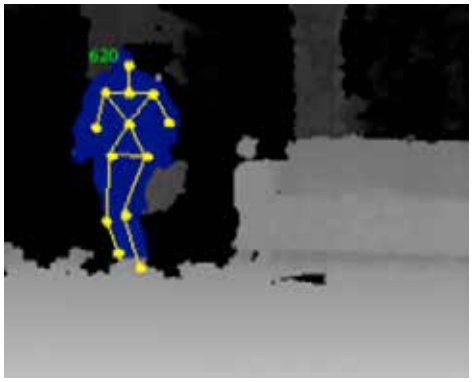

Fig. 1. Examples of worst skeleton detection. The person is far from the sensor and at least two joints are missed.

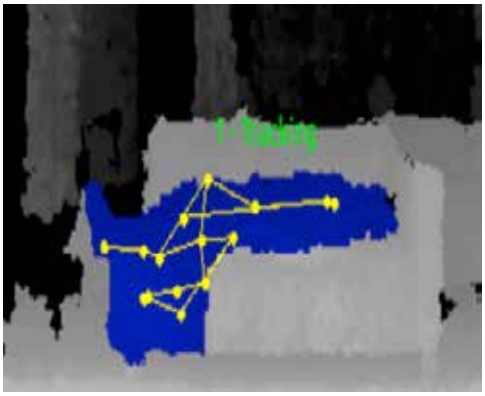

Fig. 2. Examples of worst skeleton detection. The user is lying on a sofa and the skeleton is fused with it.

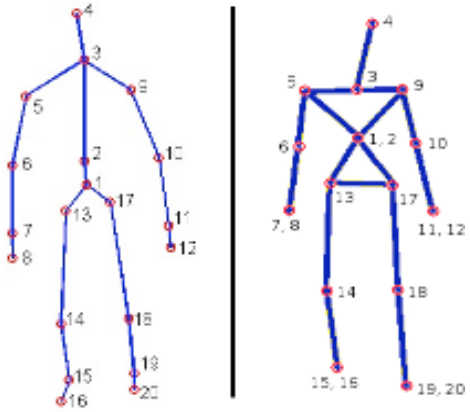

Fig. 3. Difference between skeleton representation. The Kinect NUI (left) uses 20 joints, while the NiTE SDK (right) only 15. The missing joints are replaced with the closest.

Characterization of transcriptional regulations in chronic leukemia: a network-based approach

E. Sauta[1], F. Vitali[1], A. Demartini[1], R. Bellazzi[1]
[1] *Department of Industrial and Information Engineering, University of Pavia*

***Abstract*—Transcription factors (TFs) play an essential role in regulating gene expression and in determining cell fate. Dysregulation of TFs interactions within gene-regulatory networks has been shown to cause malignancy. Focusing on chronic myeloid leukemia (CML), the study of the transcriptional relations is essential to exploit the activation of disease-specific gene programs. Using a genome-wide approach (ChIP-sequencing), we propose an integrated network framework to characterize the direct transcriptional effectors and the structure of this interactome, to potentially identify leukemic TFs signatures.**

This project is also a part of the initiative "Rete Ematologica Lombarda (REL) biotechnology cluster" for the implementation of genomic analysis and the development of new treatments for hematological diseases, with focus on myeloid neoplasms.

***Keywords*—Transcription factors, ChIP-sequencing, Bayesian Network, leukemia**

I. INTRODUCTION

Eukariotyc gene expression is the result of highly regulated networks at various molecular levels. Principal actors of these mechanisms are transcription factors (TFs), which bind specific DNA sequences to either activate or repress gene transcription. Exerting a spatial and temporal control on the expression of their targets, they modulate all complex biological process, such as cell differentiation, proliferation, and apoptosis, appearing fundamental for the cell fate [1].

The hematopoietic system provides a typical example of this concept: TFs activity is essential for the differentiation of blood stem cells, and perturbations of these transcriptional programs lead to an uncontrolled proliferation of immature blood cell lineages. Changing in transcription factors regulation, due to TF overexpression or mutations, has been regarded as the initiating lesion in leukemia [2]. Despite their importance, the specific function and downstream targets of transcription factor oncogenes are not completely known. Traditionally, medical research has focused on the study of a specific known mutated TF or small fraction of crucial TFs to elucidate their roles in biological processes [3-4]. This reductionist approach tends to isolate these molecules from the cellular environment in which they synergistically interact and may be not sufficient to investigate the transcriptional patterns underlying the considered disease. Advances in next-generation sequencing (NGS) technologies, and in particular the chromatin immuno-precipitation coupled with massively parallel sequencing (ChIP-Seq) method allowed to deeply investigate the molecular interactions of the transcriptional machinery [5]. This technique has enabled the high-throughput detection of transcription factor binding sites along the genome, and the ENCODE project [6] is actually the most complete compendium of these type of data. Using ENCODE ChIP-seq data, it is possible to integrate these genome-wide binding profiles, and resume the transcriptional state of a cell with a network description and analysis. Through a network-based approach, this interactome can be represented as a graph, in which nodes are the entities building up the system (i.e. TFs and genes) and edges correspond to the effective molecular regulation among them. Thus, the analysis of such networks enables to study the properties of the system that emerge from interactions of its individual components. Integrating this information with other sources of knowledge, i.e. gene expression profiles, could help to identify regulatory modules underlying the aberrant expression pattern of oncogenes.

In this study, we propose an integrated network method, to evaluate the roles of transcription factors, and infer their regulatory activities on the expression of their target genes. As a case study, we choose a specific pathological context, the chronic myeloid leukemia (CML), a myeloproliferative disorder caused by the oncogenic BCR-ABL gene fusion, whose transcriptional mechanisms have not yet been deeply investigated.

The framework consists in two main steps; the first one allows to build a causal network linking TFs and genes, using the ENCODE ChIP-seq data for CML. The obtained transcriptional regulatory network (TRN) is then integrated with gene expression profiles of chronic myeloid leukemia patients, available on the Gene Expression Omnibus repository [7]. The second step enables to make inference on TFs activities, and their potential effect on the gene expression, so the TRN is considered as a Bayesian Network and two different inference approaches, 'bottom-up' and 'top-down', are combined.

II. METHODS

TFs ChIP-sequencing alignment data for the chronic myeloid leukemia cell line (i.e. K562) were retrieved from the ENCODE data portal.

Only the TFs experiments with two or more biological replicates were considered and then filtered for the availability of BAM files and their relative control files. Thus, 65 TF-ChIP-seq experiments were analyzed and normalized using MACS 1.4.2 algorithm as a peak caller to identify TFs binding sites (peaks), which intersect the promoter of a target gene. Peaks were annotated to the human assembly (hg19) and then quantitatively weighted using a scoring method described in [8], taking into account the distance of each peak from a certain gene promoter and the intensity of the peak itself in that genomic region. This

procedure allows building a transcriptional regulatory network, characterized by directed edges from the 65 TFs to their targets (i.e. 20,811 genes). Since TFs are encoded by genes, when a TF binds the promoter region of another TF, in the network we also find connections between a TF to another TF. All network relationships were weighted, using the peak score as a strength index of the binding.

A Bayesian Network was defined based on the TRN structure. Each node that represents a TF or a gene is modelled as a binary variable (up/down), indicating if the node is up regulated or down regulated in the considered configuration. Each arc denotes a probabilistic influence of a TF on its target, and the type of this influence can be either activation or repression of the target expression.

The arc probabilities were obtained by properly rescaling the binding scores between 0 and 1, and by using the noisy-OR gate [9].

Since ChIP-seq does not provide any information about the TF effect, i.e. if the TF acts as a transcriptional activator or repressor, we exploited the ENCODE RNA sequencing data obtained from shRNA knockdown (KD) experiments on K562 transcription factors: silencing a specific TF allows to analyze the expression change of its target genes.

The available KD experiments cover only a small number of the TFs included in TRN. To overcome this limitation, the proposed method explores different combinations for the edges with an unknown effect given an experimental evidence of all the nodes. To evaluate the performance of each combination, a scoring index was applied to measure the accuracy of probabilistic predictions. It was defined as a sum of two Brier scores, one computed setting the evidence on the gene nodes and predicting the values for TF nodes (*bottom-up approach*), and the second calculated using the evidence on TF nodes, and estimating the states of the gene nodes (*top-down approach*).

The search algorithm for the best TF effects configuration starts with the condition of *all activations* for the unknown arcs. Then, it tries to substitute one activation at a time with an *inhibition*, and evaluates each result using the scoring index, described above. The inhibition associated to the best score is therefore considered as a known effect and definitely included in the model. The algorithm proceeds in the same way iteratively with the remaining unknown connections. The process stops when the scoring index does not improve the previous step performance.

III. RESULTS

Given the high complexity of the transcriptional regulatory network for the CML obtained from the ChIP-seq data, we extracted a sub network, characterized by 63 nodes: 58 gene nodes, 3 TFs with unknown effect and 2 TFs with an associated KD experiment, and 188 interactions, as shown in the Figure 1.

To set the binary states for each node, we performed a differential analysis on a cohort composed of 76 CML patients and 74 healthy subjects. These gene expression profiles (GSE13159) were retrieved from Gene Expression Omnibus repository.

The initial scoring index when all the unknown relationships between TF and their target genes were set to activations was 1.04. After 37 iterations, the search algorithm stopped to a 0.81 scoring value, as illustrated in the figure 2.

The estimated best TFs effect combination consists of 87 inhibitions (36 known from the KD data), and 101 activations (44 known from the KD data).

IV. CONCLUSION

This preliminary work with the final aim to characterize the transcriptional regulations in a disease context, i.e. the chronic myeloid leukemia, indicates the possibility of integrating different sources of knowledge, coming from NGS technologies (ChIP-seq and RNA-seq) and standard gene expression microarray data, with a network approach. These initial results suggest that the method can capture part of the molecular mechanisms underlying transcription process but further analysis are needed, e.g. using an independent validation dataset and a wider network, to include as much information as possible.

REFERENCES

[1] K. H. M. Prange, A. A. Singh, and J. H. A. Martens "The genome-wide molecular signature of transcription factors in leukemia", *Exp. Hematol*. 2014, vol 42 (8), pp. 637-50

[2] J. I. Silve, B. Gottgens "Transcriptional network control of normal and leukaemic hematopoiesis", *Exp Cell Res,* 2014,vol 329(2): pp 255-6

[3] M. Pimkin, A. V. Kossenkov, T. Mishra, C. S. Morrissey, W. Wu, et al, "Divergent functions of hematopoietic transcription factors in lineage priming and differentiation during erythro-megakaryopoiesis", *Genome Res*, 2014, vol 24 (12): pp 1932–1944

[4] E. Diffner, D. Beck, E. Gudgin, J. A. Thoms, K. Knezevic, et al, "Activity of a heptad of transcription factors is associated with stem cell programs and clinical outcome in acute myeloid leukemia", *Blood,* 2013, vol 121 (12): pp 2289-300

[5] T. S. Fure "ChIP–seq and beyond: new and improved methodologies to detect and characterize protein–DNA interactions", *Nature Rev. Genetics*, 2012, vol 13: pp 840-852

[6] The Encode Project Consortium. "An integrated encyclopedia of DNA elements in the human genome", *Nature,* 2012, vol 489: 57-74

[7] T. Barrett, S.E. Wilhite, P. Ledoux, C. Evangelista, I. F. Kim, et al. "NCBI GEO: archive for functional genomics data sets-update", *Nucleic Acids Res*, 2013, vol 41 (Database issue): D991-5

[8] W. Sikora-Wohlfeld, M. Ackermann, E. G. Christodoulou, K. Singaravelu, A. Beyer. "Assessing computational methods for transcription factor target gene identification based on ChIP-seq data", *PLoS Comput Biol*. 2013, vol 9 (11): e1003342

[9] J. Pearl, "Probabilistic reasoning in intelligent systems: networks of plausible inference", *Morgan Kaufmann Publishers*, 1988

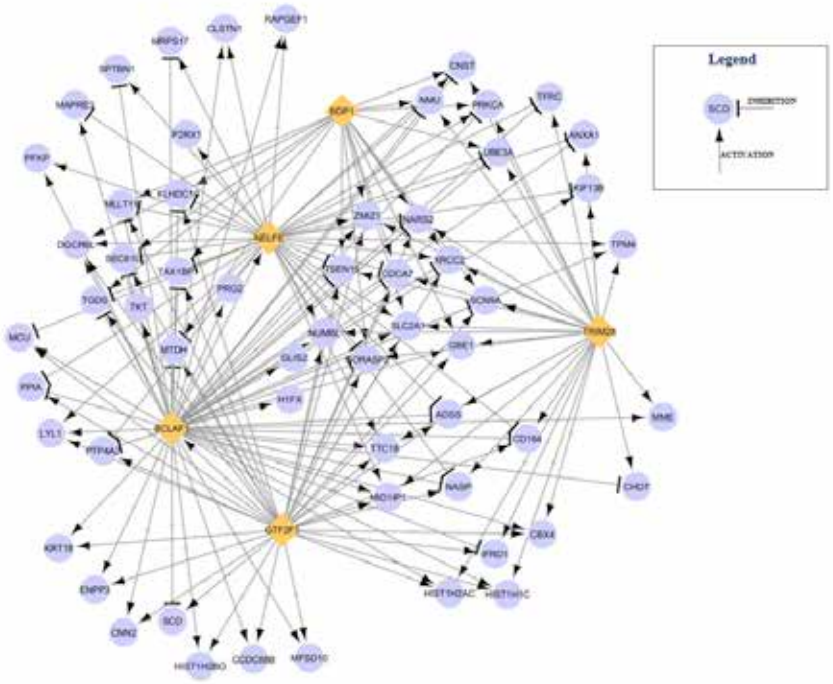

Fig. 1 The extracted sub network from the CML transcriptional regulatory network characterized by 5 transcription factors (diamond light orange nodes) and 58 target genes (ellipse violet nodes) and the 188 edges among them are represented by directed arrows.

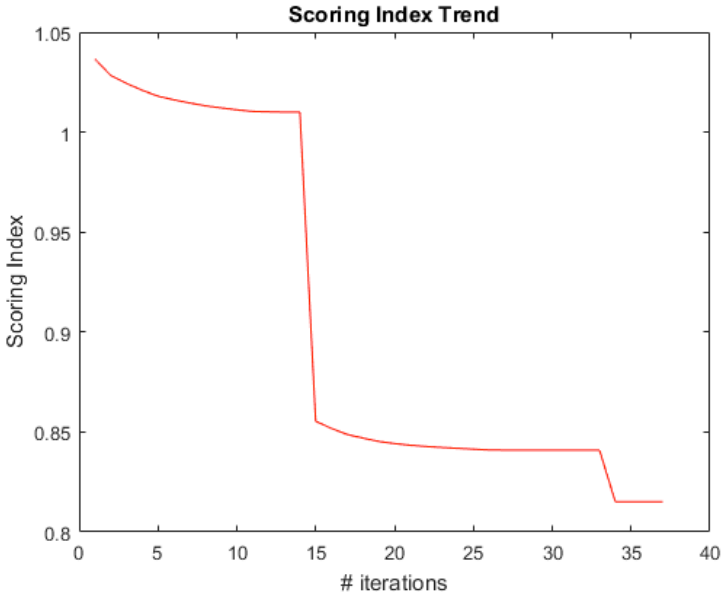

Fig. 2 Behavior of the scoring index as the iterations number of the search algorithm increases. The algorithm stops when there is no improvement of the performance.

A data driven control of a multi-compartimental physical model of electrolyte balances during dialysis

Domenico Vito[1], Giustina Casagrande[1], Camilla Bianchi[1],Maria Laura Costantino[1]
[1] *Laboratory of Biological Structure Mechanics*
Department of Chemistry, Materials and Chemical Engineering 'Giulio Natta'
Politecnico di Milano
Milan, Italy

***Abstract*— End stage uremic patients were around 3,000,000 worldwide and continue to increase, involving high percentages of elderly, predisposed to comorbidities. More than 2,000,000 of them were undergoing dialysis, with a huge socio economic impact. Dialysis is a procedure to remove waste products and excess fluid from the blood. It helps to keep the body in balance when the kidneys fail. Many different physical and mathematical models have been proposed to replicate static and dynamic phenomena related with dialysis in order to better understand them, but only few test bench were proposed and most of them are not automatically controlled. Here is presented an experimental setup for the automatic composition of a blood-like fluid used in a multi-compartmental physical simulation (mCPS) of the mass exchange phenomena during dialysis. The setup can be connected to the Dialysis Data Infrastructure (DDI) and the Dialysis MatLIB (DM), a database of clinical data acquired during dialysis treatments performed in 4 different dialysis units between Italy and Switzerland, in the framework of the Italy-Switzerland cooperation project INTERREG DialysIS. The dataset currently contains data recorded during 1018 dialysis sessions, referred to 145 patients.**

The proposed setup offered a mechatronic simulator that could reproduce the ionic exchanges during the dialysis also with a dynamic control

***Keywords*—Dialysis, physical simulator, data analysis, hypotension.**

I. Introduction

Dialysis is a widely applied therapy for the treatment of acute and chronic renal failure, when kidney transplantation is not an available option.

This therapy is often associated with several issues, which require to be focused on, from both a clinical and an engineering point of view.

A wrong assessment of the possible response of the patient to the treatment could easily lead to serious electrolyte and pressure imbalances, implying cardio-circulatory consequences and altering the efficiency of the mass and fluid exchanges with negative impact on the whole body [1].

Many different models have been proposed to replicate static and dynamic phenomena, such as solute kinetics or pressure variations, during the dialysis [2][3]. They are usually based on mathematical equations and computational simulations of mass exchanges between body compartments.

However, there are few examples of test benchs or physical simulators respectively aimed at reproducing fluid and mass exchange at the filter or among the body compartments of a patient undergoing dialysis.

Physical simulators, could help health care providers in the optimization of the clinical settings of a specific session. Furthermore they could help to avoid the long and complex process of setting up a clinical trial, especially in the earliest phases of a study.

An interesting and innovative approach could stand in combining computational models with physical simulators.

To reach this result it is necessary to automatically control the existing physical simulators with fitted algorithms to modulate the values of selected variables such as the concentration of specific solutes, the pH or the hydraulic pressure. These algorithms could be designed to reproduce clinical propile, so as to get more realistic simulations.

This work proposes an experimental setup for the automatic composition of a blood-like fluid used in a multi-compartmental physical model of the mass exchange phenomena during dialysis. The automatization implements a set of features to allow dynamic control of solute concentrations. It also allows the connection to the Dialysis Data Infrastructure (DDI) and the Dialysis MatLIB (DM), a comprehensive data structure of clinical data.

The DDI and DM have been developed in the framework of the Italy-Switzerland cooperation project INTERREG DialysIS, and currently contain data acquired during 1018 dialysis sessions, referred to 145 patients.

The database has been also used to develop predictive indexes of intra-dialysis hypotension events, based on a multivariate statistical analysis[6].

II. Materials and Methods

A. Dialysis Data Infrastructure

Clinical data have been acquired from 4 dialysis units between Lombardy and Switzerland (Dialysis Unit of Regional Hospital of Lugano, Switzerland; Nephrology and Dialysis Unit, A. Manzoni Hospital Lecco, Italy Nephlogy Unit of the Sant'Anna Hospital Como; Italy Nephrology and Dialysis Unit of the Circolo Hospital and Macchi Foundation Varese, Italy). A common platform, called DialysIS Data Infrastructure (DDI) has been developed to gather the heterogeneous information coming both from HIS (Hospital Information System), hemogas analyser, bioimpedance-meters and real–time acquisitions from dialysis machines [4].

The DialysIS Data Infrastructure has been designed to be a flexible tool allowing the sharing of clinical data among clinicians and researchers.

Accounting for their peculiar formats, it gives the possibility to separately handle the data coming from a

specific dialysis unit, through customized operations.

The DDI also allows the extraction of patient's specific data in order to perform personalized analysis.

Data are stored both in a MySQL® database a Matlab® table variables collection, designed to be interfaced with external applications.

B. Dialysis Matlib

Dialysis MATlib is a customized library, implemented in Matlab® in order to convert, harmonize and query the raw data coming from the clinical units.

Getting as input a .CVS file, the functions of the Dialysis MATlib library perform the extraction, cleaning and standardization of the input source data. Thanks to the Dialysis MATlib was possible to gather in a standard format all the information coming from the dialysis units.

Dialysis MATlib get the aim exploiting the features of the relational tables and their conversion into the Matlab table type variables. The table data type indeed, allows storing variables that are either string or numbers in a unique rows and column-oriented structure [5]. Through a dot notation is therefore possible to easily access to table rows and column, making data manipulation more simple and direct. Furthermore using the vector and matrix transformations, that are typical of the Matlab® environment, errors correction, standardization and data format conversion can be massively performed using just coding language, instead of complex SQL queries.

Dialysis MATlib is structured in macro-actions that cover all the data workflows on the DDI as in Figure 1.

C. The automatic control of the physical model

A first modular automatization mechanism has been applied to a multi-compartimental physical simulator (mCPS). The simulator considers the intra and extravascular compartments of a patient as different pools.

It models the mass exchanges between the body compartments during the dialysis theraphy.

The automatization of mCPS at this step was particularly focused on the composition of the fluids used in the mCPS to mime blood and interstitial fluids. The basic module is composed by a sensors-control actuators system as in Figure 2. A couple of Ion Selective Electrodes (ISE) produced by Vernier® (Beaverton, Oregon), ISE series (Ion Selective Electrodes), has been used to monitor the solute concentrations. A pH sensor produced by FLS R FIP division R (Genoa,Italy) PH200 model C was used to monitor pH and a Edwar TrueWave P700 pressure transducer to estimate the total volume of fluid to be conditioned.

The sensors were connected to a CY8CKIT-050 PSoC® 5LP board produced by Cypress (San Jose, CA USA) and used as control elements.

The board allows an easily firmware programming and incorporates either digital and analog memories as well peripherals on a single chip.

The actuators for the infusion of corrective solutions in the system were syringe pumps produced by New Era Pump Systems R (Farmingdale, New York), model NE-500. These pumps were equipped with a programmable internal microcontroller and a non-volatile memory, that enables to execute preset routine.

D. Firmware and Testing

The implemented firmware provides connection between sensors, actuators and software, and contains the algorithms for fluid conditioning control. The control mechanisms exploited the retroactive measure of the ionic concentration and of pH, to drive the syringe pumps, infusing the correct volumes.

The full system was tested on static and dynamic conditions, trying to stabilize and vary, according to pre-set trends, the concentration of the solutes in a container.

A LabView® interface has been also developed to allow the user to manually set the desired parameters and to work as a monitor of the system status. The interface also allows to connect the setup to the Dialysis Data Infrastrusture. The connection will allow the system to reproduce the initial composition of the compartments, on the basis of real clinical data.

III. Results and Conclusion

The proposed setup offered a mechatronic simulator that could reproduce the ionic exchanges during the dialysis also with a dynamic control. The system can also interact with a database containing clinical data, that could give a terms for comparison of the results and for the realistic set up of the controlling parameters. Going through further step of automation, it will possible to obtain a useful tool to investigate the patient response during the dialysis therapy.

Acknowledgement

This work was funded by INTERREG IT-CH EU Program DialysIS ID 33570710.

References

[1] Daurgidas J. T. Schneditz D. Compartment effects in hemodialysis. In Seminars in Dialysis, volume 14, pages 271–277, July-August 2001.

[2] Waniewski J. Mathematical modeling of fluid and solute transport in hemodialysis and peritoneal dialysis. Journal of Membrane Science, (274):24–37, 2006.

[3] Ursino, M., Innocenti, M. (1997) Mathematical investigation of some physiological factors involved in hemodialysis hypotension. Artificial Organs, 21, 891-902

[4] D. Vito, G. Casagrande, C. Bianchi, M. L. Costantino “A novel database approach to gather clinical data on dialysis treatments”, IEEE 1st RTA-CSIT Conference Proceed., December 2014.

[5] *Global Optimization Toolbox: User's Guide*, r2013, Mathworks, 2013.

[6] A. Tislér, K. Akócsi, B. Borbás et al., “The effect of frequent or occasional dialysis-associated hypotension on survival of patients on maintenance haemodialysis”, Nephrol Dial Transplant, 2003, vol. 18, pp. 2601–2605.

[7] D. Vito, G. Casagrande, G. Cappoli, C. Bianchi, G. Pontoriero, C. Schoenholzer, C. Minoretti, G. Rombolà, M. L. Costantino, “A predictive index of intra-dialysis IDH A statistical clinical data mining approach,” Int. Journal of Advances in Software Engineering & Research Methodology, vol. 2, no. 2, pp. 126–129, October 2015.

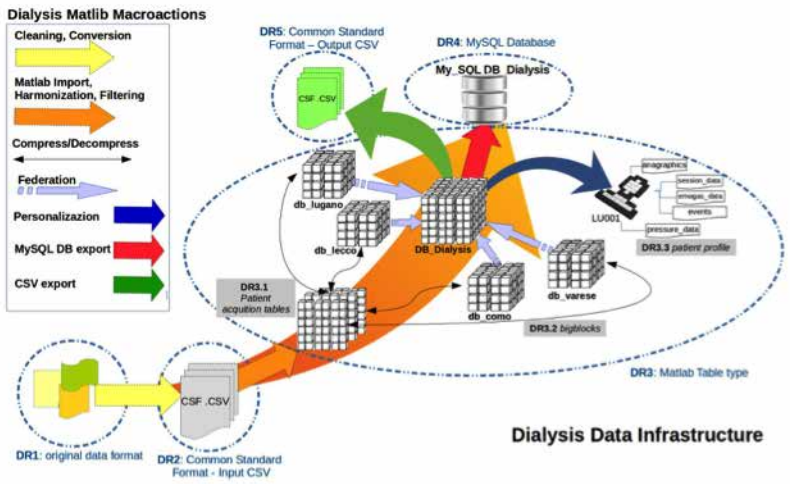

Fig. 1. Dialysis Data Infrastructure and Dialysis MATlib

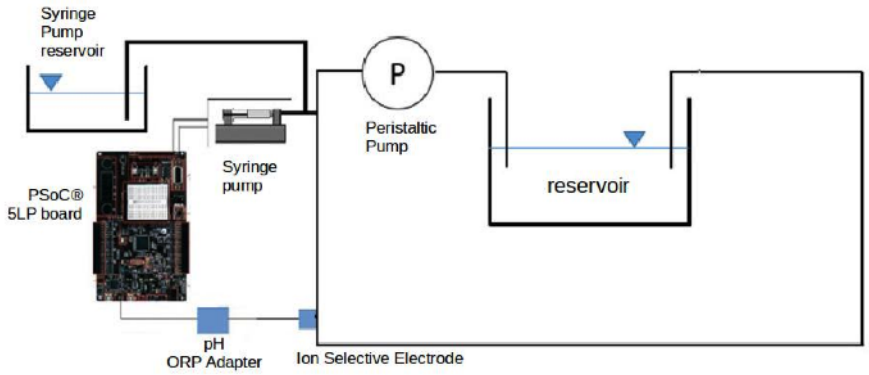

Fig. 2. Simulator experimental setup

BIOLOGIA COMPUTAZIONALE

Two-domain peptides to promote surface bio-activation of gold: a molecular dynamics study

C. Cosenza[2], F. Causa[1,2,3], and P.A. Netti[1,2,3]

[1] *Dipartimento di Ingegneria Chimica, Dei Materiali e Della Produzione Industriale (DICMAPI), University Federico II Piazzale Tecchio 80, 80125, Naples, Italy*

[2] *Interdicisplinary Research Center on Biomaterials (CRIB) University of Naples Federico II, Piazzale Tecchio 80, 80125, Naples, Italy*

[3] *Center for Advanced Biomaterials for Health Care@CRIB Istituto Italiano di Tecnologia, Largo Barsanti e Matteucci 53 80125 Napoli, Italy*

***Abstract*—The use of computational approaches in the study of the interface between biological species and inorganic materials is a rational route to design hybrid nanostructures.**
In this work we proposed classical and steered molecular dynamics to focus on the interaction between peptides and gold surface in order to promote surface bio-activation.

***Keywords*—bioactivation, steered molecular dynamics, molecular dynamics, peptides.**

I. Introduction

Researchers have developed different approaches to promote the material surface bio-activation: physical methods, based on adsorption or self-assembly processes, and chemical methods, requiring covalent surface modification [1]. Physical methods have used proteins from the extracellular matrix (ECM) or their small derived bioactive peptides merely adsorbed on biomaterial surfaces dealing with unpredictable, non-specific and potentially unstable interactions both with the cells and the material surface. Furthermore, in the last decade different amino-acid sequences have been screened for specific and strong adsorption against inorganic or synthetic materials [2]. Studying the mechanisms of interaction at the interfaces thank to molecular simulations in the context of the measurements, in an integrated approach, provides a complete vision of the interaction [3]. In a previous work, we proposed to use amino-acid sequences composed by two domains: a part combinatorially selected to bind to a given material and a bioactive part able to stimulate cell-adhesion [4]-[5]. Toward the applicability of this method it is fundamental to understand if the parts composing the two domains are still able to work together as bi-functional linkers, preserving a stable and specific interaction toward the biomaterial surface and keeping, at the same time, a suitable signal molecule display. We evaluated whether two-domain peptide ligands were able to create a mechanically stable interface, by preserving a sufficiently strong interaction of the anchoring part on the material after the pulling actions occurring during the cytoskeleton assembly [5]. Molecular simulations and experimental results discriminate the ability of ligands to preserve an anchoring domain strongly adsorbed on the material. In particular, ligands preserving a strong anchoring domain show enhancement in the cell polarization process and alignment. As a result, we have demonstrated how the mechanical resistance of ligands, upon integrin engagement, affects cell response [5].

In this work, we proposed the use of a more suitable computational approach, able to *in silico* discriminate the ligand mechanical resistance after adsorption. (Fig.1) We applied a steered molecular dynamics methodology [6] to specifically designed two-domain peptides using parameters able to describe the bio-inorganic interface [7].

II. Conclusion

We evaluate the ligand adsorption resistance and estimate the *in silico* rupture forces of two-domain peptides. We set the optimal parameters and protocol to study specifically designed peptide ligands, composed by an anchoring domain and a cell binding motif at the gold-water interface.

References

[1] M. Ventre, F. Causa, P.A. Netti, "Determinants of cell-material crosstalk at the interface: towards engineering of cell instructive materials," *J. R. Soc. Interface* , 9, pp. 2017-2032, 2012.

[2] C. Tamerler, and M. Sarikaya. "Molecular biomimetics: nanotechnology and bionanotechnology using genetically engineered peptides," *Philosophical Transactions of the Royal Society of London A: Mathematical, Physical and Engineering Sciences*, 367, 1705-1726, 2009.

[3] Z.H. Tang, J.P. Palafox-Hernandez, W.C. Law, Z.E. Hughes, M.T. Swihart, P.N. Prasad, M. Knecht and T.Walsh. "Biomolecular recognition principles for bio- nanocombinatorics: an integrated approach to elucidate enthalpic and entropic factors," *ACS Nano,* 7, 9632-9646, 2013.

[4] F. Causa, R. Della Moglie, E. Iaccino, F. Mimmi, D. Marasco, P.L. Scognamiglio, E. Battista, C. Palmieri, C. Cosenza, L. Sanguigno, I. Quinto, G. Scala, P.A. Netti. Evolutionary screening and adsorption behavior of engineered {M13} bacteriophage and derived dodecapeptide for selective decoration of gold interfaces. *Journal of Colloid and Interface Science,* 389, pp.220 – 229, 2013.

[5] C. Cosenza, V. Lettera, F. Causa, P. L. Scognamiglio, E. Battista,P.A. Netti. Cell mechanosensory recognizes ligand compliance at biomaterial interface. *Biomaterials*, *76*, pp. 282-291, 2016.

[6] N. Schwierz, D. Horinek, S. Liese, T. Pirzer, B. N. Balzer, T. Hugel & R. R. Netz.. On the relationship between peptide adsorption resistance and surface contact angle: a combined experimental and simulation single-molecule study. *Journal of the American Chemical Society,* 134(48), pp. 19628-19638, 2012.

[7] H. Heinz, R. Vaia, B. Farmer, R. Naik. "Accurate simulation of surfaces and interfaces of face-centered cubic metals using 12- 6 and 9-6 Lennard-Jones Potentials". *The Journal of Physical Chemistry C*, 112, pp. 17281–17290, 2008

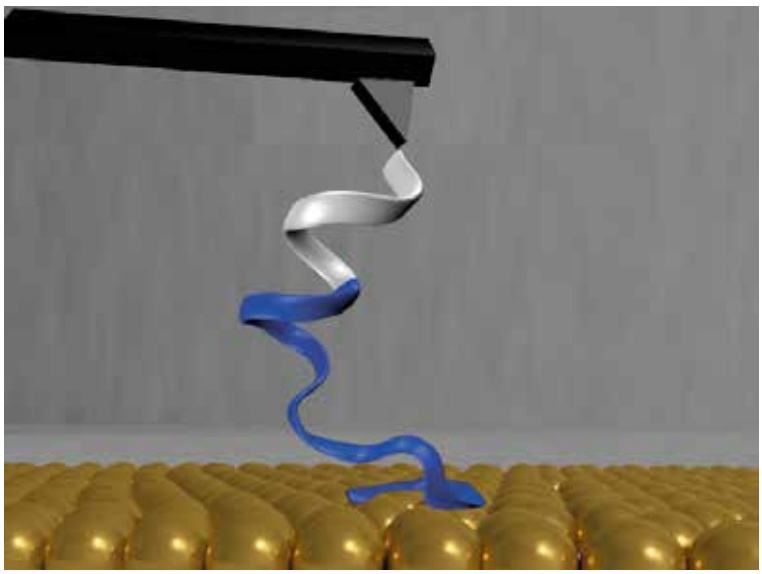

Fig. 1. A graphical representation of the Steered Molecular Dynamics approach proposed in the current work.

Modeling HPV early promoter gene expression

A. Giaretta[1], E. Bergamo[1], B. Di Camillo[1], L. Barzon[2] and G.M. Toffolo[1]
[1]Department of Information Engineering, University of Padova, Italy
[2] Department of Molecular Medicine, University of Padova, Italy

***Abstract* – Human papillomaviruses (*HPV*) are small *DNA* viruses. They infect epithelial cells and cause a variety of lesions ranging from common warts to cervical neoplasia and cancer.**

HPV life cycle is tightly linked to the infected cell differentiation program and its evolution is strictly joined to the switch between the early and the late viral polycistronic promoters.

We present a novel mathematical model condensing the available biologic knowledge on the early promoter regulation. The model includes the main regulation by *E2* viral protein as well as a recent discovered co-regulation function mediated by the viral *E1* protein. Dynamical predictions and parametric sensitivity analysis (*PSA*) revealed the importance of both *E2* and *E1* regulation to correctly predict the temporal behaviour of the early promoter switching off.

***Keywords* – HPV, gene, regulation, modeling**

I. Introduction

HPV are primarily epithelial specific viruses [1], with a life cycle strictly linked to the differentiation stage of the infected keratinocytes, and capable to induce, in their high risk form, cervical cancer. Of paramount importance, especially in the first phases of the infection, is the early promoter. This latter is policystronic, hence producing a pre-mRNA subjected to splicing and alternative splicing yielding the single early transcripts. The "regulation core" of the early promoter is represented by *E1* and *E2* gene regulation. These latter genes are essential for the viral DNA replication, while *E2* besides acting in cooperation with *E1* for the viral replication represents the main transcriptional regulator of the early promoter. In particular, the feedback on the early promoter shows both a transactivation and a strong repression function when *E2* is present in low and high concentrations, respectively [2]. Recently, it has been discovered that *E1* viral protein, whose *mRNA* is increased during the keratinocytes differentiation program, accounts for both a positive regulation of *E2* transcripts and protein stabilization [3]. This regulation of *E1* is interesting since it could allow *E2* to reach its typical differentiation levels, when the late promoter is activated, in order to optimize the viral *DNA* replication.

II. Methods

A. Model

The main mechanisms of HR-HPV early gene circuit are summarized in Fig.1:

1. The early promoter controls the primary polycistronic transcript *x*. *mRNAs* encoding all the early genes are produced by splicing of x.
2. The spliced *mRNA E2 (mE2*) encodes for *E2* protein.
3. The spliced *mRNA E1* (*mE1*) encodes for *E1* protein.
4. *E2* protein is the main regulator of the early promoter. It generates a slight positive feedback effect when present in low concentration, a negative feedback effect when present in high concentration.
5. *E1* acts with a positive regulation enhancing the *mE2* transcript and with a negative regulation on *E2* degradation, hence increasing its stability [3].

B. Model Equations

Model equations, based on mass action, are:

$$\dot{x} = S_x(E2) - k_s x \tag{1}$$

$$m\dot{E}1 = k_{1s}(t) k_s x - \delta_{1m} mE1 \tag{2}$$

$$m\dot{E}2 = k_{2s}(t) k_s x - \delta_{2m} mE2 \tag{3}$$

$$\dot{E}1 = \beta_1 mE1 - \delta_{1p} E1 \tag{4}$$

$$\dot{E}2 = \beta_2 mE2 - \delta_{2p}(E1) E2 \tag{5}$$

where the state variables are the concentrations [nM] of: the primary transcript *x*, *mRNAs mE1*, *mE2* and proteins *E1*, *E2*.

S_x refers for the transcription of *x* enhanced by low values of E2 concentration and repressed by elevated E2 concentration [2] (Fig. 2A) according to (7).

$$S_x(E2) = \begin{cases} S_b + \dfrac{a_1 E2^{q_1}}{\lambda_1^{q_1} + E2^{q_1}}, & E2 < E2_{th} \\ \dfrac{a_2 \lambda_2^{q_2}}{\lambda_2^{q_2} + (E2 - E2_{th})^{q_2}}, & E2 > E2_{th} \end{cases} \tag{7}$$

k_{1s} represents the splicing flux for the *mE1* transcript (Fig. 2B) and is modeled as a time variant forcing function (8), tightly bounded to the host cell differentiation program as reported in [10].

$$k_{1s}(t) = \begin{cases} k_{1s}^{\min} + \dfrac{a_3 t^{q_3}}{\lambda_3^{q_3} + t^{q_3}}, & t < t_h \\ \dfrac{a_4 \lambda_4^{q_4}}{\lambda_4^{q_4} + (t - t_h)^{q_4}}, & t > t_h \end{cases} \tag{8}$$

k_{2s} accounts for the splicing flux for the *mE2* transcript (9) and it is positively regulated by *E1* according to [3] (Fig. 2C).

$$k_{2s}(E1) = \frac{(f_1 - 1) k_{2s}^{\min}}{1 + \exp\left(\dfrac{\lambda_5 - E1}{\sigma_1}\right)} + k_{2s}^{\min} \tag{9}$$

δ_{2p} is the degradation of *E2* (10) which is negatively regulated by *E1* according to [3] (Fig. 2D).

$$\delta_{2p}(E1) = \delta_2^{\min} \left\{ (f_2 - 1) \left(1 - \frac{1}{1 + \exp\left(\dfrac{\lambda_6 - E1}{\sigma_2}\right)} \right) + 1 \right\} \tag{10}$$

β_1 and β_2 are the rate constants for *E1* and *E2* protein translation assumed to be linearly related to the cognate mRNAs, see (4-5).

δ_{im} and δ_{ip} are degradations of transcripts and proteins (see (2-6)), assumed to be first order processes with the only exception of $\delta_{2p,}$ see (10).

TABLE I
MODEL PARAMETERS

Parameters	*Value*	*Unit of measure*	*References*
S_b	10	[nM/min]	Assumed
k_s	0.0693	[1/min]	[6]
a_1	1.6	[nM/min]	[2]
$E2_{th}$	5	[nM]	[2]
λ_1	2.83	[nM]	[2]
q_1	2	[-]	[2]
a_2	11.21	[nM/min]	[2]
λ_2	2	[nM]	[2]
q_2	2	[-]	[2]
a_3	12.34	[-]	[4]
λ_3	3.76*1e4	[min]	[4]
q_3	4	[-]	[4]
a_4	0.38	[-]	[4]
λ_4	5*1e3	[min]	[4]
q_4	2	[-]	[4]
t_h	12	[days]	[4]
f_1	10	[-]	[3]
$k_{1s}^{\min}$	9*1e-3	[-]	[4]
$k_{2s}^{\min}$	9*1e-3	[-]	[4]
λ_5	9	[nM]	[4]
σ_1	0.7	[nM]	[4]
λ_6	13	[nM]	[3]
σ_2	0.7	[nM]	[3]
$\delta_2^{\min}$	0.0019	[1/min]	[3]
f_2	4	[-]	[3]
δ_{1m}	2.9*1e-2	[1/min]	[4] ,[5]
δ_{2m}	2.9*1e-2	[1/min]	[3]
δ_{1p}	5.7*1e-3	[1/min]	Assumed
β_1	1.5*1e-2	[1/min]	Assumed
β_2	2*1e-2	[1/min]	Assumed

C. Parametric Sensitivity Analysis (PSA)

Nominal values for all model parameters are summarized in Table I together with references used to fix/infer these values. Based on them, model equations implemented in MATLAB are simulated to assess the relative role of *E1* and *E2* regulation. Moreover, normalized sensitivity coefficients, $S_{i,j}$, were calculated:

$$S_{i,j}(t) = \frac{\partial x_i(t)}{\partial p_j}\frac{p_j}{x_i} \tag{11}$$

where x_i is the *i-th* state variabl and p_j is the *j-th* model parameter. Finally, integrated sensitivy coefficients, $S_{i,j}^{\text{int}}$, were evaluated

$$S_{i,j}^{\text{int}} = \int_{t_0}^{t} S_{i,j}(\tau)\, d\tau \tag{12}$$

where $[t_0,t]$ is the time interval of interest.

III. RESULTS

The dynamic behaviour of state variables with and without *E1* co-regulation is shown in Fig. 3. In both cases the initial phase is very fast and all transcripts reach a steady state nearly 6 hours post infection, consistently with [5]. Both *E1* effect to enhance *E2* transcript and to knock down *E2* degradation are necessary for turning off the early promoter primary transcript observed 8-12 days post infections [4].

Parametric sensitivity analysis (*PSA*) [7] shows the dominance of the parameters belonging to the negative feedback (Fig.4), but high sensitivities were shown also for the parameters acting in *E1*-coregulation. This is consistent with the beginning of the positive regulation of *E1* during the differentiation program.

IV. CONCLUSIONS

The proposed quantitative/qualitative model represents a first attempt to collect and summarize the biological knowledge spread in many literature works on the early *HPV* promoter. The model addresses the main mechanisms of the circuit involving the early promoter, two key transcripts *mE1* and *mE2* and two feedback controls exerted by the translated proteins *E1* and *E2*.

In particular, our results, in agreement with recent experimental findings [3], have confirmed the role of *E1* co-regulation function for the switching off of the early promoter. Moreover, *PSA* shows the dominance of the parameters belonging to *E2* negative feedback but high sensitivities are evaluated for the *E1* co-regulation, as well.

The proposed model incorporates the available knowledge but required numerous simplifying assumptions thus, hopefully, its validity will be further investigated on experimental time series data.

REFERENCES

[1]C. Johansson and S. Schwartz, "Regulation of human papillomavirus gene expression by splicing and polyadenylation.," *Nat. Rev. Microbiol.*, vol. 11, no. 4, pp. 239–51, 2013.

[2]S. Y. Hou, S.-Y. Wu, and C.-M. Chiang, "Transcriptional activity among high and low risk human papillomavirus E2 proteins correlates with E2 DNA binding" *J. Biol. Chem.*, vol. 277, no. 47, pp. 45619–45629, 2002.

[3]L. E. King, E. S. Dornan, M. M. Donaldson, and I. M. Morgan, "Human papillomavirus 16 E2 stability and transcriptional activation is enhanced by E1 via a direct protein-protein interaction," *Virology*, vol. 414, no. 1, pp. 26–33, 2011.

[4]M. a Ozbun and C. Meyers, "Human papillomavirus type 31b E1 and E2 transcript expression correlates with vegetative viral genome amplification." *Virology*, vol. 248, no. 2, pp. 218–230, 1998.

[5]M. a Ozbun, "Human papillomavirus type 31b infection of human keratinocytes and the onset of early transcription.," *J. Virol.*, vol. 76, no. 22, pp. 11291–11300, 2002.

[6]A. Corradin, B. DI Camillo, F. Rende, V. Ciminale, G. M. Toffolo, and C. Cobelli, "Retrovirus HTLV-1 gene circuit: a potential oscillator for eukaryotes.," *Pac. Symp. Biocomput.*, vol. 432, pp. 421–432, 2010.

[7]Perumal, T. M., & Gunawan, R. (2011). Understanding dynamics using sensitivity analysis: caveat and solution. *BMC Systems Biology*, 5(1), 41.

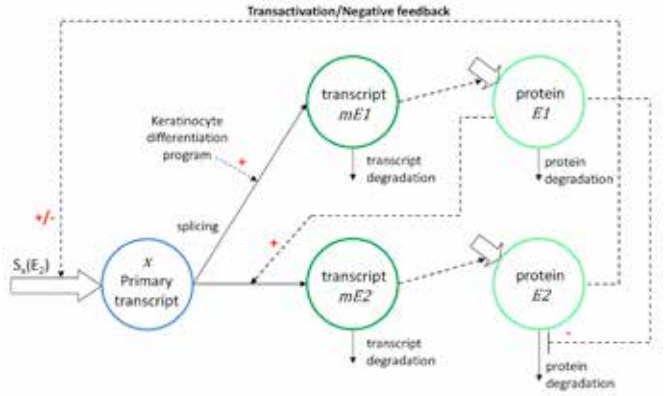

Fig.1 The model of HPV gene circuit. Solid arrows represent fluxes, dashed arrows controls. In blue the primary transcript, in green the transcripts (and their respective proteins) of early non-oncogenes and in red the early oncogenes.

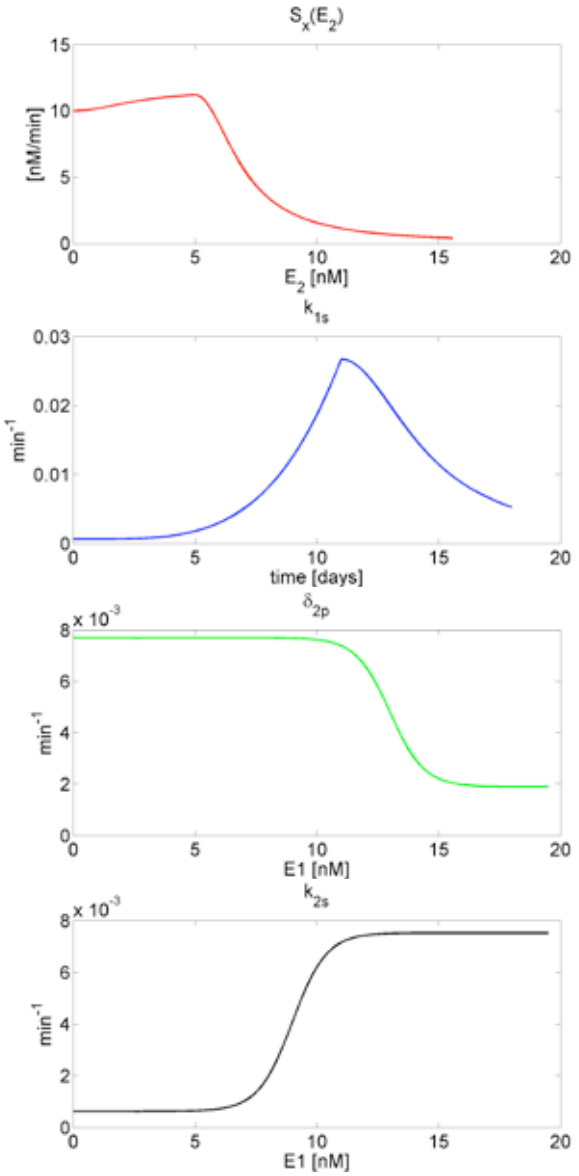

Fig.2 **First panel:** Syntesis of the primary transcript regulated by *E2* (7). **Second panel:** Rate constant for *mE1* splicing regulated by cellular differentiation (8). **Third panel:** *E2* degradation mediates by *E1* concentration (9). **Fourth panel:** Rate constant for *mE2* splicing positively regulated by *E1* concentration (10).

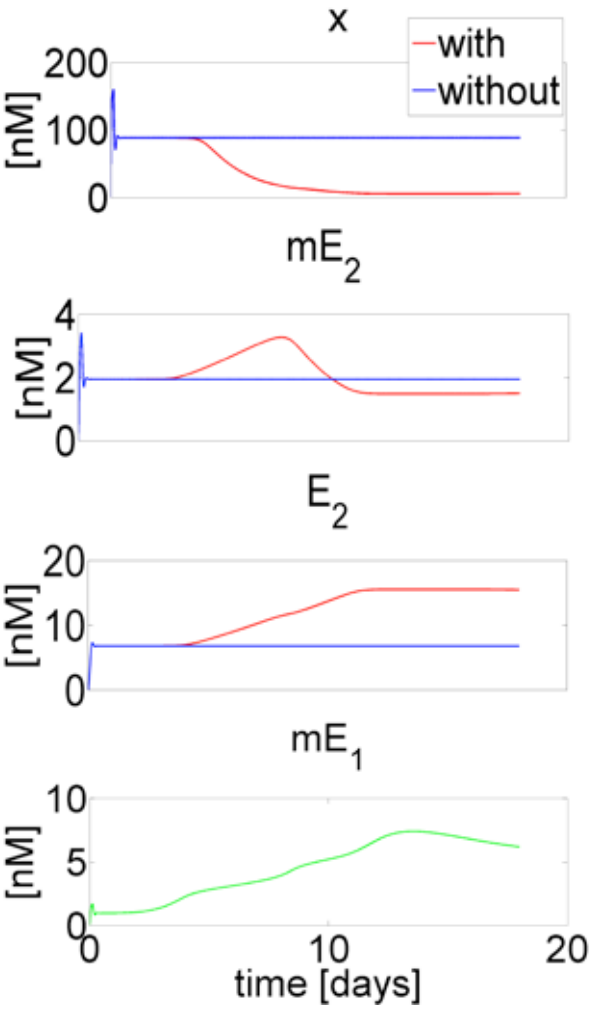

Fig.3 Model state variables with and without *E1* regulation during cellular differentiation. **First panel**: Early promoter (1). **Second panel**: *mE2* transcript (3). **Third panel**: *E2* protein (5). **Fourth panel**: *mE1* transcript (2).

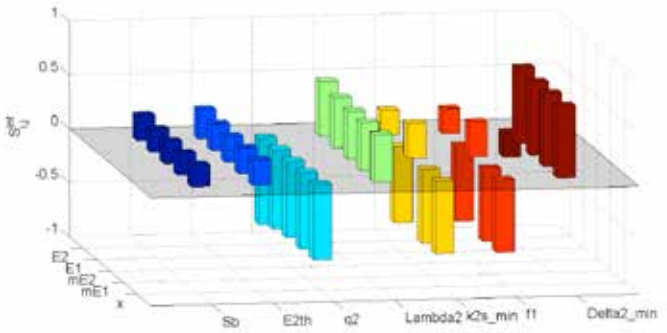

Fig.4 Integrated sensitivity coefficients (eq. 11 and 12) of the state variables with respect to the main parameters that account for the negative and positive feedback effect.

Control of gene expression for the study of neurodegenerative disorders

G. Perrino[1, 2], C. Wilson[2], M. Santorelli[2, 3] and D. di Bernardo[2, 3]

[1] *Department of Information Technology and Electrical Engineering, University of Naples Federico II, 80125 Naples, Italy*
[2] *Telethon Institute of Genetics and Medicine, 80078 Pozzuoli, Italy*
[3] *Department of Chemical, Materials and Industrial Engineering, University of Naples Federico II, 80125 Naples, Italy*

***Abstract*—Neurodegenerative disorders are characterised by the progressive disruption of specific neuronal population partly due to the formation of abnormal protein aggregates that interfere with normal cell functions. In Parkinson's disease, the role of abnormal α-synuclein protein aggregates in causing the disease is well established. Mutations in α-synuclein are known to cause familial Parkinson's disease. A quantitative understanding of the dynamics of α-synuclein protein aggregation in wild type and mutant form is however lacking. Here, we explore the feasibility of using a microfluidics-based platform for automatic control of protein expression from a galactose-inducible promoter in yeast, to model and study the human α-synuclein protein.**

***Keywords*—Synthetic biology, Modelling, Dynamics and control, Gene expression.**

I. Introduction

NEURODEGENERATIVE disorders are associated to the formation of abnormal protein aggregates that interfere with the normal functions of neurons, causing the progressive disruption of the neuronal population. The dysfunction of α-synuclein (α-syn) protein is involved in Parkinson's disease (PD) and related neurodegenerative disorders [1]. Mutations in α-syn protein are also associated with rare forms of early-onset familial PD [2]. The human α-synuclein biology has been extensively characterised [1]. A yeast model expressing wild type and mutant human α-syn protein has been used to qualitatively study its aggregation properties [2]. However, α-synuclein overexpression is toxic also for yeast cells, thus making it difficult to study, if its expression is not carefully controlled. Indeed, a quantitative study of the aggregation dynamics of the α-syn protein is still lacking.

Automatic control of gene expression can be used to precisely regulate the expression level of a protein in a population of cells [3]. Several successful attempts have been described in literature to assess the feasibility of such technology using fluorescent reporter proteins [4], [5], [6], [7], [8], [9], [10].

Here, we explore the feasibility of using a microfluidics-based platform for automatic gene expression control, which we recently developed [3], to control the expression of the human α-synuclein protein in yeast cells. The aim is to attain a quantitative understanding of the dynamics of α-syn protein's aggregation, by carefully regulating its expression and following its dynamics in real-time. Driving the expression of α-syn protein at different values, we can assess quantitatively the dynamics that lead to the formation of protein aggregates.

II. An Experimental Testbed to Study the Dynamics of the Alpha-Synuclein Protein

The toxicity of the α-syn protein has been characterised in several cell-based and organism-based models [1]. A yeast strain overexpressing normal and mutant α-syn protein fused to a green fluorescent reporter protein (α-syn-GFP) under the galactose responsive promoter has been successfully used to dissect molecular pathways involved in α-syn biology [2]. The overexpression of the human α-syn-GFP protein in yeast cells mimics the situation of the aging neurons when the capacity of the quality-control (QC) system to cope with accumulating misfolded proteins is exceeded [2]. One copy of the α-syn-GFP construct is not able to saturate the QC system of the yeast. However, when inserting multiple copies of the α-syn-GFP construct inside the yeast, the α-syn protein causes the formation of the protein aggregates that are toxic for yeast cells. Thus, the toxicity of the α-syn protein can be studied using yeast strains carrying multiple copies of the galactose-inducible α-syn-GFP construct. However, as soon as the promoter is activated by growing these cells in galactose enriched medium, α-syn toxicity causes cell death thus preventing a thorough investigation and quantification of aggregation dynamics.

Automatic control of the galactose-inducible promoter can overcome this limitation and enable quantitative analysis of α-syn-GFP dynamics in yeast strains carrying the multiple copies of the α-syn-GFP construct. Specifically, as depicted in Fig.1, automatic control of gene expression from the galactose-inducible promoter can be used to increase α-syn-GFP expression at discrete steps starting from a fully repressed promoter (glucose) thus enabling precise quantification and comparison of the aggregation dynamics of α-syn-GFP wild type and mutant forms.

In this work, we proposed a pilot study on the strain carrying the galactose-inducible α-syn-GFP construct (A53T mutant form) in single copy, in order to assess the feasibility of controlling its expression at discrete steps in yeast cells.

III. Results

A. Control strategy

To assess the dynamics of the α-syn-GFP protein, i.e. to

control the value of the protein at different levels, we implemented a Model Predictive Control (MPC) strategy, which we successfully used to control the galactose-inducible promoter in yeasts [3].

The MPC algorithm is a feedback optimisation-based technique, which uses a mathematical model of the system being controlled to predict the future values of the control error and to find the best value of the control input that minimises it [11].

B. Modelling

The MPC strategy needs a dynamical model of the system being controlled to compute the control input. Thus, we derived a two-dimensional time-discrete state-space linear dynamical model of the α-synA53T-GFP strain carrying the galactose-inducible promoter (single copy). To this end, a system identification experiment was performed on the α-synA53T-GFP yeast strain, as depicted in Fig. 2. Cells were kept in galactose enriched medium in order to fully activate the galactose promoter. The identification experiment was carried out for 40 hours, and galactose and glucose enriched media were alternatively provided to cells for 480 minutes (Fig. 2). The average fluorescence of the cell population is then quantified at each sampling time and taken as the system output (Fig. 2}, Upper Panel; black line).

A state-space identification technique was used to fit the model parameters to the data set obtained from the identification experiment (Fig. 2) [12].

C. Numerical simulations and experimental results

As we would like to increase the protein expression at discrete steps, we chose two reference signals: (*i)* a descending staircase function where each step lasts 750 min, beginning at 75% of the calibration phase average fluorescence, then stepping down to 50% and then 25%; and *(ii)* an ascending staircase function where the first and the second step last 750 min, and the third 500 min, beginning at 25% of the high steady state fluorescence value computed during the calibration phase, then stepping up to 50% and then 75%.

Numerical simulations of the control experiments confirmed the ability of the controller to follow the desired time-varying reference signals (Fig. 3a-b).

We thus decided to perform the control experiments *in vivo*, whose results are shown in Fig. 3c-d. Before each control experiment started, cells were inoculated in proper enriched medium to induce, or repress, the expression of the α-syn-GFP construct, depending on the reference signal. The experimental results confirmed the numerical simulations, demonstrating the ability of the methodology to study the dynamics of the expression of a protein in a quantitative way.

IV. CONCLUSION

Automatic control of gene expression is a key technology in synthetic biology and, so far, is enough mature to be applied to real test case to assess quantitatively the dynamics of gene expression. By means of the yeast model for the study of the Parkinson's disease, we demonstrated that a quantitative study of the neurodegenerative disorders is possible using the automatic control of gene expression through a microfluidics-based real-time platform.

REFERENCES

[1] 1. Auluck, P.K., G. Caraveo, and S. Lindquist, *α-Synuclein: Membrane Interactions and Toxicity in Parkinson's Disease.* Annual Review of Cell and Developmental Biology, 2010. **26**(1): p. 211-233.

[2] 2. Outeiro, T.F. and S. Lindquist, *Yeast Cells Provide Insight into Alpha-Synuclein Biology and Pathobiology.* Science, 2003. **302**(5651): p. 1772-1775.

[3] 3. Fiore, G., et al., *In Vivo Real-Time Control of Gene Expression: A Comparative Analysis of Feedback Control Strategies in Yeast.* ACS Synthetic Biology, 2016. **5**(2): p. 154-162.

[4] 4. Menolascina, F., et al., *In-Vivo Real-Time Control of Protein Expression from Endogenous and Synthetic Gene Networks.* PLoS Comput Biol, 2014. **10**(5): p. e1003625.

[5] 5. Danino, T., et al., *A synchronized quorum of genetic clocks.* Nature, 2010. **463**(7279): p. 326--330.

[6] 6. Olson, E.J., et al., *Characterizing bacterial gene circuit dynamics with optically programmed gene expression signals.* Nat Meth, 2014. **11**(4): p. 449--455.

[7] 7. Milias-Argeitis, A., et al., *In silico feedback for in vivo regulation of a gene expression circuit.* Nat Biotech, 2011. **29**(12): p. 1114--1116.

[8] 8. Toettcher, J.E., et al., *Light-based feedback for controlling intracellular signaling dynamics.* Nat Meth, 2011. **8**(10): p. 837--839.

[9] 9. Uhlendorf, J., et al., *Long-term model predictive control of gene expression at the population and single-cell levels.* Proceedings of the National Academy of Sciences, 2012. **109**(35): p. 14271-14276.

[10] 10. Melendez, J., et al., *Real-time optogenetic control of intracellular protein concentration in microbial cell cultures.* Integr. Biol., 2014. **6**: p. 366-372.

[11] 11. Morari, M. and J.H. Lee, *Model predictive control: past, present and future.* Computers I\& Chemical Engineering, 1999. **23**(4--5): p. 667 - 682.

[12] 12. Ljung, L., ed. *System Identification (2Nd Ed.): Theory for the User*. 1999, Prentice Hall PTR: Upper Saddle River, NJ, USA.

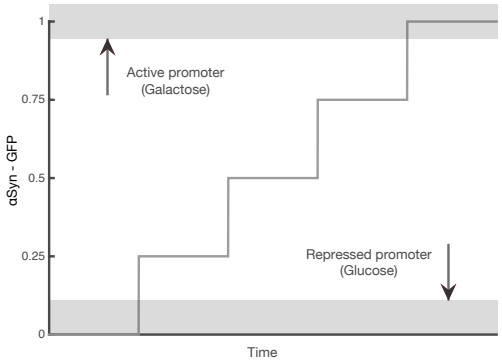

Figure 1. Proof of concept.

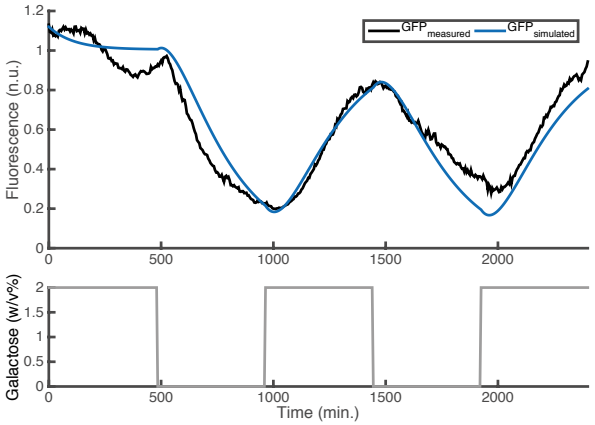

Figure 2. Identification experiment.

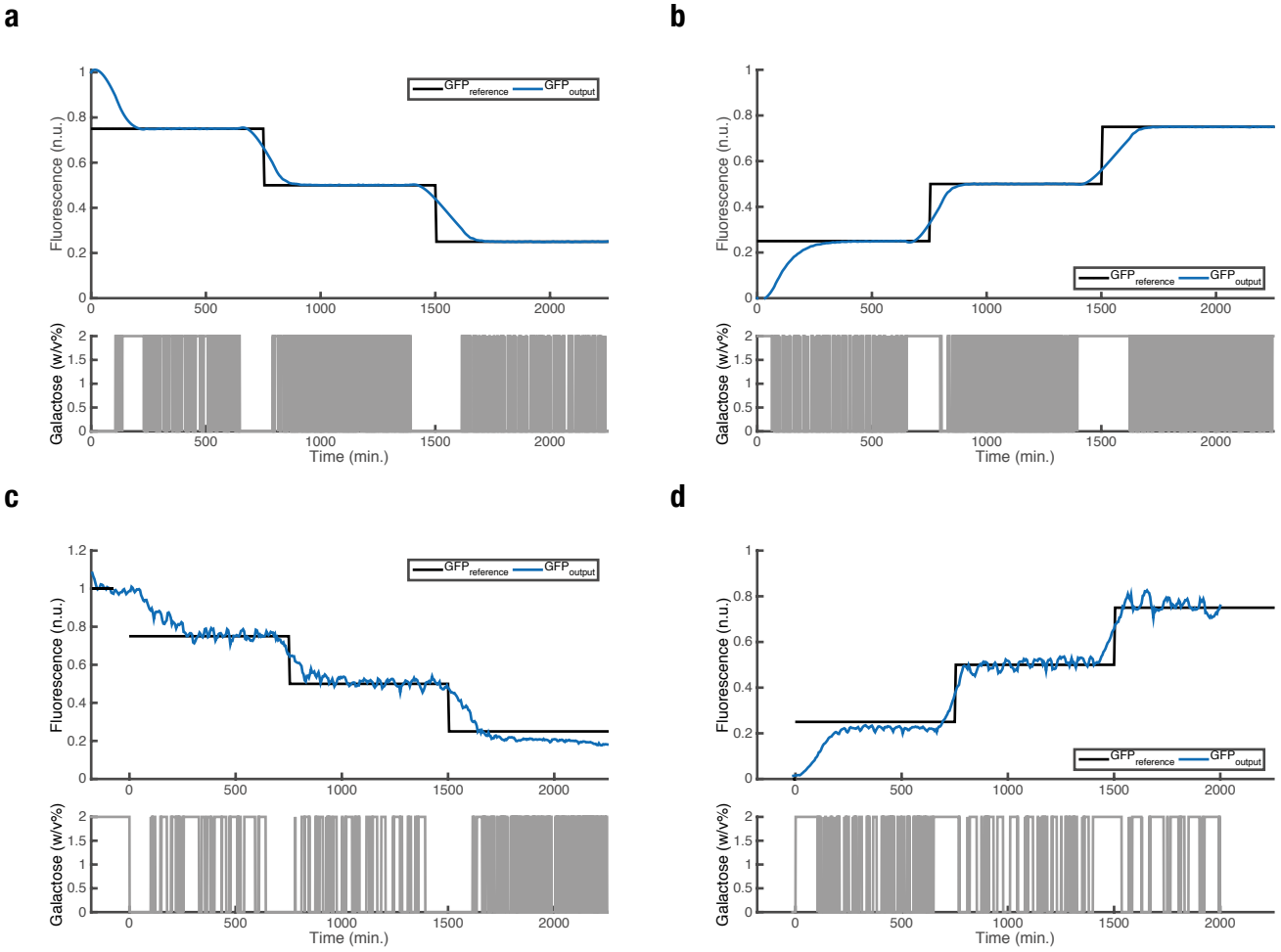

Figure 3. Numerical simulations (a-b) and experimental results (c-d).

Microfluidic-based automatic control of gene expression in mammalian cells

L.Postiglione[1,2], D. di Bernardo[1,3]
[1]Telethon Institute of Genetics and Medicine(TIGEM)Via Campi Flegrei 34, 80078 Pozzuoli (Naples), Italy
[2] Dept. of Electrical Engineering and Information Technology University of Naples "Federico II"
[3] Dept. of Chemical, Materials and Industrial Engineering University of Naples "Federico II"

***Abstract*— Real-time automatic regulation of gene expression is a key technology for synthetic biology enabling, for example, synthetic circuit's components to operate in an optimal range. We show that it is possible to regulate the expression of a reporter protein from the tetracycline-inducible promoter in a population of mammalian cells using principles from automatic control engineering.**

***Keywords*—control engineering, gene expression, mammalian cells, microfluidics.**

I. Introduction

Control engineering can be applied to biological systems to steer cellular processes towards a desired behaviour. Automatic control of gene expression in living cells is paramount importance to characterize both endogenous gene regulatory networks and synthetic circuits. In addition, such a technology can be used to maintain the expression of synthetic circuit components in an optimal range in order to ensure reliable performance.

Although the automatic control of gene expression in lesser eukaryotes has been achieved and in the last years some interesting results have already been presented [1]-[4], the application of control engineering to mammalian systems is still at its infancy. The transcriptional dynamics of mammalian cells are lesser than those of yeast cells and for this reason the time scale involved in the gene expression control is longer. Moreover, the mammalian cells need to more stringent requirements to successfully be maintained in viable terms during the all control experiment.

Recently, in [5] we demonstrated that it is possible to force a population of mammalian cells harboring the tetracycline-inducible promoter to express a predetermined level of a protein of interest by automatically administering to the cells pulses of tetracycline whose duration is computed in real time by a control algorithm.

A. Control Platform and Experimental Model

In [5], the control platform was set up to monitor fluorescent protein levels in real time and to provide the cells with precise concentrations of an inducer molecule. The Fig.1 outlines the working principles of the used experimental platform: the control scheme, in the form of a Finite State Automaton, is implemented in a computer, which actuates a fluorescence microscope capturing at 15 min intervals images both in the bright field (BF) and in fluorescence of the mammalian cells that grow in a microfluidic device within a temperature- and CO_2-controlled environment. An image segmentation pipeline is able to locate cells using BF images and to return an average measure of reporter protein fluorescence within the cells at population level at each time point. The control algorithm, then, compares the measured fluorescence with the desired level and computes the new control input to be supplied to the cells. Since we assumed that only either medium with tetracycline at its maximum concentration or medium without Tetracycline can be given to the cells, the control input is a binary signal. Computer-controlled stepper motors is programmed to translate the binary control input in heights of syringes filled with untreated and tetracycline-treated medium. Relative differences between the free surfaces of the two fluids will generate a hydrostatic pressure that will drive the flow of either medium through capillaries directly to the microfluidic device. Once the input has been applied to the cells, a new iteration starts.

In [5] as a test bed for assessing the feasibility of automatic control of gene expression in mammalian cells we chose the Tet-OFF system driving the expression of a destabilized fluorescent reporter protein [6] in a monoclonal cell population (Chinese hamster ovary cells). If cells grow in standard growth medium the reporter protein is maximally expressed. Upon addition of Tetracycline to the culture medium, the expression of reporter protein is prevented. Therefore the system can be described as a single input-single output (SISO) dynamical system in which the input is represented by the presence or absence of Tetracycline in the growth medium and the output is the measured average level of reporter protein in the cell population.

We tested two output control strategy based on Relay and Proportional-Integral controller (PI). Since we decided to use a binary control input, that is, either no inducer (i.e., just culture medium) or a single predetermined concentration of the inducer molecule, in the PI based control strategy we applied a pulse width modulation (PWM) coding scheme that, at each sampling time converts the control input to a pulse of tetracycline whose duration is proportional to the control input value. The results of the *in silico* and *in vitro* set point control experiments are reported in Fig.2.

II. From switched to continuous control input

In the pilot study made in [5], we decided to use a binary control input, that is, either no inducer (i.e., just culture medium) or a single predetermined concentration of inducer molecule. However, in principle, the difference in hydrostatic pressure between the two syringes can be used to provide any desired concentration of the inducer molecule by mixing the two fluids by properly adjusting the heights of the two

syringes. Small errors in positioning the syringes, which may be caused by the mechanical inaccuracies of motors, pulleys and belts supporting them, may accumulate over time leading to large discrepancies between the desired concentration of the molecule in the microfluidic cell chamber and its actual value. In order to overcome this problem and to pass from switched to continuous control input in order to improve the control performance of gene expression, here we present a controller that makes the actual concentration of input molecule equal to the desired concentration calculated by the gene expression controller by regulating the steps number of each motor. Specifically a certain number of motor steps number corresponds to an intermediate position of the syringes, between the highest and lowest, that finally produces an automatic dilution of inducer molecule concentration thank to the presence of a Dial-A-Wave mixer channel in the microfluidic device [7]. Thus gene expression control platform presented in Fig.1 is endowed with a new controller as Fig.3a shows. To measure the concentration of the inducer molecule, a fluorescent dye is added to the syringes containing tetracycline. The fluorescence of the dye is imaged by the microscope at regular sampling time of 1 minute and converted to a quantitative value *via* an image processing algorithm.

First with a black box identification approach (Fig.3b), a mathematical model that describes the relationship between the motor's steps number and the concentration of Tetracycline in the microfluidic chambers is identified [8] (Eq.1).

$$\begin{aligned} \dot{x} &= -0.2234x + 0.0506u \\ y &= 4.946x \end{aligned} \qquad (1)$$

Then, in order to regulate the actual concentration of tetracycline in the microfluidic device, we present a Model Predictive Control (MPC) based control strategy. However the autofluorescence of dye (no modelled by the mathematical model) interferes with detection of specific fluorescent signal. But it can be regarded as a constant disturbance and an integral action is combined to the MPC control strategy (Fig.3c) in order to ensure a zero control error.

Fig. 4 shows the results of *in silico* PI control experiments when a continuous control input is provided to the cells (control platform showed in Fig. 3a). In Fig.4, the simulations reveal how the continuous control input improves the performance of gene expression control respect to the switched control input. In the case of continuous PI controller the amplitude of oscillations of the fluorescent protein (y) around the set point (r) tends to diminish over time faster than in the case of switched PI controller. The performance indices of the control strategies and the energy of the control input signal are reported in the table I.

TABLE I
PERFORMANCE INDICES

	Switched PI control strategy	*Continuous PI control strategy*
ISE	91.0210	73.3049
IAE	372.6114	281.8001
ITAE	2.6114E04	1.0191E04
Input signal Energy	1.4382E03	1.0801E03

Performance indices and energy of control input signal calculated over the control time interval: Integral Square Error (ISE), Integral Absolute Error (IAE), Integral Time Absolute Error (ITAE).

III. CONCLUSION

In [5] we presented a microfluidics-based feedback control strategy to quantitatively regulate gene expression from a tetracycline-inducible promoter in mammalian cells by automatically administering to the cells pulses of tetracycline. Moreover in this work we present an extended control platform able to administer to the cells all intermediate levels of the inducer molecule and we show how the performance of the control experiments improves in presence of a continuous control input.

The ability to express a protein of interest at different levels or in a time-varying fashion from the same promoter would be a unique tool for several applications, including studying the effects of gene dosage in disease, probing the function of endogenous regulatory networks, and for synthetic biology applications. Moreover the opportunity to give to the cells all intermediate levels of a molecule allows us to perform automatic dose-response studies.

ACKNOWLEDGEMENT

This work was supported by Human Frontier Science Program (SFSP) grant RGP0020/2011 to D.d.B. and by the Italian Fondazione Telethon.

REFERENCES

[1] A. Milias-Argeitis, S. Summers, J. Stewart-Ornstein, I. Zuleta, D. Pincus, H. El-Samad, M. Khammash, and J. Lygeros. *In silico feedback for in vivo regulation of a gene expression circuit.* (2011) Nature Biotechnology. 29, 1114−6.

[2] J. Ulhendorf, A. Miermont, T. Delaveau, G. Chavrin, F. Fages, S. Bottani, G. Batt and P. Hersen. (2012) *Long-term model predictive control of gene expression at the population and single-cell levels*. Proc. Natl. Acad. Sci. U. S. A. 109, 14271−6.

[3] F. Menolascina, G. Fiore, E. Orabona, L. De Stefano, M. Ferry, J. Hasty, M. di Bernardo, and D. di Bernardo. (2014) *In-vivo real-time control of protein expression from endogenous and synthetic gene networks*. PLoS Comput. Biol. 10, e1003625.

[4] G. Fiore, G. Perrino, M. di Bernardo and D. di Bernardo. (2015). *In Vivo Real-Time Control of Gene Expression: A Comparative Analysis of Feedback Control Strategies in Yeast.* ACS synthetic biology.

[5] C. Fracassi, L. Postiglione, G. Fiore and D. di Bernardo. (2015). *Automatic Control of Gene Expression in Mammalian Cells*. ACS synthetic biology.

[6] V. Siciliano, F. Menolascina, L. Marucci, C. Fracassi, I. Garzilli, M.N. Moretti and D. di Bernardo. (2011) *Construction and Modelling of an Inducible Positive Feedback Loop Stably Integrated in a Mammalian Cell-Line.* PLoS Comput. Biol. 7, e1002074.

[7] M. Kolnik, L. S. Tsimring and J. Hasty. (2012) Vacuum-assisted cell loading enables shear-free mammalian microfluidic culture. Lab Chip 12, 4732−7.

[8] L. Ljung. *System Identification: Theory For the User*, Second Edition, (1999) Upper Saddle River, N.J: Prentice Hall.

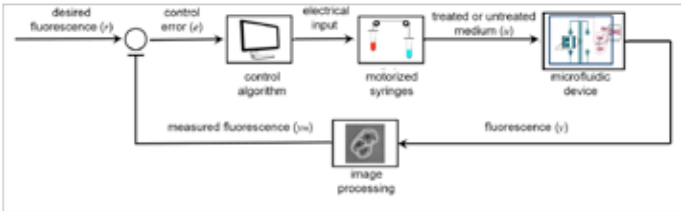

Fig.1. Experimental platform. The cells are in a microfluidic device under a microscope that takes images every 15 minutes. The control error ($e = r - y_m$), is minimized by a control algorithm that computes the necessary amount of inducer molecule (u) to be administered to the cells and then moves the motorized syringes filled with untreated and tetracycline-treated medium.

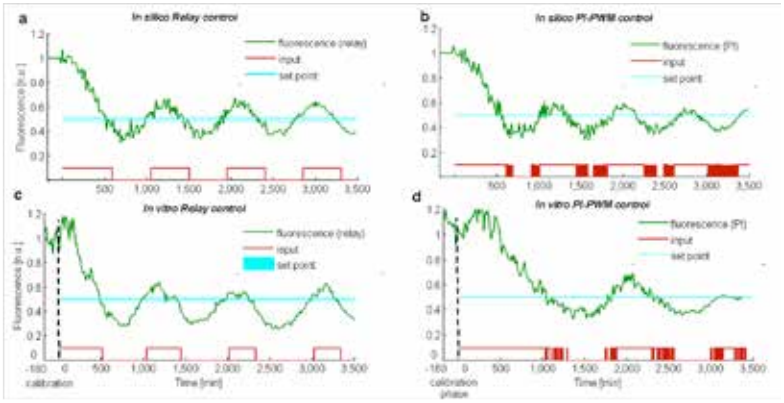

Fig.2. Results of (a, b) *in silico* and (c, d) *in vitro* set point relay and PI-PWM control experiments.. The set-point control task (cyan line) is equal to 50% of the initial fluorescence exhibited by cells in the absence of tetracycline during the calibration phase of 180 min. The red lines represent the respective tetracycline input (a, b) simulated and (c, d) provided to cells and the green lines represent the (a, b) simulated and (c, d) measured mean fluorescence of the imaged fields.

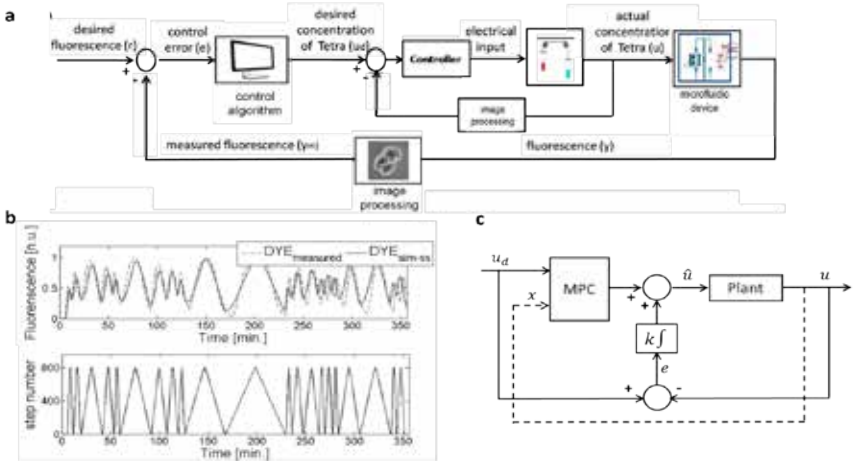

Fig.3. (a) Experimental platform endowed with a controller for the regulation of inducer molecule. A new image processing block is added to calculate the fluorescence value of the dye. (b) Black box identification. The solid line in the upper panel represents the output of the state space model identified with *prediction error minimization* algorithm and the dashed line is dye fluorescence measured during the experiment. The bottom panel shows the input represented by the motor steps number. The ideal input is used both to identify and to validate the model obtained. (c) Block scheme of MPC based control strategy for the regulation of Tetracycline concentration. u is the actual concentration of Tetracycline and u_d is the desired concentration calculated by control algorithm of gene expression.

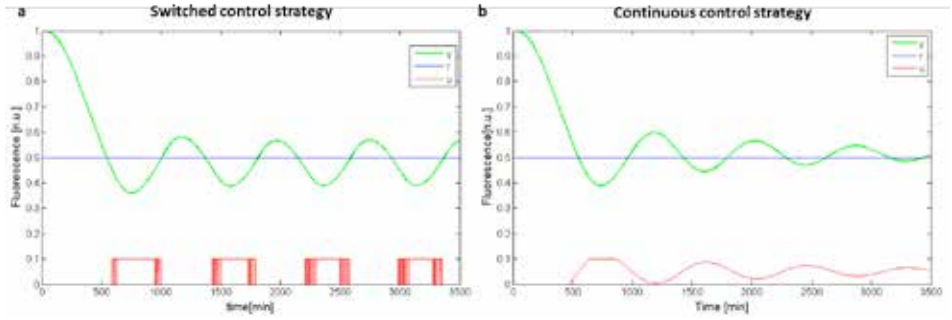

Fig.4.Comparison between the results of *in silico* and set point PI control experiments by using (a) switched and (b) continuous tetracycline input signal. The set-point control task (cyan line) is equal to 50% of the initial fluorescence exhibited by cells in the absence of tetracycline during the calibration phase of 180 min. The red lines represent the respective tetracycline input simulated (u) and the green lines represent the simulated mean fluorescence (y).

Synthesis and activity of computer-designed nanovectors for gene and drug delivery

E. Laurini[1], D. Marson[1], P. Posocco[1,2], M. Fermeglia and S. Pricl[1,2]
[1] *Molecular Simulations Engineering (MOSE) Laboratory – DEA, University of Trieste, Trieste, Italy*
[2] *INSTM, Research Unit MOSE – DEA, University of Trieste, Trieste, Italy*

***Abstract*— Due to the relative easy synthesis and commercial availability, nanovectors based on self-assembling units are among the most utilized non-viral vectors for gene/drug transfer. Contextually, recent advances in molecular simulations and computer architectures allow for accurate predictions of many structural, energetic, and eventual self-assembly features of these nanocarriers *per se* and in complex with their genetic cargoes. In the present work, we aim at reviewing our own efforts in the field of computer-assisted design, synthesis, *in vitro* and in vivo activity of these (nano)biomaterials.**

***Keywords*—Nanovectors, gene/drug delivery, computer-assisted design, *in vitro*/*in vivo* activity**

I. Introduction

With the conclusion of the human-genome sequencing project, the medical research community has an unparalleled opportunity to understand and cure diseases on a genetic level. However, translating this genomic information into drug therapies is still a major challenge facing researchers in the field – up to the preclinical stage – as well as pharmaceutical companies for the later stages of development. Providing support for the concept that drug modulation of a given target is likely to produce a therapeutic response in patients is a key step in this progression from "gene to screen". The main limitations are knowing which gene products are functionally involved in the pathology of a disease (target validation) and the druggability of the gene products by natural and/or synthetic compounds. Targeted drug therapy and, even more so, gene therapy (which holds enormous potential for therapeutic intervention in a broad range of genetic diseases including viral pathologies, gene-related disorders, and cancer), have been recognized as alternative approaches to overcome the drawbacks of "standard" therapies. In particular, gene therapy aims at delivering DNA, RNA or antisense sequences that alter gene expression within a specific cell population, thereby manipulating cellular processes and responses. Notwithstanding the wide range of nucleic acid-based therapeutics that are currently emerging as powerful, new drug entries for gene-related diseases and for lead validation, in the drug discovery process, there are still significant obstacles to be overcome before these types of therapeutics can be exploited in the clinical settings.

Perhaps, foremost among these is the issue of delivery. Injected nanoscale drug delivery systems, or nanovectors, are ideal candidates to provide breakthrough solutions to the time-honored problem of optimizing therapeutic index for a treatment. Even modest amounts of progress towards this goal have historically engendered substantial benefits across multiple fields of medicine, with the translatability from, for example, a subfield of oncology to a field as distant as the treatment of infectious diseases being granted by the fact that the progresses had a single common denominator in the underlying technological platform [1].

Under this perspective, in this work we will review some of our most recent efforts in our own efforts in the field of computer-assisted design, synthesis, *in vitro* and *in vivo* activity of nanovectors for drug/gene delivery [2]-[9], with particular focus on two new nanocarriers generated by spontaneous self-assembling of small, biocompatible, dendron-based amphiphiles.

II. Results and discussion

A. Anticancer drug nanomicelles formed by self-assembling amphiphilic dendrimer overcome drug resistance in cancer cell [2].

Drug resistance and toxicity constitute challenging hurdles for cancer therapy. The application of nanotechnology for anticancer drug delivery is expected to address these issues and bring new hope for cancer treatment. In this context, we established an original nanomicellar drug delivery system based on an amphiphilic dendrimer (*AmDM*), which could generate supramolecular micelles to effectively encapsulate the anticancer drug doxorubicin (DOX) with high drug-loading capacity (>40%) (Fig. 1). The resulting *AmDM*/DOX nanomicelles were able to enhance drug potency and contrast doxorubicin resistance in breast cancer models by significantly enhancing cellular uptake while considerably decreasing efflux of the drug (Figs. 2 and 3). In addition, the *AmDM*/DOX nanoparticles abolished significantly the toxicity related to the free drug. Collectively, our studies demonstrate that the drug delivery system based on nanomicelles formed with the self-assembling amphiphilic dendrimer constitutes a promising and effective drug carrier in cancer therapy.

B. A chameleon self-assembled nanovector for efficient siRNA delivery [3]

Small interfering RNA (siRNA) delivery remains a major challenge in RNAi-based therapy. Through the combined action of *in silico*/experimental efforts, we designed and produced for the first time an amphiphilic dendrimer *AD* able to self-assemble into adaptive supramolecular assemblies upon interaction with siRNA (Fig. 4). The resulting nanovectors can effectively deliver siRNAs to various cell lines, including human primary and stem cells, thereby outperforming the currently available non-viral vectors (Fig. 5). Most importantly, however, *AD*-mediated gene silencing

was successfully achieved also in vivo, as shown in Fig. 6.

C. Degradable self-assembling dendrons for gene delivery: experimental and theoretical insights into the barriers to cellular uptake [9]

In this work, we used a combined experimental and theoretical approach to gain unique insight into gene delivery. Specifically, we reported the synthesis and investigation of a new family of second-generation dendrons with four triamine surface ligands capable of binding to DNA, degradable aliphatic-ester dendritic scaffolds, and hydrophobic units at their focal points. According to our results, dendron self-assembly significantly enhanced DNA binding as monitored by a range of experimental methods and confirmed by multiscale modeling.

Cellular uptake studies indicated that some of these dendrons were highly effective at transporting DNA into cells (ca. 10 times better than poly(ethyleneimine), PEI, a prototypical polymeric standard employed for these experiments). Yet, levels of transgene expression were relatively low (ca. 10% of PEI). This indicated that these dendrons could not navigate all of the intracellular barriers to gene delivery. The addition of chloroquine indicated that endosomal escape was not the limiting factor in this case, whereas further experimental and theoretical work established that gene delivery could be correlated with the ability of the dendron assemblies to release DNA.

Mass spectrometric assays demonstrated that the dendrons, as intended, did degrade under biologically relevant conditions over a period of hours. Multiscale modeling of degraded dendron structures suggested that complete dendron degradation was required for DNA release. Importantly, in the presence of the lower pH associated with endosomes, or when bound to DNA, complete degradation of these dendrons became ineffective on the transfection time scale.

Therefore, we proposed this could explain the poor transfection performance of these dendrons. As such, this paper demonstrated that taking this kind of multidisciplinary approach could yield a fundamental insight into the way in which dendrons can navigate barriers to cellular uptake. Lessons learned from this work will inform future dendron design for enhanced gene delivery.

III. Conclusions

The extensive series of examples illustrated and discussed above - taken from our own experience in the field - emphasize the role and potentiality of multiscale molecular modeling and simulations in the pre-and post-development of nanodevices for gene delivery. Accurate and reliable computer-assisted design can be performed more easily than experiments. In silico evaluation can take into account the molecular specificity of the problem and dramatically reduce the time and cost required to formulate a new device and therapeutic intervention, and eventually translate it into the clinical setting. In nanomedicine, the need for accurate multiscale molecular simulations is even more pressing. Despite its rapid growth and extraordinary potential, the field is still in its infancy, is highly interdisciplinary, and aims at solving problems of extraordinary and unprecedented complexity.

With such a scenario, multiscale molecular modeling could dictate the success of nanomedicine and make the difference between several years of unfruitful research and the development of new, revolutionary therapeutic strategies readily available to the public.

Acknowledgement

Access to the supercomputers of the Consorzio interuniversitario per la gestione del centro di calcolo elettronico dell'Italia nord orientale (CINECA) was established via several Simulation of Biological Systems Projects (Iscra Supercomputing) Grants (to S.P.).

Financial support from the international ERA-Net EURONANOMED European Research project DENANORNA and from the European COST Action TD0802 "Dendrimers in Biomedical Applications" are gratefully acknowledged.

References

[1] P. Posocco, E. Laurini, V. Dal Col, D. Marson, K. Karatasos, M. Fermeglia and S. Pricl, "Tell me something that I do not know. Multiscale molecular modeling of dendrimer/dendron organization and self-assembly for gene therapy," *Curr. Med. Chem*., vol. 19, pp. 5062-5087, 2012.

[2] T. Wei, C. Chen, J. Liu, C. Liu, P. Posocco, X. Liu Q. Cheng, S. Huo, Z. Liang, M. Fermeglia, S. Pricl, X. J.Liang, P. Rocchi, L. Peng, "Anticancer drug nanomicelles formed by self-assembling amphiphilic dendrimer to combat cancer drug resistance," *Proc. Natl. Acad. Sci. USA*, vol. 112, pp. 2978-2983. 2015.

[3] D. Marson, E. Laurini, P. Posocco, M. Fermeglia, S. Pricl, "Cationic carbosilane dendrimers and oligonucleotide binding: an energetic affair," *Nanoscale*, 7, pp. 3876-87, 2015.

[4] X. Liu, J. Zhou, T. Yu, C. Chen, Q. Cheng, K. Sengupta, Y. Huang, H. Li, C. Liu, Y. Wang, P. Posocco, M. Wang, Q. Cui, S. Giorgio, M. Fermeglia, F. Qu, S. Pricl, Y. Shi, Z. Liang, P. Rocchi, J. J. Rossi, L. Peng, "Adaptive amphiphilic dendrimer-based nanoassemblies as robust and versatile siRNA delivery systems," *Angew. Chem. Int. Ed. Engl.*, vol. 53, pp. 11822-11827, 2014.

[5] S. Kala, A. S. Mak, X. Liu, P. Posocco, S. Pricl, L. Peng, A. S. Wong, "Combination of dendrimer-nanovector-mediated small interfering RNA delivery to target Akt with the clinical anticancer drug paclitaxel for effective and potent anticancer activity in treating ovarian cancer," *J. Med. Chem*., vol. 57, pp. 2634-42, 2014.

[6] P. Posocco, X. Liu, E. Laurini, D. Marson, C. Chen, C. Liu, M. Fermeglia, P. Rocchi, S. Pricl, L. Peng, "Impact of siRNA overhangs for dendrimer-mediated siRNA delivery and gene silencing," *Mol. Pharm*., vol. 10, pp. 3262-3273, 2013.

[7] X. Liu, C. Liu, E. Laurini, P. Posocco, S. Pricl, F. Qu, P. Rocchi, L. Peng, "Efficient delivery of sticky siRNA and potent gene silencing in a prostate cancer model using a generation 5 triethanolamine-core PAMAM dendrimer," *Mol. Pharm*., vol. 9, 470-81, 2012.

[8] X. Liu, J. Wu, M. Yammine, J. Zhou, P. Posocco, S. Viel, C. Liu, F. Ziarelli, M. Fermeglia, S. Pricl, G. Victorero, C. Nguyen, P. Erbacher, J. P. Behr, L. Peng, "Structurally flexible triethanolamine core PAMAM dendrimers are effective nanovectors for DNA transfection in vitro and in vivo to the mouse thymus," *Bioconjug. Chem*., vol. 22, 2461-2473, 2011.

[9] A. Barnard, P. Posocco, S. Pricl, M. Calderon, R. Haag, M. E. Hwang, V. M. Shum, D. W. Pack, D. K. Smith, "Degradable self-assembling dendrons for gene delivery: experimental and theoretical insights into the barriers to cellular uptake," J. Am. Chem. Soc., vol. 133, pp. 20288-20300, 2011.

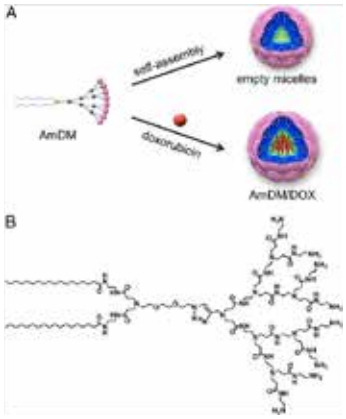

Fig. 1. *AmDM* self-assembled nanomicelles as a drug delivery platform. (A) Formation of empty *AmDM* nanomicelles and DOX-encapsulated *AmDM*/DOX nanomicelles. (B) Molecular structure of the computer-assisted designed amphiphilic dendrimer *AmDM* [2].

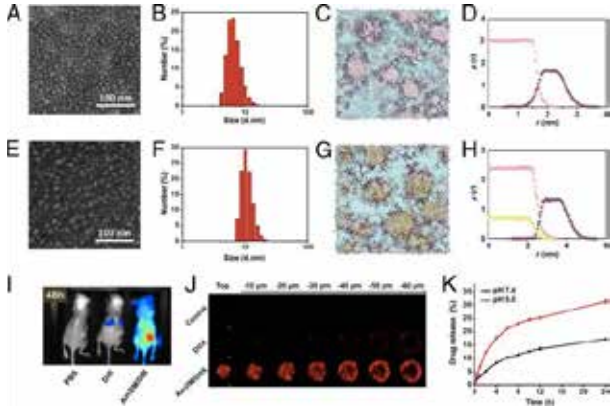

Fig. 2. (A) TEM image and (B) DLS analysis of AmDM nanomicelles. (C) Computer prediction of *AmDM* micelles morphology. Micellar hydrophilic shell and hydrophobic core are highlighted as purple and pink sticks, respectively. Solvent is depicted as light blue field. (D) Density distributions of *AmDM* hydrophobic core (pink dots) and hydrophilic shell (purple dots) segments as a function of distance from the center of the micelle. (E) TEM image and (F) DLS analysis of *AmDM*/DOX nanomicelles. (G) Computer prediction of *AmDM*/DOX micelles moprhology: *AmDM* micelles and solvent represented as in D; DOX shown as green spheres. (H) Density distributions of *AmDM* hydrophobic core (pink dots), hydrophilic shell (purple dots) segments, and DOX (green dots) as a function of distance from the center of the micelle. (I) Fluorescent imaging of biodistribution of *AmDM* nanomicelles loaded with a near-infrared fluorescent dye, DiR, 48 h postadministration via i.v. injection in NSG mice bearing MCF-7R tumors. (J) Drug penetration of *AmDM*/DOX nanomicelles into 3D-cultured MCF-7R tumor spheroids imaged with a two-photon microscope. (K) Time course of DOX released from *AmDM*/DOX micelles at pH 5.0 and pH 7.4 at 37 °C [2].

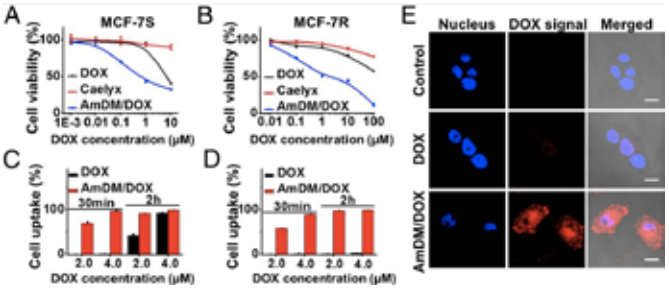

Fig. 3. Comparison of the antiproliferative activity of free DOX, commercial DOX nanodrug Caelyx, and *AmDM*/DOX nanomicelles on (A) drug-sensitive breast cancer MCF-7S cells and (B) drug-resistant breast cancer MCF-7R cells was measured using an MTT assay. The cellular uptake in (C) MCF-7S and (D) MCF-7R cells was quantified using flow cytometry after treatment with DOX and *AmDM*/DOX, respectively. (E) The cellular uptake was imaged using confocal microscope following treatment with free DOX and *AmDM*/DOX in MCF-7R cells. (Scale bar: 10 μm) [2].

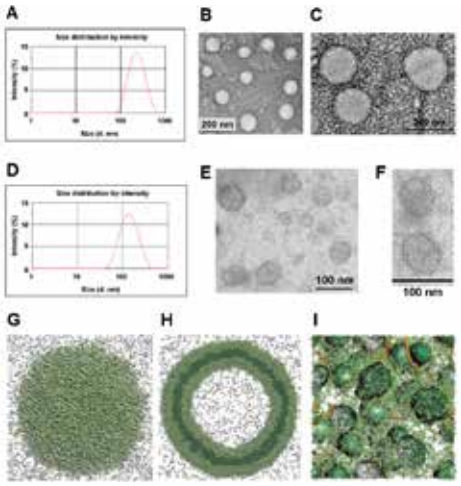

Fig. 4. The computer-aided designed amphiphilic dendron *AD* self-assembles into vesicle-like dendrimersomes which undergo structural rearrangement into smaller, spherical micelles to interact with siRNA. (A) DLS analysis and (B,C) TEM imaging of dendrimersomes formed by *AD* in water. (D) DLS analysis and (E,F) TEM imaging of the siRNA/*AD* complexes. Computer modeling predictions showing nanostructures formed by *AD* alone (H), a section plane (G) and in presence of siRNA (I). The hydrophilic units are portrayed in light green, the hydrophobic units in dark green, and siRNAs as orange sticks. Light grey spheres are used to portray some representative water molecules [3].

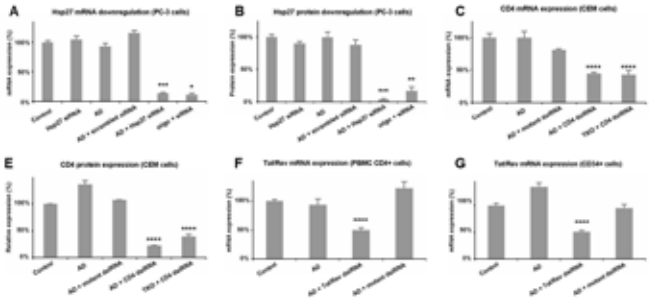

Fig. 5. *AD*-mediated siRNA delivery in human prostate cancer PC-3 cells, human CCRF-CEM T-cells, human primary cells (PBMC-CD4$^+$) and hematopoitic stem cells (CD34$^+$). Gene silencing of Heat shock protein 27 (Hsp27) at (A) mRNA and (B) protein levels in PC-3 cells treated with 20 nM siRNA and *AD* at N/P ratio 10. Down-regulation of CD4 at (C) mRNA and (D) protein expression on CEM cells treated with 50 nM dsiRNA and AD at N/P ratio 5. Knockdown of Tat/Rev mRNA expression on (E) PBMC-CD4+ cells and (F) CD34$^+$ stem cells with 50 nM dsiRNA and *AD* at N/P ratio of 5. Oligofectamine (oligo) and Trans IT-TKO (TKO) were used as controls. *, **, ***, and ****, differ from control ($p \leq 0.05$, $p \leq 0.01$, $p \leq 0.001$, and $p \leq 0.0001$, respectively) by Student's t test [3].

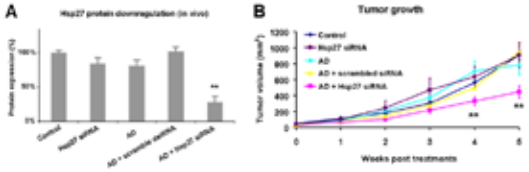

Fig. 6. Evaluation of *in vivo* siRNA delivery using prostate cancer PC-3 xenograft mice following treatment with Hsp27 siRNA/*AD* and the controls of PBS, *AD* alone, siRNA alone and scrambled siRNA/*AD*, respectively (3 mg/kg siRNA and AD at a N/P ratio of 5, injection twice a week for 5 weeks). (A) Effective gene silencing of Hsp27 at protein levels was measured using qRT-PCR and western blot, respectively. (B) Inhibition on tumor growth assessed by measuring tumor size. * and **, differ from control ($p \leq 0.05$ and $p \leq 0.01$, respectively) by Student's t test [3].

Bursting and Spiking Effectiveness in Evoking Pituitary Hormone Secretion: a Spatiotemporal Simulation Study of Calcium Diffusion and Exocytosis

A. Tagliavini[1], J. Tabak[2], R. Bertram[2], M. G. Pedersen[1]
[1] *Department of Information Engineering, University of Padua, Padua, Italy*
[2] *Department of Mathematics and Program in Neuroscience, Florida State University, Tallahassee, FL 32306, USA*

***Abstract*—Endocrine cells of the pituitary gland secrete a number of hormones, and the amount of hormone released by a cell is controlled in large part by the cell's electrical activity and subsequent Ca^{2+} influx. Typical electrical behaviors of pituitary cells include continuous spiking and so-called pseudo-plateau bursting. It has been shown that the amplitude of Ca^{2+} fluctuations is greater in bursting cells, leading to the hypothesis that bursting cells release more hormone than spiking cells. In this work, we apply computer simulations to test this hypothesis. We use experimental recordings of electrical activity as input to mathematical models of Ca^{2+} channel activity, buffered Ca^{2+} diffusion, and Ca^{2+}-driven exocytosis. To compare the efficacy of spiking and bursting on the same cell, we pharmacologically block the large conductance potassium (BK) current from a bursting cell, or add a BK current to a spiking cell via dynamic clamp. We find that bursting is generally at least as effective as spiking at evoking hormone release, and is often considerably more effective, even when normalizing to Ca^{2+} influx. Our hybrid experimental/modeling approach confirms that adding a BK-type K^+ current, which is typically associated with decreased cell activity and reduced secretion, can actually produce an increase in hormone secretion.**

***Keywords*—Ca^{2+} diffusion, exocytosis model, pituitary cells.**

I. Introduction

Endocrine pituitary cells (i.e., melanotrophs, lactotrophs, somatotrophs, thyrotrophs, corticotrophs, and gonatotrophs) secrete a wide number of hormones in response to hypothalamus stimulus [1]. Hormones secreted by pituitary gland act on other endocrine cells and other tissues including the brain to regulate physiological and behavioral aspects of growth, metabolism, water balance, and reproduction [2]. The pituitary cells express different ion channels and are electrically excitable. In particular, electrical activity induces an intracellular Ca^{2+} elevation causing hormone secretion. The two typical electrical patters observed in these cells are continuous spiking – typically observed in luteinizing hormone-secreting gonadotrophs under basal conditions – and a form of bursting known as pseudo-plateau bursting often observed in prolactin-secreting lactotrophs, growth hormone-releasing somatotrophs, and ACTH-secreting corticotrophs, where the burst duration is at most a few seconds and the spikes that ride on the elevated voltage plateau are very small [3], [4]. Simultaneously measurement of electrical activity, Ca^{2+} and release from a single cell should be performed in order experimentally test this hypothesis, however it is barely realizable on single cell. In this work, a hybrid experimental/modeling approach has been exploited to explore the hypothesis that bursting cells release more hormone than spiking cells. We used direct measurement of both the spontaneous electrical activity and the induced spiking or bursting pattern with BK channels blocker and dynamic clamp, in the same cell. We built a mathematical model of stochastic Ca^{2+} channel activity, Ca^{2+} diffusion and binding to buffer, and finally Ca^{2+}-driven exocytosis and each of the voltage traces is fed into these models.

II. Methods

A. Experimental and Dynamic Clamp

The inputs to our mathematical models are voltage time courses recorded from a mouse gonadotroph or from a GH4C1 lacto-somatotroph cell. GH4C1 cells were maintained in culture conditions in supplemented F10 medium (Sigma-Aldrich, St-Louis, MO) according to established procedures [5]. Primary pituitary cells were obtained from diestrous female rats (Sprague Dawley, aged 3-6 months) using enzymatic dispersion of pituitary fragments [6]. Animal procedures were approved by the Florida State University Animal Care and Use Committee. BK channels were blocked by bath application of 100 nM iberiotoxin (Tocris) in order to obtain continuous spiking patterns, and traces of fast pseudo-plateau bursting were obtained by adding a BK-type current to a spiking cell with the dynamic clamp.

B. Geometry, stochastic current and diffusion

To model data from pituitary cells we represented a single cell by a sphere with a diameter of 13 μm [7]. Ca^{2+} diffusion was computed in a conical region with base radius of 1.5 μm (Fig. 1), a radius obtained by dividing the sphere surface into 75 circular areas, one for each channel. This radius corresponds to an inter-channel distance of ~3 μm, in agreement with [8]. The single channel conductance was set to 20 pS [9]. the Ca^{2+} current source was located at the base center of the conical region. We implemented no-flux boundary conditions for Ca^{2+} and buffers on the sides of the cone. For the single Ca^{2+} channel, we assumed three states with kinetic mechanism described by [10]:

$$C \underset{\beta}{\overset{\alpha}{\rightleftharpoons}} O \underset{k_-}{\overset{k_+}{\rightleftharpoons}} B, \qquad (1)$$

where the states are closed (C), open (O), and blocked or inactivated (B). The stochastic channel dynamics was simulated as realizations of the discrete-state continuous-time Markov chain. In all simulations we assumed the presence of a single immobile endogenous Ca^{2+} buffer, in agreement with Kits et al. [11], The reaction-diffusion equations for the Ca^{2+} concentration and for the free unbound buffers are taken from [12] (Fig. 2 shows an example of simulation results).

C. Exocytosis Model

We used a 4-pool model (Fig. 3), which is similar to a model of exocytosis in melanotroph cells [11] in all simulations. Granule release is triggered by local Ca^{2+} levels (C_{loc}), as indicated in Fig. 3, while resupply is dependent on the bulk calcium concentration C_i, which is computed as the submembrane Ca^{2+} concentration at the distance of 1.5 μm from the channel. In order to reflect secretion experiments, all pool are initially empty.

III. RESULTS

A. Converting spiking to bursting

Adding a BK-type K^+ current to a spiking gonadotroph can change its behaviour into bursting, as shown in Fig. 4i. Figure 4 also shows the average of Ca^{2+} profiles at distances of 30, 200, and 1500 nm from the Ca^{2+} channel obtained by the Ca^{2+} diffusion model driven by either the spiking voltage pattern (left) or the bursting pattern (right). We located the exocytosis machinery at different distances from the Ca^{2+} channel and use the Ca^{2+} concentration at that location to drive the exocytosis model. Figure 5 shows the average number of fused granules over time at different distances and over the total charge entry (Q). We observed that when the release site is 100 nm far from the channel the secretion level will be the same with both spiking and bursting, however, the advantage of bursting over spiking is amplified when the release site is situated further from the channel, at 300 nm or 500 nm.

B. Converting bursting to spiking

We used recordings from a GH4 cell line, starting from the spontaneous bursting lacto-somatroph GH4C1 cell (Fig. 6 left column), then converting it to a spiking cell by the addition of the BK channel blocker iberiotoxin (middle column), and finally converting the spiking cell back to a bursting cell using dynamic clamp to inject a model BK current (right column). For each case we calculated the Ca^{2+} concentration at varying distances from the single stochastic channel, as in prior simulations, and we used the computed Ca^{2+} concentration to simulate exocytosis, locating the release sites at different distances from the Ca^{2+} channel, Fig. 7. In this case we noticed that exocytosis coupled to bursting is less superior to spiking after normalizing to Q compared to the gonadotroph results, and this result can be ascribed to the increased frequency of the spiking traces compared to spontaneous spiking behaviour of gonadothrophs.

IV. CONCLUSION

We found that bursting is typically more effective at evoking secretion than is continuous spiking. When bursting is induced in a spiking gonadotroph by injecting a BK-type K^+ current with dynamic clamp, the burst pattern is generally at least as effective as continuous spiking at evoking hormone release, and is often considerably more effective. The superiority of bursting over spiking is due to the fact that bursting brings more Ca^{2+} into the cell, thus augmenting both local and global Ca^{2+} levels, which in turn increases resupply of secretory granules and exocytosis. However, we further observed that when spiking frequency is higher, this difference between spiking and bursting in evoking exocytosis is considerably reduced.

REFERENCES

[1] S. S. Stojilkovic, H. Zemkova, and F. Van Goor, "Biophysical basis of pituitary cell type-specific Ca2+ signaling-secretion coupling.," *Trends Endocrinol. Metab.*, vol. 16, no. 4, pp. 152–9, Jan. 2005.

[2] M. E. Freeman, B. Kanyicska, A. Lerant, and N. Gyorgy, "Prolactin: Structure , Function , and Regulation of Secretion," *Physiol. Rev.*, vol. 80, no. 4, pp. 1523–1631, 2000.

[3] F. Van Goor, D. Zivadinovic, A. J. Martinez-Fuentes, and S. S. Stojilkovic, "Dependence of pituitary hormone secretion on the pattern of spontaneus voltage-gated calcium influx. Cell type-specific action potential secretion coupling," *J. Biol. Chem.*, vol. 276, pp. 33840–33846, 2001.

[4] F. Van Goor, D. Zivadinovic, and S. S. Stojilkovic, "Differential expression of ionic channels in rat anterior pituitary cells.," *Mol. Endocrinol.*, vol. 15, no. January, pp. 1222–1236, 2001.

[5] A. H. Tashjian, Y. Yasumura, L. Levine, G. H. Sato, and M. L. Parker, "Establishment of clonal strains of rat pituitary tumor cells that secrete growth hormone.," *Endocrinology*, vol. 82, no. 2, pp. 342–52, Feb. 1968.

[6] J. Tabak, M. Tomaiuolo, a. E. Gonzalez-Iglesias, L. S. Milescu, and R. Bertram, "Fast-Activating Voltage- and Calcium-Dependent Potassium (BK) Conductance Promotes Bursting in Pituitary Cells: A Dynamic Clamp Study," *J. Neurosci.*, vol. 31, no. 46, pp. 16855–16863, 2011.

[7] J. M. Dubinsky and G. S. Oxford, "Ionic currents in two strains of rat anterior pituitary tumor cells.," *J. Gen. Physiol.*, vol. 83, no. 3, pp. 309–39, Mar. 1984.

[8] S. Hagiwara and H. Ohmori, "Studies of single calcium channel currents in rat clonal pituitary cells.," *J. Physiol.*, vol. 336, pp. 649–61, Mar. 1983.

[9] J. A. Keja and K. S. Kits, "Single-channel properties of high- and low-voltage-activated calcium channels in rat pituitary melanotropic cells.," *J. Neurophysiol.*, vol. 71, no. 3, pp. 840–55, Mar. 1994.

[10] a Sherman, J. Keizer, and J. Rinzel, "Domain model for Ca2(+)-inactivation of Ca2+ channels at low channel density.," *Biophys. J.*, vol. 58, no. 4, pp. 985–995, 1990.

[11] K. S. Kits, T. a de Vlieger, B. W. Kooi, and H. D. Mansvelder, "Diffusion barriers limit the effect of mobile calcium buffers on exocytosis of large dense cored vesicles.," *Biophys. J.*, vol. 76, no. July 1998, pp. 1693–1705, 1999.

[12] V. Matveev, R. S. Zucker, and A. Sherman, "Facilitation through buffer saturation: constraints on endogenous buffering properties.," *Biophys. J.*, vol. 86, no. May, pp. 2691–2709, 2004.

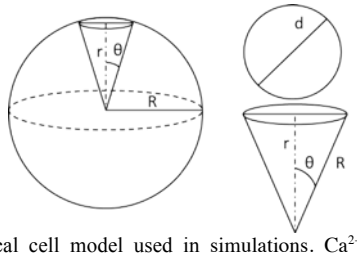

Fig. 1 Spherical cell model used in simulations. Ca^{2+} diffusion and buffering are simulated in a conical region of the sphere. The channel is located at the center of the cone base on the surface of the sphere. The base radius in the single channel case is 1.5 μm

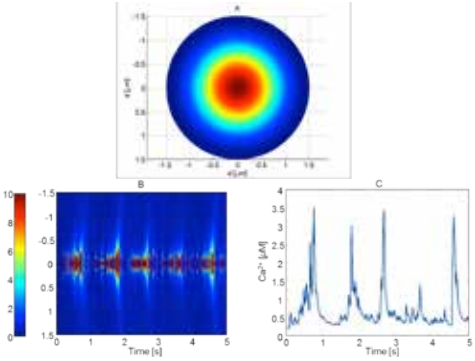

Fig. 2 A) Submembrane Ca^{2+} diffusion and buffering simulation at the base of the cone. B) Submembrane Ca^{2+} concentrations (color coded, in μM) as a function of time and the distance to the channel (d) during spiking electrical activity. C) Ca^{2+} concentration at 500 nm from the channel as function of time

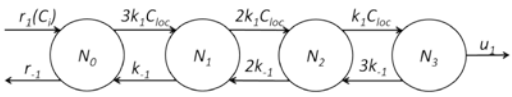

Fig 3. Kinetic scheme of the exocytosis model. The pool N_0 consists of granules primed for fusion and its resupply depends on the bulk cytosolic Ca^{2+} concentration C_i. Fusion occurs upon Ca^{2+} binding controlled by the local concentration of Ca^{2+}, C_{loc}. The pools N_1, N_2, N_3 correspond to the three Ca^{2+} bound states, and u_1 is the fusion rate.

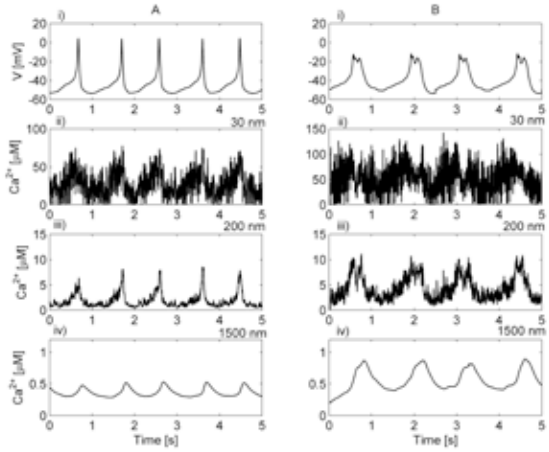

Fig. 4. Ca^{2+} concentration at different distances from a single stochastic Ca^{2+} channel on the surface of a conical region (average of 10 independent trials). The Ca^{2+} channel is placed at the center of the cone base with radius 1.5 μm. The Ca^{2+} concentration is determined using a mathematical model, in response to actual spiking (A) and bursting (B) voltage traces from a gonadotroph. The switch to bursting was obtained by injecting a model BK-current into a spiking cell using the dynamic clamp technique.

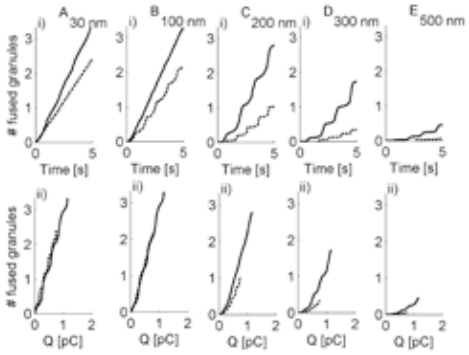

Fig. 5. Single channel exocytosis simulation results. Top panels (i) show the number of fused granules as a function of time (solid line bursting and dashed line spiking). Bottom panels (ii) show the cumulative number of fused granules during 5 seconds of simulation as function of the cumulative calcium entry Q. (A) granules located at 30 nm, (B) 100 nm, (C) 200 nm, (D) 300 nm, or (E) 500 nm from the channel.

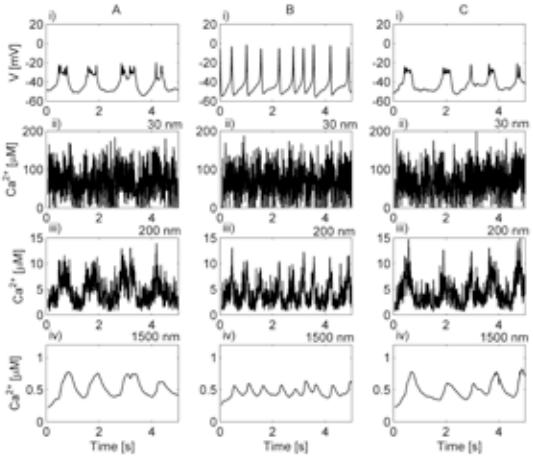

Fig. 6. Ca^{2+} concentration at different distances from a stochastic Ca^{2+} channel on the surface of a conical region (average of 10 independent trials). The Ca^{2+} channel is placed at the center of the cone base with radius 1.5 μm. (A) Bursting profile in control condition. (B) Spiking profile in the presence of the BK channel blocker iberiotoxin. (C) Bursting profile in the presence of iberiotoxin and when BK current is injected back using the dynamic clamp. Sub panels show the experimentally recorded voltage profile (i), and simulated Ca^{2+} concentrations at 30 nm (ii), 200 nm (iii), or 1500 nm (iv) from the channel.

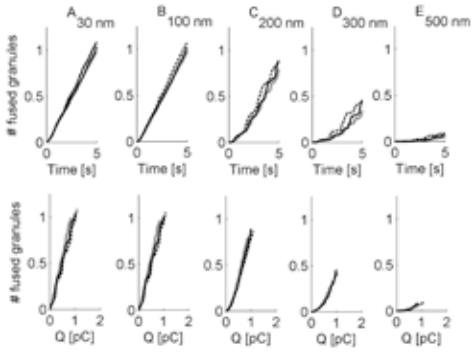

Fig. 7. Single channel exocytosis simulation for dynamic clamp-induced bursting. Top panels (i) show the number of fused granules as a function of time, evoked by a spiking voltage trace (gray curves), spontaneous bursting (black dashed curve), and bursting induced by dynamic clamp in the presence of iberiotoxin (black solid curves). Bottom panels (ii) show the cumulative number of fused granules during 5 seconds of simulation as a function of the cumulative Ca^{2+} entry Q. (A) granules located at 30 nm, (B) 100 nm, (C) 200 nm, (D) 300 nm, or (E) 500 nm from the channel.

BIOLOGIA
SINTETICA

Study of a genetic negative feedback controller via bottom-up approach and mathematical modelling

M. Bellato[1,2], L.Pasotti[1,2], F. Castronuovo[3], N.Politi[1], M.Casanova[1,2], I.Massaiu[1,2], S.Zucca[1,2], M.G. Cusella De Angelis[2] and P. Magni[1,2]

[1] *Dipartimento di Ingegneria Industriale e dell'Informazione, Università degli Studi di Pavia, via Ferrata 5, Pavia, Italy*
[2] *Center of Health Technology, Università degli Studi di Pavia, via Ferrata 3, Pavia, Italy*
[3] *Dipartimento di Fisica, Università degli Studi di Pavia, via Bassi 6, Pavia, Italy*

***Abstract*—Synthetic Biology is a branch of Bioengineering ranging over several aspects of life science; one of its aims is to develop new functionalities in living cells through manipulation of their DNA. Implementing synthetic genetic circuits, often inspired by electronic devices and control theory, is one of its aims to enable the predictable engineering of novel solutions in several application fields. Here, a study for a synthetic negative feedback control system is studied, aiming to optimize a mathematical model that predicts the dynamic behaviour of the system *in vivo*.**

***Keywords*—Synthetic biology, mathematical modelling, gene regulation, negative feedback.**

I. Introduction

EVEN sharing the same basics of molecular biology and genetics, synthetic biology differs from biotechnology and genetic engineering by the introduction of typical engineering concepts such as standardization, abstraction and modularity. This approach allows the implementation of synthetic genetic circuits exploiting the rational design advantages, i.e., bottom-up design form individually characterized genetic parts [1]-[2], in order to optimize the production of relevant bio-products such as drugs, biofuels and biomaterials in living cells.

Mathematical modelling is indispensable to support the design process aiding to manage the intrinsic complexity of biological systems. Therefore, it is possible to improve the predictability of synthetic gene circuits by a typical engineering design workflow. In order to evaluate whether any configuration of the system meets the specifications needed before physically implementing it, model systems can be used as testbed to evaluate the predictability of a model-based bottom-up design of biological systems. Importantly, unexpected conditions and relations influencing intended behaviours may be found through comparison between model predictions and *ad hoc* experiments.

Among different engineering-inspired system architectures, negative feedback control systems have been studied by synthetic biologists because of the importance of dynamically controlling and balancing fluxes in gene networks, in order to optimize production rates and possible toxic levels of a desired molecule produced by an engineered living cell.

This study aims to debug and deepen the knowledge on a previous work of our group [3], implementing a *close-loop synthetic gene controller*, which regulates the production of the signalling molecule 3-oxo-hexanohyl-homoserine lactone (HSL) in *E.coli* bacteria through a synthetic circuit developed following a rigorous bottom-up approach, using parts all from the Registry of Standard Biological Parts [4].

II. Materials and Methods

A. Genetic circuit description

The system was designed and implemented in *E.coli* MG1655-Z1 strain, based on the *quorum sensing* mechanism of some naturally-occurring bacteria (e.g., *V. fischeri*). The regulated P_{TetR} promoter, inducible by anhydrotetracycline (*aTc*), is placed upstream of the *luxI* gene, in order to tune the production of the diffusible signalling molecule HSL, while the AiiA enzyme from *Bacillus* sp. 240B1 is responsible for its enzymatic degradation. Its coding sequence is placed downstream of the P_{Lux} promoter, which acts as a sensor for HSL concentration (Fig. 1). The production and degradation process leads to a steady-state HSL level. A mathematical model of the genetic controller was derived in order to obtain predictions based on the parameters estimated separately from the individual sub-parts considered.

B. Mathematical model description

The genetic controller was modelled by the following ordinary differential equations (ODEs) system (Eq.1), describing the continuous culture (or *chemostat*) experimental set-up:

$$\begin{aligned}
\frac{dOD_{600}}{dt} &= \mu \cdot OD_{600} - D \cdot OD_{600} \\
\frac{dS_{LuxI}}{dt} &= -r_{P_{TetR}} S_{LuxI} + r_{P_{TetR}} \alpha_{P_{TetR}} \left(\delta_{P_{TetR}} + \frac{1-\delta_{P_{TetR}}}{1+\left(\frac{k_{P_{TetR}}}{[aTc]}\right)^{\eta_{P_{TetR}}}} \right) \\
\frac{dS_{AiiA}}{dt} &= -r_{P_{Lux}} S_{AiiA} + r_{P_{Lux}} \alpha_{P_{Lux}} \left(\delta_{P_{Lux}} + \frac{1-\delta_{P_{Lux}}}{1+\left(\frac{k_{P_{Lux}}}{[HSL]}\right)^{\eta_{P_{Lux}}}} \right) \\
\frac{d[LuxI]}{dt} &= S_{LuxI} - (\mu + \gamma_{LVA})[LuxI] \\
\frac{d[AiiA]}{dt} &= S_{AiiA} - (\mu + \gamma_{LVA})[AiiA] \\
\frac{d[HSL]}{dt} &= OD_{600} \left(\frac{k_{LuxI,max}}{1+\left(\frac{k_{M,LuxI}}{[LuxI]}\right)^{\eta_{LuxI}}} \right) - \left(OD_{600} \frac{k_{AiiA,max}}{1+\left(\frac{k_{M,AiiA}}{[AiiA]}\right)^{\eta_{AiiA}}} + \gamma_{HSL} + \mu \right) [HSL]
\end{aligned} \tag{1}$$

The system includes 19 parameters: first, OD_{600} (i.e. absorbance at 600 nm) enables the measurement of cellular concentration in the liquid culture, which is set by tuning the dilution rate (D) in the culture chamber. The state variables S_{LuxI} and S_{AiiA}describe the synthesis rate of the two enzymes under P_{TetR} and P_{Lux} promoters, respectively; the steady-state synthesis rates are modelled by Hill equations with parameters α_{PX}, δ_{PX}, k_{PX} and η_{PX}, for the generic *PX* promoter, while the activation dynamics is described by the pole r_{PX}. Enzyme activities were also modelled as Hill functions, depending on 3 parameters for each enzyme $k_{Y,max}$,

$k_{M,Y}$ and η_Y for the generic enzyme Y while γ_{HSL} describes the spontaneous HSL degradation rate, considered negligible in this experimental setup [5]. Parameters were estimated previously, from *ad hoc* assembled circuits [3]-[6].

C. Validation in chemostat experimental setup

The Minifor bioreactor (Lambda) was used to incubate the tested liquid cultures and maintain their absorbance to a fixed value, preventing the reaching of saturation phase. Briefly, ~30 mL cultures were grown in a 0.4-l vessel and peristaltic pumps were used to inject sterile broth and withdraw cultured broth to obtain a dilution D equal to the cell growth rate, μ, to implement a continuous culture at a user-defined OD_{600} value. This configuration is called *chemostat*. OD_{600} and HSL concentration were measured as described previously [5]-[6] over time in different experiments in which OD_{600} was set to diverse levels.

III. Results

A. Improvements in parameter identification

Since the previously described predictions overestimated the experimental data, different interventions were carried out to improve the model prediction performance. First, a new estimation of the P_{Lux}-related parameters (i.e., the promoter driving the expression of the degradation enzyme, see Fig. 1) was carried out in cells bearing a second plasmid including the *luxI* expression system, in order to characterize the promoter in a condition similar to the one of the final circuit. This analysis brought to a new set of parameters that are used to simulate the output of the final circuit. Other experiments showed that neither enzymes activity nor other parts of the circuit seemed to be influenced by this two-plasmid condition. Second, additional experiments were carried out to properly characterize the AiiA enzyme Hill function. In particular, since the P_{TetR} promoter (used to drive *aiiA* in ithe enzyme characterization phase) causes a steep switch between the low and high enzymatic activity, seven new genetic constructs were assembled with *aiiA* under the control of pre-characterized constitutive promoters with graded strength, spanning a range of AiiA levels that was hard to accurately cover with P_{tetR}.

Finally, *ad hoc* error models were selected in this work (i.e., one for each pool of experiments related to the identification of a specific group of parameters), relying on the experimentally observed variance distributions, and they were used to implement weighted least squares for parameter estimation. Taken together, these interventions enabled a significant improvement of model predictive capabilities (see below).

B. Improvements of chemostat experiments predictions

Comparison between model predictions and experimental data revealed the need for a modification of the mathematical model attempting to explain experimental oscillations in cell concentration and dilution rate. In fact, while the chemostat is implemented to keep OD_{600} around a fixed value, dilution rate is adjusted at each time point to compensate OD600 variations. These features also affect HSL levels. Hence, to describe the OD_{600} behaviour, ruling out the equivalence hypothesis between dilution coefficient D and per-cell growth rate m of Eq. 1, another equation was added to the model: a numerical evaluation of dilution coefficient evolution, described by the discrete time equation Eq.2., was carried out, by considering the proper OD_{600} time series for each experiment:

$$D(t_i) = \mu - \frac{OD_{600}(t_{i+1}) - OD_{600}(t_i)}{(t_{i+1} - t_i) \cdot OD_{600}(t_i)} \quad (2)$$

Representative results achieved are shown in Fig 2.

C. "In silico" study of system perturbations

After proving the predictive capabilities of the identified model, the system was analysed *in silico* to study the effect of disturbances and the robustness of the feedback control scheme. Impulsive and step disturbances on HSL concentration levels were taken into account: time to go back to the steady-state were calculated for several levels of cell concentrations and impulse extents while differences between HSL levels (i.e., after and before step disturbance administration) were evaluated, again for different levels of cell concentration and disturbance extents. The open-loop configuration [3]-[6], in which the feedback control was not present (i.e., AiiA enzyme not synthetized), was always used as a term of comparison to demonstrate the usefulness of the implemented control scheme when using a close-loop regulatory network.

Conclusion

This study lays the foundations for efficiently designing feedback controllers through synthetic genetic circuits in living cells. Moreover, in this work, the importance of rational design via bottom-up approach and mathematical modelling is highlighted, as well as a model refinement process for debugging purposes.

Predictions showed to be in accordance with the experimental data, overcoming the previously obtained partial predictive ability [3]-[6]. Finally, the *in silico* analysis of system response to impulsive and step disturbances revealed a greater predicted robustness of the close-loop scheme compared to the open-loop, hence the *in vivo* evaluation of this aspect are currently being studied.

Therefore, according to the obtained results, extending the use of this genetic circuit control scheme and design pipeline in all cases that aim to control a molecular concentration in living cells, seems to be a feasible step in biological engineering.

References

[1] E. Andrianantoandro, et al. "Synthetic Biology: new engineering rule for an emerging discipline" in *Mol. Sys. Biol.*, 2(1), 2006.

[2] D. Endy, "Foundation for engineering biology" in *Nat.*, 438(7067):449-453, 2005.

[3] N.Politi, "A synthetic close-loop regulator in Escherichia coli to control the concentration of a signalling molecule: bottom-up design, mathematical modelling and *in vivo* characterization", PhD thesis, UNIPV, 2013.

[4] Registry of Standard Biological Parts: http://parts.igem.org/mainpage.

[5] *N.Politi, et al. "Half-life measurements of chemical inducers for recombinant gene expression" in J. Biol. Eng. 1;8(1):5, 2014.*

[6] *N.Politi, et al. "Design and implementation of a negative feedback controller in Ecoli with a bottom-up approach"GNB abstract, 2014.*

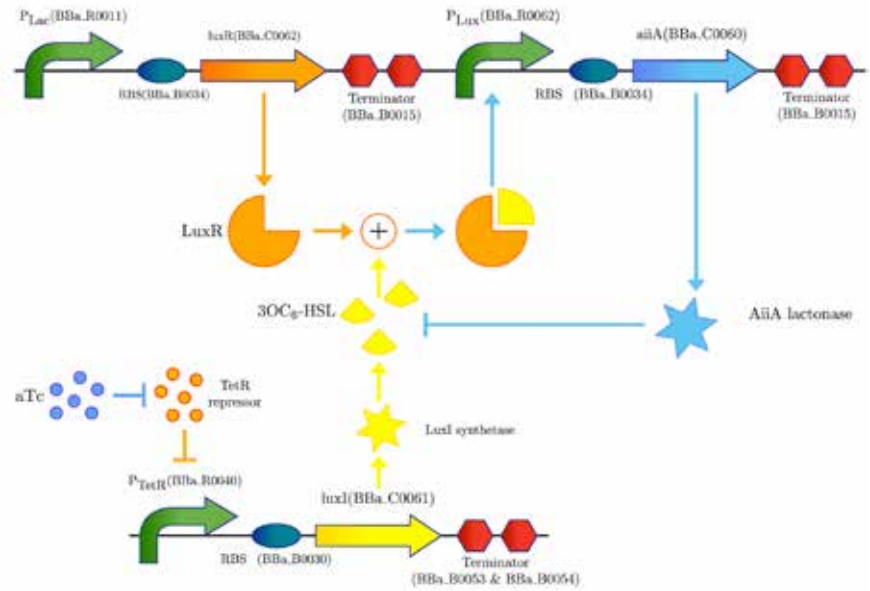

Fig. 1. Schematic representation of the negative feedback circuit.TetR repressor is constitutively produced by *tetR* gene. PTetR promoter (inducible by aTc) is placed upstream of *luxI* coding sequence, tuning its transcription rate. Once translated, LuxI enzyme produces HSL that, together with LuxR transcription factor constitutively expressed by PLac promoter, up-regulates the transcriptional output of PLux promoter. This, in turn, is placed upstream of the *aiiA* coding sequence, which encodes for a lactonase, an enzyme able to degrade HSL. This mechanism, properly tuned, is expected to regulate the concentration of 3OC6-HSL in E. coli cultures.

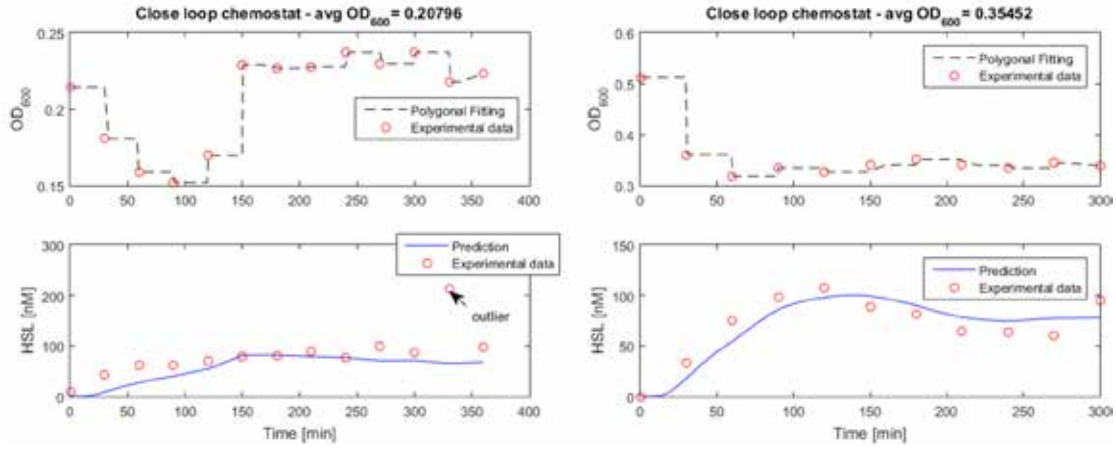

Fig. 2. Prediction of HSL dynamic in chemostat culture experiments. Two representative experiments are shown here, in which an average OD_{600} of 0.21 and 0.35 respectively was kept for the close-loop circuit. Predictions in HSL level (solid lines) can been seen to capture the experimental behavior of the measured data (circles), also as a function of the oscillatory behavior of the OD_{600} time series (circles and dashed lines).

BIOMATERIALI

Microgels as functional material for advanced label-free fiber optic biosensor

A. Aliberti,[1] A. Ricciardi,[1] M. Giaquinto,[1] A. Micco,[1] M. Ruvo,[2] A. Cutolo,[1] A. Cusano[1]
[1]Optoelectronic Division, Department of Engineering, University of Sannio, I-82100, Benevento, Italy
[2]Institute of biostructure and bioimaging, National Research Council, I-80134, Napoli

In this work, we experimentally demonstrate a novel biosensing platform consisting of a Lab on Fiber (LOF) device integrated with functionalized microgels (MGs). In presence of molecular binding events, MGs layer undergoes a volume transition and thus a change in its 'equivalent' RI. Such a RI change is than transduced as a shift of the resonant features in the LOF device reflection spectrum. In order to evaluate the performances of the developed device, in this work we have focused the attention on a well-assessed case study such as the glucose sensing. Specifically we have found that, in response to glucose binding at millimolar concentration, a large blue shift (~27nm) of the reflectance resonant feature occurs. Our results pave the way for new technological routes aimed to develop advanced label free fiber optic nanoprobes.

***Keywords*: microgel, lab on fiber, biosensors**

Rapid and sensitive detection of chemical and biological nalytes becomes increasingly important in areas such as medical diagnostics and environmental monitoring. Fusing together the world of nanotechnologies with optical fibers is leading to continuously develop novel advanced optical probes with enhanced functionalities, especially exploitable for sensing applications [1,2]. At the same time, Microgels (MGs) are increasingly receiving attention by the photonics community as direct sensing materials for environmentally responsive systems. MGs are colloidal stable hydrogel particles that can be synthesized to respond to environment changes, such as temperature, pH, and ionic strength [3-5]. In the specific case of biosensing application, the physicochemical change of a MGs is related to a protein, oligonucleotide, or ligand-binding event.

In this context, we propose a first prototype of Lab-on-Fiber biosensor based on MG system. The developed device essentially consists of a MG layer baked by a gold nanostructure, directly fabricated on the tip of a single mode optical fiber, by means of a process based on gold deposition followed by focused ion beam milling (Figure 1.a). The 50 nm thick metallic nanostructure consists of a square lattice of holes (with sub-wavelength period a=700nm and radius r=210nm) supporting plasmonic resonance, highly sensitive to local modifications of the surrounding environment such as MG layer.

To demonstrate the capability of the proposed device for biosensing application, a glucose sensing MG has been synthetized by incorporating boronic acid moieties into the gel matrix. The interaction between glucose and boronic acid rules the driving forces for gel swelling so that the MG layer undergoes a volume transition and thus a change in its 'equivalent' RI. Such a RI change is than transduced as a shift of the resonant features in the LOF device reflection spectrum. Specifically we have found that, in response to glucose binding at millimolar concentration, a large blue shift (~27nm) of the reflectance resonant feature occurs (Figure 1.b). These impressive results reveal that MG swelling effect, provides a successful amplification (on the spectral shift) with respect to the local RI changes that a small molecule (such as the glucose one) would have induced if bound at the sensor surface by a proper ligand (as in the case of a standard label-free approach).

The developed optical fiber probe represents an interesting prototype of microgel photonics technology, able to work both as biosensor but also exploitable as active tunable plasmonic device. This intriguing biosensing paradigm paves the way for developing advanced label free fiber optic nanoprobes with improved detection capability, especially in the case of small molecules. Finally, it is important to remark that the versatility offered by the MG platform, allows to extend the application of our device to the detection of many different analytes of relevant biological interest.

REFERENCES

[1] Cusano, A., Consales, M., Crescitelli, A., Ricciardi, A., [Lab-on-Fiber Technology] Springer Series in Surface Sciences, 2014.

[2] A. Ricciardi, A. Crescitelli, P. Vaiano, G. Quero, M. Consales, M. Pisco, E. Esposito, A. Cusano, *Lab-on-fiber technology: a new vision for chemical and biological sensing,* Analyst, 140, 2015, 8068-8079.

[3] X. Yin et al, "*Poly(N-isopropylacrylamide-co-propylacrylic acid) copolymers that respond sharply to temperature and pH*.", Biomacromolecules, 7, 2006,1381-1385 .

[4] A. Manikas, A. Aliberti, F.Causa, E. Battista and P.A. Netti , *Thermoresponsive PNIPAAm hydrogel scaffolds with encapsulated AuNPs show high analyte-trapping ability and tailored plasmonic properties for high sensing efficiency* Journal of . Materials Chemistry. B,3, 2015, 53–58.

[5] F. Causa, A. Aliberti, A.M. Cusano, E. Battista, P.A. Netti, "Supramolecular Spectrally Encoded Microgels with Double Strand Probes for Absolute and Direct miRNA Fluorescence Detection at High Sensitivity", J. *Am. Chem. Soc*, 137, 2015, 1758-1761.

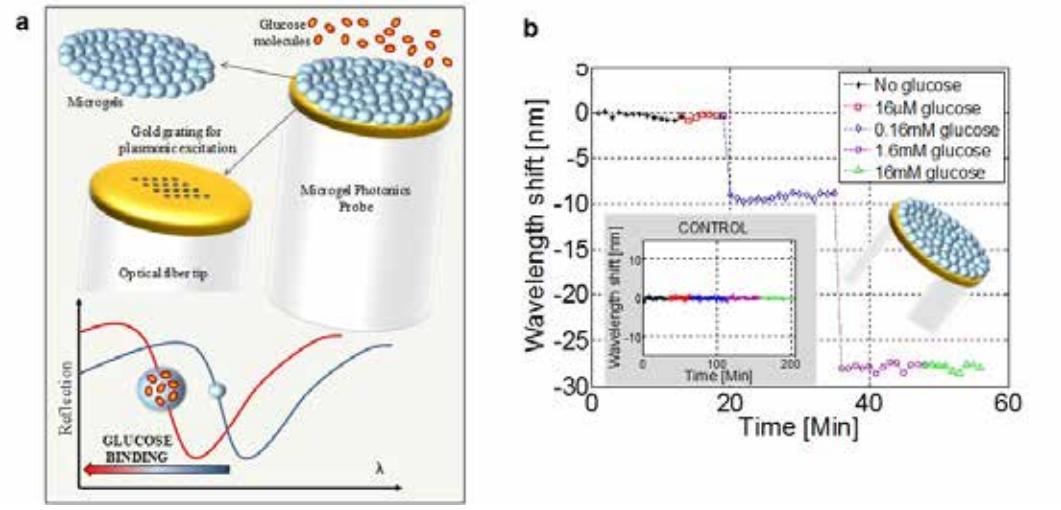

Fig 1 .**a)** Schematic of the Lab-on-Fiber biosensor based on MG system; **b)** Sensorgram at different glucose concentrations ranging from 0 to 16mM. Inset shows the sensorgram of the negative control.

Organosulfur compounds loaded poly(lactic acid) fibrous mats for tissue regeneration

Ilaria Cacciotti[1,2], Matteo Ciocci[3], Francesca Nanni[2,4] and Sonia Melino[3]
[1] University of Rome "Niccolò Cusano", Engineering Dept, Via Don Carlo Gnocchi 3, 00166-Rome, Italy
[2] Italian Interuniversity Consortium on Materials Science and Technology (INSTM), Italy
[3] University of Rome "Tor Vergata", Chemical Sci and Technol Dept, Via della Ricerca Scientifica 1, 00133-Rome, Italy
[4] University of Rome "Tor Vergata", Enterprise Engineering Dept, Via del Politecnico 1, 00133-Rome, Italy

***Abstract*—In this work organosulfur compounds (i.e. Garlic oil-soluble allyl sulfur compounds (GaOs) and diallyl disulfide (DADS)) loaded poly(lactic) acid (PLA) fibers were produced by electrospinning technique in order to be used as promising platform for tissue engineering application. The morphology was analysed by observation at scanning electron microscopy (SEM), and the mechanical properties were evaluated by uniaxial tensile tests. Finally, the potentiality of the produced systems to be used as substrates for the tissue regeneration was evaluated by preliminary *in vitro* cell tests using human progenitor cardiac cells (hCPCs).**

***Keywords*—poly(lactic acid) fibers, garlic extracts, mechanical properties, cytotoxicity.**

I. Introduction

Tissue engineering is considered as a promising and emerging alternative to the current clinical treatments for damaged tissues and organs restoration. To achieve the tissue engineering purpose, the design of a proper substrate ("scaffold") suitable to act as a temporary matrix for cell proliferation, extracellular matrix deposition, bone in-growth and neo-vascularization, is pivotal. In particular, recently a lot of attention is devoted to the device of 'bioinspired materials', materials able to resemble the composition, the morphology, the mechanical and biological features of natural tissues.

The electrospinning is a user friendly, versatile and low-cost technique , able to process different kinds of materials in fibers with diameters ranging from nanometers to microns and large surface area-to-volume ratio [1-4]. It has recently emerged as a very promising approach, due to its ability to generate structures which resemble those of the tissue extracellular matrix and to entrap biomolecules, allowing their controlled release. Moreover, since the electrospinning occurs at ambient conditions, it is very suitable to encapsulate and stabilize thermally labile substances.

Thus, in this context, organosulfur compounds (OSCs) loaded poly(lactic) acid (PLA) fibrous mats were produced by electrospinning technique. Garlic oil-soluble allyl sulfur compounds (GaOs) and diallyl disulfide (DADS) were selected in order to provide antimicrobial properties and improved biological responsiveness. In fact, it is well known that the beneficial health properties of garlic have to be ascribed to the presence of organosulfur compounds (OSCs) that provide antimicrobial, antioxidant [5,6] and anti-inflammatory properties [7], heart protection and chemo-sensitization features, including the *in vitro* inhibition of tumor cell proliferation through the apoptosis induction [7]. Their outstanding features can be associated to their ability to release H_2S, one of three natural *gas transmitters*, able to promote some specific enzymatic activities and to act as a reducing element, preventing free radicals formation.

The morphology of the obtained fibers was investigated by observation at scanning electron microscopy (FEG-SEM), the mechanical properties by uniaxial tensile tests, the ability of the OSCs loaded PLA fibers to release H_2S by methylene blue (MB) assay. Finally, the cytotoxycity and the potentiality of the produced systems to be used as scaffold for tissue repair was assessed by analysis of the *in vitro* cell viability of human Lin^- $Sca1^+$ progenitor cardiac cells (hCPCs).

II. MATERIALS AND METHODS

OSCs (5 %vol with respect to the used solvents) and PLA (15 % wt/V with respect to the used solvents) based solutions were prepared by dissolving proper amounts of PLA pellets and OSCs in a solvent mixture $CHCl_3$:DMF (67:33, in volume ratio).

Prepared solutions were poured in a glass syringe (Socorex, Switzerland) equipped with a 18 G needle, fixed in a digitally controlled syringe pump (KD Scientific, MA, USA) and electrospun in air at room temperature, setting an applied voltage of 12 kV, a flow rate of 0.5 ml/h and a needle-target distance of 15 cm. As a reference sample, neat PLA mat was also produced following the same experimental procedure.

The morphology of the electrospun mats was investigated by means of scanning electron microscopy (SEM, *Leo Supra 35*). The average fiber diameter was calculated considering around 50 randomly selected fibers from SEM micrographs (ImageJ, NIH). Mechanical properties of PLA based electrospun mats were investigated by uniaxial tensile tests performed on dog-bone specimens (width 4.8 mm, length 22.25 mm), at 1.2 mm/min to rupture by an electromechanical machine equipped with a 50 N load cell (Lloyd LRX), following ASTM D1708 and ASTM D882 for elastic modulus calculation. Four specimens were considered for each electrospun matrix. The H_2S release was estimated for both GaOS and DADS loaded PLA fibers by methylene blue (MB) assay [8,9]. The biological responsiveness of the produced systems was investigated by *in vitro* cell viability of hCPCs, up to 7 days, using MTT (methylthiazolyldiphenyl-tetrazolium bromide) assay [10].

RESULTS AND DISCUSSION

Uniform, defect-free randomly oriented fibers were obtained in all cases (Fig. 1). The addition of DADS led to bigger fibers (average value of 1.21μm vs 0.71 μm and 0.65 μm for PLA and PLA-GaOS respectively), whereas the PLA/GaOS fibers seemed very similar to neat PLA.

A remarkably significant increment of the mechanical properties, in terms of Young modulus (E) and σ_{max} (Table I), was recorded in the case of organosulfur compounds loaded PLA fibers, suggesting an interaction between the S containing compounds and the PLA chains, in agreement with differential scanning calorimetry (DSC) data (not shown) that evidenced an increased crystallinity degree in the case of organosulfur compounds loaded fibers.

In order to evaluate the potential application of the produced systems as platforms for tissue regeneration, preliminary cytotoxicity test were carried out, seeding human cardiac progenitor cells (hCPCs). Not citotoxicity of all the produced fibrous mats was demonstrated and a good cell adhesion and cell proliferation were revealed, particularly in the case of fibers loaded with DADS (Fig. 2), whereas the PLA/GaOS sample showed a behaviour comparable to that of PLA. This increment of the cell proliferation was ascribed to the higher DADS concentration which allowed an increased production of H_2S, as evidenced by the H_2S assay results (Fig. 3).

TABLE I
MECHANICAL PROPERTIES OF THE PRODUCED PLA BASED FIBROUS MATS

Sample	σ_{max} *(MPa)*	*E (MPa)*
PLA	1.1±0.1	28±1
PLA/DADS	2.4±0.2	65 ± 18
PLA/GaOS	2.7±0.3	52 ±6

III. CONCLUSIONS

Homogeneous and defect-free garlic oil-soluble allyl sulfur compounds and diallyl disulfide loaded PLA fibers were successfully pursued by electrospinning technique.

The presence of the OSCs allowed to obtain a significant increment of the mechanical properties.

Preliminary *in vitro* cell test with hCPCs evidenced not cytotoxicity of the produced systems and a remarkable enhanced cell viability in the case of fibers loaded with DADS, suggesting its ability to induce and promote cell proliferation through the production and release of H_2S.

REFERENCES

[1] S. Ramakrishna, R. Jose, P. S. Archana, A. S. Nair, R. Balamurugan, J. Venugopal, W. E. Teo, *J. Mater. Sci.*, vol. 45, pp. 6283-6312, 2010.

[2] J. M. Lagaron and A. Lopez-Rubio, *Trends in Food Science & Technology*, vol. 22, pp. 611-617, .Nov. 2011

[3] I. Cacciotti, M. Calderone, A. Bianco, *Europ. Polym. J.*, vol. 49, pp. 3210–3222, 2013.

[4] I. Cacciotti, E. Fortunati, D. Puglia, J.M. Kenny, F. Nanni, *Carbohydrate Polymers*, vol. 103, pp. 22–31, 2014.

[5] J.C. Harris, S.L. Cottrell, S. Plummer, D. Lloyd, *Appl. Microbiol. Biotechnol.*, vol. 57, pp. 282–286, 2001.

[6] F. Perez-Severiano, M. Rodriguez-Perez, J. Pedraza-Chaverri, P.D. Maldonado, O.N. Medina-Campos, A. Ortiz-Plata, A. Sanchez-Garcia, J. Villeda-Hernandez, S. Galvan-Arzate, P. Aguilera, et al., *Neurochem. Int.*, vol. 45, pp. 1175–1183, 2004.

[7] V.M. Dirsch, A.L. Gerbes, A.M. Vollmar, *Mol. Pharmacol.*, vol. 53, pp. 402–407, 1998.

[8] A.I. Bhuiyan, V.T. Papajani, M. Paci, S. Melino, *Molecules*, vol. 20, pp. 1731-1750, 2015.

[9] T.M Schmidt, B. Arieli, Y.Cohen, E. Padan, W.R. Strohl, *J Bacteriol*, vol. 169, pp. 5466-5472, 1987.

[10] F. Denizot, R. Lang, *J Immunol Methods*, vol. 89, pp. 271-277, 1986.

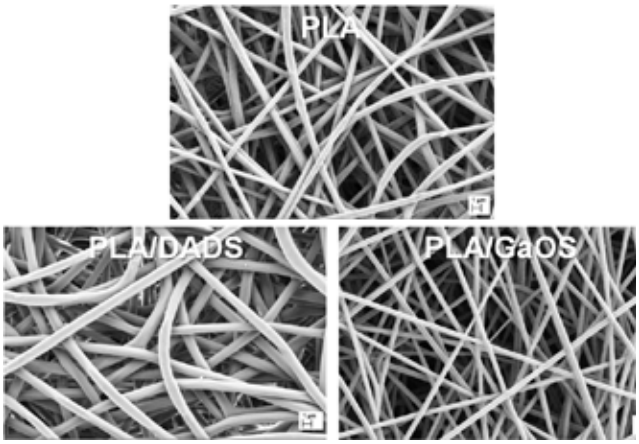

Fig. 1. SEM micrographs of PLA, PLA/DADS and PLA/GaOS fibrous mats.

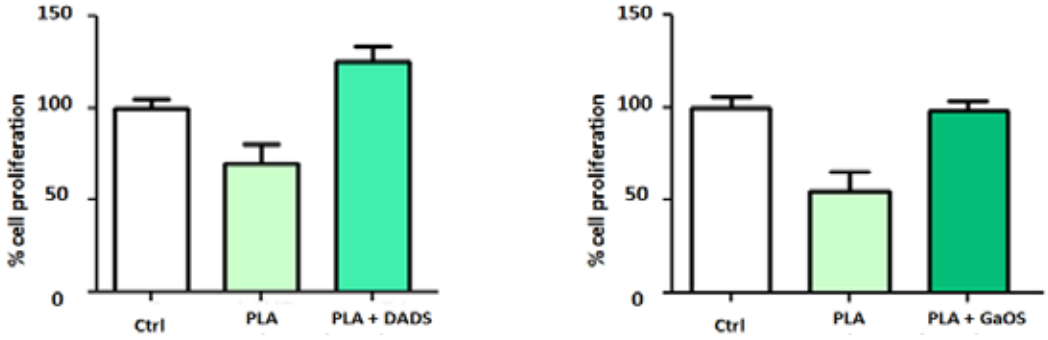

Fig. 2. MTT assay results for PLA, PLA/DADS and PLA/GaOS fibrous mats.

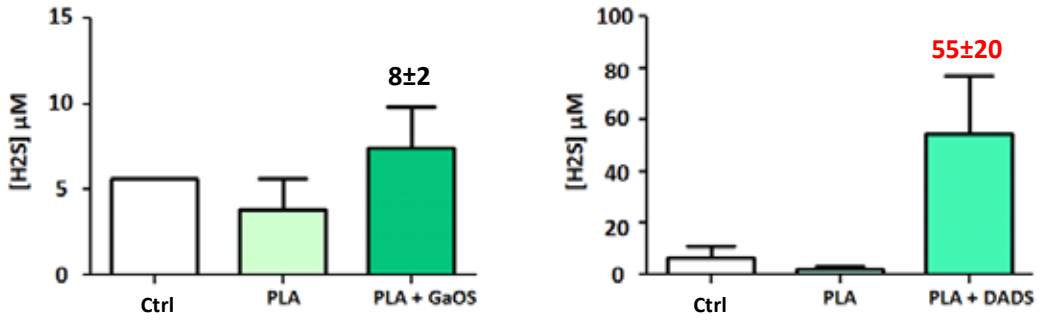

Fig. 3. H_2S assay results for PLA; PLA/DADS and PLA/GaOS fibrous mats.

Microgel Assay for miRNA analysis

T.M. Caputo[1,2], A. Cummaro[1], V. Lettera[1], E.Battista[1,2], F. Causa [1,2,3] and P.A. Netti[1,2,3]

[1] *Center for Advanced Biomaterials for Heathcare@CRIB, Istituto Italiano di Tecnologia (IIT), Largo Barsanti e Matteucci 53, 80125Naples, Italy*
[2] *Interdisciplinary Research Centre on Biomaterials (CRIB), University "Federico II", Piazzale Tecchio 80, 80125 Naples, Italy*
[3] *Dipartimento di Ingegneria Chimica del Materiali e della Produzione Industriale (DICMAPI), University "Federico II", Piazzale Tecchio 80, 80125 Naples, Italy*

***Abstract*— A new engineered method, based on a class of encoded beads for high sensitive fluorescence detection of nucleic acids is developed. In medical field, is emerging a new class of circulated biomarkers, such as miRNAs, that are related to several diseases like as cancer, viral and neurodegenerative pathologies. Direct detection of miRNAs in body fluids is particularly challenging and demands high sensitivity, specificity, and multiplexing capabilities. The conjugation of fluorescent probe onto polymeric microgels allows for sensitive detection of miRNA sequences with a dynamic range of 10^{-9}-10^{-15}M. The combination of an innovative detection assay based on micro-particles and new class of promising biomarkers represents an attractive alternative to conventional sensitive DNA detection technologies that rely on amplification methods.**

***Keywords*—miRNA, detection, assay, microgel.**

I. Introduction

MicroRNAs are a class of short non-coding single-stranded RNA molecules consisting in 20-25 nucleotides, that regulate gene expression acting at the post-transcriptional level [1]-[2]. MicroRNAs are involved in a wide range of biological processes such as cell cycle control, apoptosis and several developmental and physiological processes including stem cell differentiation, hematopoiesis, hypoxia, cardiac and skeletal muscle development, neurogenesis, insulin secretion, cholesterol metabolism, immune responses, viral replication, myopathies, cardiovascular disease , diabetes and metabolic pathologies [3]. Due to their immense regulatory power, variation of microRNAs concentration can be utilized as potential biomarkers for the diagnosis and prognosis of a variety of diseases such as cancer [4]-[5], neurological disorders [6], neurodegenerative pathologies as Alzheimer [7].

Many methodologies have been adapted for detect microRNAs expression, such as Northern blotting, microarray, polymerase chain reaction (PCR, RT-qPCR), oligonucleotide probes (molecular beacons, double strands probes), electrochemical, thermodynamic and enzymatic techniques [8]. In particular, RT-qPCR is the standard method for oligonucleotide detection because shows high sensitivity and high-throughput ability. However, extraction, amplification, and calibration steps are always necessary and time-consuming, while amplification may compromise the assay accuracy [9].

In recent years, the use of encoded beads has received considerable attention for the multiplexed detection of nucleic acids, offering high flexibility, easy probe-set modification, efficient mixing steps, and high degrees of reproducibility.

The combination of microgels beads with appropriate DNA probes proved antifouling properties and multiplex ability in miRNA identification, with outstanding performance.

We developed fluorescent probes bound to optically encoded microgel molecular network for the detection of oligonucleotide targets, by double strand displacement assay [10]-[11]. The results, here reported, show that the use of microgel platform corresponds to a 10^5 fold enhancement in sensitivity (2.6 fM) compared to the same probe no conjugated (172 pM).

II. Methods

A. Reagents and Chemicals

Poly(ethylene glycol) dimethacrylate average Mn 550 (PEGDMA), Acrylic acid (AAc), Potassium persulfate (KPS), Fluoresceine O-methacrylate, 1-ethyl-3-(3-dimethylaminopropyl) carbodiimide (EDC) and Polyvinyl alcohol 40-88 (PVA), Dimethyl Sulfoxide (DMSO), Sodium Hydroxide and MES were all purchased from Sigma-Aldrich and used as received. The dye Methacryloxyethyl thiocarbonyl rhodamine B was obtained from Polyscience Inc. Tris buffer 1M, pH 8 was supplied by Applichem GmbH. DNA and RNA oligonucleotides were purchased from Diatech Pharmacogenetics srl with HPLC purification (Table I). Human serum was supplied by Lonza. PureZOL RNA Isolation Reagent, Bio-Rad iScript™ Reverse Transcription, Supermix for RT-qPCR Bio-Rad, iTaq™ Universal Probes Supermix Bio-Rad were all purchased from Biorad. Taqman Micro RNA assays was purchased from Applied Biosystem.

B. Microgel synthesis and surface functionalization

The Multifunctional microgels were obtained through a multistep procedure combining free-radical precipitation polymerization and seeding polymerization [12].

The encoding was obtained by combining different

amounts of Rh and Fluo in the feeding solutions and noted as RxFy.

DNA-tail-Cy5 sequences were covalently immobilized to the microparticles surface by carbodiimide coupling. The amount of immobilized DNA-tail-Cy5 was calculated from the difference between the initially added and the free DNA-tail-Cy5 using confocal microscopy (excitation wavelength 633 nm, emission range 650-720 nm).

C. Quenching , miRNA displacement assay and encoded specificity

An appropriate amount of DNA-tail-Cy5 coupled microgels was mixed 1:1 ratio to the Quencher DNA probe and incubated overnight. The duplex quenched microgels were mixed to a solution containing the RNA target and the recovery fluorescence was recorded and quantified by confocal laser scanning microscope Leica SP5.

Three different encoded core double/shell microgels were used in order to indentify the three different miRNA.

III. Results and Discussion

Based on the target sequence (22nt), we designed a quencher strand fully complementary to the target and internally modified with a fluorescence quencher-Black Hole Quencher (BHQ_2) and small nucleotide tail (11-12nt) labelled with Cy5 at the 5' end, modified with an ammine group on the 3' position for the following covalent immobilization on microgels.

When Cy5 and BHQ come in close proximity, fluorescence quenching occurs. In presence of the target, the quencher and the target hybridize so that the Cy5 and BHQ are no longer in close proximity and, therefore, Cy5 fluorescence emission is recovered. The length of the tail was optimized to obtain an appropriate difference in free energy (about 20 kcal mol^{-1}) between the tail-quencher and the target-quencher duplex. The strand displacement mechanism, is therefore, driven by the free energy released from the fully complementary target-quencher duplex. In order to validate the microgels in detection applications, the miR21 sequence was chosen as a miRNA target. In Figure 1 is reported the scheme showing the detection system. The fluorescence recovery for the miR21 was measured on the microgels in a dynamic range of 10^{-9} -10^{-15} M with a LOD of 2.6 fM.

The selective detection of a triplex miRNA panel represented by miR21, miR210 and miR196a-5p was achieved by conjugating the corresponding DNA tail Cy5 probes on three different encoded microgels. The quenched microgels were mixed and incubated with a solution containing synthetic miR21 and mir196a-5p targets (3×10^9 copies of each). The Cy5 fluorescence recovery occurred only on miR21 and 196a-5p specifically encoded microgels. The ratio Fluorescein/Rhodamine indeed correlates with the specific code corresponding to miR21 and 196a-5p.

In order to compare our results with a gold standard technique, we measured the endogenous content of miR21 in healthy human serum extract by the microgels as well as by RT-qPCR. The concentration of endogenous miRNA obtained from the different technique are in fully agreement, with an improved precision for microgel assay [13].

The microgel assay allows the direct detection of single strand RNA (miRNA) with a limit of detection in order of fM, without the need for intermediate steps of extraction and amplification and with capability of performing a multiplexed assay for a panel of three targets.

IV. Conclusion

Current diagnostic techniques for cancer and other diseases are often invasive and costly, thus preventing their adoption for a larger use and limiting the possibility of detecting pathologies at early stages. Circulating microRNA have emerged as promising biomarkers; they can be detect from biological fluids tools offering the possibility of a low cost minimally invasive diagnostic procedure. With this respect, we designed and realized a simply and sensitive displacement assay in order to detect multiplex diagnostic biomarkers by using fluorescent microscopy in miniaturized system.

TABLE I

miRNA	*Sequence (5'-3')*	*ΔG (Kcal/mol)*
miR-21 DNA-tail-Cy5	**Cy5-** GACTGATGTTGA-NH_2	QF_{hyb} 11.2
mir-21 Quencher	TCAACATCAGT**BHQ** TGATAAGCTA	QT_{hyb} 24.8
hsa-mir-21 (22nt)	UAGCUUAUCAGAAC UGAUGUUGA	$\Delta_{displacement}$13.6
miR-210 DNA-tail-Cy5	**Cy5-** ACAGCGGCTGA-NH_2	QF_{hyb}13.9
mir-210 Quencher	TCAGCCGCTG**BHQ** CACACGCACAG	QT_{hyb} 34.9
hsa-mir-210 (22nt)	CUGUGCGUGUGAC AGCGGCUGA	$\Delta_{displacement}$21
miR-196a -5p DNA-tai-CY5	**Cy5-** CATGTTGTTGGG-NH_2	QF_{hyb} 11.2
miR-196a -5p Quencher	CCCAACAACAT**BH Q**AAACTACCTA	QT_{hyb} 25.8
hsa-miR-196a-5p(22nt)	UAGGUAGUUUCAUG UUGUUGGG	$\Delta_{displacement}$14.6

QF_{hyb} Free energy gained from the partially complementary DNA-tail-Cy5 and Quencher duplex; QT_{hyb} Free energy gained from the fully complementary Target and Quencher duplex ; $\Delta_{displacement}$ Free energy gained after Tail-Quencher de-hybridization and Target-Quencher hybridization

References

[1] M. Inui, G. Martello and S. Piccolo "MicroRNA control of signal transduction", *Nature Reviews Molecular Cell Biology,* Vol. 11, pp. 252-263, 2010.

[2] M. Ha, V. Narry Kim "Regulation of microRNA biogenesis", *Nature Reviews Molecular Cell Biology,* Vol. 15, pp. 509-524, 2014.

[3] V. De Guire, R. Robitaille, N.Tétrealut, R. Guérin, C. Ménard "Circulating miRNAs as sensitive and specific biomarkers for the diagnosis and monitoring of human diseases: Promises and challenges", *Clinical Biochemistry,* Vol. 46, pp 846–860, 2013.

[4] S. Lin, R.I. Gregory "MicroRNA biogenesis pathways in cancer", *Nature Reviews Cancer*, Vol. 15, pp. 321–33, 2015.

[5] M. Fernandez-Mercado, L. Manterola, E. Larrea, I. Goicoechea, M. Arestin, M. Armesto "The circulating transcriptome as a source of non-invasive cancer biomarkers: concepts and controversies of non-coding

and coding RNA in body fluids", *Journal of Cellular and Molecular Medicine,* Vol. 19, pp. 2307-2323, 2015.

[6] S.S. Hébert, B. De Strooper "Alterations of the microRNA network cause neurodegenerative disease", *Trends in Neurosciences*, Vol. 32, pp. 199–206, 2009.

[7] G.D. Femminella, N. Ferrara, G. Rengo "The emerging role of microRNAs in Alzheimer's disease", *Frontiers in Physiology*, Vol. 40, 5, 2015.

[8] R. M. Graybill, R. C. Bailey "Emerging Biosensing Approaches for microRNA Analysis", *Analytical Chemistry*, Vol. 88, pp. 431−450, 2016.

[9] C. Chen, R. Tan, L. Wong, R. Fekete, J. Halsey "Quantitation of microRNAs by real-time RT-qPCR", *Methods in Molecular Biology*, 687, pp. 113-134, 2011.

[10] F. Causa, A. Aliberti, A. M. Cusano, E. Battista, P. A. Netti "Microgels for multiplex and direct fluorescence detection ", *Proceedings SPIE,* 9529, doi:10.1117/12.2185839, 2015.

[11] A. Aliberti, A. M. Cusano, E. Battista, F. Causa, P. A. Netti "High sensitive and direct fluorescence detection of single viral DNA sequences by integration of double strand probes onto microgels particles", *Analyst*, Vol.141, pp. 1250-1256, 2016.

[12] E. Battista, A. Mazzarotta, F. Causa, A. M. Cusano, P.Netti "Core-shell microgels with controlled structural properties, *Polymer International,* DOI 10.1002/pi.5076, 2015.

[13] F. Causa, A. Aliberti, A. M. Cusano, E. Battista, P.Netti "Supramolecular Spectrally Encoded Microgels with Double Strand Probes for Absolute and Direct miRNA Fluorescence Detection at High Sensitivity", *Journal of American Chemical Society*, Vol. 137, pp. 1758–176, 2015.

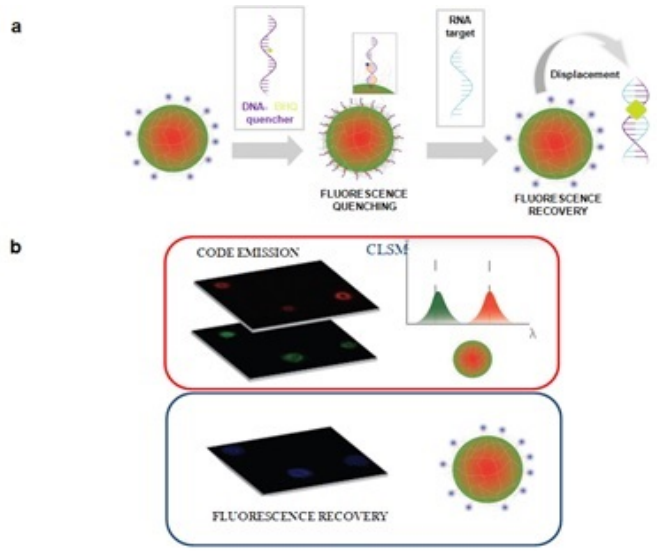

Fig. 1. Microgel based assay set up. a) Conceptual scheme showing detection mechanism. The fluorescence of DNA tail Cy5 is previously quenched by a partial hybridization with DNA quencher sequence. In presence of targets, the quencher DNA is thermodynamically driven to hybridize the target, which displaces the DNA tail Cy5, leading to a fluorescence recovery. The presence of the target is detected by the Cy5 fluorescence recovery after the displacement assay. The rhodamine B emission at l=560 nm and fluoresceine emission at l =510 nm ratio identify the encoded microgel. b) Sketch of encoded microgel assay for miRNA fluorescence quantification

Selective functionalisation of bioabsorbable stents to promote fast endothelialisation

, I Carmagnola[1], V Chiono[1], S Pacharra[2], J Salber[2], S McMahon[3], Wenxin Wang[4], C Lovell[5], P Basnett[6], B Lukasiewicz[6], R Nigmatullin[6], I Roy[6], G Ciardelli[1]

[1] *Department of Mechanical and Aerospace Engineering, Politecnico di Torino, Torino*
[2] *Zentrum für klinische Forschung, Ruhr-Universität Bochum, University Hospital Knappschaftskrankenhaus Bochum*
[3] *Vornia Biomaterials Ltd, Lab C, Synergy Centre, IT Tallaght and Charles Institute of Dermatology, UCD, Dublin*
[4] *Institute of Technology, Vornia Biomaterials Ltd, Dublin*
[5] *Lucideon Ltd, Stoke-on-Trent*
[6] *Department of Life Science, University of Westminster, London*

***Abstract*—The rapid endothelialisation of the stent surface is a critical factor to ensure healing of the vessel wall, avoiding restenosis and thrombosis.**

Innovative bioabsorbable polymers were surface functionalized with a mixture of selective pegylated pepetide and polyethylene glycol. Physico-chemical characterization confirmed the successful biochemical functionalisation and *in vitro* tests demonstrated that the selective coating effectively improved the surface endothelialisation.

***Keywords*—Bioabsorbable stent, endothelialisation, surface functionalisation, plasma treatment.**

I. Introduction

The main causes of cardiovascular stent failure are restenosis and very late thrombosis. The rapid endothelialisation of the stent surface is a critical factor to ensure healing of the vessel wall, preventing both thrombosis and restenosis [1,2]. The combination of antifouling molecules with extracellular matrix proteins is a promising strategy to design antithrombogenic surfaces able to promote fast endothelialization [3,4]. Pan et al. [5] sequentially immobilized poly(ethyelene glycole) (PEG) and collagen I on the titanium surface, improving both blood compatibility and endothelialisation.

In particular, REDV peptide was proven to selectively promote the adhesion of endothelial cells (ECs) against platelets and smooth muscle cells (SMCs) [6,7]. Biomolecules could be covalently attached to the polymer surface by employing different functional groups. Since functional groups usually are not present on synthetic polymer surface, they can be introduced by chemical or physical treatments. Through plasma treatment, surface chemistry can be modified in a controlled way without affecting the bulk material properties [8]. In this work different ratios between PEGylated-REDV and PEG were investigated in order to find the optimal coating to achieve a fast EC adhesion avoiding unspecific protein attachment. Two different chain lengths of PEG were used: PEG_6 and PEG_{12}.

II. Materials and methods

A. Materials

PEGylated REDV was provided by Biomatik, according to our specification, in particular it is formed by 6 PEG monomer repetitions (Chempep Inc.), with a $-NH_2$ terminal group. PEG oligomers were purchased from Chempep Inc. with two different chain lengths: m-PEG_6-NH_2 (295.4 Da, PEG_6) with 6 monomer repetitions and m-PEG_{12}-NH_2 (559.7 Da, PEG_{12}) with 12 monomer repetitions. Pure acrylic acid, 99% (AAc), liquid monomer, 1-(3-dimethylaminopropyl)-3-ethylcarbodiimide (EDC) and N-hydroxysuccinimide (NHS) were purchased by Sigma. All used reagents were purchased from Sigma-Aldrich, Milan, Italy. All solvents were of analytical grade and used without further purification.

B. Methods

A two-step plasma treatment was performed on different polymeric films. Polymerized acrylic acid (PAAc) coating was obtained in a Plasma Enhanced CVD reactor (RF = 13.56 MHz). Ar was used for substrate etching before PAAc deposition, for 5 min, with a flow of 20 sccm and an applied power RF = 50 W. Acrylic acid vapors were diluted in argon (flow= 20 sccm), polymerization was performed by a pulsed plasma discharge applying a discharge RF power of 200W, a duty cycle of 10% for 10 min [9]. After plasma treatment, polymeric films were rinsed two times with bidistilled water and then dried at room temperature. Plasma treated samples were dipped into a EDC/NHS solution (ratio 4:1, pH 5.5) for 1 hour at 4°C and then rinsed for two times with bistilled water. Subsequently activated polymeric films were dipped in PBS solution (100 μg/mL) containing different molar ratios between PEGylated-REDV and PEG (100/0, 80/20 and 70/30) for 20 h at room temperature. Finally functionalized films were rinsed two times and dried at room temperature.

Physico-chemical characterization was performed to confirm the successful of functionalisation process. *In vitro* cell tests were carried out to evaluate how the biochemical coating affected cell adhesion and blood biocompatibility.

III. Results and discussion

A poly(acrylic) acid (PAAc) coating was polymerised on the surface of different polymeric substrates in order to expose carboxyl groups with the aim to covalently graft biomolecules. After plasma treatment, polymeric films showed lower contact angle values compared to the untreated films; moreover ATR-FTIR spectra showed the appearance of characteristic peaks of PAAc. Colorimetric quantification through Toluidine Blue dye demonstrated successful grafting

of AAc monomers on the polymers surface as there was evidence of increased amount of carboxylic groups on the polymer surface. Physico-chemical characterization showed that PAAc coating could be successfully deposited via plasma treatment on different polymeric materials.
Different molar ratios between PEGylated REDV and PEG, by using PEG_6 and PEG_{12}, were tested to find out the optimal coating. The contact angle analysis highlighted how all tested coating caused an increase of water wettability. In particular the PEGylated REDV/PEG_{12} 70/30 coating showed the lowest contact angle value (~ 70°). Moreover the ATR-FTIR spectra confirmed the PEGylated REDV and PEG presence on the surface of polymeric films.
The PEGylated REDV functionalisation resulted in high endothelial cell adhesion accompanied by adequate cell spreading (Fig. 1). The chemical modification with PEGylated REDV also led to an elevation in platelet adhesion and activation while the unmodified polymers had low platelet adhesion. However, as a healthy endothelial cell layer is considered to be the ideal anti-hemolytic, anti-thrombotic and anti-coagulant surface, the complete and fast endothelialisation of a medical device is the best way to prevent any thrombotic or inflammatory reactions.

IV. Conclusion

In this work, a selective coating able to quickly promote a surface endothelialisation on polymeric stents was developed. In particular acrylic acid coating allowed to expose -COOH groups able to graft biomolecules; PEGylated-REDV and PEG were successful grafted on the polymeric substrates. The presence of the REDV peptide increased the EC adhesion on the materials; the fast formation of a healthy endothelial cell layer could enhance the hemocompatibility of these polymeric materials *in vivo*.

Acknowledgement

This work was funded by the European Commission 7th Framework Programme under grant agreement number 604251- ReBioStent (Reinforced Bioresorbable Biomaterials for Therapeutic Drug Eluting Stents). The authors thank all the ReBioStent partners for their support in this work.

References

[1] F. Nazneen, G. Herzog, D.W.M. Arrigan, N. Caplice, P. Benvenuto. (2012). Surface chemical and physical modification in stent technology for the treatment of the coronary artery disease. *J Biomed Mater Res B Appl Biomater*, 100B(7), 1989-2014. Available:

[2] H. Ceylan, A.B. Tekinay, M.O. Guler. (2011). Selective adhesion and growth of vascular endothelial cells on bioactive peptide nanofiber functionalized stainless steel surface. *Biomaterials*; 32(34), 8797-8805. Available:

[3] M.C. Chen, H.F. Liang, Y.L. Chiu. (2005). A novel drug-eluting stent spray-coated with multi-layers of collagen and sirolimus. *Journal of Controlled Release* ,108, 178-189. Available:

[4] S.P. Massia, J.A. Hubbell. (1992). Vascular Endothelial Cell Adhesion and Spreading Promoted by the Peptide REDV of the IIICS Region of Plasma Fibronectin Is Mediated by Integrin α4β1. *Journal of Biological Chemistry*, 267, 14019-14026. Available:

[5] C.J. Pan, Y.H. Hou, H.Y. Ding, Y.X. Dong.(2013). Enhancing anticoagulation and endothelial cell proliferation of titanium surface by sequential immobilization of poly(ethylene glycol) and collagen. *Appl Surf Sci*, 287, 443-450. Available:

[6] Hubbell, Massaia, S.P., Jeffrey, A., (1992) Vascular endothelial cell adhesion and spreading romote by the peptide REDV of the IIICS region of plasma fibronectin is mediated by integrin alpha4beta1 The journal of biological chemistry, 267(20), 14019-14026.

[7] Meyers, S.R., Kenan, D.J., Khoo, X., Grinstaff, M.W., (2011) Bioactive Stent Surface Coating That Promotes Endothelialization while Preventing Platelet Adhesion Biomacromolecules, 12, 533-539.

[8] Favia P., Sardella E., Gristina R., D'Agostino R. (2003) Novel plasma processes for biomaterials: micro-scale patterning of biomedical polymers Surface and Coatings Technology, 169-170(2), 707-711.

[9] Surface functionalization by poly-acrylic acid plasma-polymerized films for microarray DNA diagnostics, Surface and Coatings Technology, Volume 207, 25 August 2012, Pages 389–399.

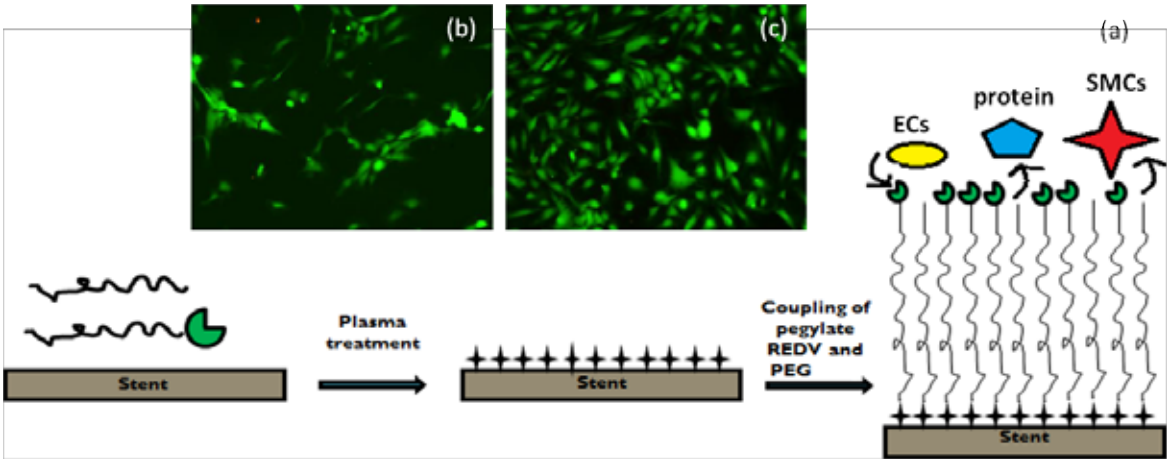

Fig. 1. (a) Scheme of functionalization steps and final main properties of functionalized surface; fluorescence microscopy images of endothelial cells cultured on different synthetic polymers (b) and on PEGylated functionalized synthetic polymers (c).

In vivo enhancement of arteriogenesis using human cell-seeded composite scaffolds

M. Carrabba[1,2], C. De Maria[2], A Oikawa[1], C Reni[1], I Rodriguez-Arabaolaza[1], H Spencer[1], S Slater[1], E Avolio[1], Z Dang[1], G Spinetti[3], P. Madeddu[1], G. Vozzi[2]

[1] *Bristol Heart Institute, School of Clinical Sciences, University of Bristol, Bristol, UK*

[2] *Research Centre 'E. Piaggio', University of Pisa, Italy*

[3] *IRCCS Multi Medica, Milan, Italy*

***Abstract*— This work is focused on the fabrication and characterization of 3D scaffolds as a promising option for revascularization of ischemic tissues. To overcome the limitations of cells therapy, we propose the design of bio-engineered scaffolds able to ensure a precise homing of cells in the area of implantation. Two classes of scaffolds were developed and compared: hydrogel (HG) and hybrid (HB). While HG are fabricated with the traditional method of Soft-Lithography, HB are achieved by the combination of microfabrication techniques as Pressure Assisted Microsyringe^2 (PAM^2) and electrospinning and by the composition of different biomaterials.**

The scaffolds were characterized, cellularized with Adventitial Progenitor Cells (APCs) isolated from saphenous veins and implanted in mice model of critical limb ischemia (LI). The effect of the procedure was studied by blood flow recovery assay and perivascular angiogenesis assays.

***Keywords*— Composite scaffolds, rapid prototyping, electrospinning, arteriogenesis..**

I. Introduction

Peripheral artery disease (PAD) is a common pathological condition that affects up to 15% of people older than 55 years [1]. Critical limb ischemia (CLI), the most severe manifestation of PAD, causes poor quality of life and requires foot amputation in 25% of cases within one year from the diagnosis. The reported amputation and mortality rates exceed 50% in CLI patients that are unsuitable for surgical or endovascular revascularization [2]. Considering these unfavourable outcomes, new therapeutic approaches are urgently needed. In this context Tissue Engineering (TE) has started to be considered like a possible solution. The fabrication of cell-engineered scaffolds for TE allow cells grow and proliferate to recreate a tissue and to be implanted around the occluded artery may obviate these limitations.

This work proposes a novel bio-engineered scaffolds providing a temporary artificial extracellular matrix (ECM) to support cell engraftment and guide the formation of a well-aligned arterial collateralization. The present study comprises 3 main work-packages: (1) design and fabrication of two classes of 3D scaffolds, (2) in vitro testing of cellularized scaffolds functionalized with human adventitial progenitor cells (APCs), and (3) in vivo perivascular transplantation of cellularized scaffolds in a mouse model of limb ischemia.

We named the two classes of microfabricated scaffolds hydrogel (HG) and hybrid (HB) respectively.

As a cellular source for scaffold functionalization, we used APCs isolated/expanded from remnants of saphenous vein of coronary artery bypass graft surgery [3], [4]. In models of limb and myocardial ischemia, transplantation of APCs promotes vascularization through the release of angiocrine factors and chemokines that recruit endothelial cells, pro-angiogenic mononuclear cells, and resident progenitor cells [5]-[8]. Following successful seeding of APCs, the functionalized scaffolds were tested in in vitro assays and then implanted around the femoral artery of mice undergoing operative limb ischemia. Results of in vivo studies indicate the feasibility and therapeutic efficacy of the proposed approach.

II. Materials and Methods

A. Scaffolds fabrication

The HG scaffolds were made by gelatin (GL) (Sigma Aldrich), a natural polymer. They were fabricated by Soft-Lithography, obtaining scaffolds with specific surface pattern consisting in 200 micrometer wide channels. Soft-Lithography exploits the lithographic process as a starting point for the construction of non-rigid structures that can reach the resolution at the scale of~10 micrometer. Two crosslinking agents, γ-glycidoxypropyltrimethoxysilane (GPTMS) [9] and Genipin (GP) [10] (Challenge Bioproducts Ltd., Taichung, Taiwan), were used to increase scaffold durability.

The HB scaffolds were manufactured with a bottom-up approach in order to mimic the hierarchical organization of biological tissue. Macrometric 3D structure was made by synthetic polymer polycaprolactone (PCL) (Sigma Aldrich). To evaluate the influence of pattern on cells functional properties we decided to design the PCL structure with two geometries: (i) channels and (ii) woodpile. Woodpile and channel-shaped PCL scaffolds were fabricated using Pressure Assisted Micro-syringe Square (PAM^2) [11] CAD/CAM system, which is a modular microfabrication system that allows to precisely dictating the internal architecture of a 3D structure at the micro-scale level. The two structures have specific patterns:

1) channels 150-200μm wide and 70μm high arranged in 100μm-wide lines. The bottom part of the channel was composed by a grid layer, built also with the PAM2 technique, with the aim at avoiding that the channel structures collapse at the time of detachment from the deposition plate;

2) woodpiles composed by 6 layers of PCL interconnected pores with size of 200μm per side and 100μm-wide lines.

The fabrication process was finely calibrated: the working parameters were the deposition plane velocity of 9 mm/s and extrusion pressure of 8 kPa [12], [13].

This step was followed by deposition of gelatin (GL) nanofibers by electrospinning (Linari Engineering S.r.l., Italy) to increase the adhesive properties of the HB scaffolds. The electrospinning system uses a high voltage field to launch a jet of GL fibers onto the scaffold, forming a nanofiber network with adhesive features similar to those of the natural ECM. Also in this stage gelatin was crosslinked by the same two different crosslinking agents

B. Scaffolds characterization

Analysis of dimensions of fibers, porosity and detected defects was a key step for tuning and optimizing the electrospinning process. (figure)

The results of mechanical uniaxial tensile tests indicated that fabrication method has the capability to control features such as anisotropy, stiffness and elasticity and to reproduce the natural physical properties of living tissues. Results showed a clear difference in rigidity between HG and HB scaffolds, with this latter displaying a more suitable values for biological tissue. In fact, the topology of HB scaffolds allows them to be shaped in tubular structure for in vivo test, giving different mechanical properties in the circumferential and longitudinal directions, mimicking the in vivo biomechanical behaviour of natural vascular structure.

C. Seeding of APCs onto scaffolds

Cell experiments were carried out at Bristol Heart Institute, School of Clinical Sciences at the University of Bristol. Adventitial progenitor cells (APCs) cells, isolated/expanded from remnants of saphenous vein of coronary artery bypass graft surgery, were cultured on the different type of scaffold to perform the in vitro assessment like cells count, MTS and EdU assays. Data from in vitro assays indicated that HB scaffolds have higher performance than HG. Moreover, among HBs, channel-shaped/GPTMS-crosslinked scaffolds confer APCs with best alignment and survival/growth characteristics.

D. Perivascular implantation of scaffolds

Based on the *in vitro* results, the type of scaffold which showed the best properties was implanted with and without APCs around the femoral artery of mice with unilateral limb ischemia (LI). Experiments were performed in three groups of mice: (i) mice with only LI (control), (ii) empty scaffolds (iii) scaffold seeded with cells. The recovery of blood flow was assessed with Flowmetry laser Doppler.

III. Results and Conclusion

The comparison of *in vitro* results was fundamental to choose the type of scaffold which shows the best property. Data from *in vitro* assays indicated that HB scaffolds have higher performance than HG. Moreover, among HBs, channel-shaped/GPTMS-crosslinked scaffolds confer APCs with best alignment and survival/growth characteristics.

Based on these results, channel-shaped/GPTMS-crosslinked scaffolds with or without APCs were implanted around the femoral artery of mice with LI.

Flowmetry assessment after *in vivo* implantation showed that the arteriogenic process is enhanced by perivascular implantation of cellularized scaffolds and, in a lesser extent, by the scaffolds themselves while the spontaneous recover is always lower, even if there is no statistical difference. Immunohistochemistry analysis was performed on the section of perivascular area with the aim at counting arterioles and infiltrating cells in the area of implantation. In the area of occluded femoral artery there was a remarkable increase in arterial collaterals in the space between the scaffold and the femoral artery, with this effect being significantly greater in mice implanted with cells-engineered scaffolds. Furthermore, the analysis of these sections, displayed that there is no evidence fibrotic tissue around the scaffold, which implies the absence of multinucleated cells and risk of immunogenicity. In summary, the described methodology using multiscale and multi-material scaffolds seeded with APCs may offer potential as a treatment for peripheral vascular disease and this approach is particularly attractive for use in patients in whom surgical revascularization is not amenable because of multiple or distal obstructions.

Acknowledgement

This research was funded by the British Heart Foundation (BHF) Centre for Vascular Regeneration (RM/13/2/30158), BHF PhD studentship (FS/15/7/31307) and Medical Research Council to Paolo Madeddu.

References

[1] WR Hiatt, “Medical treatment of peripheral arterial disease and claudication”. N Engl J Med. 2001;344:1608-21.

[2] E. Faglia , et al. “Early and five-year amputation and survival rate of diabetic patients with critical limb ischemia: data of a cohort study of 564 patients.” Eur J Vasc Endovasc Surg. 2006;32:484-90.

[3] R. Vono, G. Spinetti, M. Gubernator, P. Madeddu . “What's new in regenerative medicine: split up of the mesenchymal stem cell family promises new hope for cardiovascular repair”. J Cardiovasc Transl Res. 2012;5:689-99.

[4] H.L. Spencer, et al. “A journey from basic stem cell discovery to clinical application: the case of adventitial progenitor cells”. Regen Med. 2015;10:39-47.

[5] P. Campagnolo, et al. “Human adult vena saphena contains perivascular progenitor cells endowed with clonogenic and proangiogenic potential.” Circulation. 2010;121:1735-45.

[6] M. Gubernator M, et al. “Epigenetic profile of human adventitial progenitor cells correlates with therapeutic outcomes in a mouse model of limb ischemia”. Arterioscler Thromb Vasc Biol. 2015;35:675-88.

[7] R. Katare, et al. “Transplantation of human pericyte progenitor cells improves the repair of infarcted heart through activation of an angiogenic program involving micro-RNA-132.” Circ Res. 2011;109:894-906.

[8] E. Avolio et al. “Combined intramyocardial delivery of human pericytes and cardiac stem cells additively improves the healing of mouse infarcted hearts through stimulation of vascular and muscular repair.” Circ Res. 2015;116:e81-94.

[9] C. Tonda-Turo, et al. “Crosslinked gelatin nanofibres: preparation, characterisation and in vitro studies using glial-like cells.” Mater Sci Eng C Mater Biol Appl. 2013;33:2723-35.
[10] S. Panzavolta, et al. “Electrospun gelatin nanofibers: optimization of genipin cross-linking to preserve fiber morphology after exposure to water.” Acta Biomater. 2011;7:1702-9.
[11] A. Tirella, F. Vozzi, G. Vozzi, A. Ahluwalia. “PAM^2 (piston assisted microsyringe): a new rapid prototyping technique for biofabrication of cell incorporated scaffolds.” Tissue Eng Part C Methods. 2011;17:229-37.
[12] A. Tirella, et al. “The PAM^2 system: a multilevel approach for fabrication of complex threedimensional microstructures.” Rapid Prototyp J. 2012;18:299-307-9.
[13] D. Cei, et al. “In vitro development of engineered muscle using a scaffold based on the pressure-activated microsyringe (PAM) technique.” J Tissue Eng Regen Med. 2014.

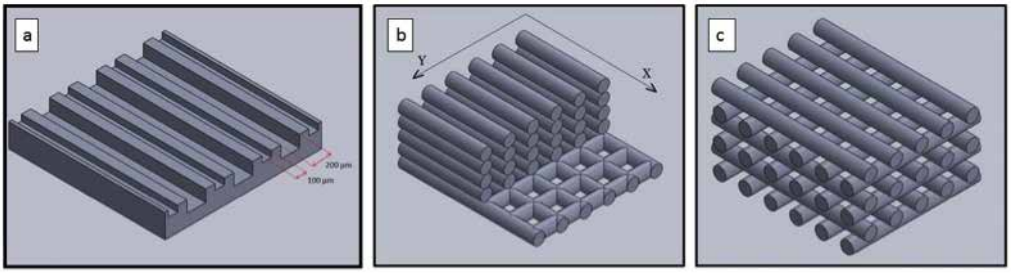

Figure 1: (a) 3D render showing the HG scaffold made by Soft-Lithography; (b-c): 3D render of channels and woodpile HB scaffold made by PAM²

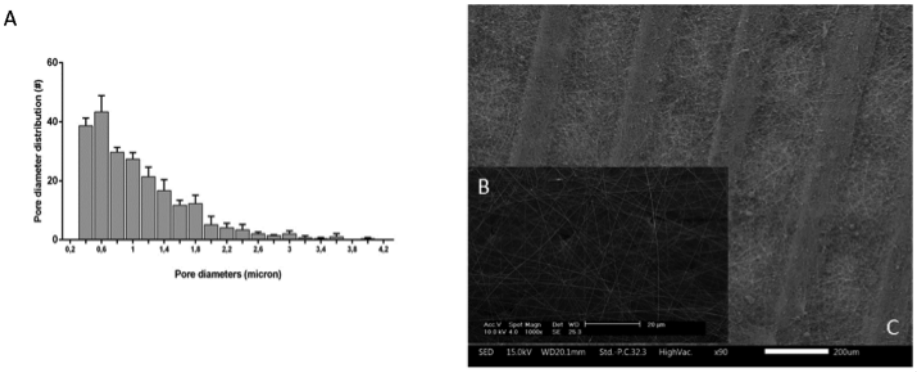

Figure 2: (A) Bar graph of pore diameter distribution of the nanofibre mat chosen after the tuning process; (B) Scanning electron microscopy microphotograph of nanofibres mat obtained after tuning of working conditions; (C) Scanning electron microscopy microphotographs showing structures obtained by combination of PAM² and electrospinning.

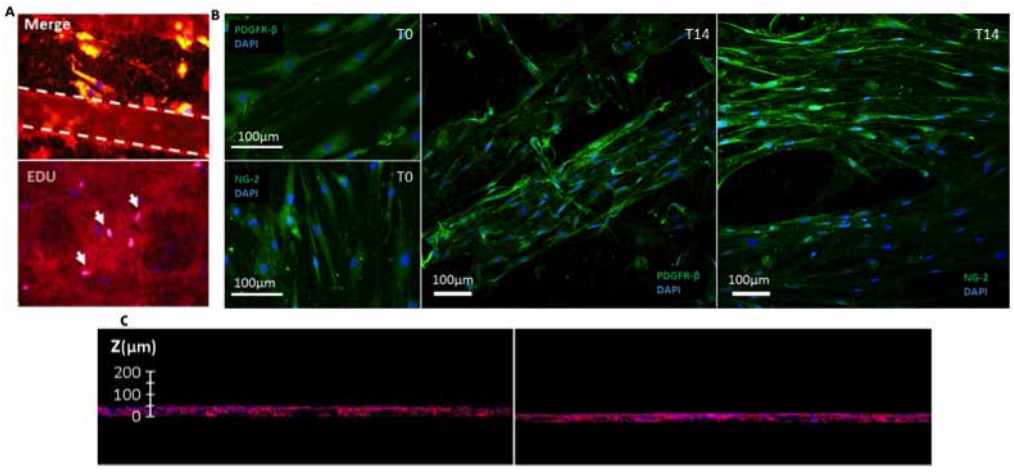

Figure 3: In vitro cellularization of scaffolds. (A) Representative fluorescent microscopy images of scaffolds seeded with APCs. Nuclei are stained blue with DAPI and cell bodies are labelled with Dil. Magnification image shows cells in the channels delimited by the wall (dotted line). Proliferating cells are stained pink by EdU. (B) Pictures show the maintaining of the APCs markers expression, PDGFR-β and NG-2, from T0, the day in which cells were seeded on scaffold, and T14, the day in which cells were analysed by cytochemistry. (C) APCs distribution in channel and woodpile scaffolds; Z stack reconstruction of confocal microscopy images from channel scaffolds (left) and woodpile scaffolds (right).

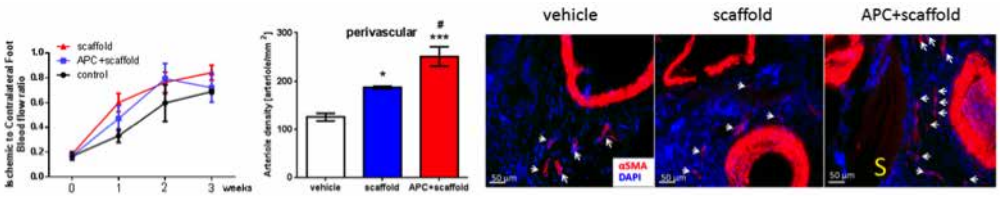

*Figure 4: Perivascular implantation of scaffolds. (A) Blood flow recovery assessed by laser Doppler flowmetry. bar graph and immunohistochemistry of vascularization around the femoral artery. Nuclei stained blue by Dapi and vascular smooth muscle cells stained red by alpha-smooth muscle actin. Arrows indicate arterioles. S indicates the scaffold. *P<0.05 and ***P<0.001 vs. vehicle. #P<0.01 vs. scaffold alone.*

Surface functionalization of polyurethane films with dendrons for stem cell culture

N. Contessi[1,2], S. Bertoldi[1,2], S. Meikle[3], A. Guildford[3], S. Farè[1,2], M. Santin[3] and M.C. Tanzi[2]

[1] *Department of Chemistry, Materials and Chemical Engineering "G. Natta", Politecnico di Milano, Milan (IT)*

[2] *INSTM local unit Politecnico di Milano, Milan (IT)*

[3] *Brighton Studies in Tissue-mimicry and Aided Regeneration (BrightSTAR), Brighton Centre for Regenerative Medicine (BCRM), School of Pharmacy & Biomolecular Sciences, University of Brighton, Brighton (UK)*

***Abstract* - The *in vitro* expansion of human mesenchymal stem cells (hMSCs) is a crucial step to obtain the adequate number of cells required for tissue engineering applications. However, *in vitro* stemness maintenance needs to be controlled by giving cells the correct cues. We produced transparent and homogenous polyurethane (PU) films with reproducible properties, eligible for 2D cell cultures. The PU films surface was decorated with poly-(ε-lysine) dendrons exposing the YIGSR peptide sequence. Mass spectroscopy and ATR-FTIR analyses allowed confirming the successful synthesis of the dendrons. Films, previously treated by plasma, were activated by NHS/EDC chemistry and dipped in dendron solutions. Surface functionalization was assessed by static contact angle and ATR-FTIR. hMSCs were *in vitro* cultured for 7 days. Spheroidal aggregates were identified on functionalised films, thus confirming the successful functionalization and promotion of *in vitro* stemness maintenance.**

***Keywords* - polyurethane, surface functionalization, dendrons, stem cell, *in vitro* culture.**

I. Introduction

The surface functionalization of a biomaterial can be used to guide a specific and desired cell response. Human mesenchymal stem cells (hMSCs) gained great interest for their use in tissue repairing and regeneration [1], [2]. However, even though a relatively high number of cells is required for the desired application, a lower number of hMSCs can be isolated from an adult tissue. Therefore, the *in vitro* expansion of hMSCs is a necessary step, but (bio)chemical cues must be finely controlled during the *in vitro* culture to ensure the stemness maintenance [3]. The *in vitro* mimicking of the stem cell niche, including the presence of laminin glycoprotein, can be used to govern stem fate [4].

In this work, we propose to functionalise the surface of 2D polyurethane (PU) films with poly-(ε-lysine) dendrons exposing the lamimin mimicking YIGSR peptide sequence. These substrates are investigated to control *in vitro* expansion of hMSCs, thus preventing uncontrolled de-differentiation.

II. Materials and Methods

A. Polyurethane film preparation

The chemical formulation of the poly-ether-urethane films was previously set up [5]. The synthesis consisted in a one step bulk polymerization. Briefly, the reaction mixture was produced by stirring for 60 s Fe-AcetylAcetonate as catalyst, water as expanding agent, a poly-ether-polyol mixture *ad hoc* prepared, and methylene diphenyl diisocyanate (MDI) prepolymer.

The reaction mixture was quickly spread on a flat glass substrate to produce the PU films (PU_notOPT). The spread mass and the water content were optimised (i.e., from 6 to 3.5 g on a 20x20 cm^2 and from 2 to 1% w/w_{polyol}, respectively) to obtain thinner and more transparent films (PU_OPT). After 48 h, films were removed from the glass substrate, purified in ethanol for 48 h and let dry at room temperature.

B. Dendron synthesis and characterization

The dendron used to bio-functionalise the PU surface is composed by an arginine root (R) and three branching generations (G3) of poly-(ε-lysine) (K) (RG3K), terminally functionalised with the linear YIGSR amino acidic sequence ($RG3K_{YIGSR}$). The dendron was synthesised by an optimised protocol [6]. Briefly, a divergent solid phase synthesis was performed by adding amino acids in sequence, following alternative coupling and de-protection steps. Dendrons were characterised by mass spectroscopy micrOTOF analysis and attenuated total reflectance Fourier Transform infrared spectroscopy (ATR-FT IR).

C. Surface functionalization with dendrons

PU_OPT films were treated by air plasma (PU_plasma) for 5 min in a vacuum chamber (PT7150 Plasma Barrel Etcher, Polaron), operating at a gas pressure of 400 Pa and a radio frequency power of 60 W. PU_plasma films were put in a 4 mM solution of 1-ethyl-3-(3-dimethylaminopropyl) carbodiimide (EDC) in 2-(N-morpholino)ethanesulfonic acid 0.1 M buffer solution (MES), in presence of N-hydroxysuccinimide 10 mM (NHS), washed twice in MES buffer solution and dipped in 0.1 M dendron solution to bind the dendrons to the PU surface (PU-RG3K). Alternatively, dendrons were firstly bound to poly-L-lysine (PLL 0.01% w/v in water, MW range 70 000 – 150 000) by preparing a 1:1 volume solution of dendrons in EDC/NHS (0.1 mg/ml) and commercial PLL solution; PU_plasma samples were then dipped in PLL/dendron solution (PU-PLL/RG3K and PU-$PLL/RG3K_{YIGSR}$).

D. Polyurethane film characterization

PU films before (PU_notOPT) and after (PU_OPT) the optimisation process, after plasma treatment (PU_plasma) and after dendron binding (PU-RG3K and PU-PLL/RG3K) were characterised in terms of thickness, transparency (stereo optical microscopy), surface morphology (SEM) and roughness (laser profilometer), and tensile mechanical properties (DMA).

E. In vitro interaction of hMSCs with functionalised films

In vitro tests were performed by seeding hMSCs (40.000 cells/cm^2) on PU samples (Ø = 10 mm, n = 4), sterilized by UV for 1 h. Cells were cultured for 7 days in mesenchymal stem cell basal medium – chemically defined, without foetal bovine serum, phenol red and antibiotics (MSCBM-CD, TheraPEAK, Lonza) and kept in Cell 150 Incubator (Hera) at 37 °C and 5% P_{CO2}. Cells seeded on tissue culture plastics (TCPS) were used as control. Cell morphology was evaluated by CellTracker staining (Life technologies) and observed by fluorescent microscopy (Nokia Eclipse TE2000-U).

F. Statistical analysis

Data normality was checked and statistical analysis performed by ANOVA (OriginPro, significance level 0.05).

TABLE I
POLYURETHANE FILMS PHYSICO-MECHANICAL PROPERTIES

	PU_notOPT	PU_OPT	PU_plasma
Physical properties			
Thickness [μm]	198.0 ± 43.6	80.0 ± 13.1	79.2 ± 22.4
R_a *[μm]*	0.24 ± 0.02	0.19 ± 0.04	0.75 ± 0.09
R_z*(ISO) [μm]*	1.50 ± 0.06	1.35 ± 0.37	4.22 ± 0.38
Mechanical properties			
Young Modulus [MPa]	2.28 ± 0.40	2.09 ± 0.05	1.73 ± 0.17
σ_{break} *[MPa]*	1.91 ± 0.99	3.00 ± 0.48	2.33 ± 0.14
ε_{break} *[%]*	181 ± 32	354 ± 12	548 ±11

III. RESULTS

A. PU film characterization

The PU films physico-mechanical properties are shown in Table 1. The thickness of PU films decreased after the optimisation from 198.0 ± 43.6 μm (PU_notOPT) to 80.0 ± 13.1 μm (PU_OPT) ($p < 0.05$). SEM (Fig. 1a-b) and optical microscope (Fig. 1c-d) images of PU_OPT showed a homogeneous, pore-free, regular surface and transparent films, eligible for 2D cell cultures, compared to the irregular surface with pores and low-transparent PU_notOPT.

B. Dendron synthesis and characterization

The complete de-protection of the terminal Fmoc-protective groups of the amino acids was qualitatively assessed by the typical violet colour assumed by dendrons with ninhydrin assay. Mass spectroscopy showed the successful synthesis of the RG3K (Fig. 2). Detected peaks correspond to the theoretical weight of the dendron (MW = 2096.79). Mass spectroscopy of $RG3K_{YIGSR}$ proved the functionalization of RG3K due to the absence of RG3K peaks. ATR-FTIR spectra of RG3K and $RG3K_{YIGSR}$ were compared to investigate the presence of YIGSR on the RG3K dendron. Typical peaks of amido acids (i.e., amide II band at 1640 cm^{-1}, C-O and C-N stretching at 1250 and 1200 cm^{-1}) were detected in both structures, thus confirming the peptide structure of the two synthesised dendrons. Peaks characteristic of aromatic structures are exhibited both in the YIGSR and $RG3K_{YIGSR}$ spectra, due to the tyrosine residue (C-H aromatic stretching at 3100 cm^{-1}, C=C stretching at 1510 cm^{-1}), thus confirming the functionalization of the RG3K dendron with the YIGSR peptide (data not shown).

C. Functionalization assessment

The tensile mechanical properties of PU films were not affected by the surface treatment: the elastic modulus and the stress at break proved to be not statistically different ($p > 0.05$) before and after the functionalization treatment. The surface roughness of PU_plasma was higher then PU_OPT, both comparing R_a and R_z(ISO) values ($p < 0.05$) due to a possible etching effect of the plasma. Statistical difference ($p < 0.05$) was detected comparing the contact angle values of PU_OPT and PU_plasma (Fig. 3), with an increase in hydrophilicity (+31%) after the plasma treatment, thus confirming the PU surface activation. The increase in wettability of PU-RG3K and PU-PLL/RG3K, in comparison to the PU_OPT films, has to be directly referred to the presence of the peptide sequences composing the dendrons on the films surface. The decrease in wettability for PU-RG3K and PU-PLL/RG3K in comparison to the PU_plasma can be referred to the interaction of the dendrons with the charges formed by the plasma treatment.

D. In vitro cell investigation

hMSCs cultured on adhesive TCPS (Fig. 4a) assumed a flat spindle-like morphology, indicative of fibroblast-like colonies associated with hMSCs de-differentiation. On the contrary, hMSCs on PU-RG3K and particularly on PU-PLL/$RG3K_{YIGSR}$ (Fig. 4c) assumed a spherical morphology and clustered in aggregates.

IV. CONCLUSION

Transparent PU films were produced with reproducible properties, eligible for *in vitro* cell cultures. Poly-(ε-lysine) dendrons were functionalised with YIGSR sequence and used as decoration for the film surface. Cultured hMSCs assumed spheroid structure on the PU modified films, promoting *in vitro* stemness maintenance and allowing *in vitro* expansion for tissue engineering applications.

ACKNOWLEDGEMENT

The authors thank NAMABIO Cost Action for providing financial support for the STSM (COSTSTSM-MP1005-15696).

REFERENCES

[1] Xi J *et al.*, "Mesenchymal stem cells in tissue repairing and regeneration: Progress and future", *Burn Trauma*,1,13–20,2013

[2] L. S. Meirelles, A. M. Fontes, D. T. Covas and A. I. Caplan, "Mechanisms involved in the therapeutic properties of mesenchymal stem cells" *Cytokine Growth Fact Rev* 20,419–427,2009

[3] I. N. Shipounova *et al.*, "Hierarchy of mesenchymal stem cells: comparison of multipotentmesenchymal stromal cells with fibroblast colony forming units", J Biomed Sci Eng 6,66-73, 2013

[4] Shin H *et al.*, "Modulation of spreading, proliferation, and differentiation of human mesenchymal stem cells on gelatin-immobilized poly(l-lactide-*co*-ϵ-caprolactone) substrates" *Biomacromolecules*, 9 (7),1772–1781,2008

[5] S. Bertoldi *et al.*, "Ability of polyurethane foams to support placenta-derived cell adhesion and osteogenic differentiation: preliminary results", J Mater Sci: Mater Med 21,1005-1011,2010.

[6] S.T. Meikle *et al.*, "Synthesis, characterisation and in vitro anti-angiogenic potential of dendron VEGF blockers", Macromol Biosci 11,1761–1765,2011.

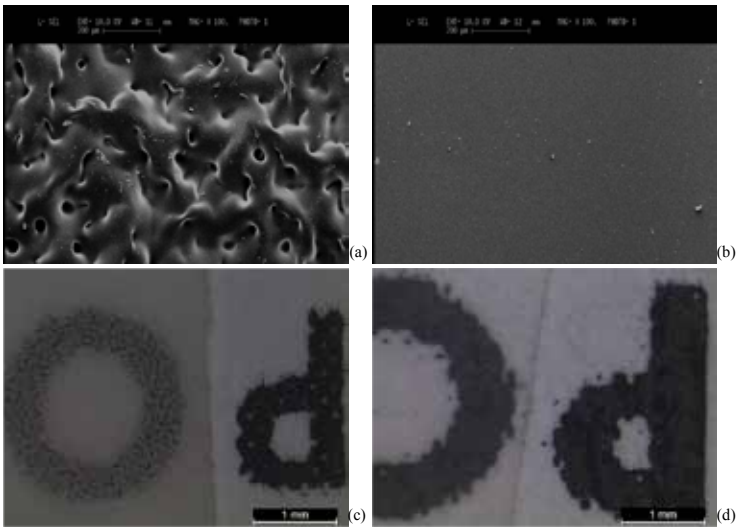

Fig. 1. Scanning electron microscopy (a - b, scale bar: 200 µm) and stereomicroscopy images (c – d, scale bar: 1mm) of (a - c) PU_notOPT films and (b - d) PU_OPT films, produced using the parameters optimised to obtain more homogeneous and transparent films.

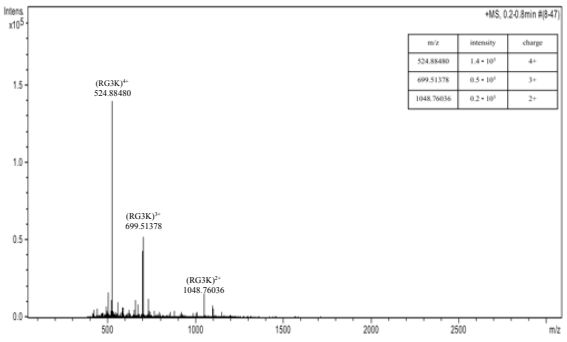

Fig. 2. Mass spectroscopy micrOTOF spectra of RG3K.

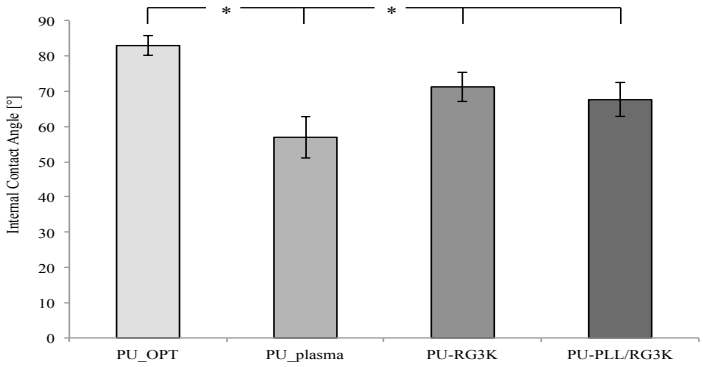

Fig. 3. Static water contact angle values of PU_OPT films, PU_plasma treated films, PU-RG3K and PU-PLL/RG3K functionalised films. (*p < 0.05). Values are expressed as mean ± SD, n = 5

Fig. 4. hMSCs morphology (CellTracker) after 7 days of culture on (a) tissue culture plastics, (b) PU-RG3K$_{YIGSR}$ and (c) PU-PLL/RG3K$_{YIGSR}$ (scale bar: 75 µm).

Assessing the role of material features on the structuring of cell derived matrix

V. Coppola[1,2], M. Ventre[1,3], and P.A. Netti[1,2,3]
[1] D.I.C.Ma.P.I., University of Naples Federico II, P.le Tecchio 80, 80125 Naples, Italy
[2] Center for Advanced Biomaterials for Healthcare IIT@CRIB,LArgo Barsanti e Matteucci 53, 80125 Naples, Italy
[3] Interdisciplinary Research Centre on Biomaterials, University of Naples Federico II, P.le Tecchio 80, 80125 Naples, Italy

***Abstract*— The architecture of the tissue microconstituents depends on the extracellular matrix assembly. Natural tissues usually display a collagen fibres matrix organized in specific spatial arrangements that provide the tissue with unique functionalities. Reproducing complex structure may be essential not only to engineer tissue able to resemble the natural function, but also to produce a complex natural platform useful for three dimensional cell mechanics studies. In this work we investigated the effect of different micro patterned substrates on the assembly of tissues. Stimulating MC3T3-E1 preosteoblasts to produce and assemble collagen rich matrix, we obtained ordered, multilayered tissues. Then, we investigated the cell derived matrix morphological feature. Our results demonstrate that by using micropatterned materials, tissue sheet displaying a structure with differential order can be generated. Therefore, contact guidance based strategies can be in principle used to modulate matrix microarchitecture.**

***Keywords*— Microtopography, cell derived matrices, mechanical properties, tissue architecture.**

I. Introduction

The unique architecture of biological tissues is dictated by the mutual organization of their microconstituents. The arrangement of these elements endow biological tissues with mechanical properties that perfectly withstand physiological loads. Signals in the form of biochemical, topographical or mechanical cues need to be presented to cells in order to control the processes of biosynthesis and protein spatial assembly [1]-[3]. In order to be effective, these signals must act on a cellular (micron scale) or sub-cellular (nano scale) level. A well-known approach to obtain in vitro ordered tissues is the cultivation of cells on planar surfaces that present on the cell-material surface topographical signals, in conditions such that cells are stimulated to secrete abundant extracellular matrix thus producing few tens of micron thick sheets [4].

Typically, linear gratings are encoded on material surface in order to orient cells and matrix in a common direction [5],[6]. The resulting membrane displays aligned ECM fibres. Therefore, surface patterning can in principle affect spatial configuration of cells and ECM fibres in a tissue [7]. This notwithstanding, in order to have a tight control on the 3D arrangement of the tissue microconstituents it is necessary that the ordering effect of the patterned signal is transmitted throughout the thickness. However, while some authors demonstrated that the surface patterning induces a cell/matrix alignment and such an alignment is maintained within the sheet, other report different trends [7]-[9].

A substantial body of knowledge has been developed on cell and tissues grown on linear patterns, but only limited pieces of information are available on the effects of different types of pattern on cell matrix deposition and organization.

We hypothesize that peculiar patterns on material surfaces, e.g. non-linear pattern, define complex spatial assemblies of ECM components. Using these different assemblies of tissues is possible to obtain a well spatially organized cell derived matrix.

Thus the aim of this work consists in exploiting the ordering effects of topographic patterns to generate cell-ECM assemblies in vitro, which possess a complex 3D collagen fibres architecture. We investigated how the pattern-induced order is transferred throughout tissue thickness, by means of multiphoton imaging.

II. Materials and Methods

A. Preparation of patterned substrates

Linear and non-linear (zig-zag) patterned substrates were obtained by replica molding of polydimethylsiloxane (PDMS, Sylgard 184, Dow Corning) on SU-8 and Poly-carbonate master respectively (Fig. 1). PDMS was prepared by mixing elastomer base and curing agent at 10:1 weight ratio. The solution was degassed, poured onto the master and then cured at 60°C for 2 h. Samples were then incubated with serum-supplemented culture medium overnight prior to cell culturing experiments.

B. Cell culture

MC3T3-E1 preosteoblasts (ATCC) were cultured in alpha MEM with deoxyribonucleosides, ribonucleosides and 2 mM L-glutamine, supplemented with 10% fetal bovine serum, penicillin (100 units ml^{-1}), streptomycin (100 mg ml^{-1}) (GIBCO) The culture medium was changed every two days. After 3 days of culture, cells were detached with trypsin/EDTA (0.25% w/v trypsin/0.02 mM EDTA) (GIBCO) and seeded on substrates at the density of $2x10^4$ cells·cm^{-2}, and cultivated for 2 weeks in presence of 25 µg/mL of ascorbic acid.

C. Cell-collagen structure characterization

Collagen rich sheets were fixed and stained with phalloidin-TRITC. Fixed samples were placed under a Leica TCS SP5 multiphoton confocal miscroscope (Leica Microsystems) in order to visualize actin and collagen fibres. Collagen fibres were visualized through second harmonic

generation microscopy. Image analysis was performed by running OrientationJ plug-in. The plug-in measures the distribution of actin filaments or collagen fibres direction.

III. Results

In order to verify how the presence of a pattern can induce an ordering effect on cell derived matrix assembly, we investigated high-density cell culture

Cell population perceived the directional cues provided by both the type of patterns. Image analysis revealed that cells were oriented along the gratings direction, in particular, in the zig-zag pattern, cells retraced the two specific directions imposed. At 5 days, cells formed a bi-layered structure in which each layer displayed different cellular arrangements (data not shown). In order to assess how the directional cues were transferred through the structure thickness we performed image analysis of the confocal micrographs at 2 weeks of culture by running OrientationJ plugin, which measures the distribution of both actin filaments and collagen fibres directions. The algorithm was applied in the basal plane, i.e. cells directly adhering to the pattern, and in the apical plane, i.e. cells in the plane more distant from the pattern. Cells on the basal plane were packed with a spindle-like morphology that followed pattern directions. In fact, the alignment directions distribution was bimodal with peaks in close agreement with the pattern directions in the non-linear case, whereas was centred around the pattern direction in the linear one (Fig. 2). Conversely, cells and collagen of the apical plane displayed a macroscopic common direction of alignment even if local orientation differing from the macroscopic one can be observed (Fig.2).

We then asked why such a mismatch in cell orientation between the apical and basal plane existed and why such a difference evolved in time. Owing to the cell contractility we hypothesized that the de novo synthesized collagen is one of the best candidates to modulate cellular orientation in the basal and apical plane. By visualizing collagen with SHG microscopy, we observed that collagen secreted by cells is aligned along the same direction of the actin filaments of the basal plane, i.e. in a wave-like configuration with a bimodal distribution of orientations (Fig. 2b). Instead, collagen close to the apical plane usually displayed a degree of alignment in the directions that corresponded with the predominant cellular orientation (Fig. 2). Afterwards, we investigated whether collagen orientation in the apical plane was the result of some kind of interactions driven by the different substrata. To verify this aspect, we cultivated MC3T3 in the same manner on flat substrates. In this case, cells and collagen of the basal plane were randomly distributed. Surprisingly, cells and apical collagen presented an elongated shape, and were coaligned, with a preferential orientation that is similar to the direction shown in the patterned cases. The distribution of cells and collagen orientation of linear, non-linear and flat were collected in scatterplots (Fig. 3).

Taken together these data suggest that the establishment of the cell-matrix architecture in the apical plane follows mechanisms that are not exclusively dictated by the microstructural features of the basal plane. Possibly, cell remodelling, as well as the macro-geometrical cues of the substratum also plays a role in matrix alignment. Additionally, the amount of collagen secreted by cells in the two conditions was apparently not significantly different, this suggest that the topographic signal we exploited does not affect collagen production but only its spatial configuration.

IV. Conclusions

We showed that the cell sculpting tissues is the result of the complex interplay of different factors identified by the constrains that cells interact with. Recognizing these factors means modulate and engineer the spatial assembly of cell-derived-matrix. Using zig-zag pattern, we obtained a complex collagen architecture that is varying trough the thickness in which the basal plane arrangement is strongly controlled by the pattern. We speculate that the interplay of matrix remodelling and the interaction between cells and sample's edges could drive the apical plane assembly. This because of the geometrical shape of the samples which was the same in every case. Therefore, contact guidance based on non-linear patterns is effective in modulating tissue assembly, however cell/ECM interplay needs to be carefully unraveled in order to predict the final structure of growing tissues in vitro.

Acknowledgement

The authors thank Dr. C. Natale for the insightful discussions.

References

[1] AW Feinberg, CM Ripplinger, P van der Meer, SP Sheehy, I Domian, KR Chien. Functional differences in engineered myocardium from embryonic stem cell-derived versus neonatal cardiomyocytes. Stem Cell Reports 2013;1:387-396.

[2] G Imparato , F Urciuolo , C Casale, PA Netti. The role of microscaffold properties in controlling the collagen assembly in 3D dermis equivalent using modular tissue engineering. Biomaterials 2013;34:7851-7861. H. Poor, An Introduction to Signal Detection and Estimation. New York: Springer-Verlag, 1985, ch. 4.

[3] H Takahashi, M Nakayama , K Itoga , M Yamato, T Okano. Micropatterned thermoresponsive polymer brush surfaces for fabricating cell sheets with well-controlled orientational structures. Biomacromolecules 2011;12:1414-1418.J. U. Duncombe, "Infrared navigation—Part I: An assessment of feasibility (Periodical style)," IEEE Trans. Electron Devices, vol. ED-11, pp. 34–39, Jan. 1959.

[4] E Cukierman, R Pankov, DR Stevens, KM Yamada. Taking cell-matrix adhesions to the third dimension. Science 2001;294:1708-1712.

[5] JH Wang, F Jia, TW Gilbert, SL Woo. Cell orientation determines the alignment of cell-produced collagenous matrix. J Biomech 2003;36:97-102.

[6] Q Xing,C Vogt, KW Leong, F Zhao. Highly Aligned Nanofibrous Scaffold Derived from Decellularized Human Fibroblasts. Adv Funct Mater 2014;24:3027-3035.

[7] BC Isenberg, DE Backman, ME Kinahan, R Jesudason, B Suki, PJ Stone. Micropatterned cell sheets with defined cell and extracellular matrix orientation exhibit anisotropic mechanical properties. J Biomech 2012;45:756-761.

[8] A Pietak, A McGregor, S Gauthier, R Oleschuk, SD Waldman. Are micropatterned substrates for directed cell organization an effective method to create ordered 3D tissue constructs? J Tissue Eng Regen Med 2008;2:450-453.

[9] MD Guillemette, B Cui, E Roy, R Gauvin, CJ Giasson, MB Esch, P Carrier, A Deschambeault, M Dumoulin, M Toner, L Germain, T Veres, FA Auger. Surface topography induces 3D self-orientation of

cells and extracellular matrix resulting in improved tissue function. Integr Biol (Camb). 2009, 1(2), 196-204.

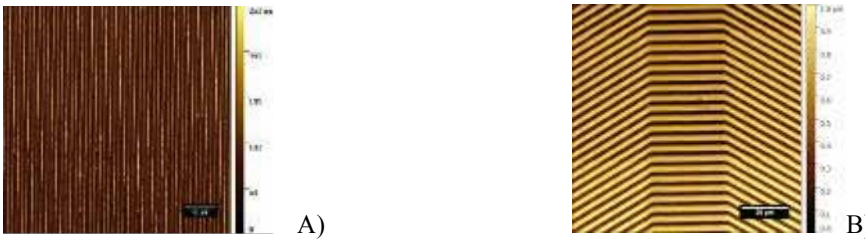

A) B)

Fig. 1. AFM of the used patterns, linear (A) and non-linear (B). In the linear pattern groove and ridge are 700nm width, the depth is 250nm. In the non-linear pattern, groove and ridge are 2μm width and the depth is 1 μm, wave period is 495 μm and the linear ramps are 255 μm. The two consecutive ramps are connected by a 20 μm straight channel.

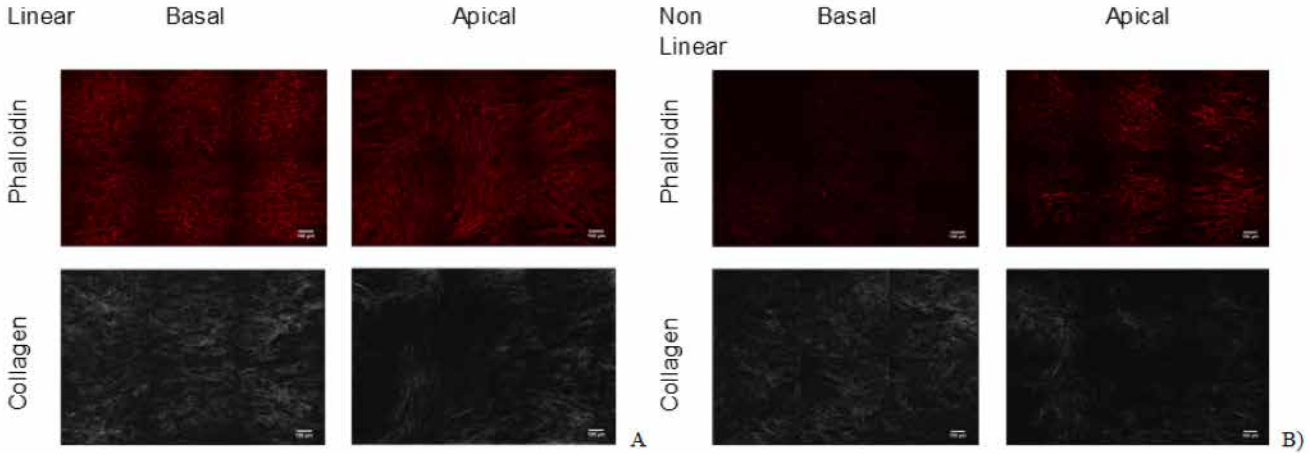

Fig. 2. Tilescans of actin filaments (top) and collagen fibres (bottom) of tissues obtained with both linear (A) and non-linear (B) pattern. Tilescans were collected merging a 3x2 grid of single z-stacks. Bars are 100 μm.

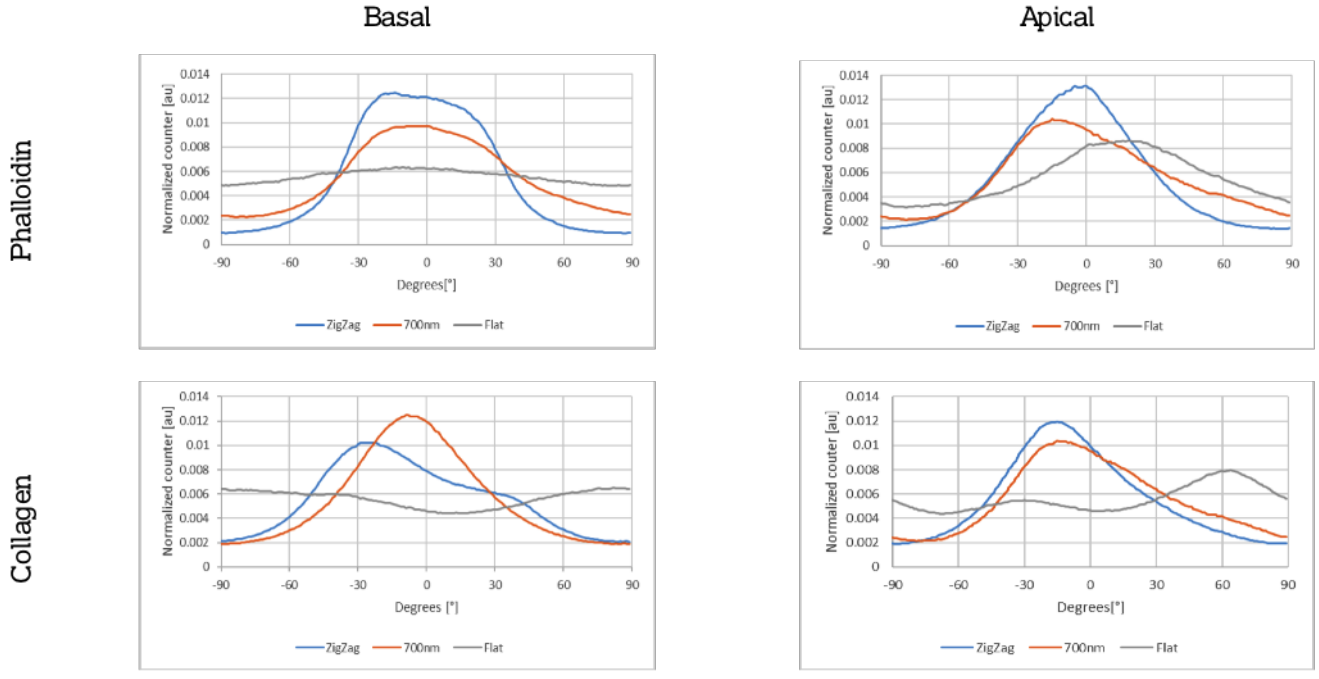

Fig. 3. Orientation distribution scatterplots. Every plot is a comparison among the different type of tissues. We reported the distribution of both the basal (left) and the apical (right) planes of the actin filaments (top) as well as collagen fibres (bottom).

3D bioprinting of aligned hydrogel fibers for the fabrication of artificial myo-structures with a microfluidic printing head.

M. Costantini[1], C.Gargioli[2], P.Mozetic[1], M.Trombetta[1], S. Cannata[2], A.Rainer[1]
[1] *Tissue Engineering Lab, Università Campus Bio-Medico di Roma, 00128 Rome, Italy*
[2] *Department of Biology, Tor Vergata University, Rome, 00133 Rome, Italy*

***Abstract*— We present a new strategy for the fabrication of artificial myo-structures with functional morphologies based on an innovative 3D bioprinting approach. This system is based on a microfluidic co-axial nozzles extruder that allowed for high-resolution 3D bioprinting of hydrogel fibers (≈100 μm) and high cell viability of muscle cells precursor (C2C12).**

To promote the differentiation of myoblast, we formulated a tailored bioink with a photocurable semi-synthetic biopolymer, namely PEGylated fibrinogen, and we encapsulate cells in 3D scaffolds composed of aligned hydrogel fibers.

After 3-5 days of culture, the encapsulated myoblast start migrating and fusing, forming multinucleated myotubes within the 3D bioprinted fibers. The development of myotubes structures was monitored up to 4 weeks. The obtained myotubes resulted to be highly aligned with an orientation parallel to the deposition direction of fibers. After 4 weeks, we checked the quality and differentiation status of obtained myotubes by means of fluorescence immunocytochemistry. The data revealed an enhanced differentiation of myoblast with the formation of long-range multinucleated myotubes. The method represents a robust and valid candidate for the regeneration of muscular tissue.

***Keywords*—Additive manufacturing, bioprinting, muscle regeneration, microfluidics**

I. Introduction

In mammalians, skeletal myogenesis is a complex phenomenon that starts from the very first weeks of embryonic development. This process involves mononucleated fusiform cells – named *myoblasts* - that progressively fuse forming plurinucleated syncytia - named *myotubes*. As development proceeds, myotubes undergo to a maturation process in which they grow in dimension and the actin-myosin based contractile apparatus, neuromuscular junctions and myotendinous junctions are assembled [1].

Skeletal muscles can naturally self-repair relatively small damage resulting from tears, small lacerations, strains or toxin damage via a three-stages process that involves a demolition, repair and remodeling phase of myotubes. Although this beneficial natural mechanism, skeletal muscle cannot restore significant tissue lost that can arise after trauma, surgeries or degenerative diseases.

Due to its biological and structural complexity, engineering an artificial muscle still represents a hurdle task. In the recent past, few methods have been developed to regenerate skeletal muscles tissue in vitro. In most of these studies, researchers primarily focused their efforts in obtaining highly oriented myotubes to mirror their natural organization present in muscle fascicles, by inducing either a mechanical - static or dynamic - or electrical pulse stimulation. These methods, although they demonstrated the possibility to obtain highly oriented myofibers, are limited with regards of creating multicellular organized structure that could better mimic the complexity of native muscles tissue. Furthermore, in most of the studies bulk hydrogels have been employed to encapsulate cells: this strategy may be on some extent detrimental for the formation of aligned myotubes, as it has been proved that muscle cells precursor may create a chaotic network of myotubes – similar to those obtained in 2D cultures – when cultured in bulk hydrogel [2].

For this reason, the development of new technologies and cell-based therapies to better regenerate *in vitro* and/or *in vivo* skeletal muscles is of utmost importance.

Among the currently available technologies, 3D bioprinting has the potential to fabricate 3D highly customizable and highly organized structures that, in theory, could be used for whole-muscle reconstruction. This emerging biofabrication technology consists of the simultaneous deposition of cells and biomaterials, in a layer-by-layer fashion, to form 3D well-organized heterogeneous structures that can mirror physiologically and morphologically relevant complex architectures.

Recently, we have developed an innovative 3D bioprinting method based on a coaxial microfluidic head enabling multi-material and/or multi-cellular deposition within a single scaffold by extruding simultaneously different bioinks or by rapidly switching between one bioink and another [3,4].

As muscular fibers have an highly aligned structural arrangement *in vivo*, the driving idea behind the presented work was that the simple geometrical confinement of muscle precursor cells into highly aligned 3D bioprinted hydrogel structures can lead to a better orientation of the arising myotubes, thus better mimicking the natural muscles morphology.

With this in mind, we tested the aforementioned method in 3D bioprinting muscle precursor cells – namely C2C12.

II. Materials and Methods

A. Biofabrication

The bioprinting apparatus consisted of a set motorized axes (miCos PLS, Physics Instruments) assembled in a gantry configuration, and featuring a coaxial microfluidic head (described elsewhere [3,4]) fed by set of independently

controlled precision syringe pumps.

We developed an innovative semi-synthetic bioink made of photocurable PEGylated fibrinogen [5] and alginate (FMC biopolymers) compatible with our microfluidic co-axial printing head. A typical bioink composition was 8 mg/ml PEG-fibrinogen, 40 mg/mL alginate a 0.05 w/w irgacure 2959 photoinitiator (Ciba Specialty Chemicals). The employment of photocurable polymers in tandem with alginate allows the formation of stable hydrogels after UV exposure that can undergo long culturing *in vitro*.

Murine C2C12 were subconfluently cultured in DMEM (high glucose, EuroClone) supplemented with 10% FBS (Lonza), 2 mM L-glutamine (Lonza), 1% pennicilin/streptomycin mixture (EuroClone).

Cells were detached by mild trypsinization and resuspended in the bioink at a concentration as high as 30×10^6 cells/mL.

A typical printing process consisted of the following steps. First, the formulated bioink was deposited in the form of Ca^{2+} ionically crosslinked hydrogel fibers to obtain a 3D multi-layered construct. After printing, photocurable PEGylated fibrinogen contained in the microfibers was covalently crosslinked by exposition to cell-compatible UV irradiation (365nm). This process guarantees a high cell viability, a good bonding among fibers belonging to adjacent layers and determines the overall mechanical properties of the scaffolds.

To mimic the skeletal muscle structure, we built all the scaffolds by depositing several layers of parallel hydrogel fibers.

Hydrogel mats with the same biopolymer composition and cell concentration were obtained by conventional casting technique followed by UV cross-linking to be used as controls.

B. Characterization

Obtained constructs and controls were incubated in DMEM at 10% FBS supplementation up to 4 weeks and timely monitored under an inverted microscope.

At selected timepoints, constructs were washed in PBS and processed for immunofluorescence analysis for myogenic markers, such as myosin heavy chain (MHC) and laminin.

III. Results and Discussion

Figure 1 shows a schematic representation of the microfluidic head working principle.

The bioprinting process led to the fabrication of highly aligned and closely packed fiber elements (ca. 100 μm in diameter) containing highly viable cells (viability >90% according to Live/Dead assay). Within few days, we observed a positive migration and differentiation of C2C12 cells that started to spread and fuse, forming multinucleated myotubes within the 3D bioprinted fibers. Interestingly, we noticed that muscle precursor cells, before fusing with adjacent cells, elongates following the orientation of the deposition direction of fibers. This may found an explanation at the molecular level as polymeric chains, when extruded, tend to orientate along the flow/extrusion direction and cells may then sense an oriented surrounding matrix.

After 4 weeks of culture, the formed myotubes reached a good differentiation status and started to deposit a physiological matrix, as confirmed by immunocytochemistry staining for myosin heavy chain (MHC) and laminin (Fig. 2). Conversely, control cast hydrogels did not show relevant cell orientation, and chaotic myostructure could be observed after 4 weeks (Fig.2a,c)

IV. Conclusion

Our preliminary results show that the confinement of muscle cells precursor is beneficial for fabricating highly aligned networks of myotubes that present a more physiological structure. Moreover, as the presented method allows for multiple dispensations of cells with extremely small dead volumes, it represents an ideal candidate for creating more complex structures for muscles tissue engineering that will include in a single construct – for example – vascular network and neuromuscular and myotendinous junctions.

Acknowledgement

MC is supported by a fellowship from Università Campus Bio-Medico di Roma.

References

[1] Leimbach A, Hacker J and Dobrindt U 2013 Intradermal Rabies Vaccination: The Evolution and Future of Pre- and Post-exposure Prophylaxis. *Curr. Top. Microbiol. Immunol.* **358** 3–32

[2] Fuoco C, Salvatori M, Biondo A, Shapira-Schweitzer K, Santoleri S, Antonini S, Bernardini S, Tedesco F S, Cannata S, Seliktar D, Cossu G and Gargioli C 2012 Injectable polyethylene glycol-fibrinogen hydrogel adjuvant improves survival and differentiation of transplanted mesoangioblasts in acute and chronic skeletal-muscle degeneration *Skelet. Muscle* **2** 24

[3] Colosi C, Shin S R, Manoharan V, Massa S, Costantini M, Barbetta A, Dokmeci M R, Dentini M and Khademhosseini A 2015 Microfluidic Bioprinting of Heterogeneous 3D Tissue Constructs Using Low-Viscosity Bioink *Adv. Mater.* 1–8

[4] Colosi C, Costantini M, Latini R, Ciccarelli S, Stampella A, Barbetta A, Massimi M, Conti Devirgiliis L and Dentini M 2014 Rapid Prototyping of Chitosan-Coated Alginate Scaffolds Through the Use of a 3D Fiber Deposition Technique *J. Mater. Chem. B* **2** 6779–91

[5] Shapira-Schweitzer K and Seliktar D 2007 Matrix stiffness affects spontaneous contraction of cardiomyocytes cultured within a PEGylated fibrinogen biomaterial. *Acta Biomater.* **3** 33–41

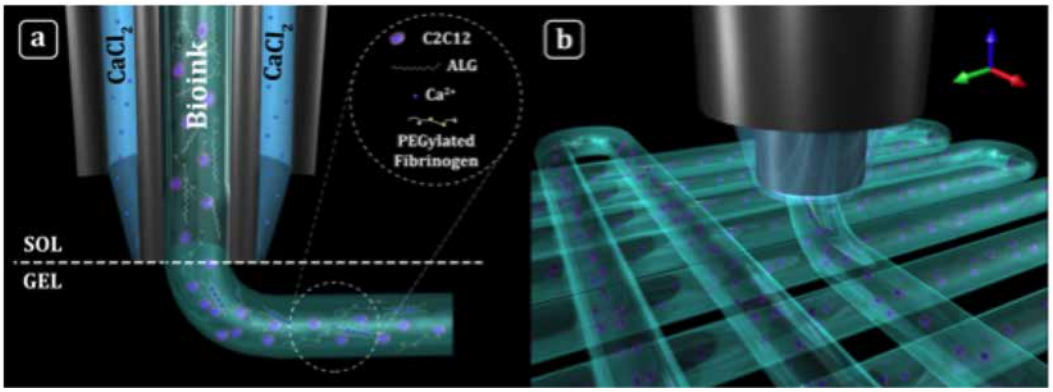

Fig. 1. a) Schematic representation of a cross-sectional view of the coaxial nozzles system: calcium chloride flows in the external nozzle while the bioink is supplied through the inner one. Hydrogel fibers form immediately at the tip of the inner nozzle when the two solutions come into contact. b) 3D illustration of hydrogel fibers deposition through coaxial nozzles printing head.

.

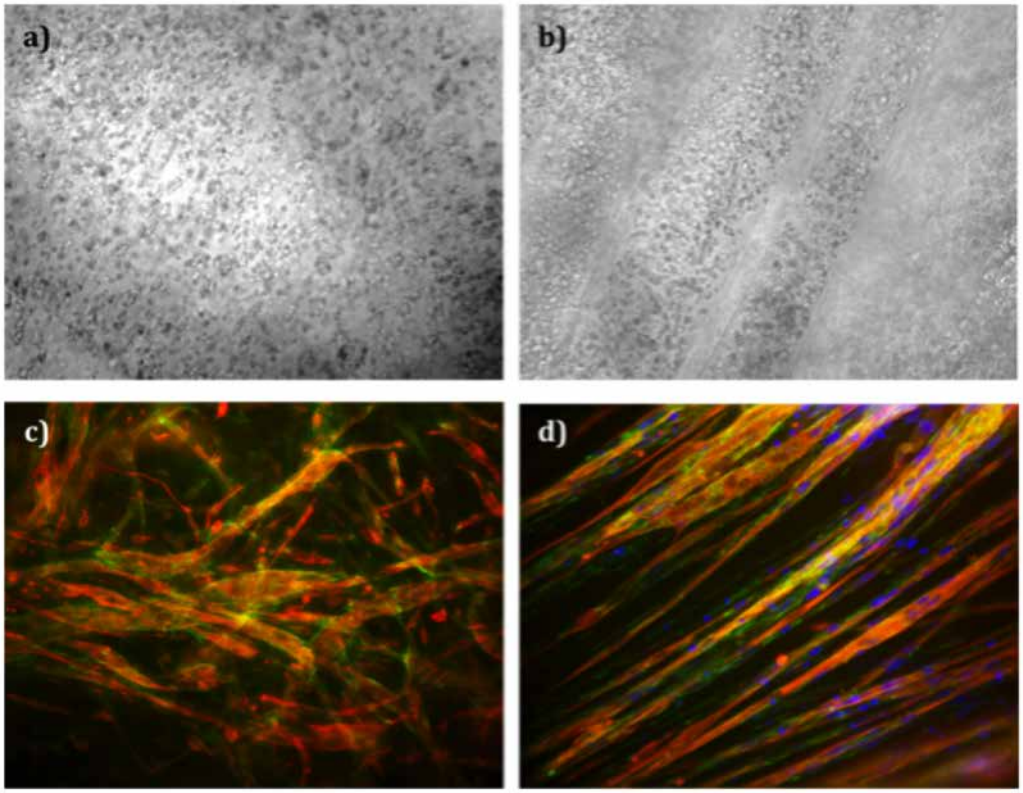

Fig. 2. a) C2C12 cells embedded in a bulk PEGylated fibrinogen hydrogel. b) 3D bioprinted C2C12 within PEGylated fibrinogen hydrogel fibers. c) Immunofluorescence micrograph showing chaotic myostructures formed in bulk (MHC in red, laminin in green). Nuclei are counterstained in blue. d) Highly aligned myotubes formed within 3D bioprinted fibers.

.

Collagen gradient on 3D printed scaffolds for interface tissue engineering

Ugo D'Amora[1], Matteo D'Este[2], David Eglin[2], Fatemeh Safari[2], Antonio Gloria[1], Roberto De Santis[1], Mauro Alini[2], Luigi Ambrosio[1,3]*

1Institute of Polymers, Composites and Biomaterials, National Research Council of Italy, Naples, Italy;

2AO Research Institute Davos, Davos, Switzerland;

3Chemical Science & Materials Technology Department, National Research Council of Italy, Rome, Italy.

***Abstract*— Interfacial tissue engineering (ITE) aims to regenerate tissue through the mimicking of continuous biological, physical and chemical transitional gradients which exist in organs and biological tissues. The introduction of rapid prototyping manufacturing allows obtaining continuous gradient of mechanical, mass transport and morphological properties, however the possibility to additionally functionalize such structures by introducing appropriate biochemical signal gradients has not been reported. Thus, the goal of this study was to optimize a two-step functionalization method in which 1) a poly(ε-caprolactone) (PCL) surface was aminolysed with a continuous gradient of amine concentration and 2) a collagen gradient was created via carbodiimide reaction. Then, the method was extended to three-dimensional (3D) morphologically-controlled scaffold as first proof of concept in the design of 3D functionalized rapid-prototyped structures for ITE.**

***Keywords*— Interface tissue engineering, PCL, functionalization, collagen, rapid prototyping manufacturing**

I. Introduction

Continuous tissue interfaces exist throughout the human body, such as the bone-cartilage and muscle-tendon interfaces. Since tightly interconnected anatomical structures present significantly different characteristics at the macro, micro, and nanoscale in terms of structural, mechanical, physicochemical, and biological properties, when considering their regeneration via tissue engineering approaches, a graded scaffold constructs able to replicate some of the key properties of the tissues is a valid approach.[Errore. L'origine riferimento non è stata trovata.-Errore. L'origine riferimento non è stata trovata.] In order to mimic the compartmental nature of tissue in organs, several biphasic, triphasic, and multilayered scaffolds have been developed. The main limitation is that they presented discrete physical and chemical gradients. Over the past years, great efforts have been devoted to the design of scaffolds with gradual change in morphological, mechanical, physico-chemical and biological performances.

Among the tools introduced to create gradients, rapid prototyping technique allows obtaining 3D custom-made scaffolds with a finely continuous gradient of mechanical, mass transport and morphological properties. However, the possibility to functionalize such structures by introducing a continuous gradient of appropriate biochemical signals has not been investigated yet. Thus, the goal of this study was to optimize a two-step functionalization method in which 1) a poly(ε-caprolactone) (PCL) surface was aminolysed with a continuous gradient of amine concentration and 2) a collagen gradient was created via carbodiimide reaction. Then, the method was extended to 3D morphologically-controlled scaffold as first proof of concept in the design of 3D functionalized rapid-prototyped structures for ITE.

II. Materials and Methods

A. PCL Surface preparation

Substrate surfaces were manufactured through melting & molding technique using PCL (M_w = 65 kDa - Sigma-Aldrich) pellets. Briefly, PCL pellets were heated at 80-100 °C and the molten polymer was then poured into a mold where it was allowed to cool down. Standard disc shaped and sheets were obtained and used for surface functionalization.

B. 3D rapid prototyped PCL scaffolds

PCL pellets were processed in a 3D Bioplotter to manufacture scaffolds with a 0/0/90/90° lay-down pattern. Specifically, 3D scaffolds were built by extruding and depositing the fibers along specific directions according to the selected lay-down pattern. PCL pellets were placed in a micro-extruder heated to a temperature of 80°C placed on the mobile arm of a 3D plotter dispensing machine (3D discovery®, RegenHU Ltd). All scaffolds were produced using a pore size (PS) of 200 μm and layer thickness (ST) of 220 μm.

C. PCL Substrate functionalization: Aminolysis and Collagen Grafting

The grafting of amino groups (NH_2) onto the PCL surface through 1,6-hexanediamine was performed as described by Zhu Y. *et al.* 2012. [4]-[6] Briefly, aminolysis was achieved by immersing the substrates in a 0.43 M 1,6 hexanediamine/isopropanol (DEA/IPA) solution at 37 °C. The NH_2 density gradient along the length of the substrate was achieved through the control of the surface exposure time to the solution using a syringe pump system (Harvard Apparatus) with a lead screw for precise linear motion. The PCL substrate was attached to the lead screw at one extremity, and then 10 mm of the other extremity was immersed for 15 minutes into the reactive solution, after that, a second substrate region was dropped into the thermostatic bath for other 15 minutes. The process was repeated three times for a total of 45 minutes to obtain a substrate characterized by four different regions made of neat PCL, to the last one in contact with the DEA/IPA solution for 45 minutes. The collagen grafting was achieved by modifying a

protocol from Chang K.Y. *et al.* [8]. Briefly, the aminolysed substrates were soaked into a 4 mg/mL collagen type I (rat tail, Sigma-Aldrich) 0.5 M acetic acid solution at RT for 1 hr. Lyophilized samples were soaked in a 50 mM 2-(N-morpholino) ethanesulfonic (MES, Sigma-Aldrich) in 70% ethanol (pH 5.4), 30 mM 1-ethyl-3-[3-dimethylaminopropyl] carbodiimide (EDC, Sigma-Aldrich) and N-hydroxysulfosuccinimide (NHS, Sigma-Aldrich) at a molar ratio of 1:1.

D. PCL Substrates characterization

The amount of NH_2 grafted onto PCL substrates was measured using a ninhydrin assay. Collagen density was quantified with a hydroxyproline assay. Confocal Laser scanning microscopy (CLSM) and fast green staining were also performed to image the NH_2 and collagen density gradient, respectively. FTIR, static contact angle and cells adhesion and proliferation analyses were also carried out.

E. Collagen gradient on 3D rapid prototyped PCL scaffolds: Characterization

Micro-Computed tomography (μCT40, Scanco) was carried out to assess the scaffold interconnectivity, the effective strut diameter, the strut spacing, and the layer thickness, which influence the overall pore size and porosity. Furthermore, the gradient of amino groups was also observed using CLSM.

III. Results and Discussion

A. PCL substrates characterization

The aminolysis represents a really fast and efficient chemical procedure to covalently bound free NH_2 groups along the polyester chains, through reaction with diamine species and formation of modified and gradient chemical polyester surfaces. These amino groups can consecutively react with biomolecules containing carboxylic groups for surface functionalization. Results from the ninhydrin assay showed that the PCL surface can be modified with amine and NH_2 concentrations ranging from $5*10^{-7}$ mol/cm^2 after 15 min of treatment, to $15*10^{-7}$ mol/cm^2 after 45 min of treatment is achieved (Fig. 1). CLSM analyses were also performed in order to visualize the NH_2 gradient after functionalization with a Rhodamine B probe. Surface spatial distribution of functional amine was assessed as well as the fluorescence intensity was also quantified. Results showed an 8-fold increase of fluorescence intensity from the neat PCL to the region aminolysed for 45 min, correlating with the ninhydrin assay. Collagen was covalently immobilized on the PCL substrates using a carbodiimide reaction. Results from hydroxyproline assay revealed that, as the NH_2 increases with the reaction time, also the amount of grafted collagen density increased from 0.08 to 0.71 μg/cm^2 (Fig. 1). FTIR spectra of collagen grafted PCL substrates showed vibrational bands specific to collagen after extensive washing. Furthermore, the positivity to the fast green staining confirmed the presence of collagen. Water contact angle of unmodified PCL surface was 76.5 ± 2.6° and dropped to 69.2 ± 1.5° after aminolysis without significant difference between the difference aminolysis time. After collagen functionalization the contact angle dropped below 40°, indicating a major change in the substrate surface hydrophilicity. Preliminary biological analyses showed that MG63 labeled cells were viable on all substrates and showed a trend toward better adhesion and faster proliferation on collagen functionalized PCL.

B. 3D rapid prototyped PCL scaffolds characterization

μCT and morphometric analysis showed that experimental PCL scaffold structural parameters had a narrow standard deviation and were close to the theoretical defined values. In particular, the strut diameter, 265.1 ± 35.0 μm was close to the inner diameter of the nozzle (330 μm). Although, the deposition speed influences the final struts diameter. The scaffolds were also characterized by a 100% interconnectivity, a porosity of 47% and a pore width of 224.0 ± 4.0 μm. Finally, CLSM analysis on the 3D rapid-prototyped scaffolds on which the gradient functionalization method was applied showed the successful production of a chemical gradient in a designed ITE construct.

IV. Conclusion

A method to create biomolecules gradient, i.e. collagen, on PCL substrate was established. The functionalization was extended to 3D rapid prototyped scaffolds, demonstrating for the possibility to manufacture combined structural and chemical gradients constructs for interface tissue engineering approaches.

Acknowledgements

The authors would like to thank FIRB MERIT project (GAE: P0000570) and the *Short Term Mobility* for providing financial support.

References

[1] A. Di Luca, C. Van Blitterswijk and L. Moroni "the osteochondral interface as a gradient tissue: from development to the fabrication of gradient scaffolds for regenerative medicin". *Birth Defects Res. C.* 105, pp. 34–52, 2015.

[2] S. Miot, A. Barbero, M. Jakob and D. Wendt. "Osteochondral tissue engineering". *J. Biomech.* 40, pp.750–765, 2007.

[3] J. Wu, Z. Mao, H. Tan, L. Han, T. Ren and C. Gao. "Gradient biomaterials and their influences on cell migration". *Interface Focus*, 2(3), pp. 337–355, 2012

[4] Z. Yang, M. ZhengWei, S. H.Yu and G.C. You. "In-depth study on aminolysis of poly(ε-caprolactone): Back to the fundamentals". *Sci. China Chem.* Vol.55 No.11, pp. 2419–2427, 2012.

[5] F. Causa, E. Battista, R. Della Moglie, D. Guarnieri, M. Iannone and P. A. Netti. Surface investigation on biomimetic materials to control cell adhesion :The case of RGD conjugation on PCL. *Langmuir,* 26 (12), pp. 9875–9884, 2010.

[6] L. Russo, A. Gloria, T. Russo, U. D'Amora, F. Taraballi, R. De Santis, L. Ambrosio, F. Nicotra and L. Cipolla. "Glucosamine grafting on poly(ε-caprolactone): a novel glycated polyester as substrate for tissue engineering". *RSC Adv.* 3**,** pp. 6286-6289, 2013.

[7] L. Russo, T. Russo, C. Battocchio, F. Taraballi, A. Gloria, U. D'Amora, R. De Santis, G. Polzonetti, F. Nicotra, L. Ambrosio and L. Cipolla. "Galactose grafting on poly(ε-caprolactone) substrate for tissue engineering: a preliminary study". *Carbohydr. Res*. 405, pp. 39–46, 2015.

[8] K. Y. Chang, L. H. Hung, I. M. Chu, C. S. Ko and Y. D. Lee. "The application of type II collagen and chondroitin sulfate grafted PCL porous scaffold in cartilage tissue engineering". *J. Biomed. Mater. Res. A*. 92(2), pp. 712-23, 2010.

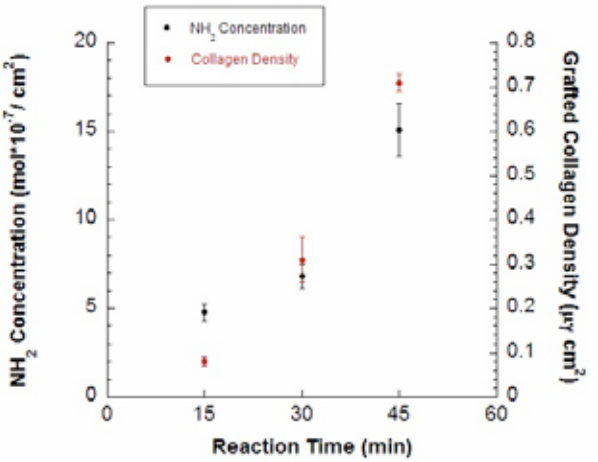

Fig. 1. Results from the ninhydrin and hydroxyproline assays reported as mean value ± standard deviation.

The effect of initial pH on in-situ synthesis of alginate-brushite hydrogel composite

Seyed Mohammad Hossein Dabiri[1*], Alberto Lagazzo [2], Fabrizio Barberis[2], Elisabetta Finochio[2], And Laura Pastorino[1]

[1] *DIBRIS, University of Genova, Genova, Italy*
[2] *DICCA, University of Genova, Genova, Italy*

Abstract **Hydrogels have emerged as versatile and viable platforms for sustained drug release, targeted drug delivery, and tissue engineering due to their excellent biocompatibility, a microporous structure with tunable porosity and pore size, and dimensions spanning from human organs, cells to viruses. In addition, their mechanical and physical properties can be tailored to meet wide range of design requirements.**

In the present study the impact of initial pH value on in-situ formation of alginate-brushite hydrogel was evaluated via performing X-ray diffraction (XRD), fourier transform infrared spectroscopy (FTIR), scanning electron microscopy (SEM). It was revealed that the proper preparation conditions obtained as the pH was regulated in the range of 7-8.

Keywords— Alginate, brushite, Hydrogel composite, in-situ synthetizes

I. Introduction

ALGINATE is a natural, biocompatible, and biodegradable polymer which has been widely used in different biomedical applications [1]. Alginate is a promising biomaterial to applicate in tissue engineering and drug delivery because it has a structure similar to that of extra-cellular matrix (ECM) and also it presents mucoadhesive characteristics and low immunogenicity [2] , [3]. However, alginate hydrogels have their own demerits including weak mechanical properties, high water content, large structural pores, and etc [4].

Numerus strategies have been proposed by scientists to overcome this limitations. These strategies includes increasing the number of crosslinks, and/or developing hydrogel composite to improve crosslinking and reduce subsequent swelling of hydrogel [4], [5]-[7].

Calcium phosphate materials have been proposed to act as a reinforcement component with alginate matrix because of their broad advantages in tissue engineering and capability of carrying different drugs [8]-[10]. Among calcium phosphate materials, brushite seems to be more proper candidate due to its particular biodegradable behavior in physiological conditions. In addition, it has been studied in different biomedical application [11].

The aim of this study was to fabricate alginate-brushite hydrogel composite for their perspective use as drug delivery and tissue engineering systems. In this work the impacts of initial pH on formation of brushite crystals inside of an alginate matrix were taken into consideration.

II. materials and methods

A. Materials

All the chemical reagents including Sodium alginate (Alg) from brown algae, calcium nitrate tetra hydrate [Ca(NO3).4H2O, 99%], diammonium hydrogen phosphate [(NH4)2HPO4, 98%], hydrochloric acid (HCl) and, sodium hydroxide (NaOH) were supplied by Sigma-Aldrich. All reagents were used without any purification process. All the solutions were prepared using purified water obtain from Milli-Q system and had the resistance of 18.2 MΩ cm.

B. Methods

First an aqueous solution containing 0.1 M of di-ammonium hydrogen phosphate and alginate 1% (w/v) was prepared. The obtained solution stirred for 2 h at room temperature to ensure that the solution would be homogenous. Then, this solution was dipped to the crosslinking solution containing 0.25 M of calcium nitrate. HCl and NaOH (0.1 M) were used to set the initial pH of both solution at different values ranging from 3-9 to investigate the impact of initial pH value on the formation of composite. The white beads formed immediately after dipping polymeric solution into the crosslinking solution and they were kept there for 24 hours. After that, the samples were centrifuged at 1000 rpm for 5 minutes and washed with water to remove excess Ca^{2+} and other impurities. This step was repeated four times. Finally the beads were dried at room temperature followed by putting them into an oven at 50 ˚C overnight. Samples are referred as C-X, where c stands for composite and X is the pH value.

The phase composition of different samples was examined via Philips PW 1800 X-ray diffractometer with Cu-k_α radiation source in the 2Θ range of 3˚ to 90˚ at 30 mA and 40 kV. In order to characterize the brushite the resulting spectra of each sample was compared with that of ICCD standard number 9-0077. A Nicolet 380 Fourier transform infrared spectrometer (Thermo Fisher scientific Inc, USA) was used to obtain FT-IR spectra of each sample to evaluate the functional group of each bead. This test was carried out at room temperature and the spectra were obtained within the wavelength of 400 to 4000 cm^{-1}. In addition, DTG was carried out TG-DTA Netzsch Gerätebau STA 409 (Germany) in nitrogen atmosphere at the heating rate of 10 ˚C.min^{-1} in the range of 25 ˚C to 450 ˚C. Finally, the surface morphology was evaluated using SEM (Hitachi S-2500).

III. results and discussion

The FT-IR spectra of the each sample along with the spectrum of reference Ca-alginate are demonstrated in fig. 1. The main alginate bands were appeared at 1649 and 1425 cm^{-1} related to the asymmetric and symmetric stretching mode of the carboxyl group. The complex envelop of bands at the frequencies ranging from 1000-1200 cm^{-1} are assigned to C-O and C-C stretching modes of the carbohydrate chain. In addition, the C-H stretching mode peak can be seen at 2922 cm^{-1} [12].

The two doublet of peaks at 3169, 3290 cm^{-1} and 3489, 3547 cm^{-1} are the characteristic peaks of brushite and relates to the O-H stretching mode of structural water molecules [13]. The absorbed peak at 1649 cm^{-1} is the O-H-O bending mode [14]. The bands at 1138, 1059 and 987 cm^{-1} relate to phosphate group. Corresponding bands of P-O-H stretching mode and P-OH bending mode can be seen at 1217 and 872 cm^{-1}, respectively [14]. Finally, the corresponding bands of P-O deformation mode of phosphate group can be detected at 667, 577 and 526 cm^{-1} [13].

The significant impact of pH value on the formation of the brushite inside the alginate matrix is represented in Fig 1. As we can see the characteristic peaks of brushite are appeared in the samples prepared at pH of 6-8. Also, it is obvious that in the lower pH the spectra are very similar to that of Ca-alginate. Brushite peaks in the sample prepared at pH 8 were more intense and the width of it were tighter than other composite samples. This can be as a result of phosphate band strengthening at pH 8. In addition, the characteristic bands of brushite almost disappeared in the sample prepared at pH 9. Besides, the alginate component can be affected by the formation of Na-alginate as the pH increase. The changes in in the region of 1650-1400 cm^{-1} of the spectrum can be explained by this phenomena.

Fig 2 demonstrates the XRD spectra of the samples prepared at different pH. These spectra were compared with that of standard brushite JCPDS card (9-0077). AS we can see the samples prepared at the pH 3-5 are completely amorphous. On the other hand, the brushite crystals can be detected in the pH range of 6-8 and those samples prepared in the pH 7 and 8 had the best crystalline structure. These preparation conditions resulted in monoclinic crystalline structure with following crystallographic parameters: a= 6.363 Å, b= 15.190 Å, c= 5.815 Å, $\alpha = \gamma = 90^{\circ}$, and $\beta = 118.5^{\circ}$. Furthermore, as the pH reached to 9 reductions in the intensity of characteristics peaks, especially at 2Θ of 20.9°, 29.25°, and 34.16°, and incensement in the width of them were noticeable. We can evolve that the degree of crystallinity decrease at pH 9.

The DTG resulting of alginate, brushite, and alginate-brushite hydrogel composite are presented in Fig 3. According to the comparison between these spectra we can see that the main weight loss occurred in alginate-brushite composite within the range of 150-300 °C. As we compared this spectra with that of reference materials, none of them exhibited this kind of phenomena in this range of temperature. This peak complexity indicates that varieties of decomposition steps happened at the same time, including organic materials degradation via glycoside bonds breaking which resulted in formation of carbonaceous material, and also dehydration of brushite. Since this phenomena occurred at lower temperature in comparison with alginate, we can say that brushite has a catalytic effect on this. These results confirmed the existence of a specific interaction between both phases of composite.

IV. conclusion

The experimental results demonstrated the significant impact of the initial pH on formation of alginate-brushite composite. In addition, it was cleared that the most proper samples obtained at the pH 7-8. This hydrogel composite is highly potential candidate biomaterial in hard tissue regeneration especially in dental and periodontal local treatment.

References

[1] Lee, Kuen Yong, and David J. Mooney. "Alginate: properties and biomedical applications." *Progress in polymer science* 37.1 (2012): 106-126.

[2] Lee, Kuen Yong, and David J. Mooney. "Hydrogels for tissue engineering."*Chemical reviews* 101.7 (2001): 1869-1880.

[3] Jain, Dharmendra, and Daniel Bar-Shalom. "Alginate drug delivery systems: application in context of pharmaceutical and biomedical research." Drug development and industrial pharmacy 40.12 (2014): 1576-1584.

[4] Hoare, Todd R., and Daniel S. Kohane. "Hydrogels in drug delivery: progress and challenges." Polymer 49.8 (2008): 1993-2007.

[5] Maiti, Sabyasachi, et al. "Adipic acid dihydrazide treated partially oxidized alginate beads for sustained oral delivery of flurbiprofen." *Pharmaceutical development and technology* 14.5 (2009): 461-470.

[6] Wang, Qin, Junping Zhang, and Aiqin Wang. "Preparation and characterization of a novel pH-sensitive chitosan-g-poly (acrylic acid)/attapulgite/sodium alginate composite hydrogel bead for controlled release of diclofenac sodium."*Carbohydrate Polymers* 78.4 (2009): 731-737.

[7] Wang, Qin, et al. "Preparation and swelling properties of pH-sensitive composite hydrogel beads based on chitosan-g-poly (acrylic acid)/vermiculite and sodium alginate for diclofenac controlled release." *International journal of biological macromolecules* 46.3 (2010): 356-362.

[8] Rajkumar, M., N. Meenakshisundaram, and V. Rajendran. "Development of nanocomposites based on hydroxyapatite/sodium alginate: synthesis and characterisation." *Materials Characterization* 62.5 (2011): 469-479.

[9] Zhang, Junping, Qin Wang, and Aiqin Wang. "In situ generation of sodium alginate/hydroxyapatite nanocomposite beads as drug-controlled release matrices." *Acta Biomaterialia* 6.2 (2010): 445-454.

[10] Amer, Walid, et al. "Smart designing of new hybrid materials based on brushite-alginate and monetite-alginate microspheres: Bio-inspired for sequential nucleation and growth." *Materials Science and Engineering: C* 35 (2014): 341-346.

[11] Tamimi, Faleh, Zeeshan Sheikh, and Jake Barralet. "Dicalcium phosphate cements: Brushite and monetite." *Acta biomaterialia* 8.2 (2012): 474-487.

[12] Ribeiro, C. C., C. C. Barrias, and M. A. Barbosa. "Calcium phosphate-alginate microspheres as enzyme delivery matrices." *Biomaterials* 25.18 (2004): 4363-4373.

[13] Hirsch, Anna, et al. "Infrared Absorption Spectrum of Brushite from First Principles." *Chemistry of Materials* 26.9 (2014): 2934-2942.

[14] Štulajterová, R., and Ľ. Medvecký. "Effect of calcium ions on transformation brushite to hydroxyapatite in aqueous

solutions." *Colloids and Surfaces A: Physicochemical and Engineering Aspects* 316.1 (2008): 104-109.

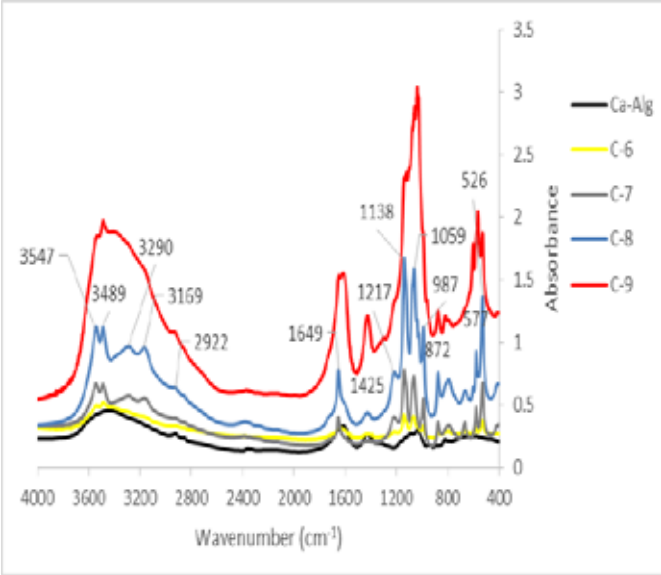

Fig.1. FT-IR spectra of composite samples prepared at different pH

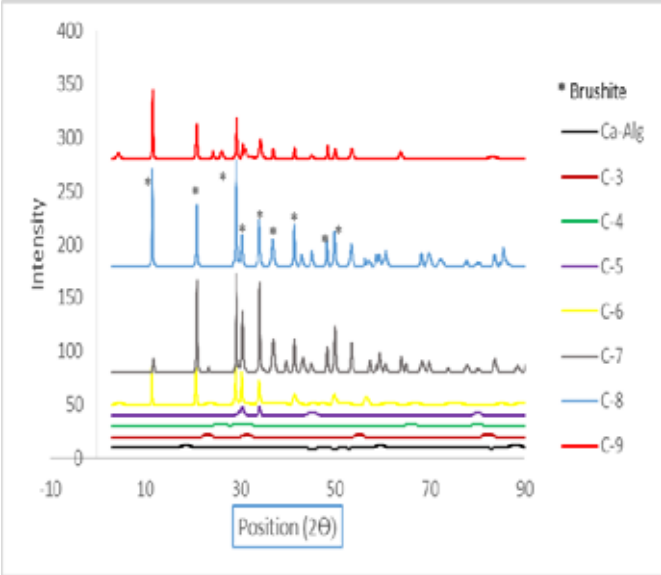

Fig.2. XRD spectra of samples prepared at different pH

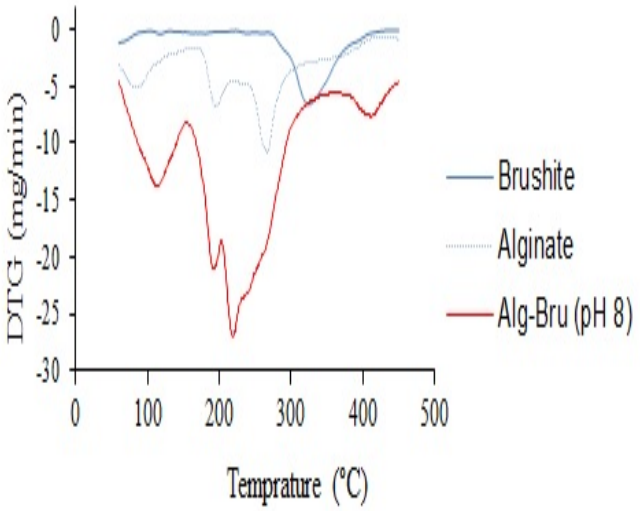

Fig.3. DTG spectra of brushite, alginate, alginate-brushite composite

Fluid Dynamic Assessment of New PHVs Prototypes under Pulsatile Flow Condition and using PIV

F. De Gaetano[1], M. Serrani[2], J. Stasiak[2], J. Brubert[2], G. D. Moggridge[2], M.L. Costantino[1]
[1] *LaBS, Department of Chemical, Material and Chemical Engineering "Giulio Natta", Politecnico di Milano, Milan, ITALY*
[2] *Department of Chemical Engineering & Biotechnology, University of Cambridge, Cambridge, UK*

***Abstract* — Two categories of heart valve prostheses are currently available in clinics: mechanical and biological valves. The former show longer duration performance, on the other hand they induce high pressure drops during operation. The latter have preferable fluid dynamic performance but do not display high durability. The potential of Polymeric Heart Valves (PHVs) is to combine the haemodynamic properties of biological valves with the durability of mechanical valves. Our group has recently developed a new PHV made of a styrenic block co-polymer obtained by compression moulding. Indeed, anisotropic mechanical properties of this material, mimicking the native tissue behaviour, can be obtained by compression and slow injection moulding. A computational tool was developed to optimize the PHV design and leaflet microstructure in order to reduce regions of stress concentration and increase the device lifetime. This work presents a hydrodynamic evaluation of the new PHV prototypes, which were manufactured by injection moulding based on the results obtained by the computational tool. The PHVs were tested under pulsatile flow conditions as prescribed by ISO 5840 Standard. Furthermore, continuous flow tests were performed to evaluate the velocity fields with the particle image velocimetry (PIV).**

***Keywords*—Heart valve, styrenic block copolymer, pulse duplicator, particle image velocimetry.**

I. Introduction

THE aim of heart valve prostheses is to replicate the function of native heart valves. Within this contest, bio-inspired polymeric heart valves (PHVs) are excellent candidate to mimic not only the shape, but also the structural and fluid dynamic properties of the native valve. Our group has recently developed a new PHV made of a styrenic block copolymer, a polymer characterised by a cylindrical morphology; in fact, the arrangement of the polymer micro domains can be optimized to enhance valve durability under physiological conditions. [1].

To find the optimised polymer microstructure in the leaflet, a computational model was developed. The mechanical properties of the polymer, were determined experimentally, while suitable boundary conditions were set to simulate a physiological pressure load on the valve. This FE model allowed to find the optimised material micro-morphology by orienting the polymeric cylinders along the maximum stress directions. Starting from this results, PHVs prototypes were produced by slow injection moulding technique in order to orient the material microstructure by controlling the polymer flow during injection. The aim of this work is to characterise the performance of styrenic block-copolymer PHVs under pulsatile flow conditions; specifically, the hydrodynamic tests were performed at 22°C and 37°C to understand the possible effect of the temperature on the PHV behaviour. Further, the velocity fields induced by the new PHVs were compared with the velocity fields of one mechanical and one biological valves currently on the market by using PIV analyses.

II. Material and Methods

According to the results of the computational model, 8 PHVs prototypes were manufactured by injection moulding technique from poly (styrene-ethylene/propylene-styrene) block copolymer with 22% wt polystyrene fraction. Hydrodynamic tests were performed under pulsatile flow conditions as recommended by ISO5840 Standard. The experimental test bench used to evaluate PHVs' performance in pulsatile flow conditions is shown in Fig. 1

The pulse duplicator consists of the following elements: the driving system made of a piston pump; the ventricular element, simulating the left ventricle; the aortic valve housing; the Resistance-Compliance-Resistance (RCR) analogue to replicate the peripheral compliance and the resistance (aortic and peripheral) of the cardiovascular system; the reservoir simulating the left atrium and the mitral valve. The pumping system was controlled by a software that allows the user to set different flow rate waveforms or different frequencies.

The PHVs were tested under different flow rates and backpressures, as required by the ISO5840 Standard. Transvalvular pressure drop was measured at a constant frequency (70 bpm) and variable flow rate (2 l/min, 3.5 l/min, 5 l/min and 7 l/min). Regurgitation volume was determined by testing each valve at a mean flow rate of 5 l/min at three different frequencies (45 bpm, 70 bpm, 120 bpm). At each frequency three backpressures were tested (80 mmHg, 120 mmHg, 160 mmHg). Each valve has been tested for at least 15 cycles at each test condition. Pulsatile flow tests were performed using distilled water at 22°C and 37°C.

The experimental set-up (Fig. 2) used for the continuous flow test with PIV is composed of a volumetric pump (0.75 hp, Lowara SGM7, Direct Industry), a free surface reservoir, a valve housing replicating the Valsalva sinus dimensions (Fig.2), a Ng:Yag pulsed laser generator (Twins Ultra, Quantel, France) and a camera (PCO SensiCam, Germany). The neutrally buoyant silver-coated seed particles were placed inside the liquid used in the system which is a mixture of glycerol and water in a 43% v/v ratio at 22°C (μ=0.003 Pa·s; ρ=1060 kg/m3). The valves were subjected to four steady flow rates: 5 l/min, 10 l/min, 15 l/min and 20 l/min. Twenty image pairs were taken for each valve at each flow rate.

III. Results and Discussion

The dimensions of the tested PHVs are shown in Fig. 3. The significance of the statistical difference between the two test temperature ($p<0.01$) was evaluated using a two sample location Student's t-test.

The PHVs exceed the minimum performance requirements provided in ISO5840 Standard (Table I), both at 22°C and at 37°C. Only the regurgitation of one valve (*Valve 2 @ 37°C*) did not meet the Standard requirements, but the mean regurgitation of this group is lower than 10% (9.04%).

TABLE I
PERFORMANCE OF PHVS

	Regurgitation [% stroke volume]	*EOA [cm^2]*
ISO 5840	<10%	>1
Valve 1 @ 22°C	9.81 ± 1.53	1.56 ± 0.27
Valve 2 @ 22°C	8.58 ± 1.28	1.33 ± 0.43
Valve 3 @ 22°C	9.40 ± 1.28	1.78 ± 0.62
Valve 4 @ 22°C	9.95 ± 0.99	1.60 ± 0.19
Valve 5 @ 22°C	9.03 ± 1.33	1.51 ± 0.49
Valve 6 @ 22°C	7.85 ± 1.06	1.44 ± 0.41
Valve 7 @ 22°C	9.90 ± 1.30	1.38 ± 0.40
Valve 8 @ 22°C	8.51 ± 1.15	1.32 ± 0.28
Valve 1 @ 37°C	8.84 ± 1.40	1.84 ± 0.21
Valve 2 @ 37°C	10.21 ± 1.22	1.56 ± 0.10
Valve 3 @ 37°C	9.34 ± 1.30	1.44 ± 0.10
Valve 4 @ 37°C	9.36 ± 1.46	1.47 ± 0.90
Valve 5 @ 37°C	8.99 ± 1.04	1.62 ± 0.42
Valve 6 @ 37°C	7.71 ± 1.22	1.85 ± 0.47
Valve 7 @ 37°C	9.60 ± 1.53	1.66 ± 0.25
Valve 8 @ 37°C	8.29 ± 1.05	1.78 ± 0.51

The table shows the ISO5840 specifications vs PHVs performance. The ISO5840 specifications correspond to the following pulsatile flow condition: beat rate = 70 cycle/min, simulated cardiac output = 5.0 l/min, mean aortic pressure 100 mmHg and systolic duration = 35%.

Pulsatile flow tests showed that the effective orifice area (EOA) at 22°C was statistically lower (1.49 ± 0.39 cm^2) than the one calculated at 37°C (1.65 ± 0.27 cm^2) ($p = 0.0019$).

Mean regurgitation volume was comparable within the two groups (9.13% ±1.24% at 22°C versus 9.04% ± 1.28% at 37°C), with no statistical significant difference at the two temperatures ($p > 0.05$). The results of this work showed that the performance of PHVs in terms of EOA and regurgitation fraction under pulsatile conditions are comparable with those of some tissue valves currently on the market, while exceed the performance of bi-leaflet mechanical prostheses having a comparable tissue annulus diameter (TAD) [2].

The fluid dynamic assessment of the PHVs were compared with a tissue valve (3000 PERIMOUNT Magna, Edwards Lifesciences) and a mechanical valve (Omniscience tilting disk) currently on the market using PIV.

At 5 l/min the flow induced by both the PHVs and in the tissue valve was characterised by a strong central orifice jet (Fig. 4). Specifically the velocity profile distribution in the presence of PHVs showed a central orifice jet flow with recirculation areas symmetrically located near the aortic wall of the Valsalva sinus. However, PHVs were found to generated higher vortex than the tissue valve due to their more constricted flow orifices. The same observation was made at the flow rate of 20 l/min (Fig. 5) (Table II).

TABLE II
PIV FLUID DYNAMIC ANALYSIS

Valves	*Velocity peak [m/s]*	*Diameter of central orifice jet [mm]*
Tissue @ 5 l/min	0.14	22.89
Mechanical @ 5 l/min	0.16	8.82
PHVs @ 5 l/min	0.16 - 0.24	10.82 - 17.39
Tissue @ 20 l/min	1.15	27.54
Mechanical @ 20 l/min	1.14	12.75
PHVs @ 20 l/min	0.85 - 1.25	17.68 - 29.86

The table shows the maximum velocity peak and the diameter of central orifice jet of the Tissue and Mechanical valve at the flow rates of 5 l/min and 20 l/min. Range of velocity peak among the PHVs are reported.

Both PHVs and tissue valve exhibit vortex flow in the sinus region generally less than 0.02 m/s at the flow rate of 5 l/min while at 20 l/min all the valves tested valves show vortex flow in the same region less than 0.2 m/s.

IV. Conclusion

An experimental hydrodynamic evaluation of PHVs manufactured from block copolymers has been performed. The result demonstrate that the behaviour of the PHVs at 37°C is better than at 22°C in terms of EOA, while no statistical differences were found between the two Groups in dynamic regurgitation tests.

The velocity profile obtained by the PIV results show how the fluid dynamic performance of the PHVs is comparable with the performance of the tested tissue valve, usually considered as the gold standard.

Moreover, the velocity profile induced by the PHVs shows a very good flow distribution when compared to the mechanical valve.

Acknowledgement

The authors thank the British Heart Foundation for the financial support to this work under Grant Nos. NH/11/4/29059 and SP/15/5/31548.

References

[1] J. Stasiak, J. Brubert, M. Serrani, S. Nair. F. De Gaetano et al. "A bio-inspired microstructure induced by slow injection moulding of cylindrical block copolymers", Soft Matter, 2014; 10(32):6077-6086.

[2] F. De Gaetano, M. Serrani, P.Bagnoli, J. Stasiak, J. Bribert et al. "Fluid dynamic characterization of a polymeric heart valve prototype (Poli-Valve) tested under continuous and pulsatile flow conditions", IJAO, 2015; 38(11):600-6006.

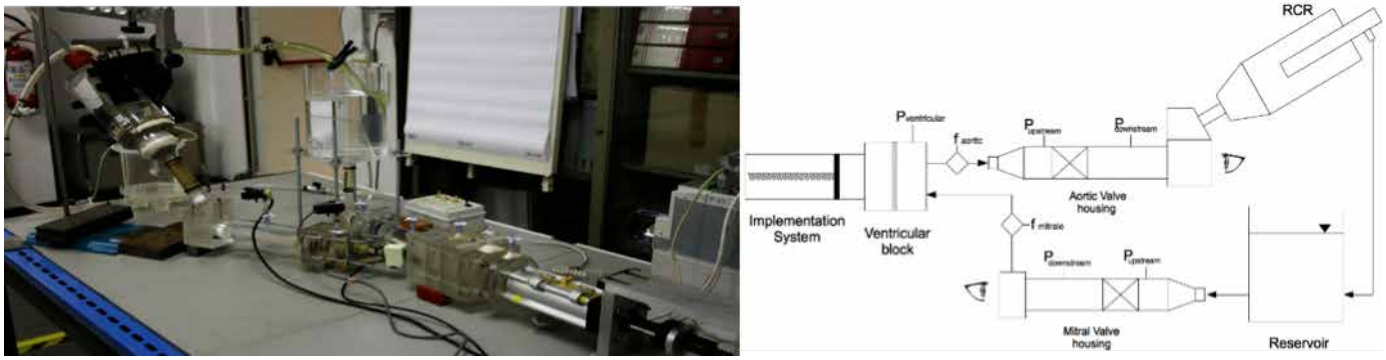

Fig. 1 Picture (left) and schematic (right) of the experimental set-up used for the pulsatile flow tests. Shown on the diagram are the locations of upstream and downstream pressure measurements, the flow rate measurement location and the observation point from which pictures of the valve opening were taken.

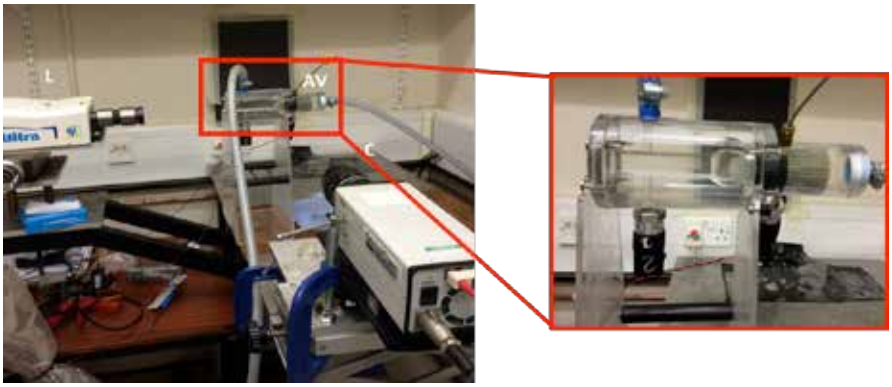

Fig. 2 On the left, picture of the experimental set-up used for the PIV tests. Shown on the diagram are the laser (L), the recording camera (C) and the valve housing mimicking the Valsalva sinus dimension obtained following the guidelines of the American Heart Association (AHA). On the right it is possible to observe a zoom of the valve housing.

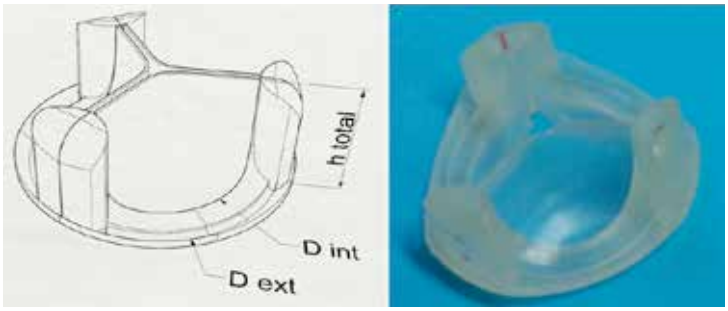

Fig. 3 Sketch (left) and picture (right) of the PHV. The dimension are: h total = 14 mm, D int = 21 mm, D ext = 32 mm, Tissue Annulus Diameter = 21 mm, thickness leaflet = 0.3 mm and height leaflet = 12 mm.

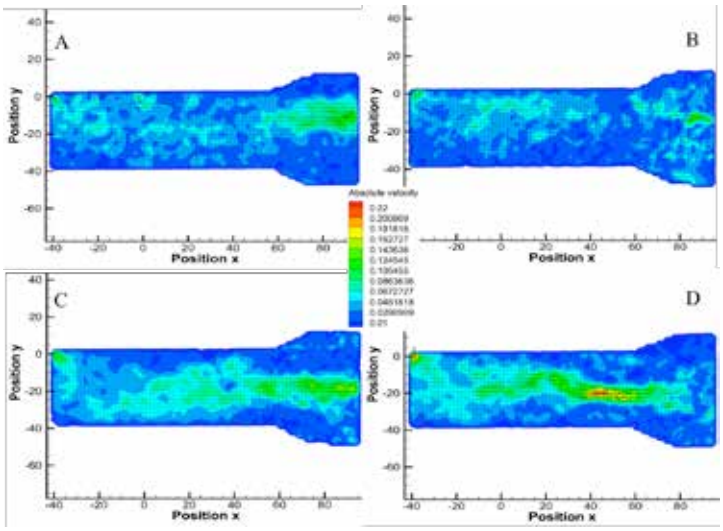

Fig. 4 Pictures of the experimental velocity at the mid plane obtained using PIV tests at the flow rate of 5 l/min. (A) Tissue valve, (B) mechanical valve, (C) PHV with the best performance and (D) PHV with the worst performance.

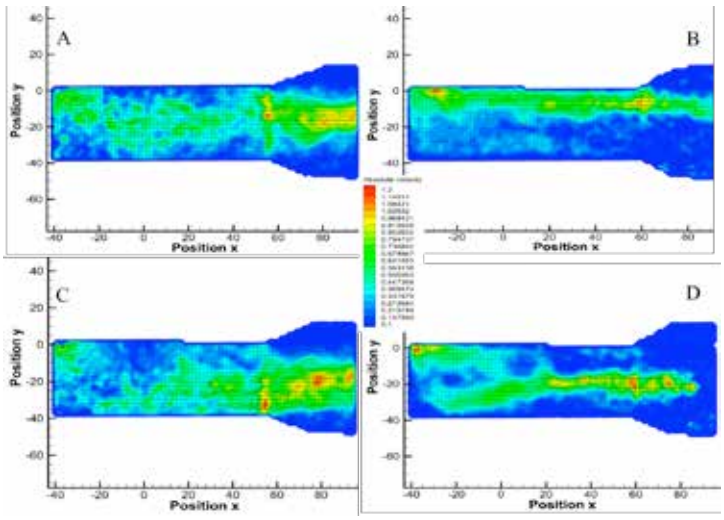

Fig. 5 Pictures of the experimental velocity at the mid plane obtained using PIV tests at the flow rate of 20 l/min. (A) Tissue valve, (B) mechanical valve, (C) PHV with the best performance and (D) PHV with the worst performance.

Polymeric scaffolds for controlled neoangiogenesis in tissue engineering

De Gregorio M[1,2], Attanasio C[1], Rossi L[4], Porzio M[3], Vilardi E[1], Netti PA[1]
[1]Center for Advanced Biomaterials for Health Care, IIT@CRIB, Istituto Italiano di Tecnologia, Napoli, Italy.
[2]Department of Veterinary Medicine and Animal Productions, University of Napoli Federico II, Napoli, Italy.
[3] Centro di Ricerca Interdipartimentale sui Biomateriali - CRIB, Università degli studi di Napoli Federico II, Napoli, Italy.
[4]CRdC Tecnologie Scarl, Napoli, Italy.

Abstract- **Vascularization is one of the great challenges that tissue engineering has to face to obtain functional replacement for damaged tissues and organs.**

An imbalance in the angiogenic cascade results in inflammation, ischemia and wound healing disorders. Engineered tissues usually trigger a complex response involving matrix, scaffold, growth factors and cells. A scaffolding matrix is often loaded with growth factors that enable the recruitment of cells from host tissues to promote tissue repair. The main goal in scaffold-guided tissue regeneration is to provide controlled release of appropriate biochemical signals over time into the site of interest. In this context, angiogenesis is a key issue. An efficient vascular network is essential to providing an adequate supply of oxygen and nutrients to obtain a functional regenerated tissue.

In the present study we investigated the performance of two polymeric porous scaffolds designed to control angiogenesis and guide tissue repair. We compared the biological response, both in vitro and in vivo, to two kind of porous scaffolds, comprised of two different polymers, polycaprolactone (PCL) and alginate.

After assaying the scaffold biocompatibility in vitro we implanted the constructs subcutaneously in rats in to assess their safety and ability to be integrated into the host tissue.

The analyses we performed after retrieval of the integrated scaffolds showed that, despite its high porosity, alginate constructs had poor biocompatibility compared to PCL.

PCL scaffolds showed the absence of any adverse reaction at the site of implantation as well as a high degree of vascularization.

Keywords—**Tissue engineering, angiogenesis, PCL, alginate.**

I. Introduction

Angiogenesis is the sprouting of new blood vessels from pre-existing ones. It occurs physiologically in embryonic life, during organ and tissue development and in tissue repair following injuries (revascularization) [1]. The proliferation of endothelial cells mediated by specific growth factors, such as Vascular-Endothelial Growth Factor (VEGF), leads to new vessel formation.

Regeneration of injured tissues is one of the main goals of tissue engineering and implies the recovery of lost biological functions[2]. In this context, angiogenesis is a key event that triggers the formation of a vascular network able to provide oxygen and nutrients to the neoformed tissue. Nevertheless, new vessels often show an altered morphology and low functionality.

Biocompatible scaffolds provide a valuable structural support together with mechanical, topographical and/or biochemical signals [3].

II. aim

The present study aims to identify the most effective scaffold to control neoangiogenesis and the following formation of a functional neoformed vasculature. We compared the performance of two scaffolds fabricated using two different polymers, alginate and polycaprolactone (PCL). Both the products were designed to guide the onset of a neoformed vasculature. We tested our hypothesis both in vitro and in vivo.

II. Materials and Methods

Scaffolds fabrication

PCL scaffolds were made of sintered microspheres produced using a single emulsion oil-in-water (O/W) technique. PCL (PCL, Sigma-Aldrich) was dissolved in dichloromethane (DCM Romil Pure Chemistry).

The polymer solution was added dropwise to the aqueous phase and then stirred for three hours at 500 rpm with a mechanical stirrer. Once obtained a micro-emulsion of dispersed particles, microspheres were isolated by three cycles of washing in distilled water and filtered in order to completely remove the emulsifier.

Scaffolds were then fabricated by placing microspheres into PDMS molds. Afterwards, a small amount of pure anisole was poured to induce microspheres sintering. To stop swelling and fix the final structure the sintered microspheres were exposed to ethanol for few seconds. Scaffolds were then removed from the mold and the solvent was allowed to evaporate overnight [4].

Alginate scaffolds were produced using the double lyophilisation technique. To obtain a porous scaffold with the desired stiffness the polymer was cross-linked with 70% CaCO3 while Arginylglycylaspartic acid (RGD) peptide was added to enhance cell adhesion. Scaffolds were then sterilized with UV for 1 hour and hydrated o/n in a 0.9% NaCl solution [5].

Scaffolds morphology and structure were assessed by scanning electron microscopy.

In vitro study

Human Umbilical Vein Endothelial Cells (HUVECs) (Lonza) were grown in Medium 200 (Live technology) supplemented by low serum and growth factor (LSGS Kit live technology) Cells were seeded into tissue culture flasks and cultured until they reached confluence.

In order to evaluate cell-material interaction PCL scaffolds were sterilized by UV exposure and seeded with HUVECs. Seeded scaffolds were cultured into 48well plates. After three days of culture the constructs were fixed with 4% paraformaldehyde, rinsed with PBS buffer and stained with Phalloidin tetramethylrhodamine B isothiocyanate (Sigma-Aldrich) and sytox green (Invitrogen). Cell adhesion and morphology were assessed by a Leica SP5 confocal laser scanning microscope.

Pre-clinical study

To test constructs biocompatibility and function in a preclinical setting we implanted the scaffolds subcutaneously in rats. The retrieval was performed at different time-points. Host response to the implants was assessed by daily observation of the area where the implants were placed and during retrieval. No immunosuppressive drugs were administered. Neovascularization of the explanted specimen comprising the scaffold and the integrated host tissue was evaluated by micro-CT and histological analyses (Fig.1 and 2).

III. Results

Cell adhesion assay showed a high in vitro biocompatibility of the two scaffolds. Confocal microscopy analysis showed cells with well-developed cytoskeleton and defined nucleus throughout the two constructs.

In contrast, scaffolds behaviour in the preclinical context was completely different. Alginate scaffolds induced a strong inflammatory reaction in the host tissue (Fig. 3). The retrieved constructs were surrounded by a thick fibrotic capsule. Sometimes signs of intra-capsular haemorrhage were also detected.

PCL scaffolds, instead, resulted perfectly integrated into the host tissue without any signs of inflammation (Fig. 3).

.

IV. Conclusion

In conclusion, the results reported in this study suggest that PCL scaffolds composed of sintered microspheres are reliable candidates for tissue regeneration in view of the high degree of biocompatibility and vascular invasion revealed in the preclinical setting. We plan to perform further experiments with bioactivated scaffolds to guide neoangiogenesis both spatially and temporally.

References

[1] Auger FA. at al. *The pivotal role of vascularization in tissue engigneering. Annu*. Rev. Biomed. Eng. 2013. 15:177-200.

[2] Lamalice L, Le Boeuf F, Huot J..*Endothelial cell migration during angiogenesis*. Circ Res. 2007 ;100(6):782-94.

[3] Zarana S. Patel and Antinios G. Micos*, Angiogenesis with biomaterial-based drug- and cell-delivery J. Biomater. Sci. Polymer Edn, Vol. 15, No. 6, pp. 701–726 (2004).*

[4] Christopher X. F. L, Dietmar W. Hutmacher, J-T, Woodruff M., *Evaluation of polycaprolactone scaffold degradation for 6 months in vitro and in vivo*. Wiley InterScience 10.1002/jbm.a.32052.

[5] Sosnik A. *Alginate Particles as Platform for Drug Delivery* by the Oral Route: State-of-the-Art. ISRN Pharm. 2014 Apr 9;2014:926157.

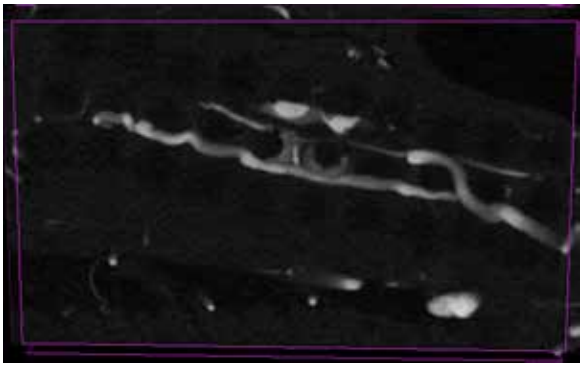

Fig. 1. MicroCT image showing the vascular invasion of a PCL scaffold after retrieval. Vessels correspond to structures in white.

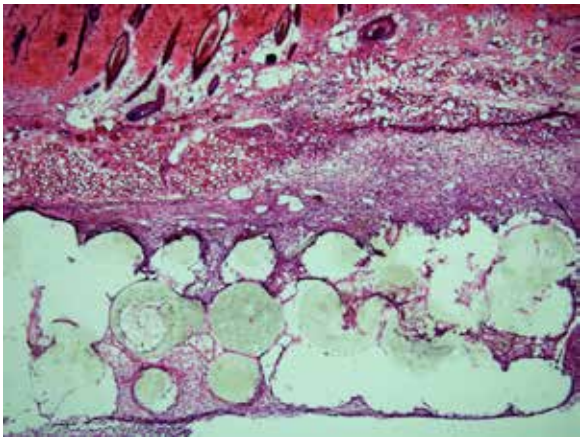

Fig. 2. Hematoxylin-Eosin staining of an explanted PCL scaffold displaying the high degree of construct

Fig. 3. Pictures of the two scaffolds after retrieval. Alginate scaffold surrounded by a thick fibrous tissue (panel on the left)and PCL scaffold free of capsule (panel on the right).

Design of Nanoparticle Probe for MRI Detection of Atherosclerotic Plaques

F. De Sarno[1,2], P. A. Netti[1,2,3], E. Torino[2,3]
[1] Department of Chemical Engineering, Materials and Industrial Production, University of Naples Federico II, Naples 80125, Italy
[2] Istituto Italiano di Tecnologia, Center for Advanced Biomaterials for Healthcare IIT@CRIB, Naples 80125, Italy
[3] Interdisciplinary Research Center on Biomaterials, University of Naples Federico II, Naples 80125, Italy

***Abstract*— Inflammation is a pivotal process in atherosclerosis development and progression, but the underlying molecular mechanisms remain largely obscure.**

The current focus of cardiovascular medicine is to identify critical cellular and molecular mechanisms of atherosclerotic disease, in order to develop novel preventive strategies.

Unfortunately, the current techniques, based on contrast analysis, do not inform specifically on the active cellular and molecular processes that drive the evolution of atherosclerotic lesions. We therefore need additional approaches to detect and prevent the atherosclerotic plaques' formation in patients at high risk for clinical events.

The nanotechnology has the potential to overcome the disadvantages of the current diagnosis of atherosclerosis by the formation of nanosized assemblies for the earlier detection of atherosclerotic lesions.

Molecular imaging, although promising, faces substantial barriers to achieve clinical utility. Imaging agents dedicated for intraplaque processes, need to achieve access to advanced human lesions. In fact, the ability of molecular imaging to interrogate biological processes rather than anatomical features could provide a new dimension of information in these applications.

In this work, we describe a new molecular probe for Magnetic Resonance Imaging (MRI) application based on nanoparticles engineered and involved in early stage of the atherosclerotic lesion.

***Keywords*— Atherosclerotic plaques, polymeric nanoparticles, molecular imaging, MRI.**

I. INTRODUCTION

Despite recent progress, cardiovascular disorders (CVD), remain a worldwide health challenge. Many of these are related to a progressive, inflammatory and chronic process, better known as atherosclerosis, that damages the medium and large-sized arteries leading to the formation of plaques [1-3]. It is often present symptomatically silent for decades until the occurrence of a major catastrophic clinical event such as coronary artery disease (CAD), leading to acute myocardial infarction (MI) and sudden cardiac death; cerebrovascular disease, leading to stroke [4].

Current imaging techniques, routinely used in cardiovascular medicine, are constantly being optimized to better detect the atherosclerotic plaques, but do not inform specifically on molecular processes associated with plaques[5], such as inflammation that is currently regarded as one of the functional features of plaques.

Magnetic resonance imaging (MRI), a non-invasive imaging modality, offers a potential approach for plaque visualization: excellent spatial resolution at submillimetre level, soft-tissue contrast, and high signal-to-noise ratio, but requires the use of a contrast agent (CA) to show the atherosclerotic plaques clearly [6].

In this scenario, the key challenge for the future is represented by development of non-invasive screening methods for early detection of atherosclerosis, based on nanotechnology and molecular imaging agents that recognize a specific biological process (for example inflammation), generate a strong signal (ideally when recognized by its target), possess favorable pharmacokinetics and biodistribution, and exhibit an excellent safety profile. In particular, a molecular imaging agent (or imaging reporter) typically consists of two components: 1) a detection moiety, such as a contrast agent; 2) a molecule-specific or cell-specific affinity ligand, such as an antibody, peptide, or small molecule.

In this work, we propose the design of a new molecular probe constituted by active molecules (imaging reporter) and hydrophilic polymers, for future production of diagnostic devices to detect pathological biomarkers in human plaque with MRI. They can be injected intravenously (as a common contrast agent) and the signal is created via the interaction between the water signal (proton density) and the magnetic properties, R1 relaxation rate and R2 transverse relaxation rate of the imaged tissues.

.

Materials and Methods

A. Tissue collection

Atherosclerotic plaques were collected from 25 patients undergoing carotid endarterectomy (CEA) for extracranial high-grade internal carotid artery (ICA) stenosis (>50% luminal narrowing). Plaque types were classified on histology according to the modified AHA (American Heart Association) plaque type criteria. Macroscopically normal specimens adjacent to endarterectomized plaques were harvested from patients as controls for MRI and histology. Inflammatory marker on human atherosclerotic plaques was detected and characterized by ex vivo magnetic resonance imaging (MRI) using antibody-conjugated polymeric nanoparticles with confirmatory immunohistochemistry.

B. Sample preparation

The plaque was cut into four sections, each of which was further subdivided into two smaller adjacent sections. One adjacent section was fixed in 4% paraformaldehyde (PFA) at 4 °C for MRI detection and characterization of inflammatory markers, while the other adjacent section was fixed in formalin and embedded in paraffin blocks for

immunohistochemistry. Concomitant immunohistochemistry was performed to correlate MRI data.

C. *Ex vivo MRI*

To explore the potential of molecular MRI probe, ex vivo MRI of human atherosclerotic plaques was performed using a 3 Tesla (Philips Achieva). The sample was placed in a quadrature birdcage coil. Sections adjacent to atherosclerotic plaques was used as controls.

D. *Immunoistochemistry*

The presence of the antigen in tissues by immunohistochemistry was performed in two steps: the first step involves the binding of the primary antibody to the antigen, followed by the detection of the bound antibody by a chromogenic system. The used detection system is based on an enzyme, horseradish peroxidase (HRP), which converts 3,3'-diaminobenzidine (DAB) into a brown product.
A standard microscope is required for the chromogenic detection.

II. Results

This study showed that the degree of inflammation associated with human atherosclerotic plaques could be imaged using antibody-conjugated polymeric nanoparticles by ex vivo MRI. We observed that exists a degree of heterogeneity in the plaque population based on the varying degree of inflammation and inflamed plaques appearing darker than non-inflamed ones. The same result was obtained by immunohistochemical experiments carried out on the collected samples.

III. Discussion and Conclusion

New molecular probe proposed here represents a potential technology in association with MRI capable of visualising plaque features and it could potentially provide clinicians with a novel imaging tool for characterization of atherosclerosis at a molecular level, In fact, our group demonstrated that non-invasive MRI imaging was sufficient to visualise and track the particles.

Furthermore, the identification of novel and specific biomarkers of atherosclerosis might represent future imaging targets able to identify patients developing unstable plaque regions susceptible to rupture, thereby allowing to: (1) accurate risk stratification; (2) prevent or slow down development of atheroma and (3) improve treatment and survival rates of patients.

References

[1] K.J. Moore, I. Tabas, Macrophages in the Pathogenesis of Atherosclerosis, Cell 145(3) (2011) 341-355.
[2] P. Libby, P.M. Ridker, G.K. Hansson, Progress and challenges in translating the biology of atherosclerosis, Nature 473(7347) (2011) 317-325.
[3] W.J.M. Mulder, F.A. Jaffer, Z.A. Fayad, M. Nahrendorf, Imaging and Nanomedicine in Inflammatory Atherosclerosis, Science Translational Medicine 6(239) (2014).
[4] M. Slevin, J. Krupinski, L. Badimon, Controlling the angiogenic switch in developing atherosclerotic plaques: possible targets for therapeutic intervention, Journal of angiogenesis research 1 (2009) 4-4.
[5] T. Quillard, P. Libby, Molecular Imaging of Atherosclerosis for Improving Diagnostic and Therapeutic Development, Circulation Research 111(2) (2012) 231-244.
[6] W.S. Kerwin, X. Zhao, C. Yuan, T.S. Hatsukami, K.R. Maravilla, H.R. Underhill, X. Zhao, Contrast-Enhanced MRI of Carotid Atherosclerosis: Dependence on Contrast Agent, Journal of Magnetic Resonance Imaging 30(1) (2009) 35-40.

Surface modification of chitosan-based hydrogels by interaction with Poly Lactic Acid

E. Dellacasa[1], P. Petrini[2], O. Monticelli[3] and L. Pastorino[1]
[1] *DIBRIS, University of Genoa, Via all' Opera Pia 13, 16145 Genova, Italy*
[2] *CMIC, Politecnico di Milano, Piazza Leonardo da Vinci 32, 20133 Milano, Italy*
[3] *DCCI, University of Genoa, via Dodecaneso 31, 16146 Genova, Italy*

***Abstract*— Chitosan is a biodegradable and biocompatible polysaccharide that has recently aroused interest in the scientific world, in particular because of its great muco-adhesive properties. As regards drug delivery applications, it was found that the release kinetics is greatly influenced by the properties of the starting polymer, as well as the resulting chitosan-based system porosity. For this reason, the modulation of such kinetics represents a goal of strong interest.**

In this work, morphological modification of chitosan based hydrogels (70 µm in diameter), through the adsorption of Poly Lactic Acid (PLA) stereocomplex by the Layer by Layer (LbL) technique, was carried out. The step by step assembly of chitosan/(PDLA/PLLA) enantiomers was monitored by quartz crystal microbalance (QCM), working in air. Chitosan based hydrogels, both untreated and PLA-functionalized, were then fabricated and characterized by FTIR.

***Keywords*— chitosan hydrogels, PLA stereocomplex, LbL technique, drug delivery.**

I. INTRODUCTION

CHITOSAN is a biodegradable and biocompatible polysaccharide that has recently aroused interest in the scientific world, in particular within biotechnology, because of its properties and low cost. It is obtained by the deacetylation of chitin, the most widely diffused polymer in nature after cellulose, present in high concentrations in the cell walls of some fungi and in the shell of many shellfish.

Its amino groups (-NH_2) can be easily protonated, forming an ionic polymeric structure. Such behavior is interesting for LbL technique applications, such as the formation of electrostatic complexes with surfactants or other polyelectrolytes.

Several applications, such as release controlled systems, the encapsulation of drugs and the creation of scaffolds for enzymes or cells immobilization, are possible [1]-[3]. For instance, the use of chitosan for the production of hydrogel based delivery systems results greatly advantageous, due to its muco- and bioadhesive properties and chemical functionalities [4]-[7].

However, one of the main obstacles to the use of chitosan is due to the release kinetics, which is difficult to control [8]. As regards the chitosan microparticles, it was found that the release kinetics is greatly influenced by the properties of the starting polymer, in particular the degree of deacetylation, molecular weight, hydrophilicity, as well as the resulting hydrogel porosity [9].
For this reason, the modulation of such kinetics, through the chitosan properties adaptation, represents a goal of strong interest.

For this purpose, the aim of this work was the morphological modification of chitosan based hydrogels through the adsorption of (PDLA/PLLA) stereocomplex by the LbL technique. The cation-dipole type interaction between chitosan amino group and PDLA carbonyl group was exploited. The hydrogels were obtained by the aerodynamically assisted jetting of chitosan solution into a neutralizing solution.

FTIR measurements were carried out in order to evaluate the effective PLA-functionalization of the hydrogel surfaces.

II. MATERIALS AND METHODS

A. Materials

Chitosan (CHI, medium molecular weight), poly(ethyleneimine) (PEI) and poly(styrenesulfonate) (PSS), sodium hydroxide (NaOH), acetic acid, acetonitrile, ethanol were purchased from Sigma–Aldrich. The average molecular weight of used PDLA and PLLA was 18300 g/mol, with a PDI of 1,49. The water solutions was purified by a Milli-Q system and had a resistance of 18.2 MΩ·cm.

B. QCM measurements

The assembly process onto planar supports was studied by a homemade QCM, with resonance frequency of 10 MHz. . The change in resonance frequency (ΔF) was measured after each assembly step and correlated to the adsorbed polymer mass (Δm) by the following Eq. (1):

$$-\Delta F\ (Hz) = 0.55\ \Delta m\ (ng) \qquad (1)$$

derived from the *Sauerbrey's equation* [10], where A was 0.205 cm^2, ρ_q was 2.648 g/cm^3 and μ_q was $2.947 \cdot 10^{11}$ $g/cm \cdot s^2$.

The crystals were immersed into the aqueous solutions of PEI and PSS (2 mg/ml) for 15 minutes and CHI (2 mg/ml in 0.1 M acetic acid) for 30 minutes, then taken out, rinsed thoroughly with pure water and dried with nitrogen. The (PEI/PSS) precursor layer preceded the deposition of CHI in order to provide a uniformly charged surface. After the CHI layer deposition, the crystal was immersed into acetonitrile solutions of PDLA and PLLA (10 mg/ml) for 20 min at 50 °C. Again, the coated electrodes were rinsed thoroughly with acetonitrile at 50 °C and dried with nitrogen. The deposition steps were repeated until the desired multilayered structure was obtained.

Surface modification of chitosan-based hydrogels by interaction with Poly Lactic Acid

E. Dellacasa[1], P. Petrini[2], O. Monticelli[3] and L. Pastorino[1]
[1] DIBRIS, University of Genoa, Via all' Opera Pia 13, 16145 Genova, Italy
[2] CMIC, Politecnico di Milano, Piazza Leonardo da Vinci 32, 20133 Milano, Italy
[3] DCCI, University of Genoa, via Dodecaneso 31, 16146 Genova, Italy

***Abstract*— Chitosan is a biodegradable and biocompatible polysaccharide that has recently aroused interest in the scientific world, in particular because of its great muco-adhesive properties. As regards drug delivery applications, it was found that the release kinetics is greatly influenced by the properties of the starting polymer, as well as the resulting chitosan-based system porosity. For this reason, the modulation of such kinetics represents a goal of strong interest.**

In this work, morphological modification of chitosan based hydrogels (70 µm in diameter), through the adsorption of Poly Lactic Acid (PLA) stereocomplex by the Layer by Layer (LbL) technique, was carried out. The step by step assembly of chitosan/(PDLA/PLLA) enantiomers was monitored by quartz crystal microbalance (QCM), working in air. Chitosan based hydrogels, both untreated and PLA-functionalized, were then fabricated and characterized by FTIR.

***Keywords*— chitosan hydrogels, PLA stereocomplex, LbL technique, drug delivery.**

I. Introduction

CHITOSAN is a biodegradable and biocompatible polysaccharide that has recently aroused interest in the scientific world, in particular within biotechnology, because of its properties and low cost. It is obtained by the deacetylation of chitin, the most widely diffused polymer in nature after cellulose, present in high concentrations in the cell walls of some fungi and in the shell of many shellfish.

Its amino groups ($-NH_2$) can be easily protonated, forming an ionic polymeric structure. Such behavior is interesting for LbL technique applications, such as the formation of electrostatic complexes with surfactants or other polyelectrolytes.

Several applications, such as release controlled systems, the encapsulation of drugs and the creation of scaffolds for enzymes or cells immobilization, are possible [1]-[3]. For instance, the use of chitosan for the production of hydrogel based delivery systems results greatly advantageous, due to its muco- and bioadhesive properties and chemical functionalities [4]-[7].

However, one of the main obstacles to the use of chitosan is due to the release kinetics, which is difficult to control [8].
As regards the chitosan microparticles, it was found that the release kinetics is greatly influenced by the properties of the starting polymer, in particular the degree of deacetylation, molecular weight, hydrophilicity, as well as the resulting hydrogel porosity [9].
For this reason, the modulation of such kinetics, through the chitosan properties adaptation, represents a goal of strong interest.

For this purpose, the aim of this work was the morphological modification of chitosan based hydrogels through the adsorption of (PDLA/PLLA) stereocomplex by the LbL technique. The cation-dipole type interaction between chitosan amino group and PDLA carbonyl group was exploited. The hydrogels were obtained by the aerodynamically assisted jetting of chitosan solution into a neutralizing solution.

FTIR measurements were carried out in order to evaluate the effective PLA-functionalization of the hydrogel surfaces.

II. Materials and Methods

A. Materials

Chitosan (CHI, medium molecular weight), poly(ethyleneimine) (PEI) and poly(styrenesulfonate) (PSS), sodium hydroxide (NaOH), acetic acid, acetonitrile, ethanol were purchased from Sigma–Aldrich. The average molecular weight of used PDLA and PLLA was 18300 g/mol, with a PDI of 1,49. The water solutions was purified by a Milli-Q system and had a resistance of 18.2 MΩ·cm.

B. QCM measurements

The assembly process onto planar supports was studied by a homemade QCM, with resonance frequency of 10 MHz. . The change in resonance frequency (ΔF) was measured after each assembly step and correlated to the adsorbed polymer mass (Δm) by the following Eq. (1):

$$-\Delta F\ (Hz) = 0.55\ \Delta m\ (ng) \qquad (1)$$

derived from the *Sauerbrey's equation* [10], where A was 0.205 cm^2, ρ_q was 2.648 g/cm^3 and μ_q was $2.947 \cdot 10^{11}$ $g/cm \cdot s^2$.

The crystals were immersed into the aqueous solutions of PEI and PSS (2 mg/ml) for 15 minutes and CHI (2 mg/ml in 0.1 M acetic acid) for 30 minutes, then taken out, rinsed thoroughly with pure water and dried with nitrogen. The (PEI/PSS) precursor layer preceded the deposition of CHI in order to provide a uniformly charged surface. After the CHI layer deposition, the crystal was immersed into acetonitrile solutions of PDLA and PLLA (10 mg/ml) for 20 min at 50 °C. Again, the coated electrodes were rinsed thoroughly with acetonitrile at 50 °C and dried with nitrogen. The deposition steps were repeated until the desired multilayered structure was obtained.

C. Hydrogels fabrication

Chitosan hydrogels were fabricated by aerodynamically-assisted jetting equipment (Nisco Encapsulation Unit VAR J30). Chitosan was dissolved in 0.1M acetic acid, to a final concentration of 1%w/v. The final solution was first filtered by a 1.20 μm syringe filter and then extruded through a conical nozzle, having a diameter of 0.25 mm, at a flow rate of 0.2 ml/min and under 80 mbar pressure. The generated microdroplets were collected into a gelling solution bath (40% H_2O, 60% Ethanol and 2% w/v NaOH) under continuous stirring. The distance from the nozzle to the gelling solution was set at 6 cm. After allowing 30 min for the completion of solidification, the obtained hydrogels were washed 3 times in distilled water by centrifugation (1000 rpm for 5 min) and kept in water until further PLA stereocomplex adsorption.

The assembly of the enantiomeric PDLA and PLLA was accomplished by alternatively suspending the hydrogels in 10 ml of 10 mg/ml PDLA and PLLA solutions in acetonitrile. The suspension was kept at 50 °C for 30 min under slow stirring. After each deposition step, three washings in acetonitrile at 1000 rpm for 5 min followed. The procedure was repeated until six PLA layers were deposited.

D. FTIR measurements

FTIR spectra were recorded on a Bruker IFS66 spectrometer in the range 400-4000 cm^{-1}. A drop of the sample solution was placed onto a glass wafer and dried overnight at room temperature.

III. RESULTS AND DISCUSSION

Figure 1 shows the step-by-step mass growth of the multilayer structure as function of each deposited layer. The (PEI/PSS)/CHI multilayer showed a total mass of 530 ng, where the CHI was found to have a mean adsorbed mass of 154 ng. The total mass of adsorbed PLA layers was found to be 201 ng, with a mean mass of 34 ng per layer. As shown in the graph, the gradual growth of the PLA layers confirmed the successful deposition of the polymers. The increasing linearity of the $(PDLA/PLLA)_3$ multilayer adsorption profile is probably due to the stereocomplex formation between PDLA and PLLA polymers [11].

In order to characterize the hydrogels treated by the LbL technique, some FTIR spectrometry measurements were carried out. The spectra obtained from PLA-functionalized hydrogels, PLLA and untreated hydrogels, are presented in Figure 2. The similarity between the spectra of functionalized hydrogels and untreated ones, in turn identical to the spectrum of chitosan (not shown), is quite evident. This clearly indicates that chitosan is the main component also of the functionalized sample. However, the presence of adsorbed PLA is confirmed by the ester group peak at 1748 cm^{-1} , together with the methine and methyl group peaks, at 2992 and 1264 cm^{-1} respectively. Since the bond between chitosan and PLA is not of covalent nature, but results from a ion-dipole type interaction, the spectra of each substance have not undergone significant changes. Consistent with this observation, the reported spectrum of the functionalized hydrogels is approximated to the sum of the individual spectra of the two components.

IV. CONCLUSION

The experimental results showed a successful fabrication of chitosan-based hydrogels. Superficial morphological changes were obtained by the novel interaction of water-soluble and organic solvent-soluble polymers . The system is then worthy for further studies, related to the modulation of the release rate of encapsulated drug molecules.

REFERENCES

[1] Bernkop-Schnurch A, Dunnhaupt A, European Journal of Pharmaceutics and Biopharmaceutics 2012, 81, 463-469.
[2] Hoffman AS, Advanced drug delivery reviews 2012, 64, 18-23.
[3] Yu L, Ding J, Chemical Society Reviews 2008, 37, 1473-1481.
[4] Anitha A, Sowmya S, Sudheesh Kumar PT, Deepthi S, Chennazhi KP, Ehrlich H, Tsurkan M, Jayakumar R, Progress in Polymer Science 2014,39, 1644-1667.
[5] Mourya VK, Inamdar NN, React Funct Polym 2008, 68, 1013–1051.
[6] Suh JKF, Matthew HWT, Biomaterials 2000, 21, 2589–2598.
[7] Muzzarelli RAA, Carbohydr Polym 2009, 76, 167–182.
[8] Gupta KC, Jabrail FH, Carbohydrate Polymers 2006, 66, 43-54.
[9] Hoare TR., Kohane DS, Polymer 2008, 49, 1993-2007.
[10] Sauerbrey G, Z. Phyz. 1959, 155, 206.
[11] Kakuta M, Hirata M, Kimura Y, Polymer Reviews 2009, 49, 107-140.

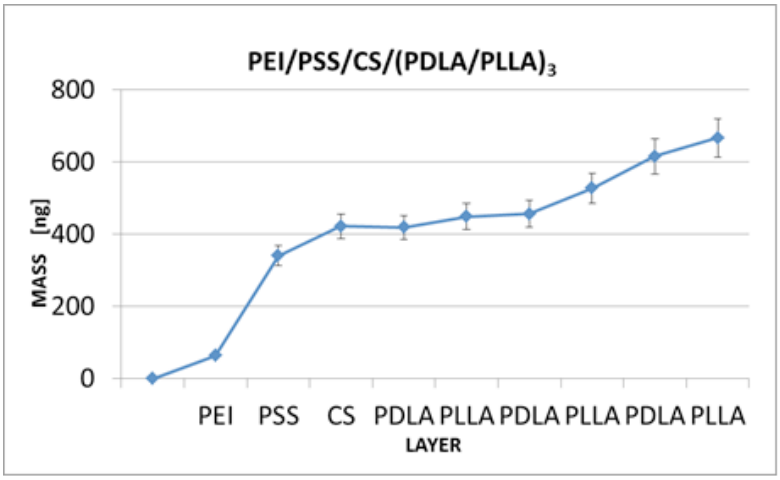

Fig. 1. Mass growth of the CHI/(PDLA/PLLA)$_3$ multilayer structure.

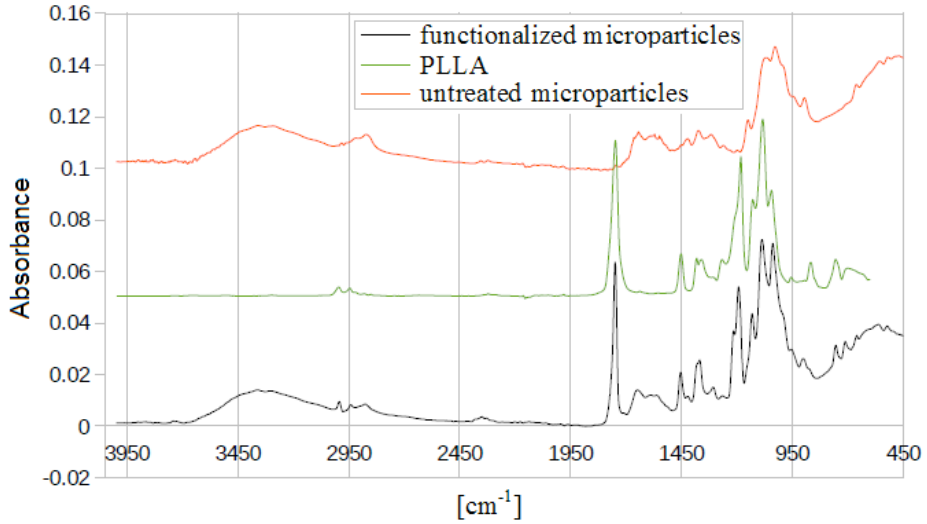

Fig. 2. FT-IR spectra of stereocomplex functionalized microparticles, PLLA and untreated microparticles.

Two different approaches to assess the chitosan scaffold bioactivation for bone tissue engineering

[1]A. Soriente, [1]I. Fasolino, [1*]M.G. Raucci, [2]C. Demitri, [1,3]L. Ambrosio

[1]Institute of Polymers, Composites and Biomaterials – National Research Council of Italy, Naples, Italy.
[2]Department of Engineering for Innovation, University of Salento, Lecce, Italy.
[3]Department of Chemicals Science and Materials Technology - National Research Council of Italy, Rome, Italy.

Abstract - **Our aim was to develop a biomimetic chitosan-based scaffold using two different approaches based on the combination of inorganic and organic components. These types of scaffold modifications provide the biochemical cues for promoting stem cell osteogenic commitment. The first approach is based on the use of a sequence of 20 amino acids corresponding to a 68-87 sequence in knuckle epitope of BMP-2 that was coupled covalently to the carboxyl group of chitosan scaffold. Meanwhile, the second approach is based on the biomimetic approach which allows the formation of hydroxyapatite deposits on the scaffold surface, improving the cell recognition of the polymeric scaffold. The results demonstrate that the presence of bioactive signals on the scaffold surface allows obtaining an osteoinductive effect on hMSC in a basal medium, making the modified chitosan scaffolds a promising candidate for bone tissue regeneration.**

***Keywords*—chitosan, scaffold, BMP-2 peptide, biomimetic treatment, hMSC differentiation.**

I. INTRODUCTION

Current tissue engineering strategies are focused on the restoration of pathologically altered tissue architecture by transplantation of cells in combination with supportive scaffolds and biomolecules. In recent years, considerable attention has been given to chitosan (CS)-based materials and their applications in the field of orthopedic tissue engineering [1-3]. Interesting characteristics such as a minimal foreign body reaction, an intrinsic antibacterial nature, and the ability to be molded in various geometries and forms like porous structures suitable for cell ingrowth and osteoconduction, make chitosan appropriate for this purpose [4]. Due to its favorable gelling properties chitosan can deliver morphogenic factors and pharmaceutical agents in a controlled fashion. Among all the properties, its chemical structure (which includes three types of reactive functional groups, an amino group as well as both primary and secondary hydroxyl groups at the C(2), C(3), and C(6) positions respectively) is the feature that allows modification of chitosan like graft copolymerization for specific applications [5]. Furthermore, these chemical groups allow many possibilities for covalent and ionic modifications that are an improvement of biological properties and also to obtain biomimetic scaffolds that induce regeneration of bone tissue [6,7]. For this purpose, biomimetic functional scaffolds can be developed by modifying scaffolds with bioactive components including inorganic particles and osteogenic growth factors/peptides and by incorporating these components into the scaffolds. These types of direct and indirect scaffold modifications provide biochemical cues for promoting stem cell osteogenic commitment.

Here, we reported the possibility to compare two different approaches based on inorganic and organic bioactive signals used to obtain biomimetic chitosan scaffolds.

II. MATERIALS AND METHODS

Chitosan scaffolds were prepared by using a foaming method based on physical foaming combined with microwave curing [8]. In the first step of the process, a stable physical foaming was induced using a surfactant (i.e. Pluronic) as blowing agent of a homogeneous blend of Chitosan (CS) and Polyethylene glycol diacrylate (PEGDA700) solutions. In the second step, the porous structure of the foaming was chemically stabilized by radical polymerization induced by homogeneous heating of the sample in a microwave. In this step2,2-Azobis[2-(2-imidazolin-2yl)propane]Dihydrochloride was used as thermoinitiator (TI). The porous structure of the foaming was chemically stabilized by radical polymerization induced by heating of the sample in a microwave (MTS 1200 Mega, Milestone Inc., Shelton, CT 06484). Some of the resulting samples were washed in acetone to evaluate the possible removal of unreacted PEGDA, and dried in a vacuum oven at 45°C. The samples were analysed without any further modification.

The biomimetic scaffolds were obtained by using two different approaches based on inorganic and organic compounds, respectively. The first one was based by treating the scaffolds with a supersaturated SBF solution (5SBF); the treatment is able to create an hydroxyapatite coating on the surface and into the porous wall in few days (7days). The second approach is based by using a bioactive peptide of Bone Morphogenetic Protein (BMP-2). The 67-87 residue of the "knuckle" epitope of hBMP-2 (NSVNSKIPKACCVPTELSAI) was synthesized by microwave-assisted Fmoc solid phase peptide synthesis (SPPS). The physicochemical, morphological and mechanical properties of materials, before and after treatments, have been evaluated. Furthermore, biological analysis by using hMSC cells to estimate the effect of the two different biomimetic approaches on cellular behaviour were performed.

III. RESULTS AND DISCUSSION

In bone tissue engineering the scaffold should provide the necessary support as artificial extracellular matrix, allowing cells to proliferate and maintain their differentiated functions [9]. On this basis, the aim of this work was to develop

biomimetic functional scaffolds by modifying polymer scaffolds with osteoinductive, bioactive signals including inorganic components like hydroxyapatite nanoparticles and osteogenic peptide and by incorporating these components into the scaffolds in order to provide biochemical cues for promoting stem cell osteogenic commitment. The possibility to perform a covalent immobilization of peptide on the scaffolds with and w/o biomineralization treatment determines a low percentage of burst release in the first 48hrs; while at long time, an important achievement was obtained by a prolonged release up to 4 weeks with an important effect on cellular behaviour. *In vitro* degradation tests showed a gradual dissolution of the foam over time, but maintaining their 3-D morphology and integrity even after 6 weeks of incubation (data not shown) allowing also an extended release of organic bioactive signal. This behaviour is a promising aspect in order to obtain a good infiltration of cells and the new tissue formation. In fact, the biological results demonstrated that the materials act as support for the hMSCs adhesion and proliferation. In this work, the expression of ALP and OCN were analyzed; in particular it was observed that at 3 and 7days no difference was observed among the group of bioactivated scaffold and 80CS20P. Meanwhile, at 14days the best expression of ALP for the 80CS20P_BMP scaffold was observed, where the peptide release of about 65-75% (12-14µg) was obtained. This behaviour was also observed at long time explaining how the interaction of peptide with the specific receptor on the cellular membrane has great effect on the hMSC differentiation in the osteoblast phenotype. Instead, biomineralized scaffold developed through biomimetic treatment (80CS20P_bio) showed a similar behaviour of 80CS20P_BMP in the first 7days, while at day 14 the ALP level was lower than 80CS20P_BMP continuing until day 21. The same behaviour was observed also for Osteocalcin expression (OCN) that the highest level was observed for scaffold with BMP2 mimic-peptide at day 21. Instead, no synergic effect was observed for the bioactivated scaffolds with both bioactive signals. However, scaffold with the single signal showed better effects on hMSC behaviour in terms of proliferation and osteogenic differentiation in basal medium by the expression of early and later signals of osteogenic differentiation then the no-biomimetic scaffold.

IV. Conclusion

This study has demonstrated the possibility to generate biomimetic structures with an highly interconnected and homogeneous structure with pores of different size from about 20 µm to 300 µm in agreement with the dimensional characteristics required for bone regeneration scaffold. The presence of bioactive signals on the scaffold surface allows to obtain an osteoinductive effect on hMSC, making chitosan a promising candidate scaffold material for bone tissue regeneration.

Acknowledgement

This study has received funding from the PNR-CNR Aging Program 2012-2014. The authors also thank Mrs. Cristina Del Barone for facilitating microscopy analysis and Mrs Stefania Zeppetelli for supporting of biological investigations.

References

[1] R. Jayakumar, N. Nwe, S. Tokura, H. Tamura, Sulfated chitin and chitosan as novel biomaterials", *International Journal of Biological Macromolecules*, 2007;40:175–181.

[2] Y. Li, X.G. Chen , N. Liu, C.S. Liu, C.G. Liu, X.H. Meng, L. Jun Yu, J.F. Kenendy, "Physicochemical characterization and antibacterial property of chitosan acetates" *Carbohydrate Polymers*, 2007;67:227–232.

[3] S. Bhaskara Rao and C.P. Sharma, "Use of chitosan as a biomaterial: Studies on its safety and hemostatic potential", *Journal of Biomedical Materials Research*, 1997; 34:21–28.

[4] D.W. Hutmacher, "Scaffolds in tissue engineering bone and cartilage", *Biomaterials*, 2000;21:2529-2543.

[5] C.K.S. Pillai, W. Paul, C.P. Sharma, "Chitin and chitosan polymers: Chemistry, solubility and fiber formation", *Progress in Polymer Science*, 2009;34(7):641-678.

[6] M.G. Raucci, M.A. Alvarez-Perez, S. Meikle, L. Ambrosio, M. Santin, "Poly(Epsilon-Lysine) Dendrons Tethered with Phosphoserine Increase Mesenchymal Stem Cell Differentiation Potential of Calcium Phosphate Gels", *Tissue Engineering Part A*. 2014;20(3-4):474-485.

[7] X. Yang, R.S. Tare, K.A. Partridge, H.I. Roach, N.M. Clarke, S.M. Howdle, K.M. Shakesheff, R.O. Oreffo, "Induction of Human Osteoprogenitor Chemotaxis, Proliferation, Differentiation, and Bone Formation by Osteoblast Stimulating Factor-1/Pleiotrophin: Osteoconductive Biomimetic Scaffolds for Tissue Engineering" *Journal of Bone and Mineral Research*, 2003;18: 47–57.

[8] C. Demitri, A. Giuri, M.G. Raucci, D. Giugliano, M. Madaghiele, A. Sannino, L. Ambrosio, "Preparation and characterization of cellulose-based foams via microwave curing", *Interface focus,* 2014;4(1):20130053.

[9] A.R. Amini, C.T. Laurencin, S.P. Nukavarapu, "Bone Tissue Engineering: Recent Advances and Challenges", *Critical Reviews in Biomedical Engineering,* 2012;40(5): 363–408.

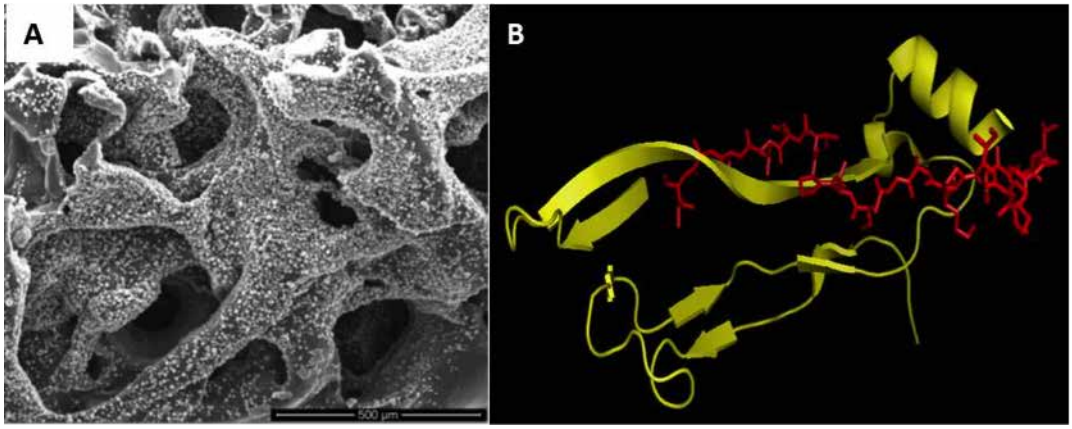

Fig. 1. (A) SEM image of biomineralized CS scaffold after 7days of biomimetic treatment; (B) 3D structure of hBMP-2, residue 283-396; in red, BMP-2 peptide

Azopolymer brushes as tunable cell-instructive materials

C. Fedele,[1,2] R. H. Kollarigowda,[1,2] S. Cavalli*[1] and P. A. Netti*[1,2]
[1] Center for Advanced Biomaterials for Healthcare, IIT@CRIB, Largo Barsanti e Matteucci 53, 80125 NA IT
[2] Department of Chemical, Materials and Industrial Engineering, Univ. Federico II, P.le Tecchio 80, 80125 NA IT
*To whom the correspondence should be addressed: nettipa@unina.it and silvia.cavalli@iit.it

***Abstract*—"Dynamic biointerfaces" are engineered surfaces that are able to modify in a predictable spatiotemporal manner the cell-material crosstalk, overcoming the limitations of static conventional biomaterials. In our work, azobenzene-containing photosensitive polymer brushes are synthesized using a controlled radical polymerization method in order to obtain patterned substrates using Lloyd's mirror photolithographic technique. An ultrasonication treatment allowed to erase the pattern, even in presence of adherent cells. Interestingly, cells seeded on these substrates showed orientation in the pattern direction and stability to the erasure process, envisioning the possibility to use these surfaces as cell-instructive biomaterials.**

***Keywords*— Azopolymer Brushes, Lloyd's mirror, Cell-instructive materials, Stimuli-responsive polymers.**

I. Introduction

"Dynamic biointerfaces" are conceived in order to be able to modify in a predictable spatiotemporal manner the cell-material crosstalk, overcoming the limitations of static conventional biomaterials [1],[2]. In order to obtain this feature, the implementation of stimuli-responsive polymers emerges as a smart way to mimic the continuous remodeling of the extracellular matrix in living systems [3].

The topographical cue on a biomaterial surface plays a significant role in the guidance of cell orientation and migration and its dynamic control can open up new strategies to develop innovative cell-instructive materials (CIMs) [4]. Among available stimuli, light as external trigger is particularly interesting because it entails several advantages such as limited chemical contamination, ease of operation and spatiotemporal precise localization of the stimulus itself.

Azobenzene-based polymers are well-known photoresponsive systems extensively used in photonic applications, but in the last decade they have been implemented also at the interface with biology [5]-[9]. In fact, azopolymers can provide an original tool for photocontrolled cell behavior studies since they can be patterned at the micro and nano scale using photolithographic techniques, such as Lloyd's mirror method [5],[10]. This system leads to the so-called surface relief grating (SRG) formation, a reproduction on the polymer surface of the interference pattern of light as a sinusoidal modulation of its thickness due to the azobenzene *trans-cis* reversible isomerization process, induced by light.

Our interest was to use for the first time these photopatterned azopolymer brushes to manipulate cell behavior and orientation instead of using spin-coated azopolymer films, thus exploiting the unique behavior of azobenzene-based materials coupled to the stability of a grafted macromolecular layer.

Moreover in this work, we used ultrasonication as mechanical stimulation over azopolymer brushes in order to disrupt the aggregation between azobenzene pendant groups, thus succeeding in the erasure of the pattern. In this way, these platforms become a new mean of patternable, erasable and reconfigurable surfaces to be used as cell-instructive materials. Finally, cells seeded on these substrates aligned along the pattern direction and resulted viable upon the erasure process, paving the way to use of these surfaces as cell-instructive biomaterials.

II. Materials and Methods

A. Synthesis of azopolymer brushes

In-house synthesized azobenzene monomer was polymerized by Reversible Addition-Fragmentation Chain Transfer (RAFT) radical polymerization technique to obtain polymer brushes sample represented in Figure 1 A and 1 D.

B. Surface Relief Gratings inscription

A 442 nm laser was used in a Lloyd's mirror configuration in order to project an interference pattern of light on the azopolymer brushes, inducing SRG formation. The pattern was analyzed with Atomic Force Microscopy (AFM).

C. Cell culture

Human umbilical vein endothelial cells (HUVEC) were cultured in gelatin-coated flasks in an incubator at 37 °C and humidified atmosphere with 5% of CO_2 and then seeded onto patterned azopolymer brushes. After 24 hours cells were imaged with either an inverted microscope or a confocal.

D. Ultrasonication procedure

Azopolymer brush glass substrate was kept in a flask with water and sonicated for 10 minutes at room temperature (or at 37 °C when the cells were present). The substrate was washed and dried in a vacuum oven for 24 hours. After that, the sample was characterized by AFM (Figure 1A).

III. Results and Discussion

Firstly, an in-house synthesized derivative of a well-known azobenzene used as monomer was prepared. Then, azopolymer brushes were synthesized by RAFT polymerization following the "grafting from" approach, resulting in a 150 nm thick layer as measured by ellipsometry. RAFT polymerization is one of the finest synthetic approaches to get polymers with a narrow polydispersity index (PDI), allowing generation of dense assemblies of macromolecules with further modifiable chain

end-functions exposed at the interface [11],[12].

The topography of azopolymer brushes was investigated by atomic force microscopy (AFM) showing a uniform distribution of the brushes on the glass surface (Figure 1 A). Moreover, we characterized the chemical composition of these azopolymer brushes using Raman spectroscopy , XPS and UV/Vis spectrophotometry, confirming the presence of azobenzene uniformly distributed over the substrate.

For what concerns the SRG inscription Lloyd's mirror setup was used. With this technique azobenzene moieties of the polymer brushes were excited with an interference pattern of a 442 nm wavelength laser. In order to obtain the highest pattern modulation possible, we tuned the orientation of linear polarized light (LPL) and illumination time increasing the pattern height up to 60 nm in 2 hours, as shown in Figure 1 B. The pattern pitch was 2.5 μm, as given by $2d=\lambda \cdot \sin(\vartheta)$, where λ is the laser wavelength and ϑ is the angle between the incident beam and the mirror. Additionally, a beam from a 632 nm laser was used for a real-time control of the inscription process by monitoring the diffraction efficiency of the inscribed grating.

So far, patterns on azopolymer brushes have not been erased, neither thermally, using circularly polarized light or by solvent treatment, thus not allowing a real "on-off" switching between patterned and flat configurations of these platforms [13],[14]. In this work we found that ultrasonication in water at room temperature was significant to erase the pattern (Figure 1 C) distorting the aggregation of polymer brushes. The summary of pre and post erasure is shown as graphical representation in Figure 1 D. The entire writing-erasing cycle was repeated more than three times and the results were consistent.

Further, our brushes were found biocompatible by seeding human umbilical vein endothelial cells (HUVECs), which are known to be quite sensitive to surface topography. Most of the cells were aligned along the grooves as can be seen in Figure 2 A and 2 B.

Also in presence of adherent HUVECs on azopolymer brushes (Figure 3 A) the pattern erasure method using mechanical stimulation resulted effective and not harmful. In fact, after 10 minutes of sonication cells were completely detached from the substrate (Figure 3 B), but, after an overnight incubation, cells adhered again (Figure 3 C). This experiment proves their viability and, thus, the feasibility of this procedure in presence of cells.

IV. Conclusion

The work reported here described the design and synthesis of new azopolymer brushes for the formation and erasure of micro-scale surface relief gratings (SRGs). From these preliminary results we envision the possibility to use such polymer brushes as erasable and rewritable interfaces to control cell fate using mild conditions.

Acknowledgement

We thank the group of Prof. Pietro Ferraro (Mr. Alejandro Calabuig, Dr. Vito Pagliarulo) of the ISASI@CNR for their essential contribution in the Lloyd's mirror illumination experiments. Dr. Carmela Rianna is acknowledged for her helpful support in the polymer brushes synthesis and characterization with AFM.

References

[1] G. Wu; P. Li; H. Feng; X. Zhang; P. K. Chu "Engineering and functionalization of biomaterials via surface modification" *Journal of Materials Chemistry B* 2015, 3, 2024.

[2] M. Ventre; P. A. Netti "Engineering Cell Instructive Materials to Control Cell Fate and Functions Through Material Cues and Surface Patterning" *ACS applied materials & interfaces* 2016.

[3] L. Moroni; M. K. Gunnewiek; E. M. Benetti "Polymer brush coatings regulating cell behavior: Passive interfaces turn into active" *Acta biomaterialia* 2014, 10, 2367.

[4] R. Singhvi; G. Stephanopoulos; D. I. Wang "Effects of substratum morphology on cell physiology" *Biotechnology and bioengineering* 1994, 43, 764.

[5] K. G. Yager; C. J. Barrett "All-optical patterning of azo polymer films" *Curr. Opin. Solid State Mater. Sci.* 2001, 5, 487.

[6] R. Barille; R. Janik; S. Kucharskic; J. Eyer; F. Letournel "Photo-responsive polymer with erasable and reconfigurable micro- and nano-patterns: An in vitro study for neuron guidance" *Colloids Surface. B* 2011, 88, 63.

[7] A. A. Beharry; G. A. Woolley "Azobenzene photoswitches for biomolecules" *Chem. Soc. Rev.* 2011, 40.

[8] A. S. Arri Priimagi "Azopolymer-Based Micro- and Nanopatterning for Photonic Applications" *J. Polym. Sci. Pol. Phys.* 2013, 52, 163.

[9] N. Hurduc; B. C. Donose; A. Macovei; C. Paius; C. Ibanescu *et al.* "Direct observation of athermal photofluidisation in azo-polymer films" *Soft matter* 2014, 10, 4640.

[10] H. Baac; J.-H. Lee; J.-M. Seo; T. H. Park; H. Chung *et al.* "Submicron-scale topographical control of cell growth using holographic surface relief grating" *Mater. Sci. Eng. C Mater. Biol. Appl.* 2004, 24, 209.

[11] J. Chiefari; Y. Chong; F. Ercole; J. Krstina; J. Jeffery *et al.* "Living free-radical polymerization by reversible addition-fragmentation chain transfer: the RAFT process" *Macromolecules* 1998, 31, 5559.

[12] G. Moad; Y. Chong; A. Postma; E. Rizzardo; S. H. Thang "Advances in RAFT polymerization: the synthesis of polymers with defined end-groups" *Polymer* 2005, 46, 8458.

[13] N. Lomadze; A. Kopyshev; J. r. Rühe; S. Santer "Light-Induced Chain Scission in Photosensitive Polymer Brushes" *Macromolecules* 2011, 44, 7372.

[14] C. Schuh; N. Lomadze; J. r. Rühe; A. Kopyshev; S. Santer "Photomechanical degrafting of azo-functionalized poly (methacrylic acid)(PMAA) brushes" *J. Phys. Chem. B* 2011, 115, 10431.

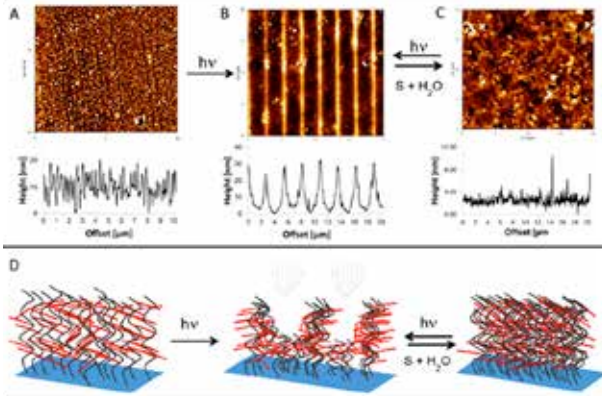

Fig. 1. AFM images of (A) before and (B) after Lloyd's mirror illumination of azopolymer brushes. (C) AFM image of erased pattern by sonication. (D) Graphical representation of azopolymer brushes before and after illumination by Lloyd's mirror method and deleted pattern by sonication (S + H_2O means sonication in water).

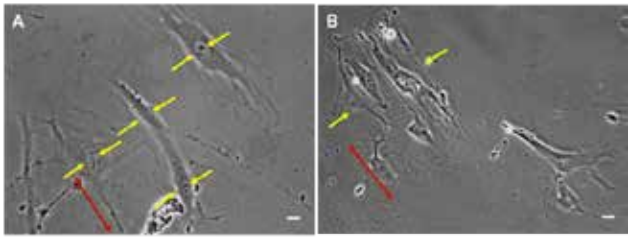

Fig. 2. (A) and (B) represent the phase contrast images (40x and 20x magnification respectively) of HUVECs on patterned azopolymer brushes after 24 hours incubation. Yellow arrows represent cells at the nuclear region while red arrows indicate pattern direction. Interestingly, most of the cells aligned along the underlying pattern.

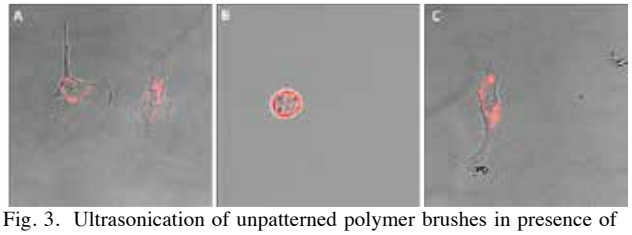

Fig. 3. Ultrasonication of unpatterned polymer brushes in presence of cells. 40x images of (A) adherent HUVECs on unpatterned polymer brushes, (B) a single cell after 10 minutes of sonication in water. (D) 40x image of a sonicated cell after an overnight incubation. Cells were stained with a vital cell tracker

Receptor quantification on cell lines: a new methodology based on the energetics of interactions

Teresa Fotticchia[1], Iolanda Fotticchia[2], Daniela Guarnieri[1], Andrea Patrizia Falanga[1], Raffaele Vecchione[1,3], Concetta Giancola[2], Paolo Antonio Netti[1,3].

[1] *Istituto Italiano di Tecnologia (IIT)@CRIB, Largo Barsanti e Matteucci 53, 80125 Naples, Italy*

[2] *Dipartimento di Farmacia, Università di Napoli Federico II, via Domenico Montesano 49, 80131 Naples, Italy*

[3] *Centro di Ricerca Interdipartimentale sui Biomateriali (CRIB), Università Federico II, P.le Tecchio 80, 80125 Naples, Italy*

A new methodology based on Isothermal Titration Calorimetry (ITC) coupled with confluent cell layers cultured around biocompatible templating microparticles was developed in order to identify the receptor overexpression on different cell lines (Fig.1). Starting from Transferrin receptors quantification on mouse brain endothelial cells (bEnd3) and primary human umbilical vein cells (HUVEC), this rapid and reliable methodology allows to gain important information to address drug design and selectively deliver therapeutics that can cross biological barriers such as the Blood-Brain Barrier.

***Keywords*: Isothermal Titration Calorimetry, Transferrin receptor, Blood Brain Barrier.**

I. INTRODUCTION

Receptor mediated Transport (RMT) relies on biological signaling for the cellular uptake of molecules [1]. This mechanism is widely used to promote drug passage through cells or a layer of cells such as the blood brain barrier (BBB). By conjugating the drug or the drug carrier to a molecule that recognizes the overexpressed receptor on the BBB, cellular uptake of molecules can be encouraged [2-3].

To identify the overexpressed receptors in each district and design the drug targeting for a desired site, it is of fundamental importance to characterize the cell membrane. Until now, several studies based on the conventional analytical methods mainly involving fluorescence (i.e. immunofluorescence microscopy, flow cytometry and immunohistochemistry), aimed to the quantification of receptors [4]. However, most of the developed assays provide only a comparative assessment of protein level, rather than absolute quantification. Herein, we propose a new methodology based on Isothermal Titration Calorimetry (ITC) coupled for the first time with confluent cell layers cultured around biocompatible templating microparticles to calculate the number of transferrin receptors (TfRs) onto cell membranes and study the energetics of their interaction with the Tf. Our study represents a new launch pad for an efficient delivery of potential therapeutical drugs that can cross biological barriers.

II. MATHERIALS AND METHODS

Cell culture

bEnd3 cells were maintained in Dulbecco′s Modified Eagle′s Medium (DMEM). HUVEC cells were cultured in Medium-200. Cells were grown at 37 °C and 5 % CO_2.

Cell seeding on Cytodex microspheres

2 ml of Dextran microcarrier beads (Cytodex, 67-80 μm) (5 mg/ml in cell culture medium) were transferred into each well of a low attachment 6-well plate. 8×10^5 cells in 100 μl of cell culture medium were added to the Cytodex in the well. The 6-well plate was kept under stirring at 80 rpm overnight in incubator at 37 °C and 5 % CO_2. The number of cells actually seeded on the microbeads was verified by counting with the Neubauer chamber. Cytodex with adhered cells were collected and cells were fixed with 4 % paraformaldehyde for 10 min before ITC analysis.

Immunofluorescence analysis

TfR expression on cell membrane was evaluated by indirect immunofluorescence. Cells were fixed with 4% paraformaldehyde and incubated overnight at 4 °C with anti-transferrin receptor polyclonal primary antibodies. Then, cells were incubated for 1 h, at RT with anti-rabbit secondary antibodies Alexa-488. Cell nuclei were stained with 4',6-diamidino-2-phenylindole blue nuclear dye (DAPI). Samples were loaded on a glass slide and detected by confocal microscope (MP Leica TCS SP5) equipped with a 63 × oil immersion objective.

Isothermal titration calorimetry (ITC)

ITC experiments were performed by Nano ITC Low Volume with a cell volume of 170μl. The sample vessel was loaded with bEnd3 or HUVEC cells cultured on Cytodex microbeads in PBS buffer solution, Tf instead was loaded into the computer-controlled microsyringe in the same buffer conditions. The titration experiments were carried out at 298 K, 10 injections of 5 μl of Tf solution were added to the vessel containing the cells cultured on Cytodex microbeads, every 250 s. All the measurements were conducted at a continuous stirring rate of 250 rpm. Tf 1μM was added to a solution of 1.8×10^6 bEnd3 cells/ml, and Tf 0.1 μM was added to a solution of 5.6×10^6 HUVEC cells/ml. The calorimetric enthalpy for each injection was calculated after correction for the heat of Tf dilution, the area under raw data peaks was integrated to give a plot of enthalpy change per mole of injectant (Tf) against the number of TfRs per cell.

The obtained plot was fitted by the analysis software of the instrument (NanoAnalyze software, version 2.4.1).

Enthalpy change ($\Delta_b H°$), binding constant (K_b), and number of binding sites (n) were obtained by fitting with an equivalent and independent binding sites model. $\Delta_b G°$ and $T\Delta_b S°$ were calculated using the typical equations of thermodynamics.

III. RESULTS AND DISCUSSION

Through indirect immunofluorescence microscopy, TfR expression levels were firstly evaluated on two different endothelial cell lines, bEnd3 and HUVEC. The choice was made on the bases of their potential expression level of TfR. The preliminary data indicated that the TfR expression in bEnd3 cells is higher than that in HUVEC cells.

Starting from these preliminary results, we optimized the procedure of cell seeding on Cytodex microspheres. The Cytodex system allowed a higher number of cells in a small volume maintaining the correct morphology of adherent cells compared to cell suspensions obtained upon trypsin treatment. At this stage, ITC experiments were performed to monitor the binding between Tf and TfRs present on the cell membrane basically measuring the heat released upon molecular interactions. The complete thermodynamic profile of interaction was obtained by the binding curve realized. The number of TfRs/cell was calculated considering the Tf moles necessary to saturate all the TfRs present in the sample and dividing by the number of loaded cells. The evaluation of the TfR number on cells by ITC, gained by the specific interaction between Tf and TfR, is very important to overcome the problem of nonspecific interactions that could occur when an excess of Tf is added.

This inconvenience is a typical aspect of the conventional analytical methods conducted adding an excess of Tf to the cell culture and then removing the unbinding molecules by washing [5]. In Fig. 2 and Fig. 3 are shown the ITC experiments, performed by using bEnd3 and HUVEC cells, respectively, cultured on Cytodex microbeads. As shown in Table 1, ITC experiments revealed that the binding reaction between Tf and TfR on bEnd3 and HUVEC cells was exothermic, the interaction is enthalpically driven accomplished by an unfavorable entropic contribution to Gibbs energy.

TABLE I

	n	Kb (M^{-1})	ΔH° (kJmol-1)	TΔS° (kJmol-1)	ΔG° (kJmol-1)
bEnd	$(2.7\pm0.3)\ 10^7$	$(2.7\pm0.5)\ 10^8$	-794±190	-746±186	-48 ± 3
HUVEC	$(4.5\pm0.4)\ 10^5$	$(2.3\pm0.4)\ 10^8$	-575±100	-528 ± 92	-47 ± 3

Thermodynamic parameters of the interaction between Tf protein and TfR on bEnd3 and HUVEC cells cultured on Cytodex microbeads.

Anyway, in both systems, the enthalpic contribution is favorable and counterbalanced by the unfavorable entropy to Gibbs energy. Consequently, the Gibbs energy is around values of a few tens of kJ mol^{-1}. The binding constant between Tf and TfR is the same and very high in both systems revealing a very good affinity, conversely the value of TfRs/cell reveals a 100-fold increase in the number of TfRs per bEnd3 cells compared to HUVEC cells. ITC experiments were also performed by injection of Tf into free bEnd3 cells in solution without Cytodex microbeads. They showed irresolvable binding isotherm, with scattered points, preventing the evaluation of the thermodynamic parameters. These findings confirmed the strength of the experiments performed on bEnd3 and HUVEC cells cultured on Cytodex microbeads. Further, thanks to the use of Cytodex, it was possible to calculate the number of receptors for a continuous layer of cells that mimic a near-physiological system, such as BBB.

IV. CONCLUSION

Through this methodology, a significant advancement in the quantification of cell membrane receptors is obtained allowing a study on the energetics of interaction between a receptor on the cell membrane and its ligand. In this study, we propose a new assay based on Isothermal Titration Calorimetry coupled with cell layers cultured around biocompatible templating microparticles to quantify TfR expression in two different kinds of endothelial cells. The developed methodology is based on a direct measurement of the number of receptors on the cell membrane together with a detailed analysis of the energetics of interaction, providing complete information on receptor overexpression in near-physiological conditions. This study represents a break through for the design of new active drug targeting to specific tissues, and sheds light on the emerging field of nanotechnology.

ACKNOWLEDGEMENT

This work was supported by National Operative Program "Research and Competitiveness 2007-2013" (Pon a3_00173 - CeSmeMo).

REFERENCES

[1] K.E. Parrish, J.N. Sarkaria, W.F. Elmquist. *Improving Drug Delivery to Primary and Metastatic Brain Tumors: Strategies to Overcome the Blood-Brain Barrier.* Clin Pharmacol Ther, 97 (2015) 336-346.

[2] I. van Rooy, E. Mastrobattista, G. Storm, W.E. Hennink, R.M. Schiffelers. *Comparison of five different targeting ligands to enhance accumulation of liposomes into the brain*. J Control Release, 150 (2011) 30-36.

[3] J.M. Lajoie, E.V. Shusta. *Targeting Receptor-Mediated Transport for Delivery of Biologics Across the Blood-Brain Barrier*. Annu Rev Pharmacol, 55 (2015) 613-631.

[4] G. Brockhoff, F. Hofstaedter, R. Knuechel. *Flow cytometric detection and quantitation of the epidermal growth factor receptor in comparison to Scatchard analysis in human bladder carcinoma cell lines*. Cytometry, 1994, 75-83.

[5] P. Nuciforo, N. Radosevic-Robin, T. Ng, M. Scaltriti. *Quantification of HER family receptors in breast cancer*. Breast Cancer Res, 17 (2015) 53.

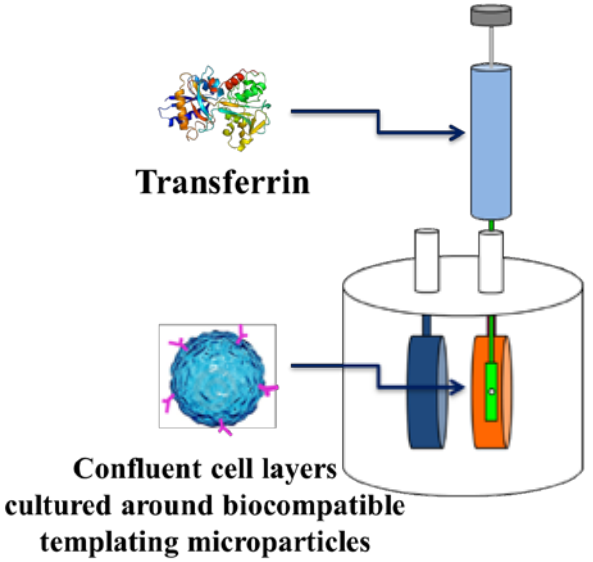

Fig.1 Schematic representation of Transferrin solution titrating a solution of cells cultured around cytodex by ITC.

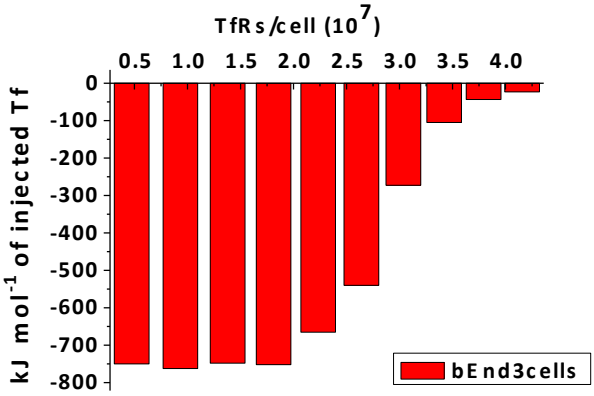

Fig.2 ITC data for titration of Tf solution into the solution of bEnd3 cells cultured on Cytodex microbeads obtained by integrating the raw data and subtracting the heat of Tf dilution into the buffer.

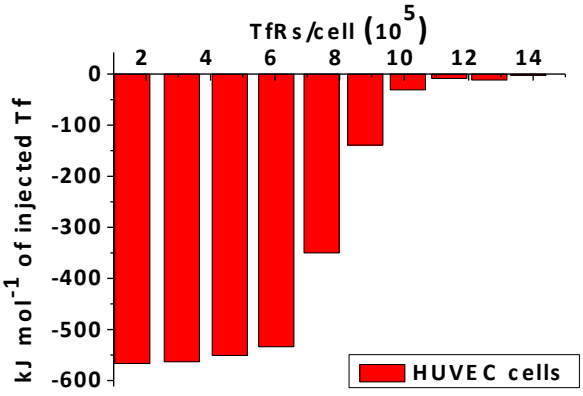

Fig.3 ITC data for titration of Tf solution into the solution of HUVEC cells cultured on Cytodex microbeads obtained by integrating the raw data and subtracting the heat of Tf dilution into the buffer.

A microfluidic device for evaluation of collagen remodelling during tumor progression

F. Gioiella[1,2,3], V. Brancato[2], G. Imparato[2], F. Urciuolo[3] and P.A. Netti[1,2,3]

[1] *Department of Chemical, Materials and Industrial Production Engineering, University of Naples Federico II, Naples 80125, Italy*

[2] *Center for Advanced Biomaterials for Healthcare@CRIB, Istituto Italiano di Tecnologia, Naples, 80125, Italy*

[3] *Istituto Italiano di Tecnologia, Largo Barsanti and Matteucci 53, Naples, 80125, Italy*

***Abstract*— In cancer research, tumor microenvironment has become recognized as a major factor influencing cancer progression and the outcome of therapy. Therefore tumor-stroma interactions have attracted particular interest due to their significant physiological relevance. Together with 3D cell cultures, recent advanced in microscale systems can contribute to developing a more realistic *in vitro* system that better mimic the complexity of *in vivo* environment. In this work, we present a microfluidic–device in which 3D microtissue model, creating by culturing normal fibroblasts (NF) or human breast adenocarcinoma cell line (MCF7) in gelatine micro-scaffolds, can be inserted in order to investigate the role of NF on cancer cell invasion and matrix remodeling.**

***Keywords*—tumor-on-a-chip, tumor microenvironment, microfluidics, cancer research.**

I. Introduction

IN the last decades, considerable attention has focused on tumor microenvironment because of its active role in cancer progression and invasion [1]. The complex stromal microenvironment is composed by several cell types like fibroblasts, endothelial cells, inflammatory and immune cells [2]. This entire structure is surrounded by extracellular matrix (ECM) that undergoes several alterations during tumor migration and invasion. In particular, matrix remodeling is a dynamic, ongoing process in which cells may deposit new matrix components and at the same time break down existing matrix with metalloproteinases (MMPs) [3].

In conventional two-dimensional (2D) monolayer systems, cells are grown on flat surfaces without the possibility to investigate cell-matrix interactions. On the other hand, although in three-dimensional (3D) models (spheroids or cell-populated biomatrices) the aforementioned cell-matrix interactions are present, the exogenous matrices are not able to replicate exactly both the structural and the morphological changes occurring during pathologic events. The stroma evolution during tumor progression can be currently detected only in xenograft animal models coupled with non-invasive optical techniques such as multiphoton microscopy or optical coherence tomography [4,5,6]. Nevertheless, animal models exhibit significant drawbacks including cost, time consuming, unpredictable characteristics and difficulty in correlating observed results with human responses [7,8]. To overcoming such limitations, microfluidic systems hold the potential to mimic complex tumoral scenario found *in vivo* and offer a number of advantages that makes it suitable in oncology research. In this direction, several studies have incorporated multicellular population and exogenous extracellular matrix components in microfluidic models to simulate the complex stroma-cancer relationship [7,8,9,10] and evaluate the efficacy of potential therapeutics against cancer pathology [7,8,11,12]. In this work, we aimed at replicating the cross talk between tumoral epithelium and its stroma in a chip. The microfluidic chip hosted two compartments separated by an interface, filled with stromal microtissue and epithelial microtissues respectively. The 3D stromal microtissue is an engineered system in which fibroblasts are continuously involved in synthesizing, assembling and disassembling their own ECM [13,14]. The stromal and epithelial compartment was kept in contact for two days to allow tumor cell invasion and ECM remodeling.

II. Materials and methods

A. Cell culture

Normal Fibroblasts (NF) and Human Breast Adenocarcinoma (MCF7) cells were cultivated on porous gelatine microcarriers in two different spinner flasks for 12 days following a previously established protocol [15] (Fig. 1).

B. Microfluidic device fabrication

The chip design comprises two chambers separated by arrays of circular pillars. The microfluidic device was created by replica molding technique. The master was carved onto a Poly(methyl methacrylate) (PMMA, Goodfellow) slab with a micromilling machine (Minitech CNC Mini-Mill). Polydimethylsiloxane PDMS (Sylgard 184, Mascherpa) base and curing agent were mixed thoroughly in the weight ratio 10:1, degassed under vacuum for 20 minutes and cured in an oven for 1 h at 80 °C. The PDMS layer and a coverslip (Menzel-Glaser 24 x 60 mm, # 1.5) were bonded by oxygen plasma treatment for 1 min at 50 W in an oxygen plasma oven (Plasma Femto, Diener) (Fig. 2).

C. Microtissue loading in a chip

NF-microtissues were loaded in the microfluidic device using a simple pipette-driven loading process. In the same way, MCF7-microtissues were added after 24 hours later. A nominal flow rate of 3.0 ml min^{-1} producing an average linear velocity similar to that of blood in tumors was performed [11].

D. *Imaging and SHG analysis*

Imaging of the tumor-microtissues and NF-microtissues was performed by using confocal microscopy every day (TCS SP5, Leica). Second Harmonic Generation (SHG) was utilized to study changes in stromal collagen during tumor progression.

III. RESULTS AND DISCUSSIONS

In this work real time invasion of tumor cells towards the adjacent stroma chamber can be detected. Cancer cell migration is facilitated by tumoral stromal collagen reorganization. SHG imaging allows on line monitoring of endogenous collagen remodelling without labelling (Fig. 3). The coupling of microtissue model with microfluidic platform enables to mimic the complex tumor microenvironment for long-term studies better than conventional 2D *in vitro* assays and allow real-time monitoring of tumor-stroma interactions and collagen remodeling.

IV. CONCLUSION

In this work a 3D microtissue model was integrated with microfluidic device in order to have a realistic model *in vitro* for study disease progression. The optical accessibility of the microdevice and the high-fidelity features of 3D tissue model allowed the on line monitoring of tumor-stroma interaction during tumor progression.

We believed that our platform holds potential as an enabling approach to future investigations in the identification of new therapeutic agents.

REFERENCES

[1] H. Li, X. Fan and J. Houghton, "Tumor Microenvironment: The Role of the Tumor Stroma in Cancer", *Journal of Cellular Biochemistry*, vol. 101, pp. 805-815, 2007.

[2] I. M. Adjei and S. Blanka, "Modulation of the Tumor Microenvironment for Cancer Treatment: A Biomaterials Approach", *Journal of functional biomaterials*, vol.6, pp. 81-103, 2015.

[3] D. Harjanto and M. H. Zaman, "Modeling extracellular matrix reorganization in 3D environments", vol. 8, *PLoS One*, pp. e52509, 2013.

[4] R. K. Jain, L. L. Munn and D. Fukumura, "Dissecting tumor pathophysiology using intravital microscopy", *Nature Reviews*, vol.2, pp. 266-276, 2002.

[5] D. Fukumura, D. G. Duda, L. L. Munn and R. K. Jain, "Tumor Microvasculature and Microenvironment: Novel Insights Through Intravital Imaging in Pre-Clinical Models", *Microcirculation*, vol. 17, pp. 206-225, 2010.

[6] R. K. Jain, "Normalizing tumor microenvironment to treat cancer: bench to bedside to biomarkers", *Journal of Clinical Oncology*, vol. 17, 2205-2219, 2013.

[7] C.R. Drifka, K. W. Eliceiri, S. M. Weber, W. J. Kao, "A bioengineered heterotypic stroma--cancer microenvironment model to study pancreatic ductal adenocarcinoma", *Lab Chip*, vol. 13, pp. 3965–75, 2013.

[8] Y. Choi, E. Hyun, J. Seo, C. Blundell, H. C. Kim, E. Lee, S. Lee, A. Moon, W. K. Moon and D. Huh, "A microengineered pathophysiological model of early-stage breast cancer", *Lab on a Chip*, vol. 15, pp. 3350-3357, 2015.

[9] L. L. Bischel, D. J. Beebe and K. E. Sung, BMC cancer, "Microfluidic model of ductal carcinoma in situ with 3D, organotypic structure", vol. 15, DOI: 10.1186/s12885-015-1007-5, 2015.

[10] N. V. Menon, Y. J. Chuah, B. Cao, M. Lim and Y. Kang, "A microfluidic co-culture system to monitor tumor-stromal interactions on a chip", *Biomicrofluidics*, vol.8, pp. 064118-11, 2014.

[11] C. L. Walsh, B. M. Babin, R. W. Kasinskas, J. A. Foster, M. J. McGarry and N. S. Forbes, "A multipurpose microfluidic device designed to mimic microenvironment gradients and develop targeted cancer therapeutics", *Lab on a Chip*, vol.9, pp. 545-554, 2009.

[12] A. Albanese, A. K. Lam, E. A. Sykes, J. V. Rocheleau and W. C. W. Chan, "Tumour-on-a-chip provides an optical window into nanoparticle tissue transport", *Nature communications*, vol. 4, DOI:10.1038/ncomms3718, 2013.

[13] C. Palmiero, G. Imparato, F. Urciuolo and P. Netti, "Engineered dermal equivalent tissue in vitro by assembly of microtissue precursors", *Acta Biomaterialia*, vol. 6, pp. 2548-2553, 2010.

[14] F. Urciuolo, A. Garziano, G. Imparato, V. Panzetta, S. Fusco, C. Casale and P. A. Netti, "Biophysical properties of dermal building-blocks affects extra cellular matrix assembly in 3D endogenous macrotissue", *Biofabrication*, vol. 8, pp. 015010, 2016.

[15] G. Imparato, F. Urciuolo, C. Casale and P. Netti, "The role of microscaffold properties in controlling the collagen assembly in 3D dermis equivalent using modular tissue engineering", *Biomaterials*, vol.34, pp. 7851-7861, 2013.

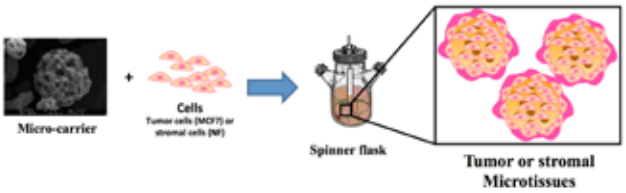

Fig. 1: Realization of tumor (MCF7) or stromal microtissues (NF) after 12 days of dynamic cultivation into spinner flasks.

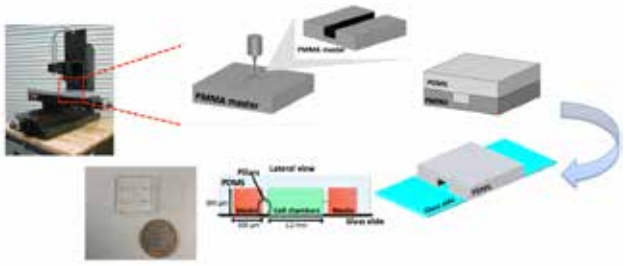

Fig. 2: Schematic representation of microfludic device fabrication by replica molding technique.

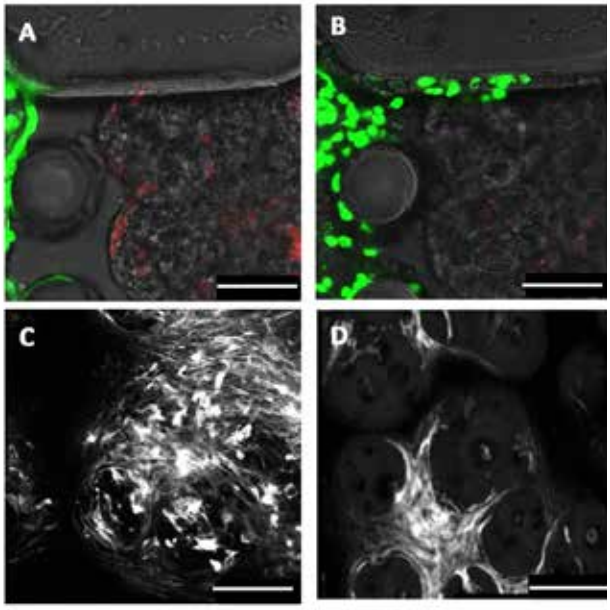

Fig. 3: Time-lapse images of MCF7 and NF-microtissues after 0 (A) and 12 (B) hours of MCF7-microtissues loading. SHG signal (gray scale) from newly formed fibrillar collagen in NF-microtissues alone (C) and after 12 hours of contact with MCF7-microtissues (D).
Scale bar = 100 μm.

A chip based system for studying liver specific functions and drug toxicity

B. Corrado[123], V. De Gregorio[1], C. Attanasio[1], F. Urciuolo[1], G. Imparato[1], P.A. Netti[123]

[1] *Center for Advanced Biomaterials for Health Care@CRIB Istituto Italiano di Tecnologia, Largo Barsanti e Matteucci n. 53, 80125 Napoli, Italy*

[2] *Department of Chemical, Materials and Industrial Production Engineering (DICMAPI), University of Napoli Federico II, P.le Tecchio 80, 80125 Napoli, Italy*

[3] *Interdisciplinary Research Centre on Biomaterials (CRIB), University of Napoli Federico II, P.le Tecchio 80, 80125 Napoli, Italy*

***Abstract*— 3D microfluidic cell culture systems offer relevant advantages for prediction of drug toxicity. In this study we describe the design and fabrication of a 3D liver-on-chip system that enables cell culture under continuous fluid flow. Through the biochip we replicate the *in vivo* microvascular environment of liver tissue. Three-dimensional liver microtissues were cultured into biochip with different ethanol concentration to tests alcoholic effects. Viability assessment through cell auto-fluorescence coupled with two-photon microscopy allows on-line monitoring of ethanol toxicity without using dyes and disintegrating the cell constructs.**

***Keywords*— Liver, microfluidic, organ-on-chip, drug toxicity**

I. INTRODUCTION

THE liver is one of the most complicated organ of human body, mainly involved in drug metabolism and body detoxification as well as plasma protein production. Because of its overall importance in drug metabolism, the liver is a major focus of pharmaceutical research [1].

Conventional 2D liver cell culture models are well-established and simple to apply but often do not reflect the morphology and functionality of their native three-dimensional phenotypes and also multi-organ interaction cannot be observed [2]. The only way to obtain *in vivo* data to predict the pharmacokinetic responses from human is the use of animal models. However, data obtained from animal tests often cannot be extrapolated to humans due to cross-species differences in metabolism. In order to overcome the limitations of conventional drug screening, multiple groups have applied microfabrication and microfluidics technologies to liver model development. Microfabrication techniques are well-suited to create structures with defined shapes and positions on the micrometer scale that can be used to position tissues and simulate organ cross talk, emulating the real *in vivo* situation [3]-[4].

In many areas of biomedical field, research is aimed at mimicking the *in vivo* organ of human body for studying its structure and function. In one early study, a flat-plate bioreactor was developed to investigate the effect of medium flow and oxygenation on the viability and function of rat hepatocytes co-cultured with fibroblasts [5].

A microfluidic liver chip described by Lee [6], contains monoculture and flow chambers, separated by a micro fabricated baffle, which shields the hepatocytes from fluid shear to mimic the LSEC-hepatocyte interface and sinusoid of the liver. A more recent study report a microfluidically perfused biochip composed of endothelial cells, macrophages and a hepatic layer comprising stellate cells co-cultured with hepatocyte [7].

One important limitation of these current *in vitro* models, is that a 2D monolayer culture of one or more cell lines is usually used, which may not replicate the physiological response in human tissues.

The issue of achieving authentic response from cells can be partially addressed with a 3D cell culture. Three dimensional tissues have been demonstrated to more closely represent *in vivo* like conditions in comparison to 2D cell cultures [8]. Three dimensional cultures help cells retain their native tissue-specific functions and differentiated state. In particular combination of a microfluidic system with 3D microtissues can improve the tissue specific functions mimicking the tissue environment with blood flow suppling oxygen and nutrients.

In this study we recreate in a microfluidic biochip the architecture of the liver sinusoid. *In vivo*, the hepatic sinusoid is a microfluidic system that carries blood from the hepatic artery and portal vein, exposing the liver to oxygen and nutrients; this blood supply can also expose the liver to toxins and infectious agents. To achieve this, we first recreate 3D hepatic microtissues *in vitro*, then develop a microfluidic device that could mimic the hepatic lobule.

The utility of the chip is demonstrated by assessing the hepatotoxicity of ethanol in a dose-dependent.

Using cell auto-fluorescence coupled with two-photon microscopy we were able to evaluate microtissues viability in a noninvasive way.

II. MATERIALS AND METHODS

The hepatic microtissues (μTPs) were obtained by dynamic cells seeding on a gelatin porous microspheres.

Gelatin porous micro-beads (GPMs) have been prepared according to a modified double emulsion technique as previously described [9].

A suspension of HepG2 cells and gelatin porous microspheres were inoculated into a siliconized spinner flask in a continuous stirring regime (Fig. 1).

The device was designed using AutoCAD (Autodesk, CA). Then the microfluidic device was fabricated using a micromilling techniques (Minitech CNC Mini-Mill) to obtain a polymethyl methacrylate (PMMA) master. The biochip was produced by replica-molding of polydimethylsiloxane

(PDMS) (Sylgard 184; Dow Corning, NY) on the master mold. In Fig. 2 the schematic illustration of biochip set-up.
From day five the μTPs were collected from the spinner culture and loaded into the microfluidic device.
For the creation of toxicity *in vitro* model, culture medium with different concentration of ethanol was perfused into the microfluidic device.
Cell viability into the biochip was assessed through cellular auto-fluorescence using two-photon microscopy (Fig. 3).
Hepatic functions of μTPs were analyzed by measuring the concentration of albumin (Albumin Human ELISA kit, ab 108788, Abcam, Cambridge, UK) and urea (Quanti ChromTM Urea Assay Kit DIUR 100) according to the manufacturer's instructions.

III. Results and discussion

We developed a biochip that recreate a physiological microenvironment for the hepatic μTPs and replicate the nutrient transport function of microvascular system in the liver. In addition we investigate if the microfluidic device provide the maintenance of the metabolic activity of liver μTPs by measuring albumin and urea production.
Using cell auto-fluorescence we assess cell viability into biochip in a noninvasive way, allowing an on-line monitoring of ethanol induced toxicity.

IV. Conclusion

This chip-based model with continuous perfusion fluid regime will serve as model for studying liver specific functions and would be a valid screening platform to evaluate the toxic effects of new developed drug.

References

[1] R. Taub, "Liver regeneration: from myth to mechanism." *Nature reviews Molecular cell biology* 5.10 (2004): 836-847.
[2] A. Abbott, "Cell culture: biology's new dimension." *Nature* 424.6951 (2003): 870-872.
[3] El-Ali J., Peter K. Sorger, and Klavs F. Jensen. "Cells on chips." *Nature*442.7101 (2006): 403-411.
[4] Park, Tai Hyun, and M. L. Shuler. "Integration of cell culture and microfabrication technology." *Biotechnology progress* 19.2 (2003): 243-253.
[5] Tilles, Arno W., et al. "Effects of oxygenation and flow on the viability and function of rat hepatocytes co-cultured in a microchannel flat-plate bioreactor."*Biotechnology and bioengineering* 73.5 (2001): 379-389.
[6] Lee, Philip J., Paul J. Hung, and Luke P. Lee. "An artificial liver sinusoid with a microfluidic endothelial-like barrier for primary hepatocyte culture."*Biotechnology and bioengineering* 97.5 (2007): 1340-1346.
[7] Rennert, Knut, et al. "A microfluidically perfused three dimensional human liver model." *Biomaterials* 71 (2015): 119-131.
[8] Griffith, Linda G., and Melody A. Swartz. "Capturing complex 3D tissue physiology in vitro." *Nature reviews Molecular cell biology* 7.3 (2006): 211-224.
[9] Imparato, Giorgia, et al. "The role of microscaffold properties in controlling the collagen assembly in 3D dermis equivalent using modular tissue engineering."*Biomaterials* 34.32 (2013): 7851-7861.
[10] Dittmar, Roman, et al. "Assessment of cell viability in three-dimensional scaffolds using cellular auto-fluorescence." *Tissue Engineering Part C: Methods* 18.3 (2011): 198-204.

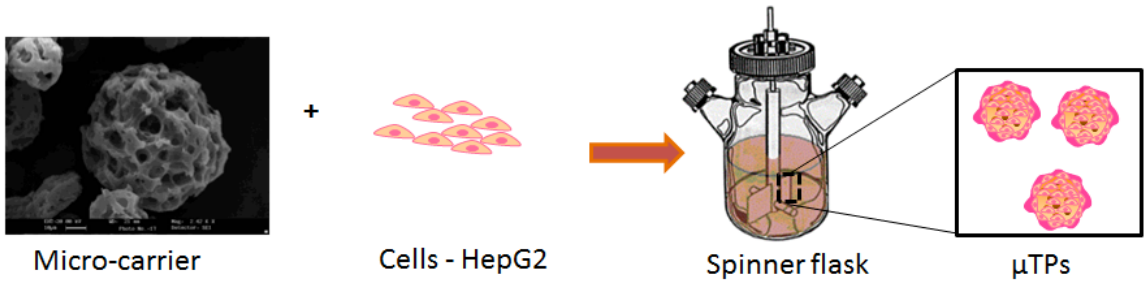

Fig. 1 Multistep process of microtissues (µTPs) fabrication**.** HepG2 cells were seeded on gelatin microcarrier in a spinner flask.

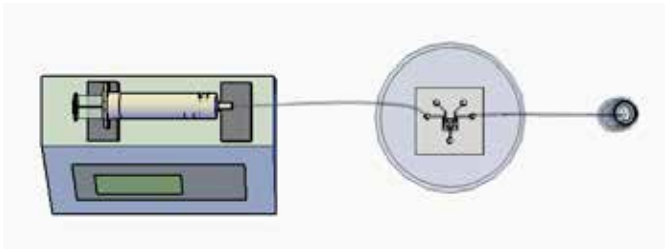

Fig. 2 Schematic illustration of microfluidic perfusion set-up**.** The biochip is connected with a syringe pump to allow fluid flow condition

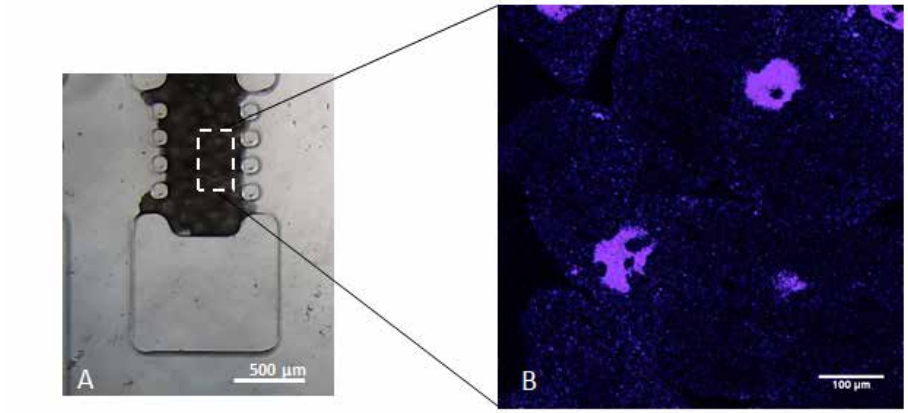

Fig. 3 In situ on line monitoring**.** (A) Bright field image of microfluidic chamber loaded with hepatic microtissues; (B) Two photon spectral images of hepatic µTPs loaded into biochip

Oil in Water Nanoemulsions as Stable Template for Controlled Deposition of Biodegradable Polymer Nanocapsules

G. Iaccarino[1, 2], R. Vecchione[1, 2],* R. Marotta[3], P. A. Netti[1, 2]

[1] *Center for Advanced Biomaterials for Health Care, IIT@CRIB, Istituto Italiano di Tecnologia, Naples, Italy*

[2] *Interdisciplinary Research Center of Biomaterials, CRIB, University Federico II, Naples, Italy*

[3] *Department of Nanophysics, Istituto Italiano di Tecnologia (IIT), Genova, Italy*

***Abstract*— Liquid-liquid interfaces are highly dynamic and intrinsically unstable, therefore not easy to handle. However, their tendency to reduce surface tension by interacting with adjacent molecules or nanoparticles may drive the assembly process in a unique fashion. Here we report on the preparation of polymeric multilayer nanocapsules based on highly concentrated oil in water O/W nanoemulsions.**

***Keywords*—Liquid-liquid interfaces, multilayer nanocapsules, ultrastable nanoemulsion, biodegradable polymers.**

I. Introduction

LIQUID-liquid interfaces possess unique properties such as elevated interfacial tension and fluidity, which provides high mobility for the achievement of an equilibrium assembly [1]. Therefore, they show great potential as viable templates for ordered assembly of molecules and nanoparticles. However, one important limitation of liquid-liquid interfaces is their poor stability, due to the intrinsic immiscible nature of the two liquids even when stabilized by surfactants [2]. This is especially relevant when multiple depositions are required, as in the case of multifunctional polymer nanocapsules. Several fields such as cosmetics, food and agriculture, drug delivery [3]-[5] would benefit from controlled biodegradable polymer nanocapsules since they combine tunable shell properties with a lipophilic liquid core capable to encapsulate high payloads.

Some attempts have been already pursued in this direction by carrying the process of multiple polymer deposition around liquid-liquid interfaces based on O/W nano-emulsions, [6] but with little control over size and stability. Following this aim, we here report on the use of a narrow distributed O/W nano-emulsion at high concentrations of oil (10 wt%) as a reliable template for multiple interfacial depositions of polymers to produce highly controllable polymer nanocapsules.

II. Experimental section

A. Nano-emulsion preparation

First a primary nano-emulsion was prepared following a two-step procedure. Preliminarily, an oil phase (soybean oil and lechitin) and an aqueous phase (Milli-Q water) were mixed up using an immersion sonicator to obtain a 20% oil pre-emulsion. Then, the initial size and dispersion of the emulsion was significantly reduced through a high-pressure homogenization step.

Afterwards, the as prepared primary nano-emulsion was mixed with a 0.1 M acetic acid solution of chitosan and kept under stirring for 15 min to allow uniform chitosan deposition. This nano-emulsion was properly re-dispersed to obtain a 10% oil - 0,1% chitosan secondary nano-emulsion.

B. Multilayer deposition

Starting from the secondary nano-emulsion, the multilayer structure was built up alternating several polyelectrolyte layers of different polymers. Experimentally, eptalayer and pentalayer capsules were fabricated by aid of two syringe pumps and an ultrasonic bath. The two liquid phases were injected at the same flow rate through two micrometric capillaries interfaced at their extremities. Due to the high surface tension, each pair of drops pouring out the two capillaries coalesced to form a unique drop hosting the very first instants of the deposition process. Each drop was then collected inside a glass tube immersed in the ultrasonic bath at room temperature.

C. Particle size and Z-potential characterization

The particle size and size distribution of all the suspensions were measured by Zetasizer (NanoSeries, Malver) using the laser dynamic light scattering ($\lambda = 632.8$ nm).

The Z-potential of all the suspensions was determined using a particle electrophoresis technique where the direction and velocity of droplet movement in a well defined electric field is monitored.

D. Cryo-TEM characterization

The morphology of the secondary nano-emulsions and multilayer nanocapsules was observed by cryo-TEM. In particular, frozen hydrated samples were prepared by applying a 3 µl aliquot to a previously glow-discharged 200 mesh holey carbon grid.

III. Results and discussion

Despite attracting increasing interest across several research fields, the use of liquid-liquid interfaces as reliable templates for polymer nanocapsules is basically discouraged by some tedious limitations. In fact, the production of highly controllable polymer nanocapsules based on O/W nano-emulsions is typically prevented by their poor stability and the lack of a deposition procedure allowing for a thorough control of the dimensional features. In particular, a narrow size distribution both of the initial liquid template and of the final polymer nanocapsule, appears to be pivotal for an effective use of O/W nano-emulsion templates for controlled Layer by Layer (LbL) of polymer nanocapsules.

Herein, we bypassed the known limitations of liquid templates starting from nano-emulsion stabilized by means of

a polymer coating, namely secondary nano-emulsion, combined with an optimal re-dispersion process allowing for enhanced stability of the final system. We monitored such secondary nano-emulsion and found them stable for more than one year while also capable to provide further polymer depositions. In order to effectively deposit further polymer layers onto highly concentrated secondary nano-emulsion (10 wt%), a new declination of the LbL procedure was proposed taking in particular account the mixing process between the polyelectrolyte solution and the nano-emulsion template [7] as depicted in Fig.1.

Small sizes (under 200 nm) and low PdI of the oil template (<0.1) were made possible thanks to the use of a high-pressure homogenizer according to a procedure previously reported [8]. For what concerns the template size, we used two different formulations, namely L_{130} and L_{90} (based on different concentrations of lecithin in oil 2.4 g/20 g and 4.8 g/20 g, respectively). These primary nano-emulsions feature a reproducible size, ranging from around 130 nm with L_{130} to around 90 nm with L_{90}.

Morphological characterizations coupled with the DLS analysis confirm the ultrastability of the proposed secondary nano-emulsion template and the use of a deposition method allowing for finely controlled biodegradable multilayer polymer nanocapsules.

Moreover, we proved the loading capability of our nanocapsules to be effective by dissolving lipophilic model drugs like Nile Red and curcumin—a lipophilic nutraceutical— inside the oily templates, without affecting size, PdI, and templating capability while making multiple polymer depositions.

In this study, we also showed the versatility of the deposition method by testing several couples of polyelectrolytes (i.e., chitosan – sodium alginate, chitosan – hyaluronic acid.

Additionally, chemically modified polyelectrolytes bearing different functionalities, such as thiols and allyls [9], were also successfully deposited on highly concentrated oil in water O/W nanoemulsions. The use of such polymers for the build-up of the polymer shell of a nanocapsule opens up a mare magnum of opportunities. Among the most appealing ones, a straightforward labeling of the polymer layers, a covalent stabilization by chemical cross-linking of the nanocapsule shell [9], the deposition of a pre-pegylated polyelectrolyte as outer layer and the possibility to decorate with specific molecules the polymer layers are certainly noteworthy.

Multilayered nanocapsules were stable over months showing no significant difference as compared to the same sample at zero time.

IV. Conclusion

In this work we propose an effective use of liquid-liquid interfaces as viable route for controlled deposition of biodegradable polymer nanocapsules. In fact, by governing their intrinsic instability one can take advantage of their unique properties to build up multifunctional nanocapsules in a relatively naïve way. The method we suggest stresses the importance to start from narrowly distributed O/W nanoemulsions as templates and finely control the deposition process of the polymer shell. This way ultrastable food grade multilayer nanocapsules were produced showing great potential particularly for nanomedicine field. Indeed, size is well under 200 nm, the concentration of the system is relatively high (we start from 10 wt% of the secondary nano-emulsion template) thus allowing for encapsulation of big amount of lipophilic molecules, compared to literature. Nevertheless, oil templates were so stable that they allowed deposition even after more than 1 year. These advantages—together with a low-cost procedure that does not involve centrifugation and rinsing steps let us imagine a very significant impact on the health care field.

References

[1] Y. Lin, H. Skaff, T. Emrick, A.D. Dinsmore, T.P. Russell, "Nanoparticle assembly and transport at liquid-liquid interfaces" *Science* 299(5604): 226-229.

[2] K. Rahn-Chique, A. M. Puertas, M. S. Romero-Cano, C. Rojas, G. Urbina-Villalba, "Nanoemulsion stability: experimental evaluation of the flocculation rate from turbidity measurements." *Advances in colloid and interface science* 2012, *178*, 1-20.

[3] Z. Teixeira, C. A. Dreiss, M. J. Lawrence, R. K. Heenan, D. Machado, G. Z. Justo, S. S. Guterres, N. Duran, "Retinyl palmitate polymeric nanocapsules as carriers of bioactives" *Journal of colloid and interface science* 2012, *382*, 36-47

[4] R. Grillo, N. Z. dos Santos, C. R. Maruyama, A. H. Rosa, R. de Lima, L. F. Fraceto, "Poly(epsilon-caprolactone)nanocapsules as carrier systems for herbicides: physico-chemical characterization and genotoxicity evaluation" *Journal of hazardous materials* 2012, *231-232*, 1-9W.

[5] D. J. McClements, D. Julian, "Edible nanoemulsions: fabrication, properties, and functional performance" *Soft matter* 2011, *7*, 2297-S. Patent 3 624 12, July 16, 1990.

[6] C. Preetz, A. Rübe, I. Reiche, G. Hause, K. Mäder, "Preparation and characterization of biocompatible oil-loaded polyelectrolyte nanocapsules" *Nanomedicine: Nanotechnology, Biology and Medicine* 2008, *4*, 106-114.

[7] R. Vecchione, G. Iaccarino, P. Bianchini, R. Marotta, F. D'Autilia, V. Quagliariello, A. Diaspro, P. A. Netti, "Ultrastable Liquid-Liquid Interface as Viable Route for Controlled Deposition of Biodegradable Polymer Nanocapsules" *Small* 2016.

[8] R. Vecchione, U. Ciotola, A. Sagliano, P. Bianchini, A. Diaspro, P. A. Netti, "Tunable stability of monodisperse secondary O/W nano-emulsions" *Nanoscale* 2014, *6*, 9300-9307.

[9] V. Calcagno, R. Vecchione, A. Sagliano, A. Carella, D. Guarnieri, V. Belli, L. Raiola, A. Roviello, P.A. Netti, "Biostability enhancement of oil core - polysaccharide multilayer shell via photoinitiator free thiol-ene 'click' reaction" *Colloids Surf B Biointerfaces* 142: 281-289.

[10] M. Dash, F. Chiellini, R. M. Ottenbrite, E. Chiellini, "Chitosan—A versatile semi-synthetic polymer in biomedical applications" *Progress in polymer science* 2011, *36*, 981-1014.

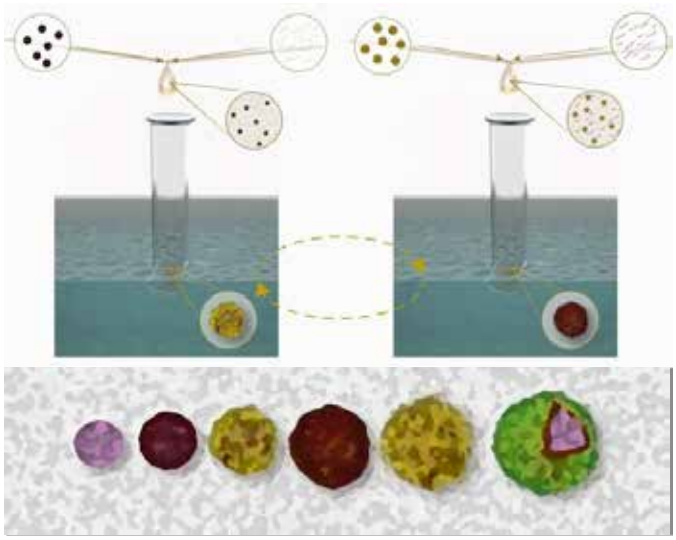

Fig. 1 Scheme of the multilayer deposition procedure on pre-loaded ultra-stable liquid template by means of sonication in a water bath of the two phases – polymer solution and suspension, which are injected dropwise.

Nanoengineered platforms for in vitro skeletal muscle self-assembly

M. Iannone[1], M. Ventre[1], O. Guardiola[2], G. Minchiotti[2], P. A. Netti[1].
[1] Department of Chemical, Materials and Industrial Production Engineering, University of Naples Federico II and Center for Advanced Biomaterials for Helathcare@CRIB, Istituto Italiano di Tecnologia, Naples, Italy;
[2]Institute of Genetics and Biophysics, National Research Council, Naples, Italy

***Abstract*— Biophysical stimuli in the local microenviroment are known to affect cell behavior in terms of cell attachment, cytoskeletal architecture and nuclear shape. However, the influence of the biophysical signals and more specifically of topographic signals, on the cells self-organization into a three-dimensional tissue is currently unclear. Here, we used nanopatterned substrates able to control the adhesion and contractility processes to generate skeletal muscles in vitro. In particular, we show that by changing the combination of the initial conditions for cell adhesion we obtained different cell behaviours in terms of self-organization, and structures development.**

***Keywords*—Topography, tissuegenesis, myotubes .**

I. Introduction

During tissuegenesis, cell behaviour is profoundly affected by biophysical and biochemical signals from surrounding extracellular matrix. Similarly, cell fate is influenced by material properties and more specifically cell-material crosstalk affects the architecture and organization of tissues, which is crucial to dictate its macroscopic functions. Within the context of myogenesis, an orderly assembly of myofibrils is required to generate functional tissues. Therefore, a precise control on cell self-organization is strictly required.

Here we report the realization of nanoengineered platforms for in vitro skeletal muscle self-assembly. The aim of this study is to define the optimal set of initial conditions that direct and control muscle supracellular self-organization leading to a development of mature and functional myofibers, in absence of differentiation medium or added growth factor.

II. Material and Methods

C2C12 murine myoblasts, were used as a model of skeletal muscle development. In order to evaluate the effect of different surface features on cell self-organization we cultured C2C12 cells in growth medium, on arrays of polydimethylsiloxane (PDMS) nanopatterned substrates displaying different properties, namely topographic features, mechanical properties and adhesivity. In more details, the array consisted in nanogrooves with dimensions of 700 nm, growing levels of adhesivity obtained by means of simple serum coating (FBS), oxygen plasma treatment (PL) or oxygen plasma treatment and subsequent incubation with Fibronectin (10mg/ml) (PL_FN); different stiffness obtained by modulating base and curing agent weight ratio during PDMS preparation.

To investigate whether hard PDMS substrates were able to induce myogenic differentiation, we performed RT-PCR on selected genes of cells cultivated on patterns with different levels of adhesivitiy. Flat substrates were used as control.

III. Results

In all conditions, surface features promoted the formation of myotubes that were aligned parallel to the pattern direction (Fig. 1). Interestingly, only C2C12 cells cultivated on hard PT_FN PDMS, were instructed to spontaneously organize towards the development of 3D cylindrical tissues assembled in myobundles oriented perpendicularly to the pattern direction (fig.1). Molecular profiles confirmed the morphologic observation indicating terminal differentiation towards myofibers. Infact, only when cultivated on hard 700nm patterned surfaces treated with oxygen plasma and fibronectin incubation (PL_FN) C2C12 cells were able to express higher level of myogenin (MYOG) and muscle creatine kinase (MCK) myosin heavy chains (MyHC) (Fig.2). Temporal evolution of myofibers formation on 700nm hard PL_FN substrates followed a precise and reproducible steps. C2C12 self-organized in myofibrils (Fig.3a), as a consequence of cell polarization and elongation along the pattern direction. At 12 days the presence of immature myotubes organized in a zipper like structures oriented perpendicularly to the pattern direction was evident. At 14 days nanopatterned surfaces were mainly populated of muscle bundles structures composed of packed mature myotubes directed orthogonally to the pattern direction (Fig.3a). Confocal images showed nuclei organization and disposition within the structures (Fig.3b). Few myotubes were still in contact with the surface of the nanopattern and follows the orientation of grooves but most of myotubes are perfectly packed within the 3D structures invariably oriented orthogonal to the pattern direction. 3D aspect of structure was confirmed by z-reconstuction, of confocal images, obtained with ImageJ software.

The development of mature and functional myofibers was evident also from Scanning Electron Microscopy images showing the development of mature myotubes closely packed in the form of parallel arrays (Fig.4a). The high level of muscle maturation was highlighted by the superficial banded pattern of sarcomeric structures (Fig.4b).

Confocal images of muscle bundles confirmed the presence of mature contractile structures as the banded pattern of myosin was clearly evident from Second Harmonic

acquisitions (Fig.5a; SHG in gray and nuclei in green) scale bar 20 mm. This observation was clarified with ultrastructural characterization (Transmission Electron Micrograph) showing well organized myofilaments, with defined sarcomeres and z-lines (Fig.5b).

IV. Conclusion

Altogether these data suggested that only the employment of a specific set of initial conditions for adhesion induces the self-organization of highly ordered and functional muscle bundles composed of well organized myofilaments, with clearly defined sarcomeres. The ability to generate engineered muscle tissue that mimics the structural and functional properties of native muscle would allow the design of platforms able to govern cellular self-organization and tissuegenesis, eventually leading to the generation of functional muscles *in vitro*. These would comprise valuable models for studying tissue development, physiology or pathological conditions. For instance, tools for studying the progression of muscle disorder or to screen the efficacy of drugs.

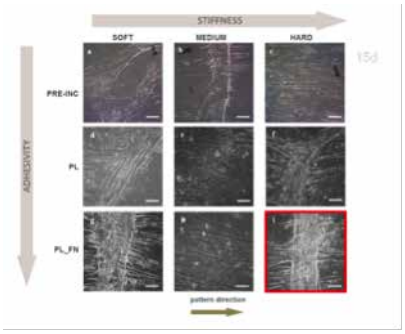

Fig. 1. Brightfield images of C2C12cell cultivated on nanopatterned array consisting in nanogrooves of 700 nm, different levels of adhesivity i.e. serum coating (FBS), oxygen plasma treatment (PL) or oxygen plasma treatment and subsequent incubation with Fibronectin (10mg/ml) (PL_FN); and growing level of stiffness (scale bar 100 mm).

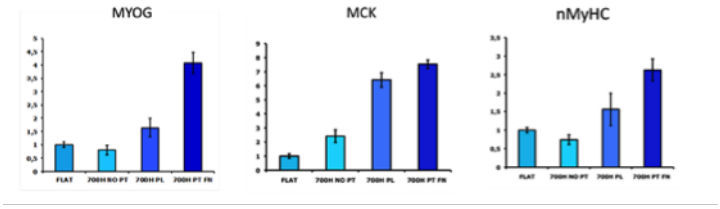

Fig. 2. Molecular profiles, obtained by Real Time PCR, of C2C12 cell seeded on array of PDMs nanopatterned substrates displaying different properties.

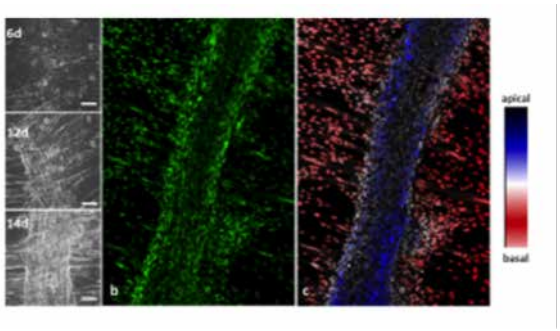

Fig. 3. Temporal evolution of myofibers formation on 700nm hard PL_FN (Fig. 3a scale bar 100 mm). 3D aspect of structure was confirmed by z-reconstuction, of confocal images, obtained with ImageJ software. Spatial arrangement of nuclei onto the surface and within the structure is reported in different colour range from the red that indicate the basal position still in contact with the surface of substrate to the blue indicating the localization on the apical plane (Fig. 3c).

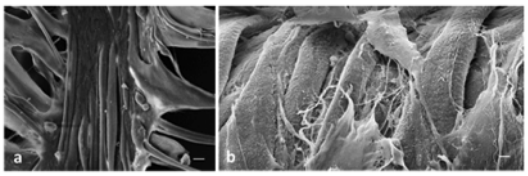

Fig. 4. The development of mature and functional myofibers was evident also from Scanning Electron Microscopy images showing the development of mature myotubes closely packed in the form of parallel arrays (Fig.4a). The high level of muscle maturation was highlighted by the superficial banded pattern of sarcomeric structures (Fig.4b). Scale bar 20 mm in a ; 3 mm in b.

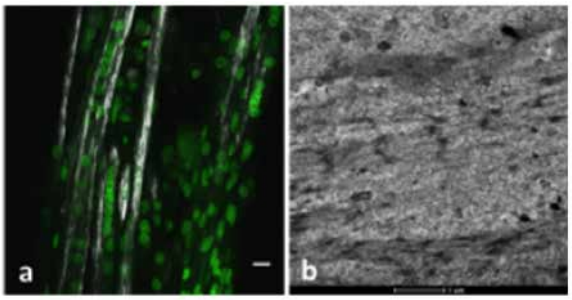

Fig. 5. Confocal images of muscle bundles showed the presence of mature contractile structures as the banded pattern of myosin was clearly evident from Second Harmonic acquisitions (Fig.5a; SHG in gray and nuclei in green) scale bar 20 mm. This observation was clarified with ultrastructural characterization (Transmission Electron Micrograph) showing well organized myofilaments, with defined sarcomeres and z-lines (Fig.5b).

Ligand recognition in complex media at material interface

V. Lettera[1], E. Battista[1,2], P. Scognamiglio[1], F. Causa[1,2,3], P. A. Netti[1,2,3]

[1] *Center for Advanced Biomaterials for Heathcare@CRIB, Istituto Italiano di Tecnologia (IIT), Largo Barsanti e Matteucci 53, 80125Naples, Italy*

[2] *Interdisciplinary Research Centre on Biomaterials (CRIB), University "Federico II", Piazzale Tecchio 80, 80125 Naples, Italy*

[3] *Dipartimento di Ingegneria Chimica del Materiali e della Produzione Industriale (DICMAPI), University "Federico II", Piazzale Tecchio 80, 80125 Naples, Italy*

***Abstract*— Aliphatic polyesters are widely used in biomedical applications after conjugation of small peptides for surface bioactivation. However, large protein adsorption occurs in serum context and little is known about the effect of physisorbed proteins on ligand presentation to cell receptors in such conditions. Here we used poly-ε-caprolactone for selective bioactivation of surface through the covalent binding of -GYGRGDS peptide by using a water soluble diepoxy linker as theter. Early stage cell-adhesion tests showed a significant increase of adhered cells when ligands are engrafted.**

Such results demonstrated an active and dynamic remodeling of cell at the interface, also providing tools to evaluate the ligand presentation in different contexts.

***Keywords*—Surfaces bioconjugation, peptide adhesion molecule, protein adsorption, material-cytoskeleton crosstalk.**

I. Introduction

In the biomedical applications, biodegradable polymers such as polyesters (poly-ε-caprolactone, PCL, polylactic acid, PLA, polylactic-co-glycolic acid, PLGA) have been extensively used as temporal supportive materials in drug delivery, guided tissue regeneration (dental and orthopaedic applications), stents, staples, sutures and tissue engineering [1]. This class of polymers has optimal tuneable mechanical properties and high processability, but often lacking specific biorecognition activity. Poly-ε-caprolactone (PCL), in particular, has been successful adopted as culture cell platforms [2] and scaffolds [3] because of its slow degradability, good mechanical and thermoplastic properties. To overcome the inertness and the poor cytocompatibility different strategies have been developed to modify the interface with cells. The encoding of biomolecular cues by chemical conjucation of peptides has been frequently adopted to integrate cell specific recognition on otherwise inhert materials.

In this context, pratical use of bioactivated material faces the adsorption of proteins present in biological fluids that could screen the conjucated signal [4]. However, some of these physisorbed proteins could provide adhesion motifs or proactive signals for cell adhesion.

In this work the presentation of GYGRGDS grafted onto aminolyzed PCL surfaces was investigated.

Early cell-adhesion tests were performed in the presence of serum and in serum-free media. Finally, the effect of cell adhesion on proteinaceus physisorbed layer was investigated during cell spreading.

II. Materials and Methods

Surface Bioactivation and Characterization

PCL thin films and their bioactivation were achived as reported by Battista et al. [5]. GYGRGDSP sequence was used as positive control, and GYGRGESP was negative control (reported below as RGD and RGE, respectively).

Serum Protein Adsorption and desorption.

1D-PAGE and micro-BCA assay were used to quantify the adsorbed proteins from FBS to polymer surfaces.

Cell-adhesion study

Cell-adhesion studies were performed in serum free conditions at short time. Mouse embryo fibroblasts NIH3T3 were grown in Dulbecco's modified Eagle medium (DMEM) and maintained at 37°C and 5% CO_2. For cell adhesion experiments, PCL, PCL-RGD and PCL-RGE materials were pre-incubated in serum free medium or in 10% fetal bovine serum (FBS) supplemented medium about 30 minutes before cell seeding. Cells were seeded on materials and incubated at 37°C .For cell area and shape factor analyses, cells were stained with fluorescein conjugate wheat germ agglutinin (WGA) and related images were acquired by CLSM (Leica).

III. Results

Effect of serum protein adsorption on NIH3T3 cell adhesion

In order to study the effect of serum protein adsorption on fibroblasts adhesion, we evaluated the density and the morphology features of cells seeded on PCL, PCL-RGD and PCL-RGE (as negative control) substrates in serum free conditions. The graph in Fig. 1A shows that after 2h from seeding, with and without serum pre-adsorption on PCL-RGD substrates the cell density was higher than on PCL and on PCL-RGE. On the substrates not pre-adsorbed with serum the density was slightly higher than in presence of adsorbed proteins. This evidence could be ascribable to the change of surface physical properties due to protein adsorption. Such effect was empirically observed during the handling of the samples by an increased wettability of our substrates pre-adsorbed with FBS (data not show).

The analysis of cell spreading area confirm the bioactivity of PCL-RGD over PCL and PCL-RGE in both conditions considered (Fig 1B, and Fig. 2). However, interestingly the cells seeded on serum pre-adsorbed substrates showed an higher spreading area than the ones on the not pre-adsorbed

substrates. The desorption of serum proteins and other growth factors from the surface protein layer could support cells during the attachment also at lower concentrations.

In addition, we studied cell adhesion behavior onto different substrates (Fig 1 C) through a shape factor, defined as the ratio of perimeter to area. This shape factor accounts for cell protrusion, such as pseudopodia per unit length. The analysis of the shape factor allow us to determine how cells behave when interact with different surfaces extending pseudopodia to sense the environment and anchor the substrate. As showed in the graph in Fig 1 C, on all the substrates cells isotropically growth with an average value ranging from 0,3 μm^{-1} to 0,2 μm^{-1}. Onto the PCL-RGD samples without serum pre-adsorption a doubled value of shape factor was registered. In this case cells experience an anisotropic ingrowth producing pseudopodia increasing the perimeter over the area and then a number of anchorage points are formed onto the bioactivated surface. In figure 2 are reported the CLSM images of cells .The shadowing of cell images help to highlight the feature of lamellipodia.

Remodelling of proteinaceus layer of physisorbed serum proteins

The effects of cell attachment on the protein adsorption patterns in PCL surfaces, before (PCL) and after bioactivation (PCL-RGD and PCL-RGE), were investigated. Using a combination of 1D-PAGE and spectrophotometric analysis we qualitatively and quantitatively monitored the adsorbed protein on different PCL surfaces after 2h, 6h and 24h of the growth from the seeding.

At first glance the total protein adsorption seems to display a similar trend in all PCL surfaces: amount of physisorbed serum proteins progressively decrease during cell spreding. However, differences were detected for each condition. Less amount of physisorbed proteins was detected in sample derived from not bioactivated PCL after 6h and 24h of cell growth respect to the ones derived from PCL-RGD supports at the same time. Moreover no significant differences were detected for the serum proteins related to PCL-RGD samples at 6h and 24h from the cell seeding, whereas a significant decrease of the amount of desorbed protein was revealed for not bioactivated PCL at 24h. from the seeding

1D-PAGE analyses showed that all bands related to the physisorbed protein content from not bioactivated PCL were also present in the ones related to PCL-RGD but several bands were only detectable in both supports after 2h of cell growth.

IV. Discussions

The most fundamental cell-substrate interaction involves cellular recognition of appropriate surface sites and subsequent cell attachment to the substrate surface. As a cell approaches a substrate, it senses both chemical and physical characteristics of that substrate surface, which includes the protein layer deposited onto these surfaces.

The effect of physisorbed proteins on the cell-recognition was evidenced combining two assays.

In the former, while RGD improved cell adhesion either in presence and absence of pre-adsorbed serum proteins (Fig. 1A and B and Fig. 2), these, nevertheless, play a relevant role in the cell-recognition of surface bound ligands. In the case of preadsorption of serum the spreading area is significantly larger than that observed on substrates without serum, whereas the cell-density is decreased.

On the contrary, when cultured on samples without serum pre-adsorption, cells experience an unspecific attachment driven mainly by hydrophobic interactions. Those interactions act more similar to an adsorption ("cell-adsorption") rather than an attempt by the cells to actively recognize the surface in a receptor mediated way [6].

Additionally, a shape factor was used as parameter to follow cell-behavior during the adhesion at different conditions (Fig. 1C). This parameter gives a measure of the approximate number of cell protrusions per unit length, generally defined as lamellipodia. Figures 1C and 2 show that cells growth isotropically on most of substrates, while on PCL-RGD in absence of pre-adsorbed serum the growth results anisotropic with production of a higher number of pseudopodia (Fig 2). As previously reported [7] [8], in serum deprived conditions cell membrane receptors are not occupied by the growth factor often found in serum (represented by small peptides and proteins) and therefore are more available for binding with substrate-bound ligands.

We also examined if the presence of NIH3T3 on PCL supports were responsible for altered the quantity and composition of the serum adsorbed protein layer during cell attachment and spreading. These data support the hypothesis of an active action of cell in modifying physisorbed serum protein layer during cell attachment and signal recruitment. Moreover, a different behavior of cells on adsorbed protein layer in presence or in absence of RGD signal was detected, which is probably driven by the active role of focal adhesion formation and mechanical strength that they exert on the anchorage point.

References

[1] B. D., Ratner,.*Biomaterials science : an introduction to materials in medicine*, 2nd ed.; Elsevier Academic Press: Amsterdam ; Boston, 2004; p xii, 851 p.

[2] R. J. McMurray, N. Gadegaard, P. M. Tsimbouri, K. V. Burgess, L. E. McNamara, R. Tare, K. Murawski, E. Kingham, R. O. Oreffo, M. J. Dalby, "Nanoscale surfaces for the long-term maintenance of mesenchymal stem cell phenotype and multipotency", Nat Mater Vol 10 pp. 637-644, August 2011.

[3] T. Calimeri, E. Battista, F. Conforti, P. Neri, M. T. Di Martino, M. Rossi, U. Foresta, E. Piro, F. Ferrara, A. Amorosi, N. Bahlis, K. C. Anderson, N. Munshi, P. Tagliaferri, F. Causa, P. Tassone, "A unique three-dimensional SCID-polymeric scaffold (SCID-synth-hu) model for in vivo expansion of human primary multiple myeloma cells", Leukemia vol. 25, pp. 707-711, April 2011.

[4] G. Marletta, G. Ciapetti, C. Satriano, F. Perut, M. Salerno, N. Baldini, "Improved osteogenic differentiation of human marrow stromal cells cultured on ion-induced chemically structured poly-epsilon-caprolactone", Biomaterials vol. 28, pp.1132-1140, June 2007.

[5] E. Battista, F. Causa, V. Lettera, V. Panzetta, D. Guarnieri, S. Fusco, F. Gentile P. A. Netti, "Ligand engagement on material surfaces is discriminated by cell mechanosensoring", Biomaterials vol. 45, pp. 72–80, March 2015.

[6] P. Parhi, A. Golas, E. A. Vogler, "Role of Proteins and Water in the Initial Attachment of Mammalian Cells to Biomedical Surfaces: A Review". J. Adhes. Sci. Technol., vol. 24, pp. 853-888, May 2010.

[7] C. A. Reinhart-King, M. Dembo, D. A. Hammer, "The dynamics and mechanics of endothelial cell spreading", Bioph. J., vol.89, pp. 676-689, January 2005.

[8] B. J. Dubin-Thaler, G. Giannone, H. G. Dobereiner, M. P. Sheetz, "Nanometer analysis of cell spreading on matrix-coated surfaces reveals two distinct cell states and STEP",. Bioph. J. vol. 86, pp.1794-1806, March 2005.

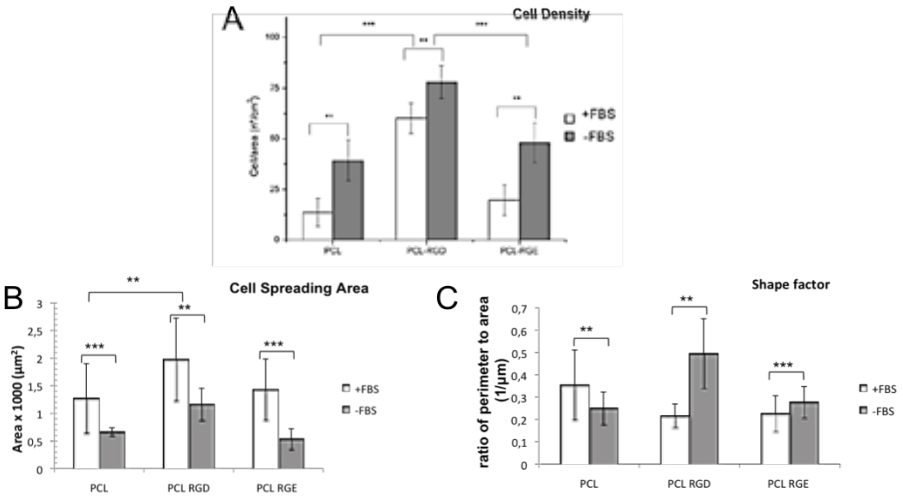

Fig 1**.** A) Cell density on PCL, PCL-DGR and PCL-RGD in presence (+FBS) and in absence (-FBS) of adsorbed serum proteins counted by nuclei staining with DAPI; B) Cell spreading area obtained from the analysis of WGA stained cells, the projected cell-area was calculated by using Image J software; C) Shape factor derived by the ratio of cell perimeter to area.

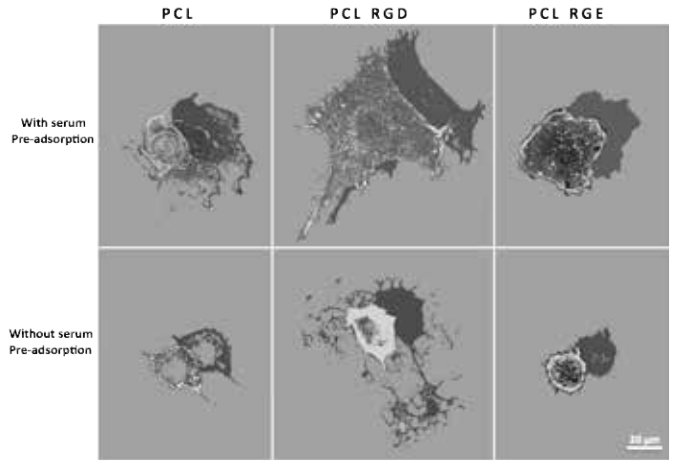

Fig 2. NIH3T3 stained with WGA after 2h from cell seeding on polyemr substrates in serum-free condition. In the first row cells seeded on substrate pre-adsorbed with 10% FBS. On the second row cells seeded on polymer surfaces without serum adsorption. The shadows highlight the features due to cell protrusions. CLSM images taken by SP5 Leica with a 63x objective.
. (** $P \geq 0,05$; *** $P \geq 0,1$)

Engineered 3D-human dermis equivalent model to study in vitro tissue repair

Bernadette Lombardi[1,2], Costantino Casale [2], Giorgia Imparato[1,2], Francesco Urciuolo[1,2], Paolo Netti[1,2]
[1] *Center for Advanced Biomaterials for HealthCare@CRIB Istituto Italiano di Tecnologia, Largo Barsanti e Matteucci n. 53, 80125 Napoli, Italy*

[2] *Interdisciplinary Research Centre on Biomaterials (CRIB), University of Naples Federico II, P.le Tecchio 80, 80125 Naples, Italy*

***Abstract*— We replicate *in vitro* the tissue repair dynamics by using a three-dimensional dermis equivalent (3D-HDE) model. The 3D-HDE is completely formed by cell-synthesized extra-cellular matrix (ECM). After damage, we observed the 3D-HDE behaved similarly to the native dermis in terms of both cells and ECM response. This model paves the way for the fabrication of a high productive platform to study tissue remodeling process *in vitro*.**

***Keywords*—3D-HDE, ECM, wound healing, *in vitro*.**

I. INTRODUCTION

THE SKIN functions as a protective physical barrier against the outside [1] and has a primary role to protect body from external influences such as pathogenic microorganisms and mechanical injuries [2]. Moreover in the skin, the interaction of cells is tightly controlled by various factors [3]. Under normal conditions, there is a balance between cell types via cell–cell contact and the extracellular matrix (ECM). The ECM provides structural scaffolding for cells, as well as contextual information [4], [5][6]. The disruption of these equilibria can result in an uncontrolled stroma degeneration during skin pathologies and alteration [7].

Wound healing is a highly organized series of processes resulting in tissue integrity and function of the damaged tissue; this process needs a complex microenvironement to be studied and represent a significant and increasing burden on healthcare systems globally. Numerous difficulties are associated to use of small animal models, for this reason *in vitro* wound models using human cells in two- and three-dimensional (2D and 3D) environments have been developed to delineate the molecular mechanisms of cellular repair.

Skin equivalents have already been developed to investigate *in vitro* wound healing. Although these studies extensively described the reepithelialization process, and the state of keratinocyte's differentiation during healing, to the best of our knowledge a few of Consequently, the development of biologically relevant three-dimensional human dermal equivalent (3D-HDE) as *in vitro* model can emerge as new challenge in tissue engineering to evaluate dermal remodeling during healing process. In this perspective, a tissue engineering bottom-up approach was used to fabricate a 3D dermis tissue. This model was composed by a cell-synthesized and responsive extracellular matrix that resembles the *in vivo* dermis. The fabrication of an endogenous stroma that interact in a complex manner with cells population allows possibility to confirm the relationship between cell migration, differentiation marker and ECM production during a wound healing process into a highly responsive endogenous matrix.

II. EXPERIMENTAL METHODS

The 3D-HDE was prepared as reported by Palmiero C. *et al*. (2010) [8]. A dermal full-thickness injury was tested on wound platform. Studies were carried oud for 20 days and a sterile scalpel (Brown 11) was used to create a gap in the tissue. During 18 days of standard culture condition wound was monitored by using time-lapse microscopy. The wound healing process and its effects were globally evaluated for 20 days. Morphological analyzes were performed on histological section at different times. Nucleus detections were assessed by using Sytox Green staining and α-smooth muscle actin (α-SMA) was detected by using anti-αSM actin antibody. HA was detected by using an Alcian blue-PAS kit.

III. RESULTS AND DISCUSSIONS

Wound healing assays were performed on a scaffold-free dermis equivalents model, realized by a bottom-up approach [8]. A cell-free gap can be created in 3D tissue by direct manipulation during the development of wound healing assay. The response to the macrotissue damaging was monitored through time-lapse acquisition for 18 days. The figure 1 showed the evolution of the wound during 20 days. It is evident a significant changing in geometry of the edge of the wound and an activation state and migratory abilities of the fibroblast. Thus, the results displayed a complete healing of the dermal wound in 18 days. In figure 2 αSMA (red) and HA production during dermal healing are reported. We found that both αSMA and HA signals presented the strongest signal at 16 days (fig. 2b, 2e). According to the literature [9] , αSMA expression was transient and it was not detectable at 20 days (fig. 2c). At this time HA levels were present (fig. 2f) but decreased compared to 16 days (fig. 2e), as well as *in vivo* happened [9], [10]. In order to demonstrate tissue capability to synthetize new collagen in neo-formed matrix we used second harmonic generation (SHG) analysis [6]. The figure 2 (2g, 2h, 2i) reported the SHG images at 10, 16 and 20 days after cutting, respectively. The signal was strong only in latter image: a relevant quantity of collagen was detected into gap 20 days after wounding (Fig. 2i). After migrating into wounds, fibroblasts commence the synthesis of ECM and the provisional extracellular matrix is gradually

replaced with a collagenous matrix as well as *in-vivo* process [10].

Taken together these results we demonstrated that some of typical proteins involved in *in vivo* wound healing, are also induced in our model by using different experimental set-ups.

IV. Conclusion

Hereby, we were able to set standardized injurie with defined dimensions in a human full-thickness 3D dermis equivalent. We demonstrated the relationship between cell migration, differentiation marker and ECM production during wound healing at same *in vivo* timing. We believe that our bioengineered 3D model of wound closure could be a starting point for a novel platform to test dermal wound therapies. As a fact, future developments could provide a complete model that will put the healthcare research into a better defined frame and more closely resembles the *in vivo* system.

References

[1] J. T. S. Iii, R. G. Tompkins, and J. F. Burke, "Artificial skin," *Rev. Med.*, no. 3, pp. 231–244, 2000.

[2] A. D. Metcalfe and M. W. J. Ferguson, "Bioengineering skin using mechanisms of regeneration and repair," *Biomaterials*, vol. 28, no. 34, pp. 5100–5113, 2007.

[3] Groeber, Florian, Holeiter, Monika, Hampel, Martina, Hinderer, Svenja, Schenke-Layland, and Katja., "Skin tissue engineering — In vivo and in vitro applications," *Adv. Drug Deliv. Rev.*, vol. 63, no. 4–5, pp. 352–366, 2011.

[4] F. A. Auger, D. Lacroix, and L. Germain, "Skin substitutes and wound healing," *Skin Pharmacol. Physiol.*, vol. 22, no. 2, pp. 94–102, 2009.

[5] H. Fernandes, L. Moroni, C. van Blitterswijk, and J. de Boer, "Extracellular matrix and tissue engineering applications," *J. Mater. Chem.*, vol. 19, p. 5474, 2009.

[6] M. J. Bissel and D. Radisky, "Putting tumors in context," *Nat. Rev. Cancer*, vol. 1, no. 1, pp. 46–54, 2001.

[7] D. Elder and D. Elder, "Melanoma Progression," no. 2015, pp. 1–8, 2016.

[8] C. Palmiero, G. Imparato, F. Urciuolo, and P. Netti, "Engineered dermal equivalent tissue in vitro by assembly of microtissue precursors," *Acta Biomater.*, vol. 6, no. 7, pp. 2548–2553, 2010.

[9] W. Y. J. Chen and G. Abatangelo, "Functions of hyaluronan in wound repair," *Wound Repair Regen.*, vol. 7, no. 2, pp. 79–89, 1999.

[10] R. A. F. C. Adam J. Singer, "Cutaneous wound healing," 1999.

[11] C. B. Raub, V. Suresh, T. Krasieva, J. Lyubovitsky, J. D. Mih, A. J. Putnam, B. J. Tromberg, and S. C. George, "Noninvasive assessment of collagen gel microstructure and mechanics using multiphoton microscopy.," *Biophys. J.*, vol. 92, no. 6, pp. 2212–2222, 2007.

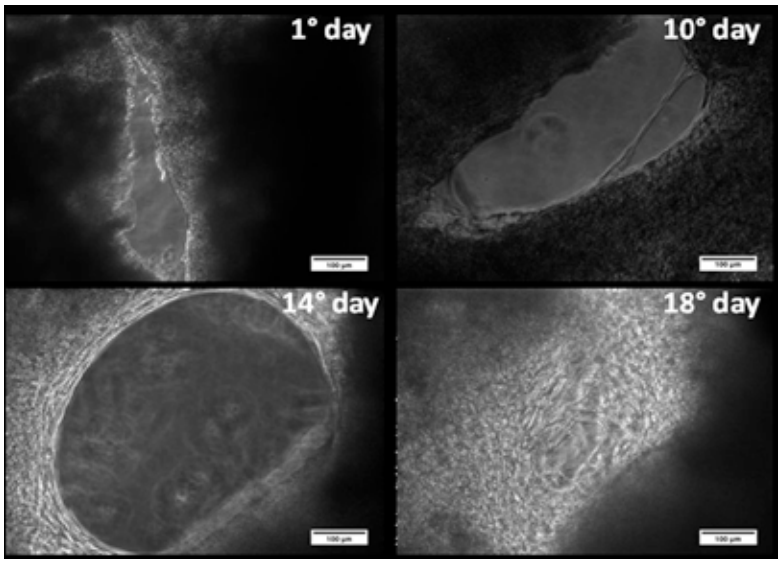

Fig. 1: Wounding and closure of 3D macrotissues. Temporal sequence of wound area showing opening and smoothing of the wound edge (original magnification- 20X and scale bar, 100 µm).

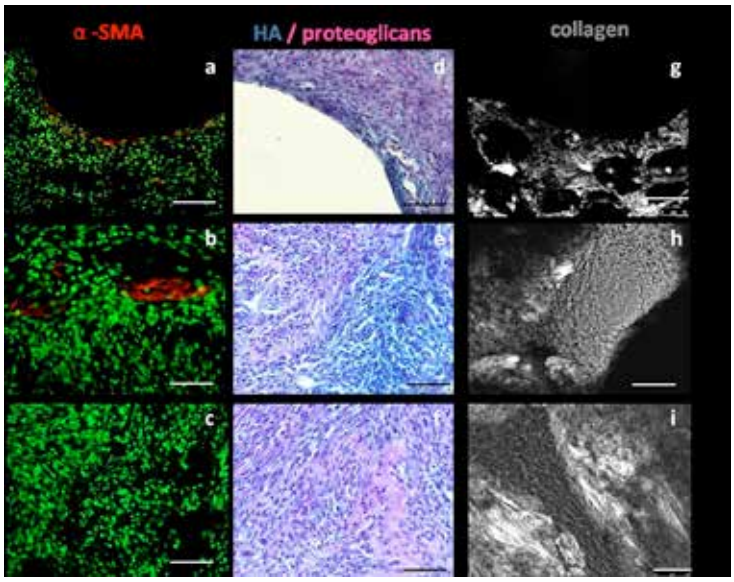

Fig. 2: Temporal sequence of micrographs showing closure progressive of wounded dermis after: 10 days of healing; 16 days of healing; 20 days of healing. Immunofluorescence of the αSMA (a, b and c, respectively) in red, and Alcian blue-P.A.S. staining for proteoglycans production (d, e and f, respectively) are showed. SHG images and collagen detection at same times (g,h,i) are showed. Frozen sections were immunostained for detection. Scale bar: a, d and g 100 µm; b,c,e,f, g, i 50 µm

Effect of SWCNTs in poly(butylene cyclohexanedicarboxylate/diglycolate) random copolymer based nanocomposites: material properties and biological response

F.Luzi[1], E. Fortunati[1], I. Armentano[1], M. Gigli[2], R. Trotta[3], I. Bicchi[3], N. Lotti[2], A. Munari[2], M. Soccio[2], S. Martino[3], M. Gazzano[4], J. M. Kenny[1], L. Torre[1]

[1] *Materials Science and Technology Center, UdR INSTM, University of Perugia, Terni, Italy.*

[2] *Civil, Chemical, Environmental and Materials Engineering Dept. (DICAM), University of Bologna, Bologna, Italy.*

[3] *Department of Chemistry, Biology and Biotechnology, Biochemistry and Molecular Biology Unit, University of Perugia, Perugia, Italy*

[4] *Organic Synthesis and Photoreactivity Institute (ISOF-CNR), CNR, Bologna, Italy*

***Abstract*— The present research proposes the potential use of novel polymeric nanostructured biomaterials developed combining newly synthesized biodegradable and biocompatible polyesters based on poly(butylene 1,4-trans-cyclohexanedicarboxylate) (PBCE) and containing different amounts of ether–linkages, P(BCE90BDG10) and P(BCE70BDG30), with single walled carbon nanotubes (SWCNTs), used as functional phase. The effect of the incorporation of different contents of SWCNTs (0.1, 0.5, 0.75 and 1wt %) on physico-chemical properties of the matrix was studied to modulate and improve the cell viability for final applications in the biomedical field.**

***Keywords*—Single walled carbon nanotubes, ether-linkages, polyesters, biocompatibility.**

I. INTRODUCTION

RECENTLY electrical conductive polymeric materials have attracted considerable interest from academic and industrial researchers for exploring their potential biomedical applications, such as in drug delivery, biosensors systems, tissue engineering and biomedical implants [1]. In this regard, nanocomposite technology permits to incorporate conductive nanostructures with unique properties in a polymer matrix in order to transfer and integrate specific properties into a single material, thereby enabling the development of new multifunctional materials [2].

In this work, we have explored the evolution and potentiality of polymeric nanostructured biomaterials developed combining newly synthesized biodegradable and biocompatible random copolymers based on 1,4-*trans*-cyclohexanedicarboxylic acid and diglycolic acid [3] with a nanocomposite approach, by using single walled carbon nanotubes (SWCNTs) as functional phase. In particular, PBCE homopolymer and two copolymers containing different amounts of ether–oxygen containing co-units, P(BCE90BDG10) and P(BCE70BDG30), have been considered as matrices of SWCNTs based nanocomposites. The effect of the incorporation of different amounts of SWCNTs (0.1, 0.5, 0.75 and 1 wt%) on physico-chemical properties was deeply investigated.

The role of SWCNT incorporation, and content, associated to the random co-unit etheroatoms, were investigated in terms of thermal, mechanical, electrical and dielectrical response whereas the biocompatibility, adhesion and proliferation studies of rat fibroblasts seeded on the biomaterials surfaces were here considered taking into account the final application in the biomedical field of the proposed formulations

II. EXPERIMETAL PART

Poly(butylene cyclohexanedicarboxylate/diglycolate) random copolymers (P(BCEmBDGn)) were synthesized in bulk by two step melt polycondensation [4].

Single walled carbon nanotube based nanocomposite films were prepared by solvent casting method in chloroform ($CHCl_3$). SWCNTs were dispersed in $CHCl_3$ by using a tip sonicator (VIBRA CELL Sonics mod. VC 750, USA) for 30 min in ice bath and for further 30 min in an ultrasonic bath (Ultrasonic bath-mod.AC-5, EMMEGI). The different polymer matrices (PBCE homopolymer, P(BCE90BDG10) and P(BCE70BDG30)) were mixed with nanotube dispersions (polymer/solvent ratio was chosen as 5 (wt/v) %) by magnetic stirring for 5 h. After complete dissolution, the mixture was cast onto a glass Petri substrate and air dried at room temperature (RT) for 24 h and for additional 48 h in vacuum.

Nanocomposite samples containing 0.1, 0.5, 0.75 and 1 wt% with respect to polymer initial weight were prepared with different matrices [5], [6].

The surface morphology of the nanocomposites was investigated by scanning electron microscope, FESEM, while wettability of different films was analysed by using static contact angle. The thermal (differential scanning calorimetry – DSC and thermogravimetric analysis – TGA), dynamic-mechanical (DMA), electrical and dielectrical characterizations were performed while long term culture biological analysis were perfomed by using primary rat fibroblasts (rFFFs), with viability and immunofluorescence study. Elongation factor (EF) and nuclear shape index (NSI) were also evaluated.

III. RESULTS AND DISCUSSION

Figure 1 shows molecular structure of the synthesized copolymers, a scheme of the SWCNTs structure and representative pictures of rat fibroblasts. Neat polymers

showed a white/transparent color, while those based on higher content of SWCNTs presented a completely black appearance, due to the carbon nanotubes and the interconnected microstructure.

The morphology and microstructure of the samples, analysed by FESEM, was affected by the SWCNT presence, while their content did not provide significant modifications. The SWCNT dispersion in the polymer plays a key role on the physical properties of nanocomposites. All nanocomposites exhibited high electrical and dielectrical properties in comparison to the neat polymers. The mechanical characterization (DMA) highlighted the reinforcement effect guaranteed by the SWCNTs for all the studied formulations with a sensible increase of the storage modulus (G') values with SWCNT content [6]. PBCE based formulations displayed the highest G' values while the presence of BDG co-unit reduced the rigidity of the film with a clear lowering in the storage modulus.

Biological investigations showed fibroblasts cultured on polymers and nanocomposites revealing no signs of toxicity, high cell adhesion and a well organization of F-actin (one of the most important protein of the cell cytoskeleton) (Figure 1 c,d), thus indicating their useful application for biological studies. Images show comparable Rat Fibroblasts (rFFFs) adhesion on polymers/SWCNTs, TCP and coverslip, confirming the biocompatibility of these substrates for somatic cell cultures, but, as revealed by the cytoskeleton organization, they also displayed a peculiar cellular organization, depending of the polymer type (Figure 1 c, d).

Thus, compared to control cultures in TCP/glass coverslip, rFFFs cultured in neat PBCE have similar morphology at 6, 14 days, while they became more enlarged at 27 day with F-actin fibres mostly structured in bundles and nuclei well evident (Figure 1 c, d; representative images). Of note, the F-actin organization revealed a more complex scenario in PBCE/SWCNTs (Figure 1 c,d). While, at both short time (6 days) and intermediate time (14 days) cell-to-cell contact decreased with the increase of SWCNTs wt % (0.5 and 1 wt %), after long-time in culture the cell interaction increase with the presence of SWCNTs. In particular at 27 days, rFFFs on PBCE/0.5SWCNTs polymer generated cell-clusters, with cells that, in many case, were attached together, whereas in PBCE/1SWCNTs, rFFFs created a structure like-network through protruding cell F-actin filipodia that interacted with those of other cells.

IV. Conclusion

The combination of new synthesized biodegradable copolymers with synthetic conductive nanostructures offers excellent capability in advanced functional materials. This approach can be extended and serve as a guide for the design of other high performance composites for biomedical applications.

References

[1] G. Kaur, R. Adhikari, P. Cass, M. Bownand P. Gunatillake, "Electrically conductive polymers and composites for biomedical applications", *RSC Adv*, vol. 5, pp. 37553-37567, 2015.

[2] I. Armentano, M. Dottori, E. Fortunati, S Mattioli, J.M. Kenny, "Biodegradable polymer matrix nanocomposites for tissue engineering: A review" *Polym. Degrad. Stab*., vol 95, 2126- 2146, 2010.

[3] M. Gigli, N. Lotti, M. Vercellino, L. Visai, A. Munari, "Novel ether-linkages containing aliphatic copolyesters of poly(butylene 1,4-cyclohexanedicarboxylate) as promising candidates for biomedical applications", *Mater. Sci. Eng. C.,* vol 34, 86-97, 2014.

[4] M. Gigli, N. Lotti, M. Gazzano, V. Siracusa, L. Finelli, A. Munari, M. Della Rosa, "Fully Aliphatic Copolyesters Based on Poly (butylene 1, 4-cyclohexanedicarboxylate) with Promising Mechanical and Barrier Properties for Food Packaging Applications", *Ind. Eng. Chem. Res*., vol. 52, 12876-12886, 2013.

[5] E. Fortunati, M. Gigli, F. Luzi, N. Lotti, A. Munari, M. Gazzano, I. Armentano, J. M. Kenny, "Poly(butylene cyclohexanedicarboxylate/ diglycolate) random copolymers reinforced with SWCNTs", *eXPRESS Polym. Letter*., vol.10, pp. 111–124, 2016,

[6] I. Armentano, E. Fortunati, M. Gigli, F. Luzi, R. Trotta, I. Bicchi, M. Soccio, N. Lotti, A. Munari, S. Martino, L. Torre, J. M. Kenny. "Effect of SWCNTs introduction in random copolymers on material properties and fibroblast long term culture stability", *Polym. Degrad. Stab*. doi.org/10.1016/j.polymdegradstab.2016.02.019

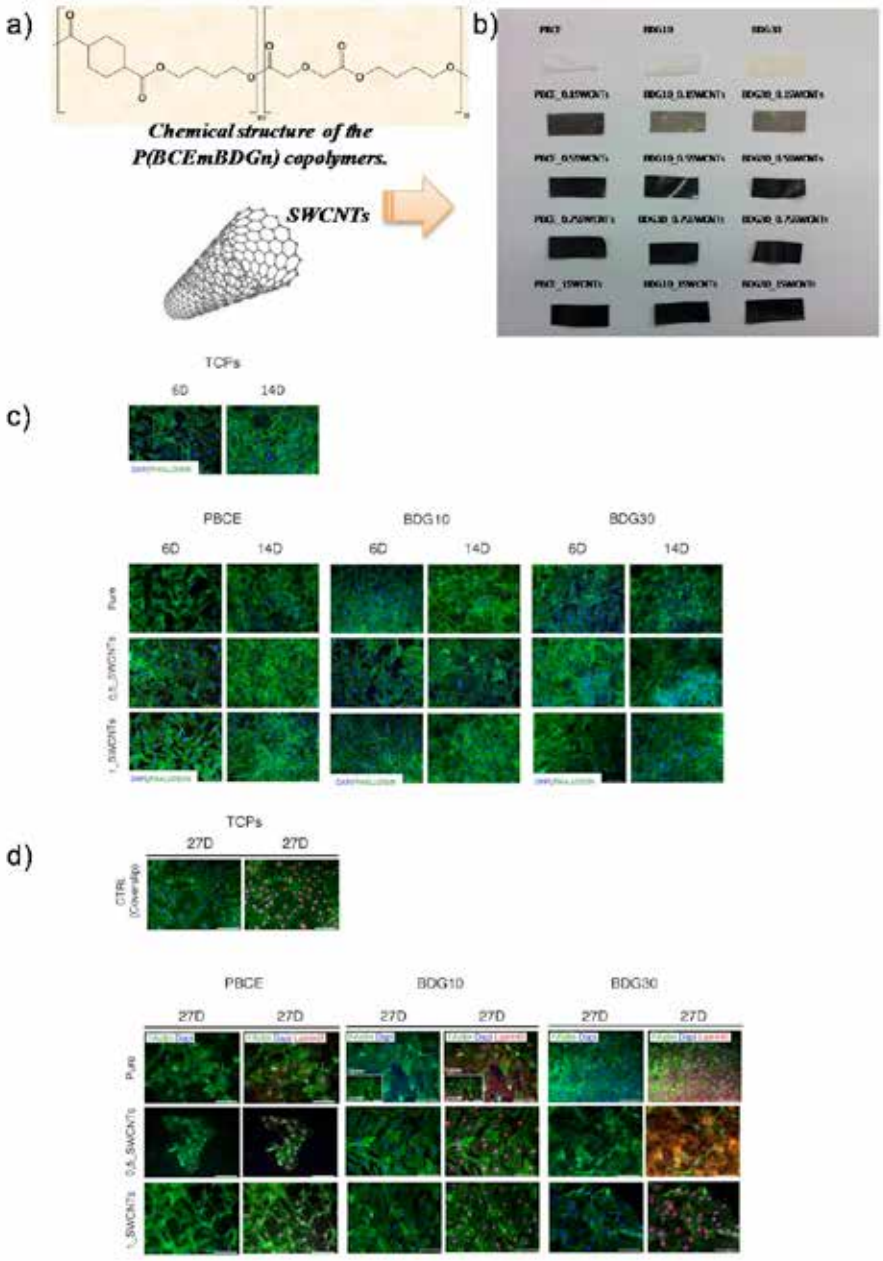

Fig. 1. Molecular structure of the synthetized copolymers (a), visual observation image of the samples (b) and fluorescence images of rat fibroblasts seeded of developed polymer and nanocomposite for 6-14 days c) and 27 days d) of incubation seeded of developed polymer and nanocomposite.(F-actin (Green fluorescence, Phalloidin), nuclei (DAPI fluorescence) and lamin B (nucleoskelethon; Cherry-fluorescence)).

Development of organotypic and vascularized *in vitro* skin models

C. Mazio[1,2,3], C. Casale[2], F. Urciuolo[1], G. Imparato[1], P.A. Netti[1,2,3]

[1] *Center for Advanced Biomaterials for Health Care@CRIB Istituto Italiano di Tecnologia, Largo Barsanti e Matteucci n. 53, 80125 Napoli, Italy*

[2] *Interdisciplinary Research Centre on Biomaterials (CRIB), University of Napoli Federico II, P.le Tecchio 80, 80125 Napoli, Italy*

[3] *Department of Chemical, Materials and Industrial Production Engineering (DICMAPI), University of Napoli Federico II, P.le Tecchio 80, 80125 Napoli, Italy*

***Abstract*— The knowledge of the evolution of endothelial structures is important to choose the right time for *in vitro* and *in vivo* applications of vascularized models. The aim of the project is the *in vitro* vascularization of a skin equivalent model produced by bottom-up approach. The endothelial cells are able to deeply penetrate into the endogenous collagen characterizing the dermal component of the model forming capillary like structures . The challenge is to obtain a stable and pervious vascular network suitable for *in vitro* an *in vivo* applications.**

***Keywords*—bottom-up, vascularized skin equivalent, capillary like structures.**

I. Introduction

Vascularization is still a great challenge in Tissue Engineering [1]. First this is important to avoid mass transfer limitation in engineered tissues [2] but also for innovative *in vivo* and *in vitro* applications. A pre-vascularized tissue can accelerate the formation of functional anastomosis with host vasculature *in vivo*. In the same time, *in vitro*, it can be a suitable model in view of fundamental research and industrial applications like drugs screening[1]-[3].

The two processes through which neo-vascularization can take place in tissues are angiogenesis and vasculogenesis.

Angiogenesis is the process through which new blood vessels are formed from pre-existing ones, whereas vasculogenesis generates new vascularization in the absence of pre-existing blood vessels [1].

When Endothelial Cells (ECs) are cultured *in vitro* in permissive conditions, especially when they are three-dimensionally co-cultured with other cell types and in a relevant ExtraCellular Matrix (ECM), they result in spontaneous capillary-like network formation. It has widely been demonstrated that fibroblasts promote ECs proliferation, migration, and angiogenesis, both *in vivo* and *in vitro*[1].

The first vascularized skin-equivalent model *in vitro* is to Auger *et al* in 1998. The tissue was obtained through a co-culture of three types of human cells: keratinocyte, fibroblasts and Umbilical Vein Endothelial Cells (HUVEC) within chitosan / collagen scaffolds. In this skin-equivalent model ECs are capable of spontaneously forming, after 31 days, capillary structures in a highly differentiated ECM showing positivity for von Willebrand factor, Weibel-Palade bodies, Laminin and Collagen IV, typical of the *in vivo* microcirculation vessels [4]. HUVEC can also grow and differentiate within artificial dermis obtained by seeding fibroblasts on hyaluronic acid scaffolds and the best ratio for the co-culture, in terms of viability and metabolic activity, is of 1:1 [5].

Recent studies show the possibility of making pre-vascularized skin engineered models with an extensive blood and lymphatic network. Reichmann *et al* seeded ECs and fibroblasts in hydrogel of collagen I/fibrin. They used Human Dermal Microvascular Endothelial Cell (HDMEC) extracted from foreskin, a population including both blood that lymphatic ECs. After 3 weeks of culture cells are able to organize themselves into capillary structures positive for the CD31 marker (pan-endothelial), Prox-1/Lyve-1 and podoplanin (lymphatic markers). Blood and lymphatic vessels never anastomose between them *in vitro*. After 2 weeks keratinocytes has been seeded on the surface construct containing fibroblasts and HDMEC. After another week of *in vitro* culture the complete model has been transplanted on the back of immunosuppressed rats. 2 weeks after implantation the tissue was surgically removed and analyzed revealing the formation of functional anastomosis between the lymphatic vessels of the construct with the host as well as to the blood vessels[6].

Despite the improvements occurred in the issue of vascularization of engineered tissues, actually there aren't dermal pre-vascularized substitutes used in the clinic. One of the major challenges is to obtain a pervious and stable vascular network within a construct with good mechanical strength, poor deformability and controlled degradation of the scaffold *in vivo*[7].

II. Methods and results

The aim of the project is the neo-vascularization of a skin equivalent model able to meet these requirements.

It is obtained *in vitro* with a bottom-up approach involving the dynamic cell seeding of fibroblasts on porous gelatine micro-spheres using a spinner flask bioreactor. Cells adhere, proliferate and synthesize a thin layer of ECM in and around the beads, generating micro-tissues (μTPs) rich in type I collagen. The assembly of μTPs in specific maturation chambers allows to obtain biohybrids dermis equivalent[8].

After the seeding and culturing of ECs on these construct we have obtained a pre-vascularized dermis model with capillary like structures growing up until 2 weeks (Fig.1) and positive for maturation markers from 1 week after EC seeding(Fig.2). The vascular network branches within the collagen rich ECM produced by the fibroblasts and able to offer pro-angiogenic signals that can guide the physiological development of the network itself. The scaffold degradation occurs *in vitro* with

known timing allowing the further synthesis of new tissue [9]. The construct has a defined micro-architecture and it is equipped with structural proteins produced by fibroblasts. These attributes award a high mechanical strength of the construct and poor deformability.

The seeding of keratinocytes on this model let the implementation of a vascularized skin equivalent as they are able to proliferate and differentiate forming a mature epithelium.

III. Conclusion

It is expected that this model could be useful for *in vivo* applications. In this way it will be possible to demonstrate that the obtained network is pervious and can form anastomosis with the host ensuring a rapid integration of the implant and its survival.

The construct could have interesting *in vitro* application for the study of drugs and molecules via topical or systemic administration, once passed the critical point to perfuse the vascular network *in vitro*.

References

[1] L. G. and D. L. François A. Auger, "The Pivotal Role of Vascularization in Tissue Engineering," Annu. Rev. Biomed. Eng., vol. Vol. 15, pp. 177–200, 2013.

[2] M. Lovett, K. Lee, A. Edwards, and D. L. Kaplan, "Vascularization strategies for tissue engineering.," Tissue Eng. Part B. Rev., vol. 15, no. 3, pp. 353–370, 2009.

[3] F. Groeber, M. Holeiter, M. Hampel, S. Hinderer, and K. Schenke-Layland, "Skin tissue engineering - In vivo and in vitro applications," Adv. Drug Deliv. Rev., vol. 63, no. 4, pp. 352–366, 2011.

[4] a F. Black, F. Berthod, N. L'heureux, L. Germain, and F. a Auger, "In vitro reconstruction of a human capillary-like network in a tissue-engineered skin equivalent.," FASEB J., vol. 12, no. 1, pp. 1331–1340, 1998.

[5] C. Tonello, B. Zavan, R. Cortivo, P. Brun, S. Panfilo, and G. Abatangelo, "In vitro reconstruction of human dermal equivalent enriched with endothelial cells," Biomaterials, vol. 24, pp. 1205–1211, 2003.

[6] D. Marino, J. Luginbühl, S. Scola, M. Meuli, and E. Reichmann, "Bioengineering dermo-epidermal skin grafts with blood and lymphatic capillaries.," Sci. Transl. Med., vol. 6, p. 221ra14, 2014.

[7] X. B. C. & D. J. S. Md. Sarker, "Experimental approaches to vascularisation within tissue engineering constructs," J. Biomater. Sci. Polym. ed., 2015.

[8] C. Palmiero, G. Imparato, F. Urciuolo, and P. Netti, "Engineered dermal equivalent tissue in vitro by assembly of microtissue precursors," Acta Biomater., vol. 6, pp. 2548–2553, 2010.

[9] G. Imparato, F. Urciuolo, C. Casale, and P. a. Netti, "The role of microscaffold properties in controlling the collagen assembly in 3D dermis equivalent using modular tissue engineering," Biomaterials, vol. 34, no. 32, pp. 7851–7861, 2013.

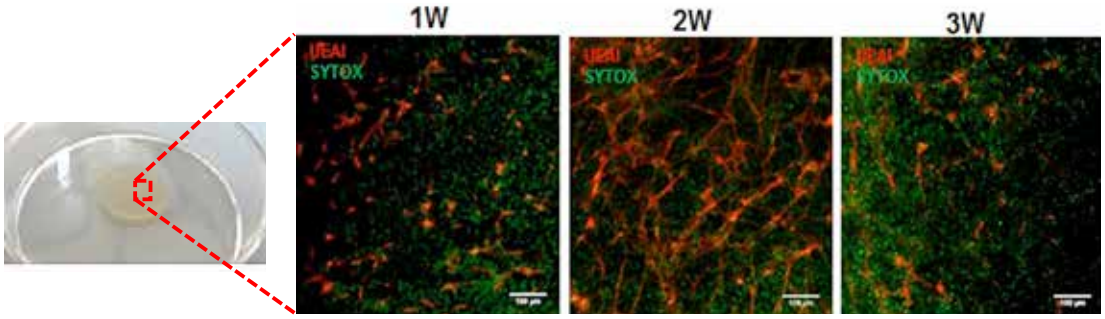

Fig. 1. Immunofluorescence showing in green all the nuclei (sytox sgreen) and in red the endothelial network (UEAI) into the dermal equivalent biohybrid 1, 2 and 3 weeks after endothelial cells seeding. The capillary network in growing up until 2 weeks and then it's going toward regression

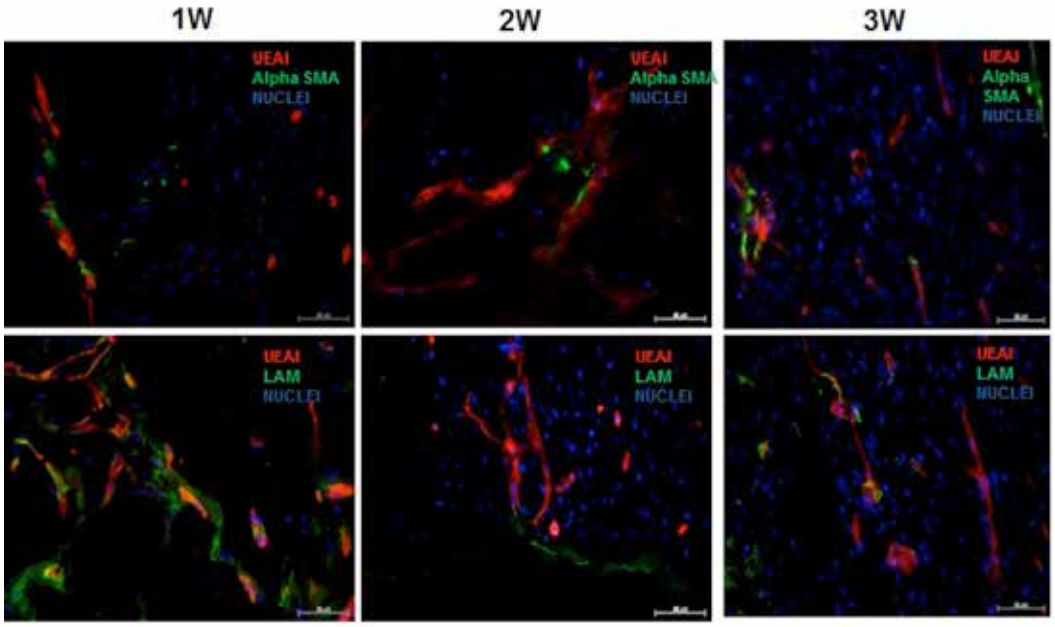

Fig. 2. Immunofluorescence of biohybrids'sections showing all the nuclei in blue (DAPI), the endothelial cells in red (UEAI) and the markers of vessels maturation in green (Alpha sma an Laminin) at 1,2 and 3 weeks after endothelial cells seeding.

Core-shell microgels: synthesis and structural characterization

A. Mazzarotta[1,2], E. Battista[1,2] F. Causa[1,2,3] P.A.Netti[1,2,3]

[1] *Interdisciplinary Research Centre on Biomaterials (CRIB), University of Naples Federico II, Piazzale Tecchio 80, 80125, Napoli, Italy*

[2] *Center for Advanced Biomaterials for Health Care@CRIB, Istituto Italiano di Tecnologia, Largo Barsanti e Matteucci 53, 80125, Napoli, Italy*

[3] *Dipartimento di Ingegneria Chimica, dei Materiali e della Produzione Industriale(DICMAPI), University "Federico II", Piazzale Tecchio 80, 80125, Naples, Italy*

***Abstract*— Microgels have become recognized as environmentally responsive systems with a great potential in smart and controlled applications such as diagnostic and in drug delivery systems. In order to correlate structure with final properties, it is necessary to know the microgels particles from a microscopic point of view. In this work, multifunctional PEG-microgels with core-shell architecture were obtained combining precipitation and seeded polymerizations. Here we demonstrated the possibility to tailor and control the bulk and surface properties accordingly to the synthesis. Moreover we characterize structurally microgels, using polymer fraction volumes from AFM images combined with the equilibrium swelling theory (Peppas–Merrill equation), in order to determine the mesh size of microgels. Such microgels can be used in multiplex assays for their favorable capability to accommodate encoding systems and anchoring groups for probes to capture circulating targets by simply changing synthesis parameters.**

***Keywords*— core−shell microgels; AFM; fluorescent encoding; swelling behaviour.**

I. INTRODUCTION

MICROGELS are intramolecularly crosslinked polymer particles, whose diameter ranges in the sub-micrometer scale (10 nm – 1μm). They have the ability to swell and shrink in suitable solvents due to their sponge-like structure,that is responsible for the final properties [1]-[2].

Recent research has focused on multifunctional hydrogel particles as materials platforms to realize next generation of diagnostic tools [3]-[4]. The most attractive feature of such materials consists on the flexibility of synthetic routes to design a multifunctional microparticle able to accommodate chemical compounds as elements to provide encoding and sensing abilities against different kind targets such as pollutants [3] or clinically relevant biomarkers [5]-[6]

In order to correlate structure with final properties, structural characterization and swelling behavior it is necessary tobe investigated. Microgels represent a versatile class of polymeric particles that allows the realization of a chemical tool box for on-demand production through the combination of various monomers, chemical approaches, architectures and microfluidic devices [7].

II. EXPERIMENTAL SECTION

A. Synthesis of Microgels

Core were prepared by free-radical precipitation polymerization, using PEGDMA (MW 550) 1% (w/v) of total concentration as monomer. Polymerization was carried out in a three-neck, 100 mL round-bottom flask to which a filtered, aqueous solution of all monomers and 1% (w/v) PVA were added. This solution was heated to ~ 65 ºC while being purged with N_2 gas and stirred vigorously for ~ 1 h. Then KPS aqueous solution (0.06 w/v) as initiator and methacryloxyethyl thiocarbamoyl rhodamine B, dissolved in dimethyl sulfoxide (DMSO) and diluted with water 0.1 mM, were added to the stirred mixture. The solution was allowed to heat and stir for an additional 7 h while being purged with nitrogen gas. The rhodamine-labelled core microgels (R1-core) were resuspended in deionized water to a concentration of 10 mg/mL and used as seeds for subsequent polymerization of additional PEGDMA cross-linked (0.5% w/v). Similarly to previous step, solution was heated at 65°, purged with N_2 gas, stirred vigorously for ~ 1 h and finally KPS was added. For the outer shell synthesis, to obtain double shell microgels with different contetnt of Fluo and AAc (R_1-F_xAAc_x), a solution of R1-PEG microgels (10mg/ml) was heated to 65 ºC, followed by the slow addition of 10 mL of aqueous monomer solution containing PEGDMA (250 mg) and Acrylic acid (AAc) (concentration ranging from 3.6-36 mM). Then KPS (1mM) and Fluo (0.1-0.3 mM) were added to initiate the polymerization. The reaction was allowed to proceed for 6 h. Afterwards double shell microgels were dialyzed for 15 days and purified several times by centrifugation (Fig. 1).

III. RESULTS AND DISCUSSION

A. Synthesis and characterization

In this work, multifunctional microgels were obtained through a multistep procedure combining free-radical precipitation polymerization and seeding polymerization, using Poly(ethylene glycol) dimethacrylate as main cross-linker. We were able to synthetize monodisperse microgels (R_1-core) with a narrow size distribution (549 ± 7 nm), that are used as seeds for synthesis of complex multishell microgels architectures. Both first and second resulted monodisperse with a narrow size distribution of 724 nm (±16 nm) for 1st shell and respectively 1389 nm (±162 nm),976 nm (±16 nm) and 1075 nm (±19 nm) for R_1-F_1AAc_{100} , R_1-F_3AAc_{10} and R_1-F_3AAc_{100} (Table I). In-situ AFM measurements were performed using ScanasystBruker, and "ScanAsyst Fluid+" as probes. Experiments were performed in order to determine morphological features and swelling parameters useful to probe the inside structure of microgels.

	PEGDA (mM)	Rhod (mM)	Fluo (mM)	Aac (mM)	KPS (mM)	PVA (mM)	Diameter (nm)
R_1	18.2	0.1	--	--	2.2	48	549±7
R_1PEG	9.1	--	--	--	1.1	48	724±2
$R_1F_1AAc_{100}$	9.1	--	0.1	36	1.1	48	1389±162
$R_1F_3\ AAc_{10}$	9.1	--	0.3	3.6	1.1	48	976±16
R_1F_3 AAc_{100}	9.1	--	0.3	36	1.1	48	1075±19

TABLE I : *Microgel's recipes and their characteristic diameter (DLS).*

In-situ AFM measurements were conducted on all samples in dried form and at different pH. First we measured dried microgels, then an amount of PBS 10 mM pH>8 was added submerging all the microgels. The system was allowed to swell for at least 30 min and images were acquired. Afterwards, measurements in acid conditions were performed on the same regions by exchanging the medium (PBS 10mM at pH<3) allowing microgels to equilibrate for a period of time (about 30 min). Our microgels results to be pH-responsive collapsing in acid and swelling to their maximum size in base above their pKa (pH>8).

As depicted in Fig. 2, microgels in the swollen state tend lose their spherical structure remaining sticked on the substrate reaching on average a height far from the original one measured by DLS in solution. Our studies show that the measure of particle volume simply through the diameter results difficult and unreliable. Infact during the drying process, microgels are dried in vacuum at 40 °C producing an alteration of their original shape due to their softness. Moreover, in wet particles we can observe an irregular shape highlighted by the profiles taken in three different directions along the center of a microgel, which describe three different areas/volumes and bring to a misinterpretation of the real volume. For that reasons we calculated the volume of each particle and swelling ratio (Q) directly form AFM images by "Laplacian volume"[8].

$$Q_s = \frac{V_s}{V_d} \qquad Q_r = \frac{V_r}{V_d} \qquad (1)$$

These values were used to apply the equilibrium swelling theory [9] to investigate structural microgels parameters such as molecular weight between two neighboring crosslinks (Mc) and mesh size (ξ) [10].

$$\frac{1}{\bar{M}_c} = \frac{2}{\bar{M}_n} - \frac{\left(\frac{\bar{v}}{V_1}\right)\left[ln(1-v_{2,s}) + v_{2,s} + \chi_1 v_{2,s}^2\right]}{v_{2,r}\left[\left(\frac{v_{2,s}}{v_{2,r}}\right)^{1/3} - \left(\frac{v_{2,s}}{2v_{2,r}}\right)\right]} \qquad (2)$$

$$\xi = v_{2,s}^{-1/3}(\bar{r}_0^2)^{1/2} \qquad (3)$$

Qs show a constant increase from R_1 to first and second shell microgels. Indeed the core result to have a higher density with respect to the adlayers according to synthesis recipe (Fig.3). On the other hand, while we were not able to calculate Qr for the not pH-responsive microgels (R1 and R1-PEG), the swelling behavior in the relaxed state of double shell microgels showed an increasing trend that basically follows the increase of the monofunctional monomers (Fluo and AAc). Indeed they represent chain extenders as the relative ratio crosslinker/ monomer increase.

IV. CONCLUSION

In conclusion, here we show a flexible synthesis of fluorescently encoded double shell microgels and the investigation of bulk and surface properties by AFM. We successfully synthetized multifunctional microgels in a combination of precipitation and seeded polymerizations demonstrating the ability of the process to obtain well defined particles in terms of inner and outer shell chemistry. In particular we have shown that is possible to realize in a two-step synthesis complex architectures to accommodate additives (i.e. fluorescent dyes) in the inner part physically separated by superimposition of different layers at different composition. Further we demonstrated the possibility to include carboxyl groups on the outer layer that give rise responsivity to pH changes and the potential anchoring group for a capture molecule. The results presented here, and in very recent studies of our group [11]-[12], suggest that such microgels represent a valuable tool for the realization of highly hydrated multifunctional particles with extreme flexibility and reproducibility to be used as carrier in diagnostics. Further work is now underway to exploit such multifunctional microgels in multiplex assays toward different clinically relevant targets.

REFERENCES

[1] Murray, M. J., & Snowden, M. J. (1995). The preparation, characterisation and applications of colloidal microgels. Advances in colloid and interface science,54, 73-91.

[2] Saunders, B. R., & Vincent, B. (1999). Microgel particles as model colloids: theory, properties and applications. Advances in colloid and interface science,80(1), 1-25.

[3] Birtwell, S., & Morgan, H. (2009). Microparticle encoding technologies for high-throughput multiplexed suspension assays. Integrative Biology, 1(5-6), 345-362.

[4] Cusano AM, Causa F, Moglie RD, Falco N, Scognamiglio PL, Aliberti A. et al., J R Soc Interface 11:20140718 (20149.

[5] Pregibon, D. C., Toner, M., & Doyle, P. S. (2007). Multifunctional encoded particles for high-throughput biomolecule analysis. Science, 315(5817), 1393-1396.

[6] Ulijn, R. V., Bibi, N., Jayawarna, V., Thornton, P. D., Todd, S. J., Mart, R. J., & Gough, J. E. (2007). Bioresponsive hydrogels. Materials today, 10(4), 40-48.

[7] Kim, J. W., Utada, A. S., Fernández-Nieves, A., Hu, Z., & Weitz, D. A. (2007). Fabrication of monodisperse gel shells and functional microgels in microfluidic devices. Angewandte Chemie, 119(11), 1851-1854.

[8] Battista, E., Mazzarotta, A., Causa, F., Cusano, A. M., & Netti, P. A. (2016). Core Shell Microgels with Controlled Structural Properties. Polymer International.

[9] Flory, P. J., & Rehner Jr, J. (1943). Statistical mechanics of cross-linked polymer networks II. Swelling. The Journal of Chemical Physics, 11(11), 521-526.

[10] Peppas, N. A., Bures, P., Leobandung, W., & Ichikawa, H. (2000). Hydrogels in pharmaceutical formulations. European journal of pharmaceutics and biopharmaceutics, 50(1), 27-46.

[11] Aliberti, A., Cusano, A. M., Battista, E., Causa, F., & Netti, P. A. (2016). High sensitive and direct fluorescence detection of single viral DNA sequences by integration of double strand probes onto microgels particles. Analyst.

[12] Manikas, A. C., Aliberti, A., Causa, F., Battista, E., & Netti, P. A. (2015). Thermoresponsive PNIPAAm hydrogel scaffolds with encapsulated AuNPs show high analyte-trapping ability and tailored plasmonic properties for high sensing efficiency. Journal of Materials Chemistry B, 3(1), 53-58.

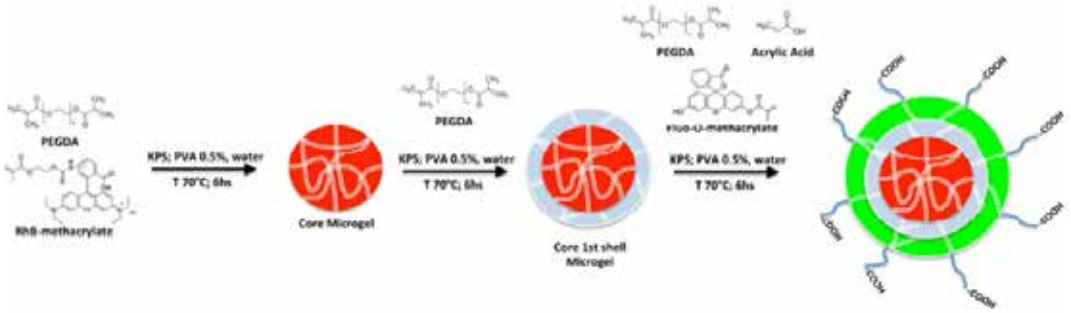

Fig. 1 Schematic representation of core−shell microgel synthesis obtained by combining precipitation and seeded polymerizations.

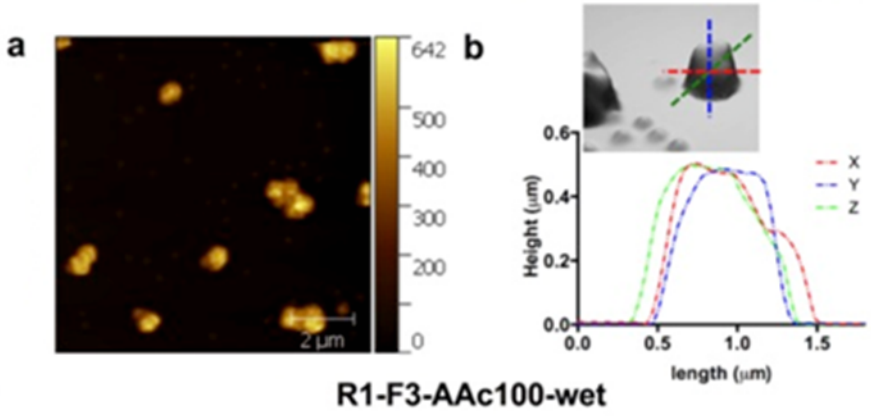

Fig. 2 (a) AFMimages of second shell microgels in the wet condition
(b)Microgel profile taken in three different directions along one microgel.

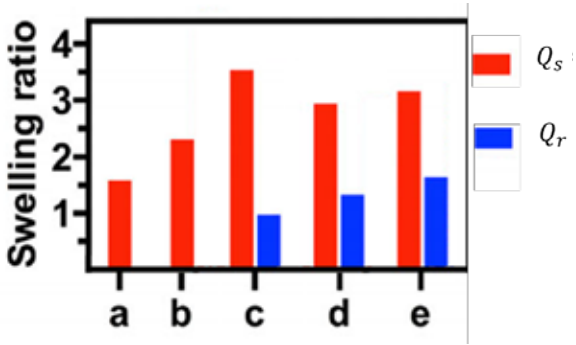

Fig. 3 Swelling ratio calculated in both the swollen and relaxed state for microgels (Qs, Qr):
(a) core microgel (R1); (b) first shell (R1PEG); (c) second shell (R1F1AAc100); (d) second shell (R1F3AAc10); (e) second shell (R1F3AAc100)

AFM investigation of Mesothelial Cells Mechanics and their mechanosensing of ECM with different stiffness

I Musella[1], S Fusco[1*], V Panzetta[1], M De Menna[2], M Volante[3], I Rapa[3], PA Netti[1,4]

1 Center for Advanced Biomaterials for Health Care@CRIB Istituto Italiano di Tecnologia, Largo Barsanti e Matteucci n. 53, 80125 Napoli, Italy.

2 Department of Experimental and Clinic Medicine, University of Catanzaro Magna Graecia, Catanzaro, Italy.

3Department of Oncology, University of Turin, Regione Gonzole 10, 10043 Orbassano, Torino, Italy.

4 Interdisciplinary Research Centre on Biomaterials (CRIB), University of Napoli Federico II, P.le Tecchio 80, 80125 Napoli, Italy.

**corresponding author (e-mail: sabato.fusco@iit.it)*

***Abstract*—Mechanical properties of cells play an important role in many biological processes such as cell growth, migration, division and differentiation. Cell mechanics is mainly determined by the cytoskeleton and changes in such a crucial structure lead to pathological condition, including cancer. Measuring a cell's rigidity provides information about its state and composition and may be viewed as a new mechanical marker. Atomic Force Microscopy (AFM) technique was performed to quantify the mechanical properties of living cells in order not only to discriminate between non-cancerous and cancerous cells, but also between cells with different metastatic potential.**

***Keywords*—Cancer, Mechanical Properties, Mechanosensing, AFM.**

I. Introduction

Cells are highly dynamic systems that continuously change their chemical and physical characteristics. Many aspects of cellular physiology rely on the ability to control mechanical stimuli across the cell. Mechanical properties of cells, indeed, play an important role in many biological processes such as cell growth, migration, division and differentiation. Cell mechanics is mainly determined by the cytoskeleton [1].The cytoskeleton carries out three broad functions: it spatially organizes the content of the cell; it connects the cell physically and biochemically to the external environment; and it generates coordinated forces that enable the cell to move and change shape. Given the widespread role of the cytoskeleton in cellular function, changes in such a crucial structure lead to pathological condition. Many diseases have now been associated with abnormalities in cytoskeleton, including cancer [2]-[4]. Intracellular pathological state influences cytoskeletal structure and function, changing the cell mechanical properties. From a general point of view, cytoskeletal strength and organization increase as a cell becomes more differentiated. In particular, during cancer progression, malignant cells undergo a transdifferentiation process, becoming softer than mature fully differentiated cells. The increased deformability allows cancer cells to infiltrate and invade tissues, and migrate to distant sites. Consequently, measuring a cell's rigidity provides information about its state and composition and may be viewed as a new mechanical marker. The decrease in cell stiffness with malignant transformation has been observed in a variety of cancers such as breast cancer, lung cancer, renal cancer, prostate cancer, oral cancer, skin cancer [5]-[7]. Furthermore, the decrease in cell stiffness seems to be greater in cells with higher malignancy and metastatic potential [8]. For a very detailed mechanical phenotyping of the tumours, it is necessary to consider the crosstalk between the cells and their surrounding extracellular matrix (ECM). Tissue mechanobiology is the result of a self-sustaining combination of interactions generating between cells and their microenvironments: i) the cell may modify the environment chemically by the metalloproteinases secretion [9],[10], or mechanically and topographically by the generation and the transmission of forces [11],[12]; ii) the ECM, thanks its mechanical and topographic features, is able to induce structural modifications of the cytoskeleton and, then, to trigger different cell functions as a responsive adaptation Thus, during tumour progression, not only cells, but also ECM is affected to transformation: cell softening is generally combined with matrix stiffening. For this reason, it could be intriguing to study if changes in ECM architecture and mechanics may be sufficient for cancer cell normalization and tumour regression.

To this aim in this work we investigated how cancer modified the mechanics of mesothelial cells. Using AFM technique we quantified the mechanical properties of a benign human mesothelium cell line, Met5A, and three human mesothelioma cell lines (MSTO, REN, MPP-89) with different metastatic potentials. First, we assessed the major compliance of the cancer cells compared to the healthy ones. Then, we associated mechanical phenotype information to the metastatic potential of each cell line by pairing analyses of migration and proliferation with mechanical classification. Finally, focusing the attention on the most aggressive cell line, the influence of ECM stiffness on cell mechanics and functions was outlined.

II. Materials and Methods

The mechanical properties of a benign human mesothelium cell line, Met5A, and three human cancer mesothelioma cell lines (MSTO, REN, MPP-89) with different metastatic potentials, were quantified using AFM technique. The mechanical phenotype was associated to the metastatic potential of each cell line by comparing the mechanical classification to analysis of migration and proliferation. Moreover, to study the effects of ECM stiffness on cell mechanics and spreading, cells were cultured on 0.15 kPa and 30 kPa polyacrylamide hydrogels (PAAm).

III. Results

A. Proliferation and Migration Analysis

Mesothelial cells were classified on the basis of cell proliferation and migration, two parameters notoriously altered in cancer. We examined single cell migration and collective migration, through wound healing. Our results suggested that REN cells were the less aggressive, while MSTO and MPP89 cells displayed an higher metastatic potential.

B. Cell Mechanics

We analysed mechanical properties of human mesothelial single cells and cell monolayer. In both cases, control cell line (Met5A) was stiffer than mesothelioma cell lines. Moreover, cancer cells showed different mechanical properties: their Young's modulus decreased with the metastatic potential.

C. Mechanosensing

In order to investigate mechanosensing capacity of mesothelial cells, we analysed the effects of substrate stiffness variation on spreading area and cell migration. As expected, cell spreading and migration increased on stiffer polyacrylamide substrates.

IV. Conclusions

Atomic force microscopy indentation using a micro-sized spherical probe was carried out to characterize the elasticity of human mesothelial cells. We observed not only that cancer cells were softer than benign control, but also that malignant cell lines had different mechanical properties. Therefore, AFM technique was able not only to discriminate between non-cancerous and cancerous cells, but also between cells with different metastatic potential. Finally, it is well known that the ability of mechanosensing may be different depending on the tumour cell line, so we confirmed the capacity of mesothelial cells to respond to stiffness substrate changes.

References

[1] Gardel ML1, Kasza KE, Brangwynne CP, Liu J, Weitz DA. Chapter 19 Mechanical Response of cytoskeleton network Methods Cell Biol. 89, 487–519 (2008).

[2] F.C.S. Ramaekers, F.T. Bosman. The cytoskeleton and disease. J. Pathol., 204 (2004), pp. 351–354

[3] Hall, A. The cytoskeleton and cancer. Cancer Metastasis Rev. 28, 5–14 (2009).

[4] C.M. Fife, J.A. McCarroll, M. Kavallaris. Movers and shakers: cell cytoskeleton in cancer metastasis. Br J Pharmacol (2014)

[5] Guck, J., Schinkinger, S., Lincoln, B., Wottawah, F., Ebert, S., Romeyke,M., et al. (2005). Optical deformability as an inherent cell marker for testing malignant transformation and metastatic competence. Biophys. J. 88, 3689–3698.

[6] Fuhrmann, A., Staunton, J. R., Nandakumar, V., Banyai, N., Davies, P. C. W., and Ros, R. (2011). AFM stiffness nanotomography of normal, metaplastic and dysplastic human esophageal cells. Phys. Biol. 8:015007.

[7] Plodinec, M., Loparic, M., Monnier, C. A., Obermann, E. C., Zanetti-Dallenbach, R., Oertle, P., et al. (2012). The nanomechanical signature of breast cancer. Nat. Nanotechnol. 7, 757–765.

[8] Swaminathan,V.,Mythreye, K.,O'Brien, E. T., Berchuck, A., Blobe, G. C., and Superfine, R. (2011). Mechanical Modeling the mechanics of cancer stiffness grades metastatic potential in patient tumor cells and in cancer cell lines. Cancer Res. 71, 5075–5080.

[9] Egeblad M, Werb Z. New functions for the matrix metalloproteinases in cancer progression. Nature Reviews Cancer. 2002;2:161-74.

[10] Deryugina EI, Quigley JP. Matrix metalloproteinases and tumor metastasis. Cancer and Metastasis Reviews. 2006;25:9-34.

[11] Malik R, Lelkes PI, Cukierman E. Biomechanical and biochemical remodeling of stromal extracellular matrix in cancer. Trends in biotechnology. 2015;33:230-6.

[12] Levental KR, Yu H, Kass L, Lakins JN, Egeblad M, Erler JT, et al. Matrix crosslinking forces tumor progression by enhancing integrin signaling. Cell. 2009;139:891-906.

Activation of Titanium surface with carboxyl groups as anchoring for bioactive molecules

S. Concolato[1], G. Sotgiu[1], M. Urbini[2], M. Orsini[1]

[1]*Department of Engineering, Roma Tre University, via Vito Volterra 62, 00146 Rome, Italy*

[2]*Department of Industrial Engineering, University of Rome "Tor Vergata", Via del Politecnico 1,00133, Roma, Italy*

***Abstract*—Activation of titanium surface with the carboxyl group was studied and the different pretreatments of titanium surface before carboxylation are analysed. The attempt to bond an important bioactive molecule as the chitosan on carboxylated titanium surface was analysed.**

***Keywords*—Titanium, surface, carboxylation, chitosan.**

I. Introduction

Titanium and its alloys are the most utilized bone and dental implant materials due to their excellent physical, chemical and biocompatible properties [1], [2].

However, titanium-based implant materials have specific complications associated with their applications, such as the loosening of implant-host interface owing to unsatisfactory cell adhesion and the susceptibility of the implants to bacterial infections [3]. Hence, it is fundamental to modify the titanium surface with bioactive molecules that enhance beneficial host cell responses, and in some cases inhibit pathogenic microbial adhesion [4].

The surface modification can be obtained *via* adsorption or covalent immobilization of bioactive molecules. Although adsorption is a simple procedure, it often requires a large quantity of reagents and suffers from a gradual loss of the adsorbed molecules from the implant site. On the other hand, the covalent functionalization results more stable than adsorption and the surface density and orientation of the immobilized molecules for specific physiological responses can be controlled [5].

The titanium surface becomes spontaneously covered by a 2−6 nm thick layer of TiO_2. This surface of oxide is often activated by –OH groups that work as anchoring point to bond bioactive molecules.

Recently we described the functionalization of poly (ε-caprolactone) (PCL) *via* hydrolysis and subsequent lactose-modified chitosan (chitlac) attachment [6].

In this study we investigated the chemical modification of titanium oxide surface by the carboxyl groups (-COOH) to immobilize later some bioactive molecules such as chitosan.

II. Results and discussion

Liu and co-workers reported the carboxylation of TiO_2 nanoparticles by an easy method using chloroaceticacid [7].

We tried to apply this procedure to bond carboxylgroups onto the oxide layer on the titanium surface.

The titanium foil was exposed to different treatments (A, B and C) before the carboxylation reaction using chloroacetic acid. In this way the best pretreatment to obtain a good activation of the surface with -COOH was evaluated.

(A) A titanium foil without previous treatment was immersed in aqueous solution of chloroacetic acid and this solution was heated at 100 °C for 7 hours.

(B) A titanium foil was heated at 400 °C for 4 hours to stabilize the layer of TiO_2 on the surface, and then it was put to react in aqueous solution of chloroacetic acid.

(C) A titanium foil was heated at 80 °C for 10 minutes in aqueous solution of HCl (18%). This acid etching pretreatment increased the surface roughness and allowed to obtain a uniform initial titanium surface before the carboxylation reaction.

The three Ti foils (A, B and C) were dried in an oven at 80 °C for 24 h to further remove the impurities, then the surface were analysed by FTIR.

The FTIR spectra of samples A (fig. 1) and C show the presence of the carboxyl group due to the stretching of C=O (1750 cm^{-1}), the methylene group (C-H stretch at 2950 cm^{-1}) and the stretching of O-H (3350 cm^{-1}) introduced by the carboxylation reaction. Instead, in the FTIR spectrum of sample B these characteristic bands were absent as in the FTIR spectrum of the sample of titanium foil that was not treated by chloroacetic acid solution at 100 °C for 7 hours.

These preliminary results showed that chemical activation of titanium surfaces with carboxyl groups takes place on untreated surfaces with native oxide layer and on surfaces pretreated by acid etching.

A preliminary analysis of sample A by ToF-SIMS (Time-of-flight secondary ion mass spectroscopy) allowed to confirm the presence of -COOH on the titanium surface.

Among the polysaccharides the chitosan presents a wide range of biomaterial applications including antibacterial activity [8]. So we tried to bond this bioactive molecule onto the carboxylated Ti foil (C) using *N*-(3-dimethylaminopropyl)-*N'*-ethylcarbodiimide (EDC), N-hydroxysuccinimide (NHS) in a 2-morpholinoethane sulfonic acid (MES) buffer system.

A preliminary analysis using ToF-SIMS of sample C treated by chitosan showed a mass spectrum that revealed a large number of peaks in common with the chitosan.

These preliminary results are promising and we are encouraged to continue our investigations in this direction.

III. Conclusion

The titanium surfaces were activated by carboxyl groups, which are very useful anchoring point to bond bioactive molecules. The procedure of carboxylation is easy and was found to be efficient on titanium surface without previous treatment. The study and the characterization of the

carboxylated titanium surfaces treated by chitosan could be investigated.

REFERENCES

[1] S. Bauer, P. Schmuki, K. von der Mark, J. Park "Engineering biocompatible implant surfaces: Part I and Systems", *Prog. Mater. Sci* vol. 58, pp. 261-326, 2013.

[2] M. Geetha, A. K. Singh, R. Asokamani, A. K. Gorgia, "Ti based biomaterials, the ultimate choice for orthopaedic implants", *Prog. Mater. Sci* vol. 54, pp. 397-425, 2009.

[3] J. M. Schierholz, J. Beuth, "Implant infections: a haven for opportunistic bacteria" *J. Hosp. Infect.* Vol. 49, pp. 87-93, 2001.

[4] D. Zheng, K. G. Neoh, E.-T. Kang "Bifunctional coating based on carboxymethyl chitosan with stableconjugated alkaline phosphatase for inhibiting bacterial adhesion andpromoting osteogenic differentiation on titanium", *Appl. Surf. Sci.* Vol. 360, pp. 86-97, 2016.

[5] S. P. Pujari, L. Scheres, A. T. M. Marcelis, H. Zuilhof "Covalent surface modification of oxide surfaces" *Angew. Chem. Int. Ed.* Vol. 53, pp 6322-6356, 2014.

[6] L. Tortora, S. Concolato, M. Urbini, S. M. Giannitelli, F. Basoli, A. Rainer, M. Trombetta, M. Orsini, P. Mozetic "Functionalization of poly(ε-caprolactone) surface with lactose-modified chitosan via alkaline hydrolysis: ToF-SIMS characterization" Biointerphases, [online] doi: 10.1116/1.4942498, Jun. 2016.

[7] B. Rajaeian, A. Heitz, M. O. Tade, S. Liu, "Improved separation and antifouling performance of PVA thin film nanocomposite membranes incorporated with carboxylated TiO_2 nanoparticles" *J. Membr. Sci.* Vol. 485, pp. 48-59, 2015.

[8] Q. Li, E. T. Dunn, E. W. Grandmaison, M. F. A. Goosen, "Applications and Properties of Chitosan" J. *Bioact.Compat. Polym.* Vol. 7, pp. 370-397, 1992.

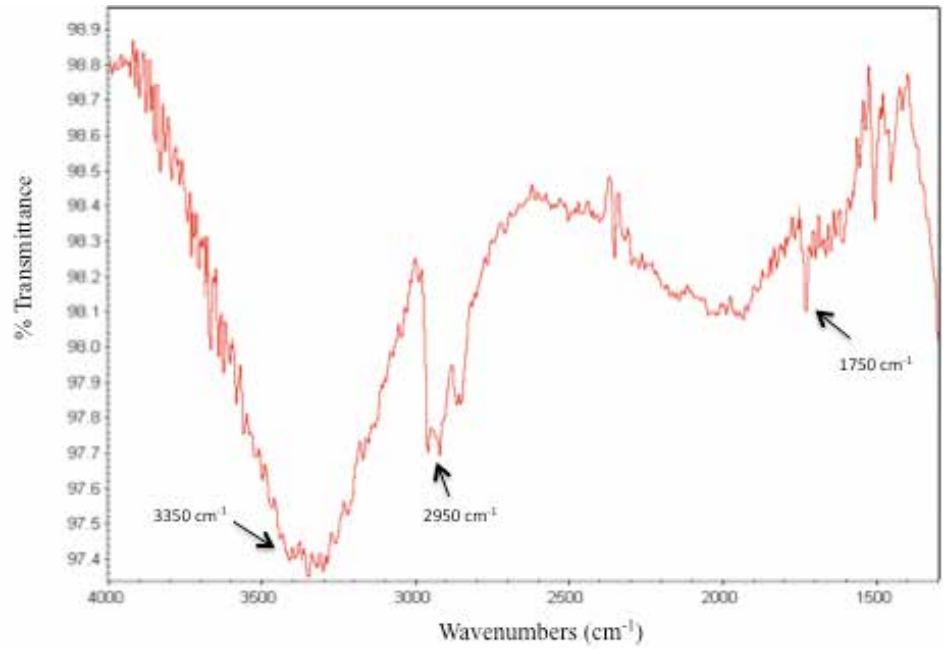

Fig. 1. ATR-FTIR spectrum of carboxylated titanium foil without previous treatment (sample A)

Nanomechanical Characterization of Healthy and Tumor Liver Tissues at Cell and Extracellular Matrix Level

V. Panzetta[1], S. Fusco[1], and P.A. Netti[2]
[1] Center for Advanced Biomaterials for Health Care@CRIB, Istituto Italiano di Tecnologia, Naples, Italy
[2] Interdisciplinary Research Centre on Biomaterials (CRIB), University of Naples Federico II, Naples, Italy

***Abstract*— Nowadays the importance of cytoskeleton and extracellular matrix (ECM) mechanical properties in cancer transformation is well established. Here we propose particle tracking microrheology as a technique to evaluate and correlate the nanomechanical properties of murine liver tissues to their pathophysiological condition at cell cytoskeleton and extracellular matrix level. We found that cancer transformation induces cell softening, as already observed in vitro systems, and extracellular matrix stiffening.**

***Keywords*—Mechanical Properties, Cancer, Particle Tracking Microrheology.**

I. Introduction

Nowadays it is well-known the critical role of cell cytoskeleton in many cell functions, such as adhesion, proliferation, migration and differentiation [1-3]. It is one of the main determinants of mechanical properties of cell [4,5]. Many works demonstrated that the complex process of malignant transformation and invasion involves marked alterations in the mechanical phenotype of the cell cytoskeleton and its surrounding microenvironment [6,7]. In particular, during cancer progression cell cytoskeleton devolves from a rigid and organized structure to a more compliant state, which confers to the cancer cells a great ability to migrate and adapt to the extracellular environment [7]. We already observed that the malignancy and aggressiveness of one transformed murine tumor cell line, SVT2, is associated with profound reduction in cell-substrate adhesion and with altered organization of the actin bundles, high motility and reduced cell mechanical properties [8]. Nevertheless, most of these investigations are conducted *in vitro* systems, ignoring the role of the surrounding extracellular matrix.
In this study, we analyzed normal and malignant murine biopsies in order to define the mechanical phenotype at cell and extracellular matrix level.

II. Materials and Methods

Experiments were performed on murine specimens of normal liver and liver metastasis from renal cancer. Samples were obtained from Department of Oncology, University of Turin, Candiolo, Italy.
In order to evaluate mechanical properties of cells and extracellular matrix we used particle tracking microrheology technique. This technique, introduced by Tseng et al. [9] allows to monitor the local viscoelastic properties of soft samples with high spatio-temporal resolution, collecting and analyzing the Brownian motions of particles introduced inside the sample using a ballistic gun (Bio-Rad, Hercules, CA).
Starting from the acquired videos of beads embedded into the cells, the particle displacements were tracked. A more extensive description of the technique was given elsewhere. Once the nanoparticle trajectories had been obtained, mean squared displacements (MSDs) were calculated as

$$\langle \Delta r^2(\tau) \rangle = \langle [x(t-\tau) - x(t)]^2 + [y(t-\tau) - y(t)]^2 \rangle$$

where angular brackets mean time average, τ is the time scale and t the elapsed time.
Local viscoelastic properties of cell were extrapolated from MSDs by using the generalized Stokes–Einstein equation

$$G^*(\omega) = \frac{K_B t}{\pi i \omega \Im_u\{\langle \Delta r^2(\tau) \rangle\}}$$

being $G^*(\omega)$ the complex shear modulus, K_B the Boltzmann constant, ω the frequency and $\Im_u$ the unilateral Fourier transform of MSDs [10,11].

III. Results

We performed particle tracking microrheology experiments in order to correlate the nanomechanical properties of murine liver tissue to its pathophysiological state. Nanobeads were introduced into the samples through a ballistic method. in order to distinguish between cells and extracellular matrix, cell nuclei were labeled with a fluorescent dye. For clarity in comparing data, we presented the only dynamic elastic modulus G', expressed as the ensemble averaged elastic modulus that nanoparticles probed once embedded in cell cytosol or extracellular matrix. Particle tracking microrheology analyses showed that cancerous transformation compromises mechanical integrity of cells and increases in a remarkable way the mechanical properties in ECM (Fig.2). In particular, cancer cells exhibited reduced mechanical properties compared to cells of healthy tissue, as consequence of a less structured cytoskeleton (Fig. 1). This result is in agreement with findings in 2D *in vitro* systems, confirming the idea that cytoskeleton cell softening is an essential prerequisite in cancer progression. Further, cancer transformation is also accompanied by extracellular matrix stiffening, as confirmed by increase of mechanical properties of matrix in tumor tissue. Many works demonstrated that matrix stiffening promotes tumor proliferation and invasiveness, by activating typical oncogenic signaling pathways.

IV. Conclusion

In this study we analyzed the mechanical properties of murine biopsy tissue at cell and extracellular matrix level. A relevant finding of the work is that cancerous transformation is characterized by decrease of cytoskeleton mechanical properties also in an *ex vivo* context. This result indicates that cell softening is an essential change, which confers to the cells the ability to escape from their native tissue and invade distant sites. The cancer progression is also accompanied by extracellular matrix stiffening, which promotes invasion and metastasis formation.

Our results indicate that particle tracking microrheology can be used to get nanomechanical characterization at different scale levels in an interpretative and diagnostic context.

References

[1] Provenzano Paolo P. and Keely Patricia J. Mechanical signaling through the cytoskeleton regulates cell proliferation by coordinated focal adhesion and Rho GTPase signaling J Cell Sci. Apr 15, 2011; 124(8): 1195–1205, **2011.**

[2] Shelly R. Peyton, Cyrus M. Ghajar. Chirag B. Khatiwala, Andrew J. Putnam. The emergence of ECM mechanics and cytoskeletal tension as important regulators of cell function. Cell Biochemistry and Biophysics, 47 (2), 300-320, **2007**.

[3] Colin Jamora and Elaine Fuchs Intercellular adhesion, signalling and cytoskeleton Nature Cell Biology 4, E101-W108, **2002**.

[4] Jacob Pourati, Andrew Maniotis, David Spiegel, Jonathan L. Schaffer, James P. Butler, Jeffrey J. Fredberg, Donald E. Ingber, Dimitrijie Stamenovic, Ning Wang. Is cytoskeletal tension a major determinant of cell deformabilità in adherent endothelial cells? American Journal of Physiology- Cell Physiology, 247 (5), C1283-C1289, **1998**.

[5] Daniel A. Fletcher and Dyche Mullins. Cell mechanics and the cytoskeleton. *Nature* 463, 485-492, **2010**.

[6] Jochen Guck, Stefan Schinkinger, Bryan Lincoln, Falk Wottawah, Susanne Ebert, Maren Romeyke, Dominik Lenz, Harold M. Erickson, Revathi Ananthakrishnan, Daniel Mitchell, Josef Kas, Sydney Ulvick, Curt Bilby. Optical deformability as an inherent cell marker for testing malignant transformation and metastatic competence. Biophysical Journal 88 (5), 2689-2698, **2005**.

[7] SE Cross, Yu-Sheng Jin, Julianne Tondre, Roger Wong, JianYu Rao and James K Gimzewski. AFM-based analysis of human metastatic cancer cells. *Nanotechnology* 38, 4003, **2008**.

[8] Panzetta, Valeria, et al. "X-Ray Irradiation affects morphology, proliferation and migration rate of healthy and cancer cells." *Journal of Mechanics in Medicine and Biology* 15.02 (2015): 1540022.

[9] Y. Tseng, T.P. Kole, D. Wirtz, Micromechanical mapping of live cells by multiple-particle-tracking microrheology, Biophys. J. 83 (2002) 3162–3176.

[10] S. Fusco, A. Borzacchiello, L. Miccio, G. Pesce, G. Rusciano, A. Sasso, et al., High frequency viscoelastic behaviour of low molecular weight hyaluronic acid water solutions, Biorheology 44 (2007) 403–418.

[11] G. Pesce, A. De Luca, G. Rusciano, P. Netti, S. Fusco, A. Sasso, Microrheology of complex fluids using optical tweezers: a comparison with macrorheological measurements, J. Opt. A: Pure Appl. Opt. 11 (2009) 034016.

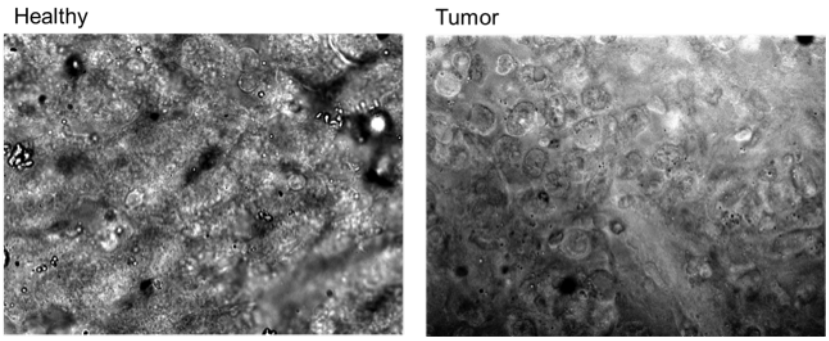

Fig. 1 Representative transmission images of healthy and tumor liver tissues.

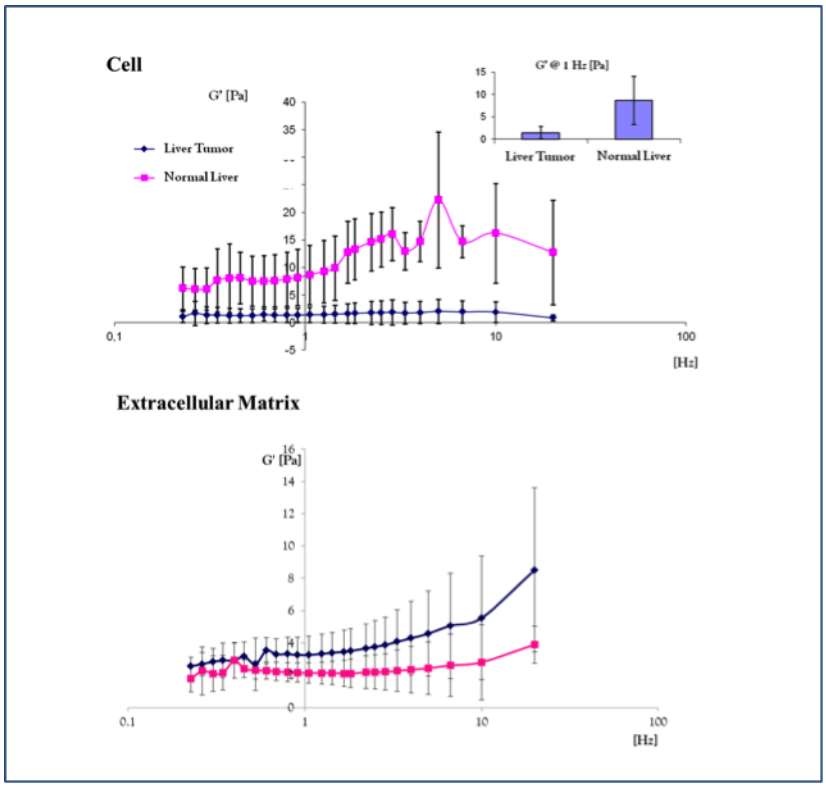

Fig. 2 Ensemble-averaged G' in cells and extracellular matrix of healthy and tumor liver tissues.

Impact of hydrogel structure on MRI contrast agents relaxometric properties

A. M. Ponsiglione[1,2], P. A. Netti[1,2,3], E. Torino[2,3]
[1] Department of Chemical Engineering, Materials and Industrial Production, University of Naples Federico II, Naples 80125, Italy
[2] Istituto Italiano di Tecnologia, Center for Advanced Biomaterials for Healthcare IIT@CRIB, Naples 80125, Italy
[3] Interdisciplinary Research Center on Biomaterials, University of Naples Federico II, Naples 80125, Italy

***Abstract*— Magnetic Resonance Imaging (MRI) represents the first-line diagnostic imaging modality for numerous indications. It is a clinically well-established, non-invasive technique providing three-dimensional whole body anatomical and functional imaging. It takes advantage of the magnetic properties of water protons present in the body and their tissue-dependent behaviour. Signal intensity in MRI can be enhanced by the administration of a contrast agent (CA) prior to scanning. The relaxivity of CAs is dependent on molecular motion, size, rigidity, and possible binding between CAs and other macromolecules. Thus, different strategies of MRI CAs design and synthesis have been developed to improve their efficacy. With the present work, we investigated the relaxometric properties of hydrogel-CA systems obtained through the combination of crosslinked hydrophilic biopolymers and commercially available MRI CAs. In this study, Hyaluronic Acid (HA) was used as the polymer due to its hydrophilic nature and established biocompatibility and biodegradability, whereas commercially available Gadolinium-DTPA (Gd-DTPA) was chosen as the contrast agent. Relaxometric properties of the HA/Gd-DTPA systems were studied by means of time-domain NMR relaxometry. Preliminary results suggest that the hydrogel matrix plays a significant role in the design of MRI CAs and can significantly impact on their relaxivity.**

***Keywords*— MRI, Contrast agents, hydrogels, relaxation enhancement**

I. Introduction

Magnetic resonance imaging (MRI) is a noninvasive diagnostic technique used to obtain high-resolution anatomical and physiological images of the body, without the use of ionizing radiations [1]. Nevertheless, it suffers from low detection sensitivity, making difficult to highlight pathological areas and perform early diagnosis [2]. In order to overcome this limitation, MRI often requires the use of contrast agents (CAs) to be administered to the patient prior to examination. These CAs utilize paramagnetic metal ions and enhance the contrast in an MR image by positively influencing the water protons in the immediate surroundings of the tissue in which they localize [3]. Among them, chelates of Gadolinium (Gd) are the most popular paramagnetic imaging CAs used to produce a positive MR contrast.

However, most of the clinically-used CAs are characterized by poor effectiveness in the high magnetic fields region (1.5 T and above), which is of particular interest for clinicians, lack in tissue specificity and, in addition, can cause heavy allergic effects and serious nephrotoxicity. In order to overcome these limitations, there has been an increasing interest in studying physicochemical properties of MRI CAs and the impact that different strategies of design and synthesis have on their efficacy.

Recently, many efforts have been devoted to the development of polymer-based carriers for MRI CAs, with particular reference to Gadolinium (Gd) chelates. Several studies, indeed, demonstrated that the polymer architecture plays a crucial role on different parameters, such as the water exchange time and the rotational correlation time, and influence the CA's relaxivity [4]. Therefore, different nanostructures have been developed by combining Gd-chelates with nanoparticles through encapsulation of the CA molecule inside an electrostatically crosslinked polymer [2] or conjugating different types of nanostructures with Gd-chelates [5], [6].

In this context, we investigated the impact of polymer-CA and hydrogel-CA systems on the relaxometric properties of MRI CAs. The characterization of these systems, obtained through the combination of commercial MRI CAs and hydrophilic biopolymers, can give an insight into the development of novel hydrogel-based CAs without inducing chemical modifications or altering the biocompatibility of the original CA.

II. Materials and Methods

A. Materials

Hyaluronic Acid (HA) (Bohus Biotech, Sweden) with an average molecular weight of 420000 Da was chosen for the polymer matrix because of its biocompatibility, biodegradability and swelling properties.

Commercially available Gd-DTPA (Sigma Aldrich) with molecular weight of 547.57 Da was used in this study as it is a well-known, low-risk CA.

Divinyl Sulfone (DVS) (Sigma Aldrich) with molecular weight of 118.15 Da was used as crosslinking agent. Milli-Q water was systematically used for sample preparation and analysis.

B. Sample preparation

Polymer-CA solutions were prepared by dispersing HA and Gd-DTPA powders in distilled deionized water and then mixing using magnetic stirrer. Solutions at various polymer/CA molar ratios were prepared for the experimentation.

Hydrogel-CA were prepared by adding Divinyl Sulfone (DVS) to the polymer solutions in order to chemically crosslink the polymer network. Hydrogels were prepared at different HA/DVS weight ratios.

C. Relaxometric measurement

Relaxation times were measured in a Bruker Minispec (mq

60) bench-top relaxometer operating at 60 MHz for protons (magnetic field strength: 1.41 T). The measurements were taken at 37°C, and before each measurement, the sample was placed into the NMR probe for about 15 min for thermal equilibration. The longitudinal relaxation times, T_1, were determined by both saturation (SR) and inversion recovery (IR) pulse sequences. The relaxation recovery curves were fitted using a multi-exponential model. Relaxivity values, r_1 ($mM^{-1}s^{-1}$), were calculated from the slope of the regression line of $1/T_1$ versus concentration with a least-squares method. Data analysis was performed by means of Origin Pro 9.1 SRO software (OriginLab Corporation, USA).

III. Results

For the polymer-CA solutions, a slight increase in the relaxivity, ranging from 2% to 7%, with respect to the reference solution (Gd-DTPA in water) was observed. For hydrogel-CA systems, the relaxivity increases to an even greater extent, ranging from 12% up to 21%.

IV. Discussion and Conclusion

According to the Solomon–Bloembergen–Morgan (SBM) theory [7], relaxivity is related to some key parameters: the number of labile water molecules coordinated to the metal ion (q), residence time of the coordinated water molecule (τ_M), rotation correlation time of the complex (τ_R) and molecular diffusional correlation time (τ_D). The Gd-chelator determines the water exchange rate (k_{ex}) and number of coordinated water molecules (q). Decreased τ_D and τ_R generally yield increased relaxation rates at low magnetic fields (<1.5 T) [1].

Relaxometric measurements confirm that the presence of a polymer matrix can influence the characteristic parameters of the metal chelate, thereby providing an increase in the relaxivity. The obtained results suggest that the modulation of the hydrogel-CA properties could lead to increased CA's relaxivity. Even though only modest increase in the relaxivity can be achieved for polymer-CA solutions, more significant relaxivity enhancement can be achieved in presence of the crosslinked structures.

This could be a starting point to further study hydrogel-CA systems in order to achieve a deeper comprehension of the mechanisms regulating the interaction between commercial MRI CAs and hydrogel matrices. Further characterization studies are necessary to better understand the behaviour of CAs within polymeric matrices and optimize these structures in order to boost the CAs' properties and, therefore, the performance of the MRI diagnosis. In addition, a better knowledge of the dynamics and properties of these complex systems could be scaled to nano-scale dimensions and inspire the development of a new class of nanostructured MRI CAs with highly tunable relaxometric properties.

References

[1] M. A. Bruckman, X. Yu, and N. F. Steinmetz, "Engineering Gd-loaded nanoparticles to enhance MRI sensitivity via T1 shortening", *Nanotechnology*, vol. 24, no. 46, pp. 462001, November 2013.

[2] T. Courant, G. V. Roullin, C. Cadiou, M. Callewaert, M. C. Andry, et al., "Biocompatible nanoparticles and gadolinium complexes for MRI applications", *Comptes Rendus Chimie*, vol. 16, no. 6, pp. 531-539, June 2013.

[3] P. Caravan, "Strategies for increasing the sensitivity of gadolinium based MRI contrast agents", *Chemical Society Reviews*, vol. 35, no. 6, pp. 512-523, June 2006.

[4] Y. Li, M. Beija, S. Laurent, L. Van Der Elst, R. N. Muller, et al., "Macromolecular Ligands for Gadolinium MRI Contrast Agents", *Macromolecules*, vol. 45, no. 10, pp. 4196-4204, May 2012.

[5] Y. Xiao, R. Xue, T. You, X. Li, and F. Pei, "A new biodegradable and biocompatible gadolinium (III) -polymer for liver magnetic resonance imaging contrast agent", *Magnetic Resonance Imaging*, vol. 33, no. 6, pp. 822-828, July 2015.

[6] S. Y. Jeong, H. J. Kim, B. K. Kwak, H. Y. Lee, H. Seong, et al., "Biocompatible Polyhydroxyethylaspartamide-based Micelles with Gadolinium for MRI Contrast Agents", *Nanoscale Research Letters*, vol. 5, no. 12, pp. 1970-1976, September 2010

[7] M. L. Wood, and P. A. Hardy, "Proton relaxation enhancement", *Journal of Magnetic Resonance Imaging*, vol. 3, no. 1, pp. 149-156, February 1993.

pH-sensitive nanoparticles for colon-targeted drug delivery

M. Porzio[1], F. Causa[1,2], P.A. Netti[1,2]
[1] *CRIB – Centro di Ricerca Interdipartimentale sui Biomateriali*
[2] *IIT – Istituto Italiano di Tecnologia*

***Abstract* — Because most episodes of back pain have inflammation as a contributing factor, anti-inflammatory medication such as non-steroidal anti-inflammatory drugs (NSAIDs) is often an effective pain medication treatment option. However oral NSAIDs consumption has been associated with significant gastrointestinal complications as ulceration and/or bleeding. Then, to reduce these drawbacks, we have designed and investigated pH sensitive nanoparticles systems for controlled and site specific delivery of diclofenac sodium, one of the most used anti-inflammatory. These nanoparticles were evaluated for surface morphology, particle size and size distribution, percentage drug entrapment and in vitro drug release.**

***Keywords*—Nanoparticles, Eudragit® S100, Diclofenac Sodium, pH-Sensitive delivery.**

I. Introduction

The outstanding contribution of polymeric nanoparticles as a physical approach to alter and improve the pharmacodynamic and pharmacokinetic properties of various types of drug entities has been studied. In addition to their advantages, various polymers were extensively employed for the formulation of nanoparticles for the delivery of drug to increase the therapeutic benefits, while minimizing side effects.

Polymeric nanoparticles systems by far the most studied organic particles in the literature. Majority of the contribution towards the field of site specificity is by polymeric nanoparticles. Wide classes of biocompatible and biodegradable polymers are available for the fabrication of drug loaded nanoparticles. The nature, surface charge and properties of the polymers controls important parameters of the formulation i.e. drug release, stability and forth (1).

Several polymers have the characteristics of protecting the drug against the action of the enzymes and gastric fluids, which are in fact very acidic (pH=1–2), and the reduction of gastrointestinal irritation caused by drugs NSAIDs (2, 3). Therefore, different types of polymer have been extensively studied, such as Eudragit® S 100, methacrylic acid co-polymers pH-dependent, that is soluble in intestinal fluid from pH 6 is widely used for the formulation of oral dosage forms (i.e., coating of tablets, matrix tablet). It is a polyacrylic resin that has been suggested to be used in microencapsulation for controlled-release applications due to its unique solubility profile (4). The free carboxylic acid groups make the polymer pH sensitive, being soluble at pH 6–7.5 (5).

Non-steroidal anti-inflammatory drugs (NSAIDs) are usually good candidates for the development of controlled release preparations, particularly through the oral route. NSAIDs are one of the most commonly used classes of medications worldwide. It is estimated that more than 30 million people take NSAID daily (6). However, gastrointestinal (GI) complications related to NSAID therapy are the most prevalent category of adverse drug reactions. Patients with arthritis are among the most frequent users of NSAID and are therefore particularly at risk for these side effects (7).

Diclofenac, a phenylacetic acid derivative, was the first non steroidal anti-inflammatory agent to be approved.It acts going to compete with arachidonic acid for binding to cyclo-oxygenase, resulting in decreased formation of prostaglandins. Diclofenac is more usually found as sodium or potassium salt with potent anti-inflammatory, analgesic, and antipyretic properties (8).

The aim of this study was to develop and characterize diclofenac sodium-loaded Eudragit® S100 nanoparticles in order to obtain a pH sensitive system. Nanoparticles were prepared by the single emulsion method and characterized the formulation in terms of morphology, size, drug loading, and release.

II. Materials and methods

A. Materials

Mowiol® 40-88 and anhydrous methanol were purchased from Sigma Aldrich (USA), Eudragit® S100 was supplied by Evonik (Germany). Diclofenac sodium was received as a gift sample from Dompé Farmaceutici (Aquila, Italy). All other chemicals and reagents were of analytical grade.

B. Preparation of Eudragit® S100-Diclofenac Sodium Nanoparticles

For encapsulating diclofenac sodium into Eudragit nanoparticles, 100 mg of Eudragit® S 100 was dissolved in anhydrous methanol. This solution was added into 8 mL of PVA solutions (Mowiol® 40-88, 3% w/v) containing diclofenac sodium in the amber glass vial, using a peristaltic pump at a flow rate of 1.0 ml/min while continuously stirring at 350 rpm with a propeller mixer. Finally, organic phases were evaporated under reduced pressure in a rotary evaporator at 40°C. After evaporation of the solvent, nanoparticles were recovered by ultracentrifugation at 20,000 rpm for 15 min and washed with distilled water. The washing step was repeated once before nanoparticles were suspended in distilled water and lyophilized overnight. All batches of nanoparticles were produced at least in triplicate.

C. Characterization of Nanoparticles

Surface Morphology: The morphological examination of the nanoparticles was performed usingtransmission electron microscope (FEI Tecnai, Eindhoven, Netherlands). Briefly, 10 µl of a suspension of nanoparticles (1 mg/ml) were laid on

a 300copper mesh grid with Lacey Carbon membrane, a specific support for TEM analysis. Then, the nanoparticles were treated with phosphotungstenic acid (2% w/v); the support was dried at room temperature and analyzed after 12 hours.

Particle Size and Zeta Potential: The size (Z-average mean) and zeta potential of the nanoparticles were analysed by photon correlation spectroscopy and laser Doppler anemometry, respectively, using a Zetasizer Nano (Malvern Instruments, UK). Size and zeta potential measurements were performed in triplicate following a dilution of the nanoparticles suspension in distilled water at 25°C. Each measurement was done in triplicate.

HPLC Methodology: HPLC determination of Diclofenac Sodium concentration was done using a Waters HPLC system (Waters, USA) at 280 nm. The column used was a reversed-phase C18 column (Phenomenex Luna, 250×4.6 mm, pore size: 5µm) with this solvent system: acetonitrile/water (60:40). An injection volume of 30 µl and a flow rate of 1.0 mL/min were used, and Diclofenac Sodium could be detected at retention time of 2.5 min. Linear correlation between peak area and Diclofenac Sodium concentration was obtained within the concentration range of 1–80 µg/mL, with a limit of quantification of 1.05 µg/mL (R^2 = 0.999).

Determination of Entrapment Efficiency and Drug Loading: To determine the diclofenac sodium content, nanoparticles were dissolved in acetone and diclofenac sodium was extracted with distilled water and determined by RP-HPLC. The experiments were performed in triplicate. The percent actual loading (DL) and percent encapsulation efficiency (EE) of nanoparticles were calculated as:

Actual loading (%) *= mg of encapsulated Diclofenac/100 mg microspheres;*

Encapsulation efficiency (%) *= (actual Diclofenac loading/ Theoretical Diclofenac loading) x 100;*

Dissolution Test: To determine the release profiles of diclofenac Sodium in simulated gastrointestinal environment, a quantity of nanoparticles was dispersed in 10ml of pH 1.2 simulating gastric fluid buffer. The drug release capacity within the fluid was tested for one hour, subsequently,0.2M sodium phosphate tribasic solution was added to the means of analysis in order to vary the pH up to value of 4 and then to 6.8. At pre-established time intervals 1ml of fluid it was collected, centrifuged and analysed at a wavelength of 280 nm using RP-HPLC method used previously. The amount of withdrawn sample was replaced with fresh buffer in order to maintain the sink conditions of the test. The parameters of temperature (37°C) and mechanical stirring (50 rpm) used are remained constant during the entire dissolution test.

III. Results and Discussions

The Eudragit® S100 nanoparticles encapsulating Diclofenac Sodium were prepared by solvent emulsion method. This method offers many advantages; for instance, avoidance of toxic solvents such as dichloromethane which require long evaporation and purification time, uniform nanoparticles formation even under moderate stirring, and high nanoparticles yield that is acceptable for industrial application.

The nanoparticles showed a narrow size distribution with average diameters in the range of 110–150 nm and low polydispersity values (Table 1).

Generally, high negative zeta potential values are expected for pure anionic polymer (PLGA, Eudragit® L100, S100, etc.) nanoparticles due to the presence of carboxyl groups on the polymeric chain extremities. However, in this case, the zeta potential values are close to zero. The factor which might be responsible for such an effect can be the presence of residual PVA on the nanoparticles surface (9).

All nanoparticles formulations showed good production yields and high entrapment efficiency of the model drug (79 ± 3.2% – 82 ± 6.6 %).

The morphology of diclofenac-loaded nanoparticles was evaluated by TEM (Fig. 1). Nanoparticles prepared displayed a well-defined spherical shape with a smooth surface and narrow size distribution.

The in vitro release profiles of Diclofenac Sodium loaded nanoparticles were studied in gradually pH-changing buffers (Fig. 2). Nanoparticles prepared exhibited a pH-dependent release property.At pH 1.2 diclofenac-loaded nanoparticles obtained are stable for the entire analysis time, similarly at pH 4.0, while at intestinal pH (7.0) the nanoparticles begin to degrade, releasing the drug over a period of about 2 hours. This test demonstrated the efficacy of these nanoparticles in sustaining the diclofenac sodium release in colon area.

In conclusion we have achieved nanoparticles from the excellent chemical-physical and morphological characteristics able to release the drug only at the colon level, thanks to the use of pH-sensitive polymer and modified preparation method.

References

[1] Polymers for Drug Delivery Systems. *Annual review of chemical and biomolecular engineering*. 2010;1; pp. 149-173.

[2] González M, Rieumont J, Dupeyron D, Perdomo I, Fernandez E,Abdón L, et al. Nanoencapsulation of acetyl salicylic acid within enteric polymer nanopaticles. Rev Adv Mater Sci. 2008;17; pp. 71–5.

[3] Piao ZZ, Lee MK, Lee BJ. Colonic release and reduced intestinal tissue damage of coated tablets containing naproxeninclusion complex. Int J Pharm. 2008;350(1–2); pp.205–11.

[4] Singh G, Triadafilopoulos G. Epidemiology of NSAID induced gastrointestinal complications. J Rheumatol Suppl. 1999 Apr; 56 pp.18-24

[5] Obeidat WM, Price JC. Preparation and evaluation of Eudragit S100 microspheres as pH sensitive release preparations for piroxicam and theophylline using the emulsion–solvent evaporation method. J Microencapsul. 2006;23 pp.195–202.

[6] Singh G, Rosen Ramey D. NSAID induced gastrointestinal complications: the ARAMIS perspective--1997. Arthritis, Rheumatism, and Aging Medical Information System. J Rheumatol Suppl. 1998 May; 51 pp. 8-16.

[7] Small, R. E. (1989). Diclofenac sodium. *Clinical pharmacy*, *8*(8), pp. 545-558.

[8] Rodriguez M, Vila-Jato JL, Torres D. Design of a new multiparticulate system for potential site-specific and controlled drug delivery to the colonic region. J Control Release. 1998;55; pp.67–77.

[9] Peppas NA, Wood KM, Blanchette JO. Hydrogels for oral delivery for oral delivery of therapeutic proteins. Expert Opinion Biological Therapy. 2004;4: pp. 881–887.

Dimensions (nm, n=5)	***132 ± 20.2***
Zeta potential (mV, n=5)	*0.095 ± 2.03*
PdI	*0.204*

Table 1 : Physicochemical characteristics of Diclofenac Sodium-loaded nanoparticles

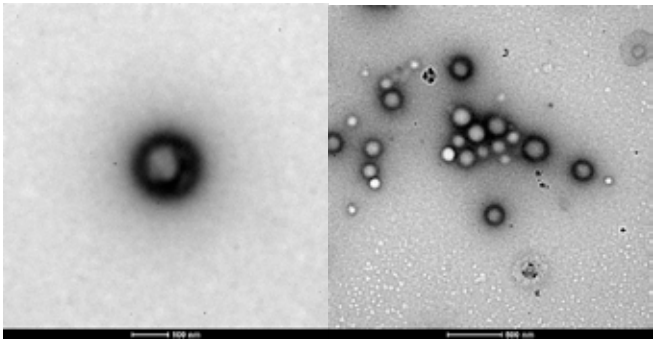

Figure 1 : Scanning electron micrographs of Diclofenac Sodium-loaded nanoparticles at different magnifications

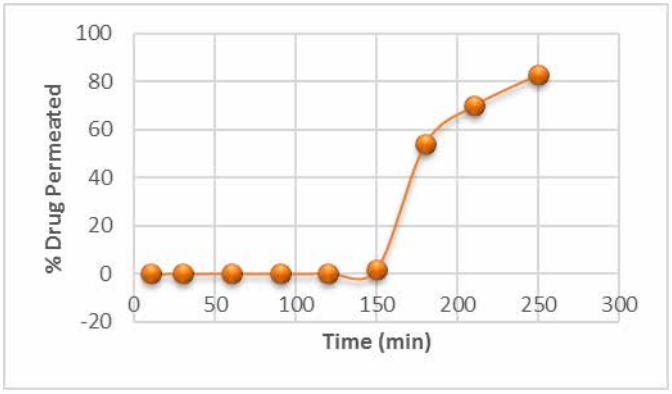

Figure 2 : Release profiles of Diclofenac Sodium from nanoparticles in gradually pH-changing buffers

Matrix Metallo-proteinase 2 Activated Prodrug Nanoparticles for on-demand Release of Doxorubicin in 3D tumor Spheroids

M. Profeta[1], M. Cantisani[1], D. Guarnieri[1,*], M. Biondi[2,3], V. Belli[1], L. Raiola[1], P. A. Netti[1,3]

[1] *Center for Advanced Biomaterials for health Care (CABHC), Istituto Italiano di Tecnologia, Largo Barsanti e Matteucci 53, Napoli, Italy*
[2] *Dipartimento di Farmacia, Università di Napoli Federico II, Via Domenico Montesano 49, Napoli, Italy*
[3] *Centro di Ricerca Interdipartimentale sui Biomateriali (CRIB), Università di Napoli Federico II, Piazzale Tecchio 80, Napoli, Italy*
* *Corresponding Author: daniela.guarnieri@iit.it*

Abstract—A common approach in cancer treatment would see the inhibition of Matrix Metalloproteinases (MMPs) expression, which are proteolytic enzymes that play a key role both in physiologic processes and in tumor metastasis progression. Since that, this kind of approach may lead to the undesired impaired of numerous homeostatic processes so, in the light of these considerations, a novel approach may be the one that benefits from MMPs over-expression, instead of inhibiting it, in order to realise a *stimuli responsive* nanocarrier.

To this aim, the purpose of this work was the design, the characterization and the *in vitro* cytotoxicity assay in 3D tumor spheroids of biocompatible and biodegradable nanoparticles made up of a poly(D,L-lactic-co-glycolic acid) (PLGA) – block – polyethylene glycol (PEG) copolymer (namely PELGA), blended with a tumor activated prodrug (TAP) composed by a MMP2-sensitive peptide bound to doxorubicin (Dox) and to PLGA molecule. The obtained devices allow the controlled release of the Dox and elicit cytotoxicity specifically upon MMP2 cleavage of the TAP. More interestingly, they sense the differences in the expression levels of endogenous MMP2 protein, thus modulating drug penetration within a three-dimensional (3D) tumor spheroid matrix, accordingly. Furthermore, the same prodrug has been produced without the MMP-sensitive linker as negative control, to evaluate the specific recognition of the MMP2 sensitive peptide sequence. Since that, the above studies hold promise for NPs testing on more complex *in vitro* tissue equivalents and for the possible application of these nanodevices in the field of nanomedicine.

Keywords— Tumor activated prodrug, matrix-metalloproteinase, stimuli-responsive biodegradable nanoparticles, 3D tumor spheroids.

I. INTRODUCTION

OVER the past few decades, there has been considerable interest in developing biodegradable polymeric nanoparticles (NPs) as effective drug delivery devices since these, when formulated correctly, can potentially reduce the drug dose needed to achieve therapeutic benefit decreasing the side effects associated with systemic drug delivery with great benefit to patients. Rather, NPs should satisfy two basic requirements such as carry the drug to reach the desired tumor sites and act specifically upon tumor cells without harmful effects to healthy tissue. These requirements may be enabled using passive targeting of drugs which takes advantages from the unique pathophysiological characteristics of the leaky tumor vasculature which permits an Enhanced Permeability and Retention (EPR) effect. A key challenge for improving passive drug delivery is to limit reticuloendothelial system uptake and to maximize the EPR effect [1]. To this aim, PEGylation, is a good strategy since, referring to an intravenous administration of drugs, promotes a prolonged circulation half-life and provide a hydrophilic environment, shielding NPs from immune recognition. This is due to specific PEG properties that are conveyed to the conjugated drug. The final structure is considered a prodrug, and the body fate of the drug reflects that of the polymer [2].

Stimuli-responsive nanocarriers, is now emerging as a family of specialized nano-sized active delivery vehicles that evolve with a specific cellular/extracellular endogenous stimuli that can modify the structural composition or conformation of the nanocarriers, promoting release of the active species to specific biological environment. Thus, NPs become an active participant in the therapeutic landscape, rather than an inert carrier molecule. An array of manifold enzymes, such as proteases, can be used as biochemical trigger [3].

Proteases, that are extracellularly expressed, such as the MMPs, are specific biomarkers of malignant tissues and are responsible for the proteolysis of the extracellular matrix and basement membranes and are required during tissue remodelling and angiogenesis associated to cancer invasion and metastasis progression [4]. So, these biochemical signatures can act as a trigger by introducing specific enzyme substrate sequence, such as peptides in NPs design.

Several potential therapeutic agents based on MMPs and their inhibitors are under investigation for their ability to decrease the invasive capacity of cancer cells [5]. Anyway, MMPs are involved in numerous physiological and homeostatic processes, so with this approach the potential for adverse effects is high [6]. In the light of these considerations, a novel overture may be the one that benefits from the MMPs over-expression in tumor sites, instead of inhibiting it, in order to realise a *stimuli responsive* nanocarrier, allowing a site specific drug release.

Guarnieri *et al.* [7] propose the use of a novel nanocarrier able to carry safely doxorubicin in tumor tissues, and to respond to MMP-2 enzyme. The nanocarrier is composed by a spherical polystyrene NP covalently bonded with a prodrug composed by polyethylene glycol (PEG), a peptide sequence sensitive to MMP-2 and doxorubicin which is an anthracycline antibiotic and works by intercalating DNA. The presence of the MMP-2 enzyme in situ, leads to the disruption of the bond between the peptide and the doxorubicin, with the consequent diffusion of the drug. These studies demonstrated that, in 2D cell culture, the produced nanocarrier is cytotoxic against all the cell lines used in the

presence of the enzyme, while no cytotoxic effects are observed in absence of the enzyme.
Inspired by these encouraging results, here we have translated the TAP production technology to the fabrication of biodegradable systems based on FDA-approved materials.

II. Materials and methods

Nanoparticles were made up of a biodegradable poly(D,L-lactic-co-glycolic acid) (PLGA) – block – PEG copolymer (namely PELGA), blended with a TAP composed by a MMP2-sensitive peptide bound to doxorubicin (Dox) at the C-terminus and to PLGA molecule at the N-terminus. The same prodrug has been produced without the MMP-sensitive linker as negative control (Figure 1). PELGA, TAP and PLGA-Dox were synthesized and synthesis purity was verified using NMR spectroscopy. TAP and Dox co-polymers were mixed with PELGA copolymer to obtain NPs according to the nanoprecipitation method. The obtained devices were characterised and tested for their Dox release and ability to diffuse within a 3D tumor matrix model. Spheroids of human glioma cell line (U87-MG) and primary human dermal fibroblasts (HDF) were used as in vitro models of 3D tumor and healthy tissues, respectively and their MMP-2 expression was also characterized. To test the biological effect of NPs, the spheroids were incubated with PELGA-TAP and PELGA-Dox NPs for 24 and 48 h to confirm the specificity of action of PELGA-TAP NPs.

III. Results and discussions

The produced NPs were characterized in terms of size, ζ-potential, stability and morphology. DLS measurements showed that NP diameter was below 100 nm with a polydispersity index (PDI) < 0.2 with and without TAP. The surface charge was negative, with very slight differences among the NPs. Moreover, NPs are stable in aqueous media up to two weeks. SEM and Cryo-TEM images of PELGA NPs, show that NPs are spherical and with a regular shape. Finally, we tested NPs ability to release Dox *in vitro* upon exposure to free MMP2 enzyme, performing a cleavage assay to obtain the *in vitro* release profiles of Dox from PELGA-TAP and PELGA-Dox NPs. Results show that in the absence of MMP2 enzyme, 25% of Dox has been released within 24 h while, in the presence of the enzyme, ~ 40% of Dox release has been observed in the same time frame. For longer release times, the effect of MMP2 is more apparent and, after 36-48 h, Dox release percentage has been found to be roughly two-fold higher in the presence of the enzyme. The release of Dox in the absence of MMP2-sensitive peptide linker was the same, with and without enzyme treatment. In particular, the percentage of released Dox in these conditions is comparable to the percentage of drug released from untreated PELGA-TAP NP (Figure 2).

The expression and the enzymatic activity of endogenous MMP2 secreted by U87-MG and HDF cells were verified by indirect immunofluorescence and results shows that tumor cells express greater levels of MMP2 protein than healthy cells. Moreover, zymography results demonstrate that, for U87-MG cell line, in cell culture medium, the amount of secreted MMP2 enzyme in its activated form was 8.4 fold higher than for HDF cells (Figure 3).

In order to demonstrate the ability of PELGA-TAP NPs to sense the differences in expression levels of endogenous MMP2 enzyme and, hence, induce Dox release upon specific enzymatic cleavage, U87-MG and HDF cell spheroids were used as *in vitro* models of a tumor and a healthy tissue, respectively and treated with PELGA-TAP and PELGA-Dox NPs. At first, the diffusion of free Dox through the spheroid matrix was evaluated by confocal microscopy analysis. Z-sectioning projection images show the presence of a fluorescence signal within U87-MG tumor spheroids after 24 h exposure to PELGA-TAP NPs. Moreover, spheroid fluorescence was found to be rapidly increasing over time, therefore indicating Dox accumulation within the spheroid bulk and, as a consequence, spheroids tend to disaggregate after 48h of incubation with PELGA-TAP NPs. On the other hand, a very low fluorescence signal was observed in the case of U87-MG spheroids treated with PELGA-Dox both for 24h and 48h incubation. More interestingly, HDF spheroids have shown a lower fluorescence signal than U87-MG spheroids, with a less significant difference in fluorescence intensity between PELGA-TAP and PELGA-Dox NP treatment than U87-MG spheroids (Figure 3).

IV. Conclusions

The results presented in this work suggest that the PELGA-TAP NPs can deliver Dox specifically upon enzymatic cleavage and promote drug penetration within 3D tumor spheroids. Therefore, the proposed PELGA-TAP NPs are able to merge the biodegradability/biocompatibility of PELGA with active mechanisms of Dox release and tumor penetration. The clear comprehension of how PELGA-TAP NPs may translate into actual therapeutic effects is still unknown and deserves further investigation. In this context, the produced NPs hold promise as a useful tool for *in vivo* investigations aimed at an improved therapeutic efficacy of the conjugated drug payload.

References

[1] You Han Bae, Kinam Park. "Targeted drug delivery to tumors: Myths, reality and possibility." *Journal of Controlled Release, Elsevier* (2011).

[2] G. P. Francesco M. Veronese) Francesco M. Veronese, Gianfranco Pasut. "PEGylation, successful approach to drug delivery." *Drug Discovery Today* (2005).

[3] Emanule Fleige, Mohiuddin A. Quadir, Rainer Haag. "Stimuli-responsive polymeric nanocarriers for the controlled transport of active compounds: concepts and applications." *Advanced Drug Delivery Reviews, Elsevier* (2012).

[4] Duffy, M. J. "The role of proteolytic enzymes in cancer invasion and metastasis." *Clinical and Experimental Metastasis* (1992).

[5] Susan A. Brooks, Hannah J. Lomax-Browne, Tracey M. Carter, Chole E. Kinch, Debbie M.S. Hall. "Molecular interactions in cancer cell metastasis." *Acta histochemics, Elsevier* (2008).

[6] Peter C. Black, Colin P. N. Dinney. "Bladder cancer angiogenesis and metastasis- translational from murine model to clinical trial." *Cancer Metastasis, Springer* (2007).

[7] Daniela Guarnieri, Marco Biondi, Hui Yu, Valentina Belli, Andrea P. Falanga, *et al.*. "Tumor-activated Prodrug (TAP)-Conjugated Nanoparticles With Cleavable Domains for Safe Doxorubicin Delivery" *Biotechnology and Bioengineering, Wiley Periodicals* (2014)

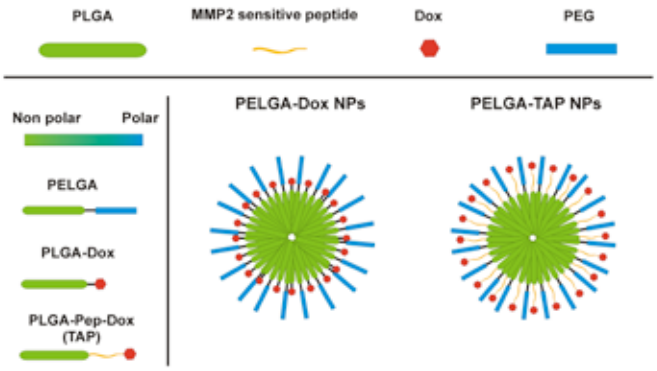

Figure 1 Schematic representation of PELGA-TAP and PELGA-Dox NP formulations

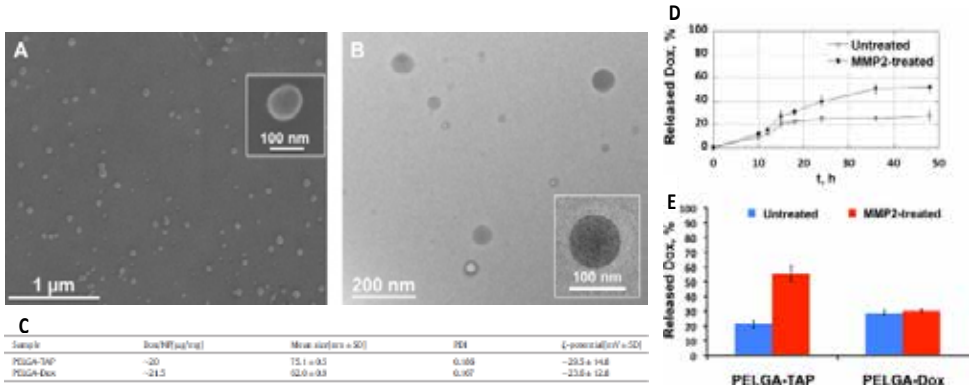

Figure 2 Scanning electron microscopy of PELGA-TAP NPs (A) and Cryo-TEM of PELGA-Dox NPs (B). The insets in A and B show images at higher magnification. Formulation, size, PDI and ξ-potential of PELGA-TAP and PELGA-DOX NPs (C) In vitro Dox release profile from PELGA-TAP NPs at 37°C in presence (black circles) and absence (white circles) of 20 nM MMP2 enzyme (D); Dox release percentage from PELGA-Dox and PELGA-TAP NPs after 24h incubation with and without MMP2 enzyme treatment at 37°C (E). Data are reported as mean ± standard deviation (SD). $p < 0.05$ was considered statistically significant.

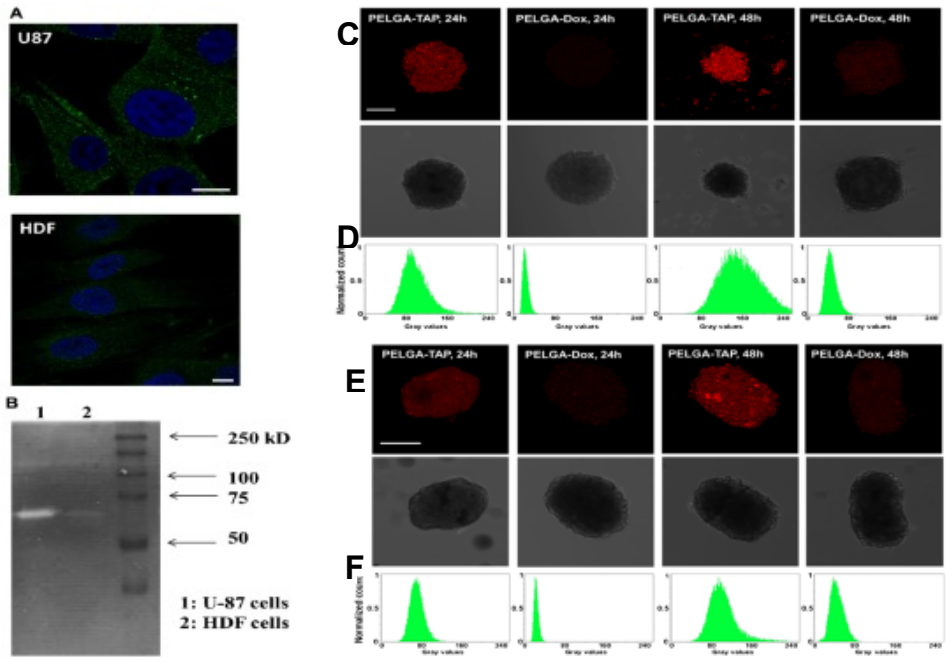

Figure 3 MMP2 expression levels in U87-MG and HDF cells. Indirect immunofluorescence of MMP2 protein (green) in U87-MG and HDF. Blue: DAPI staining of nuclei. Scale bar: 10 µm (A). Gelatin zymography showing the MMP2 activity of the two cell types used in this work (B). Distribution of Dox within U87-MG and HDF spheroid matrix upon 24 and 48 h incubation with PELGA-TAP NPs and PELGA-Dox NPs. Maximum projection of z-sectioning confocal images of Dox (red) in spheroids and transmitted light images of spheroids for U87-MG (C) and HDF (E). Fluorescence intensity distribution of Dox diffused into the spheroid matrix for U87-MG (D) and HDF (F). The y axis represents normalized pixel counts and the x axis represents the pixel fluorescence intensity expressed as gray scale values (scale range 0 – 255). Scale bar: 200 µm.

Fibrous scaffolds obtained by electrospinning for tissue regeneration

M.Putzu[1,2], F. Causa[1,2,3], and P.A. Netti [1,2,3]

[1] *Dipartimento di Ingegneria Chimica, Dei Materiali e Della Produzione Industriale (DICMAPI), University Federico II Piazzale Tecchio 80, 80125, Naples, Italy*

[2] *Center for Advanced Biomaterials for Health Care@ (CRIB) University of Naples Federico II, Piazzale Tecchio 80, 80125, Naples, Italy*

[3] *Center for Advanced Biomaterials for Health Care@CRIB Istituto Italiano di Tecnologia, Largo Barsanti e Matteucci 53 80125 Napoli, Italy*

Abstract— **In the field of tissue engineering the choice of materials is of great importance. A large number of synthetic and natural materials have been used to this purpose. In this work, we describe the use of Electrospinning technique for the manufacturing of an elastic fibrous scaffold for tissue regeneration. PCL and synthetic elastin were used as model materials and processed into nanometric fibers.**

***Keywords*—Electrospinning, tissue engineering, fibers, scaffolds.**

I. Introduction

Electrospinning is a simple and versatile top-down approach for fabricating uniform ultrafine fibers in a continuous process. Electrospinning offers several advantages, such as easy control of porosity, fiber size, and morphology among others; an effort has been made to fabricate micro/nanofibers with desired morphologies, such as aligned fibrous array and fibrous patterns (Teo WE. *et al.* 2011). The principle of electrospinning operation is based on the application of a high potential difference (Kilovolt) between two electrodes. Such electrodes are constituted, respectively, by a capillary metal (cathode) -that contains the molten or dissolved polymer to be processed- and a plate of copper or aluminum (anode) -on which the collection of the fibers takes place (Travis J. *et al.* 2008). Various materials can be electrospun including: biodegradable, non-degradable, and natural materials (Travis J. et al. 2008). A huge variety of scaffolds have been fabricated through the use of electrospinning using different types of synthetic polymers, such as PCL or PLGA (Shinoka T. *et al.* 1998). Recent research have shown promising results using electrospun scaffolds containing biopolymers blended with synthetic polymers (Swindle-Reilly *et al* 2014). Some researchers have developed nanofibrous scaffolds based on PCL blends of collagen and elastin (Li *et al*. 2005).

From the biological point of view, the scaffold should be structurally and morphologically similar to the extracellular matrix (ECM). Therefore, important tasks are cell-material interaction, sensitivity to proteases and the release of cytokines. The ECM has a fibril composition and a viscous character and such structure significantly influence the cell-biomaterial interaction (Alicia Fernandez-Colino *et al*.).

In this work, we use PCL and Elastin to obtain fibrous matrices that could be used as scaffolds for tissue regeneration. A thorough study of the influence of voltage, flow rate and distance was carried out in order to determine the appropriate parameters to obtain fibrous mats.

2,2,2-Trifluoroethanol was used as solvent to dissolve Elastin polymers at 20% (w/v). Thanks to the high volatility and chemical characteristics, we obtain fibrous matrices. PCL was dissolved using Chloroform as solvent using the same concentration as for the Elastin, 20% (w/v). Microscopy images revealed nanofibrous structures mainly composed of fibers with nanometrical dimensions (fig 1 and 2).

II. Conclusion

In this work, we describe the fabrication of nanometric fibers that could be used as biodegradable scaffold for tissue regeneration purposes. Fibers without beads and defects were obtained using different process parameters.

Acknowledgement

Authors thank Dr. Israel Gonzales De Torre from Technical Protein Nanobiotechnology (TPNCB, Valladolid, Spain) and Prof. Josè Carlos Rodriguez-Cabello from University of Valladolid (Spain) for providing us the functionalized Elastin polymers. This research was supported by funds provided through "THE GRAIL" (Tissue in Host Engineering Guided Regeneration of Arterial Intima Layer) project. The project is funded by the European Union's 'Seventh Framework' Programme for research, technological development and demonstration under Grant Agreement n° HEALTH.2011.1.4-2- 278557.

References

[1] Teo WE, Inai R, Ramakrishna S. Technological advances in electrospinning of nanofibers. Science & Technology of Advanced Materials. Vol 12, Issue 11 (2001)

[2] Travis J. Sill, Horst A. von Recum. Electrospinning: Applications in drug delivery and tissue engineering. Biomaterials. Vol. 29, Issue 13, 1989-2006 (2008)

[3] Shinoka T, Shum-Tim D, Ma PX, et al. Creation of viable pulmonary artery autografts through tissue engineering. J Thorac Cardiovasc Surg. Vol.115, Issue 3, 536–546 (1998)

[4] Katelyn E. Swindle-Reilly, Chinmay S Paranyape, Cheryl A. Miller. Electrospun Poly(Caprolactone)-Elastin scaffolds for peripheral nerve regeneration. Prog. Biomaterial 3:20 (2014)

[5] Li. M, Mondrinos MJ, Gandhi MR, Ko FK,Weiss AS, Leikes PI. Electrospun protein fibers as matrices for tissue engineering. Biomaterials, 26, 599:6608 (2005)

[6] Colino Alicia., Arias Francisco Javier, Alonso Matilde and Rodriguez-Cabello Carlos Josè. Self-Organized ECM-Mimetic Model Based on an Amphiphilic Multiblock Silk-Elastin-Like Corecombinamer with a Concomitant Dual Physical Gelation Process. Biomacromolecules 15 3781-3793 (2014)

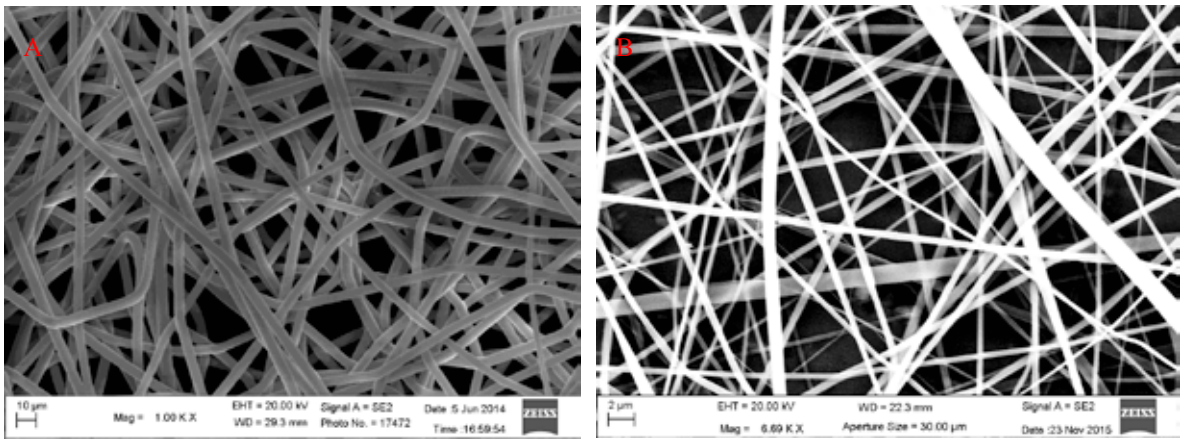

Figure 1. Scanning Electron Microscopy image of PCL and Elastin fibers obtained from 20% (w/v) solution in Chloroform and 2,2,2-Trifluoroethanol. Process parameters are 18 kV, 1 ml/h and 20 cm for PCL (A) and 20 kV, 0.3 ml/h, 20 cm for Elastin (B).

Scale-up of 3D-skin equivalent production process for cosmetics testing

F. Rescigno[1,2,3], C. Casale[3] , F. Urciuolo[1], G. Imparato[1] and P. A. Netti [1,2,3]

[1] *Center for Advanced Biomaterials for Health Care@CRIB Istituto Italiano di Tecnologia, Largo Barsanti e Matteucci n. 53, 80125 Napoli, Italy.*
[2] *Department of Chemical, Materials and Industrial Production Engineering (DICMAPI), University of Napoli Federico II, P.le Tecchio 80, 80125 Napoli, Italy*
[3] *Interdisciplinary Research Centre on Biomaterials (CRIB), University of Napoli Federico II, P.le Tecchio 80, 80125 Napoli, Italy*

***Abstract*— In recent years, advances in biomedicine are combined in the emerging field of Engineering Tissue (TE) that, by using innovative strategies, attempts to develop methods that allow for the repair and regeneration of damaged organs and tissues. The necessity of having to resort to new models *in vitro*, is born from the ban on use of animal for the study of substances and cosmetic products, as defined by the recent decree 76/768/EEC. Since recently various international companies have developed specific expertise in the design of 3D tissues *in vitro* for a variety of applications, has been explored the possibility of developing skin equivalent models as a platform for testing cosmetic products. The skin equivalent models designed by us, are realized with an innovative approach that guarantees the 3D tissue to mimic the characteristics of human skin in terms of complexity, organization, structure, and response to specific stimuli, differing from existing models present on the international market.**

***Keywords*— human skin equivalent, cosmetics, extracellular matrix.**

I. Introduction

IN recent years, the Tissue Engineering (TE), has gained ground in the biomedical and scientific and today is a new emerging discipline that consists of a series of many applications that combine the life science methods and principles with engineering ones, in order to repair and regenerate organs and tissues [1]-[4]. The first 3D tissue models made through the application of knowledge of TE were equivalent skin, bone, cornea and cartilage, most frequently damaged tissues [5].

Until the early 2000s, all that test performed cosmetic companies before putting a finished product on the market, were tested on animals [6]. Tests conducted on animal models have always aroused the need for reaching out to alternative methods what did not violate the dignity of living beings and intentions these they brought to the construction of a community regulation, the decree 76/768 / EEC what, one from leaving 2009 prohibits the use of animals for toxicological data collection of cosmetic ingredients [7],[8].

The Directive therefore puts an end to animal testing, in establishing maximum two prohibitions line:

1) testing ban is forbidden to test finished cosmetic products and their ingredients on animals;

2) prohibition of the placing on the market: the placing on the market of finished cosmetic products or contain ingredients that are tested on animals [9]-[11].

In order to study the effects of cosmetic products and various substances, a variety of three-dimensional skin model generated in vitro have been developed, by cultivating human dermal fibroblasts in exogenous collagen matrices, or biopolymers to simulate the structure of the dermis, and keratinocytes seeded on models of dermis or on polycarbonate filters at the air-liquid to allow the epithelial differentiation and support the keratinization of the epithelium. These models are known in the literature as HSE, Human Skin Equivalent and RHE (Reconstructed Human Epidermis) [12].

In the vast scenario of reconstituted skin models and in the cosmetics industry, various international companies emerge, which have developed experience and expertise in the field of cell biology and TE, producing tissue models that are now the main testing platforms available on the market. The most prestigious companies that have aroused our interest are Mattek Corporation, L'Oreal and Henkel. The models of these companies have been investigated in detail and compared by several research groups, in order to understand the features and the various uses in the cosmetic industry. These models of skin and epidermis are employed in large scale for numerous applications such as corrosion tests, tests of irritation, phototoxicity, genotoxicity, oxidative tests, transdermal drug delivery, and are currently the most used by the cosmetic and pharmaceutical industries [9]-[12].

These known models lack of complexity, and of an adequate characterization of the dermal portion , since the endogenous extracellular matrix (ECM) is completely absent [11] .

This work aimed not only, to the realization of the *in vitro* skin equivalent model in a large scale, but also to the development of protocols that are aimed at the validation of our model as an effective platform for testing cosmetic products.

II. Methods And Results

The HSEs production process is essentially divided in two phases: in the first phase, the cells (human dermal fibroblasts) are put in contact with a scaffold made from biodegradable microparticles of gelatin with interconnected porosity comprised in a range between 75-150 microns. The dynamic culture system, realized in spinner flask, allows the kinetic movement of the cell suspension in order to generate

microtissues precursors (μTPs) as “modules”. When the μTPs have produced a sufficient amount of ECM, it can proceed to the next stage, where the modules are assembled together to obtain a 3D structure, which at this stage will represent the dermis. The μTPs are assembled in a "maturation chamber", consisting of two metal grids, adapted to the passage of nutrients, and a mold of polydimethylsiloxane (PDMS) in which the modules are collected together; two teflon rings, screws and bolts seal the system. During this phase, the microtissues are assembled, thanks to the cells that migrate from one module to another, continuing to produce ECM (Fig.1). After this stage of assembly is proceeds to the next step, in which, the maturation chamber are opened to extract the dermis models and continue with the seeding of human keratinocytes on the surface. In order to ensure cell proliferation, followed by a phase of the "submerged" of about 6 days, in which the system is completely submerged by the culture medium supplemented with $CaCl_2$ at low concentrations . To enhance the differentiation of the cells and the epithelial stratification over a period of 14-21 days, we proceed to the stage of "air-liquid interface" exposing sample surface to air and increasing $CaCl_2$ concentration in the culture medium (Fig.2).

We standardize the process and develop an industrial production that requires the use of various resources, since it is essential to ensure a continuity in the production, according to precise criteria and timing perfectly scanned, so as to make available a substantial number of tissue to respond to any market applications (Fig. 3).

III. Conclusion

The development of our human skin models aims to optimize new protocols and quick tests, which exceed the limits and the timing of the histological analysis, and that they are innovative because not achievable on models already known. Our HSE could be used for the evaluation of the damage to ECM induced following exposure to UV and X-rays, analysing the reorganization of ECM and its mechanical properties; observation of elastosis phenomenon in response to UV and X-ray irradiation and oxidative stress in order to validate this models as the best platform for cosmetics testing.

References

[1] Larger R, Vacanti JP, Vacanti CA, Atala A, Freed LE, Vunjak-Novakovic G. (1995) “Tissue engineering: biomedical applications”. Tissue Engineering, 1-2

[2] Rosso F, Marino G, Giordano A et al. (2005) “Smart materials as scaffolds for tissue engineering”. Journal of Cell Physiology, 20

[3] Hubbell JA. (1995) “ biomaterilas in tissue engineering”. Nature Biotecnology, 13

[4] Bonassar LJ, Vacanti CA. (1998) “Tissue engineering: the first decade and beyond”. Journal of Cellular Biochemistry, 72

[5] Nerem RM, Sambanis A. (1995)” Tissue engineering: from biology to biological substitutes”. Tissue Engineering, 1

[6] Ott HC, Clippinger B, Conrad C. (2010)”Regeneration and orthotopic transplantation of a bioartificial lung”. Nature Medicine, 16

[7] Adler S, Basketter D, Creton S, Pelkonen O, Van Benthem J, Zuang V, Andersen KE, Loustau AA, Aptula A. (2010) “Alternative (non-animal) methods for cosmetics testing: current status and future prospects”. Archives of Toxicology, 85

[8] Netzlaff F, Lehra CM, Wertzb PW, Schaefera UF. (2005) “The human epidermis models EpiSkin, SkinEthic and EpiDerm: an evaluation of morphology and their suitability for testing phototoxicity, irritancy, corrosivity, and substance transport”. European Journal of Pharmaceutics and Biopharmaceutics, 60

[9] Ackermann K, Lombardi Borgia S, Korting HC, Mewes KR, Schäfer-Korting M. (2010) “The Phenion full-thickness skin model for percutaneous absorption testing”. Skin Pharmacology and Physiology, 23

[10] Coecke S, Corvi R, Fortaner S, Gribaldo L, Halder M, Janusch Roi A, Prieto P, Sabbioni E, Worth A and Zuang V. (2003)” ECVAM’s response to the changing political environment for alternatives: consequences of the european union chemicals and cosmetics”. ATLA, 31

[11] Fallera C, Brachera M, Damib N, Roguet R. (2002) “Predictive ability of reconstructed human epidermis equivalents for the assessment of skin irritation of cosmetics”. Toxicology in Vitro, 16

[12] Cannon CL, Neal PJ, Southee JA Kubilus J, Klausner M. (1994) “New epidermal model for dermal irritancy testing”. Toxicology in Vitro, 8

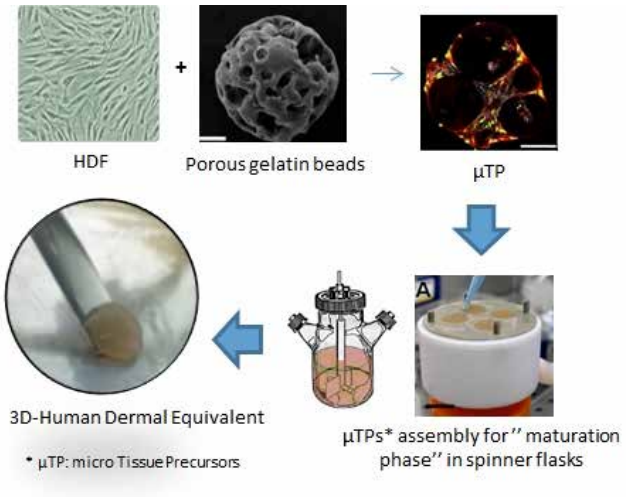

Fig. 1 The multistep process of human dermis equivalent models.

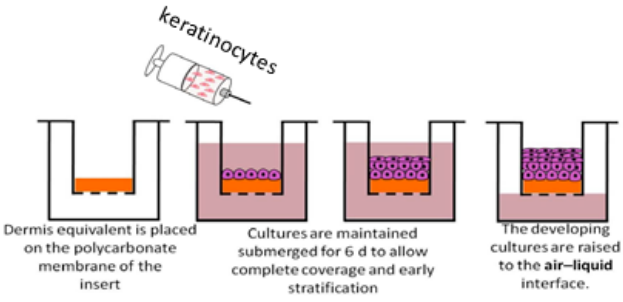

Fig. 2 Fabrication of human skin equivalent.

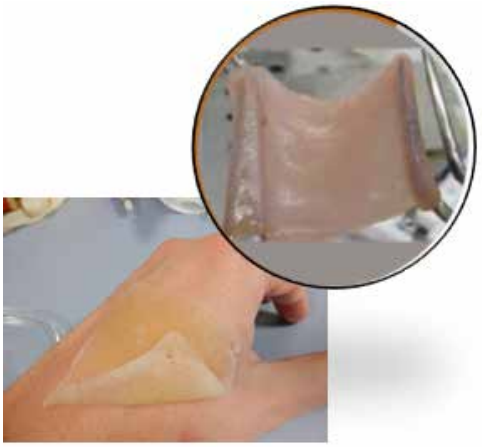

Fig. 3 Human dermis equivalent at the end of process.

Photocrosslinkable polycaprolactone for the preparation of porous scaffolds by stereolithography

A. Ronca[1], S. Ronca[2], G. Forte[2], A. Gloria[1], R. De Santis[1] and L. Ambrosio[1,3]

[1] *Institute of Composite and Biomedical Materials - National Research Council of Italy, Viale J.F. Kennedy 54, 80125 Napoli, Italy*

[2] *Department of Materials, Holywell Park Loughborough University, Leicestershire, UK, LE11 3TU*

[3] *Department of Chemical Science and Materials Technology – National Research Council of Italy, P.le Aldo Moro, 7 - 00185 Roma, Italy*

***Abstract*— A di-vinyl fumarate Polycaprolactone has been developed for tissue engineering applications using a one-step synthesis and functionalization method based on Ring Opening Polymerization (ROP) of ε-caprolactone, with Hydroxyl Ethyl Vinyl Ether (HEVE). The polymer has been successfully employed, in combination with N-vinyl Pyrrolidone (NVP), to fabricate films and computer-designed porous scaffolds by micro-stereolithography (μ-SL) with Gyroid and Diamond architectures. Characterization of the networks indicated the influence of NVP content on the network properties. Human Mesenchymal Stem Cells (hMSCs) adhered and spread onto VPCLF/NVP networks showing good biological properties and no cytotoxic effect**

***Keywords*— Photocrosslinkable polymer, Polycaprolactone fumarate, biocompatibility, stereolithography.**

I. Introduction

RAPID Prototyping technologies are increasingly demonstrating the great potential for fabricating biocompatible 3D structures with precise control of the micro- and macro-scale characteristics [1],[2]. Despite it being the first commercialized RP technology, the use of Stereolithography (SL) in Tissue Engineering has not been significantly explored, probably due to the lack of commercially available implantable or biocompatible materials [3]. An ideal scaffold design should be able to provide the necessary properties to satisfy simultaneously the biological and mechanical requirements for optimal bone tissue regeneration [4]. Stereolithography is able to reproduce with high resolution complex 3D structure that can simultaneously control the external shape that anatomically fit the bone defect but also create a perfect defined internal structure to enhance an optimum vascularization and then bone reconstruction. Typically, photocrosslinkable resins are composed of mixtures of two or more monomers that combine a relatively viscous dimethacrylate base monomer [5]. The diffusion of unpolymerized methacrylates is one of the most important factors causing irritation in tissues [6]. Stannous Octoate $Sn(Oct)_2$ has been widely used as the initiator for ROP of CL and, although very efficient, its cytotoxicity, has recently caused deep concern about biosafety of the materials synthesized from it and used for implantation purpose [7], [8]. In this work, a novel Sn-free catalyst has been used for the ROP of CL, achieving more than 95% monomers conversion at room temperature, with 4-hydroxyethyl vinyl ether (HEVE) as both initiator and photo-curable functional group. Fumarate functional group has been added to this precursor, to improve the degrees of reticulation in order to realize refined 3D scaffolds for bone tissue regeneration.

II. Experimental methods

A. Polymer synthesis

A Sn-free catalyst based on Al [9] has been used in the polymerisation of CL at room temperature, coupled with HEVE as photocurable initiator [10], according to the scheme below (Figure 1). The ratio initiator/CL has been varied to achieve a range of Mw comprised between 2000 and 5000 g/mol, as determined via rheological experiments and NMR. Following the synthesis of the vinyl-terminated PCL, its reaction with fumaryl chloride results in chains containing photocrosslinkable vinyl units at both ends and in the middle of the chain in order to obtain a divinyl-fumarate-PCL (VPCLF). Networks were formed from VPCLCF by UV irradiation (365 nm) using Lucirin TPO as a biocompatible initiator, Orasol Orange Gas dye and N-Vinyl-2-pyrrolidone (NVP) as reactive solvent.

B. Polymer characterization

The resulting polymer was characterized by its specific molecular weights, functional end groups and transition temperatures, using several techniques including Rheometry, Nuclear Magnetic Resonance (NMR), Fourier Transformed Infrared Spectroscopy (FTIR), Differential Scanning PhotoCalorimetry (DPC) and Differential Scanning Calorimetry (DSC). Photo crosslinked disk-shaped specimens (diameter 6 mm) of VPCLF/NVP were seeded with human mesenchymal stem cells (hMSCs) to assess material's biocompatibility.

C. Mathematically defined scaffolds

In order to design a suitable scaffold for tissue engineering our approach was to use the family of Triply Periodic Minimal Surfaces (TMPS) as pore morphology. TMPS structures are a remarkable class of minimal surfaces that can be generated by trigonometric equations. This advanced approach consists on designing sophisticated 3D porous structures using the periodicity of trigonometric equations Mathematically defined porous structures with Gyroid (1) architecture were prepared using the VPCLF/NVP resin [11]. The following trigonometric functions with boundary conditions x, y = [-6π,6π] and z = [-3π,3π] were used:

$$\cos(x)\cdot\sin(y)+\cos(y)\cdot\sin(z)+\cos(z)\cdot\sin(x)=C \quad (1)$$

To obtain porous structures with porosities of approximately

50-60%, offset values "C" of 0.5 are required. Rhinoceros software was used to scale the CAD-files of the two architectures to the desired dimensions.

D. Morphological characterization of scaffolds

Scanning electron microscopy (SEM) was performed in order to obtain qualitative information regarding the morphology and pore characteristics of the built VPCLF/NVP structures. The specimens were gold sputtered and observed with a FEI QUANTA 200 FEG scanning electron microscope. Nondestructive structural analysis was performed by micro-computed tomography (μ-CT) using a SkyScan 1172 micro-CT scanner (Bruker) at 5.45 μm resolution.

III. Results and Discussion

A. Synthesis of VPCLF

The polymerization of ε-caprolactone with the methylaluminum bis (2,6 ditertbutyl-4-methylphenolate) system proceeded smoothly at room temperature to give a polyester showing a reasonably narrow molecular weight distribution (MWD). PCL with a range of molecular weight ranging from 1.5 - 6 kDa were successfully synthesized but only the lower molar weight PCL (1.5kDa, VPCLC) was used for the following fumarate reaction. Nuclear Magnetic Resonance (NMR), Fourier Transformed Infrared Spectroscopy (FTIR), Differential Scanning PhotoCalorimetry (DPC) and Differential Scanning Calorimetry (DSC). NMR and FTIR confirm the presence of functional groups linked to the PCL oligomers

B. Characterization of VPCLF/NVP network

Networks were formed from VPCLF macromers and NVP by UV irradiation (365 nm) using Lucirin TPO as a biocompatible initiator. The NVP content was varied from 30 to 50 wt % and the network properties were evaluated. The gel content of the networks obtained after a photo-polymerization for 20 min was above 85% in all samples. Due to the hydrophilic character of NVP, the water uptake of the networks increases by increasing NVP content. The results suggest that hydrophilicity of the resulting networks can readily be adjusted and materials ranging from hydrophobic glassy polymer networks to hydrogels can be prepared.

To assess the suitability of these networks for cell culturing and tissue engineering, initial cell adhesion experiments were performed. hMSCs cells adhered well to the VPCLF/NVP networks, showing a spread morphology and this representative morphology is a positive sign that cells have a good biocompatibility and affinity for the VPCLF/NVP materials. Our results demonstrated that the materials appeared not to be cytotoxic neither show a negative response to cell adhesion. It can be stated that VPCLF/NVP network films are suitable substrates for cells culturing.

C. Mathematically defined structures

We prepared porous VPLCF/NVP network scaffolds with a Gyroid architectures. These architectures are mathematically defined, allowing precise control of porosity and pore size of a fully inter-connected pore network. Such built structures have been realized in less than 4 hours and they are presented in Fig. 2. Gyroid geometries have a large specific surface area and high pore interconnectivity. These characteristics make it an excellent architecture for tissue engineering, as it enables cell-seeding at high densities, and allows homogeneous distribution of cells and flow of nutrients throughout the scaffold.

IV. Conclusion

The major objective of this study was to create biocompatible PCL scaffolds with a controlled internal structure for bone tissue engineering. Results proved that it is possible to obtain biocompatible porous scaffolds with a refined micro architecture by stereolithography technique using VPCLF/NVP photocurable resin.

Acknowledgement

The authors would like to thank the Short Term Mobility 2016 (STM) Research Project co-funded by National Research Council of Italy (CNR) for providing financial support to this project.

References

[1] K. Kim, A. Yeatts, D. Dean, and J. P. Fisher, *Stereolithographic Bone Scaffold Design Parameters: Osteogenic Differentiation and Signal Expression,* Tissue Engineering: part B, Vol. 16, Issue 5, pp. 523-539 ; May 2010

[2] A. Gloria, T. Russo, R. de Santis, L. Ambrosio, *3D fiber deposition technique to make multifunctional and tailor-made scaffolds for tissue engineering applications,* Journal of Applied Biomaterials and Biomechanics, Vol. 7, Issue 3, pp 141-152; Sep 2009

[3] A. Ronca, L. Ambrosio, D.W. Grijpma, *Preparation of designed poly(d,l-lactide)/nanosized hydroxyapatite composite structures by stereolithography,* Acta Biomaterialia, Vol.9, Issue 4 pp. 5989-96; April 2013

[4] Hollister, S. J. *Porous scaffold design for tissue engineering*, Nat Mater, Vol. 4, pp. 518-524; 2005

[5] S. H. Dickens , J.W. Stansbury , K.M. Choi, and C.J.E. Floyd., *Photopolymerization Kinetics of Methacrylate Dental Resins,* Macromolecules. Vol. 36, pp. 6043-6053, July 2003.

[6] J.H. Jorge, E.T. Giampaolo, A.L. Machado, C.E. Vergani, *Cytotoxicity of denture base acrylic resins: a literature review,* J Prost Den. Vol. 90, Issue 2, pp190-193, Aug. 2003

[7] A,C, Albertsson, U. Edlund, K. Stridsberg, *Controlled ring-opening polymerization of lactones and lactides*, Macromo Symp., Vol. 157, issue 1, pp 39-46, July 2000

[8] H.R. Kricheldorf, I. Kreiser-Saunders, D.O. Damrau, *Resorbable initiators for polymerizations of lactones*, Macromol Symp. Vol. 159, Issue 1, pp. 247-258, Oct. 2000

[9] M. Akatsuka, T. Aida, S. Inoue*, Alcohol/methylaluminum diphenolate systems as novel, versatile initiators for synthesis of narrow molecular weight distribution polyester and polycarbonate,* Macromolecules, Vol. 28, pp. 1320-1322, Feb. 1995

[10] S.S. Liow, V.T. Lipik, L.K. Widjaja, M.J.M. Abadie, *Synthesis, characterization and photopolymerization of vinyl ether and acrylate functionalized hybrid oligo-caprolactone,* J Polym Res. Vol. 19, 9748, Apr. 2012.

[11] P.J.F. Gandy, J. Klinowski, *Exact computation of the triply periodic G (`Gyroid') minimal surface,* Chemical Physics Letters. Vol. 321, Issue5-6, pp. 363–371.

50-60%, offset values "C" of 0.5 are required. Rhinoceros software was used to scale the CAD-files of the two architectures to the desired dimensions.

D. Morphological characterization of scaffolds

Scanning electron microscopy (SEM) was performed in order to obtain qualitative information regarding the morphology and pore characteristics of the built VPCLF/NVP structures. The specimens were gold sputtered and observed with a FEI QUANTA 200 FEG scanning electron microscope. Nondestructive structural analysis was performed by micro-computed tomography (μ-CT) using a SkyScan 1172 micro-CT scanner (Bruker) at 5.45 μm resolution.

III. Results and Discussion

A. Synthesis of VPCLF

The polymerization of ε-caprolactone with the methylaluminum bis (2,6 ditertbutyl-4-methylphenolate) system proceeded smoothly at room temperature to give a polyester showing a reasonably narrow molecular weight distribution (MWD). PCL with a range of molecular weight ranging from 1.5 - 6 kDa were successfully synthesized but only the lower molar weight PCL (1.5kDa, VPCLC) was used for the following fumarate reaction. Nuclear Magnetic Resonance (NMR), Fourier Transformed Infrared Spectroscopy (FTIR), Differential Scanning PhotoCalorimetry (DPC) and Differential Scanning Calorimetry (DSC). NMR and FTIR confirm the presence of functional groups linked to the PCL oligomers

B. Characterization of VPCLF/NVP network

Networks were formed from VPCLF macromers and NVP by UV irradiation (365 nm) using Lucirin TPO as a biocompatible initiator. The NVP content was varied from 30 to 50 wt % and the network properties were evaluated. The gel content of the networks obtained after a photo-polymerization for 20 min was above 85% in all samples. Due to the hydrophilic character of NVP, the water uptake of the networks increases by increasing NVP content. The results suggest that hydrophilicity of the resulting networks can readily be adjusted and materials ranging from hydrophobic glassy polymer networks to hydrogels can be prepared.

To assess the suitability of these networks for cell culturing and tissue engineering, initial cell adhesion experiments were performed. hMSCs cells adhered well to the VPCLF/NVP networks, showing a spread morphology and this representative morphology is a positive sign that cells have a good biocompatibility and affinity for the VPCLF/NVP materials. Our results demonstrated that the materials appeared not to be cytotoxic neither show a negative response to cell adhesion. It can be stated that VPCLF/NVP network films are suitable substrates for cells culturing.

C. Mathematically defined structures

We prepared porous VPLCF/NVP network scaffolds with a Gyroid architectures. These architectures are mathematically defined, allowing precise control of porosity and pore size of a fully inter-connected pore network. Such built structures have been realized in less than 4 hours and they are presented in Fig. 2. Gyroid geometries have a large specific surface area and high pore interconnectivity. These characteristics make it an excellent architecture for tissue engineering, as it enables cell-seeding at high densities, and allows homogeneous distribution of cells and flow of nutrients throughout the scaffold.

IV. Conclusion

The major objective of this study was to create biocompatible PCL scaffolds with a controlled internal structure for bone tissue engineering. Results proved that it is possible to obtain biocompatible porous scaffolds with a refined micro architecture by stereolithography technique using VPCLF/NVP photocurable resin.

Acknowledgement

The authors would like to thank the Short Term Mobility 2016 (STM) Research Project co-funded by National Research Council of Italy (CNR) for providing financial support to this project.

References

[1] K. Kim, A. Yeatts, D. Dean, and J. P. Fisher, *Stereolithographic Bone Scaffold Design Parameters: Osteogenic Differentiation and Signal Expression,* Tissue Engineering: part B, Vol. 16, Issue 5, pp. 523-539 ; May 2010

[2] A. Gloria, T. Russo, R. de Santis, L. Ambrosio, *3D fiber deposition technique to make multifunctional and tailor-made scaffolds for tissue engineering applications,* Journal of Applied Biomaterials and Biomechanics, Vol. 7, Issue 3, pp 141-152; Sep 2009

[3] A. Ronca, L. Ambrosio, D.W. Grijpma, *Preparation of designed poly(d,l-lactide)/nanosized hydroxyapatite composite structures by stereolithography,* Acta Biomaterialia, Vol.9, Issue 4 pp. 5989-96; April 2013

[4] Hollister, S. J. *Porous scaffold design for tissue engineering*, Nat Mater, Vol. 4, pp. 518-524; 2005

[5] S. H. Dickens , J.W. Stansbury , K.M. Choi, and C.J.E. Floyd., *Photopolymerization Kinetics of Methacrylate Dental Resins,* Macromolecules. Vol. 36, pp. 6043-6053, July 2003.

[6] J.H. Jorge, E.T. Giampaolo, A.L. Machado, C.E. Vergani, *Cytotoxicity of denture base acrylic resins: a literature review,* J Prost Den. Vol. 90, Issue 2, pp190-193, Aug. 2003

[7] A,C, Albertsson, U. Edlund, K. Stridsberg, *Controlled ring-opening polymerization of lactones and lactides*, Macromo Symp., Vol. 157, issue 1, pp 39-46, July 2000

[8] H.R. Kricheldorf, I. Kreiser-Saunders, D.O. Damrau, *Resorbable initiators for polymerizations of lactones*, Macromol Symp. Vol. 159, Issue 1, pp. 247-258, Oct. 2000

[9] M. Akatsuka, T. Aida, S. Inoue*, Alcohol/methylaluminum diphenolate systems as novel, versatile initiators for synthesis of narrow molecular weight distribution polyester and polycarbonate,* Macromolecules, Vol. 28, pp. 1320-1322, Feb. 1995

[10] S.S. Liow, V.T. Lipik, L.K. Widjaja, M.J.M. Abadie, *Synthesis, characterization and photopolymerization of vinyl ether and acrylate functionalized hybrid oligo-caprolactone,* J Polym Res. Vol. 19, 9748, Apr. 2012.

[11] P.J.F. Gandy, J. Klinowski, *Exact computation of the triply periodic G (`Gyroid') minimal surface,* Chemical Physics Letters. Vol. 321, Issue5-6, pp. 363–371.

Dynamic reversible substrates to control cell behavior

Lucia Rossano,[1,2] Carmela Rianna,[1,2,3] Maurizio Ventre,[1,2] Silvia Cavalli,[1] Paolo A. Netti.[1,2]*

[1]*Center for Advanced Biomaterials for Health Care IIT@CRIB, Largo Barsanti e Matteucci 53, 80125 NA, IT.*
[2] *Department of Chemical, Materials and Industrial Engineering, University Federico II, Piazzale Tecchio 80, 80125 NA, IT.*
[3] *Institute of Biophysics, University of Bremen, Otto-Hahn Allee, D-28359 Bremen, Germany.*

[*]*To whom correspondence should be addressed. E-mail:* nettipa@unina.it

Abstract— Topography of material surface is known to exert a potent influence on cell fate and functions at different levels: from adhesion up to differentiation. Different techniques have been developed to fabricate micro- and nano-patterns to evaluate cell behavior. Here we investigated the response of NIH-3T3 cells to dynamic reversible topographic patterns on azopolymer films. Switchable reversible patterns were realized by single laser beam technique and were erased with incoherent light. This study paves the way toward a real-time investigation of the material−cytoskeleton crosstalk caused by the spatial and time changes of topographic signals.

Keywords— cell behavior, reversible pattern, topography, azopolymers

I. Introduction

THE most notable cellular structures that mediate material-cytoskeleton interactions are molecular complexes called focal adhesions. These are dynamic structures that involve the recruitment, interaction and turnover of several molecular components. The integrins are relevant molecules that connect ligands of the extracellular space to the cytoskeleton, and are responsible for transmitting exogenous stimuli to the cell. The number and shape of cell components and the organization of focal adhesion are of particular interest studying the dynamics of cell adhesion and migration. The topographical features play a role in cell–material interactions through the regulation of material–cytoskeleton crosstalk. Topographical signals, however, are not considered in vitro artefacts because the effects of topographical patterns on cell activity are also present in an in vivo context. Examples of native topographic micro- and nanopatterns are found in fibrils and fibre bundles (collagen and fibrin), rough surfaces (crystal deposit in bone) and porous membranes (basement membranes) [1].

In natural tissues there is a dynamical remodeling of this topographical features that influences cells behavior, in terms of adhesion, migration and differentiation. To overcome the limits of a physically static system and to develop more versatile platforms, great interest has recently arisen in using stimulus-responsive materials as dynamic supports to investigate cell response [2, 3, 4].

The azopolymers can be used to realize dynamic and light−switchable supports for cell culture [5]. They consist of polymers functionalized with azobenzene molecules. Owing to the intrinsic properties of azobenzene moieties, azopolymers belong to a class of light−responsive materials. Azobenzene is an aromatic molecule formed by an azo linkage connecting two phenyl rings. Originally, azobenzenes were used as dyes and colorants, due to their powerful colors. Azobenzenes have two stable isomeric states: a thermally stable *trans* configuration and a metastable *cis* form. Remarkably, the azobenzene chromophore can interconvert between these isomers upon absorption of a photon. For most azobenzenes, the molecule can be optically isomerized from trans to cis with light and the molecule will subsequently thermally relax back to the trans state on a timescale dictated by the substitution pattern. This photochemistry is central to azobenzene potential use as a tool for nanopatterning [6,7]. The azobenzene−type molecules have a strong absorption in the UV, and a low−intensity band in the visible. Irradiation with light produces molecular changes in azobenzenes, and under appropriate conditions, these changes can translate into larger scale motions and even modulation of material properties [8].

The azobenzene exhibits a unique and remarkable surface-mass transport under light illumination. This optical patterning represents massive material transport on a micrometer and sub-micrometer length scale and provides a unique opportunity for nanostructure formation [8].

During last decades, several phenomena arising from azopolymers−light interaction have been observed and described. Among these, surface relief gating (SRG) requires an optical set−up, made of powerful lasers, tools and filters able to induce a holographic pattern of polarized light [9].

To overcome the limits of this optical setup other techniques have been used to realize dynamic pattern in real time.

In 1998 Trypathy, Kumar and colleagues were the first to induce a deformation of an azopolymer film using a single laser beam that allows its definition and prediction [10]. Subsequently other research groups realized linear topographical patterns on azopolymer film using the laser scanning technique [11].

Here, we fabricated and characterized linear topographic patterns using a confocal technique and evaluated the behavior of NIH-3T3 cells on a dynamic reversible light sensitive polymeric biointerfaces.

II. Materials and Methods

General Materials. Poly-Disperse Red 1-methacrylate (pDR1m) was supplied by Sigma. Circular cover glasses

were purchased from Thermo Scientific. Chloroform and other solvents were purchased from Romil. Cell Tracker Deep Red dye was supplied by Life Technologies.

Substrate preparation. Circular cover glasses (12 mm diameter) were washed in acetone, sonicated for 15 min, and then dried on a hot plate prior to the spin coating process. pDR1m was dissolved in chloroform at a concentration of 5% (w/v). The solution was spun over the cover glass by using a Laurell spin coater (Laurell Technologies Corp.) at 1500 rpm.

Cell culture and staining. NIH-3T3 fibroblasts were cultured in low glucose DMEM (Dulbecco's Modified Eagle Medium) and incubated at 37°C in a humidified atmosphere of 95% air and 5% CO_2. Prior to cell seeding, pDR1m substrates were sterilized under UV light for 30 min. For confocal image acquisitions, NIH-3T3 cells were incubated with a solution of Cell Tracker Deep Red dye 1μM in serum free medium.

Atomic Force Microscopy. A JPK NanoWizard II (JPK Instruments), mounted on the stage of an Axio Observer Z1 microscope (Zeiss), was used to characterize the azopolymer films in terms of surface topography and pattern features (depth and pitch). Silicon nitride tips (MSCT, Bruker) with a spring constant of 0.01 N/ m were used in contact mode, in air at room temperature.

Micro-nanopattern inscription. A SP5 STED confocal microscope (Leica Microsystems, Germany) was used to write different topographic patterns on pDR1m substrates. In more details, the *trans−cis−trans* isomerization of the azopolymer and consequent mass transport were activated by using an Argon laser with 514 nm wavelength (2.3 mW maximum intensity).

III. Results

Confocal microscope technique is an innovative method to fabricate precise and controlled micro- and nano-patterns on azopolymer substrates. Different topographic patterns were realized by controlling the laser beam spatial position and illuminating the sample with a proper wavelength, that allows the activation of the azobenzene trans−cis−trans isomerization. Parallel lines were inscribed by illuminating the sample for 45 seconds at 514 nm (Figure 1). The realized pattern had a high of 300 nm with a pitch of 2.5μm to promote cell alignment.

An incoherent and unpolarized light beam of a mercury lamp, was used to erase the topographic pattern, indeed incoherent and unpolarized light is highly effective in randomizing azobenzene molecule orientation [8]. Starting from these observations, a linear pattern was irradiated for 30 seconds with mercury lamp, reducing the height of about 200 nm (Figure 2). This new technique is adaptable to cell environment conditions and the laser intensity power is suitable for dynamic real-time experiments with cells; in fact, the microscopy setup allows pattern feature alteration in the presence of cells without affecting their viability. Topographic stimuli influence strongly cell behavior, in particular regarding the orientation of the cell body. We realized linear patterns in presence of cells using this confocal technique and studied the time of cell alignment. Cells were stained using a cell tracker dye in order to observe the shape. Confocal images were taken at different time points (Figure 3). At t=0 cell was alive and linear patterns were embossed on the surface. Cell began to align after 150 minutes from the pattern realization and was completely aligned along the groove direction after 270 minutes from inscription.

This data confirm that the orientation of the cell body is highly influenced by topographical stimuli, and the cell is completely aligned to the linear pattern after 4 hours from inscription.

IV. Conclusions

In this work, we showed a new technique for writing and erasing topographic patterns on pDR1 films. The pattern can be easily written controlling the position of single laser beam and erased using an incoherent light. In particular, this technique is a promising strategy for real-time experiments because the microscopy setup and illumination exposure time did not affect cell viability. The initial results demonstrated that this technique may pave the way to the study of cell behavior in a dynamic and biomimetic way, owing to the versatility of optical set-up and the unique properties of the azobenzene moieties.

Acknowledgement

The authors thank Dr. Ravichandran H. Kollarigowda for his support in developing the confocal technique here described and Dr. Fabio Formiggini for his support in confocal image acquisition. Financial support was provided by IIT.

References

[1] M. Ventre, F. Causa and P. A. Netti, "Determinants of cell–material crosstalk at the interface: towards engineering of cell instructive materials," *J. R. Soc. Interface,* 2012, 9, 2017–2032.

[2] K. A. Davis, K. A. Burke, P. T. Mather, J. H. Henderson, "Dynamic Cell Behavior on Shape Memory Polymer Substrates," . *Biomaterials,* 2011, 32, 2285−2293.

[3] D. M. Le, K. Kulangara, A. F. Adler, K. W. Leong, V. S. Ashby, "Dynamic Topographical Control of Mesenchymal Stem Cells by Culture on Responsive Poly(ε-caprolactone) Surfaces," *Adv. Mater.,* 2011, 23, 3278−3283.

[4] C. Rianna, A. Calabuig, M. Ventre, S. Cavalli, V. Pagliarulo, S. Grilli, P. Ferraro and P. A. Netti, "Reversible Holographic Patterns on Azopolymers for Guiding Cell Adhesion and Orientation," *ACS Appl. Mater. Interfaces,* 2015, 7, 16984−16991.

[5] C. Rianna, M. Ventre, S. Cavalli, M. Radmacher, and P. A. Netti, " Micropatterned Azopolymer Surfaces Modulate Cell Mechanics and Cytoskeleton Structure," *ACS Appl. Mater. Interfaces*, 2015 Sep 30;7(38):21503-10.

[6] H. Zollinger, "Azo and diazo Chemistry," *Interscience* 1961.

[7] H. Rau, "Photochemistry and photophysics," *CRC Press*, 1991, 2, pp. 119–141.

[8] K. G. Yager, C. J. Barrett, "Light-Induced Nanostructure Formation using Azobenzene Polymers," *Polymeric Nanostructures and Their Applications,* Volume 0: Pages (1–38).

[9] P. Rochon, E. Batalla, A. Natansohn, "Optically induced surface gratings on azoaromatic polymer films" *Appl. Phys. Lett.* 1995, *66*, 136−138.

[10] S. Bian, L. Li, J. Kumar, D. Y. Kim, J. Williams, and S. K. Tripathy, "Single laser beam-induced surface deformation on azobenzene polymer films," *Applied Physics Letters.* 1998 *73*, 1817.

[11] A. Ambrosio, A. Camposeo, P. Maddalena, S. Patane` and M. Allegrini, "Real-time monitoring of the surface relief formation on azo-polymer films upon near-field excitation," *Journal of Microscopy.* 2008, *229*, Pt 2, pp. 307–312.

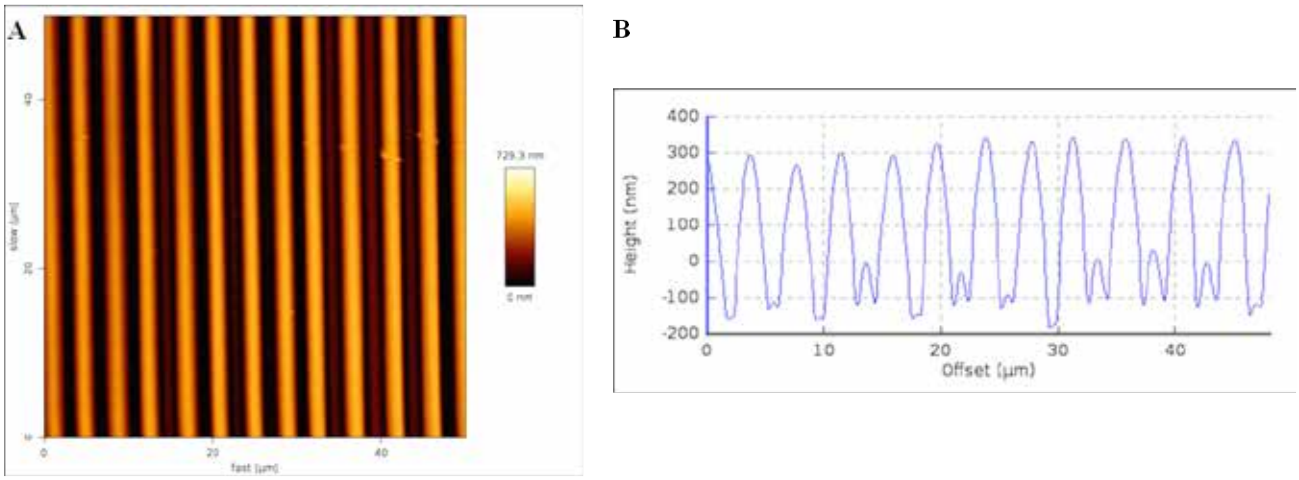

Fig. 1. AFM image of linear nano-patterns realized on pDR1 substrates, using a confocal technique. (A) Bi−dimensional topographical image, (B) cross section profile.

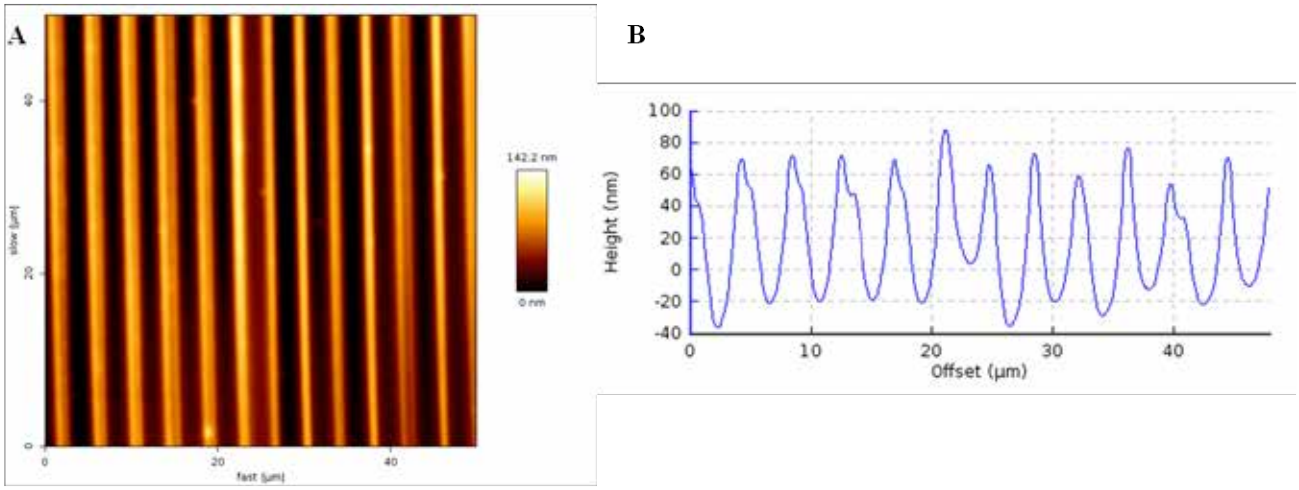

Fig. 2. AFM image of linear nano-patterns realized on pDR1 substrates after illumination with mercury lamp for 30s. (A) Bi−dimensional topographical image, (B) cross section profile.

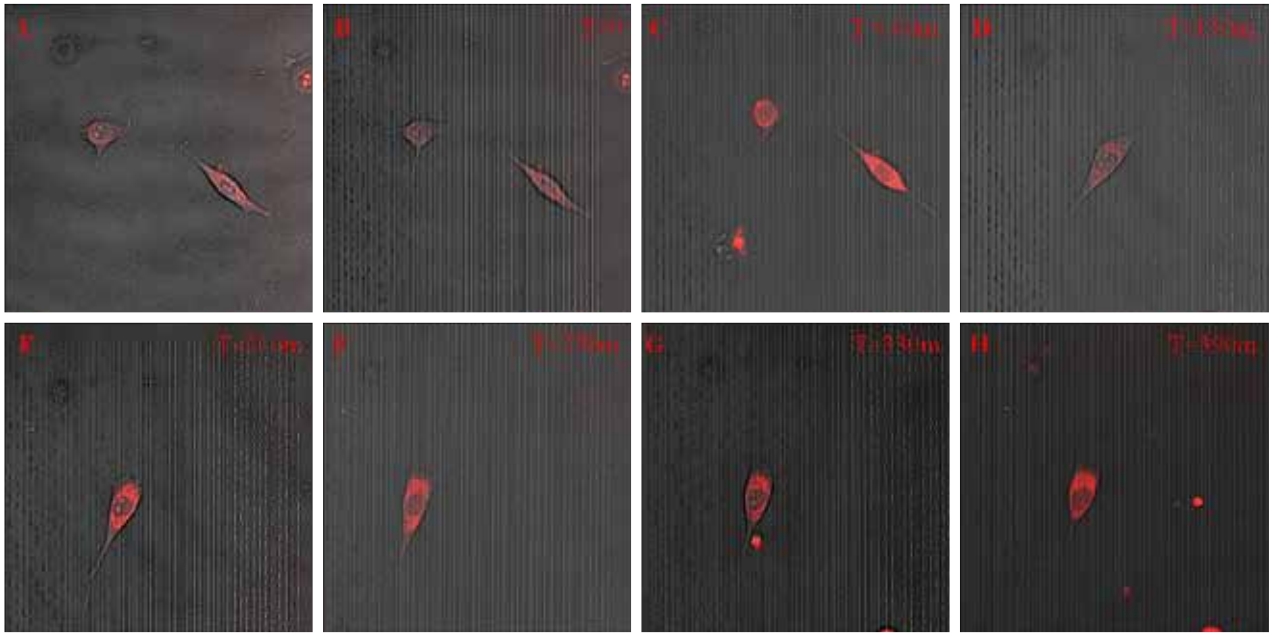

Fig.3. Cell alignment on PDR1 substrates in real-time. (A) Confocal image of a single cell on flat pDR1m, (B) same location after pattern inscription (t=0), (C-D) cell behavior after 60 and 150 minutes, (E-F-G-H) cell alignment after 210, 270, 330 and 390 minutes.

Microfluidic approach to entrap Gd-DTPA in cross-linked Hyaluronic Acid nanoparticles for enhancing MRI sensitivity

Maria Russo[1,2], Paolo A. Netti[1,2,3] and Enza Torino[1,3]
[1] Istituto Italiano di Tecnologia, Center for Advanced Biomaterials for HealthCare IIT@CRIB, 80125, Naples, Italy.
[2] University of Naples Federico II, Department of Chemical, Materials and Industrial Production Engineering, 80125, Naples, Italy.
[3] University of Naples Federico II, Interdisciplinary Research Center of Biomaterials, CRIB, 80125, Naples, Italy.

***Abstract*—Through a microfluidic flow focusing approach, cross-linked Hyaluronic Acid nanoparticles are synthesized to be used in Magnetic Resonance Imaging (MRI) applications. By fine-tuning of flow conditions and the mixing among all species the competition between nanoprecipitation behavior and crosslinking reaction is adjusted very accurately, allowing the optimization of the entrapment of Gd-DTPA within the hydrogel nanoparticles; this, in turn, improves the relaxometric properties of CAs by influencing the relaxation time of water protons. Our continuous process provides better-controlled conditions, which leads to more homogeneously sized nanoparticles than the conventional discontinuous processes. Furthermore, the ability of hydrodynamic flow focusing on tuning the properties of Gd-DTPA loaded crosslinked nanoparticles and impacting the relaxometric properties of active compounds could be proposed as a microfluidic approach to design a new class of MRI-CAs without the chemical modification of chelate.**

***Keywords*— microfluidics, nanoparticles, MRI, hydrogels.**

I. Introduction

Microfluidics is an interesting technology for different biological and medical applications because of its ability to efficient and rapidly mix reagents, provide homogeneous reaction environments and continuously vary reaction conditions. The use of microfluidic devices for nanoparticle synthesis is advantageous in many aspects, including enhanced processing accuracy and efficiency; flexibility for multi-step platform design; better controlling properties of synthesized nanoparticles, cost savings from reduced consumption of source materials and reagents. Rapid and mixing in microfluidics may allow better control over the process of nanoprecipitation [1] and also enable screening of various formulation conditions on a single platform by varying parameters such as flow rates, reagent composition, and mixing time. Flow focusing is the most frequently used and results from combining hydrodynamic forces with a specific geometry. A basic design for hydrodynamic focusing is a long microchannel with three inlets and one outlet. In the flow focused nanoprecipitation [2], [3], the non-solvent phase, flowing through two side channels, meets the solvent phase in the main channel, where the solvent phase becomes compressed, and the solvents mutually diffuse promoting the precipitation of the solute. However, investigations of the microfluidic flow focusing approach to support Magnetic Resonance field are still not studied. MRI represents the first-line diagnostic imaging modality for numerous indications and microfluidics could support this area by overcoming limitations related to the utilization of a contrast agent (CA) to improve MRI images. Indeed, despite clinical GdCAs usefulness, they still suffer from poor sensitivity [4] and low relaxivity, requiring long scan time, and rapid renal clearance, limiting the time window for clinical MRI. Several studies, based on bench reactors, have been made to obtain nanostructures encapsulating or conjugating CAs to increase their tissue specificity and reduce nephrotoxicity, but only some of them reported an increased relaxivity of Gd-based CAs without the chemical modification of the chelates [5], [6]. Here, we perform a microfluidic flow focusing approach able to produce cross-linked Hyaluronic Acid nanoparticles with improved MRI characteristics. Through our approach, we achieve a fine-tuning of the process parameters to adjust the mixing among all species very precisely and to control their nanoprecipitation behavior. Contemporarily, this fashionable approach is optimized to perform a crosslinking reaction able to retain the GdCAs in the polymer matrix of the precipitated morphology. NPs obtain an increase of MRI signal larger in r_1 than that of the commercial MRI contrast agent, Magnevist, in the common field of clinical MRI, 1.5 Tesla. Our microfluidic approach allows a strict control of the characteristics of the nanoparticles and of the entrapping of the Gd-DTPA, showing a low polydispersity of nanoparticles and a high encapsulation efficiency of CAs without long and expensive purification steps.

II. Materials and Methods

A. Materials

Sodium Hyaluronate (MW=42 kDa) was purchased from Bohus Biotech (Sweden). Gd-DTPA (MW=547.57 g/mol); Span80; Tween21; Tween85; Divinyl Sulfone (or Vinyl Sulfone) (MW=118.15 Da); Acetone; Ethanol; Sodium Hydroxide NaOH; Gadolinium Chloride Solution $GdCl_3$ (MW=263.61); Sodium Chloride NaCl were purchased by Sigma-Aldrich Co. The water, used for synthesis and characterization, was purified by distillation, deionization, and reserve osmosis (Milli-Q Plus). A quartz microfluidic device "X- Junction Chip, 190 μm", purchased from Dolomite Centre Ltd, was used to perform all the experiments.

B. Preparation of crosslinked Hyaluronic Acid nanoparticles

Nanoparticles were designed through Nanoprecipitation of the polymer by supersaturation in a microfluidic Flow focusing approach. In details, Hyaluronic Acid has been

dissolved in water and its precipitation was induced by mixing with an selected organic solvent, such as Acetone, Ethanol or Isopropanol. A new microfluidic setup was built up to obtain a sharp and stable flow focusing in order control the Nanoprecipitation process for generating HA nanoparticles entrapping Gd-DTPA. Factors such as molecular weight and concentration of polymer, the type of surfactants, the type of Anti-solvent and flow rates was investigated to study NPs properties. Different HA concentrations were tested to explore the effects of the nanoprecipitation on flow conditions. Different flow rates were tested. Precipitated nanoparticles were collected in a Petri glass containing few mL of non-solvent and kept under continuous stirring. Crosslinking reaction was performed by using Divinyl Sulfone (DVS).

C. Nanoparticles purification, recovery and characterization

Purification was performed by a solvent gradient dialysis or by ultracentrifugation. Dynamic light scattering (DLS) was used to determine nanoparticle size (Zeta sizer, Malvern). Nanoparticles were concentrated by ultracentrifugation. After these treatments, a hundred microliters of purified samples were deposited on a polycarbonate Isopore Membrane Filter (0.05, 0.1 and 0.2 μm) by ultrafiltration vacuum system. The precipitated or deposited particles were coated with gold-palladium, and their morphology was observed by ULTRA PLUS Field Emission Scanning Electron Microscope (FE-SEM Carl Zeiss, Germany). Transmission Electron Microscope (TEM) were also used to characterize the samples.

D. In vitro MRI

Empty nanoparticles and nanoparticles containing $GdCl_3$ or Gd-DTPA at different concentrations were tested by in vitro MRI and results were compared with Magnevist, Gd-DTPA and $GdCl_3$ in water as a control. After vigorous stirring, changes in relaxation time (T_1 and T_2) were evaluated at 1.5 Tesla by Minispec Bench Top Relaxometer (Bruker Corporation).

III. RESULTS AND DISCUSSION

Results show that nanoparticle sizes change varying flow rates of solvent and non-solvent phases. Indeed, at selected flow rates a more stable and narrow hydrodynamic focusing is achieved. Hyaluronic Acid concentration also affects the nanoprecipitation, and most of our experiments are conducted at a selected concentration, allowing for a longer stability of the process. All experiments are conducted at selected flow rates due to the prolonged stability of the hydrodynamic flow focusing, the absence of massive precipitation. Stable Flow Focusing and Field Emission Scanning Electron Microscopy (FE-SEM) image of the collected NPs are reported in Figure 1 A) and B). Furthermore, a crosslinking reaction is performed to improve the stability of the nanoparticles, increase loading capability and reduce swelling effects. Different crosslinking approaches are exploited to perform the simultaneous control of crosslinking reaction and nanoprecipitation. However, also at a very low Gd-DTPA concentration, we found out a strong interference on the nanoprecipitation. In order to restore optimized conditions we precisely tune pH values and, at the same time, we use an appropriate surfactant that can regulate the affinity between solvent and non-solvents. In conclusion, results clearly show that the relaxation time for Gd-DTPA entrapped within crosslinked Hyaluronic Acid nanoparticles is shorter than that of the “free” contrast agent. A very small particle size and improved MRI characteristics are obtained, achieving a signal intensity in r_1 several times larger than that of the commercial MRI contrast agent at the common field of clinical MRI.

REFERENCES

[1] P. M. Valencia, O. C. Farokhzad, R. Karnik, and R. Langer, "Microfluidic technologies for accelerating the clinical translation of nanoparticles," *Nature Nanotechnology*, vol. 7, pp. 623-629, Oct 2012.

[2] L. Capretto, W. Cheng, D. Carugo, O. L. Katsamenis, M. Hill, and X. L. Zhang, "Mechanism of co-nanoprecipitation of organic actives and block copolymers in a microfluidic environment," *Nanotechnology*, vol. 23, p. 16, Sep 2012.

[3] R. C. Souza Bicudo and M. H. Andrade Santana, "Production of hyaluronic acid (HA) nanoparticles by a continuous process inside microchannels: Effects of non-solvents, organic phase flow rate, and HA concentration," *Chemical Engineering Science*, vol. 84, pp. 134-141, Dec 24 2012.

[4] P. Caravan, "Strategies for increasing the sensitivity of gadolinium based MRI contrast agents," *Chemical Society Reviews*, vol. 35, pp. 512-523, 2006.

[5] R. Sethi, J. S. Ananta, C. Karmonik, M. Zhong, S. H. Fung, X. Liu, et al., "Enhanced MRI relaxivity of Gd3+-based contrast agents geometrically confined within porous nanoconstructs," *Contrast Media & Molecular Imaging*, vol. 7, pp. 501-508, Nov-Dec 2012.

[6] T. Courant, V. G. Roullin, C. Cadiou, M. Callewaert, M. C. Andry, C. Portefaix, et al., "Hydrogels Incorporating GdDOTA: Towards Highly Efficient Dual T1/T2 MRI Contrast Agents," *Angewandte Chemie-International Edition*, vol. 51, pp. 9119-9122, 2012.

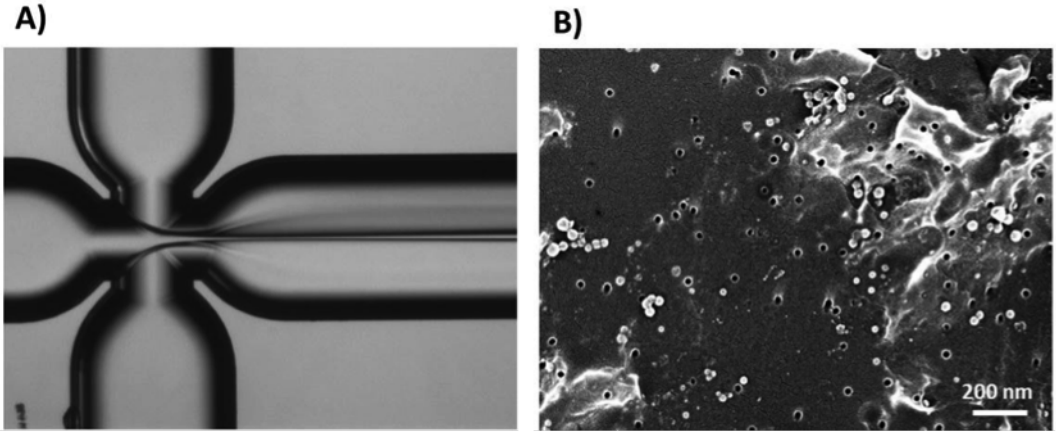

Fig. 1. A) Optical Fluorescence Microscope image of Flow Focusing; B) FE-SEM image of nanoparticles.

Different collagen-based films can differentially influence Schwann cell development in a peripheral nervous tissue regeneration system

E. Storelli[1-2], A. Romano[3], L. Salvatore[1], A. Barca[2], M. Madaghiele[1], A.L. Aloisi[3], T. Verri[2], C. Storelli[2], A. Quattrini[3] and A. Sannino[1]

[1] *Department of Engineering for Innovation, University of Salento, Via per Monteroni, 73100 Lecce, Italy*

[2] *Department of Biological and Environmental Sciences and Technologies, University of Salento, Via per Monteroni, 73100 Lecce, Italy*

[3] *Neuropathology Unit - Institute of Experimental Neurology and Division of Neuroscience - IRCCS San Raffaele Scientific Institute - via Olgettina 60, 20132 - Milan, Italy.*

***Abstract*—Collagen is one of the most used materials in scaffolding production; this is due to its peculiar characteristics that make the polymer highly biocompatible and efficient in regeneration induction and growth cone guidance. We aimed to investigate whether collagen could *per se* induce Schwann cell differentiation/proliferation and how it would do so. Results obtained in immortalized rat Schwann cells showed differential effects on several proliferation and differentiation markers depending on the type of collagen used to produce the scaffolds.**

***Keywords*—Collagen, Schwann cells, differentiation, tissue regeneration.**

I. Introduction

Tissue regeneration has been largely addressed in the last decade, becoming one of the most challenging and interesting research fields thanks to a continuous and stronger merge among different scientific categories such as medicine, biology and engineering. Efforts in this direction led to the production of more and more bioengineered scaffolding materials able to improve the physiological regenerative processes in diverse tissue types such as bone tissue or the peripheral nervous system [1], [2]. Many different kinds of materials (i.e.: synthetic, natural, autologous, composite) have been selected for their ability to support tissue regeneration and/or directional guidance [3], [4]. More recently these materials have been improved and functionalized in several ways (e.g.: filling tubular scaffolds with soluble factors like chemokines or cytokines inserting peptides and/or proteins) to increase the efficiency of the normal reconstructive mechanisms [5], [6].

Among all the materials analysed, collagen has been selected as the best performing one taking into account its high biocompatibility, its physiological adhesive properties as component of the Extracellular Matrix (ECM) and its ability in enhancing axonal regeneration, myelination and vascularisation [7]. To date, most of the work focuses to improve collagen by using molecules that can be inserted in the devices. Nevertheless, very little, is known about the direct influence of collagen-based surfaces on Schwann cells in terms of proliferation, adhesion and differentiation pathways that may be activated by the interaction between collagen and cell membranes.

In this respect, this work aims to understand if and how collagen-Schwann cells interactions may be involved in tissue regeneration and how they could affect Schwann cells proliferation and or differentiation in a 2D collagen scaffolds.

II. Materials and Methods

A. 2D collagen scaffold production

Type I collagen purchased from two different companies has been used for film production: Symatese (S) and Collagen Solution (CS). 3% (S) and 2% (CS) slurries were produced and let them dry at RT for 48 h. The resulting films were DHT and EDAC cross-linked. Successively, discs of 3 cm diameter were cut and sterilized 2h at 160°C for cell culture experiments.

B. Cells culture

RT4D6P2T schwannoma cells (250,000) were cultured directly onto S and CS films until they reach confluence. Control cells were grow directly on the plastic plate.

C. Hematoxylin-Eosin staining

S and CS films cultured with RT4D6P2T cells were fixed 12 h at 4°C in 4% PFA dissolved in PBS, the devices were washed with fresh PBS and stained with hematoxylin/eosin (Sigma Aldrich). Films were then rinsed, dehydrated, mounted with Eukitt (Sigma Aldrich) and examined under a Nikon Eclipse 800 upright light microscope.

D. RNA extraction

Total RNA extraction was performed using TRIzol® reagent (Life Technologies) followed by RNeasy plus mini kit (Qiagen) purification. Briefly, 1mL of TRIzol® was added directly to the cells to allow cell lysis. For RNA extraction 0.2 mL of chloroform was added to the solution. After centrifugation and isolation of the transparent phase the RNA was purified following the protocol of the RNeasy plus kit . The resulting RNA was stored at –20°C.

E. Protein extraction

Proteins were extracted using 1X Laemmli buffer with 200mM β-mercaptoethanol. Briefly, 300µL of this buffer were added to the cells and the resulting solution was collected in tubes that were vortexed and boiled at 100°C for 10'. Protein lysates were stored at -20°C.

F. Real-Time PCR analyses

The RNA was quantified using NanoDrop ND-1000 spectrophotometer (NanoDrop). One microgram of total RNA was retro-transcribed using iScript™ select (BioRad).

iQ™ SYBR® green super mix (BioRad) was used for the Real-Time PCR. : Specific primer pairs for MPZ, KROX20and cJun were used for the reactions. The specific gene expression levels were normalized against GAPDH (Glyceraldehyde 3-phosphate dehydrogenase) housekeeper gene expression levels.

G. Western Blot analyses

Proteins where quantified using the RC DC Assay kit (BioRad), Whole cell proteins (45µg) were separated by SDS-PAGE and transferred onto nitrocellulose membrane. Membranes were incubated with primary antibodies for KROX20 (abcam), MBP (Covance) and the appropriate secondary antibodies (anti-rabbit IgG and anti-mouse IgG; Cell Signaling) Signal detection was performed using ECL plus reagent (Thermo Scientific). Image quantifications were performed using ImageJ software (NIH) and protein levels were normalized against signals obtained using tubulin primary antibodies (Sigma Aldrich; housekeeper protein)..

III. Results and discussion

The results hereby presented indicate that collagen scaffolds and the commercial source of the collagen directly affect the behavior of Schwann cells. Histomorphological analysis of cells grown onto CS films shows that cells were highly proliferating with large network of cell-to-cell contacts (Figure 1). On the other hand, Schwann cells grown onto S scaffolds were poorly proliferating and seemed not to colonize the entire film surface (Figure 1).

Interestingly, Real-time PCR and Western Blotting analyses revealed that only Schwann cells grown on CS scaffolds up-regulate (both at mRNA and protein level) the specific Schwann cell genes KROX20, MPZ and MBP (Figure 2 and Figure 3). In particular, KROX20 (Early growth response protein 2), MBP (Myelin basic protein) and MPZ (Myelin protein zero) are genes expressed in differentiating and myelinating Schwann cells [8]. In this respect, these results suggest that CS films shift Schwann cells towards a differentiated state while S films keep the cells in an undifferentiated stage. Overall, the different behaviour of Schwann cells that we observed on diverse types of collagen may have an important role in the efficient and correct nerve regeneration given that this cells play a pivotal function in the series of events (e.g.: growth cone development, direction, path finding, etc.) occurring after injury and during nerve regeneration [9], [10]. In this context, the development of collagen scaffolds should take into account the effects of materials on Schwann cells to produce devices with higher regeneration efficiency.

IV. Conclusion

This work introduces interesting piece of information on the interactions between material and cell activity. What we discussed in this work makes clear that specific biomaterials may not only give spatial and adhesive cues to cells, but also may give differentiating signals to Schwann cells.

Studies on this research line have to be continued in order to address whether a 3D structure may have or not the same influences on Schwann cells; this being extremely interesting when it comes to the production of 3D cylindrical scaffolds for peripheral nerve regeneration.

References

[1] M. Younesi, V.M. Goldberg and O. Akkus, “A micro-architecturally biomimetic collagen template for mesenchymal condensation based cartilage regeneration”, *Acta Biomaterialia*, vol. 30, pp. 212-221, January 2016

[2] R. Parenteau-Bareil, R. Gauvin and F. Berthod, “Collagen-based biomaterials for tissue engineering applications”, *Materials*, vol. 3, pp. 1863-1887, March 2010

[3] B. Battiston, S. Genua, M. Ferrero and P. Tos, “Nerve repair by means of tubulisation: Literature review and personal clinical experience comparing biological synthetic conduits for sensory nerve repair”, *Microsurgery,* vol. 25, pp. 258-267, June 2005

[4] A.R.Nectow, K.G. Marra and D.L. Kaplan, “Biomaterials for the development of peripheral nerve guidance conduits”, *Tissue Engineering: Part B,* vol. 18-1, pp. 40-50, February 2012

[5] A. Sgambato et al. (2015, Dec.). “Different sialoside epitopes on collagen film surfaces direct mesenchymal stem cell fate”. *ACS Applied Materials and Interfaces.* Available: http://pubs.acs.org/doi/10.1021/acsami.5b08270

[6] C.T. Chalfoun, G.A. Wirth, G.R.D. Evans, “Tissue engineered constructs: where do we stand? ”, *Journal of Cellular and Molecular Medicine,* vol. 10-2, pp. 309-317, May 2006

[7] F. Stang, H. Fansa, G. Wolf and G. Keilhoff, “Collagen nerve conduits – assessment of biocompatibility and axonal regeneration”, *Biomedical Material Engineering*, vol. 15, pp. 3-12, 2005

[8] R. Mirsky et al., “Novel signals controlling embryonic Schwann cell development, myelination and dedifferentiation”, *Journal of the Peripheral Nervous System,* vol. 13, pp. 122-135, June 2008

[9] M.C.O. Rodrigues, A.A. Rodrigues Jr., L.E. Glover, J. Voltarelli and C.V. Borlongan. (2012, Jan.). Peripheral nerve repair with cultured cells: getting closer to the clinics. *The Scientific World Journal*. Volume 2012 (413091), 10 pages. Available: http://www.hindawi.com/journals/tswj/2012/413091/

[10] G.R.D. Evans, “Peripheral nerve injury: a review and approach to tissue engineered constructs”, *The Anatomical Record*, vol. 263-4, pp. 396-404, August 2001

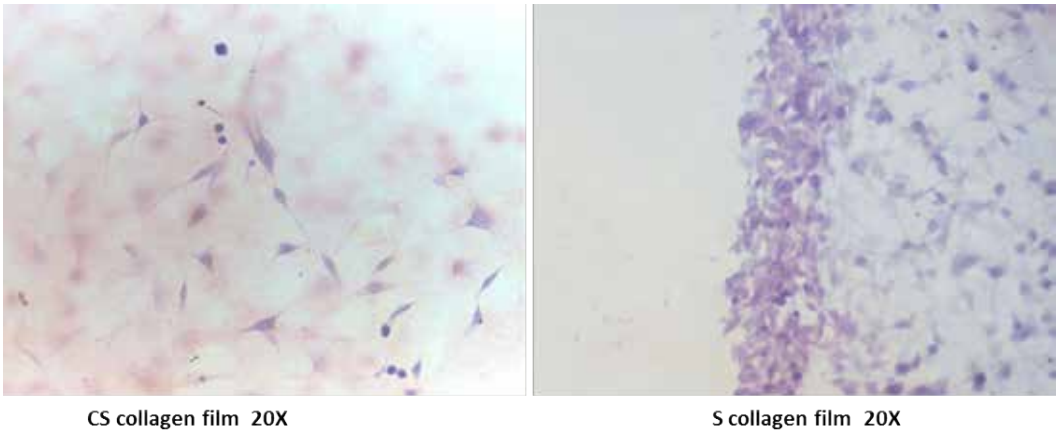

Fig. 1. Hematoxilin and Eosin staining shows different development phenotype of the cells growing either on CS or S

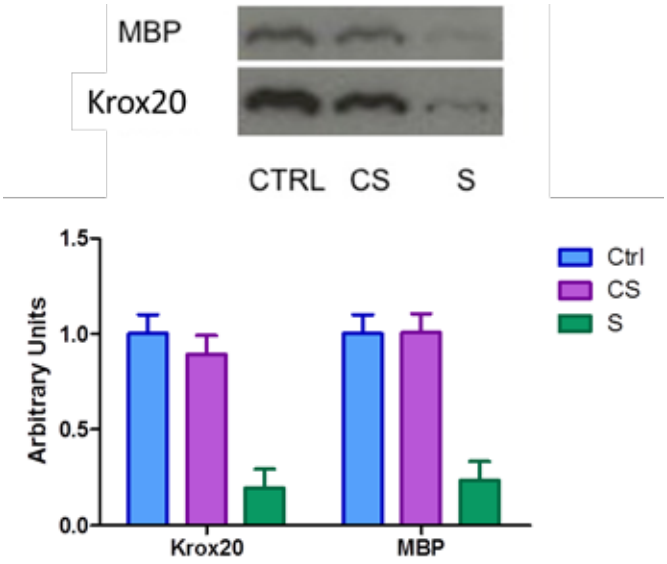

Fig. 2. Western Blot done on MBP and Krox20. The figure shows clearly the differential expression of those two proteins in cells grown on CS or S collagen films.

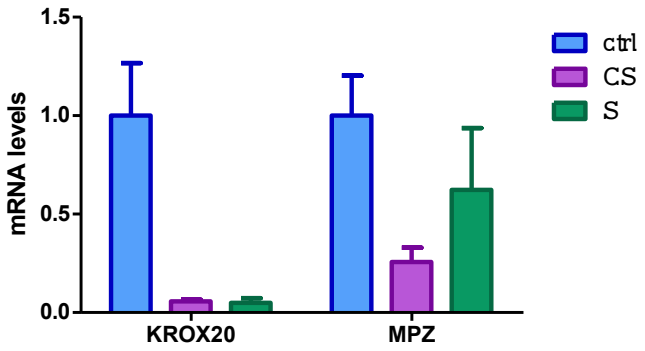

Figura 3: mRNA levels ov Krox20 and MPZ genes in cells grown on CS and S collagen films

Study of Ink-jet Printed Sensors for Monitoring Cell Cultures

S. Tonello[1], N. F. Lopomo[1], M. Serpelloni[1], M. Serzanti[2], P. Dell'Era[2] and E. Sardini[1]
[1] *Department of Information Engineering, University of Brescia, Via Branze, 38 - 25123 Brescia (s.tonello@unibs.it)*
[2] *Department of Molecular and Translational Medicine, University of Brescia, Viale Europa, 11 - 25123 Brescia*

***Abstract* — An extremely promising methodology to obtain feedbacks from cells culture is represented by the direct integration of sensitive elements capable of providing information related to cell adhesion, migration, differentiation and growth. At present, most common materials used in the implementation of sensors dedicated to 2D cell cultures monitoring are noble metals. Printed electronics instead allows an innovative approach, both from the point of view of sensor realization (inkjet printing) and of sensitive materials used. This project aims to develop and test 2D ink-jet printed sensors, focusing on biocompatible substrate and inks. Both biocompatibility and printability of two different sensor designs were in particular evaluated, before performing electronic measurements to evaluate fibroblasts adhesion. Preliminary results showed good biocompatibility of Kapton® and PEDOT:PSS, and the possibility to correlate cell adhesion with an increase of impedance module, in agreement with optical evaluations. On-going works are related to quantitative assessment of the biocompatibility on specific substrates and on the evaluation of stretchable materials aiming to a final application for monitoring cardiomyocytes activity.**

***Keywords* — Electrochemical Cells Impedance Substrate (ECIS), cells monitoring, printed electronics, ink-jet printed sensors.**

I. Introduction

Recently, a growing interest in pharmacology, regenerative medicine, and tissue engineering has been related to the identification of measuring systems and non-invasive methods that can provide real-time quantitative information regarding cell growth and differentiation, thus to obtain a feedback of cell functions and tissue development. An extremely promising methodology is represented by the direct integration into culture plates and scaffolds of sensitive elements capable of providing, information relating to cell growth, migration, differentiation or to record cellular electrical activity. Usually cell-substrate impedance measurements (ECIS) are adopted [1]–[3]. In general, the materials used so far in the realization of this type of sensors are noble metals (i.e. gold or platinum), for both two dimensional (2D) electrodes and sensitive elements (mainly nanoparticles or wires) in three dimensional (3D) environment [4]–[6]. Printed electronics instead allows an innovative approach, in terms of both implementation (inkjet printing) and use of sensitive materials, thus reducing production costs and improving the biocompatibility and the adaptability of these devices to deformable structures [7] .

Concerning 2D sensing applications, a particular interest has regarded the introduction of organic electronics (e.g. PEDOT:PSS, carbon) and of stretchable surfaces to investigate cardiomyocytes and neural cell behavior, innovating traditional technology such as Micro Electrode Arrays (MEAs) [7]–[9]. Similarly, in 3D sensing applications, nanostructured materials (e.g. carbon nanotubes), PEDOT:PSS and conductive materials are emerging as promising techniques to obtain feedbacks from cells mimicking a physiological environment.

The main goal of this study was to realize 2D printed sensors for monitoring cell cultures adhesion and growth, by means of Ink-jet printing technology, with a particular attention to the evaluation of substrate and ink biocompatibility.

II. Materials and Methods

Biocompatibility testing and ink electrical resistance evaluation after immersion in cell culture medium were performed, in order to identify the optimal materials for sensors realization. Different substrates (polyimide (Kapton®), polyethylene terephthalate (PET), PET treated to improve printability (Novele® and Coveme®), thermoplastic polyurethane (TPU from Nagase®) and inks for inkjet printing (PEDOT: PSS, carbon, silver) were considered. After that, ECIS measurements were performed to evaluate the ability to monitor cell adhesion using ECIS.

A. Qualitative Evaluation of citocompatibility

After preparing samples of proper dimensions and printing strips of inks, they were adhered to the bottom of the well with the use of high vacuum grease (Dow Corning), sterilized by exposure to UV rays, and finally seeded with fibroblasts (30000 cells/cm^2). After 24 hours, the samples were observed with an optical microscope to evaluate cell adhesion. Cell viability was evaluated using phase contrast modality. The same protocol was adopted after printing the complete sensors, before performing the electronics measurements, to evaluate cell adhesion and be able to compare results from the optical analysis with the ones from ECIS.

B. Quantitative evaluation of citocompatibility

Cell adhesion quantification was performed using a specific dye, Neutral Red, able to stain lysosomes red. More specifically, since live cells incorporate neutral red into their lysosomes, loss of neutral red uptake corresponds to loss of cell viability. In details, culture medium of the cultured samples was replaced with a Neutral Red solution and the samples were incubated at 37 ° C with controlled humidity and 5% CO2. Once washed, samples were immersed in a de-staining solution, under stirring, and then the absorbance of the solution was quantified using a spectrophotometer.

Quantification of cells adherent on each substrate was calculated referring to a calibration curve that was obtained by incubating a specific number of cells in the same assay. As blank samples, a set of substrates without any cells seeded

was used to assess the amount of absorbance due to dye absorption and thus released from the material itself.

C. Design and production of sensors and measuring system

Two different designs of the sensors were evaluated: a monopolar and an interdigitated configuration. The geometry was printed using a home ink-jet printer (Epson XP 225) and the following combinations: PEDOT: PSS on Kapton® and on PET substrates, silver on treated PET (Novele®). Before proceeding with the printing process, Kapton® and untreated PET underwent specific plasma treatment to increase surface hydrophilicity and facilitate ink absorption. In order to perform ECIS measurements, two thin copper wires were soldered on working and counter electrodes. After that, sensors were glued to the bottom of Petri dishes using the adhesive biocompatible high vacuum grease, sterilized under UV radiation and finally seeded with fibroblasts (30000 cells/ cm2). After 24 hours, cell adhesion and viability was qualitatively assessed using optical microscope in traditional and phase contrast modality.

D. Impedance Measurements

Impedance measurements were carried out using a standardized protocol before and after seeding fibroblasts on sensors, in order to correlate variations in the electrical quantities with cell cycle events (adhesion, cell growth and differentiation). Control tests were performed before cell seeding for all the samples, to evaluate impedance due to cell culture medium. Duplicate measurements for each sensor were performed by using the impedance analyzer HP4194A recording impedance magnitude and phase, in a frequency range between 200 Hz and 2 MHz.

III. RESULTS

A. Qualitative Evaluation of citocompatibility

Regarding substrate biocompatibility, Polymide (Kapton®) appeared to be the most compatible one: cells appeared to be well adherent and uniformly distributed on its surface both on the printed PEDOT:PSS and on the other areas of the sensors. On the contrary, PET substrates showed a poorer biocompatibility: interestingly, on untreated PET, where PEDOT:PSS was printed on, cells tended to migrate on the PEDOT:PSS pattern, showing no adhesion on the rest of the sensor. Novele® showed a poor cell adhesion, although plasma treatments and gelatin coatings appeared to partially improve it (Fig. 2). Among the inks, PEDOT:PSS and carbon showed a good biocompatibility with well adherent and uniformly distributed cells. Silver showed less biocompatibility in some of the sample, solved by increasing curing time to allow complete solvent evaporation.

B. Quantitative evaluation of citocompatibility

Preliminary results obtained evaluating Kapton® and PET substrates confirmed the results obtained from the qualitative assessment using optical microscopy (Fig.1). After the staining with Neutral Red, the number of cells attached on Kapton® substrate appeared to be significantly higher than the one attached on PET substrates, in agreement with what shown from optical images. On-going studies are related to the quantitative assessment of biocompatibility of all the materials described.

C. Impedance Measurements

ECIS measurements showed results in accordance to what could be observed from the optical analysis, suggesting the possibility to use this technique to assess cell adhesion and growth (Fig. 3). In particular, measurements performed on sensors realized using Kapton® and PET after cell seeding recorded an increase of impedance module in the order of a few hundred ohms compared to measurements taken with only culture medium. On the contrary, ECIS measurements performed on Novele® substrates, where the optical analysis identified a poorer cell adhesion, showed no significant changes comparing impedance before and after cell seeding.

IV. CONCLUSIONS AND FUTURE OUTLOOKS

Results obtained from qualitative and quantitative evaluation of cell adhesion suggested the possibility to pursue in the investigation of the described materials and technology.

On-going work refers to the quantification of cell adhesion using the protocol described for all the set of combination of the substrates and inks described. Once confirmed the ability of impedance measurements to assess cell adhesion through the ECIS measurements described, subsequent activities will concern the evaluation of the differences between impedance in the course of cell growth, with the objective of correlating changes in impedance to specific events of the cell cycle. Stretchable materials in particular will be evaluated, aiming to a final application for monitoring cardiomyocyte activity under mechanical conditioning. Further research interests for future development may focus on the integration of sensing elements in 3D scaffolds, in order to monitor cell functions in an environment more similar to physiological conditions.

REFERENCES

[1] S. Ramasamy, D. Bennet, and S. Kim, “Drug and bioactive molecule screening based on a bioelectrical impedance cell culture platform,” *Int. J. Nanomedicine*, vol. 9, pp. 5789–5809, Dec. 2014.

[2] S. Reitinger et al.,, “Electric impedance sensing in cell-substrates for rapid and selective multipotential differentiation capacity monitoring of human mesenchymal stem cells,” *Biosens. Bioelectron.*, vol. 34, no. 1, pp. 63–69, 2012.

[3] P. O. Bagnaninchi and N. Drummond, “Real-time label-free monitoring of adipose-derived stem cell differentiation with electric cell-substrate impedance sensing.,” *Proc. Natl. Acad. Sci. U. S. A.*, vol. 108, no. 16, pp. 6462–6467, 2011.

[4] C. K. Yeung et al., “Drug profiling using planar microelectrode arrays,” *Anal. Bioanal. Chem.*, vol. 387, pp. 2673–2680, 2007.

[5] M. E. A. Powerhouse, “Microelectrode arrays for extracellular electrophysiology.”

[6] Y. Nam and B. C. Wheeler, “In vitro microelectrode array technology and neural recordings.,” *Crit. Rev. Biomed. Eng.*, vol. 39, no. 1, pp. 45–61, 2011.

[7] A. Blau et al., “Flexible, all-polymer microelectrode arrays for the capture of cardiac and neuronal signals,” *Biomaterials*, vol. 32, no. 7, pp. 1778–1786, 2011.

[8] S. P. Lacour et al., “Flexible and stretchable micro-electrodes for in vitro and in vivo neural interfaces,” *Med. Biol. Eng. Comput.*, vol. 48, pp. 945–954, 2010.

[9] Y. Furukawa et al., “Monitoring neural stem cell differentiation using PEDOT-PSS based MEA,” *Biochim. Biophys. Acta - Gen. Subj.*, vol. 1830, no. 9, pp. 4329–4333, 2013.

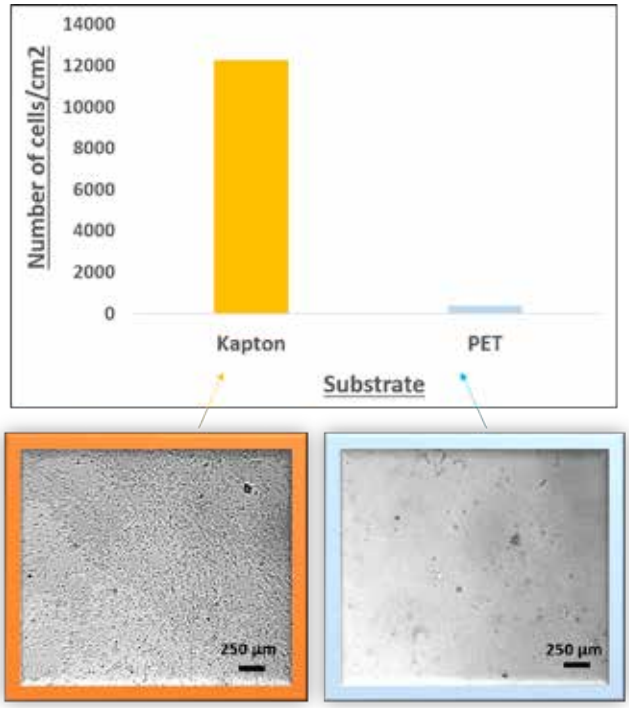

Fig. 1. Quantification of cell adhesion on Kapton® and PET

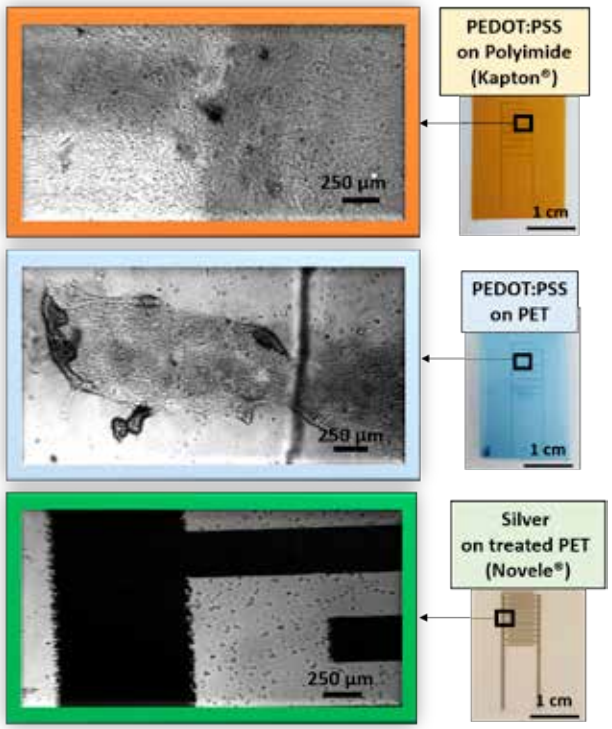

Fig. 2. Optical evaluation of cell adhesion on printed sensors, with different inks and substrates.

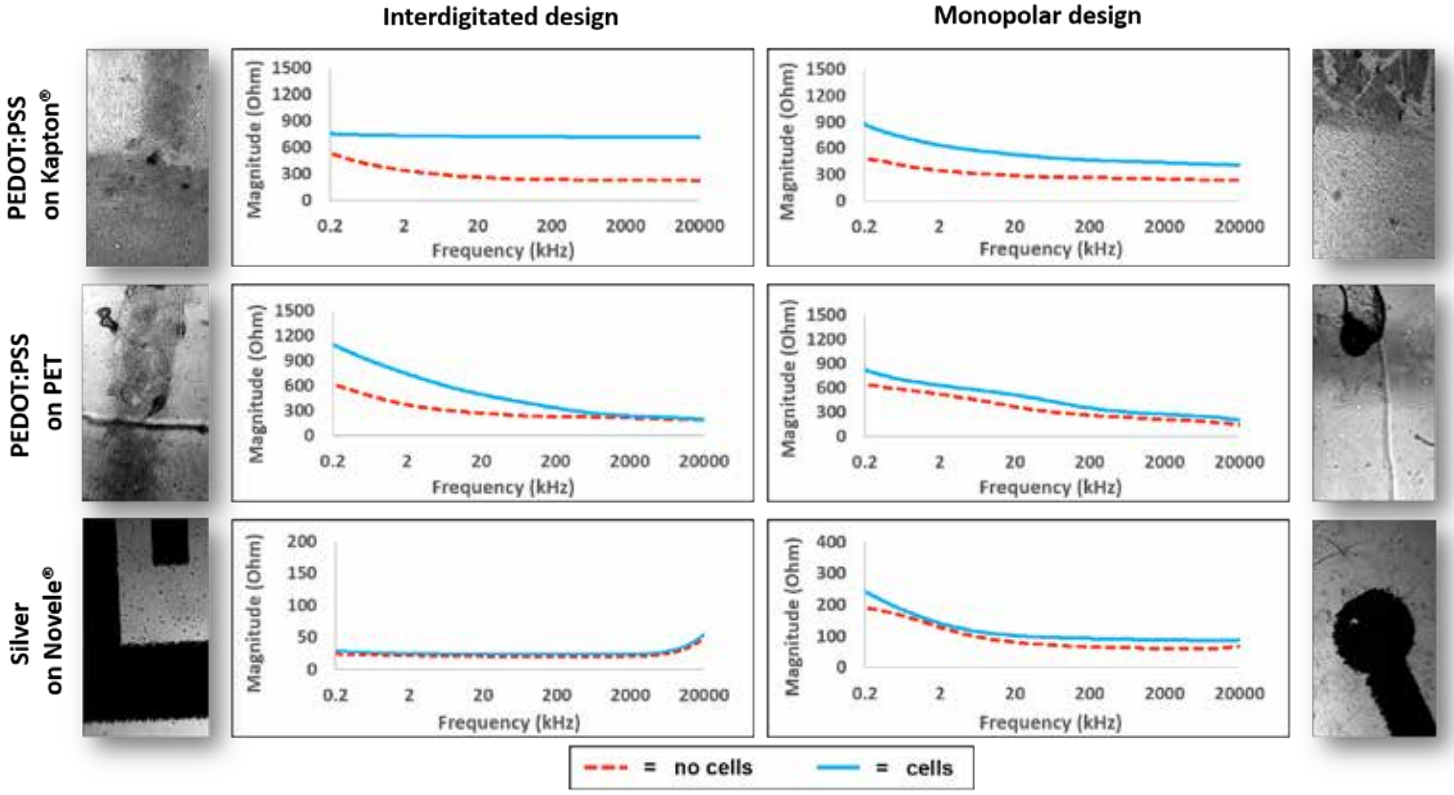

Fig. 3. Module acquired during cell-substrate impedance (ECIS) measurements performed using both sensors designs for all the materials combinations (PEDOT:PSS on Kapton®, PEDOT:PSS on PET, Silver on Novele®)

Core-Shell Nanoparticles obtained by complex coacervation for multimodal applications.

Donatella Vecchione[1,3], Paolo Antonio Netti[1,2,3], Enza Torino[1,2]
[1] *Istituto Italiano di Tecnologia, Center for Advanced Biomaterials for Health Care IIT@CRIB, 80125, Naples, Italy.*
[2] *University of Naples Federico II, Interdisciplinary Research Center of Biomaterials, CRIB, 80125, Naples, Italy.*
[3] *University of Naples Federico II, Department of Chemical, Materials and Industrial Production Engineering, 80125, Naples, Italy.*

***Abstract*— An early and effective diagnosis can increase even chances of survival that ensuring patients receive the most appropriate treatment. Nowadays diagnostic technologies could have a huge impact in the diagnosis and, therefore, in the clinical management of the pathologies at the early stages. In this context, the integrated PET/MRI plays a key role using sequentially acquired data that allows both spatial and temporal correlation of the signals. The aim of this work is the production of core-shell polymeric nanoparticles obtained by a complex coacervation method for dual imaging applications. An accurate control of the coacervation steps is realized by modulating the different process parameters, allowing the formation of a nanoparticles (NPs) that provide both MRI and PET modalities and, at the same time, reduce side effects and improve strongly the quality of the obtained images. The obtained chitosan/hyaluronic acid nanostructures are stabilized by a crosslinking able to retain active compounds. The impact of the hydrophilic properties of the hydrogel matrix on the enhancement of the relaxivity of the Gd-DTPA is evaluated, while sorption of a radiopharmaceutical substance into the polymeric matrix is discussed in terms of concentration of the radiotracers.**

***Keywords*— Coacervation, Core-shell Nanoparticles, Multimodal imaging, Enhancement.**

I. Introduction

Multimodality imaging allows integration of the strengths of individual modalities, while overcoming their limitations. Anatomical imaging technologies, such as MRI, provide unparalleled structural detail; whereas functional modalities such as positron emission tomography (PET) provide insight into morphological and functional behaviors [1],[2]. By incorporating anatomical and functional imaging in a common hybrid imaging platform, a synergism in the imaging capabilities can be achieved, thus making it possible to precisely visualize and delineate structural and functional information [2]. Integrated PET/MRI allows for both spatial and temporal correlation of the signals, differently from using sequentially acquired data [3]. Moreover, the simultaneous acquisition is able to improve the performance and information content of one instrument using the information obtained from the other instrument: the accuracy of the PET estimates might be improved by including the MRI information as the structural framework underlying the distribution of the PET signal. Reciprocally, the strength of PET to provide absolute quantitative information might help validate several MRI techniques in vivo [4],[5]. It is important to consider the acquisition times in relation to the bioaccumulation of the contrast agent for MRI and to the half-life of the radiotracers [6],[7]. Nowadays, many efforts are made in the development of integrated PET/MRI instrumentation but still no probe that allows a simultaneous acquisition of the two signals is available today. The introduction of nanotechnology has led to the development of many medical applications including the formulation of new probes that can be used for multimodal applications [8]. The aim of this work is to obtain stable nanoparticles with a fast process easy to translate into an industrial one thanks to the control of some parameters as concentration of the two polymers, the percentage of surfactants, the pH, the temperature and the duration of the different phases of the production process [9]. The nanoparticles can be encapsulated with contrast agents, fluorophores for optical imaging and radiopharmacautical substances [8]-[10].

II. Materials and Methods

A. Materials

Chitosan (Ch) low molecular weight; Sodium Tripolyphosphate (TPP) 367.86 g/mol; Glacial Acetic Acid molecular weight 60.05; Ethanol (EtOH) molecular weight 46.07; Gd-DTPA molecular weight 547.57; Mineral Oil 0.84 g/mL at 25°C (lit.); Span80 molecular weight 274.43; 1.005 g/mL at 20 C (lit.) are purchased by Sigma-Aldrich® while Hyaluronic Acid (HA) 850 kDa parenteral grade is by Hyasis®. MilliQ water is for all experiments.

B. Method of Nanoparticles Production

A Complex Emulsion-Coacervation is used for the production of polymeric core-shell nanostructures for diagnostic applications. The first step consists in the preparation of a w/o emulsion used as a template. Then, the solution containing HA as the coacervate polymer is added dropwise into the emulsion previously prepared.In different formulations, the Contrast Agent, is added alternatively to the primary and secondary emulsion at various concentrations. The coacervant phase is added dropwise to the w/o emulsion template and homogenized controlling pH and the temperature values continuously. After the coacervant phase is added to the primary emulsion, coacervation step starts as soon as HA reachs the surface of the droplet containing the chitosan solution. The reaction is stirred until a phase separation occurs.

C. Characterization

In order to characterize morphologically and chemically the system, a field emission scanning electron microscope (Fe-SEM)by Zeiss®, Transmission Electron Microscope (TEM) by FEI® in DRY, CRYO and Tomography (TOMO) modes and IR spectroscopy Thermo® are used. The SEM

characterizations are made to control the integrity of the nanostructures after ultracentrifugation and after the dialysis. Indeed, after 48 h of stirring, 200µl of the reaction are collected and diluted in EtOH, then filtered through an ISOPORE filter membrane. The TEM analyses are conducted both in DRY, CRYO and Tomography (TOMO) modes. In DRY mode the samples are prepared using Formvar/Carbon 200 mesh Cu Agar® depositing 20µl of the suspended nanoparticles. In CRYO mode the samples are prepared using VITROBOT FEI® coating Lacey Carbon film 200 mesh Cu Agar® with 3µl of nanoparticles suspension. To investigate the linkage formation between Ch, TPP and HA in the nanoparticles formation process, FT-IR studies are conducted. Experiments by Minispec 60mq are made with glass tube on nanoparticles suspension. Free Induction Decay sequence (FID) is used to evaluate the best value of the Gain to control the saturation of the signal and measure T_2*; Saturation Recovery (SR) and Inversion Recovery (IR) sequences are used to measure T_1 instead Carr Purcell sequence (CPC) to evaluate T_2. Concentrations of Gd-DTPA in the different nanostructures are evaluated by ICP-MS Agilent® to gain information about the loading capability of the produced nanocapsules. Mass spectrometry (Agilent Technologies 6530 Accurate-Mass Q-TOF LC/MS) method is dedicated to the analysis of radiopharmaceutic agent decay.

III. Results

The described process has led to the generation of nanoparticles with a chitosan core and an outer shell of hyaluronic acid. In the following image there is a physical characterization of produced nanoparticles by SEM imaging Fig. 1. The study of emulsion-coacervation system is made on a ternary diagram. The ternary diagram obtained is built analysing the behaviour of the polymer (Chitosan) at different concentration of the acetic acid solution. The Ch is not soluble in water so between these two elements there is a gap of miscibility. Adding the acetic acid dropwise, the gap between them decreases allowing the dissolution of the Ch. The use of the temperature allows a time reduction of the reaction. The innovation of this system consists in a double crosslinking that allows to control the stability and the degradation behavior of the two chosen polymers. The results show a reduction of the relaxation times and so an enhancement of MRI signal of several times respect to the signal obtained with the use of commercial Gd-DTPA . Additionally, a radiopharmaceutical agent decay sorption is reported preserving the core shell morphology. The NPs at increasing concentrations are tested in vitro and vivo on different type of cells and on C57/BALB mice to investigate the variation of the toxicity at short and long term biodistribution. Toxic effects at short and long period are not observed. The biodistribution analysis are made at different time points.

References

[1] C. Catana, A. Drzezga, W.-D. Heiss, and B. R. Rosen, "PET/MRI for Neurologic Applications," Journal of Nuclear Medicine, vol. 53, pp. 1916-1925, Dec 2012.

[2] T. E. Yankeelov, T. E. Peterson, R. G. Abramson, D. Garcia-Izquierdo, L. R. Arlinghaus, X. Li, et al., "Simultaneous PET-MRI m oncology: a solution looking for a problem?," Magnetic Resonance Imaging, vol. 30, pp. 1342-1356, Nov 2012.

[3] A. Drzezga, M. Souvatzoglou, M. Eiber, A. J. Beer, S. Fuerst, A. Martinez-Moeller, et al., "First Clinical Experience with Integrated Whole-Body PET/MR: Comparison to PET/CT in Patients with Oncologic Diagnoses," Journal of Nuclear Medicine, vol. 53, pp. 845-855, Jun 2012.

[4] S. M. Larson and L. H. Schwartz, "F-18-FDG PET as a candidate for "Qualified Biomarker": Functional assessment of treatment response in oncology," Journal of Nuclear Medicine, vol. 47, pp. 901-903, Jun 2006.

[5] L. Mosconi, W. H. Tsui, A. Pupi, S. De Santi, A. Drzezga, S. Minoshima, et al., "F-18-FDG PET database of longitudinally confirmed healthy elderly individuals improves detection of mild cognitive impairment and Alzheimer's disease," Journal of Nuclear Medicine, vol. 48, pp. 1129-1134, Jul 2007.

[6] F. F. Guglielmo, D. G. Mitchell, and S. Gupta, "Gadolinium Contrast Agent Selection and Optimal Use for Body MR Imaging," Radiologic Clinics of North America, vol. 52, pp. 637-+, Jul 2014.

[7] P. Caravan, "Strategies for increasing the sensitivity of gadolinium based MRI contrast agents," Chemical Society Reviews, vol. 35, pp. 512-523, 2006 2006.

[8] D. Wang, F. Wang, K. Gao, J. Ren, T. Li, and X. Zhao, "Control of Surface and Interface of Microencapsulated Electronic Inks by Complex Coacervation," Fine Chemicals, vol. 29, pp. 443-446,452, 2012 2012.

[9] F. Liu, L. Liu, X. Li, and Q. Zhang, "Preparation of chitosan-hyaluronate double-walled microspheres by emulsification-coacervation method," Journal of Materials Science-Materials in Medicine, vol. 18, pp. 2215-2224, Nov 2007.

[10] M. Kaloti and H. B. Bohidar, "Kinetics of coacervation transition versus nanoparticle formation in chitosan-sodium tripolyphosphate solutions," Colloids and Surfaces B-Biointerfaces, vol. 81, pp. 165-173, Nov 1 2010.

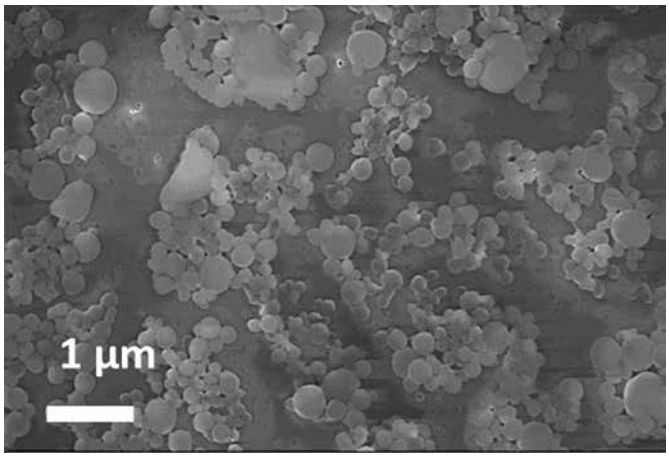

Fig. 1 – Physical characterization of produced nanoparticles by SEM imaging.

Elastic properties of Glass-Ceramic scaffolds through nanoindentation tests and microCT-based finite element models

P. Vena[1], D. Gastaldi[1], C. Vitale Brovarone[2], F. Baino[2]
[1] *Dept. of Chemistry Materials and Chemical Engineering G. Natta, Politecnico di Milano*
[2] *Institute of Materials Physics and Engineering, Department of Applied Science and Technology, Politecnico di Torino*

***Abstract*—**
In this work glass-ceramic scaffolds designed as bone tissue models are investigated through nanomechanical indentation tests; furthermore, the macroscopic elastic properties are obtained through micro Computer Tomography (micro-CT) scans and finite element models. The nanoindentation tests provided the mechanical properties of the solid walls; the computational analyses have determined the quantitative relationship between the macroscopic elastic modulus and the morphological parameters like scaffold porosity and wall thickness.

***Keywords*—Glass-ceramic scaffolds, micro-CT, finite elements, nanoindentation.**

I. Introduction

In this work 3-D bioceramic sintered scaffolds fabricated from the SiO_2-based glass formulation CEL2 are characterized. This material is particularly attractive for bone tissue engineering applications as well as for potential candidates as tissue models able to mimic healthy and diseased tissues.

The fabrication method (sponge replication) is able to produce highly-interconnected 3-D network of open macropores [1] and trabecular structures characterized by micro and nanopores. These peculiar features at different length scales substantially affect the mechanical properties of the scaffold.

The aim of this study is to establish a quantitative relationship between the mechanical properties of glass-ceramic scaffold and the nano and micro-scale properties of the constituent material with specific reference to the material stiffness. This aim is achieved through an experimental and analytical approach to the mechanical characterization of the scaffolds carried out at multiple characteristic lengths. A nanoindentation study carried out at multiple penetration depth (indentation load) is integrated with analytical homogenization models and voxel-specific micro-CT data on 3-D porous scaffolds.

Furthermore, elastic moduli of glass-ceramic scaffolds are estimated by means of finite element analyses of three-dimensional models based on micro-CT scans. The specific purpose is to determine the quantitative relationship between the morphological properties of the obtained scaffolds. More specifically the relationship between the elastic properties of the scaffolds and morphological features like macroscopic porosity and trabecular thickness are sought.

II. Methods

A. Scaffold preparation and nanoindentation tests

The scaffold samples were obtained through the sponge replica process which was shown to be very effective to obtain porous ceramics with a highly-interconnected 3-D network of open macropores; the full description of the method is reported in [2] and [3].

Three bulk samples and four porous samples were subjected to nanoindentation tests; these were performed on Nanotest Platform 3 (MicroMaterials®) at controlled temperature of 28° C using a Berkovich diamond indenter. Load-controlled indentation tests were performed at 1, 50, 100 and 200 mN maximum load. Multiload indentations at low load level were also performed with the purpose to determine the elastic properties of the full dense material.

B. Micro-CT data analysis and Finite Element modeling

The three dimensional microstructure of the scaffold was quantitatively investigated through micro-Computer Tomography (micro-CT) by using a high resolution in vitro scanner Sky-Scan1174 (Micro Photonics Inc.). Acquisition parameters for the micro-CT imaging are reported elsewhere [1-2]. The resulting pixel size is 6.5 micron. The 16bit acquired images were treated by means of a custom made analysis code in MATLAB coding environment (R2015b). All images in the stack were transformed into 8bit images with 255 grey levels. The images where then treated with a thresholding algorithm as described in [3] and a black and white stack of images is eventually obtained. Approximately about 700 slices in the stack where available for each sample and each image size was 685x730 pixels. Micro-CT data were used to assess microporosity of the whole scaffold, nanoporosity of the wall and the average wall thickness. The wall thickness was obtained as average values of the mean intercept length along the three Cartesian directions. Microporosity was used to determine the correlation with the macroscopic stiffness.

The stiffness of the scaffold was estimated my means of finite element models of the three-dimensional microstructure of the scaffold walls. Cubic Representative Volume Elements were identified with size ranging between 150x150x150 pixels and 250x250x250 pixels. A voxel-type finite element

mesh was created in which each pixel represents one single cubic three-linear finite element. The selected size is a compromise between the computational costs and the representativity of the selected volume. A total amount of 21 finite element models has been obtained, which were considered a sufficient population to obtain a meaningful mechanical characterization.

The material of the solid walls was modelled as a linear elastic isotropic material having Young modulus as obtained through the nanoindentation technique above mentioned.

The macroscopic elastic properties of the scaffolds are estimated through the well known homogenization computational method. Briefly, each three dimensional model was analysed by applying six sets of boundary conditions each representing the six unit strain modes. Macroscopic stress components were determined as a volume average of the microscopic (local) stress and the full elastic tensor was determined as stress averages per unit strain [4].

III. Results

Figure 1 shows that the indentation modulus decreases with the penetration depth. The maximum modulus found at shallow indentations is consistent with that found on bulk ideally pore-less samples (data not shown). The indentation modulus found at 200 mN is consistent with the elastic properties of a nanoporous glass-ceramic. The walls of the porous scaffold exhibit an elastic modulus of approximately 62GPa which much lower than the 100 GPa found for the full dense material. Figure 2 (left) Shows a representative image of the porous scaffold. The right panel show a representative Finite Element grid used to estimate the macroscopic elastic modulus of the scaffold.

Figure 3. Shows the estimated average modulus of the scaffold as obtained through the homogenization approach (black bullets) versus the macroscopic porosity of 21 scaffold models. The red bullets represent the average wall thickness.

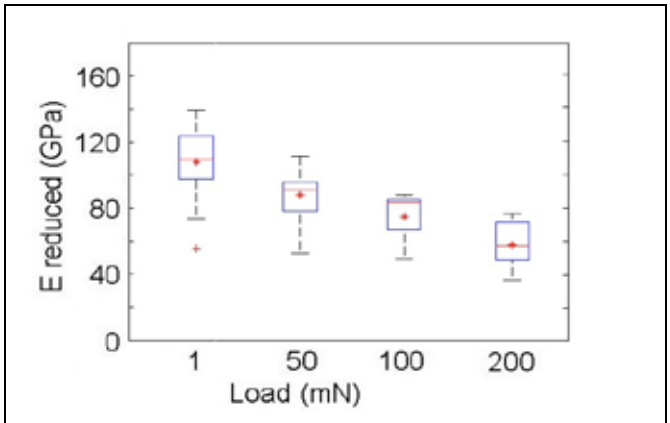

Fig. 1. Indentation modulus versus indentation load Box plots represent 95 percentile and 5 percentile of all experimental measures. Top and bottom whiskers represent the extreme measured values. Outliers are reported with cross symbols.

IV. Conclusion

Bone-like glass-ceramic scaffolds with multiscale porosity have been produced by the sponge replica method. Mechanical properties of the scaffolds at the scale of the single strut have been assessed in this work by means of a nanoindentation study. The experiments have proven that the elastic modulus of the scaffold walls is lower than that of the bulk material. Micro-porosity resulting from SEM and micro-CT investigation on the porous scaffolds explains the elastic mismatch with the bulk material which does not exhibit micro- or nano-porosity. Finite element models have shown a correlation of the scaffold stiffness with both the macroporosity as well as with the wall thickness. The results indicate that the manufacturing procedure is able to provide porous scaffold with the desired mechanical properties.

Acknowledgement

The research leading to these results has received funding from the Italian Ministry of University and Research (MIUR) in the frame of the PRIN project "Engineering physiologically and pathologically relevant organ Models for the INvestigation of age related Diseases" (MIND).

References

[1] C. Vitale-Brovarone, F. Baino, and E. Verné, "High strength bioactive glass-ceramic scaffolds for bone regeneration", in *J Mater Sci Mater Med*, 20, 2009, pp. 643-653.

[2] F. Baino, S. Caddeo, G. Novajra, C. Vitale-Brovarone, "Using porous bio-ceramic scaffolds to model healthy and osteoporotic bone", in *Journal of the European Ceramic Society* in press, 2016.

[3] M. Shahgholi, S. Oliviero, F. Baino, C. Vitale-Brovarone, D. Gastaldi, P. Vena, "Mechanical characterization of glass-ceramic scaffolds at multiple characteristic lengths through nanoindentation", in *Journal of the European Ceramic Society* in press, 2016.

[4] S. J. Hollister, N. Kikuchi, "A comparison of homogenization and standard mechanics analyses for periodic porous composites" in *Computational Mechanics* vol. 10, 1992,pp. 73-95.

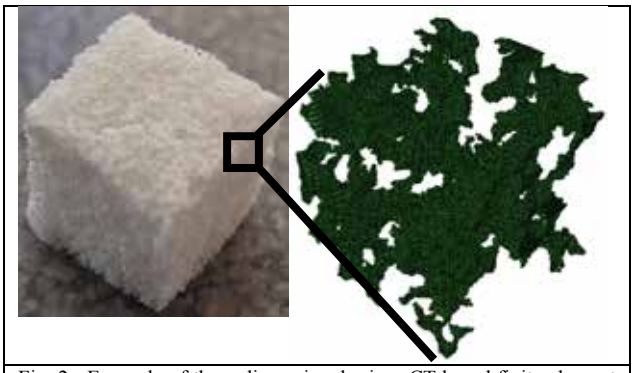

Fig. 2 Example of three dimensional micro-CT based finite element mesh with voxel elements.

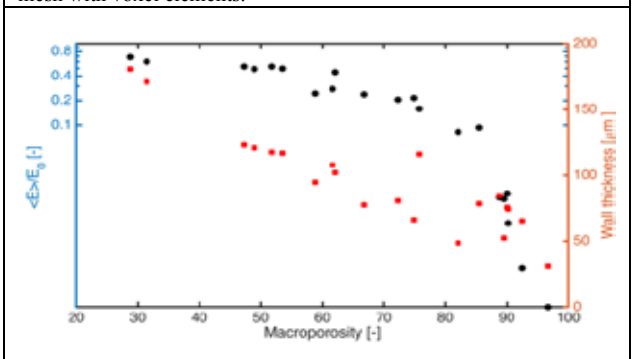

Fig. 3. Normalized elastic modulus (black bullets) and wall thickness (red bullets) vs macroporosity

Affecting Stem Cell Nuclear Stiffness with Nanopatterned Substrates

M. Ventre[1,2], A. Panico[1,2] and P.A. Netti[1,2]
[1]Center for Advanced Biomaterials for Health Care IIT@CRIB, L.go Barsanti e Matteucci 53, 80125 NA, IT.
[2] Department of Chemical, Materials and Industrial Engineering, University Federico II, P.le Tecchio 80, 80125 NA, IT.

***Abstract*—Biophysical signals in the form of topographic patterns, are known to influence cell fate and functions. Topography affects focal adhesion formation, shape and maturation, which in turn regulate the assembly of cytoskeletal structures. These dictate the mechanical properties of the cell and of the nucleus owing to a direct link between actin fibres and the nuclear envelope. Thus, patterning of adhesive sites can have profound effects on cell behaviour up to the nuclear mechanics. The aim of this work is to investigate how topographic features combined with substrate adhesivity alter the mechanical properties of stem cell nuclear region.**

***Keywords*—Nanopatterns, Nuclear Stiffness, Cytoskeleton, Cell Adhesion**

I. Introduction

Biophysical signals are known to influence cell fate and functions [1]. In particular, topographic signals dramatically affect growth and spatial positioning of focal adhesions (FAs) [2]. These not only cause FAs and actin fibres to follow the pattern contours, a phenomenon usually referred to as 'contact guidance', but also affect the structural assembly of the cytoskeleton. Adhesion conformation and contractility are known to affect stem cell lineage specification [3]-[4]. Additionally, the nuclear envelope is directly connected to the cytoskeleton through specific linker proteins [5]. Therefore, an active stress transfer exists between the nucleus and the cytoskeleton, which might eventually induce chromatin reconfiguration and possibly gene transcription [6]. Hence different topographic patterns may in principle affect contractile states of the cytoskeleton and shape of the nucleus, which both can eventually dictate cell's fate and functions. This notwithstanding, how topographic patterns alter cytoskeletal assemblies and contractility, i.e. cell mechanics, and nuclear shape is still unclear.

II. Materials and Methods

A. Sample preparation

Patterned substrates were obtained by replica moulding of Polydimethylsiloxane (PDMS, Sylgard 184) on a Polycarbonate master. Substrates were characterized by an array of parallel channels 700 nm wide and 250 nm deep. Pattern periodicity was 1.4 μm. Flat PDMS were used as control. Both types of substrates were treated with oxygen plasma and then incubated with serum (FBS, 10%) or fibronectin (FN, 10 ug/ml).

B. Cell culture and immunofluorescence

Human Mesenchymal Stem Cells (hMSCs) were cultured on the nanopatterned surfaces and flat surfaces for 48h. Immunofluorescence staining was carried out with TRITC-phalloidin (red) to stain actin bundles, FAs were recognized by incubating samples with anti-vinculin monoclonal antibody (green) and nuclei are stained with sytox (blue).

Nuclear lamins were quantified by immunofluorescence by integrating the fluorescence signal acquired in confocal mode over the nuclear volume.

C. Mechanical characterization

Mechanical properties were calculated using the CellHesion Atomic Force Microscope (AFM). A PNP-DB cantilever with a pyramidal tip was used to indent the cell surface. An upper threshold of 1.2 nN was used to indent cells. Measurements were performed on 30um x 30um square binned in a 16 x 16 map (Fig. 1).

III. Results and Discussion

A. References

Our analysis showed relevant structural and mechanical heterogeneities of the cell body and in this context both topography and substrate adhesivity played a crucial role. More specifically, cells displayed an elongated morphology and were aligned along the pattern direction. Cell cultivated on FN treated surfaces, although elongated, were larger with respect to those observed on FBS treated surface, with well-developed stress fibres on both sides of the cell. Conversely, cells cultivated on FBS treated surface had a markedly spindle-like shape (Fig. 2). On flat surfaces, cells displayed an irregular morphology. Such peculiar assemblies of stress fibres presumably induced different compressive stresses on the nuclear envelope inducing alteration of the nuclear A/R and volume. Indeed, we found higher values of A/R and smaller nuclear volumes on FBS treated substrates with respect to what measured on the other surfaces.

We then asked whether these morphological differences could reflect differences in the mechanical properties of the nuclear region. AFM measurements of the stiffness of the nuclear region revealed a positive correlation between the elastic modulus and the nucleus aspect ratio (Fig. 3a) whereas a negative correlation was found between the modulus and the nuclear volume (Fig. 3b). Additionally,

we observed a marked negative correlation between Lamins A/C content and nuclear volume (Fig. 3c), which resulted in a positive dependence of the nuclear modulus the lamins content (Fig. 3d).

IV. Conclusion

Our data demonstrate that the spontaneous elongation of cells, driven by substrate nanopatterning and its biochemical functionalization, alters not only hMSC cytoskeletal arrangement but also the nucleoskeleton, nuclear shape and possibly its mechanical properties. Our results pave the way for capturing designing concept to fabricate novel patterned platforms that effectively alters nuclear mechanics and possibly cell fate by tuning the material-cytoskeleton-nucleus crosstalk.

Acknowledgement

The authors thank Dr. Maria Iannone for the precious help during stem cell culture and Dr. Carlo Natale for his assistance for the immunofluorescence staining.

References

[1] M. Ventre, P.A. Netti, "Engineering Cell Instructive Materials To Control Cell Fate and Functions through Material Cues and Surface Patterning", *ACS Appl. Mater. Interfaces*. 2016. Available: http://pubs.acs.org/doi/10.1021/acsami.5b08658

[2] M. Ventre, P.A. Netti, "Controlling Cell Functions and Fate with Surfaces and Hydrogels: The Role of Material Features in Cell Adhesion and Signal Transduction", *Gels* Vol. 2, pp. 12, March 2016.

[3] R. McBeath, D.M. Pirone, C.M. Nelson, K. Bhadriraju, C.S. Chen, "Cell shape, cytoskeletal tension, and RhoA regulate stem cell lineage commitment", *Dev. Cell*. Vol. 6, pp. 483-495, April 2004.

[4] L.E. McNamara, R.J. McMurray, M.J. Biggs, F. Kantawong, R.O. Oreffo, M.J. Dalby, "Nanotopographical control of stem cell differentiation", *J. Tissue. Eng.* Vol. 2010, August 2010.

[5] K.N. Dahl, A.J. Ribeiro, J. Lammerding, "Nuclear shape, mechanics, and mechanotransduction." *Circ. Res*. Vol. 102, pp. 1307-1318, June 2008.

[6] J. Beyec, R. Xu, S.Y. Lee, C.M. Nelson, A. Rizki, J. Alcazar, M.J. Bissell, “Cell shape regulates global histone acetylation in human mammary epithelial cells” Exp. Cell Res. Vol. 313, pp. 3066-3075, August 2007.

Trypsin-Resistant Adhesive Sequences for Biomaterial Surfaces Grafting

A. Zamuner[1], P. Brun[2], I. Castagliuolo[2], M. Dettin[1]
[1] *Department of Industrial Engineering, University of Padova, Padova, Italy*
[2] *Department of Molecular Medicine, University of Padova, Padova, Italy*

***Abstract*—Our group recently reported that the FRHRNRKGY peptide (mapped on human vitronectin and named HVP) grafted to titanium or glass surfaces promotes h-osteoblast adhesion. In solution this peptide is cleaved by the trypsin of the serum. We have synthesized retro-inverted peptides for the stabilization of the sequence toward enzymatic degradation. The retro-inverted sequence of the dimeric form of HVP has proved to be a potent adhesive analogue completely resistant to trypsin-mediated degradation.**

***Keywords*—Bioactive surfaces, Adhesive peptides, Degradation, Retro-inverted sequences.**

I. Introduction

MANY factors are deemed to play a key role in cell adhesion process, and they are mainly due to substrate chemical composition and surface morphology. With specific regard to the surface of endosseous implants, considerable efforts have been devoted to define how surface properties can affect osseointegration process. Actually the relationships linking surface treatments (e.g. mechanical, chemical and electrochemical) with surface morphology are thoroughly investigated; moreover, surface optimization has been recently driven towards the nanometric scale to improve cell adhesion. The key role of many physiologically molecules in cell adhesion and growth has been elucidated: the acquired knowledge opens the perspective of a new approach to surface treatments, i. e. the so-called "biochemical functionalization" to improve surface to cells interactions. Several peptides able to promote osteoblast adhesion have been discovered and tested: in particular, a nonapeptide from the human Vitronectin protein has been proved to enhance osteoblast cell adhesion throught an osteoblast-specific mechanism, involving interaction between glycosaminoglycans (GAGs) from the osteoblast membrane and proteins from extracellular matrix (ECM). The peptide HVP reproducing the sequence 352-360 of human vitronectin have been used to produce biomimetic surfaces via unselective or selective grafting [1]-[5]. The biomimetic surfaces improved h-osteoblast adhesion and promoted a more strength adhesion with respect to control surfaces not-decorated with adhesion peptides. We have observed that HVP dissolved in a solution containing 10% fetal bovine serum (FBS) is cleaved in fragments by trypsin. The elucidation and the overcoming of the degradation process promoted by proteases is fundamental in the design of bioactive surfaces of last generation biomaterials. To overcome this problem, we have designed and synthesized two retro-inverted analogues (monomeric and dimeric sequences) [6]. The reproduction of a bioactive peptide of L-amino acids with inverted sequence using D-amino acid is a strategy to create a peptide that is not recognized by proteolytic enzymes (due to D-amino acids presence) but is able to orientate its side chains groups in the same way than L-sequence. It was demonstrated that a retro-inverso RGD peptide still maintains its targeting activity and selective binding affinity to integrin αvß3 [7]. The biological assays demonstrated that the dimeric retro-inverted sequence (D-2HVP) enhances h-osteoblast adhesion with respect to HVP and increases gene expression of bone sialoprotein, osteopontin and vitronectin. The incubation of D-2HVP with 10% serum and the following characterization by HPLC showed the complete stability of this innovative peptide toward trypsin-mediated degradation.

II EXPERIMENTAL PART

A. Peptide Synthesis

All peptides were synthesized by standard Fmoc chemistry using Sieber Amide resin (0.72 mmol/g; scale 0.125 mmoles) and a fully automated peptide synthesizer (Syro I, Multisynthec, Witten, Germany). The synthetized sequences are reported in Table I.

TABLE I
HVP Series of Synthetic peptides

Name	*Sequence*
HVP	FRHRNRKGY
2HVP	FRHRNRKGYFRHRNRKGY
D-HVP	YGKRNRHRF
D-2HVP	YGKRNRHRFYGKRNRHRF

The underlined sequences refer to D-amino acids.

The side chain protection employed were: Arg, Pbf; His and Asn, Trt; Lys, Boc; Tyr, tBu.
The coupling reaction was carried out using 5-fold excess of Fmoc protected amino acid and HOBt/HBTU/DIPEA. All the couplings were double. The peptides were cleaved from the solid support without contemporary side-chain deprotection using the following mixture: 1% TFA in DCM.

B. HPLC analysis of peptide degradation in the presence of serum

The assessment of peptides degradation in the presence of FBS (Fetal Bovine Serum) or Trypsin solution (300 µg/L) in PBS (phosphate buffer solution) was carried out as follows: 1 mg of each peptide was dissolved into 100 µL water, then 900 µL of 10% FBS in saline buffer or Trypsin solution was added and left at 37°C for 5 hours. The solutions were analyzed by HPLC: all peaks were collected to identify the

fragments through MALDI-TOF mass analysis. The results showed that HVP and 2HVP underwent enzymatic degradation with both solutions; in Fig.1 is reported HVP degradation caused by Trypsin. On the contrary the retro-inverted sequences didn't degrade after both FBS or Trypsin treatment. Fig.2 shows the chromatogram of D-HVP after Trypsin treatment: no fragmentation is present.

C. *Specific Peptide grafting on glass*

To verify the bioactivity and the capacity of the retro-inversed sequences D-HVP and D-2HVP to improve h-osteoblast adhesion, glass surfaces were specifically functionalized with each synthetic peptide. The glass samples (2x2 cm) were treated overnight with 2% APTES ((3-aminopropyl) triethoxysilane)/acetone solution at 40°C. After three washings with CH_2Cl_2, acetone and water, the glass surfaces were dried at 100°C for 10 minutes. The samples were treated with a solution of 10 mg glutaric anhydride and 5 mL DIPEA (*N*,*N*-Diisopropylethylamine,) in 40 mL of NMP (N-Methyl-2-pyrrolidone) for 4 hours at 25°C. The glass surfaces were washed with NMP and acetone, and finally dried under vacuum. The samples were treated with 26.7 mg of each side-chain protected peptide, 3.75 mg of HBTU, 1.34 mg of HOBT and 5 µL of DIPEA and 10 mL of NMP for 21 hours at room temperature. The glass samples were washed and dried. The side-chain protections on grafted peptides were removed with 10 mL TFA (trifluoroacetic acid), 0.25 mL EDT (1,2-Ethanedithiol), 0.1 mL TES (Triethoxysilane) and 0.23 mL water, for 1 hour at room temperature.

D. *Biological assays*

Cells (1.3×105 cells/cm^2) were seeded onto glass functionalized surfaces in 100 µL of complete culture medium. Cultures were then incubated in a humidified tissue culture incubator (Heraeus; Corston, Bath, UK) at 37°C in 5% CO_2 and 95% humidity. The incubator was also equipped with an additional pan of sterile water to prevent evaporation of tissue culture media. The volume and the pH of the complete medium were checked every 24 h.

Adhesion assay. Cellular vitality was assessed by using the MTT (3-(4,5-dimethylthia- zole-2-yl)-2,5-diphenyl tetrazoliumbromide) assay. H-osteoblasts seeded on glass were incubated at 37°C for 2 h.

Gene expression. Human Vitronectin protein (hHVP), Integrin-binding sialoprotein (IBSP) and runt-related transcription factor 2 (RUNX2), specific transcript levels were quantified in osteoblast cells cultured for 24 h on functionalized glass scaffolds as reported in [3]

Statistical analysis was performed using student't t-test with a minimum confidence level of 0.05 for statistical significance. Data are reported as mean±standard error of the mean.

II. RESULS AND DISCUSSION

Covalent grafting of adhesive molecules is considered a successful strategy to encourage the early stages of tissue-implant integration. In particular, the first adhesion phase, which precedes the proliferation, can be positively influenced by the presence of adhesive peptide sequences covalently anchored to the implant surface. To date, in literature there are not studies about the stability of such peptides with regard to the degradation operated by proteolytic enzymes present in the serum. In this paper we showed that the peptide HVP and its dimer (designed to increase the interaction with the cell surface GAGs) underwent enzymatic degradation in solution. The type of fragments, cut at basic residues level, indicates trypsin as the responsible enzyme. The two retro-inverted analogues, under the same conditions, resulted completely stable and has been recovered intact. The biological assays, performed on model glass surfaces covalently functionalized with the four peptides, have shown that only two sequences are able to improve the adhesion of h-osteoblasts compared with the control (silanized glass): HVP and D-2HVP. These results indicate that:

1. The dimer of HVP was not able to increase or even maintain the binding to osteoblasts GAGs.
2. D-HVP did not increase the adhesion of osteoblasts compared to the control.
3. D-2HVP significantly increased the adhesion of osteoblasts compared to the control. D-2HVP possessed biological activity comparable with HVP.

The D-2HVP peptide was also able to stimulate gene expression of three proteins important for osteoblasts. Conformational studies and docking analysis of the sequences with the molecular models of h-osteoblasts GAGs are underway to formulate a possible structure-function relationship.

III CONCLUSIONS

From this study it emerges that the adhesive sequence D-2HVP is capable of promoting adhesion of h-osteoblasts as the HVP peptide, is able to modulate the gene expression of hBSP, hOPN and hHVP and at the same time is not absolutely degraded by serum enzymes. In a near future, the ability of this sequence to promote osseointegration will be evaluater *in vivo*.

REFERENCES

[1] M. Dettin, et al., "Covalent surface modification of titanium oxide with different adhesive peptides: Surface characterization and osteoblast-like cell adhesion" in *J Biomed Mater Res A*, 90 (1) (2008) pp. 35-45.

[2] M. Dettin, et al., "Assessment of novel chemical strategies for covalent attachment of adhesive peptides to rough titanium surfaces: XPS analysis and biological evaluation" in *J Biomed Mater Res A*, 91(2) (2009) pp. 463-479.

[3] P. Brun, et al., "Mechanisms underlying the attachment and spreading of human osteoblasts: From transient interactions to focal adhesions on vitronectin-grafted bioactive surfaces" in *Acta Biomaterialia*, 9 (2013) pp. 6105-6115.

[4] A. Bagno, et al., "Human osteoblast-like cell adhesion on titanium substrates covalently functionalized with synthetic peptides" in *Bone*, 40 (2007) pp. 693-699.

[5] A. Bagno, et al., "Improvement of Anselme's adhesion model for evaluating human osteoblast response to peptide-grafted titanium surfaces" in *Bone*, 41 (2007) pp. 704-712.

[6] E. M. Taylor, D. A. Otero, W. A. Banks,J. S. O'Brien, "Retro-inverso prosaptide peptides retain bioactivity, are stable in vivo, and are blood-brain barrier permeable" in *J. Pharmacol. Exp. Ther.* 295 (2000) pp. 190-194.

[7] Y. Liu, et al. He, "Integrin αvß3 targeting activity study of different retro-inverso sequences of RGD and their potentiality in the designing of tumor targeting peptides" in *Amino Acids*, 47 (12) (2015) pp. 2533-2539.

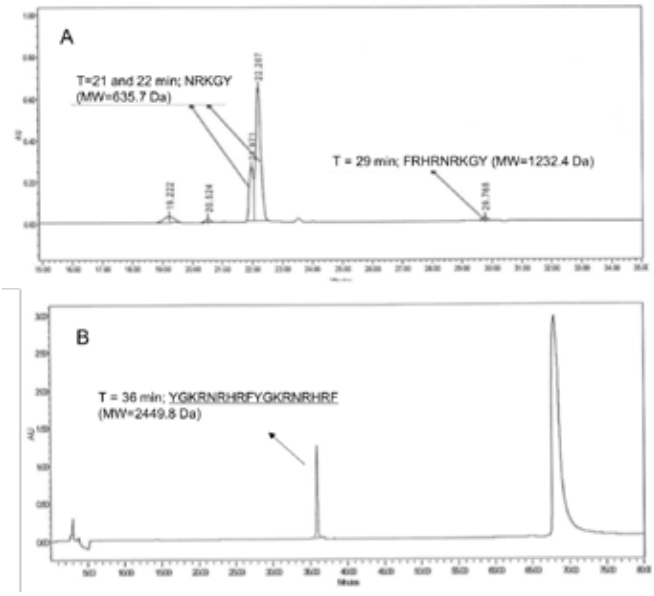

Fig. 1. Chromatograms of HVP (a detail, A) and D-2HVP (B) after Trypsin treatment, in the following conditions: column Jupiter C18 "proteo" (4 µm, 90 Å, 4.6 x 250 mm, Phenomenex); injection volume, 200 µL; flow rate, 1 mL/min; eluent A, 0.05% TFA in water; eluent B, 0.05% TFA in CH_3CN; gradient, from 0%B to 30%B in 60 min, detection at 214 nm, then 80%B for 10 min.

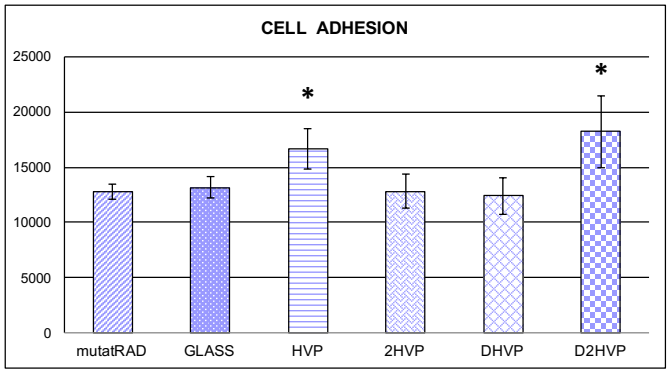

Fig. 2. Human osteoblast adhesion on functionalized glass surfaces, determined at 2 hrs from the seeding, through MTT assay. "Glass" sample refers to the silanized surface; "mutatRAD" refers to a RGD mutated sequences, not showing adhesive properties. *p-value<0.05 Student's *t-test* compared to "Glass" and "mutatRAD".

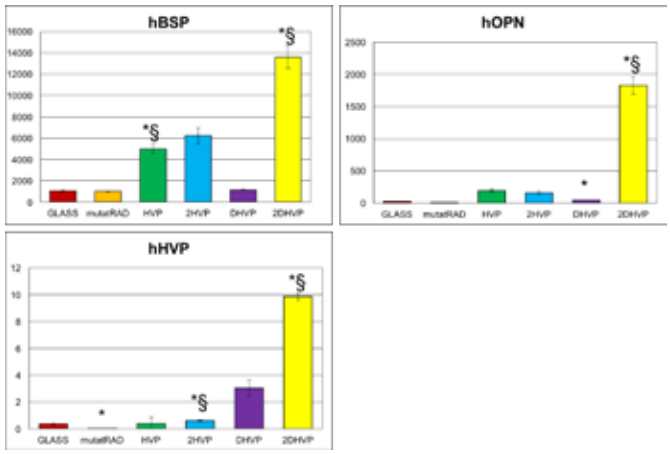

Fig. 3. Gene expression of hBSP, hOPN and hHVP, at 2 days from the seeding through q-PCR. "Glass" samples refer to silanized surface; "mutatRAD" refers to a RGD mutated sequences, not showing adhesive properties. *§p-value<0.05 Student's *t-test* compared to to "Glass" and "mutatRAD" respectivelly.

BIOMECCANICA
DEL MOVIMENTO UMANO

From gait to walk analysis: The Walk Analysis Lab

C.Basile[1], S. Magnani[1], A.E. Cifani[2], P. Galasso[1], S. Zucchi[3], A. Bray[3], R. Saggini[4]
[1] *Equipe di Biomedica Posturale, Rome*
[2] *Azienda Ospedaliera San Camillo Forlanini, Rome*
[3] *ASL VITERBO, VT*
[4] *Facoltà di Scienze dell'Educazione Motoria dell'Università G. D'Annunzio di Chieti*

***Abstract*— In this paper we wont to introduce the concept of Walk Analysis like a method to describe, in an objective way, some of the characteristics of the walk and of underlying mechanisms of gait disability. The experiences of over 25 years of research on foot pressures analysis and the innovation introduced with the ULTRASENSOR PLATFORM allow today to define a new clinical investigation path: THE WALK ANALYSIS LABORATORY, which makes possible the study of spontaneous ambulation without constraints, with acquisitions in high resolution of the foot's natural rolling, and that thanks to the optoelectronic evaluation tools and measuring the angular / linear movement also allows to assess postural influences on the body structure: the test takes few minutes and data can be consulted by any specialist.**

***Keywords*— GAIT analysis; WALK analysis; Biomechanics; New technology**

I. INTRODUCTION

THE Analysis of the human gait is the object of many research projects at the present moment. A search on the Web of Knowledge for scientific articles that include "gait" in the title shows more than 4000 publications between 2012 and 2015. Since research on this type of analysis was first begun in the 19th century, it has centered on achieving quantitative objective measurement of the different parameters that characterize gait in order to apply them to various fields such as sports [1–2], identification of people for security purposes [3–5], and medicine [6–8].

On the medical field, changes in gait reveal key information about persons' quality of life. This is of special interest when searching for reliable information on the evolution of different diseases: (a) neurological diseases such; (b) alterations in deambulation dynamic due to sequelae from stroke (c) systemic diseases; and (d) diseases caused by ageing, which affect a large percentage of the population. Accurate reliable knowledge of gait characteristics at a given time, and even more importantly, monitoring and evaluating them over time, will enable early diagnosis of diseases and their complications and help to find the best treatment.

Human gait is a complex and cyclical process requiring the synergy of muscles, bones, and nervous system [9], mainly aimed at supporting the upright position and maintaining balance during static and dynamic conditions [10]. The gait cycle is defined as the period of time from the initial contact of one foot to the following occurrence of the same event with the same foot. The correct discrimination of gait phases can be considered the starting point for several scientific applications, such as: (i) the evaluation of gait recovery status in patients after interventions or rehabilitation treatments; (ii) the classification of daily life activities; (iv) athlete coaching; and, (v) finally, distinguishing between normal and pathological gait.

The traditional scales used to analyse gait parameters in clinical conditions are semi-subjective, carried out by specialists who observe the quality of a patient's gait by making him/her walk. This is sometimes followed by a survey in which the patient is asked to give a subjective evaluation of the quality of his/her gait. The disadvantage of these methods is that they give subjective measurements, particularly concerning accuracy and precision, which have a negative effect on the diagnosis, follow-up and treatment of the pathologies.

In contrast to this background, progress in new technologies has given rise to devices and techniques which allow an objective evaluation of different gait parameters, resulting in more efficient measurement and providing specialists with a large amount of reliable information on patients' gaits. This reduces the error margin caused by subjective techniques. In this paper we wont to introduce the concept of Walk Analysis like a method to describe, in an objective way, some of the characteristics of the walk and of underlying mechanisms of gait disability[11-15].

II. MATERIALS AND METHOD

The experiences of over 25 years of research on foot pressures analysis and the innovation introduced with the ULTRASENSOR PLATFORM allow today to define a new clinical investigation path: ***THE WALK ANALYSIS LABORATORY***, which makes possible the study of spontaneous ambulation without constraints, with acquisitions in high resolution of the foot's natural rolling, and that thanks to the optoelectronic evaluation tools and measuring the angular / linear movement also allows to

assess postural influences on the body structure: the test takes few minutes and data can be consulted by any specialist.

In ***THE WALK ANALYSIS LABORATORY*** we have utilized the D.B.I.S. technology (Digital Biometry Images Scanning®) for specific investigation of posture, used for clinical activities by Postural Biomedicine Team, which includes Universities [such as: University of Chieti-Pescara, and University of Rome "Torvergata" and University of Viterbo] and Research Centre.
The data acquired through the D.B.I.S. system are the basis of Bio Postural Test that integrates the values of the following devices:
• Electronic Baropodometer, foot pressure evaluation systems
• Stabilometry Platform, body balance study systems
• Body Analysis Kapture and Image System, investigation systems
• Surfacer and B3DR, three-dimensional column and body survey systems
• Podoscanalyzer, foot morphology study system
• Myoton muscle activity detection system.

The data were analysed by the software ReBioDes, Report Biometric Description, that is an expert system of applied logic used for descriptive reporting of biometric test.
ReBioDes it allows a comparison with indicators of more biometric tests with specific conclusions on each indicator detected and at the end giving indication of any additional biometric exam needed.
The systems are used by Universities, Hospitals, Medical and Radiologic Clinics, Physiotherapy and Sport Centres; Medical Specialists(Orthopaedics, Dentistry, Otolaryngology, Ophthalmology, Phlebology, Forensic Medicine), health professionals such as Physiotherapists, Podiatrists, Osteopaths, Chiropractors, Physiotherapists, Kinesiologists, and by all those concerned with postural problems.
One of the more innovative and performance Walk Analysis Lab was performed in Viterbo, at Belcolle Hospital [ASL VT].

The next technology we will add to the "walk analysis lab" will be a new kind of innovative UltraSensor platform.
The UltraSensor platform represent a concrete answer for a "trustable analysis of the walk employing foot pressure measurement", to be used in the Walk Analysis Lab. For a correct acquisition of the parameters of the walk the SCIENTIFIC literature suggests a path of at least 6 meters. The standard required from most of the Gait Analysis Labs in the USA are indicated in a length of at least 5 m and a width of 1 m.

We have realized a new UltraSensor patented platform in order to meet the gait evaluation needs, having a surface expandable up to 20 meters in length and 2 meters in width.
To properly detect the characteristics of the pressure of the foot, to study the functional responses of each subsequent support of the same foot, to evaluate changes in the overall dynamic center of mass (COM, calculated from the single pressure points) is required the acquisition in high resolution.
The sensor acquisition surface should at least have a detail with more than **6 sensors each cm2 and the UltraSensor Platform has 7 sensors each cm2**.

III. CONCLUSION

In the last decades, interest in obtaining in-depth knowledge of human gait mechanisms and functions has increased dramatically. Thanks to advances in measuring technologies that make it possible to analyse a greater number of gait characteristics and the development of more powerful, efficient and smaller sensors, gait analysis and evaluation have improved. In contrast to the traditional semi-subjective methods which depend on the specialist's experience, the different parameters being studied can now be objectively quantified. These new methods have great impact in various fields such as human recognition, sports, and especially in the clinical field, where objective gait analysis plays an important role in diagnosis, prevention and monitoring of neurological, cardiopathic and age-related disorders.

IV. REFERENCES

[1] Gouwanda D., Senanayake S.M.N.A. Emerging Trends of Body-Mounted Sensors in Sports and Human Gait Analysis. In: Osman N.A.A., Ibrahim F., Abas W.A.B.W., Rahman H.S.A., Ting H.N., editors. 4th Kuala Lumpur International Conference on Biomedical Engineering 2008. Volume 21. Springer; New York, NY, USA: 2008. pp. 715–718.
[2] Di Stasi S.L., Logerstedt D., Gardinier E.S., Snyder-Mackler L. Gait patterns differ between ACL-reconstructed athletes who pass return-to-sport criteria and those who fail. Am. J. Sports Med. 2013;41:1310–1318. [PMC free article] [PubMed]
[3] Fathima S.M.H.S.S., Banu R.S.D.W. Human Gait Recognition Based on Motion Analysis Including Ankle to Foot Angle Measurement. Proceeding of 2012 International Conference on Computing, Electronics and Electrical Technologies (ICCEET; Nagercoil, India. 21–22 March 2012; pp. 1133–1136.
[4] Wang L., Tan T., Ning H.Z., Hu W.M. Silhouette analysis-based gait recognition for human identification. IEEE Trans. Pattern Anal. Mach. Intell. 2003;25:1505–1518.
[5]Han J., Bhanu B. Individual recognition using Gait Energy Image. IEEE Trans. Pattern Anal. Mach. Intell. 2006;28:316–322. [PubMed]
[6]Sutherland D.H. The evolution of clinical gait analysis part I: Kinesiological EMG. Gait Posture. 2001;14:61–70. [PubMed]
[7] Giacomozzi C, Caselli A, Macellari V, Giurato L, Lardieri L, Uccioli L: Walking strategy in diabetic patients with peripheral neuropathy. Diabetes Care 2002, 25:1451–1457.

[8] Sutherland D.H. The evolution of clinical gait analysis part III—kinetics and energy assessment. Gait Posture. 2005;21:447–461. [PubMed]
[9] Saggini R, Pizzigallo E, Vecchiet J, et al. Alteration of spatial temporal parameters of gait in chronic fatigue syndrome patients. J Neurol Sci 1998; 154: 18-25
[10] Ayyappa E. Normal human locomotion. Part 1: Basic concepts and terminology. J. Prosthetics Orthot. 1997;9:10–17. doi: 10.1097/00008526-199710000-00004. [Cross Ref]
[11] Giacomozzi C., Macellari V., Saggini R. Spatial-temporal parameters of gait. ISTISAN Report 95/36, 1995.
[12] Macellari V, Giacomozzi C, Saggini R:Spatial-temporal parameters of gait: reference data and a statistical method for normality assessment. Gait Posture 10:171– 181, 1999

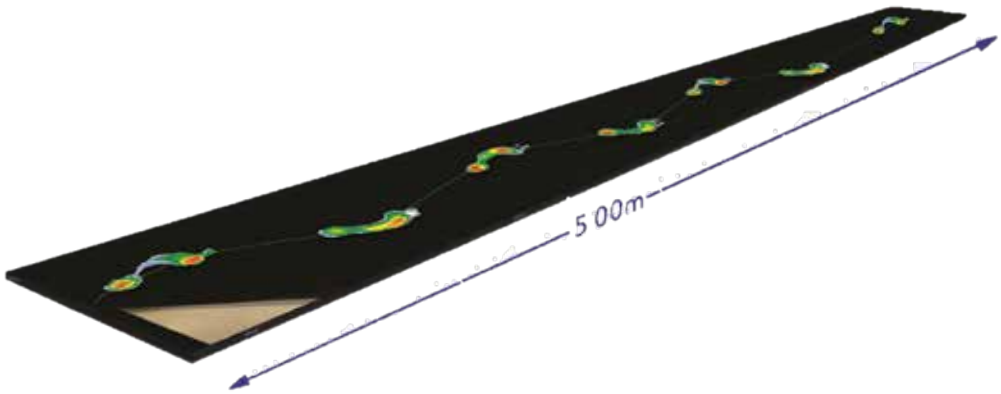

Fig. 1. ULTRASENSOR PLATFORM

Identification of multiple U-turns using gyroscopes: comparative assessment of two methods

M. Bertoli, A. Cereatti and U. Della Croce
POLCOMING Department, University of Sassari, Sassari (SS), Italy, mbertoli@uniss.it
Interuniversity Centre of Bioengineering of the Human Neuromusculoskeletal System, Sassari, Italy

***Abstract* — The identification of turnings segments during walking trials including the U-turns represents the first preliminary step required for the analysis of gait featuring straights and turns. To this purpose IMU-based methods were developed, however many of them rely on the a-priori knowledge of the number of turns. In this study, we selected two methods and compared them to evaluate their ability to detect the number of turns in continuous gait with multiple U-turns without further assumptions. Gyroscope data were recorded during gait trials performed at different speeds by two groups of subjects (healthy elderly and patients with Parkinson disease).**

Results show that the method that employs a sensor on the back yields better results than the one making use of a sensor on the ankles.

***Keywords*—Turning, Gait, Gyroscopes, IMU**

I. Introduction

QUANTITATIVE gait analysis traditionally focuses on the study of straight walking, the determination of spatio-temporal parameters and joint kinematics are typical goals of it [1]. However, some classical clinical evaluations of gait, such as the Time-Up-and Go (TUG) and the Six-Minutes-Walking test, include one or more turns. The correct identification of the turning occurrences is the first step for properly segmenting the walking trials into portions of straight walking and turns.

Recently, the use of miniaturized inertial measurement systems which include accelerometers and gyroscopes (IMUs) and specific signal analysis techniques have allowed, in addition to the quantitative analysis of standardized gait parameters, also for the recordings and analysis of composite gait tasks, as those including turnings [2], [3]. Moreover, the use of wearable IMUs can allow for the analysis of gait outside the laboratory, in more ecological conditions, therefore including turns.

Several studies in the literature have focused on the analysis of turnings during instrumented clinical test featuring a predefined number of straight gait and turnings. For instance, in the TUG test a 180 degrees turn is expected in the middle of the trial plus a second toward the end of it. Methods for the analysis of the IMU-instrumented TUG found in the literature exploit the information about these imposed motor tasks sequence [4]-[7].

Very few studies have been proposed for the analysis and turn-straight gait segmentation of walking trials including with an unknown number of turns [8]. In this study, we selected two published methods based only on gyroscopes recordings for the analysis of gait tasks featuring a known number of turns. These methods were extended to analyse gait trials that did not have a number of turns known a-priori. Aim of this study was to test their capability of detecting the correct number of turns during walking trials including U-turns. To this purpose, we applied them to gait trials performed at different speeds by two different groups of subjects: healthy elderly and patients with Parkinson disease.

II. Materials and Methods

A. Experimental setup

The study included 10 healthy elderly (ELD) and 12 subjects with Parkinson's disease (PD). The Declaration of Helsinki was respected, all subjects provided informed written consent, and local ethic committee approval was obtained. Two IMUs (Opal, APDM) were attached to the ankles just above the malleoli and a third one to the trunk, between L4 and S2. Gait data were acquired using the IMUs and an instrumented mat (GAITRite®), simultaneously. The signals from the IMUs were recorded at 128 Hz, streamed wirelessly to a laptop and stored for offline analysis.

Subjects walked back and forth along a 12-m walkway for one minute. They performed straight walking portions on the instrumented mat and the U-turns outside of it. The setup and the sensors placement are depicted in Figure 1. Subjects stood still for a few seconds after the beginning of the acquisition before walking. For each subject, two gait conditions were tested: normal walk (NW – self selected, comfortable speed) and fast walk (FW – walking as fast as possible). The total number of passages on the instrumented mat and U-turns recorded during the one minute acquisition varied with the subject speed.

B. Methods description

Two published methods were selected and implemented for comparison [9], [10]. For both methods, only gyroscope signals are required for the identification of the U-turns.

Method A

The method is based on the work of Nguyen [9], which requires a gyroscope on the back and it identifies turns from the analysis of the angular velocity about the gyroscopic axis approximately aligned to the yaw axis. A band pass filter was first applied to the angular velocity component (low and high cut off frequencies set at 0.0025 Hz and 0.7 Hz, respectively). The filtered signal was then de-trended and normalized. The timing of peaks of the resulting signal corresponded to timings of turns. Two or more peaks occurring within the same turns (<4 seconds) were associated to a single turn.

Method B

The method is based on the work of Greene et al [10]

which requires a gyroscope applied on the ankle and identifies turns from the analysis of the angular velocity about the medio-lateral (ML) axis. Greene and colleagues determined through empirical tests that the amplitude of the ML angular velocity signal during turning was lower than during straight walking. Threshold values used in the original paper were not reported. In this study, the determination of the ML angular velocity threshold was carried out by analysing the gait trials recorded on the ELD group at normal speed. In particular, the threshold was varied until the number of turning identified on the data recorded by the gyroscope attached to the left side was equal to that measured by the instrumented mat.

C. Data analysis

The performance of the two methods was evaluated by comparing the number of turns they detected with the number of turns obtained from the instrumented mat (actual turns). The last was obtained from the number of passages on the walkway minus one, given that the trial did not end with a turn.

Since the method B was applied to the data recorded by each of the two gyroscopes attached to the left and right ankles, two independent estimates of the total number of turns were obtained for each subject.

III. Results and Discussion

The number of actual turns as measured by the instrumented mat (reference data) and the total number of detected turns estimated using both method A (back gyroscope) and method B (right and left gyroscopes), are reported in Table I.

Method A detected the 100% of the actual turns across groups and gait speeds.

Method B missed 3 turns (6% overall) on the left side (L) and none on the right (R) in the PD group. The number of errors increased at higher walking speed (respectively on R and L sides 8% and 11% in ELD, and to 7% and 18% in PD).

TABLE I
NUMBER OF ACTUAL AND DETECTED TURNS

Algorithm	*ELD NW*	*PD NW*	*ELD FW*	*PD FW*
Actual turns	**48**	**47**	**64**	**56**
Detected turns Method A	48	47	64	56
Detected turns Method B, R	48	47	59	52
Detected turns Method B, L	48	44	57	46

IV. Conclusions

The better performance of the method A is probably due to the low variability, which characterizes the yaw angular velocity recorded at the low back level. On the contrary, angular velocity at the ankles is characterized by higher variability and it changes with gait speed. Since the threshold used in the method B was defined on comfortable walking speed, the performance of the method worsened at higher walking speed. A similar conclusion can be drawn with respect to the differences found between right and left sides.

It is important to mention that the identification of the number of turns during walking trials including U-turns represents the first preliminary step required for the analysis of gait featuring straights and turns. Once the number of turns is correctly determined it is necessary to identify when each turn begins and ends, to then segment the straight and turning portions of the walking trial. Once walking trials are segmented, it is possible to extract the relevant gait parameters by using algorithms specifically devoted for the analysis of either straight or curvilinear gait, [1],[11],[12].

The observations presented in this study are encouraging but still preliminary. For more definitive conclusions, a larger number of subjects must be included in the analysis and, above all, different pathological groups should be analyzed to test the methods performance when the deviations of the angular velocity patterns from those typical of normal gait are not negligible [13].

As future development, the use of the magnetometer signals in addition to the angular velocities will be explored.

References

[1] A. Köse, A. Cereatti, and U. Della Croce. "Bilateral step length estimation using a single inertial measurement unit attached to the pelvis." *Journal of neuroengineering and rehabilitation* 9.1 (2012): 1.

[2] C. Bonnyaud, D. Pradon, N. Vuillerme, D. Bensmail, and N. Roche. "Spatiotemporal and kinematic parameters relating to oriented gait and turn performance in patients with chronic stroke." *PloS one* 10.6 (2015): e0129821.

[3] F. Huxham, J. Gong, R. Baker, M. Morris, and R. Iansek. "Defining spatial parameters for non-linear walking." *Gait & posture* 23.2 (2006): 159-163.

[4] A. Weiss et al. "An instrumented timed up and go: the added value of an accelerometer for identifying fall risk in idiopathic fallers." *Physiological measurement* 32.12 (2011): 2003.

[5] P.C. Fino, C.W. Frames, and T.E. Lockhart. "Classifying step and spin turns using wireless gyroscopes and implications for fall risk assessments." *Sensors* 15.5 (2015): 10676-10685.

[6] S. Reinfelder, R. Hauer, J. Barth, J. Klucken, & B.M. Eskofier. "Timed Up-and-Go phase segmentation in Parkinson's disease patients using unobtrusive inertial sensors." *Engineering in Medicine and Biology Society (EMBC), 2015 37th Annual International Conference of the IEEE*. IEEE, 2015.

[7] M.R. Adame, et al. "TUG test instrumentation for Parkinson's disease patients using inertial sensors and dynamic time warping." *Biomedical Engineering/Biomedizinische Technik* 57.SI-1 Track-E (2012): 1071-1074.

[8] M. El-Gohary, et al. "Continuous monitoring of turning in patients with movement disability." *Sensors* 14.1 (2013): 356-369.

[9] H.P. Nguyen, et al. "Auto detection and segmentation of physical activities during a Timed-Up-and-Go (TUG) task in healthy older adults using multiple inertial sensors." *Journal of neuroengineering and rehabilitation* 12.1 (2015): 1.

[10] Greene, Barry R., et al. "Quantitative falls risk assessment using the timed up and go test." *Biomedical Engineering, IEEE Transactions on* 57.12 (2010): 2918-2926.

[11] P.C. Dixon, J. Stebbins, T. Theologis & A.B. Zavatsky. "Spatio-temporal parameters and lower-limb kinematics of turning gait in typically developing children." Gait & posture 38.4 (2013): 870-875.

[12] D. McGrath, et al. "Reliability of quantitative TUG measures of mobility for use in falls risk assessment." *Engineering in Medicine and Biology Society, EMBC, 2011 Annual International Conference of the IEEE*. IEEE, 2011.

[13] D. Trojaniello, et al. "Estimation of step-by-step spatio-temporal parameters of normal and impaired gait using shank-mounted magneto-inertial sensors: application to elderly, hemiparetic, parkinsonian and choreic gait." *Journal of neuroengineering and rehabilitation* 11.1 (2014): 1.

Fig 1. A schematic representation for the experimental setup and sensors placement

The influence of filtering on spatio-temporal gait parameters estimation from inertial sensors

C. Caramia, I. Bernabucci, B. Fida, A. Proto, M. Schmid
Department of Engineering, Roma Tre University, via Vito Volterra 62, 00146 Rome, Italy

Abstract— **The aim of this study is to compare some specific gait parameters extracted by one inertial sensor against those obtained through a marker-based motion capture system, and to check whether differences in filtering lead to relevant changes in estimation accuracy. To this end, a population sample of 4 healthy young individuals repeated walking trials at different speeds, while wearing an inertial sensor allocated on the lower back. Stride time, gait speed, step length, stride frequency, step symmetry and stride regularity were estimated from the two systems. For both step length and gait speed, different values of high-pass frequency for displacement estimation from accelerometer data were considered. Coefficients of determination (R^2) between parameters calculated by motion capture data and those estimated by the inertial sensor were extracted. Stride time, stride frequency and gait speed showed values of R^2 higher than 0.9, and step length showed a clear dependence of the regression accuracy from frequency; this appeared also for the gait speed estimation, though to a minor extent. A cut-off frequency of 1.3 Hz is then suggested for high-pass filtering for step length estimation, as it showed the highest R^2 values. Step symmetry and stride regularity showed low values for R^2, and this may be related to the reduced availability of consecutive steps upon which these parameters were calculated.**

Keywords— **gait parameters, accelerometer, validation**

I. Introduction

Gait refers to the style of walking of an individual. A normal walk presents repetitive gait sequences, with a nearly periodic behavior [1]. The measurement of gait parameters allows to have a synthetic sketch that may help identify deviations from normal patterns or values and, thus, to understand the reason of these differences. Different are the application fields, such as the assessment of children with cerebral palsy in orthopedic treatment planning, or the assessment of people with other movement disorders, or the evaluation of fall risk in the elderly, a theme that is becoming increasingly topical [2]. Recent advances in miniaturized technological tools brought the availability of having wearable high-resolution devices, the inertial sensors, able to capture some kinematic variables associated with gait. Thanks to them, the analysis has been brought outside the lab and, so, used for applications in daily life, in such a way that motor behavior is not modified or hindered by the use of a limited space or of a controlled environment.

In terms of user acceptability, the smaller the number of sensors to be placed, the lower the computational cost – and obviously the more comfortable the set-up for the user. The inertial sensor placement is also crucial in terms of wearability, as it is recommendable to be in a position accepted by people. A common practice, in these regards, is to allocate one sensor on the lower trunk, in such a way that information about kinematics of both legs can be gathered.

While the definition of the spatio-temporal parameters is agreed in the literature, different techniques for their calculation and validation from inertial sensors data have been proposed in the literature [3], [4], with varying choices as per the pre-processing parameters (filtering being one among them). The purpose of this study is thus to specifically study the effect of different numerical choices for filtering in the estimation of gait parameters from inertial sensors, through a validation based on motion capture data.

II. Materials and Methods

A. Participants and procedure

4 healthy volunteers (age range 24-39 years, height range 1.64-1.79 m) with no referred motor disorders, participated to the experiments. Subjects were instructed for the experimental procedure described in the following, and all of them gave written informed consent according to the declaration of Helsinki.

The experiment included five repetitions of gait within a 6 m-long walkway at three different speeds freely chosen by each participant (slow, normal, fast), thus summing a total of 15 trials with at least two entire strides for each participant.

B. Signal recording

Each participant worn a wireless inertial measurement unit (Shimmer3, Shimmer sensing, Dublin, Ireland) placed on the back of the lower trunk. Linear accelerations and angular velocities around the three major axes (range ±2 g) were captured at 102.4 samples/s and stored for offline processing. Smart-DX (8 cameras, BTS Bioengineering, Milan, Italy) captured marker data positions in the calibrated volume at a sampling rate of 250 samples/s. Markers used for the experimentation were placed on top of the inertial sensor, and bilaterally on each heel, lateral malleolus, and fifth metatarsophalangeal joint. Offline resampling and synchronization were performed for data validation.

C. Data processing and parameter extraction

From the marker dataset, it was possible to directly determine the spatio-temporal parameters of gait: stride time, gait speed, step length, stride frequency, step symmetry and stride regularity.

The same parameters were, then, estimated from inertial sensor data, through the procedure detailed in the following: stride time is the time lag which maximizes the signal resulting by the sum of the unbiased auto-covariance of the acceleration components along the three directions [6]; gait speed and step length are modeled using the method proposed by Gonzales et al. [7], where the single stance phase follows the concept of an inverted pendulum, while the double stance phase is calculated by a value proportional to

foot length: for this parameter, initial and final contact of the foot were also estimated. Step symmetry – which describes the similarity between right and left steps – and stride regularity – which refers to similarity between successive strides – are calculated by the harmonics of the auto-covariance along the vertical direction [5]; stride frequency considers the modal frequencies of the spectra along the three directions [6].

In particular, the calculation of stride velocity and step length through inertial sensor data requires double integration of acceleration. In order to minimize drift, high-pass filtering before each integration step is necessary. In the present research, the cut-off frequency of this filter was varied in a range between 0.1 and 1.6 Hz, with steps of 0.1 Hz.

Furthermore, the chosen method for step length estimation [7] is a modification of the method of Zijlstra and Hof [8], which allows to decrease the error of the estimation introducing a proportionality constant K which multiplies the length of the foot of the subject. Two different values from literature [7] are assigned to K, respectively 0.67 and 0.83, and for both of them the calculation was made.

All recorded data were processed together: indeed, fast, slow and normal velocities are referred to a single individual, and they do not represent different classes, since each participant chose their own selected speed for the three classes.

D. Gait parameter validation

The extracted parameters from both systems were compared, and the coefficient of determination for each parameter was extracted. In order to determine the influence of high-pass filtering on both step length and stride velocity, the value of the coefficient of determination was calculated for each individual frequency lying in the range [0.1-1.6] Hz. This made it possible to check whether an optimum frequency for high-pass filtering was present in the recorded dataset.

III. RESULTS

Linear regression resulted very high for both stride time and stride frequency (R^2 = 0.9968 and 0.9896, respectively). Step length estimation accuracy resulted highly variable with the cut-off frequency (R^2 resulted varying in the range 0.5207-0.8401, for K = 0.83, see figure 1), and the best linear regression appeared with f_{cut} = 1.3 Hz. These results were practically identical with K = 0.67: changes of K essentially introduce a subject-dependent bias, that is only minimally captured by R^2. Stride speed estimation accurately matches values obtained from motion capture data with a slight dependence from filtering frequency (R^2 higher than 0.91 for every f_{cut} and maximum value = 0.9732, for f_{cut} = 1.4 Hz).

Figure 2 shows the scatter plots of the parameters mentioned above, with the respective trend lines and R^2.

As per the step symmetry, inertial-based values lie in the range 0.9519±0.0451, while motion capture data lead to values in the range 0.9630±0.0154 (R^2 around 0.0095). Stride regularity gives 0.8251±0.0830 vs. 0.9798±0.0088, with R^2 around 0.3943. It is to be highlighted that the definition of both these parameters is inherently different if calculated by the two systems. Moreover, given the rather small number of steps that were captured within one trial, results on these parameters – which rely on the availability of multiple steps to be accurately estimated – may be influenced by that.

IV. DISCUSSION AND CONCLUSION

The results obtained for stride time and stride frequency are good, and the used method showed high accuracy on a variety of different speeds and anthropometric factors.

Regarding step length and stride speed estimation, we decided to choose the optimum cut-off frequency as the one that maximized the coefficient of regression R^2 of the step length. The motivation behind this choice is the fact that stride speed is calculated by combining two estimated parameters – step length and stride time – thus introducing uncertainties coming from the combination of two different sources of error.

We did not choose frequencies higher than 1.6 Hz, as this brought to the introduction of peaks in the signal, that needed some manual identifications of gait events. If automatic detection had been done, gait temporal events would have been misidentified, and the corresponding estimation of gait parameters would have been largely affected.

Step symmetry and, especially, stride regularity give results that are only loosely correlated with the expected values coming from motion capture data. This is probably due to the fact that only few strides were made available for each repetition, whereas it would make sense to apply these estimations to longer paths, with more strides.

Thanks to the results obtained, the direction to follow is to assess the correlation between cut-off frequency and the velocity of walking, in such a way that a gait speed-dependent cut-off frequency may help reduce the inter-individual variability. Finally, the idea is to use the developed methods to longer walking sessions, thus increasing the accuracy in parameters extracted from inertial sensor data, in order to apply them, later, to other population samples, including elderly people.

REFERENCES

[1] M. W. Whittle, "Clinical gait analysis: A review", *Human Movement Science*, pp. 369-387, 1996.

[2] M. Marschollek, K. H. Wolf, M. Gietzelt, G. Nemitz, H. M. zu Schwabedissen, R. Haux, "Assessing elderly person's fall risk using spectral analysis on accelerometrici data", in *2008 Proc. IEEE EMBS Conf.*, 3682-3685.

[3] F. Bugané, M.G. Benedetti, G. Casadio, S. Attala, F. Biagi, M. Manca, A. Leardini, "Estimation of spatio-temporal gait parameters in level walking based on a single accelerometer: Validation on normal subjects by standard gait analysis", *Computer methods and programs in biomedicine*, 108.1: pp. 129-137, 2012.

[4] D. Trojanello, A. Cereatti, U. Della Croce, "Accuracy, sensitivity and robustness of five different methods for the estimation of gait temporal parameters using a single inertial sensor mounted on the lower trunk", *Gait & Posture*, 40.4, pp. 487-492, 2014.

[5] R. Moe-Nilssen, J. L. Helbostad, "Estimation of gait cycle characteristics by trunk accelerometry", *Journal of Biomechanics*, 37.1, pp. 121-126, 2003.

[6] S. M. Rispens, K. S. van Schooten, M. Pijnappels, A. Daffertshoofer, P. J. Beek,J. H. van Dieen, "Identification of Fall Risk Predictors in Daily Life Measurements: Gait Characteristics' Reliability and Association With Self-reported Fall History", *Neurorehabilitation and Neural Repair,* 1-8, 2014.

[7] R.C. Gonzales, D. Alvarez, A. M. Lopez, J.C. Alvarez, "Modified pendulum model for mean step length estimation", in *2007 Proc. IEEE EMBS Conf.* pp. 1371-1374.

[8] W. Zijlstra, A. L. Hof, "Assessment of spatio-temporal gait parameters from trunk accelerations during human walking", *Gait & Posture*, 18.2: pp. 1-10, 2003.

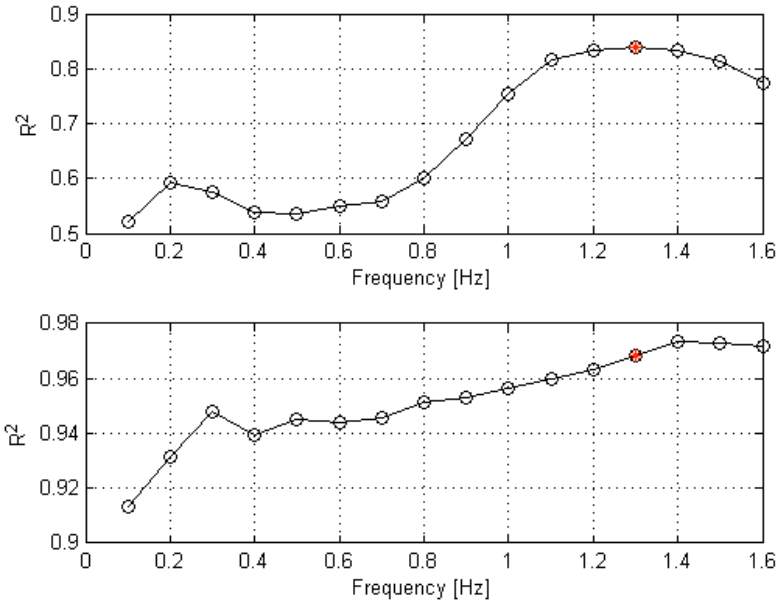

Fig.1. The graph on the upper panel represents the regression coefficient under varying frequencies for K equal to 0.83, relative to the estimation of step length, while the one on the lower panel is relative to the estimation of stride speed. The red point shows which is the frequency chosen.

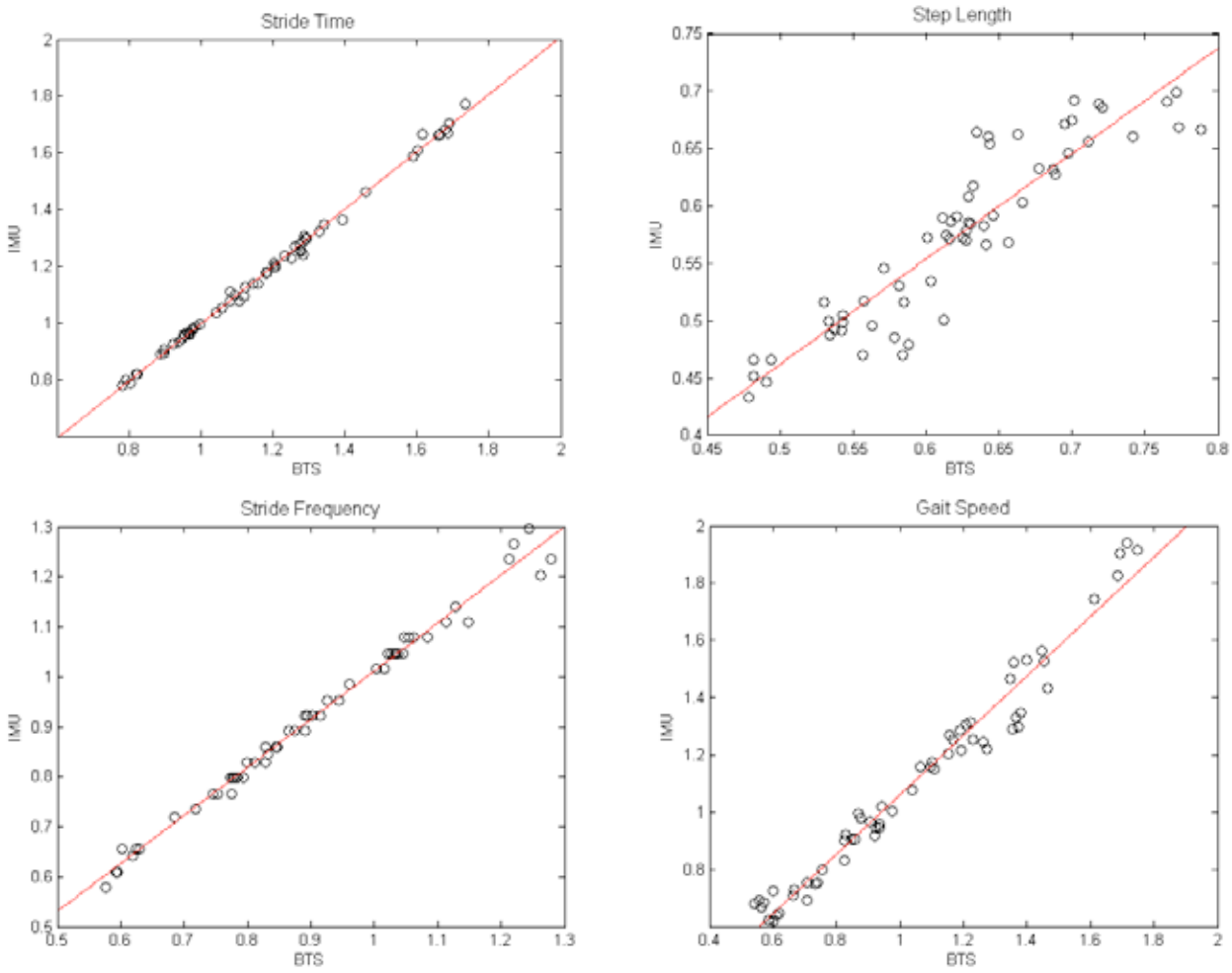

Fig. 2. Scatter plots of stride time, step length, stride frequency and gait speed, with the respective trend lines and R^2.

Experimental framework for human hand biomechanical analysis

F. Cordella[1], R.A. Romeo[1], A.G. Cutti[2], R. Sacchetti[2], A. Davalli[2], E. Guglielmelli[1] and L. Zollo[1]
[1]*Unit of Biomedical Robotics and Biomicrosystems, Department of Engineering, Università Campus Bio-Medico di Roma, IT*
[2] *Centro Protesi INAIL, Vigorso di Budrio (BO), IT*

***Abstract*—Studying human grasping is of paramount interest for advancing on the comprehension of human sensorimotor strategies and for imparting similar skills to robotic hands. This paper wants to propose and validate an experimental framework for hand biomechanical analysis composed of (i) a set of instrumented objects for force analysis during grasping aimed at evaluating the behaviour of human as well as robotic hands and (ii) a kinematic protocol for assessing the hand functionality in terms of range of motion and joint angles. A combined kinematic and dynamic analysis has been performed on 7 subjects during grasping a set of instrumented objects. Information about motion kinematics have been obtained from data acquired with an optoelectronic system.**

***Keywords*—Kinematic reconstruction, hand biomechanical analysis, instrumented objects, grasping force.**

I. Introduction

BIOMECHANICAL analysis of the human hand during grasping is a fundamental issue to be faced while studying human grasping strategies as well as robotic grasping capabilities. In case of studies on humans, force analysis in addition to kinematic analysis allows investigating sensori-motor mechanisms responsible for human grasp control, with important implications both in neuroscience and in robotics.

Different approaches have been proposed in the literature to acquire information about forces and hand kinematic behavior during the grasping action. Sensors embedded in gloves or directly positioned on the hand have been adopted in [1] and [2], respectively, to measure grasping forces. Instrumented objects, i.e. objects embedding tactile or force sensors, have been used for studying grip force during pinch, tripod and power grasps. Different transduction technologies have been embedded in these objects for providing information about force values and spatial distribution of contact points, such as force transducers, strain gauges [3], tactile sensors [4] and force-torque sensors [5]. The main limitations of these solutions are represented by the impossibility of recognizing the forces applied by each finger in correspondence of the contact points and, in some cases, the high costs.

As regards the hand kinematic analysis, different methods for human hand joint motion reconstruction from 3D marker positions acquired with optoelectronic motion analysis systems [6], as well as different kinematic models [7] have been proposed.

The objective of this paper is to propose an experimental framework for performing hand kinematic and force analysis through a purposely developed protocol for optoelectronic systems and a set of instrumented objects during grasping. The protocol for positioning markers on the hand has been chosen in such a way to minimize artefacts, due for example to skin movements or marker occlusions, and to obtain information about wrist position. The set of instrumented objects is conceived to be low-cost and able to analyze the force applied by each finger during the task and to detect slippage.

II. Methods

A. Kinematic protocol for hand motion analysis

In order to describe finger behaviour during grasping, a kinematic model consisting of 21 degrees of freedom (five for the thumb and four for each of the long fingers) and a protocol for tracking hand motion and reconstructing joint angles starting from the marker positions acquired with an optoelectronic motion analysis system have been adopted [8] (Fig. 1). In particular, finger joint trajectories and angles have been determined placing 25 reflective markers of 6 mm diameter on the subject's right hand. For each image frame, the 3D marker positions acquired with the optoelectronic system are used for obtaining unit vectors representing the axes of joint reference frames. The angular parametrization of Euler angles in configuration *ZYX* has been chosen in order to obtain the hand joint angles from the rotation matrices.

B. Instrumented objects for grasping force evaluation

A set of instrumented objects has been conceived to be jointly used with the system for motion analysis in order to obtain a complete grasp analysis of human hands. In particular, in this paper the development and testing of two spherical objects for tripod and pinch grasp analysis is discussed.

Each object embeds (Fig. 2): (i) Force Sensing Resistor sensors (FSR, Model 400 by Interlink Electronics, Inc.), (ii) an electronic board for acquisition and amplification of the output signals provided by the aforementioned sensors, (iii) movable parts, one for each contact point, sliding on mechanical springs lodged into rails, and (iv) a triaxial accelerometer (ADXL330 Analog Devices, Inc.) for slip detection. The location of the contact areas on the object surface answers the requirement of ensuring grasp stability for human hands.

The CAD of the two objects is shown in Fig. 3. Three piezoresistive sensors have been located in order to measure the forces applied by the hand fingers during grasping. Each sensor has a circular active area (diameter of 5.08 mm), a discrimination threshold of 0.2 N and a measurement range up to 20 N. The input-output relationship of the FSR sensor is described by the equation

Robotic Hand", *International Journal of Advanced Robotic Systems*, vol. 11, no. 37, 2014.

Figure 1. Protocol for marker positioning.

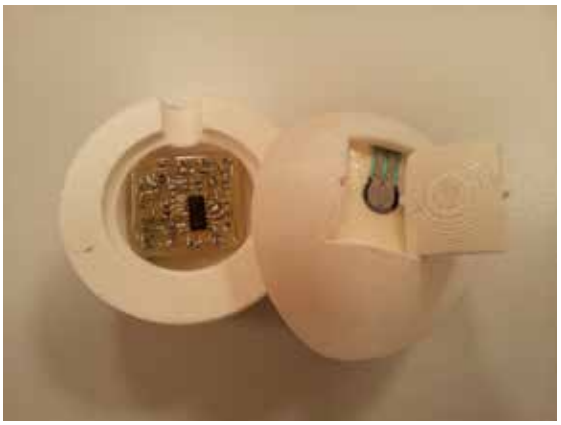

Figure 2: The electronic circuit is collocated inside the developed instrumented objects.

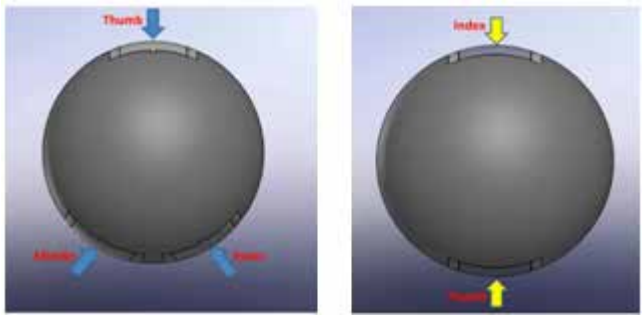

Figure 3. CAD model of the instrumented objects for tripod (left) and pinch (right) grasps. The arrows point to the contact areas.

Figure 4. Final grasping configuration.

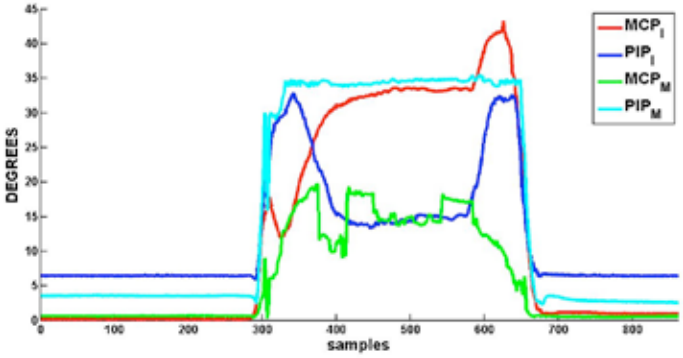

Figure 5. Flexion/Extension angle behavior of the index and middle fingers MCP and PIP joints.

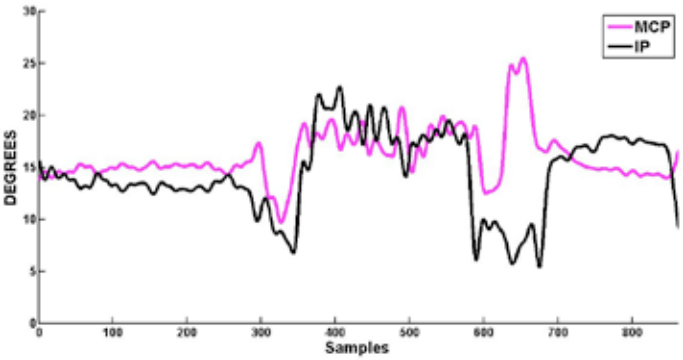

Figure 5. Flexion/Extension angle behavior of the thumb TM and IP joints.

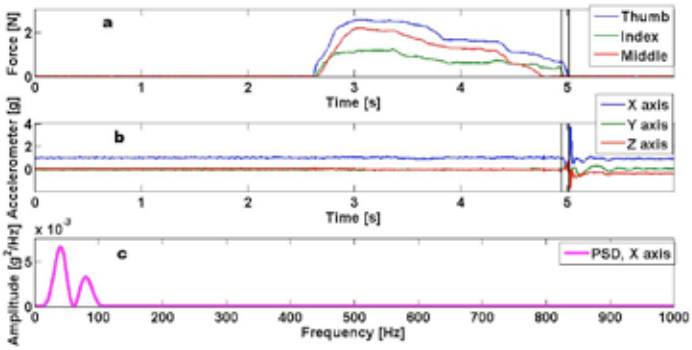

Figure 6. Finger forces (a), components of acceleration (b), and PSD (c).

Evaluation of the center of rotation with MIMUs: impact of the experimental conditions

M. Crabolu[1], D. Pani[1], L. Raffo[1], A. Cereatti[2]
[1] *Dept. of Electrical and Electronic Engineering, University of Cagliari, Italy*
[2] *University of Sassari, Italy*

***Abstract*—The automatic estimation of the centre of rotation (CoR) is a challenging issue in the identification of the kinematic chains representing the human body from a biomechanical perspective. When accurate enough, such models could be used to provide quantitative evaluation of the range of movements in different biomedical applications, such as rehabilitation and functional evaluation.**

In this paper, we investigate the possibility of identifying the CoR by means of magneto-inertial sensors in a mechanical analogue of the gleno-humeral joint. By exploiting a "functional approach", the CoR location can be identified without taking any mechanical measurement on the system, just relying on the sensors output. The influence of the experimental conditions on the quality of the solutions are analysed, revealing how performing fast movements, with the MIMU close to the CoR has a positive impact, whereas the range of motion during the trial has a negligible influence. Such information can be exploited in order to design the trial for a CoR identification with MIMUs maximizing the performance of the functional approach.

***Keywords*—inertial sensors, centre or rotation, functional approach, biomechanics.**

I. Introduction

FUNCTIONAL evaluation, human-assisted rehabilitation and self-managed rehabilitation, are typically characterized by the evaluation of range of movements by eye. Instrumenting such practices could improve the quality of the evaluation, opening new possibilities in rehabilitation. In the field, the adoption of magneto-inertial measurement units (MIMUs) could provide substantial benefits over other techniques, thanks to the unobtrusive monitoring, without the occlusion problems typical of optical and depth-sensing technologies. However, the adoption of MIMUs is hampered by the low accuracy and the complex setup, requiring anthropometric measurements and precise sensors placement on the human body. The so-called "functional approach" requires the subject to perform *ad hoc* joint movements in order to identify the parameters of the kinematic model of his body. Such an approach can be used to locate the centre of rotation of the spherical joints between the bony segments [1]. This is a well-known issue with stereo-photogrammetry techniques [2], but it is still to be evaluated with MIMUs.

In this paper, we proposed a functional approach to identify the position of the centre of rotation (CoR) of a spherical joint model from the movement data recorded using a MIMU [3]. In particular, we investigated the impact of the experimental conditions (sensors location, movement velocity and range of motion) on the CoR estimate accuracy.

II. Material and Methods

A. The mathematical model

Consider a model composed of two rigid segments connected by a spherical joint, and consider one of them fixed and the other free to move. The acceleration of a point on the moving segment, by considering a global frame (GF) with the CoR in the origin, is given by:

$$\mathbf{a} = \frac{d\boldsymbol{\omega}}{dt} \times \mathbf{r} + \boldsymbol{\omega} \times (\boldsymbol{\omega} \times \mathbf{r}) \qquad (1)$$

where $\boldsymbol{\omega}$ is the angular velocity and $\mathbf{r}$ is the distance of the point from the CoR. Eq. (1) can be re-arranged in order to exhibit the form:

$$\mathbf{K}(\boldsymbol{\omega}, \dot{\boldsymbol{\omega}})\mathbf{r} = \mathbf{a} \qquad (2)$$

where $\mathbf{K}$ is function of $\boldsymbol{\omega}$ and its time derivative $\dot{\boldsymbol{\omega}}$.

This equation is linear in the unknown vector **r,** which represents the CoR position (latent variable). The vectors $\mathbf{a}$ and $\boldsymbol{\omega}$ represent the observable variables, whereas the angular acceleration is computed as the discrete-time derivative of $\boldsymbol{\omega}$. Computing (2) for each of the N sampled instant of time recorded during an *ad hoc* movement, an oversized linear system can be obtained:

$$\overline{\mathbf{K}}\mathbf{r} = \overline{\mathbf{a}} \qquad (3)$$

Where $\overline{\mathbf{K}}$ is a 3N×3 matrix and $\overline{\mathbf{a}}$ is a 3N×1 array. The least-squares solution for $\mathbf{r}$ can be obtained by computing the pseudoinverse of $\overline{\mathbf{K}}$.

B. Validation framework

A commercial MIMU (MTx, by Xsens) has been firmly attached to a non-ferromagnetic mechanical device (Fig. 1), consisting of a rigid aluminum bar (segment 1) connected through a ball-and-socket joint to a fixed basement and built based on the dimensions of the human shoulder complex. The nominal position of the center of the spherical joint was determined from the device geometry with a tolerance of 1 mm. A cylinder with its axis orthogonal to the basement and passing through the joint, can be used to limit the range of motion of the aluminum bar to a maximum angle. The device can be manually operated, to generate movements with plausible patterns and velocities. The functional movement consisted in a cross (two arcs on two perpendicular planes). Three trials for every conditions were recorded.

The MIMU orientation was estimated using the Kalman filter by Xsens. The gyroscopes and magnetometers were calibrated before the experiments using the calibration tool

provided in the vendor's software (MT manager). The experimental conditions are reported in Table I.

TABLE I
EXPERIMENTAL CONDITIONS TESTED

Sym.	*description*	*Parameters value*
P1	MIMU close to joint	309 mm, 25 mm, 3 mm, d= 310 mm
P2	MIMU far from joint	559 mm, 25 mm, 3 mm, d= 560 mm
θ1	Smaller range of motion	45°
θ2	Larger range of motion	90°
V1	Slow motion	6 s
V2	Quick motion	2 s

For P1 and P2, the parameters represent the position of the CoR with respect to the sensor, in the LF.

C. Processing

Data processing was performed off-line with Matlab. A static acquisition phase (5 s), before and after the dynamic phase, was used to evaluate and compensate the constant bias in the gyroscope data and to verify the effectiveness of the gravitational contribution removal. The constant gyroscope bias was partially compensated by subtracting from the gyro signals the values obtained by averaging the first 4 s.

For each trial, the error was computed as the absolute value of the difference between the CoR nominal position and the estimated position. A comparison between different experimental conditions was carried out in terms of mean and standard deviation of the error over the three trials repetitions.

III. RESULTS

Results are reported in the bar charts in Fig. 2. Each bar represents the mean error (± std) of the estimated distance between the CoR and the origin of the sensor's reference.

The different experimental conditions have different impact on the quality of the CoR estimation from MIMUs. Variations in the methodology implementation largely affected the CoR estimation. The most critical factor resulted to be the speed of the joint movement used for the CoR estimation, followed by the distance of the sensor from the CoR and, lastly, the range of motion. Such results are important for a perspective biomedical applications since they suggest that this methodology can be applied to impaired patients with limited range of motion. Conversely, since the motion speed is the most critical aspect, larger errors can be expected on patients with bradykinesia.

IV. CONCLUSION

The findings of the present study encourage the application of this technique for studies on human subjects. Since the achieved accuracy levels are comparable with state-of-the-art optoelectronic stereo-photogrammetry techniques [4], the potentialities of the proposed approach can be investigated in clinical scenarios. Currently we are investigating the quality of the approach on human subjects on the gleno-humeral joint, evaluating the accuracy and the effect of the soft tissue artefacts.

REFERENCES

[1] A. Cappozzo, "Gait analysis methodology", *Human Movement Science* 3, 27–50, 1984.
[2] V. Camomilla, A. Cereatti, G. Vannozzi, A. Cappozzo, "An optimized protocol for hip joint centre determination using the functional method," *Journal of Biomechanics*, 39, 1096–1106, 2006.
[3] H.E. Veeger, "The position of the rotation center of the glenohumeral joint," *Journal of Biomechanics* 33, 1711-1715, 2000.
[4] Piazza, S.J., Okita, N., Cavanagh, P.R. "Accuracy of the functional method of hip joint centre location: effects of limited motion and varied implementation," *Journal of Biomechanics* 34, 967–973, 2001.

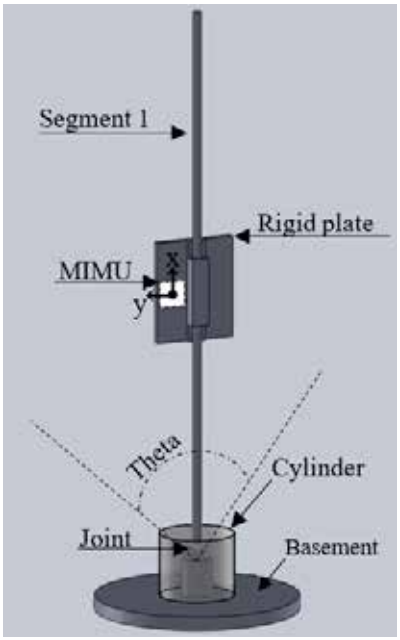

Fig. 1. A mechanical analogue of the shoulder joint. The MIMU is oriented with the x axis aligned to segment 1 and pointing to its tip; the y axis is parallel to the plane of the rigid plate and directed perpendicularly away from segment 1; z axis is oriented according to the right-hand rule.

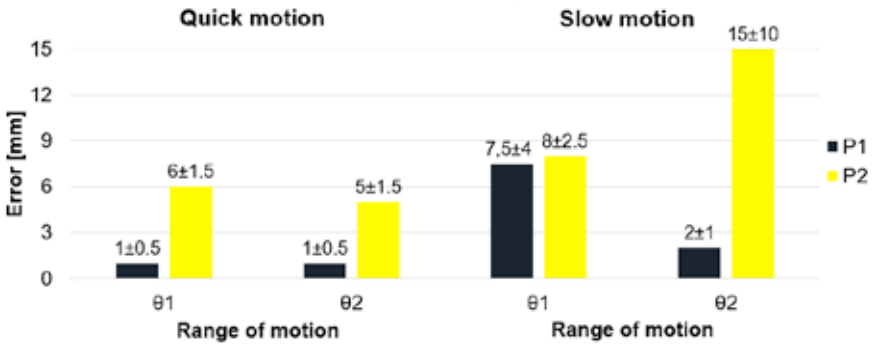

Fig. 2. Summary of the results (mean ± std) of the trials performed at different experimental conditions: different speed of motion (quick and slow), different range of motion (θ1 and θ2) and different distance of the sensor from the CoR (P_1 and P_2).

Describing the effect of different visual biofeedback presentations on postural strategies in quiet stance: a case study

C.D'Anna[1], D. Bibbo[1], M. Goffredo[1], M. Schmid[1] and S. Conforto[1]
[1] *Department of Engineering, Roma Tre University, Rome, Italy*

***Abstract*—The modality of Visual Biofeedback (VBF) presentation influences the postural performance during quiet stance. Analysis of posturographic parameters taken from force plate data revealed that the use of a discretized VBF improves the postural performance and favours a more natural postural behaviour. Conversely, literature is lacking in studying kinematics to evaluate postural strategies in quiet stance during VBF tasks. Therefore, this paper aims at studying the correlation between kinematic data obtained from motion capture, and dynamics taken form force plate data, during a baseline condition (no VBF) and during the tasks in which a continuous and a discretized VBF were randomly presented.**

During required tasks, motion capture data were used to estimate ankle and hip joint flexion-extension, while a force plate collected the centre of Pressure (CoP) coordinates. These latter ones were processed in real-time to be used in the VBFs presentations, shown on a screen in front of the subject.

The correlation between the CoP and both the hip and ankle angles was calculated, to check possible variations between postural strategies coming from the presentation of VBF. Preliminary results show different correlation values depending on the presented VBF, with an inverse correlation between hip and ankle With the small sample size now at hand, no definite behaviour appears in terms of differences, while it can be speculated that, with an extended sample it may be possible to infer on the presence of an effect of the VBFs on the contribution of hip and ankle postural strategies in quiet stance.

***Keywords*—Posture, Visual Biofeedback, Optoelectronic System, Force Plate.**

I. Introduction

Posturography is one of the biomechanical techniques dealing with the study of the neuromuscular control system and tries to provide quantitative information on the strategies underlying balance mechanisms. Upright stance, in fact, is a not trivial task and deals with keeping several joints and muscle groups in a geometric relationship with the environment [1]. Even when required to stand still, the human body cannot be considered as a motionless structure and continuous action of the central nervous system is necessary to maintain balance. Therefore, despite its seemingly simplicity, maintaining balance is a rather complex task that requires the integration of information coming from different sensory channels including proprioception, vestibulum, and vision [2].

In particular, the vision is one of the most important sources of information to keep balance [3].

Among systems developed to improve balance performance, the Visual BioFeedback (VBF) consists of delivering additional artificial visual information about body motion to supplement the natural visual information, to help improve human balance [4]. The use of real-time VBF obtained from the Centre of Pressure (CoP) during a standing task is a common tool for the evaluation and training of the postural control [5]. The CoP position is presented in real time on a monitor screen and the subject is required to confine it to the narrowest possible zone]. Literature includes a wide range of VBFs [6-8] showing that the modality of VBF presentation influences the postural performance. In particular, in a recent study [7] two different VBFs were compared: one based on the traditional CoP presentation, and a second based on the presentation of a discretized information. The analysis of the traditional postural parameters has shown that the use of a discretized VBF, as compared to the continuous VBF, favoured a more natural postural behaviour by promoting a natural intermittent postural control strategy. The possible impact on the control strategies adopted to maintain balance needs to be studied by integrating dynamics data necessary to extract CoP, with those directly related to the multi-segmental kinematics. The scientific literature on this topic, in fact, includes few studies on the kinematic analysis of upright stance maintenance with VBFs [8,9], although the importance of assessing the kinematic compensations occurring when balance is challenged under different conditions is acknowledged [10].

The aim of the present case study is to describe the effect of the two different modality of VBF presentation assessing the correlation between the anterior-posterior coordinate of CoP and the kinematic data (hip and ankle angles).

II. Materials and Methods

A. Experimental set-up and procedure

The preliminary experiments were conducted on a young volunteer (aged 32, weight 80kg, height 1.70m). He did not report neuropathies at the peripheral level, or vestibular pathologies, they had normal visual acuity and no colour blindness. He was instructed as for the experimental procedure that will be described in the following.

During the experiments the subject stood barefoot, feet together on a custom force plate and he was asked to maintain an upright natural posture with arms along his sides.

Kinematics was collected using an eight-camera BTS SMART-DX6000 (BTS Bioengineering, Milano, Italy) motion analysis system (fc = 250 Hz), calibrated over a collection volume measuring approximately 3x4x3m. Twenty-two spherical reflective (9mm) markers were applied to assess the body segment movements, according to the Davis protocol [11]. Anatomical markers were positioned on

both lower limbs over the iliac crest, the greater trochanter, the half thigh, the femoral condyle, the tibial plateau, the half shank, the malleoli, the fifth metatarsal head, the heel in addiction to ones positioned on the sacrum on both shoulders and on the 7th cervical vertebrae.

Visual biofeedback was displayed on a computer LCD 21" monitor placed in front of the subjects at a viewing distance of 1 m (Fig.1).

Three different conditions were considered, with the following instructions:

- **noVBF** : we asked to maintain a natural posture looking at a black screen positioned in front of him
- **$VBF_{continuous}$**: we asked to maintain a white spot within a red square displayed on the same black screen. The spot is a real-time representation of the CoP and the red square represents the area of stability.
- **$VBF_{discretized}$**: we asked to maintain a smiling emoji on.

In the $VBF_{continuos}$ case, a time continuous biofeedback was displayed, thus providing a detailed temporary information regarding their balancing.

In the $VBF_{discretized}$ case, a time discrete biofeedback consisting in a set of five emoticons were selected and displayed in real time on the basis of the current CoP displacement. A smiling emoji was displayed if the CoP position was inside the stability area (defined as in the $VBF_{continuos}$ task) while a sad emoticon was displayed in the opposite case, changing in shape and size depending on the direction [7]. Each condition consisted of three 30 s trials, the interval among the trials was 60 s.

B. Data acquisition and Processing

Analogue signals were low-pass filtered (10 Hz) and sampled at 100 samples/s (NI USB-6210, by National Instruments). A custom LabView code (National Instruments Corporation) was used to control the VBFs in real time and to store the CoP coordinates for offline processing. The LabView code execution was synchronized with the motion capture system by means of an external trigger communication.

From the kinematic data, the following joint rotations were calculated: ankle dorsiflexion and hip flexion-extension.

III. Preliminary Results

The correlation (*corr*) was calculated between the ankledorsiflexion angle (A_{df}) and the antero-posterior (AP_{CoP}) coordinate of the CoP, and between the hip flexion-extension angle (H_{fe}) and the AP_{CoP} coordinate.

Preliminary results show a positive correlation between AP_{CoP} and A_{df}, in each repetition, when the subject stood on force plate without a VBF (*mean_corr*=0.23) and during the $VBF_{discretized}$ task (*mean_corr* = 0.15).

Conversely, when the $VBF_{continuous}$ was presented on the screen the correlation resulted negative (*mean_corr* = -0.12, Fig.2).

At the same time, slight negative correlation between AP_{CoP} and H_{fe} appeared, in each repetition, when the subject stood on the force plate without VBF(*mean_ corr* =-0.1) and during the $VBF_{discretized}$ task (*mean_corr* = -0.28).

Conversely, when the $VBF_{continuous}$ was presented on the screen the correlation was positive (*mean_corr* = 0.15, Fig.3).

IV. Discussions and Conclusions

The aim of this preliminary study was to evaluate if the modality of VBF presentation influences the postural strategies. The first conducted experiments on a single subject show that the continuous and discretized VBFs have different effects on the adopted postural strategy.

In particular, during the $VBF_{continuous}$ presentation, ankle dorsiflexion was negatively correlated with $AP_{CoP.}$, while hip flexion-extension was positively correlated with it.

Conversely, during the $VBF_{discretized}$ presentation, ankle dorsiflexion was positively correlated with AP_{CoP}, while hip flexion-extension appeared negatively correlated with it. Moreover, the results obtained with the $VBF_{discretized}$ tasks appeared more similar to the postural strategies used in the case of noVBF.

From these results it can be observed that, when VBF is presented, hip and ankle main rotations are inversely correlated with CoP excursions, thus in agreement with a compensating postural strategy. These preliminary results encourage in the ongoing of the measurement campaign on a larger sample population.

References

[1] A. S. Pollock, B. R. Durward, P. J. Rowe, J.P Paul, "What is balance?," Clinical rehabilitation, vol. 14(4), pp. 402-406, 2000.

[2] M.G Wade, G. Jones, "The role of vision and spatial orientation in the maintenance of posture," Physical therapy, vol. 77(6), pp.619-628, 1997.

[3] N. Pinsault, N. Vuillerme, "The effects of scale display of visual feedback on postural control during quiet standing in healthy elderly subjects," Archives of physical medicine and rehabilitation, vol. 89(9),pp. 1772-1774, 2008.

[4] J. Laurens, L. Awai, C.J Bockisch, S. Hegemann et al., "Visual contribution to postural stability: interaction between target fixation or tracking and static or dynamic large-field stimulus," Gait & posture, vol. 31(1), pp.37-41, 2010.

[5] Z. Halicka, J. Lobotkova, K. Bučková, F. Hlavačka, "Effectiveness of different visual biofeedback signals for human balance improvement," Gait & posture, vol. 39(1), pp. 410-414, 2014.

[6] R.P. Cawsey, R. Chua, M.G Carpenter, D.J & Sanderson, "To what extent can increasing the magnification of visual feedback of the centre of pressure position change the control of quiet standing balance?," Gait & posture, vol. 29(2), pp. 280-284, 2010.

[7] C. D'Anna, M. Schmid, D. Bibbo, M. Bertollo, S. Comani, S. Conforto, " The Effect of Continuous and Discretized Presentations of Concurrent Augmented Visual Biofeedback on Postural Control in Quiet Stance," PloS one, 10(7), e0132711, 2015.

[8] Z. Halicka, J. Lobotkova, K. Bučková, F. Hlavačka,"Effectiveness of different visual biofeedback signals for human balance improvement," Gait & posture, vol. 39(1), pp. 410-414, 2014.

[9] S. Freitas, M. Duarte, "Joint coordination in young and older adults during quiet stance: effect of visual feedback of the center of pressure," Gait & posture, vol. 35(1), pp. 83-87, 2012.

[10] D. Abrahámová, M. Mancini, F. Hlavačka, L. Chiari, "The age-related changes of trunk responses to Achilles tendon vibration," Neuroscience letters, vol. 467(3), pp. 220-224,2009.

[11] R.B Davis, S. Ounpuu, S., D. Tyburski, J.R Gage, "A gait analysis data collection and reduction technique," Hum Movement Sci, vol. 10, pp. 575–587, 1991.

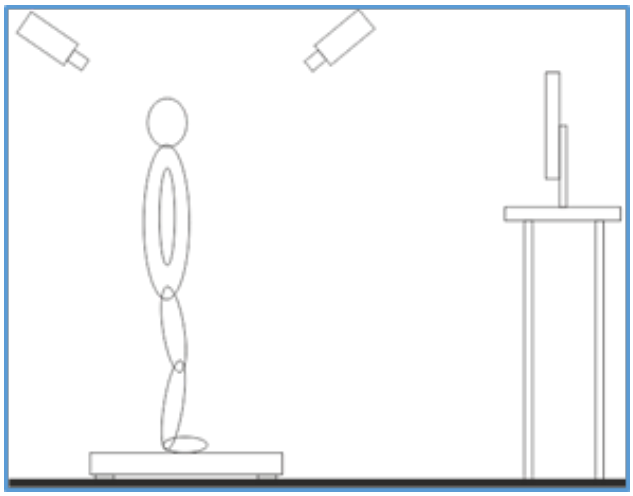

Fig.1. the experimental setup

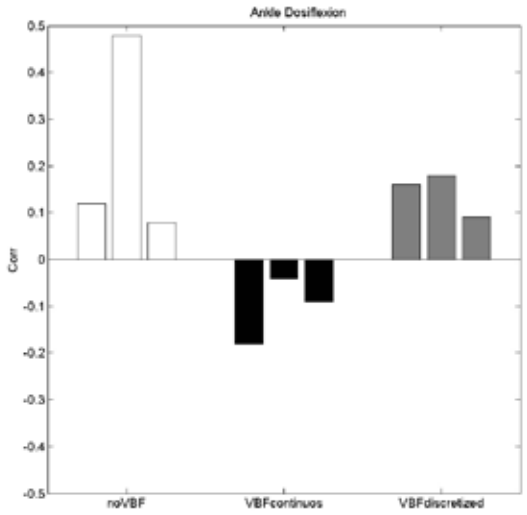

Fig.2. correlation between the AP_{CoP} and the Ankle Dorsiflexion, for each condition (noVBF, $VBF_{continuos}$, $VBF_{discretized}$) and all trials.

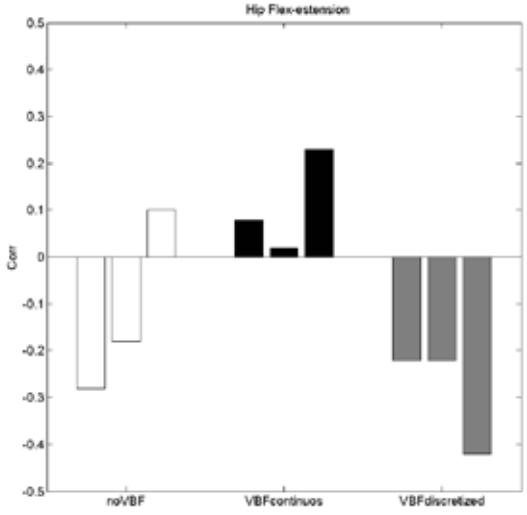

Fig.3. correlation between the AP_{CoP} and the Hip Dorsiflexion for each condition (noVBF, $VBF_{continuos}$, $VBF_{discretized}$) and all trials.

Relation between velocity and curvature of the trajectory in cursive handwriting

A. Accardo[1], P. D'Antrassi[1]
[1] *Department of Engineering and Architecture, University of Trieste, Trieste, Italy*

***Abstract*— The 2/3 power law links the kinematics of handwriting with a movement trajectory but lack of precision for handwriting movement. In order to study a more appropriate relationship between velocity and curvature in handwriting movements we examined the writing responses of 204 children from 2nd and 5th primary school. Cursive writing was acquired by a digital tablet and its dynamic aspects were studied in five different experimental conditions:two repetitive sequences of le and uno, a series of numbers (in letters) in ascending order and a sentence written in accurate and fast conditions. We found a limit law that identify the maximum velocity required to perform a specific curvature.**

***Keywords*— Handwriting, Kinematic analysis, Graphic tablet.**

I. Introduction

Since the early 1980s the study of drawing and handwriting movements has come to be known as the field of graphonomics. The main aim of this field is to identify the relationships between the planning and generation of drawing and handwriting movements. This permits to define the nature and limitations of the processes taking place at various levels of the neuromotor system as these movements evolve [1]. Nowadays, graphic tablets and appropriate software simplify and enhance graphonomics, allowing the extraction of precise kinematic features from digitally recorded writing samples [2]. In particular, the factors concerning the basic elements of writing, such as components and strokes [3] have shown to be very promising for hand motor performance quantification. A component represents the segment between two successive penlifts, while a stroke is the basic element of writing movements, delimited by the points of minimal curvilinear velocity.

According to the 2/3 power law [4], the nonlinear relationship between tangential velocity and radius of curvature of the endeffector trajectory, a very high velocity of motion does not permit the execution of accurate movements with small radius of curvature (large curvature). However, studies on this law show that it is not reliable for handwriting movements [5]. Indeed, the velocity is not proportional to the curvature because their relationship is influenced by several factors. Due to the kinematic structure of the human arm and the constraint of the central nervous system in the smooth rhythmic trajectory, the 2/3 power law is applicable only to the planar drawing patterns of relatively small size [6], and when fewer or simpler joint systems are involved (e.g. better for finger than for wrist motion) [7]. Furthermore, the power law can be considered a good model in high speed condition, when movement execution time has been set [8].

In this paper we investigated possible relation between velocity and curvature of the trajectory in cursive handwriting; in particular we examined the writing of school children from 2nd grade to the 5th grade of Primary school. Each participant had to produce two repetitive cursive sequences, about independent from linguistic aspects, then a task, partly dependent on the mathematical knowledge acquired by the child, and finally had to copy a short meaningful sentence, for which adequate linguistic competences were required.

II. Materials and Methods

A. Participants

In order to study the relation between velocity and curvature of the trajectory in cursive handwriting, 204 pupils was recruited from different primary schools of Trieste, Italy. No selection was performed on subject: Italian and no-Italian mother-tongue, both right and left-handed, with or without handwriting problems or organic pathologies, were considered. The distribution of subjects along the four considered classes and ages was: 48 in 2nd (Mean = 7.9 years ± 0.4), 43 in 3rd (Mean = 9.0 years ± 0.4), 50 in 4th (Mean = 10.0 years ± 0.3), 42 in 5th (Mean = 10.9 years ± 0.4).

Before starting the tests, written informed consent was obtained from the parents. In this study no specific neurological and neuropsychological assessments were conducted.

B. Test

All children undertook a series of five exercises: the first two tests (LE and UNO tasks) were partially independent from linguistic aspects; it required students to write in fast way, for 60 seconds, a cursive sequence of 'le' or 'uno', respectively. The third test (NUM task) was partly dependent on the mathematical knowledge acquired by the child; it required students to write in 60 seconds, as quickly as possible, numbers in cursive letters and in ascending order. In the last two tests (A and F tasks) adequate linguistic competences were required; it asked students to copy in cursive the Italian sentence: *L'elefante vide benissimo quel topo che rubava qualche pezzo di formaggio*. This sentence was constructed in order to contain all the letters of the Italian alphabet and several phonological rules. In the A task child had to write, as accurately as possible, while in the F task, he/she had to write as Fast as possible.

As regard the posture and the prehension to keep, no indication was given to the students.

C. Apparatus

Wacom Intuos 3 Tablet with Intuos Ink Pen, and ruled paper appropriate to the grade attended were used for the data acquisition. The digitizing tablet has a spatial resolution of

5µm and samples horizontal and vertical pen displacement at 200Hz. The Intuos Ink Pen enables simultaneous collection of both digital and hardcopy data, reproducing a normal pen and paper context.

D. Data Analysis

A proprietary MATLAB program [9] was used to perform this analysis.

At first, for each test, the components were identified as the written tracts between two consecutive pen lifts. Then, the horizontal and vertical pen positions were separately filtered by means of a second order lowpass Butterworth filter (10Hz cut-off frequency) with phase compensation and the curvilinear motion characteristics, i.e. position, and velocity curves were derived. To identify the strokes, an automatic segmentation procedure detected points of minimal curvilinear velocity, hypothesizing that each velocity minimum corresponds to a different motor stroke, as claimed by the bell-shaped velocity profile theory [10].

The curvature, with its direction, was calculated using the Eq (1). Positive curvature values indicate a clockwise rotation and negative curvature values a counter clockwise rotation in handwriting movements.

$$C = \frac{(v_x \cdot a_y) - (v_y \cdot a_x)}{(v_x{}^2 + v_y{}^2)^{3/2}} \qquad (1)$$

In Eq (1), v_x and v_y are respectively the maximum horizontal and vertical velocities of the considered stroke (mm/s) and a_x and a_y their first derivative with respect to time.

To study possible relation between velocity and curvature with schooling advances, at first the max value of velocity was calculated for each value of curvature and averaged across students of the same grade. For each class a curvilinear velocity-curvature curve was plotted and grouped by task.

III. Results and Discussion

A. LE task

(Fig. 1) Regarding positive values of curvature (clockwise rotation) the velocity required to perform them is the same for 4th and 5th classes. In 3rd class, the velocity for curvature values greater than 0.3 starts to move away from the curves of higher classes. This explains that, only when radius values are larger enough, pupils from 3rd can achieve the same velocity of older students; their velocity execution decreases for larger curvatures. Instead, pupils from 2nd class always keep a lower velocity respect the higher classes.

In LE task execution we expect only clockwise rotation. However some negative values of curvature was detected due to inaccurate strokes of the pen.

B. UNO task

(Fig. 2) The curve for 2nd class is different in trajectory respect the other classes: for curvature closer to zero, 2nd class achieves higher velocity and, with a higher gradient, decrease increasing the curvature.

C. NUM task

(Fig. 3) For positive curvature, we can discriminate two different trend in that 3rd with 5th and 2nd with 4th have similar curves. Regarding negative curvature, 2nd class has a different curve respect the higher classes.

D. A task

(Fig. 4) For little positive curvatures, all classes achieve the same velocities. Decreasing radius values, differences between classes become evident. Younger students cannot perform fine movements with the same velocity of older students. For negative curvatures, 2nd and 3rd classes has the same curve, velocities increase from 4th to 5th class.

E. F task

(Fig. 5) 4th and 5th have the same curves. For each curvature values the maximum velocity that students can achieved is proportional to the class attended.

IV. Conclusion

A relationship between curvature and velocity exists but it is not a close relation. The power law is applicable only to simple geometric patterns (e.g. circles, ellipses); it is not applicable to complex movements like handwriting movements.

Curvilinear velocity-curvature curves vary considerably over task although only children between 7 and 10 years was considered. On the other hand, clockwise (positive values) and counter clockwise (negative values) curvatures are different for each task and subjects.

In conclusion, the relationship between velocity and curvature is influenced by several factors that make difficult the identification of a precise and universal law describing any type of movement. In this paper we found the limit law identified by the curves that identify for each curvature value the maximum velocity value required to perform it.

References

[1] R.G. Meulenbroek, A.W. Van Gemmert, "Advances in the study of drawing and handwriting," Human Movement Science, vol.22(2), pp.131-5, 2003.

[2] L.P. Erasmus, S. Sarno, H. Albrecht, M. Schwecht, W. Pöllmann, N. König, "Measurement of ataxic symptoms with a graphic tablet: standard values in controls and validity in Multiple Sclerosis patients," J.Neursci. Methods, vol.108, pp.25-37, 2001.

[3] G.P. Van Galen, J.F. Weber, "On-line size control in handwriting demonstrates the continuous nature of motor programs," Acta Psychol. (Amst) vol.100, pp.195-216, 1998.

[4] F. Lacquaniti, C. Terzuolo, P. Viviani, "The law relating the kinematic and figural aspects of drawing movements," Acta Psychol, vol. 54, pp. 115-130, 1983.

[5] J.G. Phillips, "Can the relationship between tangential velocity and radius of curvature explain motor constancy?" Human Movement Science, vol. 27(5), pp.799-811, 2008.

[6] S. Schaal, D. Sternad, "Origins and violations of the 2/3 power law in rhythmic three-dimensional arm movements," vol.136(1), pp.60-72, 2001.

[7] L.L. Saling, J.G. Phillips, "Variations in the relationship between radius of curvature and velocity as a function of joint motion," Human movement science, vol. 24(5-6), pp.731-743, 2005.

[8] J. Wann, I. Nimmo-Smith, A.M. Wing, "Relation between velocity and curvature in movement: Equivalence and divergence between a power law and a minimum-jerk model," Journal of Experimental Psychology: Human Perception and Performance, vol. 14(4), pp. 622-637, 1988.

[9] A. Accardo, M. Genna, M. Borean, "Development, maturation and learning influence on handwriting kinematics," Human Movement Science, vol. 32, pp. 136-146, 2013.

[10] M. Djioua, R. Plamondon, "A new algorithm and system for the characterization of handwriting strokes with delta-lognormal parameters," IEEE Trans Pattern Anal Mach Intell, vol. 31(11), pp. 2060-2072, 2009.

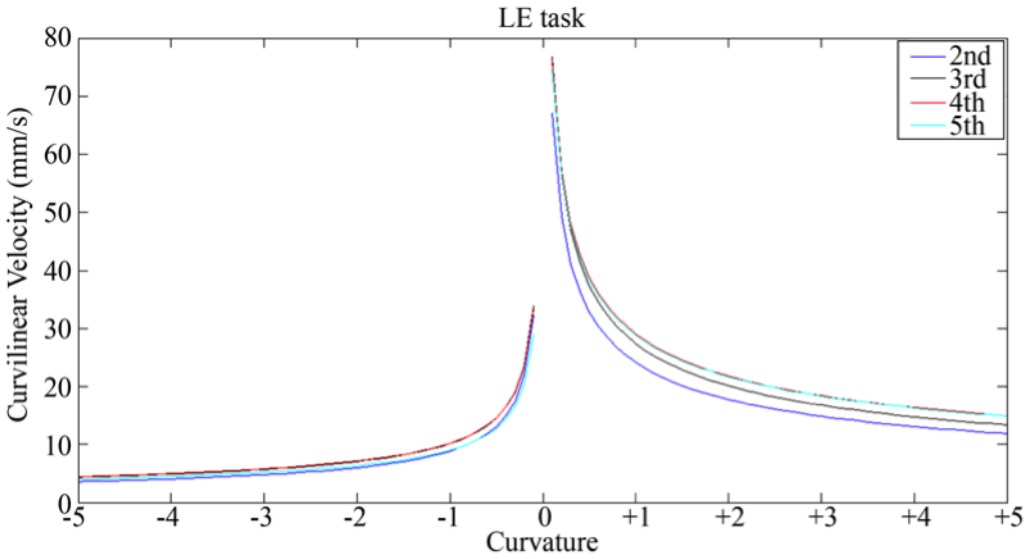

Fig. 1. Curvilinear velocity-curvature curve for each class regarding LE task's execution

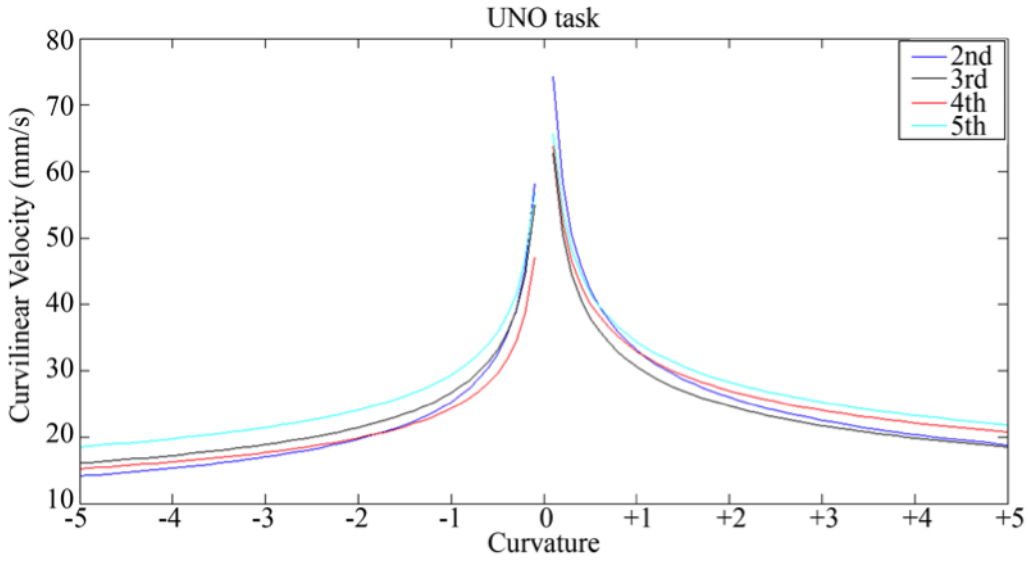

Fig. 2. Curvilinear velocity-curvature curve for each class regarding UNO task's execution

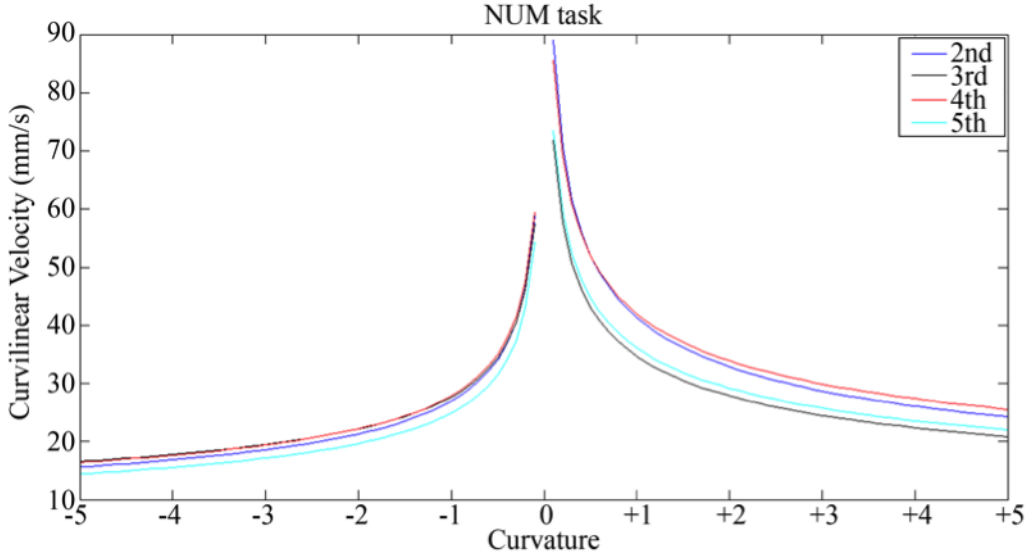

Fig. 3. Curvilinear velocity-curvature curve for each class regarding NUM task's execution

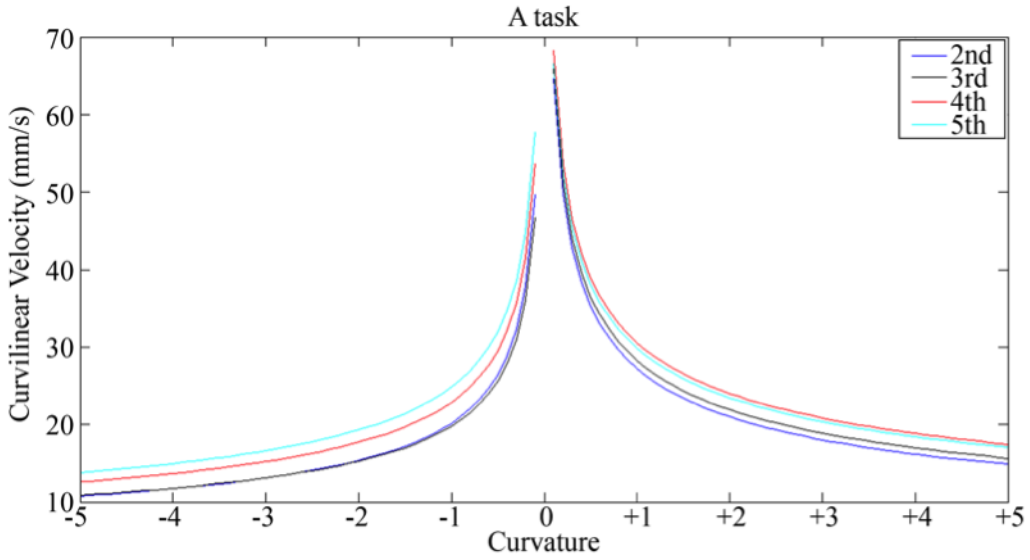

Fig. 4. Curvilinear velocity-curvature curve for each class regarding sentence task's execution in accurate (A) modality

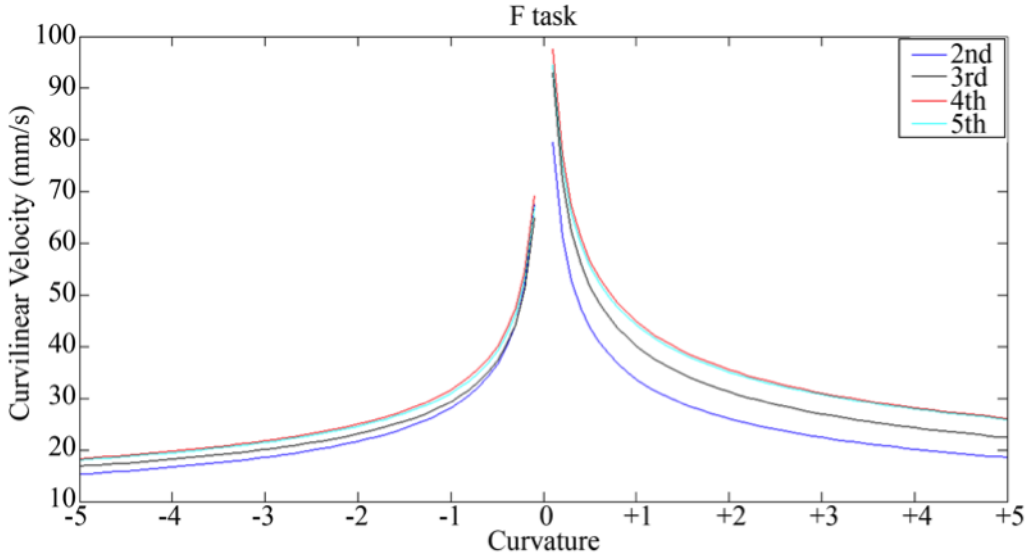

Fig. 5. Curvilinear velocity-curvature curve for each class regarding sentence task's execution in fast (F) modality

Sonification of pre and post rehabilitation writing

F. De Dea, A. Accardo, L. Cerni, and F. Costa
University of Trieste, Dept. of Engineering and Architecture

Abstract – Handwriting is considered a silent movement since the friction of the pen on the paper does not produce sound and generally it is examined by visual analysis starting from the written trace. Recently, many studies were carried out on writing acquisition performed by means of digitizing tablets that allow objective quantitative kinematic analyses of the writing quality. Duration, length, velocity, legibility, direction of letters and numbers of strokes or components are the typical kinematic parameters of handwriting movements that provide information about the development level achieved by a subject [1] and they can be also used in the evaluation of a handwriting rehabilitation treatment.

In this work a new technique for the assessment of the handwriting, useful also in the evaluation of a rehabilitation program, based on writing sonification is proposed. This technique is suitable for silent movements such as writing and it is able to help an external examiner to evaluate hidden features in order to better understand movement characteristics. The sound was associated to the handwriting velocity profile of children with handwriting problems.

In order to examine the goodness of this technique, thirteen volunteers listened two different sounds generated before and after rehabilitation, and compared their fluency. The results showed that sounds associated to different handwriting could help to distinguish between good writing and not.

***Keywords*—sonification, graphomotor rehabilitation, handwriting, dysgraphia.**

I. Introduction

Handwriting is a motor learning process that involves the coordination of several abilities. In particular phonologic, visuo-perceptive, motor and visuo-spatial abilities are the most important. Alterations in the grapho-motor production could bring to a not legible writing that both is not precociously identifiable and needs a rehabilitation process to regain a correct writing. The method based on visuo-motor feedback is widely adopted in the rehabilitation processes but also alternative proprioceptive methods have been recently proposed.

The adoption of sound feedback for the recovery of the dysgraphia could represent an alternative and complementary method besides the previous ones.

The sonification (i.e. the use of a sound for representing a physical quantity different from a sound), like visualization, can be applied to many kind of data in order to simplify the communication. In particular, it can be a valuable tool in the evaluation/transformation of a movement as well as in the motion perception supporting the possibility to use it beside the visualization feedback for physical training and rehabilitation [2]. Furthermore, the association of a sound to some kinematic parameter of a movement like, for example, velocity, fluency or pressure [3] could be also used for supporting the identification of either a good or a bad writing (dysgraphia). In the literature, many techniques to sonify a physical quantity are proposed [2], for the majority based on pitch modulation.

By handwriting sonification, we might help both therapists and teachers to evaluate the children writing, only by listening thus supporting a more precise identification of dysgraphic subjects.

Until now, very few experiments have been carried out to test the effects of handwriting movement sonification; however, preliminary results showed that the sonification of handwriting of a child without writing problems generates a more fluent and regular sound [4].

Since the curvilinear velocity profile is considered one of the most significant parameter in discerning a bad trace from a good one, in this study we sonified this kinematic parameter. In order to verify if the sonification could be an useful support in the discrimination between good and bad writing, the reproduced sound of some writing of dysgraphic children before and after a rehabilitative program was heard by a group of evaluators.

II. Materials and Methods

A. Subjects

The handwriting of 10 dysgraphic children (of primary school) recorded before and after a rehabilitation treatment, for a total of 100 sounds, was examined. The pair of sounds produced for the same writing exercise before and after rehabilitation was compared by each evaluator.

B. Tasks

Five type of writing tests were used in the following order: LE, UNO, NUM, A task and F task.

The LE test required pupils to write as quickly as possible a cursive sequence of *lelele* for a minute; the UNO task required pupils to write as quickly as possible, for a minute, a repetitive cursive sequence of the word *uno*; the NUM task required the child to write in cursive, as fast as possible, numbers (in letter) in ascending order, for a minute.

In the A and F tasks the pupils have to copy in cursive the Italian sentence: *L'elefante vide benissimo quel topo che rubava qualche pezzo di formaggio* (meaning *The elephant clearly saw that mouse stealing some pieces of cheese*). In the A task the child had to write as Accurate as possible, while in the F task he had to write as Fast as possible.

C. Handwriting acquisition

Data were acquired by means a commercial digitizing tablet (Wacom, Inc., Vancouver, WA, Model Intuos 3.0), using an ink pen and a lined paper of the adequate school grade. The pen displacement across the tablet was sampled at 200Hz and acquired with a spatial resolution of 0.02 mm.

The size of the tablet is a little bit bigger that an A4 sheet. The acquisition was carried out by a program based on the Wacom SDK (Software Development Kit, LCS/Telegraphics) and optimized for the purposes of research at the Laboratory of Biomedical Instrumentation, University of Trieste. Analysis was performed using a proprietary program written in MATLAB® [5]. The horizontal and vertical pen positions were filtered separately by means of a second order low-pass Butterworth filter (10Hz cut-off frequency) with phase compensation, and the curvilinear motion signal was derived together with the corresponding velocity.

D. Methods

For the sonification, the sound was generated by using a frequency modulation; the range of frequencies were obtained by Eq.(1).

$$frequency = curvilinear\ velocity * 30 + 200 \quad (1)$$

We multiplied the curvilinear velocity by a factor 30 and summed 200 in order to create a range of possible frequencies between 200 Hz and 2200 Hz. For each instantaneous velocity value, a sinusoidal wave with a frequency following the eq. (1) was created with a duration corresponding to a single handwriting sample interval (5ms); in this way a sequence of sounds, variables in accordance with the velocity profile, between 200 Hz (relative to the null velocity) and 2200 Hz (representing the maximum velocity) was produced. In this way a high frequency sound corresponds to a greater velocity while a low frequency sound represents a lower handwriting velocity.

E. Method assessment

In order to assess the handwriting differentiation by means of the proposed sonification method, we asked a group of 13 adult volunteers (7 females and 6 males, average age 30.2 years) to listen, for each child and each test, the two sounds corresponding to the handwriting before and after the treatment. The couple of the two sounds were presented randomly in the order (before/after or after/before treatment) and they could also be the same sound. Each sound had the same total duration of the corresponding written trace.

The evaluators were not experienced in writing and did not know the project. No one of them was hearing impaired. Their task was to tell if a difference between the two listened sounds was present (and which of them seemed more or less fluent); they could express only four type of judgment: more fluent, less fluent, equal and not catch.

III. RESULTS

Figure 1 shows an example of the written production in the test UNO with the corresponding curvilinear velocity profile.

Test A is the most recognized, indeed 62% of sounds were properly associated with pre or post rehabilitation (Fig.2), while test NUM is the least recognized (47% of sounds correctly associated).

The other tests showed a percentage of association greater than 50%, in particular the F task presented 60% of success, the LE test 53% and the UNO test 52%.

The results clearly proven that in some tests the identification of the differences before and after rehabilitation are well recognizable, demonstrating that sounds derived from less legible writings are discriminated against those readable; however, the writings with slight differences are not well discriminated yet.

IV. CONCLUSION

The purpose of this study was to study how to translate dynamic characteristics of handwriting into sounds and if these sounds could be used to identify different kind of writing. The latter could be employed to improve the diagnosis of grapho-motor problems, like dysgraphia.

The results showed that sounds are able to give information on writing and to discriminate a fluent writing from a not one. Hence, the sonification could be a very useful tool both in the diagnosis and in the rehabilitation of dysgraphia.

ACKNOWLEDGEMENT

The authors wish to thank the U.L.S.S. 7 of Pieve di Soligo (TV). Work partially supported by Master in Clinical Engineering, University of Trieste.

REFERENCES

[1] Mergl R, Juckel G, Rihl J, Henkel V, Karner M, Tigges P, Schröter A, Hegerl U. (2004) Kinematical analysis of handwriting movements in depressed patients. Acta Psychiatr Scand. 109(5):383-91.

[2] Dubus G, Bresin R (2013) A Systematic Review of Mapping Strategies for the Sonification of Physical Quantities. PLoS ONE 8(12): e82491.

[3] Thoret E. (2015) The effect of real-time auditory feedback on learning new characters, Human movement science 43:216-228.

[4] Danna J., Velay JL (2015) Basic and supplementary sensory feedback in handwriting. Frontiers in Psychology, 6:1-10.

[5] Accardo A., Chiap A., Borean M., Bravar L., Zoia S., Carrozzi M., Scabar A. (2007) A device for quantitative kinematic analysis of children's handwriting movements. Proceed. MEDICON 2007, Lubljiana 26-30 june 2007, pp 445-448.

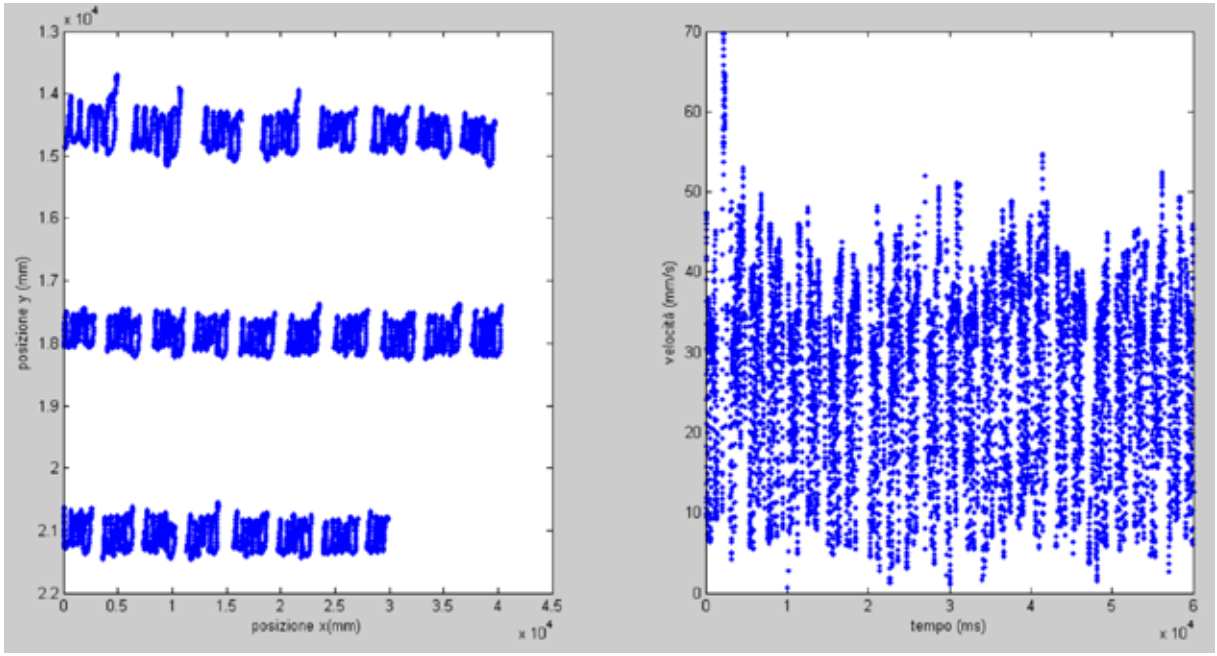

Fig. 1 Example of test UNO (left side) and corresponding curvilinear velocity profile (right side).

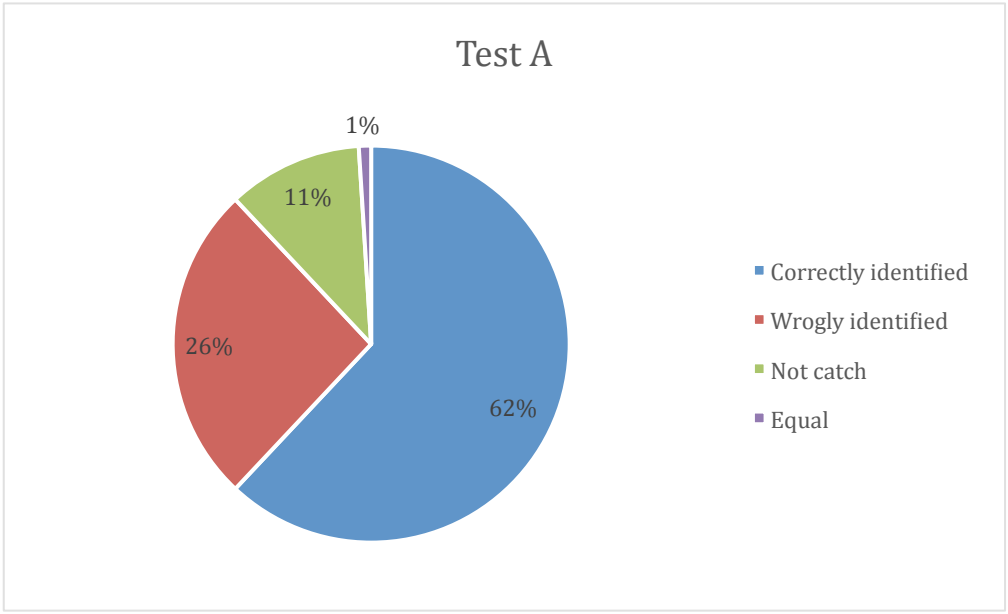

Fig. 2. Percentage of responses in the test A association between sound and writing.

Validation of a real-time gait event detection algorithm across different walking speeds

B. Fida[1], I. Bernabucci[1], D. Bibbo[1], C. Caramia[1] and M. Schmid[1]
[1] *Department of Engineering, Roma Tre University, Rome, Italy*

***Abstract*—this paper presents in-time detection of heel strike (HS) and toe-off (TO) events at three different walking speeds; slow, normal and fast. Shank mounted gyroscope was used to gather gait data from four participants. Proposed modified algorithm correctly identified the all events thus without causing any delay in events detection. The aim of the study was to build a system which can facilitate the online deployment of the algorithm with less complexity. Validation of the algorithm using optical motion analysis system shows that algorithm detects HS event earlier (4 ms) with 95% confidence interval of [-8, 0] and FO event earlier (44 ms) with 95% confidence interval of [-56, 32] than the motion capture system.**

***Keywords*—gait event detection, gyroscope, heel strike, Toe-off.**

I. INTRODUCTION

The ability to automatically and robustly segment individual strides from gait sequences derived from inertial sensors is crucial for monitoring gait variations and helps answer specific clinical needs, such as identifying disease-related patterns or quantifying gait impairments associated with movement disorders [1-3].

The development of a system able to capture these variables needs to incorporate sequentially the following three functions: (1) an accurate and robust segmentation of the gait sequences into individual strides; (2) a detection of temporal events within each stride, and a calculation of the corresponding gait parameters; (3) a comprehensive evaluation of these parameters in the context of the clinical questions [4]. This work focusses on the first function, presenting and testing a novel technique for the identification of gait events and the identification of single strides from gait performed at different velocities on a flat surface.

A number of approaches have been used to identify gait events: Aminian *et al.* [5] used gyroscopes on the shank and thigh to identify strides during straight walking, based on wavelet-based decomposition and threshold-based event detection; Catalfamo *et al.* [6] and Lee *et al.* [7] identified the initial contact and foot off events with the an average delay of 120 and 320 ms respectively; in [8], each foot-off event was detected based on the local minimum search from the expected foot-off point to zero-crossing of the next swing phase; Trojanello *et al.* [9] combined data coming from inertial sensors taken bilaterally to increase accuracy in the estimation of temporal events in gait of both controls and people with a variety of movement disorders.

This paper presented a modified gait event detection algorithm based on real-time identification from raw gyroscope data. The performance of the gyro-based system was validated against temporal events identified by a motion capture system. The remainder of this article is organized as follows: the second section presents the materials and methods used in this study; the third section elaborates the results on experiments; in the last section the conclusions are drawn.

II. MATERIALS AND METHODS

A. Methods

Inertial sensor

An inertial measurement unit (Shimmer3, Shimmer sensing, Dublin, Ireland) including one tri-axial gyroscope (±2000 deg/s) was placed on the shank of the left leg to collect the walking data at 102.4 samples/s, then resampled for validation. Only the component on the sagittal plane of the angular velocity recorded by the gyroscope was used for the analysis.

Motion capture

An optical motion capture system (Smart-DX, BTS Bioengineering, Milan, Italy) has been used as ground truth to validate the gyroscope measuring method. Eight cameras were mounted to capture the motion analysis data on a calibrated volume of around 35 m³. Four markers were placed over the foot complex of the preferred leg (over the IMU, ankle, heel and toe). The data were sampled at 250 samples/s.

Protocol

Four healthy young adults participated in this study. They walked inside the motion capture calibrated volume with three different self-selected speeds; slow, normal and fast. Each task was repeated five times to collect the sufficient data.

B. Data processing

Data obtained from the markers were processed in SMART Analyzer. Heel strike and toe-off events were obtained from the heel and toe markers.

1) Detection of gait events: Identification of the gait events *was performed on the raw gyroscope angular velocity* data. Temporal locations of h*eel strike (*HS) *and toe-off (*TO) were identified through *a modified gait event detection algorithm* that uses the sagittal component of the angular velocity: It is agreed that the two successive local minima after mid swing (maximum angular velocity) correspond to HS and TO, respectively. The algorithm thus searches for two successive zero-crossings (a negative zero-cross followed by a positive zero-cross) that are hypothesized as characteristic of the swing phase: the swing phase is thus identified if the maximum value of the angular velocity in that direction is greater than a specified threshold (2.7 rad/s). Once the swing phase is identified, the algorithm starts searching for the

following minimum value (HS). Once HS is found, the algorithm searches for the local maximum t_{max} and local minimum t_{min} and verifies the following condition:

$$if\,(t_{min} - t_{max} \geq 20\text{ ms} \,\&\, g_z\,(t_{min}) \leq -1.4\text{ rad/s} \,\&\, t_{max} - HS \geq 45\text{ ms})\ \text{then TO} = t_{min}$$

If this condition is not satisfied within 1.3 s, then the algorithm discards the current saved swing phase and starts the search for the next swing phase. A single stride is then segmented with duration as the temporal distance between two successive HSs. Figure 1 shows the algorithm detections over a single stride.

2) Accuracy of detection: to determine the accuracy of the gait event detection algorithm, HS and TO as estimated from gyro-based method were compared against those taken from the motion capture system. Difference in the events timings and in stride duration was calculated in terms of root mean square error and in percentage of the gait cycle duration, respectively.

III. RESULTS

The event detection presented in this work is a simple rule-based algorithm that detected all events, thus showing high reliability across a variety of different speeds.

Table 1 shows the mean differences in events timings estimation from those calculated from motion capture data. HS events were detected, on average approximately 4 ms earlier, with a 95% confidence interval of [-8, 0]; TO events were detected on average around 44 ms earlier, with a 95% confidence interval of [-56, 32]. As the average stride time is 1.2 s, 44 ms corresponded to around 3.6% of the gait cycle. Table 2 shows the average stride time of each subject with standard deviation.

TABLE I
DETECTION TIMING DIFFERENCE BETWEEN BOTH SYSTEMS; MEAN (RMSE) [95% CONFIDENCE INTERVAL]

	HS(ms)	*TO (ms)*
Slow	-4 (16) [-8, 0]	-60 (40) [-68, -52]
Normal	0 (16) [-4, 4]	-36 (56) [-48, -24]
Fast	0 (16) [-4, 4]	-40 (48) [-52, -28]

TABLE II
STRIDE TIMES (S): MEAN (STANDARD DEVIATION)

	Slow	*Normal*	*Fast*
Subject 1	1.26 (0.05)	0.95 (0.01)	0.98 (0.01)
Subject 2	1.32 (0.05)	1.11 (0.03)	0.88 (0.01)
Subject 3	1.29 (0.04)	1.19 (0.04)	0.98 (0.02)
Subject 4	1.69 (0.03)	1.09 (0.05)	0.9 (0.02)
Average	**1.39 (0.19)**	**1.08 (0.1)**	**0.92 (0.04)**

IV. DISCUSSION AND CONCLUSION

The present study investigates the detection of HS and TO events from a shank-mounted gyroscope. The algorithm performed well on all three walking speeds with the same threshold values, although data showed variability in walking speeds among the subjects. The results obtained in this study are comparable with others even though the position of the sensors and reference systems used are varied.

Catalfamo *et al* [6] reported a mean difference between gyroscope and reference system was <-25 ms and < -75 ms for initial contact (IC) and foot-off (FO) events respectively. Additionally, a delay of approximately 120 ms is also reported to detect FO based on the window search. Selles *et al* [10] used two uni-axial shank-mounted accelerometers to detect IC and FO, and obtained an average error of 34 ms with a 95% confidence interval of [3, 66] ms for IC and of 19 with a 95% confidence interval of [-36, 76] ms for FO. In [7], the algorithm detected FO earlier (-8 ms) and IC later (19 ms) than the reference system. Moreover, the algorithm produced a delay of 0.32 s (320 ms) to detect the gait events.

The studies cited for comparison added filtering and the use of a search window to detect the gait events. Instead, the algorithm presented in this work, which performs accurately among different walking speeds, does not add any pre-processing (except for resampling, needed for validation purposes) and the absence of search windows does not lead to additional delays for event detection. It may thus be considered as a valid alternative when real-time detection of gait events is needed.

REFERENCES

[1] T. Liu, Y. Inoue and K. Shibata., "Development of a wearable sensor system for quantitative gait analysis," *Measurement*, vol. 42, no. 7, pp. 978-988, 2009.

[2] A. Salarian, H. Russmann, F. J. Vingerhoets, C. Dehollain, Y. Blanc, P. R. Burkhard and K. Aminian, "Gait assessment in Parkinson's disease: toward an ambulatory system for long-term monitoring," *IEEE Trans Biomed Eng*, vol. 51, no. 8, pp. 1434-43, 2004.

[3] B. Mariani, C. Hoskovec, S. Rochat, C. Büla, J. Penders, K. Aminian, "3D gait assessment in young and elderly subjects using foot-worn inertial sensors," *J. Biomech*, vol. 43, pp. 2999–3006, 2010.

[4] J. Barth, O. Cäcilia, P. Cristian, S. Samuel, G. Heiko et al, "Stride segmentation during free walk movements using multi-dimensional subsequence dynamic time warping on inertial sensor data," *Sensors*, vol. 15, no. 3, pp. 6419-6440, 2015.

[5] K. Aminian, B. Najafi, C. Büla, P. F. Leyvraz and P. Robert, "Spatio-temporal parameters of gait measured by an ambulatory system using miniature gyroscopes," *J Biomech*, vol. 35, no. 5, pp. 689-99, 2002.P. Catalfamo, S. Ghoussayni and D. Ewins, "Gait Event Detection on Level Ground and Incline Walking Using a Rate Gyroscope," *Sensors*, vol. 10, no. 6, pp. 5683-702, 2010.

[6] J. K. Lee and E. J. Park, "Quasi real-time gait event detection using shank-attached gyroscopes," *Medical & Biological Engineering & Computing*, vol. 49, pp. 707-712, 2011.

[7] M. A. Azhar, D. Gouwanda and A. A. Gopalai, "Development of an Intelligent Real-Time Heuristic-Based Algorithm to Identify Human Gait Events*," In Proceedings of the IEEE-EMBS International Conference on Biomedical and Health Informatics* (BHI), Valencia, Spain, 1–4 June 2014.

[8] D. Trojanello, A. Cereatti, E. Pelosin, L. Avanzino, A. Mirelman, J.M. Hausdorff, U. Della Croce, "Estimation of step-by-step spatio-temporal parameters of normal and impaired gait using shank-mounted magneto-inertial sensors: application to elderly, hemiparetic, parkinsonian and choreic gait," *Journal of Neuroengineering and Rehabilitation*, vol. 11, no. 152, 2014.

[9] R. Selles, M. A. G. Formanoy, J. B. J. Bussmann, P. J. Janssens, H. J. Stam, "Automated Estimation of Initial and Terminal Contact Timing Using Accelerometers; Development and Validation in Transtibial Amputees and Controls," *IEEE Trans. Neural Syst. Rehabil. Eng,* vol. 13, pp. 81–88, 2005.

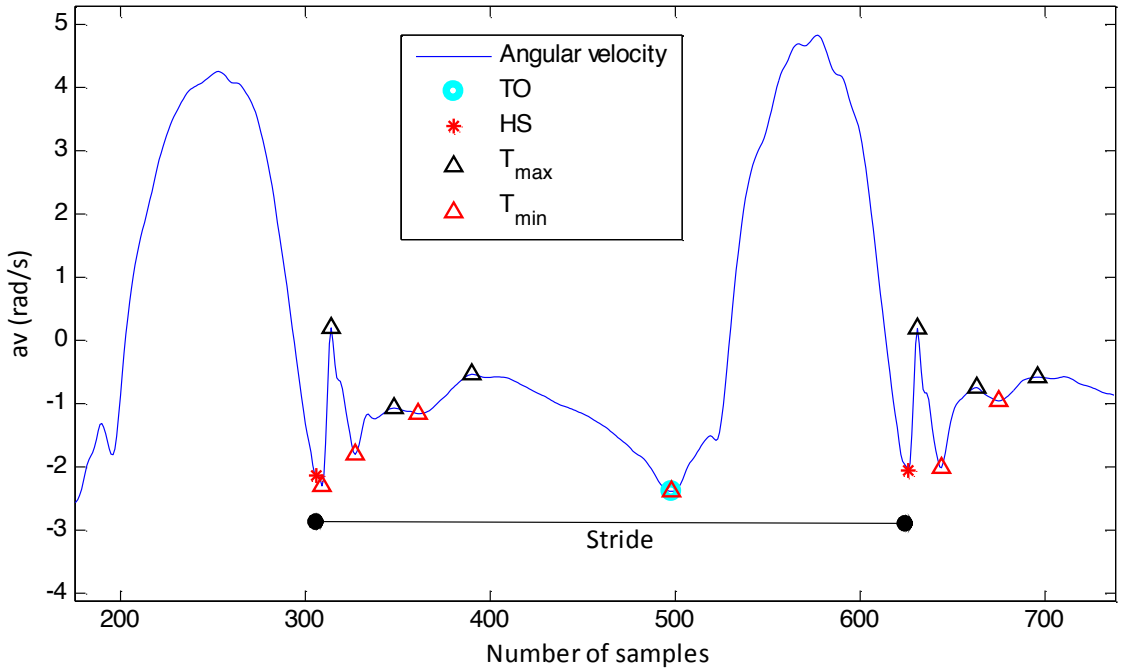

Fig. 1. Segmentation algorithm detection for a walking step, where black and red triangles are t_{min} and t_{max}, red asterisks are heel strike and aqua circles are toe-off

Correlation between clinical scales and quantitative analysis of balance and gait

L. Iuppariello[1], G. D'Addio[2], P. Bifulco[1], M. Romano[3], F. Gallo[2] , B. Lanzillo[2] and M Cesarelli[1]
[1] *Department of Electric Engineering and Information Technologies (DIETI), School of Engineering, University of Naples Federico II, via Claudio 21, 80125 Naples, Italy*
[2] *2 S. Maugeri Foundation, Rehabilitation Institute of Telese Telese Terme (BN), Italy*
[3]*DMSC, University "Magna Graecia", Catanzaro, Italy.*

***Abstract*— One-third to one-half of the population over age 65 reports some difficulties with balance or ambulation. A comprehensive clinical assessment of balance is important for both diagnostic and therapeutic reasons in clinical practice. Balance disorders can have serious consequences for physical function (leading to fall-related injuries) as well as social function (fear of falls leading to activity restriction and social isolation). The aim of this study was to investigate the correlation between the traditional clinical scales and quantitative assessment obtained by means inertial sensors in evaluating the balance and gait impairment in hemiparetic patients.**

***Keywords*—inertial sensors, rehabilitation, balance, gait.**

I. INTRODUCTION

The neuromotor rehabilitation field is among the medical specialties of greater development in the last decade and with a rapidly growing demand.

Primarily this is due to the recent advances in emergency medicine and intensive rehabilitation programs which often allow the patients to overcome the acute phase of several diseases, such as stroke, while in past often led with high probability the patient's death.

One of the critical aspect and current clinical interest in rehabilitation, is the evaluation of outcome rehabilitation, particularly in the evaluation of functional results of the rehabilitation treatments that often are exclusively entrusted by means of the qualitative and subjective methods.

One of the most appealing features of new rehabilitation programs consists in the possibility measure the clinical outcomes be means of quantitative evaluations, while traditional clinical scales permit only qualitative and potentially disagreeing evaluations[1].

Until now, the prevailing technology used in motion analysis laboratories has based on optoelectronic stereo-photogrammetric systems or systems based on the placement of passive markers, allowing the acquisition of kinematic variables non-invasively.

The optoelectronic systems that use cameras operating in the visible or near infrared range, together with the markers, representing the most widespread technological solution for the estimation of human movement.

These systems, although guaranteeing high accuracy, provide an estimate and not a direct measurement of kinematic variables.

The advantages in the use of such systems can certainly be identified in the possibility of an extremely detailed study of the kinematics of all body segments involved in the journey, but the main limits which have also limited the use in clinical practice, consist in the high cost of the instrumentation, ranging around some hundreds of thousand euro, in the long times of the examination, the need for large and perfectly mackerel spaces devoted to the laboratory and the need of a carefully trained staff to ensure the quality of the measures.

Recently an alternative method based on accelerometer systems is spreading [2-4], allowing a quantitative assessment of gait kinematics that although more simplified than the traditional method, however, often provides the clinician the main measurements of clinical interest, taking advantage of an extremely simple method, with examinations lasting a few minutes and more economic compared to the optoelectronic stereophotogrammetric systems.

The aim of this work is to study the correlation between the quantitative parameters of measurements of gait and balance measured by instrumental analysis accelerometer, and the assessment of motor disability performed with the traditional clinical scales, usually used in the medical rehabilitation field.

II. MATERIALS AND METHODS

A. Mobility Lab

The system used for the study of the way was the APDM's Mobility Lab ™ (Figure 1), which represents a new system of gait analysis and balance assessment, composed by a set of wearable inertial sensors and their docking stations. There is an Access Point for wireless data transmission, an user-friendly software to help the user and subject through the testing protocols. Finally, there is an automated analysis and reporting of the recorded data.

Three Opals are attached to the body with Velcro. The clinician, guided through the protocol, can easily abort, repeat, or comment trials as necessary.

Mobility Lab™ provides immediate access to measures of gait and balance along with matching control values to aid in research or clinical decision-making.

B. Protocol and Sway analysis

This study involved 19 hemiparetic patients enrolled through the assistance of neurologists and psychiatrists and they were be able of walking without assistance.

Three Opals sensors have been attached to the patient body with Velcro straps (one on the low back for postural sway, two on the shanks for gait). The vibrating units have been

fixed to the splenius muscles of the neck for the whole duration of the measure.
Subjects have been instructed to stand quietly for 30 s and then have been asked to walk at their comfortable speed for 7m, turn 180° and walk back to the starting point.
This protocol (Figure 2), named Instrumented Stand and Walk (ISAW) and offered by the APDM system permits to combine measures of postural sway, anticipatory postural adjustments (APA) during step initiation, gait and turning into one.
The Berg Balance Scale (BBS), the Barthel Index (BI) and the Trunk Control Test (TCT) were used to assess the impairment in balance and mobility.
The inertial sensors provided several kinematic indexes related to the balance, straight and turning gait [5-7]:
The sensors and the vibrating units have been removed after finishing 3 ISAW trials and after each ISAW trial the subjects were allowed to rest. All patients signed a consent form before involvement in the study.
In order to quantifies the degree to which the inertial balance and gait variables are related to the clinical scales, the results have been analyzed by means of the Pearson correlation.

III. RESULTS

The most interesting results are now illustrated. Figure 3 shows the highly significant correlation between the BBS and frequency variable Centroidal, 95% Frequency.

Among the several gait parameters, we have found a highly significant correlation between the BBS and RoM Shank Left and RoM Shank, as shown in Figure 4.

Moreover, we have found, a highly significant correlation between the TCT and frequency variable Centroidal (figure 5). Related to straight and turning gait, we found moderate correlation between TCT and RoM Shank L e RoM Shanke (Figure 6).

Finally we found highly significant correlation between the BI and frequency variable Centroidal and 95% Frequency (Figure 7). Related to straight and turning gait, we found moderate correlation between BI and RoM Shank Left e RoM Shanke (Figure 8).

IV. CONCLUSIONS

Summarizing, the frequency variable Centroidal, RoM Shank Left e RoM Shanke simultaneously showed significant correlations with all the considered scales. The 95% Frequency Variable has simultaneously shown correlations with Berg Balance Scale and Barthel Index.

Firstly, this study demonstrates the full clinical validity of the assessments carried out by mean of the accelerometer methodology.

We found, in fact, a significant consistency between the kinematic parameters evaluated using accelerometer sensors, and the assessment obtained by completing the clinical scales in evaluating the motor impairment.

Secondly, some of the kinematic parameters calculated by means of accelerometric system show simultaneously significant and strong correlations with multiple clinical scales. This is clear for the Centroidal Frequency Variable which significantly correlated with the scales of Berg Balance Scale, the Trunk-scale and the Barthel Index.

This consideration allows to infer that the quantitative assessment of Centroidal Frequency variable can provide the same information resulting from the compilation of qualitative three different clinical scales.

The latter observation is very interesting because could lead to the conclusion that the evaluation of a single parameter, such as the Centroidal Frequency variable, could substitute the qualitative scores obtained with Berg Balance Scale, the Barthel Index and the Trunk Control Test, making this parameter as one of the most promising rehabilitative clinical outcome of the motor impairment.

V. REFERENCES

[1] Krebs HI, Volpe BT, Aisen ML et al (2000). Increasing productivity and quality of care: robot-aided neuro-rehabilitation. J Rehabil Res Dev; 37:639-52.
[2] K. M. Culhane, M. O'Connor, D. Lyons, and G. M. Lyons,"Accelerometers in rehabilitation medicine for older adults," Age Ageing, vol. 34, no. 6, pp. 556–560, Nov. 2005.
[3] R. E. Mayagoitia, A. V. Neneb, and P. H. Veltink, "Accelerometer and rate gyroscope measurement of kinematics: an inexpensive alternative to optical motion analysis systems," J. Biomech., vol. 35 no. 4, pp. 537-542, Apr. 2002.
[4] C. V. Bouten, K. T. Koekkoek, M. Verduin, R. Kodde, and J. D. Janssen, "A triaxial accelerometer and portable data processing unit for the assessment of daily physical activity," IEEE Trans. Biomed. Eng., vol. 44, no. 3, pp. 136-147, Mar. 1997
[5] Mancini M, Salarian A, Carlson-Kuhta P, Zampieri C, King L, et al. (2011) iSWAY: a Sensitive, Valid and Reliable Measure of Postural Control. J Neuroeng Rehabil Under Review.
[6] Mancini M, Horak FB, Zampieri C, Carlson-Kuhta P, Nutt JG, et al. (2011) Trunk accelerometry reveal postural instability in untreated Parkinson's disease. Parkinsonism Relat Disord 17 : 557-562.
[7] Mancini M, Zampieri C, Carlson-Kuhta P, Chiari L, Horak FB (2009) Anticipatory postural adjustments prior to step initiation are hypometric in untreated Parkinson's disease: an accelerometer-based approach. Eur J Neurol 16 : 1028-1034.

Figure 1: A. Sensor dimension. B. Mobility Lab system and components

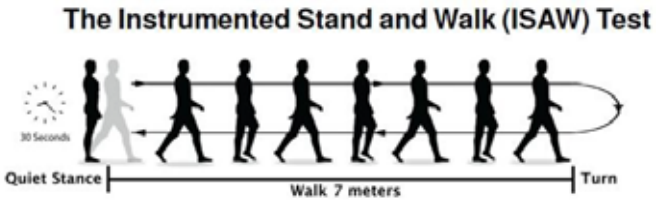

Figure 2. the ISAW protocol.

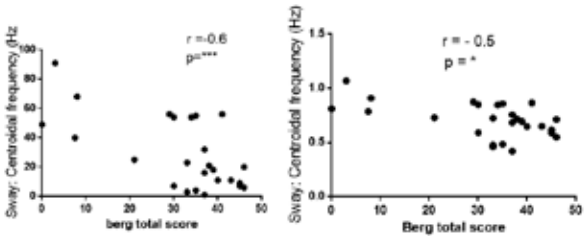

Figure 3. Correlation analysis between BBS and frequency variable Centroidal and frequency 95%.

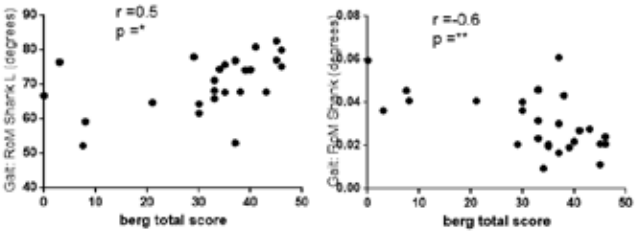

Figure 4. Correlation analysis between BBS and RoM Shank Left (degrees) and RoM Shank (degrees).

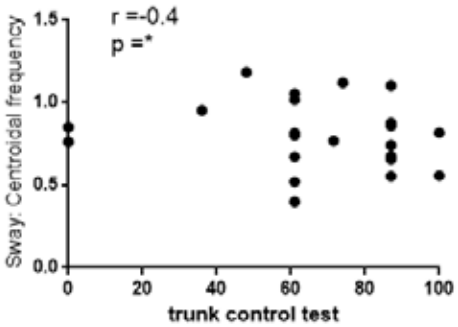

Figure 5. Correlation analysis between TCT and frequency variable Centroidal.

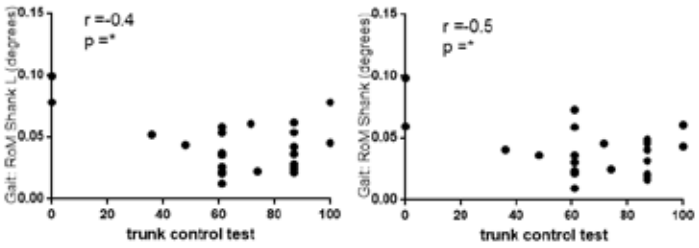

Figure 6. Correlation analysis between TCT RoM Shank Left e RoM Shanke.

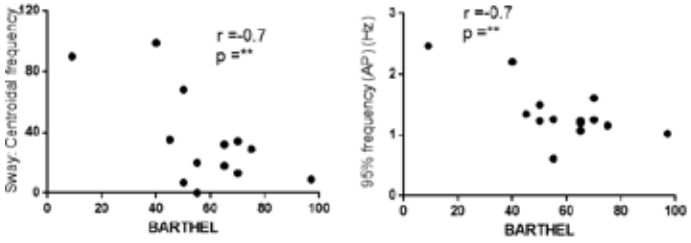

Figure 7. Correlation analysis between BI and frequency variable Centroidal and frequency 95%.

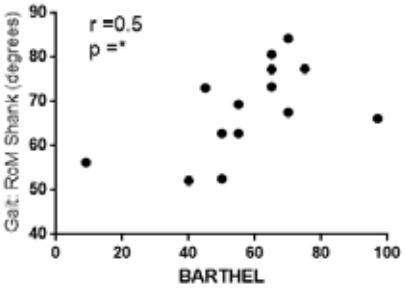

Figure 8. Correlation analysis between BI and RoM Shank (degrees).

Comparison between methods for gait events detection in Parkinson's disease

L. Pinna[1], A. Mannini[1], A. M. Sabatini[1], C.Dolciotti[2], P. Bongioanni[2], F. Saponara[3] and G. De Petris[3]
[1] The BioRobotics Institute, Scuola Superiore Sant'Anna, Pisa, Italy
[2] *Neurorehabilitation Unit, Department of Neuroscience, Pisa University Hospital, Italy*
[3] Tim, WHITE Lab, Pisa, Italy

***Abstract*—The aim of this work is to compare three methods to extract gait events for normal and pathological gait. Methods used data from wearable inertial measurement units (IMU) placed on the body centre of mass (BCOM, 1 method) or on the shanks (2 methods). Twenty-one subject with early to moderate Parkinson's disease (PD) and thirteen healthy individuals were included in this study. All subject repeated the 7 meter Timed Up and GO (TUG) test three times. Foot strike and toe off detection, obtained using the three different methods, were compared. A paired t-test was run to evaluate the shank-based gait segmentation outcomes referring to the BCOM-based segmentation method as a reference. Statistical tests did not report significant differences across the BCOM-based method and the shank–based methods when testing either healthy or pathological gait.**

Keywords—gait events, inertial sensors, gait segmentation.

I. Introduction

Accurate and efficient detection of gait events is essential for the analysis of human gait. The determination of foot strike (FS) and toe off (TO) events allows walking trials to be segmented into strides and discriminating the stance and the swing phases. This eases the comparison across multiple strides and walking trials. Gait data are usually assessed in clinical settings with reference to gait events or phases, to estimate variables such as knee flexion at heel strike or knee moment at fifty percent of stance phase. Then an accurate and consistent gait events detection throughout a trial is critical.

Researchers have used several experimental methods to determine gait events. The current gold standard solutions for gait phases segmentation require structured environment with complex instrumentation such as optoelectronics systems, force sensitive walkway, or a walkway containing multiple force plates [1][2]. Alternative wearable-sensors based solutions can use for example pressure sensitive foot switches that have been employed to detect when a load is placed on or removed from the foot, allowing then to determine FS and TO events [3][4]. However, this approach requires the modification of the subject's footwear. Furthermore it has limited use in subject populations with abnormal gait, especially in populations in which the subject lacks sufficient foot clearance during the swing phase. Novel techniques, based on the use of miniature gyroscopes have also been used to determine the timing of gait events and looks promising for the application to abnormal gait conditions [5][6][7].

In this work, three computational methods of determining gait events from wearable sensors (accelerometers and gyroscopes) data during TUG test are compared. The overall objective of this study was to evaluate the ability of the three algorithms to predict gait events by comparing the computationally predicted events among each other. In order to evaluate the robustness of the algorithms, data were collected from a variety of subject populations including healthy and Parkinson's disease (PD) subjects.

II. Materials and Methods

Data were collected from 13 healthy adult subjects, with no history of gait issues, age 70.7 ± 6.9 years, weight 72.5 ±12.1 kg, and from 21 people with PD, from stage 1 to 4 of Hoehn and Yahr scale, age 70 ± 8.4 years, weight 68.8 ±14.9kg.

Participants were asked to perform the TUG test: rise from a chair, walk seven metres at their normal comfortable speed, turn around, walk back to the chair, and sit down.

During the test, the subjects wore their regular footwear and did not use any mobility aid. Three inertial measurement units (IMUs) have been used for this study at the body sites of interest: body centre of mass (BCOM), right and left shank to detect some gait events.

A. Data Acquisition

A dedicated custom-made Android application was used to connect, synchronize, stream and save data from wearable sensors during the exercises. Three custom-made IMUs [8] sampling at 100 Hz, were placed on participant during tests using elastic bands. Each IMU contained a tri-axis angular rate sensor (gyro) with a sensitivity up to 131 LSBs/dps and a full-scale range of ±250dps and a tri-axis accelerometer with a programmable full scale range of ±2g. One sensor was secured on the region around the third lumbar vertebrae L3, (BCOM), and the others were placed on the anterior aspect of the right and left tibia, For our purposes, only accelerometer and gyroscope signals were retained.

B. Data Analysis

Data processing was done offline in MATLAB® (Math-Works, Inc., Natick, MA, USA). Inertial sensors data were then filtered using a 2nd order Butterworth band-pass filter with cut-off frequencies of 0.2 and 15 Hz. Gait data were then automatically located into the trials and separated from data corresponding to sit to stand transition (SiST) and stand to sit transition (StST). To do so the angular velocity of BCOM along the vertical and the medial lateral axis was used. The numerical integration of these quantities allowed an estimation of the trunk tilt angles along the two axis, indicated as θ and ϕ respectively. In particular, the zero cross of θ nearest the local maximum peak of ϕ identifies the SST transitions, Fig. 1. Once gait data were isolated, the three

segmentation methods for the extraction of FS and TO were evaluated. In synthesis the used
methods were:

- '*Peak Detection Method* (PDM)' [9]. Pattern of antero-posterior (AP) acceleration of BCOM were used to identify the FS events. The medio-lateral (ML) acceleration was used to discriminate left and right support. The vertical acceleration was used to locate the TO as the point in which the vertical acceleration was still larger than gravity, as a result of a contralateral knee extension due to activity in the quadriceps muscle, Fig. 2. This BCOM-based method, previously validated on PD subjects was used as a reference in this preliminary analysis to evaluate the efficacy of the two shank-based methods [10].
- '*Local Maximum Peaks* (LMP)'[11]. Events were determined based on shank angular velocity in the ML axis. First, the time events corresponding to the mid-swing of shank angular velocity were individuated as the local maximum peak. Mid-swing was used as reference to select the intervals in which negative peaks reminiscent of TO and FS were to be found. The nearest local minimum after mid-swing was selected as FS while the minimum preceding the mid-swing was selected as TO, Fig.3.
- *'Hidden Markov models method* (HMM)*'* [12][13]. This segmentation approach was based on the use of Hidden Markov Models (HMMs). In synthesis, such statistical method was used to provide a statistical modelling framework for gait data (accelerometers and gyroscopes). In the model definition, gait phases were paired to model states. New signals were then processed using the model to extract the more likely sequence of model states that could better explain data, corresponding then to gait phases sequence. This approach confirmed its efficacy on healthy and pathological gait and look as a promising research approach, because it could also find application on gait classification tools.

The difference in the events detection was recorded and evaluated graphically using box plots of the error occurring on the normalized stride profile, Fig. 4. Paired difference Student's t-test, was returned to determine whether significant change occurred between methods (significance level $\alpha = 5\%$). The test was done for all the combinations between the methods.

III. Results

A. Healthy Subjects

A total of 785 gait events (during TUG) were used for comparison of gait events. LMP and HMM methods determined all the gait events within a range of -10 to +10 data samples for TUG- 7 meters when compared to PDM.
No statistical differences were observed when comparing gait events using *t*-tests (*p*-values higher than 0.1).

B. PD Subjects

PD provided a total of 1658 gait cycles. Such number is larger than the one obtained by healthy subjects due to the characteristic of the pathology (make a lot of small step near the transitions: turn and StST). Confirming the tendency of previous case the LMP and HMM methods determined all the gait events within a similar range of variability and no statistical differences were observed with a p-value higher than 0.3. Table 1, shows the distribution of the bias in gait events determination between LMP and HMM methods, using PDM as reference.

TABLE I
BIAS MEAN , STANDARD DEVIATION AND MEAN ABSOLUTE ERROR (SAMPLES) IN RELATION TO PDM METHOD

	Gait Event (method)	*MEAN ± STD, MAE*
Controls	*FS (LMP)*	-0.03 ± 4.94, 3.55
	FS (HMM)	-0.42 ± 5.15, 3.71
	TO (LMP)	2.26 ± 5.45, 4.94
	TO (HMM)	1.22 ± 5.56, 4.66
PD	*FS (LMP)*	0.80 ± 5.34, 4.04
	FS (HMM)	0.83 ± 5.20, 3.81
	TO (LMP)	-1.11 ± 5.98, 5.28
	TO (HMM)	-0.31 ± 5.97, 5.17

IV. Discussion

Results from this study verified the applicability of the three tested methods to gait events detection in both healthy and PD subjects. While event detection for the healthy unimpaired subjects showed closer behaviour to the PDM, the algorithms appear to be valid for use in population where altered gait patterns are present. The large amount of gait cycles used in this work and the small average value of errors respect to the previously validated PDM approach in event prediction demonstrate the ability of the three methods to calculate gait events even in the presence of altered gait pattern.

Acknowledgement

The author s would like to thank Tim Joint White Lab, Pisa, Italy for their support.

References

[1] Brodland GW, Thornton-Trump AB. *Gait reaction reconstruction and a heel strike algorithm*. J Biomech 1987
[2] Hansen AH, Childress DS, Meier MR. *A simple method for determination of gait events*. J Biomech 2002
[3] Nilsson J, Stokes VP, Thortnensson A. *A new method to measure foot contact*. J Biomech 1985
[4] Hausdorff JM, Ladin Z, Wei JY. *Footswitch system for measurement of the temporal parameters of gait*. J Biomech. 1995.
[5] Tong K, Granat MH. A practical gait analysis system using gyroscopes. Medl Eng Phys. 1999
[6] Aminian K, Najafi B, Bula C, Leyvraz PF, Robert PH. *Spatio-temporal parameter of gait measured by an ambulatory system using miniature gyroscopes*. J Biomech. 2002
[7] Mannini, A., & Sabatini, A. M. (2012). *Gait phase detection and discrimination between walking–jogging activities using hidden Markov models applied to foot motion data from a gyroscope.* Gait posture, 36(4), 657-661.
[8] Buonocunto, Pasquale, and Mauro Marinoni. "*Tracking limbs motion using a wireless network of inertial measurement units*." 9th IEEE Internat Symp on Industrial Embedded Systems (SIES), 2014.
[9] W. Zijlstra, A. Rutgers, A. Hof, and T. Van Weerden, *Voluntary and involuntary adaptation of walking to temporal and spatial constraints*, Gait Posture, 1995.
[10] Dijkstra, Baukje, et al. "*Detection of walking periods and number of steps in older adults and patients with Parkinson's disease: accuracy of a pedometer and an accelerometry-based method*." Age and ageing 37.4 (2008): 436-441.
[11] Salarian, Arash, et al. *Gait assessment in Parkinson's disease: toward an ambulatory system for long-term monitoring.* IEEE Transact Biomed Eng, 51.8.2004
[12] Mannini, A., Trojaniello, D., Della Croce, U., & Sabatini, A. M. (2015). "*HMM-based strategy for gait segmentation using inertial sensors: Application to elderly, hemiparetic patients and Huntington's disease patients"*. Proc IEEE-EMBC (pp. 5179-5182), 2015.

[13] Mannini, A., Trojaniello, D., Cereatti, A., & Sabatini, A. M. (2016). *A Machine Learning Framework for Gait Classification Using Inertial Sensors: Application to Elderly, Post-Stroke and Huntington's Disease Patients*. Sensors, 16(1), 134.

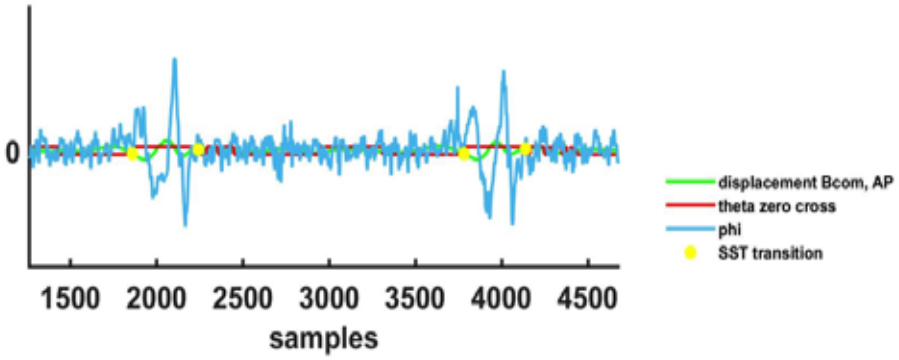

Fig 1: Integrated BCOM angular velocities, θ and ϕ variables. θ zero-crosses for the identification of sit-to-stand transitions (SST) closer to the maximum peak of ϕ are indicated with yellow dots.

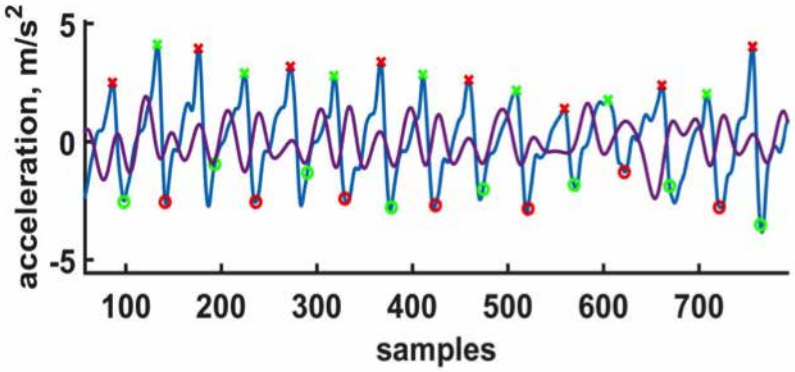

Fig 2: AP (blue) and ML(violet) acceleration data of BCOM. Cross indicates FS and the circles indicates TO, as detected from left (red) or right (green) shank.

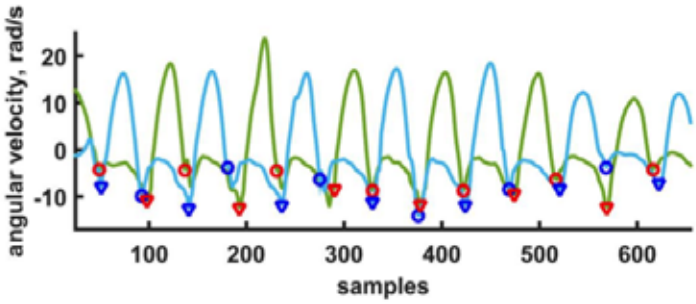

Fig 3: ML angular velocity of right (green) and left (light blue) shank. Circles indicate FS and triangles indicate TO, as detected from left (blue) or right (red), LMP method.

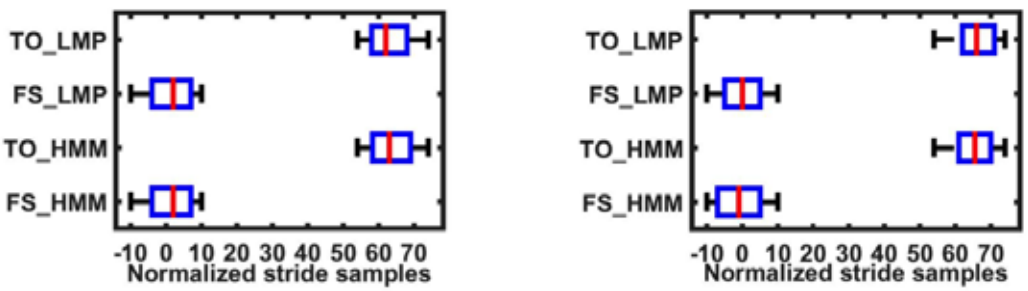

Fig 4: Box plots of gait event bias respect to the PDM approach on the normalized stride. Strides were normalized referring to the FS obtained from PDM. Left plot refers to PD subjects, right plot refers to healthy controls.

Locomotion in patients with Hereditary Spastic Paraparesis

M. Rinaldi[1], M. Serrao[2,3], A. Ranavolo[4], G. Martino[5,6], L. Leonardi[2], T. Varrecchia[1], F. Draicchio[4], F. Lacquaniti[5,6,8], G. Chini[1], C.Casali[3] and F.Pierelli[3]

[1] *Department of Engineering, Roma TRE University, 00154 Rome, Italy*
[2] *Rehabilitation Centre, Policlinico Italia, 00162 Rome, Italy*
[3] *Department of Medico-Surgical Sciences and Biotechnologies, University of Rome Sapienza, 40100 Latina, Italy*
[4] *Department of Occupational and Environmental Medicine, Epidemiology and Hygiene, INAIL, 00078 Monte Porzio Catone, Rome, Italy*
[5] *Centre of Space Bio-Medicine, University of Rome Tor Vergata, 00173 Rome, Italy*
[6] *Laboratory of Neuromotor Physiology, Istituto Di Ricovero e Cura a Carattere Scientifico Santa Lucia Foundation, 00179 Rome, Italy*
[7] *Fondazione Don Gnocchi, 20121 Milan, Italy*
[8] *Department of Systems Medicine, University of Rome Tor Vergata, 00133 Rome, Italy*

***Abstract*—The aim of this study is to completely describe (temporal, kinetic, kinematic and surface electromyographic parameters) gait in Hereditary Spastic Paraparesis (HSP) in order to individuate specific gait patterns in subgroups of patients according to lower limb joint kinematics. Forty HSP patients were evaluated by computerized gait analysis system and compared to healthy subjects. When patients were subdivided as subgroups 1 to 3, according to their kinematic behaviour, three distinctive gait patterns were observed Particularly, patients were classified as having deficits at all hip, knee and ankle level (subgroup 1), at knee and ankle level (subgroup 2), and higher activation at hip level (subgroup 3). Identifying specific gait patterns, related to both primary motor deficits and secondary compensatory mechanisms, are helpful in individualizing the pharmacological and rehabilitative treatments and better evaluating the effects over the time.**

***Keywords*—HSP, gait analysis, kinematics, sEMG.**

I. Introduction

HSP is a heterogeneous group of inherited neurodegenerative disorders characterized by retrograde degeneration of the long axonal fibers of the corticospinal tracts. Lower limb spasticity, which predominates on the muscle weakness, is the key clinical feature in patients with HSP [1] and greatly impairs their walking ability [2], [3].

Only antispastic drugs and physiotherapy [4]-[7] may be helpful to preserve gait function, then characterizing the gait impairment is crucial in HSP in order to better focus pharmacological and rehabilitation treatments. However most of the reports are based on clinical observations [1], [8]-[10] and only few studies quantitatively evaluated the gait impairment in HSP [11]-[13]. Nevertheless, the pathologic gait pattern does not reflect the clinical heterogeneity of HSP disease. Our assumption was that different joint kinematics behavior in HSP patients, due to spasticity, generated specific gait patterns.

The aims of this study were: i) to perform a comprehensive analysis of kinematics, kinetics and sEMG parameters in a sample of HSP patients; ii) to individuate specific gait patterns in subgroups of patients classified according to lower limb joint kinematics.

II. Materials and Methods

Patients and controls were evaluated and compared by computerized gait analysis system (BTS System) which recorded kinematic (8 infrared cameras-300 Hz), kinetic (two dynamometric platforms-1200 Hz) and surface electromyography (16-channel wireless system-1000 Hz). They walked at comfortable self-selected speeds along a walkway with 22 reflective spherical markers attached on the anatomical landmarks [14] and 12 bipolar electrodes placed on the right leg on the Tibialis Anterior (TA); Gastrocnemius Lateralis (LG); Gastrocnemius Medialis (MG); Soleus (SOL); Peroneus Longus (PL); Vastus Lateralis (VL); Vastus Medialis (VM); Rectus Femoris (RF); Biceps Femoris (BF); Semitendinosus (ST); Tensor Fascia Latae (TFL); and Gluteus Medium (GM) [15]-[16]. Acquisition of kinematic, kinetic and electromyographic data was integrated and synchronized. All participants provided informed written consent (Helsinki Declaration and had local ethics committee approval). After each acquisition performed by SMART Capture, 3D markers trajectories were reconstructed using SMART Tracker. Data were processed using SMART Analyzer and MATLAB.

We evaluated time-distance gait parameters (i.e. walking speed, step length, step width, stance and swing duration) and the joint range of motion (RoM) for hip, knee, ankle, trunk and pelvis. Angular impulse [17] was calculated from joint moment curves. The raw sEMG signals were band-pass filtered using a filter at 20–400 Hz, rectified, and low-pass filtered at 10 Hz. For each individual, the EMG signal from each muscle was normalized to its peak value across all trials. The co-activation of ankle muscles through the time-varying multi-muscle co-activation function (TMCf) [18] were assessed ($TMCf_{Area\_Ankle}$).

In order to classify patients according to lower limb joint kinematic behavior we used a z-test choosing a z-score of mean±1.5*SD of the joint RoMs of the control group as threshold. T-test for between-group differences and post hoc analyses between patients subgroups were performed, when significant differences were observed in the ANOVA.

III. Results

According to the z-score thresholds, three subgroups of patients were identified: i) subgroup 1: patients with hip, knee and ankle joint RoMs reduced; ii) subgroup 2: knee and ankle joint RoMs reduced and hip joint RoM close to those of controls; iii) subgroup 3: ankle and knee joint RoMs close to those of controls and hip joint RoM increased.

When comparing the whole sample of patients with controls group, significant differences were found in step length, step width, knee, ankle, trunk and pelvis RoMs and $TMCf_{Area\_Ankle}$ (Table I).

A significant effect of patients' subgroup was found on walking speed, stance, swing duration and double support duration, step length, hip, knee ankle and pelvis tilt RoMs (Fig. 1).

TABLE I
TIME-DISTANCE, KINEMATIC, KINETIC AND SEMG PARAMETERS

	HSP	*Controls*
Step length [%]	0.60	0.71
Step width[%]	0.33	0.29
Knee RoM[°]	45	59
Ankle RoM[°]	21	28
Trunk RoM[°]	26	12
Pelvis RoM[°]	17	12
$TMCf_{Area\_Ankle}$	23	13

Mean values for the whole sample of HSP patients and healthy subjects. Differences between HSP and Controls are statistically different.

IV. Discussion

In the present study we investigated the gait pattern in patients with HSP by performing a comprehensive analysis of all time-distance, kinematic, kinetic and sEMG parameters. According to previous studies [11]-[13], when comparing the whole sample of patients with controls, we found a pathologic gait pattern (Table I). However some specific biomechanical features were hidden within the global walking strategy.

Conversely, when subgrouping patients three clear gait patterns were identified. The gait pattern of subgroup 1 patients (the most severely affected with the slowest speed) was characterized by reduced hip, knee and ankle joint RoMs. The gait pattern of subgroup 3 patients (the mildest affected with the highest speed) was characterized by increased hip joint RoMs and close to controls knee and ankle joint RoMs. The gait pattern of subgroup 2 patients (disease severity and gait speed between the subgroups 1 and 3), was characterized by close to controls hip joint RoM values and decreased knee and ankle joint RoMs.

Identifying specific gait patterns allow to distinguish both primary motor deficits and secondary compensatory mechanisms and may be helpful in individualizing the pharmacological and rehabilitative treatments and better evaluating the effects over the time.

References

[1] I. Faber, K. R. Servelhere, A. R. Martinez, A. D'Abreu, I. Lopes-Cendes, M. C. França-Jr, Clinical features and management of hereditary spastic paraplegia, Arq Neuropsiquiatr, vol. 72(3), pp. 219-226, 2014.

[2] S. Klimpe, R. Schüle, J. Kassubek, S. Otto, Z. Kohi et al., Disease severity affects quality of life of hereditary spastic paraplegia patients, Eur J Neurol, vol. 19(1), pp. 168-171, 2012.

[3] D. Orsucci, L. Petrucci, E. C. Ienco, L. Chico, P. Simi et al., Hereditary spastic paraparesis in adults, A clinical and genetic perspective from Tuscany, Clin Neurol Neurosurg, vol. 120, pp. 14-19, 2014.

[4] J. K. Fink, Hereditary spastic paraplegia, Curr Neurol Neurosci Rep, vol. 6(1), pp. 65-76, 2006.

[5] Y. Zhang, R. Roxburgh, L. Huang, J. Parsons, T. C. Davies, The effect of hydrotherapy treatment on gait characteristics of hereditary spastic paraparesis patients, Gait Posture, vol. 39(4), pp. 1074-1079, 2014.

[6] H.W. Heetla, J. P. Halbertsma, R. Dekker, M. J. Staal, T. van Laar, Improved gait performance in a patient with hereditary spastic paraplegia after a continuous intrathecal baclofen test infusion and subsequent pump implantation: a case report, Arch Phys Med Rehabil, vol. 96(6), pp. 1166-1169, 2015.

[7] F. Bertolucci, S. Di Martino, D. Orsucci, E. C. Ienco, G. Siciliano et al., Robotic gait training improves motor skills and quality of life in hereditary spastic paraplegia, NeuroRehabilitation, vol. 36(1), pp. 93-99, 2015.

[8] R. D. Adams, M. Victor, A. H. Ropper, M. A. Samuels, J. Klein, Principles of neurology, 10th ed. New York: McGraw-Hill Education Medical, 2015.

[9] L. P. Rowland, T. A. Pedley. Neurologia de Merritt, 12nd ed. Nederland: Wolters Kluwer Health, 2011.

[10] T. Lo Giudice, F. Lombardi, F. M. Santorelli, T. Kawarai, A. Orlacchio, Hereditary spastic paraplegia: clinical-genetic characteristics and evolving molecular mechanisms, Exp Neurol, vol. 261, pp. 518-539, 2014;.

[11] S. Klebe, H. Stolze, F. Kopper, D. Lorenz, R. Wenzelburger et al., Gait analysis of sporadic and hereditary spastic paraplegia, J Neurol, vol. 251(5), pp. 571-578,2004.

[12] L. Piccinini, V. Cimolin, M. G. D'Angelo, A. C. Turconi, M. Crivellini, M. Galli, 3D gait analysis in patients with hereditary spastic paraparesis and spastic diplegia: a kinematic, kinetic and EMG comparison, Eur J Paediatr Neurol, vol. 15(2), pp. 138-145, 2011.

[13] J. Marsden, G. Ramdharry, V. Stevenson, A. Thompson, Muscle paresis and passive stiffness: key determinants in limiting function in hereditary and sporadic spastic paraparesis, Gait Posture, vol. 35(2), pp. 266-271, 2012.

[14] III R. B. Davis, S. Õunpuu, D. Tyburski, J. R. Gage, A gait analysis data collection and reduction technique, Hum Mov Sci, vol. 10, pp. 575–587, 1991.

[15] H. J. Hermens, B. Freriks, C. Disselhorst-Klug, G. Rau, Development of recommendations for SEMG sensors and sensor placement procedures, J Electromyogr Kinesiol, vol. 10(5), pp. 361-374, 2000.

[16] M. Barbero, R. Merletti, A. Rainoldi, Atlas of muscle innervation zones: understanding surface electromyography and its applications, New York: Springer, 2012.

[17] R. Don, M. Serrao, P. Vinci, A. Ranavolo, A. Cacchio et al., Foot drop and plantar flexion failure determine different gait strategies in Charcot-Marie-Tooth patients, Clin Biomech, vol. 22(8), pp. 905-916, 2007.

[18] A. Ranavolo, S. Mari, C. Conte, M. Serrao, A. Silvetti et al., New muscle co-activation index for biomechanical load evaluation in work activities, Ergonomics, vol. 58(6), pp. 966-979, 2015.

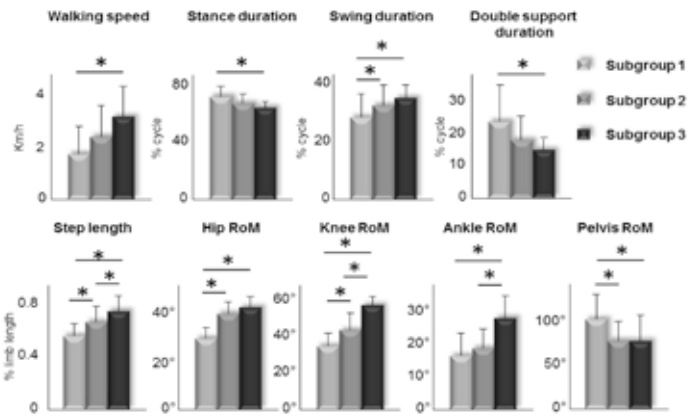

Fig. 1. Mean values (±SD) of time distance and kinematic parameters (RoM) in HSP subgroups. * significant differences among the three subgroups at post hoc analysis.

NNSVD Based Method to Extract Muscle Synergies

Mumtaz Hussain Soomro, Cristiano De Marchis, Silvia Conforto, Gaetano Giunta
Department of Engineering, Roma TRE University, Via Vito Volterra 62, 00146 Rome, Italy.

***Abstract*— In this paper a novel method based on Non-negative Singular Value Decomposition (NNSVD) to extract muscle synergies is proposed. The proposed method is compared with traditional and commonly used Non-negative Matrix Factorization (NNMF) method on simulated data. Simulated data are generated from synthetic synergies, whose activation coefficients are corrupted either by making them highly correlated or by adding noise in order to obtain low SNR levels. The performance of both methods (i.e. NNSVD and NNMF) are assessed by using quality of identification of the original simulated synergies, starting from the decomposition of a simulated dataset. Simulation results demonstrate that NNSVD has achieved better quality of reconstruction in extracting muscle synergies than NNMF in the presence of correlation in the data and low SNR levels.**

***Keywords*—Electromyography (EMG), Muscle synergy, NNMF, NNSVD.**

I. Introduction

MUSCLE synergies are a pattern of synchronized activations of a group of muscles which are used by the central nervous system (CNS) to create muscle activity for movement production [1-2]. Muscle synergies are extracted from surface myoelectric data. Recently, various dimensionality reduction methods have been used to extract and analyse muscle synergies for neuromuscular control including: Factor analysis (FA) [3], Principle Component Analysis (PCA) [4], Independent Component Analysis (ICA) [4], and Non-negative Matrix Factorization (NNMF) [4-7]. Among the above mentioned methods, NNMF is the most commonly and prominently used method to extract muscle synergies from EMG data. In [4] and [7], the performance of these methods (i.e. FA, PCA, ICA and NNMF) were compared and discussed in detail. The authors suggested that the PCA performance were lower than other methods whereas FA and ICA were almost at the same level in identifying muscle synergies. However, NNMF was better than FA and ICA due to its non-negativity constraints and low computational complexity but it was found that likewise FA and ICA, NNMF also could not accurately identify existing muscle synergies in the following cases: 1) when data was contaminated with noise and 2) when synergy activation coefficients were correlated. Therefore, considering these facts, a study has been carried out to overcome the limitations of NNMF. In this regards, a novel method based on Non-negative singular value decomposition (NNSVD) is proposed. In [8], NNSVD has been applied successfully on the microarray data of spermatogenesis to have correlated biological processes and it was demonstrated that NNSVD has achieved better results than NNMF.

In this work, muscle synergies are extracted from EMG data using NNSVD method based on the Weixiang Liu algorithm [8]. NNSVD is adopted by incorporating non-negativity constrains in singular value decomposition (SVD) and multiplicative update rules. The preliminary results of extraction of muscle synergies from simulated EMG data reveal that that NNSVD in extracting muscle synergies performs better than traditional NNMF.

The rest of the paper is organised as follows. Section II presents the simulation of muscle synergies and muscle activation coefficients with controlled signal to noise ratio (SNR) and controlled correlation among muscle activation coefficients. Section III gives a brief description of the methods. Section VI discusses preliminary results of the proposed method and finally conclusion is provided for future direction in Section V.

II. Generation of Simulated Data

The main goal of simulating EMG data is to assess the performance of the proposed NNSVD method in extracting muscle synergies. This is done by assessing the quality of synergy identification, by using different SNR values and different ranges of correlation between muscle activation coefficients. Non-negative simulated data were generated with two numbers of basis vectors (i.e. synergies), four data dimensions (i.e. muscles) and the data were consisted of 1000 data points; such as [4]

$$D = w \times c + E \qquad (1)$$
$$s.t. \quad c \geq 0 \quad and \quad w \geq 0,$$

where $c \varepsilon \mathbf{R}_{+}^{k \times 1000}$ is the synergy activation coefficient matrix containing the activation of a single synergy in each row, and k denotes number of synergies, $w \varepsilon \mathbf{R}_{+}^{4 \times k}$ is the synergy matrix where each column is a synergy vector and contains four dimensions (i.e. muscles) in each synergy vector, $E \varepsilon \mathbf{R}^{1000 \times 4}$ is additive Gaussian noise (AGN) which is levied to the generated data based on different signal to noise ratio (SNR) levels and $D \varepsilon \mathbf{R}_{+}^{4 \times 1000}$ is the data generated from the simulated synergies. In this simulation study, for every trial, activation coefficients are generated randomly with controlled correlation between them.

III. Methods

A. Nonnegative Matrix Factorization (NNMF)

Nonnegative matrix factorization (NNMF) has been widely explored and it has been proven to be a powerful method for analysis of nonnegative data [2], [4], [6-7]. Concisely, NNMF factorizes the given nonnegative data $D \varepsilon \mathbf{R}_{+}^{m \times n}$ into two nonnegative matrices w and c such that:

$$D \approx w \times c, \qquad (2)$$

where $w \varepsilon \mathbf{R}_{+}^{m \times k}$ is matrix of muscle synergy vectors, $c \varepsilon \mathbf{R}_{+}^{k \times n}$ is activation coefficient matrix and k is the number of synergies. Typically, NNMF minimizes the nonnegative

matrices Frobenius norm $\| D - wc \|_{Fro}^2$ iteratively by incorporating multiplicative update rules explained in [5], such that:

$$w_{ik} \leftarrow w_{ik} \frac{(Dc^T)_{ik}}{(wcc^T)_{ik}}, \; c_{kj} \leftarrow c_{kj} \frac{(w^T D)_{kj}}{(ww^T c)_{kj}}. \quad (3)$$

NNMF considers nonnegativity constraint on *w* and *c* matrices which makes it advantageous over traditional ICA and PCA [4], particularly in muscle synergy extraction [4], [7]

B. Nonnegative Singular Value Decomposition (NNSVD)

The proposed NNSVD for the extraction of muscle synergies from nonnegative EMG data is summarized as below:

Step 1. Apply SVD on data matrix $D \varepsilon \mathbf{R}_+^{m \times n}$ to decompose *D* into two left and right real orthonormal matrices $U \varepsilon \mathbf{R}^{m \times m}$ and $V^T \varepsilon \mathbf{R}^{n \times n}$, and nonnegative diagonal matrix $S \varepsilon \mathbf{R}_+^{m \times n}$, such that:

$$D = USV^T \quad s.t. \quad S \geq 0. \quad (4)$$

Step 2. In order to achieve nonnegativity in SVD, optimize eq. (4) as

$$\min \quad f_D(U,S,V) = \frac{1}{2} \| D - USV^T \|_{Fro}^2 \quad (5)$$

$$s.t. \qquad \{U, V \; and \; S\} \geq 0. \quad (6)$$

Where $\|.\|_{Fro}$ is a known as Frobenius norm.

Step 3. To solve the problem for *w* and *c* in eq. (1), multiplicative updates are derived as [5], [8]

$$u_{ik} \leftarrow u_{ik} \frac{(DV^T S)_{ik}}{(USVV^T S)_{ik}} \quad (7)$$

$$v_{lj} \leftarrow v_{lj} \frac{(D^T US)_{lj}}{(V^T SU^T US)_{lj}} \quad (8)$$

$$s_{kl} \leftarrow s_{kl} \frac{(U^T DV^T)_{kl}}{(UU^T SVV^T)_{kl}} \quad (9)$$

where *u*=*w*, *v*=*c* and *s* contains singular values which may use for sorting the learned basis vectors.

Step 4. Stop updating factors (i.e. *u*, *v*, and *s*), if $\| D - USV^T \|_{Fro} \leq thr$, where *thr* is a certain set threshold (i.e. *thr* = 0.01).

In order to validate the proposed method NNSVD, a statistical parameter, i.e. the quality of reconstruction (QR), is used. QR calculates an average similarity based on correlation between generated muscle synergies and the synergies extracted by an algorithm. The QR gives a value between -1 and 1, with 1 indicating highest similarity between extracted muscle synergies and simulated muscle synergies. The proposed method is compared with traditional NNMF method in extracting synergies using this performance metric.

QR is computed with NNSVD and NNMF for simulated data presenting different SNR values (i.e. 20dB, 15dB, 10dB and 5dB) along with different ranges of correlation (using 10 steps from 0 to 1) among muscle activation coefficients. The average value of QR over 30 runs is computed between the original muscle synergies, synthetically generated, and the synergies extracted by NNSVD and NNMF.

IV. Results

Fig. 1, 2, 3, and 4 shows the comparison between NNSVD and NNMF when SNR level is 20dB, 15dB, 10dB, and 5dB respectively. From the figures, it can be seen how the performance of NNMF and NNSVD are similar when the correlation among muscle activation coefficients is low and the SNR level is high. The results also demonstrate that the performance of NNMF decrease dramatically when correlation among muscle activation coefficients increases and SNR level decreases. Vice versa NNSVD maintains the same level of performance, thus presenting a behaviour that seems to be independent from SNR and correlation.

V. Discussion and Conclusion

In this paper, the performance of the proposed method NNSVD in extracting muscle synergies is investigated and compared with traditional method NNMF. Simulation results of an average of 30 runs show that NNDSVD has achieved better quality of reconstruction than NNMF over different range of correlation among muscle activation coefficients along with different SNR levels. Hence, NNSVD may be used more effectively than NNMF for those applications where muscle activation coefficients are highly correlated and the extraction of accurate structure of synergies is required, such as; execution of movement after stroke [9-10], muscle synergy analysis in children with dystonia [11] and cerebral palsy [12]. In addition, proposed method has an advantage over NNMF: NNMF has only two factor matrices while NNSVD has three; one extra factor i.e. '*S*', that can be used to identify additional features in the data.

References

[1] P.J. Cordo, C.C. Bell, S. Harnad, " Motor Learning and Synaptic Plasticity in the cerebellum," *Cambridge, UK: Press Syndicate of the University of Cambridge, Cambridge University Press*, 1997.

[2] T. Wojtara, F. Alnajjar, S. Shimoda, H. Kimura, " Muscle synergy stability and human balance maintenance," *Jr. of NeuroEngineering and Rehabilitation*, vol. 11, no.129, pp. 1-9, 2014.

[3] L.A. Merkle, C.S. Layne, J.J. Bloomberg, J.J. Zhang, "Using factor analysis to identify neuromuscular synergies during treadmil walking," *Jr. of NeurosciMethods*, vol. 82, pp. 207–214, 1998.

[4] M. C. Tresch, V. C. K. Cheung, A. d'Avella, "Matrix Factorization Algorithms for the Identification of Muscle Synergies: Evaluation on Simulated and Experimental Data Sets," *Jr. of Neurophy.,*Vol. 95, no. 4, pp. 2199-2212, 1 April 2006.

[5] D.D. Lee, and H.S. Seung, " Algorithms for non-negative matrix factorization," *Adv. Neural Inform. Process. Syst.* Vol. 13, pp.556–562, 2001.

[6] D.J. Berger, and A. d' Avella, "Effective force control by muscle synergies" *Frontiers in Computational Neuroscience*, vol. 8, article 46, pp. 1-13, 2014.

[7] K. M. Steele, M. C. Tresch, E. J. Perreault, "Consequences of biomechanically constrained tasks in the design and interpretation of synergy analyses," *Jr. of Neurophy.* Vol. 113, no. 7, pp. 2102-2113, 2015.

[8] W. Liu, A. Tang, D. Ye and Z. Ji, "Nonnegative singular value decomposition for microarray data analysis of spermatogenesis," *In proc. of 5th Int. conf. on Information Technology and Applications in Biomedicine (ITAB)*, pp. 225-228, 2008.

[9] M. G. Bowden, A. L. Behrman, R. R. Neptune, C. M. Gregory, S. A. Kautz, "Locomotor Rehabilitation of Individuals With Chronic Stroke: Difference Between Responders and Nonresponders," *Arch. of Phy Med and Rehabil,* Vol. 94, Issue 5, pp. 856-862, May 2013.

[10] J. Roh, W. Z. Rymer, E. J. Perreault, S. B. Yoo, R. F. Beer, "Alterations in upper limb muscle synergy structure in chronic stroke survivors," *Jr. of Neurophys.* Vol. 109, No. 3, pp. 768-781, 2013.

[11] F. Lunardini, C. Casellato, M. Bertucco, T. D. Sanger and A. Pedrocchi, "Muscle synergies in children with dystonia capture "healthy" patterns regardless the altered motor performance," In the proc. of *37th Annual Int. conf. of IEEE on Engineering in Medicine and Biology Society (EMBC)*, pp. 2099-2102, Milan, 2015.

[12] L. Tang, F. Li , S. Cao , X. Zhang ,DeWu and X. Chen, "Muscle synergy analysis in children with cerebral palsy," *Jr. Neural Eng.* Vol. 12, pp. 1-14, 2015.

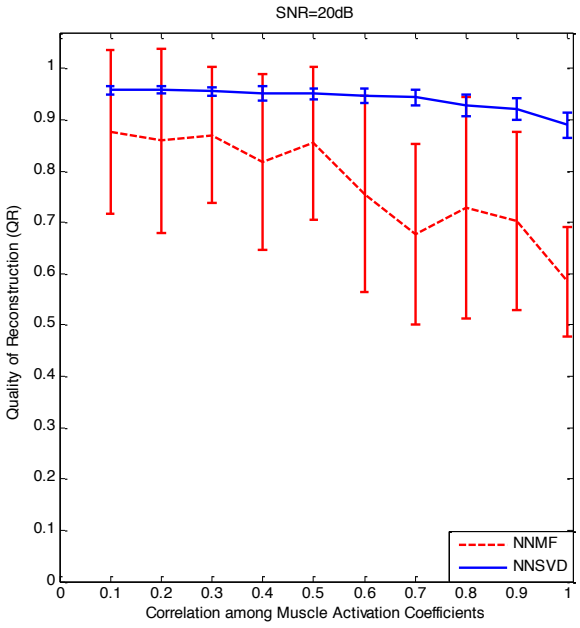

Fig. 1. Comparison between NNMF and NNSVD when SNR = 20dB

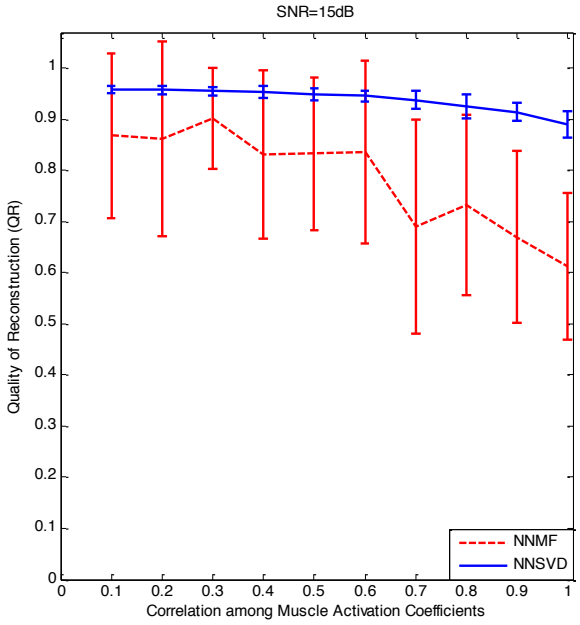

Fig. 2. Comparison between NNMF and NNSVD when SNR = 15dB

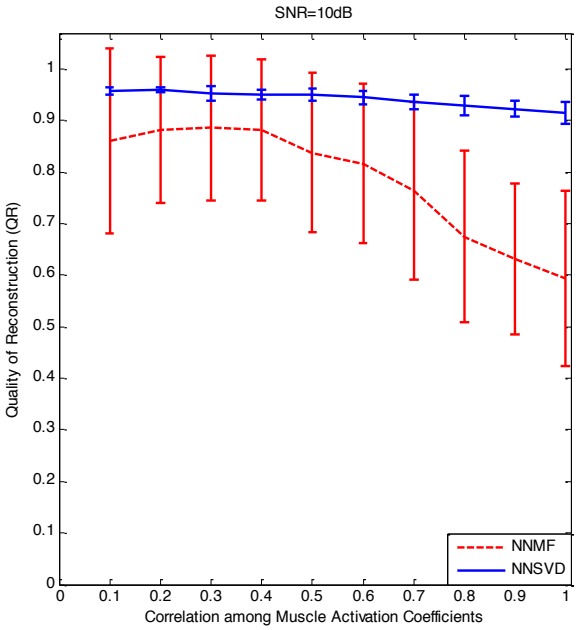

Fig. 3. Comparison between NNMF and NNSVD when SNR = 10dB

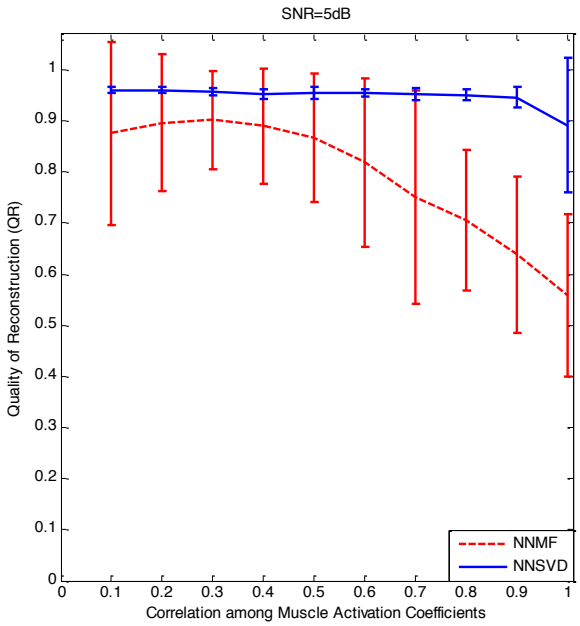

Fig. 4. Comparison between NNMF and NNSVD when SNR = 5dB

Inter-foot distance measured during gait with wearable IMU and IRR sensors

N. Valeri[1], D. Trojaniello[1,2], A. Cereatti[1], K. Aminian[3] and U. Della Croce[1]
[1] *Information Engineering Unit, POLCOMING Dept. University of Sassari, Sassari, Italy*
[2] *e-Services for Life and Health - San Raffaele Scientific Institute, Milan, Italy*
[3] *Laboratory of Movement Analysis and Measurements, EPFL, Lausanne, Switzerland*

***Abstract*— Inter-foot distance (IFD) is an important indicator of gait stability. The aim of this work was to evaluate the accuracy of the IFD estimate at mid-swing obtained on 13 healthy subjects with a wearable system integrating an infrared range sensor (IRR) and an inertial measurement unit (IMU). Data were acquired during gait performed at two different self-selected gait speeds and two bases of support. The IFD gold standard measurement was obtained with a stereo-photogrammetric system. The error found was larger for gait tasks performed at a greater base of support regardless the speed, while it was limited when gait was performed without overextending the base of support especially at slow gait speed. The study supports the potential use of the proposed technology for estimating IFD in daily living conditions.**

***Keywords*—Gait analysis, IMU, step width, inter-foot distance.**

I. Introduction

INTER-FOOT distance (IFD) is the projection along the medio-lateral direction of the distance between corresponding points of the feet. It is an indicator of the stability of gait throughout the gait cycle [1]. Its value at heel strike coincides with the step width (SW) which is used in clinical gait analysis to evaluate the stability of gait and risk of falls [2,3]. SW is commonly measured in laboratory settings with instrumented treadmills and instrumented gait mats [4,5]. Conversely, to measure the entire IFD pattern during the gait cycle (including SW), conventional stereo-photogrammetric (SP) systems [1] are used. However, IFD or SW measurements obtained in laboratory settings may not represent the subject specific gait characteristics in real life. Few studies proposed the measurement of IFD using wearable sensors, such as those based on ultrasounds (US) and infrared light (IR), often integrated into the shoes [6-9]. The US unit and inertial measurement units (IMUs) were fused together, however the resulting measurement system was bulky and needed to be calibrated [6,7]. IR based systems proposed in [8,9] included a micro camera and a panel with LEDs and were integrated with IMUs, resulting in bulky devices affecting walking patterns. Infrared range sensors (IRR) integrated with IMUs have shown their potential [10]. IRR sensors employ the single point optical triangulation principle for measuring the distance from a target object and are competitive in terms of response time, resolution, beam width, power consumption and size.

The aim of this work was to evaluate the accuracy of the previously proposed IRR-IMU device applied to the subject shoes in estimating the IFD at the mid-swing phase of gait. Data acquired during gait were compared to those acquired simultaneously with a SP system used as gold standard to evaluate the accuracy of the IRR-IMU system in dynamic conditions.

II. Material and Methods

A. Instrumentation

The IRR sensor (GP2Y0A41SK0F, Sharp Corp™, 29.5×13×13.5mm) was preliminary calibrated [10]. According to the manufacturer's specifications, the measuring range is 40÷300 mm and the short measuring cycle is ~16ms. The IRR sensor was wired to an IMU (Shimmer 2R, Shimmer Sensing) through a dedicated expansion board (Shimmer AnEx), and a white paper screen (120×200mm) reflecting the emitted IR signal was manufactured. A 6-camera SP system (Vicon T20, 128 frames/s) was used as gold standard. Additional IMUs (OPAL, APDM) were applied on the feet for synchronization with the SP system purposes.

B. Experimental setup

The IRR-IMU system was positioned on the right foot (the IRR just below the medial malleolus and the IMU over the dorsal aspect). The white paper screen was positioned on the medial aspect of the left foot. Three spherical markers were positioned on each foot to form a local reference frame (over the IMUs, the toes and the heels). Two additional markers were positioned over the IRR sensor and the screen during a static acquisition for system position calibration purposes [11]. The additional IMUs were also applied on the dorsal aspect of each foot.

C. Subjects and acquisition protocol

13 healthy subjects (6 F, 7 M; 29.2 ±3.2 y.o; H: 1.69 ± 0.1 m) were recruited for this study. They were asked to walk along a 10 m walkway including the SP system calibrated volume at two self-selected speeds, comfortable gait (CG) and slow gait (SG), and with normal (N) and wide (W) base of support.

D. IFD Estimation

To determine the minimum IFD during gait the following steps were performed:

- the right foot mid swing phase was isolated from the rest of the cycle by identifying the time interval in which ML angular velocity, as recorded by the IMU on the right foot, exceeded 60% of its maximum value [12];
- the measurements obtained from the IRR sensor within the central 20% duration of the above mentioned time interval was isolated (as it was supposed to include the time when the white paper screen reflected the emitted IR light);

- the minimum value of the above mentioned measurements was determined and assumed to represent the minimum IFD estimate.

The gold standard values were obtained from the distance between the IRR and the white paper screen as measured by the SP system after the calibration of their position with respect to the local reference frame identified by the three markers attached to each foot [11]. The IFD was then obtained as the projection of the above mentioned distance along the ML direction. The minimum IFD values, obtained at right foot mid swing, were finally used as gold standard measurements.

E. Data analysis

For each gait condition the gold standard IFD (IFD_{SP}) and the IFD estimates obtained with the IRR-IMU ($IFD_{IRR\text{-}IMU}$) were estimated as the relevant mean values of the IFDs measured at each gait cycle. The error (*e*) was then calculated as the difference between the two above mentioned IFD measurements (e=$IFD_{IRR\text{-}IMU}$–IFD_{SP}). A Wilcoxon signed ranked test was performed to verify if statistically significant differences between errors resulting in different gait conditions were found (CG vs SG – both with N and W base of support and N vs W – both at CG and SG speeds). The significance level was set to 0.05 and then adjusted using the Bonferroni's correction.

III. Results and Discussion

A. Error dependency on gait speed and IFD

Descriptive statistics of *e* together with gait speed and gold standard IFD_{SP} values observed in each gait condition are reported in Table I.

TABLE I

Gait Condition	*e [mm] mean (sd)*	*Gait Speed [m/s] mean (sd)*	*IFD_{SP} [mm] mean (sd)*
SG-W	-22 (13)	0.64 (0.11)	174 (31)
SG-N	0 (6)	0.65 (0.1)	89 (23)
CG-W	-32 (23)	0.97 (0.15)	171 (37)
CG-N	-7 (8)	0.95 (0.11)	87 (26)

Errors for each subject and in each gait condition are reported in figure 1 as a function of gait speed (fig. 1a) and of IFD_{SP} (fig.1b). No correlation between *e* and gait speed was found (r= -0.23), while a considerable correlation between *e* and IFD_{SP} was found (r= -0.80).

The Wilcoxon signed rank test showed that *e* was statistically different between the N and W base of support both for SG and CG speeds. Statistically significant differences were also found for *e* between CG and SG speeds, but only for the N base of support.

Overall, the results of this study showed that the IRR-IMU system may provide a satisfactory estimate of the IFD when its value is lower than about 110 mm especially when walking at slow speed, while it tends to underestimate the IFD when it is greater than about 110 mm and the underestimation increases as the IFD increases.

Noteworthy, most of the subjects walking with a N base of support showed an IFD lower than 110 mm, while when walking with a W base of support showed an IFD greater than 110 mm. While obtaining better IFD estimates at slower gait speed is promising for applications of the proposed technology on elderly subjects at risk of fall, the larger error found for greater IFD values may be detrimental. In fact, greater IFD at mid swing may be representative of larger base of support also in elderly populations. However, if the IFD measured on elderly does not reach the values observed in this study for the trials performed with a W base of support, errors in estimating IFD may be limited to 10 to 20 mm.

IV. Conclusion

The technology tested in this study based on the combination of a wearable IMU connected to a IRR sensor applied on the shoe allows estimating the minimum IFD during gait with a satisfactory accuracy, especially at slow gait speed. Performance deteriorates as the minimum IFD increases regardless the gait speed.

References

[1] D.E. Krebs, D. Goldvasser, J.D. Lockert, L.G. Portney, K.M. Gill-Body, "Is base of support greater in unsteady gait?" *Phys Ther*, vol. 82, No. 2, pp. 138–47, 2002.

[2] P.O. Riley, B.J. Benda, D.E. Krebs, "Phase plane analysis of stability in quiet standing", *J. Rehabil Res Dev*, Vol. 32, pp.227–235, 1995.

[3] J.S. Brach, J.E. Berlin, J.M. Vanswearingen, A.B. Newman, and S.A. Studenski, "Too much or too little step width variability is associated with a fall history in older persons who walk at or near normal gait speed," *J. Neuroeng Rehabil*, vol. 8, pp. 1–8, 2005.

[4] T.M. Owings and M.D. Grabiner, "Step width variability, but not step length variability or step time variability, discriminates gait of healthy young and older adults during treadmill locomotion", *J. Biomech*, Vol. 37, No.6, pp. 935–8, 2004.

[5] J.S. Brach, R. Berthold, R. Craik, J.M. Van Swearingen, and A.B. Newman, "Gait variability in community-dwelling older adults". *J. American Geriatrics Society*, vol. 49, pp.1646-50, 2001.

[6] S.J. Morris, A.Y. Benbasat, D.M. Scarborough, D.E. Krebs and J.A. Paradiso, "Gait analysis using a shoe-integrated wireless sensor system", *IEEE Trans. information technology in biomedicine*, vol.12, pp. 413–23, 2008.

[7] C. Wada, S. Ikeda, F. Wada, K. Hachisuka, T. Ienaga, Y. Kimuro and T. Tsuji, "Improvement study for measurement accuracy on wireless shoe-type measurement device to support walking rehabilitation", in *2012*, *Proc. ICME*, pp. 471–474.

[8] B. Mariani, G. Lisco, K. Aminian, "New gait analysis method based on wiimote technology and fusion with inertial sensors", in *2012 Proc. 1st Joint World Congress ISPGR & Gait and Mental Function*.

[9] T.N. Hung and Y.S. Suh "Inertial Sensor-Based Two Feet Motion Tracking for Gait Analysis", *Sensors* Vol.13, pp.5614-5629, 2013.

[10] D. Trojaniello, A. Cereatti, A.K. Burke, K. Aminian, U. Della Croce, "A wearable system for the measurement of the inter-foot distance during gait", in *2014 Proc. 20th IMEKO TC4*, pp 765-76.

[11] A. Cappozzo, F. Catani, A. Leardini, U. Della Croce, "Position and orientation in space of bones during movement: anatomical frame definition and determination", *Clin Biomech*, vol. 10, pp.171-178, 1995.

[12] D. Trojaniello, A. Cereatti, E. Pelosin, L- Avanzino, A. Mirelman, J.M. Hausdorff, U. Della Croce, "Estimation of step-by-step spatio-temporal parameters of normal and impaired gait using shank-mounted magneto-inertial sensors: application to elderly, hemiparetic, parkinsonian and choreic gait", *J Neuroeng Rehabil.*, vol. 11:152, 2014.

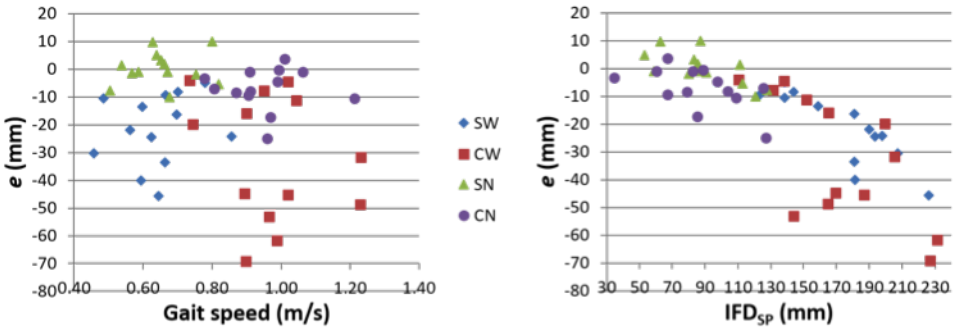

(a) (b)

Fig. 1. Error in estimating IFD (mm) as a function of gait speed (a) (m/s) and of IFD true value (b) (mm) with the IRR-IMU system employed. For each subject, errors resulting from gait performed in the four conditions tested are grouped in four categories.

A sEMG-based approach for biomechanical risk assessment derived from the NIOSH equation

T. Varrecchia[1], A. Ranavolo[2], A. Marchesi[3], M. Rinaldi[1], M. Serrao[4], M. Cesarelli[5], S. Conforto[1], S. Del Ferraro[2], V. Molinaro[2], A. Silvetti[2], G. Rotriquenz[5] and F. Draicchio[2]

[1] *Department of Engineering, Roma TRE University, Via Ostiense 159, 00154 Rome, Italy*
[2] *Department of Occupational and Environmental Medicine, Epidemiology and Hygiene, INAIL, 00078 Monte Porzio Catone, Rome, Italy*
[3] *Department of electric and information engineering, University of Cassino and Lazio Meridionale, 03043 Cassino, Italy*
[4] *Department of Medico-Surgical Sciences and Biotechnologies, University of Rome Sapienza, 40100 Latina, Italy*
[5] *Department of Electrical Engineering and Information Technology, University of Naples Federico II, 80125 Naples, Italy*

***Abstract*—The objectives of the work are: to identify surface electromyography (sEMG)-based indices acquired during the execution of controlled lifting tasks designed to have growing lifting index (LI); to verify the sensitivity of these indices to the risk level and their relationship with forces at the L5-S1 joint. During the execution of lifting tasks in three conditions, kinematic, kinetic and sEMG data of 16 workers were recorded. We found differences between each pairs of lifting conditions for each muscular parameters investigated (average rectified value, maximum value of trunk muscles, simultaneous activation of all the trunk muscles by using the time-varying multi-muscle co-activation function). Correlation analysis showed a significant relationship between sEMG parameters and kinetic variables. It is possible designing a quantitative sEMG-based lifting pattern recognition toolbox.**

***Keywords*—Biomechanical risk assessment, lifting index (LI), sEMG, work-related low-back disorders (WLBDs).**

I. Introduction

Work-related low-back disorders (WLBDs) are the costly and most common musculoskeletal problems, principally caused by manual lifting tasks, [1], [2]. Revised NIOSH (National Institute for Occupational Safety and Health) Lifting Equation (RNLE), published by the NIOSH to prevent and reduce the risk of WLBDs, was an approach used in overall the world to assess two-handed manual lifting demands [3], [4]. Its strength lies in the fact that the risk of WLBD increases as the lifting index (LI) increase from 1.0 to 3.0 [5]-[8]. On the other hand, RNLE does record also some weakness: the parameters and equation restrictions represent a limit in the RNLE usability [9], [10]. These limits are the rationale to develop further quantitative methods for lifting tasks risk assessment. In this study, we investigated the surface electromyography (sEMG) activities of the trunk muscles and forces at the L_5-S_1 joint (F_{L5-S1}) to identify sEMG-based indices acquired during the execution of controlled lifting tasks designed to have growing LI and to verify the sensitiveness of these indices to the risk level and their relationship with F_{L5-S1}.

II. Materials and Methods

Sixteen workers were recruited in this study. They gave their informed consent prior to taking part in the study, which complied with the Helsinki Declaration and was approved by the local ethics committee. An eight infrared cameras (sampling frequency 340 Hz) optoelectronic motion analysis system (BTS System, Milan, Italy) was used to detect the movements of 4 spherical reflective markers placed on a plastic crate and of 33 spherical markers covered with aluminum powder reflective material, placed over prominent anatomical bony landmarks (suprasternal notch, sternum, sacrum, cutaneous projections of the spinous processes of the seventh and tenth cervical vertebra and bilaterally over the temple, posterior-superior parietal bone, anterior superior iliac spine, great trochanter, lateral femoral condyle, fibula head, lateral malleoli, metatarsal head, heel, acromion, olecranon, styloid ulnar and radial processes and head of the third metacarpal bone) [11]-[15]. Four dynamometric platforms were used to record ground reaction forces at a sampling rate 680 Hz. Surface myoelectric signals were acquired at a sampling rate of 1 kHz using a 16-channel Wi-Fi transmission surface electromyography. Six electrodes were placed on the right side of the trunk: Latissimus Dorsi (LD), Erector Spinae Longissimus (ESL), Erector Spinae Iliocostalis (ESI), Multifidus (M), Rectus Abdominis Middle (RAM) and Rectus Abdominis Superior (RAS) muscles.

TABLE I
LIFTING CONDITIONS

LI	1	2	3
L (kg)	~21 kg	~21 kg	~20 kg
LC	23 kg	23 kg	23 kg
H (m)	0.25	0.50	0.63
V (m)	0.75	0.75	0.30
D (m)	0.25	25	0.45
A (°)	0	0	0
F (lift/s)	0.033	0.033	0.033
C	good	good	good

The values of the load weight (L), the horizontal (H) and vertical (V) locations, the vertical travel distance (D), the asymmetry angle (A), the lifting frequency (F) and the hand-to-object coupling (C) for each lifting condition (LI=1, 2 and 3).

The subjects were asked to perform the manual material lifting task of a load with handles using both hands in three different lifting conditions (LI=l, 2 and 3), according to the RNLE [3] (see Table I). Subjects also performed the isometric maximum voluntary contractions (iMVCs), according to SENIAM recommendations [16]. After each acquisition performed by Smart Capture (BTS, Milan, Italy), three-dimensional marker trajectories were reconstructed

using a tracking system (SMART Tracker, BTS, Milan, Italy). Data were processed using SMART Analyzer software (BTS, Milan, Italy) and Matlab software (MathWorks, Natick, MA, USA). The vertical displacement and velocity of markers placed over the vertex of the crate were evaluated to define the onset and termination of the lifting task. Using a polynomial procedure, kinematic, kinetic and sEMG data were then time normalized to the duration of the lifting tasks and reduced to 101 samples. According to the multi-segment upper body model (hands, forearms, arms, head and trunk) [17], the compression ($Fcompr_{L5-S1}$) and shear ($Fshear_{L5-S1}$) forces at the L5-S1 joint were calculated in the local reference system on the trunk in which the y axis is oriented as the vector C7-sacrum and x-z represents the orthogonal plane to y. sEMG signals were processed as follows: the iMVC and the sEMG raw data of the lifting tasks were band-pass filtered (30 and 400 Hz) [18], [19], full-wave rectification and low-pass filtered using filter at 5; the rectified and filtered sEMG data related to the lifting tasks were expressed as a percentage of the sEMG peak value calculated as the mean of the maximum values detected for each of the two iMVCs. From the elaborated sEMG signals of each lifting task, we evalueted the average rectified value (ARV) and the maximum value (Max) within the cycle, to characterize differences in the sEMG activity between different conditions. Furthermore, we have calculated the simultaneous activation of all the trunk muscles by using the time-varying multi-muscle co-activation function (TMCf) proposed by Ranavolo [20] and we considered the area of total TMCf ($TMCf_{Area}$) within the cycles. Using SPSS 17.0 software, the Shapiro-Wilk test was used to analyze the Gaussian distribution of the data. We analyzed a one-way ANOVA to determine any significant differences between the three risk levels. Post-hoc analyses were performed using a paired t test with Bonferroni's corrections. The Pearson test was used to investigate any correlations between each muscular parameters and forces.

III. Results

The repeated measures ANOVA revealed a significant effect of the lifting condition on ARV and Max for all the muscles except RAM. Fig. 1 shows the significant differences of the paired *t* test with Bonferroni's corrections for the ARV and Max of all the muscles investigated. We also observed significant differences for $TMCf_{Area}$, between each pair of lifting conditions. Correlation analysis showed a significant relationship between each muscular parameters (ARV, Max and $TMCf_{Area}$) and $Fshear_{L5-S1}$, and also between Max and $TMCf_{Area}$ and $Fcomp_{L5-S1}$.

IV. Conclusion

Our experimental data support the proposed hypothesis by demonstrating that a sEMG-based indices (ARV, Max and $TMCf_{Area}$) would serve to estimate risks associated with lifting tasks to place side by side the NIOSH protocol or to assess a vast range of conditions in which the NIOSH protocol cannot be used.

References

[1] M.L. Lu, T.R. Waters, E. Krieg, , D. Werren, Efficacy of the Revised NIOSH Lifting Equation to Predict Risk of Low-Back Pain Associated With Manual Lifting: A One-Year Prospective Study, Hum Factors, vol. 56(1), pp. 73–85, 2014.

[2] NIOSH. Work practices guide for manual lifting. NIOSH Technical Report No. 81-122 (U.S. Dept. of Health and Human Services, National Institute for Occupational Safety and Health Cincinnati, OH). 1981.

[3] T.R. Waters,V. Putz-Anderson, A. Garg, Applications Manual for the Revised NIOSH Lifting Equation. Cincinnati, OH: U.S. Department of Health and Human Services,1994.

[4] T.R.Waters, V. Putz-Anderson, A. L.J. Garg, Fine, Revised NIOSH Equation for the Design and Evaluation of Manual Lifting Tasks, Ergonomics, vol. 36 (7), pp. 749–776, 1993.

[5] T.R.Waters, S.L. Baron, L. Piacitelli, V. Anderson, T.Skov, et al., Evaluation of the Revised NIOSH Lifting Equation, Spine, vol. 24 (4), pp.386–395,1999.

[6] T.R.Waters, M. Lu, L.A. Piacitelli, D. Werren, J.A. Deddens, Efficacy of the revised NIOSH lifting equation to predict low back pain due to manual lifting: Expanded crosssectional analysis, J Occup Environ Med, vol. 53, pp.1061–1067, 2011.

[7] A. Garg, S. Boda, K.T. Hegmann, J.S. Moore, J.M. Kapellusch, et al. Malloy, The NIOSH lifting equation and low-back pain, Part 1: Association with low-back pain in the backworks prospective cohort study, Hum Factors, vol. 56(1), pp. 6-28, 2014.

[8] R. Sesek, D. Gilkey, P. Drinkaus, D.S. Bloswick, R. Herron, Evaluation and quantification of manual materials handling risk factors, Int J Occup Saf Ergon, vol. 9(3), pp. 271-87, 2003.

[9] W.S. Marras, L.J. Fine, S.A. Ferguson, T.R. Waters, The effectiveness of commonly used lifting assessment methods to identify industrial jobs associated with elevated risk of low-back disorders, Ergonomics, vol. 42(1), pp. 229-45, 1999.

[10] P.G. Dempsey, Usability of the revised NIOSH lifting equation, Ergonomics, vol. 45(12), pp. 817-28, 2002.

[11] G. Wu, S. Siegler, P. Allard, C. Kirtley, A. Leardini, et al., Standardization and Terminology Committee of the International Society of Biomechanics, ISB Recommendation on Definitions of Joint Coordinate System of Various Joints for the Reporting of Human Joint Motion, Part I. Ankle, Hip, and Spine, J Biomech, vol. 35(4), pp.543–548, 2002.

[12] G. Wu, F.C. van der Helm, H.E. Veeger, M. Makhsous, P. Van Roy, et al., Buchholz, International Society of Biomechanics. ISB Recommendation on Definitions of Joint Coordinate Systems of Various Joints for the Reporting of Human Joint Motion. Part II. Shoulder, Elbow, Wrist and Hand, J Biomech, vol. 38(5), pp.981–992, 2005.

[13] E.M. Gutierrez-Farewik, A. Bartonek, H. Saraste, Comparison and evaluation of two common methods to measure center of mass displacement in three dimensions during gait, Hum Mov Sci, vol. 25, pp.238-256, 2006.

[14] G. Rab, K. Petuskey, A. Bagley, A Method for Determination of Upper Extremity Kinematics, Gait & Posture, vol. 15(2), pp.113–119, 2002.

[15] R.B. Davis III, S. Õunpuu, D. Tyburski, J.R. Gage, A gait analysis data collection and reduction technique, Hum Mov Sci, vol. 10, pp.575–87, 1991.

[16] H.J. Hermens, B. Freriks, C. Disselhorst-Klug, G. Rau, Development of Recommendations for SEMG Sensors and Sensor Placement Procedures, J Electromyogr Kinesiol, vol.10(5), pp.361–374, 2000.

[17] A. Plamondon, M. Gagnon, P. Desjardins, Validation of two 3-D segment models to calculate the net reaction forces and moments at the L5/S1 joint in lifting, Clin Biomech, vol.11(2), pp.101-110, 1996.

[18] J.D. Drake, J.P. Callaghan, Elimination of electrocardiogram contamination from electromyogram signals: An evaluation of currently used removal techniques, J Electromyogr Kinesiol, vol.16(2), pp.175-87, 2006.

[19] H.L. Butler, R. Newell, C.L. Hubley-Kozey, J.W. Kozey, The Interpretation of Abdominal Wall Muscle Recruitment Strategies Change when the Electrocardiogram (ECG) is Removed from the Electromyogram (EMG), J Electromyogr Kinesiol, vol.19(2), pp.102–113, 2009.

[20] A. Ranavolo, S. Mari, C. Conte, M. Serrao, A. Silvetti, et al., A new muscle co-activation index for biomechanical load evaluation in work activities, Ergonomics, vol.2, pp.1-14, 2015.

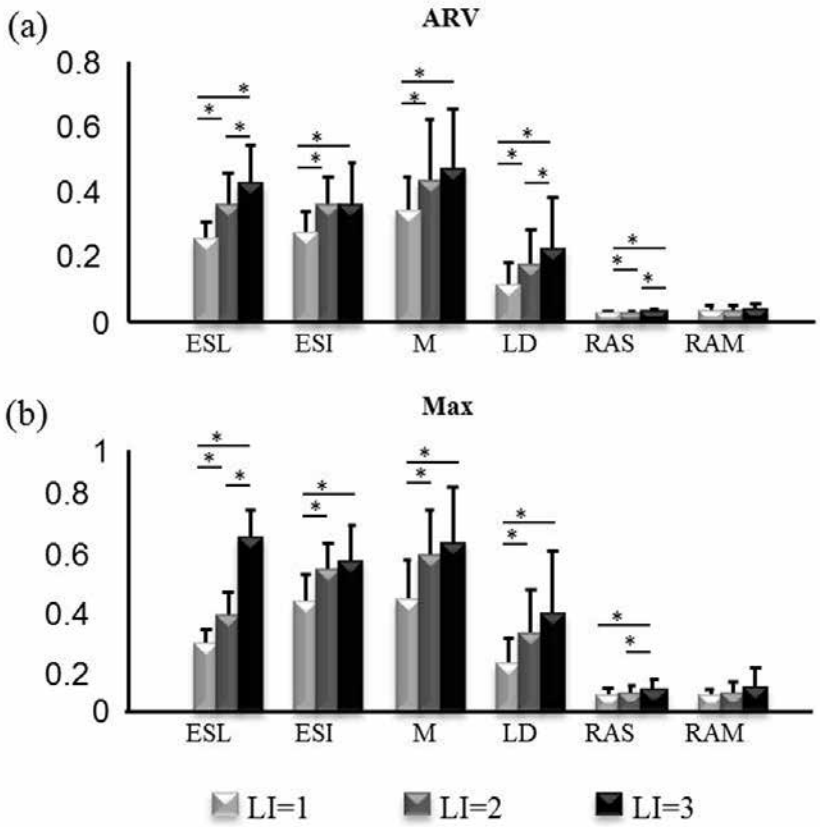

Fig. 1. Means and standard deviations of the ARV (a) and Max (b) calculated while performing manual material lifting tasks in the three different conditions (LI=1, LI=2 and LI=3) for the six muscles ESL, ESI, M, LD, RAS and RAM on the right side of the trunk. * Significant differences at post hoc analysis.

BIOMECCANICA STRUTTURALE

Methods and procedures in bariatric surgery: a biomechanical approach

E.L. Carniel[1,2], A. Frigo[1,2], C.G. Fontanella[2,3], L. Polese[2,4], G.M. De Benedictis[2,5], A. Rubini[2,3], S. Merigliano[2,4] and A.N. Natali[1,2]

[1] *Department of Industrial Engineering, University of Padova, Padova, Italy*
[2] *Centre for Mechanics of Biological Materials, University of Padova, Padova, Italy*
[3] *Department of Biomedical Sciences, University of Padova, Padova, Italy*
[4] *Department of Surgery, Oncology and Gastroenterology, University of Padova, Padova, Italy*
[5] *Department of Animal Medicine, Production and Health, University of Padova, Italy*

Abstract **- Bariatric surgery includes a variety of procedures performed on obese people. The common surgical techniques aim to reduce the size of the stomach and are traditionally performed by laparoscopic surgery. The post-surgical conformation of the stomach is usually defined mostly on clinical basis. Instead, the optimal geometrical configuration should be defined by analysing the mechanical functionality of the stomach and the relationship between food intake, nutrient adsorption, mechanical stimulation of stomach wall and feeling of satiety.**

A novel approach to bariatric surgery is required, integrating competences in the areas of biomechanics, physiology and surgery, based on a strong interaction between engineers and clinicians. Preliminary results from coupled experimental and computational investigations are here reported. The analyses aimed to develop computational tools for the investigation of stomach mechanical functionality in the pre- and post-surgical configurations.

Keywords **- Bariatric surgery, stomach mechanics, experimental methods, computational biomechanics.**

I. INTRODUCTION

OBESITY is an epidemic disease associated with multiple co-morbidities, whose prevalence in the developed countries is increasing. Behavioural and pharmacological treatment approaches are modestly effective and not durable. Bariatric surgery remains the most effective intervention for persons with body mass index of 35 or greater [1]. Bariatric surgery aims to decrease the intake of food and calories. Some operations obtain this goal by reducing the stomach capacity, as adjustable gastric banding, some others by reducing the absorbing capacity, finally there are operations that exploit both the effects. The use of adjustable gastric band is the most common and successful operation. In general, bariatric surgical procedures are effective, but are associated with major complications in 25% of patients and the mortality incidence is 7.6% [1].

The specific bariatric procedure and the post-surgical conformation of the operated gastrointestinal region are usually evaluated on clinical basis, taking into account the food intake requirement and surgical parameters. Further physiological and mechanical processes should be considered, as the functionality of the gastrointestinal region and the relationship between food intake, mechanical stimulation of gastrointestinal wall, adsorbing capacity and feeling of satiety. Mostly qualitative activities have been previously performed to evaluate how the food consumed affects satiety [2]. Methods and procedures of bariatric surgery should be consequently defined by integrating competences in the area of surgery, physiology and biomechanics. Computational models of the gastrointestinal region can be developed and applied to investigate the mechanical stimulation of the gastrointestinal wall because of food intake and depending on the surgical procedure. Subsequently, physiological investigations can be performed to better identify the relationship between mechanical stimulation of the gastrointestinal wall, adsorption capacity and feeling of satiety. Depending on such parameters, an optimized bariatric procedure can be identified for the specific patient.

The here reported activities aimed at developing preliminary computational tools for the mechanical analysis of bariatric procedures. A coupled experimental and numerical approach was adopted. Experimental activities on pig stomachs aimed at providing information about stomach structural behaviour and geometrical configuration. Computational models were developed by the analysis of experimental data. Finally, computational analyses made it possible to investigate the stomach mechanical functionality in pre- and post-surgical configurations.

II. MATERIALS AND METHODS

A. Experimental investigation

The structural behaviour of the stomach was analysed by inflation tests. Stomach of eight piglets (weight: 30 ± 2 Kg) were provided by a local abattoir. The samples were composed of the stomach and short portions of the oesophagus and the duodenum. Samples were gently washed with physiological saline (0.9% NaCl) to remove any residual chime and maintained in saline at low temperature (4°C), up to the development of mechanical testing. Preliminarily, the sample was placed on a laminated graph paper and spread out to its physiological bean-shape conformation (Fig. 1a). A peristaltic pump (VerderFlex Vantage 3000 P EZ, Verder Ltd, UK) and a pressure transducer (142 pc 01d, Honeywell, USA) were connected to the sample by rubber tubes. Pump and transducer tubes were fixed to esophageal and duodenal stubs, respectively, by means of surgical elastic seams. The transducer was interfaced to a laptop PC by a microcontroller (Arduino MEGA, Arduino, USA). Data storage was fixed at 4 Hz sample rate. The instrumented stomach was completely

immersed in saline to prevent gravity effects (Fig. 1b). Sample testing was performed by a multi-step procedure (Fig. 1c). Each step was composed of 100 ml inflation of saline (50 ml/s) and 300 s of rest to allow the development of relaxation phenomena. The step was repeated up to 1000 ml inflation. Subsequently, the stomach was completely deflated at 50 ml/s. The overall procedure was repeated three times on each stomach.

B. Computational model definition

Digital processing of stomachs pictures in unstrained configuration and morphometrical data from the literature made it possible to develop an average virtual solid model of the pig stomach. Finite element discretization by three-nodes tetrahedral hybrid elements led to the computational model (Fig. 2a). The mechanical response of the stomach wall was specified by a visco-hyperelastic formulation [3]:

$$\mathbf{P}(\mathbf{C},t) = \mathbf{P}^0(\mathbf{C}) - \sum_i \mathbf{q}^i(\mathbf{C},t) \quad (1)$$

$$\mathbf{P}^0(\mathbf{C}) = -p\mathbf{F}^{-T} + C_1 \exp\left[\alpha_1 (I_1 - 3)\right]\left(2\mathbf{F} - 2/3\, I_1 \mathbf{F}^{-T}\right) \quad (2)$$

$$\dot{\mathbf{q}}^i + \frac{1}{\tau^i}\mathbf{q}^i = \frac{\gamma^i}{\tau^i}\mathbf{P}^0 \quad (3)$$

where $\mathbf{P}$ is the first Piola-Kirchhoff stress tensor, $\mathbf{F}$ is the deformation gradient, p specifies hydrostatic pressure, I_1 is the first invariant of the right Cauchy-Green strain tensor $\mathbf{C}=\mathbf{F}^T\mathbf{F}$, $\mathbf{q}^i$ are viscous variables. Constitutive parameters were identified by the inverse analysis of tensile tests that were developed on pig stomach samples [4].

C. Computational analyses of stomach functionality

Numerical analyses were performed by the general purpose finite element software Abaqus 6.14 (Dassault Systèmes Simulia Corp., Providence, RI). A fluid filled-cavity was defined to characterize the internal region of the stomach and to simulate the inflation process. The upper and lower extremity of the cavity, at the gastroesophageal and gastroduodenal junctions, were fixed. The volume of the cavity was progressively raised up to a 1000 ml volume increment.

The numerical model of a gastric band was developed by six-nodes wedge elements. The mechanical behaviour was specified by an Ogden hyperelastic formulation and parameters were identified by the inverse analysis of tensile tests on silicon rubber. The gastric band was located around the stomach model. Computational models contemplated different band positions, which were defined on the basis of the standard surgical activity (Figs. 2b, 2c, 2d). Friction contact condition (0.01 friction coefficient) allowed characterizing interaction between the stomach and the band. Numerical analyses were finally developed to simulate stomach inflation in the post-surgical configuration.

III. RESULTS AND DISCUSSION

A. Experimental activities

Experimental testing provided data about the structural behaviour of pig stomachs. Post-processing of experimental results (Fig. 3a) made it possible to characterize the stomach structural behaviour. The collection of pressure-volume data at the end of the rest stages led to equilibrium curves (Fig. 3b), while the analysis of pressure-time results during the constant volume stages led to relaxation curves (Fig. 3c).

B. Computational activities

The comparison of computational and experimental results from inflation tests on stomachs in the pre-surgical configuration made it possible to assess the reliability of the model developed. Experimental data and computational results are compared in Fig. 4a.

The developed computational models allowed preliminarily investigating the influence of bariatric surgery on stomach mechanical functionality. The comparison of stomach structural behaviour in pre- and post-surgical configurations is reported in Fig. 4a. The analysis of tensile stress distribution allows better evaluating the stomach functionality. Typical stress contours are reported in Fig. 4 for the pre-surgical configuration (Fig. 4b) and the different post-surgical configurations (Figs. 4c, 4d and 4e).

IV. CONCLUSION

Preliminary outcomes are reported from activities that are under development in the research field of stomach mechanics and bariatric surgery. Further efforts are mandatory for a more reliable analysis of the problem. For example, experimental activities are under development on stomach in different post-surgical configurations. A more refined constitutive characterization of stomach tissues is being defined and aims at considering stomach tissues non homogeneous configuration, wall stratification and muscular fibres distribution.

Nevertheless, the results show the potentiality of the methods of experimental and computational biomechanics for the investigation and optimization of bariatric surgery techniques. Computational models allow evaluating the stomach functionality depending on the specific bariatric procedure. The computational approach makes it possible to identify the stress and strain fields in stomach tissues. Such mechanical parameters depend on stomach filling and regulate the feeling of satiety. The topic has been only qualitatively analysed. Further physiological investigations are required aiming at the quantitative identification.

REFERENCES

[1] S.H. Chang, C.R. Stoll, J. Song, J.E. Varela, C.J. Eagon, G.A. Colditz, "The effectiveness and risks of bariatric surgery: an updated systematic review and meta-analysis, 2003-2012" *JAMA Surg*, vol. 149, pp. 275-287, 2014.

[2] S.C. Woods, "Gastrointestinal satiety signals I. An overview of gastrointestinal signals that influence food intake", *Am J Physiol Gastrointest Liver Physiol*, vol. 286, pp. 7-13, 2004.

[3] E.L. Carniel, C.G. Fontanella, C. Stefanini, A.N. Natali, "A procedure for the computational investigation of stress-relaxation phenomena", *Mech Time-Depend Mater*, vol. 17, pp. 25-38, 2013.

[4] J. Zhao, D. Liao, P. Chen, P. Kunwald, H. Gregersen, *J Biomech*, vol. 41, pp. 3441-3447, 2008.

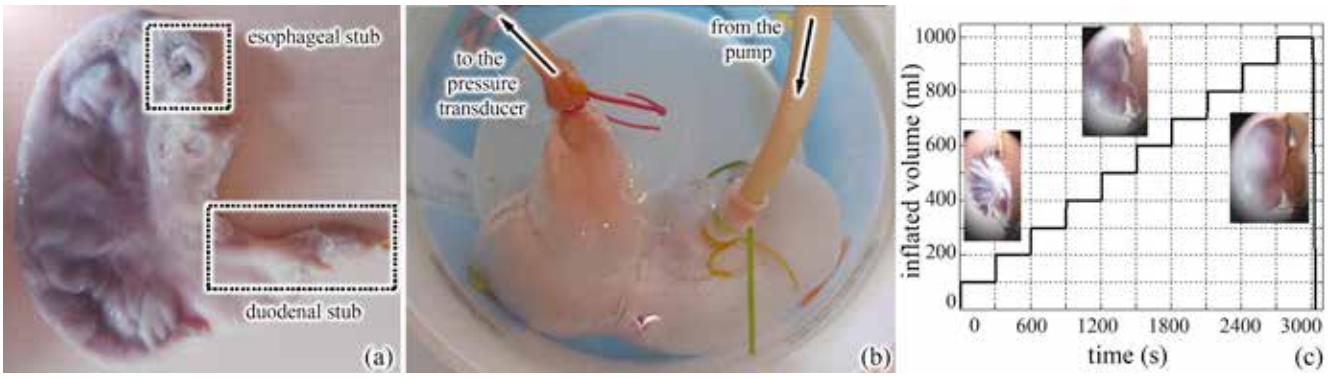

Fig. 1. Pig stomach spread out to physiological bean-shape (a) and during inflation test (b). Inflated volume history (c).

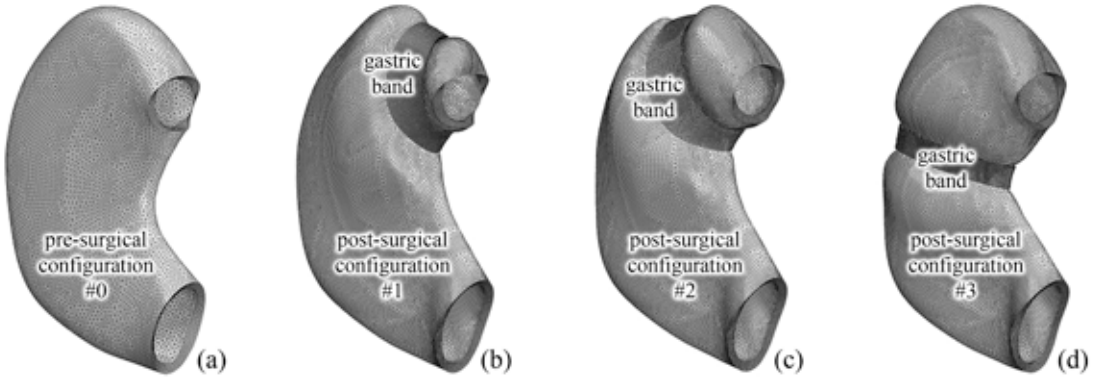

Fig. 2. Finite element models of the stomach in the physiological bean-shape conformation (a) and in different post-surgical configurations (b, c).

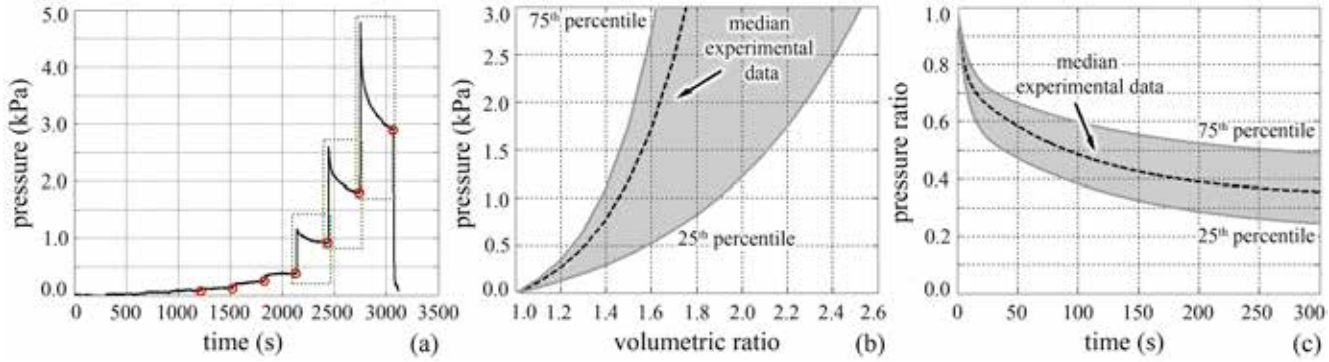

Fig. 3. Experimental results from inflation tests: typical pressure-time data (a), statistical distribution of equilibrium pressure-volume (b) and relaxation curves (c).

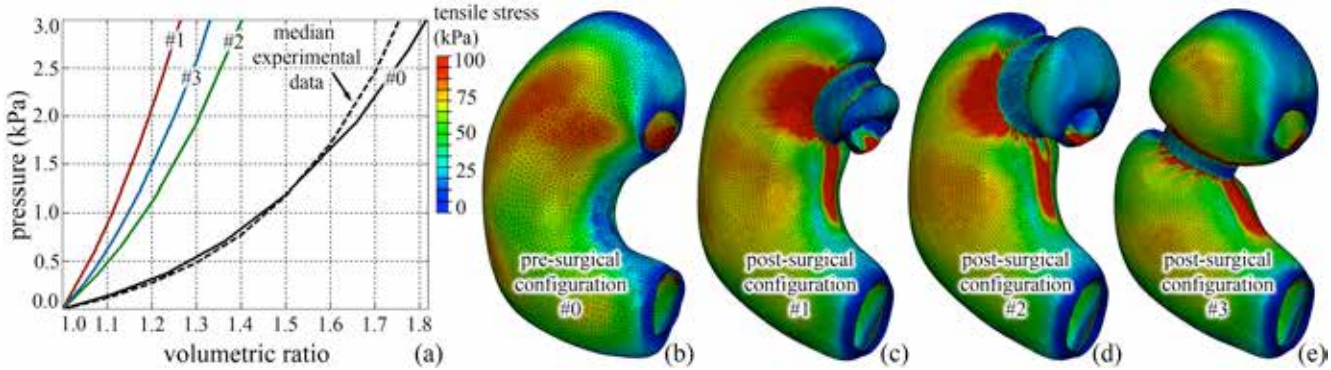

Fig. 4. Comparison of stomach structural behavior in pre- and post-surgical configurations (a); for the pre-surgical configuration model results are compared with median experimental data. Contours of tensile stress fields at 3 kPa internal pressure for pre-surgical configuration (b) and different post-surgical configurations (c, d, e).

Biomechanical behaviour of Hoffa's fat pad

C.G. Fontanella[1,2], E.L. Carniel[1,3], V. Macchi[1,4], A. Frigo[1,3], A. Porzionato[1,4], R. De Caro[1,4], and A.N. Natali[1,3]

[1] *Centre for Mechanics of Biological Materials, University of Padova, Italy*
[2] *Department of Biomedical Sciences, University of Padova, Italy*
[3] *Department of Industrial Engineering, University of Padova, Italy*
[4] *Department of Molecular Medicine, University of Padova, Italy*

Abstract - **The infrapatellar fat body (Hoffa's fat pad, IFP) is situated between the patellar tendon, the femoral condyle and the tibial plateau of the knee. The IFP consists of white adipose lobules delimited by thin connective septa. The structural functionality of the IFP is debated and may pertain to a cushioning role in the knee joint, providing to distribute and to damp mechanical stresses during articular activity.**

The present study aimed at assessing the IFP mechanical role and at analysing the correlation between micro-structural configuration and mechanical properties. Histological and ultrastructural methods were exploited to analyse the microscopic anatomy. Finite element micro-models were developed by using the resulting histo-morphometric data. Typical loading conditions, as compressive and shear ones, were investigated. Numerical analyses pointed out the IFP mechanical functionality. The comparison of numerical results and data about the mechanical behaviour of other fat tissues demonstrated the mechanical relevance of IFP.

Keywords **- Fat tissue, Hoffa's fat pad, soft tissue mechanics, computational biomechanics.**

I. Introduction

RECENT advances in medical research address to the evidence that some body fat tissues have not only the classic role of energy storage but also mechanical function. The infrapatellar fat pad (IFP), or Hoffa's fat pad [1], is located in the knee, between patellar tendon, femoral condyles and tibial plateau, underneath the patella. It is covered by synovial membrane posteriorly and is closely related also to articular cartilage, being intra-capsular and extra-synovial. It is hypothesized that the IFP provides cushioning of the knee, facilitates the distribution of synovial fluid and acts to absorb forces through the knee joint [1].

The reliable identification of fat tissue mechanical behavior requires deeply investigating the micro-structural configuration and composition [2],[3]. The action aims at identifying the quantity and the spatial distribution of tissue sub-components, making it possible to develop mechanical models that interpret the micro-structural configuration. In general, subcutaneous fat consists of white adipose tissue, of lobular type, with lobules delimited by thin connective septa. The dimension of lobules and the thickness of interlobular septa change between the different fat tissues, with a consequent differentiation of the mechanical roles.

With regard to the IFP, the geometrical conformation and the composition of adipose lobules and of interlobular septa were studied through histological and ultrastructural methods [4]. Results from the investigations made it possible to develop computational models, which allowed investigating the IFP mechanical functionality. Finite element micro-models of the fat tissue were developed by considering the specific adipose lobules dimension, fibrous septa thickness and the mechanical properties of the different sub-components. The mechanical behavior of the lobules and the fibrous septa was specified by hyperelastic constitutive formulations. Numerical analyses were developed taking into account of compression and shear loads, aiming at evaluating the mechanical response in typical physiological situations.

II. Materials and Methods

A. Histo-morphometric configuration

The histo-morphometric conformation of IFP was studied through histological and immuno-histo-chemical methods on samples from bodies of the Body Donation Program '*Donation to Science*' of the University of Padova. Thick sections of 10 μm were obtained from paraffin embedded specimens. Different image analysis procedures allowed the identification and the quantification of the sub-components, in particular elastic and collagen fibers.

The thickness of the septal walls was measured on magnified sections (Fig. 1a). Using specific imaging software (Adobe Photoshop CS5, Adobe Systems Incorporated, USA), the septal walls were identified and highlighted (Fig. 1b). Subsequently, images were converted to 8-bit binary images for the elaboration with a specifically developed algorithm implemented in Matlab R2012b (The MathWorks, Inc., USA). Parallel lines, with an interline distance of ~200 μm, were randomly overlaid on rotated 4x images. Orthogonal lines to the left aspect of the septal walls were drawn, leading to the measurements of the intercept length (Fig. 1c). Using a similar procedure, the dimension of adipocyte lobules was calculated [4]. Statistical distributions, as median, 25th and 75th percentile data were finally computed: septa thickness 229 μm [145 μm; 424 μm]; lobules dimension 1160 μm [650 μm; 1983 μm].

B. Finite element models

Basing on the results of histo-morphometric studies, a three-dimensional micro-model of the IFP was developed. Histological data were increased of a 25% factor to correct the shrinkage that inevitably occurred during tissue processing [5].

Adipose lobules were modeled by spheres, which were separated by connective septa (Fig. 2). The virtual solid model was composed by different layers, which were shifted each other according to a hexagonal scheme. This configuration well interprets the actual histo-morphological conformation of the tissue [2],[3]. The numerical model was obtained by finite element discretization of the virtual solid model, using four node tetrahedral elements (Fig. 2a). Hybrid pressure-displacement formulation was assumed because of the almost incompressible behavior of soft biological tissues.

The typical cylindrical conformation of compression specimens and the symmetry of tests suggested considering a wedge model for the analysis of compression loading conditions. A cubical shape was assumed for the shear specimen (Fig. 2).

The further step of the micro-model development pertained to the definition of sub-components mechanical response. Because of the micro-structural conformation of adipose tissue, a hyperelastic isotropic formulation was assumed for the adipose lobules [2]. The specific constitutive parameters were identified by the inverse analysis of data from compression tests that have been developed on adipose tissue specimens from healthy pigs [3],[6].

The performed histological examinations revealed the typical fibre-reinforced conformation of connective septa. In the IFP there was a prevalence of collagen I fibers (43%) with respect to collagen III fibers (18%), while elastic fibers were almost absent (<1%). The mechanical behavior of the interlobular septa was described by an anisotropic hyperelastic formulation, considering two groups of fibres distributed around each lobule, one running in a clockwise and one in an anticlockwise direction [2]. The identification of septa parameters was performed by the inverse analysis of data from tensile tests that have been developed on anterior talo-fibular human ligament tissues [7], because of the similar amount and typology of collagen fibers [2],[3].

C. *Numerical analyses*

Numerical analyses were developed by using the general purpose finite element code Abaqus 6.14 (Dassault Systèmes Simulia Corp., Providence, RI). The constitutive formulations were implemented by specific user subroutines UMAT.

The developed wedge model was constrained to analyze the tissue compressive behavior. The bottom side of the model was fixed, the top side was moved downward up to about 40% structural compressive strain (Fig. 2b), the planar lateral faces were constrained to ensure the symmetric configuration, while the circular lateral face was unconstrained. With the aim of evaluating the pure shear behavior, shear tests were analyzed by fully constraining the bottom face of the cubic model, while a purely transversal displacement was imposed to the opposite face of the specimen (Fig. 2c) up to 0.35 rad structural shear strain.

III. Results and Discussion

The comparison of results from microscopical investigations on IFP and other fat tissues [4] highlighted the peculiar conformation and composition of IFP adipose lobules and interlobular connective septa. The results enforced the mechanical role of the IFP.

Results from numerical analyses made it possible to compare the structural behavior of IFP and other fat tissues (Fig. 3). The comparison considered data from compression and shear tests that were developed on foot plantar [8],[9] and abdominal [9] fat tissues. Such tissues were selected because of the relevant and negligible mechanical role of plantar and abdominal tissues, respectively. The similarity between IFP and plantar fat mechanical behavior finally suggested the real mechanical role of the Hoffa's fat pad, as a cushioning element in the knee joint.

Post-processing of numerical results allowed better elucidating the contribution of tissue sub-components to the IFP mechanical functionality. Typical contours of stress were reported in Figure 4 for both compressive and shear conditions. With specific regard to compressive loading, compressive stresses mainly develop within the adipose chambers because of their relevant volumetric stiffness. Transverse tensile stresses develop within interlobular connective septa and oppose bulging of the chambers. Adipose lobules exhibit low iso-volumetric stiffness and shear loadings mainly determines stresses within septa.

IV. Conclusion

In conclusion, the present study describes the organization of the IFP in microscale and the resulting mechanical behavior. The specific configuration of the tissue and the peculiar mechanical environment within the knee suggest the mechanical role of IFP in damping impulsive loads and distributing stresses on the adjacent biological elements.

The results of the investigation should represent a support in the procedures of knee surgery, with particular regard to total knee arthroplasty (TKA). Nowadays, the removal of IFP during TKA is strongly affected by surgical practice results. The preservation of the IFP is associated with an improved outcome, although it is also reported that IFP excision in minimally invasive TKA resulted in a percentage of patients with anterior knee pain after surgery. Thus, the identification of IFP actual mechanical role can be an useful tool for the choice of whether to remove the IFP during TKA.

Acknowledgement

The authors are grateful to Dr. Anna Rambaldo and Dr. Maria Martina Sfriso for their skillful technical assistance.

References

[1] A. Hoffa, "The influence of the adipose tissue with regard to the pathology of the knee join", *J Am Med Assoc*, vol. 43, pp. 795-796, 1904.

[2] A.N. Natali, C.G. Fontanella, E.L. Carniel, "A numerical model for investigating the mechanics of calcaneal fat pad region", *J Mech Behav Biomed*, vol. 5, pp. 216-223, 2012.

[3] C.G. Fontanella, F. Nalesso, E.L. Carniel, A.N. Natali, "Biomechanical behavior of plantar fat pad in healthy and degenerative foot conditions", *Med Biol Eng Compu,* In press.

[4] V. Macchi, A. Porzionato, G. Sarasin, L. Petrelli, D. Guidolin, M. Rossato, C.G. Fontanella, A.N. Natali, R. De Caro, "The infrapatellar adipose body: an histotopographic study", *Cell Tissue Organs,* In Press.

[5] P-B. Dobrin, "Effect of histologic preparation on the cross-sectional area of arterial rings", *J Surgical Research,* vol. 61, pp. 413-415, 1996.

[6] K. Comley, N.A. Fleck, "The compressive response of porcine adipose tissue from low to high strain rate", *Int J Impact Eng*, vol. 46, pp.1-10, 2012.

[7] J.R. Funk, G.W. Hall, J.R. Crandall, W.D. Pilkey, "Linear and quasi-linear visco-elastic characterization of ankle ligament", *J Biomed Eng,* vol. 122, pp.15-22, 2000.

[8] W.R. Ledoux, J.J. Blevins, "The compressive material properties of the plantar soft tissue", *J Biomech*, vol. 40, pp. 2975-2981, 2007.

[9] S. Pai, W.R. Ledoux, "The shear mechanical properties of diabetic and non-diabetic plantar soft tissue", *J Biomech*, vol. 45, pp. 364-370, 2012.

[10] G. Sommer, M. Eder, L. Kovacs, H. Pathak, L. Bonitz, C. Mueller, P. Regitnig, G.A. Holzapfel, "Multiaxial mechanical properties and constitutive modeling of human adipose tissue: a basis for preoperative simulations in plastic and reconstructive surgery", *Acta Biomater*, vol. 9, pp. 936-948, 2013.

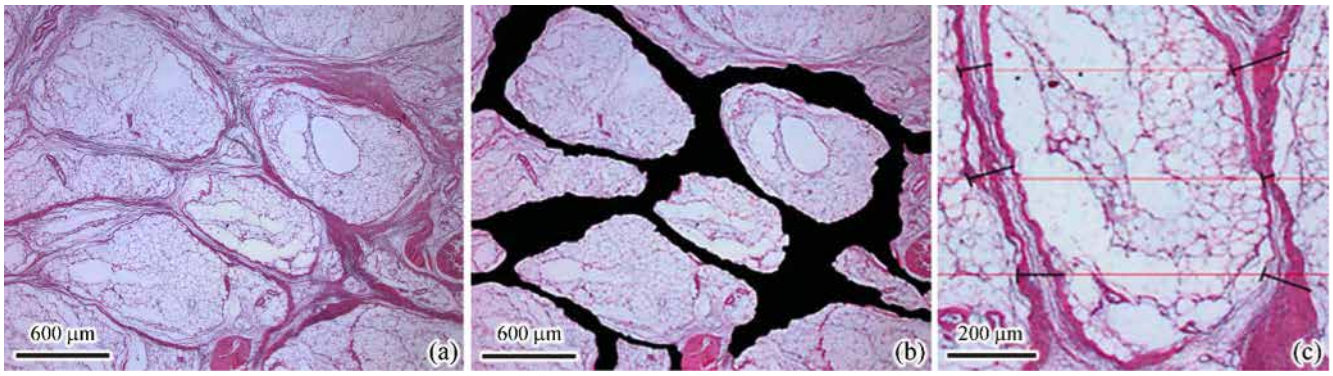

Fig. 1. Microscopic appearance of Hoffa's fat pad (a); identification of interlobular septa (b); measurement of septa thickness (c).

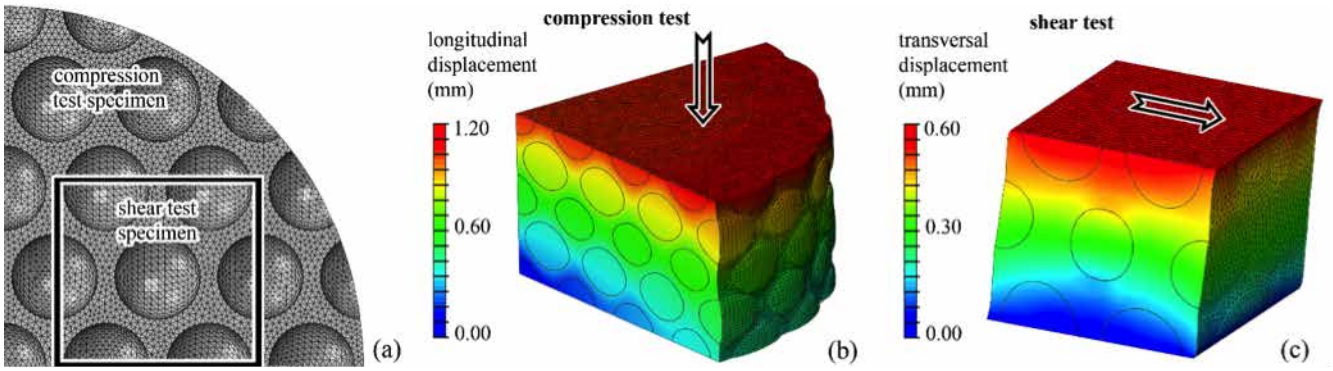

Fig. 2. Finite element micro-models of tissue samples (a), compression (b) and shear (c) loading conditions.

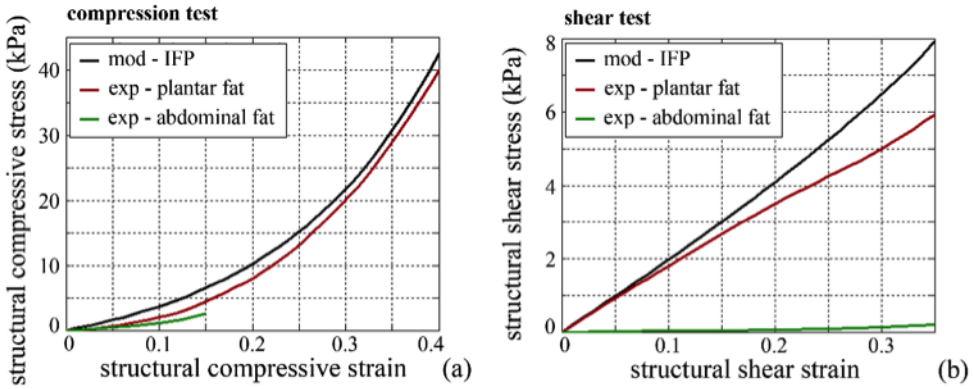

Fig. 3. Comparison of the structural behavior of the different fat tissues for compression (a) and shear (b) loading conditions.

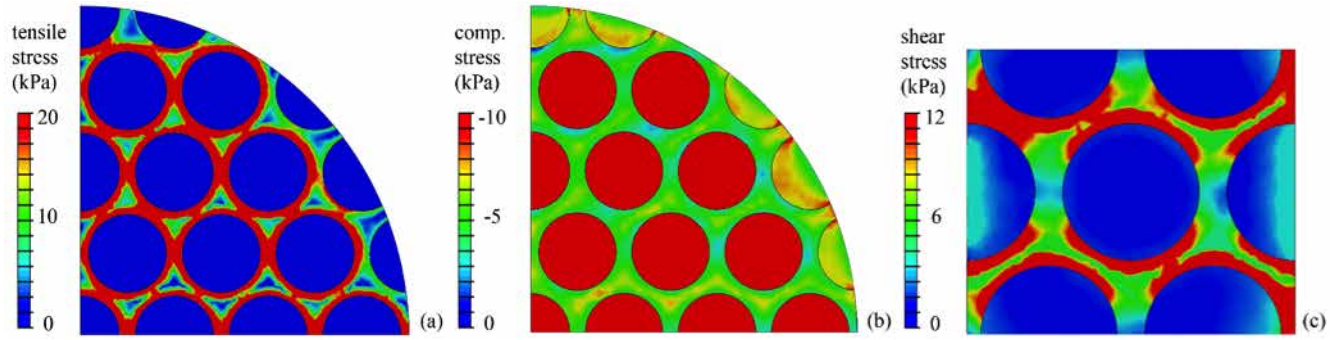

Fig. 4. Results from the numerical analysis of compression tests: contours of tensile stress (a), as the maximum principal stress, and compressive stress (b), as the minimum principal stress, for a 20% structural compressive strain condition. Results from the numerical analysis of shear tests: distribution of shear (c) stress field for a 0.2 rad structural shear strain condition.

Mechanics of urethral duct: tissue constitutive formulation and numerical modelling with regard to lumen occlusion

A.N. Natali[1,2], E.L. Carniel[1,2], P.G. Pavan[1,2], C.G. Fontanella[2,3], S. Todros[1,2], A. Frigo[1,2], P. Pachera[1,2], W. Artibani[4], M.A. Cerruto[4], R. De Caro[2,5], V. Macchi[2,5], A. Porzionato[2,5], A. Rubini[2,3], L. Cavicchioli[6], G.M. De Benedictis[2,7]

[1] *Department of Industrial Engineering, University of Padova, Padova, Italy*
[2] *Centre for Mechanics of Biological Materials, University of Padova, Padova, Italy*
[3] *Department of Biomedical Sciences, University of Padova, Italy*
[4] *Department of Urology, University of Verona, Verona, Italy,*
[5] *Department of Molecular Medicine, University of Padova, Padova, Italy*
[6] *Department of Comparative Biomedicine and Food Science, University of Padova, Italy*
[7] *Department of Animal Medicine, Production and Health, University of Padova, Italy*

***Abstract*— The research activity belongs to a general project on the mechanics in urology, with specific reference to bladder, urethra and overall functional response of the lower urinary system. The present work pertains to the mechanics of urethral duct, in consideration of the adoption of artificial sphincteric devices or slings to overcome the incontinence problems. Experimental activity is performed on urethral tissues and also structural test are carried out on the overall urethral duct, to provide constitutive parameters definition within the formulated hyperelastic model. The numerical analysis developed leads to a valid set of results addressed to the definition of the mechanics of urethral lumen occlusion under the action of prosthetic device, stressing the integration with surgical practice.**

***Keywords*—mechanics in urology, urethral duct, experimental testing, computational biomechanics.**

I. Introduction

URINARY incontinence represents a pathology with a relevant social and economic impact. Different prostheses are currently adopted for incontinence surgical therapy, among which the artificial urinary sphincter is considered the most effective solution at present [1].

The prosthesis exerts a variable pressure field on the urethra, occluding the duct. However, several complications, as tissue atrophy and erosion, were observed after medium-long term implantation, leading to surgical recurrence. The artificial sphincter conformation and mechanical action are mostly based on data from surgical practice, while prosthesis should be also evaluated trough a biomechanical analysis of urethral tissues and structure, in particular during the occlusion of the duct.

At this purpose, an integrated experimental and computational approach is exploited. A computational framework of urethra mechanics is here proposed, based on experimental investigation of the mechanical properties of urethral tissues and structure. Histological data are processed to make virtual solid and finite element models of urethral duct. A specific hyperelastic formulation is developed to characterize the non-linear mechanical behaviour of urethral tissues. The inverse analysis of tensile tests on a urethra samples enables to define preliminary constitutive parameters. The parameters are defined also with reference to data form inflation tests.

Finally, the computational model of a urethra is exploited to evaluate the mechanical response when external actions are applied, aiming at the interpretation of the conditions for urethral lumen occlusion.

II. Materials and Methods

A. Histological analysis

Horse urethra samples were cut both in transversal and longitudinal directions after a histological fixation process [2]. Masson trichrome staining was used to identify tissue morphological properties, collagen and muscular fibres amount and preferred orientation (Fig. 1).

B. Mechanical testing

Mechanical tests on urethral tissues were performed on specimens from both distal and proximal urethra, along longitudinal and circumferential directions.

A Bose® ElectroForce® (Bose Corporation, ElectroForce Systems Group, Eden Prairie, MN, USA) equipment was used. Each specimen was stretched up to 60 % strain, kept constant for 300 s to investigate stress relaxation phenomena. As an example, the statistical distribution of results from tensile tests on distal tissue samples is reported in Fig. 2a.

Inflation tests were carried out on tubular segments of the urethral duct pertaining to distal and proximal regions. A mechano-electrical transducer (142 pc 01d pressure transducer, Honeywell, USA) interfaced to a data storage device (1326 Econo Recorder, Biorad, Italy) was used for data collection. The tests followed a two-step procedure. The first step was an almost instantaneous liquid in-flow, up to different inflated volumes (in a range between 5 and 50 ml), aiming at the definition of the elastic response. In the second step, the volume of the sample was kept constant for about 300 s to allow the development of visco-elastic processes, up to steady state.

Inflation tests on distal samples are reported in Fig. 3a.

C. Computational modelling

Histological analysis showed strong similarity between horse distal urethra and human anterior urethra [3]. Distal samples were considered for the computational modelling. A virtual geometrical model of urethra section was developed from histological images (Fig. 2b). Different layers compose the urethral tissue, namely a columnar epithelium around the lumen, a thin layer of dense connective tissue and a thick stratum of loose tissue comprising corpora spongiosa, connective septa and blood vessels. The geometrical model was imported into the finite element pre-processing software Abaqus/CAE 6.14-1 (Dassault Systèmes Simulia Corp., Providence, RI) and meshed by triangular elements (Fig. 2c). The representation of the epithelial layer was not provided with regard to its contribution to the mechanical response, as it is almost negligible. On the contrary, the epithelium effectively contributes to the overall behaviour, mostly when lumen surfaces interact because of compression loads. Specific self-contact condition allowed to properly take into account such interaction phenomena.

The mechanical behaviour of dense connective and loose tissue was specified by a hyperelastic formulation. The hyperelastic model adopted derives from previous constitutive analyses and proved its capability to interpret the typical features of soft tissue mechanics [4,5]. The general stress-strain relationship is here recalled:

$$\mathbf{P} = -p\mathbf{F}^{-T} + C_1 \exp\left[\alpha_1 \left(I_1 - 3\right)\right]\left(2\mathbf{F} - 2/3\, I_1 \mathbf{F}^{-T}\right) \qquad (1)$$

where $\mathbf{P}$ is the first Piola-Kirchhoff stress tensor, $\mathbf{F}$ is the deformation gradient, p is a Lagrange multiplier that specifies hydrostatic pressure and ensures the almost incompressibility of the material, I_1 is the first invariant of the right Cauchy-Green strain tensor $\mathbf{C} = \mathbf{F}^T\mathbf{F}$. The inverse analysis of results from tensile tests allow for the identification of constitutive parameters.

Additional investigations were required to assess the model reliability. A finite element analysis was consequently provided to evaluate experimental results from inflation tests that were developed on urethra tubular specimens. A homogeneous hydrostatic pressure field was applied to the intraluminal border of the urethra model. Pressure value was progressively increased to simulate the experimental progressive inflation.

The computational model allowed the definition of the urethra tissues mechanical response when external occluding load is applied. With the aim to mimic the action of artificial sphincters, a pressure field was applied all around the external boundary of the urethra model, according to the specific conformation. Considering the configuration of commercial devices, the occluding pressure can reach the limit of 10 kPa, while the intraluminal pressure was assumed between 0 and 10 kPa. Numerical analyses were performed by a two steps procedure. During the first step, the urethra was progressive inflated up to the target intraluminal pressure. During the second step, the occluding pressure was increased up to 10 kPa.

III. Results

The analysis of data from experimental investigations, at both tissue and structure level, is the basis for the constitutive parameters identification and assessment. Model results and statistical distribution of experimental data are compared in Figs. 2a and 3a, taking into account tensile tests on tissue samples and inflation tests on tubular specimens, respectively.

The numerical analysis of inflation tests allowed evaluating the tissues mechanical response when intraluminal pressure is applied. Typical contours of radial displacement and tensile stress (as the maximum principal stress) fields are reported in Figs. 3b and 3c, respectively.

Finally, urethral duct was investigated when external occluding action is applied. The numerical analyses took into account different situations, as different intraluminal pressure and progressive occluding load. Reference results are reported in Fig. 4. The compressive strain (as the minimum principal strain) field is reported for both loose tissue and dense connective tissue layer for different values of the occluding pressure conditions, while intraluminal pressure is kept at 1 kPa.

IV. Conclusion

The development of reliable computational models of the urethral tract requires a comprehensive experimental characterization of the constituent tissues and structure, through histologic analysis and mechanical testing.

Experimental data allow the definition of an appropriate constitutive formulation and the identification of constitutive parameters. The histological analysis aims at characterizing tissues configuration and is correlated with urethra mechanical behaviour. Tissue mechanical tests allow the preliminary identification of the constitutive model and the related parameters. Additional tests are developed on the overall urethra, in order to evaluate additional data from the structural response. The evaluation of animal and human urethra mechanical properties is not extensively discussed in the literature and was deeply investigated on the basis of histomorphometric data. The characterization of human urethra is in progress by additional experimental activities on human samples.

The present integrated experimental and computational protocol allows evaluating the mechanical behaviour of urethral duct during lumen occlusion, simulating the mechanical action of an artificial urinary sphincters and slings and offering a valid reference for surgical activity.

References

[1] E. Chung. (2014, August). A state-of-the-art review on the evolution of urinary sphincter devices for the treatment of post-prostatectomy urinary incontinence: past, present and future innovations. *J. Med. Eng. Technol. 38(6).* pp. 328-332.

[2] H. D. Dellmann, J. A. Eurell. (1998). Textbook of Veterinary Histology, 5th edn. Lippincott Williams &Wilkins, Baltimore,MD, USA.

[3] A. N. Natali, E. L. Carniel, A. Frigo, P. G. Pavan, S. Todros, P. Pachera, C. G. Fontanella, A. Rubini, L. Cavicchioli, Y. Avital, G. M. De Benedictis. (2016, February). Experimental investigation of the biomechanics of urethral tissues and structures. *Exp. Physiol.* DOI: 10.1113/EP085476

[4] A. N. Natali, E. L. Carniel, H. Gregersen. (2009, November). Biomechanical behaviour of oesophageal tissues: material and structural configuration, experimental data and constitutive analysis. *Med Eng Phys. 31(9).* pp. 1056-1062.

[5] A. N. Natali, P. G. Pavan, C. Venturato, K. Komatsu. (2011, November). Constitutive modeling of the non-linear visco-elasticity of the periodontal ligament. *Comput Methods Programs Biomed. 104(2).* pp. 193-198.

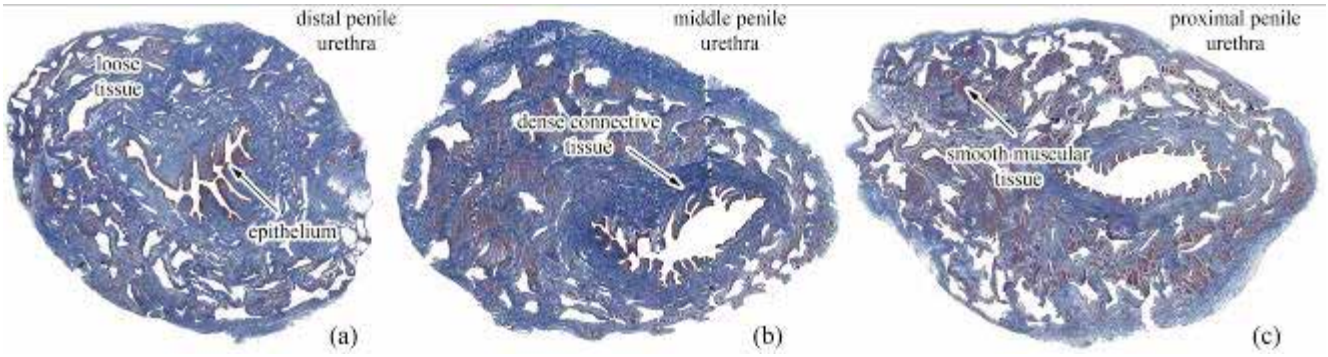

Fig. 1. Histological investigation of horse penile urethra. Specimens were collected from distal (a), middle (b) and proximal (c) regions.

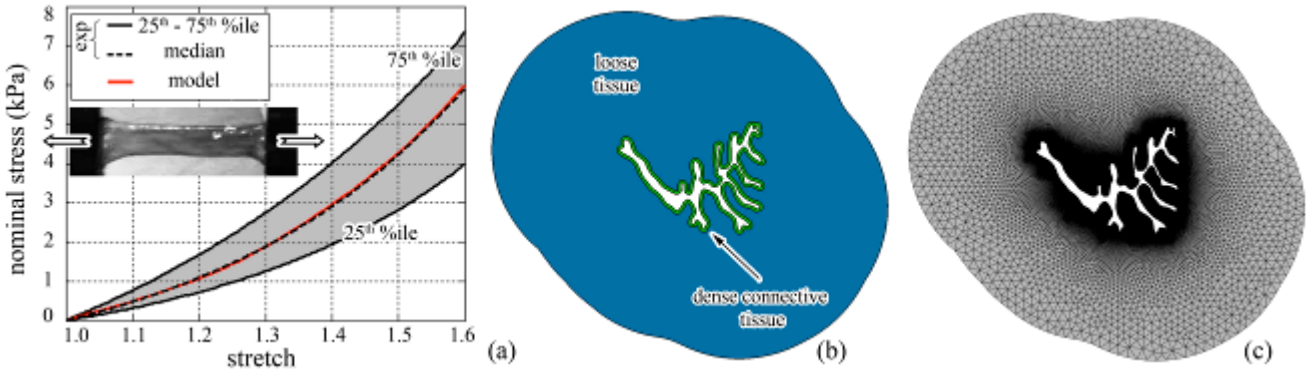

Fig. 2. Urethral tissue analysis and lumen modelling. Results from tensile tests (a) for identification of constitutive parameters by inverse analysis; virtual solid model of urethral section (b) and finite element discretization (c).

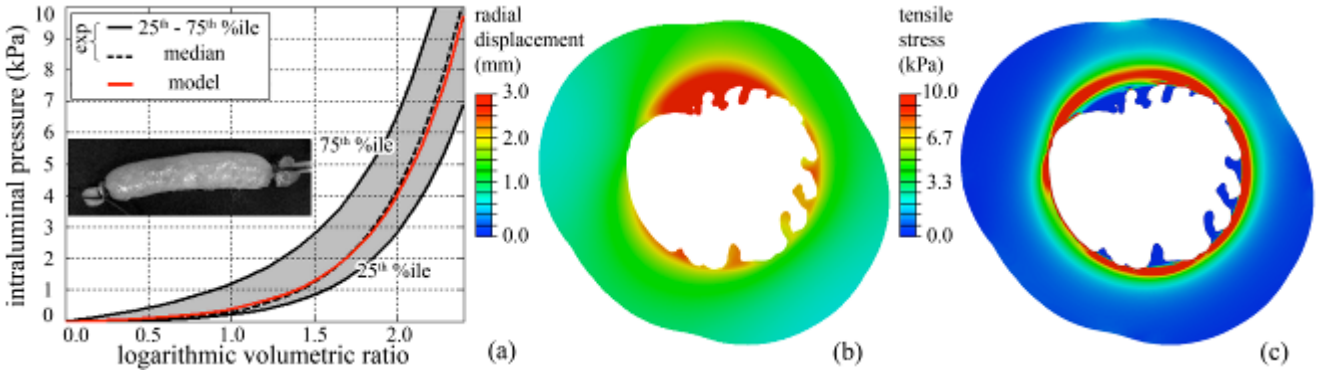

Fig. 3. Urethral duct analysis. Comparison of model results and experimental data from inflation tests (a); contours of radial displacement (b) and tensile stress (c) fields at a 4 kPa intraluminal pressure.

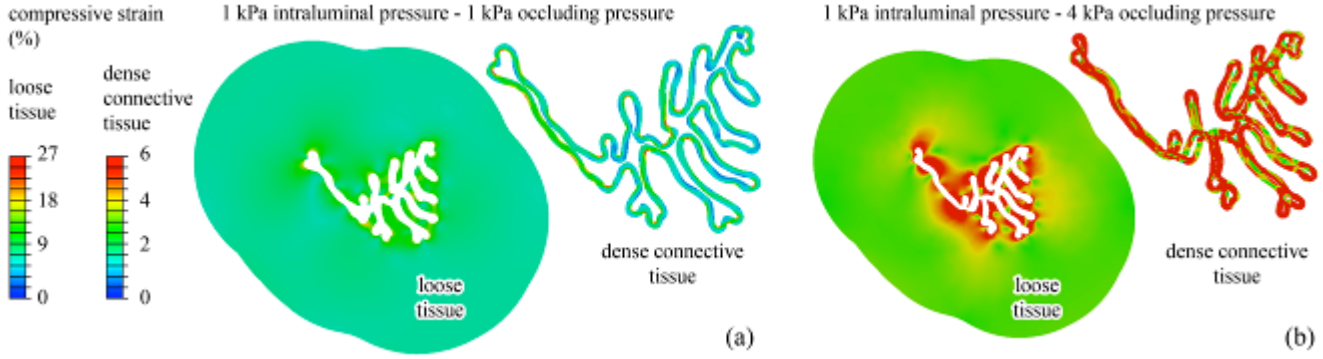

Fig. 4. Numerical analysis of lumen occlusion. Compressive strain field is separately depicted for loose and dense connective tissues: results are reported at 1 kPa intraluminal pressure and 1 kPa (a) or 4 kPa (b) occluding pressure.

A numerical approach to abdominal hernia repair with surgical mesh

P. Pachera[1,2], P.G. Pavan[1,2], S. Todros[1,2], C.G. Fontanella[1,2], N. Baldan[2,3], S. Merigliano[2,3], and A.N. Natali[1,2]
[1] *Department of Industrial Engineering, University of Padova, Padova, Italy*
[2] *Centre for Mechanics of Biological Materials, University of Padova, Padova, Italy*
[3] *Padova General Hospital, Padova, Italy*

***Abstract*— The present work proposes the numerical modelling of the abdominal wall repair by means of surgical meshes. The development of the numerical model of the abdominal wall is performed starting from images of Computed Tomography (CT) and data from literature, allowing the definition of the different abdominal components. Firstly, the global passive mechanical behaviour in the heathy condition is analysed. Then, a hernia defect is anteriorly introduced to mimic the presence of an incisional hernia, which is repaired by means of different surgical meshes with mechanical properties corresponding to xenograft and synthetic prostheses. Numerical analyses are performed by applying a uniform intrabdominal pressure (IAP) up to the physiological limit of 170 mmHg (0.023 MPa) which is observed while jumping. The global mechanical behaviour of the healthy and repaired abdominal wall are compared. The present work intends to provide a useful tool for a preliminary evaluation of the mechanical effects induced by a surgical mesh in the abdominal wall.**

***Keywords*—abdominal wall repair, surgical mesh, hyperelastic formulation, finite element analysis.**

I. INTRODUCTION

ABDOMINAL hernia consists in the protrusion of the internal viscera through a weakened region of the abdominal wall. Several factors can induce the hernia occurrence through the increase of the abdominal pressure.

Another important cause of hernia is the weakening of the abdominal tissues after operations at the site of the surgical incision (incisional hernia). Independently on the hernia origin, the surgical intervention is necessary to restore a condition which is as similar as possible to the initial physiological condition, by means of the insertion of a prosthesis. Nowadays, more than 500,000 hernia repair operations are performed worldwide each year, stressing the clinical relevance of this disease. Surgical meshes can have different origin and can be classified as biologic or synthetic, characterized by specific mechanical and biochemical characteristics and, consequently, by different biomechanical performances. Several factors can affect the success of the substitution as the mesh characteristics of chemical compatibility and biocompatibility. These aspects are correlated with this work, which is mainly focused on mesh biomechanical compatibility. The aim of this study consists in analysing and comparing, via numerical modelling, the mechanical response of the abdominal wall in the healthy condition and after the surgical repair. At the purpose, the numerical model of a healthy abdominal region is developed from Computed Tomography images. A hernia defect, characterized by size and position in accordance to clinical evidences, is introduced in the abdominal wall. This herniation is virtually repaired by means of different grafts, such as xenografts and synthetic meshes. In this study it is reported the example of surgical reparation by means of a xenograft (Permacol™), mechanically characterized in a previous work [1], and of a polypropylene mesh. A hyperelastic and fibre reinforced formulation is adopted to describe the mechanical behaviour of the different abdominal components. Experimental data from uniaxial tensile tests on human abdominal tissues [2] are considered for the constitutive parameters definition for each region by means of an optimization algorithm, which minimizes the difference between experimental data and numerical results. Surgical meshes are modelled according to their mechanical characteristics with an isotropic or anisotropic hyperelastic formulation. Numerical analyses are performed by applying a uniform IAP. The comparison of numerical results in physiological and pathological conditions allows a preliminary evaluation of the mesh effects on the global mechanical behaviour of the abdominal wall.

II. MATERIALS AND METHODS

A. Constitutive model

Since the long term condition is considered in the investigation of the abdominal wall tissues, a hyperelastic formulation is adopted. With this assumption the viscous phenomena are considered as completely developed.

Histological analyses highlight a transversal isotropic symmetry of the abdominal tissues, composed of a ground matrix reinforced by a family of collagen fibres, characterized by a preferential orientation. Because of the high water content of these tissues, it is possible to assume an almost incompressible behaviour that implies the splitting of the strain energy function into a volumetric and an iso-volumetric part.

$$W = U_m(J) + \bar{W}_m(\bar{I}_1) + \bar{W}_f(\bar{I}_4) \tag{1}$$

By defining the volume-preserving part of the right Cauchy-Green strain tensor as $\bar{\mathbf{C}} = \det J^{-2/3}\mathbf{C}$ it is possible to modify the invariants as $\bar{I}_1 = \mathrm{tr}(\bar{\mathbf{C}})$, $\bar{I}_4 = \bar{\mathbf{C}}:(\mathbf{m}_0 \otimes \mathbf{m}_0)$ obtaining the following strain energy function:

$$W = \frac{k_m}{2}\left(J^2 - 1 - 2\ln J\right) + \frac{\mu_m}{2}\left(\bar{I}_1 - 3\right) + \frac{\alpha_1}{2\alpha_2}\left[\exp\left(\alpha_2\left\langle \bar{I}_4 - 1\right\rangle^2\right) - 1\right] \tag{2}$$

k_m is the initial bulk modulus of the ground matrix, μ_m represents its initial shear stiffness and α_1 (stress-like), α_2

(dimensionless) are constitutive parameters related to the response of collagen fibres.

A hyperelastic formulation with isotropic or anisotropic characteristics is adopted for the constitutive modelling of the surgical meshes depending on their mechanical behaviour and characteristics. Also in this case the long term condition is considered.

B. Constitutive model fitting

The constitutive model fitting is performed by exploiting uni-axial tensile tests, along different directions, on the tissues of the abdominal wall, namely linea alba, rectus sheath, rectus muscles, lateral muscles [2,3]. Tensile tests on Permacol™ [1] and polypropylene mesh are considered for the mechanical characterization of surgical meshes. The constitutive parameters are identified by iteratively minimizing a cost function, which expresses the difference between the experimental data and the numerical results.

C. Finite element model

The volumes of linea alba, rectus abdominis muscle, aponeurosis and a structure comprising the lateral muscles are all included in the numerical model (Fig. 1). Then an incisional hernia characterized by an elliptic shape, having dimensions of 24 mm x 32 mm, is introduced along the linea alba. The surgical mesh is modelled with a rectangular shape, characterized by dimensions usually adopted in surgical procedures. The solid model is discretized by means of CAE ABAQUS® software (SIMULIA, Daussault Systems).

Muscles, aponeurosis and linea alba are discretized using linear tetrahedral elements. The fascial tissues that cover the muscles are characterized by a small thickness and are modelled by using linear membrane elements. The abdominal symmetry with respect to the sagittal plane is assumed allowing then consideration of half of this anatomical region, with consequent computational advantages.

An incremental and uniform IAP of 0.023 MPa is applied to the internal surfaces of the abdomen with the aim to span all the physiological range of pressure.

III. RESULTS

The comparison between experimental data and numerical results is reported in Figure 2a for the rectus sheath and the rectus muscle.

Figures 2b and 2c report the data fitting of Permacol™ and of the polypropylene mesh.

Figure 3 allows the comparison between the displacements magnitude computed at a IAP of 45 mmHg in the case of the healthy abdominal wall (a) and after surgical repair by means of Permacol™ (b). In Figure 3c it is reported the graph of the incremental stiffness.

The displacements magnitude are reported in Figure 4 for two paths of nodes chosen along the craniocaudal (a) and the transversal direction (b), taking into account the three above-mentioned conditions.

IV. CONCLUSION

A validation of the model in the healthy condition is achieved by comparing numerical results with experimental findings from literature. A strain along the linea alba of 15.2% is computed at 150 mmHg; the same measurement is in agreement with experimental data from inflation tests that highlight a strain of 16.5 ± 4.6% [4]. Another experimental study measures, by means of a system of infrared markers placed on the skin, an increase in the abdominal area of about 15% at a pressure of 12 mmHg [5]. The same calculation is performed on the numerical model obtaining a variation of the area up to 14% confirming the reliability of the results.

At present, there are no references in literature about experimental findings on the repaired abdomen. Therefore, this condition can be investigated through numerical models.

By comparing numerical data, it appears that the introduction of a biologic or a synthetic surgical mesh induces a global stiffening of the overall structure in terms of incremental stiffness (Fig. 3c). This latter is reported starting from the pressure value of 12 mmHg that is the value at which the mesh is positioned. The comparison of the deformational behaviour among the healthy and repaired conditions highlight very closed results (Fig. 4).

Some limitations of this work should be mentioned. Experimental data at disposal are limited as the number of subjects from which data are drawn. Only uni-axial mechanical tests are performed on tissues, omitting to consider the biaxial characterization. Further, only the passive behaviour on the abdominal wall is taken into account, neglecting muscles active contraction. Moreover, the mechanical behaviour of these biological structures is considered on the long term, neglecting the viscous phenomena.

Despite these limitations, the present work represents an improvement of the studies at disposal that often assume strong exemplifications. Furthermore, the proposed model supplies a tool for a preliminary evaluation of the mechanical effects due to the application of a surgical mesh. Future developments include also an extension different synthetic meshes with different materials and structures.

REFERENCES

[1] P. G. Pavan, P. Pachera, S. Todros, C. Tiengo, A. N. Natali (2015, June). Mechanical characterization of animal derived grafts for surgical implantation. J. Mech. Med. Biol. DOI: 10.1142/S0219519416500238

[2] M. H. S. Cardoso (2012). Experimental study of the Human Abdominal Wall. PhD thesis.

[3] B. Hernández, E. Peña, G. Pascual, M. Rodríguez, B. Calvo, M. Doblaré, J. M. Bellón (2011, December). Mechanical and histological characterization of the abdominal muscle. A previous step to modelling hernia surgery. J. Mech. Behav. Biomed. Mater. 4(3). pp. 392—404

[4] M. A. Konerding, M. Bohn, T. Wolloscheck, B. Batk, J. L. Holste , S. Wohlert, J. Trzewik, T. Förstemann, C. Hartung (2011, February). Maximum forces acting on the abdominal wall: Experimental validation of a theoretical modeling in a human cadaver study. Med. Eng. Phys. 33. pp. 789—792.

[5] C. Song C, A. Alijani A, T. Frank T, G. B. Hanna GB, A. Cuschieri A (2006, May). Mechanical properties of the human abdominal wall measured in vivo during insufflation for laparoscopic surgery. Surg. Endosc. 20. pp. 987—990.

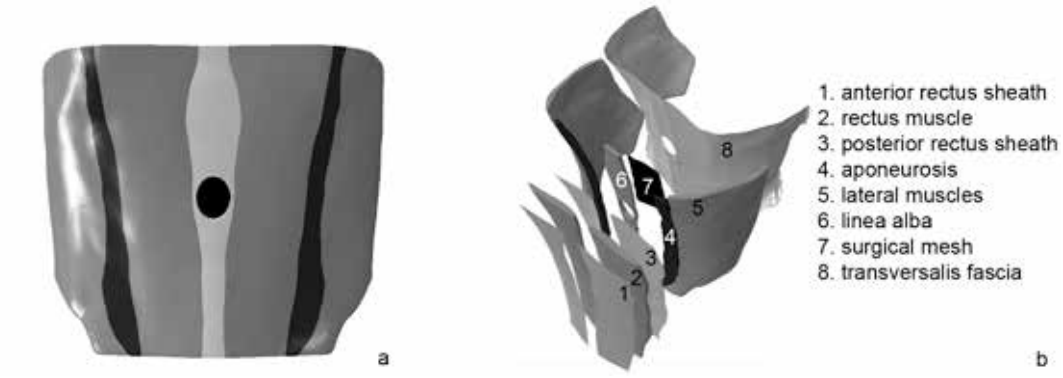

Fig. 1. Frontal view of the numerical model (a) and splitted view of the abdominal structures on different layers (b).

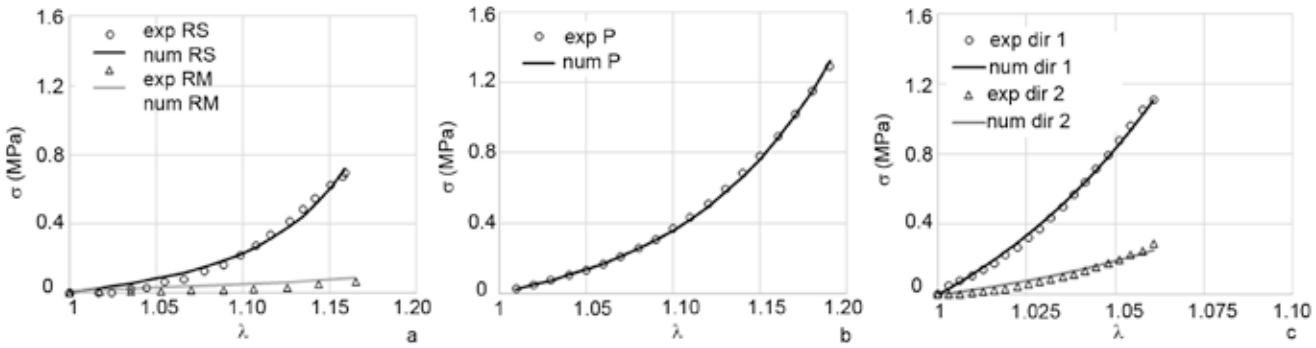

Fig. 2. Cauchy stress versus stretch behaviour for the mechanical response of rectus sheath (RS), rectus muscle (RM) (a), Permacol™(b) and polypropylene mesh along two mutual perpendicular directions (c). The solid lines are obtained by the numerical model, while open symbols represent experimental data.

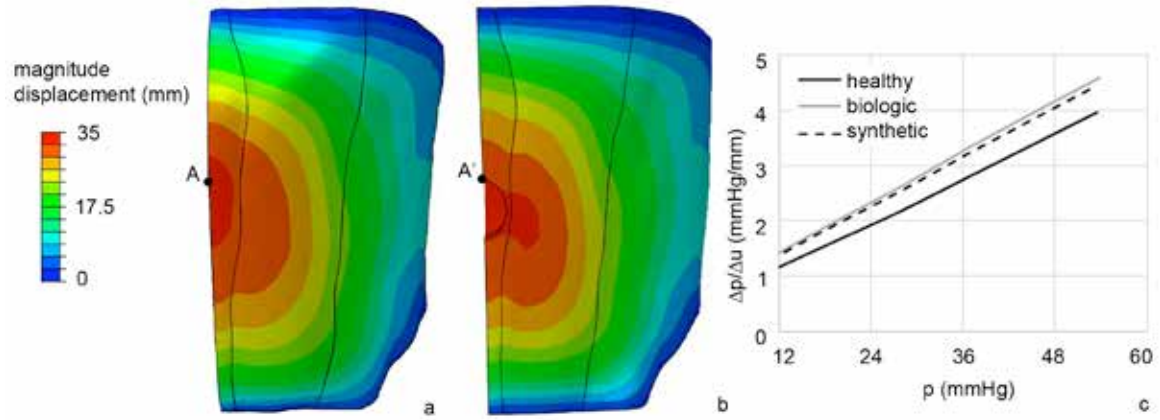

Fig. 3. Contour of the displacements magnitude on the external front view of the left abdomen in the case of the healthy condition (a) and after surgical repair by means of Permacol™ (b) mesh. Measure of the incremental stiffness calculated at specific points (A, A') as ratio between incremental IAP and incremental displacement (c) for the healthy condition and after surgical repair by means of Permacol™ (biologic) and of a polypropylene mesh (synthetic). Curves are reported starting from 12 mmHg that is the pressure value at which the mesh is positioned.

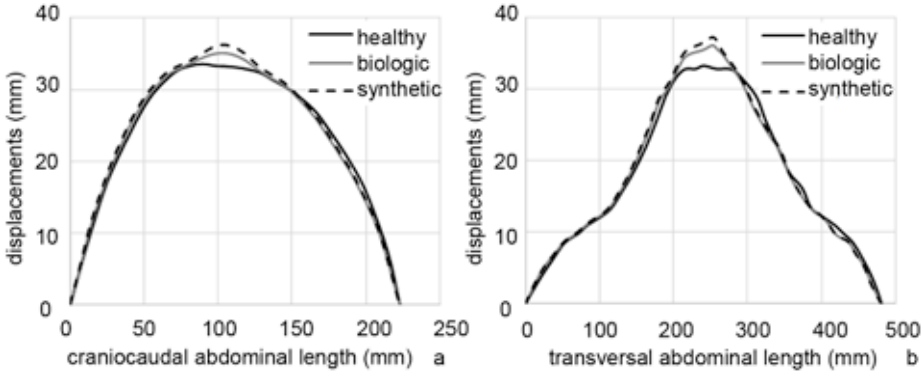

Fig. 4. Magnitude displacements evaluated along the craniocaudal (a) and the transversal direction (b) in the case of the healthy condition (H) and after surgical repair by means of Permacol™ (biologic) and a polypropylene mesh (synthetic) considering a IAP value of 45 mmHg.

Numerical modelling of human diaphragm mechanics: from fibres to whole muscle

P.G. Pavan[1,3], L. Marcucci[2,3], L. Toniolo[2], L. Cancellara[2], C. Reggiani[2,3] and A.N. Natali[1,3]
[1] *Department of Industrial Engineering, University of Padova, Padova, Italy*
[2] *Department of Biomedical Sciences, University of Padova, Padova, Italy*
[3] *Centre for Mechanics of Biological Materials, University of Padova, Padova, Italy*

***Abstract*— The diaphragm is the most important muscle of respiratory system. Its dysfunctions are related to alterations at morphological and/or tissue level and entail mechanical aspects. Therefore, in this work, we investigated diaphragm mechanics with a bottom-up approach. The mechanical response of single type I (slow) and type II (fast) muscle fibres was considered. Finite Element (FE) models of these fibres including a three elements Hill's constitutive formulation of the single sarcomere were developed to reproduce experimental tests. A FE model of a muscular bundle composed of type I and type II fibres was then obtained to estimate its force-length curve and adjust the Hill's constitutive model at a tissue level. Finally, a FE model of a human diaphragm was developed and its capability to describe the action of the diaphragm during respiratory activity was evaluated. This work represents the basis to investigate pathologies of respiratory system.**

***Keywords*—human diaphragm, muscle fibres, constitutive modelling, Finite Element Analysis.**

I. INTRODUCTION

THE DIAPHRAGM is the most important inspiratory muscle and its mechanical response is at the basis of possible dysfunctions of the respiratory system. Its morphology is complex, as well as the spatial distribution of embedded muscle fibres. Characterized by a dome-shaped structure, the diaphragm separates the thoracic cavity from the abdomen, mechanically interacting with the surrounding organs during its contractile function. Its peripheral part consists of muscular fibres that take origin from the circumference of the inferior thoracic aperture and converge to the central tendon.

The computational modelling [1] of diaphragm mechanics during the respiratory event in physiological and pathological conditions can have important applications in clinical treatment. To improve model predictability, it is necessary to keep a tight relationship of the constitutive model of active contraction with experimental data at any level, not only macroscopically, but also microscopically. Thus, to define the diaphragm model, we adopted a bottom-up approach, simulating the muscle behaviour at tissue level starting from single fibre characterization [2].

We developed models for single fibres based on a three elements Hill's model. We defined the model parameters for both type I and type II human skeletal muscle fibres, based on original experimental data (Vastus lateralis) obtained at low temperature (12°C), then extrapolating the results at body temperature.

The human diaphragm is composed approximatively by the same amount of type I and type II fibres, each with a diameter of few tens of micron. The fibres are finely mixed into bundles of hundreds of micron of diameter. Including a FE for each fibre is computationally too expensive To describe the mechanical response of muscle at tissue level, the characterization of mixed fibre bundles is then necessary. We therefore modelled bundles made of type I and type II fibres to reproduce the mixing effect on the force-velocity curve. Finally, we included our results in a three-dimensional FE model of human diaphragm, reproducing its mechanical behaviour during normal breathing.

II. MATERIALS AND METHODS

A. Experimental testing of muscle fibre mechanics

The fibre segment was transferred from the dissection to the experimental set-up (Fig. 1a) and mounted in a drop of relaxing solution between the force transducer equipped with a displacement transducer. The fibre segment, after measuring length, diameters and sarcomere length, was stretched by approximately 20%. Then, the fibre segment was transferred from relaxing solution into pre-activating solution for at least 2 min and, finally, maximally activated by immersion in activating solution (pCa 4.6). During maximal activation, isometric tension (P_0) was measured and unloaded shortening velocity (V_0) was determined according to the slack test procedure [3].

B. Constitutive model of muscle tissue

A three elements Hill's model was used for the mechanical characterisation of muscle contraction. The model includes an elastic element in parallel (PE) with a contractile element (CE) and a second elastic element in series (SE). Hill's models are rather phenomenological, despite that some relationship between elements and real muscle structures can be derived. In particular, the PE accounts for the passive elasticity and SE represents the elastic component in the muscle fibre, like tendons or even smaller structures (cross-bridges elasticity, titin, filaments compliance etc.). The CE represents the active force generation of muscle. Stretches of muscle fibre λ_f, active part λ_m and passive part λ_s of sarcomeric elements are related as:

$$\left(1+k\right)\lambda_f = \lambda_m + k\lambda_s \tag{1}$$

with k = 0.3, according to the literature. The stretch of the fiber is obtained as

$$\lambda_f = \sqrt{J^{-2/3}\mathbf{F}^T\mathbf{F} : \left(\mathbf{n}_0 \otimes \mathbf{n}_0\right)} \tag{2}$$

being $\mathbf{n}_0$ a unit vector representing the fibre direction in the undeformed configuration, $\mathbf{F}$ the deformation gradient and J the Jacobian. The first Piola-Kirchhoff stress is defined by the sum of passive isotropic and passive-active anisotropic terms:

$$\mathbf{P} = \mathbf{P}_{iso} + \left(P_p + P_a\right)\mathbf{F}\mathbf{n}_0 \otimes \mathbf{n}_0 \tag{3}$$

The isotropic part is obtained via a standard derivative from a strain energy function. The passive anisotropic part is set to

$$P_p = 4P_0\left(\lambda_f - 1\right)^2 \quad (4)$$

The active contribution given by the element CE is:

$$P_a = f_a f_l f_v P_0 \quad (5)$$

where P_0 is the maximum isometric stress, f_a the activation function, f_l the force-length function, f_v the force-velocity function. Contrary to usual approach in the literature [4,5], we have included the stretching of the SE at the maximum activation into the definition of f_l. In this way, the actual muscle length is taken into consideration instead of the sole CE length. This makes the model more consistent with physiologic aspects. The constitutive model was implemented with a user-subroutine in the general-purpose FEM software ABAQUS® (SIMULIA, Daussault Systems).

C. Constitutive model fitting

FE models of both muscle single fibres and bundles were developed by using linear hexahedral hybrid elements, because of the assumed almost-incompressible behaviour. Slack test of single fibres were simulated and the constitutive parameters defined by fitting the mechanical response to experimental data. Mixed type I and type II fibre bundles were also modelled according to the previous setting of the constitutive model. Isometric and isotonic contractions of the bundles were simulated to deduce the parameters of the Hill's model for the bundles. These models were based on histological cross sections of muscles, mimicking the original geometry obtained in the biopsy, as shown in Fig. 2a-b. The obtained characteristics curves were then adopted to fit the constitutive model at the tissue level.

D. F.E. model of human diaphragm

A human diaphragm FE model (Fig. 3a) was obtained from a 3D virtual representation, by using linear tetrahedral hybrid elements. For the muscle, the constitutive model described in Section C was adopted. A hyperelastic neo-Hookean model was assumed for the tendons.

A uniform pressure was applied on the inferior surface of the whole structure to simulate the mechanical action of abdominal region on diaphragm. The inferior region of the crura and the attachment to the ribs were considered fixed. The contraction of the diaphragm was simulated by applying an activation function corresponding to a respiratory rate of 12-20 min^{-1}.

III. Results and Discussion

Slack test experiments (Fig. 2c) shown a clear linear relationship between the amount of relative shortening and the time needed to recovery a non-zero tension. The slope of the fitting line obtained in FE analysis is the maximum velocity of the fibre, which has a clear distinction between type I and type II fibres. The intercept of the line at time zero indicates the stretch of the elastic components in the muscle during the isometric contraction (almost equal for the two fibres in the figure).

The FE model for the fibre allowed describing very severe protocols as the one used in the experimental characterisation of the muscles. As a novelty, we constrained the parameters of SE to reproduce slack test experimental data for both fast and slow fibres. As shown in Fig. 2a, the FE model for the fibre quantitatively reproduces both the minimum length step able to make the whole fibre unloaded and the increasing time in force recovery after increasing step length. The same FE model was used to reproduce the force velocity curve for both type I and type II fibres and the bundle.

Figure 2d shows the comparison of force-velocity curves for single type I and type II fibres, as well as a whole bundle composed with a type I / type II ratio of 1.079. When the diagram is shown in terms of normalized force, the bundle shows an intermediate curve, but more shifted toward the type II curve in the part of the diagram related to high velocity.

As introductory phase of the work, we tested the capability of the diaphragm model to replicate physiological conditions of normal breathing, verifying the mechanical response in terms of vertical excursion of the model. Figure 3b shows values that are in the range of those experimentally reported in the literature [6].

IV. Conclusion

A computational model based on an effective morphology may help in understanding the effects of diaphragm related pathologies, such as chronic obstructive pulmonary disease, diaphragm inactivity induced by mechanical ventilation, or amyotrophic lateral sclerosis.

On the other side, several diaphragm pathologies are associated to strong changes of single muscle fibre properties, such as contractile weakness, atrophy, or reduced cross sectional area. Moreover different muscle fibre isoforms affect in different way the whole muscle behaviour.

A bottom-up approach based on the effective behaviour of single fibres could be particularly useful to predict how different pathologies at fibre level can influence the whole muscle performance. This represents the main focus of the present work. The development of patient specific models of diaphragm will follow.

References

[1] M.P. Pato, N.J. Santos, P. Areias, E.B. Pires, M. de Carvalho, S. Pinto, D.S. Lopes, “Finite element studies of the mechanical behaviour of the diaphragm in normal and pathological cases”, *Comput Methods Biomech Biomed Engin*, vol. 14(6), pp. 505–513, 2011.

[2] R.K. Josephson, K.A. Edman, “The consequences of fibre heterogeneity on the force-velocity relation of skeletal muscle”, *Acta Physiol Scand*, vol. 132(3), pp. 341–52, 1988.

[3] K.A. Edman, “The velocity of unloaded shortening and its relation to sarcomere length and isometric force in vertebrate muscle fibres”, *J Physiol*, vol. 291, pp. 143–159, 1979.

[4] T. Joahansson, P. Meier, R. Blickhan, “A finite-element model for the mechanical analysis of skeletal muscle”, *J Theoret Biol*, vol. 206, pp. 131–149, 2000.

[5] S.M. Mijailovich, B. Stojanovic, A. Ko Liang, V.J. Wedeen, R.J. Gilber, “Derivation of a finite-element model of lingual deformation swallowing from the mechanics of mesoscale myofiber tracts obtained by MRI”, *J Appl Physiol*, vol. 109, pp. 1500–1514, 2010.

[6] J.G. Houston, A.D. Morris, D.G. Grosset, K.R. Lees, N. McMillan, I. Bone, “Ultrasonic evaluation of movement of the diaphragm after acute cerebral infarction”, *J Neurol Neurosurg Psychiatry*, vol. 58, pp. 738–741, 1995.

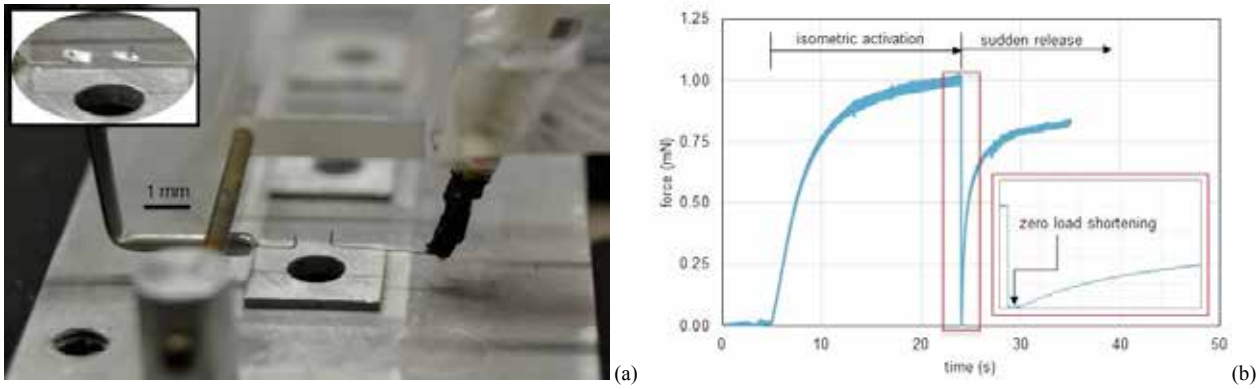

Fig. 1. Experimental set up for the mechanical testing of single muscular fibres, with enlarged detail of a clamped fibre (a). Typical force-time curve obtained from slack-test protocol (b).

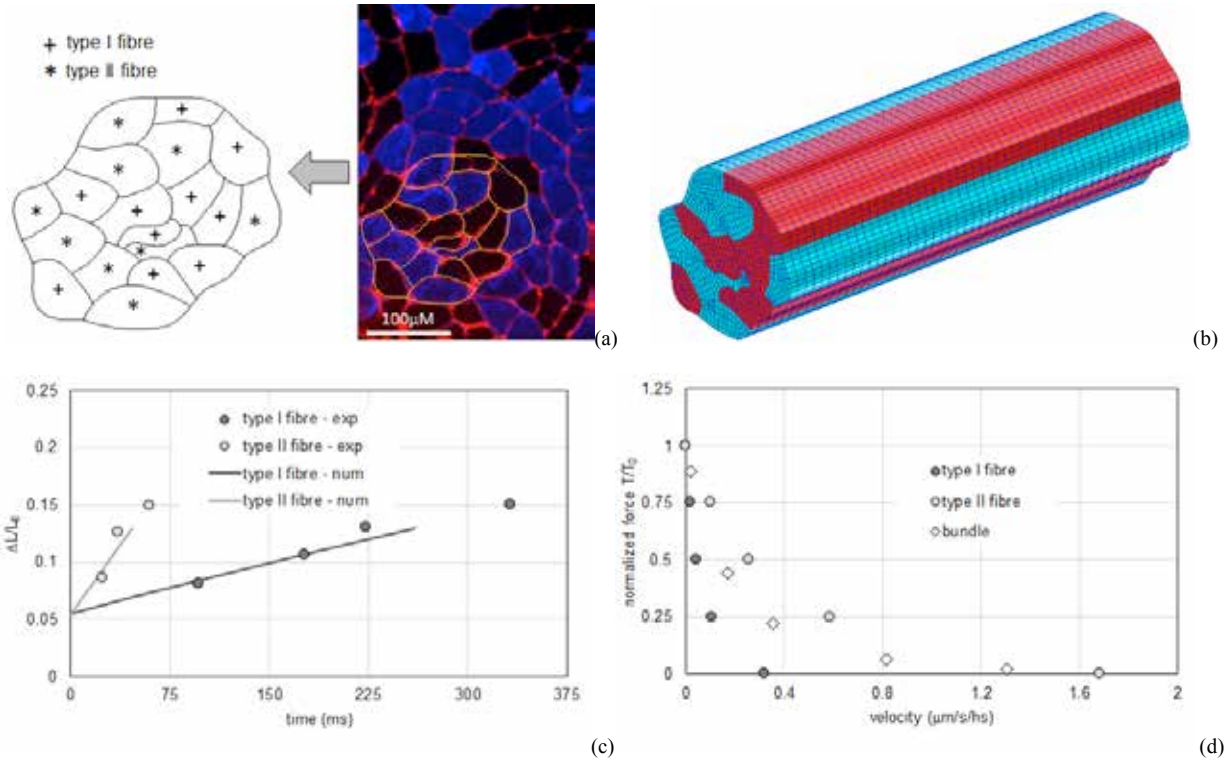

Fig. 2. Cross sectional area of muscle bundles (a), with identification of the modelled bundle. Reconstructed F.E. model of the bundle (b). Fitting of the model to mechanical response of single type I and type II muscle fibres (c), shown as ratio of length shortening and initial length vs. time. Simulated force-velocity response of a bundle compared to muscular type I and type II fibres response (d): the force is normalized to the isometric value, while the velocity is normalized to the length of half sarcomere (hs).

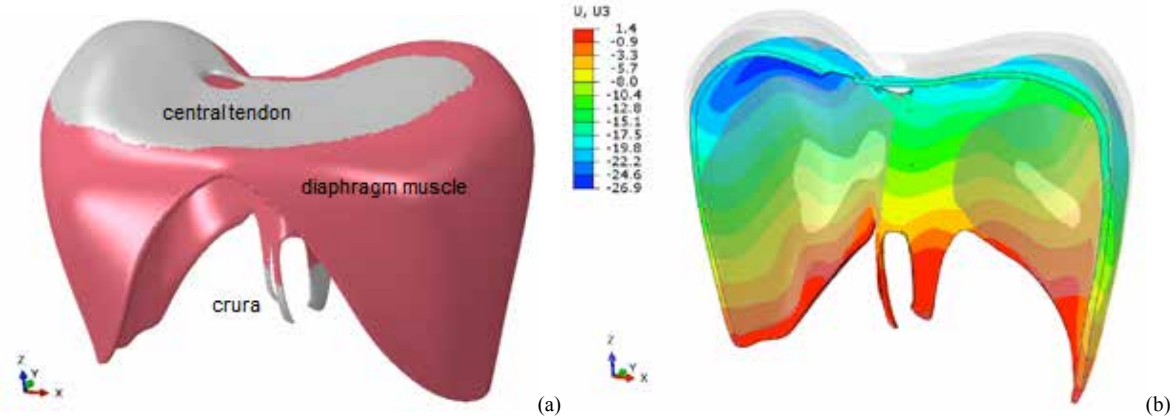

Fig. 3. F.E. model of human diaphragm (a) with indication of connective (grey coloured) and muscular (red coloured) tissue regions. Comparison of simulated relaxed and contracted shapes on a frontal section of the diaphragm corresponding to quite breathing (b); negative values (mm) represent displacements in the cranial-caudal direction.

Canine anterior cruciate ligament rupture: evaluation of functional recovery with multibody analysis

M. Gandaglia[1], M. Frapiccini[1], A. L. Audenino[1], P. Costa[2], M. Terzini[1], E. M. Zanetti[3], C. Bignardi[1]
[1] *Department of Mechanical and Aerospace Engineering - Politecnico di Torino, ITALY*
[2] *Intrauma S.r.l. – Rivoli (TO), ITALY*
[3] *Department of Industrial Engineering – Università di Perugia, ITALY*

***Abstract*—The aim of this study was to compare Tibial Plateau Levelling Osteotomies (TPLO) and CORA Based Levelling Osteotomies (CBLO) in treating canine Cranial Cruciate Ligament rupture. The two osteotomies were modelled using Solidworks® (Dassault Systemes SolidWorks Corporation, Massachusetts, USA) and Adams® (MSC Software Corporation, California, USA) codes and the simulations of both Cranial Drawer Test and Tibial Compression Test were performed. The results obtained in terms of tibial displacements were compared with those found *in vivo* in literature.**

***Keywords*—multibody analysis, canine cruciate ligaments, TPLO, CBLO**

I. INTRODUCTION

BEING one of the most involved articulation in dog injury, stifle joint is also one of the most studied; in particular, diseases related with the rupture of the Cranial Cruciate Ligament (CrCL) are the most frequent. Although diffused traditional techniques focus on the replacement of damaged ligaments with autologous, allogenic or synthetic structure, nowadays an increasing number of surgical procedures are based on tibial osteotomies, even if they are more expensive for dog owners (osteotomies can cost twice as much a traditional operation).

With this study, a multibody simulation of canine stifle was conducted to analyse forces and displacements acting firstly on a physiological limb and on a pathological one and then on the limb with osteotomies trying to understand how these ones can help a dog to regain normal lifestyle without lameness or pain. There are not many studies using multibody dynamic models of canine stifle, but, starting from works by Kim et al. [1], Helms et al. [2] and Olcott [3], an enough realistic model could be made.

II. MATERIALS AND METHODS

Four different models were created to analyse four different situations: Physiological (Physio), Pathological (Patho), tibia with TPLO (Tibial Plateau Levelling Osteotomy) osteotomy and tibia with CBLO (CORA (Center of Rotation of Angulation) Based Levelling Osteotomy) osteotomy.

Using Solidworks® (Dassault Systemes SolidWorks Corporation, Massachusetts, USA), on an existing CAD model of a canine complete posterior limb, origin and insertion points of Medial Collateral Ligament (MCL), Lateral Collateral Ligament (LCL), Cranial Cruciate Ligament (CrCL), Caudal Cruciate Ligament (CdCL) and Patellar Ligament (PL) were positioned, respectively on the femur and on the tibia, following anatomical indications taken from Evans et al. [4]. The model files relative to bones and ligaments were then imported in Adams® (MSC Software Corporation, California, USA).

For each bone part imported, markers were positioned at origin and insertion points relative to ligaments found in Solidworks®; Cranial Cruciate Ligament markers were only used in physiological model, because in the others the ligament was not present since it was ruptured.

For the construction of TPLO and CBLO models, the osteotomies were firstly carried out in Solidworks® following veterinary instructions and then the files were imported in Adams®. TPLO and CBLO plates, bushes and screws were positioned directly using Adams®.

Physiological and pathological models were created connecting femur and tibia without osteotomy: forces simulating ligaments action were applied in correspondence of markers using a subroutine in C language (Olcott [3]) that simulates their non-linearity.

The same procedure was followed for the construction of TPLO and CBLO models; in addition, the two parts composing the tibia with osteotomy, were connected using TPLO and CBLO plates, bushes and screws.

As regards materials the following characteristics were assigned: bone (density = $1.3*10^{-6}$ kg/mm^3 [3], E = 20 GPa [5]), steel (density = $7.81*10^{-6}$ kg/mm^3 , E = 207 GPa) for plates and Ti6Al4V (density = $4.43*10^{-6}$ kg/mm^3 , E = 114 GPa) for bushes and screws; for all the materials Poisson's Ratio was chosen as 0.3.

The tests were performed simulating a standing dog, i.e. with an angle between the femur and the tibia of about 135° (starting configuration) (Fig.1).

The Cranial Drawer Test was performed on each model leaving respectively the femur free to move vertically (one degree of freedom) without any force applied and the tibia free to move horizontally (one degree of freedom) applying on it a 44.5 N caudo-cranial force.

The Tibial Compression Test was performed with the same previous configuration, but growing forces (from 10 N to 80 N), corresponding to about 30% of canine weight of different dog sizes, were applied to the femur in order to simulate the load on the limb during standing.

III. RESULTS

In Table I the forces acting on ligaments in the four models in the starting configuration are compared. It results an increase of forces in TPLO and CBLO models; in particular, the patellar ligament (PL) seems to be more pre-stretched in CBLO than TPLO because in the latter the proximal part of the tibia is wedged, while in the former PL acts as a tie-rod.

In Table II Ultimate Tensile Strength (UTS) is compared with stress acting on ligaments in the starting configuration:

it can be seen that values reached after osteotomies are sufficiently lower than UTS, therefore ligaments do not reach premature damage situations. In addition, soft tissues, like ligaments, adapt to increased or decreased mechanical loadings by adjusting their size, their material properties, or both. This adaptation allows the tissues to withstand the mechanical loads imposed on them during normal activities of daily living [6].

TABLE I
FORCES ACTING ON LIGAMENTS IN THE STARTING CONFIGURATION [N]

	Physio	Patho	TPLO	CBLO
MCL	14.53	14.52	64.84	93.10
LCL	0.00	0.00	8.09	117.50
PL	5.56	5.57	8.39	107.20
CdCL	0.16	0.16	0.09	0.00
CrCL	0.00	-	-	-

TABLE II
LIGAMENTS STRESS IN THE STARTING CONFIGURATION [MPa] COMPARED WITH ULTIMATE TENSILE STRENGHT (UTS) [MPa]

	UTS	TPLO	CBLO
MCL	25.00	2.03	2.92
LCL	25.00	0.44	6.39
PL	25.00	0.35	4.53

In Table III displacements measured *in vivo* by Lopez [7] are compared with those obtained from simulations of Cranial Drawer Test.

TABLE III
DISPLACEMENTS OBTAINED WITH EXPERIMENTAL (*IN VIVO*) TEST AND NUMERICAL SIMULATIONS [mm]

	Physio	Patho
Lopez [7]	1.100	3.200
Adams model	1.347	2.835

In Fig. 2 results obtained after numerical simulations of the Tibial Compression Test are depicted. As can be expected, after the rupture of Cranial Cruciate Ligament (Patho), a significant increase in the cranial displacement of the tibia respect to the femur can be seen if compared with the Physio results. Looking at TPLO and CBLO results, it can be said that both osteotomies reach their purpose, i.e. creating a dynamic stabilization of the canine stifle. CBLO seems to be better than TPLO for small size dogs because it already reaches a good stability at low weight, while, with the increasing of dog sizes, both osteotomies tend to reach the same results, even better than physiological ones.

IV. Conclusion

As expected from theory, both Tibial Plateau Levelling Osteotomy (TPLO) and CORA Based Levelling Osteotomy (CBLO) increase their efficacy with the increments of dog weight; CBLO results the best choice for small size dogs.

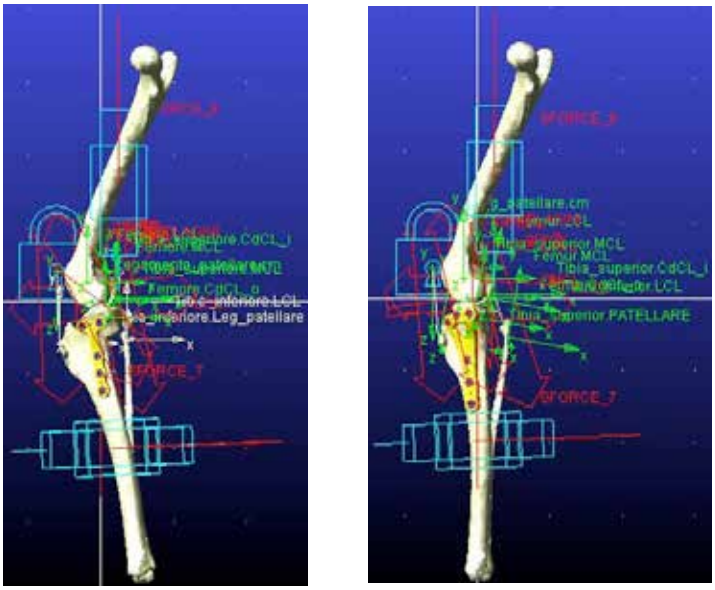

Fig. 1. TPLO (left) and CBLO (right) Adams® models

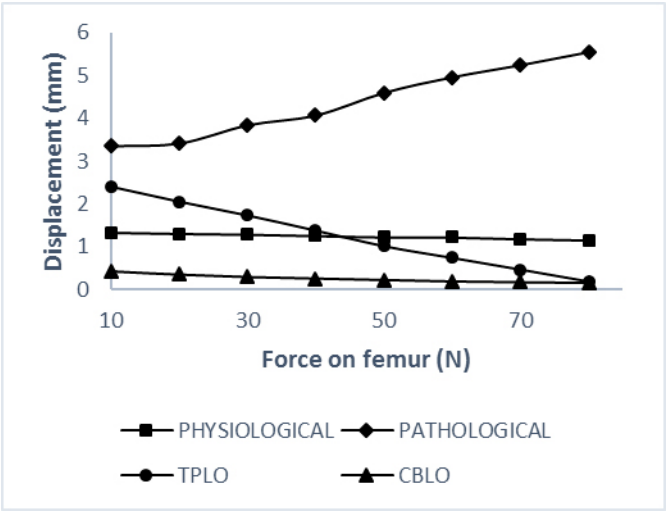

Fig.2. Tibial Compression Test results

References

[1] Kim S. E., Pozzi A., Banks S. A., Conrad B. P., Lewis D. D., Effect of Tibial Plateau Leveling Osteotomy on femorotibial contact mechanics and stifle kinematics. Veterinary Surgery, 2009, 38, 23-32.

[2] Helms G., Behrens B.-A., Stolorz M., Wefstaedt P., Nolte I., Multi-body simulation of a canine hind limb: model development, experimental validation and calculation of ground reaction forces. BioMedical Engineering OnLine, 2009, 8:36.

[3] Olcott L. E., Validation of a Subject Specific Canine Hind Limb Model with Emphasis on an Anatomical Stifle. 2011. PhD Thesis. University of Missouri-Kansas City

[4] Evans H. E., De Lahunta A., Miller's Anatomy of the Dog 4th ed. Elsevier Saunders,2012.

[5] Ashman R. B., Rosinia G., Cowin S.C., Fontenot M. G., Rice J. C., The bone tissue of the canine mandible is elastically isotropic, Journal of Biomechanics, 1985, 9, 18, 717-721.

[6] Ullrich R., Hulse D., Hauptman J. G., Effects of Tibial Plateau Leveling on Stability of the Canine Cranial Cruciate-Deficient Stifle Joint: An In Vitro Study. Veterinary Surgery, 2002, 31, 147-154.

[7] Lopez M. J., Hagquist W., Jeffrey S. L., Gilbertson S., Markel M. D., Instrumented measurement of in vivo anterior-posterior translation in the canine knee to assess anterior cruciate integrity. Journal of Orthopaedic Research, 2004, 22, 949-954.

Biomechanical analysis of synthetic surgical meshes for hernia repair

S. Todros[1,2], P. Pachera[1,2], P.G. Pavan[1,2], N. Baldan[2,3], S. Merigliano[2,4], and A.N. Natali[1,2]
[1] *Department of Industrial Engineering, University of Padova, Padova, Italy*
[2] *Centre for Mechanics of Biological Materials, University of Padova, Padova, Italy*
[3] *Padova General Hospital, Padova, Italy*
[4] *Department of Oncologic and Gastroenterologic Surgical Science, University of Padova, Italy*

***Abstract*— Abdominal wall surgery requires the use of surgical meshes, currently available in a variety of materials and structural conformations. Physicochemical and mechanical properties, as elastic, time dependent and anisotropic response, affect mesh conformation in the interaction with surrounding tissues and play a crucial role in a successful post-operative outcome. The aim of this study is to provide an experimental approach to study mesh biomechanical characteristics. Results refer to an integrated experimental and computational investigation, in direct correlation with surgical practice, aiming at the definition of suitable surgical meshes for the use in specific abdominal wall repair.**

***Keywords*—Synthetic surgical mesh, abdominal wall surgery, polymeric materials, mechanical properties.**

I. Introduction

THE use of surgical meshes is a frequent procedure for the repair of abdominal wall hernia (Fig. 1) or organs prolapse, in general [1]. Ventral hernias may arise for different reasons, including obesity, pregnancy, injuries and recurrent weight lifting [2]. Since laparotomy became established, incisional hernias occur after about 20% of interventions, in case of incomplete healing of the incision. Recurrence rates of post-laparotomy hernia are very high [3].

The investigation of surgical meshes in interaction with the abdominal wall is extremely important, in order to understand the role of material and structural properties in prosthesis performance [4]. Currently used meshes were repeatedly associated with complications, including chronic pain, bowel adherence, bacterial colonization and infection [2]. Due to the availability of many different prostheses and to patient-specific conditions, the efficacy of surgical meshes is not easy to predict.

The objective of this study is to acquire necessary data for mechanical analysis of surgical meshes. Experimental results on physicochemical and mechanical properties in this work are the basis for an integrated experimental and computational investigation.

In detail, the characterization of physicochemical properties of mesh materials and the morphologic analysis of mesh structures will allow for the comprehension of mesh mechanical behaviour. The main role of hernia prostheses is to strengthen the abdominal wall. At the same time, the prosthesis should not reduce the mobility and flexibility of the abdominal wall and should mimic the local anisotropy of the host tissue [5]. These mechanical requirements, which depend on mesh material and structural conformation, will be addressed and evaluated by mechanical testing. Moreover, the progress of this activity will let to evaluate, via computational tools, the mechanical behaviour of surgical meshes interacting with the tissues of the abdominal wall [6], after virtual surgical repair of hernia.

II. Materials and Methods

A. Materials

Synthetic surgical meshes were selected according to their use and diffusion for ventral hernia repair. The most widespread polymeric materials for the manufacturing of meshes were taken into account. Moreover, for the same mesh material, implants with different textile structure were selected.

B. Morphological characterization

Synthetic meshes are based on a polymeric fibre, which is generally knitted by interlacing it in a complex topology and with a wide range of possible textile patterns.

Optical and electronic microscopy allowed evaluating mesh conformation, polymeric fibre size and structure. A Zeiss Stemi 2000-C Stereo Microscope equipped with AxioCam ERc5s camera and an E-SEM XL30 Philips microscope were used for imaging.

C. Physicochemical characterization

Fourier Transform Infra-Red Spectroscopy (FT-IR) and Differential Scanning Calorimetry (DSC) were carried out in order to evaluate chemical composition and crystalline structure of mesh materials. FT-IR spectra were collected using a Nicolet TM iSTM 50 spectrometer. The spectra were obtained in ATR mode. A Q200 DSC (TA Instruments) equipped with a liquid N_2 cooling system was used to probe the thermal phase transitions.

D. Mechanical characterization

Mechanical tests were carried out on a Bose Electro-Force Planar Biaxial Test Bench Instrument, under displacement control. Different test protocols were adopted to evaluate the stress-strain response of surgical implants replicating physiological loading conditions, the time dependent mechanical behaviour and anisotropy of the prostheses. This was achieved via uni-axial tensile tests along structure symmetry axes, biaxial and equi-biaxial tensile tests (as shown in Fig. 2a). All tests were developed at different strain rates and with repetitive loading cycles to evaluate the mechanical behaviour after pre-conditioning.

III. RESULTS

A. Morphological conformation.

Optical images allowed a preliminary evaluation of mesh textile pattern. A repetitive unit was identified and measured. The analysis of unit cell geometry and orientation is fundamental for tensile specimen sizing and for the definition of test directions (Fig. 2b and 2c). Moreover, electron microscopy provided an insight on fibre diameter and structure. In most of the meshes, monofilament fibre were found, with a diameter of about 0.15 mm. Some SEM details of the structural conformation of different meshes are reported in Fig. 3.

B. Physicochemical properties.

FT-IR and DSC results confirmed that the different meshes investigated in this work are made by isotactic polypropylene, polyethylene terephthalate and polyvinylidene fluoride. This characterization provides the basis for comparing mechanical properties of meshes with the same chemical composition and different textile patterns. Moreover, the effect of crystalline structure of polymers on their mechanical properties may be investigated.

C. Mechanical properties.

Uni-axial and biaxial tests were carried out on different meshes. Uni-axial testing does not accurately mimic physiological loading conditions, while biaxial tests are preferable for a more accurate biomechanical evaluation. Biaxial testing for surgical meshes characterization is infrequently reported in the literature [7,8]. The results revealed a wide range of different mechanical behaviour depending on mesh type, including a non-linear stress-strain behaviour with a stiffening response.

By way of example, the experimental results of equi-biaxial tensile tests along two orthogonal directions are shown in Fig. 4a for a polyvinylidene fluoride surgical mesh, in terms of membrane force vs. nominal strain. The tensile response was evaluated in the strain range up to 0.1 that can be considered a moderate strain in physiological conditions. The results clearly demonstrated that the mesh has an anisotropic behaviour. Mesh and host-tissue anisotropy should be correlated within surgical planning.

The results of uni-axial tensile tests along two orthogonal directions, at different strain rate, are shown in Fig. 4b for a polypropylene mesh. In this case, the prosthesis did not show a significant viscoelastic behaviour.

In Fig. 4c, a comparison of tensile data for the same polypropylene mesh in different test conditions is reported. Results showed the stiffness measured via equi-biaxial testing is typically higher than the stiffness in uni-axial tension or in plane strain state. This means that uni-axial testing by itself can lead to an underestimation of mesh stiffness with possible negative implications after in-vivo positioning.

IV. CONCLUSION

Synthetic surgical meshes are frequently used for hernia repair, but their implantation may bring complications and surgical recurrence. For this reason, prostheses compatibility should be carefully evaluated, with regard to biochemical and mechanical aspects. At present, the lack of standardization in test procedures for surgical meshes is determining problems in evaluating their performances, even in correlation with host tissues mechanical behaviour. It is advisable to identify main morphological, chemical and mechanical features, which could provide a whole picture of mesh properties. Mesh membrane stiffness must be evaluated, because significant difference in stiffness between the host tissue and the prosthesis may cause pain and complications. Moreover, the viscoelastic properties of surgical meshes should be investigated, to assess their mechanical response depending on loading rate.

In this work, several surgical meshes were taken into account, according to their diffusion and use in hernia repair. Physicochemical and mechanical properties of these prostheses were characterized and compared. Based on the acquired experimental data, a biomechanical analysis of mesh behaviour in vivo is already in progress. At this purpose, experimental results on mesh mechanical properties let to formulate an appropriate constitutive model. Constitutive parameters are identified by the comparison between experimental data and model results. Numerical analyses are performed in order to evaluate the mechanical performances of different meshes in interaction with the tissues of the abdominal wall. This activity entails a multidisciplinary approach, involving surgeons and biomechanical engineers, in order to interpret properly the functional response of the mesh.

REFERENCES

[1] S. Todros, P.G. Pavan, A.N. Natali (2016, March). Biomechanical properties of synthetic surgical meshes for pelvic prolapse repair, *J. Mech. Behav. Biomed. Mater. 55.* pp. 271—285.

[2] R. W. Luijendijk, W. C. J. Hop, P. van den Tol, D. C. D. de Lange, M. M. J. Braaksma, J. N. M. Ijzermans, R. U. Boelhouwer, B. C. de Vries, M. K. M. Salu, J. C. J. Wereldsma, C. M. A. Bruijninckx, J. Jeekel. (2000, August). A comparison of suture repair with mesh repair for incisional hernia. *New Engl. J. Med. 343(6).* pp. 392—398.

[3] V. J. Hesselink, R. W. Luijendijk, J. H. de Wilt, R. Heide, J.Jeekel. (1993, March). An evaluation of risk factors in incisional hernia recurrence. *Surg. Gynecol. Obstet. 176(3).* pp. 228—234.

[4] S. Todros, P. G. Pavan, A. N. Natali. (2015, December). Synthetic surgical meshes used in abdominal wall surgery: part I - materials and structural conformation. *J. Biomed. Mater. Res. B Appl. Biomater.* DOI: 10.1002/jbm.b.33584

[5] S. Todros, P. G. Pavan, P. Pachera, A. N. Natali. (2015, December). Synthetic surgical meshes used in abdominal wall surgery: part II - biomechanical aspects. *J. Biomed. Mater. Res. B Appl. Biomater.* DOI: 10.1002/jbm.b.33586

[6] P. G. Pavan, P. Pachera, S. Todros, C. Tiengo, A. N. Natali. (2015, June). Mechanical characterization of animal derived grafts for surgical implantation. *J. Mech. Med. Biol.* DOI: 10.1142/S0219519416500238

[7] C. R. Deeken, D. M. Thompson, R. M. Castile, S. P. Lake. (2014, October). Biaxial analysis of synthetic scaffolds for hernia repair demonstrates variability in mechanical anisotropy, non-linearity and hysteresis. *J. Mech. Behav. Biomed. 38.* pp. 6—16.

[8] M. T. Wolf, C. A. Carruthers, C. L. Dearth, P. M. Crapo, A. Huber, O. A. Burnsed, R. Londono, S. A. Johnson, K. A. Daly, E. C. Stahl, J. M. Freund, C. J. Medberry, L. E. Carey, A. Nieponice, N. J. Amoroso, S. F. Badylak. (2014, January). Polypropylene surgical mesh coated with extracellular matrix mitigates the host foreign body response. *J. Biomed. Mater. Res. A. 102(1).* pp. 234—246.

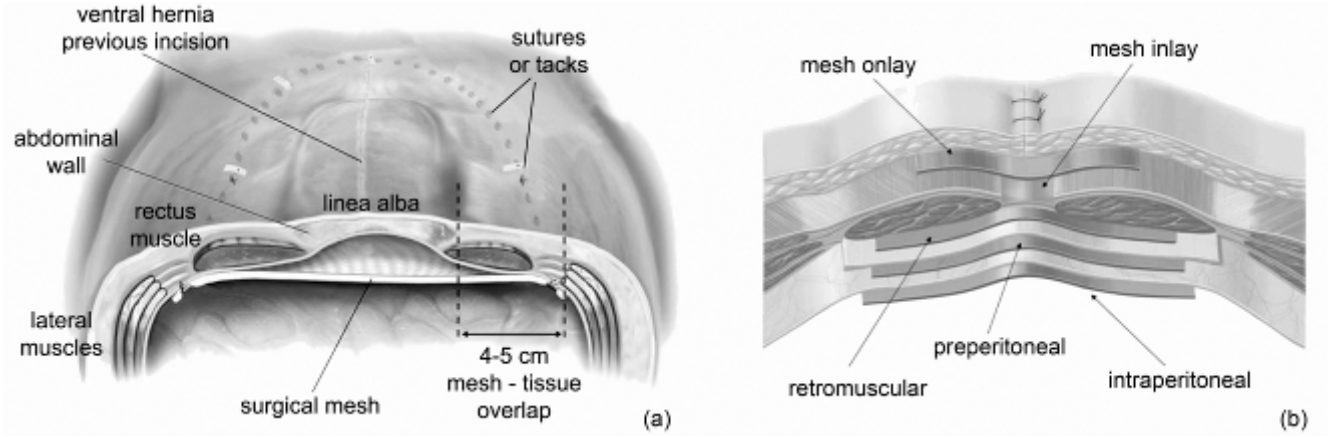

Fig. 1. Position of synthetic surgical mesh for abdominal hernia repair (a) with regard to abdominal wall layers (b).

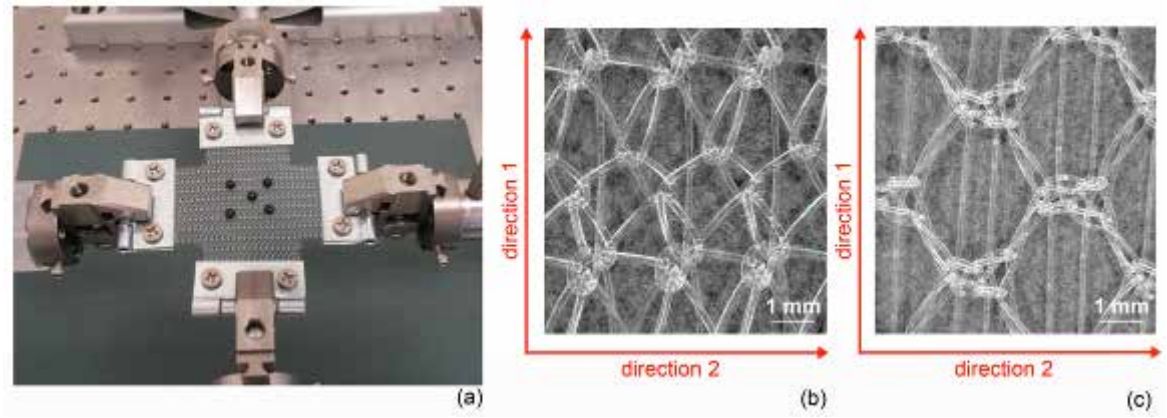

Fig. 2. Experimental set-up for biaxial tensile tests on a surgical mesh (a). Markers in the central area of the sample are used to obtain the local strain by an integrated system of image analysis. Different mesh conformations (b,c) and corresponding test directions.

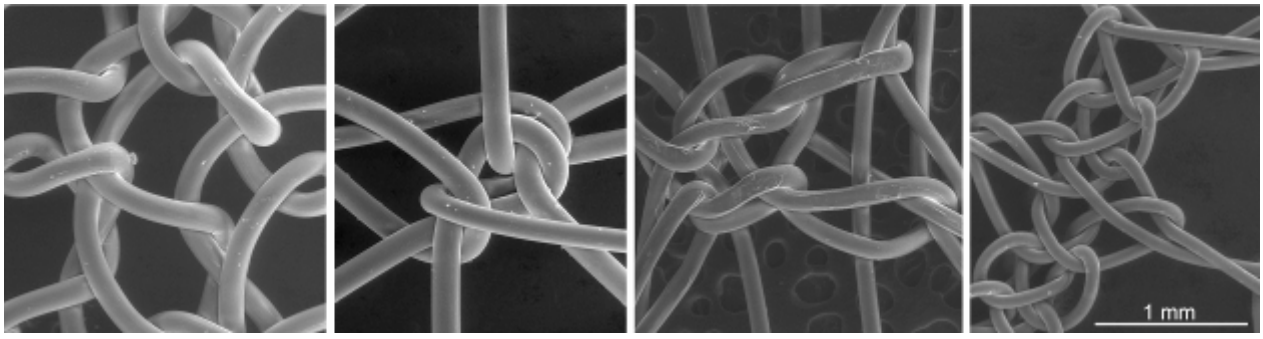

Fig. 3. SEM images of different synthetic surgical meshes: details of the structural conformation.

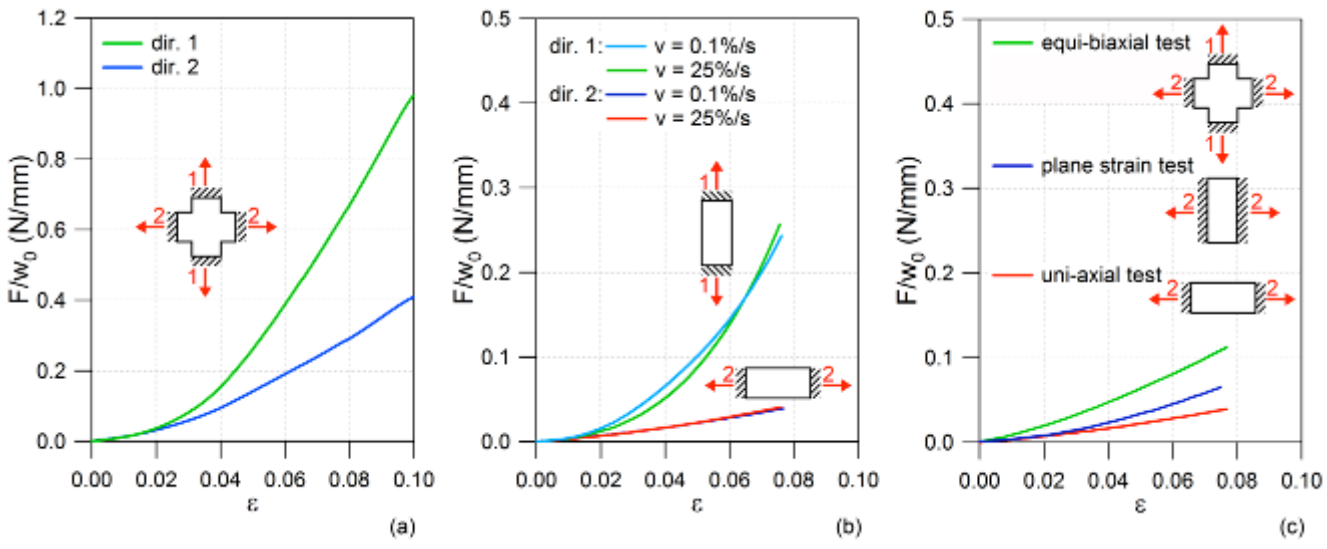

Fig. 4. Tensile test results reported as force per unit width vs. strain. Equi-biaxial tests of the mesh in Fig. 2b (a); uni-axial tests of the mesh in Fig. 2c at different strain rates along two different directions (b); comparison of tensile results for the mesh in Fig. 2c in different test conditions, at a strain rate of 0.1 % s^{-1}, along direction 2.

BIOROBOTICA

Multilevel control of an anthropomorphic prosthetic hand for grasp and slip prevention

R. Barone[1], A.L. Ciancio[1], R.A. Romeo[1], A. Davalli[2], R. Sacchetti[2], E. Guglielmelli[1] and L. Zollo[1]
[1]*Laboratory of Biomedical Robotics and Biomicrosystems, Università Campus Bio-Medico di Roma, Via Alvaro del Portillo 21, I00128 Roma, Italy*
[2]*INAIL Centro Protesi, Via Rabuina, 14, 40054 Vigorso di Budrio (BO), Italy.*

***Abstract*—Actual upper limb commercial prostheses mainly rely on amputee visual feedback to allow the objects to be stably grasped. This is due to the lack of force/tactile sensors in the prostheses and force/slippage controls. This paper proposes a multilevel control for sensorized hand prostheses based on two distinct levels, i.e. i) a policy search learning algorithm combined with Central Pattern Generators in the higher level control for planning motion strategies, and ii) a parallel force/position control for managing slippage events in the lower level. The control has been tested on an anthropomorphic robotic hand for prosthetic application endowed with force sensors; bi-digital and tri-digital tasks with and without slip information have been carried out. The acquired data demonstrate that proposed control has the potential to adapt the changes in the environment and guarantees grasp stability, by avoiding object fall thanks to prompt slippage event detection.**

***Keywords*—Prosthetics, Biomechatronics, Control, Tactile sensors.**

I. Introduction

COMMERCIAL prostheses are typically velocity- or position controlled; no tactile system is integrated in the hand and the success of the grasp is based on the visual feedback of the amputee [1]. In robotic applications, tactile systems are used for objects recognition tasks, force control, objects grasp and surfaces servoing [2]. The control approaches can control fingers torque, force, velocity and trajectory and include classical PID, adaptive, robust, neural, fuzzy sliding-mode and their combinations [3]. In addition, a well-consolidated approach to ensure grasp stability relies on the concept of friction cone, thus implying that the ratio between the normal force and the tangential force during grasping, multiplied by the static coefficient of friction, has to exceed one. This method is very effective; however, it suffers from some limitations that make it unsuitable for prosthetics, e.g. it requires sensors able to measure both normal and tangential forces (even though estimations can be used as in [4]) and requires to a priori know the static friction coefficient. Alternative and more recent approaches able to still guarantee grasp stability can be found in [5-8].

In this work, a new control architecture for prosthetic hands is proposed. It is distributed on two levels: a high level based on learning algorithm (Policy Improvement Black Box, i.e. PIBB), for trajectory planning and finger coordination, and a low-level for force and position control (a parallel force/position control) endowed with slippage prevention capability. In this paper, low cost FSR sensors have been positioned on the tip of thumb, index and middle fingers and used for measuring the normal force component. Furthermore, FSR output is properly processed to extract information about slippage events, without requiring further sensing units (as in [6]) or supplementary equipment [8].

II. Materials and Methods

A. Control architecture

The control architecture distributed on high and low level control is shown in Fig. 1. The high level control has the aim of planning the desired grasping task and identifying the optimal strategy for finger coordination. The PIBB learning algorithm has been employed in order to autonomously search the CPG parameters necessary to define the desired finger trajectory suitable for the grasping task. The learning phase has been characterized by several repetitions of the trial, grouped into periods. The set of optimal CPG parameters for a specific task is so obtained and the desired trajectories for the fingers motion is generated accordingly.

The parallel force/position control (i.e. the low level control) produces the motor commands for the hand actuation system starting from force and position references and proprioceptive and tactile sensory feedback. The implemented low level control is a parallel force/position control equipped with slippage detection and control.
The proposed control law is expressed as follows

$$\tau = \tau_g + k_p\left(x_f + x_d - e_s - x\right) - k_d\dot{x} + J^t f_a \quad (1)$$

$$x_f = C_f(f_d - f_a). \quad (2)$$

The parallel force/position control consists of two loops: the outer, with c_f as a gain, is a PI force control (with k_{fp} and k_{fi} as proportional and integral gains respectively), while the inner loop is a PD position control, where k_p and k_d are the proportional and derivative gains; x_f is the position reference from the outer loop, f_d and f_a are the desired and the actual normal forces respectively; τ is the actuation torque to command each joint of the hand (x), τ_g is the torque needed to compensate the gravity action. x_d is the desired joints position, e_s the slippage signal which acts as an additional error of the position inner control loop as shown in [7]. $\dot{x}$ is the joint velocities vector and J_{fa}^t is the term needed to compensate the force between the fingers and the object.

The proposed architecture aims at being used both during grasping and (rhythmic and discrete) manipulation tasks. The desired forces have been experimentally retrieved with the prosthetic hand while the position references have been generated by the high level control.

B. Implementation on the prosthetic hand

In this study the IH2 anthropomorphic robotic hand (by Prensilia s.r.l.) has been used (Fig. 2). It is a 5-finger bio-mechatronic underactuated human-sized hand for prosthetic applications.

The learning phase (high-level control) has been carried out in simulation with simulated objects in order to avoid overwork and exclude unexpected behaviour or damages in the real setting with the IH2 hand. The learned parameters have been tested on the real robotic hand during the object grasp. Grasp forces during the experimental trials have been collected by three FSR sensors, each one mounted respectively on the distal phalanx of thumb, index and middle finger (Fig. 2). A quasi-static calibration of the three sensors has been carried out over the range [0.2; 8.0] N. Each sensor has been covered with a prosthetic silicon cap, in order to simulate a prosthetic glove (Fig. 2). As regards slippage, after preprocessing of the FSR output, a threshold mechanism has been adopted to extract a real-rime binary slip signal.

C. Experimental setup

The experimental set-up for the validation of the two-level control is depicted in Fig. 3. Three widely used objects during activities of daily living (ADLs) have been selected for performing two kinds of grasp: bi-digital and tri-digital (Fig. 4). The former has been performed with an egg (Fig. 4B) and a highlighter (Fig. 4D), the latter with the egg (Fig. 4A) and a cylindrical plastic cup (Fig. 4C). The masses of the objects were around: 60 g (egg), 50 g (cup) and 10 g (highlighter). Slippage has been automatically induced by means of a robotic arm (KUKA/LWR4+), whose end effector has been equipped with a thin, cylindrical probe. Experiments without considering the slip information (i.e., only relying on the force/position control) have been carried out as well for comparison. In all cases, six repetitions have been performed, resulting in a total of 72 trials. All the data have been acquired at a sampling frequency of 2 kHz by a NI DAQ (NI-6009) device.

III. Results and Discussions

A. Results of the training phase

Cost time course during the learning of bi-digital and tri-digital grasp of an egg are shown in Fig. 5. The decrease of the cost values during training clearly indicates the improvement of the performance during learning.

B. Experimental results of the test phase

The results of the experimental tests on grasping with and without slippage control are shown in Figs. 6 and 7. They show: (a), (c) the measured forces compared with the desired force; (b), (d) the slider positions compared with the desired positions. When there is no slippage control, the grasped object is perturbed by two identical perturbations of 1 cm at the maximum robot speed (4 cm/s), in order to verify whether the object falls, or at least is unstably grasped. When the slippage control is active, one perturbation of 1 cm at two different velocities (2 cm/s and 4 cm/s) is produced; as expected, the system is able to immediately detect slippage .

Figures 6(a) and 6(b) show a tri-digital grasp of the plastic cup with the slip prevention algorithm disabled and perturbation set to 4 cm/s. The controller reacts to the perturbation by avoiding the cup fall thanks exclusively to the parallel force/position control; grasp is maintained but it is no longer stable. In fact, as the subsequent perturbation occurs, index and thumb fingertips lose their contact with the object and the precision grasp fails. The middle fingertip casually continues touching the object because the object remains unstably grasped. Figures 6(c) and 6(d) show a further tri-digital grasp trial of the cup, but this time the slippage prevention algorithm is active and the perturbation set to 2 cm/s. As the slip event due to perturbation is detected, the grip is strengthened and the grasp becomes stable. In Fig. 7 the bi-digital grasp of the highlighter is reported. In this case, when the control of the slippage is inactive (i.e. 7(a) and 7(b)) there is no incisive increase in the grasp forces after the two perturbations. Instead, forces diminution can be observed in the force plot, confirming that the object is not grasped in a stable manner as a consequence of the perturbations. Slider positions remain unvaried; forces change is uniquely due to the under-actuated behaviour of the fingers. Figures 7(c) and 7(d) illustrate the reaction of the controller to a perturbation applied at 4 cm/s. The slip event is followed by a fast increase of index and thumb forces. After the adjustment due to slippage control, grasp stability is reached.

Acknowledgement

This work was supported by the Italian Ministry of Instruction, University and Research with PRIN project "HANDBOT " (CUP: B81J12002680008), by the Italian Institute for Labour Accidents (INAIL) with PPR 2 project (CUP: E58C13000990001), by the European Project H2020/AIDE, CUP J42I15000030006.

References

[1] Ninu A, et al. Closed-loop control of grasping with a myoelectric hand prosthesis: Which are the relevant feedback variables for force control?. NSRE 2014; 22: 1041-1052.

[2] Kappassov Z, et al. Tactile sensing in dexterous robot hands-Review. RAS 2015; 74: 195-220.

[3] Huang HP, et al. Rehabilitation Robotic Prostheses for Upper Extremity. In: Zhou M, Li HX and Weijnen M (eds) Contemporary Issues in Systems Science and Engineering. USA: Wiley, 2015, pp.661-697.

[4] Wettels N, et al. Grip control using biomimetic tactile sensing systems. IEEE/ASME Trans. on Mechatronics 2009; 14: 718-723.

[5] Pasluosta CF and Chiu AW. Evaluation of a neural network-based control strategy for a cost-effective externally-powered prosthesis. Assistive Technology 2012; 24: 196-208.

[6] Mingrino AR, et al. Slippage control in hand prostheses by sensing grasping forces and sliding motion. IROS, Munich, Germany, September 12 - 16, 1994, pp.1803-1809.

[7] Engeberg ED et al., Adaptive sliding mode control for prosthetic hands to simultaneously prevent slip and minimize deformation of grasped objects. IEEE/ASME Trans. on Mech. 2013; 18: 376-385.

[8] Sriram G, et al. Slippage control for a smart prosthetic hand prototype via modified tactile sensory feedback. In: EIT, Milwaukee School of Engineering Milwaukee, WI, 05 Jun - 07 Jun 2014, pp.225-230.

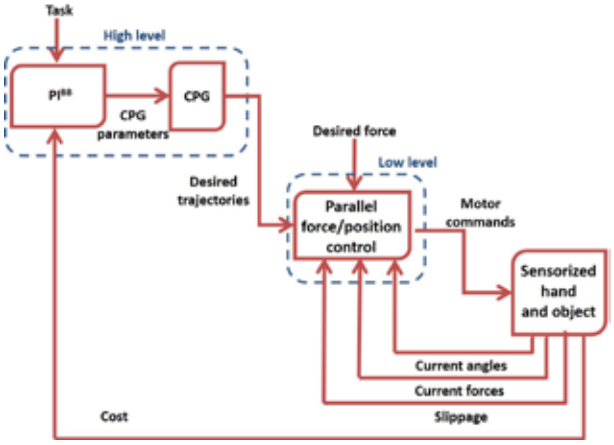

Fig. 1. Control architecture characterized by the following components: Policy Improvement with Black Box, Central Pattern Generators, Parallel force/position control, sensorized hand and object.

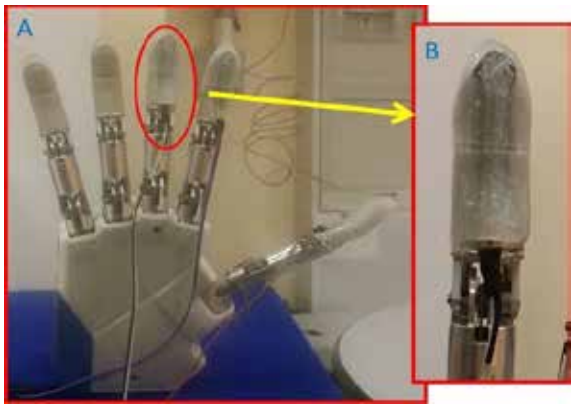

Fig. 2. Prosthetic hand IH2 mounted with FSRs on the fingertips of thumb, index and middle finger (A). The sensorized fingertips are covered with prosthetic silicon caps, as detailed in (B).

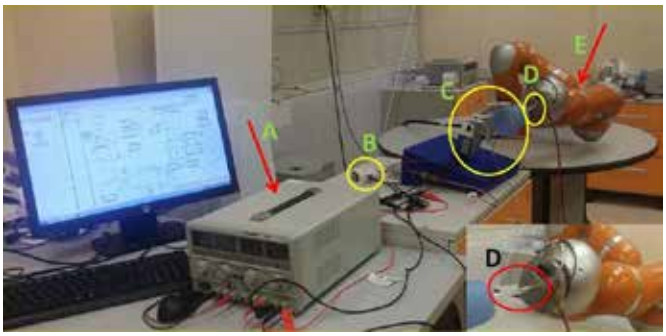

Fig. 3. Experimental set-up. DC power supply for electronics, sensors and prosthetic hand (A); NI-DAQ device (B) for data acquisition; prosthetic hand grasping a cup (C); end effector inducing slippage (D); KUKA-LWR 4 robotic arm (E).

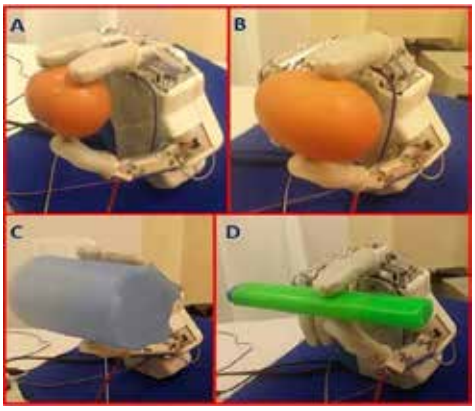

Fig. 4. Grasps performed by the IH2 hand during the experiments: tri-digital with egg (A) and cup (C), bi-digital with egg (B) and highlighter (D).

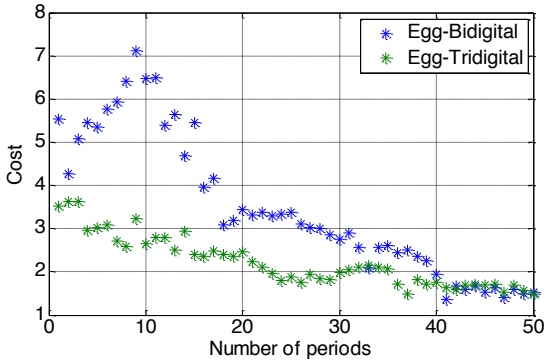

Fig. 5. Cost during the learning of two grasping tasks of an egg: bi-digital grasp (blue) and tri-digital grasp (green). The stars indicates the cost value at each period of the training.

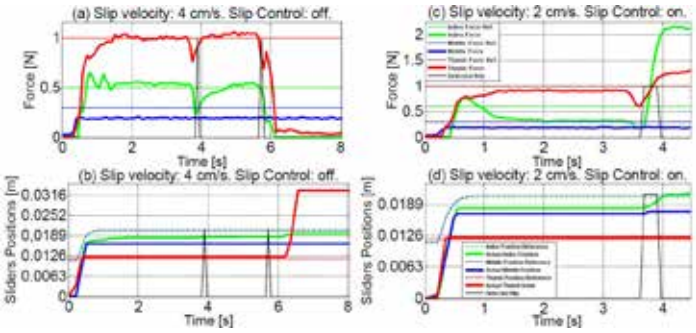

Fig. 6. Experimental results with the plastic cup. (a) and (b): Slippage control: off. (c) and (d): Slippage control: on.

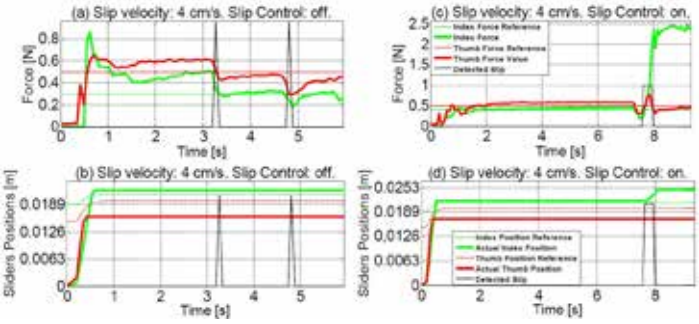

Fig. 7. Experimental results with the highlighter. (a) and (b): Slippage control: off. (c) and (d): Slippage control: on.

Robotic platform for Focused Ultrasound Surgery

A. Cafarelli[1], A. Diodato[1], A. Schiappacasse[2], S. Tognarelli[1], G. Ciuti[1] and A. Menciassi[1]
[1] *The BioRobotics Institute, Scuola Superiore Sant'Anna, Pisa*
[2] *Camelot Biomedical Systems S.r.l, Genova*

***Abstract*— Focused Ultrasound Surgery (FUS) is an early-stage, non-invasive therapeutic technology that has the potential to change the treatment of many medical disorders by serving as an alternative to surgery and radiotherapy. The use of a robotic-assisted approach for Ultrasound guided Focused Ultrasound Surgery (USgFUS) may reduce problems related to predictability and repeatability of current procedures by enhancing accuracy, safety and flexibility, and thus enabling a large use of FUS for the treatment of different pathologies. FUTURA (Focused Ultrasound Therapy Using Robotic Approaches) project proposes an innovative robotic-assisted platform for non-invasive FUS therapy under US imaging. The use of two dedicated anthropomorphic manipulators provides the platform with a high flexibility in terms of workspace, thus allowing to choose suitable acoustic windows during the procedure. The aim of this work is to demonstrate the workflow of the procedure (*i.e.* target identification, sonication and lesion assessment phases), the effective use of two US imaging probes during the treatment, and the possibility to monitor the lesion progress during sonication.**

***Keywords*—Focused Ultrasound Surgery; Computer-assisted robotic platform; HIFU, Cancer treatment.**

I. Introduction

FOCUSED Ultrasound Surgery (FUS), also referred as High Intensity Focused Ultrasound (HIFU) is a non-invasive therapeutic technology that enables the treatment of several pathologies [1]. FUS implies the transmission of acoustic energy through the body from an external source; being the transducer focused, large levels of energy can be deposited in very small spots, thus causing hyperthermia and necrosis in the targeted area (*e.g.*, tumour) without harming adjacent tissues. This emerging technology has an enormous potential being it based on an extracorporeal delivery of non-ionizing radiations; thus, it results to be intrinsically non-invasive and safe. Although Ultrasound guided FUS (USgFUS) does not guarantee high quality images and quantitative temperature maps if compared with Magnetic Resonance guided FUS (MRgFUS), it offers advantages such as lower cost and system size, the possibility to verify the treatment acoustic window, and an intrinsic higher frame rate that allows real-time therapy monitoring and compensation of physiological movements. The use of a robotic-assisted approach for USgFUS may relieve the problems related to the predictability and repeatability of the current procedures by enhancing accuracy, safety and flexibility of the treatment, and thus enabling a larger use of FUS. The most widespread commercial USgFUS robotic platform is the HAIFU JC (Chongqingd Haifu Medical Technology Co. Ltd, Chongqing, China), which mainly performs treatment of uterine fibroids, breast and liver tumours. Nevertheless, HAIFU JC is not able to monitor and track moving organs during the sonication, because the US images are completely distorted by the noise generated by the HIFU transducer, normally operating in continuous mode. These limitations are already overcome in some research platforms exploiting a Pulse With Modulation (PWM) signal for the HIFU transducer [2]; an all-in-one robotized HIFU system was developed for real-time intra-abdominal organ motion compensation by exploiting a US visual servoing scheme based on the US confocal probe imaging. This platform is equipped with a 2D US confocal probe; anyway for a moving 3D targeting, it is necessary to use a further US probe in a different plane with respect to the US 2D confocal probe [3]. In this framework, the FUTURA (Focused Ultrasound Therapy Using Robotic Approaches) project (www.futuraproject.eu) stemmed from the idea to develop an autonomous, multi-functional and multi-robotic assisted platform for flexible non-invasive FUS therapy.

The possibility to manage two dedicated anthropomorphic manipulators (therapeutic manipulator with a US confocal probe and monitoring manipulator with a 3D US probe) provides the FUTURA platform with a high flexibility in terms of workspace, thus allowing to choose suitable acoustic windows during the procedure. The aim of this work is to demonstrate the workflow of the FUTURA procedure (*i.e.* target identification, sonication and lesion assessment phases), the effective use of two US imaging probes during different phases of the lesion treatment, and the possibility to monitor the lesion progress during sonication.

II. Materials and Methods

A. Robotic platform architecture

The architecture of the FUTURA platform (Fig. 1A) includes the following modules: (1) a *Robotic Module*, composed by two identical 6 degrees of freedom (DoFs) anthropomorphic manipulators (IRB 120, ABB); (2) a *Therapeutic Module*, composed by a dedicated broadband wave generator (16 channels, 20W/channel, IGT) and a HIFU transducer (16 channels annular array, IMASONICS); (3) a *Monitoring Module*, composed by 2 US imaging probes (a 2D imaging US probe, PA7-4/12 confocal to the HIFU transducer, and a 3D imaging US probe 4DC7-3/40, Analogic Ultrasound), both connected to an acquisition system (SonixTablet, Analogic Ultrasound); (4) a *Sensor Module* for the calibration and registration of the platform, and for improving safety of the overall procedure (NDI Polaris Spectra and Microsoft Kinect V2).

A dedicated control software, developed with Robot

Operating System (ROS), allows for the communication and the synchronization between the different modules composing the platform.

Finally, a dedicated Human Machine Interface (HMI) was developed for controlling all the components (*i.e.*, robotic, monitoring and therapeutic modules) involved in FUS treatments with an accurate real-time visualization of the working environment (Fig. 1B).

B. Experimental procedure

The general workflow of the robotic-assisted FUS procedure is represented in Fig. 2 (Top) and includes the following steps: *A) Pre-Treatment phase:* during this step, pre-operative images (*i.e.* MR or Computer Tomography images) are registered with the on-line US images, the target is identified and the therapy is planned; *B) Treatment phase*: HIFU therapy is delivered under US monitoring; for each single sonication a target point is selected, the HIFU transducer is switched on and the lesion progress is assessed using both the US probes; *C) Post-Treatment phase*: after the last sonication, the treatment is finally evaluated using both US images probes.

The assessment of the HIFU procedure and the demonstration of therapy monitoring with 2 different US probes has been performed in *in-vitro* and *ex-vivo* static conditions.

The FUS procedure was accomplished by using an home-made phantom, made up by a bulk of agar gel with internal cylinders(representing the targets of the therapy), based on polyacrylamide gel (PAA) mixed with egg white. This material is a good mimicking phantom for HIFU ablation because it becomes opaque only in proximity of the HIFU focus and the formed lesion is clearly visible by eyes and in US B-mode images. The phantom was immersed in a tank with degassed water ensuring a correct acoustic coupling for the two US imaging probes and HIFU transducer.

The first phase of the FUS procedure entails the identification of the target through the US probes (Fig. 2B_I). A 3D US phantom reconstruction is performed; thus, by selecting the centre of the target to be sonicated (using the HMI integrated software), the therapeutic manipulator adjusts its position for performing the desired spot sonication. The images provided by the confocal 2D US probe guarantee the correctness in manipulator position (the visualized blue cone in all the 2D US images indicates the HIFU focus position). After checking the therapeutic manipulator positioning, a sonication composed by 10 repetitions of 1 second with 90% duty cycle is set. Frequency and acoustic power of the sonication are 1200 kHz and 120 Watts, respectively. During the sonication procedure the confocal 2D US probe is active for monitoring the lesion progress when the HIFU is switched off (10% of the time) (Fig. 2B_II). Finally the last phase of the FUS procedure is the lesion assessment performed through both the US imaging probes (Fig. 2B_III).

The same procedure has been repeated also using *ex-vivo* material (*i.e.* porcine liver instead of PAA cylinders into an Agar structure).

III. RESULTS

Fig. 2 describes the different phases of the FUS procedure. During the target identification phase, both the US imaging probes are used. The manipulator positions at the end of these phases are depicted in Fig. 1. Although the US confocal probe is rigidly attached to the HIFU transducer, the FUTURA platform maintains US imaging flexibility thanks to the 3D US probe mounted on the second manipulator. Indeed, the 3D US probe can be positioned according to the requirements of the FUS procedure and based on the available acoustic window. The 3D US phantom reconstruction and the related 2D US confocal images (Fig. 2B_I) acquired before sonication show the target without any lesion. In addition, the estimated HIFU transducer focus, located in the center of the target, assesses the correctness in positioning of the therapeutic manipulator. During the sonication process an on-line monitoring of the lesion is performed by exploiting a PWM signal for the HIFU transducer generator. Fig. 2B_II shows the 2D US confocal images acquired during the target sonication. As expected, when the HIFU transducer is on, only blurry images were acquired. Instead, useful US images for monitoring the lesion progress are acquired when the HIFU transducer is off. Finally, the lesion assessment phase (Fig. 2B_III) shows the 3D US phantom reconstruction and the related 2D US confocal images acquired after sonication with the lesion performed on the center of the target (*i.e.,* accuracy better than 1 mm [4]).

An optical assessment on the sectioned targets in proximity of the performed lesion was also carried out. Fig. 3 shows the visualization of the lesion induced by the HIFU into tissue-mimicking phantom (A) and into porcine liver (B).

IV. CONCLUSION

This work assesses the possibility to use a robotic platform for USgFUS treatment, using two US imaging probes for the different phases of the procedure. Synchronizing the HIFU transducer shot with the US imaging acquisition enables to monitor the lesion progress during the sonication phase, which is very important for patient safety. In addition, the use of both US probes during the sonication phase enables the tracking of moving 3D organs. Further tests will be performed in order to assess the accuracy of USgFUS treatment under dynamic condition.

ACKNOWLEDGEMENT

Research supported by the European Commission in the framework of FUTURA project, grant agreement n. 611963.

REFERENCES

[1] J. L. Foley, *et al.*, "Image-guided focused ultrasound: state of the technology and the challenges that lie ahead", *Imaging in Medicine*, vol. 5, pp. 357-370, 2013.

[2] L.-A. Chanel, F. Nageotte, J. Vappou, J. Luo, L. Cuvillon, "Robotized High Intensity Focused Ultrasound (HIFU) system for treatment of mobile organs using motion tracking by ultrasound imaging: An in vitro study", in *2015 Proc. EMBC 2015 Conf.*, pp. 2571-2575.

[3] N. Koizumi, *et al.,* "An extremely robust US based focal lesion servo system incorporating a servo recovery algorithm for a NIUTS", in *2015 Proc. IROS*, pp. 2625-2632.

[4] A. Cafarelli, *et al.*, "A computer-assisted robotic platform for Focused Ultrasound Surgery: Assessment of high intensity focused ultrasound delivery", in *2015 Proc. EMBC 2015 Conf.*, pp. 1311-1314.

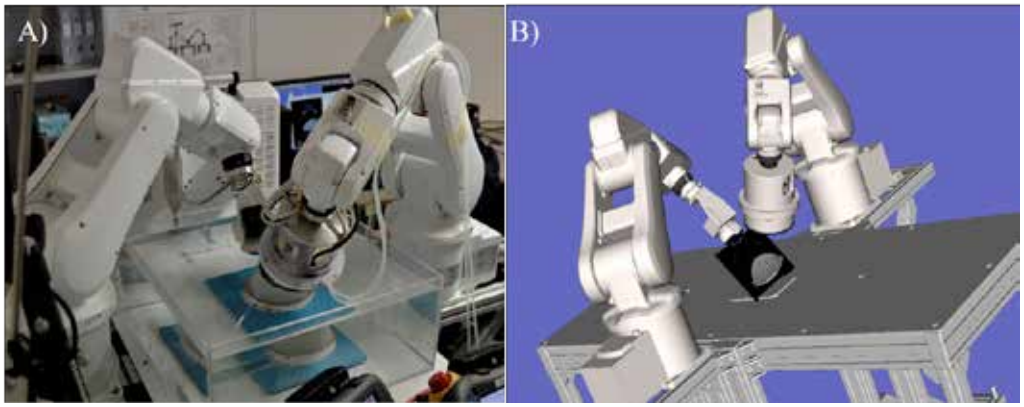

Fig. 1. A) FUTURA platform: robotic, monitoring and therapeutic modules. B) Real-time visualization of the simulated FUTURA working environment.

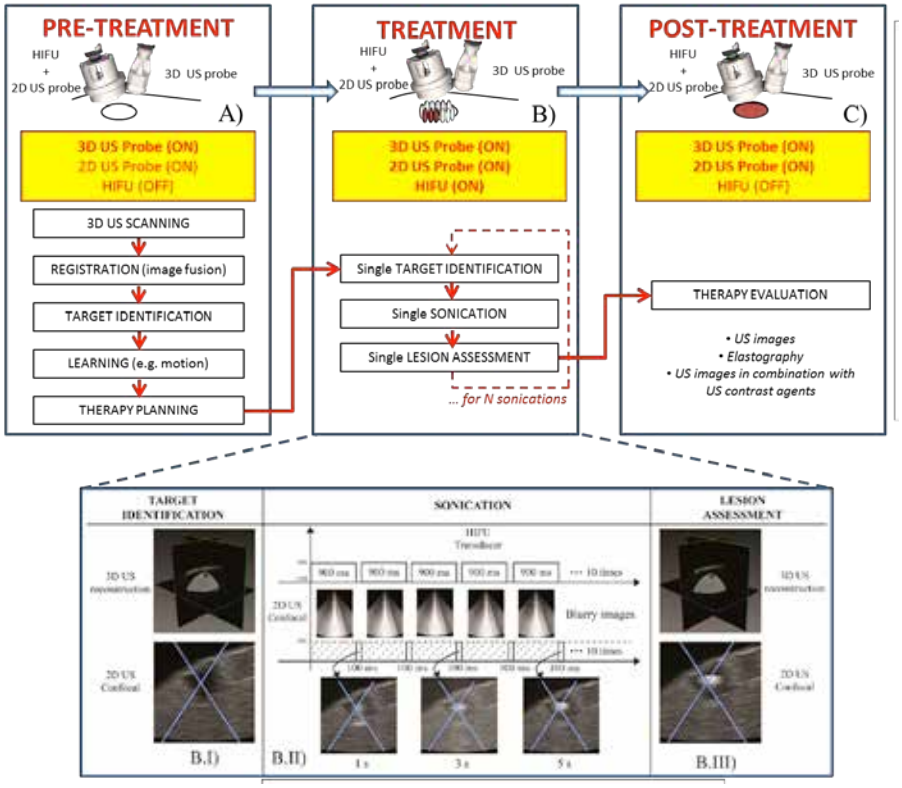

Fig. 2. Workflow of the robotic-assisted FUS procedure (Top) that includes: A) *Pre-Treatment;* B) *Treatment* and C) *Post-Treatment* phases. Each single sonication can be divided in three further stages: B_I): *Target identification phase*: both US probes are used to identify the point to be sonicated; B_II) *Sonication phase*: the HIFU is switched on and the lesion progress is assessed through US confocal probe; B_III) *Lesion assessment phase*: the created lesion is assessed with both US imaging probes.

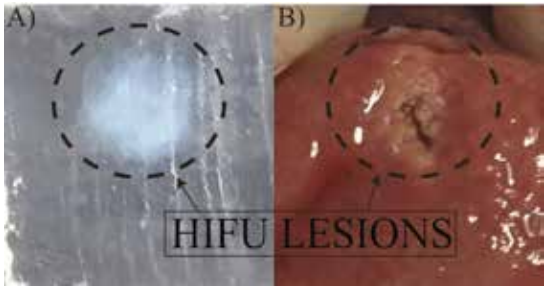

Fig. 3. Optical images of the lesion induced by the HIFU into a tissue-mimicking phantom (A) and into a porcine liver (B).

Disassembly Robotic Tasks for Circular Economy: a Preliminary Study

P. Dario[1], A. Morachioli[1], I. Strazzulla[1], C. Laschi[1]and F. Bonsignorio[1]
[1] *The BioRobotics Institute, Scuola Superiore Sant'Anna, Italy*

***Abstract*— The continued development of our economy and the fast growth of the population are endangering our world's ecological stability. Not only natural resources are finite, but also the capability of the ecosystem to support the global economy's side effects is limited. An eco-sustainable solution to guarantee a high quality of life to the billions of people living on Earth by 2040 can be moving away from the current paradigm of the "Linear Economy" towards the emerging paradigm of the "Circular Economy" (defined as a mode of economic development based on ecological circulation of natural materials and artefacts). Robotics will have a crucial role in the emergence and implementation of Circular Economy. Disassembly and recycling are fundamental procedures for Circular Economy, allowing to introduce the concept of the "Robotic Circular Production" (RCP), which closes the loop production cycle. According to this concept, products will be conceived not only to be assembled but also to be effectively disassembled by "disassembly robotic lines" and then more efficiently recycled. The objective of this study is to present preliminary evidences on how intelligent robotics technologies, such as bio-inspired dexterous dual-arm manipulation combined with vision, could be used to implement disassembly tasks that form the building blocks of more complex processes of the Circular Economy paradigm.**

***Keywords*— Robotics, Disassembly, Circular Economy, Dual-arm.**

I. Introduction

At the very beginning the robotic manipulators were actually dual-arm systems. The first models were dual-arm manipulators developed by Goertz in the 1940's and 1950's [1]. They were supposed to handle radioactive goods through two arms, having the operator controlling one with each hand. But later on, especially in the 1980's and 1990's, a lot of applications faced the use of single arm manipulators combined with the "newly developed" visual servoing [2].

At present times, dual-arm robots are gaining attention back as a potential solution because of their flexibility and the ability to work in a similar way to a human operator [3]. When it is required to equip a production site with robots, the modification of the working environment represent the most serious problem. In particular, industrial robots have the necessity to operate in unstructured and improved environments in order to enable operations within each robot's workspace. The challenges that concern dual-arm manipulation, especially in *unstructured environments*, can be seen also as a motivator for development in basic research areas, and provide relevant application scenarios for various enabling technologies [2]. One example is the Circular Economy's one (CE), defined as a method of economic development based on ecological circulation of natural materials and artefacts. CE represent an alternative to the actual paradigm of the "Linear Economy", defined as 'take-make-dispose' economy has been relying on the inputs of cheap and available resources.

A possible application in CE is disassembly, which, together with recycling, could become fundamental in a CE paradigm. Robotized dismantling can be seen as the reversed process of robotized manufacturing, or as replacing human labour by robot in repeatable operations during dismantling process [5].

The study of disassembly problems in the robotic field implies several fundamental dissimilarities with corresponding assembly tasks, one crucial difference is that in disassembly used objects have a past "life", which could have most probably modified them unpredictably both in their aspect and in their internal structure [6].

It is worth notice that in these problems bio-inspiration is at two levels: 1) the robot bi-manual manipulation is inspired by humans and primates 2) the Circular Economy paradigm of production is inspired by the biosphere ecology.

II. Methods

The bimanual manipulation was implemented using an industrial Comau Dual-arm robot (cfr. Fig. 1a). Each robot arm has a six-revolute-joint anthropomorphic geometry, with non-null shoulder and elbow offsets and non-spherical wrist. Each arm is mounted on a central revolute-joint (torso) that allows yaw movements to the arms. The joints are actuated by brushless motors via gear trains; shaft absolute resolvers provide motor position measurements. The robot is controlled by the C5G control unit, which has a VME-based architecture with two processing boards (robot and servo CPUs), both based on a Motorola 68020/68882, where the latter has an additional DSP and is in charge of trajectory generation, inverse kinematics, and joint position servo control. Independent joint control is adopted, in which the individual servos are implemented as standard PID controllers. The native robot programming language is PDL 2, a high-level Pascal-like language with typical motion planning instructions. The robot presents cooperative motion and synchronized movements among the arms and torso, its design is best suited to perform human-like movements, that require high degree of dexterity and precision. In order to study the disassembly tasks for the Circular Economy, it has been set up an experimental environment where the Comau Dual-arm robot [7] has been integrated over a TCP/IP connection with a Matlab computer server together with a series of smart 3D cameras: Kinect v1 [8] (cfr. Fig. 1b), Festo SBOx-Q [9], Bumblebee 2 [10] and the Dexter's humanoid head (cfr. Fig.1c) [9]. The end-effectors planned to be tested are: Festo grippers DHDS-50-A [10] (cfr. Fig. 2a), Prensilia IH2 Azzurra [13] (cfr. Fig. 2b), Universal Gripper [14]. The preliminary task that has been explored, presented in this

paper, is a basic one in *dismantling*. The Comau *Dual-arm* robot *sorts and classifies* a bag of components previously disassembled by another robot or human operator. The robotic system is integrated with the Festo *grippers* and a Kinect *vision system* that controls the robot movement and trajectory planning.

The *sorting and classifying* task is performed by positioning a full shopping bag in the workspace of the robot. The vision system elaborates the image of the bag and the objects inside. The planning system running on the computer server receives through the dedicated sockets the information and generates the trajectories for the two end-effectors. The manipulation of the objects is performed by means of two bio-inspired grippers. The final expected task is to empty the bag and classify every object on the table.

III. Results

The unpacking task carried out by the robotic system was divided into five stages:

1. Object recognition: the vision system identifies the shopping bag and the coordinates of the first object to grasp, by knowing the shape of the object it determines its central point.
2. Motion planning: the control system determines the joints trajectories in the range of motion of the Dual-arm robot.
3. Error/Collision Avoidance: a secondary parallel control loop ensures that the robot didn't collide with the objects present in the working space.
4. Manipulation phase: each arm gripper grasps the planned object and manipulates it as necessary.
5. Object classification: the vision system classifies the objects based on their colour, shape or other features.

The *object recognition* phase starts with the triggering of the system by means of new objects presented on the work table. The vision system recognizes the shape and colour of the object, extracts its centroid coordinates and send an operational command to the arm closest to the object, in order to grasp it. At this point the *motion planning* and *error/collision avoidance* phases start: the *control system* computes the correct space trajectory that the arm assigned to grasp the object need to execute, in order to safely reach and grasp the object without any collision with the environment and the other arm. When the gripper touches the object the *manipulation* phase begins: the object is grasped with a proper force (using the touch sensors on the fingertips) and, if needed by the *object classification* protocol, manipulated in order to sort out the object with similar features or dismantling a complex object into its basic components.

IV. Conclusions

To date, outside of structured environments, robots have only performed sophisticated manipulation tasks when tele-operated by humans. In the context of ongoing digitalization of manufacturing processes (industry 4.0) agile adaptive factories are becoming less structured than they were before and researchers are pursuing a variety of approaches to overcome the current limitations of autonomous robot manipulation in semi-structured environments [15]. Since heavier object could induce larger deviations of the end effector, *visual manipulator tracking* is a fundamental requirement [16].

The choice to adopt dual-arm manipulation, especially in unstructured environments, is motivated by several advantages such as the flexibility and dexterity, the reduced usage of fixtures, the similarity to operator and the manipulability, which is remarkably suitable for disassembly tasks like those required by the Circular Economy paradigm (cfr. Fig. 3)[17]. Disassembly and recycling are indeed fundamental procedures for Circular Economy, allowing to introduce the concept of the "Robotic Circular Production" (RCP), which closes the loop production cycle (cfr. Fig. 4). By following this concept, products will be conceived not only to be assembled but also to be effectively disassembled by specific "disassembly robotic lines" and then more efficiently recycled [6]. The challenges raised by Robotics and Intelligent solutions for CE can be regarded as bio-inspired under two different aspects: 1) the proposed technical solution mimics the vision and haptic guided process of bimanual manipulation in the humans and the primates; 2) the envisioned production process is designed as information driven, self-regulated very similar to the ecological cycles maintaining the equilibrium of the biosphere.

References

[1] Goertz, R. C. (1952). Fundamentals of general purpose remote manipulators. Nucleonics, 10(11), 36-42.

[2] Smith, C., Karayiannidis, Y., Nalpantidis, L., Gratal, X., Qi, P., Dimarogonas, D. V., & Kragic, D. (2012). Dual-arm manipulation—A survey.Robotics and Autonomous systems, 60(10), 1340-1353.

[3] Do, H. M., Choi, T. Y., & Kyung, J. H. (2015). Automation of cell production system for cellular phones using dual-arm robots. The International Journal of Advanced Manufacturing Technology, 1-12.

[4] Yuan, Z., Bi, J., & Moriguichi, Y. (2006). The circular economy: A new development strategy in China. Journal of Industrial Ecology, 10(1-2), 4-8.

[5] He, W., Li, G., Ma, X., Wang, H., Huang, J., Xu, M., & Huang, C. (2006). WEEE recovery strategies and the WEEE treatment status in China. Journal of hazardous materials, 136(3), 502-512.

[6] Dario, P., Rucci, M., Guadagnini, C., & Laschi, C. (1993, November). An experimental robot system for investigating disassembly problems. In Advanced Robotics, 1993. Can Robots Contribute to Preventing Environmental Deterioration? Proceedings, 1993 IEEE/Tsukuba International Workshop on(pp. 37-42). IEEE.

[7] http://www.robotics.comau.com/product_Dual_Arm_RML_Robot.html accessed online Apr 2016.

[8] https://msdn.microsoft.com/en-us/library/jj131033.aspx accessed online Apr 2016.

[9] https://www.festo.com/cat/en_en/products__97102 accessed online Apr 2016.

[10] https://www.ptgrey.com/bumblebee2-firewire-stereo-vision-camera-systems accessed online Apr 2016.

[11] Laschi, Cecilia, et al. "An anthropomorphic robotic head for investigating gaze control." Advanced Robotics 22.1 (2008): 57-89.

[12] https://www.festo.com/cat/en_en/products__69071 accessed online Apr 2016.

[13] http://www.prensilia.com/index.php?q=en/node/40 accessed online Apr 2016.

[14] Brown, Eric, et al. "Universal robotic gripper based on the jamming of granular material." Proceedings of the National Academy of Sciences 107.44 (2010): 18809-18814.

[15] Kemp, Charles C., Aaron Edsinger, and Eduardo Torres-Jara. "Challenges for robot manipulation in human environments." IEEE Robotics and Automation Magazine 14.1 (2007): 20.

[16] Hebert, P., Hudson, N., Ma, J., & Burdick, J. W. (2013, May). Dual arm estimation for coordinated bimanual manipulation. In Robotics and Automation (ICRA), 2013 IEEE International Conference on (pp. 120-125). IEEE.

[17] MacArthur, Ellen. "Towards the circular economy." Journal of Industrial Ecology (2013).

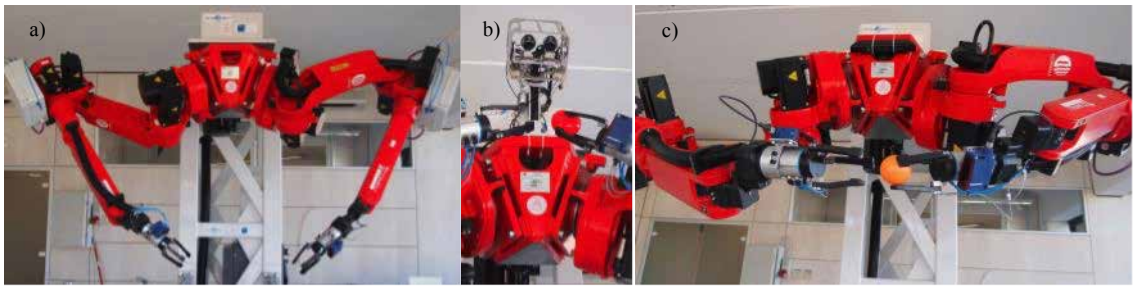

Fig. 1.
a) the Dual Arm robot from Comau is a 13 DoF robot, composed by two arms and a third central joint (torso joint) that allows yaw movements. The robot presents cooperative motion and synchronized movements among the arms and torso, its design is best suited to perform human-like movements, that require high degree of dexterity and precision.
b) Dexter's humanoid head: biomechatronic and anthropomorphic 7 DoF robotic head, able to perform human eye and neck movements. The system integrates a 3D vision system to perform object recognition in a 3D space.
c) Kinect v1: it is provided of a 3D RGB camera, an infrared (IR) emitter, an IR depth sensor, a multi-array microphone and a 3-axis accelerometer.

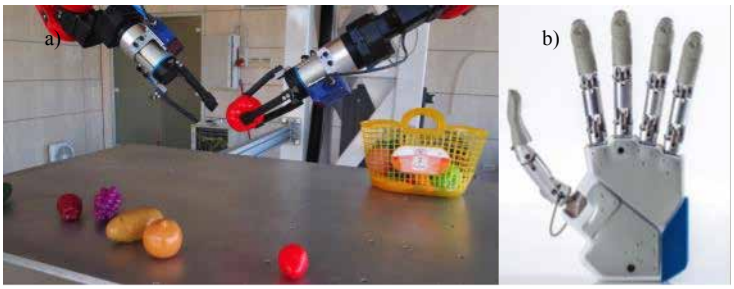

Fig. 2.
a) Three-point gripper mounted on each arm of the robot. They ensure operational flexibility and force grip with objects of various shape and dimensions.
b) Palm view of IH2 Azzurra (left hand version).

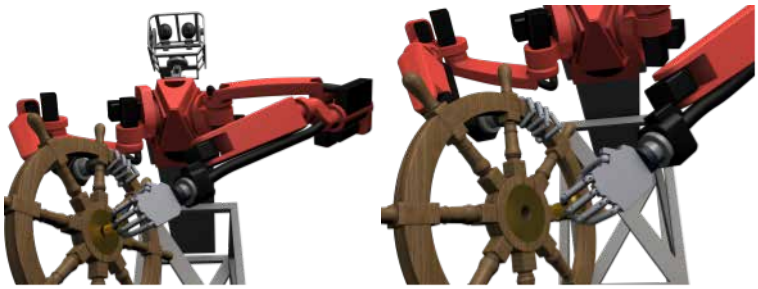

Fig. 3. A potential task in the Circular Economy: the dismantling of a ship's wheel. An exemplary task in the Circular Economy: the dismantling of a ship's wheel. The execution of this task without fixtures requires bimanual manipulation: the left hand holds the wheel, the right hand performs the disassembly tasks. Dismantling procedures require to cope with the disassembly of a large variety of mechatronic systems. Reducing the number of needed dedicated set-ups is key for the economic viability of the process.

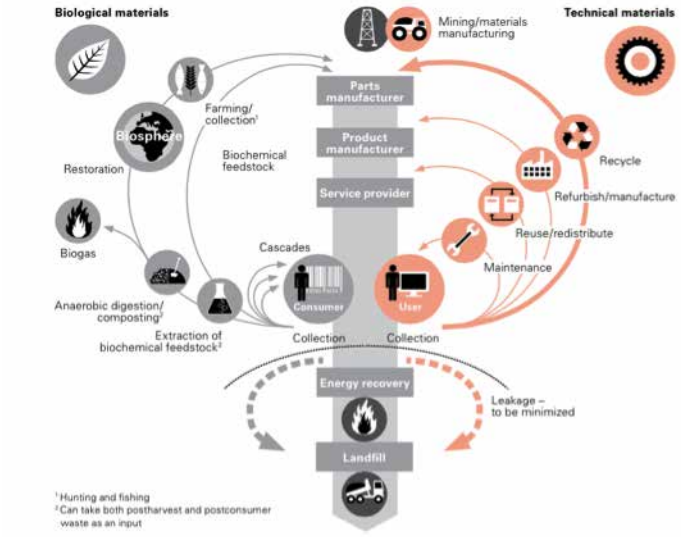

Fig. 4. Circular Economy scheme

Prototypes design and fabrication of bio-ispired distributed actuation systems

A. De Acutis[2], A. Bau[2], and G. Vozzi [1,2]
[1] Research Center E. Piaggio – University of Pisa, Pisa, Italy
[2] Department of Ingegneria dell'Informazione – University of Pisa, Pisa, Italy

***Abstract*—Soft robotics technologies paved the way to design actuators mimicking natural biological systems and structures. Thus, inspired by the small human intestinal peristalsis, we provide two prototypes of a bio inspired soft robotic platforms characterized by a wave-like motion. Peristaltic movements were obtained by a specific logic of actuation of an array hydrostatically coupled dielectric elastomer actuators. Device's possible opportunities in biomedical application can be found.**

***Keywords*—Dielectric elastomer actuator (DEA), distributed actuators, peristalsis, biomimetic.**

I. Introduction

In nature the peristaltic motion is the common example of distributed actuators systems found in several number of biological organism, including humans. The peristalsis consists of a wave of contraction and relaxation by which tubular organs with muscles integrated in their side-walls propel their contents. In humans, for example, esophagus, stomach and intestine, but also some extra-gastrointestinal districts as ureters and the uterine tubes perform peristaltic involuntary movements to propel their contents onward. Instead some animals use peristalsis as form of locomotion.
Researches on robotics have addressed great attention on this concept of biological distributed actuators to develop efficient actuators that do not influence the shape and the macroscopic characteristics of place where they are located. Research on distributed actuation began last century with the work by Hirose and Umetani [1], but developments in soft robotics technologies, such in soft or stimuli-responsive materials, have enabled researchers to engineer biological functionality such as muscle contractions [2], [3]. Thus, following the concept idea proposed by Menon et al. [4], the paper present an ongoing development of a biomimetic distributed actuation systems that mimick the peristaltic motion of human small intestine exploiting hydrostatically coupled dielectric elastomer actuators (HC-DEAs). At first, a functional proof-of-concept prototype was developed to validate the feasibility of the peristaltic surface motion generation. Then an organotypic technical prototype was fabricated as starting point towards a tool for a real-word-application. Finally, after discussing about the future work some interesting application of the technical prototype in biomedical field are provided.

II. General design specifications

HC-DEAs were used to fabricate both the proof of concept and the technical prototype. The HC-DEAs are based on dielectric elastomers (DE) principle of operation, providing high scalability, versatility, low power consumption and low cost, even if they require the application of high electric fields (~V/μm) for their operation. In particular, for the fabrication of the bio-inspired distributed actuation systems an array of independent HC-DEAs was designed. As shown in Figure 1A, each rectangualar actuator was developed by mechanically coupling an active and passive element by means of an incompressible fluid to enable hydrostatical trasmission. The active element is the DE based actuation component while the passive element is the contact surface interfaced with the load that has to be propelled [5]. The strategy of activation each array's actuation unit showed in Figure 1B was adopted to generate the surface peristaltic motion on both prototypes: at each actuation step a couple of actuators are always in an activated state so that their passive surfaces are a contact with the load and at a lower height than that of the other actuators. At each step an actuator is turned off and the other is activated. Returning to the off state, the actuator exerts a force that induces the rolling forward of the load.

III. Proof Of Concept manufacture

The proof of concept prototype consists of an array of five HC-DEAs in a planar configuration (Fig. 2). The active and the passive element of each HC-DEA were made of a membrane of VHB 4910 (3M, USA), an acrylic elastomer of 1 mm in thickness. The VHB was mechanically biaxially prestretched to enlarge its surface area up to 16 times in order to increase its dielectric stiffness and reduce its thickness. In this way, for the same voltage applied, the actuator can achieve higher deformations. The electrodes were made by coating a thin layer of carbon grease (846, M.G. Chemicals, CND) on both faces of the dielectric, and applying two electrodes of aluminum for the connection to the supply circuit. For the hydrostatical coupling 7 ml of silicone grease (8462, M.G. Chemicals, CND) were used causing a half height's actuator of about 6 mm in the apical point. All the active and passive elements were held together by two rigid frames designed to minimize the distance between two adjacent actuation units. Each HC-DEA had a 50 mm x 20 mm rectangular shape to maximize the contact surface with the load and to make the fabrication process easier. The various structural elements were designed with SolidWorks and printed in ABS (acrylonitrile-butadiene-styrene) using a FMD 3D printing machine (Fortus 250mc, Stratasys, USA)

IV. Technical prototype manufacture

The technical prototype was fabricated following the same design approach of the proof of concept. To reproduce also the intestinal morphology, the prototype was based on an array of four HC-DEAs in a half-tube configuration (Fig. 3).

This arrangement was guaranteed by two rigid frames properly designed and printed in ABS to replicate a 70 mm longitudinal section of a tube with a radius of 25 mm. Each actuator was also scaled in dimensions up to a 25 mm x 10 mm rectangular shape filled with 2 ml of silicone grease causing a half height's actuator of about 5 mm in the central point. Since the carbon grease can rub off and smear easily, in this prototype a polydimethylsiloxane (PDMS) (Sylgard 184 (1:30), Dow Corning, USA) composite having a 25 wt% of carbon black (CB) (Vulcan XC 72R, Cabot Corporation, USA) was used as electrodes material. This was an important step to the fabrication of compliant electrodes using coventional microfabrication techniques for improving the reliability and repeatability of the device. To obtain an organotypic configuration, two of these devices were coupled.

V. ELECTRONIC CONTROL UNIT

To make possible the peristaltic surface propulsion an electronic actuation unit was developed on purpose. A common 9V battery was used as principal power supply. A voltage converter (Q50, EMCO High Voltage Corporation). was used to obtain the actuation tension (respectively 4kV in the proof of concept prototype and 2.5 kV in the technical one) for each HC-DEA. Each actuator was connected in parallel to a 50MΩ resistor in order to facilitate the dissipation of the accumulated charge on the active layer's DE. MOSFETs (IXTF02N450, IXYS) in low-side configuration were used as switches. Additionally drivers (TC 1427CPA, Microchip Technology) were used to speed up the MOSFETs state transitions and to externally manage the control signals. To implement the logic control describe above, an Arduino Duemilanove was used to generate a square wave with a period of 5T and duty cycle of 40% in input to each driver. A temporal offset equal to T to was given control adjacent actuators.

VI. ACTUATION PERFORMANCES: PRELIMINARY REUSULTS

Each HC-DEA of the proof of concept unit was characterizated in term of deformation-voltage behavior using a laser sensor (optoNCDT 1800, Micro-Epsilon, GE). In the proof of concept the apical point of each actuator unit showed a maximum deformation of about 60% at 4 kV (Fig. 4A). The proof of concept was also characterized in term of each HC-DEA's blocking force-voltage behavior with a compression test using a Zwick/Roell Z005 testing device (ZwickGmbH & Co, GE) equipped with a 100 N load cell (Fig. 4B). These tests were performed with a dedicated indenter at 10 mm/min up to the maximum deformation. Finally the surface peristaltic propulsion of both systems was tested using five control signals with different frequencies of activation (1 s <T< 8 s). With these parameters the proof of concept prototype was able to generate a surface propulsive motion to move in a fixed direction an axial-symmetric load of about 50 gr.

VII. CONCLUSIONS AND FURTHER WORK

In this paper an ongoing work on the development of soft platfroms that exhibit a peristaltic surface motion inspired by typical small intestinal motility was presented. In particular we have presented the design, development, and preliminary results of two distributed actuation system prototypes based on an array of HC-DEAs actuated with a specific logic. Although the development of these novel bio-inspired distributed actuators is only at the conceptual level, it provides a evidence to support the basic theoretical idea. We proposed only a starting point toward functional prototypes, with the potential to be introduced in the biomedical field as substrate for the fabrication of in vitro small intestine dynamic model or as novel system for the validation of robotic capsule endoscopes. Structure modifications and a more complete mechanical characterization will be required in the future to make these devices available in the biomedical field.

REFERENCES.

[1] S. Hirose and Y. Umetani, "Kinematic Control of Active Cord Mechanism withTactile Sensors", *Proceedings of 2nd CISM-IFToM Symposium on Theory and Practice of Robots and Manipulators*, pp.241-252, 1976

[2] C. D. Rahn, W. M. Kier, and I.D. Walker, 2Soft robotic: biological inspiration, state of the art, and future research", Applied Bionics and Biomechanics, vol. 2, pp.99-117, 2008

[3] S. Spano and H. H. Asada, "Kinematic analysis and design of surface wave distributed actuators with application to a powered bed for bedridden patients," in *IEEE Transactions on Robotics and Automation*, vol. 16, no. 1, pp. 1-11, Feb 2000.

[4] C. Menon, F. Carpi, and D. De Rossi, "Concept design of novel bio-inspired distributed actuators for space applications," *Acta Astronautica*, vol. 65, no. 5-6,

[5] F. Carpi, G. Frediani, and D. De Rossi, "Hydrostatically coupled dielectric elastomer actuators," *IEEE/ASME Transactions on Mechatronics*, vol. 15, no. 2, pp. 308–315,

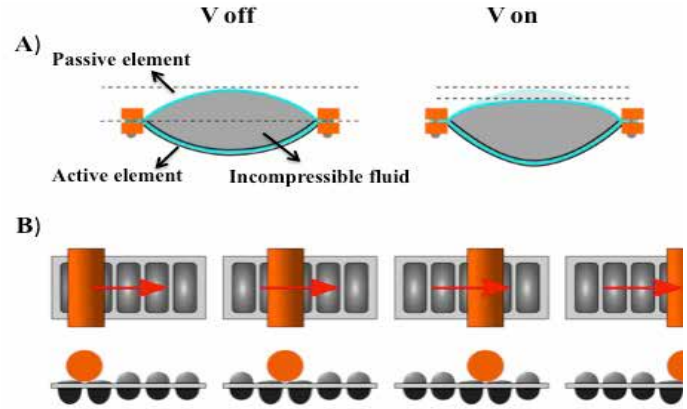

Fig. 1. A) An illustration of HA-DEA's a lateral section in its activated and inactivated state; B) an illustration of the strategy of actuation of HC-DEAs array to generate the surface peristaltic wave.

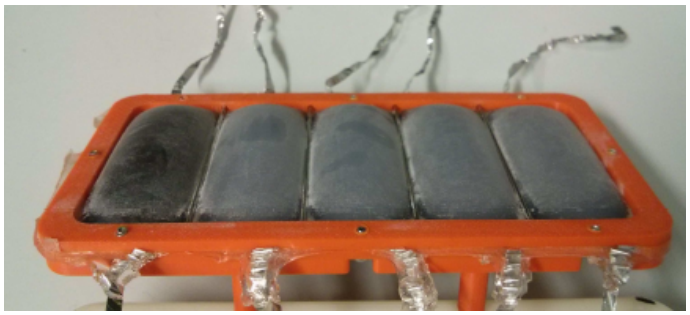

Fig. 2. A picture of the proof of concept prototype.

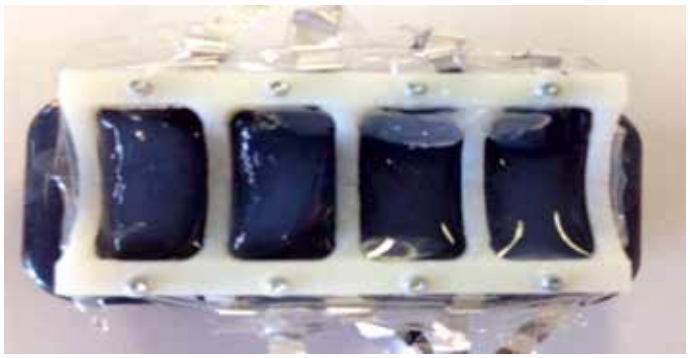

Fig. 3. A picture of the technical prototype.

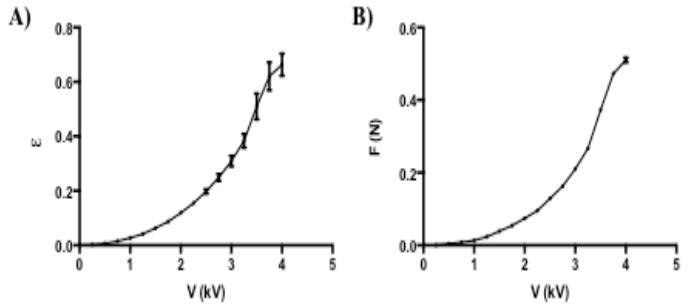

Fig. 4. A) Blocking force - behavior and B) blocking force - voltage behavior of an actuation unit in the proof of concept.

Toward biomorphic central pattern generator system for controlling lamprey robot

E.Donati[1], G. Indiveri[2], C. Stefanini[1,3]
[1] The Biorobotics Institute, Scuola Superiore Sant'Anna, Pontedera (PI), Italy
[2] Institute of Neuroinformatics, University of Zurich and ETH Zurich, Switzerland
[3] Department of Biomedical Engineering, Khalifa University, Abu Dhabi, UAE

***Abstract*— The study proposed describes a preliminary results of a spiking implementation of lamprey's Central Pattern Generator (CPG) using Neuromorphic VLSI devices. Due to the relative simplicity, the lamprey's CPG has been studied in great detail by neurobiologist and nowadays it is one of the best known vertebrate CPG. Several robotic implementations have been built to test the models in a real physical bio-mimetic artefact but, in these systems there is a clear separation between the actuators and body of the system, and their control part. This study proposes to implement a CPG control to directly interface to the actuators of the Lamprey robot, creating a biomimetic robot both from mechanical and electronical point of view.**

***Keywords*—Central pattern generator, neuromorphic engineering, bioinspired robotics.**

I. INTRODUCTION

Living organisms are far superior to artificial robotic platforms in both motor skill and computational abilities, for sensory-motor tasks executed in uncontrolled environments.

One of the motor skills that has been most studied in neuroscience is locomotion. The neural circuits that implement CPG are central for animal locomotion in general, and are also of fundamental importance for processes required for survival (e.g., breathing, chewing, etc.). As CPG circuits can be implemented with spike-based neuromorphic circuits, they represent a promising computational primitive for producing and controlling motor outputs in biomimetic robotic platforms.

In this project spiking neural networks have been used to reproduce the behaviour of the lamprey's central pattern, and control the actuators of bioinspired lamprey robot [1]. Event based systems have had a recent upsurge in scientific interest, for their benefits in control, communication and signal processing. In event-based systems, signals are communicated and processed asynchronously (without clocks) only when data is present. The asynchronous and event-based nature of this representation drastically reduces latencies and significantly decrease power consumption.

Energy efficiency is a fundamental aspect in robotics that we will try to address both at the level of the neural computation and motor control aspects. Another advantage of neuromorphic locomotion control is the possibility to maximize parallelism in computation from systems having a large number of simple equivalent components (neurons), unlike with the classical digital approach where there are one or more central processing units (CPU). Large number of components that work in the same way make the system redundant and, therefore, fault tolerant. Fault tolerance is a crucial aspect in robotics, as robots need the ability to effectively detect and tolerate internal failures in order to continue performing their tasks without an external intervention.

II. MATERIALS AND METHODS

The Lamprey robot [1] is a bio-inspired autonomous swimming robot, inspired by the real animal, used as a tool for neuroscientist to investigate neural control mechanism. The actuation system is based on the use of direct interaction between permanent magnets to generate actuation forces. The orientation or position of the magnets, driven by motors, control the forces between magnets. The actuation system is composed by three vertebrae: one active, with the motor that rotates the permanent magnet and two passive with two fixed magnets.

Lamprey animals have networks to control swimming that are arranged, at the segmental level, with reciprocal inhibition between left/right side of the body [2,3]. The CPG network is initialized in the reticulospinal neurons (RS), where a group of excitatory neurons interact close to the sensory feedback. The basal ganglia maintains the CPG networks under tonic inhibition. For a given task, the relevant CPG needs to be disinhibited. The signal to start the dis-inhibition comes from rostral brain structures activated by sensory stimuli (i.e, vestibular system). The mesencephalic locomotor region (MLR) and diencephalic locomotor region (DLR) are brainstem locomotor control system areas and connect directly with the first segment of CPG into the spinal cord. In the lamprey the spinal cord system consists of about 100 units, each containing an oscillatory neural network. In each of these segments the left-right alternated spiking activity has a frequency range ranging from 0.1 Hz to 8-10 Hz. A pool of interactive excitatory interneurons (EIN) produces burst when activated by an excitatory drive (emulated by using a oscillatory network). The mechanism for terminating each burst is a set of inhibitory interneurons, contralateral and lateral (CIN, LIN) that feed back onto the excitatory cells and contribute to the burst termination. The motor neurons (MN) project the output directly to the muscles (see Fig. 1). A lamprey swims forward because an ondulatory wave is transmitted along the body through the segments. Forward swimming is achieved by a lag between the onset of activity in consecutive segments rostro-caudally, vice versa in backward locomotion. The time lag between segments is variable, but, it is always a fixed proportion of the cycle duration and it is reverse proportional to the speed.

The same characteristics and connections of CPG have been reproduced on the Reconfigurable On-line Learning Spiking Neuromorphic Processor (ROLLS) [4], (see Fig. 2). ROLLS comprises spiking neurons that can exhibit a wide range of realistic behaviours and biologically realistic response properties. It comprises a row of 256x1 silicon neuron circuits, an array of 256x256 synapses that have on-chip spike-driven plasticity mechanisms to change their weights, an array of 256x256 programmable synapses with short-term plasticity circuits, and a peripheral analog/digital in/out circuits for both receiving and transmitting spikes in real-time off-chip.

III. RESULTS

To reproduce the burst observed in CPG patterns of activity a strong neural adaptation current [5,6], a weak synaptic weights, and slow time synaptic constants have been set. Figure 3 shows measurement results from one of such neuron circuits integrated on the chip [7]. The parameter of the network have been chosen to recreate the behaviour of the burst, as in the real animal. In this case, the neuron produces periodic bursting, lasting approximately 60 ms. with an inter-burst interval of about 1.5 s. Fig. 4 shows the hardware measurements of the first segment. It is possible see the alternate activity of the right and left side. The frequency of activity is about 1Hz. In the lamprey the alternate activation ranges from 0.1 Hz to 8-10 Hz.

The oscillatory network can be connected to either the first or the last segment. In forward locomotion the oscillators are connected to the first segment through a delay interneurons. The delay interneurons receives spikes from EIN and projects excitatory synapses on all neurons of the EIN pool of consecutive segments. The delay is a function of synaptic straight, time constant of neuron, and firing threshold. Keeping fixed the parameters of synaptic straight and firing threshold, it is possible control the time before the neuron firing by setting the value of time integration. Fig. 5, shows the delay produce between segments by increasing the number of interneurons. Synaptic circuits are strongly affected by mismatch and the delay is different in different neurons.

To control the bio-inspired actuators of Lamprey robot it is necessary to convert the neurons output in a value of motor position. By changing the DC, Cascode and inhibition currents, the values of frequency, duration and mean rate of burst change. The output is parameterized and each value corresponds to a specific value of motor position. The loop is closed with hall sensors that can be used directly at "low" level to update the PID controller, or, as in this project, to emulate the behaviour of lampreys stretch receptors (SR) (see Fig. 5). The SR are sensors at lateral margin of spinal cord. They sense the lateral bending during swimming and they have a local effect. They receive phasic inhibition and excitation from the CPG during the locomotion cycle. SR are two types: excitatory and inhibitory. In the hardware CPG each hemisegment is connected to two pool of SRs. The excitatory ones provide excitation to the EIN and MN ipsilateral CPG neurons, while the inhibitor SRs to the controlateral side.

IV. DISCUSSIONS AND CONCLUSION

This study presents a neuromorphic implementation of lamprey's CPG to directly control the bioinspired actuators of Lamprey robot. An hardware model of CPG has been implemented to reproduce the same behaviour and the same connectivity of the real animal at level of single segment. Furthermore, an intersegmental connectivity has been investigated in order to reproduce the intersegmental delay. The results showed that the characteristic behaviour of burst activity and alternating movement have been reproduced. Parameters as, mean rate of spiking, frequency and burst duration have been used as input for the actuators control.

Currently, with this configuration and forward and backward solutions, it is possible to control up to five vertebrea. Further developments will be increasing the number of controllable vertebrae and realizing a complete neural control (a PFM control) by eliminating the interface board to create a complete bio-inspired system, from a mechanical, electronic and control point of view.

REFERENCES

[1] Manfredi, L., Assaf, T., Mintchev, S., Marrazza, S., Capantini, L., Orofino, S., ... & Stefanini, C. (2013). A bioinspired autonomous swimming robot as a tool for studying goal-directed locomotion. Biological cybernetics, 107(5), 513-527.

[2] Grillner, Sten. "The motor infrastructure: from ion channels to neuronal networks." Nature Reviews Neuroscience 4.7 (2003): 573-586.

[3] Grillner, S., Kozlov, A., Dario, P., Stefanini, C., Menciassi, A., Lansner, A., & Kotaleski, J. H. (2007). Modeling a vertebrate motor system: pattern generation, steering and control of body orientation. Progress in brain research, 165, 221-234.

[4] Qiao, N., Mostafa, H., Corradi, F., Osswald, M., Stefanini, F., Sumislawska, D., & Indiveri, G. (2015). A reconfigurable on-line learning spiking neuromorphic processor comprising 256 neurons and 128K synapses. Frontiers in neuroscience, 9.

[5] Russell, D. F., & Hartline, D. K. (1978). Bursting neural networks: a reexamination. Science, 200(4340), 453-456.

[6] Marder, E., & Calabrese, R. L. (1996). Principles of rhythmic motor pattern generation. Physiological reviews, 76(3), 687-717.

[7] Donati, E., Corradi, F., Stefanini, C., & Indiveri, G. (2014, October). A spiking implementation of the lamprey's Central Pattern Generator in neuromorphic VLSI. In Biomedical Circuits and Systems Conference (BioCAS), 2014 IEEE (pp. 512-515). IEEE.

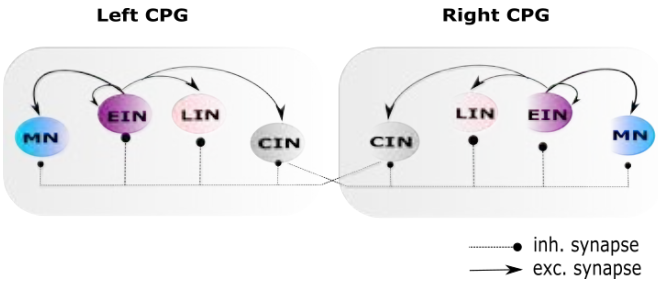

Figure 1 CPG neural organization, it comprises two sides coupled both excitatory and inhibitory connections.

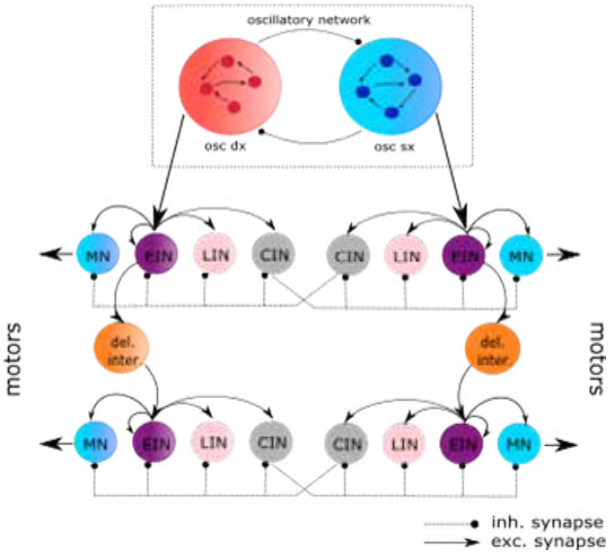

Figure 2 Schematic diagram of the hardware model.

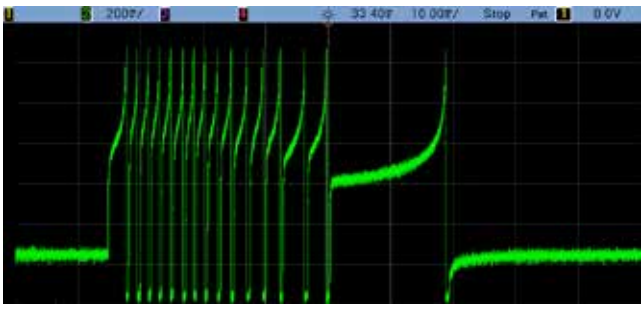

Figure 3 Burst activity measured on a silicon neuron.

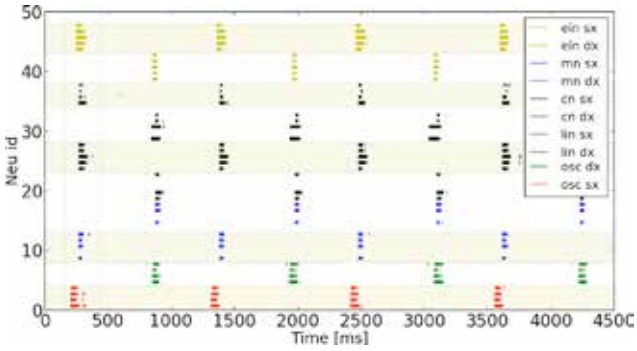

Figure 4 Alternate movement left/right in the first segment.

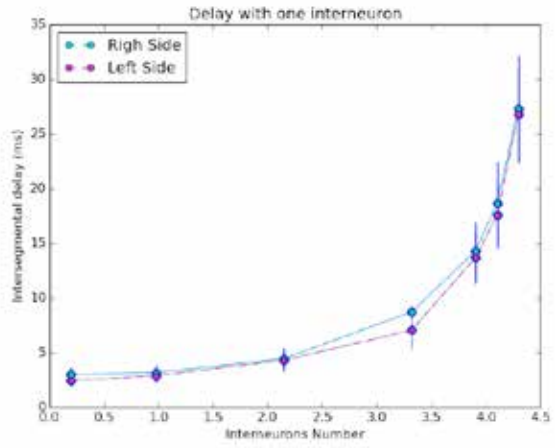

Figure 5 Intersegmental delay between segments, by increasing value of input current.

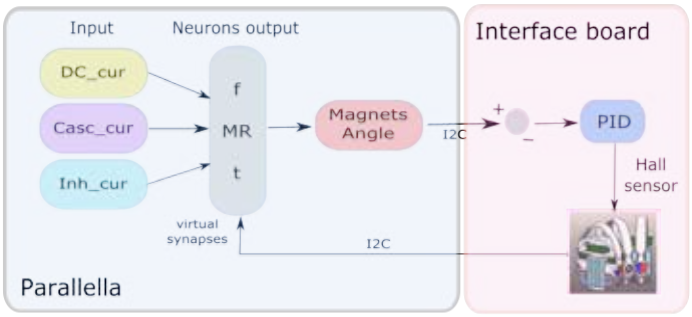

Figure 6 Block diagram of Lamprey control system.

Gait segmentation with a wearable non contact capacitive sensory system

S. Manca[1], A. Parri[1], T. Yan[1], E. Zheng[2], M. Cortese[1], R. Molino Lova[3], Q. Wang[2], N. Vitiello[1,3]
[1] The BioRobotics Institute, Scuola Superiore Sant'Anna, viale Rinaldo Piaggio 34, 56025, Pontedera (PI), Italy.
[2] Robotics Research Group, College of Engineering, Peking University, Beijing 100871, China.
[3] Don Carlo Gnocchi Foundation, via di Scandicci 256, 50143, Firenze, Italy.

***Abstract*—In this paper a novel method to analyze and segment the gait cycle based on capacitive sensors is presented. Capacitive signals indicate the volume variation of the lower-limb segments due to muscular contraction/relaxation during the gait cycle. In order to correlate the lower limb deformations to biomechanical gait related events, six capacitive signals were recorded from the distal segment of the lower limb, simultaneously with the vertical ground reaction forces (vGRF). Data collected from five subjects walking on a treadmill at three different speeds show a repeatable correlations between the capacitive signals and the vGRF.**

***Keywords*—Capacitive sensors, gait segmentation, wearable sensors, gait analysis, real-time gait monitoring, exoskeleton.**

I. Introduction

Gait phase estimation is fundamental to study human gait biomechanics for robotics applications. In the specific field of lower-limb assistive robotics, the computation of the gait phase, i.e. the time-scaled reference of the stride period, is still a major open challenge. The cognitive interface of a wearable lower-limb robot should be able to decode the gait-phase of the user in order to deliver proper mechanical power in specific phases of the stride cycle. Many approaches have been proposed for designing intuitive and effective human-robot interfaces exploiting different kinds of sensory apparatus. Inertial sensors are one of the most popular solutions for reconstructing the kinematics and kinetics in a walking task [1]. Nevertheless, they consist of an expensive technology and require complex preconditioning. Among mechanical sensors, instrumented foot soles gain a great interest in several robotics applications [2]. However, the lifespan of foot soles is always a limitation for long-time utilization since they are supposed to bear the weight of adult persons for several cycles. In addition, they often need to be placed inside shoes which could cause discomfort for the user and, moreover, it is necessary to change their size to comply with different anthropometries. Surface electromyography (sEMG) is a common approach to decode the user intentions in assistive robotics field since it represents a direct measurement of the muscular activity. Nevertheless, its utilization is always associated with complex procedures for electrodes placement and skin preparation that can easily affect their effectiveness [3]. To overcome the limitations of the above mentioned sensory system, in this paper, a novel method based on non contact capacitive sensors is presented to detect the gait cycle and estimate relevant gait events. This wearable sensory apparatus (WSA), which measures the lower limb muscle deformations during walking, has been previously used to recognize different locomotion modalities in transtibial amputees [5], [6]. Differently from instrumented insoles, the device is positioned on the leg thus not being stressed by the entire body weight. As a consequence, it ensures a longer lifespan of utilization. Furthermore, this WSA does not have to be placed directly on the skin but can be worn above clothes, reducing the possibility of motion artifacts and increasing the user acceptability. In order to segment the gait cycle by utilizing capacitive signals, we propose to identify the relationship between the recorded lower-limb muscle deformations with biomechanically relevant gait event such as heel strike (HS) measured with sensitive insoles, which represents the gold standard in the gait segmentation field [3], [4]. The related materials and methods, including the validation experiments, are described in Section II. In Section III, experimental results are reported. Finally, results are discussed and conclusions are drawn in Section IV.

II. Materials and Methods

A. Capacitive sensing system

The capacitive technology used in this work is known in literature as C-Sens [5], [6], and was developed at the College of Engineering of the Peking University (Beijing, People Republic of China), to measure the lower limb muscles deformations during human walking by means of capacitive electrodes. C-Sens is composed by a custom print circuited board (PCB), powered at 5V, and two orthopaedic cuffs that can be placed on the distal and proximal lower-limb segments [Fig. 1(a)-(c)]. Each cuff, made of thermoplastic material, is instrumented with six flexible copper made capacitive electrodes, placed in the inner side of the cuffs. Three electrodes are located on the anterior side of the cuff and three on the posterior side [Fig. 1(b)]. The electrodes are connected to the dedicated PCB by means of a RS232 connection. A layer of silicon rubber (2.5 mm thickness) is placed above the electrodes to electrically isolate them from the contact surface. An additional electrode, namely the reference electrode, must be placed directly in contact with the skin. The capacitive signals are sampled at 100 Hz and are measured between each capacitive electrode and the reference one. As it is known, the value of the capacitance is directly proportional to the surface of the plates and to the dielectric constant and inversely proportional to the distance between the plates. Indeed, as the muscles shape varies during the gait cycle, due to contractions and relaxations, at the same time, the distance between the skin and the copper changes resulting in a variation of the capacitance. Up to twelve capacitive signals can be collected simultaneously but it is worth noticing that in this study only the six capacitive signals from the distal segment were unilaterally recorded.

B. Instrumented insoles

The instrumented insoles, developed at Scuola Superiore Sant'Anna (Pontedera, Pisa, Italy), are made of 64 optoelectronic pressure sensors embedded into a PCB and covered with a silicon layer. The data from all the sensors are sampled at 100 Hz and transmitted to the PC via a Bluetooth connection. When a load is applied on the top of the cover, the silicone gradually closes the light path between the emitter and the receiver resulting in a variation of the output voltage [7]. The size of the insoles is 41- 43 EU size. Each insole is connected by means of a flat cable with the dedicated electronic board powered at 4.2V with a Li-Io battery. The electronic board is devoted to signal transmission and the computation of vGRF and longitudinal position of the centre of pressure (CoP).

C. Experimental protocol

In order to evaluate the possibility to detect some relevant biomechanical gait related events by means of the capacitive signals, five subjects were enrolled (four males and one female, 26.8±2.4 years, 67.40±7.99 kg, 174±11 cm). The experiment was conducted at Scuola Superiore Sant'Anna. Each subject worn the distal C-Sens cuff on the left shank and both the instrumented insoles. Before the data acquisition started, each subject was asked to walk on the treadmill in order to select his/her slow, fast and normal self-selected speeds hereafter indicated as SS, SF and SN respectively. After twenty seconds of standing still on the treadmill the subject walked at the three different speeds, each one maintained for three minutes, in the following order: SN, SF, SN, SS, SN. Finally, the subject stopped walking and stood still on the treadmill for twenty seconds.

D. Data analysis

The data were processed in real-time by using the NI, single Board RIO (sBRIO) 9626. The experiment was monitored in real-time by means of a graphical user interface (GUI). In particular, the capacitive signals were filtered on line by means of a second-order band-pass Butterworth filter (pass band: 0.1÷1 Hz). The off-line analysis was performed on Mathworks, Matlab. The six capacitive signals were segmented with respect to the HS detected by the vGRF. Then, the signals were interpolated as the percentage of the gait cycle (0% - 100%) and their averaged envelopes along with the standard deviation were computed. Furthermore the capacitive signals collected from each subject were normalized for their maximum in absolute value in order to compare the six capacitive signals for all of the five subjects with the vGRF. The segmented data are presented in Fig. 2. The same analysis was conducted for the vGRFs [Fig. 3].

III. Results and Discussion

The comparison of the capacitive signals from different subjects showed that there is a minimal inter-subject variability in some channels, in particular, the signals recorded from the channels #1, #4 and #6. Channel #4 and #6 are positioned on the rear part of the lower limb as shown in Fig. 1 (b) while channel #1 is on the upper part of the anterior side. For this reason we identified these channels as the most suitable to identify any possible relationship between the signal from the muscular deformation and vGRFs. Signals measured from channel #1 presented a negative peak in 22.60±7.47% of the stride and a consecutive positive peak next to 82.40±2.70% of the stride. The signal crosses the zero at around 59.10±6.59% of the gait cycle. Signals measured from channel #6 showed a similar trend: a negative peak occurs between 39.60±17.36% of the stride, while the positive peak is next to 85.60±7.79% of the stride; the transition from the negative to the positive values is next to 63.60±11.72% of the stride. Better results come from the segmentation of the signals measured from channel #4. Indeed, these signals have a more periodic behavior and are less affected by inter- and intra-subject variability with respect to the signals measured from channel #1 and #6 which have an higher variability as showed by their standard deviation. Effectively, the transition from negative to positive for the signals from channel #4 occurs for all of the subjects immediately after the second hump of the vGRF, in correspondence of the swing phase next to 65.72±3.35% of the stride period. Nevertheless, there is an inter-subject variability in the minimum peak of the signals recorded from channel #4 which is next to 36.76±10.46% of the stride. Finally, this signal has a maximum peak 20% in advance with respect to the HS (85.80±3.19% of the gait cycle). We believe that the minimal inter-subject variability observed in these three signals is related to the sensors placement; indeed, those channels are placed on the muscles that are more active during the gait cycle (on the distal segment) and, as a consequence, show evident deformations, i.e. the Gastrocnemius and the Tibialis Anterior. Hence, this novel WSA has three major advantages to record biomechanical gait related events reliably with respect to other sensors as sEMG and instrumented insoles. Firstly, contrarily to sEMG, skin preconditioning is not needed and motion artifacts are avoided. Then, with respect to the instrumented insoles, this system does not require a calibration and it is not necessary to account for different sizes to improve wearability. In addition, the sensors can be worn above clothes making the system more acceptable for users with respect to insoles or sEMG and usable in activities of daily living.

IV. Conclusions

This paper showed that the muscles deformations measured by means of capacitive sensors can be used to estimate the gait cycle, without involving in any other sensory apparatus. Experimental results showed a reliability of gait event detection and gait-phase estimation, comparable with instrumented insoles. In addition, it was proved that at the posterior side of the lower-limb distal segment a capacitive signal is minimally affected by inter-subject and intra-subject variability. In the future, this device could be used to segment the gait cycle in robotics applications, for instance in the cognitive interface of lower-limb powered exoskeletons or prostheses. A future achievement could be the integration of the sensors inside clothes and textiles to further facilitate and improve the system wearability and utilization in an out-of-lab scenario.

Acknowledgement

This work was supported by Fondazione Pisa within the IUVO project (prog. 154/11).

REFERENCES

[1] M. Boutaayamou, C. Schwartz, J. Stamatakis, V. Denoel, D. Maquet, B. Forthomme, J.L. Croisier, B. Macq, J. G. Verly, G. Garraux, O. Bruls, 'Development and validation of an accelerometer-based method for quantifying gait events', *Medical Engineering and Physics* vol. 37, pp. 226–232, 2015

[2] A.B. Zoss, H. Kazerooni, A. Chu, 'Biomechanical design of the Berkeley lower extremity exoskeleton (BLEEX)', *IEEE/ASME Transactions on Mechatronics*, vol.11, pp. 128–138, 2006

[3] J. Taborri, E. Palermo, S. Rossi, P. Cappa,"Gait partitioning methods: a systematic review", *Sensors*, vol.66, pp.1-20, 2016

[4] W. Tao, T. Liu, R. Zheng, H. Feng, "Gait analysis using wearable sensors", *Sensors*, vol.12, pp.2255-2283, 2012

[5] E. Zheng, L. Wang, K. Wei, Q. Wang, "A noncontact capacitive Sensing System for recognizing locomotion modes in transtibial amputees", *IEEE Transactions on Biomedical Engineering*, pp. 2911-2920, vol. 61, no. 12, Dec. 2014.

[6] E. Zheng, N. Vitiello, Q. Wang, "Gait phase detection based on non-contact capacitive sensing: preliminary results", *IEEE International Conference on Rehabilitation Robotics*, pp. 43-48, 2015.

[7] S. Crea, M. Donati, S.M. M. De Rossi, C: M. Oddo, N. Vitiello, "A wireless flexible sensorized insoles for gait analysis", *Sensors*, vol. 14, pp. 1073-1093, 2014

.

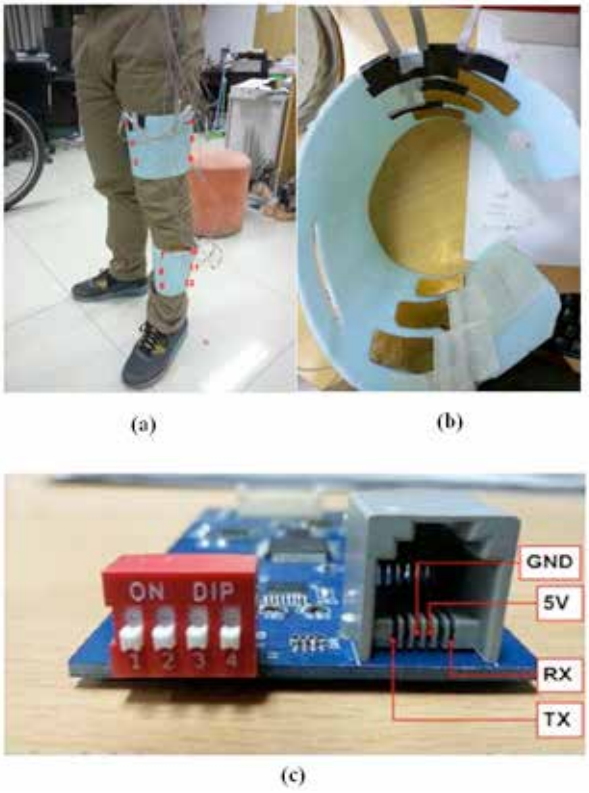

Fig. 1 C-Sens technology: (a) the two orthotic cuffs, (b) C-Sens sensors, (c) C-Sens board

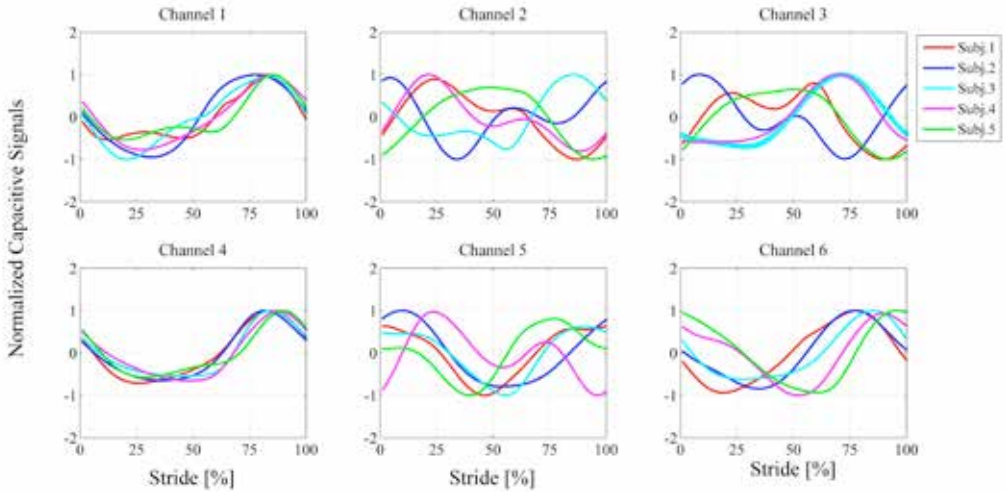

Fig. 2 Averaged normalized capacitive signals measured from the left shank of the five subjects.

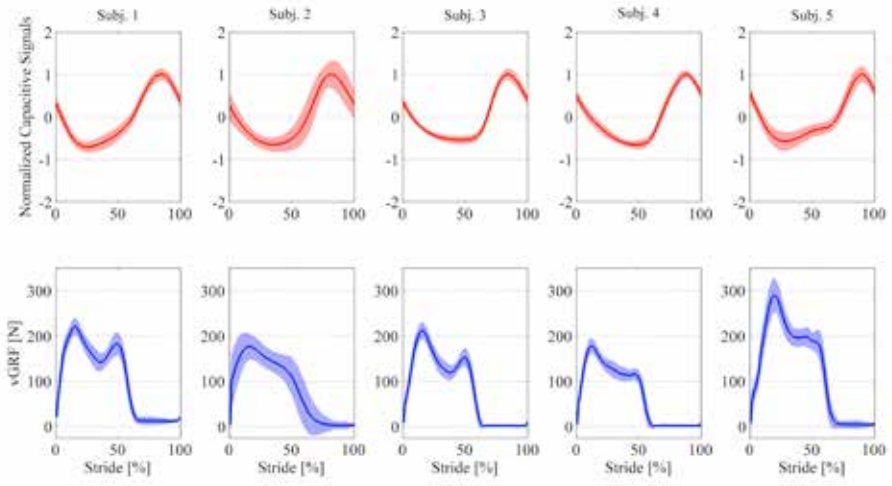

Fig. 3 Overview of results from channel 4. The first row reports the normalized capacitive signals for the five subjects; the

A novel soft manipulator for assistive robotics based on soft fluidic actuators

M. Manti, A. Pratesi, M. Cianchetti and C. Laschi
The BioRobotics Institute of the Scuola Superiore Sant'Anna, Pisa, Italy.

***Abstract*— The authors focus on the possibility to adapt technologies and basic concepts of Soft Robotics for building a new generation of soft manipulators as shower arm that can safely come into direct contact with humans in a novel scenario which is the bathing activity. The paper points out the manipulator design and a preliminary characterization of its performances in terms of shortening, elongation and bending capabilities. The outcomes of this work represent a first step in the application of soft mechatronics technologies in assistive robotics for developing functional tools in the bathing activities.**

***Keywords*— soft robotics, soft modular manipulator, assistive robotics, personal care robot.**

I. Introduction

The rapid advances occurred in the field of robotics in recent years enable the development of robotic assistive systems to improve the independence and quality of life of elderly people with ageing-related disabilities [1]. The development of assistive technologies is seen as an enabler for a human doing an activity of daily living (ADL), thus facing challenging scenarios as for example the intimate bathing task. The main issues related to the disabilities derive from the lack of user-oriented tools for overcoming the barriers during the interaction between people and the environment, for performing critical and high risk ADLs, like the bathing activity [2]. This highlights that a support in bathing activities will improve independent living for persons prone to loss of autonomy, thus lightening the users' caring issues [1]. Although the importance of the bathing activity as a basic ADL, literature analysis on assistive technologies for bathing task suggests us only two commercially available shower devices: the Oasis Seated Shower system [3] and the Seat Lift Device [4]. In this view, a service robotics system that targets bathing tasks should be safe, reliable, adaptable to users' actions [5] during the direct contact and interaction with the elderly people for accomplishing the shower task. Moreover, the system could be exploited in different real life applications, thus it should be modular and flexible for addressing a safe human-robot interaction (HRI). Among the useful technologies that satisfy the previous requirements, we evaluated the possibility of exploiting soft robotics ones. Our purpose is to apply, for the first time, soft robotics concepts in a new challenging scenario, like the showering activities, by designing and developing a modular manipulator which safely comes into direct contact with humans.

II. Materials and Methods

A. Technological concept for the shower arm

The aim of the work is the use and adaptation of soft robotics technologies for developing a robotic shower arm considering the constraints imposed by the bathing scenario. The final design will take into account two issues: (i) the target workspace to be covered defines the dimension of the complete shower arm; (ii) the expected performances (dexterity) establish the type of actuation technology. For addressing these features, we combined cables and flexible fluidic actuators. Figure 1 presents a typical scenario with two identical soft robotic arms mounted on the wall respect to the user that, seated on a chair, approaches the robotic shower. Moreover, a CAD overview related to the single module is provided in order to show the main technical components. The starting point for delivering our technological concept of the robotic shower arm has been a literature analysis regarding the design of manipulators based on soft technologies [6]–[10]. Considering the main achievements of these works, we designed our device by combining three cables, for shortening and bending movements, and three McKibben-based flexible fluidic actuators, enablers of bending and elongation movements in soft structures [11].

B. Design and manufacturing of the module

Our module embeds three flexible fluidic actuators 120° spaced and three cables that are 60° spaced respect to the previous elements (Figure 1). The flexible fluidic actuators McKibben-based are made of an internal balloon anchored to two end-caps covered by a braided structure that has been properly designed in order to have a bellow-type shape. All the components are concentrically arranged around an internal channel that provides water and/or soap. In order to avoid lateral buckling of the fluidic actuators, a flexible helicoidal structure has been inserted along the entire module thus constraining any lateral movements. The single module is 60 mm in diameter and 205 mm in length (Figure 1), with a total weight of 180 g. Cables and chambers are decoupled, each one has a dedicated activation line for respectively tension and pressure regulation.

C. Experimental set-up

The set-up consists of a single module attached to an acrylic box and a pneumatic circuit that allows to independently control the pressure in each valve (0÷1.2 bar). The air source, provided by a compressor, is regulated through a ROS interface. Instead, cable tension is produced by connecting them to a load cell moving on a rail. The position and orientation of the module tip in the space has been tracked with an Aurora® Tracking system (NDI) with a six-DOF probe fixed on the tip of the module (Figure 2).

D. Preliminary experimental evaluation

In order to characterize the system, we measured elongation, shortening and bending capabilities in the 3D space according to the following patterns: (i) elongation by pressurizing all the three chambers; (ii) shortening by

tensioning all the three cables; (iii) bending by pressurizing at different steps a single chamber (**Activation pattern 1**) or two chambers (**Activation pattern 2**) and then by tensioning the cable until a 180° rotation of the module tip in order to measure the maximum force. The last part of the experimental characterization aims at defining the boundaries of the workspace for the two different patterns of activation (A1, A2 and A3; A1-A2, A2-A3 and A1-A3).

III. Results and Discussion

The experimental evaluation starts by activating the chambers respect to the cables in order to firstly exploit the global movement of the module due to the fluidic capabilities and then to adjust the position (curvature and orientation) with the cables tensioning. The single McKibben-based actuator has been characterized at increasing pressure values. The bellows-type design of the external sheath enables an elongation up to 85% respect to its initial length (@ P=1.2 bar).

A. Elongation

The activation of the three chambers at 1.2 bar of pressure allows an elongation up to 345 mm, with an increase of its length of 68%. It means that each chamber undergoes to 72% of deformation respect to its initial length (195 mm). The lower elongation achieved by the flexible fluidic actuators when embedded into the module is caused by the constraints and limitations imposed by the structural elements of the module (e.g. the helicoidal structure).

B. Shortening

Shortening capabilities are achieved by a simultaneous tensioning of the three cables. Starting from a total length of 205 mm, the module achieves a 25% shortened position (155 mm) by applying 18 N.

C. Bending

Bending performances have been analysed at increasing pressure values. In particular, even if the working pressure range was from 0 bar to 1.2 bar (with 0.1 bar of resolution), we noticed no movements from 0.0 bar to 0.5 bar, due to the non-linear response of the actuator.

Activation pattern 1: The overall movement of the module in the 3D space is shown in Figure 3A. The tip undergoes a displacement along the z-axis of 100 mm respect to the rest position, against gravity effects (see Figure 3B). Another observation regards the role played by the single opposite cable (B1) respect to the overall movement of the module. A 180° rotation of the module is achieved by applying 2N of tension in the cable. The behaviour of the module respect to the yz plane (Figure 3C) shows a lateral displacement of 25 mm (@ 1.2 bar), due to a slight asymmetry introduced during the manual manufacturing procedure of the module.

Activation pattern 2: Figure 3D shows the global movement of the module, by co-activating two chambers (A2-A3) where the module tip undergoes a vertical displacement of 30 mm (Figure 3E). It implies that, the module is firstly elongated and then, the distal portion of the total length produces the bending. While, the lateral displacement is approximately 45 mm (@ 1.2 bar), due to the asymmetry of the module (Figure 3F). Regarding the effect produced by the cables co-activation (B2-B3), the module tip is able to produce a 180° rotation respect to the base, by applying 1N in each cable.

D. Workspace

The evaluation of the workspace aims at defining the boundaries of the reachable positions of the module tip (Figure 4). These points are acquired by applying the activation patterns 1 and 2 to all the three chambers and combination of them respectively.

IV. Conclusion

The proposed work addresses, for the first time, the challenge of developing a modular shower arm that safely interacts with the user for carrying out one of the most critical ADLs as the bathing tasks. The present shortening, elongation and bending outcomes are promising and encouraging; they guarantee that the connection of three identical modules will be helpful for accomplishing the bathing activity in the worst reachable body parts. This aspect represent the starting point for the development of the first soft assistive robot for personal care of elderly people.

Acknowledgement

Research supported by the I-Support project in HORIZON 2020 PHC19, Grant Agreement #643666 and the RoboSoft CA in FP7 ICT FET-Open project #619319. The work is also supported by the Italian Ministry of Foreign Affairs and International Cooperation DGSP-UST through Joint Laboratory on Biorobotics Engineering project.

References

[1] S. W. Brose, D. J. Weber, B. A. Salatin, G. G. Grindle, H. Wang, J. J. Vazquez, and R. A. Cooper, 'The role of assistive robotics in the lives of persons with disability', *Am J Phys Med Rehabil*, vol. 89, no. 6, pp. 509–521, Jun. 2010.

[2] T. Bock, C. Georgoulas, and T. Linner, 'Towards robotic assisted hygienic services: Concept for assisting and automating daily activities in the bathroom', *Gerontechnology*, vol. 11, no. 2, p. 362, Jun. 2012.

[3] http://www.seatedshower.com/

[4] http://www.drivemedical.co.uk/sections/bathroom-toilet-aids/

[5] Q. Meng and M. H. Lee, 'Design issues for assistive robotics for the elderly', *Advanced Engineering Informatics*, vol. 20, no. 2, pp. 171–186, Apr. 2006.

[6] A. Loeve, P. Breedveld, and J. Dankelman, 'Scopes Too Flexible...and Too Stiff', *IEEE Pulse*, vol. 1, no. 3, pp. 26–41, Nov. 2010.

[7] G. Immega and K. Antonelli, 'The KSI tentacle manipulator', in *, 1995 IEEE International Conference on Robotics and Automation, 1995. Proceedings*, 1995, vol. 3, pp. 3149–3154 vol.3.

[8] W. McMahan, V. Chitrakaran, M. Csencsits, D. Dawson, I. D. Walker, B. A. Jones, M. Pritts, D. Dienno, M. Grissom, and C. D. Rahn, 'Field trials and testing of the OctArm continuum manipulator', in *Proceedings 2006 IEEE International Conference on Robotics and Automation, 2006. ICRA 2006*, 2006, pp. 2336–2341.

[9] W. McMahan, B. A. Jones, and I. D. Walker, 'Design and implementation of a multi-section continuum robot: Air-Octor', in *2005 IEEE/RSJ International Conference on Intelligent Robots and Systems, 2005. (IROS 2005)*, 2005, pp. 2578–2585.

[10] M. B. Pritts and C. D. Rahn, 'Design of an artificial muscle continuum robot', in *2004 IEEE International Conference on Robotics and Automation, 2004. Proceedings. ICRA '04*, 2004, vol. 5, pp. 4742–4746 Vol.5.

[11] A. De Greef, P. Lambert, and A. Delchambre, 'Towards flexible medical instruments: Review of flexible fluidic actuators', *Precision Engineering*, vol. 33, no. 4, pp. 311–321, Oct. 2009.

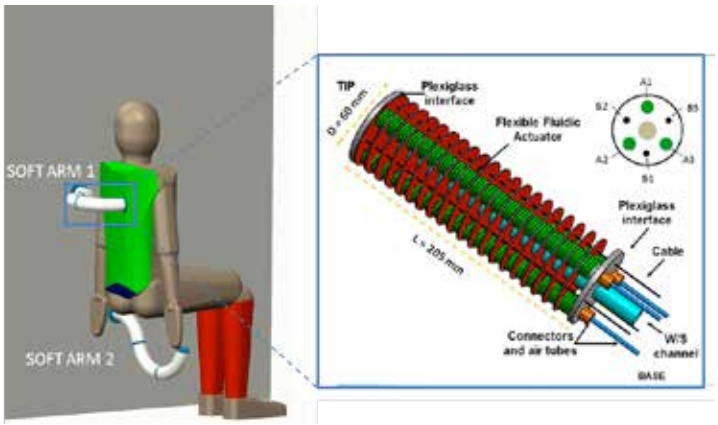

Fig. 1. Concept overview: soft robotic shower arms mounted on the wall (critical body parts: back region and lower limbs). CAD design of the single module.

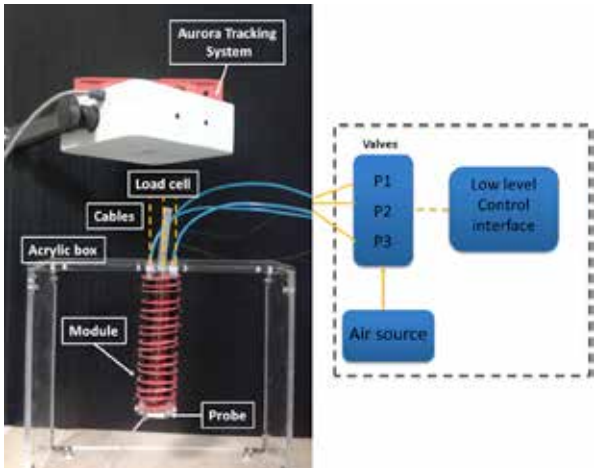

Fig. 2. Experimental set-up for module characterization.

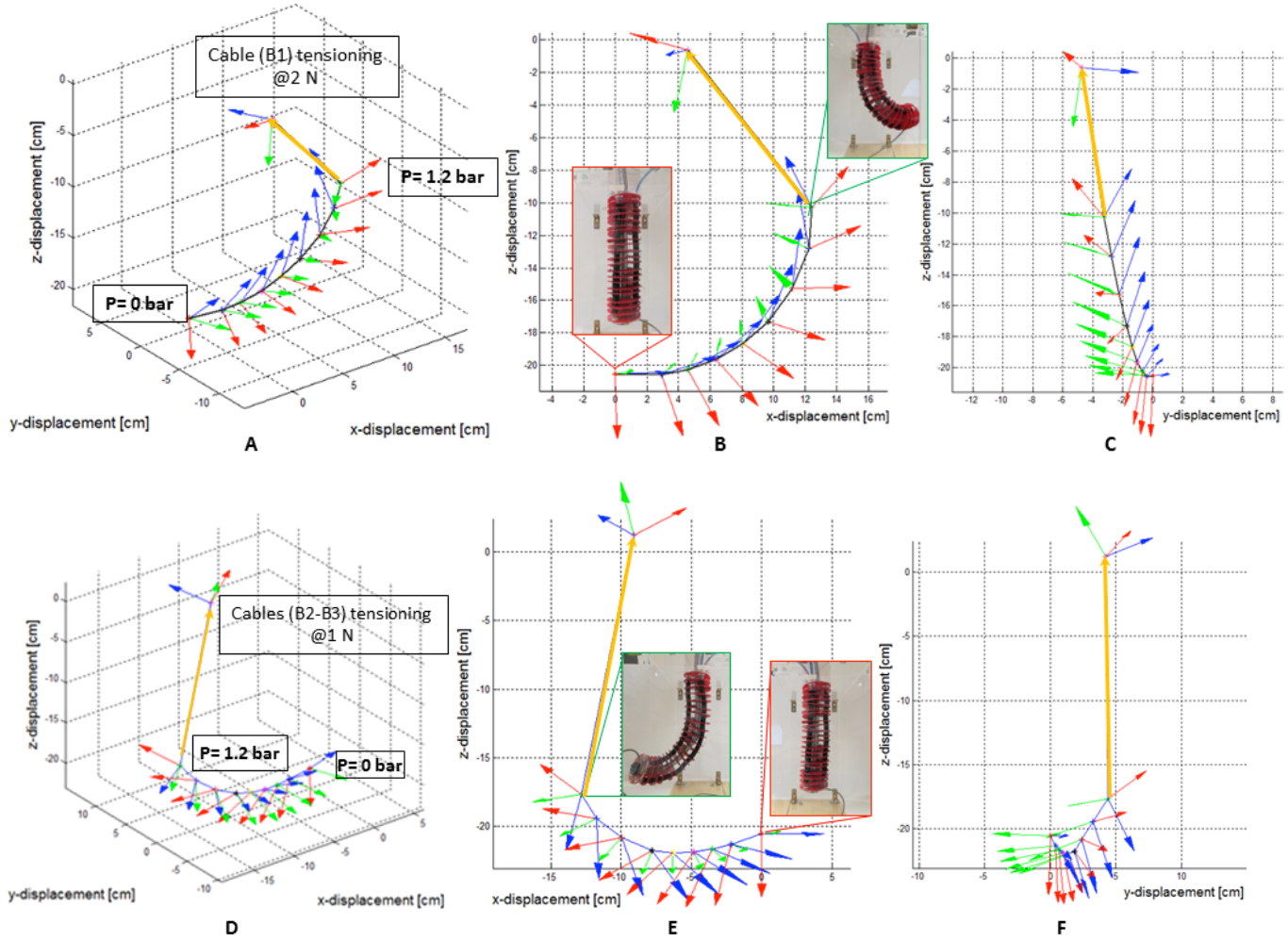

Fig. 3. Bending performances of the two activation patterns. A) 3D view of pattern 1 (A1 + B1); B) xz view of pattern 1; C) yz view of pattern 1; D) 3D view of pattern 2 (A2-A3 + B2-B3); E) xz view of pattern 2; F) yz view of pattern 2.

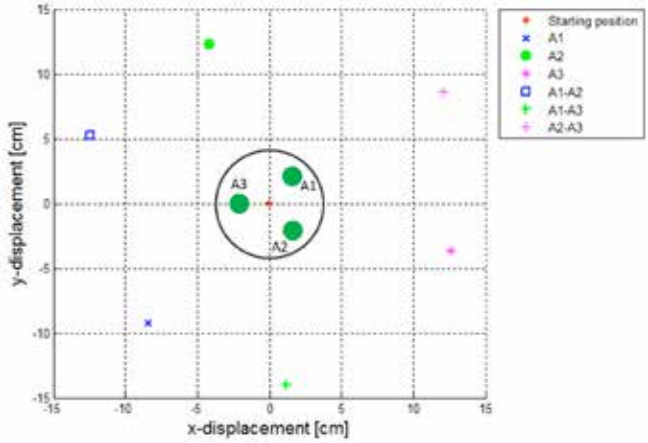

Figure 4. Module workspace (xy view): maximum positions reached by the module tip for different patterns of activation.

A novel strategy for assisting Sit-to-Stand and Stand-to-Sit tasks through a lower-limb exoskeleton

D. Marconi[1], A. Parri[1], T. Yan[1], F. Giovacchini[1], M. Fantozzi[1], M. Cortese[1], R. Molino Lova[2] and N. Vitiello[1,2]

[1] *The BioRobotics Institute, Scuola Superiore Sant'Anna, viale Rinaldo Piaggio 34, 56025, Pontedera (PI), Italy.*
[2] *Don Carlo Gnocchi Foundation, via di Scandicci 256, 50143, Firenze, Italy.*

***Abstract*—Gait impairments or lower-limb muscular weaknesses are inevitable issues associated with aging and neurological diseases. In this paper, a novel assistive strategy to aid the Sit-to-Stand and Stand-to-Sit tasks was proposed, In fact these are two of the most demanding activities in daily living. The assistance was provided by a multi-joint lower-limb orthosis. The strategy consists of two levels: firstly the intended task is recognized by a finite-state machine controlled via thresholds, then the assistive torque is delivered based on a function of the hip angles. Validation experiments involved one healthy subject performing the sitting down and standing up tasks 12 times while receiving the designed assistive torque. The assistance proved to be well received by the user without hindering his natural movement.**

***Keywords*—Active lower-limb orthosis, wearable assistive technology, elderly people, lower-limb weakness**

I. Introduction

THE issue of population aging is attracting a great attention especially in Europe and the US [1]. According to several population-based studies ([2], [3]), gait impairments are prevalent in about 80% of the general population over 85 years old. The degenerated mobility holds the elderly individuals away from an independent life and could result in more severe health deteriorations, such as cardiovascular conditions, cognitive and neurological decline, risk of fall and subsequent traumas. As a valuable solution to cope with this perspective, wearable robotic devices, also known as powered orthoses or exoskeletons, have been designed to assist impaired and elderly people's movements. An exoskeleton is defined as a portable mechatronic anthropomorphic device, worn by the users and fitting closely to their body. Current state-of-the-art exoskeletons include devices distinguished by different features, such as the number of actuated joints (full body, lower limb, hip, etc.), the targeted utilization (assisting, rehabilitation, force augmentation), the mechatronics design (mechanics, actuation system, control strategies), and the human-robot interface [4].

In this paper, a modular unilateral active orthosis was used to provide assistive torque to the user. The full device was composed of two parts: an Active Pelvis Orthosis (APO) and a Knee-Ankle-Foot Orthosis (KAFO) (**Errore. L'origine riferimento non è stata trovata.**a). An early validation of this device was carried out in **Errore. L'origine riferimento non è stata trovata.**. The device encompasses all of the leg joints (hip, knee and ankle). The orthotic system was used to provide assistive torque to the corresponding human joints during sit-to-stand and stand-to-sit movements, which can be considered very demanding activities of daily living for people with mild gait impairments, such as frail elderly people or amputees. The control system proposed in this study implements a threshold-based algorithm and a finite-state machine to automatically identify the intended task in real-time, providing appropriate assistive torque.

In this paper a brief description of the mechatronic system of APO and KAFO is presented, together with a description of the control algorithm (Section II). Then a feasibility experiment is described, and results are discussed (Section III). Conclusions are drawn in Section IV.

II. Material and Methods

A. APO-KAFO mechanics

The APO (overall weight: ~8 kg) consists of a backpack containing the main electronic components, two actuators placed below the backpack itself, two carbon fibre links interfaced distally with thighs and coupled to the actuation units and three orthotic cuffs. The plastic cuffs ensure a comfortable human-robot interaction as they were designed with a large contact surface to reduce pressure on the wearer's skin. The torque generated by the actuators is transmitted to the flexion-extension joints through a steel cable transmission embedded into the carbon fibre lateral arm. The device has an active hip flexion-extension degree of freedom (DoF), with a range of motion (RoM) in the range [-110°÷20°] (positive while extending). Moreover, the device is endowed with a passive hip adduction-abduction DoF with a RoM in the range [-15°÷20°] (positive in abduction), and a passive intra-extra rotational DoF with a RoM in the range [-10°÷10°]. Both passive DoFs are necessary to ensure a comfortable wearability by different wearers. The actuation units rely on the approach of Series Elastic Actuators (SEA) [5], thus providing a compliant actuation with minimum joint output impedance within the frequency spectrum of gait [7].

The KAFO (overall weight: ~6 kg) is interfaced with the APO through a removable linkage. Both the knee and ankle joints are actuated in the sagittal plane, with the RoMs equal to [-150°÷0°] and [-52°÷29°] respectively. The knee joint is actuated via a SEA, while the ankle joint is actuated via a MACCEPA, a non-linear series elastic actuator with a variable stiffness [8] assembled in series with a 4-bar linkage mechanism. Nevertheless, the proposed assistive strategy aimed to deploy assistance only to the hip and knee joints with the ankle joint in zero-torque mode.

B. Control system

The control system of the device consists of a hierarchical structure, i.e. a low-level layer implementing closed-loop torque control and a high-level layer implementing the

assistive strategy. The strategy aims at providing a desired torque reference variable over the task phase.

The output torque of the active joints is estimated by measuring the deformation of the SEA springs by means of absolute encoders. The assistive torque profile was mapped over the hip joint angles and was designed to have a Gaussian shape, in order to ensure a smooth torque delivery as described in the following equation:

$$\tau_{des} = Ae^{-\frac{1}{2}\left(\frac{\varphi-\sigma}{\partial}\right)^2} \quad (1)$$

where τ is the delivered torque, A is the amplitude of the curve peak, and σ and ∂ are respectively the peak shift and the width of the Gaussian curve as a function of φ. Specifically, φ is an index of task completion based on the two thresholds θ_1 and θ_2 - set on the hip joint angles - defining the 0 - 100 % of the Sit-to-Stand task and vice versa, as illustrated in **Errore. L'origine riferimento non è stata trovata.**b. A finite state machine was designed for discerning between situations of Quite Sitting, Quite Standing, Sitting Down or Standing Up. When the subject is in Quite Sitting or Quite Standing positions, no torque is provided. Then, the variation of the mean hip angle:

$$\bar{\theta} = \frac{\theta_L + \theta_R}{2} \quad (2)$$

- being θ_L, θ_R the left and right hip joint angles respectively - is used to trigger the switch of the task identification when overcoming the thresholds θ_1, θ_2 (**Errore. L'origine riferimento non è stata trovata.**b). Moreover, in order to ensure robustness and safety, the following condition has to apply:

$$\theta_{LR} = |\theta_L - \theta_R| < \Delta_\theta \quad (3)$$

where θ_{LR} is the difference between θ_L, θ_R, averaged over the span of 40 samples and Δ_θ is a set threshold. This is an indicator of the symmetry of the user movement, with θ_{LR} increasing with asymmetry between left and right hip angles. The task switch occurs only if θ_{LR} is below Δ_θ, preventing the device from delivering torques during possibly odd movements.

C. Experiment

In order to verify the feasibility of the assistive torque profiles and the control algorithm, a prototypical experimental setup was designed and tested by a healthy volunteer (male, 27 years old, 71 kg, 1.65 m). The experiment was carried out at the premises of Don Carlo Gnocchi Foundation (Florence, Italy). The subject was requested to sit down and stand up 12 times while receiving the assistance from the exoskeleton. Collected variables, including the time taken to complete each task and the joints angles and torques, were segmented and re-sampled between 0% and 100% of the analysed tasks, i.e. for the standing up task 0% means sitting position and 100% means standing position, and vice versa. The joint velocities and assistive powers were then offline calculated. It is worth noting that hip and knee joint angles and velocities were assumed positive when the joints were extending.

TABLE I
AVERAGE ASSISTIVE POWERS OF HIP AND KNEE JOINTS DURING STANDING UP AND SITTING DOWN TASKS

	Peak Joint Powers [W]		*Average Joint Powers [W]*	
	Standing Up	*Sitting Down*	*Standing Up*	*Sitting Down*
Hip	16.94±7.01	-5.99±6.84	1.95±4.26	-1.04±1.23
Knee	11.6±4.53	-5.73±4.66	1.18±3.04	-1.26±1.71

III. RESULTS

In this section, results of the experimental session are reported. The average angle, torque and power profiles of the hip and knee joints were presented in Fig. 2 with the standard deviation contour. The assistive torque is set to be 0.14 N·m/kg (based on the subject bodyweight), for both hip and knee namely about 10% of the maximum physiological torque during sitting and rising from a chair tasks [7], [10]. Joint powers are positive during the Standing Up task, with peak values of 16.94±7.01 W for the hip and 11.6±4.53 W for the knee. During the Sitting Down task the joint powers were mostly negative with a hip power of -5,99±6.84 W and a knee power of -5.70±4.66 W. Mean mechanical power transmitted to the user during task accomplishment was calculated and results are shown in Table 1. As expected, the Standing Up tasks displays a mainly positive power, as the user need active power to help him perform the task. On the contrary, Sitting Down shows a mainly negative power delivery, as the device has to resist the subject's fall, slowing down his movement. Lastly, the average time needed for the subject to rise from the chair was reduced compared to the same task performed without assistance, being 1.21 s and 0.98 s respectively, while the time during the sitting task was increased from 1.46 s to 1.79 s.

IV. CONCLUSION

In this paper, an assistive strategy for Sit-to-Stand tasks was designed and validated with an active lower-limb orthosis composed by an APO and a KAFO modules. The proof-of-concept experiments was carried out with an healthy volunteer wearing the system and performing multiple sitting down and standing up tasks. Under the assistive controller, the device was able to transfer mechanical power to the subject consistently as demonstrated by the delivered power. Moreover, it was also proved that the assistance reduced the Standing Up time while increasing the Sitting down time which was significantly important to augment the subject's locomotion capability while protecting the joints from getting injured.

ACKNOWLEDGEMENT

This work was supported in part by the EU within the CYBERLEGs project (FP7-ICT-2011-2.1 Grant Agreement #287894), by Fondazione Pisa within the IUVO project (prog. 154/11).

REFERENCES

[1] Healthy ageing: keystone for a sustainable Europe, http://ec.europa.eu/health7ph_information/indicators, 2007. W.-K. Chen, *Linear Networks and Systems* (Book style). Belmont, CA: Wadsworth, pp. 123–135, 1993.

[2] A. H. Snijders, B. P. van de Warrenburg, N. Giladi, and B. R. Bloem, "Neurological gait disorders in elderly people: clinical approach and classification," *Lancet Neurol.,* vol. 6, no. 1, pp. 63–74, Jan. 2007.

[3] B.R. Bloem, et al., "Investigation of Gait in Elderly Subjects Over 88 Years of Age", *J Geriatr Psychiatry Neurol,* vol.5, no.2, pp.78-84, April/June, 1992.

[4] A. M. Dollar and H. Herr, "Lower Extremity Exoskeletons and Active Orthoses: Challenges and State of-the-Art," *IEEE Trans. Robot.,* vol. 24, no. 1, pp. 144–158, Feb. 2008.

[5] T. Yan et al., "A novel adaptive oscillators-based control for a powered multi-joint lower-limb orthosis", *IEEE, Rehabilitation Robotics (ICORR)*, pp. 386-391, 2015.

[6] G. A. Pratt and M. M. Williamson, "Series elastic actuators," *in Proceedings IEEE/RSJ International Conference on Intelligent Robots and Systems. Human Robot Interaction and Cooperative Robots*, vol. 1, pp. 399-406, 1995.

[7] F. Giovacchini et al., "A light-weight active orthosis for hip movement assistance" *Robotics and Autonomous Systems*, 2015.

[8] B. Vanderborght, N. G. Tsagarakis, R. Van Ham, I. Thorson, and D. G. Caldwell, "MACCEPA 2.0: compliant actuator used for energy efficient robot Chobino 1D", *Auton Robot*, pp. 31:55–65, 2011.

[9] K.L. Kang, S.Y. Lee, H.C. Kang and J.H. Jeong, "Study of Knee and Hip Joints' Moment Estimation by Biomechanical Simulation DuringVarious Motion Changes", *Proceedings of the World Congress on Engineering and Computer Science (WCECS, San Francisco, USA),* Vol 2, October 20-22, 2009.

[10] A.B. Schultz, N.B. Alexander and J.A. Ashton- Miller "Biomechanical Analysis of Rising from a Chair" *J Biomechanics*, Vol. 25, No. 12, pp. 1383-13911, 1992.

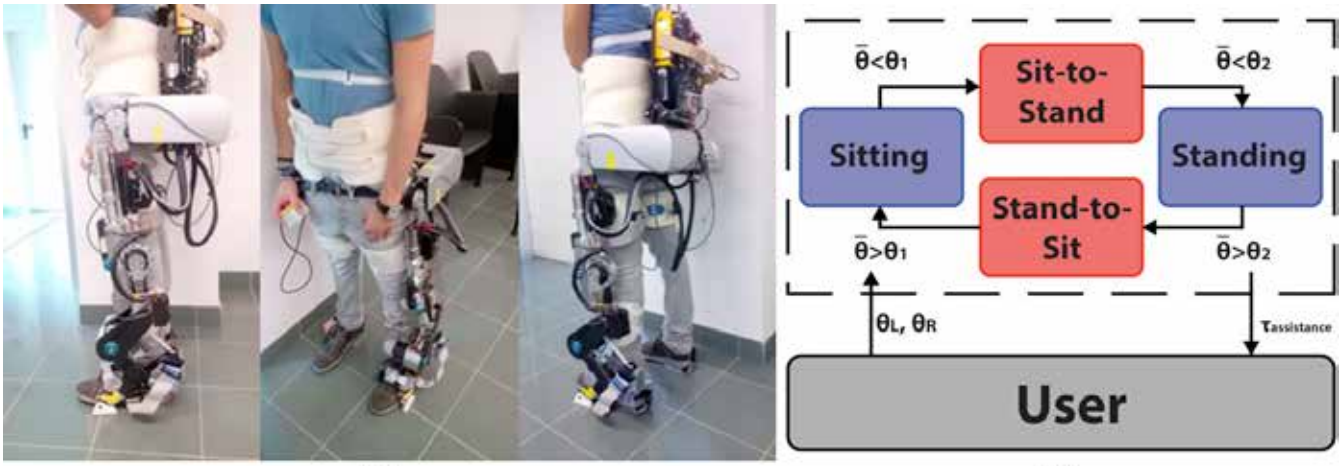

Fig. 1. (a) Overview of the full experimental setup (APO+KAFO), (b) Finite-state machine diagram for task identification. Quite Standing and Quite Sitting are static tasks, and therefore are not assisted by the device. The device switches to the dynamic states (i.e. sit-to-stand and stand-to-sit) when the hip angles reach set thresholds.

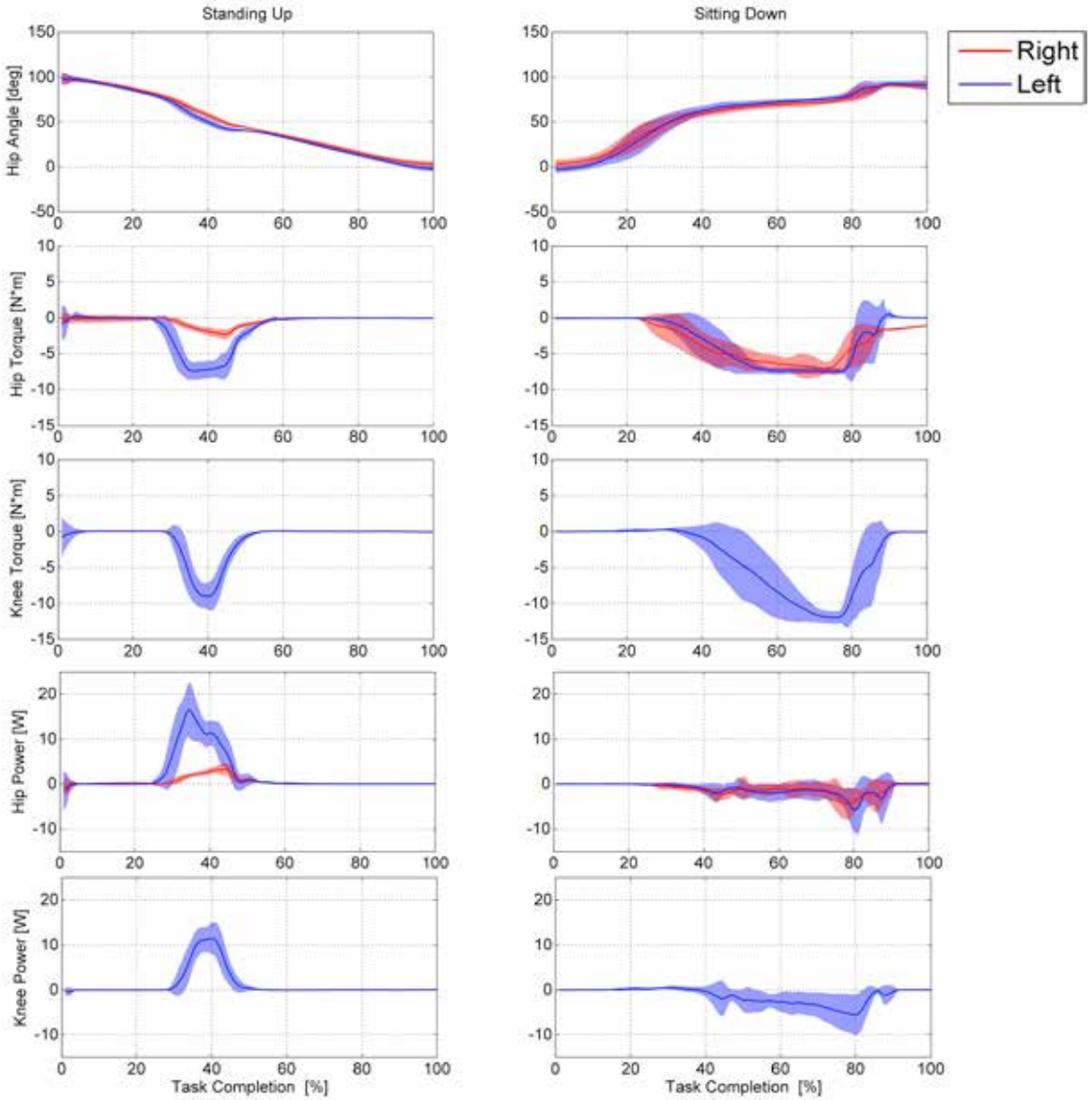

Fig. 2. Standing Up and Sitting Down tasks, displayed across the task completion percentage and averaged across multiples trials. The following variables are reported from top to bottom: hip angles, hip torques, knee torques, hip powers and knee powers. For each graph the average curve (solid line, blue for left and red for right joints) is shown along with the standard deviation contour.

A new cardioscopic device for paravalvular leak repair

M. Mencattelli[1], C. Kim[2], Z. Machaidze[3], I. Berra[4], B. Rosa[3], C. Stefanini[1], and P. E. Dupont[3]
[1] *The Biorobotics Institute, Scuola Superiore Sant'Anna, Pontedera (PI), Italy*
[2] *Health Care Robot Group, Korea Institute of Science and Technology, Seoul, Korea*
[3] *Cardiovascular Surgery, Boston Children's Hospital, Harvard Medical School, Boston (MA), USA*
[4] *Cardiovascular Surgery and Transplant, Hospital de Pediatria J. P. Garrahan, Bueons Aires, Argentina*

***Abstract*—Despite the substantial progress in catheter-based technologies for treating valvular diseases (e.g. paravalvular leak, PVL), significant problems like the limited dexterity and visualization during tissue contact, still remain. By integrating cardioscopy into the catheter tip, the surgeon can rely on high-resolution cardioscopic images to reach and deliver the occluding device, with direct visibility of the anatomy. To this aim, a cardioscope with an 8 mm diameter, clear silicone-optical-window is developed. *Ex vivo* testing on porcine models has been carried out. The capability to provide clear visualization of intracardiac structures is demonstrated.**

***Keywords*—Cardioscopy, paravalvular leak repair, clear silicone optical window.**

I. INTRODUCTION

VALVULAR heart disease is a significant health issue that accounts for 10% to 20% of all cardiac procedures in the US [1]. Much progress in catheter-based technologies and imaging techniques have been made to address this problem, avoiding the risk of cardiopulmonary bypass [2]. However, significant drawbacks remain, like the limited ability to optimally manipulate tools and tissue, and the reduced visibility during tissue contact. A relevant example is the closure of a paravalvular leak (PVL) during beating heart surgery. PVL is a complication of surgical valve replacement, which occurs in 5% to 17% of surgical implanted valves [3]. The PVLs shape, small size, and location, make their identification and repair very challenging tasks [4].

Decreasing or completely avoiding the need for fluoroscopy, together with a direct visualization of device deployment, are benefits that can make the PVL repair procedures easier. The combination of cardioscopy, which involves making contact with the tissue to displace the blood and look through a clear optical element [5], and catheter techniques, is a reasonable solution. In related research, a cardioscope enabling high-resolution imaging has been developed by Padala et al. [6]. It consists of a CCD camera embedded on the tip of a straight endoscope and covered by a convex Plexiglass tip to allow identification of structures on a beating porcine heart. A similar device, with the addition of an instrument channel, has been developed by Vasilyev et al. [7]. By pressing the plastic window against the tissue, the blood can be displaced, allowing visualization of heart structures through the clear window. The tool channel can be also used for saline flushing, which improves the visualization.

In our new design, the rigid optical window is replaced by a soft silicone bulb that can conform better to irregular tissue surfaces and enable a more compliant and soft contact. This solution has been applied on a cardioscope for heart tissue removal [8]. Within this study, we present a cardioscope with a silicone optical window to be used for PVL repair.

II. MATERIALS AND METHODS

The cardioscope (Fig. 1) consists of a 3 mm outer diameter (OD) straight metallic tube, 78 mm long, with a distal silicone optical window (8 mm OD) and an ergonomic handle. The optical-window size is chosen in order to optimize the trade-off between minimally invasive design and maximum field of view (FOV). The distal tip, on which the optical window is molded, holds a 1x1 mm CMOS camera (NanEye Camera System, Awaiba), a light source (1.6x1.6 mm LED) and a working channel (2 mm internal diameter, ID) (Fig. 2a). The working channel is positioned off center to facilitate the delivery of the vascular plug (Fig. 2b) at the targeting point. It is made of a polyimide tube all the way until the silicone tip. Then, inside the optical-window, a fully transparent channel is molded. In that way, the FOV is unobstructed by the tool, prior to its release. A valve positioned at the proximal end of the cardioscope enables insertion and removal of the tool without air or blood leaking.

The silicone tip, fabricated with a QSil 218 (Quantum Silicones LLC), has a planar-bevelled shape ($\theta = 20°$, see Fig. 2c). This geometry, along with enabling the surgeon to constantly monitor the vascular plug extension even before tissue contact, allows navigation all around the valve annulus. The silicone window is partially enclosed into the custom-designed tip, and partly in direct contact with the tissue. This feature enables a softer touch, by avoiding scratching the tissue because of the rigid mold. Furthermore, to prevent fogging and sealing issues, the silicone window is poured directly into the tip of the device, creating a seal around the embedded chip-on-tip camera and allowing optimal visualization through the silicone

Once the optical window is pressed against the heart tissue, the blood in front of the camera is displaced, thus allowing a clear view of the anatomy and providing direct visual guidance for delivering the occluder to repair the leak. Also, if PVL localization is difficult, saline solution can be injected through the working channel to improve the visibility.

A pericardial bioprosthetic valve (Carpentier-Edwards PERIMOUNT Magna, Edwards Lifesciences) was used to replace the native aortic valve, while leaving space for

regurgitant flow between valve and aortic wall. *Ex-vivo* experiments were performed in pig hearts, with aortic PVL, to evaluate the ability of the cardioscope to visualize intracardiac structures. The surgical procedure requires a transapical access into the left ventricle of the heart, as shown in Fig. 3.

III. RESULTS

Ex-vivo testing was performed on porcine hearts submerged in a water tank to evaluate PVL localization and vascular plug deployment under cardioscopic imaging. The experiments have been performed first in clear saline, and then with porcine heparinized blood to mimic the real surgical scenario.

Experiments in pig hearts filled with clear saline (Fig. 4) showed excellent visualization of all the structures and PVL location by the cardioscope, which allowed successful deployment of a vascular occluder. Fig. 5 shows the vascular plug occluding the PVL, after having removed the heart from water.

During similar experiments using hearts filled with heparinized blood, cardioscopy provided clear images of cardiac anatomy in contact with the tip, including the aortic valve (Fig. 6a). Fig. 6b shows the advancing tool inside the working channel, while Fig. 6c, 6d show the assessment carried out after successful deployment of the closure device in blood, respectively without and with the help of a bolus of saline. As expected, it took more time (around 10 min) for the operator to locate the PVL and successfully repair it in blood than in clear fluid.

IV. DISCUSSIONS AND CONCLUSION

Within this study, a cardioscope with a distal silicone optical-window has been developed and successfully tested in *ex-vivo* experiments. The main purpose is optimizing PVL closure procedures in terms of enhancing the visibility of the anatomical structures thanks to high-resolution cardioscopic images. Direct visualization of occluding device deployment is also provided. Furthermore, the amount of fluoroscopy currently required to navigate and identify the leak should decrease.

Ex-vivo tests demonstrate the ability of the cardioscope to visualize intracardiac structures and components of a prosthetic valve. Further optimization and experiments are underway for the delivery of an occluding device to repair a PVL.

Future developments will be related to the design of a steerable cardioscope tip to deal with the issue of limited dexterity of current technologies, and to the *in vivo* testing of both rigid and steerable cardioscopes, in beating heart surgery.

REFERENCES

[1] K. Maganti, V. H. Rigolin, M. E. Sarano, R. O. Bonow, "Valvular Heart Disease: Diagnosis and Management", *Mayo Clinic Proceedings*, vol. 85, n. 5, pp: 483-500, 2010.

[2] R. Zahn, U. Gerckens, E. Grube, A. Linke, H. Sievert, H. Eggebrecht, R. Hambrecht, S. Sack, K. E. Hauptmann, G. Richardt, H. R. Figulla, J. Senges, "Transcatheter aortic valve implantation: first results from a multi-centre real-world registry", *European Heart Journal,* vol. 32, n. 2, pp. 198-204, 2010.

[3] R. K. Binder, J. G. Webb, "Percutaneous mitral and aortic paravalvular leak repair: indications, current application, and future directions", *Current Cardiology Reports*, vol. 15, n. 3, 2013.

[4] P. Généreux; S. J. Head, R. Hahn, B. Daneault, S. Kodali, M. R. Williams, N. M. van Mieghem, M. C. Alu, P. W. Serruys, A. P. Kappetein, M. B. Leon, "Paravalvular leak after transcatheter aortic valve replacement", *Journal of the American College of Cardiology*, vol. 61, n. 11, pp. 1125-1136, 2013.

[5] A. Shiose, T. Takaseya, H. Fumoto, T. Horai, H. I. Kim, K. Fukamachi, T. Mihaljevic, "Cardioscopy-guided surgery: intracardiac mitral and tricuspid valve repair under direct visualization in the beating heart", *The Journal of Thoracic and Cardiovascular Surgery"*, vol. 142, n. 1, pp. 199-202, 2010.

[6] M. Padala, J. H. Yoganathan, A. Chin, V. H. Thourani, "Transapical beating heart cardioscopy technique for off-pump visualization of heart valves", *The Journal of Thoracic and Cardiovascular Surgery*, vol. 144, n. 1, pp. 231-234, 2012.

[7] N. V. Vasilyev, J. F. Martinez, F. P. Freudenthal, Y. Suematsu, G. R. Marx, P. del Nido, "Three-Dimensional echo and videocardioscopy-guided atrial septal defect closure", *The Annals of Thoracic Surgery,* vol. 82, n. 4, pp. 1322-1326, 2006.

[8] A. Ataollahi, I. Berra, N. V. Vasilyev, Z. Machaidze, P. E. Dupont, "Cardioscopic tool-delivery instrument for beating-heart surgery", *IEEE/ASME Transactions on Mechatronics,* vol. 21, n. 1, pp. 584-590, 2016.

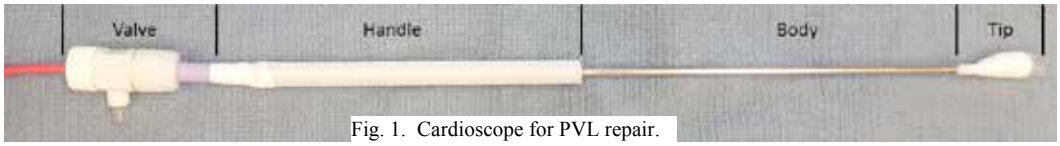

Fig. 1. Cardioscope for PVL repair.

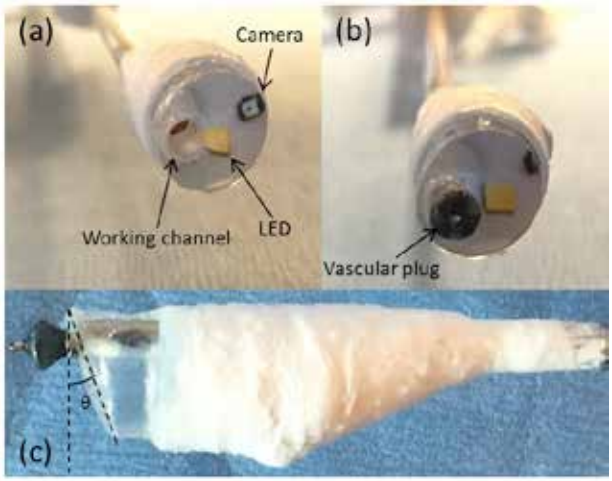

Fig. 2. Cardioscope tip. (a) Camera, LED, and working channel. (b) Vascular plug. (c) Beveled optical window.

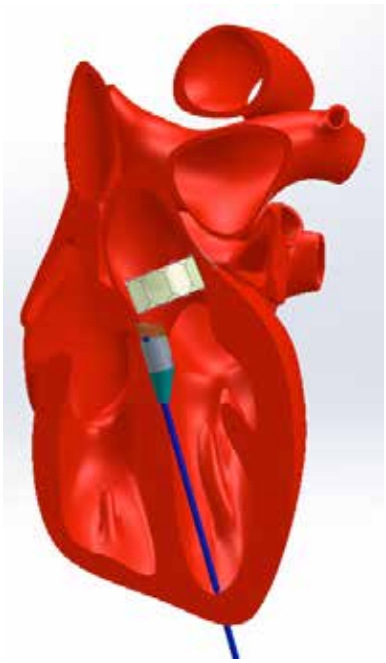

Fig. 3. Schematic of transapical access for cardioscopically-guided PVL repair.

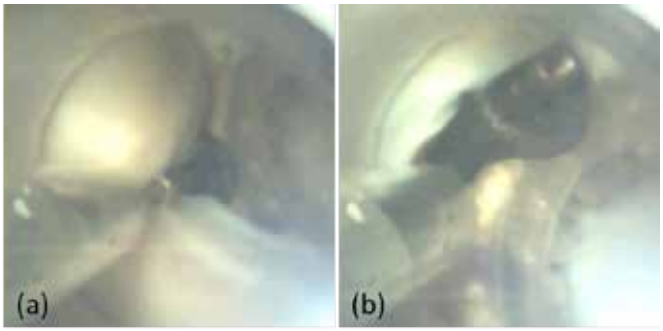

Fig. 4. Vascular plug deployment in clear saline. (a) Tool deployment. (b) Assessment of occluder position inside the defect

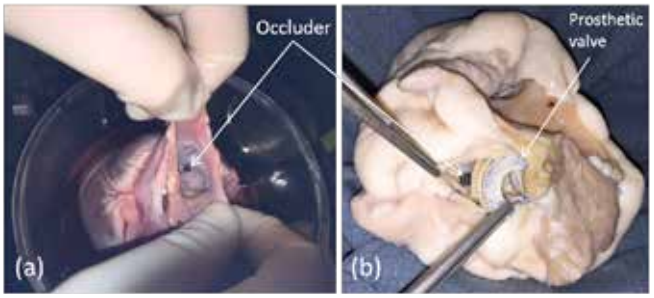

Fig. 5. Vascular plug checking from the outside.

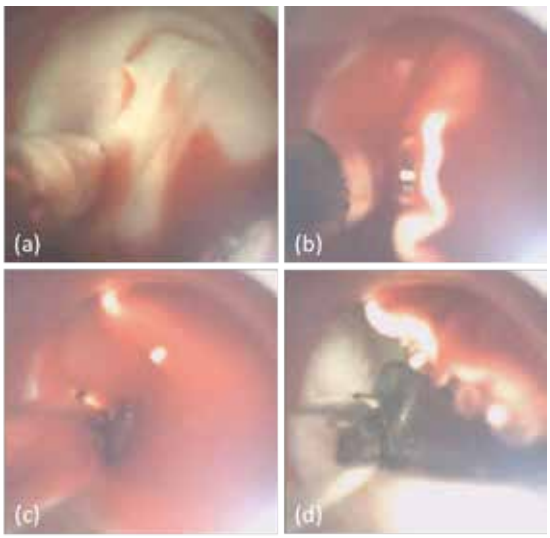

Fig. 6. Vascular plug deployment in blood. (a) Clear view of the anatomical structures. (b) Tool deployment. (c) Tool checking. (d) Tool checking with a bolus of saline.

Kinematic and muscles activity assessment of upper limb in stroke survivors during reaching tasks

M. Mugnosso*[1,2], A. Cherif*[1], L. Pellegrino*[1], P. Giannoni[1], L. Marinelli[3] and M. Casadio[1]
[1] Dept. Informatics, Bioengineering, Robotics and Systems Engineering, University of Genoa, Italy
[2] Dept. of Robotics, Brain and Cognitive Sciences (RBCS), Istituto Italiano di Tecnologia, Genoa, Italy
[3] Dept. of Neuroscience, Rehabilitation, Ophthalmology, Genetics, Maternal and Child Health of University of Genoa, Italy
*Equal contribution

***Abstract*—The goal of this study was to extract information about the strategies adopted by chronic stroke survivors compared to healthy subjects during reaching task in different environments. The experimental protocol aimed at evaluating muscles activity and kinematic parameters of both upper limbs. The experimental apparatus includes an impedance-controlled planar manipulandum, an EMG acquisition device and a force sensor. Preliminary results suggest that stroke survivors adopt different strategies to control both arms, in terms of kinematic and muscle activation patterns, with respect to the healthy controls in dynamic environments conditions.**

***Keywords*—Kinematic, EMG, stroke survivors**

I. Introduction

Stroke is one of the most prevalent causes of impairment in many countries and its incidence continues to rise [1].

Usually, motor impairments of the upper limbs cause functional limitations during activities of daily living [2]. Generally, a stroke results in motor damages mainly in the body side contralateral to the affected brain hemisphere. Often the ability to perform fine movements is replaced with the execution of stereotyped and less efficient movements, involving also the other side of the body. Although this movement reorganization may be successful in helping subjects to solve basic motor tasks, such strategies do not assure a normal movement execution. Previous studies suggest that stroke influences not only the performance of the contralesional, but also the ipsilesional side of the body with respect to the cerebral lesion [3].

This study aimed at evaluating the muscle activity and kinematic parameters of both "impaired" (I) and "less impaired" (LI) upper limbs in stroke survivors while they control their upper arm motion and/or forces under different environment conditions.

II. Material and Methods

A. Subjects

Sixteen chronic stroke survivors (SS: 10 Male (M) and 6 Female (F); 59±11 years old) and sixteen healthy subjects (HS: 10 M – 6 F; 60±11 years old) participated in the study, see Table I. The two groups are age and sex matched.

We divided the stroke survivors depending on their affected side (nine with left hemiparesis and seven with right hemiparesis). The inclusion criteria for stroke survivors were: (i) chronic stroke (>1 year after stroke event), (ii) Modified Ashworth Scale Bohannon & Smith (MAS) ≤ 3 and (iii) mini-mental state examination ≥20 (moderate/mild cognitive impairment). The research conforms to the ethical standards of the 1964 Declaration of Helsinki, which protects research subjects and was approved by the ethics committee of ASL3 Genovese. Each subject signed a consent form conforming to these guidelines.

B. Experimental set-up and protocol

Subjects were seated on a chair, in front of a computer screen and grasped the handle of a planar manipulandum [5] - characterized by low friction, low inertia, zero backslash, large elliptical workspace (80 × 40 cm) - or of a fixed force sensor (Gamma SI 13010, ATI Industrial Automation Inc.) see Fig.1 Panel A. Movements were restricted to the horizontal plane, with no influence of gravity.

The robot recorded the end-effector position and interactions forces during: (i) Reaching movements in free space (FS)- the subject's hand moved freely with no presence of any force field; (ii) Reaching movements with assistive force (AF) - a force field attracted the subject's hand towards the target (iii) Reaching movements with opposing force (SF) - a spring opposed the movement of the hand and (iv) Force trajectories in isometric conditions IF - the subject controlled the movement of a cursor applying forces in the isometric condition to a force sensor.

Subjects were required to perform reaching movements toward 8 targets (14 cm or 10 N distance from the center) randomly presented five times each (40 center-out movements in total) for each condition. The cursor position was continuously displayed during the execution of the tasks. Muscle activity was recorded with surface electrodes for electromyography (EMG) using the CometaWavePlus system. The activities of the following 16 muscles of both arms were recorded: Biceps brachii long and short head, Triceps brachii long head and lateral, Brachioradialis, Extensor carpi radialis, Flexor carpi radialis, Pronator Teres, Trapezius, Latissimus Dorsi, Rhomboid Major, Anterior-Middle-Posterior Deltoids, Infraspinatus, Pectoralis major.

C. Data analysis

Movement and force trajectories were sampled at 60 Hz and smoothed using a 6th order Savitzky–Golay filter (cut-off frequency ~11Hz), which was also used to estimate the subsequent time derivatives of the trajectory. For each movement, we computed the time elapsed between, respectively, movement onset (defined as the first time when the speed exceeded the10% of the maximum speed) and the time when speed reaches a max peak (acceleration duration) as well as the time between the peak speed and that the movement termination defined as the time of deceleration duration. We focused on the following performance indicators: Average speed, Acceleration/Deceleration duration, 300-ms aiming error **Errore. L'origine iferimento non è stata trovata.** and Jerk index **Errore. L'origine riferimento non è stata trovata.**. Repeated measures ANOVA was used to compare the

performance measures in all tasks, arms and targets' directions. Effects were considered significant when $p<0.05$. Specifically, we ran a repeated measure ANOVA with 3 between-subject factors: arm (impaired vs less impaired arm) and task (Free Space, Assistive Force and Spring Force); and one within-subject factor disease (healthy vs pathology).

EMG signals were acquired at 2 kHz, band-pass filtered (30-550 Hz), rectified, low-pass filtered (cut-off frequency of 20 Hz), and then integrated over 25 ms intervals to obtain the EMG envelope time series. The EMG signals of each muscle were normalized with the median value obtained over all tasks: this normalization is robust against high-amplitude spikes arising from noise **Errore. L'origine riferimento non è stata trovata.**. Then, for each environment condition, we evaluated the Root Mean Square (RMS) of the signal **Errore. L'origine riferimento non è stata trovata.**.

TABLE I
SUBJECT RECRUITED

	Sex	*Age (ys)*	*PH*	*E*	*DD (ys)*	*FMA (A-D) /66*	*FMA (H) /12*
P01	F	40	R	I	10	22	10
P02	F	65	L	H	16	42	7
P03	F	64	L	H	10	17	2
P04	M	62	R	H	3	14	3
P05	M	67	L	H	13	5	11
P06	F	61	R	I	7	21	12
P07	M	57	L	I	1	6	7
P08	F	40	L	I	11	9	1
P09	M	61	L	H	8	39	5
P10	F	44	R	I	12	18	12
P11	M	67	L	I	3	26	9
P12	M	68	L	H	2	40	12
P13	M	68	R	I	2	25	12
P14	M	55	R	I	2	20	5
P15	M	78	R	I	8	33	12
P17	M	48	L	I	1	19	7

* Sex=Female/Male; PH=Paretic hand: (Right/Left); E=Etiology: Ischemic/Hemorrhagic; DD=disease duration (years); FMA= Fugl-Meyer Assessment (section motor function (A-D) and sensation (H) in upper limb).

III. RESULTS

All subjects were able to perform the dynamic tasks (FS, AF and SF) with both hands. Instead 10 out of 16 subjects were not able to perform the isometric force task with the I arm and 4 out of 16 were not able to perform this task even with the LI. For this reason here the statistical analysis is limited to the dynamic tasks.

As we expected, all kinematic and EMG features of the movement of the stroke survivors differed significantly from the healthy subjects' ones. Stroke survivors generated less straight and smooth trajectories compared to the healthy subjects, not only with the I arm, but also with the LI arm. The I arm had lower average speed with respect to the LI arm ($p=0.004$); but, interestingly, their LI arm was slower than the correspondent healthy subjects' arm ($p=0.03$); see Fig.2 panel A. The duration of the deceleration phases confirmed these differences for the I and LI arms ($p<0.001$); Moreover, the phase of deceleration was longer in the LI arm respect to the correspondent healthy subjects' arm ($p<0.001$), Fig. 2 panel B. Conversely, the acceleration phase of the LI arm was equal between healthy subjects and stroke survivors; but we observed a longer acceleration phase in the I arm respect to LI arm ($p=0.02$). The 300-ms aiming error showed that stroke survivors had more problems in planning the movements with the I arm than LI arm ($p<0.001$); see Fig.2 Panel C. Movements of the I arm were less smooth than the one of the LI side ($p=0.0026$). Also for the LI arm movement smoothness was lower (higher jerk index) in stroke survivors than in healthy subjects ($p<0.001$). In the assistive force tasks the LI arm performance become more similar to the ones of healthy subjects, probably because in this task subjects were helped by the assistive force of the robot.

As for the EMG signals relative to the LI arm for left and right hemiparetic subjects, we noticed an important co-contraction of biceps and triceps, especially in the upper directions during the execution of the free space and spring force task (Fig. 3). As we expected this result is more evident in the I arm. As for forearm muscles in the I arm, they used pronator in an abnormal way to reach targets that required the extension of the elbow against resistance. The trapezius and trunk muscles (infraspinatus and rhomboid) showed a similar feature: prolonged activation and different modulation only for I arm (Fig.4).

IV. CONCLUSION

The aim of this study was to characterize the abnormalities in terms of muscle activation and kinematic behavior during reaching tasks in different environments for a population of chronic stroke survivors. As expected, stroke survivors adopted different movement strategies and muscle activation patterns in controlling the impaired arm with respect to their less impaired arm and to the matched healthy controls. Most interesting, the performance of the LI side showed significant differences from the healthy subjects' ones. Both arms had lower average speed, higher aiming error and a longer movement deceleration phase with respect to the correspondent arm of the healthy controls. The longer deceleration phase could be due to the need to correct for the greater 300-ms aiming errors in both LI and I arms. This error indicates difficulties in movement planning. In the impaired side we also observed various abnormalities in muscle activation patterns: prolonged activation, incorrect co-contractions of the biceps and triceps during arm extensions, abnormal shoulder/elbow muscle co-activation patterns.

ACKNOWLEDGEMENT

The research was supported by Marie Curie Integration Grant FP7-PEOPLE-2012-CIG-334201 (REMAKE).

REFERENCES

[1] V. L. Feigin, et al., *"Worldwide stroke incidence and early case fatality reported in 56 population-based studies: a systematic review,"* Lancet Neurol,(2009) vol. 8, pp. 355-69

[2] Nichols-Larsen et al. *"Factors influencing stroke survivors' quality of life during subacute recovery."* Stroke 36.7 (2005): 1480-1484.

[3] Schwerin et al. "Ipsilateral versus contralateral cortical motor projections to a shoulder adductor in chronic hemiparetic stroke: implications for the expression of arm synergies." *Experimental brain research* 185.3 (2008): 509-519.

[4] Wetter et al.. *"Functional implications of ipsilesional motor deficits after unilateral stroke."* Archives of physical medicine and rehabilitation 86.4 (2005): 776-781.

[5] Casadio M., Sanguineti V., et al.. *Braccio di Ferro: a new haptic workstation for neuromotor rehabilitation*. Technol Health Care (2006) 14(3): 123-142

[6] Casadio M.,et al.., *"Abnormal control, but intact force field adaptation in multiple sclerosis subjects with no clinical disability"* Multiple sclerosis 14.3 (2008): p. 330-342.

[7] Teulings, H.L. et al., Adler C.H. *"Parkinsonism reduces coordination of fingers, wrist, and arm in fine motor control."* Exp Neurol, (1997). 146(1): p.159-70.

[8] Cheung V.C., et al. *"Stability of muscle sinergie for voluntary actions after cortical stroke in humans."* Proceedings of the National Academy of Sciences, (2009) 106(46), 19563-19568.

[9] S. G. Boe,et al., *"Estimating Contraction Level Using Root Mean Square Amplitude in Control Subjects and Patients With Neuromuscular Disorders," Arch. Phys. Med. Rehabil.*(2008) vol. 89, no. 4, pp. 711–718

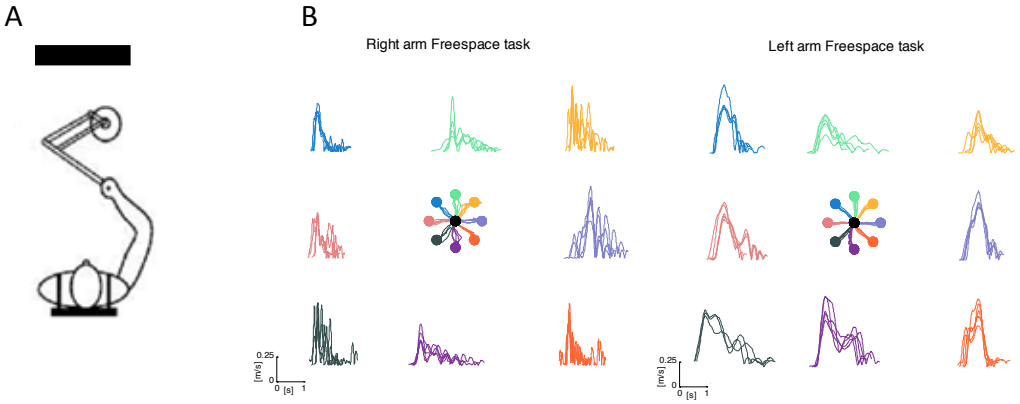

Fig. 1 Panel A: Experimental set-up; Panel B: Speed profiles and trajectories of subject P01 with right paretic arm during the Free Space Task.

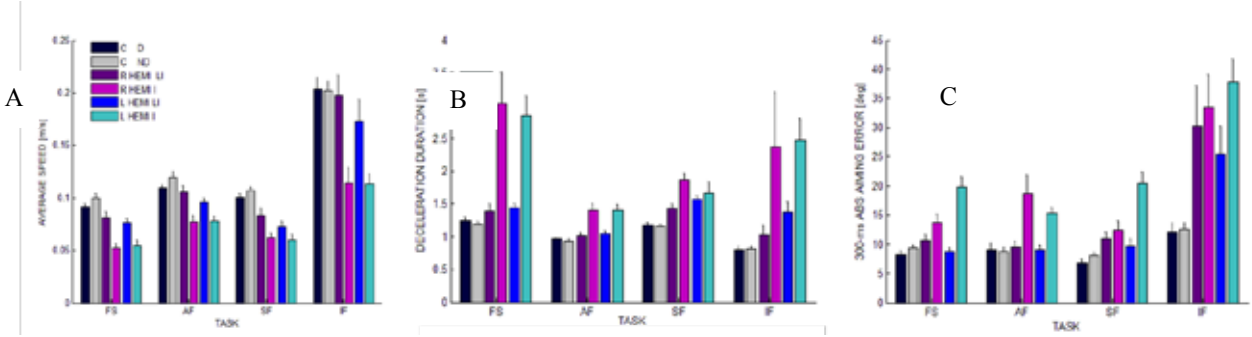

Fig. 2 Average speed (A), deceleration duration (B) and 300-ms aiming error (C) during the free space (FS), assistive force (AF), spring force (SF) and isometric force IF tasks. Control subjects (C), subjects with right hemiparetic arm (R hemi) and subjects with left hemiparetic arm (L hemi) are shown with different colors. The darker colors represent the dominant arm for C and Less Impaired (LI) arm for stroke survivors while the light colors represent the non-dominant arm for C and the Impaired arm (I) for stroke survivors. The error bars correspond to the standard deviation of the indicators.

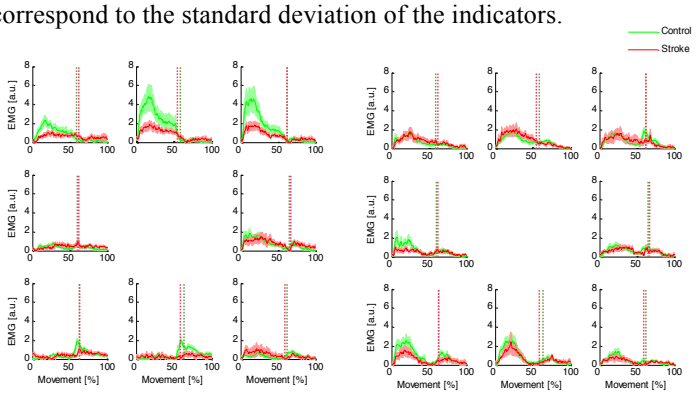

Fig. 3 Activation of the Triceps (left panel) and Biceps (right panel) head long muscle of right arm during reaching movements in eight directions in the Spring Force task. The green line represents the control subjects and the red line the stroke survivors with left hemiparesis. Dotted lines represent the beginning of backward movements.

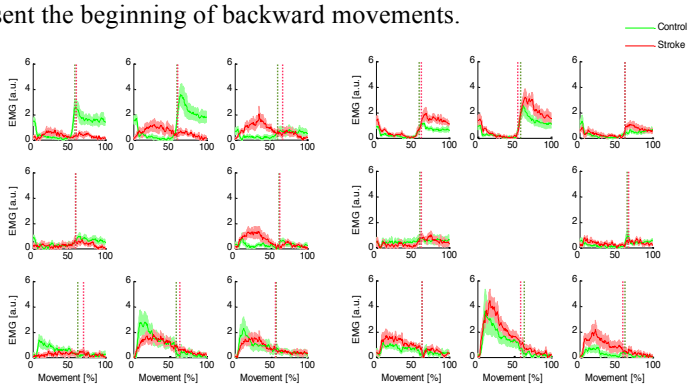

Fig 4 Activation of the Trapezius muscle during reaching movements in eight directions in the Spring Force task. The green line represents the control subjects and the red line the stroke survivors with left hemiparesis .The task was performed both with the left arm (left panel) and the right arm (right panel). Dotted lines represent the beginning of backward movements.

Relationship between Neural and Muscular Recordings during Hand Control

E. Noce[1], L. Zollo[1], A. Davalli[2], R. Sacchetti[2] and E. Guglielmelli[1]
[1] *Laboratory of Biomedical Robotics and Biomicrosystems, Università Campus Bio-Medico di Roma, IT*
[2] *INAIL centro protesi di Vigorso di Budrio (BO), IT*

***Abstract*—This paper aims to find a mathematical relationship between electromyographic (EMG) and neural (ENG) signals recorded simultaneously on one amputee subject during the ENG control of a hand prosthesis. The EMG signal was processed with standard techniques while the neural signal processing steps involved the use of a moving average algorithm to evaluate the energy of the recording and an amplitude thresholding to detect action potentials inside the recording. This allowed generating a new signal extracted for the original neural one that accounts for both amplitude and temporal allocation of the spikes. A correlation analysis with the EMG envelope is then performed by means of a purposely defined parameter *R*. The proposed approach has been applied on *little finger flexion* and *open hand* tasks. A comparative analysis with the Pearson coefficient has been carried out.**

***Keywords*—EMG signal, ENG signal, Upper-limb prosthesis.**

I. Introduction

EMG extraction is a non-invasive process and is generally well-tolerated by the patients. To date, it is the most robust and accurate way for controlling upper-limb prostheses [1]. In combination with pattern recognition techniques, it is possible to discriminate up to 11 gestures, although the classification error is still too high [2].

EMG-based prosthesis control has the main limitation of not providing the amputees with sensory feedback, paramount to enhance the performance of the amputee in grasping tasks [4].

Recently [4][5][6], through neural electrodes it is possible to return a sensory feedback by stimulating the Peripheral Nervous System (PNS) and activating the sensory fascicles within the nerves.

Neural electrodes can be used not only to stimulate but also to record neural activity. In [7], the ENG signals recorded from the PNS were used to control a hand prosthesis, thus providing one of the first feasibility study on that and implicitly showing that the EMG signals can be regarded as the expression of the ENG ones. However, to our knowledge, no study has been carried out on the relationship between EMG and ENG signals in amputee subjects controlling a hand prosthesis. Hence, this work intends to investigate such a relationship by simultaneously analysing the features of the neural recordings, such as the amplitude of the action potentials (AP) or the interspike interval (ISI), and the envelope of EMG signals.

II. Materials and Methods

A. Signal acquisition, processing and spike detection

Data were acquired during the experimentation reported in [7] where intraneural electrodes (tf-LIFE4) were implanted on the median and the ulnar nerve of male trans-radial amputee. Clinical trials wanted to assess the use of the ENG signals to control a hand prosthesis.

EMG signal was recorded by surface electrodes, sampled at 48 kHz and amplified with a gain factor of 5000. , the raw EMG was filtered with a 4th order passband Butterworth IIR filter between 50 Hz and 450 Hz [8]. The recording, then, was rectified and lowpass filtered to compute the envelope of the EMG. The filter was modeled as a 2nd order Butterworth IIR filter. The cut-off frequency was 50 Hz.

ENG signals were recorded with intraneural electrodes (tf-LIFE4 [7]) at a sampling rate of 48 kHz and amplified by a factor of 10000. The raw ENG signal was filtered with an elliptic IIR [9] passband filter between 500 Hz and 7000 Hz to retain only the useful components of the recording [10]. In Fig. 1 an ENG signal and the related EMG signal recorded during the little finger flexion task are shown. In this study the *open hand* and *little finger flexion* recordings were used.

One typical approach for ENG signal processing consists of adopting amplitude thresholds to identify the outliers of the signal [11]. The threshold is evaluated as N times the value of the standard deviation (SD) of a pure noise recording.

An efficient method to improve the performance of the detection algorithms consists in evaluating the energy of the registration by means of a moving window [12]. Energy E[i] of a neural recording can be computed as

$$E[i] = \frac{1}{W}\sum_{i-\frac{W}{2}}^{i+\frac{W}{2}}(x_i - x_M)^2 \qquad (1)$$

where x represents the neural recording, W is the width of the window and x_M is the mean of the signal within the window.

An amplitude threshold applied on the outcome signal E[i] has been used to detect the action potentials. In particular, W has been set to 120, N to 9 and the SD has been computed by means of the *Mean Absolute Deviation* (MAD) [13].

Signal processing was performed in Matlab in a Macintosh environment.

B. Relation between EMG and ENG

Muscle activity is the expression of the intention of the subject to execute a certain movement. Before producing the muscular contraction, the information is given to the fibers through the Peripheral Nervous System (PNS). To relate EMG envelope and ENG signals, once amplitudes and occurrence of the spikes in the ENG signal have been found by means of the detection algorithm, the following parameter

is computed

$$F[i] = \frac{\alpha A_{i+1} + \beta A_i}{2} \, e^{-\frac{O_{i+1}}{O_i}} \quad (2)$$

where $\alpha \leq 1$ and $\beta \leq 1$ are two weight factors and A_i and O_i are the amplitude and the time bin of the *i-th* action potentials.

In order to verify if *F* and the EMG envelope are correlated, the parameter *R* is introduced. It is expressed as

$$R(\alpha, \beta) = \frac{A^F}{A^{EMG}} \quad (3)$$

where A^F is the area under the curve identified by *F* when α and β are varied and A^{EMG} is the area under the EMG signal. For comparison purposes, also Pearson coefficient between the two curves, i.e. *F* and the EMG, has been computed.

By analogy with *R*, also the Pearson coefficient will be evaluated as a function of α and β.

III. Results and Discussion

The action potentials in the neural recording are extracted to compute parameter *F*. Since the amplitude of the neural signal is one order of magnitude lower than the EMG one, parameter F is multiplied by 2 times the mean of the electromyographic signal and then biased by the mean of the EMG signal.

The results of the parameter *R* and the Pearson coefficient are reported in Fig. 2. From the data reported, it emerges that there is not a unique solution (i.e. a unique pair (α,β)) that clearly maximizes parameter *R*. As for the Pearson coefficient, the best value of the R is ideally 1. Hence, the best pair (α,β) is searched for. In both the little finger and open hand tasks, the best results are obtained when the sum of α and β is 0.9 giving a restricted range of possibilities.

The highest correlation between the EMG envelope of the *little finger movement* and the Pearson coefficient is obtained when α and β are respectively 0.1 and 1.0. The Pearson coefficient, however, is low (i.e. 0.157). As clearly visible in Fig. 3, the EMG envelope shows its oscillating nature while the R parameter does not exhibit the same trend. This may justify the low results obtained with the Pearson coefficient. The capability of F to follow the trend of the EMG envelope is shown in Fig. 3. In it two cases are reported where F has been evaluated with different pairs (α, β). Both of them well overlap the EMG envelope, as also confirmed by parameter R equal to 0.954 (red line) and 1.048, respectively (yellow line).

R seems to be an efficient parameter to compare the EMG signals with the ENG ones. The neural signal and the myoelectric signal are simultaneous, as it can be easily seen in Fig. 1, revealing a high temporal correlation. But such a correlation can be also found from the features of the neural signal, since the neural activity drives somehow the muscle activity. Thus, the amplitude of the action potentials and the firing rate seem to be a valid tool to relate the ENG with the EMG

IV. Conclusion

In this study, a simple mathematical relationship between EMG and ENG signals has been investigated by means of a new parameter *F* computed by the amplitude and the occurrences of the action potentials and by the ratio *R* between the area under *F* and the EMG envelope.

The proposed method allows relating the envelope of the muscle activity with the amplitude and the occurrence of the spike of the neural recording with a correlation value of *1.017* and *0.995* for the *open hand* and *little finger flexion* movement, respectively. These results can be helpful in developing algorithms and systems that use ENGs as the main information. The relation can be further studied and improved to better relate the muscle and the neural activity, enhancing its robustness and usability.

Acknowledgement

This work was supported partly by the Italian Institute for Labour Accidents (INAIL) with PPR 2 project (CUP: E58C13000990001), partly by the Italian Ministry of Instruction, University and Research with PRIN HANDBOT project (CUP: B81J12002680008).

References

[1] D Farina and O Aszmnann, "Bionic limbs: clinical reality and academic promises," Science Translational Medicine, vol. 6, 2014, pp 1-4

[2] LJ Hargrove et al., "Principal compo- nents analysis preprocessing for improved Classification accuracies in pattern-recognition-based myoelectric control", IEEE Transaction on Biomedical Engineering, vol. 56, 2009, pp. 1407-1414

[3] C Cipriani et al., "On the shared control of an EMG-controlled prosthetic hand: analysis of user-prosthesis interaction", IEEE Transaction on Robotics, vol. 24, 2008, pp. 170-184

[4] S Raspopovic et al., "Restoring natural sensory feedback in real-time bidiriectional hand prostheses", Science Translational Medicine, vol. 6, 2014, pp. 1-10

[5] DW Tan et al., "A neural interface provides long-term stable natural touch perception", Science Translational Medicine, vol. 6, 2014, pp. 1-11

[6] M Ortiz-Catalan, "An osseointegrated human-machine gateaway for long-term sensory feedback and motor control of artificial limbs", Science Translational Medicine, vol. 6, 2014, pp. 1-8

[7] PM Rossini et al., "Double nerve intraneural interface on human amputee for robotic hand control", Clinical Neurophisiology, vol. 121, 2010, pp. 777-783

[8] CJ De Luca, "The use of surface electromyography in biomechanics", Journal of Applied Biomechanics, vol. 13, 1997, pp. 135-163

[9] RQ Quiroga, "What is the real shape of extracellular recordings?", Journal of Neuroscience Methods, vol. 177, 2009, pp.194-198

[10] S Micera et al., "Control of hand prostheses using peripheral information", IEEE Reviews in Biomedical Engineering, vol. 3, 2010, pp. 48-68

[11] C Pouzat et al., "Using noise signature to optimize spike-sorting and to assess neuronal classification quality", Journal of Neuroscience Methods, vol. 122, 2002, pp.43-57

[12] E Rutishauser et al., "Online detection and sorting of extracellularly recorded action potentials in human medial temporal lobe recording", Journal of Neuroscience Methods, vol. 154, 2006, pp. 204-224

[13] RQ Quiroga et al., "Unsupervised spike detection and sorting with wavelets and superparamagnetic clustering", Neural Computation, vol. 16, 2004, pp. 1661-1687

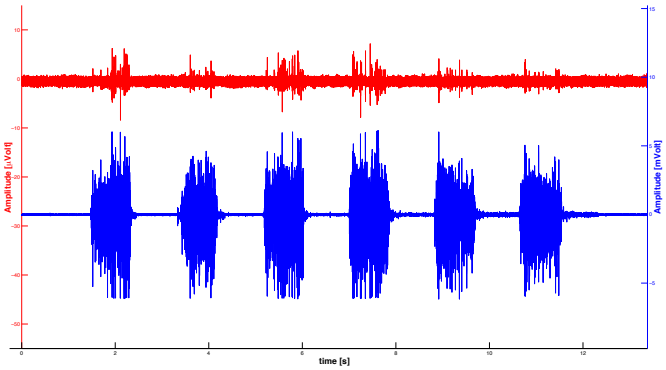

Figure 1. EMG signal (in blue) and ENG signal (in red) recorded simultaneously when the patient was asked to move the little finger of his phantom limb.

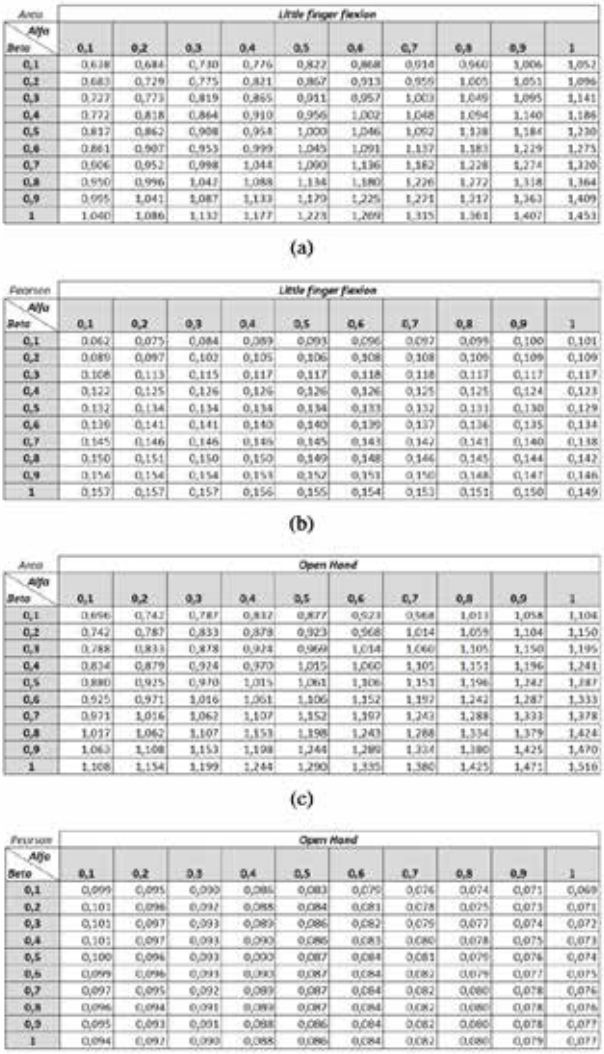

Area — Little finger flexion

Alfa / Beta	0,1	0,2	0,3	0,4	0,5	0,6	0,7	0,8	0,9	1
0,1	0,638	0,684	0,730	0,776	0,822	0,868	0,914	0,960	1,006	1,052
0,2	0,683	0,729	0,775	0,821	0,867	0,913	0,959	1,005	1,051	1,096
0,3	0,727	0,773	0,819	0,865	0,911	0,957	1,003	1,049	1,095	1,141
0,4	0,772	0,818	0,864	0,910	0,956	1,002	1,048	1,094	1,140	1,186
0,5	0,817	0,862	0,908	0,954	1,000	1,046	1,092	1,138	1,184	1,230
0,6	0,861	0,907	0,953	0,999	1,045	1,091	1,137	1,183	1,229	1,275
0,7	0,906	0,952	0,998	1,044	1,090	1,136	1,182	1,228	1,274	1,320
0,8	0,950	0,996	1,042	1,088	1,134	1,180	1,226	1,272	1,318	1,364
0,9	0,995	1,041	1,087	1,133	1,179	1,225	1,271	1,317	1,363	1,409
1	1,040	1,086	1,132	1,177	1,223	1,269	1,315	1,361	1,407	1,453

(a)

Pearson — Little finger flexion

Alfa / Beta	0,1	0,2	0,3	0,4	0,5	0,6	0,7	0,8	0,9	1
0,1	0,062	0,075	0,084	0,089	0,093	0,096	0,092	0,099	0,100	0,101
0,2	0,089	0,097	0,102	0,105	0,106	0,108	0,108	0,109	0,109	0,109
0,3	0,108	0,113	0,115	0,117	0,117	0,118	0,118	0,117	0,117	0,117
0,4	0,122	0,125	0,126	0,126	0,126	0,126	0,125	0,125	0,124	0,123
0,5	0,132	0,134	0,134	0,134	0,134	0,133	0,132	0,131	0,130	0,129
0,6	0,139	0,141	0,141	0,140	0,140	0,139	0,137	0,136	0,135	0,134
0,7	0,145	0,146	0,146	0,145	0,145	0,143	0,142	0,141	0,140	0,138
0,8	0,150	0,151	0,150	0,150	0,149	0,148	0,146	0,145	0,144	0,142
0,9	0,154	0,154	0,154	0,153	0,152	0,151	0,150	0,148	0,147	0,146
1	0,157	0,157	0,157	0,156	0,155	0,154	0,153	0,151	0,150	0,149

(b)

Area — Open Hand

Alfa / Beta	0,1	0,2	0,3	0,4	0,5	0,6	0,7	0,8	0,9	1
0,1	0,696	0,742	0,787	0,832	0,877	0,923	0,968	1,013	1,058	1,104
0,2	0,742	0,787	0,833	0,878	0,923	0,968	1,014	1,059	1,104	1,150
0,3	0,788	0,833	0,878	0,924	0,969	1,014	1,060	1,105	1,150	1,195
0,4	0,834	0,879	0,924	0,970	1,015	1,060	1,105	1,151	1,196	1,241
0,5	0,880	0,925	0,970	1,015	1,061	1,106	1,151	1,196	1,242	1,287
0,6	0,925	0,971	1,016	1,061	1,106	1,152	1,197	1,242	1,287	1,333
0,7	0,971	1,016	1,062	1,107	1,152	1,197	1,243	1,288	1,333	1,378
0,8	1,017	1,062	1,107	1,153	1,198	1,243	1,288	1,334	1,379	1,424
0,9	1,063	1,108	1,153	1,198	1,244	1,289	1,334	1,380	1,425	1,470
1	1,108	1,154	1,199	1,244	1,290	1,335	1,380	1,425	1,471	1,516

(c)

Pearson — Open Hand

Alfa / Beta	0,1	0,2	0,3	0,4	0,5	0,6	0,7	0,8	0,9	1
0,1	0,099	0,095	0,090	0,086	0,083	0,079	0,076	0,074	0,071	0,069
0,2	0,101	0,096	0,092	0,088	0,084	0,081	0,078	0,075	0,073	0,071
0,3	0,101	0,097	0,093	0,089	0,086	0,082	0,079	0,077	0,074	0,072
0,4	0,101	0,097	0,093	0,090	0,086	0,083	0,080	0,078	0,075	0,073
0,5	0,100	0,096	0,093	0,090	0,087	0,084	0,081	0,079	0,076	0,074
0,6	0,099	0,096	0,093	0,089	0,087	0,084	0,082	0,079	0,077	0,075
0,7	0,097	0,095	0,092	0,089	0,087	0,084	0,082	0,080	0,078	0,076
0,8	0,096	0,094	0,091	0,089	0,087	0,084	0,082	0,080	0,078	0,076
0,9	0,095	0,093	0,091	0,088	0,086	0,084	0,082	0,080	0,078	0,077
1	0,094	0,092	0,090	0,088	0,086	0,084	0,082	0,080	0,079	0,077

Figure 2. Results of the *R* and the Pearson coefficient for the little finger (a-b) and open hand recording (c-d).

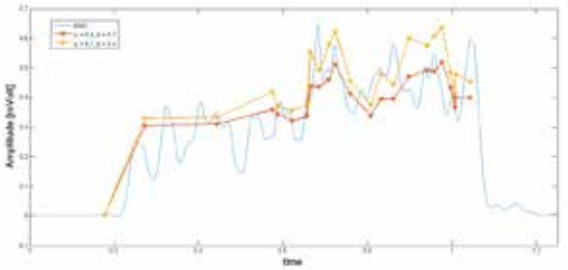

Figure 3. Effects of the parameter α and β on the parameter *F*.

A novel positioning system for surgical cannulae insertion procedure in spine surgery

I. Portaccio[1], S. Valentini[1], N. L. Tagliamonte[2], F. Russo[3], R. Papalia[3], V. Denaro[3], G. Vadalà[3] and D. Accoto[1]

[1] *Università Campus Bio-Medico di Roma, Laboratory of Biomedical Robotics and Biomicrosystems, Center of Integrated Research (CIR), Via Alvaro del Portillo, 21 - 00128 Rome,Italy.*

[2] *Fondazione Santa Lucia, Laboratory of Robotic Neurorehabilitation, Via Ardeatina, 306 - 00179 Rome, Italy.*

[3] *Università Campus Bio-Medico di Roma, Department of Orthopaedic and Trauma Surgery, Via Alvaro del Portillo, 200 - 00128 Rome, Italy.*

***Abstract*— In this work we present the design of a surgical positioning system for handling and orienting a cannula for Minimally Invasive Spine Surgery (MISS), keeping a fixed remote center of motion. The proposed system guides the percutaneous and transpedicular insertion of a cannula into the intervertebral space using a few fluoroscopic images. A dedicated software computes joint angles of the positioning system starting from a planned route, traced by the surgeon through a Graphical User Interface.**

***Keywords*—Technology for assisted surgery and diagnosis; Image and model-guided interventions; Surgical navigation and robotics**

I. Introduction

Over the past decades many robotic systems have been developed to allow effective surgical procedures and to provide assistance to surgeons. Robot-assisted MISS has the potential of improving surgical outcomes thanks to an increased accuracy in the preparation of bone surfaces, better reliability and reproducibility of results, and greater spatial precision [1]-[5]. Furthermore, the combined use of surgical navigation systems and robotic manipulators can reduce the X-ray exposure and the related biological damages.

In surgical practice fluoroscopy is widely used as a support to navigation. Fluoroscopy allows the construction of an intra-operative map following the principles of stereotactic surgery. In particular, C-arm fluoroscopes are widely used in orthopaedic procedures.

In this work we describe the design of a new Surgical Positioning System (SPS) to support spine surgeons in MISS to treat degenerative intervertebral disc diseases. This procedure entails an access to the intervertebral space through a transpedicular route and can be performed percutaneously, overcoming the disadvantages of open surgery [6]-[8].

The surgeon using a k-wire establishes an access to the intervertebral disc space by drilling the bone of the vertebra. Nowadays this action is performed manually by the surgeon and the proper positioning of the k-wire is verified by acquiring several antero-posterior and medio-lateral fluoroscopic images taken during the drilling procedure, thus exposing the patient to a high dose of radiations. Once the vertebra has been drilled up to the disc endplate, biological materials are delivered into the IVD by using a needle.

To this aim it is necessary to orient a cannula to guide the bone (vertebra) driller along a planned route, for creating the access to the intervertebral disc through the vertebral pedicle. The system that we present includes *i)* a software for the identification of the target cannula orientation, starting from a desired insertion point and a pre-planned insertion direction, and *ii)* a Mechanical Positioning Device (MPD) capable of handling the cannula and orienting it as required. Starting from two perpendicular fluoroscopic images, the software assists the surgeon in planning a safe route to reach the intervertebral space preserving neural structures.

II. Design of the Positioning System

A. SPS requirement

In order to treat the intervertebral disc degeneration a new transpedicular approach has been proposed in [6]-[8]. To support this surgical procedure, the SPS should be compatible with the space available in the operating area and with the equipment used during surgery, such as the C-arm fluoroscope, and it should be anchored to a single side of the operating table. The C-Arm fluoroscope should provide two perpendicular images to a software that support the surgeon in planning the transpedicular route. The SPS includes a MPD, which supports and orients the cannula and whose passive joints are manually locked by the surgeon into the configuration computed by the software. The complete surgical procedure is described in Fig. 1.

B. Kinematic structure of the MPD

The kinematic architecture of the MPD is depicted in Fig. 2. It includes: *i)* a linear 3-DoFs Cartesian stage, that can be anchored to the lateral bars of the operating table (prismatic joints are indicated with d_i) for the initial rough positioning of the tool before the subsequent fine orientation adjustment; *ii)* a Planar Double Parallelogram (PDP) with 1-DoF Remote Center of Motion (RCM), as further detailed in Fig. 2, that, in combination with the additional rotary joint j_1, orients the cannula around two rotation axes. The whole system, composed by the Cartesian stage and the PDP mechanism, is positioned on one side of the operating table and allows 5 DoFs overall.

C. Software for orientation reconstruction

The cannula placement is reconstructed from its projections on two orthogonal planes.

The orientation problem can be described considering the global reference frame *x-y-z* as reported in Fig 3. In particular: *i)* the *y* axis is directed towards the longitudinal axis of the patient, that is prone on the operating table*; ii)* the PDP lies on a plane perpendicular to the sagittal one; *iii)* the C-arm lies on a plane parallel to the axial one and it can be rotated around an axis parallel to the *y* one to obtain two perpendicular images that represent the projections on the frontal and sagittal planes (antero-posterior and medio-lateral views, respectively). Starting from the two fluoroscopic images (Fig. 3) the software can calculate the angles of the rotary joints of the SPS, θ_1 and θ_2 in Fig. 2, for a desired orientation of the cannula. Specifically, it can reconstruct the three orientation angles of an arbitrarily oriented segment (cannula) in the Cartesian reference frame, α, β and γ, and then the MDP configuration simply results from the intrinsic construction of the problem: $\theta_1 \equiv \beta$ and $\theta_2 \equiv \pi - \alpha$. The software has been implemented in MATLAB (Mathworks, Natick MA, USA).

With reference to Fig. 3; it is possible to identify the tip of the cannula (point P_2) and its other visible extremity (point P_1) and their projections. Hence, the reconstructed segment $\overline{P_1P_2}$ has the same spatial orientation of the cannula (see link a_6 in Fig. 2); its direction is represented by the vector $\bar{r} = [x_1 - x_2; y_1 - y_2; z_1 - z_2]$ and the inclination angles α, β and γ can be calculated through the inverse relation of the direction cosines. The orientation planning can be then divided in the following steps:

a) The surgeon identifies the tip of the cannula (red points on Fig. 4.A) on the sagittal and frontal projections through a GUI. These points must have a common *y** coordinate. If during the images acquisition the C-arm is inadvertently moved from its position in the *x-y* plane the software can perform a calibration/correction procedure for matching the *y* coordinates of the two projections. The offset calculation is done by evaluating $y_{off} = y_2 - y_1$ so that the images have the same reference frame.

b) The surgeon chooses the desired access points to the IVD space on the frontal projection, which has coordinates x_a, y_a (blue point in frontal projection of Fig. 4.B). The software draws a straight line ($y = y_a$) on the sagittal view in *y-z* plane (Fig. 4.B), along which the surgeon has to select the access point in the sagittal view (blue point in sagittal projection of Fig. 4.B).

c) The software plots on both images a line representing the transpedicular route (yellow straight lines in Fig. 4.C) so that the surgeon can visualize and analyze the planned route. If it does not meet the safety requirements for the patient (e.g. it is too close to nervous structures) the surgeon can redefine a new route.

d) When the surgeon has fixed the planned route then the software gives as output the values of the joint angles needed to adjust the configuration of the MPD (θ_1 and θ_2).

III. Discussion and Conclusion

This work presented the design a surgical positioning system for handling and orienting a cannula for MISS; a mechanical support can be regulated based on the pre-planning of the cannula insertion route through fluoroscopic images.

The insertion planning, starting from the identification of the insertion point and of the desired orientation of the cannula, is simply based on the information coming from two perpendicular images (antero-posterior and medio-lateral views) acquired though a C-arm fluoroscope. This approach minimizes the radiation dose administered to the subject since fluoroscopic images have not to be acquired through the whole insertion procedure but only at its beginning, to identify the access point, and at its end, to verify the correctness of the cannula orientation.

The presented solution provides an adjustable RCM in a compact design that does not interfere with the presence of other instruments in the surgical space. Since the insertion procedure is only based on the use of a C-arm, which is commonly available in surgical rooms, and since the SPS is designed to be connected to standard operating tables, a wide potential widespread of the system is expected.

Moreover, the simple kinematic structure directly maps one-to-one the orientation of the cannula with the rotation of the joints of the positioning system thus avoiding the need for calculating inverse kinematics to adjust the structure configuration given a desired insertion route.

The proposed SPS is potentially usable for different spine surgical procedures such as percutaneous transpedicular screw fixation in MISS. Finally, the presented system is suitable to be provided with actuated joints in order to allow a quicker positioning, thus shortening the duration of the preoperative phase. In particular, the adoption of actuators with intrinsic elasticity [9]-[10] would allow to safely cope with small vertebrae motion, e.g. caused by breathing.

Acknowledgement

This work was supported by Università Campus Bio-Medico di Roma within the project START-Disc (Smart Surgical platform for the Transpedicular delivery of Advanced Regenerative Therapies into the intervertebral DISC space), and by the Research Grant for Young Investigator of the Italian Minister of Health (GR-2010-2318448).

References

[1] R. H. Taylor and D. Stoianovici, "Medical robotics in computer-integrated surgery," IEEE Trans. Robot. Autom., vol. 19, no. 5, pp. 765–781, 2003.

[2] A. M. DiGioia, B. Jaramaz, and B. D. Colgan, "Computer assisted orthopaedic surgery: Image guided and robotic assistive technologies." Clin. Orthop. Relat. Res., vol. 354, pp. 8–16, 1998.

[3] R. A. Beasley, "Medical robots: current systems and research directions," Journal of Robotics, vol. 2012, 2012.

[4] J. Lang, S. Mannava, A. Floyd, M. Goddard, B. Smith, A. Mofidi, T. Seyler, and R. Jinnah, "Robotic systems in orthopaedic surgery," J. Bone Jt. Surg. , Br. Vol., vol. 93, no. 10, pp. 1296–1299, 2011.

[5] A. Adili, "Robot-assisted orthopedic surgery," Surg. Innov., vol. 11, no. 2, pp. 89–98, 2004.

[6] G. Vadalà, F. De Strobel, M. Bernardini, L. Denaro, D. D'Avella, and V. Denaro, "The transpedicular approach for the study of intervertebral disc regeneration strategies: in vivo characterization," Eur. Spine J., vol. 22, no. 6, pp. 972–978, 2013.

[7] G. Vadalà, F. Russo, A. Di Martino, and V. Denaro, "Intervertebral disc regeneration: from the degenerative cascade to molecular therapy and tissue engineering," J. Tissue Eng. Regener. Med., 2013.

[8] G. Vadalà, F. Russo, G. Pattappa, D. Schiuma, M. Peroglio, L. M. Benneker, S. Grad, M. Alini, and V. Denaro, "The transpedicular approach as an alternative route for intervertebral disc regeneration," Spine, vol. 38, no. 6, pp. E319–E324, 2013.

[9] N. L. Tagliamonte, F. Sergi, G. Carpino, D. Accoto, and E. Guglielmelli, "Design of a variable impedance differential actuator for

wearable robotics applications," IROS 2010, pp. 2639 – 2644, 2010.
[10] D. Accoto, G. Carpino, F. Sergi, N. L. Tagliamonte, L. Zollo, and E. Guglielmelli, "Design and characterization of a novel high-power series elastic actuator for a lower limbs robotic orthosis," Int. j. adv. robot. syst., vol. 10.

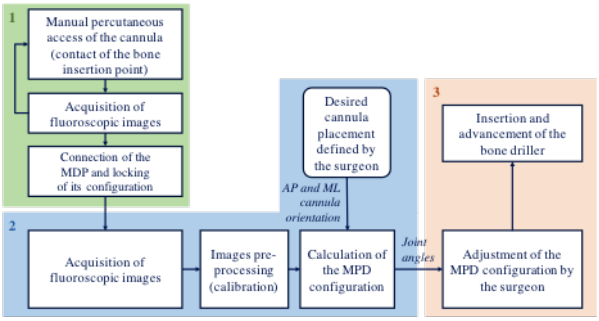

Fig. 1. Block diagram of the surgical procedure. 1: Percutaneous access of the cannula; 2: Orientation planning; 3: Adjustment of the MPD.

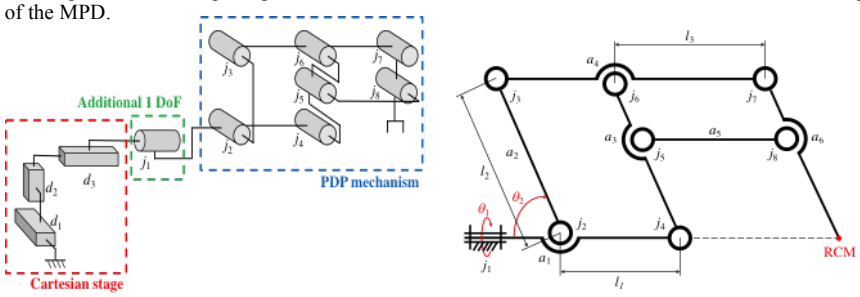

Fig. 2. Left: Kinematic structure of the proposed 5-DoFs MPD. Rotary joints j_i (i=2,…,8) implement a planar double parallelogram for the orientation of the cannula in the sagittal plane while joint j_i is added to regulate the orientation in the axial plane (see also Fig. 3). Prismatic joints d_i (i=1,…,3) are added for the initial rough position regulation of the tool before the final fine adjustment. The ground indicates the operating table on which the positioning system is connected. Right: Kinematic representation of the PDP mechanism plus the additional rotary joint j_i which are combined to orient the cannula in the sagittal plane (angle β) and in the axial plane (angle α).

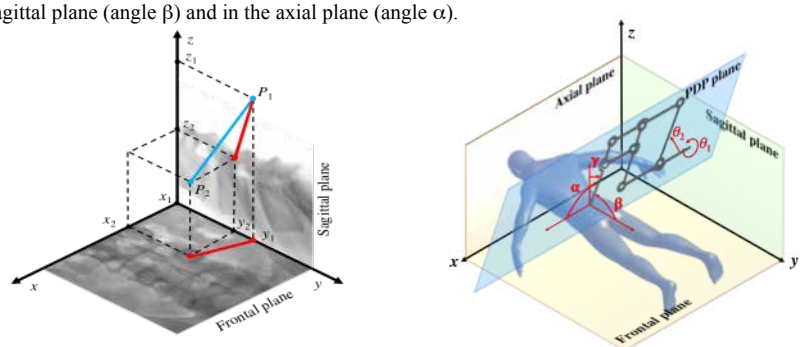

Fig. 3. Left: Schematic representation of the cannula orientation (segment $\overline{P_1P_2}$ in light blu) starting from the desired placement (red) identified by the surgeon on the antero-posterior view (frontal plane) and medio-lateral view (sagittal plane). Right: Reference anatomical planes and cannula orientation angles, α, β and γ, with respect to the global reference frame. The angles θ_1 and θ_2 represent the joint angles of the MPD.

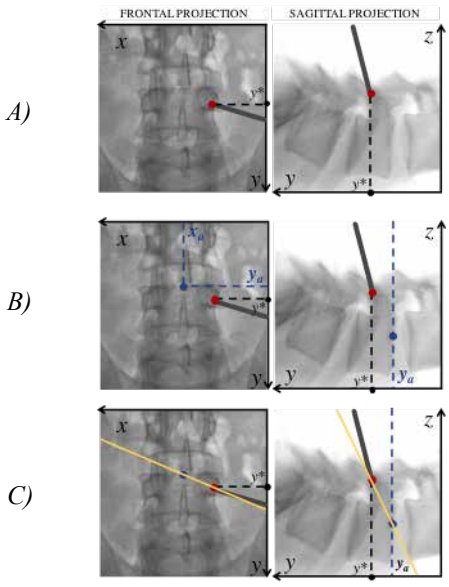

Fig. 4. Orientation planning: *A)* Identification of the current position of the cannula tip (red points). *B)* Identification of the desired final position of the cannula tip (blue point). *C)* Planned insertion direction (yellow line).

A computational framework to study physical human-human interaction

Vinil Thekkedath Chackochan and Vittorio Sanguineti
Dept. of Informatics, Bioengineering, Robotics and Systems Engineering
University of Genoa

***Abstract*—Systematic analysis of the mechanisms of physical human-human interaction (pHHI) requires adequate computational modelling framework. Recently differential game theory models - a multi-agent counterpart of optimal control - have been used to analyse sensorimotor collaborative strategies. A task can be defined by a pair of quadratic cost functionals (one per partner). The 'plant' is constituted by the two partners' body dynamics plus their mechanical links (if any). Every partner has his/her own sensory system. In analogy with single-agent dynamics, we assume that each partner maintains an internal model or state observer of own and partner's dynamics. The framework naturally incorporates the effects of noisy or incomplete sensory information about own body state. Different interaction strategies can be simulated, ranging from 'optimal' collaboration (Nash equilibrium) to no collaboration (two separate LQG controllers). We compared the model predictions with an experimental scenario in which two partners have partly conflicting goals – a reaching task with different via-points. This framework also reproduces behaviours – like 'slacking'- that are typical of the robot-human interaction in robot-assisted adaptation or rehabilitation trials.**

***Keywords*—game theory, physical human-human interaction, LQG, Nash equilibrium.**

I. Introduction

SENSORY motor interaction between two humans have important implications in many tasks of daily living. We interact with peers in most actions, it is challenging new field of research. The mechanisms of sensorimotor interaction between two humans are currently little understood and are the basis for the development of collaborative strategies that are common in everyday life. This is important in the design of robots that interact with humans. Another important clinical implication is to study motor interaction with another person in individuals with Autism Spectrum Disorder [1].

Computational models are widely used to study the dynamics of biological movements. Recently studies have focused on motor interaction between two agents that were physically connected (a dyad) and had a common goal [2]–[4]. 'Motor' versions of classical non-cooperative games like the prisoner's dilemma, rope pulling etc. [5], signalling games [6], have been used to study optimal strategies developed by dyads. These applications used a differential game theory-based modelling framework to interpret the observed behaviours.

When partners have different goals, they can negotiate a collaborative strategy if they have perfect knowledge of their respective target and their partner's intention. It is unclear how the development of collaborative strategy is affected by incomplete or unreliable information about their partners' intention and current state.

Here we outline a modelling framework based on differential game theory to study the development of collaborative strategies for some aspects of movement control between partners in a dyad.

II. Materials and Methods

A. Dynamic model

The purpose of simulations was to characterize an ideal scenario, in which both partners know everything about the plant, about their task and that of the partner, but they autonomously determine their actions. This optimal solution within this non-cooperative scenario is a so-called Nash equilibrium [7] - a situation in which each partner cannot decrease his cost by unilaterally changing his own strategy. Differential game theory predicts that in determining his/her control strategy, each agent must infer what the other partner intends to do. In other words, it must establish a model of the partner controller. To simulate dyad movements, we approximated the plant dynamics as a two-point mass connected by a spring:

$$M_i\ddot{p}_i = f_i + k(p_{-i} - p_i) - b\dot{p}_i$$

where $p_i(t)$ is the hand position vector of agent i, (with $-i$ being its partner), M_i is the arm's inertia matrix and $f_i(t)$ is the muscle-generated force vector, all expressed in the Cartesian space, for agent i, $i = 1,2$.

Realistic values for the inertia matrices were calculated from estimates of arm configuration at the center of the workspace, arm geometry and body mass for each individual subjects. Mass and moments of inertia of arm and forearm, and positions of their center of mass were taken from normative data [8]. We modelled the dynamics of muscle force generation as second order system with τ=40 ms:

$$\tau^2\ddot{f}_1 + 2\tau\dot{f}_1 + f_1 = u_1$$
$$\tau^2\ddot{f}_2 + 2\tau\dot{f}_2 + f_2 = u_2$$

Where $u_1(t)$ and $u_2(t)$ are the muscle activations. Defining the state vector as:

$$x = \begin{bmatrix} p_1 & \dot{p}_1 & p_2 & \dot{p}_2 & f_1 & \dot{f}_1 & f_2 & \dot{f}_2 \end{bmatrix}^T$$

and discretizing, the state-space equation takes the form:

$$x(t+1) = Ax(t) + B_1\left[u_1(t) + w_1(t)\right] + B_2\left[u_2(t) + w_2(t)\right]$$

where $w_1(t)$ and $w_2(t)$ denote motor command noise for each of the partners. We also assume that each partner has a sensory system:

$$y_i(t) = Cx(t) + v_i(t)$$

where $v_i(t)$ is sensory noise for partner i. As both partners have incomplete information about the state, they need to use a state observer in order to estimate plant state, so two separate state estimates are available.

The task can be defined by a pair of quadratic cost functionals $J_1[u_1,u_2]$ and $J_2[u_1,u_2]$.

B. Feedback controllers and state observers

The strategy of interaction is specified by a pair of feedback controllers (one per partner). We assume that each partner has a feedback controller of the type:

$$u_i(t) = -L_i(t)\, x(t)$$

The possible strategy outcomes can be studied in terms of two possibilities:

1) Collaborative: Game theoretic controller

Under the differential game theoretic framework, the motor control system of dyad is modelled as a dual feedback controller block schematic as shown in Fig 1. In this system the controllers of respective subjects' compute to achieve a goal given in its environment that minimise the quadratic cost incurred by the dyad plant. This requires each agent has perfect knowledge of plant and the both partners' cost functions (see Fig 2).

2) Non-collaborative: Linear Quadratic Gaussian (LQG) controller

Lack of collaboration can be modelled through two separate LQG controllers. In this case in addition to plant dynamics, each agent only needs to know his own cost function.

III. Results

A. Case study: reaching task with different via-points

To substantiate our hypothesis of tendency of collaboration with respect to subjects' uncertainty about the goals of their partner, we consider an example illustrated in Fig. 3, were two partners have partly conflicting goals in a shared motor task. Subjects were supposed to make reaching movements such that he/she has to pass a via-point and to reach the target at a pre-specified time, but location of via-points are different for each partners. While doing the task the two partners were mechanically connected through a virtual spring simulated through the robotic interface (see Fig. 3). The task was defined by the following cost functional (*i=1,2*):

$$J_i[u_1,u_2] = w_p \cdot \left\|x_T - x_i(T)\right\|^2 + w_v \cdot \left\|\dot{x}_i(T)\right\|^2 + w_{vp} \cdot \left\|x_{VP_i} - x_i(T_{VP_i})\right\|^2 + \frac{w_f}{T}\sum_{t=1}^{T}\left\|x_{-i}(t) - x_i(t)\right\|^2 + r \cdot \frac{w_u}{T} u_i(t)^2$$

The first two terms enforce stopping on target at the end of the movement. The third term reflects the requirement to pass through the via-point. The fourth term accounts for minimizing the distance between agents throughout the movement. The last term penalizes the effort incurred in the action by the corresponding subject.

B. Model predictions

We looked at the model predictions contrasting the two situations: (i) Collaborative: the two subjects establish an optimal form of cooperation (Nash equilibrium); (ii) Non-collaborative: the two subjects plan their movements by accounting for the dyad dynamics but ignoring each other, i.e. each partner treats the other as noise; see Fig 4.

IV. Discussion and Conclusions

We introduced a modelling framework to analyse human-human sensory motor collaborative strategies, where the task and interacting subjects' constraints are described by a pair of cost function. In our specific example, simulation results demonstrate that the model forms predicts that optimal collaboration between partners (Nash equilibrium) is characterized by overlapping paths, approximately same crossing times at both via points and near-zero interaction forces. In contrast, in the LQG model the overlap between paths is incomplete and each partner crosses their partner's via point with a significant delay. Also, the interaction forces suggest that partners switch between leader-follower roles during movements (Fig. 4.A).

The simulations suggest that different 'roles' during an interaction can be predicted by the interaction modality. In principle, this same framework could be used to investigate the patient-therapist or patient-robot interaction in neuromotor rehabilitation. In particular, it may explain 'slacking'- a distinctive observation in human-robot or robot-assisted rehabilitation in which voluntary control diminishes over trials when assistance keeps the errors low.

References

[1] D. A. Gonzalez, C. M. Glazebrook, B. E. Studenka, J. Lyons, and J. M. Abdullah, "Motor interactions with another person : do individuals with Autism Spectrum Disorder plan ahead ?," *Front. Integr. Neurosci.*, vol. 7, no. April, pp. 1–9, 2013.

[2] G. Ganesh, A. Takagi, R. Osu, T. Yoshioka, M. Kawato, and E. Burdet, "Two is better than one: physical interactions improve motor performance in humans.," *Sci. Rep.*, vol. 4, p. 3824, Jan. 2014.

[3] K. B. Reed and M. A. Peshkin, "Physical Collaboration of Human-Human and Human-Robot Teams," *IEEE Trans. on Haptics.,* vol. 1, no. 2, pp. 108–120, 2008.

[4] N. Jarrassé, T. Charalambous, and E. Burdet, "A Framework to Describe, Analyze and Generate Interactive Motor Behaviors," *PLoS One*, vol. 7, no. 11, 2012.

[5] D. A. Braun, P. A. Ortega, and D. M. Wolpert, "Nash equilibria in multi-agent motor interactions," *PLoS Comput. Biol.*, vol. 5, no. 8, 2009.

[6] F. Leibfried, J. Grau-Moya, and D. A. Braun, "Signaling equilibria in sensorimotor interactions.," *Cognition*, vol. 141, pp. 73–86, Aug. 2015.

[7] Tamer Başar and Geert Jan Olsder, *Dynamic Noncooperative Game Theory*, 2nd Edition. SIAM, Philadelphia, 1999.

[8] D. A. Winter, *Biomechanics and Motor Control of Human Movement*, Fourth Edi. John Wiley & Sons, Inc., 2009.

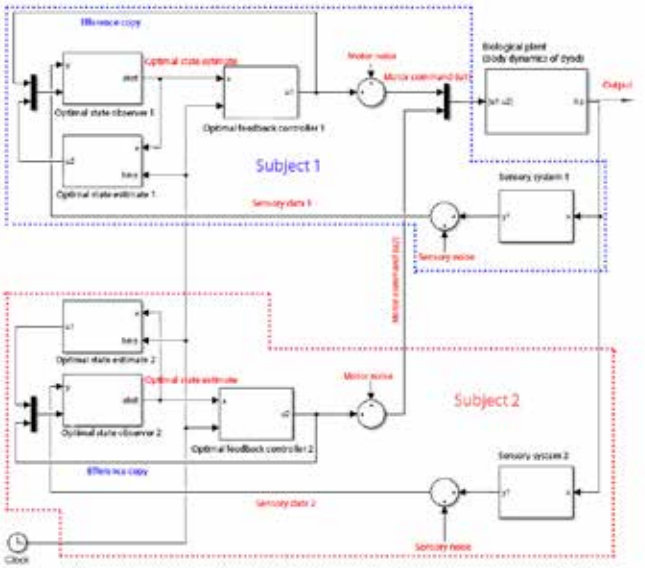

Fig 1. Feedback control system for dyad dynamics

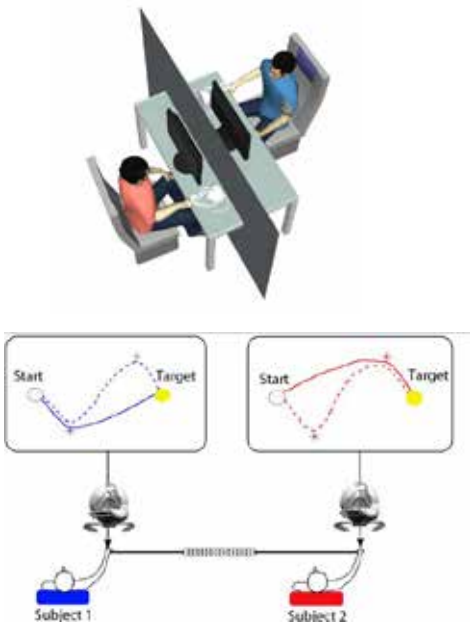

Fig 3. Dyad haptic experiment setup and task

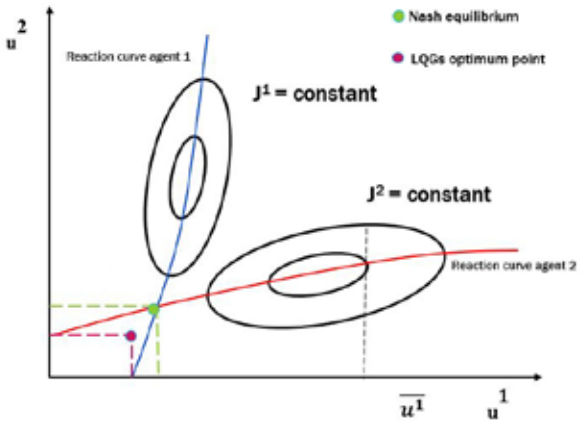

Fig 2. Nash equilibrium incurred by game theoretic controller and (green point). Equilibrium incurred by LQG controllers (violet point).

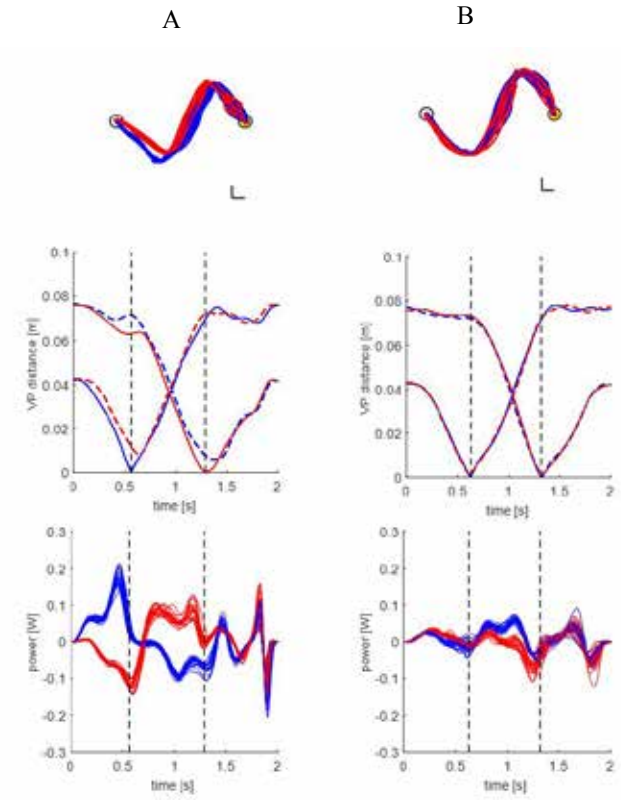

Fig 4. A, model predicted trajectories in two conditions; LQG(left), Nash(right). B, via-point crossing times vs distance

A Multi-Degree-of-Freedom Arm Exoskeleton with Compliant Actuators

E. Trigili[1], S. Crea[1], M. Cempini[1], M. Moisè[1], A. Baldoni[1], D. Marconi[1], M. Cortese[1], F. Giovacchini[1], F. Posteraro[2], N. Vitiello[1]

[1] *The BioRobotics Institute, Scuola Superiore Sant'Anna, viale Rinaldo Piaggio 34, Pontedera (PI), Italy.*

[2] *Rehabilitation Department, Versilia Hospital, USL Nord Ovest Toscana, Italy*

***Abstract*—In this paper, a novel exoskeleton for shoulder and elbow rehabilitation is presented. The robot (NESM) has four active degrees of freedom, allowing the shoulder flexion/extension, adduction/abduction and intra/extra rotation, and the elbow flexion/extension. Each of the active joints is provided with a series elastic actuation unit, which enables both position and torque control, and ensures a safe physical human-robot interface. Eight passive degrees of freedom allow the exoskeleton joints to self-align with the anatomical joint axes, in order to avoid delivering undesired loads to the articulations.**

***Keywords*—Arm Exoskeleton, Robotic Rehabilitation, Series Elastic Actuators**

I. Introduction

Robots have recently seen a notable increase in their applications in medical field, especially as wearable devices for rehabilitation and assistance, with the aim to help people suffering from motion impairments to improve their quality of life [1]. The general trend of modern clinical rehabilitation suggests the employment of a robotic device, provided with many sensors able to register a large amount of quantitative data, to allow the physician a more objective and repeatable evaluation of the patient's condition [2]. Although there is still no consensus about the effectiveness of robot-aided therapy with respect to conventional physical therapy [3], a robotic system gives the possibility to employ the long, repetitive and sometimes-strenuous rehabilitation sessions reducing the burden for the therapist, as well as the time and cost of the therapy [4]. Robotic devices for rehabilitation can be divided into three main architectures, depending on their physical human-robot interface (p-HRI): first, end-point manipulators interface with the user only at the end-effector (e.g. MIT-MANUS [5]); second, cable suspension devices actuate the attached part by means of hanging cables (e.g. DIEGO® [6]); third, powered exoskeletons consist of a series of rigid links running parallel to the human body segments, replicating their kinematic structure (e.g. NEUROExos [7], Armeo®Power by Hocoma). The advantage of exoskeletons over the first two architectures is the possibility to mobilize each joint independently, activating specific muscular groups at the same time similarly to the natural movement. Indeed, it is well known that retaining the natural muscular synergies leads to a more beneficial therapy [8]. The use of an exoskeleton implies a close physical interaction with the human user. A p-HRI must be realized to meet often-contrasting requirements, such as lightness and robustness, safety and high power transmission, comfort and tight fitting, to execute the movement in the most accurate way, without harming the user [9]. A common solution is to provide the robot with additional passive degrees of freedom (DOFs), so that the exoskeleton joint and the respective human joint axes are always aligned and no parasitic load is transferred to the articulations [10]. NESM (Fig. 1) is a powered exoskeleton for shoulder and elbow rehabilitation, designed to meet the above-mentioned requirements. The main novelty with respect to other exoskeleton devices is the employment of compliant actuation units, namely series elastic actuators (SEA), for each active joint. They are realized with a motor and a custom spring arranged in series, enabling the direct measurement of the applied torque and enhancing the safety for the user, who interfaces with a compliant, elastic element (the spring) instead of a rigid one. In the following sections, the description of the device and preliminary experimental data for the validation of the position controller are presented.

II. System description

A. Mechanical structure

The NESM kinematic chain consists of four active rotational joints enabling the shoulder abduction/adduction (sA/A), the shoulder flexion/extension (sF/E), the shoulder intra/extra rotation (sI/E), and the elbow flexion/extension (eF/E). Each actuation unit employs a brushless DC motor, a reduction stage and a custom torsional spring equipped with two absolute encoders, one at each of the two sides. The device has a modular structure with three main blocks, each bearing its own actuation units. The first, namely the *shoulder section* (Fig. 1 - green contour), comprises drivers and actuators for sA/A and sF/E. It is composed of an L-shape aluminium flange, which encompasses the user's shoulder leaving the actuators behind. Since the two units are placed next to each other, a cable and pulley mechanism is employed to allow the rotation around two perpendicular axes. In particular, two idle pulleys at the corner of the "L" route the cables from the sF/E driver carter to the s/FE actuation pulley, placed on the lateral side. Each actuation unit can supply a maximum torque of 60 N·m. The second, i.e. the *arm section* (Fig. 1 - blue contour), is dedicated to the sI/E joint. The core structure comprises two hemi-cylindrical shells rotating one around the other and both around a common axis, perpendicular to both sF/E and sA/A axes. The relative motion is achieved through an external linkage composed of two articulated parallelograms, which transmit the motion to the arm cuff by means of two capstan pulleys, rolling one to the surface of the other. Finally, the *elbow section* (Fig 1 - red contour) includes the elbow joint. The

actuator lies perpendicular to the elbow axis and the motion is achieved by means of two bevel gears with perpendicular axes. Both eF/E and sI/E actuators can deliver a torque up to 30 N·m. Moreover, the robot is provided with eight passive degrees of freedom, allowing the self-alignment with the human joint axes. Three of them are embedded within the vertical stand of the support structure, to allow shoulder elevation/depression, retraction/protraction and the rotation of the exoskeleton around a vertical axis. A bar linkage connects the exoskeleton to the human's trunk support and is endowed with four passive DOFs (a rotational one, for the robot side, and a ball joint for the user side) to leave the scapular motion free during the shoulder adduction/abduction. Finally, a slider allows the translation of the elbow axis along the forward/backward direction. In addition, five size regulation have been designed to adapt the height and orientation of the support structure, as well as the arm and forearm cuffs, to different body sizes.

B. *Control system*

The control system runs on a sbRIO-9636 (National Instrument, Austin, Texas, US) and has a hierarchical architecture. The high-level control layer runs at 100 Hz on a real-time processing unit, while the low-level control runs at 1 kHz on a field programmable gate array (FPGA). Two low-level control strategies have been implemented. The *position control* is used for the passive mobilization of the user's arm, commanding each joint to follow a predefined reference trajectory. When the user has some residual motion capabilities, the *torque control* can be used to assist the movement or to let the user completely free to move. Both the controllers rely on PID regulators, operating on the error between the reference value (i.e. joint angle or torque) and the measured variable. It is worth to notice that the torque control is possible thanks to the series elastic actuators: the two absolute encoders measure the deformation of the spring at both sides and, being the stiffness known, the resulting torque can be calculated and controlled in closed loop. Moreover, an algorithm for gravity compensation running in real-time has been implemented when the device is in torque control. The torque due to the action of the gravity in each joint is estimated in static condition, according to the joints configuration, so that the SEA units can provide the compensatory torque to cancel it. Under gravity compensation, when the device is used in transparent mode (i.e. zero torque) the output impedance can be reduced to a nearly-zero value.

III. Preliminary Experimental validation

A preliminary experimental validation has been carried out to evaluate the performance of the position controller. Two weights of 1.5 kg were attached to the arm and forearm cuffs, to simulate the average inertia of a human limb. Forty sinusoidal inputs (frequency = 0.4 Hz, amplitude = 10 deg) were commanded simultaneously as a reference position to each joint and root-mean-square error (RMSE) was calculated to evaluate the tracking capability of the controller. As shown in Fig. 2, the measured outputs present no overshoots. RMSE was 1.23 deg for sA/A, 1.06 deg for sF/E, 0.73 deg for sI/E and 0.98 deg for eF/E. Sinusoidal inputs were preferred over step inputs, since in a typical rehabilitation task the movements must be as smooth as possible, without any abrupt changes.

IV. Conclusions

In this paper, a novel shoulder-elbow exoskeleton with self-aligning mechanisms and compliant actuation units has been presented, together with a preliminary experimental evaluation of the implemented position controller. The use of SEAs allowing to implement both position and torque control strategies opens the way to different scenarios for rehabilitation. Indeed, the device can be used at different stages of the rehabilitation process, from the very beginning where passive mobilization is required, to the late phase, where the user has regained some motion capabilities and the robot can provide only a certain amount of assistance needed to achieve the movement. Finally, different biosignals such as EMG or EEG can be exploited to detect user's intention and trigger the robot movement, thus broadening the possibilities for control strategy.

Acknowledgement

This work was supported in part by the European Union within the AIDE Project H2020-ICT-22-2014 under Grant Agreement 645322.

References

[1] Poli P., Morone G, Rosati G, Masiero S. Robotic technologies and rehabilitation: new tools for stroke patients' therapy, Biomed Res Int. Volume 2013, Article ID 153872, 8 pages.

[2] Krebs, H. I., Hogan, N., Aisen, M. L., & Volpe, B. T. (1998), "Robot-aided neurorehabilitation", *Rehabilitation Engineering, IEEE Transactions on*, *6*(1), 75-87.

[3] N. Norouzi-Gheidari, P. S. Archambault, and J. Fung, “Effects of robot-assisted therapy on stroke rehabilitation in upper limbs: systematic review and meta-analysis of the literature”, *J. Rehabil. Res. Dev.*, vol. 49, no. 4, pp. 479–96, 2012.

[4] Masiero S., Poli P., Armani M., Ferlini G., Rizzello R. and Rosati G., “Robotic Upper Limb Rehabilitation after Acute Stroke by NeReBot: Evaluation of Treatment Costs,” BioMed Research International, vol. 2014, Article ID 265634, 5 pages

[5] H. I. Krebs, M. Ferraro, S. P. Buerger, M. J. Newbery, A. Makiyama et al., “Rehabilitation robotics: pilot trial of a spatial extension for MIT-Manus,” J. Neuroeng. Rehabil., vol. 1, p. 5, 2004.

[6] Tyromotion, “Modern Hand- and Arm Rehabilitation. The Tyrosolution concept,” 2007

[7] N. Vitiello, T. Lenzi, S. Roccella, S. M. M. De Rossi, E. Cattin et al., “NEUROExos: A powered elbow exoskeleton for physical rehabilitation,” IEEE Trans. Robot., vol. 29, no. 1, pp. 220–235, 2013.

[8] A. Safavynia, G. Torres-Oviedo, L. H. Ting," Muscle Synergies: Implications for Clinical Evaluation and Rehabilitation of Movement", Topics in Spinal Cord Injury Rehabilitation 2011, 17(1):16–24. doi: 10.1310/sci1701-16

[9] R. Alami, A. Albu-Schaeffer, A. Bicchi, R. Bischoff, R. Chatila et al.,‘‘Safe and dependable physical human–robot interaction in anthropic domains: State of the art and challenges,’’ in Proc. IROS’06.

[10] A. H. A. Stienen, E. E. G. Hekman, F. C. T. van der Helm, H. van der Kooij, “Self-aligning exoskeleton axes through decoupling of joint rotations and translations,” IEEE Trans. Robot., vol. 25, no. 3, pp. 628–633, 2009.

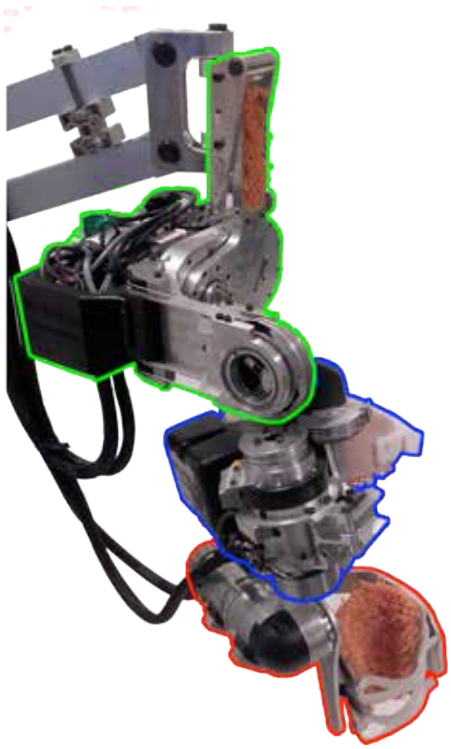

Fig. 1. Lateral view of the exoskeleton with the modular architecture: shoulder section (green contour), arm section (blue contour) and elbow section (red contour).

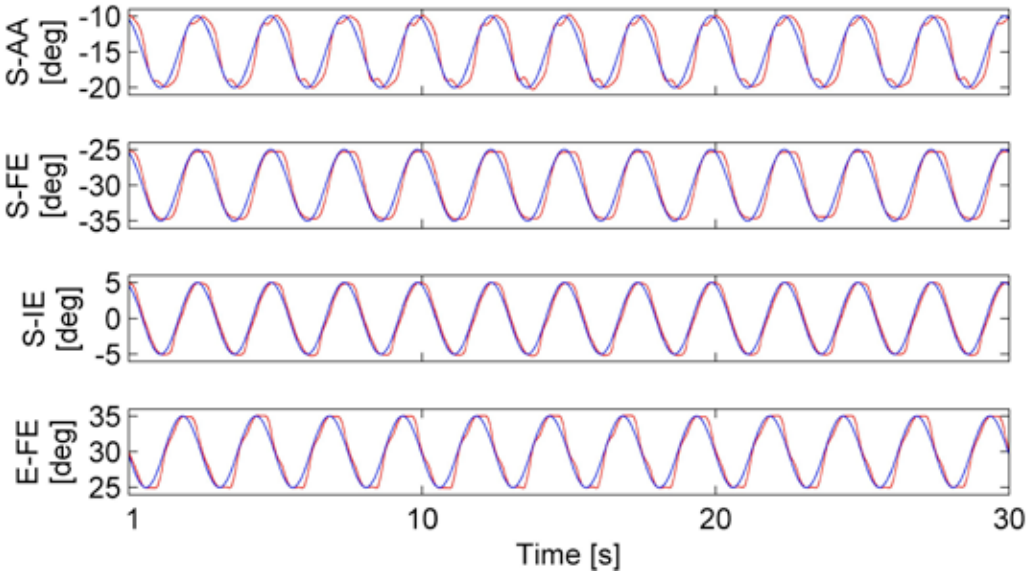

Fig. 2. Sinusoidal joint angle inputs with 10 deg of amplitude and 0.4 Hz frequency for the position control: reference trajectory (blue) and measured joint angles (red).

Visual tracking based on retinal colour-opponency implemented through spiking neural networks on a humanoid robot

L. Vannucci, A. Ambrosano, U. Albanese, M. Kirtay, E. Falotico and C. Laschi
The BioRobotics Institute, Scuola Superiore Sant'Anna

***Abstract*—The `red-green' pathway of the retina is classically recognized as one of the retinal mechanisms allowing humans to gather colour information from light, by combining information from L-cones and M-cones in an opponent way. In this paper, we simulate the red-green opponency process and we integrate this model within a visual tracking controller implemented as a spiking neural network to guide eye movements in a humanoid robot. Tests conducted in the Neurorobotics Platform confirm the effectiveness of the whole approach. This work is the first step towards a bio-inspired smooth pursuit model embedding a retina model using spiking neural networks.**

***Keywords*—retinal vision, bioinspired controllers, spiking neural networks, humanoid robotics.**

I. Introduction

ONE of the most important characteristics of the primate visual system is represented by the space-variant resolution retina with a high-resolution fovea that offers considerable advantages for a detailed analysis of visual objects. Even if in the retina three photoreceptors cell types are present, each more responsive to a different wavelength, signals from a single cone type can't carry any colour clue, but at least two types of cone must be compared in order to get actual colour information[1].

Two processes of this sort are known to happen inside the retina: the *red-green opponency*, where M-cones and L-cones responses are taken into account in order to get colour information in the red-green axis, and *yellow-blue opponency*, where all three kinds of cones are considered to get colour information in the yellow-blue axis[2].

The space-variant resolution of the retina requires efficient eye movements, such as smooth pursuit, for correct vision. The purpose of smooth pursuit eye movements is to minimize the retinal slip, i.e. the target velocity projected onto the retina, and several robotics implementation of this eye movement have been developed. While some are integrated alongside other oculomotor behaviours[3], others includes cognitive aspects such as the prediction of the target motion and are implemented with artificial neural networks[4,5], but no robotic model of visual pursuit exists that integrates retinal image processing.

In this paper we present a first attempt of embedding a retina model inside a visual pursuit controller suitable for a robotic implementation that makes use of biologically inspired Spiking Neural Networks. Thus, a proper framework that combines robotics and neural simulations has been used: the Neurorobotics Platform.

II. The Neurorobotics Platform

The Neurorobotics Platform (NRP) is developed as part of the Human Brain Project[1] to run coupled neural and robotics simulations. The NRP aims at offering a platform that combines the neuroscientific and robotic fields, therefore it includes state of the art neural and physics simulators such as NEST[6] and Gazebo[7]. The platform is capable of synchronizing the two simulations and also offers functions that translate information coming from one simulation in a suitable input for the other one (called transfer functions), thus providing full closed loop architecture. Access to the simulation interface is provided via a web frontend where an experiment can be designed from scratch, by choosing the robot model, the environment, the brain model and the transfer functions. The platform also offers live visualization tools for brain activity and robot status.

In order to simulate the retinal image processing, a computational framework for retinal simulation was integrated inside the NRP. The chosen framework was COREM[8], a general framework that includes a set of retinal microcircuits that can be used as building blocks for the modelling of different retinal functions. The simulation engine allows the user to create custom retina scripts and to easily embed the retina model in the neural simulator.

Using the NRP, we set up and experiment by placing a virtual screen in front of a simulated iCub robot[9]. The simulated robot has cameras with a resolution of 320x240 pixels. The screen showed a red background with a moving green circle that had to be pursued by the robot, as depicted in Figure 1.

III. Retina based controller

An overview of the proposed controller can be seen in Figure 2. Images coming from the robot camera are fed to the retina model, whose output are in turn translated into current values and sent as an input to a brain model. Measures on the activity of the neural network are then used to generate an appropriate motor command.

The retina model implements the red-green opponency and comprises two symmetric subcircuits. The $L^{+}M^{-}$ circuit subtracts the output of the M-cones (more sensitive to green) from the L-cones (more sensitive to red) output, then the combined cones signal is processed by all retina layers: horizontal, bipolar, amacrine and ganglion cells. Due to the

[1] https://www.humanbrainproject.eu/

opponency, ganglion cells are more sensitive to a red centre on a green background in their receptive field. The neural response is even more elicited, due to the ganglion temporal characteristics, when a green objects appears in receptive fields that were earlier impressed by red objects. The other subcircuit (L^-M^+) does the opposite, having a greater response for red appearing over green.

A horizontal stripe of the output from the retinal processing (corresponding to 320 pixel, intersecting the target) is given as an input to a brain model made of 1280 integrate and fire neurons, organized in two layers: the first one acts as current to spike converter, while each neuron in the second layer receives projections from 7 adjacent neurons from the first one, acting as a spike integrator, filtering out the background noise and thus extracting the target edges position from the retinal processed output.

By measuring the spike frequency of the second layer of neurons, information about the two edges of the target can be inferred. Therefore, the target centroid can be estimated by computing the mean between the position of the edges on the horizontal stripe represented by the two most frequently spiking neurons and a motor command suitable for moving the eye towards it can be generated and sent to the simulated robot.

IV. Results

In order to assess the performances of the proposed controller, two different kind of test were conducted.

A. Static target

In this experiment the controller has been validated by testing its response towards a statically placed target. During the experiment, data about both target perceived location and the neural network response was collected and it is reported in Figure 3, where it can be noticed that, after an initial phase where some overshoot is present, the eye remains stable on the target. Moreover, the filtering action of the second neuron layer can be observed in the spike raster plot.

B. Moving target

In this test we used the same setup of the previous experiment, but we moved the target with a horizontal sinusoidal trajectory (Figure 4).

It can be observed that the controller is able to make the eye follow the target even if with some delay due to the fact that no prediction on the target motion is present, unlike what would happen in human behaviour. The estimation is still effective even with a moving eye, which validates our choice of a retina simulator as a data source for the controller.

V. Conclusion

In this paper we propose a retinal red-green opponency based robot controller, processing image from the outside world through a retina model instead of using classic image-processing methods. We set up a framework by integrating an existing retina simulator in the NRP, implementing a custom retina circuit and a custom neural network and finally setting up an experiment in the NRP with suitable transfer functions.

Two experiments allowed us to validate the effectiveness of this setup for both detection and pursuit of a moving green target on a red background, although with the limitations of a single retina pathway and a single image stripe processed by the brain model. This work represents a first attempt towards a bio-inspired visual pursuit controller embedding a retina model and we plan on extending it in the future by processing the whole retinal output in the brain model and make use of bioinspired models of visual cortex to perform such processing. Moreover, this controller could be used on a real robotic platform by using real-time neural simulations such as the ones provided by neuromorphic hardware like SpiNNaker[10].

Acknowledgement

The research leading to these results has received funding from the European Union Seventh Framework Programme (FP7/2007-2013) under grant agreement no. 604102 (Human Brain Project). The authors would like to thank the Italian Ministry of Foreign Affairs, General Directorate for the Promotion of the "Country System", Bilateral and Multilateral Scientific and Technological Cooperation Unit, for the support through the Joint Laboratory on Biorobotics Engineering project.

References

[1] Baylor, D., Nunn, B. Schnapf, J., "Spectral sensitivity of cones of the monkey macaca fascicularis" in *The Journal of Physiology*, vol. 390, 1987, pp. 145-160.

[2] Dacey, D.M., "Primate retina: cell types, circuits and color opponency", *Progress in retinal and eye research,* vol.18(6), 1999, pp. 737–763.

[3] Shibata, T., Vijayakumar, S., Conradt, J., Schaal, S., "Biomimetic oculomotor control", *Adaptive Behavior,* vol.9(3-4), 2001, pp. 189–207.

[4] Vannucci, L., Cauli, N., Falotico, E., Bernardino, A., Laschi, C., "Adaptive visual pursuit involving eye-head coordination and prediction of the target motion", *Proceedings of the 14th IEEE-RAS International Conference on Humanoid Robots (Humanoids 2014)*, 2014, pp.541–546.

[5] Vannucci, L., Falotico, E., Di Lecce, N., Dario, P., Laschi, C., "Integrating feedback and predictive control in a bio-inspired model of visual pursuit implemented on a humanoid robot", *Biomimetic and Biohybrid Systems*, 2015, pp.256–267.

[6] Gewaltig, M.O., Diesmann, M., "*NEST (NEural Simulation Tool)*", Scholarpedia, vol. 2(4), 2007, p. 1430.

[7] Koenig, N. Howard, A., "*Design and use paradigms for gazebo, an open-source multi-robot simulator*", Proceedings of the IEEE/RSJ International Conference on Intelligent Robots and Systems (IROS 2004), 2004, pp. 2149-2154.

[8] Martínez-Cañada, P., Morillas, C., Nieves, J.L., Pino, B., Pelayo, F., "*First stage of a human visual system simulator: The retina*", Computational Color Imaging, 2015, pp. 118-127.

[9] Metta, G., Natale, L., Nori, F., Sandini, G., Vernon, D., Fadiga, L., Von Hofsten, C., Rosander, K., Lopes, M., Santos-Victor, J., "*The iCub humanoid robot: An open-systems platform for research in cognitive development*", Neural Networks, vol. 23(8), 2010, pp. 1125-1134.

[10] Painkras, E., Plana, L.A., Garside, J., Temple, S., Galluppi, F., Patterson, C., Lester, D.R., Brown, A.D., Furber, S.B., "*Spinnaker: A 1-w 18-core system-on-chip for massively-parallel neural network simulation*", Solid-State Circuits, vol. 48(8), 2013, pp. 1943-1953.

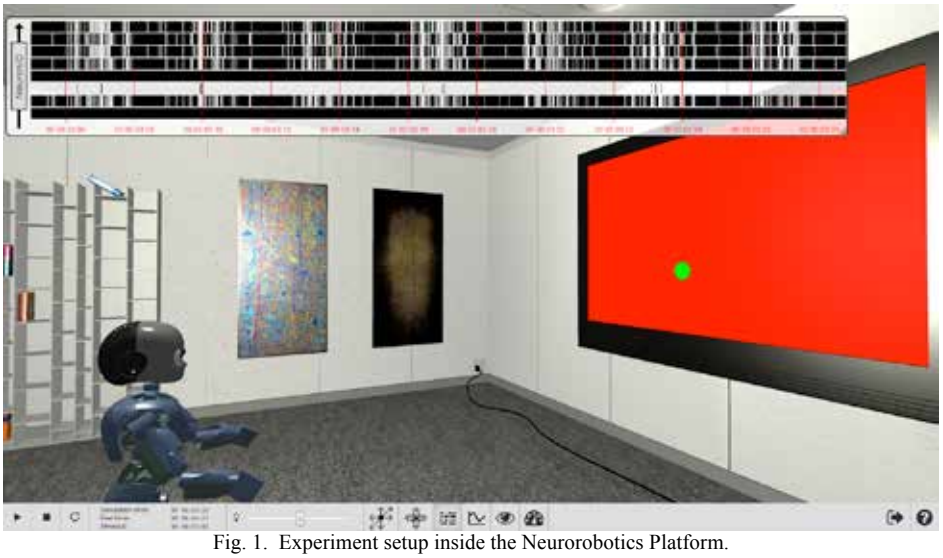

Fig. 1. Experiment setup inside the Neurorobotics Platform.

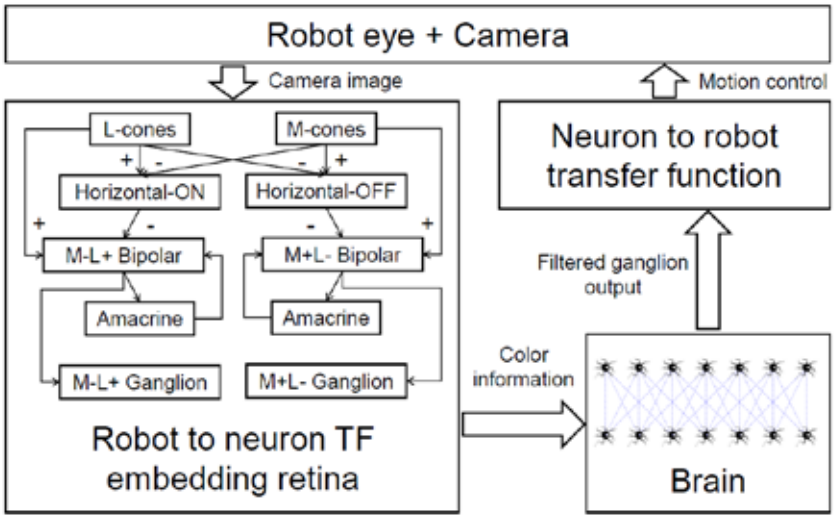

Fig. 2. Proposed visual tracking controller.

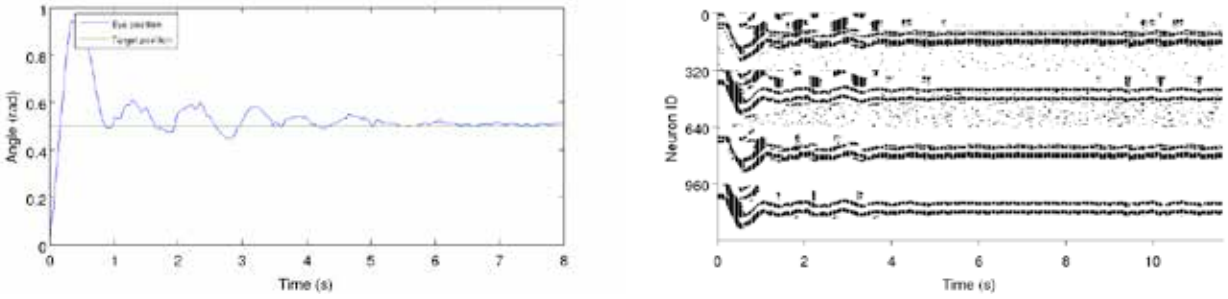

Fig. 3. Results for step response towards a static target, target and eye position on the left, brain response on the right.

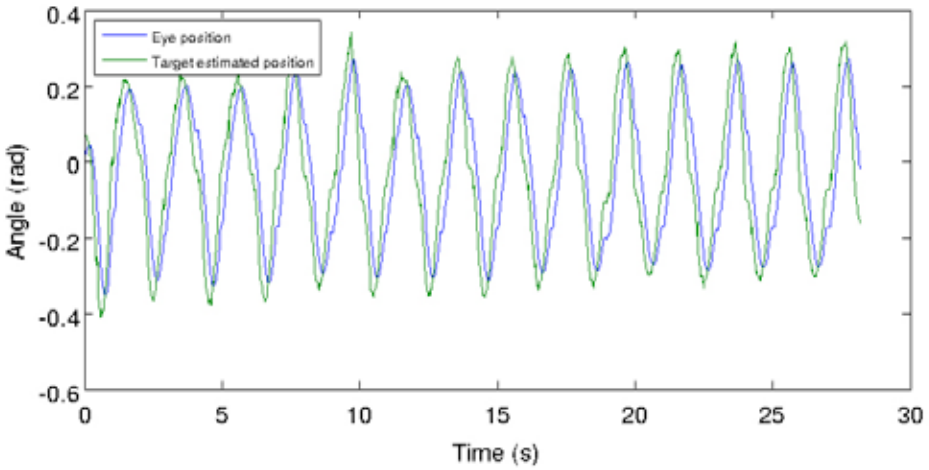

Fig. 4. Results for the tracking of a moving target with a sinusoidal motion.

Artificial Neural Network for Grasp Learning in a Synergy-based Framework

F. Ficuciello[1], D. Zaccara[1], and B. Siciliano[1]
[1] *Department of Electrical Engineering and Information Technology, University of Naples Federico II, {fanny.ficuciello, bruno.siciliano}@unina.it, damianozaccara@libero.it.*

Abstract—**In this work, a supervised learning strategy has been applied in conjunction with a control strategy to provide anthropomorphic hands of autonomous grasping capabilities. Both learning and control algorithms have been developed in a synergy-based framework in order to address issues related to high dimension of the configuration space that typically characterizes robotic hands with human-like kinematics. The experiments have been conducted on the SCHUNK 5-Finger Hand (S5FH).**

Keywords—**Supervised Learning, Postural Synergies, Artificial Hands.**

I. Introduction

The S5FH hand is an under-actuated hand provided of its own mechanical synergies. Nevertheless, the needs of specifying 9 parameters to determine the hand configuration can still makes difficult to successfully apply a learning algorithm. On the other hand, another issue holding for underactuated hands is the impossibility of independently assign the position of the five fingers in the Cartesian space. For this reason a planning strategy for grasp synthesis should disregard an accurate definition of the desired contact points on the object while guaranteeing robustness with respect to variability on shape and size. To overcome these problems, synergies concept is used to develop control and learning algorithms. The synergies subspace and the control strategy have been computed and tested in [3]. The method used for synergies computation has been developed in [4] and then adapted to the kinematics and actuation system of the S5FH. The experiments conducted in [3] demonstrate that the method provide good results since the hand can be suitably controlled in a three dimension synergies subspace. Moreover, the evaluated features of the first three synergies are very similar to those of fully actuated anthropomorphic hands. In order to autonomously grasp an object in the synergy subspace, the association of proper synergies coefficients to the geometrical characteristics of the object and to the task requirements is needed [5]. However, it is hard to derive a model that describes accurately such relationship. For this reason it is of great interest to use control strategies together with learning strategies. In this work, supervised learning based on Multiple Neural Networks (MNN) has been adopted to generalize the results obtained with a synergy-based control strategy. The main idea is to use the control strategy, developed in [3], to optimize the execution of planned grasps synthesized in the synergies subspace by projecting known hand configurations associated with known objects. The synergy coefficients corresponding to the final grasp configuration will be used to train the artificial neural network and, in turns, to generalize grasp planning of unknown objects.

II. Materials and Methods

A multilayer feedforward neural network with non linear transfer function has been adopted thanks to the ability to learn any function with a finite number of discontinuities. The use of synergies reduce the search space of the learning algorithm addressing a simplification in the neural network architecture design, especially regarding the number of hidden layers and the neurons in each of them. In order to train the neural network, a library of grasp synergies of the hand is needed. The training set is constituted by twelve spherical objects, whose diameters are included in a range between 1.5 [cm] and 9.6 [cm], eight cylindrical objects, with height between 6.8 [cm] and 25 [cm] and diameters included in a range between 1.5 [cm] and 7.5 [cm]. Since the input patterns must have the same dimension for all the objects, about the spheres a second parameter, namely the height, is introduced and obviously it is chosen equal to the diameter. Finally, a third object category of parallelepiped-shaped objects is considered. For this category a further input it is needed, i.e. the length, and it is included in a range between 8.5 [cm] and 12 [cm], while, for both cylinders and spheres, this parameter is set to zero. Furthermore, in order to identify the type of the grasp, an additional binary input has been introduced. The latter, for both cylinders and spheres, it assumes unitary value for precision grasp and zero value for power grasp. Instead, for the parallelepiped-shaped objects this input assumes unitary value for a lateral grasp and zero value for the other cases. In summary, the network receives in input four parameters: diameter, height and length of the object and the ”grasp type input”. The outputs are the three coefficients of the postural synergies. The neural network has been implemented in MatLab using the Neural Network Toolbox (NN Toolbox). The network architecture has been experimentally chosen by changing the number of neurons and hidden layers, and in turns by analyzing the corresponding NN performance in terms of Mean Squared Error (MSE). As a result of those experimental evaluations, the network model has been chosen as a feedforward NN with two hidden layer and ten sigmoid neurons for each layer. Furthermore, in order to improve the generalization, multiple neural networks have been trained and an average of their outputs has been considered for the experiments. Precisely, in this work, fifty neural networks have been trained and their mean squared errors have been compared to the means squared error of their average. The result of this comparison that reveals a striking result, i.e. the mean squared error for the averaged output is at least an order of

magnitude less if compared with all the individual performance. Therefore, the use of multiple neural networks greatly improves the network generalization. In this way, it is possible to find the synergies coefficients corresponding to the object geometric features with higher accuracy. The effectiveness of the exposed method will be demonstrated through experimental tests, whose results are presented in the following.

III. Results

The method has been tested for a total amount of 9 grasps. In order to assess the quality of the proposed planning method, those objects are chosen within the set used for synergies computation. In this way, the original configuration used for Principal Component Analysis (PCA) computation and the relative projection in the synergies subspace is known. The goal is to demonstrate that the initial configuration, planned in the synergies subspace can be improved using a learning strategy. In order to compare the initial configurations planned using PCA and learned using MNN, the control of the hand is constituted by a low-level algorithm that simply moves the hand toward the target introducing motor current thresholds to avoid fingers configurations that can cause high contact forces on the object. The comparison between the two configurations is shown in Figures (1-5), where the planned grasps obtained using PCA and learned grasps using MNN are represented on the left and on the right respectively. For saving space, not all the experiments have been reported.

IV. Conclusion

The experiments demonstrate that multiple neural networks are able to approximate with a high quality level the relationship between the synergies coefficients and the geometrical object features. Thus, MNN is a useful tool to plan grasps directly in the synergies subspace, with obvious advantage both from a computational and algorithmic point of view. Indeed, on the base of object shape and size information, the synthesized synergies coefficients produce the desired grasp distinguishing among precision, power and lateral grasps, and also the number of fingers involved.
In conclusion, the use of synergies and neural networks allows to plan and execute grasps of a wide variety of objects used in the Activities of Daily Living with a reduced number of control signals.

Acknowledgement

The research leading to these results has been partially supported by the RoDyMan project, funded by the European Communitys Seventh Framework Programme (FP7/2007 2013) under ERC AdG-320992.

References

[1] "Schunk hand webpage," http://mobile.schunk-microsite.com/en/\\produkte/produkte/servoelektrische-5-finger-greifhand-svh.html.
[2] S. Ruehl, C. Parliz, G. Heppner, A. Hermann, A. Roennau, and R. Dillman, "Experimental evaluation of the schunk 5-finger gripping hand for grasping tasks," in Proc. IEEE Int. Conf. on Robotics and Biomimetics, Bali, Indonesia, 2014, pp. 2465–2470.
[3] F. Ficuciello, A. Federico, V. Lippiello, and B. Siciliano, "Synergies evaluation of the schunk s5fh for grasping control," in 15th International Symposium on Advances in Robot Kinematics, accepted, 2016.
[4] F. Ficuciello, G. Palli, C. Melchiorri, and B. Siciliano, "A model-based Strategy for mapping human grasps to robotic hands using synergies," in IEEE/ASME International Conference on Advanced Intelligent Mechatronics (AIM), Wollongong, Australia, 2013, pp. 1737–1742.
[5] J. Vilaplana and J. Coronado, "A neural network model for coordination of hand gesture during reach to grasp," Neural Networks, vol. 19, no. 1, pp. 12–30, 2006.

Figure. 1. Power Grasp: orange.

Figure. 2. Precision Grasp: cylindrical object.

Figure. 3. Precision Grasp: strawberry.

Figure. 4. Precision Grasp: pin.

Figure. 5. Lateral Grasp: card.

CONTROLLO MOTORIO E SENSORIALE

Correlation of COP-COM sway in postural evaluation of elderly subjects

P. Colagiorgio, F. Romano, A. Buizza, and S. Ramat
Department of Electrical, Computer and Biomedical Engineering, University of Pavia, Pavia

***Abstract*— Traditionally, postural control during quiet standing is assessed analyzing the sway of the Center of Pressure (CoP), easily measured using a force platform. Today, the recent proliferation of motion capture systems makes an estimate of the CoM location easily available. CoP-based measures presented in literature provide information about age-related changes in postural stability and fall risk. We investigated, on an age-matched group of subjects, the relationship between classical CoP-based measures computed on sway path and statistical mechanics parameters on diffusion plot, with those extracted from CoM time-series. The aim of this work is to understand which of these parameters, computed on CoM sway, can discriminate postural abnormalities.**

***Keywords*—COM, COP, posturography, balance control**

I. Introduction

MEASURES of postural steadiness evaluate the postural control system in maintaining balance during quite standing, providing useful information in identifying postural abnormalities and fall risk [1]. The goal of the balance control system during quiet standing is that of maintaining the ground projection of the center of mass (CoM) of the body within the base of stability. The sway of the CoM is therefore the controlled variable of the postural control system. The control variable is instead the center of pressure (CoP), i.e. the point of application of the ground reaction-force vector, which is actively moved by the balance control system through muscular activations [2]. Despite the CoP can be easily measured using a force platform, the location of the CoM in space is the weighted average of the CoM of each body segment, and can be accurately estimated only by means of stereo-photogrammetric systems and anthropomorphic statistics. Thus several studies propose the analysis of CoP-based measures to evaluate postural control and stability [1], [3], [4]. Nowadays, the proliferation of commercial motion tracking systems makes it possible to easily access an estimate of the CoM sway in space. In this context, the Kinect device (Microsoft Corp., 2011), i.e. a low-cost 6-DoF marker-less tracking system, which has been previously validated [5], [6] and appears promising for assessing postural control in clinical settings [7], [8].

During quite standing an inverted pendulum model of the body can be assumed, thus CoP sway can be used as an indirect measure of postural sway since CoM trajectory can be estimated from CoP using a filtering approach [9] or biomechanical models [10]. Consequently, we aim to: 1) evaluate the correlation between common CoP-based parameters used in literature for the assessment of postural stability and the relative CoM-based parameters, for understanding which CoM-based parameters can better discriminate pathological subjects; 2) use a video tracking system to evaluate both balance and motor capabilities by monitoring all the exercises taken from common balance assessment scales [7].

II. Materials and Methods

A. Data Set

We observed the changes in postural steadiness related to age by recruiting 43 voluntary subjects divided in two age groups: 1) 8 young adult subjects (26±4 years), 2) 35 elderly subjects (71±5 years), recorded in the clinic "Istituto Santa Margherita" in Pavia.

B. Experimental setup

Subjects had to maintain a standing position for 45 seconds, in four distinct conditions or items, in order to evaluate the contribution of each sensory system involved in balance control. The analyzed items were: standing with eyes open (SEO), in which all sensory information are available; standing with eyes closed (Romberg Test, SEC), to test balance without the contribution of vision; standing with eyes open on foam (SEOF) and standing with eyes closed on foam (SECF), in which we used a soft foam cushion to alter proprioceptive information.

CoM and CoP sway were acquired using respectively the Kinect and the Nintendo Wii Balance Board (our custom developed software [7] allowed synchronized acquisition at 30Hz). The AP and ML time-series (for both CoM and CoP) were filtered with a 2.5 Hz, second order Butterworth low pass filter (the chosen cutoff frequency is compatible with the range of frequencies of movements). We calculated the resultant distance time-series as the Euclidean distance between each pair of points in AP and ML time-series [1]; such time series is not sensitive to the relative orientation of the coordinate systems.

C. Features Set

Two different kinds of CoP-based measures were compared: 1) five Summary Statistical Scores (SSS) computed directly on sway path [1] (Fig. 1 A,B), 2) three postural control parameters estimated by means the Stabilogram Diffusion Analysis (SDA) [3], [11] (Fig. 1 C,D). Despite several SSS CoP-based features were available [1], [12], we discard those features affected by biomechanical factors (i.e. anthropometry and foot placement) [13], and we selected the most sensitive measures to discriminate changes in postural steadiness related to age or to item type (i.e. eyes open, EO; or eyes closed, EC) [1]:

1. *RDIST*, a distance measure, i.e. the root mean square distance from the mean of the sway path;
2. *MVEL*, a velocity measure, i.e. the average velocity of the sway path;
3. *CEA*, an area measure, i.e. the 95% confidence ellipse area that encloses approximately 95% of the points on the sway path;

4. *FD*, a "hybrid" combination of distance and area measures, i.e. the fractal dimension, that is a unitless statistical index of complexity or irregularity, of the stabilogram;

5. *PWRF50*, a frequency domain measure, i.e. the median frequency of the sway path power spectrum.

As regarding the SDA, we selected the only 3 meaningful parameters of Collins et al. model [3], which allow to identify the critical point, i.e. the point of transition between the short-term (open-loop control) and long-term region (closed-loop control) and detect age-related differences in the in the "quasi-static" dynamics of the control system [11]:

6. Δt, time coordinate of the critical point;

7. $\langle \Delta r^2 \rangle$, mean square displacement of the critical point;

8. D_s, the diffusion coefficient, i.e. the slope of the diffusion plot in the short-term region, indicating the stochastic activity of the open-loop postural control mechanism.

III. Results

Pearson's Correlation Coefficient and linear regression were computed for each feature.

A. A. Summary Statistical Scores

All features estimated on CoM sway result being underestimated (Fig.2, $\beta_1<1$), in agreement with the hypothesis that the CoM sway could be seen as a filtered version of COP sway (Fig.2) [9]. Consequently, while the distance, velocity and area measures have a high correlation ($\rho>0.90$) and high significance ($p<0.001$) (Fig. 2), the frequency domain measures, as PWRF50 result less correlated ($\rho \sim 0.60$, $p<0.05$). As final remark, the "Hybrid feature" FD, being linked to the complexity, irregularity and shape of sway path, results less correlated ($\rho \sim 0.70$, $p<0.05$).

B. Stabilogram Diffusion Analysis

Parameters related to the *critical point* of the diffusion plot (i.e. Δt, $\langle \Delta r^2 \rangle$ and D_s), are highly correlated ($\rho>0.90$, $p<0.001$). In agreement with SSS results, $\langle \Delta r^2 \rangle$ and D_s parameters are strongly influenced and attenuated by the low frequency behavior of CoM (Fig. 3, $0.3< \beta_1<0.5$). Δt results also highly correlated ($\rho>0.90$, $p<0.001$) but a little delayed by the smoothness of the CoM sway.

YOUNG VS ELDERLY SUBJECTS.

SSS CoP			SSS CoM		
RDIST (mm)	***CEA (mm^2)***	***MVEL (mms^{-1})***	***RDIST (mm)***	***CEA (mm^2)***	***MVEL (mms^{-1})***
8.3 ±1.5 15.8 ±2.9°	6.5 ±1.5 26.4 ±5.2°	18.3 ±1.9 34.5 ±3.1°	6.6 ±1.4 10.7 ±2.2°	4.0 ±1.5 10.0 ±3.0 <	8.3 ±2.0 14.0 ±2.5 <
10.8 ±1.8 19.9 ±3.3 <	15.3 ±4.3 49.6 ±14 <	30.9 ±5.4 44.5 ±6.4*	7.2 ±2.2 14.9 ±4.3*	7.0 ±3.0 18.0 ±8.8*	10.8 ±1.9 17.2 ±3.5*
SDA CoP			**SDA CoP**		
$\langle \Delta r^2 \rangle$ (mm^2)	***D_S ($mm^2\ s^{-1}$)***		***$\langle \Delta r^2 \rangle$ (mm^2)***	***D_S ($mm^2\ s^{-1}$)***	
116.3 ±7.3 566.0 ±116.2°	35.7 ±9.7 242.8 ±75.4°		61.3±7.5 229.5 ±61.2°	15.0 ±5.0 89.1 ±35.3°	
297.6 ±83.0 935.5 ±440.3 <	126.1 ±44.4 385.2±110.5 <		96.8 ±24.8 393.7 ±250.4*	35.7 ±7.9 138.4 ±82.1*	

Row represents one item, respectively: SEOF, SECF;
Significance of comparison between young (top row value and elderly (bottom row value subjects:
* p< 0.05 ; < p<0.01 ; ° p< 0.001 (Wilcoxon rank sum test

C. Age Related changes

In comparing young and elderly subjects RDIST, CEA and MVEL are the most age sensitive among SSS measures both for CoP and CoM, according to correlation results. In particular, differences are emphasized in the items performed on foam (SEOF, SECF; data shown in Table I). In SDA comparisons, among the two coordinates of the critical point only $< \Delta r^2 >$ has a high discriminant power both on CoP and CoM, because aging increases sway oscillation, as also shown by both area and velocity measures. Finally, also the stochastic activity in open loop control, summarized by D_s, resulted highly informative for both CoP and CoM.

IV. Conclusion

We investigated whether traditional CoP-based parameters proposed in the literature remain powerful also when based on CoM sway analysis. We analyzed 5 SSS parameters directly computed on the sway path (area, distance velocity and frequency measures and 3 parameters resulting from diffusion plot analysis (related to the open-loop an closed-loop postural control). We found that RDIST, CEA, MVEL, Δt, $\langle \Delta r^2 \rangle$ and D_s are highly correlated and can thus be considered relevant also when computed on CoM sway. The more informative features that distinguishing between young and elderly subjects in CoP analysis (RDIST, CEA, MVEL, $\langle \Delta r^2 \rangle$, D_s) remain informative also when they are computed on the sway of the CoM. These parameters can then be used to evaluate balance with a video tracking system, in order to evaluate both static equilibrium and dynamic motor abilities with a single experimental instrument, a useful scenario in clinical settings.

References

[1] T. E. Prieto, J. B. Myklebust, R. G. Hoffmann, E. G. Lovett, and B. M. Myklebust, "Measures of postural steadiness: differences between healthy young and elderly adults.," *IEEE transactions on bio-medical engineering*, vol. 43, no. 9, pp. 956–66, Sep. 1996.

[2] D. A. Winter, A. E. Patla, F. Prince, M. Ishac, and K. Gielo-Perczak, "Stiffness control of balance in quiet standing.," *Journal of neurophysiology*, vol. 80, no. 3, pp. 1211–21, Sep. 1998.

[3] J. J. Collins and C. J. De Luca, "Open-loop and closed-loop control of posture: a random-walk analysis of center-of-pressure trajectories.," *Experimental brain research*, vol. 95, no. 2, pp. 308–18, Jan. 1993.

[4] M. Piirtola and P. Era, "Force platform measurements as predictors of falls among older people - a review.," *Gerontology*, vol. 52, no. 1, pp. 1–16, Jan. 2006.

[5] R. A. Clark, Y.-H. Pua, K. Fortin, C. Ritchie, K. E. Webster, L. Denehy, and A. L. Bryant, "Validity of the Microsoft Kinect for assessment of postural control.," *Gait & posture*, vol. 36, no. 3, pp. 372–7, Jul. 2012.

[6] A. Fern'ndez-Baena, A. Susin, and X. Lligadas, "Biomechanical Validation of Upper-Body and Lower-Body Joint Movements of Kinect Motion Capture Data for Rehabilitation Treatments," in *2012 Fourth International Conference on Intelligent Networking and Collaborative Systems*, 2012, pp. 656–661.

[7] P. Colagiorgio, F. Romano, F. Sardi, M. Moraschini, A. Sozzi, M. Bejor, G. Ricevuti, A. Buizza, and S. Ramat, "Affordable, automatic quantitative fall risk assessment based on clinical balance scales and Kinect data.," *Conference proceedings : ... Annual International Conference of the IEEE Engineering in Medicine and Biology Society. IEEE Engineering in Medicine and Biology Society. Annual Conference*, vol. 2014, pp. 3500–3, Jan. 2014.

[8] L. F. Yeung, K. C. Cheng, C. H. Fong, W. C. C. Lee, and K.-Y. Tong, "Evaluation of the Microsoft Kinect as a clinical assessment tool of body sway.," *Gait & posture*, vol. 40, no. 4, pp. 532–8, Sep. 2014.

[9] B. J. Benda, P. O. Riley, and D. E. Krebs, "Biomechanical relationship between center of gravity and center of pressure during standing," *IEEE Transactions on Rehabilitation Engineering*, vol. 2, no. 1, pp. 3–10, 1994.

[10] P. G. Morasso, G. Spada, and R. Capra, "Computing the COM from the COP in postural sway movements," *Human Movement Science*, vol. 18, no. 6, pp. 759–767, Dec. 1999.

[11] J. J. Collins, C. J. De Luca, A. Burrows, and L. A. Lipsitz, "Age-related changes in open-loop and closed-loop postural control mechanisms.," *Experimental brain research*, vol. 104, no. 3, pp. 480–92, Jan. 1995.

[12] A. Hufschmidt, J. Dichgans, K. H. Mauritz, and M. Hufschmidt, "Some methods and parameters of body sway quantification and their neurological applications.," *Archiv für Psychiatrie und Nervenkrankheiten*, vol. 228, no. 2, pp. 135–50, Jan. 1980.

[13] L. Chiari, L. Rocchi, and A. Cappello, "Stabilometric parameters are affected by anthropometry and foot placement.," *Clinical biomechanics (Bristol, Avon*, vol. 17, no. 9–10, pp. 666–77, Jan.

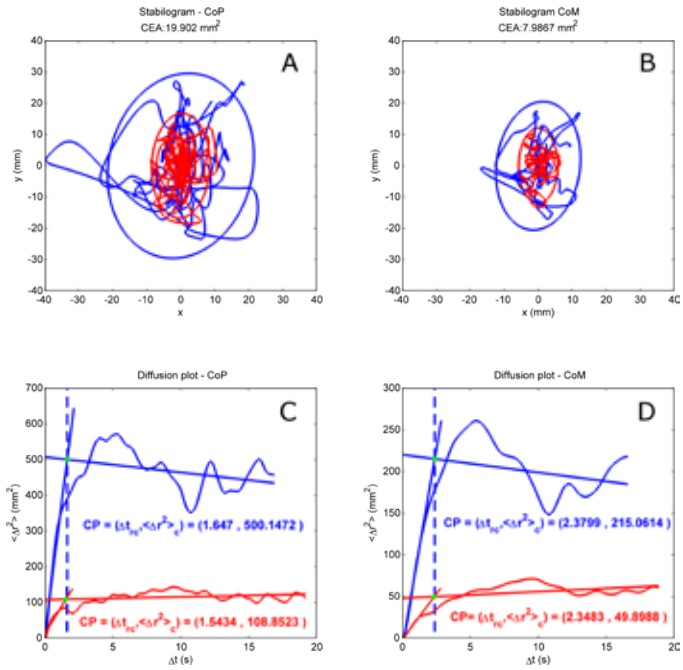

Fig. 1. A, B) Stabilogram of the SEC execution of an elderly subject (blue line) and of a young subject (red line), respectively on CoP and CoM sway. C,D) diffusion plot of the SEC exercise for an elderly subject (blue line) and of a young subject (red line), respectively on CoP and CoM sway. The green dot indicates the critical point, i.e. the intersection between the linear regression lines of short-term and long-term areas

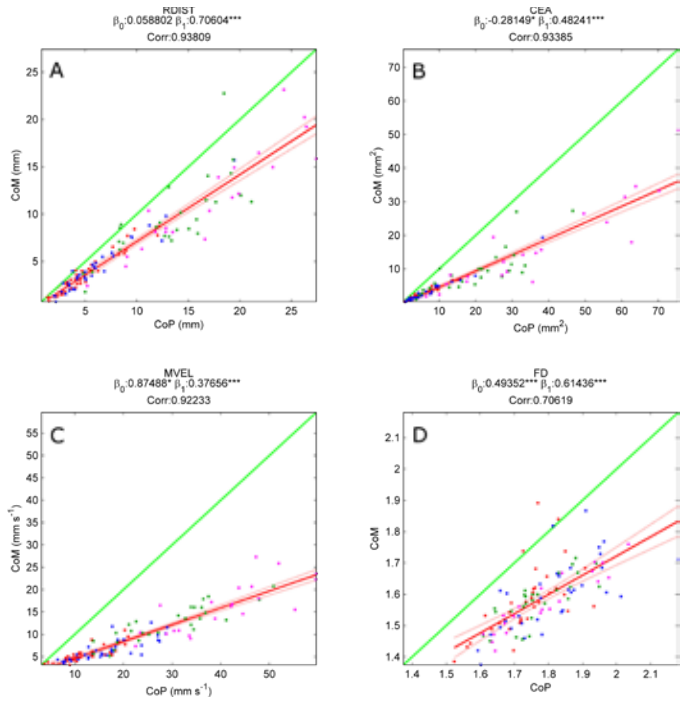

Fig. 2. CoP vs C CoP vs CoM SSS features (fCoP fCoM). All item are plotted for each subject: Red dots SEO, Blue dots SEC, Green dots SEOF and Magenta dots SECF. Green line represents the bisector line. Red solid line represents the regression line (fCoM = β0+ β1•fCoP ; βi ≠ 0 ,* p< 0.05, ** p< 0.01, *** p< 0.001), red dotted lines represent the coefficent confidence interval bounds. All Pearson's correlation coefficients, between fCoM , fCoP , reported in the figures title, are statistically significant (p < 0.01). The PWRF50 data are not presented, since show weak correlation between COM and COP values (ρ < 0.4).

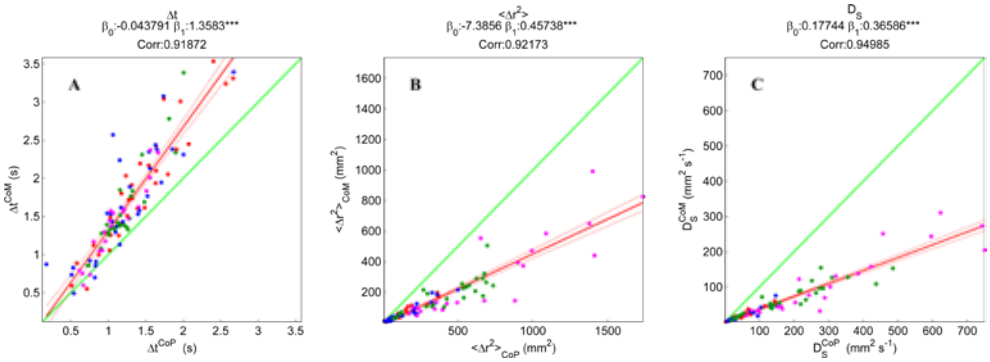

Fig. 3. CoP vs CoM SDA features normalized between [0,1] (f_{CoP} f_{CoM}). All items are plotted for each subject: Red dots SEO, Blue dots SEC, Green dots SEOF and Magenta dots SECF. Green line represents the bisector line. Red solid line represents the regression line ($f_{CoM} = \beta_0 + \beta 1 \cdot f_{CoP}$; $\beta_i \neq 0$,* p<0.05, ** p<0.01, *** p<0.001), red dotted lines represent the coefficent confidence interval bounds. All Pearson's correlation coefficients, between f_{CoM} , f_{CoP} , reported in the figures titles, are statistically significant (p < 0.01).

Visuomotor Behaviour in 3D Visual Exploration: Dominant and Non-Dominant Eye

A. Gibaldi, A. Canessa, and S.P. Sabatini
DIBRIS – University of Genova

***Abstract*—Saccades are fast ballistic eye movements that redirect the fovea of the eyes onto the object of interest. When exploring the three-dimensional environment, different amplitudes are necessary to make the eyes land on the target at the same time, thus requiring an effective processing of the visual information from both eyes.**

We asked 30 human observers, with normal or corrected-to-normal vision and normal stereopsis, to perform a visual exploration of natural images, while binocularly recording their eye movements. Three stimulations where used: 2D image of a natural scene, and 3D image of the same scene, presented dichoptically, either with its actual texture, or with pink noise texture preserving the disparity of the scene. Kinematic performances with significant differences were measured between the two eyes, depending on the visual information presented. Whereas the dominant eye is almost unaffected by the presence of depth information, the non-dominant one shows a decreased peak velocity, particularly on pink-noise images, where object texture is removed.

Our results suggest how this asymmetry in the saccadic motor control can be interpreted as a significant role of monocular visual processing in the neural mechanism underlying the generation of the binocular coordination of saccadic movement.

***Keywords*—Eye Movements, Binocular Saccade, Binocular Coordination.**

I. Introduction

WHEN an attracting stimulus is detected within the visual field, the visual system performs a saccadic movement to redirect the foveae of the eyes onto the object of interest. The neural circuits associated to saccade generation thus transform the visual position of the target on the two retinas into an open-loop motor command [10]. The obtained movement is synchronous and coordinated for both eyes, and allows us to binocularly foveate the target [11,13]. Besides conjugate saccades, by which both eyes rotate together in the same direction, during disjunctive saccades the point of fixation changes in both depth and direction, due to different retinal location on the two eyes of the object of interest. How the brain transform the visual signal into a motor command, considering that they have such different representations and that the visual information from the two eyes should be integrated into a single representation, is still a matter of research (see [12,13] as review).

In this work we aim to investigate the possible role of texture and disparity information on the generation of the binocular coordination of the saccade. To this purpose, we used three different kinds of images, one containing texture information only, one combining texture and disparity information, and one where the normal texture is replaced with a pink noise texture, thus contains disparity information, only. Considering the tight relationship evidenced between the peak velocity and the amplitude of saccadic eye movements [10,11], we used these variables, together with duration, to describe the kinematic characteristics of saccades.

The results evidence a significantly different effect of disparity information between the saccadic movement of the dominant and the non-dominant eye.

II. Materials and Methods

A. 3D Virtual Environments

In the recent years, the novel technologies for 3D range laser scanner allowed for the implementation of realistic experimental setups for a quantitative characterization of binocular vision in a direct relation with the three-dimensional environment [1,2,3,4,5]. We used a 3D laser scanner (Konica Minolta Vivid 910) to create 3D virtual models of peripersonal space. Two naturalistic virtual scenes were used, both bounded inside the peripersonal space (within distances of ~2m): an office desk (top) and a kitchen table. We obtained a full VRML model of more than 13,000,000 of points. Off-line registrations of data guarantee an accuracy of about 0.1 mm (Fig. 1, left).

B. Virtual Reality Simulator

Once obtained the VRML models of our 3D environment, we used a Virtual Reality (VR) simulator to render realistic stereoscopic images that project on the retinas of a human observer in front of the scene. Differently from the commonly used approach, which considers parallel optical axes [2,3,4,5], we took into account the natural viewing posture of the human visual system, *i.e.* with the eyes verging on a point in space. To this purpose, we specifically used a recently developed virtual simulator [6] that allows pointing each camera at a single focal point (the fixation point) through a proper rotation. Together with the stereoscopic image (Fig. 2, middle), the simulator computes also the ground truth disparity map.

C. Visual Stimuli

For each of the two virtual models, we considered 10 different vantage points for the virtual head. For each head position, the binocular line of sight is chosen to ensure the gaze to be always directed to the peripersonal workspace. For each vantage point, we obtained three different visual stimuli: 1) the 2D image acquired by a "cyclopean" camera placed between the two eyes, 2) the 3D stereoscopic image acquired by the cameras corresponding to the left and right eyes, and 3) a 3D stereoscopic image where normal texture has been substituted with a pink-noise texture with coherent disparity information.

D. Experimental Setup

The stereo pairs were displayed on a 42-inch (930x523mm) LG 42LW450A stereoscopic LCD screen. The screen had a resolution of 1920x1200 pixels, with a refresh rate of 100 Hz. Stereoscopy was obtained with a pair of passive circularly polarized glasses (RealD 3D technology). The subjects were placed at a fixed distance of 1150 mm from the screen, with the head stabilized with a chin rest (see Fig. 1, left). SMI RED 250 mobile eye-tracker was used to record the eye movements. The accuracy of the eye-tracker declared by the manufacturer is 0.4 degree.

E. Experimental Procedure

Thirty subjects were included in the experiment, 22 males and 8 females (age between 18 to 52 years old, mean 26.5 years old). The human subjects' protocol was approved by the Ethics Committee of San Martino Hospital of Genova, Italy. All the participants signed an informed consent document before starting the experiment. The subjects, all with normal vision and normal stereoacuity, were unaware of the goal of the experiment, and were instructed to freely explore the scenes. The Miles test was used to determine the eye dominance [7]. Subjects were selected in order to have half of them with right dominant eye, and half with left dominant eye. In order to mitigate possible error due to fixation disparity [8], the calibration procedure provided by the manufacturer was modified, calibrating each eye separately, so to increase the accuracy of the device in binocular tasks [9]. Each subject was shown 60 images, 20 for each of the visual stimulations considered. Each image pair was presented dichoptically for 18.5 seconds on the screen, while recording the binocular eye movements with the eye tracker. Each stereo pair was preceded by a white cross on a gray background, presented for 1.5 sec.

F. Data Analysis

For each image pair, the kinematic characteristics of the scan paths were computed separately for the left and the right eyes (see Fig. 2, top). For each of the identified saccadic movement, we measured the saccade initiation, duration, amplitude, and peak velocity. The performance of each saccade was thus computed as the ratio between its amplitude and peak velocity [10,11]. A one-sample *t*-test was used to compare the kinematic characteristics measured for the same eye on different types of visual stimulations, and for the left and right eyes on the same stimulation.

III. Results

The obtained results evidence how, on most of the subjects involved, a different effect of the visual information is present in the generation of the visuomotor behaviour in the dominant and the non-dominant eye. With the first set of stimuli, the 2D image projects almost symmetrically on the two retinae, and the two eyes have similar kinematic characteristics (see Fig. 3, top). When binocular disparity information is introduced, the dominant eye control likely maintains its characteristics, while the performance of the non-dominant one is slightly but significantly (p<10e-3) reduced, particularly when normal texture is removed (see Fig. 3, middle and bottom).

IV. Conclusion

Our results suggest a direct relation between the *monocular* visual performance, and the resulting *binocular* motor control for saccade movements. In fact, a significant motor asymmetry has been measured between the dominant and the non-dominant eye, depending on the depth information present in the visual scene. It is worth considering that, in pathological conditions like amblyopia, the visual dysfunction of the lazy eye also results in a degraded motor performance, compared to the fellow eye [14]. From this perspective, physiological interocular difference occurring in the healthy visual system is likely to provide a qualitatively similar effect to amblyopia. This suggests how the generation of the saccade, binocular and coordinated, likely relies on monocular processing of the visual information.

References

[1] Liu, A. Bovik, L. Cormack, "Disparity statistics in natural scenes", *Journal of Vision* 8 (2008) 19.

[2] L. Jansen, S. Onat, P. Konig, "Influence of disparity on fixation and saccades in 1063 free viewing of natural scenes", *Journal of Vision* (2009) 29.

[3] Gautier, O. Le Meur, "A time-dependent saliency model combining center and depth biases for 2d and 3d viewing conditions", *Cognitive Computation* 4 (2012) 141–156.

[4] Lang, T.V. Nguyen, H. Katti, K. Yadati,M. Kankanhalli, S. Yan, "Depth matters: Influence of depth cues on visual saliency", in: *Computer Vision–ECCV 2012*, Springer, 2012, pp. 101–115.

[5] Wang, M.P. DaSilva, P. LeCallet, V. Ricordel, "Computational model of stereoscopic 3D visual saliency", *Image Processing, IEEE Transactions on* 22 (2013) 2151–2165.

[6] M. Chessa, F. Solari, S. Sabatini, "Virtual reality to simulate visual tasks for robotic systems", in: J.J.K. Ed., *Virtual Reality*, 2010, pp. 71–92.

[7] Roth HL, Lora AN, Heilman KM (2002). "Effects of monocular viewing and eye dominance on spatial attention". Brain 125 (Pt 9): 2023–35.

[8] E.D. Cornell, H.G.Macdougall, J. Predebon, I.S. Curthoys, et al., "Errors of binocular fixation are common in normal subjects during natural conditions", *Optometry & Vision Science* 80 (2003) 764–771.

[9] Gibaldi, A. Maiello, G.,Vanegas, M. and Bex, P.J. "Evaluation of the Tobii EyeX Eye Tracking Controller and Matlab Toolkit for Research",*Behavior Research Methods* in press.

[10] Westheimer, G. "Mechanism of saccadic eye movements". *Archives of Ophthalmology* 52, (1954)7 10-724.

[11] Collewijn, H., Erkelens, C.J. and Steinman, R.M.. "Binocular co-ordination of human horizontal saccadic eye movements." *The Journal of Physiology* 404 (1988): 157.

[12] Meeter, M., Van der Stigchel, S. and Theeuwes, J. "A competitive integration model of exogenous and endogenous eye movements." Biological cybernetics 102.4 (2010): 271-291.

[13] Kirkby, J. A., Webster, L. A., Blythe, H. I., & Liversedge, S. P. "Binocular coordination during reading and non-reading tasks." *Psychological Bulletin*, 134 (2008), 742.

[14] Niechwiej-Szwedo, E., Goltz, H. C., Chandrakumar, M., Hirji, Z. A., & Wong, A. M.. Effects of anisometropic amblyopia on visuomotor behavior, I: saccadic eye movements. Investigative ophthalmology & visual science, 51 (2010), 6348-6354.

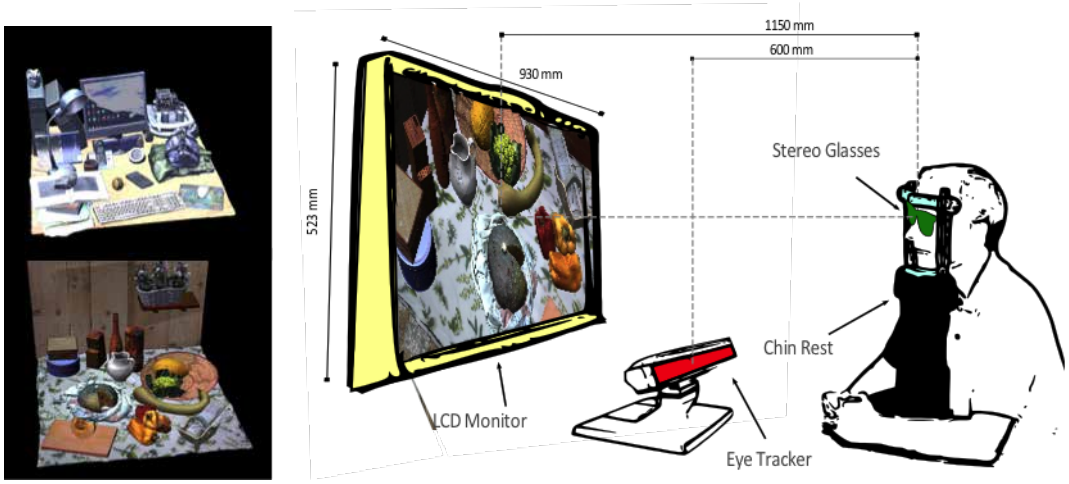

Fig. 1. Sketch representing the two naturalistic virtual scenes used (left): an office desk (top) and a kitchen table (bottom). Representation of the setup for measuring binocular fixations on subjects (right).

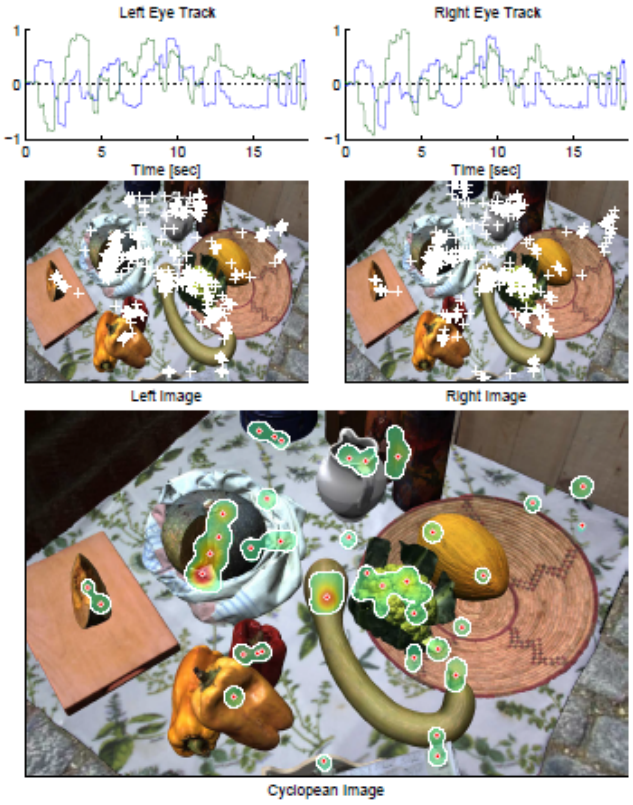

Fig.2 Example of the horizontal (green) and vertical (blue) scan paths measured for the left and the right eyes (top), together with the fixation points on the left and right images (middle), and the binocular heat map of fixations (bottom).

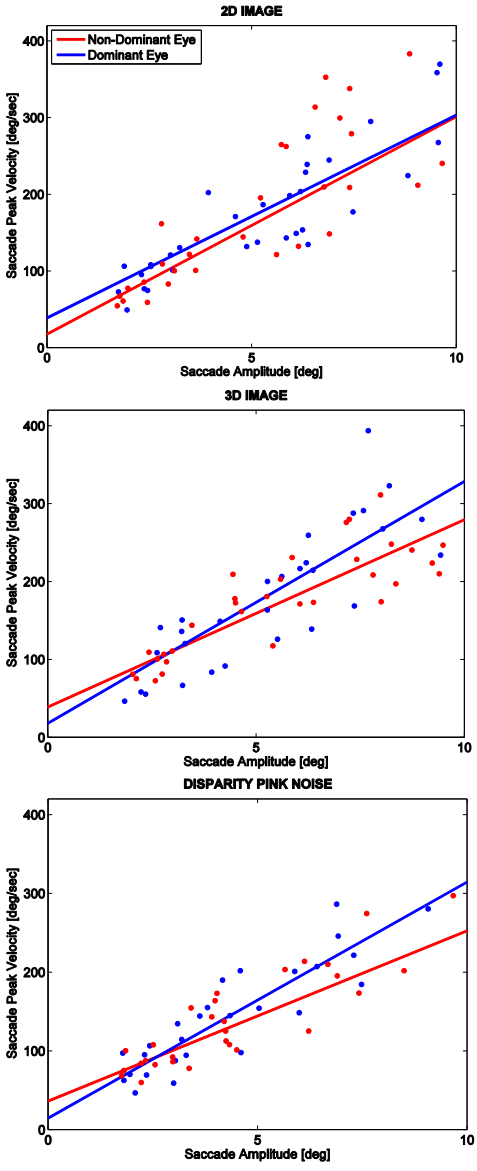

Fig. 3 Example of kinematic performance of the dominant (blue) and non-dominant (red) eye. Each subfigure shows the amplitude versus the peak velocity of the saccades (dots) and the associated regression lines, performed on 2D images (top), 3D stereoscopic images (middle), and 3D stereoscopic images with pink-noise texture.

An Android application to assess attention deficits in persons with multiple sclerosis

Francesca Florio[1], Martina Venturini[1], Andrea Tacchino[2], Giampaolo Brichetto[2] and Vittorio Sanguineti[1]
[1]*Department of Informatics, Bioengineering, Robotics and Systems Engineering, University of Genoa*
[2] *Italian Multiple Sclerosis Foundation, Genoa*

***Abstract*—Attention is an important cognitive function for individual survival and it is often compromised in persons with multiple sclerosis (PwMS). The goal of the study is the assessment of attention between PwMS and healthy individuals through the Attention Network Test-Interaction (ANT-I). The attention state will then be related to the state of fatigue and different clinical measures related to all subjects. Furthermore, the study includes the development of an Android application: the administration of the test on tablet (touch-screen version) will be compared with the administration on the PC (keyboard).**

***Keywords*—Android application, Attention Network Test-Interaction, multiple sclerosis.**

I. Introduction

Attention is essential for individual survival and is crucial in many daily activities. In 1990, Posner and Petersen [1] postulated that attention is mediated by three distinct subsystems: alerting, orienting and executive. The alerting network is responsible for increasing and maintaining vigilance and readiness to an upcoming stimulus. Orienting is responsible for selecting an information in the context of numerous inputs. Finally, the executive network underlies the selection and resolution of conflicts. The performance of these separate subsystems can be assessed by the Attention Network Test (ANT) [2], later modified into the Attention Network Test-Interaction (ANT-I) [3]. In persons with multiple sclerosis (PwMS), a gradual cognitive decline is relatively common (60% of subjects) though only in 10% it translates into significant disability. A number of studies has addressed attention deficits in PwMS using the ANT or ANT-I tests. With respect to healthy subjects, PwMS exhibit a degradation in the alerting network [4] and in the executive network [5]. However, no correlation was observed between attentional performance and clinical conditions [4]. The original version of the ANT-I test was implemented in Python by Michael A. Lawrence for use on a personal computer, with the keyboard as interface. A mobile version of the same application (e.g., Android) would provide an opportunity for patients to perform the test independently, given a greater accessibility than traditional PCs. A study involving healthy subjects [6] reported no differences in performance between the administration of the test through keyboard and touchscreen, but it is unclear if it is still the case in PwMS. Here we investigate the determinants of ANT-I performance in PwMS. We used the ANT-I version of the test because previous studies found it more reliable [7]. We also developed an Android version of the same test and we compared the ANT-I performance in either PwMS and healthy subjects as measured by either a PC-based or a tablet-based version of the test.

II. Materials and Methods

A. Participants

This study included a group of twenty-six healthy control participants (C) and thirty PwMS. All participants were between twenty-five and seventy years of age. Patients were recruited from Italian Multiple Sclerosis Foundation (FISM) and they were diagnosed with relapsing remitting multiple sclerosis (RR-MS) and secondary progressive multiple sclerosis (SP-MS). Inclusion criteria for the patients were disability ratings determined by the Expanded Disability Status Scale (EDSS) at the time of recruitment ranged from 1.0 to 8.0 and fatigue score measured by Modified Fatigue Impact Scale (MFIS) greater than 38. All the participants signed an informed consent provided by FISM.

All participants completed self-reported questionnaires of Edinburgh Inventory (EI), ABILHAND, Beck Depression Inventory (BDI), Fatigue Severity Scale (FSS), Modified Fatigue Impact Scale (MFIS). Moreover, the oral version of the Symbol Digit Modalities Test (SDMT) and the Nine Hole Peg Test (9-HPT) were administered.

B. Attention Network Test-Interaction

The test consists of one practice block followed by four experimental blocks. Each block consists of 72 trials. In each trial, warning tones or/and visual cues precede a central target (a fish, either looking toward left or right). The target can be flanked by other distractors (other fishes, looking in congruent or incongruent directions). The participants' task is to indicate the direction of the target fish as quickly and accurately as possible. The ANT-I allows for the examination of three attention networks. The alerting network is evaluated by examining differences in the reaction time in trials where the alerting tone was either present or absent. The orienting network is evaluated comparing reaction times in the valid cue conditions (the cue appears in the same location of the target) with reaction times in the invalid cue conditions (the cue appears in the opposite location of the target). Finally, the executive network is measured by comparing reaction times for congruent flanker trials (two flanker fishes on each side point in the same direction of the target fish) with reaction times from incongruent flanker trials (two flanker fishes on each side point in the opposite direction of the target fish) [8]. Greater scores of alerting and orienting indicate stronger effects, whereas greater scores of executive indicate a weaker executive function [9]. All fifty-six subjects performed the ANT-I on PC and only a subgroup (seventeen PwMS and eighteen healthy controls) performed the test on tablet.

C. Android application

The original version of ANT-I was implemented in Python and used modules for writing games (Pygame) and for providing high-quality drawing (Aggdraw, Python Imaging Library). Different methods allow to package Python code into Android APKs. We used the Pygame Subset for Android (PGS4A), which allows to port a game written in Python with Pygame to Android. To make it work, all code using Aggdraw and Python Imaging Library was replaced by equivalent Pygame functions. In the original ANT-I code, Pygame functions were used for the reproduction of sound signals. As these functions are not supported by PGS4A, we used Pyjnius, a Python interface to the Android Java classes. The modified version only uses Python and the Pygame and Pyjnius packages. In conclusion the following programs and packages are necessary to port the ANT-I application to Android: Java Development Kit, Python 2.7 and Pygame, Device Drivers for Android device, PGS4A [10].

D. Statistical analysis

We are interested in assessing the overall effect of the multiple sclerosis on attention performance. A mixed effects model for multivariate regression [11] is implemented to evaluate the relationship between scores on the clinical scales and the attention coefficients (alerting, orienting, executive). The model is defined as:

$$Indicator_i = \beta_0 + b_{0i} + \beta_1 \cdot \mathrm{FSS}_i + \beta_2 \cdot \mathrm{BDI}_i + \beta_3 \cdot 9\mathrm{HPT}_i + \beta_4 \cdot \mathrm{SDMT}_i + \beta_5 \cdot \mathrm{AGE}_i + \varepsilon_i$$

where β_i (i = 0,…,5) is a fixed factor common to all subjects, b_{0i} is a random factor for each subject, ε_i represents noise.

To compare the ANT-I results obtained from the PC and the tablet, we used a two-way ANOVA for repeated measures with group as a between-subjects factor and device as within-subjects factor. For all statistical calculations, we used the R statistical package and the Matlab software.

III. RESULTS

A. Multivariate regression

The average response time and the coefficients of alerting, orienting and executive are related to FSS, BDI, 9-HPT, SDMT and age through the mixed effects model. The average response time is significantly correlated with FSS, 9-HPT and SDMT. Fatigue is significantly correlated with the response times of all the subjects ($p < 0.0001$): a lower score of FSS corresponds to a shorter reaction time (Fig. 1). The 9-HPT is significantly correlated with the response times of all the subjects ($p < 0.0001$): a greater score of 9-HPT corresponds to a higher reaction time (Fig.2). The processing speed of the information is significantly correlated with the response times of all subjects ($p < 0.0001$): a lower score of SDMT corresponds to a higher reaction time (Fig.3). The executive is the only coefficient significantly correlated with the processing speed of information ($p < 0.0001$): a greater score of SDMT corresponds to a better executive control (Fig. 4).

B. PC vs tablet

The difference between the two devices (PC, tablet) is highly significant (effect of the device, $p < 0.0001$) in all groups (C, RR-MS, SP-MS). The difference in response times between groups is significant both the PC and the tablet (group effect, $p = 0.011$). However, there are no significant interactions between group and device. In other words, the effect of the device (increase of reaction time) is substantially similar for all groups (Fig. 5). The component 'executive' is the only coefficient in which the difference between the two devices is significant (Fig. 6).

IV. DISCUSSION AND CONCLUSION

We found that major determinants of the reaction time are fatigue (FSS), symbolic processing speed (SDMT) and incoordination (9-HPT). Symbolic processing speed also correlates with an improved executive function.

As regard the PC vs tablet comparison, with the tablet the reaction time consistently increases in all subject groups. Executive function also exhibits a difference between the two devices (better executive performance with the tablet).

These results suggest a clear relation between attentional performance and clinical state, which is not necessarily specific to PwMS. We also show that, different from previous studies, the interface used in administering the test has consequences on the assessment and should therefore be taken into account when interpreting the outcomes.

ACKNOWLEDGEMENT

We wish to thank M. Lawrence of Dalhousie University for having kindly provided his original implementation of the ANT-I test.

REFERENCES

[1] M. I. Posner and S. E. Petersen, “The attention system of the human brain,” *Annual Review of Neuroscience*, vol. 13, pp. 25–42, 1990.

[2] J. Fan, B. D. McCandliss, T. Sommer, A. Raz, and M. I. Posner, “Testing the efficiency and independence of attentional networks,” *Journal of Cognitive Neuroscience*, vol. 14, pp. 340–347, 2002.

[3] A. Callejas, J. Lupiàñez, M. J. Funes, and P. Tudela, “Modulations among the alerting, orienting and executive control networks,” *Experimental Brain Research*, vol. 167, pp. 27–37, 2005.

[4] C. Urbanek et al., “Attention Network Test reveals alerting network dysfunction multiple sclerosis,” *Multiple Sclerosis (Houndmills, Basingstoke, England)*, vol. 16, pp. 93–99, 2010.

[5] M. Wojtowicz, A. Omisade, and J. D. Fisk, “Indices of cognitive dysfunction in relapsing-remitting multiple sclerosis: intra-individual variability, processing speed, and attention network efficiency,” *Journal of the International Neuropsychological Society: JINS*, vol. 19, pp. 551–558, 2013.

[6] M. Canini et al., “Computerized neuropsychological assessment in aging: testing efficacy and clinical ecology of different interfaces,” *Computational and Mathematical Methods in Medicine,* pp. 1-13, 2014.

[7] Y. Ishigami and R. M. Klein, “Repeated measurement of the components of attention using two versions of the Attention Network Test (ANT): stability, isolability, robustness, and reliability,” *Journal of Neuroscience Methods*, vol. 190, pp. 117–128, 2010.

[8] M. A. Wojtowicz, Y. Ishigami, E. L. Mazerolle, and J. D. Fisk, “Stability of intraindividual variability as a marker of neurologic dysfunction in relapsing remitting multiple sclerosis”, *Journal of Clinical and Experimental Neuropsychology*, vol. 36, pp.455-463, 2014.

[9] A. K. Roth, D. R. Denney, and S. G. Lynch, “Information processing speed and attention in multiple sclerosis: Reconsidering the Attention Network Test (ANT),” *Journal of Clinical and Experimental Neuropsychology*, vol. 37, pp. 518–529, 2015.

[10] J. Henze (2014, Oct 29) [Online]. Available: http://www.gamedev.net

[11] D. M. Bates and J. C. Pinheiro, lme and nlme—mixed-effects methods and classes for S and S-PLUS. Madison, 1998.

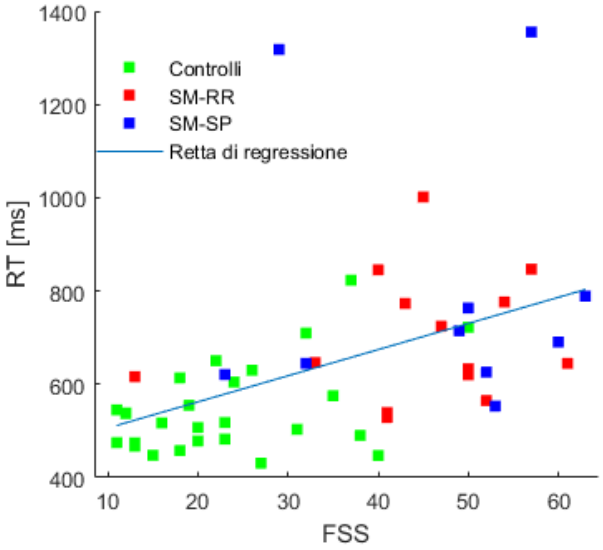

Fig. 1. Correlation between score FSS and reaction time.

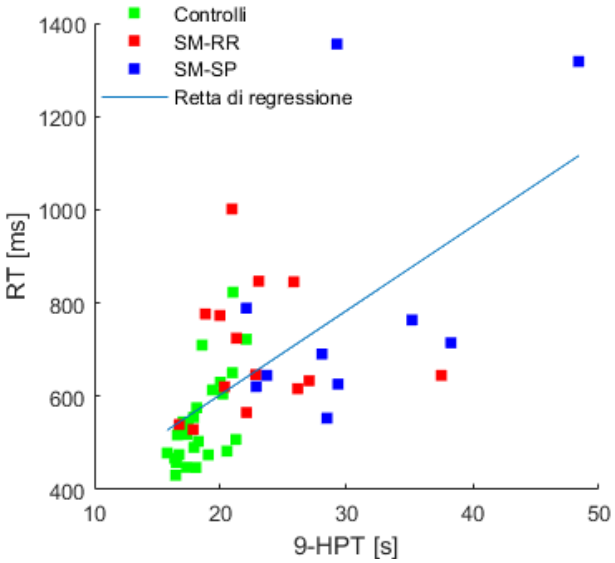

Fig. 2. Correlation between score 9-HPT and reaction time.

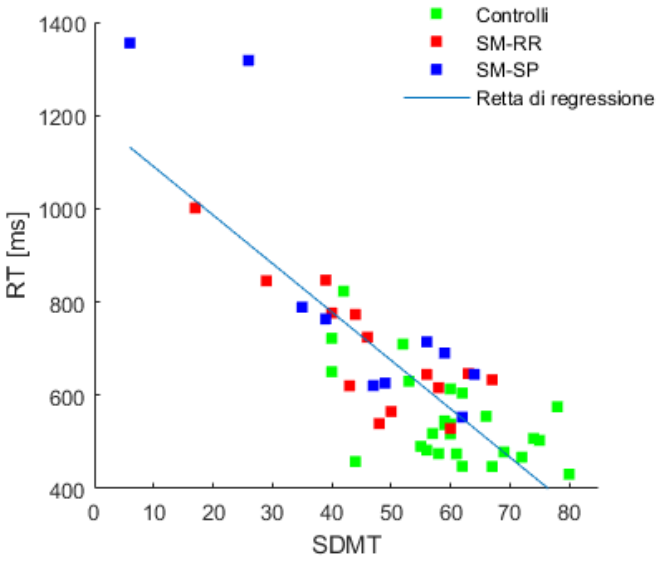

Fig. 3. Correlation between score SDMT and reaction time.

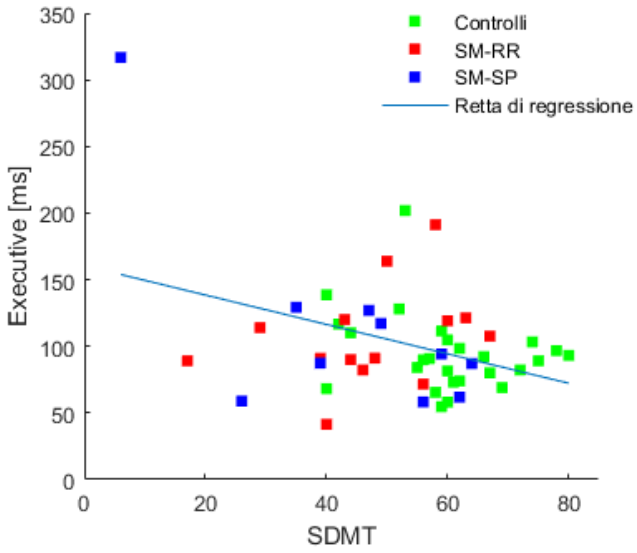

Fig. 4. Correlation between score SDMT and executive.

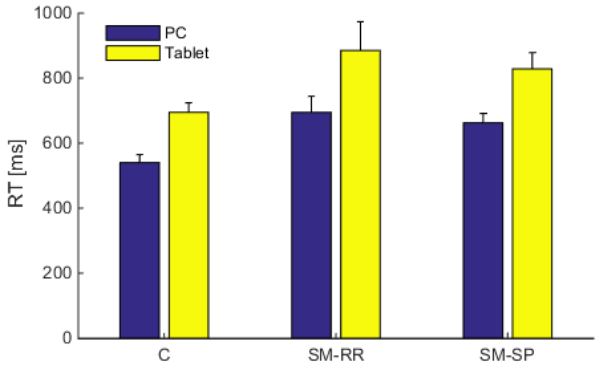

Fig. 5. Reaction time: PC vs tablet.

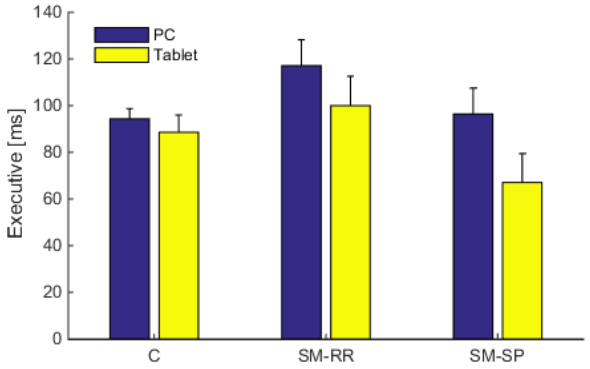

Fig. 6. Executive: PC vs tablet.

Effect of negative velocity-dependent forces on reaching movements at different speeds

S. Summa[1,2], M. Casadio[2] and V. Sanguineti[2]

[1] *Unit of Biomedical Robotics and Biomicrosystems, Department of Engineering, Università Campus Bio-Medico di Roma, Italy*

[2] *Department of Informatics, Bioengineering, Robotics and Systems Engineering, University of Genoa, Italy*

***Abstract*— In hand movements, speed is determined by the conflicting needs of maximizing accuracy and minimizing mechanical effort. Dynamic perturbations, e.g. force fields, may be used to manipulate movements in order to investigate these mechanisms. Here we focus on how negative velocity-dependent force fields affect the relation between speed and accuracy during hand reaching movements. We focused on endpoint error, distinguishing between bias and variability components. Negative viscosity resulted in increased variability during force field adaptation and in a reduction of the endpoint bias, which was maintained in the subsequent after-effect phase. These findings confirm that training within negative viscosity force fields improves movement accuracy.**

***Keywords*—Insert up to 4 keywords, separated by commas.**

I. Introduction

In target-directed movements the inter-relation between speed and accuracy - speed/accuracy trade-off (SAT) - has been studied for more than a century. Experiments on speed/accuracy trade-off can be classified into two categories: spatially constrained or temporally constrained [1]. In experiments with temporal constraints, subjects are required to move to a fixed target within a specified time. In this case, movement time is controlled and the spatial variability of the movement is measured to reflect accuracy. These experiments suggested that achieving a greater speed requires a larger motor command; but motor commands are affected by noise whose variance increases with the magnitude of the command [2]. As a consequence, increasing movement speed increases movement variability, which ultimately affects reaching accuracy.

Endpoint error can be decomposed into two components. The 'systematic' component (bias) reflects the mismatch with respect to the motor plan. The 'random' component (variability) reflects how repeatable our movements are. Both components of the endpoint error may be affected by changes in the dynamic environment.

Here we asked if exercise against a dynamic perturbation can alter – temporarily or permanently – the relationship between speed and accuracy (SAT curve). Specifically, we investigate how the SAT relation is modulated by body dynamics (inertia, in particular) and by negative viscous external perturbations, during temporally constrained hand reaching movements.

II. Materials and Methods

A. Experimental Set-up

Study participants sat in front of a 19" computer monitor placed vertically about 1 m away, at eye level. They grasped with their right hand the handle of a planar manipulandum with two degrees of freedom [3]. Seat position was adjusted so that, with the cursor pointing at the center of the workspace, the elbow and the shoulder joints were flexed about 90° and 45°.

B. Task and Experimental Protocol

Participants were instructed to perform reaching movements under visual control in two directions, corresponding to different arm inertia (45°: low inertia, LI; 135°: high inertia, HI). The subjects were required to maintain four different movement durations (very slow: 1.5 s; slow: 1.2 s; fast: 0.9 s; very fast: 0.6 s). The experimental protocol consisted of three phases (8 epochs per phase): (i) Null Field (Null1) - the robot generates no force; (ii) Force Field - the robot generates a velocity-dependent force field with negative viscosity (B = -10 Ns/m); and (iii) Null Field (Null2) - no force. The B value was set to get maximum force magnitudes of approximately 6 N, (at maximum speed). The study involved a total of 7 subjects (4 M + 3 F).

C. Data Analysis

Hand trajectories were sampled at 60 Hz and smoothed with a 6th order Savitzky-Golay filter with a 127 ms time window (cut-off frequency: 7.5 Hz). We used the same filter to estimate hand velocity and jerk.

We first looked at path curvature and trajectory smoothness. Path curvature was measured as the percent increase of the trajectory length with respect to the ideal path length. Trajectory smoothness was quantified in terms of the normalized jerk index. We then looked at the final hand position. Specifically we calculated projections of the norm of the bias and of the average norm of the endpoint variability (respectively $Bias_{lon}$, $Bias_{lat}$ and $Variability_{lon}$, $Variability_{lat}$), as in [4].

D. Statistical Analysis

To quantify whether and how the movement parameters change in the different experimental phases, we ran a repeated-measures 3-way ANOVA with three within-subjects factors - Phase (Null 1, Force Field - Null 2), Inertia (low inertia, LI; high inertia, HI) and Time (very fast, fast, slow, very slow). We additionally looked (planned comparisons) at (i) perturbation effect, expressed as the difference between the Null 1 and Force Field phases; (ii) carryover effect, expressed as the difference between the Null 1 and the Null 2 phases, (iii) inertia effect, i.e. the difference between LI and HI. We took p=0.05 as threshold for statistical significance.

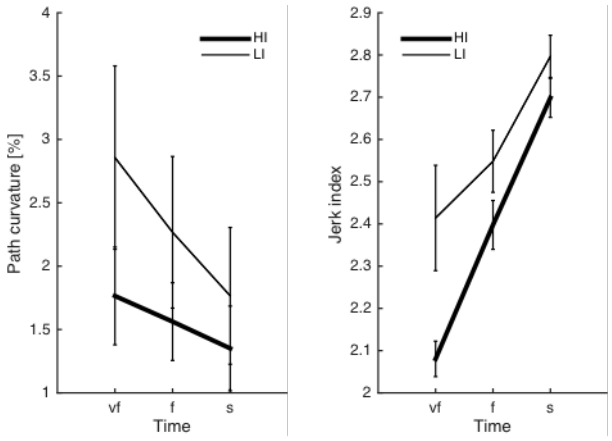

Fig. 1. Dependence of path curvature (left) and jerk index (right) curves on inertia. Thin and thick lines denote, respectively, low (LI) and high inertia (HI) directions. Vertical bars denote the SE

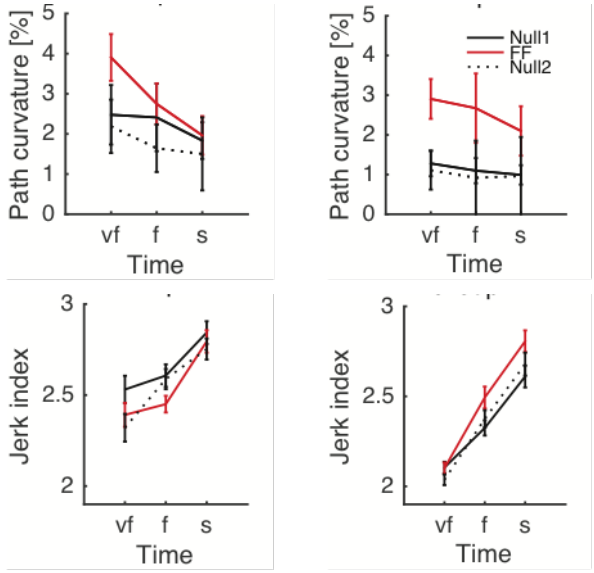

Fig. 2. Path curvature and Jerk index vs Movement Time for Low inertia (LI, left) and high inertia (HI, right). Curves are averaged over subjects for each velocity constraint and for each phase – Null1 (black), FF (red) and Null2 (dot- ted black). The differences between Null1 and FF indicate perturbation effects. The differences between Null1 and Null2 indicate carryover effects. Vertical bars denote the SE

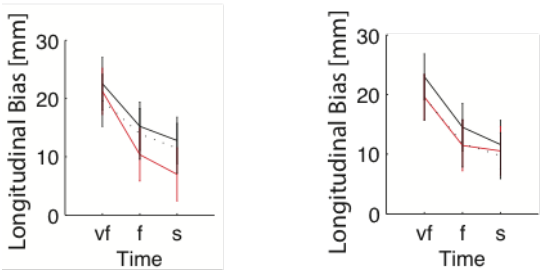

Fig. 3. Longitudinal Bias vs Movement Time, for Low inertia (LI, left) and high inertia (HI, right). Curves are averaged over subjects for each velocity constraint and for each phase – Null1 (black), FF (red) and Null2 (dot- ted black). The differences between Null1 and FF indicate perturbation effects. The differences between Null1 and Null2 indicate carrvover effects. Vertical bars denote the SE

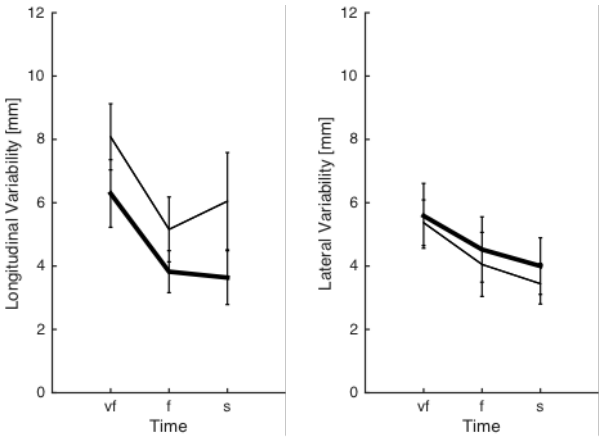

Fig. 4. Dependence of Longitudinal Variability (left) and Lateral Variability (right) curves on inertia. Thin and thick lines denote, respectively, low (LI) and high inertia (HI) directions. Vertical bars denote the SE

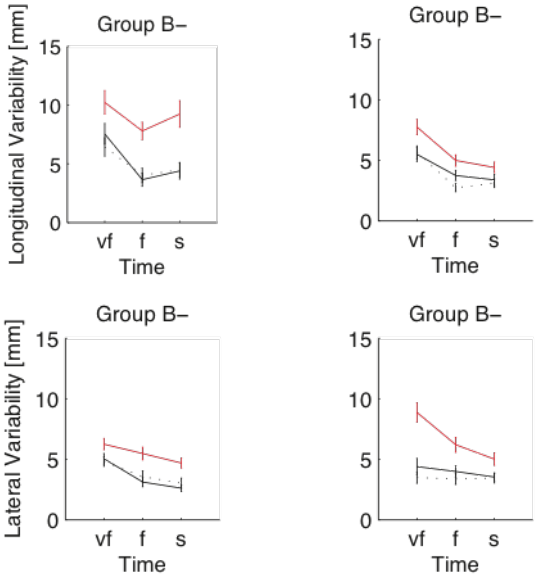

Fig. 5. Longitudinal Variability and Lateral Variability vs Movement Time, for Low inertia (LI, left) and high inertia (HI, right). Curves are averaged over subjects for each velocity constraint and for each phase – Null1 (black), FF (red) and Null2 (dot- ted black). The differences between Null1 and FF indicate perturbation effects. The differences between Null1 and Null2 indicate carryover effects. Vertical bars denote the SE

Dyadic learning of motor control strategies in complex tasks

J. Zenzeri[1], E. J. Avila Mireles[1], P. Morasso[1] and D. De Santis[2]
[1]Robotics, Brain and Cognitive Sciences Unit, Istituto Italiano di Tecnologia, Genova, Italy
[2]Department of Physiology, Northwestern University and Rehabilitation Institute of Chicago, Chicago, Illinois, USA

***Abstract*—It is known that physical coupling among active individuals can be beneficial and increase the performance of the dyad compared to an individual. However, the factors that may result in a performance benefit are still poorly understood. The aim of this work is to understand how the different initial skill levels of the interacting partners influence the learning of a stabilization task. Twelve subjects divided in two groups trained in couples in a joint stabilization task. In the first group the couples are made of two novices, while in the second a novice trains together with an expert. Results show that training with an expert results in the greatest performance in the joint task. However, this benefit is not transferred to the individual when performing the same task alone.**

***Keywords*—Dyads, Motor Learning, Physical Human Robot Interaction, Control Strategies.**

I. INTRODUCTION

Developing a machine capable of understanding the intention of a movement and interactively cooperate with a human is among the frontiers of the research in robotics as well as rehabilitation. A distinctive feature that makes joint actions in a haptic task particularly interesting, is their ability to induce to increase their sense of agency proportional to the performance of the interacting subjects[1]. On one side, physical coupling between two subjects was shown to be an advantageous solution in many cooperative contexts [2]–[5]. The behavior and performance of the dyad, however, is strongly dependent on the individual capabilities of the two partners. For instance, interacting with a partner that is more skilled will result in an improvement over the individual performance. Interestingly though, when it comes to a novel task, the interaction between partners with a similar skill level leads to better performance than with an expert or target in the tracking task [4]. On the other side, little is known about how two people mutually exchange information to exploit the coupling. Some findings suggest that dyads may adopt force amplification as a possible strategy to improve their performance especially in contexts that are challenging from the point of view of coordination [6]. Some other studies have shown that dyads may have a disadvantage in coping with noise and unforeseen disturbances [7]. In the present study, we were interested in testing how the presence of an expert partner affects the skill learning process of a novice individual in a challenging dyadic stabilization task. We asked subjects to learn to jointly manipulate a compliant tool under the action of an unstable force-field. In order to characterize the learning process in the dyad, we compared the case of two interacting individuals to one individual alone.

II. METHODS

A. Experimental setup

In this experiment, the haptic interface was rendered by a double Braccio di Ferro robot [8] consisting of two planar manipulanda mounted in a mirror configuration. During the first part of the experiment, the subjects had to work in dyads, so that each subject had to grasp the end effector of one manipulandum always with the right hand. In the second part of the experiment, instead, the two robotic arms were brought close to each other, allowing a single person to control it using both hands.

B. Task & protocol

The subjects were requested to stabilize a virtual mass (1 cm diameter with a weight of 15 Kg) inside a target location for 4 seconds. This was repeated for 9 different target locations (8 equally distributed on a circle of 10 cm diameter and 1 in the center). The targets were presented in an out-center-out sequence. The handles of the robot were indirectly attached to the virtual mass through a couple of non-linear virtual springs. The virtual environment was composed by a saddle-like force field to provide instability in the task (for details see [9]). The experiment was divided in 5 sessions having an approximate duration of 2.5 hours. Sessions from 1 to 4 were the training sessions, while session 5 was considered as the assessment session. The training and assessment were split down in target sets (TS). In each of them, the subject had to complete 16 stabilizations, 8 in the peripheral targets and 8 in the central one. The order of presentation of the peripheral targets within each TS was randomized. In every session, the subject had to complete between 6 and 10 TS with the unstable force-field active, during which one catch trial per TS was introduced (trial in which the instability was removed). The subjects were divided in 2 different groups. In the Naïve – Naïve group (N-N) each dyad was composed by 2 subjects with no experience in the task. The dyads in the Expert – Naïve group (E-N) were formed by a subject skilled in the task (the expert) and a naïve one. Subjects had to complete the training sessions following the next protocol:

Session 1: i) Familiarization: 6 TS, unstable force-field off; ii) Adaptation: 6 TS, unstable force-field on; iii) Wash-out: 3 TS, unstable force field off.

Session 2-3: i) Training: 10 TS, unstable force-field on.

Session 4: i) Training: 10 TS, unstable force-field on; ii) Wash-out: 3 TS, unstable force field off.

Session 5: This session is divided in two parts, first the subjects have to work in dyads and complete the following sequence (Part 1): i) Training: 3 TS, unstable force-field on; ii) Wash-out: 3 TS, force-field off.

Once the subjects completed the training on Session 5, they proceeded to work bimanually performing the following sequence (Part 2): i) Familiarization: 6 TS, unstable force-field off; ii) Adaptation: 6 TS, unstable force-field on; iii) Wash-out: 3 TS, unstable force-field off.

Twelve right handed (according to the Edinburgh test) subjects took part in the experiment (26±4 year-old): 5 male and 5 female naïve in the stabilization task, and 1 male and 1 female subjects expert in the task. Among the group of

subjects, 3 naïve males and 3 naïve females were selected to be part of the N-N group and the E-N group was composed of the remaining subjects. The study was approved by the local ethics committee, Comitato Etico of the ASL3 of Genova (Italy), which is legally competent for approving experiments involving human subjects. During the sessions 1, 2, 4, and 5, surface EMG signals were recorded from 10 relevant muscles from the arm and trunk. Surface electrodes were used to record the signals (OTBiolab EMG-USB2+ system). The sampling frequency was 2048Hz, and the signals were amplified with a gain that could vary from 1000 to 2000 depending on the amplitude of the EMG of each subject. The cut off frequencies of the internal bandpass filter of the device was set at 10-900 Hz to avoid aliasing problems and to reduce movement artifacts. At the beginning of the experimental session, the maximum voluntary contractions (MVC) of each subject were recorded in order to normalize the EMG signals.

C. Outcome Measures

Several measures were computed in order to quantify the relationship between the EMG and the kinematic results: 1) *EI* (Effort Index): EI = F1+F2 (N) where F1 and F2 represent forces applied to the left and right manipulandum by the subjects; 2) *Time to target* (seconds). Corresponds to the time that the subjects consumed to bring the mass in the target location and stabilize it. We also computed a Principal Component Analysis on the EMG signals to understand which muscles contribute mostly to the corrective movements produced in the stabilization phases of the task.

III. Results

Both groups of subjects were able to complete the training and significantly improve their performance in the end of Session 3. The E-N group in particular reduced the time to target faster and more consistently than the N-N group troughout the target sets. Moreover, the E-N group employed a much lower effort than 2 over 3 N-N dyads since the first session. As the training proceeds, however, the N-N dyads greatly decrease the overall effort compared to the initial pahses of the training. The N-N dyads employed more effort by strecthing the springs much more than the E-N group with the objective of increasing the overall stiffness of the hand-mass-hand system. Regarding the time to target, since the very first target set the 6 subjects in the N-N group are able to reach the 8 targets within half the time needed to the 4 naive subjects of the E-N group. The N-N subjects did not achieve this performance at the cost of a greater effort. In fact, both at the beginning and at the end of the assessment phase with the force-field they employed a much lower effort than the naive subjects who trained with the experts. Moreover, in the solo condition the N-N naives were actually able to apply less effort than with the partner. The behaviour of the naïve subjects in the E-N group was more etherogeneous, with a tendency to apply a greater effort compared to the N-N group and almost double the effort they employed in the training. It is interesting to notice that, despite not reducing the effort index they are able to accomplish the stabilization within much less time since the very beginning of the session. An explanation for the observed difference among groups could be that the E-N naives were subject to an 'interference effect' of the previuos training with an expert, while the N-N naives experienced a positive transfer of the acquired skills. In order to find a possible explanation for the observed kinematic performance, we conducted some analysis on the EMG data during the stabilization phase for the task. A PCA was used in order to identify the muscles that could account more for the observed corrective actions during the 4s stabilization inside the target area. The PCA reconstructions represent the muscles for which the variation in the EMG signal envelope accounts for at least 80% of the total variability of the signal in a group of representative subjects when reaching the target n.5 (180 deg). The N-N group shows more co-contraction of agonist and antagonist muscles, at least in the initial phases of the training. This observation is consistent with the higher effort index in this group during the training.

IV. Conclusion

The main findings of the present work can be summarized as follows: dyads are not only susceptible of adaptation, but they can also quickly learn new skills in a shared context; the amount of knowledge that can be transferred from a dyadic to an individual condition is limited by the interaction itself. Therefore, in addition to what already stated in the introduction, physical interactions are not always beneficial to the individual performance of the interacting partners. Our results suggest that the initial level of the performers has a strong impact on the learning of a context-independent representation of the dynamics of the task. In particular the interaction with an expert is detrimental in this sense. While interacting with an expert brought to a greater advantage over working with a pair, it partially manipulated the dynamics that the naïve perceived. As a consequence, the naïve subjects may have learnt how to cope with a leading expert rather than the background perturbation.

Acknowledgement

Research supported by the Robotics, Brain and Cognitive Sciences Unit of the Istituto Italiano di Tecnologia, and partially by the European CODEFROR project (FP7-PIRSES-2013-612555).

References

[1] R. P. R. D. van der Wel, N. Sebanz, and G. Knoblich, "The sense of agency during skill learning in individuals and dyads.," *Conscious. Cogn.*, vol. 21, no. 3, pp. 1267–79, Sep. 2012.

[2] J. Masumoto and N. Inui, "Motor control hierarchy in joint action that involves bimanual force production," *J. Neurophysiol.*, p. jn.00313.2015, 2015.

[3] R. P. R. D. van der Wel, G. Knoblich, and N. Sebanz, "Let the force be with us: dyads exploit haptic coupling for coordination.," *J. Exp. Psychol. Hum. Percept. Perform.*, vol. 37(5), pp. 1420–31, Oct. 2011.

[4] G. Ganesh, A. Takagi, R. Osu, T. Yoshioka, M. Kawato, and E. Burdet, "Two is better than one: physical interactions improve motor performance in humans.," *Sci. Rep.*, vol. 4, p. 3824, Jan. 2014.

[5] J. Masumoto and N. Inui, "Two heads are better than one: both complementary and synchronous strategies facilitate joint action.," *J. Neurophysiol.*, vol. 109, no. 5, pp. 1307–14, Mar. 2013.

[6] A. Melendez-Calderon, V. Komisar, and E. Burdet, "Interpersonal strategies for disturbance attenuation during a rhythmic joint motor action.," *Physiol. Behav.*, vol. 147, pp. 348–58, Aug. 2015.

[7] K. B. Reed and M. A. Peshkin, "Physical Collaboration of Human-Human and Human-Robot Teams," *IEEE Trans. Haptics*, vol. 1, no. 2, pp. 108–120, Jul. 2008.

[8] M. Casadio, V. Sanguineti, P. G. Morasso, and V. Arrichiello, "Braccio di Ferro: a new haptic workstation for neuromotor rehabilitation.," *Technol. Health Care*, vol. 14, no. 3, pp. 123–42, Jan. 2006.

[9] E. J. A. Mireles, D. De Santis, V. Squeri, P. Morasso, and J. Zenzeri, "Motor control strategies in the bimanual stabilization of an unstable virtual tool," in *Proceedings of the IEEE International Conference of Engineering in Medicine and Biology*. 2015, pp. 3472–3475.

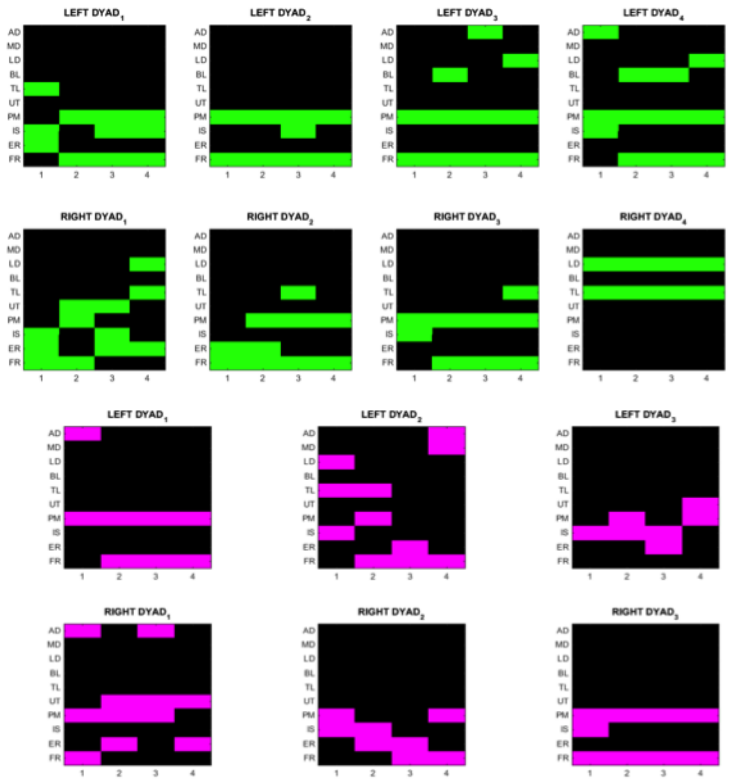

Fig. 1. Reconstruction of the muscle activation in the projection of the first 3 Principal Components for the N-N group (top two rows) and 3 representative subjects of the E-N group (bottom two rows). The muscles which projection over the 3 first components was greater or equal to the 80% is shown in purple and in green respectively. In each group of panels the top row shows the subject manipulating the left arm and the bottom row the subject on the right.

DISPOSITIVI, SISTEMI E TECNOLOGIE DIAGNOSTICHE E TERAPEUTICHE

Metal-enhanced fluorescence on gold nanoparticles clusters

Edmondo Battista[1], Maria Laura Coluccio[2], Marianna Barberio[3], Enzo Di Fabrizio[2,4], Paolo Antonio Netti[1], Francesco Gentile[5]

[1]*Interdisciplinary Research Center on Biomaterials (CRIB), University Federico II, P.le Tecchio 80, Napoli, Italy*
[2]*Department of Experimental and Clinical Medicine, University of Magna Graecia, 88100 Catanzaro, Italy*
[3]*Ipat-lab, INRS-EMT, 1650 Boul Lionel Boulet, Varennes (Qb), Canada*
[4]*PSE division, King Abdullah University of Science and Technology, Thuwal 23955 − 6900, Saudi Arabia*
[5]*Department of Electrical Engineering and Information Technology, University Federico II, Naples, Italy*

***Abstract*— We used conventional optical lithography and electroless deposition methods to realize arrays of gold nanoparticles in which the size and spacing of the (i) arrays and of the (ii) particles are controlled at the nano-meter level. In the chips, gold nanoparticles enable metal enhanced fluorescence (MEF) effects, whereby fluorescence signal of fluorophores in close proximity to the rough gold surface is amplified of several orders of magnitude. We demonstrated the device in the analysis of fluorescein derived GBP-FITC peptides. This technology may be employed in protein microarrays where the increased sensitivity of the device may enable the early detection of cancer biomarkers or other proteins of biomedical interest.**

***Keywords*— Electroless deposition, gold nanoparticles, Metal Enhanced Fluorescence (MEF), Fluorescence Lifetime Microscopy (FLIM).**

I. Introduction

The new paradigm of Materials Science is realizing materials in which the structure of the material itself is controlled at a molecular level [1, 2]. Similar nano-scale materials display enhanced properties with respect to their macro-scale counterparts. Advanced materials and a nano-scale design may lead to major changes in biology and bio-engineering. Metal enhanced fluorescence (MEF) is an effect that may support biologists in analytical chemistry and early detection. MEF is a physical effect that occurs when fluorophores are located in close proximity to a rough metal surface [3]. Compared to conventional fluorescence, MEF benefits of increased spontaneous emission rate, quantum yield and photo-stability, decreased fluorescent lifetime of fluorophores, directional emission [3]. In MEF, fluorescence amplification depends on three separate mechanisms, that are, (i) energy transfer from the fluorophore to the metal; (ii) enhancement of the local electromagnetic field; (iii) modification of the radiative decay rate of the fluorophore. Mechanisms from (i) to (iii) are driven by the geometry of metal/fluorophore interface. Controlling the fabrication of metal nano-patterns with a nano-meter accuracy is a binding condition to obtain highly efficient MEF devices. Here, we used in combination optical lithography techniques and electroless deposition to obtain arrays of gold nanoparticles clusters in which the distance between the clusters and the particle size are controlled at the micro- and nano-meter level. We selectively adsorbed a fluorescein derived GBP-FITC peptide onto the gold nanoparticles and verified peptide/metal binding and resulting enhancement of fluorescence through fluorescence microscopy and fluorescence lifetime microscopy.

II. Methods

A. Fabrication

We used P type, (100) Silicon wafers as substrates. After cleaning with acetone, we spin coated the substrates with a positive tone resist (S1813). We used optical lithography techniques to generate arrays of holes in the resist, with an average size $D = 10\ \mu m$. Gold nanoparticles were deposited into the holes using electroless deposition techniques as described elsewhere [4, 5]. Electroless deposition is based on an autocatalytic chemical reduction of metal ions in an aqueous solution when silicon nanoparticles are present. Gold ions exchange electrons with the silicon substrate that is the reducing agents itself [6]. The reaction occurs in a $0.15\ M$ solution of fluoridric acid (HF) solution containing the silicon substrate and auric chloride ($AuCl_3$). The gold salt concentration C and the process conditions: temperature T and reaction time t are adjusted as $C = 5\ mM$, $T = 50°C$, $t = 120\ s$.

B. Sample characterization

SEM images of the Gold Nanoparticles clusters were captured using a Dual Beam (SEM-FIB) - FEI Nova 600 NanoLab system. During acquisition, the beam energy and the corresponding electron current were fixed to 15 keV and 0.14 nA, respectively. Atomic force microscopy (Veeco MultiMode with NanoScope V controller) was used for the measurement and characterization of the structures as reported elsewhere [7].

C. Deriving the fractal dimension of the nanoclusters

The AFM profiles were processed to obtain the corresponding Power Spectrum density functions $PS(q)$ of the samples [5]. In a loglog plot, the power spectrum density appears as a line with a slope β. The slope β is related to the fractal dimension D_f of the surface as $D = (8 - \beta)/2$.

D. Surface Functionalization

The device surface was treated by fluorescent $GBP - FITC$ (gold binding peptide fluorescein), made of a sequence previously selected by phage display to be selective for gold ($AuPi_3$: TLLVIRGLPGAC) [8, 9] and at flanking region with the sequence $-\mathrm{G4} - \mathrm{RGDSPKC}$ (FITC) (MW: 2469.82 Da, purchased from Proteogenix, France). Peptide was dissolved

in HBS at the concentration of 30 µM. Gold surface was cleaned in a 5% (w/v) water solution of sodium hypochlorite for 5 min, then washed with ethanol (95 %) and dried with nitrogen. The molecular binding was carried out by dropping 4 µl of solution on surfaces. The drop was left to adsorb for 30 min, rinsed with 3 ml HBS afterward and then dried with nitrogen.

E. Fluorescence microscopy

Confocal fluorescence and lifetime images (FLIM) were recorded by means of a Leica inverted microscope SP5 from Leica Microsystems using a water immersion objective 25× (NA 0.95). To investigate the binding of GBP − FITC, the system was excited with an Ar^+ laser at 488 nm and the emission bandwidth was from 520 to 600 nm. All the images were collected at 12 bit color depth with a resolution of 1024×1024. Fluorescence lifetime images + of GBP − FITC adsorbing nanostructures were acquired by using a pulsed Multiphoton Laser source (120 fs, 80 MHz, Ultra, Chamaleon, Coherent, Santa Clara CA, US) implemented in the time-domain using a time-correlated single photon counting (TCSPC) module. The laser was tuned to 780 nm for two-photon excitation of fluorescein derivative by TCSPC, operating the laser at excitation 800 nm. Images and lifetime data were analyzed by using SymPhoTime software (PicoQuant, Germany).

III. Results

The proposed top down/bottom up approach delivers the ability to produce clusters of gold nanoparticles with a tight control over the physical characteristics of the system, including size and shape of the particles. Several SEM images (**Figure 1**) were taken to assess sample uniformity and reproducibility. In **Figure 1a**, gold nanoparticles clusters are 10 µm wide and are separated by 20 µm (the scale bar in the image is 100 µm). Higher magnifications as in **Figure 1b** (scale bar: 5 µm) and **c** (scale bar: 100 nm) reveal the morphology of the particles at a smaller scale. Gold nanoparticles have a quasi-circular shape with an average size S = 60 nm and small deviations from the mean. Surface nano-topography of the samples (**Figure 2a**) was acquired using standard AFM. From the surface profile we derived a power spectrum (**Figure 2b**) that delivers the information content of the surface over different scales[10]. In a log-log diagram, the power spectrum exhibits a linear behaviour with slope β in a region of the diagram. β and the fractal dimension D_f are not independent and from the measure of β one may obtain D_f. For this particular configuration $D_f \sim 2.3$. The described aggregates of gold nanoparticles were functionalized with a fluorescent $GBP - FITC$ gold binding peptide. **Figure 3** shows the fluorescent profile of a pattern of structures with (**a**) and without (**b**) the clusters of gold nanoparticles. As precedently demonstrated by Causa et al [8, 9], the $AuPi_3$ sequence, selected by phage display, can bind selectively with higher affinity gold surfaces. This explains the increased fluorescence signal on the gold nanoparticles (**a**) and, conversely, the reduction of the signal (**a**) in absence of gold in the structures. **Figure 3c** is a FLIM image of gold nanoparticles arrays without the FITC peptide. Differently, **Figure 3d** shows a FLIM profile of the device functionalized with the peptide. Taken together, **Figure 3a-d** show significant fluorescence enhancements when fluorophores interact with rough metal surfaces. This is made evident by the decrease of fluorescent lifetime in correspondence to the gold nanostructures (roughly in the $0.5 - 1.5\ ns$ range) as predicted by MEF theory. In addition to this, MEF is correlated to an enhanced fluorophore photo-stability as the fluorophores stay less time in an excited state, before falling to their pristine ground state, and are therefore less susceptible to photo-destruction [11].

IV. Conclusion

We demonstrated arrays of gold nanoparticles for metal enhanced fluorescence. Dividing the fabrication process of the chip into two separate stages permits to realize devices in which the spacing and size of the (i) array spots and of the (ii) gold nano-grains are controlled separately at the micro to nano level in a hierarchical architecture. This, in turn, enables to operate site specific measurements of biological samples with increased sensitivity and low detection ranges. The described technology may be principally used in in protein microarrays, enabling multiplexed protein assays with detection limits as low as few femto-molar and high dynamic range, for the early detection of cancer biomarkers or other proteins.

References

[1] S. Glotzer, "Nanotechnology: Shape Matters," *Nature,* vol. 481, pp. 450-452, 2012.

[2] S. C. Glotzer and J. A. Anderson, "Nanoparticle Assembly: Made to Order," *Nature Materials,* vol. 9, pp. 885-887, 2010.

[3] W. Deng, F. Xie, H. T. M. C. M. Baltarac, and E. M. Goldys, "Metal-enhanced fluorescence in the life sciences: here, now and beyond," *Physical Chemistry Chemical Physics,* vol. 15, pp. 15695-15708, 2013.

[4] M. L. Coluccio, F. Gentile, M. Francardi, G. Perozziello, N. Malara, P. Candeloro, *et al.*, "Electroless Deposition and Nanolithography Can Control the Formation of Materials at the Nano-Scale for Plasmonic Applications," *Sensors,* vol. 14, pp. 6056-6083, 2014.

[5] F. Gentile, M. Coluccio, A. Toma, E. Rondanina, M. Leoncini, F. De Angelis, *et al.*, "Electroless deposition dynamics of silver nanoparticles clusters: A diffusion limited aggregation (DLA) approach " *Microelectronic Engineering,* vol. 98, pp. 359-362, 2012.

[6] S. Yae, Y. Morii, N. Fukumuro, and H. Matsuda, "Catalytic activity of noble metals for metal-assisted chemical etching of silicon," *Nanoscale Research Letters,* vol. 7, pp. 352-6, 2012.

[7] F. Gentile, M. L. Coluccio, P. Candeloro, M. Barberio, G. Perozziello, M. Francardi, *et al.*, "Electroless deposition of metal nanoparticle clusters: Effect of pattern distance," *Journal of Vacuum Science and Technology B,* vol. 32, pp. 031804:1-12, 2014.

[8] C. Cosenza, V. Lettera, F. Causa, P. Scognamiglio, E. Battista, and P. Netti, "Cell mechanosensory recognizes ligand compliance at biomaterial interface," *Biomaterials,* vol. 76, pp. 282-291, 2015.

[9] A. M. Cusano, F. Causa, R. D. Moglie, N. Falco, P. L. Scognamiglio, A. Aliberti, *et al.*, "Integration of binding peptide selection and multifunctional particles as tool-box for capture of soluble proteins in serum," *Journal of the Royal Society: Interface,* vol. 11, pp. 20140718:1-11, 2014.

[10] F. Gentile, E. Battista, A. Accardo, M. Coluccio, M. Asande, G. Perozziello, *et al.*, "Fractal Structure Can Explain the Increased Hydrophobicity of NanoPorous Silicon Films," *Microelectronic Engineering,* vol. 88, pp. 2537-2540, 2011.

[11] G. Das, E. Battista, G. Manzo, F. Causa, P. Netti, and E. Di Fabrizio, "Large-scale plasmonic nanocones array for spectroscopy detection," *ACS Applied Materials and Interfaces,* vol. 7, pp. 23597-23604, 2015.

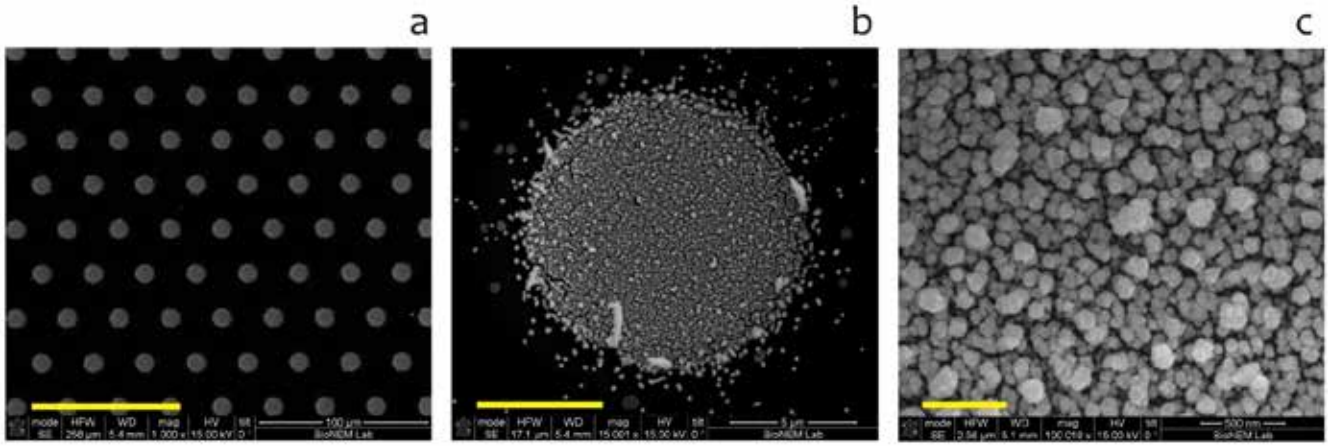

Fig. 1

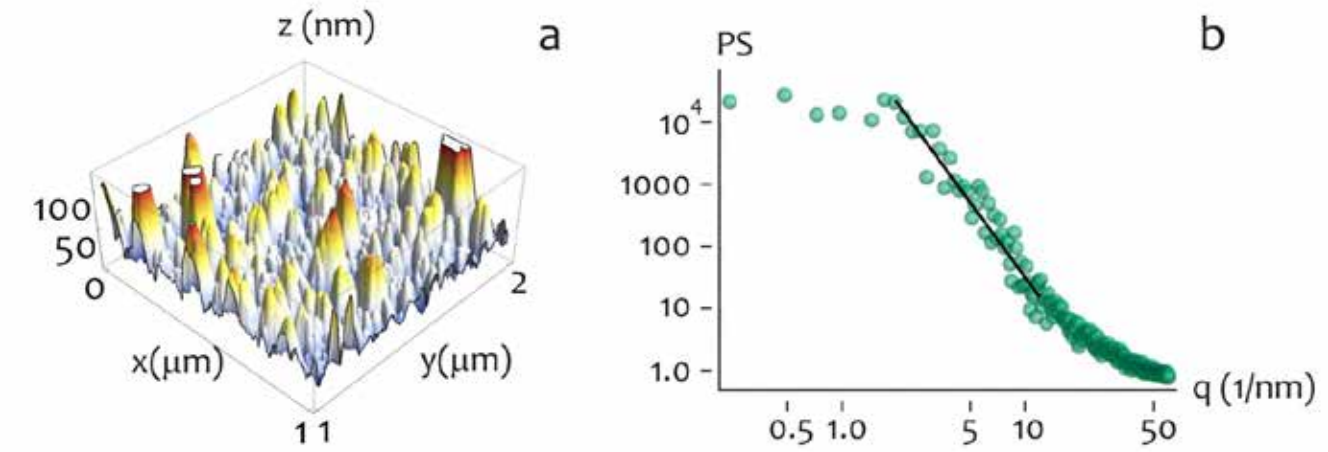

Fig. 2

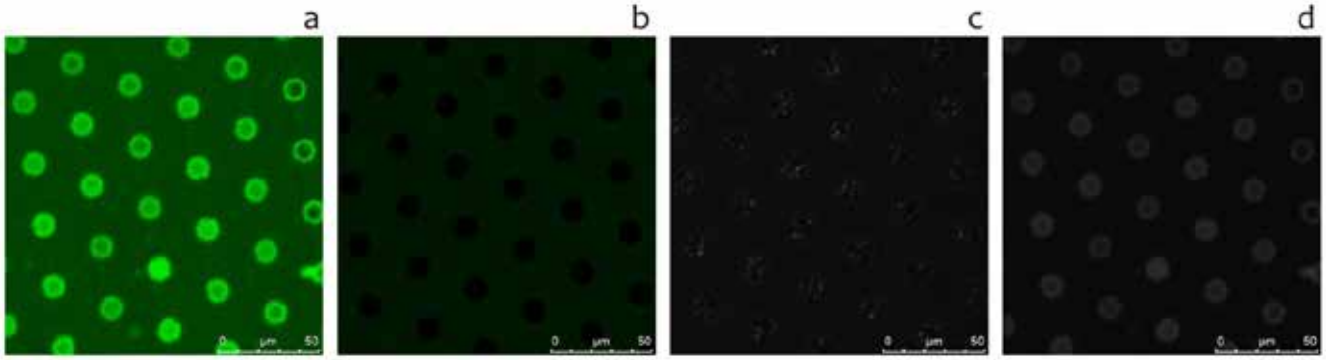

Fig. 3

Patient-specific modelling of multi-compartment fluid and mass exchange during dialysis.

C. Bianchi[1], G. Casagrande[1], and M.L. Costantino[1]
[1]*Dipartimento di Chimica, Materiali ed Ingegneria Chimica "Giulio Natta", Politecnico di Milano, Milan, Italy*

***Abstract*—This work aims at developing a patient-specific multi-compartment model of fluid and mass kinetics during hemodialysis therapy.**

The validation of the model, made through the comparison with clinical data, allows to consider the model as a support decision tool for the nephrologist.

***Keywords*— Hemodialysis, patient-specific model, solute kinetics**

INTRODUCTION

End Stage Renal Disease implies the need to treat the patients by hemodialysis (HD). Despite the improvements made in the last years, several co-morbidities [1] are still associated to the treatment. A need for treatment customization emerged over the years because individual tolerance might vary even in the presence of similar treatments. Moreover, due to the therapy discontinuity, HD procedure induces considerable changes in osmotic balances and rapid variations in fluid volumes [2-4] and electrolytic concentrations [5] within the patient's body compartments.

An innovative approach would be to provide the clinician an instrument to simulate and predict the single patient response to the treatment in terms of solutes and catabolite kinetics, so as to identify the most suitable therapy, reducing intra-dialysis complications and associated long-term dysfunctions.

To this aim, a parametric multi-compartment model has been developed, capable to account for several patient specific characteristics. The peculiarity of the proposed model is the possibility to perform a real time simulation which can allow quantitative appraisal of hemodynamic and hematochemical quantities whose direct measurement is in general prohibitive.

MATERIALS AND METHODS

A. The mathematical model

The model (fig. 1) is a multi-compartment parametric kinetic model, implemented in Matlab®, based on mass and fluid balance equations both in the patient and across the dialyzer membrane. The body compartments have been represented as two pools for the mass exchange analysis (intra and extra-cellular) of the considered solutes and three pools (plasmatic, interstitial and intracellular) for fluids transfer.

The model allows to simultaneously evaluating the behavior of different plasmatic electrolytes as sodium (Na^+), potassium (K^+), chloride (Cl^-), calcium (Ca^{2+}), bicarbonate (HCO_3^-), and breakdown products such as urea in the patient's blood.

In terms of mass and fluid exchange, the patient's specific control is achieved by identifying three specific parameters related to the membranes across which the fluid and mass transports occur.

B. Dialyzer-side equations

Across the dialyzer membrane, the mass exchange for each solute can be quantified through the sum of the diffusive and convective flows [6].

A useful equation for clinical practice has been found, dependent on input flow rate, dialysance for the specific filter and for the specific solute and the input concentrations (identified as $\Phi_{hd/hdf}$ in fig. 1).

The flow across the dialyzer membrane changes its expression in the model, according to the dialysis technique (HD or HDF).

The patient-specific parameter η represents the performance of the dialyzer membrane in terms of filtration.

C. Patient-side equations

In fig.1 mass, fluid and pressure balance equations accounting for mass and fluid exchanges among the body patient compartments are reported.

There are two equations for the mass balance, related to the intra and extra cellular compartments; three equations for the fluid balance, related to the intracellular, interstitial, plasmatic compartments; two equations for the pressure balance (arterial capillary and interstitial pressures).

The patient-specific parameters k allows to modulate the mass transfer efficiency across the cellular membrane.

ρ is the patient dependent parameter representing the relative capillary wall permeability.

All the mass, fluid and pressure balance equations, compose a system of Ordinary Differential Equations (ODE) that is solved by the 4th order Runge-Kutta numerical method. Each variable of the ODE system is calculated with a time step of one minute.

D. Clinical input data for the model

Clinical data have been acquired during the DialysIS project at the Dialysis and Nephrology Units of the Regional Hospital of Lugano (Lugano, Switzerland). A total of 20 patients, undergoing Haemo-Dia-Filtration (HDF) treatment thrice a week, have been enrolled.

A total of 131 sessions have been considered.

Clinically recorded data were: the therapy prescription for each patient, patient initial conditions, patient registry and medical records. All of these data were used to correctly set and initialize the mathematical model in order to simulate a specific dialysis session.

To allow the validation of the model and compare the simulation results with the clinical data, electrolytes and catabolites concentrations have been evaluated by

hemogasanalysis at the beginning of the treatment and every hour until the end of the session. Along the same treatment, the blood volume reduction has been directly acquired every minute by the dialysis monitors. The clinical blood volume curve can be an indicator comparable with the blood volume curve simulated by the mathematical model.

E. Optimization of the model to characterize the patients

To identify the patient-specific membrane parameters (ρ, k, η), a constrained non-linear optimization algorithm has been used [7-8]. By means of this method, it is possible to extract the set of parameters that minimize a criterion function, which is the sum of the mean squared errors weighed on different parameters influence on different outputs (different solutes concentrations):

$$J_i = \sum_{j=1}^{N} w_{ij} E_{ij} \quad (1)$$

G. Validation of the descriptive ability of the model

The model reliability and its descriptive capability have been evaluated comparing the outputs of the model, in terms of solute blood concentrations, with the clinically recorded data, using the identified patient-specific parameters.

RESULTS AND DISCUSSION

The developed model allows describing electrolytes and catabolite concentration trends into the different body compartments along each dialysis session. The results are summarized in fig.2.

Evaluating the overall deviation between clinical and simulated solutes and catabolite concentrations, it can be noticed that the optimized model allows the description of plasmatic concentrations trend of Na^+, Cl^-, and Ca^{2+}, and HCO_3^- with an average percent error lower than 2,1%, the concentration of K^+ with an average percent error lower than 5% and Urea concentration with an average percent error around 7% (fig.3).

The developed model allows to correctly describing the concentration trends of solutes and catabolites in the plasmatic compartment along a dialysis session. Its peculiarity, with respect to the literature [2-3, 5, 9-13], is the possibility to consider the evolution of different solutes at the same time, among which also the trends of those solutes which are not always considered by the clinician in the clinical routine, but that have demonstrated to be relevant in the correct definition of the therapy.

More importantly, the developed multi-compartment parametric model, due to the identification of the patient-specific parameters, allows an accurate description of the patient-specific response to the treatment, giving the clinician useful information about the patient response to dialysis session settings. The possibility to quantitatively appraise also the intra-Dialysis variations of hemodynamic and hematochemical quantities whose direct measurement is generally prohibitive, is a further value in the view to use the model to support clinical prescriptions.

CONCLUSION

The developed model allows the patient-specific description of the mass transfer. The information given by the model can be helpful for a more accurate planning of the dialysis therapy; implying the improvement of the treatment outcomes but, above all the improvement of the patients' quality of life.

ACKNOWLEDGEMENT

This work was part of the "DialysIS (Dialysis therapy between Italy and Switzerland)" project funded by the cross-boarder cooperation program INTERREG IT/CH 2007-2013.

REFERENCES

[1] H. Palmer, F. Biff, L. William, "Recent Advances in the Prevention and Management of Intradialytic Hypotension", *Journal of the American Society of Nephrology*, Vol. 19, p. 8-11, 2008.

[2] Prakash S., Reddan D., Heidenheim P. et al. "Central, Pheripheral, and other Blood Volume Changes During Hemodialysis", *ASAIO J.*; vol 48, pp 379-382, 2002.

[3] Tapolyai, Faludi, Fülöp et al, "Which fluid space is affected by ultrafiltration during hemodiafiltration?" *Hemodial Int.*18:384-90, 2014.

[4] Daugirdas T., "Dialysis hypotension: a hemodynamic analysis", *Kidney Int* 39: 233-246, 1991.

[5] Santos SF, Peixoto AJ., "Sodium balance in maintenance hemodialysis", *Semin Dial.* Nov-Dec; 23(6):549-55, 2010.

[6] N. A. Hoenich., "Membranes and filters for haemodiafiltration", *Contrib Nephrol*, 158:57–67, 2007.

[7] A. Saltelli, M. Ratto, T. Andres, F. Campolongo, J. Cariboni, D. Gatelli, M. Saisana, and S. Tarantola, "Global Sensitivity Analysis. The primer". Wiley, 2008.

[8] J. I. Myung, Y. Tang, and M. A. Pitt., "Evaluation and comparison of computational models", *Meth. Enzymol.,* 454:287–304, 2009.

[9] Prado M, Roa L, Palma A, Milan JA., "A novel mathematical method based on urea kinetic modeling for computing the dialysis dose" *Computers Methods and Prog in Biomedicine*, 74: 109-128, 2004.

[10] Ursino, L. Coli, E. Magosso, P. Capriotti, A. Fiorenzi, P. Baroni, and S. Stefoni."A mathematical model for the prediction of solute kinetics, osmolarity and fluid volume changes during hemodiafiltration with on-line regeneration of ultrafiltrate (HFR)", *IJAO*, 29:1031–1041, 2006.

[11] Waniewski J., "Mathematical modeling of fluid and solute transport in hemodialysis and peritoneal dialysis", *Journal of Membrane Science*; 274:24-37, 2006.

[12] Leypoldt, J.K., Agar, B.U., Akonur, A., Gellens, M.E.,Culleton, B.F., "Steady state phosphorus mass balance model during hemodialysis based on a pseudo one-compartment kinetic model", *IJAO*, 35 (11), 969-980, 2012.

[13] Agar, B.U., Culleton, B.F.,Fluck, R., Leypoldt, J.K., "Potassium kinetics during hemodialysis", Hemodialysis International, 19 (1), 23-32, 2015.

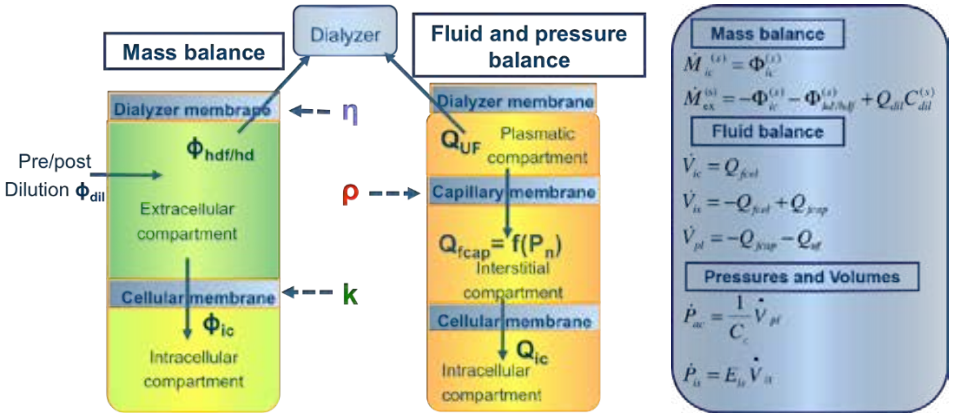

Fig. 1. Scheme of the body compartments as considered in the model. Fluid and mass exchanges across the relevant biological and artificial membranes were represented. Q_{UF} is the ultrafiltration flow rate. On the right, there is a scheme of the system of ODE implemented in Matlab.

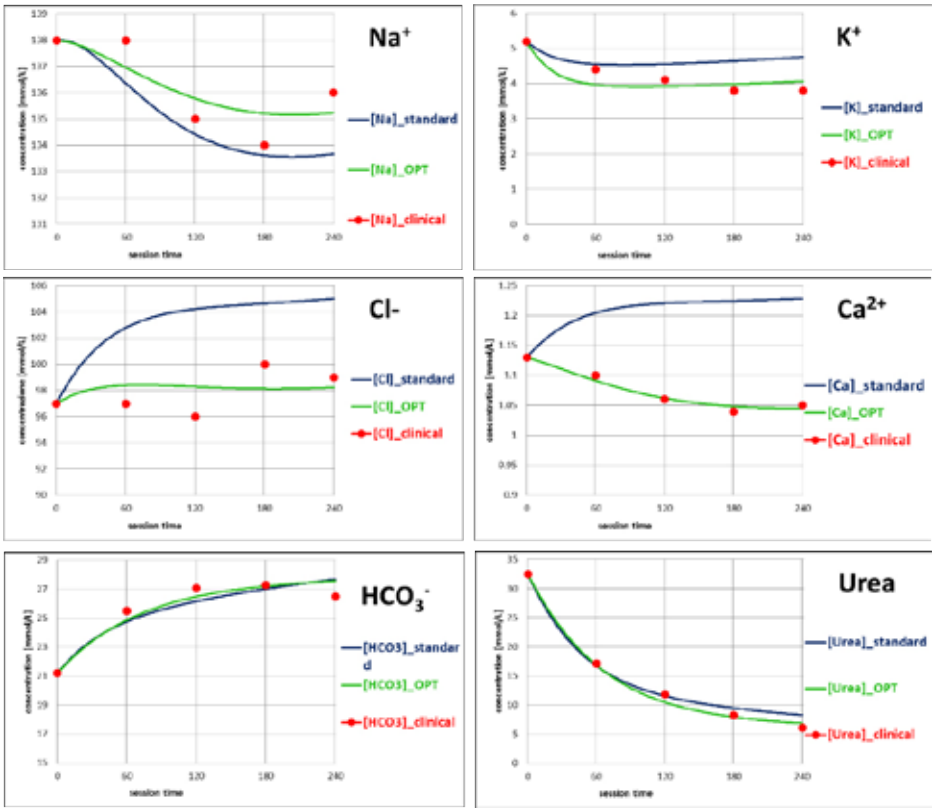

Fig. 2. Plots of the main model outputs, on which the results are focused. Red dots represent the clinically acquired data to be compared with solutes concentrations trends in the optimised model (green line) and in the model set with standard values for the patient-dependent parameters (blue line).

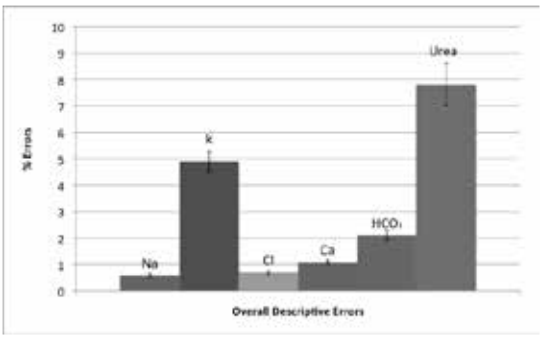

Fig. 3. Overall averaged descriptive errors evaluated for each solute, once the model is optimized on the single session (identification of the patient-specific

Emulsion templated silica-biopolymer nanocapsules for theranostic and co-delivery

V. Calcagno[1,2,3], R. Vecchione[1,2], G. Luciani[2,3], A. Jakhmola[1], B. Silvestri[2,3], and P.A. Netti[1,2]
[1] *Istituto Italiano di Tecnologia, IIT@CRIB, Largo Barsanti e Matteucci, 53 80125 Napoli, Italy*
[2] *Centro di Ricerca Interdipartimentale sui Biomateriali CRIB, Università di Napoli Federico II, Piazzale Tecchio, 80 80125 Napoli, Italy*
[3] *Dipartimento di Ingegneria Chimica dei Materiali e della Produzione Industriale, Università di Napoli Federico II, Piazzale Tecchio, 80 80125 Napoli, Italy*

***Abstract*—A simple, novel, strategy to design a multi-shell nanocapsule featuring an oil-core/hybrid polymer/silica-shell is reported. The final nanocarrier results to be a multifunctional platform, allowing the co-delivery of lipophilic and hydrophilic drugs, the confinement of tracers and contrast agents, the coating with PEG for antifouling activity and the interface decoration for active targeting.**

***Keywords*—silica nanocapsules, oil core, theranostic, multifunctional platform.**

I. Introduction

A GREAT deal of effort has been spent in searching new materials for the development of smart nanocarriers [1-3] with high stability, biocompatibility [4], [5] biodegradability,[5] together with high payloads of contrast agents and/or drugs,[4-6] selective cell targeting[7], [8] and release of active compounds at the molecular level.[2], [9-12]
It is widely recognised that, due to molecular complexity of many diseases (in particular, cancer, cardiovascular diseases, neurological disorders, malaria, and AIDS), smart combination of drugs can better modulate cell-signalling network and maximize therapeutic effect, reducing drug resistance as well as side effects.[13] Therefore, developing novel systems that could jointly encapsulate two different types (hydrophilic and/or hydrophobic) of drugs into a single vehicle is still a major challenge for smart drug delivery.[14]
To this end, a capsule-like configuration with different compartments to encapsulate both hydrophilic and hydrophobic agents is highly desirable. Furthermore, the presence of a silica gel outside layer could act as hydrophilic biocompatible compartment for hydrophilic drugs.
Here, we propose a synthetic strategy to obtain oil core-multilayered shell nanocapsules.[15] In situ deposition of tunable silica shells was carried out directly around a mono-disperse oil in water nano-emulsion system,[16-18] stabilized by polymer bilayers via LbL. The lipophilic core – with a size ranging from 100 to 200 nm – shows the ability to confine high payloads of lipophilic tracers (CdSe quantum dots, Nile Red) or drugs (Paclitaxel). The polymeric inter-layers confer stability to the emulsion and can be independently exploited if properly functionalized – as demonstrated by conjugating chitosan with fluorescein isothiocianate. The outer silica shell, was prepared by an in situ short (2-4 h) synthesis process, optimized to easily tune the thickness, and combines several properties. It has been coated with polyethylenglycol (PEG), thus showing antifouling properties. It can be loaded with hydrophilic drugs, as demonstrated by embedding sulforhodamine B in the porous structure. It results to be an optimal bio-interface for bio-conjugations and targeting, as demonstrated by the decoration of the PEGylated shell with the folate-doxorubicin adduct. Silica nanostructures were characterized by a variety of analytical and spectroscopic techniques and in vitro degradation of silica shell was also assessed (Fig. 1).

II. Experimental section

A. Nanoemulsion realization

A homogenous oil phase was realized by simply adding a certain amount of surfactant (Lipoid E 80, Lecithin (1.2g)) to a predetermined volume of soy-bean oil (20 ml) at 60 °C followed by sonication for a few min to homogenize and mix. Then, a pre-emulsion was prepared by a step-by-step addition of the as-prepared oil phase to a weighted amount of aqueous phase (Milli-Q water) so as to obtain a final concentration of 10 wt% in the oil phase. The mixture was thoroughly mixed through the immersion sonicator for a few minutes in a beaker. Finally, the pre-emulsions were passed at 1000 bar through a high-pressure homogenizer (Microfluidics M110PS) with a combination of individual cycles and continuous steps until a minimum size and PDI was reached. The nanoemulsion has also been loaded with several hydrophobic species by adding a miscible solvent – usually ethanol – containing the desired drug, dye or contrasting agent.

B. Biopolymer-silica shell realization

Monolayer of chitosan, or chitosan labelled with FITC, was deposited at a final concentration of 0.01% wt (at pH=4) whereas oil concentration was 1% wt. Bilayer emulsion was prepared by mixing 4 ml of monolayer to 2.5 ml of heparin solution (0.044% wt) in water.
After the formation of the bilayer, heparin carboxyl (–COOH) groups, were coupled to amino groups of APTS molecules, through EDS/NHS chemistry.[19] Reaction was allowed to proceed under stirring for 15 min at 4 °C in an ice bath. Then, reaction mixture was removed from ice bath and silica shell synthesis was initiated at room temperature using a modified Stöber method. In summary, the pH of dispersion was adjusted to 10.0 and a TEOS solution in 2-propanol was added drop-wise.[20] Stirring was continued for another 1 h at room temperature after which the dispersion was mixed with equal volumes of Milli-Q water and subjected to further stirring for variable timings, ranging from 5 min to 3 h, thus

obtaining a tunable shell thickness. To carry out PEGylation of the nanocapsules, equal volumes of an aqueous PEG solution 0.220 M, were added to the nanocapsule dispersion during the second step (1:2 dilution), thus obtaining a PEG grafting by means of a transesterification reaction.[21]

C. *Decoration with folate-doxorubicin adduct.*

Carboxyl group of FA was first activated with EDC, thanks to the formation of the corresponding isourea, that is more reactive then the carboxylic acid. [22] Briefly, FA (4.5 mg, 0.01 mmol) was dissolved in 5 ml of PBS and EDC (3.0 mg, 0.01 mmol) and NHS (23.3 mg, 0.20 mmol) were added and the resulting solution was stirred for 2h. PEGylated nanocapsules samples were added and stirred for 2h, at room temperature. The anticancer drug doxorubicin (2 mg) was dissolved in 2 ml of tris(hydroxymethyl) aminomethane buffer solution at pH 7, added to the nanocapsules solution and stirred over night at room temperature. Finally, the sample was dialyzed (MWCO 25 kDa) against water.

III. Results and discussions

Silica nanostructures were characterized by a variety of analytical and spectroscopic techniques like Raman Spectroscopy, Dynamic Light Scattering (DLS), Electron microscopy (SEM, TEM), and fluorescence microscopy (Confocal and STED).

The hydrodynamic diameter of the emulsion before and after deposition of the bilayer was 114.8 nm (PDI=0.055) and 145.4 nm (PDI=0.0) respectively. Samples collected at 1 and 3 h of seeded growth were submitted to Electron microscopy (FESEM, TEM) for morphological analysis, thus showing a continuous shell formed around the bilayer (Fig. 2). Samples with just 1 h of reaction had thin and continuous shells with a thickness of around 20 nm; particles after 3 h of reaction possessed a thicker continuous shell of about 45 nm. In order to confirm nano-confinement of solid hydrophobic materials in the oil core, we performed characterization with fluorescence microscopy. For this analysis, two different sets of experiments were designed. The first was carried out with hydrophobic CdSe quantum dots, thus proving the nano-confinement capability of these capsules, where in place of CdSe also other types or nanoparticles, such as gold or iron oxide (which can make these capsules suitable for X-ray or MRI imaging, depending on the applications) may be used. In the second experiment we used two different dyes: Nile Red to tag the oil and FITC to tag the chitosan layer, thus confirming that these nanocapsules can act as efficient nanocarriers for lipophilic drugs and demonstrating that the polymeric layers can be properly functionalized.

The negative surface charge limits their efficacy due to increased interaction with blood proteins which can result in rapid capture and removal by reticuloendothelial system. [13], [23] To potentially reduce these obstacles, the surface of nanocapsules was coated with PEG (MW 5000). PEG coating was also exploited for the decoration of the nanocapsules with a stable ligand, folic acid, conjugated with an anticancer drug, doxorubicin.

IV. Conclusion

One intriguing route for *in vivo* imaging, as well as drug delivery, is the use of core shell type structures that effectively allow confinement or protection of both tracers and/or drugs in the inner core. In the present work, an emulsion templated silica-biopolymer nanocapsule with antifouling properties was realized. The presence of different compartments confers to the final nanocarrier simultaneous functionalities, such as co-delivery of drugs, diagnostic and active targeting. Therefore, this is an innovative, low cost, effective and green way to produce new nanocarriers to be used in nanomedicine.

References

[1] D. Peer, J. M. Karp, S. Hong, O. C. Farokhzad, R. Margalit and R. Langer, Nature nanotechnology, 2007, 2, 751-760.

[2] F. M. Kievit and M. Zhang, Advanced Materials, 2011, 23, H217-H247.

[3] D.-E. Lee, H. Koo, I.-C. Sun, J. H. Ryu, K. Kim and I. C. Kwon, Chemical Society Reviews, 2012, 41, 2656-2672.

[4] R. M. Fratila, S. G. Mitchell, P. del Pino, V. Grazu and J. s. M. de la Fuente, *Langmuir*, 2014.

[5] L. Zhang, Y. Li and C. Y. Jimmy, Journal of Materials Chemistry B, 2014, 2, 452-470.

[6] M. Colombo, S. Carregal-Romero, M. F. Casula, L. Gutiérrez, M. P. Morales, I. B. Böhm, J. T. Heverhagen, D. Prosperi and W. J. Parak, Chemical Society Reviews, 2012, 41, 4306-4334.

[7] R. Rossin, S. Muro, M. J. Welch, V. R. Muzykantov and D. P. Schuster, Journal of Nuclear Medicine, 2008, 49, 103-111

[8] M. Shokeen, E. D. Pressly, A. Hagooly, A. Zheleznyak, N. Ramos, A. L. Fiamengo, M. J. Welch, C. J. Hawker and C. J. Anderson, ACS nano, 2011, 5, 738-747.

[9] X. Guo, C. Shi, G. Yang, J. Wang, Z. Cai and S. Zhou, Chemistry of Materials, 2014, 26, 4405-4418.

[10] F. Tang, L. Li and D. Chen, *Advanced Materials*, 2012, **24**, 1504-1534.

[11] V. P. Torchilin, *Advanced drug delivery reviews*, 2012, **64**, 302-315.

[12] M. Ding, N. Song, X. He, J. Li, L. Zhou, H. Tan, Q. Fu and Q. Gu, *ACS nano*, 2013, **7**, 1918-1928.

[13] S.-H. Hu, S.-Y. Chen and X. Gao, *ACS nano*, 2012, **6**, 2558-2565.

[14] C.-W. Su, C.-S. Chiang, W.-M. Li, S.-H. Hu and S.-Y. Chen, *Nanomedicine*, 2014, **9**, 1499-1515.

[15] R. Vecchione, G. Luciani, V. Calcagno, A. Jakhmola, B. Silvestri, D. Guarnieri, V. Belli, A. Costantini and P. A. Netti, *Nanoscale*, 2016. (DOI: 10.1039/C6NR01192F)

[16] S. Sivakumar, V. Bansal, C. Cortez, S. F. Chong, A. N. Zelikin and F. Caruso, *Advanced Materials*, 2009, **21**, 1820-1824.

[17] R. Vecchione, U. Ciotola, A. Sagliano, P. Bianchini, A. Diaspro and P. Netti, *Nanoscale*, 2014, **6**, 9300-9307.

[18] I. Fotticchia, T. Fotticchia, C. A. Mattia, P. A. Netti, R. Vecchione and C. Giancola, *Langmuir*, 2014, **30**, 14427-14433.

[19] B. Silvestri, A. Pezzella, G. Luciani, A. Costantini, F. Tescione and F. Branda, *Materials Science and Engineering: C*, 2012, **32**, 2037-2041.

[20] F. Branda, B. Silvestri, G. Luciani and A. Costantini, *Colloids and Surfaces A: Physicochemical and Engineering Aspects*, 2007, **299**, 252-255.

[21] F. Branda, B. Silvestri, G. Luciani, A. Costantini and F. Tescione, *Colloids and Surfaces A: Physicochemical and Engineering Aspects*, 2010, **367**, 12-16.

[22] B. Silvestri, D. Guarnieri, G. Luciani, A. Costantini, P. Netti and F. Branda, *Journal of Materials Science: Materials in Medicine*, 2012, **23**, 1697-1704.

[23] F. Alexis, E. Pridgen, L. K. Molnar and O. C. Farokhzad, *Molecular pharmaceutics*, 2008, **5**, 505-515

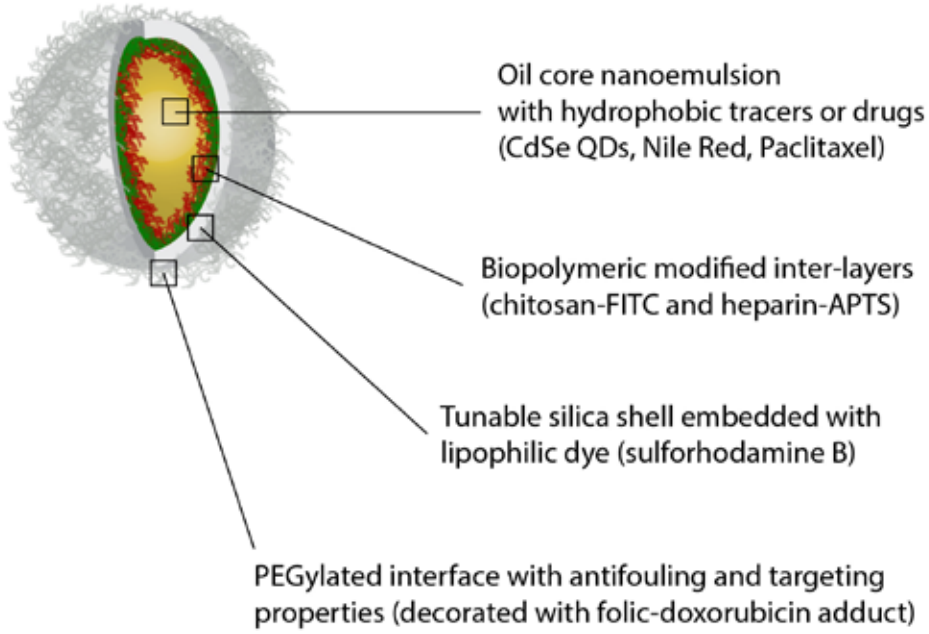

Fig. 1. Schematic representation of the emulsion templated silica-biopolymer nanocapsules for theranostic and co-delivery. Each compartment can be exploited to add functionalities to the final nanocarrier

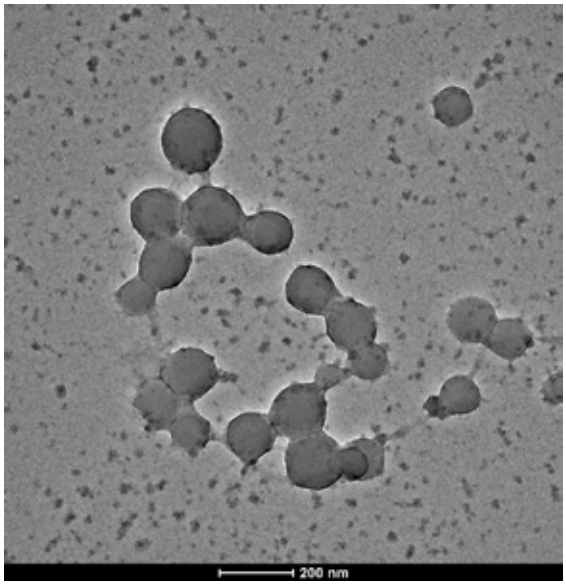

Fig. 2. TEM micrograph of silica nanocapsules after 1 h of seeded growth time. Sample has been stained with OsO4 vapors.

A portable device based on a custom IC for impedance measurement in neural interfaces.

C. Carboni[1], R. Puddu[1], L.Bisoni[1], L. Raffo[1] and M. Barbaro[1]
[1] *University of Cagliari*

***Abstract*—A multi-channel device able to measure neural impedances is proposed in this paper. The system is composed of an analog front-end based on a custom designed IC realized in a CMOS 0.35 µm process and of a digital back-end implemented in a FPGA. The device generates a current by means of a current DAC and acquires the correspondent voltage drop across the impedance, using a sigma delta converter. An user-friendly GUI implemented in LabView environment allows the user to configure the system and to acquire the data. The device was realized and successfully tested with electrical tests showing a capability of measuring impedances in the range from 10kΩ to 100kΩ.**

***Keywords*—Biomedical device, bioimpedance measurement, neural interface.**

I. Introduction

THE human machine interfaces have been deeply investigated by the researcher in the last decades. Many systems have been proposed to record and stimulate the neural activity, both in the Central Nervous System (CNS) and in the Peripheral Nervous System (PNS) [1, 2]. The possibility to acquire the neural signals and to elicit the neurons with electrical signals, in fact, opens interesting perspectives in the treatment of a large number of diseases. Neural interfaces (NI) can be useful in the therapy of degenerative illness of the neural system such as Parkinson disease and multiple sclerosis, and they have also been used in patients affected by epilepsy, in patient with permanent damages to spinal cord and in neuroprosthetics [3, 4, 5, 6]. Several different electrodes have been proposed for neural applications [7, 8], they are characterized by impedances that can range from 10 kΩ to 1 MΩ [9]. Nowadays, the research trend is to try to reduce the impedance contact to few kΩ. Nevertheless, the electrochemical reactions at the interface with the tissue cause the impedance increase with the time, degrading the recording/stimulation performance in long term implant. For this reason, a key factor for the NI is represented by the electrode-tissue impedance measurement. Evaluating the impedance before the stimulation/recording session in fact, allows, on one hand, to set properly the device parameters such as the gain in the recording and the pulse amplitude in the stimulation and, on the other hand, to monitor the eventual degradation of the electrode inserted in the nerves. Several method have been proposed for bioimpedance measurements. In [10], a device based on a Commercial Off-The-Shelf (COTS) sine wave generator and a gain-phase detector, has been used to evaluate the impedance of a cuff electrode. While in [11], in a complex multi-channel ASIC for cortical neural recording with MEA electrodes, a square-current generator for impedance measurement has been embedded. In this paper we present a system able to measure neural impedances in the range 10 kΩ – 100 kΩ. The device has been implemented in an IC realized in a CMOS 0.35 µm technology and it is embedded in a wider biomedical interface for neural recording and stimulation. The device has been successfully evaluated by means of electrical test with laboratory equipment confirming the capability of measuring impedances in the range of interest.

II. System Overview

In Fig. 1, the system overview is presented. The device is composed of two main parts: a custom integrated IC and a digital control module implemented in a FPGA. The chip includes 8 different channels for measuring the impedance of multi-channel electrodes. Each channel has two main parts: a current generator, that injects a programmable current into the electrode site, and a voltage recorder able to measure the voltage drop between the active site and the reference. The device can be used in two different operating mode, by changing the reference current of the current generator. In the first mode, a I_{Bmax} = 2.1 µA current is used, and impedances in the range 10kΩ - 50kΩ can be measured, while with the second operating mode (I_{Bmin} = 20nA), it is possible to evaluate impedances from 50kΩ to 100kΩ. The digital module embedded on chip, besides handling the communication with the FPGA with an SPI link, can also configure the chip according to the settings chosen by the user in the Graphical User Interface (GUI) on PC. The FPGA manages the communication between the chip (SPI interface) and the control PC (Ethernet link). The whole system can be easily programmed by the PC by means of an user friendly GUI developed in LabView environment. The results can be displayed in real time in the PC and can be stored in a file for further processing. A picture of the whole system is shown in Fig. 2, the main blocks have been highlighted: on the right the test board that hosts the custom designed chip (indicated with a white box) can be observed, in the center the red box shows the FPGA and finally on the left the GUI has been indicated with a green box.

III. Experimental Results

The chip layout is reported in Fig. 3, the total area occupation is *3.7 mm x 4.1 mm*. It was designed using a special care on track minimization, realizing the matched parts symmetrically and using a common centroid approach. Considering that a fully differential topology was used, a layout that guarantees a good matching is, in fact, of crucial importance. The device has been tested in DC conditions modelling the electrode-impedance tissue with a simple

Resistance. Different values have been chosen to cover the most likely values at the electrode-tissue interface in both operating modes (I_{Bmax} and I_{Bmin}) available for the proposed device. For each test a known DC current value has been injected into the load, and the corresponding voltage drop across the resistance has been measured. Increasing the injected current by steps of 2.1 μA and 20 nA respectively for the first and the second working range, it has been possible to estimate the load resistance by measuring the slope of the linear interpolation of the collected data. Fig. 4 shows the results achieved for different resistance values (5.6 kΩ, 15 kΩ, 27 kΩ, 39 kΩ and 56 kΩ) using the 2.1 μA reference current. The voltage values versus the injected current measured have been reported, for each series of data the linear interpolation has been calculated and plotted, the corresponding equation is reported in the legend. The equation slope corresponds to the estimated Resistance value. As reported in Table 2, the system is able to detect the load used with an error lower than 15% for values higher than 10kΩ.

TABLE I
DC IMPEDANCE MEASUREMENT FOR THE RANGE 10KΩ-56KΩ

Nominal Value	*Measured Value*	*Error*
5.6 kΩ	7.6 *kΩ*	35%
15 kΩ	17.3 *kΩ*	15%
27 kΩ	28.8 *kΩ*	6.7%
39 kΩ	39.2 *kΩ*	0.5%
56 kΩ	50.2 *kΩ*	10%

The same tests have been performed using the second operating range of the device (i.e. the 20 nA current) in this way the range 56 kΩ – 100 kΩ can be covered. In Fig. 5 the results are shown for the resistance value 56 kΩ; 68 kΩ; 82 kΩ and 100 kΩ, the linear interpolation allows to estimate the resistance values giving the results summarized in Table 3, in all cases the error is lower than 10% allowing a good estimation of the measured impedance.

TABLE II
DC IMPEDANCE MEASUREMENT FOR THE RANGE 56KΩ-100KΩ

Nominal Value	*Measured Value*	*Error*
56 kΩ	56 *kΩ*	<1%
68 kΩ	68 *kΩ*	<1%
82 kΩ	75 *kΩ*	8.5%
100 kΩ	92 *kΩ*	8%

IV. Conclusion

An IC based system for neural impedance measurements has been designed and tested. The proposed device is able to measure impedances in the range 10kΩ - 100kΩ. The chip is intended to be used with multi-channel electrodes and includes eight separate channels, each of which is composed by a current generator and by a recording module based on a sigma delta converter. The chip occupies a total area of 3.7 mm x 4 mm and consumes a power of 16 mW. The device has been successfully tested, confirming the capability to detect impedance in the range of interest with an maximum error of 15%.

Acknowledgement

This work was partially funded by MIUR (Italian Ministry of Education, University and Research) through project HANDBOT (PRIN 2010/2011), by Italian Ministry of Health through project NEMESIS and by the European Commission, ICT-2013.9.6 FET Proactive: Evolving Living Technologies (EVLIT), through project NEBIAS (n.611687).

References

[1] R. R Harrison and C. Charles, "A low-power low noise cmos amplifier for neural recording applications," IEEE Journal of Solid-State Circuits, vol. 38, pp. 958–965, 2003.

[2] R. Rieger, M. Schuettler, D. Pal, C. Clarke, P. Langlois, J. Taylor, and N. Donaldson, "Very low-noise eng amplifier system using cmos technology," IEEE Transactions on Neural Systems and Rehabilitation Engineering, vol. 14, pp. 427–437, 2006.

[3] E. Pereira, A. Green and D. Nandi, "Deep brain stimulation: indications and evidence," Expert Rev Med Devices, vol. 4, pp. 591–603, 2007.

[4] W. Liu, K. Vichienchom, M. Clements, S. DeMarco, C. Hughes, E. McGucken, M. Humayun, E. D. Juan, J. Weiland, and R. Greenberg, "A neuro-stimulus chip with telemetry unit for retinal prosthetic device," IEEE Journal of Solid-State Circuits, vol. 35, pp. 1487–1497, 2000.

[5] G. Loeb, F. Richmond, D. Olney, T. Cameron, A. Dupont, K. Hood, R. Peck, P. Troyk, and H. Schulman, "Bionic neurons for functional and therapeuticelectrical stimulation," IEEE Engineering in Medicine and Biology Society, 1998.

[6] J. VonArx and K. Najafi, "A wireless single-chip telemetry-powered neural stimulation system," IEEE Journal of Solid-State Circuits, pp. 214–215, 1999.

[7] X. Navarro, T. Krueger, N. Lago, S. Micera, T. Stieglitz, and P. Dario, "A critical review of interfaces with the peripheral nervous system for the control of neuroprostheses anf hybrid bionic systems," J. Peripheral Nervous System, vol. 10, pp. 229–258, 2005.

[8] T. Boretius, A. Pascual-Font, E. Udina, T. Stieglitz, and X. Navarro, "Biocompatibility of chronically implanted transverse intrafascicular multichannel electrode (TIME) in the rat sciatic nerve," IEEE Transaction on Biomedical Engineering, vol. 58, no. 8, pp. 2324–2332, 2011.

[9] R. R. Harrison, "A versatile integrated circuit for the acquisition of biopotentials," Custom Integrated Circuits Conference, pp. 115–122, 2007.

[10] Y.-T. Li, J.-J. Chen, and C.-C. Lin, "Application of implantable wireless biomicrosystem for monitoring electrode-nerve impedance of animal after sciatic nerve injury," in Circuits and Systems, 2008. ISCAS 2008. IEEE International Symposium on, May 2008, pp. 1112–1115.

[11] C. Lopez, A. Andrei, S. Mitra, M. Welkenhuysen, W. Eberle, C. Bartic, R. Puers, R. Yazicioglu, and G. Gielen, "An implantable 455-active-electrode 52- channel cmos neural probe," Solid-State Circuits, IEEE Journal of, vol. 49, no. 1, pp. 248–261, Jan 2014.

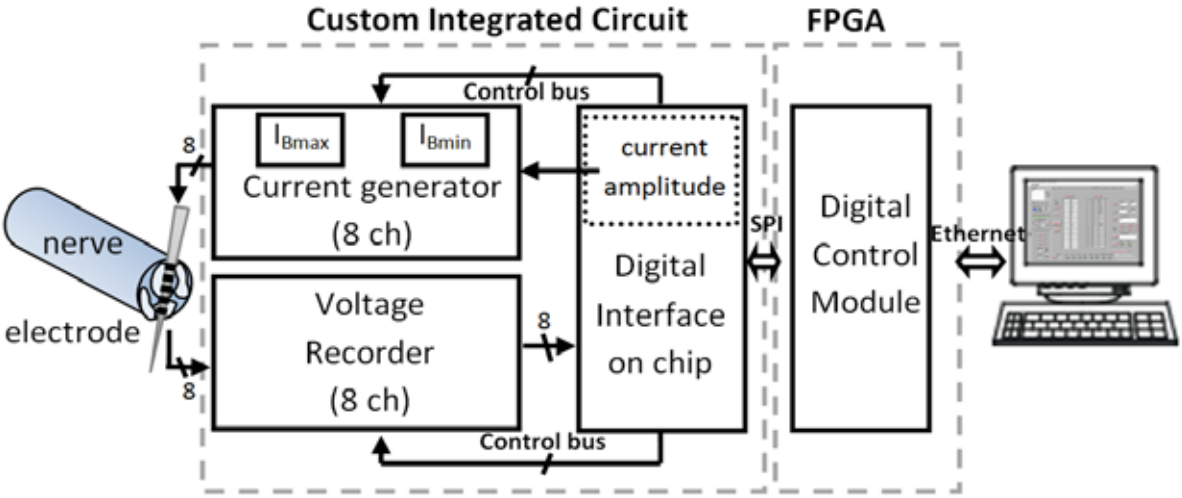

Fig. 1: System architecture

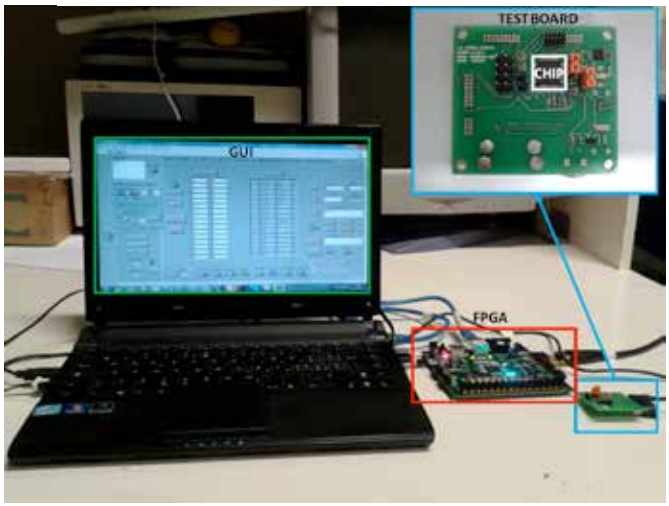

Fig. 2: System picture

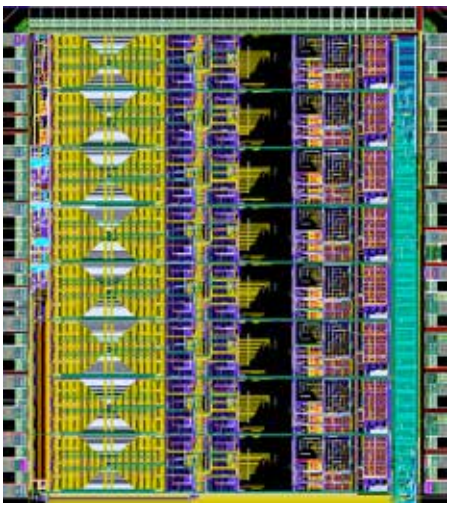

Fig. 3: Chip Layout

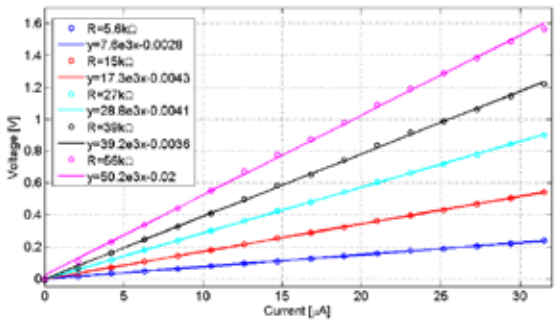

Fig. 4: DC Impedance measurement for the range 10kΩ - 56kΩ: data collected and linear interpolation

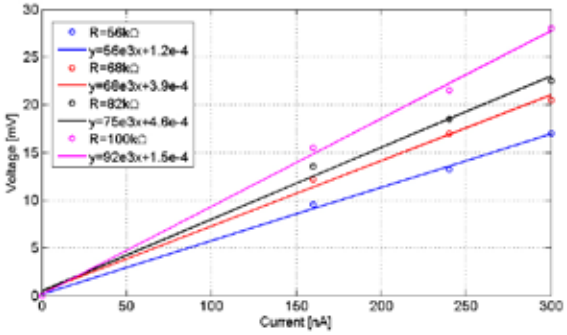

Fig. 5: DC Impedance measurement for the range 56kΩ - 100kΩ: data collected and linear interpolation

Non-invasive glucose sensor based on enzyme functionalized organic transistor

M. Celentano[1], R. Vecchione[1], A. Jakhmola[1], P. A. Netti[1]
[1] *Center for Advanced Biomaterials for Health Care – IIT@CRIB – Largo Barsanti e Matteucci, Napoli, Italy*

***Abstract*—We developed a disposable, hybrid organic/inorganic sensor for D-glucose based on a porous PEG/Polyaniline/Gold Nanowires composite transistor functionalized with Glucose Oxidase Enzyme (Gox). This sensor responds to glucose in the range 1μM – 100 mM, which includes typical glucose concentrations in human blood and saliva. The devices could represent a general strategy to bloodless glucose monitoring by detecting low concentrations of glucose in saliva.**

***Keywords*—D-Glucose sensor, transistor, heterogeneous composite, porous polymer matrix.**

I. Introduction

Diabetes mellitus is a metabolic disorder characterized by a chronic hyperglycemia resulting from defects in insulin action. This chronicity is correlated with long-term damage, dysfunction, and failure of various organs (eyes, kidneys, nerves, heart, and blood vessels). Therefore, the development of high sensitive glucose sensors is a mandatory need. Heterogeneous conducting composites have been object of extensive studies in the last decades. The combination of conducting polymers with inorganic materials having different properties opens up new avenues for the development of innovative hybrid materials with interesting features.[1-4]

Polyanilines have been extensively studied in recent years due to many advantages among other conducting polymers such as low cost, easy synthesis, range of electrical conductivities and unique reversible proton doping-dedoping processes.[5]

At the same time, gold nanoparticles have been applied both in biology and in technology due to their tunable chemical-physical properties. Moreover, they can be easily conjugated with biological molecules.[6] Combination of organic and inorganic materials having biological moieties could be potentially applied in biosensor devices.[7]

We report the realization and characterization of a new heterogeneous conducting organic/inorganic material, easily functionalizing with Glucose Oxidase Enzyme, and its implementation in a high sensitive glucose sensor.

II. Methods and Materials

$PEG\text{-}DA_{250}$ (macromer), Pluronic F68 (surfactant), camphor sulfonic acid (CSA), aniline hydrochloride, ammonium peroxide, chloroauric acid and sodium citrate were purchased from Sigma Aldrich, photoiniziator darocure 1173 from Ciba.

AC electrical response of the composites was investigated thought Impedance Spectroscopy Analysis using a two probe method formed by two aluminium disc as electrodes connected to an AUTOLAB PGSTAT302N (potentiostat/galvanostat) equipped with a FRA32M module (frequency response analysis module). Impedance spectra were recorded in potentiostatic mode with an amplitude of 0.01V and frequencies ranging from 100kHz to 0.01Hz between the electrodes. For each measurements 3 reading and 50 data points (logarithmic frequency step) per reading were collected. The least-square optimization method was used to fit the measured impedance data to an electrical equivalent circuit model (brick layer model [8]). Morphological characterizations were carried out by TEM (FEI Tecnai G2 transmission electron microscope at 200 kV and images were acquired by Eagle 2K CCD-HS camera) and SEM (Ultra Plus Zeiss Germany, FEG-SEM). Elemental microanalysis was carried on composites using SEM equipped with EDS detector (Oxford Instruments) Transistor sensor prototypes were realized using two PEDOT:PSS strips as gate and source-drain channels, while heterogeneous composite materials were used as transducer. Transistor sensors were tested with control (phosphate buffer) and D-glucose solutions in the concentration range from 1μM and 100mM.

III. Synthesis

Porous materials were prepared using a reverse micro-emulsion strategy. PANI-CSA, prepared with the standard method [9], was dispersed at different weight percentage in PEG-DA by sonication, after that the photo-iniziator darocure 1173 was added (2% w/w). A water buffered solution (PBS, ph= 7.4, 100mM) of Pluronic F68 (180 mg/mL) and Gold Nanowires (NWs, obtained with the Turkevich route [10]) or Gox, or both, was added to PEG-DA/PANI-CSA dispersion at several weight percentages. The resulting dispersion was sonicated and photo-polymerized under UV light to obtain a solid porous material.

IV. Results and Discussion

In this work conducting polyaniline doped with was dispersed into PEG porous matrix containing gold nanowires in network form.

The electron microscopy (TEM and SEM) of the composites reveals a porous morphology. The AC electrical behavior was also studied by Impedance Spectroscopy. Electrical conductivity of the heterogeneous composite, extrapolated from impedance data, shown a changing from insulator to conducting behavior. The relation among composition, morphology and AC electric response was taken into account.

Morphological and spectroscopic analysis have revealed that the gold nanowires were included only in the pores, while the

polyaniline was dispersed in the PEG matrix. When both these two fillers were present in the matrix, at the same concentration of the previous cases, the percolation threshold was surpassed. Probably, the two fillers exerted a synergic effect on the AC conductivity. Indeed, the pores may be electrically interconnected through the polyaniline chains inside the PEG matrix.

The composite was functionalized with Glucose Oxidase Enzyme and integrated as transducer in a full-organic transistor device. The device shows a good D-Glucose response in the range 1μM – 100 mM (Figure 1), which includes typical glucose concentrations in human blood and saliva. The devices represent a new general strategy to bloodless glucose monitoring by detecting low concentrations of glucose in saliva. Furthermore, the composites could be easily functionalized with other Enzymes to obtain sensors for specific metabolites.

V. CONCLUSION

A new heterogeneous porous composite (porous PEG/PANI/gold NWs composite) was realised and electrically and morphologically characterized. The composite shown a good electrical conductivity and could be easily conjugated with the Glucose Oxidase Enzyme. The composite was integrated in a full-organic transistor device and tested as D-Glucose sensor. This sensor device shown a good response to glucose molecules in the range 1μM – 100 mM, which includes typical glucose concentrations in human blood and saliva. The sensor could be applied to bloodless glucose monitoring by detecting low concentrations of glucose in saliva.

REFERENCES

[1] C.G.Wu, D.C. Degroot, H.O. Marcy, J.L. Schindler, C.R. Kannewurf, Y.J. Liu, W. Hirpo, M.G. Kanatzidis, Chem. Mater. 8 (1996) 1992.
[2] T.A. Kerr, H. Wu, L.F. Nazar, Chem. Mater. 8 (1996) 2005.
[3] E.R. Hitzky, P. Aranda, B. Casal, J.C. Galvan, Adv. Mater. 7 (1995) 180.
[4] W.J. Bae, K.H. Kim,W.H. Jo, Y.H. Park, Mac-romolecules 37 (2004) 9850.
[5] Trivedi, D. C., 1997. “Handbook of Conducting Molecules and Polymers”, (ed.) by Nalwa, H. S., John Wiley and Sons 2:505.
[6] P. M. Tiwari, K. Vig, V. A. Dennis and S. R. Singh, Nanomaterials, 1, 31-63 (2011).
[7] T. A. Kumar , E. Capua , M. Tkachev , S. N. Ad-ler, and R. Naaman, Adv. Funct. Mater., 24(37), 5833-5840 (2014).
[8] Barsoukov E., Macdonald J.,“Impedance Spectroscopy: Theory, Experiment, and Applications” , Wiley, 2nd Edition, 2005.
[9] Heeger, Alan (2001). "Nobel Lecture: Semiconducting and metallic polymers: The fourth generation of polymeric materials". Reviews of Modern Physics 73 (3): 681.
[10] Turkevich, J., Stevenson, P.C., Hillier, J.: A study of the nucleation and growth processes in the synthesis of colloidal gold. Discuss. Faraday Soc. 55–75, (1951)

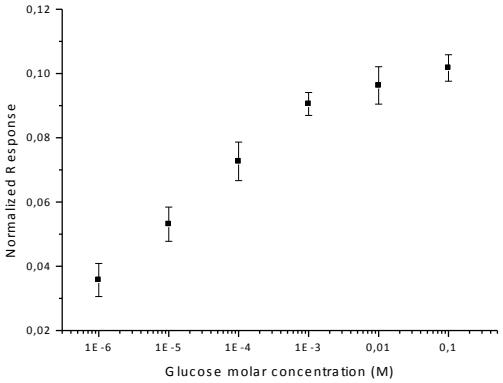

Fig. 1. Normalized response of heterogeneous sensor device at different D-Glucose molar concentrations.

CardioMon: an implantable catheter with a 3D gyro for continuous monitoring of cardiac rotation

L. Cercenelli[1], B. Bortolani[1], and E. Marcelli[1]
[1]*Laboratory of Bioengineering, DIMES-Experimental Diagnostic and Specialty Medicine Dept., University of Bologna, Bologna, Italy*

***Abstract*— Cardiac rotation is a sensitive indicator of cardiac performance. We present CardioMon, a newly developed implantable catheter equipped with a 3D MEMs gyro to provide the continuous monitoring of cardiac rotation.**

Preliminary lab tests on CardioMon catheter were performed to assess reliability of angular velocity signals measured by the 3D MEMs gyro included in the catheter.

***Keywords*—cardiac rotation, 3D MEMs gyro, implantable sensor, cardiac monitoring.**

I. Introduction

CARDIAC torsion is the wringing motion of the heart around its long axis created by oppositely directed apical and basal rotations and is determined by contracting myofibers which are arranged in opposite directions between the subendocardial and subepicardial layers [1]. This motion is essential for regulating cardiac systolic and diastolic functions, and changes in the pattern or amplitude of cardiac rotation have been associated with various cardiovascular diseases, including Heart Failure (HF), one of the major health problem worldwide [2].

Recent advances in echocardiography techniques [3], [4] have allowed for quantification of cardiac rotation; however these examinations are used on an intermittent basis and are not addressed to continuous monitoring of patient status.

We present CardioMon, a novel implantable sensorized catheter equipped with a tri-axis (3D) MEMs gyro for the continuous monitoring of cardiac rotation. Starting from our previous results on using an "off-the-shelf" single-axis (1D) gyro for epicardial assessment of apical rotation in sheep [5], [6], we assembled an implantable sensorized catheter that may detect rotation at endocardial sites.

Cardiac rotation monitoring by an implantable gyro holds the premise for early detection of impairment in cardiac mechanics, that may predict decompensation in HF patients and prevent recurrent hospitalizations, by tailoring an effective drug therapy on the basis of gyro detections.

II. Materials and Methods

A. CardioMon catheter

The CardioMon catheter is composed of a sensorized capsule in the catheter tip and a flexible main body including the electrical connections required for the sensor (Fig.1).

The capsule, a cylindrical box in Delrin (Ø=4.4mm, L=6.6mm), includes a capacitive 3D MEMs gyro (CMR3100-D01, Murata Electronics Oy, Kyoto, Japan), which is a very small size sensor (3.0x3.0x0.9mm) with a detection range of ±500 °/s and a digital SPI/I_2C interface for output reading. The capsule contains also a miniaturized printed circuit board (PCB) designed to be housed in the capsule. On one end, the capsule is provided with a titanium screw to allow its anchoring to the endocardium. The capsule is also provided with a removable silicone flange with two holes to allow it to be sewn on epicardial sites (Fig.1).

The flexible main body of the catheter is made of a standard silicon tubing (Nusil MED-4750) for implantable electrocatheters and it includes 4 spiral wound insulated wires, connected to the pin terminals of the PCB in the capsule. A standard stylet (steel AISI 304, Ø=0.4 mm) for inserting the catheter is also provided (Fig.1).

B. Data Reading Unit

We assembled a data reading unit to implement the I_2C digital communication protocol required for the output reading of the 3D gyro in the CardioMon catheter. The I_2C interface was selected (rather than SPI protocol) since it allows communication with a minimum of 4 lines (Vdd, GND, SCL, SDA), thus minimizing the total number of wires to be included in the silicon tubing of the catheter. The reading unit is composed of a microcontroller board (Arduino Mega ADK 5V/16MHz, Arduino, Italy), three adapters to adjust voltage levels between the Arduino board and the 3D gyro, and three D/A converters, one for each sensitive axis of the gyro. The analog output signals from the reading unit are then collected and analyzed using a data acquisition system (MP100, Biopac System, Goleta, CA, USA).

C. Functional lab tests

A mechanical simulator was used to test CardioMon catheter. The simulator is composed of a DC brush motor (Escap 17N78-210E-F16, Portescap, West Chester, PA, USA), controlled by a programmable automation controller (CompactRIO, National Instruments, Austin, TX, USA). A supporting board, anchored to the rotating shaft of the motor and rotating with it, is used to position the sensors to be tested (Fig.2).

An "off-the-shelf" single-axis gyro (1D gyro) with analog output (ENC-03R Murata Manufacturing Co., Kyoto, Japan) was used as reference sensor.

Both the CardioMon catheter including the 3D gyro and the 1D gyro were mounted on the supporting board and fixed in stable position by means of adjustable clips attached to the board (Fig.2).

The simulator was programmed to provide target angular velocities (V_T) in both clockwise and counterclockwise directions (V_{T+} = +200°/s and V_{T-} = -100°/s, respectively) that may be representative of cardiac twist velocities (200°/s for a tachycardia condition, 100°/s for sinus rhythm).

To evaluate the single-axis response of the 3D gyro, the CardioMon catheter was sequentially arranged on the

supporting board in order to align each detecting *x*-, *y*-, *z*-axis parallel to the rotating shaft of the motor ("X alignment", "Y alignment", "Z alignment"), while the 1D gyro remained in the same position (Fig.2). For each alignment, five repetitions of the sequence V_0 / V_{T+} / V_T- / V_0 (with V_0 = stop motion) were carried out, while angular velocity signals were collected simultaneously from the two sensors.

D. Data collection and calculations

For each alignment of the 3D gyro, the three components of angular velocities (*Vx, Vy, Vz*) were collected and the modulus of angular velocity ($\boldsymbol{V_{3Di}}$, with *i*=X, Y, Z alignment) was calculated as in Eq. (1).

$$\boldsymbol{V_{3Di}} = \sqrt{Vx^2 + Vy^2 + Vz^2} \qquad (1)$$

For the 1D gyro, the single-axis velocity (V_{1D}) was recorded. Steady-states velocities (corresponding to the set target velocities: V_{T+}, V_T-) were considered and were reported as Mean±SD, obtained by averaging angular velocities from the five repetitions of the test sequence.

Noise level was estimated for the 3D gyro (N_{3Di}, with *i*=X, Y, Z alignment) and for the 1D gyro (N_{1D}): in both cases the noise was calculated as peak-to-peak amplitude of velocity signals at V_0 condition (Fig.3).

Measurement errors were defined, for both the 3D gyro (E_{3Di}, with *i*=X, Y, Z alignment) and the 1D gyro (E_{1D}), as in Eq. (2) and Eq. (3).

$$E_{3Di} = mean\left\{\left(V_{3Di+} - V_{T+}\right); \left(V_{3Di-} - |V_{T-}|\right)\right\} \qquad (2)$$

$$E_{1D} = mean\left\{\left(V_{1D+} - V_{T+}\right); \left(|V_{1D-}| - |V_{T-}|\right)\right\} \qquad (3)$$

TABLE I
MEASUREMENTS PROVIDED BY 3D GYRO (CARDIOMON CATHETER) AND BY 1D GYRO

		3D MEMs Gyro (CardioMon catheter)						*1D Gyro (control)*		
	V_T[°/s]	Vx[°/s] *(M±SD)*	Vy[°/s] *(M±SD)*	Vz[°/s] *(M±SD)*	$\mathbf{V_{3Di}}$ [°/s] *(M±SD)*	E_{3Di} [°/s]	N_{3Di} [°/s]	$\lvert V_{1D}\rvert$[°/s] *(M±SD)*	E_{1D}[°/s]	N_{1D}[°/s]
X alig.	V_{T+} = **200.0**	*200.7±3.7*	0.1±3.4	1.0±5.4	**200.8**±3.7	2.5	6.7	**204.6**±3.3	3.5	8.8
	V_T- = **-100.0**	*-103.9±2.8*	-2.7±5.0	-1.6±4.2	**104.1**±2.8			**101.0**±3.1		
Y alig.	V_{T+} = **200.0**	-3.9±8.0	*200.2±8.9*	1.0±8.9	**201.1**±7.9	2.3	7.1	**206.7**±2.2		
	V_T- = **-100.0**	1.4±1.8	*-103.5±1.6*	-0.9±1.9	**103.6**±1.6			**98.0**±5.5		
Z alig.	V_{T+} = **200.0**	8.7±1.7	-6.5±8.8	*190.7±4.5*	**191.5**±4.3	5.8	7.4	**202.9**±3.7		
	V_T- = **-100.0**	-14.1±3.6	-0.9±6.1	*-95.0±1.4*	**96.9**±3.1			**103.8**±3.2		

X, Y, Z-alig.= alignment of *x, y, z*-axis of the 3D gyro parallel to the rotating shaft of the simulator; V_T= target angular velocities; $\mathbf{V_{3Di}}$= modulus of angular velocity measured by the 3D gyro (*i*=X, Y, Z alignment); E_{3Di}= calculated error for the 3D gyro (*i*=X, Y, Z alignment); N_{3Di}= estimated noise for the 3D gyro (*i*=X, Y, Z alignment); V_{1D}= single-axis angular velocity for the 1D gyro; E_{1D}= calculated error for the 1D gyro; N_{1D}= estimated noise for the 1D gyro.

III. RESULTS

Angular velocity signals provided by the 3D gyro encapsulated in the CardioMon catheter were reliable and comparable with signals obtained with the "off-the-shelf" 1D gyro. Examples of the recorded signals are reported in Fig.3.

The output velocities from the 3D gyro and the 1D gyro were comparable (Table I): differences between $\boldsymbol{V_{3Di}}$ and the corresponding V_{1D} fell within noise levels estimated for both the 3D gyro (N_{3DX}=6.7°/s, N_{3DY}=7.1°/s, N_{3DZ}=5.4°/s) and the 1D gyro (N_{1D} =8.8°/s).

For all X, Y, Z alignments, measurement errors (E_{3DX}, E_{3DY}, E_{3DZ}) were below the corresponding estimated noise level N_{3DX}, N_{3DY}, N_{3DZ} (Table I).

IV. CONCLUSION

The newly developed CardioMon catheter including the 3D MEMs gyro was reliable and accurate in detecting angular velocities within the range of cardiac twisting velocities.

The novel device can provide information that complement standard cardiac function indices, offering new diagnostic and therapeutic perspectives.

Animal experiments will be planned to further evaluate the CardioMon catheter in *in vivo* environment and to investigate possible implantation sites for the catheter within the heart.

REFERENCES

[1] C.C. Beladan, A. Călin, M. Roşca, C. Ginghină, B.A. Popescu, "Left ventricular twist dynamics: principles and applications," *Heart*, vol. 100(9), pp. 731-40, 2014.

[2] D. Mozaffarian et al, "Heart disease and stroke statistics--2015 update," *Circulation,* vol.131(4), pp. e29-322, 2015.

[3] M. Biswas *et al*, "Two-and three-dimensional speckle tracking echocardiography: clinical applications and future directions," *Echocardiography*, vol. 30(1), pp.88-105, 2013.

[4] J. Gorcsan, H. Tanaka, "Echocardiographic Assessment of Myocardial Strain," *JACC*, vol.58(14), pp.1401–13, 2011.

[5] E. Marcelli, G. Plicchi, L. Cercenelli, F. Bortolami, "First experimental evaluation of cardiac apex rotation with an epicardial Coriolis force sensor," *Asaio J*, vol. 51(6), pp.696-701, 2005.

[6] L. Cercenelli, E. Marcelli, "Cardiac apex rotation assessed by an implantable gyro sensor: correlation with a LV pressure-derived myocardial performance index in experimentally induced ischemia" *JMMB*, vol.15(2), pp.1540013-1 - 1540013-6, 2015.

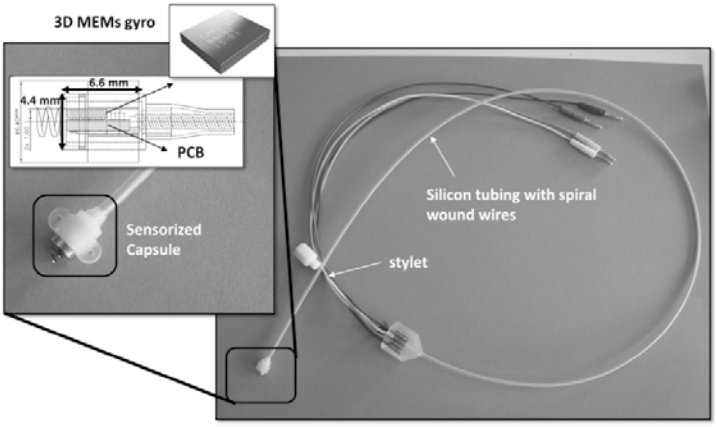

Fig. 1. The CardioMon catheter.

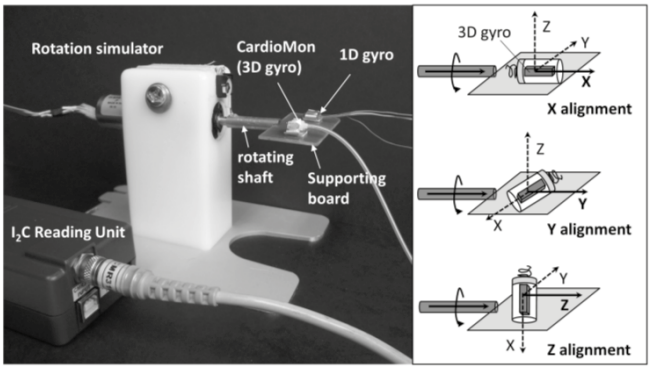

Fig. 2. Set-up for lab functional tests.

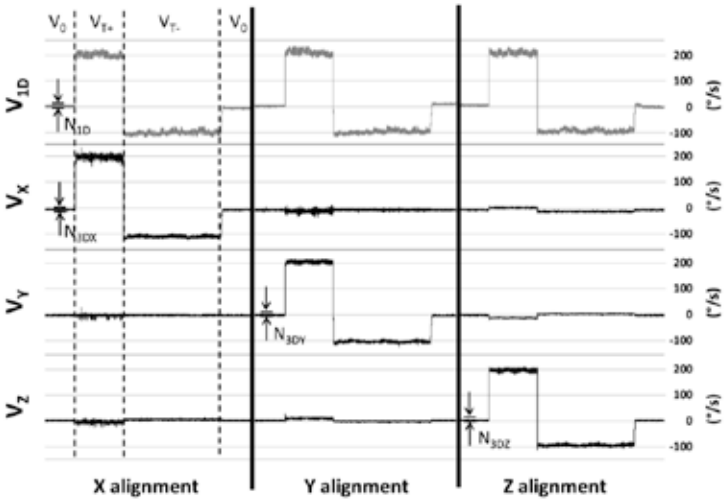

Fig. 3. Angular velocity signals recorded with the 1D gyro (grey curve) and with the 3D gyro included in the CardioMon catheter (black curves); N_{1D}= estimated noise for the 1D gyro; $N_{3Di\ (i=X,\ Y,\ Z\ alignment)}$= estimated noise for the 3D gyro.

Microwave spectroscopy for biomarker detection

R. Chignola[1], P. Donato[2], R. Massa[2], E. Milotti[3]

[1]Dipartimnto di Biotecnologie, Università di Verona
[2]Dip. Fisica " Ettore Pancini" Università di Napoli Federico II e INFN Sezione di Napoli
[3]Dipartimento di Fisica, Università di Trieste e INFN, Sezione di Trieste

***Abstract*— Lactic acid is considered a biomarker for several pathologies. The aim of this work is to evaluate the feasibility of a real time measurement of lactic acid levels in a tissue under test by means of its dielectric characterization. We present preliminary results of broad-band measurements (0.5 GHz-4.5 GHz) of the permittivity of lactic acid solutions (in water or culture medium) carried out with the truncated coaxial cable technique. The obtained data are encouraging and show a correlation between conductivity and concentration and/or pH of the solution.**

***Keywords*—dielectric measurements, lactic acid, biomarker, microwaves.**

I. Introduction

THIS work presents preliminary results on the feasibility of real time monitoring of lactic acid concentrations by dielectric measurements at microwave frequencies. Lactic acid levels are considered a metabolic biomarker of several pathologies. For instance, it has been proposed as an early marker of brain injury in inflicted traumatic brain [1], as a metabolic biomarker of prostate cancer [2] or of the development of nodal or distant metastases in head-and-neck cancer patients [3], as a predictive value in infants with perinatal asphyxia in the early postnatal period [4] or for detecting spinal cord ischemia [5]. High lactate concentration are well known to accumulate in the interstitium of solid tumors as the consequence of hypoxia and/or aerobic glycolysis [6]

In addition, lactate sensing is important in sport medicine and food processing as well, and design of lactate sensors are proposed for emerging new technologies [7]. In this context a low power microwave sensor for analysis of lactic acid in cerebrospinal fluid (CSF) has been proposed in [8] by measuring the amplitude of the reflection coefficient when samples were inserted in a cylindrical cavity working in the 950 MHz – 1150 MHz frequency range. In our study the lactic acid concentrations were related to the variations of the solution conductivities measured by means a truncated coaxial cable. In this way we use a well-known technique which is more general and less critical than the measurement of the reflection coefficient amplitude (in terms of choice of applicator, shape and volume of the sample, etc.).

II. Materials and Methods

A. Sample Preparation

Solutions (25 ml) of L(+)-lactic acid BIOXTRA (Sigma – Aldrich) in both distilled water and culture medium (RPMI) were prepared to cover a concentration range from low, physiological up to supra-physiological levels (0 mM, 0.5 mM, 2 mM, 4 mM, 8 mM, 16 mM, 32 mM, 64 mM). We adopted the same concentrations reported in [8] in order to compare the results. Immediately after the preparation, pH was measured (Crison Basic 20 pH meter) and permittivity measurements were carried out on the same day and after 15 days and 30 days in order to evaluate the stability of the samples. Samples were stored in a refrigerated unit at 4°C and were taken only for measurement purposes. L(+)-lactic acid RPMI solutions were heated at 37°C by water thermostatic bath immersion, then permittivity and non-perturbing temperature measurements were carried out simultaneously, the latter by using a fiber optic thermometer (Luxtron 652).

B. Permittivity Measurements

Dielectric measurements in the 0.5 – 4.5 GHz frequency range were carried out by means of the truncated coaxial cable technique, that is widely used for permittivity evaluations of biological tissues [9]. The method is based on the measurement of the reflection coefficient (amplitude and phase) at the tip of a truncated coaxial cable immersed in the sample and connected to a Vector Network Analyzer (Agilent E5071C-240) once the calibration with a short circuit, an open circuit and a known liquid is carried out. Permittivity values are then calculated following the approach described in [10]. Uncertainty budget was evaluated on distilled water samples (5 independent measurements) as described in [11] and reported in Table 1.

III. Results

Permittivity measurements of lactic acid solutions were stable up to one month. Among the considered frequencies, a regular trend of the conductivity with the concentration was observed at 800 MHz and 850 MHz for water and culture medium solutions, respectively. The conductivity behaviors of lactic acid solutions in water and in RPMI as function of concentration and pH are shown in Fig. 2 and Fig 3. The trend observed in water solutions was consistent with that reported in [8] while in the case of RPMI solutions, that are closer to human physiology, the trend appears to be different and depend on concentration. In particular conductivity increases up to the concentration of 2 mM and decreases for higher concentrations. Even though for saline solutions it is known that dielectric parameters increase monotonically up to 4 mM where the trend reverses [12], more accurate

measurements should be carried out in our case in order to establish the sensitivity of our technique to low-concentration solutions.

IV. Conclusions

We have presented the results of a microwave broad-band characterization of a biomarker that is relevant in several pathologies, with particular attention to the possibility of relating the concentration and pH with the conductivity. The preliminary results are encouraging and future measurements will be carried out with samples that simulate tissues or small tumours in order to propose this technique as a non invasive diagnostic tool.

TABLE 1
UNCERTAINTY BUDGET OF THE MEASURED PERMITTIVITY (ϵ') AND EFFECTIVE CONDUCTIVITY (σ_{eff}) OF DISTILLED WATER

	ϵ'	σ_{eff} (S/m)
Repeatability(SDM) (%)	0.65	5.18
Deviation from reference (%)	1.36	6.99
Combined uncertainty (%)	1.50	8.70
Expanded uncertainty k=2 (%)	3.01	17.39

V. References

[1] K. L. Makoroff , K. M. Cecil, M. Care and W. S. Ball Jr, "Elevated lactate as an early marker of brain injury in inflicted traumatic brain injury", *Pediatr Radiol* , vol. 35, pp. 668–676, 2005

[2] M. B. Tessem et al., "Evaluation of lactate and alanine as metabolic biomarkers of prostate cancer using H HR-MAS spectroscopy of biopsy tissues", *Magnetic Resonance in Medicine,* vol. 60, pp. 510–516, 2008.

[3] D. M. Brizel et al., "Elevated tumour lactate concentrations predict for ann increased risk of metastases in head-and-neck cancer", *Int. J. Radiation Oncology Biol. Phys*., vol. 51, No. 2, pp. 349–353, 2001.

[4] M. K. Zarifi et al., "Prediction of adverse outcome with cerebral lactate level and apparent diffusion coefficient in infants with perinatal asphyxia", *Radiology* vol. 225, pp. 859–870, 2002.

[5] N. Khaladj et al., "The role of cerebrospinal fluid S100 and lactate to predict clinically evident spinal cord ischaemia in thoraco-abdominal aortic surgery", *Eur J Vasc Endovasc Surg* vol. 36, 11-19, 2008.

[6] F. Hirschhaeuser, U.G.A. Sattler, W. Mueller-Klieser. "Lactate: a metabolic key player in cancer", *Cancer Research,* vol. 71, pp. 6921-6925, 2011.

[7] L. Rassaei, W. Olthuis, S. Tsujimura, E. J. R. Sudhölter and A. van den Berg, "Lactate biosensors: current status and outlook", *Anal Bioanal Chem* vol. 406, pp. 123–137, 2014.

[8] J. H. Goh, A. Mason, A. I. Al-Shamma'a, M. Field and P. Browning, "Lactate detection using microwave spectroscopy for in-situ medical applications*", International Journal on Smart Sensing and Intelligent systems*, vol. 4 (3), pp. 336-352, 2011.

[9] M. Lazebnik, L. McCartney, D. Popovic, C.B. Watkins, M.J. Lindstrom,J. Harter, S. Sewall, A. Magliocco, J.H. Booske, M. Okoniewski and S. C. Hagness, "A large-scale study of the ultrawideband microwave dielectric properties of normal breast tissue obtained from reduction surgeries", *Phys Med Biol* vol. 52 , pp. 2637–2656, 2007.

[10] R. Massa et al Wide Band Permittivity Measurements of Palm (*Phoenix Canariensis*) and *Rhynchophorus. ferrugineus* (Coleoptera Curculionidae) for RF Pest Control, *Journal of Microwave Power and Electromagnetic Energy*, 48 (3), pp. 158-169, 2014,.

[11] C. and A. Peyman, "Dielectric measurement: error analysis and assessment of uncertainty", *Phys Med Biol,* vol. 51, pp. 6033–6046, 2006.

[12] A.Peyman, C.Gabriel, and E.H.Grant, Complex Permittivity of Sodium Chloride Solutions at Microwave Frequencies, *Bioelectromagnetics J.* vol. 28, pp. 264-274, 2007.

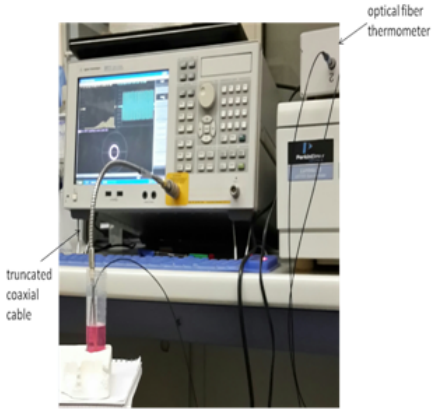

Fig.1 Experimental set-up for permittivity measurements.

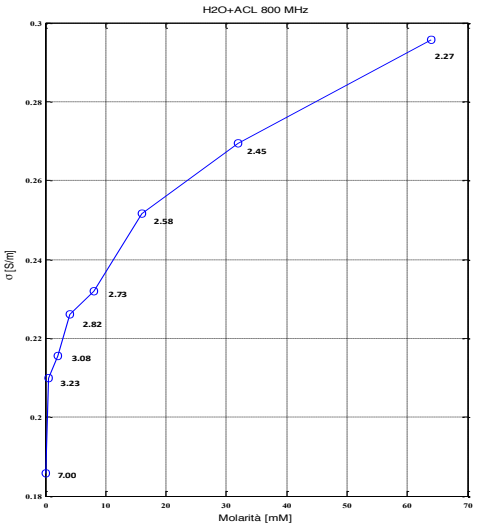

Fig.2 Conductivity behaviour of Acid Lactic solution in water as a function of concentration and pH.

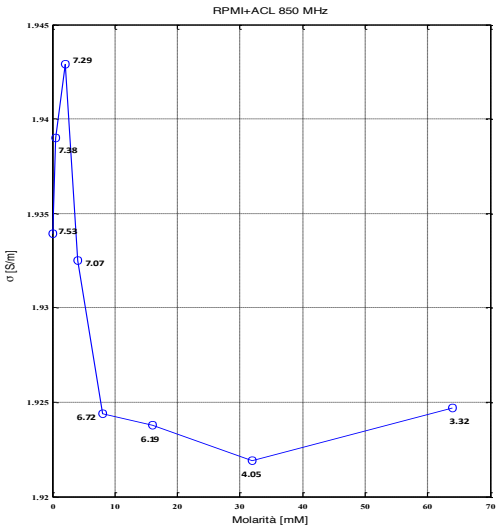

Fig.3 Conductivity behaviour of Acid Lactic solution in RPMI culture medium as a function of concentration and pH.

Viscoelastic induced single particle/cell investigation in microfluidic flow

David Dannhauser[1], Domenico Rossi[1], Filippo Causa[1,2] and Paolo Antonio Netti[1,2]
[1]Center for Advanced Biomaterials for Healthcare@CRIB, Istituto Italiano di Tecnologia (IIT), ITALY
[2]Interdisciplinary Research Centre on Biomaterials (CRIB), Università degli Studi di Napoli "Federico II", ITALY

***Abstract*— A versatile microfluidic tool for the characterization and classification of individual viscoelastic aligned particles as well as peripheral blood mononuclear cells is described. Our approach exploit the fact, that even low concentrations of viscoelastic polymers can be used to induce particle or cell alignment to the centerline of a capillary or squared channel. Using biocompatible viscoelastic substances it is even possible to create naive measurement conditions, useful, for instance to investigate morphological living cell properties in flow.**

***Keywords*— Scattering, Viscoelastic, Microfluidic, Cells.**

I. Introduction

We present a universally usable tool for the investigation of individual viscoelastic aligned particles or cells in microfluidic flow conditions. For this purpose we take advantage of the fact, that even low concentrations of a biocompatible viscoelastic substance can be used to induce particle or cell alignment in the centerline of a capillary or squared channel.[1-5]

For instance, naive measurement conditions can be realized to investigate morphological living cell properties in flow conditions. Indeed, several optical measurement techniques can be simply combined with our cost effective and easy to adapt versatile microfluidic tool to achieve multiplex information of particle or cells.[6,7] Here, several measurement techniques can be utilized, such as the digital holography approach, static light scattering technique or ordinary microscope observations.[6-8]

II. Materials and Methods

The essential alignment -in our microfluidic tool- takes place in a round shaped capillary (inner diameter of 50 μm), induced by a pressure driven viscoelastic polymer solution (Polyethylene oxide – 4 MDa, SIGMA ALDRICH), which is combined with a highly transparent rectangular shaped measurement channel (cross section = 380x400 μm) as shown in Fig.1. Indeed, due to the adaptive centerline probability as well as flow velocity -by the used set of alignment parameters- and the relative big channel size compared to the investigated particles or cells (typically object size 1 – 20 μm), a wide field of possible observation application can be applied.

III. Results

For instance, using a standard bright field microscope opens up the possibility to investigate unknown viscoelastic polymer properties, which cannot be obtained by standard rheological measurement techniques.[3,7] Moreover particle or cell size, shape or relative amount of objects, while passing a defined measurement area can be obtained.[4,7] Note that for most of our measurement conditions no deformation of cells or soft particles can be assumed, due to the relatively low shear forces in the measurement channel.

In addition combining our versatile microfluidic tool with more sophisticated microscope systems can be used to investigate, for instance, an automatic barcode readout system for fluorescent based multi-shell particles or dyes inflow. For example the multiplex fluorescence signal detection of microRNA (miRNA) concentrations in small sample volumes, without pre-treatments as PCR amplification steps are therefore from growing interest.[9-13]

Furthermore coupling our tool with a static light scattering (SLS) approach, open up the possibility to label-free investigate physical cell properties (size, shape, refractive index or cell-to-nucleus ratio) in flow.[6,14] We used a light scattering apparatus, whose design and principles are shown elsewhere[6]. In general, our apparatus is able to instantly obtain precise experimental optical signatures of individual peripheral mononuclear blood cells in a continuous angular range from 2° up to 30°. The hereby achieved angular resolution of 0.1022°, gives the possibility to distinguish cell dimensions within the submicron range at throughput rates of up to 1.2 cells per second.[7] Therefore, peripheral human blood cells have been successfully investigated by our SLS apparatus, without causing them any structural damages. (see Fig. 2)

In fact, traditional cell alignment approaches, using fast -and potentially damaging- sheath fluids, could damage living cells.[15] Note that sheath fluids are, a critical variable to be chosen, whenever cells are desired to be collected for further analysis. Indeed, only few commercial available measurement systems are suitable for living cell investigations, retaining pH and osmotic pressure values adequate for their surviving.

Recurring to our SLS approach, several different surface or volume based scattering simulation models can be used to achieve unknown cell's parameters or to discriminate separate cell subpopulations. To name but a few, the discrete source method, discrete dipole approximation or Lorenz-Mie theory. By using such theoretical particle or cell simulation approaches it gets possible to obtain a counting and characterization of cell subpopulations without the use of Ab-labeling.

IV. Conclusions

We presented a versatile tool for the characterization and classification of individual viscoelastic aligned particles or cells -as well as the possibility to even characterize the utilized viscoelastic solution- based on the fact, that even low concentrations of a viscoelastic substance can be used to induce particle or cell alignment in the centerline of a capillary or squared channel. In fact, by using biocompatible viscoelastic substances it becomes possible to create naive measurement conditions, for instance needed to investigate morphological living cell properties in flow. Such capability can be useful to create, reference panels for morphologic cell characteristic and compare in real time obtained measurement values to identify morphologic cell aberrations caused by pathologic events.

References

[1] G. Romeo, G. D'Avino, F. Greco, P.A. Netti and P.L. Maffettone, "Viscoelastic flow-focusing in microchannels: scaling properties of the particle radial distributions," *Lab Chip*, 13(14), 2802–2807 (2013).

[2] G. D'Avino, G. Romeo, M.M. Villone, F. Greco, P.A. Netti and P.L. Maffettone, "Single line particle focusing induced by viscoelasticity of the suspending liquid: theory, experiments and simulations to design a micropipe flow-focuser," *Lab Chip*, 12(9), 1638-1645 (2012).

[3] F. Del Giudice, G. Romeo, G. D'Avino, F. Greco, P.A. Netti and P.L. Maffettone, "Particle alignment in a viscoelastic liquid flowing in a square-shaped microchannel," *Lab Chip* 13(21), 4263-4271 (2013).

[4] S. Yang, S.S. Lee, S.W. Ahn, K. Kang, W. Shim, G. Lee, K. Hyun and J.M. Kim, "Deformability-selective particle entrainment and separation in a rectangular microchannel using medium viscoelasticity," *Soft Matter*, 8(18), 5011-5019 (2012).

[5] K. Kang, S.S. Lee, K. Hyun, S.J. Lee and J.M. Kim, "DNA-based highly tunable particle focuser," *Nat. Commun.*, 4, (2013).

[6] D. Dannhauser, G. Romeo, F. Causa, I. De Santo and P.A. Netti, "Multiplex single particle analysis in microfluidics," *Analyst*, 139(20), 5239-5246 (2014).

[7] D. Dannhauser, D. Rossi, F. Causa, P. Memmolo, A. Finizio, T. Wriedt, J. Hellmers, Y. Eremin, P. Ferraro and P.A. Netti, "Optical signature of erythrocytes by light scattering in microfluidic flows,", *Lab Chip*, 15(16), 3278-85 (2015).

[8] D. Dannhauser, P. Memmolo, D. Rossi, F. Merola, L. Miccio, F. Causa, P. Ferraro and P.A. Netti, "Cells characterization in microfluidic flows by small angle light scattering and 3D holographic technique." In SPIE Optical Metrology, pp. 95290D-95290D. International Society for Optics and Photonics, (2015).

[9] A.M. Cusano, F. Causa, R. Della Moglie, N. Falco, P.L. Scognamiglio, A. Aliberti, R. Vecchione, E. Battista, D. Marasco, M. Savarese, U. Raucci, N. Rega and P.A. Netti, "Integration of binding peptide selection and multifunctional particles as tool-box for capture of soluble proteins in serum", *J. R. Soc., Interface* 11:20140718, (2014).

[10] F. Causa, A. Aliberti, A.M. Cusano, E. Battista and P.A. Netti, "Supramolecular spectrally encoded microgels with double strand probes for absolute and direct miRNA fluorescence detection at high sensitivity," *J. Am. Chem. Soc.*, 137(5), 1758-1761 (2015).

[11] A.C. Manikas, A. Aliberti, F. Causa, E. Battista and P.A. Netti, "Thermoresponsive PNIPAAm hydrogel scaffolds with encapsulated AuNPs show high analyte-trapping ability and tailored plasmonic properties for high sensing efficiency", *J. Mater. Chem. B*, 3(1), 53-58. (2015).

[12] E. Battista, A. Mazzarotta, F. Causa, A.M. Cusano and P.A. Netti, "Core−shell microgels with controlled structural properties" *Polym. Int.*, (2016).

[13] A. Aliberti, AM. Cusano, E. Battista, F. Causa and PA.Netti, "High sensitive and direct fluorescence detection of single viral DNA sequences by integration of double strand probes onto microgels particles" *Analyst*, 8;141(4):1250-6.U, (2016).

[14] D. Dannhauser, D. Rossi, F. Causa, and P.A. Netti, "Individual erythrocyte analysis in microfluidic flow by different light scattering methods." Light Scattering by Complex Particles (ScattPort Series, 2), (2015).

[15] H.M. Shapiro, "Practical flow cytometry," *John Wiley & Sons*, 2005.

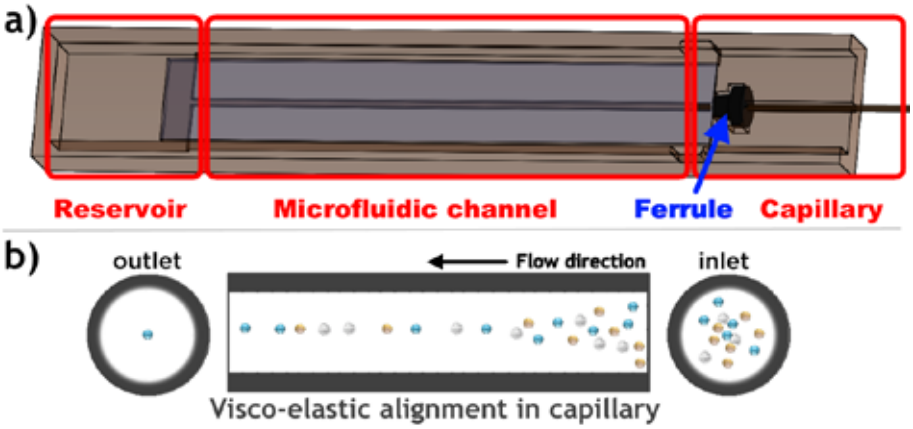

Fig. 1. Microfluidic alignment and observation tool. a) show the microfluidic system with a round capillary entering from the left side a rectangular shaped microfluidic channel, sealed by a soft ferrule. Finally at the end of the channel is placed a reservoir to collect the measured sample. b) the viscoelastic alignment principle which takes place in a round capillary is illustrated.

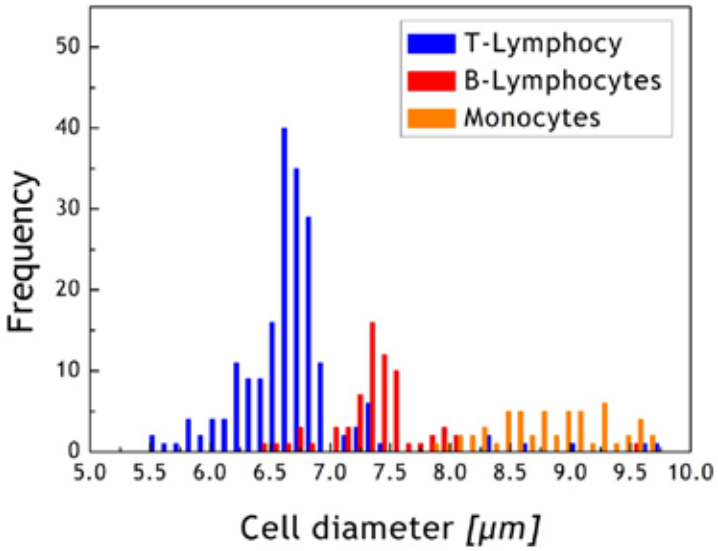

Fig. 2. Size distribution of peripheral human mononuclear cells analyzed by our microfluidic tool combined with a SLS approach is shown.

Clinical Validation of an Artificial Pancreas: From Hospital to Home

S. Del Favero[1], L. Magni[2] and C. Cobelli[1]

[1]*Department of Information Engineering, University of Padova, Italy*
[2]*Department of Civil Engineering and Architecture, University of Pavia, Pavia, Italy*

***Abstract*—An Artificial Pancreas (AP) is a minimally-invasive device for automated glycemic control in Type 1 diabetes, that modulates insulin infusion on the basis of the measurements collected by a real-time continuous glucose monitoring sensor.**

AP research has progressed to an impressive pace in the last decade. In 2007 we developed a Model Predictive Control (MPC) algorithm for blood glucose regulation and performed, entirely in silico, the pre-clinical validation. We then moved to in-hospital testing of this AP algorithm running on a bulky laptop. From 2012 we moved outside the hospital, in environments more closely resembling daily life and free from strict protocol prescriptions. Recently we completed a 2 month long trial where the patients carried an MPC based wearable AP, wirelessly connected with pump and sensor, granting them tighter blood glucose control and less hypoglycemia during their daily activities and overnight.

Thorough a review of Padova's group experience in this field, this contribution gives a taste of the large research effort performed by the AP community.

***Keywords*—Artificial Pancreas, Blood Glucose Control, Clinical Trial, Inpatient testing, Outpatient testing.**

I. Background

Type 1 diabetes is a disease induced by autoimmune pancreatic beta-cells destruction, causing inability to produce insulin and hence characterized by severely disturbed blood glucose (BG) homeostasis. Type 1 diabetic patients are dependent on external insulin administration to restore glucose utilization and to maintain their BG concentration is the nearly normal range [70, 180] mg/dL. Low BG levels (hypoglycemia) poses the patient at immediate risk, possibly leading to hypoglycemic coma and ultimately to death. Sustained high BG levels (hyperglycemia) are associated with long term complications such as neuropathies, retinopathies, nephropathies and cardio-vascular diseases. Therefore, type 1 diabetics face every day an extremely challenging control problem, complicated by the strong disturbance actions of meals and physical activity.

Artificial Pancreas (AP) systems aim to artificially restore the severed regulation and improve patient quality of life, by reducing onset of complications and alleviating diabetes management burden. An AP system is a device that automatically modulates insulin injection, infused by a subcutaneous insulin pump, on the basis of the measurement provided by a minimally-invasive subcutaneous glucose sensor (CGM, continuous glucose monitor). The insulin injection requested to maintain patient BG in the nearly normal range is computed by a control algorithm.

In 2007 we developed a Model Predictive Control (MPC) algorithm for blood glucose control, [1], and performed the pre-clinical validation entirely in silico [2].

II. In Hospital Testing (2007-2012)

The first step toward the clinical validation of an AP was its testing on hospitalized patient. To guarantee the higher level of patient safety medical and technical personnel were closely monitoring the patient throughout the study and operating on the AP prototype. Moreover, the collection of frequent blood samples was usually a mandatory requirement at this stage. The consequent need of an open intravenous access strongly limited patient freedom of movement.

A. Hardware for Inpatient Studies

In view of this, technological requirements for in-patient AP prototypes were very limited: the algorithm was running on laptop and was implemented in Matlab. Data transfer with sensor and pump was performed first manually and later automated through wired connection.

B. Inpatient Results

From 2007 to 2012, Padova was involved in 4 international studies in hospital. Overall, 127 adult patients were recruited in 11 centers of 7 different countries. Here we mention, as an example [3], where the MPC based AP controller was tested on 12 hospitalized patients in a randomized 22h study. The study started after lunch, prescribing a moderate physical exercise and facing the challenge of dinner and breakfast. The study showed that overall percent time in near normoglycemia (70-180 mg/dL, time-in-target from now on) increased significantly from mean(standard deviation) = 76.8(5.0)% to 90.1(3.4)%, p=0.05 and that percent time-in-tight-target (80-140 mg/dL) increased significantly overnight from 42.7(11.2)% to 79.3(8.1)%, p=0.04, while improvements in tight control on the overall data were not statistically significant, due to the effect of meal perturbation. Moreover, overnight average plasma glucose was significantly reduced and so was the dispersion around the average (i.e. standard deviation, measured intra-subject). Improved glucose control was achieved without significant increase in the risk of hypoglycemia (1.4 vs. 1.6 events/patient in open loop vs. eCTR, p = 0.43) and with a significant decrease in the overall average plasma glucose.

III. Getting outside the hospital(2012-2014)

By 2012 several hospital studies provided solid evidences on superior safety and efficacy of closed-loop control with respect to standard therapy. The frontier of the AP research moved to the testing of this technology in environments more close to real-life and free from strict protocol prescription.

A. Hardware for outpatient use

Apparently, the previously employed technology, based on bulky laptop and wired connections is not suited for out-patient real-life studies, since it strongly limits patient's mobility. An important step forward for the ambulatory use

of an AP, was the introduction of the Diabetes Assistant (DiAs), University of Virginia [4]. The system is capable to run a closed-loop control algorithm and to wirelessly connect with pump and sensor, granting patient freedom of movement. The central component of the DiAs system is an off-the-shelf smart phone running the Android operating system (OS). To ensure the operation of the smart phone as a medical device, its OS was modified to disable processes not related to clinical operation and to include self-checks of system integrity. Patient-DiAs interaction takes place using a Graphical User Interface (GUI) [5]. This is a critical part of the system, since in out-patient AP studies the patient interacts with the system without supervision.

B. Telemedicine

One of the critical issues in moving outside the hospital is to guarantee the highest possible level of safety for the patient. Apparently, having the attending personnel directly watching the patient cannot be proposed, as it would interfere with the study, especially overnight, and limit the patient in its activities. Instead, the DiAs streams patient and system data in real-time to a telemonitoring website, exploiting the smartphone 3G connectivity. Accessing to the website via an ordinary PC, the study team can monitor from a remote location the status of several patients and to check the correct functioning of the system throughout the trial [6].

C. Hotel Studies

From 2012 to 2014, Padova was involved in 5 studies performed outside the hospital. Overall, 85 adult patients were recruited in 5 centers of 4 countries. Here we mention, as an example, [7] where the MPC based AP running on the DiAs platform was tested outside the hospital in 13 patients in a 42h non-randomized protocol (the first 14h were in open-loop and the remaining 28h in closed-loop). The study was conducted in a hotel and the subjects were free to move in the facility and in its immediate vicinities. The study team, physically located in the same facility, monitored the trial through the telemedicine system without interfering/interacting with the experiment, unless needed for safety or to solve technical issues. The study started before dinner and the controller was activate before breakfast of the second study day, therefore both during open- and closed-loop the glycemic control was challenged by a dinner and both periods included one night. Closed-loop was further challenged by two breakfasts of study day 2 and 3 and by the lunch of study day 2. Meals were consumed at the hotel restaurant where patients were invited to choose a menu in line with their daily habits, both in terms of meal amount and composition.

The AP relevantly improved overnight control vs open-loop. Statistically significant improvement in time-in-target, 64.0 (32.8)% open-loop vs 92.2(8.0)% closed-loop ($p = 0.01$) were recorded combined with statistically significant reduction of time-in-hypo (glycemia < 70mg/dl) median[25th perc, 75th perc]=0[0, 25.3]% vs 0[0, 0]%, $p=0.03$. Joint evaluation of dinner and overnight shows a significant reduction of time-in-hypo from 6.0[1.6, 19.4]% to 5.96[1.6, 19.5]% ($p < 0.01$), together with a significantly improved time-in-target 62.4(29.0)% open-loop vs. 83.6% (14.0)% closed-loop ($p=0.04$).

IV. AT PATIENT HOME (2014-2015)

Given the encouraging results in hotel, in 2014 the MPC based AP running on the DiAs platform was tested at patients' home for 2 consecutive months in a randomized trial that involved N=32 adult patients [8]. Blood glucose control achieved with the AP was compared with the one achieved in 2 months of open-loop therapy. The AP system was active only during dinner and night portions, when the patient is usually at home. From 20:00 to 08:00 h, the mean time-in-target was higher with AP than with open-loop: 66.7(10.1)% versus 58.1(9.4)% $p<0{\cdot}0001$, through a reduction in both mean time-in-hyper (glycemia >180 mg/dl): 31.6(9.9)% vs 38.5(9.7)%, $p<0.0001$, and time-in-hypo: 1.7[0.8, 2.5] vs 3.0[1.6, 4.9]%, $p<0.0001$. Of note, taking a period effect into account ($p=0.0034$), the decrease in mean HbA1c during the AP period was significantly greater than during the open-loop period (–0·3% vs –0·2%, $p=0.047$). No serious adverse events occurred during this study, and none of the mild-to-moderate adverse events was related to the study intervention

V. CONCLUSION

In this contribution we reviewed our trials assessing efficacy of an AP system relying on an MPC algorithm. Of all the experiments performed we selected one short study performed in hospital, one short study performed outside the hospital mimicking patient daily life and a two-month long study assessing independent use of a wearable AP system at home.

In all these increasingly challenging set-ups, the MPC based AP showed superior safety and efficacy with respect to standard therapy. Future works include AP efficacy assessment in other diabetic populations, such as children and adolescents.

REFERENCES

[1] L. Magni et al. "Model predictive control of type 1 diabetes: an in silico trial," J Diabetes Sci Technol, vol. 1, no. 6, pp.804–812, 2007.

[2] B. P. Kovatchev, M. Breton, C. Dalla Man, C. Cobelli, "In silico preclinical trials: a proof of concept in closed-loop control of type 1 diabetes," *J Diabetes Sci Technol*. 2009;3(1):44-55.

[3] M. Breton et al, "Fully integrated artificial pancreas in type 1 diabetes: modular closed-loop glucose control maintains near normoglycemia," Diabetes, vol. 61, no. 9, pp. 2230–2237, Sep 2012.

[4] P. Keith-Hynes, B. Mize, A. Robert, and J. Place, "The Diabetes Assistant: A smartphone-based system for real-time control of blood glucose," Electronics, vol. 3, no. 4, pp. 609–623, 2014.

[5] P. Keith-Hynes, S. Guerlain, B. Mize, C. Hughes-Karvetski, M. Khan, M. McElwee-Malloy, and B. Kovatchev, "DiAs User Interface: A Patient-Centric Interface for Mobile Artificial Pancreas Systems," J Diabetes Sci Technol, vol. 7, no. 6, pp. 1416–1426, 2013.

[6] G. Lanzola, et al. "Monitoring Artificial Pancreas Trials Through Agent-based Technologies: A Case Report," J Diabetes Sci Technol, vol. 8, no. 2, pp. 216–224, Mar 2014

[7] S. Del Favero et al "Multicenter outpatient dinner/overnight reduction of hypoglycemia and increased time of glucose in target with a wearable artificial pancreas using modular model predictive control in adults with type 1 diabetes," Diabetes Obes Metab, vol. 17, no. 5, pp. 468–476, May 2015.

[8] J. Kropff et al, "2 month evening and night closed-loop glucose control in patients with type 1 diabetes under free-living conditions: a randomised crossover trial." Lancet Diab. End.3(12):939-47. Dec 2015

Fig. 1. AP hardware for the studies in hospital (left), in hotel (center) and at patient's home (right)

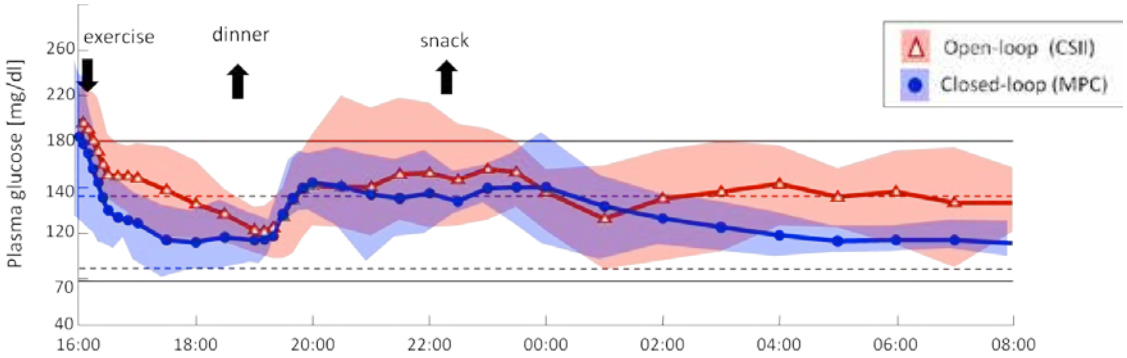

Fig. 2. Blood Glucose Control achieved by the MPC in hospital setting [3]. Thick lines, representing population mean results, are depicted together with their ± standard deviation envelope. Red dashed line represent open-loop, blue solid lines MPC.

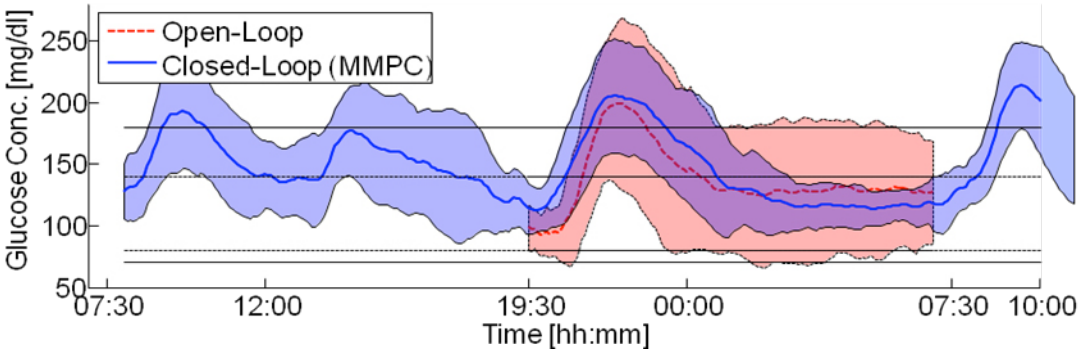

Fig. 3. Blood Glucose Control achieved by the MPC in hotel setting [7]. Thick lines, representing population mean results, are depicted together with their ± standard deviation envelope. Red dashed line represent open-loop, blue solid lines MPC.

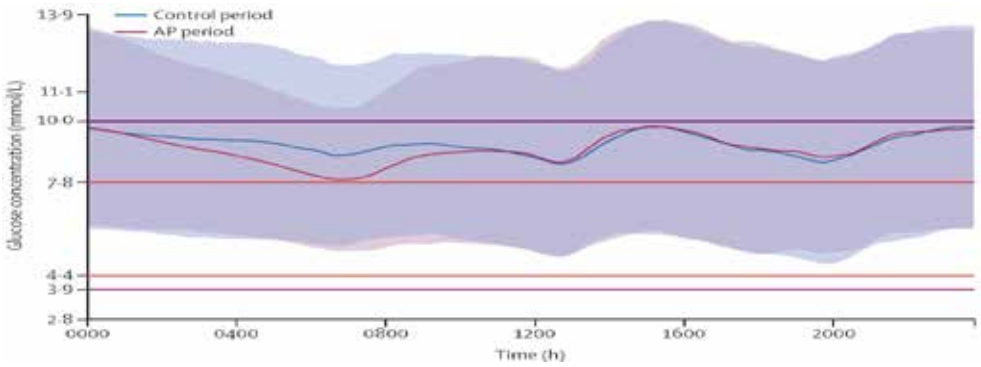

Fig. 3. Blood Glucose Control achieved by the MPC at patients home [8]. Thick lines, representing population mean results, are depicted together with their ± standard deviation envelope. Red dashed line represent MPC, blue solid lines open-loop.

CT study of the tissue shrinkage occurring during a microwave thermal ablation procedure

L. Farina[1], V. Lopresto[2], R. Pinto[2], D. D'Alessio[3], S. Minosse[3], L. Strigari[3], M. Cavagnaro[1]
[1] *Dept of Information Engineering, Electronics and Telecommunications, Sapienza University of Rome, Italy*
[2] *Div of Health Protection Technologies, Casaccia Research Centre, ENEA, Rome, Italy*
[3] *Medical Physics Laboratory, Regina Elena National Cancer Institute, Rome, Italy*

***Abstract*—This work aims to study the shrinkage phenomenon that occurs in the biological tissue treated with a Microwave Thermal Ablation procedure, in correlation with the induced temperature increase. An experimental set up is used to evaluate under real-time CT control the displacement of fiducial markers placed into thermally ablated specimens of *ex vivo* bovine liver tissue. Fibre-optic sensors are used to measure the tissue temperature during the procedure. A correlation in the kinetic of the two processes, i.e. tissue shrinkage and temperature increase, was observed.**

***Keywords*—Microwave Thermal Ablation, Tissue Shrinkage, Image-guidance.**

I. Introduction

MICROWAVE Thermal Ablation (MTA) is an interstitial procedure used to destroy un-healthy cells inducing cytotoxic temperatures. It is mainly adopted to treat unresectable tumours and it exploits the interaction between biological tissue and electromagnetic energy at microwave (MW) frequencies (usually 915 MHz and 2.45 GHz). The absorption of the electromagnetic fields, in facts, induces temperature increases above 55-60 °C [1]. Thermal ablation can be used in combination with image-guiding technologies to supervise and control the whole procedure and the final induced necrosis [2].

MTA induces physical and structural modifications in the biological tissue: in particular, changes in the dielectric and thermal properties occur, and the tissue shrinks as a function of the increasing temperature [3]–[6]. The temperature increase can reach values as high as 100 °C and beyond [7]. It is thus fundamental to properly characterize the behaviour of the treated biological tissue in order to improve the technique efficiency and standardize the treatment results. To this purpose, several experimental studies have been conducted in the recent years [7]–[13].

Aim of this work is to use Computed Tomography (CT), i.e. the most suitable imaging technique for the guidance and supervision of a tumour ablation procedure, to experimentally study in real-time the shrinkage process that occur in the tissue as a function of the temperature increase.

II. Materials and Methods

A set up involving a CT scan (Figure 1), lead markers and temperature sensors was purposely developed and tested. It foresees a plastic box, transparent to the electromagnetic field, purposely designed to host a block of *ex vivo* bovine liver and to allow accurate positioning inside the tissue sample of the MTA antenna, the lead markers, and the temperature sensors. Ad hoc holes on the box walls consent the insertion of a grid of spherical markers and fibre-optic probes around the MW antenna in predefined and reproducible positions. A generator working at 2.45 GHz supplies to the internally cooled 14G MW antenna 60 W for 10 minutes. The box set up is placed in the CT gantry and the ablation procedure is performed under CT monitoring. The CT system is able to detect and track the markers movements, whereas the temperature sensors are remote controlled through a dedicated LabVIEW program. Then, at the end of the experiment, the tissue specimen is sectioned along a horizontal plane containing the antenna axis to evaluate and measure the dimensions of the final necrosis, with the extension of the carbonised and coagulated areas. The first is the portion of tissue closer to the antenna axis that reaches temperatures above 100 °C and appears highly dehydrated, whereas the latter concerns the tissue undergoing temperatures between 60 °C and 100 °C (Figure 2).

The proposed set up was used to perform several experiments placing up to 27 markers and 4 fibre-optic sensors. The collected data were then processed with a dedicated MATLAB program developed to analyse the CT images acquired over time before and during ablation procedure: the markers positions were correlated with the temperature data recorded by the fibre-optic sensors and the tissue modifications in terms of shrinkage.

III. Results

Thanks to the MATLAB program, each marker was identified based on CT images and its absolute and relative positions were recorded during the thermal ablation procedure (Figure 3). It was then possible to classify the markers based on their distance from the antenna axis: knowing the dimensions of the induced necrosis and the extension of the carbonised and coagulated tissue, it was possible to discriminate in which of the two regions the markers were positioned at the end of the ablation. At the end of the ablation (i.e. after 600 s), in the radial direction with respect to the antenna axis, in correspondence of the antenna feed, an average extension of 6.0 ± 1.4 mm and of 19.8 ± 1.6 mm were observed for the carbonised and coagulated area, respectively; at the same time, an average displacement of 2.7 ± 0.5 mm and of 2.4 ± 0.5 mm were measured for the markers that were positioned inside the carbonised and the coagulated area, respectively. The displacement was evaluated considering the marker's distance from the antenna axis at the given time-step of the ablation procedure with respect to its initial position. One fibre-optic sensor was

placed at the edge of the carbonised region (initial radial distance from the antenna axis 11.7 ± 1.3 mm), and a temperature increase of 70 °C was measured, at the end of the ablation procedure. A second fibre-optic sensor was placed at the edge of the coagulated region (initial radial distance from the antenna axis 20.3 ± 1.6 mm), and a temperature increase of 35 °C was measured after 600 s. The first sensor, located in the carbonised region, showed a higher rate of the temperature increase with respect to the sensor located in the coagulated area. A similar behaviour was observed for the markers placed in carbonised tissue, since already after 300 s, an average displacement of2.4 ± 0.4 mm was noted; while the markers placed in the coagulated tissue reached such value of displacement only at the end of the ablation time (i.e. after about 600 s).

IV. Conclusion

Both the temperature increase and the markers' displacement pointed out a similar kinetic behaviour, highlighting the dependence of the tissue shrinkage from the temperature increase, and thus from the heating deployed into the tissue. Further analysis are needed to better characterize and quantify this correlation.

Acknowledgement

The authors acknowledge the R&D Unit of HS Hospital Service S.p.A., Rome, Italy, for providing the antenna applicators and the MW power generator.

References

[1] M. Ahmed, C.L. Brace, F.T. Lee Jr, S.N. Goldberg,"Principles of and advances in percutaneous ablation,"*Radiology*, vol. 258, pp. 351–369,2011.

[2] M. Ahmed, L. Solbiati, C.L. Brace, D.J. Breen, M.R. Callstrom, *et al.*,"Image-guided tumor ablation: standardization of terminology and reporting criteria-a 10-year update,"*J Vasc Interv Radiol*, vol. 25(11), pp. 1691–1705,2014.

[3] D. Yang, M.C. Converse, D.M. Mahvi, J.G. Webster,"Measurement and analysis of tissue temperature during microwave liver ablation,"*IEEE trans Biomed Eng*, vol. 54, pp. 150–155,2007.

[4] C.L. Brace, T.A. Diaz, J.L. Hinshaw, F.T. Lee Jr,"Tissue contraction caused by radiofrequency and microwave ablation: A laboratory study in liver and lung,"*J Vasc Interv Radiol*, vol. 21, pp.1280–1286, 2010.

[5] Z. Ji, C.L. Brace,"Expanded modelling of temperature-dependent dielectric properties for microwave thermal ablation,"*Phys Med Biol*, vol. 56, pp. 5249–5264, 2011.

[6] V. Lopresto, R. Pinto, G.A. Lovisolo, M. Cavagnaro,"Changes in the dielectric properties of ex vivo bovine liver during microwave thermal ablation at 2.45 GHz,"*Phys Med Biol*,vol. 57, pp. 2309–2327, 2012.

[7] V. Lopresto, R. Pinto, M. Cavagnaro,"Experimental characterisation of the thermal lesion induced by microwave ablation,"*Int J Hyperthermia*, vol. 30, pp. 110–118, 2014.

[8] D. Liu, C.L. Brace. "CT imaging during microwave ablation: analysis of spatial and temporal tissue contraction,"*Med Phys*,vol. 41(11), pp. 113303-1–9, 2014.

[9] C.M. Sommer, S.A. Sommer, T. Mokry, T. Gockner, D. Gnutzmann,*et al.*,"Quantification of tissue shrinkage and dehydration caused by microwave ablation: experimental study in kidneys for the estimation of effective coagulation volume,"*J Vasc Interv Radiol*, vol. 24, pp. 1241–1248, 2013.

[10] C. Rossmann, E. Garrett-Mayer, F. Rattay, D. Haemmerich,"Dynamics of tissue shrinkage during ablative temperature exposures,"*Physiol Meas*, vol. 35, pp. 55–67, 2014.

[11] L. Farina, N. Weiss, Y. Nissenbaum, M. Cavagnaro, V. Lopresto, *et al.*,"Characterisation of tissue shrinkage during microwave thermal ablation," *Int. J. Hyperthermia*, vol. 30, pp. 419–428, 2014.

[12] N. Weiss, S.N. Goldberg, Y. Nissenbaum, J. Sosna, H. Azhari,"Planar strain analysis of liver undergoing microwave thermal ablation using X-ray CT,"*Med Phys*,vol. 42, pp. 372–380, 2015.

[13] M. Cavagnaro, R. Pinto, V. Lopresto,"Numerical models to evaluate the temperature increase induced by ex vivo microwave thermal ablation,"*Phys Med Biol*, vol. 60, pp. 3287–3311, 2015.

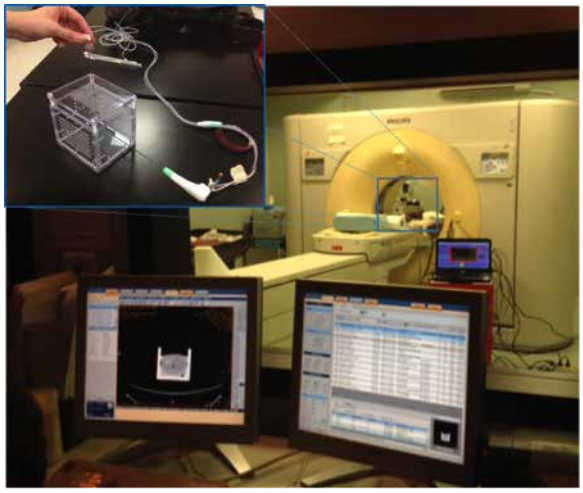

Fig. 1. Experimental set up with the box detail.

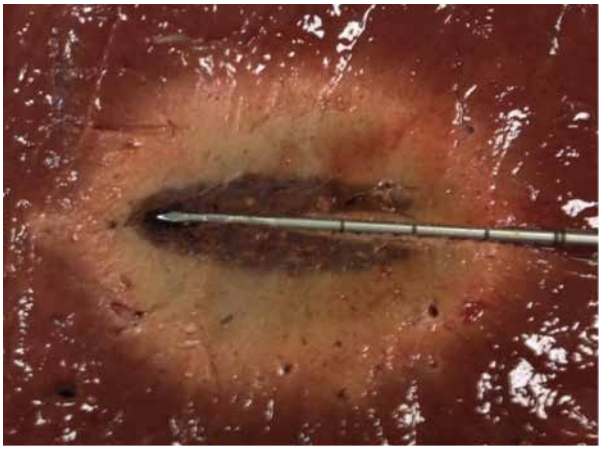

Fig. 2. Appearance of the necrosis induced from the MTA procedure: the inner part is the carbonized region (dark brown), surrounded from the coagulated region (light brown) and then from the untreated tissue (red).

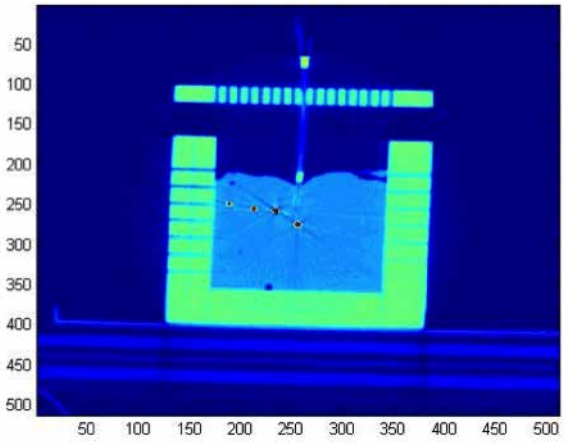

Fig. 3. CT image: section of the tissue sample with the antenna (central red dot) and three markers (red dots in the left side). The plastic introducer of a temperature sensor is also visible on the top.

Soft-Rigid Collision Algorithm for Surgery Realistic Simulation in an Open-Source Engine

F. Fazioli[1], F. Ficuciello[1], G. A. Fontanelli[1], B. Siciliano[1] and L. Villani [1]
[1] *Department of Electrical Engineering and Information Technology, University of Naples Federico II, f.fazioli@studenti.unina.it, fanny.ficuciello@unina.it*

***Abstract*—The aim of this work is to integrate a soft-rigid collision algorithm in an open source physics engine, Bullet Physics, which simulates collision detection, soft and rigid body dynamics. In surgical applications this can be the case of a clamp grabbing deformable organic material or of a spatula opening a brain fissure. The goal is to realize a collision detection algorithm to handle the collision between the soft body (deformable organ) and the rigid body (spatula), assuming that the position of the spatula in the space is given by the Novint Falcon 3D Haptic Controller. The visual rendering has been realized using OpenGL, a cross-language for rendering 2D and 3D vector graphics.**

Keywords—**Surgical Simulation, Soft-Rigid Collision Detection, Real-Time Physics Simulation**.

I. Introduction

It is worth noting that the default soft-rigid collision algorithm proposed by Bullet Physics [1] is not very effective in the case of a thin tool interacting with a deformable object. In particular, if the rigid body (surgical tool) moves slowly, i.e. its displacement covers a small distance compared to the simulation step size, the collision is detected regularly. On the other hand, if the rigid object moves too fast, the Bullet default algorithm does not recognize the collision. As a consequence, the object penetrates into the soft body, and it appears located inside and not in collision. The implemented simulation scene is very essential. There are one rigid body, one soft body and a ground plane. The rigid body is a (1 m x 1 m x 0.125 m) parallelepiped while the soft body is a sphere of radius 3 m and composed by a 328 triangular mesh nodes. In the lack of interaction with the rigid object, the sphere rests on the ground plane.

II. Materials and Methods

To implement the soft-rigid collision algorithm [2], nodes are discretely located on the spatula surfaces. From these nodes rays are casted to detect the collision with the triangles of the soft body mesh. The ray casting algorithm used in this work is the one proposed in [3] by Möller and Trumbore. The rays are cast internally to the rigid body of the object (Figure 2), so as to find collisions as soon as a minimum intersection between the rigid and soft bodies is verified. Typically, for the scope of the work, the ray casting direction is the normal to the surface to which the node belongs. When the spatula (parallepiped) performs a very rapid displacement with respect to the simulation time, it will be detected by the algorithm as completely internal to the deformable organ (sphere, see Fig. 1) and the nodes on both parallel surfaces of the parallepiped would find a mesh on which collide. This problem also depends on the thickness of the rigid body. The thicker the more difficult to occur. To overcome this problem we can distinguish between feasible and non-feasible collisions with the flags method proposed by Fukuhara [2].
The algorithm, at each simulation step, executes a check for each node on the surfaces of the rigid body with the following steps.

A. First Step

To each node is associated a Boolean flag, that describes whether or not the relative node is colliding (flag equal to one means true). When a node is checked, at the beginning it is verified if the collision flag, relative to the opposite node on the parallel surface, is true. If this is true, we have to verify that the body is not fully contained in the deformable object. Thus, the node that presents flag true has to cast a ray, this time externally (see Fig. 1). If this ray finds a mesh, then the collision of the studied node is unfeasible, the collision flag (for the next simulation step) is turned to zero and the study goes to the next node of the rigid body. Otherwise, if the ray cast algorithm does not find a result, the algorithm continues checking the current node.

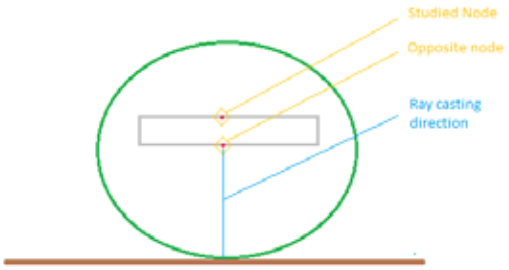

Figure. 1. First step of the algorithm, the opposite node casts the ray.

B. Second Step

The checked node casts a ray along the opposite direction of the normal to the surface which the node belongs to. If the ray casting algorithm gets a positive result, then an auxiliary condition has to be verified. Called N the normal to the triangle belonging to the soft body surface and N_r the normal to the surface of the rigid body to which the node belongs, the sign of the scalar product N·N_r must be evaluated. If negative, then the collision is taking place and

the collision flag relative to the node in exam is set equal to one (true), otherwise the collision flag is set equal to zero.

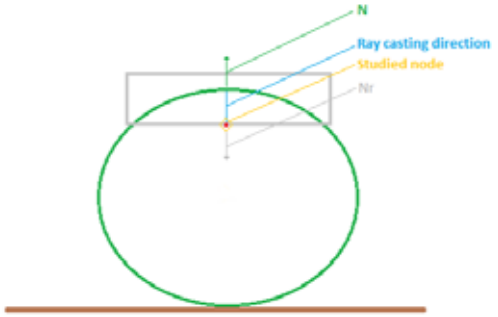

Figure. 2. Second step of the algorithm, the studied node casts the ray.

III. Results

By applying the default collision detection method proposed by Bullet Physics, it follows that the spatula collides with the soft body in a consistent way only for small displacements and slow motion. Fast displacement of the spatula can cause a complete penetration into the soft body surface without further collision (see Fig. 3).

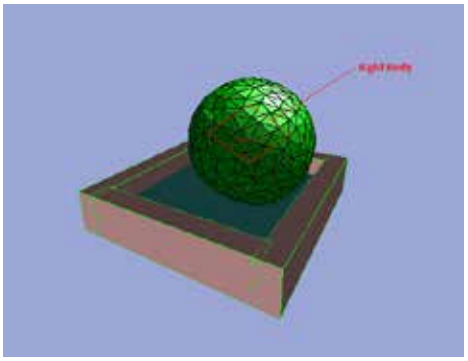

Figure. 3. Soft-rigid collision without the proposed algorithm. The rigid body is located inside

It is worth noticing that the application of only the second step of the algorithm causes drawbacks (see Fig. 4). In fact, the algorithm would work fine if the dimension of the rigid body along the collision direction is large enough to not allow entering, inside the soft body, to both the parallel surfaces (orthogonal to the colliding direction) during a single simulation step. If this is not verified, as in the case of Fig. 4, the collision appears unstable. This happens because both nodes belonging to the two opposite surfaces apply collision forces to the soft body even if some of these collisions are unfeasible. This drawback is overcome by applying also the first step of the algorithm, that detects the unfeasible collisions and excludes them from the study at the current simulation step (see Fig. 5).

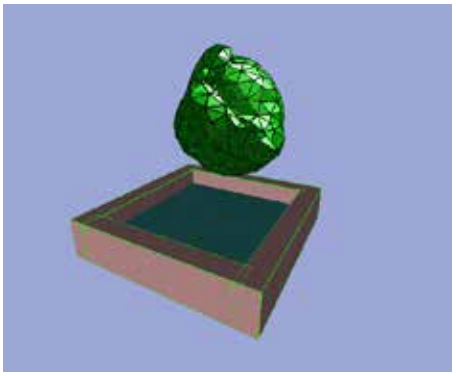

Figure. 4. The rigid body interacts badly with the soft object because of some unfeasible collisions.

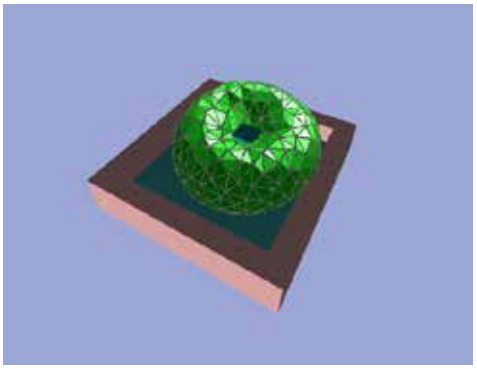

Figure. 5. Soft-rigid collision with the proposed algorithm.

IV. Conclusion

The simulation results of the collision detection method between a thin rigid body (spatula) and a soft object (organ), proposed in [1] and implemented in Bullet Physics, are promising if compared to the results obtained using the default algorithm of the physics engine. Despite the algorithm limitations related to shape, thickness and surfaces interested by the contact of the spatula (i.e. only collision detection with the two largest planes of the spatula are considered), it is worth continuing to investigate toward improved solutions, and future integration within different engines such as SOFA [4].

Acknowledgement

The research leading to these results has been partially supported by the RoDyMan project, funded by the European Communitys Seventh Framework Programme (FP7/2007 2013) under ERC AdG-320992.

References

[1] http://bulletphysics.org/wordpress/.
[2] Akira Fukuhara et al., "Proposition and evaluation of a collision detection method for real time surgery simulation of opening a brain fissure", ROBOMECH Journal 2014, 1:6.
[3] T. Moller et al. "Fast, minimum storage ray/triangle intersection" Journal of Graphics Tools, 1997.
[4] https://www.sofa-framework.org/.

A procedure for the autonomic diagnosis of esophageal motility disorders

A. Frigo[1,2], E.L. Carniel[1,2], M. Costantini[2,3], R. Salvador[2,3], S. Merigliano[2,3] and A.N. Natali[1,2]
[1] *Department of Industrial Engineering, University of Padova, Padova, Italy*
[2] *Centre for Mechanics of Biological Materials, University of Padova, Padova, Italy*
[3] *Department of Surgery, Oncology and Gastroenterology, University of Padova, Padova, Italy*

***Abstract* – Functional disorders and tissues degenerative phenomena may affect the esophageal motility and functionality causing chest pain and inability to swallow, representing a relevant social-health problem. The diagnosis is usually performed considering results from High Resolution Manometry (HRM), but inter- and intra-operator variabilities may affect the procedure with regard to the final problem definition. An autonomic diagnosis procedure was here defined, aiming to support the clinical staff during the traditional diagnostic process and to reduce the margin of personal interpretation. Such algorithm accounts for a physiological model designed to interpret data from HRM and to summarize results into specific model parameters.**

A training set (N=226) of healthy volunteers and pathological subjects was assumed and model parameters distributions of different groups of subjects were defined. Different pathologies were investigated: Achalasia pattern I, Achalasia pattern II, Hypertensive Lower Esophageal Sphincter (Hypertensive LES), Nutcracker esophagus and Diffuse Esophageal Spasm (DES). According to the developed algorithm, a patient is classified by comparing the patient-specific parameters to the distributions of the different groups of subjects and selecting the "most similar" group.

Results address the suitability of model to interpret data from HRM (R^2=86% to 99% between experimental data and model results) and the reliability of the developed procedure as a valid support to clinicians during the traditional diagnostic activity.

***Keywords* - Esophageal functionality, High Resolution Manometry, physiological model, autonomic diagnosis.**

I. INTRODUCTION

THE esophagus is a tubular organ whose main function pertains to the food transport from mouth to stomach. The upper (UES) and the lower (LES) esophageal sphincters are located at the proximal and distal extremities of the esophagus, respectively. In healthy conditions, longitudinal and lumen-occluding esophageal muscular fibres are precisely coordinated in a peristaltic sequence, propelling food downwards. The swallowing reflex begins when the UES relaxes for less than 1 second, allowing the bolus transit to the proximal esophagus and preventing ingestion of air. Simultaneously, the LES relaxes from its basal tone, while peristaltic contractions take place within the proximal tract of the esophagus. Subsequently, low peristaltic pressure values characterize the central transition zone of the esophagus. Finally, peristaltic contractions take place within the distal esophagus, before the LES contracts to a hypertonic pressure value to prevent gastric reflux. Pathologies and degenerative phenomena may affect the described motion, preventing the correct transfer of food, causing dysphagia and chest pain, as a relevant social-health problem.

Esophageal motility disorders are detected by analysing the pressure field determined within the lumen by muscular contractions. High Resolution Manometry (HRM) is a widespread clinical test designed to record the pressure field within a duct by means of a special catheter (Fig. 1a) characterized by N>36 equally spaced sensors. Each sensor is able to detect pressure (Fig. 1b) that is recorded and processed to obtain a coloured pressure map (Fig. 1c). Different techniques have been proposed to interpret data from HRM, but their principal lack pertained to the requirement of a specialized interpreter of data, introducing inter- and intra-observer variabilities [1]. To this purpose, parameters should be defined to interpret the physiological properties of the esophageal structures and to identify the healthy or pathologic condition of subjects.

Several models were proposed in literature [2] to interpret the HRM pressure maps, but they faced relevant difficulties because of the heterogeneous distribution of physiological properties along the esophagus. The model parameters should be related to specific physio-mechanical properties and models identification must analyse data sets composed by a reasonable number of subjects.

The investigation proposed here aims to provide an autonomic diagnostic system based on a physiological model designed to interpret data from HRM. The model and the corresponding parameters were defined accounting for the heterogeneous distribution of biomechanical and functional properties of the esophagus. The autonomic diagnosis procedure aims at detecting the healthy or pathological condition of a patient by analysing the corresponding HRM data. In detail, the patient-specific model parameters are identified and compared with the parameters distributions of different groups of subjects, and the "most similar" group is chosen for the autonomic diagnosis. Model parameters distributions were obtained from a set of N=226 subjects, providing a statistically relevant description of the parameters. Relationships between the identified model parameters and pathologies were found, aiming to define more reliable criteria for the diagnostic activity.

II. MATERIALS AND METHODS

A. Clinical diagnostic activities

High Resolution Manometry tests were performed by means of ManoScan HRM (Given Imaging Ltd, Israel) according to standard procedures. During an HRM test, a catheter is placed inside the patient's esophagus and the intraluminal pressure evolution over time is measured by each one

of the 36 equally spaced sensors of the probe. Each patient was tested in a supine position, required to rest for 20 sec to identify the positions of the sphincters and to evaluate the basal pressure distribution, before starting 10 deglutitions of 5 ml of water each. Clinical measurements have been performed on different groups of subjects referred to the Clinical Hospital of the University of Padova, Italy. Activities on both healthy volunteers and pathologic subjects have been previously approved by the local human research ethics committee. All subjects provided written informed consent. Subjects were divided into groups, accounting for the different health conditions, as healthy subjects, Achalasia pattern I, Achalasia pattern II, Hypertensive LES, Nutcracker esophagus and DES.

Pressure data were analysed by ManoViewTM (Given Imaging Ltd, Israel) and the actual pathologies were identified by clinicians with high degree of expertise, according to standard criteria [3]. Data were subsequently exported and post-processed by specific routines in MatLab (The MathWorks Inc., Natick, MA).

B. Physiological model definition

A physiological model was developed to interpret pressure evolution over time at different positions along the esophagus:

$$p(x,t) = s(x,t) + \delta(x,t)$$

$$p(x,t) = p_0(x) + \left[p_{max}(x) - p_0(x)\right] sech\left\{\frac{\beta(x)}{L}\left[x - \eta(x)t\right]\right\}$$

$$\delta(x,t) = \frac{5}{4}\Delta(x)\left\{tanh\left[\frac{2}{\phi(x)}\left(t - \frac{x}{\eta(x)}\right)\right] - \frac{1}{5}tanh\left[\frac{2}{5\phi(x)}\left(t - \frac{x}{\eta(x)}\right)\right]\right\}$$

where t is time; x is the normalized position along the esophagus; L is the esophageal length; p_0 is the basal pressure; p_{max} is the difference between the maximum pressure and the resting pressure; β is related to the contraction persistence ϕ; η is related to the propagation speed of the pressure wave, the pressure peak occurs at $t_{max}=x/\eta$ and Δ represents the difference between the pressure measured after and before the bolus transit (Fig. 2).

C. Parameters identification

With regard to the mean deglutition of each subject, data from each sensor of the probe were fitted by the model, leading to the identification of the local values of the model parameters. The identification of the parameters for each sensor defines a curve for each parameter, as $p_0(x)$, $p_{max}(x)$, $t_{max}(x)$, $\beta(x)$ and $\Delta(x)$. $v(x)$ was computed as the numerical derivative of $t_{max}(x)$, representing the actual propagation speed of the peristaltic wave.

The parameter curves of each subject were statistically analyzed within each group of subjects, in order to identify the corresponding distributions. Finally, the parameters distributions were compared to evaluate their capability to interpret the different healthy or pathologic conditions.

D. Autonomic diagnosis

A specific procedure was defined and implemented accounting for the distribution of the parameters within the different groups of subjects. The procedure analyses HRM data of a specific subject by the following main steps:

- computation of the mean deglutition from the HRM measurement;
- identification of the model parameters;
- computation of "similarity indexes" between the specific subject and the different groups of subjects;
- diagnosis: selection of the group of subjects showing the highest similarity index.

III. RESULTS

A physiological model able to interpret data from HRM measurements was defined and the coefficient of determination R^2 between clinical data and model results was evaluated for each subject. The range of variation is from 0.83 to 0.96 within the different groups of subjects. An autonomic procedure was developed to identify the physiological model parameters that optimally interpret a HRM map of a mean deglutition. The parameters curves were statistically processed and summarized in order to achieve the parameters distributions for each group (Fig. 3). The pathologic situations showed significant differences at the specific regions affected.

The autonomic diagnostic system was able to match the correct diagnosis for the 79.8% of the considered subjects. The performance of the algorithm was even higher (86.2%) if the difference between the two patterns of Achalasia was not considered. The success rate of the algorithm can be represented by means of a grayscale map in order to compare autonomic diagnoses with actual healthy or pathologic conditions (Fig. 4).

IV. CONCLUSIONS

A general framework for the post-processing of clinical data from HRM was developed, aiming to provide an autonomic decision support system for a more reliable diagnosis of esophageal motility diseases. The suitability of the physiological model was assessed endorsing its reliability as a tool to interpret HRM data. The high success rate of the algorithm suggested the application of the procedure for the diagnostic activity. Obviously, the reliability of the procedure depend on the size and quality of the database. A preliminary database was here assumed, but it should be extended and continuously updated in order to improve the autonomic diagnosis procedure efficiency and reliability.

REFERENCES

[1] D.S. Nayar et al. (2005). Esophageal manometry: assessment of interpreter consistency. *Clinical Gastroeneterology and Hepatology 3*. pp. 218–224.

[2] E.Toklu (2011). A new mathematical model of peristaltic flow on esophageal bolus transport. *Scientific Research and Essays 6(31)*. pp. 6606–6614.

[3] S.J. Spechler, D.O. Castell (2001). Classification of oesophageal motility abnormalities. *Gut 49(1)*. pp. 45–151.

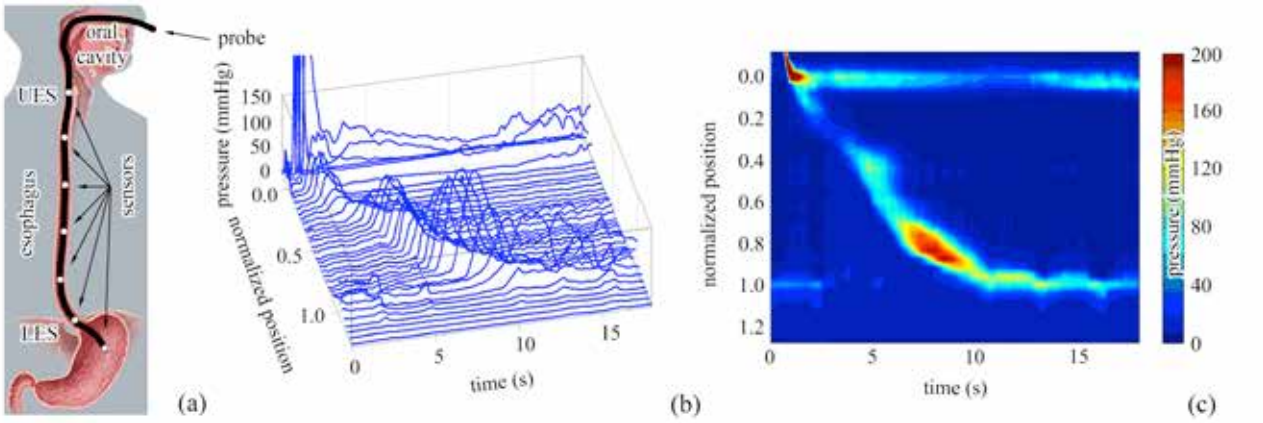

Fig. 1. Scheme of a HRM test: probe placement (a), measured signals (b), pressure map (c).

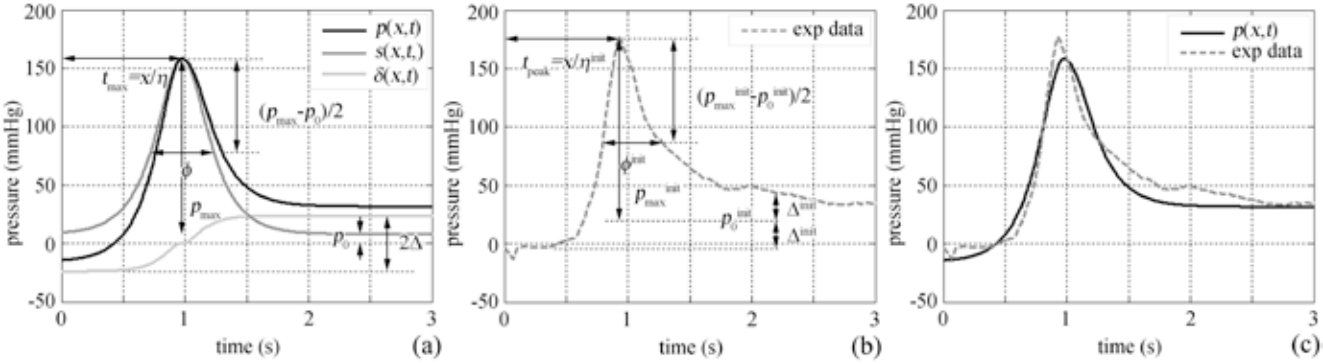

Fig. 2. Model parameters in a pressure versus time diagram (a); identification of initial values of parameters by processing experimental data (b); comparison of model results and experimental data after discrepancy minimization (c).

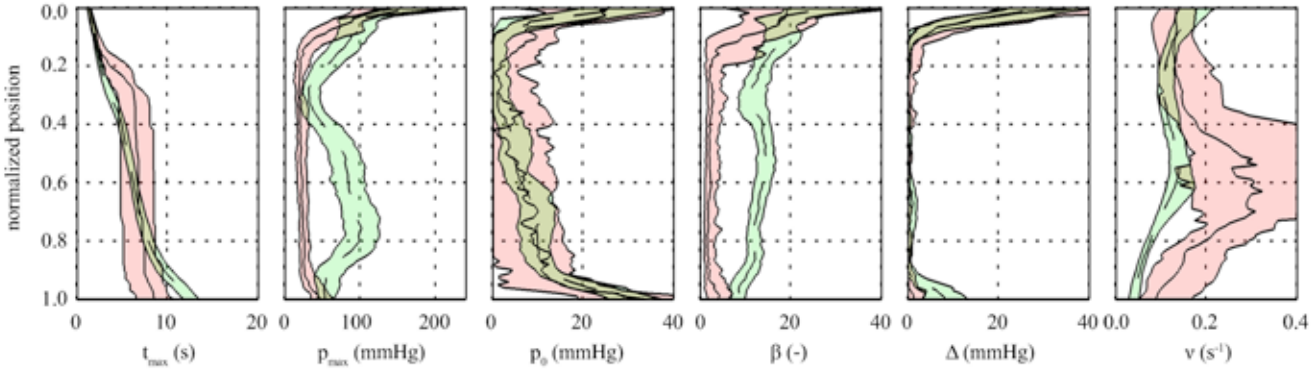

Fig. 3. Example of parameters distributions regarding the group of subjects with Achalasia pattern I. Distributions are reported as 50% scatter bands (colored areas) and median values (continuous or dashed lines). The parameters distributions of healthy subjects (green areas) are overlapped to the parameters distributions of Achalasia pattern I group (pink areas), in order to emphasize the differences.

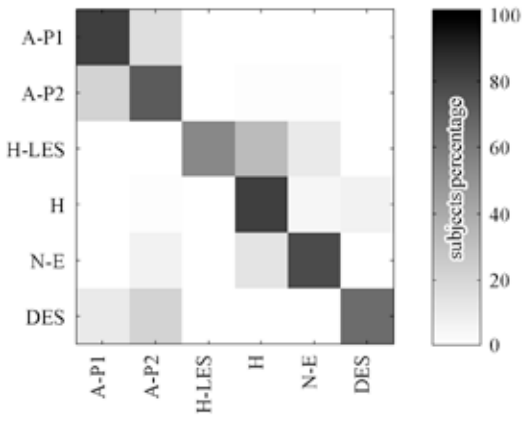

Fig. 4. Results of the autonomic diagnosis algorithm with regard to the different healthy and pathological conditions, as Achalasia pattern I (A-P1), Achalasia pattern II (A-P2), Hypertensive LES (H-LES), healthy (H), Nutcracker esophagus (N-E) and Diffuse Esophageal Spasm (DES). Rows correspond to the actual healthy or pathological conditions, while columns correspond to the results of the autonomic diagnoses.

Ocular surface temperature in healthy subjects: a preliminary study

S. Matteoli[1], F. Vannetti[2], S. Tchuente[1] and A. Corvi[1]
[1]*Bioengineering Laboratory, Department of Industrial Engineering, University of Florence, Florence, Italy*
[2]*Don Gnocchi Foundation, Rehabilitation Center IRCSS, Florence, Italy*

***Abstract*— The aims of this study were 1) to measure by thermography the ocular surface temperature (OST) of a healthy population (68 subjects, 34M/34F), and 2) to investigate the influence of subject factors (i.e. age, gender, BMI, body temperature, physical activity and smoke) on the OST. Specifically, the OST of five anatomical areas on both eyes were measured. Statistical analyses showed the repeatability of the measurements and the significant difference among three areas: nasal, central and temporal. Moreover, there was no significant difference between left and right eyes (P-value>0.05). Age, body temperature and smoke did influence significantly the OST of both eyes (P-value<0.001), while gender, BMI and physical activity and did not influence significantly the OST (P-value>0.05). The strong correlations OST-age and OST-body temperature indicates the importance of these two subject factors when investigating different populations.**

***Keywords*—Insert up to 4 keywords, separated by commas.**

I. Introduction

Interest in the temperature of the eye spans almost 130 years [1,2], but accurate quantitative measurements of the profile of the ocular surface temperature (OST) has been possible only in the last few decades, thanks to the infrared thermography (IR) - a non-invasive, cheap and easy-to-use technique which allows measuring the OST with more accuracy, resolution, and speed than previously possible [2-5]. It is widely known that the ability to measure accurately the OST will increase the understanding of ocular physiology and should be a decisional support to the therapy integrated with classical diagnostic procedure. The use of ocular thermography offers great opportunities for monitoring the temperature of the anterior eye and analyzing the effects of some pathology in the OST [6-13]. However, it is firstly necessary to establish a normal range of the OST in order to correlate OST alterations to parameters, which might describe pathologies. Unfortunately, the literature cannot be used as a reference as previous studies focused only on the temperature of the central cornea [5,14], or examined only a group of Chinese young adults [15]. The aims of this study were to measure the OST of a healthy population and to investigate the influence of subject factors (*i.e.* age, gender, height, weight, body temperature, physical activity and smoke on the OST.

II. Material and Methods

A. Subjects

68 subjects (34M/34F of age 14-80) were enrolled in this study. Exclusion criteria were: ophthalmic pathologies, diabetes and a body temperature above 37.5°C. All participants were volunteers, who signed the informed consent before starting the measurements. Furthermore, each subject was asked to fill a questionnaire regarding personal data as well as general and ocular anamnesis. Table 1 shows the characteristics of the subjects investigated.

Table 1: Subjects' characteristics expressed as mean ± SD.

	Females	Males
Subjects	34	34
Age (years)	50±15	47±17
Weight (kg)	67.3±13.6	77.5±12.3
Height (cm)	162.9±6.0	174.5±6.5
BMI (kg/m^2)	25.5±3.7	25.4±5.4
Body Temperature (°C)	36.1±0.4	36.2±0.4

B. Experimental setting

The thermocamera used to acquire the OST was the FLIR 320A with an image resolution of 320x240 pixels, and image frequency of 30 Hz. The detectors time constant is 12 ms with accuracy ±2°C and a sensibility of 0.05 °C at +30 °C.

Only one examiner carried out OST measurements in order to avoid inter-examiner variation, in a room without windows, illuminated with neon lights. Both temperature and humidity were constantly monitored and maintained to an average of 22.1±0.5°C and 43±4% by using an air conditioning system.

The same procedure was applied for each thermographic acquisition. Subjects remained in the test-room for 20 minutes [11], so that the own body temperature could adapt to the climatic condition of test-room. Then, subjects' chin was positioned on an ophthalmic chinrest in front of the thermocamera, whose lens was positioned at 500 mm. the subject was asked to keep both eyes closed for 10 s before starting the measurement. Subjects were asked to keep both eyes widely open during the thermographic acquisition (7 s at 30 Hz), so that both eyes could be measured in just one recording. Three recordings were taken for each subject.

For each thermographic acquisition only the first frame corresponding to the eye opening was selected for further analysis, in order to avoid the influence of the tear-film evaporation [13].

C. Image processing

A semi-automatic image processing procedure written in Matlab (2012, Mathworks, USA) was used to calculate from the selected frames the ocular temperatures. As shown in Figure 1, the eye was divided into five anatomical areas: 1) nasal, 2) central, 3) temporal, 4) superior and 5) inferior. The average temperature was calculated for each area.

D. Statistcal analysis

One-way ANOVA was applied in order to assess the measurements repeatability as well as the difference among the temperature of the five areas selected.

Paired t-test was carried out in order to compare right (RE) and left (LE) eyes, while a multivariate regression analysis was then used to evaluate which predictors were significantly influencing the OST. *Unpaired t-test* was applied to analyze the effect of smoke on the OST of all ocular areas.

A P-value<0.05 was chosen to indicate a significant difference.

III. Results

ANOVA tests confirmed the repeatability of the measurements (P-value>0.05), so for each subject the OST was calculated as the average of the three temperatures, and a significant difference (P-value<0.0001) among the temperature belonging to three areas: nasal, central and temporal for both RE and LE.

Paired t-test showed that there was no significant difference between RE and LE.

In order to carry out the multivariate regression analysis, the level of physical activity was classified as: none, mild, moderate or intense.

Table 2 shows P-values obtained by the multivariate regression analysis. Gender, BMI and physical activity did not influence significantly the OST ocular area, whereas body temperature influenced significantly the OST. Specifically, results showed a positive correlation between body temperature and OST. The effect of age was found to be significant only in the nasal region.

Table 2: P-values found by multivariate regression analysis

	Nasal	Central	Temporal	Superior	Inferior
BMI	0.256	0.141	0.220	0.224	0.462
Age	0.032	0.253	0.098	0.150	0.231
Gender	0.577	0.931	0.394	0.623	0.834
Body Temperature	0.000	0.000	0.000	0.000	0.000
Physical activity	0.569	0.838	0.773	0.901	0.708

When evaluating the smoking history, subjects were divided into two groups: smokers and non-smokers. Specifically, the non-smokers included also those who had stopped smoking for more than fifteen years. Results obtained from the unpaired t-test showed a significant difference (P-value<0.04) between smokers and non smokers in all 5 areas (Figure 2). Specifically, smokers showed always a higher temperature than non smokers.

IV. Discussion

Results confirmed the repeatability of the measurements as well as a significant difference among the temperature obtained from the nasal, central and temporal areas. The latter finding confirms the necessity to evaluate the OST of these anatomical regions of the eye.

Gender does not influence significantly the OST, but females showed a tendency to have higher temperatures than males (Figure 3). This may be explained with hormonal factors as most of females were women of childbearing age.

Smokers showed a higher temperature than non smokers in all regions; this may be related to the inflammation process caused by nicotine and other components present in tobacco. It is known, indeed, that inflammation is usually associated with an increase in blood perfusion that should lead to OST increase.

Furthermore, the strong correlations OST-age (even though only for the nasal area) and OST-body temperature indicate the importance of these two subject factors when investigating different populations.

Acknowledgement

Authors would like to thank all volunteers who were enrolled in the study.

References

[1] A. Holmberg, "The temperature of the eye during the application of hot packs, and after milk injections". *Acta Ophthalmol*, vol. 30, pp. 347-364, 1952.

[2] C. Purslow, and J. S. Wolffsohn, "Ocular surface temperature: a review", *Eye & Contact Lens*, vol. 31, pp. 117-123, 2005.

[3] R. Mapstone, "Measurement of corneal temperature", *Exp Eye Res*, vol. 7, pp. 237-243, 1968.

[4] P. B. Morgan, M. P. Soh, N. Efron, and A. B. Tullo, "Potential applications of ocular thermography., *Optom Vis Sci*, vol. 70, pp. 568–576, 1993.

[5] H. Fujishima, I. Toda, M. Yamada, N. Sato, and K. Tsubota, "Corneal temperature in patients with dry eye evaluated by infrared radiation thermometry", *Br J Ophthalmol*, vol. 80, pp. 29-32, 2006.

[6] A. Sodi, B. Giambene, G. Falaschi, R. Caputo, B. Innocenti, A. Corvi, and U. Menchini, "Ocular surface temperature in central retinal vein occlusion: preliminary data" *Eur J Ophthalmol*, vol. 17, pp. 755-759, 2007.

[7] D. Martin, and I. Fatt, "The presence of a contact lens induces a very small increase in the anterior corneal surface temperature." *Acta Ophthalmol (Copenh)*, vol. 64, pp. 512-518, 1986.

[8] S. Betney, P. B. Morgan, S. J. Doyle, and N. Efron, "Corneal temperature changes during photorefractive keratectomy", *Cornea*, vol. 16, pp. 158-161, 1997.

[9] A. Corvi, B. Innocenti, and R. Mencucci, "Thermography used for analysis and comparison of different cataract surgery procedures based on phacoemulsification", *Physiol Meas*, vol. 27, pp. 371-384, 2006.

[10] F. Vannetti, S. Matteoli, L. Finocchio, F. Lacarbonara, A. Sodi, U. Menchini, and A. Corvi, "Relationship between ocular surface temperature and peripheral vasoconstriction in healthy subjects: a thermographic study", *Proc Inst Mech Eng H*, vol. 228, pp. 297-302, 2014.

[11] S. Matteoli, L. Finocchio, I. Biagini, G. Giacomelli, A. Sodi, A. Corvi, G. Virgili, and S. Rizzo, "A thermographic study on eyes affected by Age-related Macular Degeneration: Comparison among various forms of the pathology and analysis of risk factors", *Infrared Physics & Technology,* Mar 2016.

[12] A. Sodi, S. Matteoli, G. Giacomelli, L. Finocchio, A. Corvi, and U. Menchini, "Ocular surface temperature in age-related macular degeneration", *J Ophthalmol*, vol. 2014, pp. 281010, 2014.

[13] P. B. Morgan, "Ocular thermography in health and disease", PhD Thesis University of Manchester, 1994.

[14] U.R. Acharya, E. Y. Ng, G. C. Yee, T. J. Hua, and M. Kagathi, "Analysis of normal human eye with different age groups using infrared images", *J Med Syst*, vol. 33, pp. 207-213, 2009.

[15] L. Tan, Z. Q. Cai, and N.S. Lai, "Accuracy and sensitivity of the dynamic ocular thermography and inter-subjects ocular surface temperature (OST) in Chinese young adults", *Contact Lens & Anterior Eye,* vol. 32, pp. 78-83, 2009.

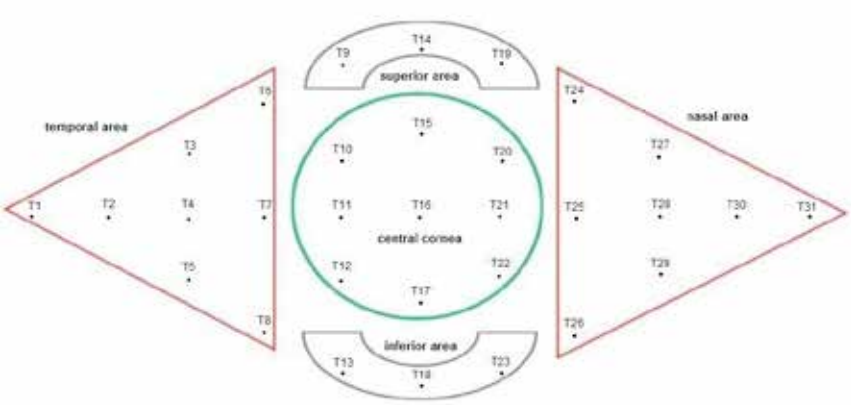

Figure 1 Scheme of the eye divided into 5 main areas for the calculation of the Ocular Surface Temperature

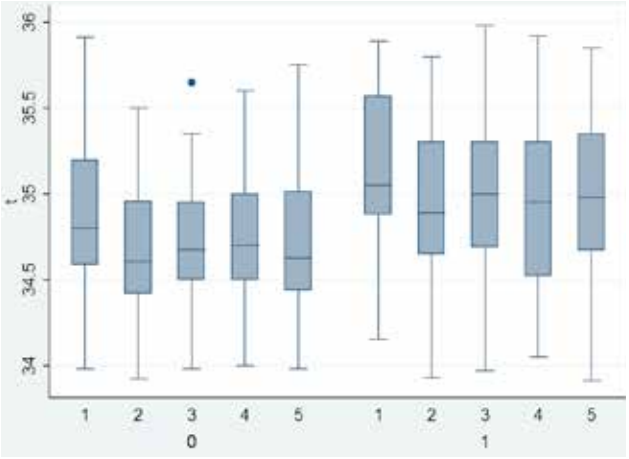

Figure 2 Comparison among the OSTs of smokers (1) and non smokers (0) in all 5 ocular areas

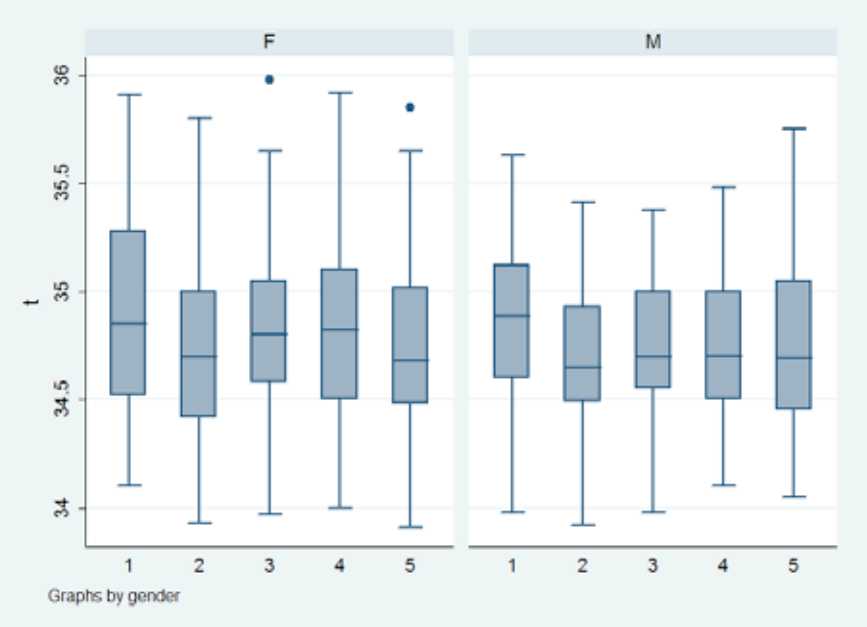

Figure 3 Comparison among the OSTs of females (F) and males (M) in all 5 ocular areas

Fully textile electrodes for wearable electrophysiological signal monitoring systems

D. Pani [1], G. Barabino [1], A. Achilli [1], B. Fraboni [2] and A. Bonfiglio [1]
[1] *Dept. of Electrical and Electronic Engineering - University of Cagliari, Italy*
[2] *Dept. of Physics and Astronomy - University of Bologna, Italy*

***Abstract*— In recent years, there has been a particular interest in wearable electronics due to the continue miniaturization of electronic devices. This led to the use of this technology in various fields as fashion, fitness or medical devices. The ultimate goal is the integration of sensors and electronics in clothes and garments.**

In this work, textiles electrodes obtained by treating natural cotton fabric with the conductive polymer poly-3,4-ethylenedioxythiophene doped with poly(styrene sulfonate) (PEDOT:PSS) are presented. The intrinsic ionic conductivity of the PEDOT:PSS coated fabrics eliminates the need of electrolytes, pastes or solutions for acquiring bioelectrical potentials directly from the human skin. The electrodes have been tested on human volunteers, in dry and wet conditions, at rest and during physical activity.

The achieved results reveal that these electrodes can be effectively used to acquire ECG signals. The performance of fabric electrodes in term of skin-electrode impedance and noise level is comparable to gelled Ag/AgCl electrodes. A printing technique able to achieve good definition and control over the quantity of deposited polymer is also presented as an alternative to the treatment of the whole tissue.

***Keywords*—Textile electrodes, conductive textiles, e-textiles, wearable electronics.**

I. INTRODUCTION

TODAY, the development of wearable technologies able to unobtrusively and accurately monitor bioelectric signals in various everyday life conditions is an important goal of biomedical engineering research. Traditional Ag/AgCl gelled electrodes are still the gold standard for clinical and short-term evaluation but their short operation time and low comfort limit their use in wearable applications [1]. Electro-conductive textiles can represent a valuable solution. Cotton, polyester and polyamide are three of the most common textile materials universally appreciated for their comfort, soft handle, water absorbency, strength and easy maintenance. In recent years, with the development of stable and highly conductive polymers it has been possible to transform those standard non-conductive textile fibers into flexible and reliable conductors [2]. PEDOT:PSS is one of the most commercially successful conductive polymers that can be exploited to this aim [3].

In this paper, we present the development of textile electrodes based on the treatment of common textile fabrics with a highly conductive PEDOT:PSS solution. PEDOT:PSS coating has been obtained with two distinct techniques: the immersion in a PEDOT:PSS solution and a screen printing with an ink obtained with a modified PEDOT:PSS solution. Despite less investigated for the time being, the second method allows selectively creating conductive areas, with a high geometrical precision and the chance to control the amount of ink on the fabric surface. This is promising for the realization of smart clothes with biopotentials acquisition features.

II. MATERIALS AND METHODS

A. Fabrication of soaked textile electrodes

A highly conductive PEDOT:PSS dispersion (Clevios PH 500, Heraeus Clevios – Germany) was mixed with a second dopant to improve conductivity. The substrate of tissue was immersed for at least 48h at room temperature in the polymer solution, then passed through metallic rolling cylinders that apply pressure in order to remove the solution in excess, and finally annealed at 180°C. The conductive fabric was then sewed to a nonconductive 35 mm × 35 mm layered structure of foam (4 mm) and polyester, and a snap button was attached to provide the possibility to use the electrode with snap-on ECG cables (Fig. 1). The introduction of foam layers allows improving the contact between the electrode and the skin, also preserving the electrode wet when naturally or artificially wetted, with a positive impact on the skin contact impedance [4].

B. Fabrication of printed textile electrodes

The same kind of tissue was used also as substrate for the printed electrodes. The ink used in this case was obtained adding a reticulating agent and heating for 50 minutes until it reaches a semisolid state. Then, the ink is deposited through a mask on the fabric surface to impress the electrode with the desired shape. Samples are then annealed as in the previous case. Printed electrodes are characterized by an extreme versatility in the fabrication technique and, treating pre-defined portions of the garment, enable the integration of the electrodes in finished clothes. For these reasons, such electrodes have not been equipped neither with snap fastener nor with foam layers.

C. Instrumentation and measurements

Since the first technology is mature whereas the second one is currently under development, the reported evaluation has been carried out on the soaked electrodes only, not on the printed ones. Dry and wet conditions (about 0.10 ml of saline, to emulate human sweat [4]) have been tested. This study followed the principles outlined in the Helsinki Declaration of 1975, as revised in 2000, and involved 10 voluntary subjects.

Skin-electrode contact impedance at 10 Hz was measured with an FDA cleared Prep-Check impedance meter by General Devices between two adjacent points on the chest.

For ECG signal acquisition, the single-lead standard Holter

placement (second lead for 7- electrode configuration) was chosen. Textile electrodes were attached with adhesive tape on the chest. In order to record some ECG traces, simultaneously and independently using textile and commercial disposable electrodes (FIAB F9079 Ag/AgCl foam electrodes), a custom battery-powered recorder has been designed. Based on the analog front-end ADS1292 by Texas Instruments, it applies minimal and known signal conditioning before analog to digital conversion [5]. The ADS1292 is interfaced to a local host microcontroller MSP430F5515 via an SPI port, in charge of configuring it, reading the data and writing them to a microSD card. The recorder was set to acquire at a sampling frequency of 512 Hz (24-bit). The input referred noise of the recorder is about 5 μV rms.

The experimental protocol was designed to include both rest and dynamic conditions (step and stairs climbing), and was carried out in the lab facilities.

III. Results

The impedance measurements provided, as expected, better values for the wet electrodes (22.3 kΩ ± 9 kΩ) compared to the dry ones (96.6 kΩ ± 54 kΩ). Remarkably, both values are largely acceptable.

Dry electrodes are more sensitive to baseline wandering and motion artefact. This is clearly visible in Fig. 2, which reveals that wet textile electrodes could perform even better than commercial Ag/AgCl electrodes in some cases. This is also confirmed by a QRS detection analysis, performed with the Pan-Tompkins algorithm [6]. The manual annotation of an expert, performed analyzing contemporarily all the readable signals (an R peak is annotated when visible in at least one signal) has been used as ground truth. At rest, no signal is discarded because unreadable, for both dry and wet textiles, whereas during exercise some unreadable records appear for the dry electrodes. The performance of the QRS detector has been analysed in terms of Sensitivity (S defined as TP/(TP + FN)) and Positive Predictivity (P+ = TP/(TP + FP)) in Fig. 3, confirming that wet electrodes are comparable to wetted commercial ones, whereas dry ones does not.

About baseline wandering, which is a typical issue of textile electrodes fabricated with different technologies, we estimated its trend using the non-linear filter described in [7]. Its standard deviation is presented in Fig. 4, and again confirm the superiority of the wet electrodes compared to the dry ones. The same difference can be seen with other performance metrics, such as the *rms* around the baseline, the kurtosis index, etc. [8].

IV. Conclusion

In this paper, we introduced light, flexible and comfortable electrodes made of conductive polymer-treated common textiles. By completely treating the fabrics with doped PEDOT:PSS solutions, very conductive textiles can be obtained, revealing good performance as surface electrodes for biopotential recordings.

Compared to soaked electrodes, the printed ones do not have the same amount of PEDOT:PSS solution in the fibers and so they present a worst conductivity. Nevertheless, it is possible print the sensors to be in contact with the skin even when the cloth has been already manufactured. Such electrodes also showed a better reproducibility and manufacturability and this can be the first step towards the production of clothes able to unobtrusively acquire physiological biopotentials. This kind of products can have different uses because, potentially, they can also detect signals different from the ECG.

At the moment, a clinical trial is starting to evaluate the quality of the ECG signals acquired with textile electrodes produced with the described technology, targeting the most common ischemic and congenital heart diseases. Future work includes the study of the best strategies for integrating fabric electrodes in everyday clothes for long-term monitoring applications.

References

[1] M. Stoppa, A. Chiolerio, "Wearable Electronics and Smart Textiles: A Critical Review," *Sensors*, vol. 14, pp.11957–11992, 2014.

[2] G. Mattana, P. Cosseddu, B. Fraboni, G. G. Malliaras, J. P. Hinestroza, and A. Bonfiglio, "Organic electronics on natural cotton fibres," *Organic Electronics*, vol. 12, no. 12, pp. 2033–2039, Dec. 2011.

[3] S. Tsukada et al., "Conductive polymer combined silk fiber bundle for bioelectrical signal recording," *PloS one*, vol. 7, no. 4, p. e33689, Jan. 2012.

[4] J. Löfhede et al., "Textile Electrodes for EEG Recording – A Pilot Study," *Sensors*, vol. 12, no. 12, pp. 16907–16919, 2012.

[5] G. Barabino, D. Pani, A. Dessì and L. Raffo, "A configurable biopotentials acquisition module suitable for fetal electrocardiography studies," *Medical Measurements and Applications (MeMeA), 2015 IEEE International Symposium on*, Turin, 2015, pp. 479-483.

[6] J. Pan, W. J. Tompkins, "A Real-Time QRS Detection Algorithm," *IEEE Trans. on Biomedical Engineering*, vol. BME–32, no. 3, pp. 230–236, Mar. 1985.

[7] J. M. Łeskia, N. Henzel, "ECG baseline wander and powerline interference reduction using nonlinear filter bank," *Signal Processing*, vol. 85, no. 4, pp. 781–793, Apr. 2005.

[8] D. Pani et al., "Fully Textile, PEDOT:PSS Based Electrodes for Wearable ECG Monitoring Systems," *IEEE Transactions on Biomedical Engineering*, vol. 63, no. 3, pp. 540-549, March 2016.

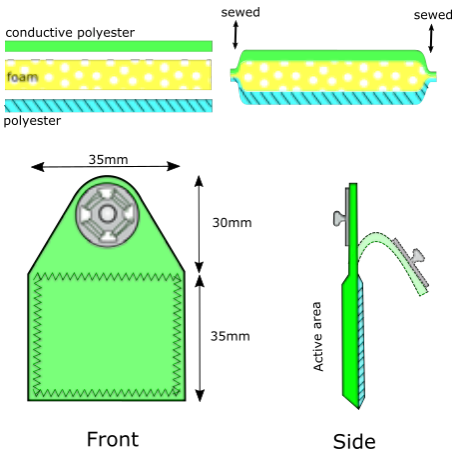

Fig. 1. The drawings of the soaked textile electrodes.

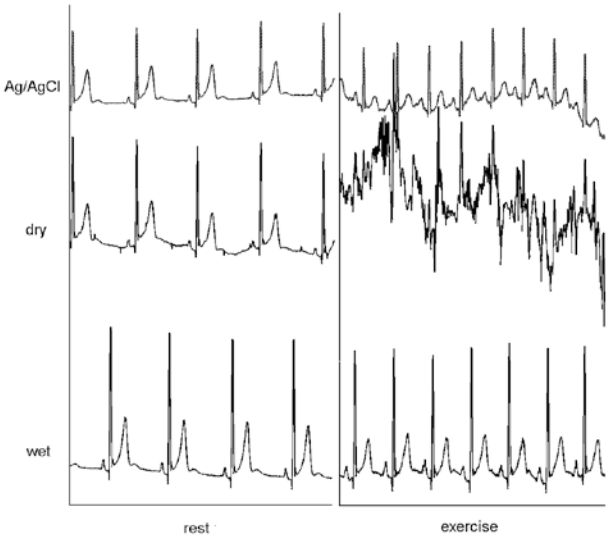

Fig. 2. From top to bottom, the ECG signals acquired with commercial disposable electrode, with soaked dry textile electrodes and with soaked wet (saline) textile electrodes, both at rest and during a moderate physical activity (stairs climbing).

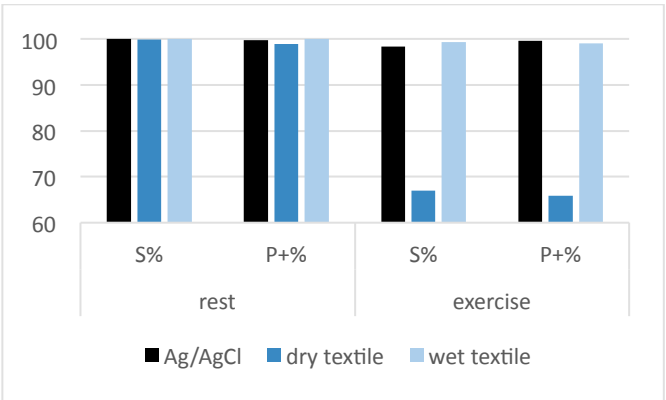

Fig. 3. The performance of the electrodes evaluated in terms of Sensitivity and Positive Predictivity in different conditions.

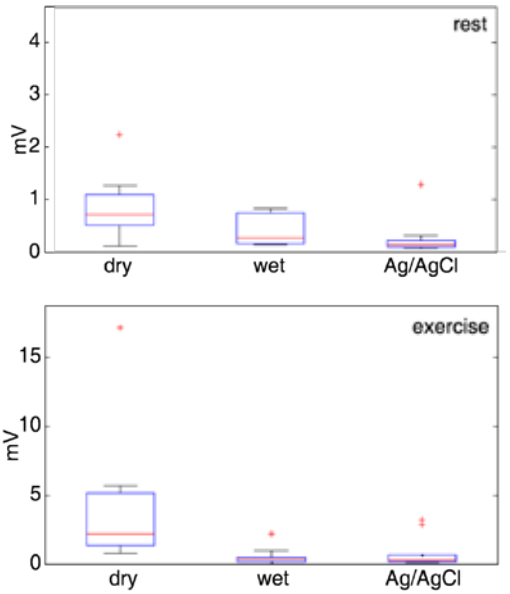

Fig. 4. Standard deviation of the baseline wandering in the ECG traces at rest and during exercise, with commercial disposable electrodes, and with the proposed textile (dry and wet) electrodes.

In situ laser fenestration of a standard stent graft

R. Piazza[1,2], S. Condino[1], F. Rossi[3], V. Ferrari[1,4] and M. Ferrari[1,2]

[1] *EndoCAS Center, Department of Translational Research and of New Surgical and Medical Technologies, University of Pisa, Pisa, Italy.*
[2] *Unit of Vascular Surgery of the Department of Translational Research and of New Surgical and Medical Technologies, University of Pisa, Pisa, Italy.*
[3] *Institute of Applied Physics, Italian National Research Council (CNR), Florence, Italy.*
[4] *Department of Information Engineering, University of Pisa, Pisa, Italy.*

***Abstract*— Complex morphology of abdominal aneurysms is the main limiting factor for the eligibility of patients to endovascular aneurysm repair. During these years, custom made stent grafts have been developed, such as fenestrated and branched ones. These devices are expensive, depend on accurate preoperative imaging and their implantation is time consuming. For these reasons, alternative procedures, such as the in situ fenestration of a standard stent graft have been proposed. The reliability of this procedure is today principally limited by the difficulties in guiding the endovascular tools to the proper fenestration site. In this work we propose an innovative fenestration strategy based on a laser technology integrated into a 3D computer-assisted guidance platform.**

***Keywords*— In situ fenestration, laser, 3D EM navigation, EVAR.**

I. Introduction

EVAR (Endovascular Aneurysm Repair) is a minimally invasive surgical procedure that involves, under fluoroscopic guidance, the placement of a stent graft within the aorta to exclude an aortic aneurysm. Advantages of this technique comprise quicker recoveries, shorter hospitalization, and lower risk of complications. However it is not free of complications and intraoperative technical problems can arise when traversing very narrow irregularly shaped, highly tortuous and heavily branched vessels to reach the treatment site. Aorta anatomy is a key aspect for a reliable endograft anchoring and for maintaining continued blood flow through the collateral vessels [1, 2]. For example, in the cases of juxtarenal aneurysms, where the dilation extends up to but does not involve the renal arteries, the implantation of a standard endograft may be problematic: since the length of suitable aorta suitable for a proper attachment of device is inadequate [3]. In these cases custom-made grafts with fenestrations (made before surgery) may be useful to maintain the perfusion of branches extending from aorta [4, 5]. Fenestrated grafting however is technically challenging and time consuming since fenestrations should be aligned with the collateral vessels ostia. Moreover, the use of customized grafts is expensive and requires significant preplanning, and such grafts are not available for acute syndromes and for emergency situations. Alternative procedures, such as the *in-situ fenestration of a standard stent grafts* have been proposed in order to avoid custom fabrication of endoprosthesis and find a simple, accurate and cost-effective way to obtain fenestrated stent grafts and preserve blood flow to essential visceral arteries.

II. In Situ Fenestration

Due to an unfavourable anatomy of the patient's aorta, sometimes, a proximal portion of the stent graft needs to be secured to the aortic wall including the branch vessel origins, thereby obstructing the passage of blood through them. In order to restore patency to visceral vessels, stent grafts can be modified intraoperatively with the in situ creation of a fenestration close to the location of the involved branch vessels.

A. Fenestration methods

Today, one limitation for the reliability of the in situ fenestration is the lack of a safe method to perforate the graft, preventing injuries to the arterial wall. Different techniques exist to form openings in the graft material: penetration by a needle or the sharp end of a guidewire [6-9]; use of a radiofrequency probe [10-12]; use of laser systems [13-15]. Restoration of blood flow is relatively difficult to perform with a needle because the exerted forces can suddenly cause the crossing of the needle through the material damaging adjacent aortic tissues. Fenestrations with radiofrequency probe and laser consist of melting or vaporizing the graft fabric by transferring energy from tip of the fenestration tool. Fabric particles and/or coagulated blood could potentially embolize during such a procedure.

Among fenestration methods, laser generated fenestration can be potentially considered the safest and most promising procedure because it can be selective for the graft material and thus it can avoid injuries to surrounding tissues. Several research studies indeed reported the use of laser atherectomy catheters as an equivalent solution to perforate the graft material. Regardless of the method used, the perforation must be enlarged, for example, with a catheter balloon.

B. Identification of fenestration site

Most of aforementioned approaches to create openings in endoprosthesis are performed with a retrograde approach [6, 7, 10, 16-19], which require the percutaneous access to the downstream vessel, with the fenestration of the fabric from the external surface of the graft. Using this approach it is easy to fenestrate a thoracic stent graft from aortic arch vessels (left subclavian artery, carotid arteries). Because of anatomical considerations, a similar methodology cannot be applied for creating holes in an abdominal graft (in correspondence to visceral vessels such as renal or mesenteric arteries) which require an antegrade approach [8, 9, 20]. In this case the graft is fenestrated from the inside. This technique is more difficult due to mechanical reasons (including mechanical stability of the fenestration device) and the difficulty in precisely identifying the target fenestration site: indeed, after the coverage of arteries ostia

due to stent graft realising, the collateral vessels cannot be visualized by angiography since the contrast medium flow is blocked by the endograft wall.

In previously studies, our research group [21, 22] have demonstrated that a 3D computer-assisted guidance system, based on the electromagnetic (EM) tracking of the surgical tools, is a reliable solution for guiding endovascular instruments (catheters and guidewires) to a target site, allowing avoidance of the need for real-time fluoroscopy and angiography, thus reducing X-ray exposure and contrast medium injection. This system can use intraoperative data acquired just before the endograft deployment, such as 3D rotational angiography volumetric radiological images, to reconstruct a 3D model of the patient anatomy.

C. Reaching and positioning at the correct fenestration site

Our research group is working to provide guidelines for the design of adequate endovascular tools for the abdominal aortic aneurysm repair via the EM guided in-situ laser fenestration of a traditional stent graft. The idea is to use a laser fiber incorporated into a guidewire (Fig.1) to deliver laser energy, and a sensorized guiding catheter (Fig.2) for the navigation and positioning of the laser tool at the correct fenestration site. The guiding catheter must be easily advanced through the aorta until the proper axial positioning is reached, then it must be easily rotated in order to correctly orient its tip at the collateral arteries ostium. Then, the laser fiber, and thus the catheter tip, should be positioned perpendicular to the graft surface. This requires a proper bending of the catheter tip (Fig. 3). Finally, once the proper longitudinal and rotational alignments are reached and the catheter tip is perfectly aligned with the target site, the catheter should guarantee mechanical support and stability during fenestration.

III. CONCLUSION

In-situ fenestration presents an alternative option for the treatment of patients in case of emergency situations and who are unsuitable for a standard EVAR. To overcome the limitations linked to this procedure, our idea is to integrate a laser system into a 3D EM navigation platform to provide the surgeon with a selective fenestration tool whose position and orientation can be accurately tracked and showed in real time within the 3D model of the patient vasculature.

ACKNOWLEDGEMENT

The research is supported by the scientic project LASER (Electromagnetic guided in-situ laser fenestration of endovascular endoprosthesis, November 2014 - November 2017) funded by the Italian Ministry of Health and Regione Toscana through the call "Ricerca Finalizzata 2011-2012".

REFERENCES

[1] E. D. Dillavou, S. C. Muluk, R. Y. Rhee, E. Tzeng, J. D. Woody, N. Gupta and M. S. Makaroun, "Does hostile neck anatomy preclude successful endovascular aortic aneurysm repair?," *J Vasc Surg*, vol. 38, pp. 657-663, Oct 2003.

[2] E. Choke, G. Munneke, R. Morgan, A. M. Belli, I. Loftus, R. McFarland, T. Loosemore and M. M. Thompson, "Outcomes of endovascular abdominal aortic aneurysm repair in patients with hostile neck anatomy," *Cardiovasc Intervent Radiol*, vol. 29, pp. 975-980, Nov-Dec 2006.

[3] H. G. Bertoni, G. Girela, M. Peirano, J. H. Leguizamón, S. Ludueña and H. Barone, "Endovascular Exclusion of an Abdominal Aortic Aneurysm with a Fenestrated Balloon-Expandable Stent-Graft," *Revista argentina de cardiología*, vol. 76, pp. 2008.

[4] E. L. Verhoeven, C. J. Zeebregts, M. R. Kapma, I. F. Tielliu, T. R. Prins and J. J. van den Dungen, "Fenestrated and branched endovascular techniques for thoraco-abdominal aneurysm repair," *J Cardiovasc Surg (Torino)*, vol. 46, pp. 131-140, Apr 2005.

[5] R. K. Greenberg and M. Qureshi, "Fenestrated and branched devices in the pipeline," *J Vasc Surg*, vol. 52, pp. 15S-21S, 2010.

[6] R. G. McWilliams, S. J. Fearn, P. L. Harris, D. Hartley, J. B. Semmens and M. M. Lawrence-Brown, "Retrograde fenestration of endoluminal grafts from target vessels: feasibility, technique, and potential usage," *J Endovasc Ther*, vol. 10, pp. 946-952, Oct 2003.

[7] R. G. McWilliams, M. Murphy, D. Hartley, M. M. Lawrence-Brown and P. L. Harris, "In situ stent-graft fenestration to preserve the left subclavian artery," *J Endovasc Ther*, vol. 11, pp. 170-174, Apr 2004.

[8] L. W. Tse, B. T. Bui, S. Lerouge, I. Salazkin, E. Therasse, A. Benko, H. Heon, V. L. Oliva and G. Soulez, "In vivo antegrade fenestration of abdominal aortic stent-grafts," *J Endovasc Ther*, vol. 14, pp. 158-167, Apr 2007.

[9] C. V. Riga, C. D. Bicknell, D. Wallace, M. Hamady and N. Cheshire, "Robot-assisted antegrade in-situ fenestrated stent grafting," *Cardiovasc Intervent Radiol*, vol. 32, pp. 522-524, May 2009.

[10] F. Numan, H. Arbatli, W. Bruszewski and M. Cikirikcioglu, "Total endovascular aortic arch reconstruction via fenestration in situ with cerebral circulatory support: an acute experimental study," *Interact Cardiovasc Thorac Surg*, vol. 7, pp. 535-538, Aug 2008.

[11] L. W. Tse, S. Lerouge, B. T. Bui, E. Therasse, H. Heon and G. Soulez, "Radiofrequency perforation system for in vivo antegrade fenestration of aortic stent-grafts," *J Endovasc Ther*, vol. 17, pp. 192-198, Apr 2010.

[12] L. A. Eadie, G. Soulez, M. W. King and L. W. Tse, "Graft durability and fatigue after in situ fenestration of endovascular stent grafts using radiofrequency puncture and balloon dilatation," *Eur J Vasc Endovasc Surg*, vol. 47, pp. 501-508, May 2014.

[13] E. H. Murphy, J. M. Dimaio, W. Dean, M. E. Jessen and F. R. Arko, "Endovascular repair of acute traumatic thoracic aortic transection with laser-assisted in-situ fenestration of a stent-graft covering the left subclavian artery," *J Endovasc Ther*, vol. 16, pp. 457-463, Aug 2009.

[14] S. S. Ahanchi, B. H. Almaroof, C. L. Stout and J. M. Panneton, "In Situ Laser Fenestration and Stenting during TEVAR: A New Approach to Subclavian Artery Revascularization," *J Vasc Surg*, vol. 53, pp. 552-553,

[15] R. E. Redlinger, Jr., S. S. Ahanchi and J. M. Panneton, "In situ laser fenestration during emergent thoracic endovascular aortic repair is an effective method for left subclavian artery revascularization," *J Vasc Surg*, vol. 58, pp. 1171-1177, Nov 2013.

[16] B. Sonesson, T. Resch, M. Allers and M. Malina, "Endovascular total aortic arch replacement by in situ stent graft fenestration technique," *J Vasc Surg*, vol. 49, pp. 1589-1591, Jun 2009.

[17] B. J. Manning, K. Ivancev and P. L. Harris, "In situ fenestration in the aortic arch," *J Vasc Surg*, vol. 52, pp. 491-494, Aug 2010.

[18] B. Sonesson, T. Resch, N. Dias and M. Malina, "New temporary internal introducer shunt for brain perfusion during total endovascular arch replacement with in situ fenestration technique," *J Vasc Surg*, vol. 56, pp. 1162-1165, Oct 2012.

[19] D. S. Kassavin and G. Constantinopoulos, "Repair of a disconnected stent-graft limb facilitated by in situ fenestration," *J Endovasc Ther*, vol. 19, pp. 434-438, Jun 2012.

[20] T. Kolbel, S. W. Carpenter, H. Diener, S. Wipper, E. S. Debus and A. Larena-Avellaneda, "Antegrade in situ stent-graft fenestration for the renal artery following inadvertent coverage during EVAR," *J Endovasc Ther*, vol. 20, pp. 289-294, Jun 2013.

[21] S. Condino, V. Ferrari, C. Freschi, A. Alberti, R. Berchiolli, F. Mosca and M. Ferrari, "Electromagnetic navigation platform for endovascular surgery: how to develop sensorized catheters and guidewires," *Int J Med Robot*, vol. 8, pp. 300-310, Sep 2012.

[22] S. Condino, E. M. Calabro, A. Alberti, S. Parrini, R. Cioni, R. N. Berchiolli, M. Gesi, V. Ferrari and M. Ferrari, "Simultaneous tracking of catheters and guidewires: comparison to standard fluoroscopic guidance for arterial cannulation," *Eur J Vasc Endovasc Surg*, vol. 47, pp. 53-60, Jan 2014.

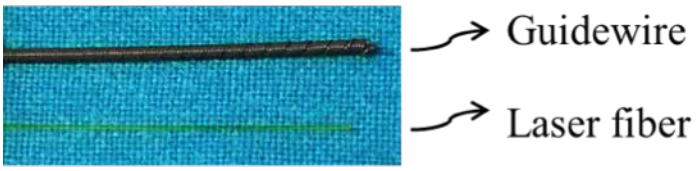

Fig. 1. The laser fenestration tool consists of a nitinol micro tube, used as guidewire, and a laser fiber.

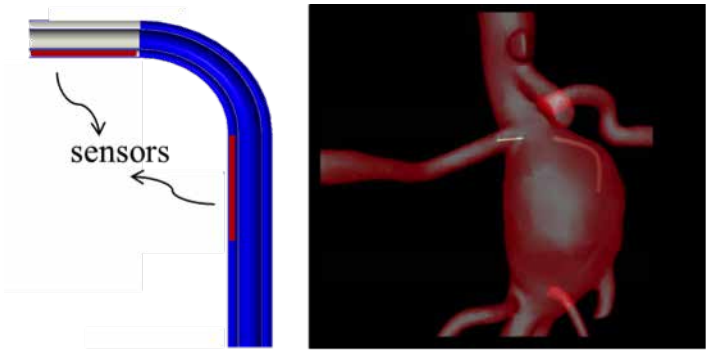

Fig. 2. On the right a screenshot of the navigation system during the targeting of the fenestration site. On the left the proposed sensor configuration [21] which allows the real time tracking of the catheter tip position and the reconstruction of the distal part curvature.

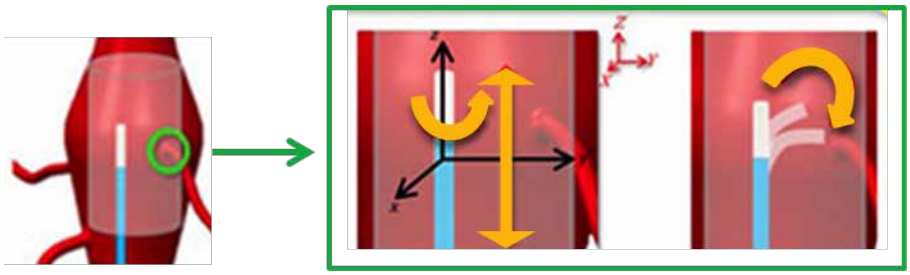

Fig. 3. Schematic representation showing the fenestration site targeting (the target ostium is highlighted with a green circle) during an EVAR procedure. Two coordinate systems are represented: a global system (XYZ) in red, and local coordinate system (xyz) in black related to the guiding catheter body. A precise targeting requires a proper catheter positioning along the longitudinal direction (Z axis), rotation around the catheter main axis (z axis) and bending of the catheter tip (in the yz plane).

Spectral encoded microgel readout system inflow for miRNA bioassay characterizations

Domenico Rossi[1], David Dannhauser[1], Edmondo Battista[1], Filippo Causa[1,2] and Paolo Antonio Netti[1,2]
[1]*Center for Advanced Biomaterials for Healthcare@CRIB, Istituto Italiano di Tecnologia (IIT), ITALY*
[2]*Interdisciplinary Research Centre on Biomaterials (CRIB), Università degli Studi di Napoli "Federico II", ITALY*

Abstract – A microfluidic based multiplex fluorescence signal detection system, able to accurately detect microRNA concentrations in small sample volumes without pre-treatments as PCR amplification steps is presented. Preliminary results show a variable particle speed -ranging from 1 up to 12 µm s-1- while an automatized fluorescent acquisition and microgel counting routine was able to detect the desired miRNA concentrations in microfluidic flow conditions.

***Keywords*—miRNA, Microfluidic, Viscoelasticiy**

I. Introduction

A microfluidic based multiplex fluorescence signal detection system, able to accurately detect microRNA (miRNA) concentrations in small sample volumes, without pre-treatments as PCR amplification steps is presented. In general, miRNAs are a class of short, single-stranded, non-coding endogenous RNAs, which play an important role in the regulation of gene expressions via target miRNA degradation or translational repression.[1] Recently it has been demonstrated that circulating miRNA expression levels in the human blood stream can be straightforward related to various diseases states, including, for instance, cancer, neurodegenerative disorders and cardiovascular diseases.[2] Accurate and reliable quantification of circulating miRNA in blood is challenging. Metastatic or recurrent diseases are still a major challenge due to high levels of sequence homology, complex secondary structures and low concentrations.

More recently, a number of new miRNA detection methods including droplet digital PCR, nanopore-based detection, sequencing and electrochemical sensing methods have been introduced for miRNA measurements.[3-6] However, all of them need large sample pre-treatments.

II. Materials and Methods

Recently, our research group has presented a microgel based multiplexing approach using microgel particles with a core-shell structure presenting two different fluorescent dyes -for multiplex spectral analyses- and endowed with an additional fluorescent probe for miRNA detection.[7] Indeed, the antifouling properties of microgels permit a direct measurement of miRNAs in the human blood serum, even though the microgels possessed all the requirements for direct in-serum detection, their application for a micro total analytical system (µTAS) is impaired. In fact, a cost effective automatized device, where microgels can be easily manipulated and optically analysed is still not available. To gain such an aim, microgel alignment in a specific measurement area of a highly translucent microfluidic device is needed, as well as a fast, automatized and highly sensitive multiplexed spectral analysis is mandatory.

Here, we present an optimized viscoelastic induced microgel alignment system for the automatic spectral encoding of multiplexed microgel codes (see Fig. 1). The utilized microgel alignment takes place in a self made PMMA measurement device, with a given channel cross section of 380x400 µm, connected to a round shaped glass capillary with inner diameter of 50 µm, where the general viscoelastic particle alignment takes place.[8,9]

However, such an alignment is mainly induced by a pressure driven viscoelastic polymer solution (Polyethylene oxide – 4 MDa), which in our case is combined with a highly transparent rectangular shaped measurement channel, where three alternating excitation wavelengths are striking the passing particles from below, exciting the corresponding fluorescence codes. Moreover our measurement tool allows collecting in a reservoir, positioned at the end of the channel, all of the measured microgel particles. In such a way all particles can also be recovered for further optical analysis. In fact, such a µTAS device is cheap and simple to be produced, permitting the possibility of real time detection of passing microgel particles.

However, we have designed microgel particles with altering ratio of two emitting fluorescent dyes for the mentioned multiplex spectral analyses and endowed with diverse fluorescent emitting molecules for the specific miRNA type detection. Preliminary results show a variable particle speed -ranging from 1 up to 12 µm s^{-1}- while an automatized fluorescent acquisition and microgel counting routine was able to detect the desired miRNA concentrations in microfluidic flow conditions.

III. Conclusions

We realized a microfluidic layout allowing continuous fluorescence signal acquisitions according to several

emission wavelengths. A multiplex fluorescence signal detection system has been employed, able to accurately detect microRNA (miRNA) concentrations in small sample volumes, without pre-treatments. In such a way sample volumes of around 250 microgel particles could be analyzed in 10 minutes with a given miRNA detection limit in the femtomolar range. Such results open up new roots for lab-on-chip application of any microgel based suspension assays with high sensitivity.

REFERENCES

[1] D.P. Bartel, "MicroRNAs: genomics, biogenesis, mechanism, and function," Cell, 2004. 116(2), 281-297.

[2] H. Schwarzenbach, N. Nishida, G.A. Calin and K. Pantel, "Treatment of HCV infection by targeting microRNA," *Nat. Clin. Pract. Oncol.*, 11(3), 145-156 (2014).

[3] C.M. Hindson, J.R. Chevillet, H.A. Briggs, E.N. Gallichotte, I.K. Ruf, B.J. Hindson, R.L. Vessella and M. Tewari, "Absolute quantification by droplet digital PCR versus analog real-time PCR" Nat. Methods, 10(10), 1003-1005 (2013).

[4] AM. Cusano, F. Causa, R. Della Moglie, N. Falco, PL. Scognamiglio, A. Aliberti, R. Vecchione, E. Battista, D. Marasco, M. Savarese, U. Raucci, N. Rega and P.A. Netti, "Integration of binding peptide selection and multifunctional particles as tool-box for capture of soluble proteins in serum", *J. R. Soc., Interface*, 11:20140718, (2014).

[5] A. Aliberti, AM. Cusano, E. Battista, F. Causa and PA.Netti, "High sensitive and direct fluorescence detection of single viral DNA sequences by integration of double strand probes onto microgels particles" *Analyst*, 8;141(4):1250-6.U, (2016).

[6] Y. Wang, D.L. Zheng, Q.L. Tan, M.X. Wang and L.Q. Gu, "Nanopore-based detection of circulating microRNAs in lung cancer patients" *Nat. Nanotechnol.*, 6(10), 668–674 (2011).

[7] J. Das, I. Ivanov, L. Montermini, J. Rak, E.H. Sargent and S.O. Kelley, "An electrochemical clamp assay for direct, rapid analysis of circulating nucleic acids in serum" *Nat. Chem.*, 7.7 569-575. (2015).

[8] E. Battista, A. Mazzarotta, F. Causa, A.M. Cusano and P.A. Netti, "Core−shell microgels with controlled structural properties" *Polym. Int.*, doi: 10.1002/pi.5076, (2016).

[9] A.C. Manikas, A. Aliberti, F. Causa, E. Battista and P.A. Netti, "Thermoresponsive PNIPAAm hydrogel scaffolds with encapsulated AuNPs show high analyte-trapping ability and tailored plasmonic properties for high sensing efficiency", *J. Mater. Chem. B*, 3(1), 53-58. (2015).

[10] M. Murtaza, S.J. Dawson, D.W.Y. Tsui, D. Gale, T. Forshew, A.M. Piskorz, C. Parkinson, S.F. Chin, Z. Kingsbury, A.S.C. Wong, F. Marass, S. Humphray, J. Hadfield, D. Bentley, T.M. Chin, J.D. Brenton, C. Caldas and N. Rosenfeld, "Non-invasive analysis of acquired resistance to cancer therapy by sequencing of plasma DNA" Nature, 497(7447), 108–112 (2013).

[11] F. Causa, A. Aliberti, A.M. Cusano, E. Battista and P.A. Netti, "Supramolecular spectrally encoded microgels with double strand probes for absolute and direct miRNA fluorescence detection at high sensitivity" *J. Am. Chem. Soc.*, 137(5), 1758-1761 (2015).

[12] D. Dannhauser, G. Romeo, F. Causa, I. De Santo and P.A. Netti, "Multiplex single particle analysis in microfluidics," *Analyst*, 139(20), 5239-5246 (2014).

[13] G. Romeo, G. D'Avino, F. Greco, P.A. Netti and P.L. Maffettone, "Viscoelastic flow-focusing in microchannels: scaling properties of the particle radial distributions" *Lab Chip*, 13(14), 2802–2807 (2013).

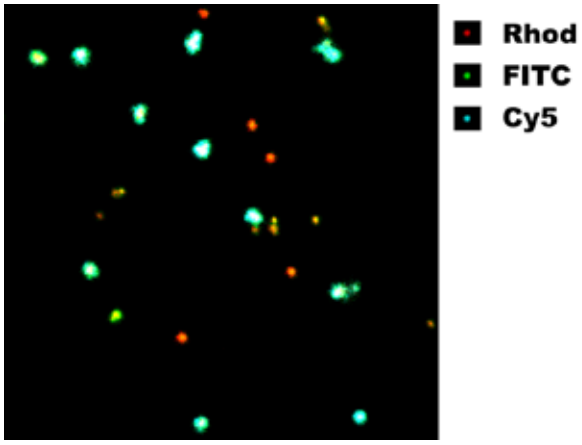

Fig. 1. Multiplex microgel based miRNA target detection. Quiescent measurements performed in a 512x512 pixel field of view. The PMT signal for each separate fluorescence signal is overlaid according to the shown colour code and its relative intensity.

Closed-Loop Control Benefits of A New Insulin Formulation: Assessment using the University of Virginia/Padova Type 1 Diabetes Simulator

M. Schiavon PhD[1], M. Messori PhD[2], C. Dalla Man PhD[1], L. Magni PhD[2], and C. Cobelli PhD[1]
[1] *Department of Information Engineering, University of Padova, Padova, Italy*
[2] *Department of Computer Engineering and Systems Science, University of Pavia, Pavia, Italy*

***Abstract*— In the last years, the University of Virginia (UVA)/Padova Type 1 Diabetes (T1D) Simulator has been extensively used for the design of artificial pancreas control algorithms. However, it also offers the possibility to test in silico new insulin molecules for the treatment of T1D.**

In this work, the UVA/Padova T1D Simulator was used to in silico assess the potential benefits of new insulin formulations for closed-loop control (CLC). To do this, pharmacokinetic and pharmacodynamic data of new ultra-fast vs. fast acting insulin formulations were successfully modeled and incorporated into the UVA/Padova T1D Simulator.

Results showed that the overall glucose control is significantly improved using the new ultra-fast vs. fast acting insulin formulation without increasing the risk of hypo- and hyperglycemic events.

In conclusion, the UVA/Padova T1D Simulator was successfully employed for evaluating in silico the potential benefits for CLC introduced by newly under-development ultra-fast acting insulin molecules.

***Keywords*—Artificial pancreas, in silico trial, type 1 diabetes, insulin analogues, pharmacokinetic/pharmacodynamic, closed-loop control.**

I. INTRODUCTION

SIMULATION models of the glucose-insulin system are fundamental for studying the pathophysiology of diabetes and for the design and evaluation of decision support systems for its treatment. In particular, for type 1 diabetes (T1D), the development of artificial pancreas, i.e. a system aiming to automatically administer exogenous insulin to restore glucose homeostasis in people with T1D, has been greatly accelerated in the last decade. This was mainly due to the availability of minimally invasive glucose sensors and insulin pumps, but also to the development of the University of Virginia (UVA) and Padova T1D Simulator (T1DS), accepted by the U.S. Food and Drug Administration (FDA) as a substitute for preclinical trials of certain insulin treatments, including closed-loop control (CLC) algorithms [1][2]. As a matter of fact, the T1DS has been largely employed for developing and testing of CLC algorithms [3][4][5]. However, another important use of the T1DS, despite less known, is the in silico testing of new insulin molecules.

The current artificial pancreas adopts the well-established subcutaneous route for insulin delivery [6], but a well-known key limiting factor for closed-loop control is represented by the delay and variability in subcutaneous absorption of commercially available fast acting insulin analogues, particularly relevant when compensating the postprandial glucose excursion due to meal intake. Thus, the research of the pharma companies producing insulin analogues is focusing on the development of ultra-fast acting insulin formulations able to mitigate such issues.

The aim of this work was to in silico assess CLC benefits of ultra-fast vs. fast acting insulin analogues using the UVA/Padova T1DS. To do this, one has first to equip the UVA/Padova T1DS with a module describing the pharmacokinetics of both fast and ultra-fast acting insulin analogues and, secondly, to compare in silico the performance of a properly tuned MPC controller, widely used in clinical trials [7], for both insulin formulations.

II. METHODS

A. PK/PD data

Thirty-eight T1D subjects (age = 44±13 years, BW = 81±10 kg, BMI = 25±2 kg/m^2) underwent a double-blind, randomized, controlled, single dose (0.2 U/kg) cross-over study of subcutaneous insulin bolus injection of fast (commercially available) vs. ultra-fast (under-development) acting insulin analogues after ingestion of a standardized meal (Ensure Plus Abbott®, 400 ml containing 80g of carbohydrates).

B. Model identification

PK/PD data were identified using two models:

- *PK*: a new subcutaneous insulin absorption model [8] (Fig. 1, red box), coupled with the two-compartment model of insulin kinetics currently incorporated into the UVA/Padova T1DS [2], was used to predict plasma insulin data. The model was numerically identified (Fig. 2, top) with a Bayesian Maximum a Posteriori (MAP) estimator, assuming the error on insulin measurements to be uncorrelated, Gaussian, with zero mean and unknown standard deviation (SD) [9], and the prior distribution extracted from the joint parameter distribution of the UVA/Padova T1DS [2].
- *PD*: the UVA/Padova T1DS model (Fig. 1) [2] was used to predict plasma glucose data. The model was numerically identified (Fig. 2, bottom) using a Bayesian MAP estimator, as detailed in [10], assuming the error on glucose measurements to be uncorrelated, Gaussian, with zero mean and known constant coefficient of variation (CV) of 2%.

C. Incorporation into the time-varying UVA/Padova T1DS [11]

For each insulin formulation, the joint parameter distribution of the above PK/PD models was estimated and used to randomly generate a new virtual subjects population, as described in [2], matching PK/PD dynamics observed in clinical data.

D. In silico clinical trial

The entire virtual population underwent, for each insulin formulation, a 7-day scenario including 3 meals per day with 50g, 60g and 80g at 8am, 1pm and 8pm, respectively, with insulin administered according to the MPC controller of [7], properly tuned for each insulin formulation.

III. Results

A. Model identification

The models well predicted both PK and PD data, as shown in Fig. 2, and parameters were estimated with precision (CV<100%). Parameters k_{a1}, k_d and τ of the subcutaneous insulin absorption model (Fig.1, red box) were statistically different ($p<0.05$) when estimated from the ultra-fast vs. fast acting insulin analogue data (k_{a1} = 0.001 vs. 0.0002 min^{-1}, k_d = 0.041 vs. 0.030 min^{-1} and τ = 4 vs. 11 min) while this was not the case for k_{a2} (k_{a2} = 0.014 vs. 0.015 min^{-1}). All the other parameters were not statistically different in the two experiments.

B. In silico clinical trial

Fig. 3 shows the average ± SD plasma glucose concentrations obtained with ultra-fast (blue) vs. fast (pink) acting insulin analogue for the entire scenario. Average glucose concentration was significantly decreased ($p<0.05$) both at night (155.7 vs. 159.4 mg/dL) and in the postprandial phase (179.2 vs. 186.3 mg/dL) with the ultra-fast vs. fast acting insulin analogue, respectively, without increasing the risk of hyper- and hypo-glycemic events. Ultra-fast vs. fast acting insulin analogue achieved an overall significant reduction in time spent above 180 mg/dL (36.5 vs. 40.1%), increase in time spent between 70 and 180 mg/dL (60.7 vs. 56.9%) and in time spent between 80 and140 mg/dL (34.4 vs. 31.4%), while no differences were reported both in time below 70 mg/dL and time below 50 mg/dL.

In Fig. 4 the Control Variability Grid Analysis (CVGA) [5] shows the improved glycemic control for the entire population using the ultra-fast (blue) vs. fast (pink) acting insulin analogue with an increased number of subjects in the regions A-B (optimal and good control) and a reduced number in regions C-D (bad control).

IV. Conclusion

In this work the UVA/Padova T1DS was employed for in silico testing the possible benefits for CLC introduced by newly under-development ultra-fast acting insulin molecules.

In particular, PK/PD data of ultra-fast vs. fast acting insulin analogues were used to estimate the parameters of a subcutaneous insulin absorption model and the UVA/Padova T1DS. Then, the estimated model parameters allowed the generation of a new in silico T1D population, matching PK/PD dynamics observed in clinical data.

The new virtual population underwent an in silico trial showing that glucose control is significantly improved with the ultra-fast acting insulin formulation.

Acknowledgement

This study was partially founded by Italian Ministero dell'Università e della Ricerca Scientifica (Progetto di Ateneo dell'Università di Padova, 2014).

References

[1] Kovatchev B. P., Breton M., Dalla Man C., Cobelli C., *In silico preclinical trials: a proof of concept in closed-loop control of type 1 diabetes*, J Diabetes Sci Technol, 3(1): 44–55, 2009.

[2] Dalla Man C., Micheletto F., Lv D., Breton M., Kovatchev B.P., Cobelli C., *The UVA/PADOVA Type 1 Diabetes Simulator: New Features*, J Diabetes Sci Technol, 8(1): 26–34, 2014.

[3] Lee H., Buckingham B.A., Wilson D.M., Bequette B.W., *A closed-loop artificial pancreas using model predictive control and a sliding meal size estimator*, J Diabetes Sci Technol, 3(5): 1082-1090, 2009.

[4] Grosman B., Dassau E., Zisser H., Jovanovic L., Doyle F.J. 3rd., *Zone model predictive control: a strategy to minimize hyper- and hypoglycemic events*, J Diabetes Sci Technol, 4(4): 961-975, 2010.

[5] Toffanin C., Messori M., Di Palma F., De Nicolao G., Cobelli C., Magni L., *Artificial pancreas: model predictive control design from clinical experience*, J Diabetes Sci Technol, 7(6):1470-1483, 2013.

[6] Cobelli C., Renard E., Kovatchev B.P., *Artificial pancreas: past, present, future*, Diabetes, 60(11): 2672–2682, 2011.

[7] Kropff J., Del Favero S., Place J., Toffanin C., Visentin R., Monaro M., Messori M., Di Palma F., Lanzola G., Farret A., Boscari F., Galasso S., Magni P., Avogaro A., Keith-Hynes P., Kovatchev B.P., Bruttomesso D., Cobelli C., De Vries J.H., Renard E., Magni L., AP@home consortium, *2 month evening and night closed-loop glucose control in patients with type 1 diabetes under free-living conditions: a randomised crossover trial*, Lancet Diabetes Endocrinol, 3(12): 939-947, 2015.

[8] Schiavon M., Dalla Man C., Krasner A., Pichotta P., Cobelli C., *Modeling subcutaneous insulin kinetics in type 1 diabetes*, 6th International Conference on Advanced Technologies & Treatments for Diabetes, Paris, France, 2013.

[9] Cobelli C., Foster D.M., Toffolo G.M., *Tracers kinetics in biomedical research: from data to model*. New York: Kluwer Academic/Plenum, 2000.

[10] Visentin R., Dalla Man C., Cobelli C., *One-day bayesian cloning of type 1 diabetes subjects: towards a single-day UVA/Padova type 1 diabetes simulator*, IEEE Trans Biomed Eng, 2016 (Epub ahead of print).

[11] Visentin R., Dalla Man C., Kudva Y.C., Basu A., Cobelli C., *Circadian variability of insulin sensitivity: physiological input for in silico artificial pancreas*, Diabetes Technol Ther, 17(1): 1-7, 2015.

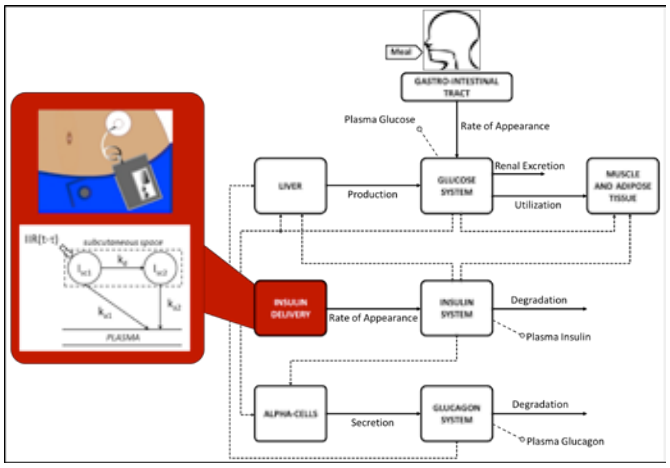

Fig. 1 Schematic diagram of the T1DS model [2] incorporating a new model of the subcutaneous insulin absorption (red box) [8].

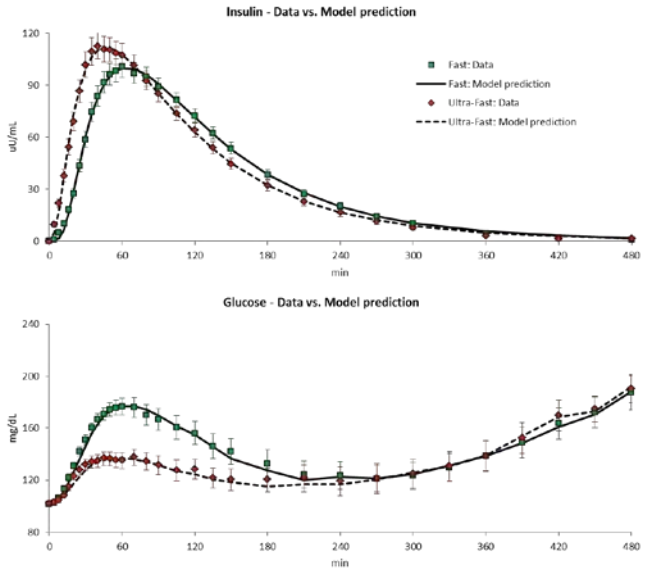

Fig. 2 Data vs. model prediction for each insulin formulation (ultra-fast, in red, vs. fast, in green, acting insulin analogues): PK (top) an PD (bottom) model.

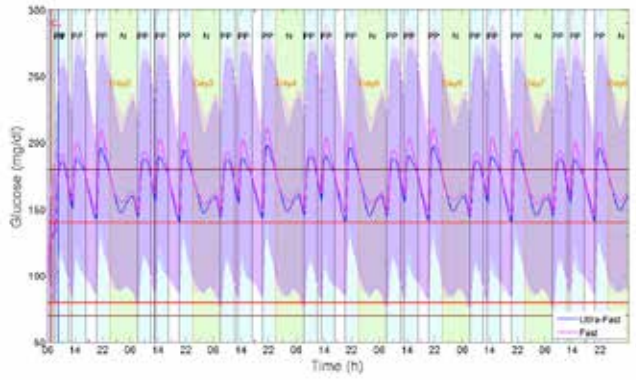

Fig. 3 Average ± SD plasma glucose concentrations obtained with ultra-fast (blue) vs. fast (pink) acting insulin analogues in the 7-day scenario.

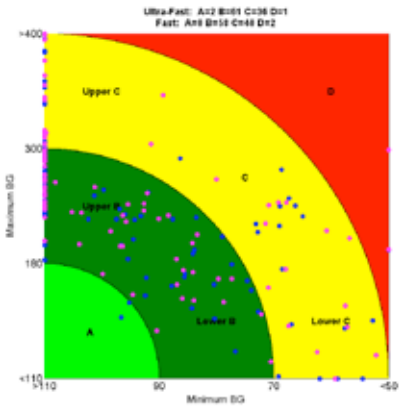

Fig. 4 Control Variability Grid Analysis (CVGA) [5]. Each point (ultra-fast, in blue, vs. fast, in pink, acting insulin analogues respectively) represents the extreme value (*x-axis* is a function of the minimal and *y-axis* is a function of the maximal glucose value) of a patient over the entire simulation.

Multifunctional Particles for Diagnostic tools using a microfluidic flow-focusing device

P.L. Scognamiglio[1], A. Mazzarotta[1], E. Battista[1], F. Causa[1,2,3] and P.A. Netti[1,2,3]
[1] *Center for Advanced Biomaterials for Heathcare@CRIB, Istituto Italiano di Tecnologia (IIT), 80125Naples, Italy*
[2] *Interdisciplinary Research Centre on Biomaterials (CRIB), University "Federico II", 80125 Naples, Italy*
[3] *Dip. di Ing. Chimica del Materiali e della Produzione Indus. (DICMAPI), University "Federico II", 80125 Naples, Italy*

***Abstract*—Multifunctional polymeric microparticles have received considerable attention for many applications. Especially in biomedical fields, polymeric microparticles with advanced functions such as targeted delivery, controlled encapsulation, as imaging agents for analytics and diagnostics, or as microreactors for confined bioreactions. Generally, the functions of these microparticles rely on both their structures and the properties of their component materials (monomers). Thus, creating unique structures from different multi-reactive monomers provides an important strategy for developing advanced functional polymeric microparticles. Poly(ethylene glycol) (PEG) is a bioinert polymer that can be easily tailored to capture specific biomolecules within different biological fluids. Microfluidic methods offer excellent control of droplets synthesis, thereby providing a powerful platform for continuous, reproducible, scalable production of polymeric microparticles with unprecedented control over their monodispersity, structures, and compositions. In this work, we describe the development of advanced monodisperse PEG microparticles for potential diagnostic applications through microfluidic techniques.**

***Keywords*—multifunctional microparticles, poly(ethylene glycol), microfluidic device.**

I. Introduction

RECENT research has focused on multifunctional polymeric microparticles as materials platforms to realize the next generation of polymeric microparticles with advanced functions, such as targeted delivery and controlled encapsulation or capture and release, show great importance in numerous applications, including drug delivery, diagnostic imaging, and confined microreactions. The most attractive feature of such materials consists in the flexibility of synthetic routes to design a multifunctional microparticle able to accommodate chemical compounds as elements to provide encoding and sensing abilities against different kinds of targets such as pollutants or clinically relevant biomarkers [1],[2]. Changes in the physical and chemical characteristics of the employed polymer, as well as changes in microsphere size and morphology, may be exploited to allow the realization of a chemical toolbox for on-demand production [3]. Microfluidics offers a versatile platform for synthesizing uniform polymeric microspheres harboring a variety of biologics under relatively mild conditions. Prior reports have demonstrated the ability of microfluidic-based platforms to synthesize, functionalized and encoded microparticles with multiple bioactive agents [4],[5] in a single step, overcoming the conventional emulsion polymerization methods [6]. Droplet microfluidics facilitates fabrication of spherical microparticles (i.e., microspheres) or microparticles with complex chemical compositions, and potentially enables higher throughput synthesis [7] Polymeric microspheres containing multiple reagents and biologics are synthesized by adding polymer and biomolecules to the precursor solution and polymerizing the resulting microparticles [8]. Even if it is possible to take advantage of particular orthogonal, "click" chemistries for post-polymerization functionalization reactions combining fundamental organic chemistry, biology and bioconjugation chemistry.

Given such biologics are sensitive to chemical microenvironments, it is important to identify appropriate polymer formulations. Poly(ethylene glycol) (PEG) is a well-established hydrophilic anti-fouling polymer, and has been widely used to form hydrogels for a broad range of biomedical applications due to its tunable chemical and physical properties. In this paper, a preparation method of monodispersed poly(ethylene glycol) (PEG) microparticles using a microfluidic flow-focusing device is presented. Important physic parameters such as surface tensions, viscosity and capillary number, that characterize emulsion stability and could influence the droplet formation processes, were considered. After that various experimental conditions such as the surfactant concentrations, flow rates of the dispersed phase (PEG solution) and continuous phase (mineral oil), and concentration of the PEG solution were investigated and optimized to fabricate monosized PEG microparticles that could easily functionalized through the implementation of different acrylic reactive monomers.

II. Materials and Methods

A. Materials

PEG diacrylate (PEGDA M_n= 700 g mol^{-1}), the non polar solvent light mineral oil, the nonionic detergent sorbitan monooleate (Span 80), fluorescein O-methacrylate (Fluo), and acrylic acid (AAc) were all purchased from Sigma-Aldrich (St Gallen, Switzerland) and used as received.

B. Microparticles synthesis and Microfluidic device

Microparticles were synthesized using light mineral oil containing nonionic surfactant Span 80 (5 wt%) as a continuous phase and poly(ethylene glycol) diacrylate (PEGDA) (range 20-60 wt%), with fluorescein O-methacrylate (0.01 wt%) and acrylic acid (0.01 wt%) as disperse phase. Polyethylene tubes were connected to the inlets and outlets and the solutions were injected using high-precision syringe pumps (neMesys-low pressure) to ensure a reproducible, stable flow. This system was mounted on an inverted microscope (IX 71 Olympus) and the droplets formation was visualized using a 4× objective and recorded with a CCD camera Imperx IGV-B0620M. The uniform

PEG-droplets were collected and washed three times with a solution of propan-2-ol (70 v/v%) and water (30 v/v%) to remove the oil. The average microsphere diameter was measured via image processing. Briefly, microsphere area was determined by quantifying the number of pixels per microsphere and converting that value to micrometers based on the Zeiss program standards. Ten images per group were assessed. The wettability of the different PEG concentrations was assessed by static water contact angle measurements, using a Optical Contact Angle/Surface Tension Meter KSV's CAM 200. Three measurements were taken on each surface using Milli-Q water as probe liquid (2 μL drop size) and the experiments were repeated on three independent samples

III. RESULTS AND DISCUSSION

A. Generation of PEG Droplet in the Microfluidic Device

The formation of droplets at a junction is governed by the competition between the viscous stress and the surface tension stress [9]. In emulsification processes, the effect of the interfacial tension on droplet size and stability is significant. For this reason, we investigated the surface tension (γ) increasing the polymer concentration; in particular, γ was changed from 4.175 to 1.547 to mN/m (Table I) and it was observed that when γ increased, droplets diameter increased (data not shown).

TABLE I
SURFACE TENSION DATA

Solutions	*Surface tension [mN/m]*
20% PEGDA + 80% water	4.175 ± 0.172
40% PEGDA + 60% water	2.678 ± 0.171
60% PEGDA + 40% water	1.547 ± 0.240

In order to stabilize droplets against uncontrolled coalescence, the use of a surfactant is necessary, e.g. the nonionic detergent sorbitan monooleate (Span 80). These molecules populate the water/oil interface and prevent droplet coalescence. To determine the influence of this surfactant on the viscosity oh the oil phase, we investigated the viscosity of the different solutions. As shown in the Table II, the viscosity did not change between the oil without and with a solution of 5% Span80.

TABLE II
VISCOSITY DATA

Solutions	*Viscosity (Pa.s)*
20% PEGDA + 80% water	μ =0,002±0,001
40% PEGDA + 60% water	μ =0,005±0,001
60% PEGDA + 40% water	μ=0,023±0,003
Light Mineral Oil	μ =0,025±0,002
Light Mineral Oil + 5% SPAN 80	μ =0,024±0,001

The capillary number ($Ca=U\mu/\gamma$) is a value showing the relative importance of these two effects, where U is the flow rate of continuous phase, μ is the viscosity of the continuous phase, and γ is the interfacial tension between the hydrophilic and continuous phases. Choi et al. also investigated on the flow patterns to obtain stable polymeric droplets [9]. They found that stable and monodisperse emulsions were generated in a limited range of Ca (0.5×10^{-2}~ 0.5×10^{-1}) and a flow rate of disperse phase (0.2~1.1 μL/min). In this case a regime of flows of the two phases has been obtained to allow the production of monodisperse particles in the range of 150-20μm. As shown in Figure 1.A, the microfluidic device, purchased from Dolomite-Microfluidics, consists of two inlets of continuous fluids with hydrophobic light mineral oil solution and one inlet of hydrophilic PEG prepolymer as a dispersed phase. Light mineral oil and PEG prepolymer solution are immiscible because of two distinctive properties such as hydrophilic or hydrophobic and then they can easily form W/O emulsion in the microfluidic channel. Disperse phase having PEG prepolymer was supplied from one central microchannel, and the oil phase as continuous phase was injected perpendicularly from two side microchannels, where W/O emulsion are reproducibly formed by rupturing of hydrodynamic instability under the our experimental condition (Figure 1.B). Figure 1.B shows that droplets of PEG prepolymer are clearly pinched off from X-junction and surrounded in continuous oil without attachment on the wall. The PEG-droplets were collected in a reservoir containing light mineral oil and then washed before an image analyses (Figure 1.C) to determine diameter and dispersity.

IV. CONCLUSION

The microfluidic technique has been demonstrated a simple but efficient tool to generate PEG microspheres. Using continuous droplet formation, we have synthesized microspheres with high monodispersity. The average microspheres could be easily manipulated by the change of interfacial tension, and the flow rate of the droplets and continuous phases. This approach represents a starting point for a easily droplet functionalization through the implementation of different acrylic reactive monomers to obtain encoded microparticles with multiple bioactive agents.

REFERENCES

[1] AM. Cusano, F. Causa, R. Della Moglie, N. Falco, PL. Scognamiglio, A. Aliberti et al.," Integration of binding peptide selection and multifunctional particles as tool-box for capture of soluble proteins in serum", *J R Soc Interface* 11:20140718, 2014.

[2] R.V. Ulijn, N. Bibi, V. Jayawarna, P.D. Thornton, S.J. Todd, R.J. Mart, A.M. Smith, J.E. Gough, "Bioresponsive hydrogels", *Materials Today*, 10, 40-48, April 2007.

[3] E. Battista, A. Mazzarotta, F. Causa, AM. Cusano and PA. Nettia, "Core−shell microgels with controlled structural properties", *Polym Int,* doi: 10.1002/pi.5076, February 2016.

[4] F. Causa, A. Aliberti, AM. Cusano, E. Battista and PA. Netti, "Supramolecular spectrally encoded microgels with double strand probes for absolute and direct miRNA fluorescence detection at high sensitivity", *J Am Chem Soc* 137:1758−1761, 2015.

[5] A. Aliberti, AM. Cusano, E. Battista, F. Causa, PA.Netti, "High sensitive and direct fluorescence detection of single viral DNA sequences by integration of double strand probes onto microgels particles", *Analyst*, 8;141(4):1250-6.U, Feb 2016.

[6] K. Landfester, "Miniemulsion polymerization and the structure of polymer and hybrid nanoparticles", *Angew Chem Int Ed Engl,* 48(25):4488-507, 2009.

[7] T. Nisisako, T. Torii, "Microfluidic large-scale integration on a chip for mass production of monodisperse droplets and particles", *Lab Chip*, 8 (2),287−93,2008.

[8] WJ. Duncanson, T. Lin, AR. Abate, S. Seiffert, RK. Shah, DA. Weitz, "Microfluidic synthesis of advanced microparticles for encapsulation and controlled release", *Lab Chip*, 12 (12), 2135−45, 2012.

[9] CH.Choi, JH. Jung, TS. Hwang, and CS. Lee, "In Situ Microfluidic Synthesis of Monodisperse PEG Microspheres", *Macromolecular Research*, Vol.17, No.3, pp163-167, 2009.

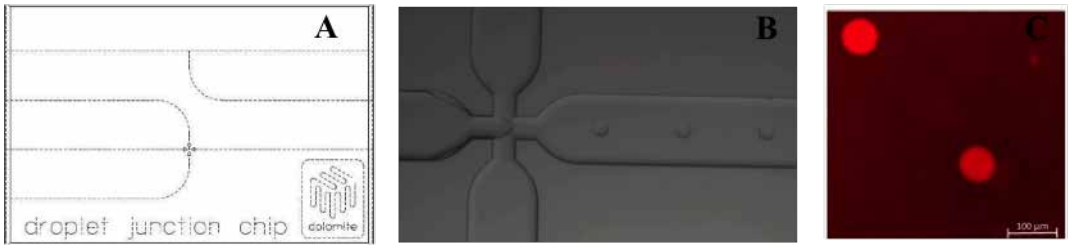

Fig. 1. Generation of PEG Droplet in the Microfluidic device. A. Microfluidic chip used in this work. B PEGDA microparticles (20%PEGDA). C. Fluorescent image of Fluorescein encapsulation.

Training in ultrasound: an hybrid simulator for diagnostic and interventistic procedure

S.Sinceri[1], M. Carbone[1], C. Freschi[1], G. di Candio[2], V. Ferrari[1,3] and M.Ferrari[1]

[1]*EndoCAS Center, Department of Translational Research and of New Surgical and Medical Technologies, University of Pisa, Pisa, Italy*

[2] *General Surgery, Department of Oncology Transplantation and New Technologies, University of Pisa, Italy*

[3]*Department of Information Engineering, University of Pisa, Pisa, Italy.*

***Abstract*—In recent years the clinical interest for structured training, in every medical specialization, has increased. Currently, the learning model for ultrasound imaging follows the traditional approach based on learning by doing. This study describes an integrated system for training ultrasound (US) to learn diagnostic and interventional procedures. The structured training is based on an hybrid simulator that provides a support to acquire skills in term of 3D perception and hand-eye coordination. Actually the ultrasound structured training is tested on 5 clinicians.**

All clinicians agreed that the structured training for ultrasound is very useful for improving the learning of the ultrasound procedure.

***Keywords*— training, learning, ultrasound, simulator.**

I. INTRODUCTION

Knowledge of ultrasound and its diagnostic and therapeutic applications has became essential in the daily clinical practice thanks to the advantages offered by this imaging modality, but it is highly operator dependance. Ultrasound is considered safe, but lack of operator skills may lead to diagnostic errors. Currently, the training in ultrasound imaging uses a traditional approach, where the patient is exposed to the whole learning curve of the novice. The increased attention to patient health and the continued development in diagnostic and therapeutic procedures has led to a growing interest in the use of simulators for medical training. Training based on simulation [1] may enable trainees to learn the image optimization and probe orientation, and finally to practice the ultrasonography procedures. In the ambulatory stage the trainees are not allowed for legal reasons to perform procedures on patients, in particular for interventional tasks, so, there is need to identify training methods structured, repeatable and certifiable [2, 3]. However, in literature, there is limited evidence on how to assess simulated performance, what elements the training should include and how much practice is needed [4, 5].

The aim of this study is to evaluate and improve a training structured, with a panel of experts in the ultrasound procedures, so, to draw a comprehensive training course.

In particular the training structured will be composed by a specific curriculum so to transfer to the trainee the skills to:

- to perform ultrasound in vitro diagnostic;
- to assess and recognize anatomical structures, discriminating between normal and pathological findings in vitro;
- to perform interventional ultrasound in vitro.

To obtain these purposes an innovative hybrid simulator was used[6].

II. MATERIALS AND METHODS

A. Hybrid simulator

The simulator used in the training structured is an hybrid interactive system, based on mixed reality [7]; this simulator has been preliminary validated for face, content and construct validity. The hybrid simulator appears to the clinicians with an ultrasound phantom and a software application with 3D virtual scene (Fig.1). In this scene the 3D representation of the internal structures of the ultrasound phantom is combined with the model of the probe and its scan plane. The visualization of the internal structures in their real position is given by a tracking system realized through an electromagnetic localizer.

The ultrasound phantom, implemented in collaboration with an expert radiologist, simulates the patient's abdomen, in particular reproduces the echogenicity of hepatic tissue[8, 9]. The phantom is constituted with innovative inorganic material.

The phantom is realized with inorganic materials and through a controlled procedure that allows for the realization of different complexity level of phantom. Inside each phantom the trainee will find: ribs, vessel (linear or bifurcated), lesions (hypoechoic, hyperechoic and anechoic).

Moreover, the hybrid simulator allows interventional procedure thanks to a sensorized needle to simulate US guided biopsy.

The augmented reality application enriches the phantom allowing for independent training and speeding up the process of transferring fundamental skill as the hand–eye coordination for diagnostic US and the hand-eye-needle [10].

B. Procedure and tasks

The training course is structured in two modules: diagnostic and interventistic. The course is structured as described in the flow diagrams proposed (Fig. 2 and Fig. 3). The ultrasound structured training is tested on five specialist sonographers.

The trainees can start the interventistic module only when they has passed the diagnostic one. Before to start training session, all trainees received the same explanation on the hybrid simulator through an educational video.

At the end of each module the trainees have to do a final exam.

C. Diagnostic module

The Diagnostic module consists in answering a series of questions about the "anatomy" of the phantom of increasing difficulty. The diagnostic module is structured as described in the flow diagram proposed (Fig. 2).

The trainee to pass the module has to correctly answer the questions, in a defined time interval, on two consecutive different ultrasound phantoms.

At first the trainee executes free-hand ultrasound exams without the augmented reality on a first ultrasound phantom. After answering all the questions the augmented reality screen is activated. Through the augmented reality the trainee is able to understand whatever has done wrong; once corrected all the answers the trainee starts again with a second ultrasound phantom and without augmented reality. In the eventuality that even with augmented reality support the trainee is not able to understand his/her mistakes an expert clinician guides him through the exercises, after that the trainee start again the cycle with a different ultrasound phantom.

When the trainee is able to answer correctly to all the questions without the need of the augmented reality correction on two different ultrasound phantoms consecutively, the trainee exits successfully the diagnostic module.

D. Interventistic module

The trainee enters the interventistic module only after he has finished the diagnostic module. The interventistic module is structured as describe in the flow diagram proposed (Fig 4).

The trainee starts the interventistic training on a randomly selected ultrasound phantom. Each ultrasound phantom contains four anechoic lesions different in dimension and positioning. These lesions are the target for biopsies. To successfully exit the module the trainee has to execute four increasing difficulty biopsies at first try.

If at the first try the lesion is not reached augmented reality guide is added; if even with augmented reality guide the trainee doesn't reach the lesion, an expert guides him through the exercise. At the end of the four biopsies if the trainee needed augmented reality or expert guide to complete the biopsies, the trainee starts again with a second ultrasound phantom, else, if four biopsies were correctly executed consecutively the interventistic module is completed.

III. Conclusion

All trainees agreed that the structured training for ultrasound is very useful for speeding the learning of the ultrasound procedure and improve training methods. Ultrasound training with hybrid simulator should not be as a replacement for traditional clinical training, but rather as a preparation before entering clinical practice. The proposed training course may be used as a basic training program to learn the basic skills for ultrasound procedures; in particular the ultrasound structured training should be used to determine when the trainees are fit for clinical practice, that it is when the trainees will reach a positive feedback on both simulation sessions.

The results obtained show that the trainees need up to three days to obtain a positive feedback on simulation session, in particular, one day for diagnostic module (two consecutive hours) and two days for interventistic module (four consecutive hours).

Acknowledgement

The research is supported by "SThARS Project" (Grant "Ricerca finalizzata e Giovani ricercatori 2011-2012" Young Researchers – Italian MOH).

References

[1] H. Samia, S. Khan, J. Lawrence, and C. P. Delaney, "Simulation and Its Role in Training," *Clin Colon Rectal Surg,* vol. 26, pp. 47-55, Mar 2013.

[2] S. B. Issenberg, W. C. McGaghie, I. R. Hart, J. W. Mayer, J. M. Felner, E. R. Petrusa*, et al.*, "Simulation technology for health care professional skills training and assessment," *JAMA,* vol. 282, pp. 861-6, Sep 1 1999.

[3] D. P. Mandavia, J. Aragona, L. Chan, D. Chan, and S. O. Henderson, "Ultrasound training for emergency physicians--a prospective study," *Acad Emerg Med,* vol. 7, pp. 1008-14, Sep 2000.

[4] R. E. Lewiss, B. Hoffmann, Y. Beaulieu, and M. B. Phelan, "Point-of-care ultrasound education: the increasing role of simulation and multimedia resources," *J Ultrasound Med,* vol. 33, pp. 27-32, Jan 2014.

[5] K. Kunkler, "The role of medical simulation: an overview," *Int J Med Robot,* vol. 2, pp. 203-10, Sep 2006.

[6] C. Freschi, S. Parrini, N. Dinelli, M. Ferrari, and V. Ferrari, "Hybrid simulation using mixed reality for interventional ultrasound imaging training," *Int J Comput Assist Radiol Surg,* Sep 12 2014.

[7] M. Francesconi, C. Freschi, S. Sinceri, M. Carbone, C. Cappelli, L. Morelli*, et al.*, "New training methods based on mixed reality for interventional ultrasound: Design and validation," *Conf Proc IEEE Eng Med Biol Soc,* vol. 2015, pp. 5098-101, Aug 2015.

[8] A. Pacioni, M. Carbone, C. Freschi, R. Viglialoro, V. Ferrari, and M. Ferrari, "Patient-specific ultrasound liver phantom: materials and fabrication method," *Int J Comput Assist Radiol Surg,* Oct 1 2014.

[9] M. Carbone, S. Condino, L. Mattei, P. Forte, V. Ferrari, and F. Mosca, "Anthropomorphic ultrasound elastography phantoms - characterization of silicone materials to build breast elastography phantoms," *Conf Proc IEEE Eng Med Biol Soc,* vol. 2012, pp. 492-4, 2012.

[10] J. McVicar, A. U. Niazi, H. Murgatroyd, K. J. Chin, and V. W. Chan, "Novice performance of ultrasound-guided needling skills: effect of a needle guidance system," *Reg Anesth Pain Med,* vol. 40, pp. 150-3, Mar-Apr 2015.

Fig. 1. Hybrid simulator set up

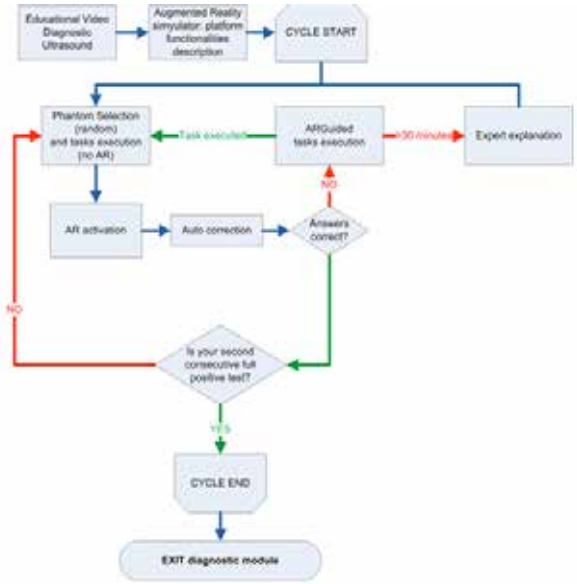

Fig. 2. Flow diagram of diagnostic module

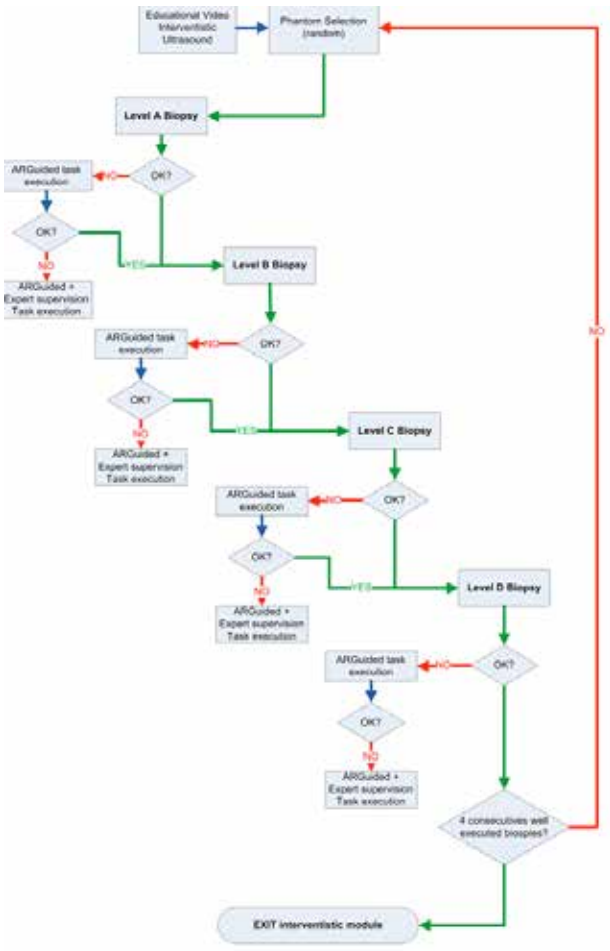

Fig. 3. Flow diagram of interventistic module

Cognitive rehabilitation in multiple sclerosis: an app for attention and memory at-home interventions

A. Tacchino[1], L. Pedullà[2], G. Brichetto[1]
[1] *Italian Multiple Sclerosis Foundation, Research Area*
[2] *University of Genoa, Department of Experimental Medicine*

***Abstract* — Cognitive impairments are common in people with Multiple Sclerosis and severely affects their social and professional life. It has been shown that intensive and personalized cognitive rehabilitation, leads to improved cognitive status of healthy and cognitive-impaired subjects. New technologies would help to promote accessible, at-home, and self-managed cognitive interventions. An app for attention and memory at-home interventions (COGNI-TRAcK) has been developed by the Research Area of the Italian Multiple Sclerosis Foundation for cognitive rehabilitation in people with Multiple Sclerosis.**

***Keywords* — mobile device; cognitive rehabilitation; self-management; adaptive working load algorithms**

I. Introduction

MULTIPLE Sclerosis (MS) is a chronic neurological disease with an unpredictable course, affecting around 2.3 million people in the world (600,000 in Europe, 68,000 in Italy) [1]. The exact cause of MS is not known, but it is thought to be an autoimmune disease in which an immune system dysfunction produces an inflammatory attack directed against the myelin in a process called demyelination that interferes with nerve conduction and is at the basis of the permanent impairments due to the disease (loss of vision, stiffness, weakness, imbalance, loss of coordination, fatigue, emotional changes, intellective impairment, etc.). Thus, the effects of MS are wide-ranging, having an impact on physical, cognitive, psychological, social well-being and consequently on health-related quality of life (QoL) [2], [3].

To date, for a better disease management and consequently to make cost/patient ratio more efficient for Public Health System, in addition to pharmacological treatment, interdisciplinary rehabilitation interventions become crucial, reducing MS relapses, alleviating symptoms and improving social participation in order to achieve the highest possible independence and the best QoL for people with MS (PwMS) [4].

Despite their relevance for the disabling effects on the major part of daily activities of PwMS, only recently cognitive impairments [5] involving complex attention, memory, information processing speed, executive functions, and visuospatial abilities [6] have been seriously considered for more structured cognitive interventions; the main aspect determining this reticence could be found in the difficulty to deliver effective cognitive rehabilitation (CR) to PwMS as consequence of the use of devices only allowing not intensive outpatient CR, contrary to what recent works demonstrated and suggested [7]. However, new technologies such as mobile phones and tablets have made more feasible intensive cognitive interventions to PwMS.

In this context, the traditional interdisciplinary team, composed by medical practitioners, such as physiatrist, physiotherapist, occupational therapist and psychologist, increasingly needed and needs the biomedical competences of bioengineers as support for technological issues.

II. Cognitive intervention in PwMS

Approximately 40-65% of PwMS show cognitive impairments, especially attention and memory, with severe consequences for daily life activities. Recent works showed that specific CR can improve some aspects of cognitive status of PwMS [7], by describing the mostly used methodologies with particular focus on the factors affecting the training efficacy. Among the cited characteristics, besides task types, subject motivation and arousal status, adaptability (i.e. the adjustment of the difficulty of the task depending on the subject's performance) and intensiveness (i.e. how the same amount of training is massed in to shorter time of periods or in to longer ones) of training are mentioned as fundamental features enhancing the effects of the administered intervention [8], [9]. Indeed, it has been clearly shown that an adaptive and intensive cognitive intervention based on specific training, for example for attention and working memory, unlike non-adaptive training, produces significant changes in brain structure (white and gray matter) associated with an improvement in cognitive functions [9], [10].
Nevertheless, some limitations seriously affect the possibility to deliver actual adaptive and intensive cognitive interventions. In an era of inadequate economic resources to invest in health care, it is not possible to guarantee a constant and intensive outpatient administration of cognitive rehabilitation, severely limiting the effects of the interventions. Indeed, proper cognitive rehabilitation programs based on traditional tools (e.g., paper and pencil) require qualified professionals, outpatient facilities, and intensive treatment sessions which often lead to economic burdens at the expense of the user or the health care system. In this context, computerized systems are particularly helpful to overcome this gap by guaranteeing efficient and user-friendly cognitive rehabilitation tools [10]-[12]. However, these tools are usually implemented on laptops and/or desktop computers, whose the costs, the manageability and the transportability still severely limit the adherence to the treatment and, consequently, their full efficacy. The recent technological innovations gave researchers the possibility to provide cognitive treatment programs for mobile phones and tablets, thus making home-based cognitive rehabilitation exercise management and the (self)-administration of

intensive cognitive interventions more feasible to patients. In addition, particular attention must be devoted to implement algorithms for automatic working load adaptation and automatic procedures for intensiveness regulation that only recently it was introduced [14] although the most current computer-based cognitive rehabilitation tools do not incorporate.

III. A NEW APP FOR COGNITIVE REHABILITATION IN MS

In order to provide an ad-hoc computer-based tool for intensive cognitive mobile rehabilitation a new app, named COGNI-TRAcK, has been developed by the team of the Research Area of Italian Multiple Sclerosis Foundation (FISM) with C# programming language, by using the platform Xamarin Studio 4.0.10 for Android (API level 15 and following). The app allows to program a personalized training schedule of attention and working memory exercise; it includes user-friendly interfaces for personal data input and management and for CR intervention configurations.

Inner routines for adaptive working load algorithms allow to automatically set the difficulty level at the participant maximal working threshold taking into account the previous task results. Seven exercises for attention (reaction time; trade off speed-accuracy; auditive, visual, spatial selectivity and concentration; attention span through direct and inverse repetition of digits; distributed attention; inattention resistance; multiple searching through verbal and visual stimuli) and three exercises based on working memory are implemented.

Preliminary results on the disposability-to-use of COGNI-TRAcK were obtained by means of a questionnaire administered to 30 PwMS at the end of an 8-week (5 daily scheduled 30-minute sessions per week) at-home intervention administered by the app. The adherence to the treatment was >85%. Of the participants, 97% understood the instructions given, 100% felt independent to use COGNI-TRAcK at-home, 82% found the exercises interesting, and 88% found the exercises useful and were motivated to use the app again. Moreover, during the exercises, PwMS were highly motivated to perform well (mean score 3.32/4), experienced rather low levels of stress (mean score 1.98/4), were not bored (mean score 1.61/4), and felt amusement (mean score 2.60/4).

Thus, the participants showed a cognitive improvement and compliance with the device, allowing to hope in facilitated at-home self-administered rehabilitation treatments.

IV. CONCLUSION

COGNI-TRAcK is highly usable, motivating, and well-accepted by PwMS. To improve COGNI-TRAcK, new releases should contain more exercises, especially for other cognitive domains affected in MS.

The use of computer-based cognitive rehabilitation is increased because of its numerous advantages, such as the possibility both to administer in-home intensive training and to implement self-management programs and personalized treatments. In particular, computer-based cognitive rehabilitation is shown to be effective in improving cognitive functions; practitioners should be encouraged to use validated tools to enhance cognitive functions. In addition, researchers are challenged to find new tools to make more effective, more accessible, and user-friendlier this type of rehabilitation.

ACKNOWLEDGEMENT

The authors would like to thank all the personnel of Italian Multiple Sclerosis Society and especially to Prof. Mario Alberto Battaglia and Mrs Paola Zaratin. Special thanks to all the collaborators and especially to Prof. Marco Bove and its research team at the University of Genoa.

This work was supported by the Italian Multiple Sclerosis Foundation – FISM (project n. 2011/R/8).

REFERENCES

[1] Atlas of MS 2013. Available: http://www.msif.org/wp-content/uploads/2014/09/Atlas-of-MS.pdf (Access March 2016).

[2] A. Forbes, A. While, L. Mathes and P. Griffiths, "Health problems and health related quality of life in people with multiple sclerosis," *Clinical Rehabilitation*, vol. 20, pp. 67–78, 2006.

[3] A.J. Mitchell, J. Benito-León, J.M. González and J. Rivera-Navarro, "Quality of life and its assessment in multiple sclerosis: integrating physical and psychological components of wellbeing," *Lancet Neurology*, vol. 4, pp. 556–566, 2005.

[4] S. Beer, F. Khan and J. Kesselring, "Rehabilitation interventions in multiple sclerosis: an overview," *Journal of Neurology*, vol. 259, pp. 1994–2008, 2012.

[5] A.R. O'Brien, N. Chiaravalloti, Y. Goverover and J. Deluca, "Evidenced-based cognitive rehabilitation for persons with multiple sclerosis: a review of the literature," *Archives in Physical Medicine Rehabilitation*, vol. 89(4), pp. 761-769, Apr 2008.

[6] D. Schulz, B. Kopp, A. Kunkel and J.H. Faiss, "Cognition in the early stage of multiple sclerosis," *Journal of Neurology*, vol. 253(8), pp. 1002-1010, Aug, 2006.

[7] H. Takeuchi, Y. Taki and R. Kawashima, "Effects of working memory training on cognitive functions and neural systems," *Review Neuroscience*, vol. 21(6), pp. 427–449, 2010.

[8] S.M. Jaeggi, M. Buschkuehl, J. Jonides and W.J. Perrig, "Improving fluid intelligence with training on working memory," *Proceedings of the National Academy of Sciences*, vol. 105(19), pp. 6829-6833, May 13, 2008.

[9] H. Takeuchi, A. Sekiguchi, Y. Taki, S. Yokoyama, Y. Yomogida, N. Komuro, T. Yamanouchi, S. Suzuki, and R Kawashima, "Training of working memory impacts structural connectivity," *Journal of Neuroscience*, vol. 30(9), pp. 3297-3303, Mar 3, 2010.

[10] H. Takeuchi, Y. Taki, Y. Sassa, H. Hashizume, A. Sekiguchi, A. Fukushima and R Kawashima, "Working memory training using mental calculation impacts regional gray matter of the frontal and parietal regions," *PLoS One*, vol. 6(8), pp. e23175, 2011.

[11] Y. Cha and H. Kim. "Effect of computer-based cognitive rehabilitation (CBCR) for people with stroke: a systematic review and meta-analysis," *NeuroRehabilitation*, vol. 32(2), pp. 359-368, 2013.

[12] L. Tárraga, M. Boada, G. Modinos, A. Espinosa, S. Diego, A. Morera, M. Guitart, J. Balcells, O.L. López and J.T. Becker, "A randomised pilot study to assess the efficacy of an interactive, multimedia tool of cognitive stimulation in Alzheimer's disease," *Journal of Neurology, Neurosurgery, and Psychiatry*, vol. 77(10), pp. 1116-1121, Oct, 2006.

[13] S. Bonavita, R. Sacco, M. Della Corte, S. Esposito, M. Sparaco, A. d'Ambrosio, R. Docimo, A. Bisecco, L. Lavorgna, D. Corbo, S. Cirillo, A. Gallo, F. Esposito and G. Tedeschi, "Computer-aided cognitive rehabilitation improves cognitive performances and induces brain functional connectivity changes in relapsing remitting multiple sclerosis patients: an exploratory study," *Journal of Neurology*, vol. 262(1), pp. 91-100, Jan, 2015.

[14] A. Tacchino, L. Pedullà, L. Bonzano, C. Vassallo, M.A. Battaglia, G. Mancardi, M. Bove and G. Brichetto, "A New App for At-Home Cognitive Training: Description and Pilot Testing on Patients with Multiple Sclerosis," *JMIR Mhealth Uhealth*, vol. 3(3), pp. e85, Aug 31, 2015.

Screen-Printed Biosensors for the Early Detection of Biomarkers Related to Alzheimer Disease

S. Tonello[1], M. Serpelloni[1], N. F. Lopomo[1], G. Abate[2], D. L. Uberti [2] and E. Sardini[1]

[1] *Department of Information Engineering, University of Brescia, Via Branze, 38 - 25123 Brescia (s.tonello@unibs.it)*
[2] *Department of Molecular and Translational Medicine, University of Brescia, Viale Europa, 11 - 25123 Brescia*

***Abstract* — Alzheimer Disease (AD) represents the most common cause of dementia in elderly, for which an early diagnosis is still missing. A potential biomarker for early diagnosis of AD is the open isoform of p53, redox sensitive protein, currently quantified using a specific blood-based enzyme-linked immunosorbent assay (ELISA). In order to overcome ELISA limitations (limit of detection, standardization and reliability), this study aimed to realize a low cost highly sensitive portable point-of-care (PoC) testing system based on screen printed electrochemical sensors (SPES).**

The study specifically reported the design of the platform, including the sensing probe and the electronic circuit devoted to the conditioning and acquisition of the electric signal. Considering the whole testing workflow and without losing the possibility of generalization, preliminary results were obtained from circuit testing using controlled concentrations of electrolytic solutions and from a preliminary calibration using Anodic Stripping Voltammetry (ASV) measurements. After a proper calibration, the circuit is intended to be optimized to quantify unknown concentration of unfolded p53 in samples of peripheral blood of AD patients, aiming to realize a low cost, easy to use and highly precise platform.

***Keywords*—Screen-Printed Electrochemical Sensors, Biomarkers, Alzheimer disease, Point of Care testing.**

I. Introduction

Among neurodegenerative diseases, Alzheimer Disease (AD) represents one of the most investigated and serious pathology, for which an early diagnosis is still missing. The ability to diagnose the pathology at an early stage is one of the actual priority of biomedical research in term of neurology and geriatrics [1]. To date, the most advanced and accepted methods to diagnose AD are represented by enzyme-linked immunosorbent assay (ELISA) measurements in cerebrospinal fluid (CSF) and imaging biomarkers [2]. Recently, among several studies addressing this issue, different approaches to identify the specific AD biomarkers have been established and novel one discussed. In particular a peculiar expression of an altered conformational isoform of p53 protein was reported to be able to distinguish AD subjects from healthy population with high values of sensitivity and specificity [3]–[5]. On this basis, the levels of p53 unfolded could represent an interesting starting point to a reliable blood-based ELISA performed with a specific conformational anti-p53 antibody. Even if ELISA assay actually represents the gold standard technique used for the detection and quantification of this p53 biomarker, some limitations are related to its diffusion. These issues specifically include high costs of the assay implementation, high operator dependence, lack of standardization and impossibility to lower the limit of detection, thus to detect the biomarker in the early stage of the disease when it would be more useful for the clinicians.

Biosensors represent the emerging technology that promises to address this challenge, bringing promising solutions in term of cost and sample use reduction, ease of use, high portability and sensitivity [6]–[8].

In light of this, the main objective of this work addressed the preliminary study of a low-cost portable point-of-care testing platform, intended to improve the detection and sensitive quantification of the unfolded p53 protein as a specific AD biomarker.

II. Methods

A. Point of care design and production

The development of the platform specifically included both the design of the screen printed sensing probe with particular attention to the choice of the materials and geometry, and of the electronic circuit devoted to the conditioning and acquisition of the transduced electric signal (Fig.1). After designing the sensor geometry and producing the proper mask to perform the printing process, silver, carbon and silver-silver chloride were selected respectively to realize conductive tracks, working (WE) and counter electrode (CE), reference electrode (RE), with a three-electrodes configuration focusing on ASV measurements.

Parallelly to the realization of the electrochemical sensor, the conditioning and acquisition circuit was designed in order to allow the production of a complete PoC testing platform. The design of the circuit was in particular performed by following the scheme of common potentiostats. In these, a varying potential is applied to the WE with respect to the RE (which is analogous to system ground) and, thanks to the electrons movement generated by the effect of the applied electromotive force in the sample, the generated current is then detected by the CE. Operational amplifiers were carefully selected depending on the specific function they had to perform in the circuit to ensure precision and accuracy. After all the SMD components were soldered, the board was inserted in a metallic box to avoid noises on the signal recording and to improve the sensor sensitivity and precision.

B. Circuit testing using conductive solutions

The first test was performed using a saline solution, varying the concentration of NaCl in order to change the conductivity of the solution, and evaluating the ability of the circuit to quantify these variations as changes in the current peak between WE and CE. In the second test, EIS principle

was applied in order to measure changes of system impedance, resulting in changes in the current detected between WE and CE deriving from different concentrations of the primary antibodies released and adhered on WE surface after an overnight coating. EIS measurements were performed in presence of a conductive electrolytic an solution of 5 mM K3[Fe(CN)6] in 1 M KCl. In both protocols, drops of 2 ml of the conductive solution were released on WE, CE and RE in order to allow current flow, ensuring that the drop stayed correctly in place by using a mask applied on top of the sensor. Triangular waves were given as input at specific frequencies using a pulse generator and the output current flowing between WE and CE was recorded using an oscilloscope.

C. *Anodic Stripping quantification of interleukin proteins*

ASV protocol adopted for interleukin quantification in the calibration phase of the circuit was characterized by a specific functionalization of the WE using immucomplexes formed by a capture and a detection antibody, using a dedicated kit (DuoSet® development system for ELISA). In order to perform the detection step, Alkaline Phosphatase (AP) was used to label the secondary antibodies, thus allowing a selective silver deposition, proportional to the amount of proteins detected. Finally, after placing a drop of buffer solution on the three electrodes, a ramp input was given to the WE, causing the oxidation of the deposited silver, and the current flowing between WE and CE was measured, allowing a sensitive quantification of the proteins.

III. Results

A. *Circuit conditioning using conductive solutions*

Results from the evaluation of circuit response to changes in saline solution conductivity showed a particular trend, characterized by two different slopes respectively for concentration of NaCl lower and higher than 1.0 mg/ml.

In particular (Fig.2), a higher sensitivity was shown for concentrations lower than 1.0 mg/ml, indicating a higher sensitivity of the sensor (0.2 mA/(mg/ml)) for small changes of conductivity and small currents, and a lower sensitivity (20 µA/ (mg/ml)) for higher concentration. This is probably due to the specific features of the SMD components chosen, which makes them from one side really precise and sensitive to detect small changes in ionic current, but from the other unable to detect with the same sensitivity higher conductivity variations, which brings to current which cause the circuit to saturate.

Results from EIS measurements showed a proportional decreasing of the peak of current flowing between CE and WE, indicating an increased impedance of the system due to an increasing concentration of antibodies coated on WE surfaces resulting in a reduced electrons exchange between WE surface and electrolytic solution (Fig. 3). Increasing the concentration of antibodies coated on the WE resulted in reducing the differences of currents exchanged at different frequencies. The sensitivity of the sensor in detecting the change in antibodies coating concentration was of 80 µA/µg.

B. *Anodic Stripping quantification of interleukin proteins*

Results from ASV measurements showed an increase in the maximum peak of current proportional to the increase of interleukin concentration. A linear increase of current peaks recorded when decreasing the input potential from 0 to -0.6 V could be observed, with a sensitivity of 35 µA/ng (Fig.4). The reliability of this result will be confirmed with a complete calibration curve, and a better evaluation of the contribution of the buffer solution and ionic silver during the anodic stripping.

IV. Conclusion

The obtained results during testing with conductive solutions and during preliminary ASV measurement showed good reproducibility, reliability and sensitivity, promising for the future developments with lower values of proteins concentrations. On-going activity refers to the proper calibration of the circuit using interleukin and then the specific unfolded p53, essential in order to proceed with the quantification of unknown concentration of unfolded p53 protein. After the validation, the proposed methodology and the platform design will be optimized in order to be easily accessible for a routine automatized diagnosis technique in the clinical environment. Particular attention will be addressed to reduce the variability between sensors and to increase the sensitivity of the method itself, with the introduction of nanostructured materials.

All this, with the aim to realize an innovative self-standing portable point-of-care, a low cost, easy to use and highly precise platform able to support clinicians to diagnose AD from its earliest stages.

References

[1] C. Humpel, “Identifying and validating biomarkers for Alzheimer’s disease,” Trends Biotechnol., vol. 29, no. 1, pp. 26–32, Jan. 2011.

[2] L. J. Thal, K. Kantarci, E. M. Reiman, W. E. Klunk, M. W. Weiner, H. Zetterberg, D. Galasko, D. Praticò, S. Griffin, D. Schenk, and E. Siemers, “The Role of Biomarkers in Clinical Trials for Alzheimer Disease,” Alzheimer Dis. Assoc. Disord., vol. 20, no. 1, pp. 6–15, 2006.

[3] L. Buizza, G. Cenini, C. Lanni, G. Ferrari-toninelli, C. Prandelli, E. Buoso, M. Racchi, M. Barcikowska, M. Styczynska, A. Szybinska, D. A. Butterfield, M. Memo, and D. Uberti, “Conformational Altered p53 as an Early Marker of Oxidative Stress in Alzheimer ’ s Disease,” vol. 7, no. 1, pp. 1–11, 2012.

[4] C. Lanni, M. Racchi, G. Mazzini, A. Ranzenigo, R. Polotti, E. Sinforiani, L. Olivari, M. Barcikowska, M. Styczynska, J. Kuznicki, A. Szybinska, S. Govoni, M. Memo, and D. Uberti, “Conformationally altered p53 : a novel Alzheimer ’ s disease marker ?,” pp. 641–647, 2008.

[5] D. Uberti, C. Lanni, T. Carsana, S. Francisconi, C. Missale, M. Racchi, S. Govoni, and M. Memo, “Identification of a mutant-like conformation of p53 in fibroblasts from sporadic Alzheimer ’ s disease patients,” vol. 27, pp. 1193–1201, 2006.

[6] P. Yager, G. J. Domingo, and J. Gerdes, “Point-of-care diagnostics for global health.,” Annu. Rev. Biomed. Eng., vol. 10, pp. 107–144, 2008.

[7] D. Polese, A. Convertino, L. Maiolo, A. Ferrone, L. Pazzini, M. Marrani, F. Maita, A. Pecora, G. Fortunato, and G. Fiaschi, “Investigation on nanostructured biosensor for Biotin detection,” SENSORS, 2014 IEEE. pp. 1627–1630, 2014.

[8] S. Feng, L. E. Roseng, and T. Dong, “Quantitative detection of Escherichia coli and measurement of urinary tract infection diagnosis possibility by use of a portable, handheld sensor,” Medical Measurements and Applications (MeMeA), 2015 IEEE International Symposium on. pp. 586–589, 2015.

[9] A. P. Dhawan et al., “Current and Future Challenges in Point-of-Care Technologies: A Paradigm-Shift in Affordable Global Healthcare With Personalized and Preventive Medicine,” Translational Engineering in Health and Medicine, IEEE Journal of, vol. 3. pp. 1–10, 2015.

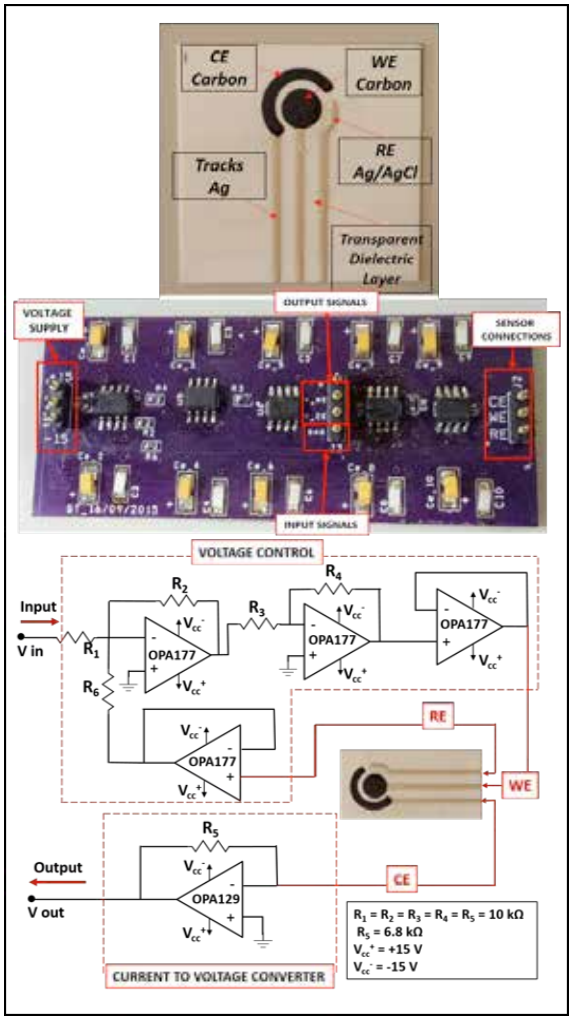

Fig. 1. Final layout of the Biosensor and of the conditioning circuit

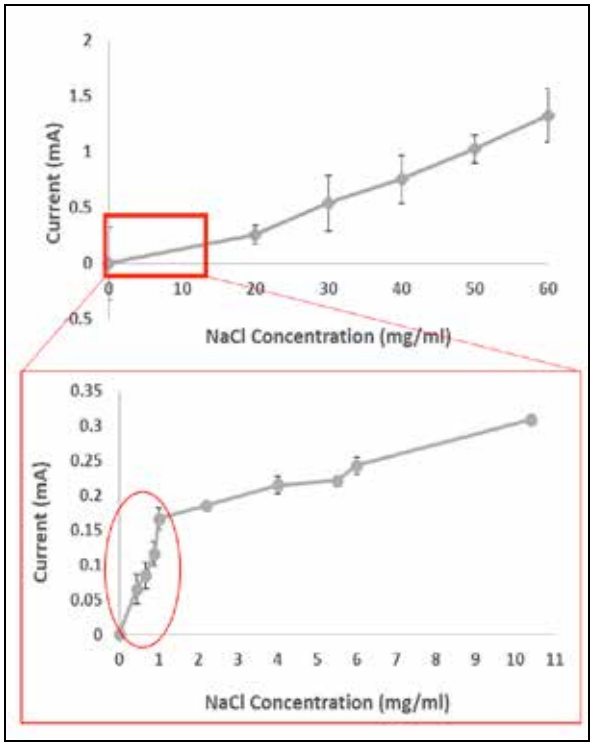

Fig. 2. Calibration of SPES with NaCl solution.

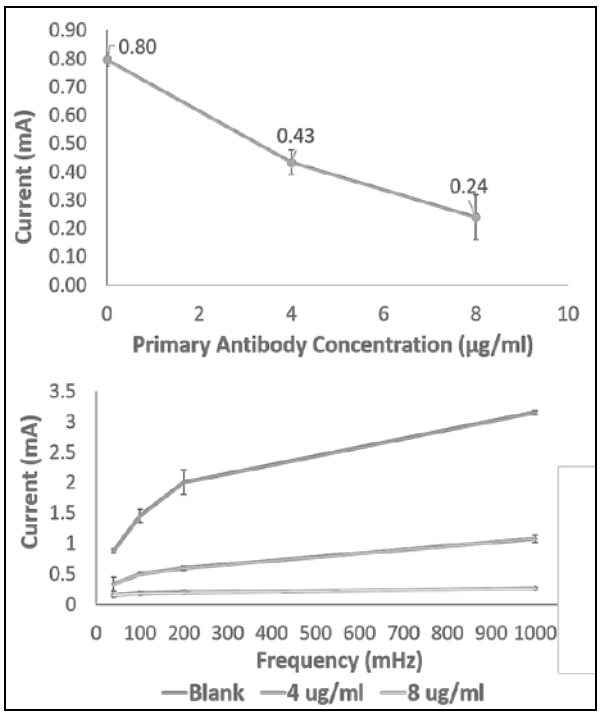

Fig. 3. EIS at low frequencies and at 50 mHz using different primary antibodies concentrations for WE coating

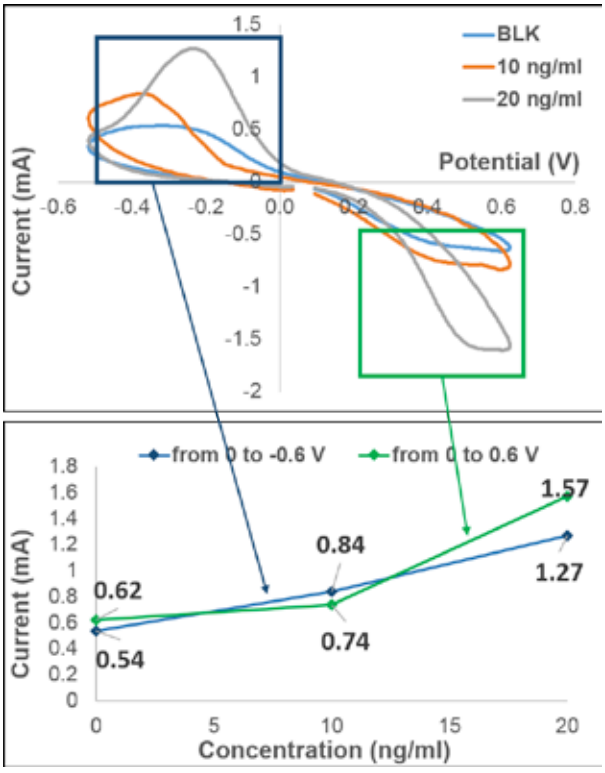

Fig. 4. ASV measurements in a preliminary calibration of SPES using human interleukin proteins.

The UVA/Padova Type 1 Diabetes Simulator for Optimizing the Dosing Regimen of Inhaled Insulin

R. Visentin[1], T. Klabunde[2], M. Grant[3], C. Dalla Man[1], and C. Cobelli[1]
[1]*Department of Information Engineering, University of Padova, Italy*
[2] *Sanofi-Aventis Deutschland GmbH, Frankfurt, Germany*
[1] *MannKind Corporation, Danbury CT, USA*

***Abstract*—Besides its extensive use in closed-loop testing, the UVA/Padova type 1 diabetes simulator (T1DS) has great potential for testing novel type 1 diabetes treatments. Here we describe the use of the T1DS to evaluate the effects of the novel inhaled Technosphere® Insulin (TI). A TI pharmacokinetic (PK) module has been successfully developed and incorporated into the T1DS. This allows running several in silico trials to evaluate the optimal TI dosing regimen to control post-prandial glucose, with the potential to inform clinical study design.**

***Keywords*—Glucose control, inhaled insulin, in silico trial, pharmacokinetic.**

I. Introduction

SINCE its acceptance by U.S. FDA as substitute for preclinical trials of certain insulin treatments, the Universities of Virginia (UVA) and Padova type 1 diabetes simulator (T1DS) [1] allowed relevant time- and cost-savings providing in silico evaluations of various treatments of type 1 diabetes (T1D). In the last eight years, the T1DS has been continuously refined ([2]-[5]), and its principal application to date has been the test of artificial pancreas closed-loop control algorithms, e.g. [6]-[8]. However, another important application area of the T1DS is in testing new insulin products developed by pharma companies.

Here the in silico testing of a recombinant human insulin is presented: the novel ultra-rapid Technosphere® Insulin (TI) inhalation powder (Afrezza®), which has been approved by U.S. FDA to control high blood glucose in adults with type 1 and type 2 diabetes. Afrezza is a dry powder formulation of recombinant human insulin administered by pulmonary route directly before the meal using a new drug delivery system. It is characterized by fast absorption (with a peak serum concentration achieved in about 15 minutes) and short duration of action (2-3 h) due to a short half-life [9]. This fast absorption of insulin reduces the delay inherent in the current subcutaneous insulin therapy, but introduces the challenge of covering the full duration of post-prandial glucose elevation, which might take 4 to 6 hours to return to pre-meal values.

A comprehensive survey of alternative dosing regimens in vivo is unfeasible, but a modeling study could identify promising strategies to achieve optimal post-prandial glucose control. The aim of this work was thus to incorporate a pharmacokinetic (PK) model of TI insulin into the T1DS in order to simulate post-prandial glucose response in T1D subjects treated with TI administered at different times (e.g. before the meal or within the meal period), or in different fashions (e.g. split dosage rather than a single bolus).

II. Methods

A. Database

Twelve T1D subjects (9 male, age = 39±9 years, BW = 84.2±8.8 kg, BMI = 26.6±1.9 kg/m^2) underwent a hyperinsulinemic-euglycemic clamp study (MKC-TI-177, Mannkind, NCT01544881). During treatment visits, subjects received 20 U TI. Blood samples were taken from -20 to 360 min after dosing, for plasma insulin measurements.

B. PK model

PK model of TI is a variation of the single-compartment model described in [10]. Model equations is:

$$\dot{I}_{TI}(t) = -k_{aTI} \cdot I_{TI}(t) + F_{TI} \cdot D \quad I_{TI}(0) = 0 \tag{1}$$

where I_{TI} (pmol/kg) is the amount of insulin in the alveolar space; D (pmol/kg/min) is the TI dose; F_{TI} is the fraction of inhaled insulin which actually appears in plasma; and ka_{TI} (min^{-1}) is the rate constant of insulin absorption from the lungs. Plasma insulin kinetic is described using the two-compartments configuration currently included into the simulator [2]:

$$\begin{cases} \dot{I}_l(t) = -(m_1 + m_3) \cdot I_l(t) + m_2 \cdot I_p(t) & I_l(0) = I_{lb} \\ \dot{I}_p(t) = -(m_2 + m_4) \cdot I_p(t) + m_1 \cdot I_l(t) + k_{aTI} \cdot I_{TI}(t) & I_p(0) = I_{pb} \\ I(t) = I_p(t)/V_I & I(0) = I_b \end{cases} \tag{2}$$

where I_p and I_l (pmol/kg) are the mass of insulin in plasma and liver respectively; I (pmol/L) is the plasma insulin concentration; suffix b denotes basal state; m_1, m_2, m_3, m_4 (min^{-1}) are rate parameters; and V_I (L/kg) is the insulin distribution volume.

C. Model identification

PK model parameters were identified on plasma insulin concentrations by nonlinear weighted least squares implemented in Matlab. Error in insulin measurements was assumed to be uncorrelated, Gaussian, with zero mean and a variance linked to insulin measurements as reported in [11]. Insulin bolus is the model input, assumed to be known without error. Bayesian Maximum a Posteriori estimator was employed, with a-priori information on FTI set according to [10].

D. T1DS incorporating inhaled insulin PK

In silico PK parameters of TI insulin have been generated paralleling what is described in [2], i.e. they were randomly extracted from the joint parameter distribution that has been created using the parameter estimates obtained from model identification. Then, each individual PK has been randomly assigned to each in silico subject. The T1DS incorporating TI insulin PK, shown in Fig. 1, was thus validated by simulating the same 20 U TI protocol and comparing the resulting insulin profiles with the clinical observations.

E. In silico experiments

The effect of different dosing regimens of TI insulin on post-prandial glucose after a meal test has been explored in 100 virtual patients for pre-meal and post-meal dosing as well as for split dosing scenarios. In particular, a meal test with 50 g CHO has been simulated, with TI doses ranging from 10 to 80 TI Units, with timing ranging from 0 to 120 min after meal, as illustrated in Fig. 2.

For all the simulations, the expected risk (e.g. number of expected hypoglycemic events) and benefit (e.g. mean plasma glucose of meal test) were evaluated. To select the most suitable dose for each virtual patient, a titration rule has been followed, based on the glucose level at 90 min after meal ingestion ($BG_{90'}$): if $BG_{90'}$ is between 110-160 mg/dL, TI dose is considered as adequate; if $BG_{90'}$>160 mg/dL, TI dose has to be increased; if $BG_{90'}$<110 mg/dL, TI dose has to be decreased.

III. Results

A. T1DS incorporating inhaled insulin PK

Model fit of TI data was excellent, as shown in Fig. 3. Estimates of model parameters were: V_I = 0.044 ± 0.008 L/kg, m_1 = 0.178±0.031 min^{-1}, m_2 = 0.322±0.079 min^{-1}, m_3 = 0.267±0.047 min^{-1}, m_4 = 0.129±0.032 min^{-1}, k_{aTI} = 0.026 ± 0.010 min^{-1}, F_{TI} = 0.14 ± 0.03.

The comparison between simulated vs. measured insulin in response to 20 U TI dose is shown in Fig. 4. Results are satisfactory: in particular, the simulated over-basal insulin time courses strongly resemble the observed data, in terms of both average profiles and inter-subject variability.

B. In silico experiments

Simulations of different dosing regimens are shown in Fig. 5 for one illustrative in silico subject (VP#004). The effect of inhaled insulin on post-prandial glucose excursion depends on dose: too low doses lead to suboptimal control of post-prandial glucose; on the other hand, due to fast TI appearance, too high pre-meal doses lead to sharp glucose decline and risk of early hypoglycemic events (Fig. 5, upper panel). A flatter profile can be obtained by giving the dose after meal (Fig. 5, middle panel) or by splitting the insulin amount in two doses, one directly before the meal and one after a certain time interval (Fig. 5, lower panel). In these cases, higher total doses may be selected gaining additional efficacy on post-prandial glucose control, without inducing hypoglycemia. Numerical results of this analysis are reported in detail in Table 1, which reports, for each dosing pattern, both the optimal insulin dose satisfying the titration rule and the highest dose not leading to hypoglycemia.

IV. Conclusion

So far, the UVA/Padova T1D simulator has been extensively used for the in silico testing of artificial pancreas closed-loop control algorithms. However, its employment in supporting the test of novel insulin compounds or administration routes is of interest. In this contribution we presented the first use of T1DS to model prandial response to a novel inhaled insulin powder, i.e. the ultrafast-acting Technosphere® Insulin (TI) inhalation powder (Afrezza®).

TABLE I
OPTIMAL MEAL DOSING IN SUBJECT VP#004

TI dose (U)	*BG_{4hr} (mg/dL)*	*BG<70mg/dL (Y/N)*	*Optimal dose by titration rule*	*Highest dose with BG<70mg/dL*
Pre-meal dosing				
10	177.1	N	§	
20	133.2	N		†
30	85.2	Y		
Post-meal dosing				
10	181.1	N		
20	143.2	N	§	
30	113.2	N		†
Split dosing				
10-10	139.0	N	§	
10-20	104.0	N		
20-10	91.9	N		†

For each insulin dose administered (TI dose, second column), the glucose value obtained 4 hours after meal (BG4hr, second column) and whether hypoglycemia occurs (BG<70 mg/dL, third column) are reported. For each dosing pattern (i.e. pre-meal, post-meal, split) both the optimal insulin dose satisfying the titration rule ("§" in fourth column) and the highest dose not leading to hypoglycemia ("†" in fifth column) are indicated.

In particular, a TI insulin PK module was successfully developed and incorporated into the T1DS. This allowed performing a total of more than 20,000 simulations in which the virtual subjects underwent different TI dosing regimens.

The in silico clinical trials are being used to inform the design of clinical studies evaluating different TI treatment regimens in T1D.

Acknowledgement

This work was supported by Sanofi-Aventis Deutschland.

References

[1] B. P. Kovatchev, M. Breton, C. Dalla Man, C. Cobelli, "In silico preclinical trials: a proof of concept in closed-loop control of type 1 diabetes," *J Diabetes Sci Technol*. 2009;3(1):44-55.

[2] C. Dalla Man, F. Micheletto, D. Lv, M. Breton, B. Kovatchev, C. Cobelli, "The UVA/PADOVA Type 1 Diabetes Simulator: New Features," *J Diabetes Sci Technol*. 2014;8(1):26-34.

[3] R. Visentin, C. Dalla Man, B. Kovatchev, C. Cobelli, "The University of Virginia/Padova Type 1 Diabetes Simulator Matches the Glucose Traces of a Clinical Trial," *Diabetes Technol Ther*. 2014;16(7):428-34.

[4] R. Visentin, C. Dalla Man, Y. C. Kudva, A. Basu, C. Cobelli, "Circadian variability of insulin sensitivity: physiological input for in silico artificial pancreas," *Diabetes Technol Ther*. 2015;17(1):1-7.

[5] R. Visentin, C. Dalla Man, C. Cobelli, "One-Day Bayesian Cloning of Type 1 Diabetes Subjects: Towards a Single-Day UVA/Padova Type 1 Diabetes Simulator," *IEEE Trans Biomed Eng*. 2016 Feb 26. [Epub ahead of print].

[6] B. Grosman, E. Dassau, H. C. Zisser, L. Jovanovic, F. J. Doyle 3rd, "Zone model predictive control: a strategy to minimize hyper- and hypoglycemic events," *J Diabetes Sci Technol*. 2010 Jul 1;4(4):961-75.

[7] H. Lee, B. A. Buckingham, D. M. Wilson, B. W. Bequette, "A closed-loop artificial pancreas using model predictive control and a sliding meal size estimator," *J Diabetes Sci Technol*. 2009 Sep 1;3(5):1082-90.

[8] C. Toffanin, M. Messori, F. Di Palma, G. De Nicolao, C. Cobelli, L. Magni, "Artificial pancreas: model predictive control design from clinical experience," *J Diabetes Sci Technol*. 2013 Nov 1;7(6):1470-83.

[9] A.H. Boss, R. Petrucci, D. Lorber, "Coverage of prandial insulin requirements by means of an ultra-rapid-acting inhaled insulin," *J Diabetes Sci Technol*. 2012;6(4):773-9.

[10] E. Potocka, R. A. Baughman, H. Derendorf, "Population Pharmacokinetic Model of Human Insulin Following Different Routes of Administration," *J Clin Pharmacol*. 2011;51:1015-1024.

[11] G. Toffolo, M. Campioni, R. Basu, R. A. Rizza, C. Cobelli, "A minimal model of insulin secretion and kinetics to assess hepatic insulin extraction," *Am J Physiol Endocrinol Metab*. 2006;290:E169-E176.

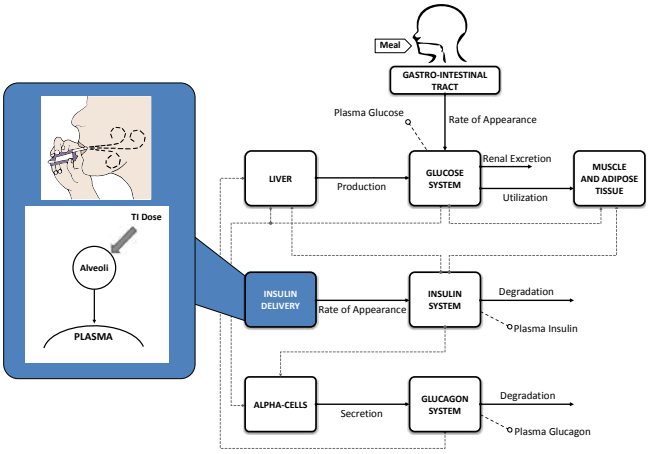

Fig. 1. Scheme of the T1D simulator incorporating TI insulin PK model.

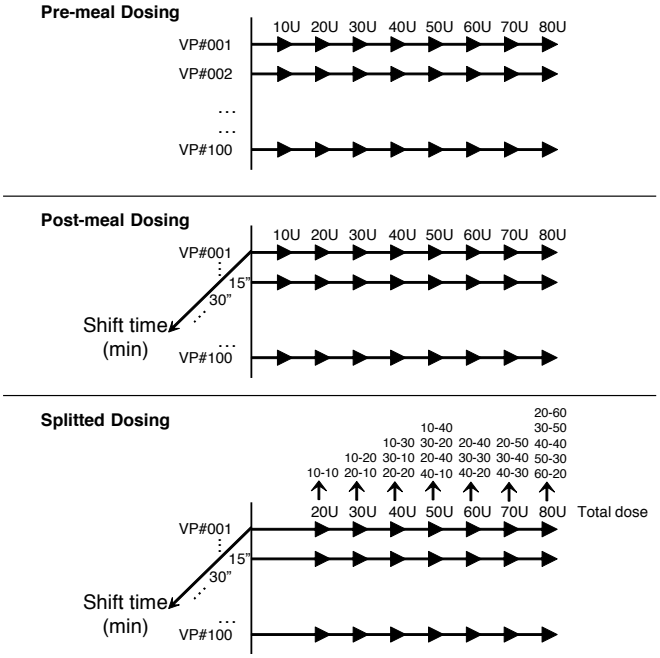

Fig. 2. Scheme of different dosing regimens explored in simulation: pre-meal dosing (upper panel), post-meal dosing (middle panel), split dosing (lower panel).

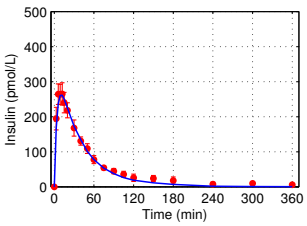

Fig. 3. Results of PK model fit. Mean ± SE data are shown as red dots and bars, average model fit is shown as blue line..

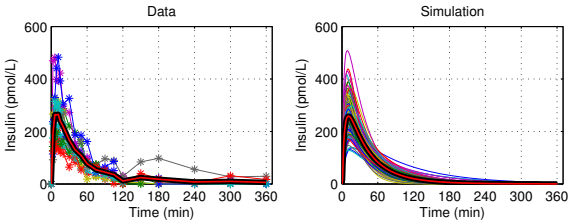

Fig. 4. Comparison between over-basal insulin data (left panel) and simulations (right panel) obtained after an administration of 20 U TI. Individual profiles are shown, with averages plotted as thick red lines.

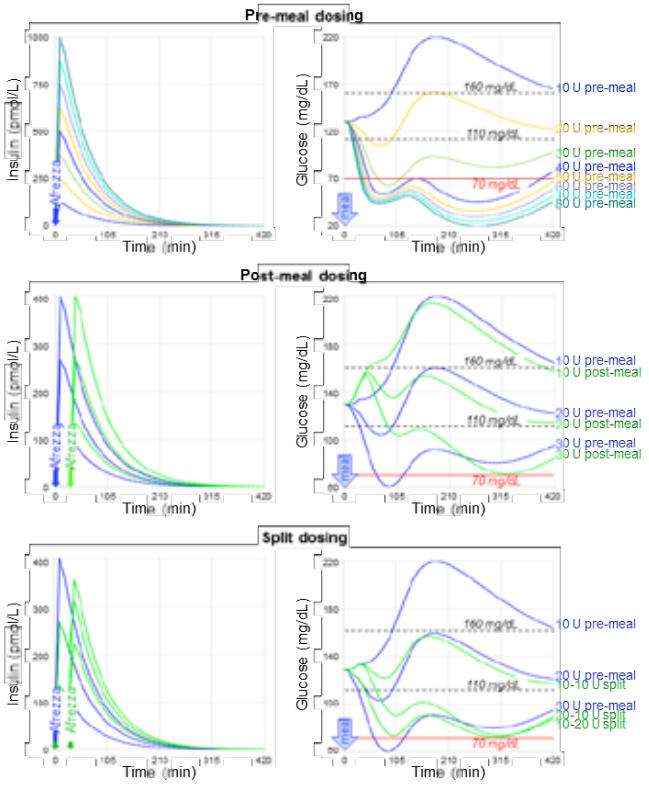

Fig. 5. Meal experiments in one illustrative in silico subject (VP#004). Upper panels: insulin (left) and glucose (right) in response to pre-meal administration of eight different dosages, indicated with different colors. Middle panels: insulin (left) and glucose (right) in response to post-meal dosing (green lines) compared to pre-meal dosing (blue lines). Lower panels: insulin (left) and glucose (right) in response to split dosing (green lines) compared to pre-meal dosing (blue lines).

ELABORAZIONE DI DATI E SEGNALI BIOMEDICI

Smart calibration of Continuous Glucose Monitoring sensors: utility of Bayes estimation

G. Acciaroli[1], M. Vettoretti[1], A. Facchinetti[1], G. Sparacino[1] and C. Cobelli[1]
[1]*Department of Information Engineering, University of Padova, Padova, Italy*

***Abstract*—In continuous glucose monitoring sensors, the current signal generated by glucose-oxidase is transformed to glucose concentration by a calibration function whose parameters are periodically updated by matching self-monitoring of blood glucose references, usually twice a day, to compensate for sensor variability in time. This contribution aims to reduce the frequency of calibrations, which obviously create discomfort to the patient, by employing a Bayesian methodology in the estimation of the calibration function parameters.**

***Keywords*—Diabetes, glucose sensors, continuous glucose monitoring, calibration, Bayesian estimation.**

I. Introduction

DIABETES management can be improved by using minimally-invasive continuous glucose monitoring (CGM) sensors [1]-[3], able to frequently measure interstitial glucose (IG) concentration in the subcutis for up to 7-10 consecutive days. In particular, CGM sensors physically measure a current signal, which is generated by glucose-oxidase and real-time transformed to IG by a calibration function, whose parameters are estimated using self-monitoring of blood glucose (SMBG) references [4], [5] collected by the patient by lancet devices. Since the relation between measured current and IG varies during the monitoring period [6], [7], calibration parameters need to be updated, usually every 12h. This process, refereed to as "in vivo calibration", is considered reason of discomfort, thus, reducing the frequency of calibrations is desirable for both practical and commercial reasons. The aim of this work is to evaluate whether the formulation of the calibration process in a Bayesian setting [8], in which information brought by SMBG measurements could be replaced by prior knowledge on calibration function parameters, allows to reduce the frequency of calibrations without worsening CGM sensor accuracy.

II. Materials and Methods

A. Database

The database consists of 57 diabetic subjects monitored for 7 days by the DexCom G4 Platinum sensor [9]. The raw sensor current signal is available together with SMBG references acquired for calibration and IG profile originally calibrated by the manufacturer. High-accuracy YSI measurements (YSI Inc., Yellow Springs, OH) are also available as references. A representative dataset is reported in Fig. 1.

B. The calibration algorithm

The Bayesian calibration algorithm [8] processes, as in real-time, the raw current signal and the SMBG references, acquired at time instants t_i, i=1,…N (see Fig. 1). Defining a calibration window as the time interval between two consecutive SMBGs, i.e. from t_i to t_{i+1}, the following time-varying calibration model is used to relate the interstitial current signal $y_I(t)$ to the correspondent IG $u_I(t)$ inside each calibration window:

$$y_I(t) = a \cdot u_I(t) + b + c \cdot \Delta t \quad (1)$$

where Δt is the time from sensor insertion and a, b, c are the calibration function parameters, which are updated each time a new SMBG is available (and a new calibration window starts), following a three-step procedure:

1. Non-parametric deconvolution of the measured current $y_I(t)$ to compensate for blood glucose - interstitial glucose (BG-IG) kinetics [10], [11], obtaining the deconvoluted signal $y_B(t)$ that corresponds to an hypothetical current signal measured in plasma.
2. Estimation of calibration parameters $\hat{a}, \hat{b}, \hat{c}$ in a Bayesian linear minimum variance framework, using day-specific prior information [12], by fitting $y_B(t)$ against the last two SMBGs available.
3. Conversion of the sensor current signal $y_I(t)$ into IG signal $u_I(t)$:

$$u_I(t) = \frac{y_I(y) - \hat{b} - \hat{c}\Delta t}{\hat{a}} \quad (2)$$

C. Calibration scenarios: simulation and assessment

To test the performance of the Bayesian algorithm with only one calibration per day, the original SMBG vector, which has a 12h periodicity and is used by the manufacturer for calibration, has been down-sampled, passing to a 24h periodicity. The so obtained IG profiles are then compared, in terms of accuracy, with the ones originally calibrated by the manufacturer. Accuracy of CGM calibrated profiles is assessed by three popular metrics, which use YSI measurements as reference: mean absolute relative differences (MARD), percentage of accurate glucose estimates (PAGE) and percentage of pairs YSI-CGM in the A-zone of the Clark Error Grid [13]-[15]. For all subjects in the dataset YSI measurements were collected in days 1, 4 and 7, allowing a separate accuracy evaluation in these three days as well as a global evaluation in all three days.

D. Implementation

YSI references were also used to build day-specific priors on calibration function parameters (step 2 of algorithm described above), fitting the following non-linear model:

$$y_I(t) = a \cdot u_B(t) \otimes \frac{1}{\tau} e^{-\frac{t}{\tau}} + b + c\Delta t \quad (3)$$

where τ is the equilibration time characterizing the BG-IG kinetics. The method is tested implementing a leave-one-out

cross-validation technique in which, at each iteration, day-specific priors are built fitting the model of Eq. 3 against the training set, while accuracy is evaluated on the subject under test, both for the Bayesian calibration algorithm and for the IG profiles originally calibrated by the manufacturer, for comparison.

III. Results

Comparing the original manufacturer calibration against the Bayesian algorithm using the same number of SMBGs (two per day), CGM accuracy improves, as shown in [8], [12]. Here we tested the performance of the Bayesian algorithm, fed with only one SMBG per day, against the original manufacturer calibration, which is always fed with two SMBGs per day. As shown in Table I (and visible comparing CGM profiles of Fig. 2), a statistically significant improvement in accuracy is achieved for MARD in day 1, PAGE in day 1 and 4, CEGA-A in day 1. In particular, MARD is overall reduced from 13.05% to 11.81%, PAGE is overall increased from 78.01% to 87.23% and CEGA-A is overall increased from 77.78% to 84.75%.

TABLE I
PERFORMANCE METRCS MEDIAN VALUES

Metric	*Day*	*Original manufacturer calibration (12h periodicity)*	*Bayesian calibration algorithm (24h periodicity)*
MARD	*1*	15.98^{+}	13.29^{+}
	4	9.07	9.59
	7	8.81	10.13
	1,4,7	13.05^{+}	11.81^{+}
PAGE	*1*	76.92^{+}	80.95^{+}
	4	93.33^{+}	94.87^{+}
	7	93.75	93.74
	1,4,7	78.01^{+}	87.23^{+}
CEGA-A	*1*	81.25^{+}	85.11^{+}
	4	91.67	92.86
	7	93.62	91.62
	1,4,7	77.78	84.75

$^{+}$ *Wilcoxon signed-rank test, p-values (not shown) lower than 0.05*

IV. Conclusions and Future Developments

The use of day-specific Bayesian priors and a time-varying calibration function allows to calibrate the DexCom G4 Platinum sensor only once a day. Future developments regard the application of the Bayesian methodology to the design of new calibration algorithms that rely much more on prior knowledge, allowing to further reduce, or even eliminate, the need of in vivo calibrations. In particular, the Bayesian methodology here applied to the estimation of the parameters of a time-varying calibration function (Eq. 1), allowed to halve the frequency of calibrations from two to one per day, extending the calibration windows to 24h. However, using the model of Eq. 1, the calibration windows cannot be further extended, becoming the linear assumption introduced by the model critical for time windows wider than 24h. This limitation can be overcome by changing the calibration model of Eq.1, which is valid inside each calibration window, with a new model whose domain of validity is the entire monitoring period, e.g.:

$$y_I(t) = g(t) \cdot u_I(t) + f(t) \quad (4)$$

where g(t) and f(t) are functions describing respectively the variability [6], [7] of sensor sensitivity and offset over time. Different models, either linear or nonlinear, described by a set of parameters $\vec{P}_g$ and $\vec{P}_f$, can be used to approximate g(t) and f(t). Once the choice of the best models is done, prior knowledge on calibration parameters $\vec{P}_g$ and $\vec{P}_f$ is derivable fitting the model of Eq. 4 against a training set. Then, the calibration procedure described in Section II can be applied to the new model, modifying the estimation procedure of step 2. Indeed, having extended the domain of validity of the calibration model to the entire monitoring period, parameters can be estimated in the Bayesian framework fitting the model on all SMBGs acquired, with no need of limiting the calibration windows to the time between two consecutive SMBGs, and thus allowing to further reduce the frequency of calibrations.

Acknowledgement

DexCom Inc. (San Diego, CA) is acknowledged for having provided the data already published in [9].

References

[1] T. Battelino, M. Phillip, N. Bratina, R. Nimri, et al.: "Effect of continuous glucose monitoring on hypoglycaemia in type 1 diabetes". *Diabetes Care* 2011;34(4):795-800.

[2] N. Mauras, L. Fox, K. Englert, R.W. Beck: "Continuous glucose monitoring in type 1 diabetes". *Endocrine* 2013;43(1):41-50.

[3] D. De Salvo, B. Buckingham: "Continuous glucose monitoring: current use and future directions". *Curr Diab Rep* 2013;13(5):657-662.

[4] P. Rossetti, J. Bondia, J. Vehí, C.G. Fanelli: "Estimating plasma glucose from interstitial glucose: the issue of calibration algorithms in commercial continuous glucose monitoring devices". *Sensors* 2010;10(12):10936-10952.

[5] B.W. Bequette: "Continuous glucose monitoring: real-time algorithms for calibration, filtering, and alarms". *J Diabetes Sci Technol* 2010;4(2):404–418.

[6] K.L. Helton, B.D. Ratner, N.A. Wisniewski: "Biomechanics of the sensor-tissue interface—effects of motion, pressure, and design on sensor performance and the foreign body response—part I: theoretical framework". *J Diabetes Sci Technol* 2011;5(3):632-646.

[7] U. Klueh, Z. Liu, B. Feldman, T.P. Henning, et al.: "Metabolic biofouling of glucose sensors in vivo: role of tissue microhemorrhages". *J Diabetes Sci Technol* 2011;5(3):583-595.

[8] M. Vettoretti, A. Facchinetti, S. Del Favero, G. Sparacino, C. Cobelli: "On-line calibration of glucose sensors from the measured current by a time-varying calibration function and Bayesian priors". *IEEE Trans Biomed Eng* 2015;DOI 10.1109/TBME.2015.2426217.

[9] M. Christiansen, T. Bailey, E. Watkins, D. Liljenquist, D. Price, et al.: "A new-generation continuous glucose monitoring system: improved accuracy and reliability compared with a previous-generation system". *Diabetes Technol Ther* 2013;15(10):881-888.

[10] M. Schiavon, C. Dalla Man, S. Dube, M. Slama, et al.: "Modeling plasma-to-interstitium glucose kinetics from multitracer plasma and microdialysis data". *Diabetes Technol Ther* 2015;17(11):825-831.

[11] G. Sparacino, A. Facchinetti, C. Cobelli: ""Smart" continuous glucose monitoring sensors: on-line signal processing issues". *Sensors* 2010;10(7):6751-6772.

[12] G. Acciaroli, M. Vettoretti, A. Facchinetti, G. Sparacino, C. Cobelli: "Glucose sensors for diabetes management: no need of 24h warm-up time by use of Bayes estimation". *Proc 37th Annual International Conference of the IEEE Engineering in Medicine and Biology Society* 2015, August 25-29.

[13] I.M.E. Wentholt, A.A.M. Hart, J.B.L. Hoekstra, J.H. Devries: "How to assess and compare the accuracy of continuous glucose monitors?" *Diabetes Technol Ther* 2008;10(2):57-68

[14] T. Bailey, H. Zisser, A. Chang: "New features and performance of a next-generation SEVEN-day continuous glucose monitoring system with short lag time". *Diabetes Technol Ther* 2009;11(12):749-755.

[15] W.L. Clarke: "The original Clarke error grid analysis (EGA)". *Diabetes Technol Ther* 2005;7(5):776-7.

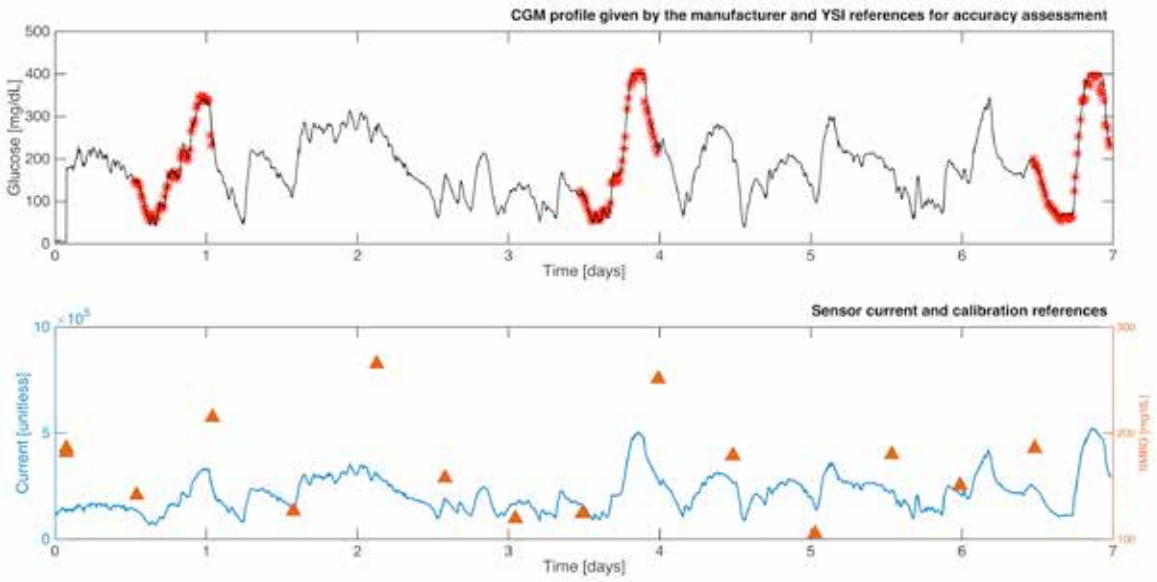

Fig. 1. Representative dataset. First panel: CGM profile given by the manufacturer (continuous black line) and YSI references for accuracy assessment (red stars). Bottom panel: current signal (continuous blue line) and SMBG measurements (orange triangles) with 12h periodicity used by the manufacturer for calibration.

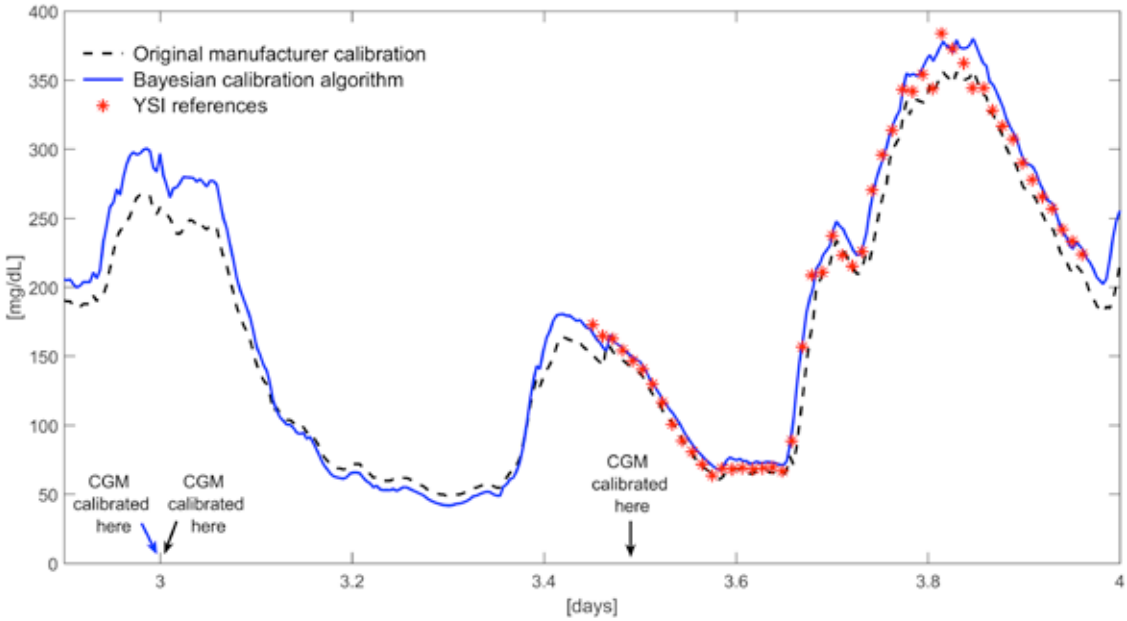

Fig. 2. Day 4. CGM profiles obtained with the manufacturer calibration every 12h (dashed black line) and with the Bayesian calibration algorithm every 24h (continuous blue line) vs. YSI references (red stars).

Stability over Finite Domains of 2D-Systems

C. Cosentino[1], A. Merola[1], M. Romano[1], M. Cesarelli[2] and F. Amato[1]
[1] *Dipartimento di Medicina Sperimentale e Clinica, Università degli Studi Magna Graecia di Catanzaro*
[2] *Dipartimento di Ingegneria Elettrica e delle Tecnologie dell'Informazione, Università degli Studi Federico II di Napoli*

***Abstract*—In this paper we investigate the stabilization over a finite region of two-dimensional (2D)-systems. Such class of systems plays an important role in the biomedical engineering context, with particular reference to the field of image processing. Often 2D-systems are defined over a finite domain of the plane, where each independent variable attains values into a given interval (for example they represent the coordinates of the pixels of a given image). On the basis of these considerations, it is quite straightforward the idea to exploit for 2D-systems the finite-time stability (FTS) theory developed in the context of the classical one-dimensional system framework. Indeed the FTS approach is a more practical concept than classical Lyapunov asymptotic stability, useful to study the behaviour of a system within a finite (possibly short) interval, and therefore it finds application whenever it is desired that the state variables do not exceed a given threshold during the transients.**

***Keywords*—2D-systems, finite-time stability, image processing, linear matrix inequalities.**

I. Introduction

TWO-DIMENSIONAL (2D)-systems [1], [2], [3], [4] play an important role in the biomedical engineering context, since they have a wide application in the fields of digital filtering [3], image processing [2], X-ray image enhancement [5], gas absorption [6], thermal and industrial processes [7], etc.

Structural properties of 2D-systems, namely Lyapunov stability, controllability, observability, as well as optimal control techniques, like linear quadratic and $\mathcal{H}_\infty$ control, have been widely investigated in the last decades, see among others [4], [8]-[10].

2D-systems are characterised from the fact that the state variable vector depends on two arguments; in principle, such arguments can be viewed as time variables; more often they represent space coordinates. When the independent variables of a 2D-system do not have the physical dimension of time, as it is the case, for instance, of image processing, where the two arguments represent the pixel coordinates, the 2D-system under consideration is generally defined over a finite domain of the two-dimensional space. Therefore classical Lyapunov asymptotic stability, which looks to infinite domains, is not applicable in such cases.

To overcome this problem, a possible strategy is to extend the finite-time stability (FTS) theory, developed in the context of one-dimensional systems, to the class of 2D-systems.

Nowadays FTS can be considered a mature field of research, which has attracted the interest of many researchers in the last fifteen years (see [11] for an overview). The first studies on FTS date back to the Sixties, when this concept was introduced in the control literature [12], [13]. The development of effective optimization tools to solve linear matrix inequalities (LMIs) and differential LMIs (DLMIs) feasibility problems has fuelled new interest on this topic at the end of the last century, since practical results to checking whether a given linear system is finite-time stable or not have become available [14]-[17].

Roughly speaking, a system is said to be finite-time stable if, given a bound on the initial condition, its state (weighted) norm does not exceed a certain threshold during a specified time interval. Hence FTS is a more practical approach than Lyapunov asymptotic stability, useful to study the behaviour of a system within a finite (possibly short) interval, and therefore it finds application whenever it is desired that the state variables, for example the reconstruction error of a filter, do not exceed a given threshold over the given finite interval.

Based on the above considerations, the goal of this paper is to investigate the extension of the FTS theory to the class of 2D-systems. In particular we shall provide a sufficient condition for the stability over a finite region of a 2D-system in terms of the solvability of a convex feasibility problem constrained by LMIs.

II. Main result

Consider the following 2D-system in Roesser form (see [2]):

$$\frac{\partial x(t_1,t_2)}{\partial t_1} = A_1 x(t_1,t_2) \qquad (1a)$$

$$\frac{\partial x(t_1,t_2)}{\partial t_2} = A_2 x(t_1,t_2) \qquad (1b)$$

where $x \epsilon \mathbb{R}^n$ is the system state, and we assume that the two system matrices are commutative, i.e. $A_1A_2=A_2A_1$.

A. Definition 1: Stability over a finite domain

Given a scalar $c > 1$, and two positive scalars T_i, i=1,2, system (1) is said to be stable over the finite domain $[0, T_1] \times [0, T_2]$ with bound c, if the condition:

$$\begin{cases} \|x(0,t_2)\|_2^2 \leq 1, & t_2 \in [0,T_2] \\ \|x(t_1,0)\|_2^2 \leq 1, & t_1 \in [0,T_1] \end{cases} \qquad (2)$$

implies, for all $(t_1, t_2) \in [0, T_1] \times [0, T_2]$,

$$\|x(t_1,t_2)\|_2^2 < c.$$

Now, let us consider the Lyapunov function $V(x)$ and assume that, for some nonnegative scalars, α and β,

$$\left.\frac{\partial V(x)}{\partial t_1}\right|_{(1a)} < \alpha V(x) \qquad (3a)$$

$$\left.\frac{\partial V(x)}{\partial t_2}\right|_{(1b)} < \beta V(x) \qquad (3b).$$

Under condition (2), if, as usual, we assume that $V(x)$ is a quadratic form, i.e. $V(x) = x^T P x$, with P being a positive definite matrix, we obtain from (3a) that, for any $t_2 \in [0, T_2]$,

$$\begin{aligned} x^T(t_1,t_2)\, P\, x(t_1,t_2) &\le x^T(0,t_2)\, P\, x(0,t_2) e^{\alpha t_1}, \quad t_1 \in [0,T_1] \\ &\le \lambda_{max}(P)\, \|x(0,t_2)\|_2^2\, e^{\alpha T_1} \\ &\le \lambda_{max}(P)\, e^{\alpha T_1} \qquad (4) \end{aligned}$$

where $\lambda_{max}(.)$ denotes the maximum eigenvalue of the argument, and we have used the fact that α is nonnegative.

In the same way, from (3b) we obtain that, for any $(t_1, t_2) \in [0, T_1] \times [0, T_2]$,

$$x^T(t_1,t_2)\, P\, x(t_1,t_2) \le \lambda_{max}(P)\, e^{\beta T_2} \qquad (5).$$

We can conclude that:

$$x^T(t_1,t_2)\, P\, x(t_1,t_2) \le \lambda_{max}(P) min\{ e^{\alpha T_1}, e^{\beta T_2}\} \quad (6).$$

On the other hand we have, for all $(t_1, t_2) \in [0, T_1] \times [0, T_2]$,

$$x^T(t_1,t_2)\, P\, x(t_1,t_2) \ge \lambda_{min}(P)\, \|x(t_1,t_2)\|_2^2 \qquad (7).$$

Putting together (6) and (7), we obtain:

$$\begin{aligned} \|x(t_1,t_2)\|_2^2 &\le \frac{1}{\lambda_{min}(P)} x^T(t_1,t_2)\, P\, x(t_1,t_2) \\ &< cond(P)\, min\{ e^{\alpha T_1}, e^{\beta T_2}\} \qquad (8) \end{aligned}$$

where *cond(P)* denotes the condition number of the positive definite matrix P, i.e. the ratio between the maximum and minimum eigenvalue of P.

From the last inequality, we can derive the following theorem.

B. Theorem 1

Assume there exist a positive definite matrix P, and nonnegative scalars α, β, such that, defined $V(x) = x^T P x$, assumptions (3) are satisfied. Then system (1) is stable with bound c over the finite domain $[0, T_1] \times [0, T_2]$ if:

$$cond(P)\, min\{ e^{\alpha T_1}, e^{\beta T_2}\} \le c \qquad (9).$$

In order to obtain computationally tractable conditions we note that:

$$\left.\frac{\partial V(x)}{\partial t_1}\right|_{(1a)} = x^T(A_1^T P + P A_1 - \alpha P)x \qquad (10)$$

therefore condition (3a) is guaranteed if the following linear matrix inequality (LMI) in the variable P

$$A_1^T P + P A_1 - \alpha P < 0 \qquad (11)$$

is satisfied.

In the same way condition (3b) is guaranteed by the LMI

$$A_2^T P + P A_2 - \beta P < 0 \qquad (12).$$

III. CONCLUSIONS

The extension of FTS theory to 2D-systems can be useful when it is desired that the state variables do not exceed some given thresholds over a given finite domain of the plane.

This is the case, for example, of image processing, where the reconstruction error has to be bounded, according to a prespecified level, over a finite domain represented by the picture under consideration.

To this regard, a sufficient condition guaranteeing that a given 2D-system in the form (1) is stable with a given bound c over a given finite domain has been provided. Such condition requires the existence of a positive definite matrix P, and nonnegative scalars α, β, such that the LMIs (11), (12) and condition (9) are satisfied. Such feasibility problem can be turned into a convex optimization problem following the guidelines of [11], [15].

REFERENCES

[1] T. Kakzorek, "Two-dimensional linear systems", *Springer-Verlag*, 1985.

[2] R. Roesser, "Discrete state-space model for linear image processing". *IEEE Trans. On Auto. Contr.*, vol. 20(1), 1975, pp. 1–10.

[3] E. Fornasini and G. Marchesini, "State-space realization theory of two dimensional filters". *IEEE Trans. Auto. Contr.*, vol. 21(4), 1976, pp. 484–492.

[4] E. Fornasini and G. Marchesini, "Doubly indexed dynamical systems: State-space models and structural properties". *Mathematical systems Theory*, vol. 12(1), 1978, pp. 59–72.

[5] M. Bisiacco, E. Fornasini and G. Marchesini, "Dynamical regulation of 2D systems: A state space approach". *Linear Algebra and its Application*.

[6] D. Bors and S. Walcza, "Application of 2-D systems to investigation of a process of gas filtration". *Multidimensional Syst. Signal Process*, vol. 23(1), 2012, pp. 119–130.

[7] S. Foda and P. Agathoklis, "Control of the metal rolling process: A multidimensional system approach". *J Franklin Institute*, vol. 329(2), 1992, pp. 317–332.

[8] D.B.O. Anderson, P. Agathoklis, E.I. Jury and M. Mansour, "Stability and the matrix Lyapunov equation for discrete 2-dimensional systems". *IEEE Trans. Circ. Syst. I*, vol. 33(3), 1986, pp. 261–267.

[9] J.S.H. Tsai, J.S. Li and L.S: Shieh, "Discretized quadratic optimal control for continuous-time two-dimensional systems". *IEEE Trans. Circ. Syst. I*, vol. 49(1), 2002, pp. 116–125.

[10] C. Du, PL. Xie and C. Zhang, "$\mathcal{H}_\infty$ control and robust stabilization of two-dimensional systems in Roesser models". *Automatica*, vol. 37(2), 2001, pp. 205–211.

[11] F. Amato, R. Ambrosino, M. Ariola, C. Cosentino and G. De Tommasi, "Finite-Time stability and Control". *Springer Verlag*, 2014.

[12] P. Dorato, "Short time stability in linear time-varying systems", in *1961 Proc. IRE International Convention Record Part 4*, pp. 83-87.

[13] L. Weiss and E.F. Infante, "Finite time stability under perturbing forces and on product spaces". *IEEE Trans. Auto. Contr.*, vol. 12, 1967, pp. 54–59.

[14] F. Amato, M. Ariola, C.T. Abdallah and P. Dorato, "Finite-time control for uncertain linear systems with disturbance inputs", in *1999 Proc. American Control Conference*, San Diego (CA), pp. 1776-1780.

[15] F. Amato, M. Ariola and P. Dorato, "Finite-time control of linear systems subject to parametric uncertain and disturbances". *Automatica*, vol. 37, 2001, pp. 1459–1463.

[16] F. Amato, M. Ariola and C. Cosentino, "Finite-time stabilization via dynamic output feedback". *Automatica*, vol. 42, 2006, pp. 337–342.

[17] F. Amato, M. Ariola and C. Cosentino, "Finite time stability of linear time-varying systems: Analysis and controller design". *IEEE Trans. Auto. Contr.*, vol. 55(4), 2010, pp. 1003–1008.

Neuroelectrical Signatures of Attentional Network Task

A. Anzolin[1,2], D. Mattia[2], J. Toppi[1,2], A. Riccio[2], F. Pichiorri[2], F. Cincotti[1,2], L. Astolfi[1,2]
[1]*Dept. of Computer, Control and Management Engineering, Sapienza University of Rome, Italy*
[2]*Neuroelectrical Imaging and BCI Lab, IRCCS Fondazione Santa Lucia, Rome, Italy*

***Abstract*—The Attention Network Task (ANT) was developed to provide a measure of the efficiency for each of three components of attention: alerting, orienting and executive control. Several fMRI studies have already provided evidences on the anatomical separability and interdependency of these three networks and EEG studies have also characterized the associated brain rhythms. What is still missing is a characterization of the brain circuits subtending the attentional components in terms of directed relationships between the brain areas and their frequency content. The idea of this study was to exploit the high temporal resolution of the EEG, improving its spatial resolution by means of advanced source localization methods, and to integrate the resulting information with the connectivity analysis and graph theoretical approach. In particular, this work aims at the extraction of the connectivity patterns providing at the same time spatial and spectral information, and at the definition of neuro-electrical descriptors for their main local and global properties. The results showed in the present study demonstrated the possibility to associate a specific circuit to each attention component and to identify synthetic indices able to selectively describe their neurophysiological, spatial and spectral properties.**

***Keywords*—Attention, Source Reconstruction, Effective Connectivity, Graph Theory.**

I. Introduction

The comprehension of the neural mechanisms underlying attentional processes has been a subject of studies in neuroscience and neuro-engineering for decades, due to its theoretical and practical implications. Posner and Petersen proposed a theoretical model in which attention is defined as a complex system of multiple networks in the brain, responsible for three different functions: alerting, orienting and executive control [1]. Fan et al. developed the Attention Network Task (ANT), a paradigm providing measures of the functionality of these networks [2]. Several studies demonstrated that they are independent [3], involve different anatomical areas (fMRI studies) [4] and each of them has a distinct oscillatory activity and time course (EEG study) [5]. Current evidences suggest: the activation of frontal and parietal cortical sites and a high involvement of the right hemisphere for alerting; a large lateralization in favour of the left hemisphere and the involvement of top-down processes for orienting; the executive control network appears spread out on several brain areas with a particular involvement of the pre-frontal cortex (PFC) and the anterior cingulate (ACC). Despite the advancements in this field, a single framework able to provide a connection between the different levels of description and to take into account at the same time i) the location of the involved areas, ii) the directed connectivity patterns including such areas, iii) the frequency content of the signals is still missing. The use of techniques of brain sources localization allows to increase the spatial resolution of EEG by keeping its excellent temporal resolution, leading to an accurate estimation of effective connectivity to describe the involved brain circuits. The aim of this study was to integrate together spatial and temporal information into a single circuit (connectivity pattern), and to provide neuro-physiological descriptors able to characterize the different attention processes.

II. Material and Methods

A. Standardized Low Resolution Tomography (sLORETA)

The algorithm sLORETA [6] is a method for the reconstruction of cortical and subcortical activity from hdEEG scalp signals. It allows to estimate neuro-electrical activities in the whole grey matter from hdEEG recordings by solving the linear inverse problem. sLORETA estimates the current source density distribution on a dense grid of 6239 voxels at 5 mm spatial resolution, modeling the entire brain volume.

B. Partial Directed Coherence (PDC)

PDC is a causality-based connectivity estimator characterized by high accuracy and stability in the evaluation of directed influences between any given pair of signals in a multivariate dataset [7]. Such estimator provides a spectral measure of the causal information flows, by representing a spectral version of Granger causality approach. The original formulation of the PDC is the following:

$$\pi_{ij}(f) = \frac{|A_{ij}(f)|^2}{\sum_{m=1}^{M}|A_{im}(f)|^2} \quad (1)$$

where $A_{ij}(f)$ represents the entry (i,j) of the matrix of MVAR model coefficients A at frequency *f*.

C. Graph Theory (GT)

Cerebral networks are sets of nodes (vertices) linked by connections (edge) indicating the presence of an interaction between them, thus they can be mathematically described as graphs. GT allows to synthetize the main local and global properties of a complex network by means of simple indices:
Density: index used to quantify the percentage of existing connections with respect to the totality of possible links. Such index can be adapted to quantify the percentage of connections relative to a specific area.
Out-Degree: measure used to characterize the outputs links of individual areas or nodes. Such index allows to identify sources in the network [8].
Clustering: measure of the tendency of the network to segregate the information in subnetworks;
Influence: measure of the difference in the number of inter connections between two different spatial regions [9].
Divisibility - Modularity: indices computed considering two subnetworks and able to describe the relationship between them in terms of inter (divisibility) and intra (modularity) connections: strict interconnection or isolation [10].

For the evaluation of such indices we considered three couples of subnetworks derived from previous studies in literature: left and right hemisphere, frontal and parietal lobes, cerebral areas involved in Bottom-Up (flow from lower to higher centers-frontal gyrus, temporal parietal junction) and Top-Down processes (flow from cortical areas to lower centers-PFC, visual cortex, parietal lobule)[4].

D. Experimental Design

HdEEG data were collected on 17 healthy subjects during the execution of the ANT. Participants were presented with a row of 5 black arrows pointing left or right. They were asked to indicate the direction of the central arrow (target stimulus). Trials were *Congruent* if the 4 lateral *flankers* and the central arrow had the same direction, *Incongruent* if the flankers pointed at the opposite direction. In addition there were three cue (an asterisk sign) conditions: *No cue*, *Center cue* (in the center of the screen for alerting), and *Spatial cue* (at the target location, above or below a fixation cross, for alerting plus orienting) [3]. The comparison between these experimental conditions allowed to extract the attentional components: i) *Center cue* and *No cue* conditions define the alerting, ii) *Spatial cue* and *Center cue* the orienting, iii) *Incongruent* and *Congruent* the executive control.

E. EEG Data Analysis and Connectivity Estimation

EEG data were pre-processed and segmented in cue and target windows. Through the reconstruction of the cortical and subcortical brain activity (sLORETA), we identified regions of interest (ROIs) (the complete list of the considered ROIs is reported in Fig 1). Connectivity between the ROIs was estimated by PDC, for each experimental condition and each frequency band. The salient properties of these networks were derived by means of the graph theory approach described in the previous paragraphs. In order to describe each attentional component, statistical comparisons between appropriate couple of conditions (according to ANT theory) were performed. Finally we reconstructed the brain circuits at the basis of the three processes by means of a group statistical non-parametric test.

III. Results

A. Average Connectivity Maps

In Figs.1a, 1c, 1e, we reported the statistical connectivity patterns elicited in specific frequency bands, for the different attentional components (Alpha, Gamma, Beta bands, respectively for alerting, orienting and executive control). The arrows color represents the strength of the connections between the considered ROIs.

B. Attentional Components Characterization

GT application provided descriptors quantifying the main properties of the single experimental conditions and their variations. Alerting contrast showed a significant increase, in Alpha band, of: Bottom-Up *Out-Degree, Influence* of the Bottom-Up network on the Top-Down, *Influence* of the frontal lobe on the parietal one (Fig. 1b). Bottom-Up network plays an important role as source and is independent from the Top-Down processes. The main flow direction in this phase comes from the frontal lobe.

Results related to orienting, reported in Fig.1d, revealed a significant increase, in Gamma band, in terms of Left *Density*, Left/Right *Influence* and Bottom-Up/Top-Down *Influence* (Fig 1d). Such results showed that this attentional component is characterized by a high involvement of the left hemisphere, that exerts an influence on the area of the right side, and by a larger participation of Top-Down processes.

The analysis related to executive control showed a significant increase of the Clustering index and a significant decrease of *Modularity* and *Divisibility* between Bottom-Up and Top-Down networks, in Beta band. Conflict resolution is the most complex phase in the ANT and, as expected, was described by the cooperation between Bottom-Up and Top-Down processes and showed a more efficient organization in smaller subnetworks.

IV. Conclusion

Our results showed the possibility to identify the specific cerebral areas involved in attention processes from EEG recording, using advanced methods for source reconstruction. Furthermore, the integration between source localization methods, connectivity estimation and GT indices allowed to provide spatial and temporal informations, and to extract synthetic neurophysiological indices directly related to the cerebral processes which underlie the attentive functions. Such indices allowed to highlight important neuro-electrical properties (sources and dynamics) of the circuits related with the analysed attentional function.

Acknowledgement

Research partially supported by the University of Rome Sapienza: “Progetti di Ateneo per la Ricerca Scientifica anno 2014”.

References

[1] M. I. Posner and S. E. Petersen, “The attention system of the human brain,” *Annu. Rev. Neurosci.*, vol. 13, pp. 25–42, 1990.

[2] J. Fan, B. D. McCandliss, T. Sommer, A. Raz, and M. I. Posner, “Testing the efficiency and independence of attentional networks,” *J. Cogn. Neurosci.*, vol. 14, no. 3, pp. 340–347, Apr. 2002.

[3] J. Fan, B. D. McCandliss, J. Fossella, J. I. Flombaum, and M. I. Posner, “The activation of attentional networks,” *NeuroImage*, vol. 26, no. 2, pp. 471–479, Jun. 2005.

[4] M. Corbetta and G. L. Shulman, “Control of goal-directed and stimulus-driven attention in the brain,” *Nat. Rev. Neurosci.*, vol. 3, no. 3, pp. 201–215, Mar. 2002.

[5] J. Fan, J. Byrne, M. S. Worden, K. G. Guise, B. D. McCandliss, J. Fossella, and M. I. Posner, “The Relation of Brain Oscillations to Attentional Networks,” *J. Neurosci.*, vol. 27, pp. 6197–6206, 2007.

[6] R. D. Pascual-Marqui, “Standardized low-resolution brain electromagnetic tomography (sLORETA): technical details,” *Methods Find. Exp. Clin. Pharmacol.*, vol. 24, pp. 5–12, 2002.

[7] L. A. Baccalá and K. Sameshima, “Partial directed coherence: a new concept in neural structure determination,” *Biol. Cybern.*, vol. 84, no. 6, pp. 463–474, Jun. 2001.

[8] R. Kötter and K. E. Stephan, “Network participation indices: characterizing component roles for information processing in neural networks,” *Neural Netw. Off. J. Int. Neural Netw. Soc.*, vol. 16, no. 9, pp. 1261–1275, Nov. 2003.

[9] J. Toppi, M. Petti, F. De Vico Fallani, G. Vecchiato, A. G. Maglione, F. Cincotti, S. Salinari, D. Mattia, F. Babiloni, and L. Astolfi, “Describing relevant indices from the resting state electrophysiological networks,” *Conf. Proc. Annu. Int. Conf. IEEE Eng. Med. Biol. Soc. IEEE Eng. Med. Biol. Soc. Annu. Conf.*, vol. 2012, pp. 2547–2550, 2012.

[10] M. E. J. Newman, “Finding community structure in networks using the eigenvectors of matrices,” *Phys. Rev. E*, vol. 74, no. 3, Sep. 2006.

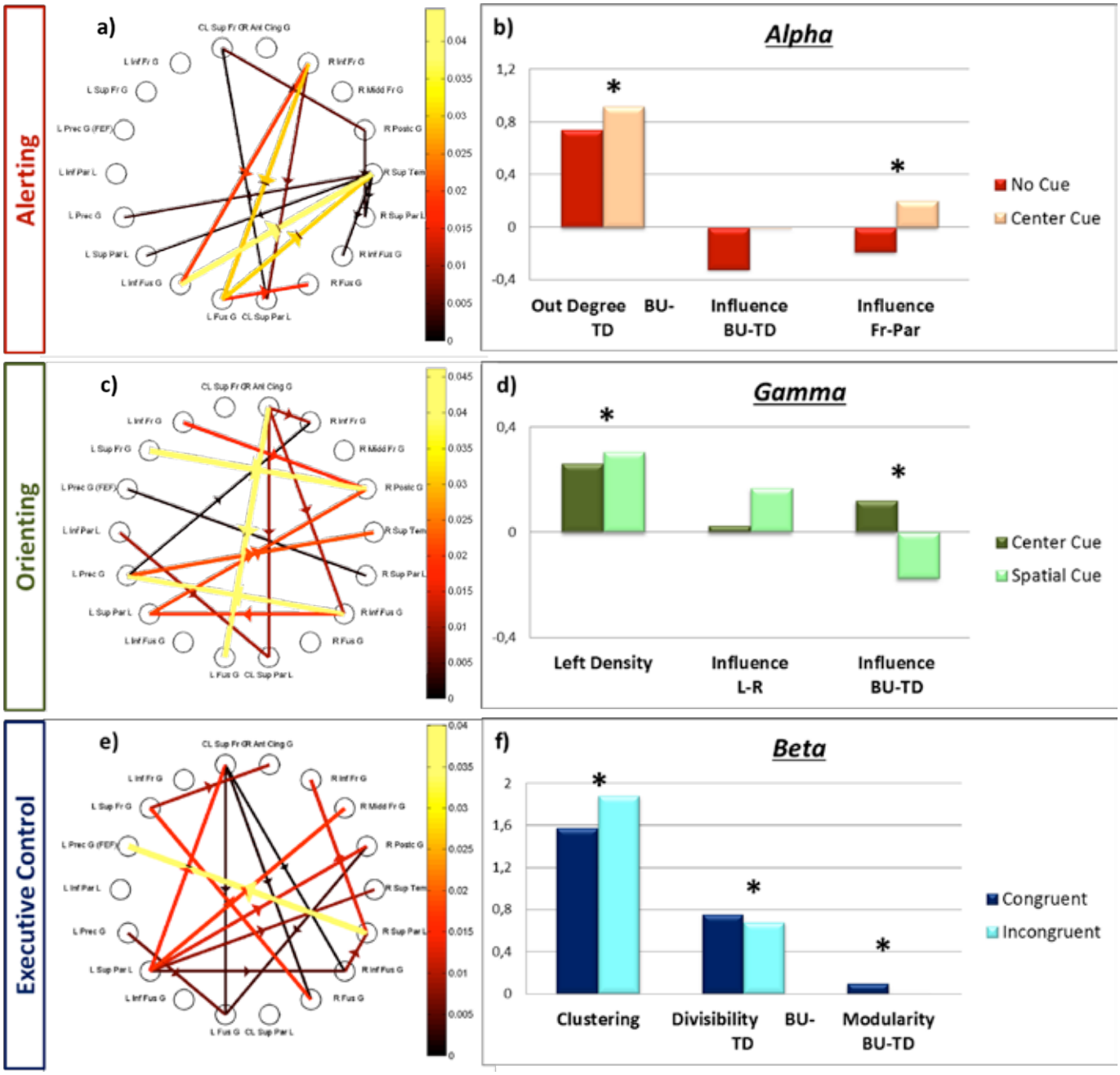

Fig. 1- Connectivity maps and their descriptors extracted for the three attentional networks. The considered ROIs are: *left inferior\superior frontal gyrus, left precentral gyrus, left inferior\superior parietal lobule, left fusiform gyrus, left inferior fusiform gyrus, right anterior cingulate gyrus, right inferior\middle frontal gyrus, right post-central gyrus, right superior temporal gyrus, right superior parietal lobule, right fusiform gyrus, right inferior fusiform gyrus*. a,c,e) Statistical connectivity patterns elicited by healthy subjects performing ANT in a specific frequency band for each attention component: a) alerting, alpha band; c) orienting, gamma band; e) executive control, beta band. Connectivity patterns are represented on a 2D model in which nodes are the cortical ROIs and the edges are the causal significant connections. The arrows color codes for the strength of the connection. b,d,f) Bar diagrams reporting the values achieved for a specific graph index averaged on the population. The asterisk highlights a statistical significant variation of the index in an experimental condition corresponding to a specific attentional component with respect to a baseline condition (permutation test; $p<0.05$).

Entropy and uniformity as CT perfusion measures may predict survival in lung cancer

S. Baiocco[1], D. Barone[2], G. Gavelli[2] and A. Bevilacqua[1,3]
[1] *Advanced Research Centre on Electronic Systems(ARCES), University of Bologna, Bologna, Italy*
[2] *Radiology Unit, IRCCS - Istituto Scientifico Romagnolo per lo Studio e la Cura dei Tumori (IRST), Meldola (FC), Italy*
[3] *Dept. of Computer Science and Engineering (DISI), University of Bologna, Bologna, Italy*

***Abstract*— Computed Tomography perfusion (CTp) is a functional imaging technique, which allows detecting the presence of tumour abnormal vascular patterns, through the temporal analysis of the tissue density variations. The aim of this study is to extract meaningful statistical features from CTp colorimetric maps of lung cancers that could act as a surrogate prognostic image-based biomarker.**

***Keywords*— quantitative imaging, tumour heterogeneity, clustering, time-concentration curves**

I. Introduction

Lung tumour is characterised by an extraordinarily heterogeneity both at genetic and histopathological levels [1], mainly due to angiogenesis, a process involving the formation of new blood vessels from pre-existing ones [2].

Imaging technologies have a great potential, being able to capture the *in vivo* intra-tumoral heterogeneity [3]. In particular, Computed Tomography perfusion (CTp) has shown to be widely applicable in oncology for evaluation and monitoring of tumours angiogenesis through perfusion colorimetric maps [4].

However, the hemodynamic heterogeneity emerging from CTp maps is difficult to extract because of the contemporary presence of structural artefact due to, for instance, beam hardening, partial volume effects and not negligible motion [5], particularly problematic in abdomen application where movements, mostly due to breathing, are almost inevitable even for the short first-passage studies [6].

Heterogeneity is also considered a plausible explanation for the differences in treatment outcomes observed in clinic [7]. Indeed, survival for non-small-cell lung cancer (NSCLC) is varying for patients stratified in the same stage grouping [8]. Therefore, further quantitative studies focusing on hemodynamic heterogeneity are needed to derive more effective and reliable biomarker of prognosis, with strong implications in treatment choices [8].

The aim of this work is to exploit voxel-based information and to find out features able to capture the information conveyed by the hemodynamic heterogeneity patterns of the CTp maps. In this way, it is possible to obtain data to predict patient survival since the diagnosis stage. Accordingly, the regions undergoing CTp artefacts, that could hamper the assessment of the heterogeneity, were automatically removed from the image sequences [5].

II. Materials and Methods

A. CT perfusion protocol

16 patients (age range 36-79 years) with a primary NSCLC lesion, at the diagnosis stage, underwent axial CTp with a 256-slice CT system, feet first in the supine position. Survival data were included in the study.

An initial low-dose unenhanced full-body CT scan was performed to identify the target lesions at baseline condition. A 50 mL intravenous bolus of contrast agent was then injected at 5 mL/s for axial contrast enhanced CT. The study was approved by the medical ethics committee.

A single acquisition, lasting 25 s, was performed at 0.8 Hz for each patient, instructed for breath-hold, yielding 20 scans, with 55 mm of z-coverage (11 slices, 5-mm slice thickness, at 80 kV, 250 mA, 100 mAs). On the whole, a sequence of 220 cine images (512 × 512 pixel, 350 mm × 350 mm, 5-mm slice spacing) was achieved for each patient.

B. Perfusion maps

The target lesions and the arterial input (aorta) were selected in agreement by two radiologists on a reference slice. For each lesion, a reference sequence made of slices at the same coach position was considered. The radiologists manually drawn on a reference slice the region of interest (ROI) and translated it on the remaining ones, so that the borders of the lesion visually match. Finally, a 3D rigid alignment is performed by radiologists by also exploring the adjacent slices, looking for the best match with the reference section [6], so as to achieve the "best" sequence. Blood flow (BF) functional maps of the reference slice were obtained by fitting the concentration values of the best temporal sequence relative to each voxel, using a sigmoid-shape model, arising from the Hill Equation [9], and applying the Maximum-Slope method [5] during the first-pass phase:

$$BF = \frac{\frac{dC_T(t)}{dt}\Big|_{max}}{C_A(t)|_{max}} \quad (1)$$

where $C_T(t)$ is the time concentration curve (TCC) of the tissue and $C_A(t)$ is the TCC of the arterial input. BF values, expressed in mL/min/100 g, are graphically represented using functional colorimetric maps.

In particular, BF values undergoing high fitting errors were automatically removed. Similarly, BF values strictly lower than 1 mL/min/100 g were considered as being unlikely compliant with physiological values and rather ascribed to numerical errors, since the computing method forces BF to have positive values only [5]. Both the errors have been highlighted in the colour map with the pink colour.

C. Data Processing

Overall survival (OS) was defined as the time between the date of diagnosis and the date of death. Median OS for the

entire cohort was calculated and resulted to be 8 months.

Among the features generated, we selected two relevant first-order statistics, the Shannon entropy (*E*) and the uniformity (*U*), measures of irregularity and homogeneity respectively. *E* and *U* were computed on all BF maps and analysed both separately and jointly in couples. Whereas *E* is widely known, *U* is described in Eq. (1), where *l* represents the pixel value, ranging from 1 and k, and *p(l)* its frequency in the overall map:

$$U = \sum_{l=1}^{k} [p(l)]^2 \quad (2)$$

Unsupervised classification was performed on the whole dataset through the *k*-means (*k*=2) algorithm, where the Squared Euclidean distance was considered as the similarity measure. Subsequently, a multivariate analysis of variance (MANOVA) was performed to assess the statistical separability of the two clusters identified by the algorithm.

Finally, the prognostic power of the features couple, that is, their capability to predict OS based on clusters attained, was assessed by comparing the clustered patients with OS data.

III. Results

Results in terms of *E* and *U* for each patient are summarized and reported in arbitrary units (a.u.) in Table I, along with the information regarding OS.

TABLE I

ID	*OS*	*E*	*U* ($\times 10^{-2}$)
ID1	6	7,44	0,74
ID2	4	8,64	0,33
ID3	14	5,20	3,53
ID4	13	5,81	2,06
ID5	5	8,02	0,43
ID6	8	8,07	0,45
ID7	5	7,51	0,64
ID8	6	7,53	0,76
ID9	16	6,57	1,33
ID10	6	7,24	0,81
ID11	6	7,71	0,59
ID12	10	6,35	1,63
ID13	8	8,02	0,50
ID14	8	7,20	0,86
ID15	12	6,65	1,27
ID16	0	7,19	0,90

Summary of overall survival (OS), entropy (E) and uniformity (U) for each examination (ID). E and U are reported in arbitrary units (a.u.).

E and *U* used together show a high discriminatory power to separate the two groups of patients with OS≤8 and OS>8. Indeed, Cluster 1 (highlighted in red in Fig. 1), characterized by higher entropy and lower uniformity values, encloses the patients with the worst prognosis (OS≤8). On the contrary, the patients belonging to the Cluster 2 (highlighted in blue in Fig. 1) are those characterised by the best prognosis in this study (OS>8). Moreover, the outcome of MANOVA proves that the means *E* and *U* of the two clusters differ significantly, with a *p*-value = $1{,}52\times10^{-5}$.

In addition, we report BF maps and related histograms of the most significant cases: the most heterogeneous examination (ID2, Fig. 2), the most homogeneous one (ID3, Fig. 3), and the borderline examinations with the closest distance, in terms of *E* and *U* values (ID15, Fig. 4 and ID16, Fig. 5). ID15 is correctly assigned to the higher OS group, being generally homogeneous and low perfused, but with the upper region more heterogeneous and highly perfused. On the contrary, ID16 correctly falls in the lower OS group although it shows two different and separate behaviours: the upper region is heterogeneous and highly perfused, while the lower region is homogeneous with a very low perfusion.

IV. Conclusion

The results prove that simple features, *E* and *U*, strongly correlate with OS when computed on perfusion maps where the unlikely BF values have been automatically removed.

In addition, BF maps of the group with the highest OS expectation are much more homogeneous than those of the other group, which is characterized by a narrowed range of BF values. On the contrary, BF maps of the group with the lowest OS expectation are generally more perfused, and values in the histograms are more homogeneously distributed. This implies a greater heterogeneity of BF values and, consequently, a greater functional heterogeneity of the lesions. These results show that a higher heterogeneity correlates with a higher tumour aggressiveness, which strongly reflects on the OS parameter.

In conclusion, this finding proves that the quantitative measurements of the intra-tumour hemodynamic heterogeneity could represent a promising surrogate biomarker for OS prediction. These results prompt us to plan a prospective study aiming at predicting OS of the single patients, hence to assess whether CTp-based heterogeneity measures can be utilized in clinics as a prognostic biomarker.

References

[1] P. Lambin, *et al*., "Radiomics: extracting more information from medical images using advanced feature analysis.", *Eur. J. Cancer*, (2012) 48(4):441-446.

[2] W. van Elmpt, *et al*., "Characterization of tumor heterogeneity using dynamic contrast enhanced ct and fdg-pet in non-small cell lung cancer." *Radiother. Oncol*., (2013) 109(1): 65-70.

[3] R. Colen, *et al.,* "NCI workshop report: clinical and computational requirements for correlating imaging phenotypes with genomics signatures.", *Transl. Oncol,.,* (2014) 7(5):556-569.

[4] K. A. Miles, M. R. Griffiths, "Perfusion CT: a worthwhile enhancement?", *Br. J. Radiol.*, (2003) 904(76):220-231.

[5] A. Bevilacqua, D. Barone, S. Malavasi, and G. Gavelli, "Automatic detection of misleading blood flow values in CT perfusion studies of lung cancer.", *Biomed. Signal Process. Control*, (2016) 26:109-116.

[6] A. Bevilacqua, D. Barone, S. Malavasi, G. Gavelli, "Quantitative assessment of effects of motion compensation for liver and lung tumors in CT perfusion.", *Acad. Radiol.*, (2014) 21(11):1416-1426.

[7] Z. Chen, C. M. Fillmore, P. S. Hammerman, C. F. Kim, K. K. Wong, "Non-small-cell lung cancers: a heterogeneous set of diseases.", *Nat. Rev. Cancer*, (2014) 14(8):535-546.

[8] S. G. Spiro, *et al*., "Lung cancer: progress in diagnosis, staging and therapy.", *Respirology*, (2010) 15(1):44-50.

[9] S. Goutelle *et al*., "The Hill equation: a review of its capabilities in pharmacological modelling.", *Fundam. Clin. Pharmacol.*, (2008) 22(6):633-648.

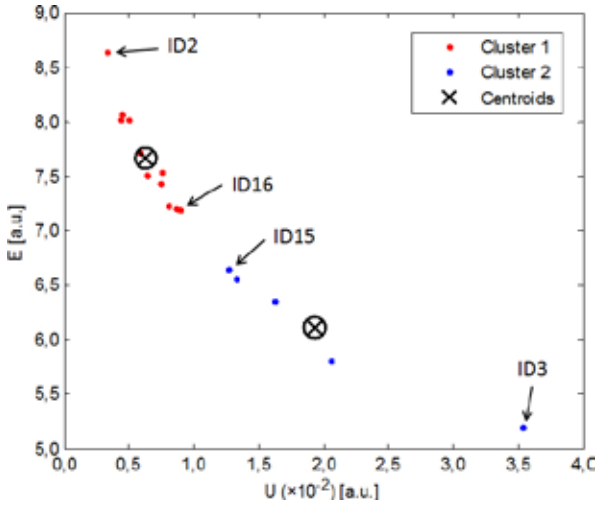

Fig. 1. Scatter plot of entropy (E) and uniformity (U) values related to all the examinations are reported and given in arbitrary units (a.u.). 11 examinations belong to Cluster 1 (in red), 5 to Cluster 2 (in blue).

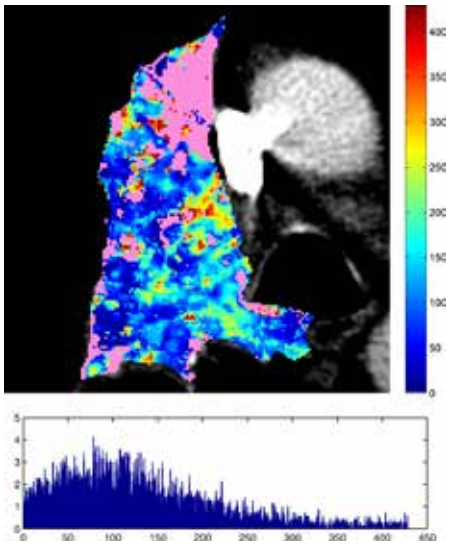

Fig. 2. ID2: Blood flow (BF) colorimetric map (top) and corresponding BF histogram (bottom). The pink colour points out unreliable BF values.

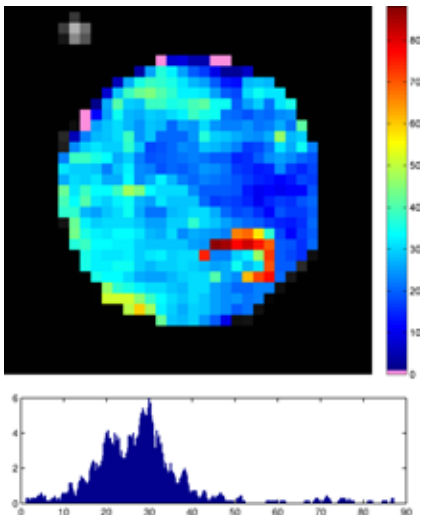

Fig. 3. ID3: Blood flow (BF) colorimetric map (top) and corresponding BF histogram (bottom). The pink colour points out unreliable BF values.

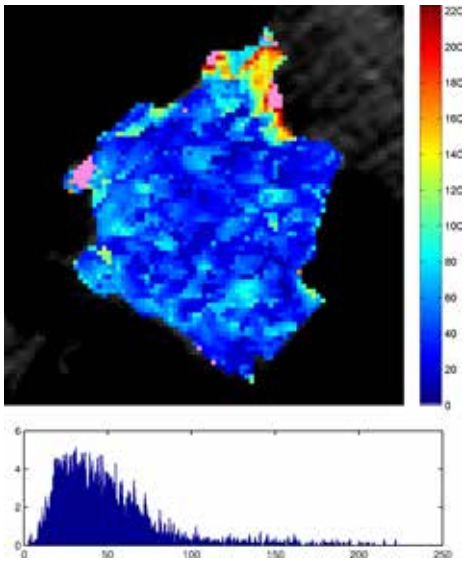

Fig. 4. ID15: Blood flow (BF) colorimetric map (top) and corresponding BF histogram (bottom). The pink colour points out unreliable BF values.

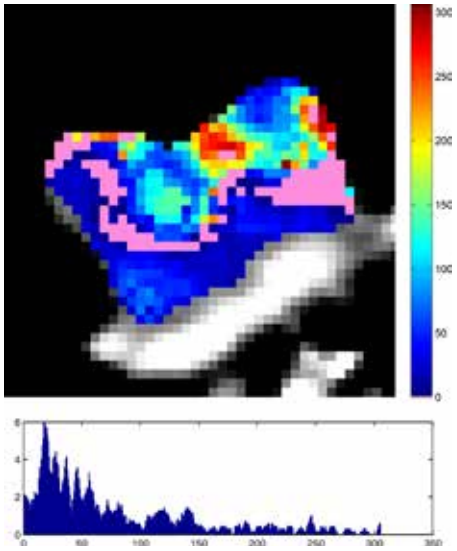

Fig. 5. ID16: Blood flow (BF) colorimetric map (top) and corresponding BF histogram (bottom). The pink colour points out unreliable BF values.

A wearable embedded platform for real-time hand neuroprostheses control

G. Barabino, D. Pani and L. Raffo
DIEE- Dept. of Electrical and Electronic Engineering, University of Cagliari, Italy

***Abstract*—The control of upper limb neuroprostheses through the peripheral nervous system (PNS) can allow restoring motor functions in amputees. Beyond having a system that could manage the prosthetic device with a satisfactory power efficiency, another crucial aspect is the real-time implementation of neural decoding algorithms, which necessarily need to run on a custom embedded system. This aspect is usually overlooked, notwithstanding the actual portability and the impact that limited hardware resources have on the efficiency/effectiveness of the decoding algorithms.**

This paper presents an embedded system that could allow controlling a neural hand prosthesis by decoding in real-time the movement intention extracted from the PNS activity. By interfacing this system with the robotic hand and an analogue front-end for signal acquisition and neural stimulation, it is possible to implement a wearable solution for the neuroprosthesis control. The final embodiment demonstrates the real-time performance onto a low-power off-the-shelf Digital Signal Processor (DSP), opening to experiments exploiting the efferent signals to control a hand neuroprosthesis.

***Keywords*—Neural prosthesis, real-time processing, embedded systems.**

I. Introduction

ACTIVE upper limb prostheses, such as those extracting the patient's movement intention from the Electromyogram (EMG), already entered the market. Alternative and more natural ways to access the movement intention can rely on the neural signals decoding. Compared to the coarse compound signal, the neural one is finer and potentially able to provide more information to control more degrees of freedom. Thanks to the evolution of the neuronal interfaces with the peripheral nervous system PNS, now characterized by better selectivity [1], in principle it is possible to perform decoding on the PNS signals with techniques similar to those exploited for the CNS. However, on the peripheral nerves, the SNR is typically lower [2]. Such an aspect, and the limited electrodes selectivity, require enhanced signal processing techniques, at the expenses of the computational power.

Unfortunately, the decoding algorithms must be implemented onto embedded platforms, characterized by limited resources, low operating frequencies and tight real-time bounds to fulfil. Overlooking this issue could have severe consequences on the validity of decoding algorithms in real scenarios. In this paper, an embedded wearable system, developed with such constraints in mind, is presented and evaluated. A particular effort has been put on the optimization and characterization of different decoding algorithms implemented onto an off-the-shelf Digital Signal Processor (DSP) powering a custom board. The real time performance of the implemented algorithms will be presented.

II. Materials and Methods

The embedded system developed to perform the real-time neural signal decoding can be interfaced to a custom recording/stimulation front-end [3] and can communicate with the robotic hand to provide high-level commands (grasping types). It consists of a 11cm × 13cm × 4.7cm box (shown in Fig. 1), embedding all the electronics. The system is battery powered and, beyond several communication interfaces, embeds a 4.2" LCD display for user interaction. Its core is the MityDSP-L138F (shown in Fig. 2) platform (hosted on a custom motherboard), a so-called System-On-Module (SOM), which in a small form-factor PCB board integrates the dual-core OMAP-L138 CPU, an ARM9 + C674x DSP processor, along with a Xilinx Spartan-6 FPGA. Moreover, the SOM hosts a 256MB RAM memory and a 512MB NAND flash memory. The system is capable of controlling up to 54 channels in stimulation and can record up to 8 user selected channels among the 54 available, supporting data logging and visualization features. Its internal structure, shown in Fig. 3, is composed of:

- The ARM9, managing the overall system operation, providing external connectivity and exporting a portable graphical interface (GUI) to the user
- The DSP, which runs the neural decoding algorithms and handles the data coming from the recording front-end
- The FPGA, implementing a custom interface to the recording/stimulation front-end
- I/O buses to interface the system to the other system components (sensors, robotic hand).

A custom communication protocol, based on a shared memory region and on the IPC 3.x APIs, is used to synchronize the ARM9 – DSP operation. The ARM application is able to load different precompiled signal processing routines, which can be selected from the GUI by the user, onto the DSP, configuring its operation via a set of parameters stored into the shared memory. The communication between the ARM9 and the front-end (for its configuration and management) and between the recording chip and the DSP are implemented via two individual SPI buses. The system also provides additional standard ports for communicating with the robotic hand (UART), along with additional communication interfaces (SPI) which can be exploited to connect the device to neural stimulation systems to provide afferent stimuli to the PNS. Notably, the system offers a significant degree of flexibility, which is desirable in a first experimentation phase.

A. Decoding algorithms

Two different decoding algorithms have been implemented and characterized. The first one (A1) it's a spike sorting algorithm, whose real-time implementation has been deeply analysed in [4]. Its structure consists of four stages: a wavelet denoising pre-processing (WD), spike detection (SD), spike sorting by template matching (SS) for feature extraction and classification (CL). The latter exploits a SVM classifier. The template matching approach adopted in this algorithm is critical in terms of computational complexity in the perspective of a real-time implementation. To cope with the real-time requirements, a block-on-line approach has been selected, exploiting a virtual sliding window for the first three stages, the last one being in charge of preserving a memory of the spike sorting results for the latest *N* blocks (which represent the time window on which CL operates) to compute the features used for the classification. In order to enhance the real-time performances of the same algorithm, also its fixed-point version (A2) has been implemented. Several changes have been applied throughout the code, to avoid overflows and to reduce round-off errors in math operations such as square root. The SVM has been substituted with a neural network (2 layers, 10 hidden neurons, M outputs, where M stands for the number of classes to discriminate), which more easily can be implemented in fixed-point arithmetic. This second version has been characterized both in terms of efficacy (affected by the limited precision of fixed-point arithmetic) and efficiency.

Along with the spike-based algorithms, another one, suited for cumulative activity decoding (A3), based on [5], has been implemented. This algorithm implements a first pre-processing band-pass filtering the signals with a 128-tap least-square FIR filter with 0.8kHz and 2.2kHz cut-off frequencies. The choice of the order is a good trade-off between performance and spectral behaviour. The features (Mean absolute value, Variance, Wave length and Energy in this implementation) are extracted over 100ms windows, with an overlap of 50%. The extracted features are saved in a data structure of predetermined size and labelled automatically on the basis of the experimental protocol. This phase ends when a data structure containing the training set for the classifier (an SVM) has been completely filled. Training is performed creating as many classifiers as the number of classes to discriminate, according to the technique of One-Vs-All.

For all the algorithms, samples labelling is performed automatically exploiting a trigger identifying the signals parts characterized by a given event. However, a sample is labelled only if the absolute value of the feature is greater than the threshold of baseline activity.

B. Evaluation methods

The system has been evaluated both in terms of real-time performance (efficiency) and decoding quality (effectiveness). For the former, a cycle-accurate profiling analysis on the real hardware platform (C6748 DSP) has been carried out, evaluating the number of machine cycles needed to perform the different parts of the algorithm. A less accurate energy consumption estimation has been also performed. For the latter, the algorithms have been trained to decode different afferent stimuli (up to 4) starting from the recorded neural activity on the PNS of rodents.

III. Results

TABLE I
DECODING ALGORITHMS PROFILING RESULTS IN CPU CYCLES

	Pre-processing	*Feature extraction*	*Classification*	*Tot ($\times 10^6$)*
A1	331185	~198692*n_{sp}	795900	36.8
A2	70610	~149557*n_{sp}	2155	26.9
A3	168047	4227732	795900	5.2

Real-time performances can be compared through Table I. Considering a DSP operating frequency of 300 MHz, a sampling frequency of 12 kHz and a block size of 3000 samples, the real-time bound is set at 75×10^6 CPU cycles. Results obtained for the three algorithms are not immediately comparable, since A1 and A2 cycle count depends on the number of spikes present in a block n_{sp}. All the algorithms satisfy the real time bound in real working conditions, A3 being the less computationally intensive.

Nevertheless, in terms of efficacy in the decoding phase, the latter has also the worst performance (particularly when working with selective electrodes tfLIFE), in contrast with the spike-based algorithms, which are able to obtain better performances (Fig. 4). It is also noticeable how the fixed point version of A1 does not pay excessive penalties in the classifier performance, due to the limited precision.

From a power analysis, it results that the most demanding algorithm could run for 24 hours with a battery by 2300 mAh, supposing the DSP operating at a maximum load.

IV. Conclusion

The developed system demonstrated in the preliminary tests to be efficient from a power consumption perspective and to be also effectively able to run in real-time decoding signal processing routines aimed at controlling a neuroprosthesis. The device will be employed during in-vivo experiments on humans in range of the E.U. founded project Nebias and the PRIN project HandBot, starting from June 2016.

Acknowledgments

The authors wish to thank Prof. Xavier Navarro (Universitat Autonoma de Barcelona) and his team for providing the signals from rodents. The research leading to these results has received funding by the Region of Sardinia in the ELoRA project (Fundamental Research Programme, L.R. 7/2007, grant agreement CRP-60544), by the European Commission in the NEBIAS project (FP7, FET Proactive, grant agreement 611687) and by Italian Government in the HANDBOT project (PRIN 2010/11, prot. 2010YF2RY_003).

References

[1] A. Kundu et al "Stimulation Selectivity of the Thin-Film Longitudinal Intrafascicular Electrode (tfLIFE) and the Transverse Intrafascicular Multi-Channel Electrode (TIME) in the Large Nerve Animal Model," *IEEE Trans. Neural Systems and Rehabilitation Engineering,* vol 22, pp.400-410, 2014.

[2] X. Navarro et al., "A critical review of interfaces with the peripheral nervous system for the control of neuroprostheses and hybrid bionic systems," *J. of the peripheral nervous system*, vol 10, pp.229-258, 2005.

[3] C. Carboni et al., "An integrated interface for peripheral neural system recording and stimulation: system design, electrical tests and in-vivo results," *Biomedical Microdevices*, vol. 18, pp. 1–17, 2016.

[4] D. Pani et al., "Real-time neural signals decoding onto off-the-shelf DSP processors for neuroprosthetic applications," *IEEE Trans. Neural Systems and Rehabilitation Engineering*, in press.

[5] S. Raspopovic, J. Carpaneto, E. Udina, X. Navarro, S. Micera, "On the identification of sensory information from mixed nerves by using single-channel cuff electrodes," *J. of Neuroengineering and Rehabilitation* 2010, 7:17

Fig. 1: pictorial view of the prototypical control system for a neuroprosthesis

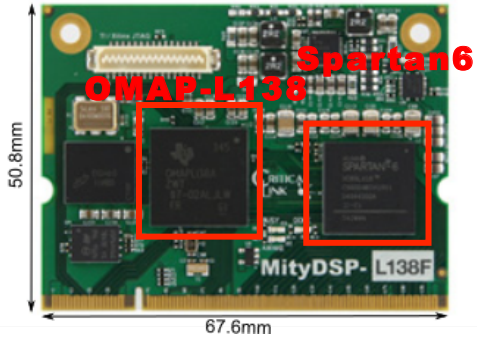

Fig. 2: the System-On-Module MityDSP-L138

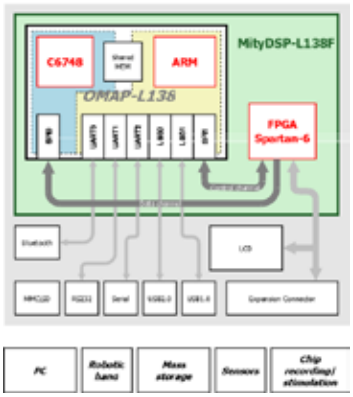

Fig. 3: Block diagram representing the internal structure of the embedded system for the closed loop control of a neuroprosthesis

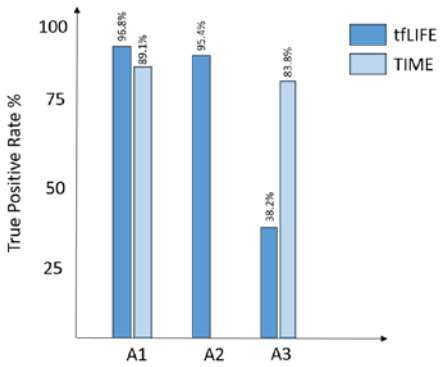

Fig. 4: Decoding algorithms performance on signals acquired with different intrafascicular electrodes.

A targeted metabolomics approach for mortality risk stratification in septic shock patients

A. Cambiaghi[1], L. Brunelli[2], R. Pastorelli[2], M. Ferrario[1]
[1] *Dipartimento di Elettronica, Informatica e Bioingegneria (DEIB), Politecnico di Milano*
[2] *IRCCS Istituto di Ricerche Farmacologiche Mario Negri, Milano*

***Abstract*— The occurrence of septic shock remains a major problem in Intensive Care Unit (ICU), with high mortality rate and difficulties in predicting the outcome. In this preliminary study we examined plasma metabolome and clinical features in a subset of 20 patients with severe septic shock (SOFA score>8), enrolled in the multicenter Albumin Italian Outcome Sepsis study (ALBIOS, NCT00707122). Our aim was to elucidate early biomarkers signatures that might help clinicians in prioritizing individual patient treatment during shock. Data-mining techniques were used to highlight metabolite levels associated with 28-day and 90-day mortality in order to investigate the possibility to predict short-term and long-term outcomes by means of a univariate and multivariate analysis of plasma quantitative metabolome and clinical features. Our findings show that early changes in the plasma levels of low unsaturated long-chain phosphatidylcholines, lysophosphatidylcholines and kynurenine were associated with long-term mortality, with potential implications for early intervention and discovering new target therapy.**

***Keywords*—Metabolomics, mortality prediction, septic shock.**

I. Introduction

SEPTIC shock is the most severe complication of sepsis and one of the main causes of death in ICUs [1]. Although treatment has improved over the last decades, outcome is still poor and difficult to predict [2]. As for therapies, current strategies are targeted to reduce symptoms of shock but they are unable to act at the "beginning of the cascade" because of the lack of a model explaining the molecular basis of shock-induced tissue injury and of ensuing organ damage. To shed light on the complexity of this pathological status, the use of emerging omics tools able of examining physiological responses at system level is thus particularly promising.

In the present study, we used a targeted mass spectrometry-based quantitative metabolomics approach focusing our attention on several series of metabolites, such as glycerophospholipids, aminoacids, biogenic amines and acylcarnitines, some of which have already been identified as part of key biochemical pathways in septic shock [3,4]. We applied our metabolomic strategy on a well defined class of patients with severe septic shock (serum lactate concentration > 4 mmol/L) with multiple organ failures (SOFA score > 8) enrolled in the recent multicenter, randomized clinical trial ALBIOS, which is a large study with 1818 severe sepsis or septic shock patients enrolled [5]. Metabolomics analyses provided absolute quantitative information on plasma metabolite levels measured at first day (initial acute phase) and after seven day. The association between metabolic changes and mortality was assessed with univariate and multivariate analyses adjusted for clinical relevant variables. The primary goal of this pilot investigation was to verify the feasibility of the target metabolomics and the statistical approach in a small cohort of patients (20 subjects). This is meant as preliminary for another ongoing study named ShockOmics (NCT02141607), which aims at elucidating early multilevel markers signatures and metabolic pathways involved, a necessary step for a target therapy.

II. Materials and Methods

A. Study population

The following demographic, clinical and laboratory variables were considered: (i) information about the patient collected at ICU admission: age (years), sex, body mass index, pathological conditions before hospitalization (presence of hepatic insufficiency, renal insufficiency, respiratory pathologies, immunocompromised state, cardiovascular pathologies); (ii) hemodynamic parameters: heart rate (bpm), mean arterial pressure (mmHg), venous central pressure (mmHg), daily urinary output (ml/die); (iii) ventilation parameters: positive end-expiratory pressure (cmH_20), FiO_2 (%); (iv) blood gas analysis: central venous O_2 saturation, venous partial pressure of CO_2, arterial partial pressure of CO_2, arterial partial pressure of O_2, central venous partial pressure of O_2, arterial and venous pH; (v) laboratory and clinical parameters: serum concentrations of creatinine (mg/dL), biliuribin (mg/dL), and lactate (mmol/L); (vi) Sequential Organ Failure Assessment Score (SOFA) [6], need of renal replacement therapy (RRT); (vii) outcome: mortality at 28 and 90 days. Details of the selected patients are reported in Table 1.

B. Plasma metabolomics analysis

Plasma samples were collected at day 1 and 7 after diagnosis of septic shock. A targeted quantitative approach using a combined direct flow injection and liquid chromatography tandem mass spectrometry assay (AbsoluteIDQ 180 kit, Biocrates, Innsbruck, Austria) was applied for the metabolomics analysis. In total, 137 metabolites were identified: 1 hexose, 21 amino acids, 14 biogenic amines, 3 acylcarnitines, 14 sphingomyelins, 84 glycerophospholipids.

C. Statistical analysis and mortality prediction model

The patients (pts) were grouped into survivors (S, 11 and 9 pts according to their 28-day and 90-day survival, respectively) and non survivors (NS, 9 and 11 pts).

The comparisons between survivors (S) and non-survivors (NS) were performed by unpaired Wilcoxon Test for clinical parameters and metabolite concentrations (μM), whereas the comparisons between day 1 and day 7 by paired Wilcoxon signed rank test. To overcome the problem of the large number of statistical comparisons, we calculated also the false discovery rate (FDR).

We used a bootstrapping technique of oversampling with

replacement to obtain a sample size of 20 patients for each group (S and NS).

TABLE I
STUDY POPULATION

Clinical variable	*DAY 1*	*DAY 7*
Heart Rate (bpm)	*103.5 ± 20.3*	85.4 ± 10.3
MAP (mmHg)	*75.7 ± 14.3*	87.3 ± 15.8
VCP (mmHg)	11.7 ± 5.1	7.9 ± 3.7
PEE (cmH2O)	*8.8 ± 2.6*	*6.6 ± 4.6*
FIO_2 (%)	*57.8 ± 15.2*	*44 ± 16.1*
$SvCO_2$ (%)	*76.3 ± 9.3*	*76 ± 6.8*
$PvCO_2$ (mmHg)	*47.3 ± 5.9*	*48.9 ± 6.2*
$PaCO_2$ (mmHg)	*43.4 ± 6.7*	*43.3 ± 6.1*
Lactate (mmol/L)	*4 ± 2.2*	*1.8 ± 1.4*
SOFA	*11.6 ± 2.7*	*6.8 ± 4*
Diuresis (ml)	*2006.2 ± 1323.7*	*2944.7 ± 1870.2*
Creatinine (mg/dL)	*2.3 ± 1.1*	*1.8 ± 1.5*
Biliuribin (mg/dL)	*3 ± 3.5*	*4.6 ± 7.6*
Arterial pH	*7.4 ± 0.1*	*7.4 ± 0.1*
PaO_2 (mmHg)	*115.3 ± 48.3*	*115 ± 44.9*
Venous pH	*7.4 ± 0.1*	*7.4 ± 0.1*
PvO2 (mmHg)	*45.1 ± 5.9*	*42.9 ± 6.3*
RRT (#pts)	*3*	*3*

Clinical and laboratory variables at day 1 and day 7 for the 20 patients. Data are presented as mean ± SD. No significant differences were found between D1 and D7.

Multivariate analysis was performed using the Elastic Net technique, a shrinkage regression method effective in case of several highly correlated variables [7]. The Elastic Net performs continuous variable selection causing some of the regression coefficients to be exactly zero, thus reducing the variance of the regression estimates by eliminating redundant predictors. Furthermore, the subset of variables corresponding to non-zero coefficients can be considered as the predictors mainly associated to the outcome. Firstly, metabolomics data and clinical parameters were normalized to have unitary variance and zero mean. Different models were built with 2, 4, 5 and 10-fold cross validation (CV) and the model with the minimum Mean Squared Error (MSE) was selected. As for the FDR, we used a bootstrapping technique of oversampling with replacement to obtain a sample size of 20 patients for each group (S and NS) by maintaining the same percentage of events. The outcome (survivors = 0, non-survivors = 1) was considered as output of the model. The best model was selected among the different CV models based on one-standard error rule.

III. RESULTS AND DISCUSSION

Our analyses showed that NS were characterized by an overall decrease from day 1 to day 7 in levels of different species of lysophosphatidylcholines (LPC) and phosphatidylcholines (PC) together with a significant increase in kynurenine (KYN), both at 28-day (Fig 1a) and 90-day (Fig 1b) (Wilcoxon test $p<0.05$, FDR<0.05).

In the multiparameter model (Fig 2), low unsaturated long-chain PC species and LPC a C24:0 were associated with long-term mortality (90 days) together with circulating KYN. Moreover, LPC a C24:0 and PC aa C32:3 were negatively correlated to the event at 28 days and 90 days in combination with clinical variables (the cardiovascular SOFA score for the 28-day mortality model, and the renal replacement therapy during the 7 day ICU staying for the 90-day mortality model).

IV. CONCLUSION

The data presented here confirm the feasibility of our approach in determining changes in circulating metabolites, which characterize the progress of septic shock condition. In line with recent findings [4], our results show that low unsaturated long-chain phosphatidylcholines and lysophosphatidylcholines species are associated with long-term survival together with circulating KYN. Moreover, these glycerophospholipids are negatively correlated to the event at 28-day and 90-day in combination with clinical variables such as cardiovascular SOFA score (28-day mortality model) or renal replacement therapy (90-day mortality model). Overall, the association of early changes in the plasma levels of both lipid species and KYN with mortality may have implications for early intervention and discovering new target therapy.

ACKNOWLEDGEMENT

The research was supported by the “ShockOmics” grant #602706 of the European Union. Part of the presented results are published in [8]

REFERENCES

[1] Russell, J. A. Management of sepsis. N Engl J Med 355, 1699–713, (2006).
[2] Angus, D. C. & van der Poll, T. Severe sepsis and septic shock. N Engl J Med 369, 840–51, (2013).
[3] Rogers, A. J. et al. Metabolomic derangements are associated with mortality in critically ill adult patients. PLoS One 9, e87538, (2014).
[4] Langley, R. J. et al. An integrated clinico-metabolomic model improves prediction of death in sepsis. Sci Transl Med 5, 195ra95, (2013).
[5] Caironi, P. et al. Albumin replacement in patients with severe sepsis or septic shock. N Engl J Med 370, 1412–21, (2014).
[6] Vincent, J. L. et al. The SOFA (Sepsis-related Organ Failure Assessment) score to describe organ dysfunction/failure. On behalf of the Working Group on Sepsis-Related Problems of the European Society of Intensive Care Medicine. Intensive Care Med 22, 707–10, (1996).
[7] Hui, Z. & Hastie, T. Regularization and variable selection via elastic net. Journal of Royal Statistical Society: Series B (Statistical Methodology) 67, 301–10, (2005).
[8] Ferrario, M, Cambiaghi A, Brubelli, L, et al., Mortality prediction in patients with severe septic shock: a pilot study using a target metabolomics approach. Sci Rep. 2016 Feb 5;6:20391.

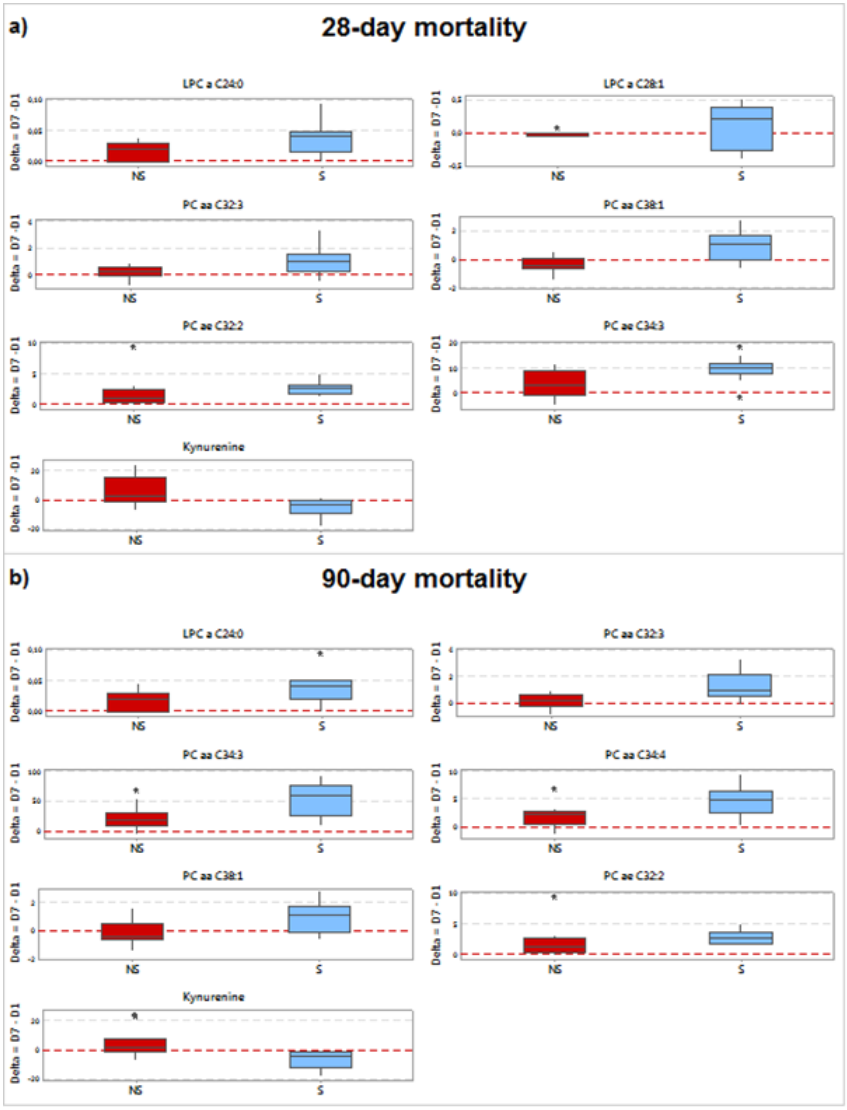

Fig. 1. Comparison of the absolute differences in metabolite concentrations (μM) from day 1 to day 7 (Delta = D7–D1) in survivors (S) and non-survivors (NS) at 28 days (a) or 90 days (b). Distribution of differences is shown as box-plots, where the central mark is the median concentration, the edges of the box are the 25th and 75th percentiles.

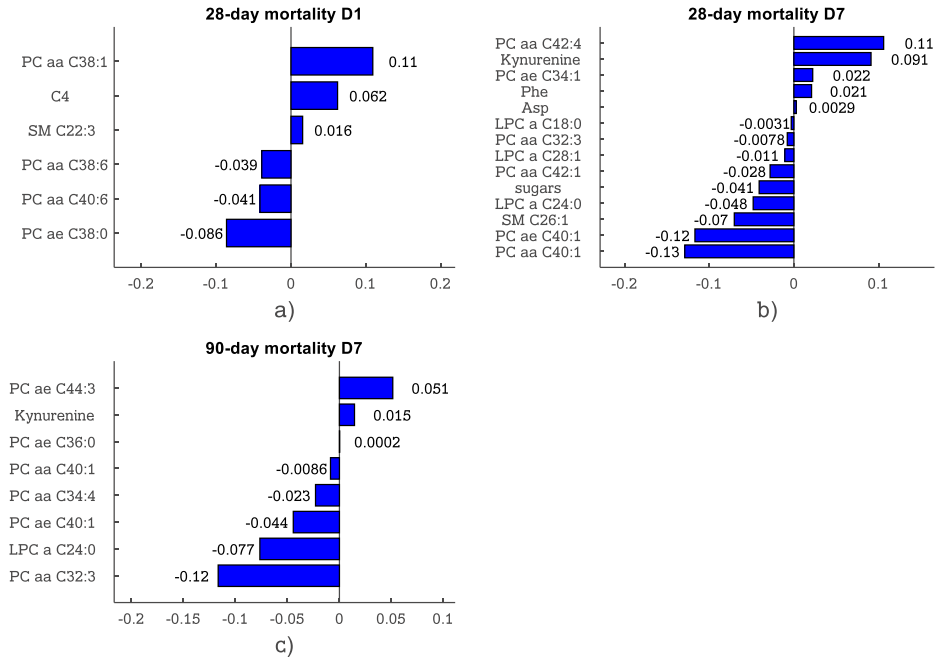

Fig. 2. Elastic Net coefficients built on metabolites concentration at day 1 (a) and day 7 (b) for 28-day and 90-day (c) mortality prediction model.

Multiscale modelling of mortality risk in a septic shock population

M. Carrara[1], G. Baselli[1], and M. Ferrario[1]
[1] *Dipartimento di Elettronica, Informazione e Bioingegneria (DEIB), Politecnico di Milano*

***Abstract*— Septic shock patients were selected from the public database MIMIC-II and were used to explore the critical issue of mortality stratification in intensive care. For each patient different types of variables were extracted of the first 48 hours after the onset of the shock, as hemodynamic data, laboratory and clinical information and they were used to build a multivariate prediction model of 7-day mortality. With this contribution, we want to underline the importance of a multilevel data integration approach and its possible usefulness in critical care contexts.**

***Keywords*—shock, mortality, multiscale, prediction .**

I. Introduction

Mortality related to sepsis and septic shock in intensive care is still one of the highest worldwide and clinicians are constantly pointing attention to new possible therapies and clinical guidelines to improve the available treatments [1]. Important medical societies also dedicate great attention to the topic, as recently demonstrated by the "Third International Consensus Definitions for Sepsis and Septic Shock (Sepsis-3)" convened by the Society of Critical Care Medicine and the European Society of Intensive Care Medicine [2].

The complex and heterogeneous nature of sepsis together with the wide inter-subject difference in the response to infection has given birth in the recent years to new approaches based on multiscale and multilevel data integration. The so called "personalized medicine" [3] is in line with the new definitions by Sepsis-3 Consensus which states that "septic shock should be defined as a subset of sepsis in which particularly profound circulatory, cellular, and metabolic abnormalities are associated with a greater risk of mortality than with sepsis alone", and calls for new methods for data integration.

In this work, we analysed values and trends of different types of data routinely collected in Intensive Care Unit (ICU) to predict mortality in the following 7 days; the aim is to highlight the potential of this approach and to assess its benefit in septic shock patients stratification and in timely delivery of care.

II. Materials and Methods

A. Patients and Data

A total of 73 adult septic shock patients at their first hospital and ICU admission were selected from the public database MIMIC-II; septic shock was defined according to the criteria proposed by Angus et al [4] (i.e. presence of both ICD-9 codes for fungal or bacterial infection and acute organ dysfunction).

For each patient the following ICU data were considered:

- Hemodynamic data: systolic, diastolic and mean arterial blood pressure (SBP, DBP, MAP, mmHg), heart rate (HR, bpm), respiratory rate (RR, breath per minute), central venous pressure (CVP, mmHg), cardiac output (CO, L/min).
- Clinical and laboratory data: temperature (T, °C), arterial pH (units), creatinine (mg/dL), blood glucose (mg/dL), lactate (mmol/L), haematocrit (%), white blood cell count (WBC, cells/cmm), oxygen saturation SpO2 (%).
- Amounts of fluids administered: total intake including all intravenous infusion given to the patient (mL).

Missing data (7.03%) were replaced by mean imputation.

B. Univariate and Multivariate Analyses

Septic shock onset was firstly identified following the criteria proposed in [5].

Data of the first 48 hours after the onset were extracted and for each series statistical and trend indices were computed: mean, standard deviation, minimum and maximum values, median, kurtosis, skewness, the regression slope of the series and the delta between the start and the end of the series.

The patients were dived into survivors (S, n=53) and non survivors (NS, n=20) based on their mortality within 7 days.

Univariate statistic was applied to compare the two groups, using the Wilcoxon Rank-Sum Test and False Discovery Rate (FDR) correction to take into account the multiple comparisons. A p-value < 0.05 was adopted for significance.

A prediction model of 7-day mortality was developed from all the features. We used a linear regression model with a variable selection method named Elastic Net [6]. Also, the Variance Inflation Factor (VIF) was computed and constrained to be lower than 5 to avoid multicollinearity.

The performance of the model was evaluated by means of the Area Under the Curve (AUC) assessed by building a linear regression model with the features selected by the Elastic Net and tested by a 5-folds cross-validation.

Finally, the performance of the model was compared with scores currently available in clinical practice for mortality risk assessment, i.e. the Sequential Organ Failure Assessment, SOFA, and the Simplified Acute Physiology Score, SAPS-I.

III. Results

Figure 1 shows an example of vital signs time series and shock onset detected by the algorithm.

Univariate analysis reported 43 features, which significantly distinguish between the two groups. The most relevant results are that NS have higher HR, increased RR and Lactate, greater CVP, lower arterial blood pressure,

reduced blood pH and oxygenation with respect to S (see Table I).

The NS group showed negative values of regression slope and delta for arterial pressure, pH and SpO2 whereas S group showed opposite sign (results are not reported here).

Table II reports the values of the coefficients and VIF of the features selected from the Elastic Net regression model. The Mean Squared Error of the model is 0.11.

The AUC values computed for the indices and our model are the following: SOFA score 0.74 ± 0.17, SAPS I 0.95 ± 0.04, and proposed model 0.97 ± 0.03.

TABLE I
MEDIAN (25°,75°) VALUES OF INDICES SIGNIFICANTLY DIFFERENT BETWEEN THE GROUPS

	Survivors	*Non Survivors*	*p-value*
Mean HR	103.1 (93.6,110.4)	115 (104,124)	< 0.01
Mean RR	22.8 (19,25.6)	24.9 (23.3,27.2)	0.025
Mean Lactate	3.2 (1.7,5.1)	6.7 (3.8,12.7)	< 0.01
Mean CVP	14.3 (12.1,18.5)	17.3 (16.3,19.9)	0.012
Mean SBP	98.3 (94.4,106.9)	88.3 (79.6,98.9)	< 0.01
Mean DBP	59 (50.7,63.3)	53.5 (48,55.5)	0.013
Mean MAP	73.9 (68.6,77.9)	65.3 (62.8,69.5)	< 0.01
Mean pH	7.35 (7.3,7.41)	7.28 (7.22,7.3)	< 0.01
Mean SpO2	97 (95.5,98.3)	94.7 (92.5,96.6)	< 0.01

TABLE II
COEFFICIENT AND VIF VALUES OF ELASTIC NET REGRESSION

	Coefficients	*VIF*
*Delta SpO2 (%) **	- 0.0323	1.6
*Slope SBP (mmHg/h) **	- 0.0191	1.52
*Delta ph (units) **	- 0.0154	1.63
*Max pH (units) **	- 0.0114	1.48
*Delta DBP (mmHg/h) **	- 0.0047	1.91
*Mean HR (bpm) **	0.0012	1.32
Skewness Creatinine	0.033	1.13
*Std WBC (cells/cmm) **	0.0443	1.38
*Std T (°C) **	0.0827	2.03
*Min Lactate (mmol/L) **	0.1431	1.93

*parameters significant also in the univariate analysis

IV. DISCUSSION AND CONCLUSION

In this study a preliminary analysis on a small unspecific subset of septic shock patients was carried out resulting in a multivariate model able to predict mortality within 7 days with a good performance, using data collected in the first 48 hours after the onset of the shock.

As expected, we found common clinical signs which characterize septic patient at high risk of mortality: NS have significant higher HR, RR and T, typical symptoms of systemic inflammatory response syndrome (SIRS) which, combined to persistent hypotension despite fluid delivery, is known to lead to multiple organ dysfunction and death.

Lactate was found to be crucial both in univariate analysis (p-value < 0.01) and in the multivariate model, where it assumes the largest coefficient as absolute value, supporting the general knowledge of hyperlactatemia being a symptom of poor outcome in intensive care [7].

Of interest CVP turned up to be positively associated with higher risk of death. Current clinical guidelines consider it to be a good marker of fluid resuscitation, based on the idea that CVP reflects intravascular volume. However, recent works published results underlining a poor relation between CVP values and blood volume and a limited ability of CVP to predict fluid responsiveness [8]. Our result show high CVP as not beneficial for a better outcome similarly to the findings of Legrand et al. [9]: a higher mean CVP in the first 24 hours from admission is associated to an increasing risk of new or persistent acute kidney injury (AKI) in septic patients.

The analyses of trends reveal that information related to time evolution (e.g. slope and delta) and time distribution (e.g. skewness and kurtosis) of the variables should be included in addition to absolute values since they add information on pattern evolution or pattern changes.

Finally, the proposed model provided the highest value of AUC with respect to the traditional scores, supporting our approach.

It's noticeable to observe that not all the variables included in the regression model were also significant in the univariate analysis (e.g. skewness of Creatinine values). Indeed, sepsis and septic shock arise from a very complex and still unclear interdependence among different physiological systems, encompassing phenomena taking place at different scales which is at the basis of the big heterogeneity of the disease. These observations emphasize the need for innovative, ground breaking multiscale models of disease, which drive a global understanding of the patient status and could improve precision and promptness of therapies [10].

ACKNOWLEDGEMENT

This research is supported by EU FP7 Health Programme (HEALTH.2013.2.4.2-1) #602706. Part of the presented results are published in [11].

REFERENCES

[1] K.E Henry. et al, "A targeted real-time early warning score (TREWScore for septic shock", Sci. Transl. Med., Vol 7, Issue 299ra122, 2015.

[2] M. Singer et al., "The Third International Consensus Definitions for Sepsis and Septic Shock (Sepsis-3)", JAMA, 315(8):801-810, 2016.

[3] H.R. Wong, "Personalized medicine, endotypes, and intensive care medicine", Intensive Care Med., vol. 41, no. 6, pp. 1138-1140, 2015.

[4] D. C. Angus et al., "Epidemiology of severe sepsis in the United States: analysis of incidence, outcome and associated costs of care", in Crit. Care Med., vol. 29, no. 7, pp. 1303-1310, 2001.

[5] D. Shavdia, "Septic Shock: Providing Early Warnings Through Multivariate Logistic Regression Models," 2007.

[6] H. Zou and T. Hastie, "Regularization and variable selection via the elastic net," J. of the Royal Stat. Soc.Series B: Statistical Methodology, vol. 67, no. 2, pp. 301–320, 2005.

[7] H.B. Nguyen et al., "Early lactate clearance is associated with improved outcome in severe sepsis and septic shock" Crit. Care Med., vol. 32, no. 8, pp. 1637–1642, 2004.

[8] P.E. Marik et al., "Does central venous pressure predict fluid responsiveness? A systematic review of the literature and the tale of seven mares" Chest, vol. 134, no.1, pp. 172–178, 2008.

[9] M. Legrand et al., "Association between systemic hemodynamics and septic acute kidney injury in critically ill patients: a retrospective observational study," Critical Care, vol. 17, article R278, 2013.

[10] F. Aletti et al., "ShockOmics: multiscale approach to the identification of molecular biomarkers in acute heart failure induced by shock", Scandinavian Journal of Trauma, Resuscitation and Emergency Medicine, 24:9, 2016.

[11] M. Carrara, G. Baselli, M. Ferrario, "Mortality Prediction Model of Septic Shock Patients Based on Routinely Recorded Data," Computational and Mathematical Methods in Medicine, vol. 2015, Article ID 761435, 7 pages, 2015.

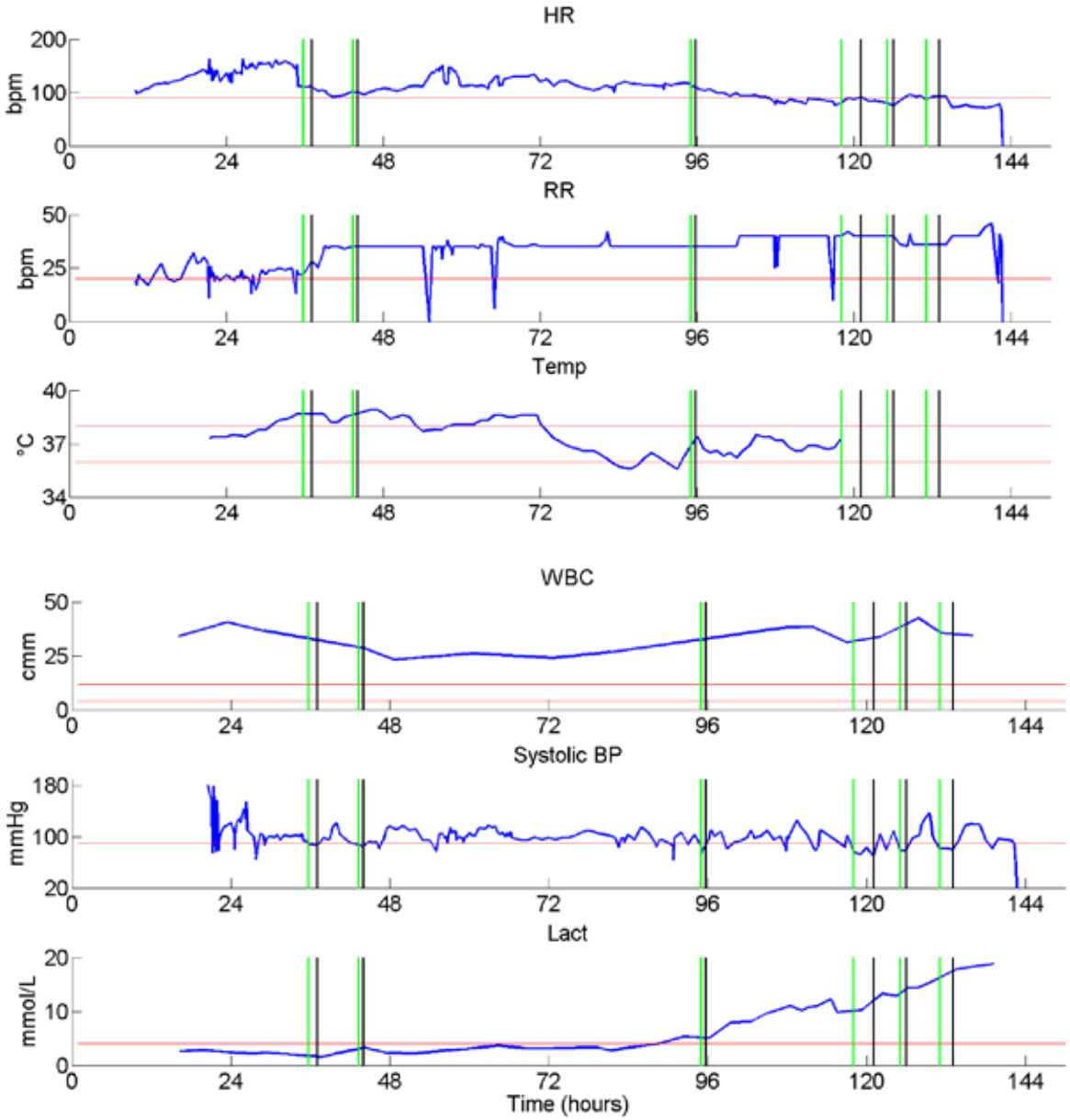

Fig. 1. Example of parameters series from one patient (ID 6471). Green and black lines mark the start and the end of a shock episodes, respectively. The red lines indicate the threshold value for abnormality according to the SIRS criteria. After 6 days in ICU the patient dies. Notice that the values of lactate monotonically increase hinting organ dysfunction, hypoperfusion, and tissue injury. The values for WBC are maintained clearly over the threshold during the entire ICU staying, sign of a systemic inflammatory response. Observing the trend for the RR series, it is clearly visible that there is a sharp increase of the values till a plateau, synchronous with the shock onset.The patient receives about 1200mL of fluids but he shows a persistent hypotension despite fluid resuscitation

Effective interhemispheric connectivity and corticospinal tract integrity interdependency after unilateral stroke

S. Caschera[1,2], F. Pichiorri[1], M. Petti[1,2], F. Cincotti[1,2], L. Astolfi[1,2] and D. Mattia[1]
[1] *IRCSS Fondazione Santa Lucia, Rome, Italy*
[2] *Dept. of Computer, Control and Management Engineering, 'Sapienza' University of Rome, Italy*

***Abstract*— The aim of this study is to explore whether the EEG-derived sensorimotor interhemispheric connectivity (nIHS) at rest can vary in relation to the corticospinal tract integrity and excitability in subacute stroke patients. Thirty unilateral first ever stroke patients participated in the study. High Density EEG was recorded during 5 minutes of resting state with eyes closed. Effective connectivity was computed by means of Partial Directed Coherence (PDC). Patients with disrupted corticospinal tract showed a reduction of nIHS specific to the sensorimotor scalp electrodes. Our results of EEG-derived connectivity could reflect the functional reorganization in motor IHC related to corticospinal tract damage.**

***Keywords*—Electroencephalography/EEG, Partial Directed Coherence, Stroke, Corticospinal tract/CST.**

I. Introduction

In the healthy adult brain, activation of the primary motor cortex (M1) region contralateral to the motor task inhibits the homologous region of the opposite hemisphere. This process is known as interhemispheric inhibition [1]. Such motor interhemispheric balance is altered in unilateral brain lesions such as stroke [2]. Recent studies using functional magnetic resonance imaging (fMRI) have shown that altered interhemispheric connectivity (IHC) in resting state is associated with lesions of the corticospinal tract (CST) [3]. Motor impairment reflects the dual contribution of corticospinal damage and altered network functional connectivity. The recognition and understanding of the complex relationship between functional and structural impairments in the pathological brain may have important implications for neurorehabilitation. The use of Electroencephalography, with respect to fMRI, provides several advantages: EEG is an inexpensive and portable device that enhances ecological validity without sacrificing experimental control. Because of its unique temporal resolution, EEG constitutes one of the most eligible techniques for stroke rehabilitative interventions. Furthermore, strategies to restore the regular interhemispheric balance between the lesioned and healthy hemispheres is at the foundation for a number of neurorehabilitation training approaches [4].This study has the aim to quantify functional changes in motor IHC related to corticospinal tract damage by applying advanced signal processing techniques for EEG-derived connectivity.

II. Materials and Methods

A. Participants

Thirty subacute patients (mean age: 64 ± 9 years; time course after lesion: 2 ± 1 months) with first-ever unilateral stroke were recruited. All patients were assessed for clinical stroke severity. Stroke-related neurologic disability was evaluated using the *European Stroke Scale* (ESS) and the *Fugl-Meyer Assessment* (FMA). For each patient, corticospinal integrity was studied by means of single pulse Transcranial Magnetic Stimulation (TMS); Motor Evoked Potentials (MEPs) were recorded from the affected First Dorsal Interosseus muscle to determine their presence or absence (at maximum stimulator output). Ten patients had preserved corticospinal integrity (presence of MEP on affected side). No statistical difference was found in terms of age, time after stroke and lesioned hemisphere between patients without MEP on affected side and patients with MEP. The research was approved by a human experimentation ethics committee. After receiving information about the aims of the study, all participants gave informed consent before participation.

TABLE I
PATIENTS CHARACTERISTICS

	CST integrity preserved (n = 10)	*CST integrity disrupted (n = 20)*
Age (years)	63 ± 10	66 ± 8
Months after stroke	1.9 ± 1	1.8 ± 1.5
Lesioned hemisphere	6 Right / 4 Left	10 Right / 10 Left
ESS	83.6 ± 7.1	60.4 ± 9.2
FMA	50 ± 10	15 ± 12

Data are presented as means ± SD.

B. HD-EEG analysis

High Density EEG (HD-EEG) signals were recorded during 5 minutes of eyes-closed resting state from 61 scalp positions. During measurements, the impedance of all electrodes was kept below 5KΩ. EEG data were pre-processed (1-45 Hz filtering, down-sampling at 100 Hz, artifact rejection and 1s-ephocs segmentation).

To allow a statistical group analysis across all participants, EEG signals were flipped in the Left / Right direction in order to ensure that the lesioned hemisphere was on the left

side for all subjects.

C. Connectivity analysis

Effective connectivity provides insights about the communication between different brain regions that goes beyond the simple mapping of their activity. Brain connectivity patterns were computed my means of Partial Directed Coherence (PDC) [5]. Based on Granger causality [6], PDC reveals the existence, the direction and the strength of a functional relationship between the activities in different sites of the brain, starting from EEG data. Such estimator is based on the use of Multivariate Autoregressive (MVAR) models and is defined both in time and frequency domain. Frequency bands of interest were Theta (IAF-6; IAF-3), Alpha (IAF-2; IAF+2), lower Beta (IAF+3; IAF+11), upper Beta (IAF+12; IAF+20) and Gamma (IAF+21; IAF+35) whose band limits were defined according to Individual Alpha Frequency (IAF) [7].

D. Graph theoretical analysis

To extract quantifiable indices to be subjected to a statistical analysis, the neuronal connectivity patterns were analysed by means of a theoretical graph approach. Indeed salient networks properties can be described by quantifiable indices like those derived from classical graph theory (e.g. measures of integration, measure of centrality, network motifs) [8]. A new index was defined ad hoc in order to underline the distinctive topographic property of alteration of the communication between hemispheres. The new synthetic index, called *normalized Inter-Hemispheric Strength* (nIHS), was defined as the fraction of the sum of weights w_i of inter-hemispheric links to the total weight w_{TOT} of the network:

$$nIHS = \frac{\sum_{i=1}^{N_{IHC}} w_i}{w_{TOT}} \quad (1)$$

with:

$$w_{TOT} = \sum_{i=1}^{N} w_i \quad (2)$$

For every subject and every frequency band, nIHS was computed and extracted from the connectivity patterns involving the whole scalp and for those focused in three different subareas (12 electrodes each): a central zone (corresponding to motor and premotor cortices) and occipital and frontal zones, used as control areas.

E. Statistical analysis

A statistical analysis was performed (unpaired two-tailed Welch t-tests; significance level was set at $p < 0.05$) to identify differences between patients' subgroups in the nIHS computed for the entire scalp and for each specific area. False Discovery Rate correction for multiple comparisons was applied to avoid the occurrence of type I errors. A Pearson correlation analysis was performed between the nIHS index and both the ESS and FMA clinical indices.

III. Results

The nIHS index obtained for whole scalp connectivity patterns showed a statistically significant higher mean ($p = 0.004$) in Beta bands in patients with preserved corticospinal integrity with respect to the group with disrupted corticospinal tract. A statistically significant difference ($p = 0.01$) was observed between the two subgroups in the motor area in lower Beta band (figure 1). Positive correlations were obtained both between nIHS computed in the central zone with ESS index ($R = 0.4$, $p = 0.02$) and with FMA index ($R = 0.4$, $p = 0.02$). No between group differences were noted in nIHS computed for occipital and frontal areas.

IV. Conclusion

Coherently with previous neuroimaging findings [2], we found a reduction of interhemispheric connectivity specific to the sensorimotor scalp electrodes in patients with disrupted corticospinal tract in the Beta band. This spectral band is peculiarly related to motor tasks. The specifically computed index showed correlations with both clinical scales utilized. This study shows how the estimation of EEG-based connectivity and the extraction of related indices can contribute to our understanding of the functional modifications in the brain after stroke damage. Further studies based on the described approach and the evaluation of the implemented neurophysiological index during different rehabilitation interventions in stroke patients could increase our understanding of stroke recovery process and eventually suggest new, neurophysiologically driven and patient-tailored interventions.

Acknowledgement

Research partially supported by the University of Rome Sapienza "Progetti di Ateneo per la Ricerca Scientifica anno 2014".

References

[1] M. A. Perez and L. G. Cohen, "Interhemispheric inhibition between primary motor cortices: what have we learned?", *The Journal of Physiology*, 2009, pp.725-726.

[2] B. A. Radlinska, Y. Blunk, I. R. Leppert, J. Minuk, G. B. Pike et al., "Changes in callosal motor fiber integrity after subcortical stroke on the pyramidal tracy)," in *Journal of Cerebral Blood Flow & Metabolism*, 2012, pp. 1515–1524.

[3] A. R. Carter, K. R. Patel, S. V. Astafiev, A. Z. Snyder, J. Rengachary et al., "Upstream Dysfunction of Somatomotor Functional Connectivity after Corticospinal Damage in Stroke" in Neurorehabil Neural Repair, 2012

[4] F. Pichiorri, G. Morone, M. Petti, J.Toppi, I. Pisotta et al., "Brain-Computer Interface Boosts Motor Imagery Practice during Stroke Recovery", in *Annals of Neurology*, 2015, pp. 851:865

[5] L. Baccalà and K. Sameshima, "Partial directed coherence: a new concept in neural structure determination", *Biological Cybernetics*, 2001, pp. 463-474

[6] C. W. Granger, "Investigating causal relations by econometric models and cross-spectral methods", *Econometrica*, Vol. 37, 1969, pp. 424-438

[7] M. Doppelmayr, W. Klimesh, T. Pachinger and B. Ripper, "Individual differences in brain dynamics: important implications for the calculation of event-related band power", *Biological Cybernetics*, 1998, pp. 49-57

[8] M. Rubinov and O. Sporns, "Complex network measures of brain connectivity: Uses and interpretations", *NeuroImage*, 2010, pp. 1059-1069

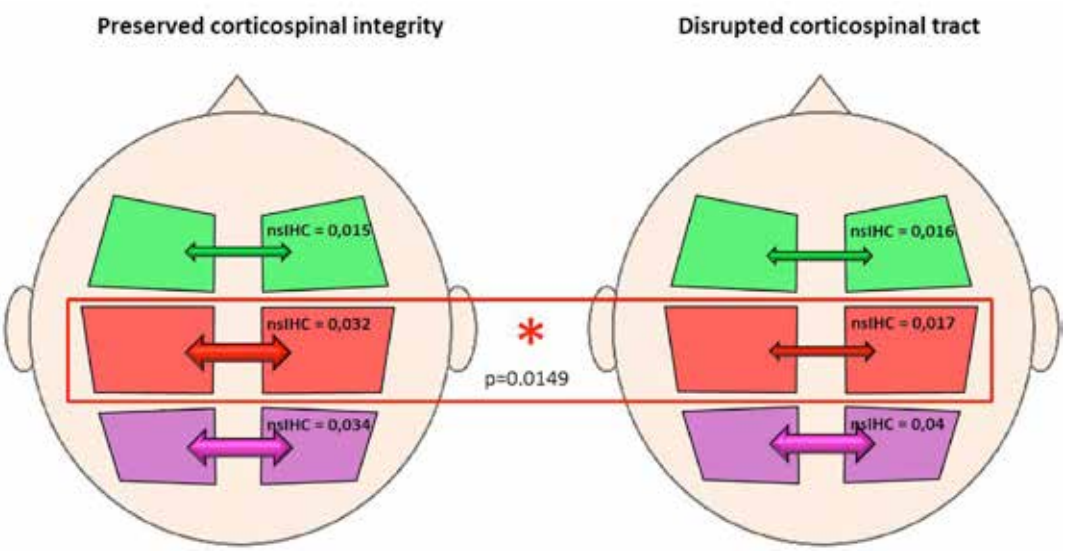

Fig. 1. Results of t-tests for nIHS index between patients with preserved corticospinal integrity (left) and patients with disrupted corticospinal tract (right) for lower Beta band. Green areas identify frontal zone, Red areas identify central zone and Violet areas identify occipital zone. * Statistically significant result ($p < 0.05$).

Software-based enhancement of microfluidic impedance cytometry

F. Caselli, P. Bisegna
Department of Civil Engineering and Computer Science, University of Rome Tor Vergata

***Abstract* — This work reports on recent advances in the field of microfluidic impedance cytometry, which is a promising label-free approach for single-cell analysis and discrimination. In particular, original software-based strategies that improve the discrimination capabilities of the widely used parallel facing electrode design are presented.**

***Keywords* — single-cell analysis, impedance, microfluidics, signal processing.**

I. Introduction

The schematic and the working principle of a typical impedance cytometer are illustrated in Fig. 1(a) [1]. Two pairs of facing microelectrodes are integrated into the wall of a fluid-filled microchannel (parallel electrode design). An AC excitation signal is applied to the top electrodes, and the differential current flowing through the bottom electrodes is measured by means of a differential amplifier. When a cell passes through the electrode region, a variation of the differential signal is recorded, which exhibits a typical odd-symmetric pattern [2]. In fact, when the cell passes position A, it begins to pose a hindrance to the current collected at the left bottom electrode. Such a hindrance is maximal when the cell is aligned with the center of the left electrode pair (position B), where the signal peak amplitude is recorded. The signal then progressively decreases and reaches zero when the cell is in the middle of the sensing region (position C), which corresponds to a symmetric configuration. Past position C, a specular and reversed profile is recorded.

Multifrequency impedance measurements in the radio-frequency range can give multiparametric, high-content data that can be used to distinguish cell populations [3]. Low frequency (< 500 kHz) impedance is used to size particles because at these frequencies (and in high conductivity buffer) the particle volume is related to the real part of the complex impedance signal, in a similar manner to a Coulter volume measurement. At intermediate frequencies (around 1 MHz), the signal conveys information about membrane capacitance, and at high frequencies (above some MHz) measurements give information about cytoplasm conductivity and permittivity.

Recently, microfluidic impedance cytometers have been successfully applied to analyze micro-organisms [4], erythrocytes [5], leukocytes [6], platelets [7], and animal and human cell lines [8]. However, impedance cytometry has not yet reached full maturity, and sensitivity, specificity and throughput still need to be improved. In this regard, effort has focused on devising novel designs of microdevice and developing new detection techniques, but there has been little attempt at developing ways of extracting meaningful data from measured signals using signal processing [2]. The latter issue represents the subject of this work.

II. Materials and Methods

A. Event-detection algorithm

The first step in impedance cytometry data processing is the event-detection, which is the identification of a cell passing through the sensing region of the device (Fig. 1(b)). This step provides the total cell count and is critical to the further steps of feature extraction and classification. A reliable event-detection strategy is especially important in case that rare cells (e.g., circulating tumor cells) or small particles (e.g., platelets) have to be detected.

In this work a simple and robust event-detection algorithm is presented [9], which fruitfully exploits the odd-symmetric nature of the measured differential signal. The algorithm acts in two steps: a preliminary segmentation is followed by an event-quality check. The segmentation is based on the correlation of the data stream with the simplest odd-symmetric template, which emphasizes the odd-symmetric structures present in the data stream; the quality of a detected event is then established by evaluating its E_2O index, that is, a measure of the ratio between the magnitudes of its even and odd parts. If such an index is too high, the event is rejected (Fig. 1(c)). Few parameters are involved in the algorithm, whose setting is non-critical, and a preliminary denoising step is not required. Implementation is quite simple and computational complexity limited.

The performance of the algorithm is evaluated on the basis of the fraction of false positives and missed events. In particular, sensitivity and positive predictive value (PPV) are taken as metrics. In order to achieve an objective and reproducible performance analysis, effort has been devoted to build reference datasets of synthetic impedance cytometry data, which reproduce with high fidelity experimentally measured data. Very good overall performances are achieved (94.9% sensitivity and 98.5% PPV). The algorithm has also been tested on experimentally measured data, showing the efficacy and soundness of the approach.

B. Feature extraction

The processing step following event detection is the extraction of features suitable for cell classification. In particular, the peak amplitude is usually extracted from the experimental event traces and is used to determine the dielectric properties of the particle at the relevant frequency. However, for the widely used parallel electrode geometry (Fig. 1(a)), the measured impedance signal also depends on the position of the particle between the electrodes, i.e. the

trajectory of the particle as it flows through the channel. This is because the electric field in the channel is not uniform and the particle can influence the current in the reference arm of the sensor [10]. This manifests itself as an error in the measured "volume" of the particle for off-centre particles (i.e. close to the top or bottom electrodes).

To obtain high quality (low CV) data, nearly all cytometers use some form of particle focusing [11]. Typically, hydrodynamic focusing is adopted, which has been introduced in 1968 for the Coulter counter, and then developed in several modalities, like sheath flow or inertial focusing. Hydrodynamic focusing is a passive technique, depending entirely on the channel geometry or intrinsic hydrodynamic forces. However, sheath flow increases the complexity of the layout and control for microfluidic devices and consumes additional fluid, while inertial focusing requires high flow-rates that may induce stress in the cell, and restricts simultaneous measurement of heterogeneous populations (RBCs had to be sphered prior to measurement). Alternatively, active focusing systems like dielectrophoresis (DEP) or acustophoresis can be applied, which rely on an external force field and generally have limited throughput, because particles must be exposed to the outer force field for sufficient duration to achieve effective functionality. Other approaches have been also presented in the literature, like dielectric focusing, optimized electrode layout, and DEP-inertial microfluidics. In all systems, particle position depends on particle properties, hence it can be difficult to optimize them for heterogeneous samples.

In this work, an original approach to compensate via signal-processing for the variation in signal caused by the random position of a particle is described [12]. In particular, the transit times of particles through the device using two simultaneous current measurements, a transverse current and an oblique current, are recorded. Their ratio gives a new metric that can be used to estimate the vertical position of the particle trajectory through the microchannel. This parameter can be effectively used to compensate for the height-dependent variation of impedance due to non-uniform electric field in the channel. The new technique is developed and validated using numerical modelling. Then, it is applied to experimental impedance data relevant to a mixture of 5, 6 and 7 μm polystyrene beads. As a result, the height-dependent variation of impedance is completely eliminated, i.e. all particles of a given size show the same corrected impedance, irrespective of trajectory through the channel. The method gives a Coefficient of Variation in (electrical) radius of particles of 1% for a sheath less configuration.

III. Conclusion

Digital signal processing can greatly enhance the quality and information content of impedance measurement, thus fostering the role of impedance cytometry in single-cell analysis. Effective strategies for event-detection and off-centering compensation have been here presented, suited to the parallel electrode design. Perspectives include the extension to co-planar electrode designs (e.g., [4]) and the development of signal processing strategies for the treatment of coincidences (i.e., two cell simultaneously present in the sensing region). Real-time GPU implementations will also be pursued.

Acknowledgement

This work was supported by the Scientific Independence of Young Researchers Programme (SIR 2014) under Grant RBSI14TX20 - "Multidimensional Single-Cell Microfluidic Impedance Cytometry."

References

[1] S. Gawad, K. Cheung, U. Seger, A. Bertsch and P. Renaud, "Dielectric spectroscopy in a micromachined flow cytometer: theoretical and practical considerations," *Lab Chip*, vol. 4, pp. 241–251, 2004.

[2] T. Sun, C. V. Berkel, N. G. Green and H. Morgan, "Digital signal processing methods for impedance microfluidic cytometry," *Microfluid. Nanofluid.*, vol. 6, pp. 179–187, 2009.

[3] K. C. Cheung, M. Di Berardino, G. Schade-Kampmann, M. Hebeisen, A. Pierzchalski, J. Bocsi, A. Mittag and A. Tarnok, "Microfluidic impedance-based flow cytometry," *Cytometry, Part A*, vol. 77A, pp. 648–666, 2010.

[4] M. Shaker, L. Colella, F. Caselli, P. Bisegna, P. Renaud, "Impedance-based flow micro-cytometer for single cell morphology discrimination," *Lab Chip*, vol. 14, pp. 2548–55, 2014.

[5] C. Küttel, E. Nascimento, N. Demierre, T. Silva, T. Braschler, P. Renaud and A. G. Oliva, "Label-free detection of babesia bovis infected red blood cells using impedance spectroscopy on a microfabricated flow cytometer,"*Acta. Trop.*, vol. 102, pp. 63–8, 2007.

[6] D. Holmes, D. Pettigrew, C. H. Reccius, J. D. Gwyer, C. van Berkel, J. Holloway, D. E. Davies and H. Morgan, "Leukocyte analysis and differentiation using high speed microfluidic single cell impedance cytometry," *Lab Chip*, vol. 9, pp. 2881–2889, 2009.

[7] M. Evander, A. J. Ricco, J. Morser, G. T. A. Kovacs, L. L. K. Leung and L. Giovangrandi, "Microfluidic impedance cytometer for platelet analysis," *Lab Chip*, vol. 13, pp. 722–9, 2013.

[8] J. L. Hong, K. C. Lan and L. S. Jang, "Electrical characteristics analysis of various cancer cells using a microfluidic device based on single-cell impedance measurement," *Sens. Act. B Chem.*, vol. 173, pp. 927–34, 2012.

[9] F. Caselli and P. Bisegna, "A simple and robust event-detection algorithm for single-cell impedance cytometry," *IEEE Trans Biomed Eng*, vol. 63, pp. 415–422, 2016.

[10] D. Spencer and H. Morgan, "Positional dependence of particles in microfludic impedance cytometry," *Lab Chip*, vol. 11, pp. 1234–39, 2011.

[11] D. Spencer, G. Elliott and H. Morgan, "A sheath-less combined optical and impedance micro-cytometer," *Lab Chip*, vol. 14, pp. 3064–3073, 2014.

[12] D. Spencer[§], F. Caselli[§], P. Bisegna, and H. Morgan, *submitted paper* (§ equal contribution).

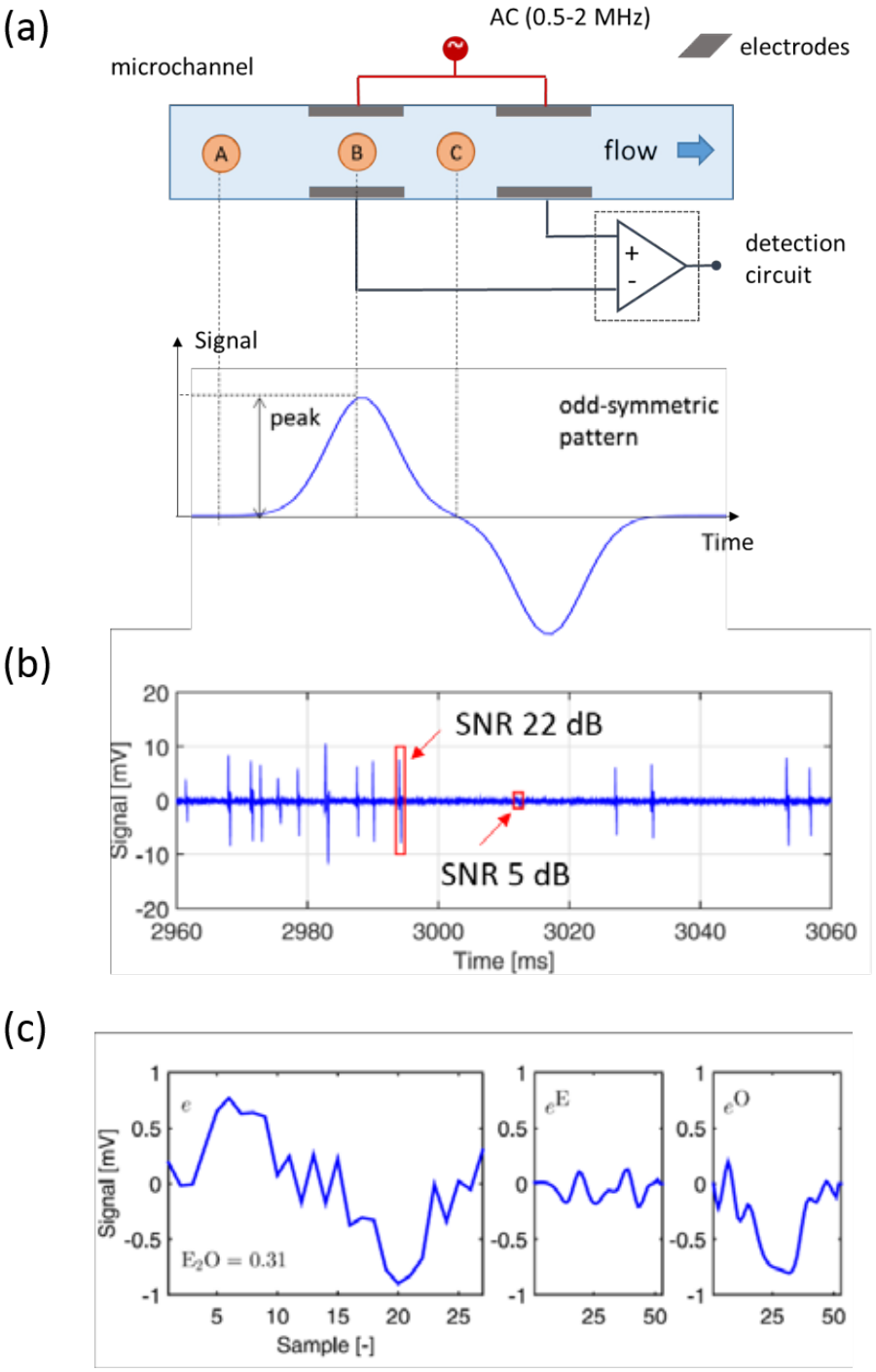

Fig. 1. (a) Schematic diagram of a single-cell impedance analysis system. The device consists of two sets of parallel facing electrodes fabricated inside a microfluidic channel. AC excitation signals are applied to the top pair of electrodes, and the difference in electrical current flowing through the bottom two electrodes is measured using a differential amplifier. The differential impedance signal exhibits an odd-symmetric profile. Cells suspended in an electrolyte flow through the microchannel one at a time, so that the circuitry can determine the ac electrical properties of single cells. (b) Impedance cytometry data at 0.5 MHz, real part shown. Two events with different signal-to-noise ratio (SNR) are highlighted with a box. (c) Measured event e (SNR = 6 dB) along with its even and odd parts, e^{E} and e^{O}, respectively, upsampled at a rate R = 4. The relevant E2O index is sufficiently small (E_2O = 0.31), testifying the odd-symmetric pattern.

Concentric-ring electrodes reduce crosstalk in surface EMG

E. Colamarino[1,2], E. Merlo[3], G. Boccia[4,5], J. Toppi[1,2], D. Mattia[2], F. Cincotti[1,2]
[1] *Department of Computer, Control, and Management Engineering Antonio Ruberti, Sapienza University of Rome, Italy*
[2] *Neuroelectrical Imaging and BCI Lab, Fondazione Santa Lucia IRCCS, Rome, Italy*
[3] *OT Bioelettronica s.n.c., Turin, Italy*
[4] *Motor Science Research Center, Department of Medical Sciences, University of Turin, Italy*
[5] *CeRiSM, "Sport, Mountain, and Health", University of Verona, Italy*

***Abstract*—Signals generated from muscles other than the muscle of interest can confound the interpretation of surface electromyograms (crosstalk). The work aims to compare bipolar and concentric-ring electrodes about crosstalk. Surface myoelectric signals were detected from the skin surface above the tibialis anterior, gastrocnemius lateralis, gastrocnemius medialis, soleus and peroneus tertius muscles during voluntary submaximal isometric contractions (dorsiflexion and plantar flexion of ankle joint) in 11 healthy subjects. The average rectified value (ARV) index is computed for each pair muscle-contraction. The ratio of the signal ARV index calculated over the non-active muscle to the active muscle during the contraction estimates the crosstalk index. The corresponding crosstalk indices are evaluated also on components extracted from signals, using an algorithm based on independent component analysis. The Wilcoxon statistical tests between crosstalk indices estimated in bipolar and concentric-ring recordings lead to the conclusion that (a) the latest are significantly less sensitive to the crosstalk phenomenon than bipolar electrodes, (b) the algorithm chosen reduces crosstalk only for bipolar recordings.**

***Keywords*—Crosstalk, Bipolar electrode, Concentric-ring electrode, Surface electromyography.**

I. Introduction

CROSSTALK is one of the main drawback in surface electromyography [1]-[3]. It is defined as the signal detected over a non-active muscle and generated by other nearby muscle [1], [4]. This phenomenon confounds the interpretation of muscular signals: in the gait analysis [4] it can mislead the identification of the activation timing and force magnitude of the muscle of interest [5].

No methods are available to completely eliminate crosstalk [6]. Still, the appropriate choice of a suitable detection system [1] and the use of blind signal separation (BSS) algorithms [7] can reduce it.

Bipolar electrodes are the most common sensors. The configuration with electrodes along the muscular fibre direction shows better longitudinal and poorer transversal spatial selectivity than configuration with electrodes transversally placed to the fibres [8]. There are also systems with electrodes mounted in two dimensional (2D) configurations, which show the same longitudinal and transversal selectivity [8] and are more selective than bipolar configuration [9], [10]. Concentric-ring electrode belongs to 2D systems. Compared to others, it requires only two leads and it is perfectly isotropic.

Beside the spatial selectivity, there are some BSS algorithms for crosstalk reduction. Kong et al. [7] show the efficacy of one of them applied to forearm muscles in a static task.

The aims of the study are (a) to compare the effects of crosstalk in bipolar and concentric-ring electrodes used for electromyographic recordings, (b) to evaluate for both types of electrodes the efficacy of BSS methods to reduce crosstalk during voluntary isometric contraction of the leg muscles.

II. Materials and Methods

A. Subjects

Eleven volunteers (three female; mean ± SD, age: 27.6 ± 5.5 years; height: 1.77 ± 0.07 m; weight: 68.7 ± 8.9 kg) participated in the study. All subjects reported having no orthopaedic or neuromuscular disorders. Each subject gave written informed consent priori to inclusion. The study conforms to the guidelines in the Declaration of Helsinki.

B. Surface electromyographic (EMG) recordings

Surface EMG signals were acquired with bipolar or concentric-ring electrodes, in separate sessions. Bipolar electrodes consisted of two (24 mm diameter) silver-chloride disks. Concentric-ring electrodes consisted of Ag/AgCl circular (16 mm) electrode and surrounding external circular ring (outside and inside diameter of 42 mm and 28 mm, respectively). EMG potentials from multiple muscles were fed into a 64-channels system, which amplified, bandpass filtered (10-500 Hz, 3 dB bandwidth), sampled signals (2048 samples/s per channel) and converted to digital data by a 12 bit A/D converter.

C. Experimental protocol

Surface EMG signals were detected from tibialis anterior (TA), gastrocnemius lateralis (GL), gastrocnemius medialis (GM), soleus (S) and peroneus tertius (P) muscles.

Each muscle innervation zone (IZ) position was identified. The recording electrodes were placed between the IZ and the proximal tendon region for the tibialis anterior and soleus muscles and the distal tendon region for the gastrocnemius lateralis and medialis and peroneus tertius muscles. Bipolar electrodes were placed parallel to the muscle fibres direction with the inter-electrode (centre to centre) distance of 25 mm. Concentric-ring electrodes, for their geometry, are invariant to rotations. A common ground electrode was at the left wrist.

The subject sat comfortably in a chair with his right leg fixed in the ergometer for isometric contraction of the ankle flexors. Four inelastic straps secured the contact. The angle of the ankle and the hip was 85° and 110°, respectively. The

angle of the knee ranged between 120° and 140°, depending on the height of the subject.

Maximal voluntary contraction (MVC) forces for plantarflexion and dorsiflexion were measured. The greatest value in two repetitions was the reference level for the strength feedback. The subject performed plantarflexion and dorsiflexion of the ankle joint in isometric conditions at 25%, 50% and 75% MVC. Each contraction was kept for 5 s. Among successive contractions, a rest period of one minute was included to reduce fatigue phenomena. The order of electrode type, plantar-/dorsi-flexion and contraction level were randomized among subjects. Signals were visualized and stored using the OTBioLab software (version 1.8, OT Bioelettronica, Turin, Italy).

D. Data processing

Using Matlab, signals were bandpass filtered (20-450 Hz) with a forth order Butterworth filter. They were rectified and divided in contiguous epochs of 0.25 s. The average rectified value (ARV) was estimated for each epoch. For each combination of muscle-contraction levels, the ARV index was the mean of the ARVs computed in its epochs. The crosstalk index [4] is the ratio of ARV index of non-active to active muscles. Each index was normalized with the measured strength level.

To evaluate the efficacy of BSS, the corresponding crosstalk index (CI) was computed on components extracted from bandpassed signals. We used the fast independent component analysis (fastICA), with convergence rate and approach set to cubic and symmetric, respectively.

E. Statistical analysis

Crosstalk indices were compared with a nonparametric test for paired samples (one tail Wilcoxon signed rank) between the two types of electrodes and between the two types of analysis (on signals and on components). Threshold for statistical significance was set to $p < 0.05$. False discovery rate was used to correct for multiple comparisons.

III. Results

Figure 1 shows crosstalk indices for the couples GL/TA and GL/P in dorsiflexion task and P/S in plantarflexion task. In the dorsiflexion and plantarflexion the active muscles are TA, P and S, GL, GM, respectively. Data are presented as median and 25^{th} and 75^{th} percentiles with boxplots.

During the plantarflexion at 25% MVC the amplitude of the EMG signal was comparable to the instrumental noise. Consequently, this condition was excluded from further analysis.

A. Bipolar vs concentric-ring electrodes

Crosstalk indices estimated on signals and on components (from fastICA application) in bipolar recordings are significantly larger than those in concentric-ring recordings.

B. Efficacy of crosstalk reduction method

The effect of fastICA algorithm on crosstalk indices is not the same for both types of electrodes. For concentric-ring electrodes the CIs estimated on signals and on components do not change significantly. In the pair P/S muscles for bipolar recordings the effect is similar. CI decreases significantly, instead, for GL/TA and GL/P muscles.

The ratio of medians of bipolar CIs to concentric-ring CIs decreases of 14%, passing from evaluations on signals to evaluations on components.

IV. Discussion and conclusion

The high value of CIs between peroneus tertius and soleus respect with the CI values for GL/TA and GL/P (as it is shown in Figure 1) underlines the need to reduce crosstalk. Moreover, peroneus tertius and soleus are of functional importance in gait and balance studies.

In surface EMG choosing a detection system based on its spatial selectivity is not the only method to reduce crosstalk. Our results suggest that the application of the BSS method improves crosstalk contamination (CIs decrease) in bipolar recordings when a muscle of the pair is a surface pennate muscle. On the other hand, it does not enhance this feature in concentric-ring recordings. Nevertheless, crosstalk indices estimated in bipolar recordings on ICA components are significantly larger ($p < 0.05$) than that on signals for concentric-ring recordings. These electrodes, as we have experimentally verified and as spatial selectivity suggests, are less sensitive to the crosstalk phenomenon.

Based on the results of this study, concentric-ring electrodes reduce crosstalk significantly better than bipolar electrodes in static condition. Performances, evaluated in dynamic tasks, could add information for choosing the detection system and the separation algorithm.

References

[1] D. Farina, R. Merletti, B. Indino and T. Graven-Nielsen, "Surface EMG crosstalk evaluated from experimental recordings and simulated signals: reflections on crosstalk interpretation, quantification and reduction," *Methods of Information in Medicine*, vol. 43, pp. 30-35, 2004.

[2] T. J. Koh and M. D. Grabiner, "Cross talk in surface electromyograms of human hamstring muscles," *Journal of Orthopaedic Research*, vol. 10, pp. 701-709, 1992.

[3] G. V. Dimitrov, C. Disselhorst-Klug, N. A. Dimitrova, E. Schulte and G. Rau, "Simulation analysis of the ability of different types of multi-electrodes to increase selectivity of detection and to reduce cross-talk," *Journal of Electromyography and Kinesiology*, vol. 13, pp. 125-138, 2003.

[4] D. Farina, R. Merletti, B. Indino, M. Nazzaro and M. Pozzo, "Surface EMG crosstalk between knee extensor muscles: experimental and model results," *Muscle and Nerve*, vol. 26, pp. 681-695, 2002.

[5] C. J. De Luca, M. Kuznetsov, L. D. Gilmore and S. H. Roy, "Inter-electrode spacing of surface EMG sensors: reduction of crosstalk contamination during voluntary contractions," *Journal of Biomechanics*, vol. 45, pp. 555-561, 2012.

[6] K. S. Frahm, M. B. Jensen, D. Farina and O. K Andersen, "Surface EMG crosstalk during phasic involuntary muscle activation in the nociceptive withdrawal reflex," *Muscle and Nerve*, vol. 46, pp. 228-236, 2012.

[7] Y.-K. Kong, M. S. Hallbeck and M.-C. Jung, "Crosstalk effect on surface electromyogram of the forearm flexors during a static grip task," *Journal of Electromyography and Kinesiology*, vol. 20, pp. 1223-1229, 2010.

[8] D. Farina, L. Arendt-Nielsen, R. Merletti, B. Indino and T. Graven-Nielsen, "Selectivity of spatial filters for surface EMG detection from the tibialis anterior muscle," *IEEE Trans. on Biomedical Engineering*, vol. 50, pp. 354-364, 2003.

[9] L. Mesin, S. Smith, S. Hugo, S. Viljoen and T. Hanekom, "Effect of spatial filtering on crosstalk reduction in surface EMG recordings," *Medical Engineering & Physics*, vol. 31, pp. 374-383, 2009.

[10] D. Farina and C. Cescon, "Concentric-ring electrode systems for noninvasive detection of single motor unit activity," *IEEE Trans. on Biomedical Engineering*, vol. 48, pp. 1326-1334, 2001.

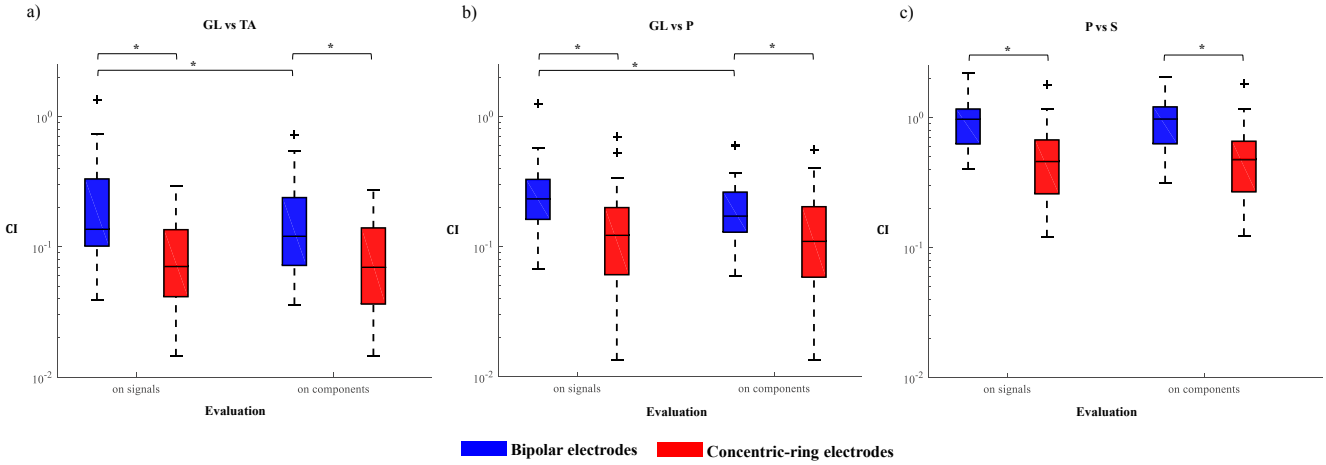

Fig. 1. Crosstalk indices (CIs) evaluated for bipolar and concentric-ring recordings, on signals and on components (from fastICA algorithm application) between (a) gastrocnemius lateralis (GL) and tibialis anterior (TA) muscles, (b) gastrocnemius lateralis (GL) and peroneus tertius (P) muscles during the dorsiflexion of the ankle joint, (c) peroneus tertius (P) and soleus (S) muscles during the plantarflexion of the ankle joint, in isometric condition in eleven healthy subjects. The plots (box-plot representation, in logarithmic scale) show boxes which range from the first to the third quartile, a line across the box indicating the median, the whiskers and the individual marks representing the most extreme data points not considered outliers and the outliers, respectively. Comparing bipolar and concentric-ring electrodes with nonparametric test (one tailed, paired samples Wilcoxon sign rank), both on signals and on ICA components, CIs in bipolar recordings are significantly (*) larger than those in concentric-ring recordings (familywise $p < 0.05$, false discovery rate correction applied). Evaluating for both types of electrodes the efficacy of BSS method chosen to reduce crosstalk, for bipolar recordings CIs decrease significantly (*) for the pairs GL/TA (panel a) and GL/P (panel b).

Association between Smartphone-based Activity Monitoring and Traditional Clinical Assessment Tools in Community-Dwelling Older People

Alice Coni[1], Sabato Mellone[1], Marco Colpo[2], Stefania Bandinelli[2], and Lorenzo Chiari[1]
[1] *Department of Electrical, Electronic and Information Engineering, University of Bologna, Bologna, Italy*
[2] *Local Health Unit Tuscany Centre, Firenze, Italy*

Smartphones are used in the framework of the FARSEEING-InCHIANTI study for gaining information on activities of daily living to ultimately define objective physical activity profiles. In this study we aimed to investigate the association between mean and extreme values of physical activity and gait characteristics derived from daily living activities and well-established clinical tools. 171 persons from the InChianti cohort study, were recruited. Factor analysis was performed in order to extract the underlying structure of physical activity and gait features for both mean and extreme values. Outcomes of the smartphone-based home monitoring are coherent with clinical assessments. Extreme values seems to be more informative than the mean values and are more closely related with the clinical assessment.

***Keywords*—Activity monitoring, smartphone, factor analysis, older people.**

I. Introduction

Smartphones (SP) are used in the framework of the FARSEEING-InCHIANTI study for gaining information on activities of daily living to ultimately define objective physical activity profiles [1].

The InCHIANTI study [2] is a longitudinal cohort study of factors contributing to loss of mobility in late life started in 1998 and is aimed to translate epidemiological research into geriatric clinical tools that allows for more precise diagnosis and more effective treatment in older persons with mobility problems. Data from InChianti were used to develop and test smartphone based applications in the FARSEEING project.

Previous studies used the mean or median of a gait characteristic under the hypothesis that this would be the most representative estimate for the person's capacity [3]. However, extreme values of gait characteristics may better reflect the capacity of adapting the gait pattern to the variety of daily life conditions.

Situations where people show "high gait quality" might be informative about the best possible performance they can achieve, which may be closely related to the performance in a lab [4].

In this study we aimed to investigate the association between mean and extreme values of physical activity and gait characteristics derived from daily living activities and well-established clinical tools for quantifying motor and cognitive impairments in a cohort of community-dwelling older subjects.

II. Materials And Methods

A. Population

171 persons (79.72± 6.55 years old, 87 females), a subsample of the InChianti cohort study, were recruited. Participants had worn a SP at home for at least 5 days (up to 9). SP was equipped with a custom Android application designed for long-term monitoring of physical activity. A set of sensor-based features was extracted from the signals recorded by the 3D accelerometer and gyroscope embedded into SPs. Ethical approval was obtained by Local Ethical Committee (approval number: 584/2012).

The following clinical data were collected from the subjects: Mini-Mental State Examination (MMSE), the Activity of Daily Living (ADL), i.e. the number of activity for which the person requires help (e.g. bathing, dressing, eating, etc.); the Instrumental Activity of Daily Living (IADL), i.e. the number of instrumental activity in which the person requires help (e.g. preparing meals, performing housework, getting to places outside of walking distance, and managing medications, etc.); the Epidemiologic Studies Depression Scale (CESD), a questionnaire used to assess depressive symptoms [5]; the Physical Activity (PA) assessed through a questionnaire [6]; The Hand-Grip strength test (HG); the Trail Making Test A (TMTA), a neuropsychological test that assesses various cognitive abilities, including visual-conceptual, visuospatial, and visual-motor tracking; the lower extremity muscle power measured using the Nottingham leg extensor Power Rig (PR) [7]; the Survey of Activities and Fear of Falling in the Elderly, a questionnaire that inquires about fear of falling (FEAR) [8]; and the Short Physical Performance Battery (SPPB), a measure of mobility function [9].

B. Instrumentation

Instrumental features representative of the person's motor profile were obtained from the analysis of the signals derived from the long-term monitoring, including the percentage of sedentary, active, and walking time, duration and intensity (METs) of the activities, gait and turning characteristics. Mean or extreme (5^{th} or 95^{th} percentile) values of each variable were computed in order to define two sets of features: the first set represents the mean performance, the second set represents the best performance observed during the activity monitoring.

C. Statistical Analysis

Robust linear regression was performed in order to remove the effect of age, gender, height, weight, and MMSE. Factor analysis was performed in order to extract the underlying structure of physical activity and gait features. Subjects that were identified as outliers in the linear robust regression analysis were excluded from this analysis. Factor analysis scores were obtained from the fitted model for all subjects. Spearman's correlation analysis was used for investigating the association between factors and clinical variables.

III. Results

Sixteen features were obtained from the smartphone-based activity monitoring dataset for both mean and extreme values.

Three factors were obtained using the dataset of mean values, explaining the 56% of variance (Table I). The first factor is associated with gait regularity, the second with the activity level of the person, and the third with his/her turning ability.

Eight factors were obtained using the dataset of extreme values, explaining the 73% of variance (Table I). According to the meaning of grouped features, factors were labelled as follows: activity level, turning velocity, gait variability, gait regularity, Medio-Lateral (ML) gait regularity, turning duration, sprint, and cadence.

Table I also reports Spearman's correlation coefficient between factors obtained using both mean and extreme values and clinical variables. Only significant correlations ($p<0.05$) are displayed.

IV. Discussion And Conclusion

The factor associated with the Activity Level was defined by the same set of features for both the mean values and the extreme values. It is important to note that there is a significant association between the Activity Level and the self-reported PA meaning that those reporting a high/low activity level were actually moving more/less during the day. People that are less sedentary also have a lower fear of falling (FEAR) and are less prone to depression (CESD); they also have higher lower limbs strength (PR) and higher scores in the functional assessment (SPPB). Gait Variability factor in both mean values and extreme values does not seem to be related to any of the clinical variables; this could be due to the high number of confounders that can affect variability values as environmental factors (e.g. how large is the home environment) and dual tasking (e.g. walking while talking). The Turning Ability factor derived from the mean values of the features is significantly associated with the self-reported PA, the SPPB, and the PR meaning that the ability to turn seems to be a motor task very much related with the fitness of the person; the association with TMTA can reflect the motor planning component that is also associated with this motor task.

The Turning Ability factor splits into two factors in the extreme values dataset: the Turning Velocity and the Turning Duration. The Turning Velocity, as the Turning Ability factor, is associated with the self-reported PA, the SPPB, a strength-related variable (HG), and a cognitive component (TMTA); while the Turning Duration is not associated with the clinical variables meaning that the best performance observed in term of movement duration seems to be dependent on the context more than on the person's fitness.

With regards to the other gait-related factors derived from extreme values, ML Gait Regularity and Sprint factors are not associated with the clinical scores and this fact could again be explained by the impact of the environment and the context on those factors. The Gait Regularity factor is instead significantly associated with strength-related scores (HG and PR) and on the functional status of the person (SPPB); those with the higher gait regularity seems to be also the stronger and healthier ones. This is also reflected in the Cadence factor since the higher values of cadence are associated with the lower limbs strength (PR) and the functional level of the person (SPPB).

Outcomes of the SP-based home monitoring are coherent with clinical assessments performed in institutions supporting the hypothesis that SPs can become an effective solution for ecological, quantitative behavioural analysis of community-dwelling older subjects with a clear clinical value. As hypothesised, extreme values of the features seems to be more informative about the functional status of the person and are more closely related with the motor performance assessed in a supervised clinical setting.

Acknowledgement

Research has received funding from the EU FP7/2007-2013 under grant agreement FARSEEING n° 288940

References

[1] Mellone S, Tacconi C, Schwickert L, Klenk J, Becker C, Chiari L, Smartphone-based solutions for fall detection and prevention: the FARSEEING approach, Zeitschrift für Gerontologie und Geriatrie, Vol. 45, No 8, pp. 722-7, December 2012.

[2] http://inchiantistudy.net/wp/

[3] S. M. Rispens, K. S. van Schooten, M. Pijnappels, A. Daffertshofer, P. J. Beek, and J. H. van Dieën, "Identification of fall risk predictors in daily life measurements: gait characteristics' reliability and association with self-reported fall history.," Neurorehabil. Neural Repair, vol. 29, no. 1, pp. 54–61, Jan. 2015

[4] Rispens, S. M., Schooten, K. S. Van, Pijnappels, M., Daffertshofer, A., Beek, P. J., & Die, J. H. Van. "Do Extreme Values of Daily-Life Gait Characteristics Provide More Information About Fall Risk Than Median Values ?",vol. 4, pp. 1–9, 2015.

[5] L. S. Radloff, "A Self-Report Depression Scale for Research in the General Population," *Appl. Psychol. Meas.*, vol. 1, no. 3, pp. 385–401, 1977.

[6] K. V Patel, A. K. Coppin, T. M. Manini, F. Lauretani, S. Bandinelli, L. Ferrucci, and J. M. Guralnik, "Midlife physical activity and mobility in older age: The InCHIANTI study.," *Am. J. Prev. Med.*, vol. 31, no. 3, pp. 217–24, Sep. 2006.

[7] A. P. Marsh, M. E. Miller, A. M. Saikin, W. J. Rejeski, N. Hu, F. Lauretani, S. Bandinelli, J. M. Guralnik, and L. Ferrucci, "Lower extremity strength and power are associated with 400-meter walk time in older adults: The InCHIANTI study.," *J. Gerontol. A. Biol. Sci. Med. Sci.*, vol. 61, no. 11, pp. 1186–93, Nov. 2006.

[8] N. Deshpande, E. J. Metter, F. Lauretani, S. Bandinelli, J. Guralnik, and L. Ferrucci, "Activity restriction induced by fear of falling and objective and subjective measures of physical function: A prospective cohort study," *J. Am. Geriatr. Soc.*, vol. 56, no. 4, pp. 615–620, 2008.

[9] J. M. Guralnik, L. Ferrucci, E. M. Simonsick, M. E. Salive, and R. B. Wallace, "Lower-extremity function in persons over the age of 70 years as a predictor of subsequent disability.," *N. Engl. J. Med.*, vol. 332, no. 9, pp. 556–561, 1995.

TABLE I
FACTORS DEFINITIONS AND SPEARMAN'S CORRELATION COEFFICIENT BETWEEN FACTORS AND CLINICAL VARIABLES

feature	E.V.	factor	ADL	IADL	CESD	FEAR	PA	FALL	HG	PR	TMTA	SPPB
FACTOR ANALYSIS OF THE EXTREME VALUES OF THE FEATURES												
• Sedentary time % • Active time % • Walking time %	0.13	Activity Level			-0.16	-0.15	0.28			0.17		0.21
• Mean turning velocity (95) • Peak turning velocity (95)	0.12	Turning Velocity					0.26		0.16		-0.20	0.48
• St. Dev. step duration (5) • CV step duration (5)	0.11	Gait Variability										
• AP Harmonic Ratio (95) • AP step regularity (95) • V step regularity (95)	0.10	Gait Regularity							0.18	0.15		0.19
• ML Harmonic Ratio (95) • ML step regularity (95)	0.09	ML Gait Regularity										
• Mean turning duration (5)	0.07	Turning Duration										
• Step duration (5) • Coordination Index (5)	0.06	Sprint										
• Cadence (95)	0.04	Cadence								-0.16		-0.16
FACTOR ANALYSIS OF THE MEAN VALUES OF THE FEATURES												
• St. Dev. step duration • CV step duration • Coordination Index • AP Harmonic Ratio • V Harmonic Ratio • AP step regularity • V step regularity	0.26	Gait Variability										
• Sedentary time % • Active time % • Walking time % • Mean sedentary time	0.16	Activity Level			-0.16	-0.15	0.27	0.15		0.17		0.21
• METs • Mean turning duration • Mean turning velocity • Peak turning velocity	0.14	Turning Ability					0.25			0.17	-0.16	0.42

ACRONYMS: ML = Medio-Lateral; AP = Antero-Posterior; V = Vertical; E.V = Proportion of Explained Variance; St. Dev = Standard Deviation; CV = Coefficient of Variation; METs = Metabolic Equivalents.

A correlational study between speech-related features and alexithymia trait

A. Guidi[1, 2], C. Gentili[3], E. P. Scilingo[1, 2] and N. Vanello[1, 2]
[1] *Research Center "E. Piaggio", University of Pisa, Pisa, Italy*
[2] *Dipartimento di Ingegneria dell'Informazione, University of Pisa, Pisa, Italy*
[3] *Department of General Psychology, University of Padua, Padua, Italy*

***Abstract*—Voice signal has been widely investigated to characterize mood and emotional states. A further interesting dimension could be related to the personality traits, whose effects might overlap to the ones related to emotion and/or mood. According to the literature, speech production can be related to personality traits evaluated by others. This relationship is not yet fully understood and the correlation between personality traits and specific speech features requires further investigation. In this study, a correlational analysis between some prosodic features and an alexithymia score is performed. An experimental protocol was administered to eighteen healthy subjects to investigate fundamental frequency related features. Results showed that the proposed prosodic features are positively correlated with the alexithymia score.**

***Keywords*—Fundamental frequency, speech-related features, personality trait, alexithymia.**

I. Introduction

ALMOST the whole central nervous system is involved in voice production. Laryngeal muscles, mucosae, tongue and lips are finely controlled by the speech motor system. The activation of mouth and laryngeal muscles is controlled by the vagus nerve, that supplies motor parasympathetic fibers [1]. Again, the speakers' prosody is controlled by both autonomic and somatic nervous systems via respiratory system. Noteworthy, since speech production is modulated by different psychological and/or mental states, speech analysis represents an interesting, non-invasive and economic approach to study speaker's mental state [2].

Many studies aimed at investigating psychological dimensions by means of the speech signal. Emotion [3], mood [4], and stress [5] were studied in relation to the speakers' speech production. Several studies attempted to characterize mood swings in patients affected by bipolar disorder [6], [7] as well as the depression severity [4]. A further interesting psychological variable is the speaker's personality. The trait theory [8] distinguishes personality traits from personality states. Traits can be defined as "stable internal characteristics that people display consistently over time and across situations", while states refers to temporary and short behaviours or feelings that depend on the personal situation and particular time. Many studies investigated the relation between voice and personality. Prosodic, spectral and voice quality features were investigated in relation to personality perception, e.g. competence, benevolence, extraversion, dominance and political charisma [9]-[11]. The INTERSPEECH 2012 Speaker Trait Challenge [12] showed that the classification of personality traits is feasible.

Although some useful indications about the relation between personality traits and voice production can be drawn from the literature review, the work on this topic is far from being concluded. For instance, the currently available studies mostly rely on the estimation of the perceived personality traits, without exploring the possibility of using dedicated personality tests, while, the relationship between personality traits and specific speech features have still to be clarified.

When speech analysis is addressed, three categories of features can be considered: excitation source, vocal tract and prosody-related features [3]. Excitation source features describe the vocal fold dynamics. Vocal tract features describe the different configurations of the vocal tract section during the articulatory process. Finally, prosodic features describe the modulation of intonation and intensity of speech. In particular, this kind of feature has been widely investigated, since prosody play a crucial role in conveying emotional messages. Moreover the prosodic feature estimation is usually quite robust against noise.

The aim of this study is the investigation of the alexithymia, a personality trait that is related to the incapability of recognizing and describing the emotions in the self [13]. More specifically this trait is characterized by the difficulty in identifying feelings and distinguishing between feelings and the bodily sensations of emotional arousal and by the difficulty in describing feelings to other people [14]. Usually such a trait can be assessed by the Toronto Alexithymia Scale (TAS-20) [15], an instrument characterized by high objectivity, good internal consistency, reliability and validity [16]. In this study a correlational analysis between prosodic features related to the speech fundamental frequency (F0) dynamics and the score returned by the TAS-20 will be conducted. This study will be performed on healthy subjects using a structured speech task.

II. Materials and Method

A. Experimental protocol

Eighteen healthy subjects (12 females, 23.66 ± 2.28 year) without any history of psychiatric disorder were enrolled. Subjects were asked to fill out the TAS-20 about 4 days before performing the experimental protocol. The TAS-20 is a self-report questionnaire based on 20 items and provides information about alexithymia trait in terms of three factors: difficulty identifying feelings, difficulty describing feelings, and external-oriented thinking. In this study, the TAS-20 sum score was investigated. The experimental protocol consisted in commenting a set of five Thematic Apperception Test (TAT) [17] images, a traditional projective test used to assess

personality disorders. Audio signals were acquired by means of a high quality system (AKG P220 Condenser Microphone, M-Audio Fast-Track), with a sampling frequency equal to 48 KHz and a resolution of 32 bits.

B. Algorithms

The proposed method consisted in a three-step procedure. In the first step, signal intensity and zero crossing rate were evaluated to detect voiced part of syllables [7]. Only the segments showing high intensity values and low zero crossing rates were considered as voiced. Then, in the second step, the F0 contour is estimated according to the double Camacho's SWIPE' [18] iteration method as described in [8]. SWIPE' is an algorithm that estimates the vocal F0 via a spectral-match approach. Finally, in the third step, the speech-related features proposed in [6] and describing the F0 profile were estimated. Such features, extracted within every voiced segment, aim at characterizing rising and falling F0 events in terms of amplitudes and durations. They can be defined as in Eq. (1)-(3):

$$Amplitude^* = \frac{|A_{rise}|-|A_{fall}|}{|A_{rise}|+|A_{fall}|} \quad (1)$$

$$Duration^* = \frac{D_{rise}-D_{fall}}{D_{rise}+D_{fall}} \quad (2)$$

$$Tilt^* = \frac{Amplitude^*+Duration^*}{2} \quad (3)$$

where A_{rise} and A_{fall} are the F0 change during the rising and falling section within a segment, and D_{rise} and D_{fall} are the duration of the rising and falling sections. Finally the features were averaged to obtain a single value for each subject.

The non-parametric Spearman method is used to estimate the correlation coefficient between the TAS-20 sum score obtained from each enrolled subject, and the corresponding mean prosodic features. The Benjamini-Hochberg procedure is used to correct p-values for the false discovery rate.

III. Results

The enrolled subjects reported a median TAS-20 sum score equal to 44.5 and a median absolute deviation equal to 8. Three subjects out of 18 reported a score corresponding to a possible alexithymia trait (52<score<61), while two of them reported a score corresponding to the alexithymia trait (score>60) [16].

The correlational analysis revealed that the prosodic features and the TAS-20 sum score are positively correlated. Amplitude*, duration* and tilt* reported correlation coefficients equal to 0.56 (corrected p-value=0.0307), 0.48 (corrected p-value=0.0428), and 0.54 (corrected p-value=0.0205) respectively.

IV. Conclusion

The obtained results indicate that the investigated speech-related features are significantly positively correlated with the TAS-20 sum score. This features aim at describing the F0 contour within every voiced segment and therefore their prosodic behaviour. Hence, the results let us suppose that information about speakers' prosodic production might be related to alexithymia scores.

Notwithstanding the limited number of enrolled subjects, the obtained results may be interesting. In fact, alexithymia seems to be associated with a generally weakened neural response to speech prosody. This reduced prosodic processing might be partially responsible for an impaired social communication in people with this personality trait [19]. We might speculate that the impaired prosody processing might also affect the prosodic speech production.

Finally, since high alexithymia scores were observed in people with eating disorders [20], this study might be relevant for clinical practice.

References

[1] J. Kreiman and D. Sidtis, Foundations of voice studies: An interdisciplinary approach to voice production and perception. John Wiley & Sons, 2011.

[2] C. S. Hopkins, R. J. Ratley, D. S. Benincasa, and J. J. Grieco, "Evaluation of voice stress analysis technology," in *System Sciences, 2005. HICSS'05. Proceedings of the 38th Annual Hawaii International Conference on. IEEE*, 2005, pp. 20b–20b.

[3] S. G. Koolagudi and K. S. Rao, "Emotion recognition from speech: a review," *International journal of speech technology*, vol. 15, no. 2, pp. 99–117, 2012.

[4] N. Cummins, et al., "A review of depression and suicide risk assessment using speech analysis," *Speech Communication*, vol. 71, pp. 10–49, 2015.

[5] N. Sharma and T. Gedeon, "Objective measures, sensors and computational techniques for stress recognition and classification: A survey," *Computer methods and programs in biomedicine*, vol. 108, no. 3, pp. 1287–1301, 2012.

[6] A. Guidi, et al., "Automatic analysis of speech f0 contour for the characterization of mood changes in bipolar patients," *Biomedical Signal Processing and Control*, vol. 17, pp. 29–37, 2015.

[7] N. Vanello, et al., "Speech analysis for mood state characterization in bipolar patients," in *Engineering in Medicine and Biology Society (EMBC), 2012 Annual International Conference of the IEEE. IEE*E, 2012, pp. 2104–2107.

[8] D. Bernstein, Essentials of psychology. Cengage Learning, 2013.

[9] K. R. Scherer and U. Scherer, "Speech behavior and personality," *Speech evaluation in psychiatry*, pp. 115–135, 1981.

[10] F. Weninger, J. Krajewski, A. Batliner, and B. Schuller, "The voice of leadership: Models and performances of automatic analysis in online speeches," *Affective Computing, IEEE Transactions on*, vol. 3, no. 4, pp. 496–508, 2012.

[11] G. Mohammadi and A. Vinciarelli, "Automatic personality perception: Prediction of trait attribution based on prosodic features," *Affective Computing, IEEE Transactions on*, vol. 3, no. 3, pp. 273–284, 2012.

[12] B. Schuller, et al., "The interspeech 2012 speaker trait challenge." in *INTERSPEECH*, vol. 2012, 2012, pp. 254–257.

[13] Sifneos, Peter E. "The prevalence of 'alexithymic'characteristics in psychosomatic patients." *Psychotherapy and psychosomatics* 22.2-6 (1973): 255-262.

[14] G. J. Taylor, R. M. Bagby, and O. Luminet. "Assessment of alexithymia: Self-report and observer-rated measures." The handbook of emotional intelligence (2000): 301-319.

[15] R. M. Bagby, J. D. A. Parker, and G. J. Taylor. "The twenty-item Toronto Alexithymia Scale—I. Item selection and cross-validation of the factor structure." *Journal of psychosomatic research* 38.1 (1994): 23-32.

[16] M. Franz, et al. "Alexithymia in the German general population." *Social psychiatry and psychiatric epidemiology* 43.1 (2008): 54-62.

[17] H. A. Murray, "Uses of the thematic apperception test," *American Journal of Psychiatry*, vol. 107, no. 8, pp. 577–581, 1951.

[18] A. Camacho and J. G. Harris, "A sawtooth waveform inspired pitch estimator for speech and music," *The Journal of the Acoustical Society of America*, vol. 124, no. 3, pp. 1638–1652, 2008.

[19] K. S. Goerlich-Dobre, et al. "Blunted feelings: Alexithymia is associated with a diminished neural response to speech prosody." *Social cognitive and affective neuroscience* (2013): nst075.

[20] K. Kucharska-Pietura, N. Vasilis, and M. Masiak. "The recognition of emotion in the faces and voice of anorexia nervosa." *International Journal of Eating Disorders* 35.1 (2004): 42-47.

Detection of Sensor Artifacts by Using Continuous Glucose Monitoring, Meal and Insulin Delivery Information.

Y. Leal[1], L. Gonzalez-Abril[2], S. Del Favero[1], A. Facchinetti[1], G. Sparacino[1] and C. Cobelli[1]
[1]Department of Information Engineering, University of Padova, Italy
[2] Department of Applied Economics I, University of Seville, Spain

***Abstract*—Geometric mean support vector machines (GSVMs) are an attractive option for detecting faults in continuous glucose monitoring (CGMs) sensor, because their learning mechanism usually considers a small subset of patterns to separate failure from fault-free situations. This work is aimed to introduce a methodology for online detection of sensor artifacts by using CGM, meal and insulin delivery information, in order to improve the CGM sensor reliability. To develop this approach, a dataset of 100 virtual patients was used. For each patient, 7 fault-free days of closed-loop control with 3 meals per day were simulated starting from midnight.**

***Keywords*—Support vector machines, Fault detection, Continuous glucose monitoring sensors.**

I. Introduction

Continuous Glucose Monitoring (CGM) faults, even if of limited time duration, can expose diabetic patients to severe risks and deteriorate effectiveness of automated insulin therapies. Typical faults originated by mechanical sources include occasional spikes and temporary attenuations induced by e.g. pressure made by the patient lying or sleeping on the sensor. Fault detection methods for CGMs have been scarcely investigated, being the current version of CGMs still not able to detect and compensate for failures that can corrupt the local reliability of the CGMS trace. The glucose estimations are unreliable, particularly in the hypoglycemic range [1], in comparison with SMBG measurements and laboratory systems. In order to improve reliability, self-monitoring capabilities must be embedded in the CGMs for detecting abrupt faults. Some notable works about this fact can be found in [2-3].

Geometric Mean Support Vector Machine (GSVM) [4] are learning machines that implement the structural risk minimization inductive principle to obtain generalization on a limited number of learning patterns [5], improving the geometric mean between specificity and sensitivity. For CGM fault detection, GSVMs are an attractive option, because their learning mechanism usually considers a small subset of patterns that allow separating failure from fault-free situations.

This work is aimed to detect such failures by exploiting CGM, meal and insulin delivery information by employing an online method based on a GSVM.

II. Methods

A. Subjects

100 virtual patients provided to capture inter-patient variability were generated by using the UVA/Padova Type-1 diabetic simulator [6], it was accepted in 2008 by USA FDA as substitute of animal trials prior to Artificial Pancreas clinical trials on humans. This is a highly accurate simulator based on complex physiology studies.

Model parameters of these virtual-subjects are sampled from probability distributions learned from the data. For each patient, seven fault-free days of closed-loop control with three meals per day were simulated starting from midnight.

B. Fault Scenarios

Several artificially generated fault episodes were added at random time instants (see Fig. 1). For each fault type, different amplitudes A = [-7.5, -10, -15, -20, -25, -30 mg/dL], and durations D = [5, 10, 20, 30, 40, 50, 60 min] were considered.

Spikes: An anomalously large error of amplitude A was added to the CGM reading at the random time t_f, for a fixed duration of D = 5 min.

$$CGM_{faulty}(t_f) = CGM(t_f) + A \tag{1}$$

Pressure-Induced Sensor Attenuation (PISA): A sequence of consecutive large errors of amplitude A were added to the CGM readings from the random time t_f, for a fixed duration of D = [10, 20, 30, 40, 50, 60 min].

$$CGM_{faulty}(t_f, t_f + D) = CGM(t_f, t_f + D) + A \tag{2}$$

C. Metrics to evaluate the performance of a classifier

Performance of the fault detection method were assessed thorough the metrics describing in (3), (4), (5) and (6). For each CGM sample, fault-detection output was classified as True/False Alarms or True/False Positives (t_{pos}/f_{pos}), depending on weather it did/did not detect the artifact and as False/True Negatives (f_{neg}/t_{neg}), in case it did/did not alarm in a not-faulty condition.

$$Accuracy = \frac{t_{pos} + t_{neg}}{t_{pos} + f_{neg} + f_{pos} + t_{neg}} \tag{3}$$

$$Sensitivity = \frac{t_{pos}}{t_{pos} + f_{neg}} \tag{4}$$

$$Specificity = \frac{t_{neg}}{f_{pos} + t_{neg}} \tag{5}$$

$$G_{mean} = \sqrt{Sensitivity * Specificity} \tag{6}$$

D. The Geometric Mean Support Vector Machine (GSVM)

Let $Z = \{(x_1, y_1) \ldots (x_N, y_N)\}$ be a training set with $x_i \in X$ as the input space, $y_i \in \{+1, -1\}$ as the output space, and $z_i = (x_i, y_i)$. Let $\varphi: X \rightarrow F$, $x = \varphi(x)$ be a feature mapping with a dot product denoted by $\langle \cdot, \cdot \rangle$. A binary linear classifier $f: X \rightarrow R$, defined as $f(x) = \langle x, w \rangle - b$, is sought where $w \in F$, $b \in R$. Outputs are obtained as $h(x) = sign(f(x))$.

The solution of the optimization problem of the standard

SVM [7] can be expressed as $w_0 = \sum_i \alpha_i y_i x_i$, where w_0 defines the orientation of the classifier and α_i are the Lagrange multipliers for dual formulation. The classifier can be written as in (7), where bias b determines the position of the optimal hyperplane and $K(x,y)=<x,y>=<\varphi(x),\varphi(y)>$, is called the kernel function, defined in (8).

$$f(\vec{x}) = sign\left(\sum_{i=1}^{N} \left[\vec{\alpha}_i y_i K(\vec{x}_i, \vec{x}) \right] - b \right) \quad (7)$$

$$K(\vec{x}_i, \vec{x}) = e^{-0.5 \frac{\|\vec{x}_i - \vec{x}\|^2}{\sigma^2}} \quad (8)$$

The GSVM is based on the consideration that the bias b is a parameter to be tuned. The function learned by a standard SVM will be adjusted through the bias to improve its performance, measured in terms of (6). Hence, once the solution vector w_0 is obtained, starting from w_0, a set of classifiers $F(w_0)$ is considered. The GSVM classifier ($\Theta b_G(x)$) is defined by modifying the standard bias b. The $\Theta b_G(x)$ is defined, such that given an input vector x, it assigns a label as follows in (9), where the new bias b_G is obtained as (10):

$$\Theta_{bG}(\vec{x}) = sign\left(f_{bG}(x)\right) = \begin{cases} +1 & if \quad \left\langle x, w_0 \right\rangle \geq b_G \\ +1 & if \quad \left\langle x, w_0 \right\rangle < b_G \end{cases} \quad (9)$$

$$b_G = \arg\max_{i=1,\ldots,N_{pos}} G_{mean}\left(b_i\right). \quad (10)$$

According to the previous theoretical results, the new classifier attains a more balanced performance between the true positive rate and the true negative rate.

E. Online detection of sensor artifacts by using individualized GSVM models

An individualized GSVM model was trained offline using past CGM sensor readings, rate of appearance of glucose (R_{aG}) and rate of appearance of insulin (R_{aI}) as it is shown in Fig. 2. R_{aG} and R_{aI} were simulated using the population parameter values estimated in [8-9]. Then, the model and inputs were used online to detect sensor faults. The first four data days were used for training. The remaining three days were used for testing, simulating an online scenario. GSVMs with RBF kernel were tuned and validated using five-fold cross-validation.

III. Results

From all patients, 75940 fault-free readings and 10160 failures readings were obtained for testing. Whether only the CGM information is used as model inputs, 83.6% of accuracy, 70.5% of specificity and 85.3% of sensitivity were reported. However, when the meal and insulin delivery information are added, metrics improve significantly, as it is shown in Table I and Fig. 3.

TABLE I
AVERAGE METRICS FOR 100 PATIENTS

Metrics	*Number of Samples*	*CGM, R_{aG} and R_{aI} (%)*	*CGM (%)*	*p-value < 0.05*
Accuracy	86100	92.8	83.6	†
Sensitivity	10160	83.4	70.5	†
Specificity	75940	94.0	85.3	†
G_{mean}	86100	88.5	77.6	†

Average metrics for two inputs combination are indicated: option 1 (only CGM information) and option 2 (CGM, meal and insulin delivery information). The symbol "†" indicates significant differences between them.

TABLE II
AVERAGE SENSITIVITY FOR 100 PATIENTS ACCORDING TO FAULT AMPLITUD AND DURATION

Faults	*Number of Samples*	*CGM, R_{aG} and R_{aI}*	*CGM*	*p-value < 0.05*
Faults Amplitudes (mg/dL)				
7.5	1560	57.6	55.1	
10	1691	72.3	60.8	†
15	1655	89.1	70.9	†
20	1599	93.0	71.0	†
25	1626	92.2	80.0	†
30	2029	93.1	82.1	†
Faults Durations (min)				
5	546	94.1	96.3	
10	378	92.2	94.4	
20	300	83.3	72.4	†
30	301	82.1	68.1	†
40	225	83.4	69.2	†
50	195	83.9	67.5	†
60	175	78.0	60.2	†

Average sensitivity for two inputs combination is indicated: option 1 (only CGM information) and option 2 (CGM, meal and insulin delivery information), according to fault amplitude and fault duration. The symbol "†" indicates significant differences between them.

In the same way, the incorporation of meal and insulin delivery information has significantly improved the sensitivity, when the analysis is done considering the fault amplitude and duration, as it is shown in Table II. Regarding fault amplitude (see Fig. 4), sensitivity was between 89.0% and 93.0%, except for 7.5 mg/dL (57.6%) and 10 mg/dL (72.3%). Regarding fault duration (see Fig. 5), sensitivity was around 83.0%, except for 5 min (94.1%), 10 min (92.2%), and 60 min (78.0%).

False positives are limited for all simulated amplitudes and durations. Except for amplitudes A = 7.5 mg/dl and 10 mg/dl, sensitivity is around 90%, when meal and insulin delivery information are included.

The spike detection can be considered highly sensitive (94.1%). A representative example of spikes detection is illustrated on Fig. 6. The PISA detection (fault duration above 5 min) can be considered satisfactory, exhibiting only a slight deterioration when the fault duration is above 60 min (78.0%) respect to results obtained only with CGM information. Fig. 7 shows a representative case of PISA detection.

IV. Conclusion

The method shows good sensitivity by detecting CGM faults for mid and large amplitudes (above 10 mg/dL), and for duration faults shorter than 60 min. Validation of the proposed method with real-data is needed.

Unlike previous works in this direction, this method includes a technique that allows more balanced performance between detection of fault-free and failures situations.

Additionally, the incorporation of R_{aG} and R_{aI}, together with CGM readings, allows an effective detection of spike and PISA artifacts.

Acknowledgement

This work is supported partially by the Agency for Management of University and Research Grants (AGAUR) of the Government of Catalonia, Spain (Beatriu de Pinós (BP-DGR 2013)).

REFERENCES

[1] Y. Luijf, J. Mader, W. Doll, T. Pieber, A. Farret, J. Place, E. Renard, D. Bruttomesso, A. Filippi, A. Avogaro, S. Arnolds, C. Benesch, L. Heinemann, and J. Devries. "Accuracy and reliability of continuous glucose monitoring systems: A head to-head comparison", *Diabetes Technol Ther*, 2013:15: 722–727.

[2] S. Del Favero S., M. Monaro, A. Facchinetti, A. Tagliavini, G. Sparacino and C. Cobelli. "Real-time detection of Glucose Sensor and Insulin Pump Faults in an Artificial Pancreas", *IFAC*, 2014.

[3] A. Facchinetti, S. Del Favero, G. Sparacino and C. Cobelli. "An online failure detection method of the glucose sensor-insulin pump system: Improved overnight safety of type-1 diabetic subjects", *IEEE Transactions on Biomedical Engineering* 2013:60(2):406-416.

[4] L. Gonzalez-Abril, H. Nuñez, C. Angulo and F. Velasco. "GSVM: An SVM for handling imbalanced accuracy between classes", *Applied Soft Computing*, 2014:17:23–31.

[5] V. Vapnik. "Statistical Learning Theory", *John Wiley & Sons*, New York, 1998.

[6] M. Breton, C. Cobelli, C. Dalla Man, B.P. Kovatchev. "Method, system and computer simulation environment for testing of monitoring and control strategies in diabetes", *Patent WO/2008/157781*, 2008.

[7] L. Gonzalez-Abril, C. Angulo, F. Velasco and A. Català. "Dual unification of biclass support vector machine formulations", *Pattern Recognition,* 2006:39:1325–1332.

[8] C. Dalla Man, M. Camilleri and C. Cobelli. "A System Model of Oral Glucose Absorption: Validation on Gold Standard Data". *IEEE Transactions on Biomedical Engineering,* 2006:53(12):2472-2478.

[9] C. Dalla Man, D. M. Raimondo, R.A. Rizza and C. Cobelli. "GIM, Simulation Software of Meal Glucose–Insulin Model". *IEEE Transactions on Biomedical Engineering,* 2007:1(3):323-330.

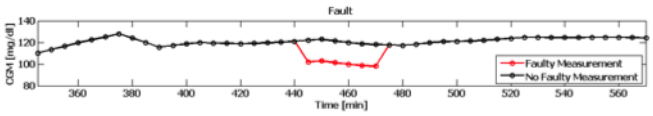

Fig. 1. Scheme of typical sensor faults originated by mechanical sources.

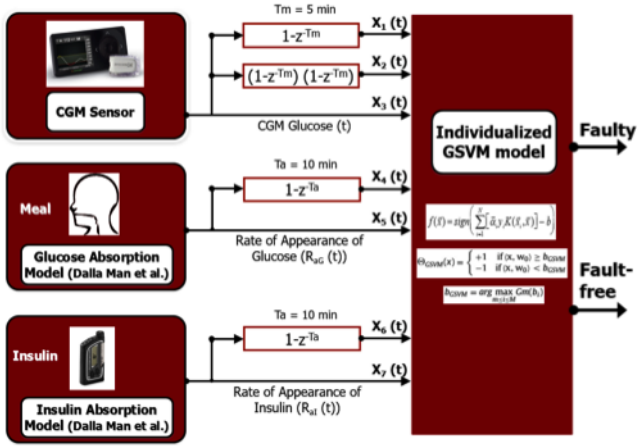

Fig. 2. Scheme of the online detection of sensor artifacts method by using individualized GSVM model.

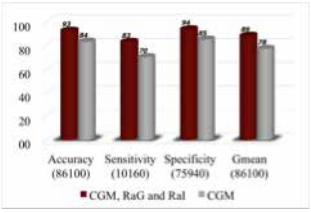

Fig. 3. Results of average metrics for two inputs combination are shown: option 1 as gray bars (only CGM information) and option 2 as red bars (CGM, meal and insulin delivery information).

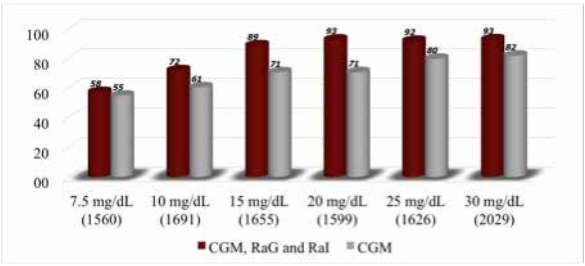

Fig. 4. Sensitivity comparison regarding fault amplitude for two inputs combination are shown: option 1 as gray bars (CGM information) and option 2 as red bars (CGM, meal and insulin delivery information).

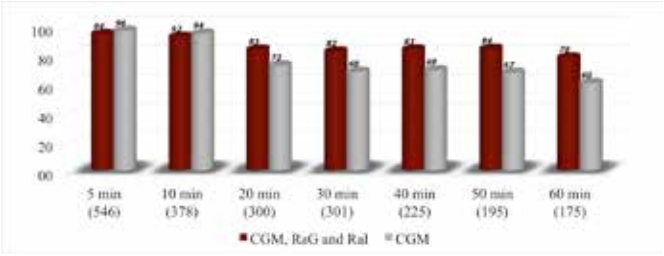

Fig. 5. Sensitivity comparison regarding fault duration for two inputs combination are shown: option 1 as gray bars (CGM information) and option 2 as red bars (CGM, meal and insulin delivery information).

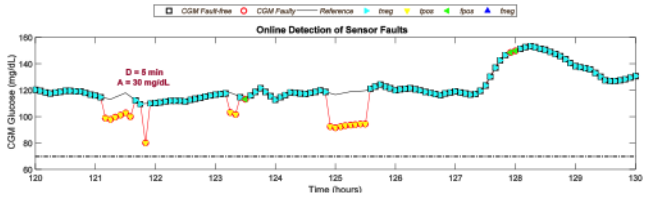

Fig. 6. A representative example of spikes detection is illustrated.

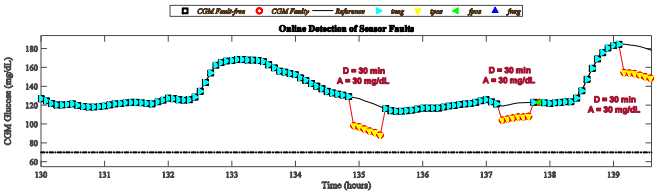

Fig. 7. A representative case of PISA detection is shown.

Cardio-respiratory control in Full-term Newborn and Late-Preterm One-Month Infants

M. Lucchini[1], M.G.Signorini[1], and W.P.Fifer[2]
1 Dipartimento di Elettronica, Informazione e Bioingegneria (DEIB), Politecnico di Milano, Italy
2 *Department of Psychiatry, Columbia University College of Physicians & Surgeons, New York, NY, USA*

***Abstract*— Cardio-respiratory control is a crucial mechanism for newborn survival and proper development as it is tightly related to Autonomic Nervous System (ANS) behavior. ANS branches, sympathetic and parasympathetic, work together to keep homeostasis. Premature birth is a strong stressor for ANS and might then impact cardio-respiratory control.**

We collected Hear Rate (HR) and respiration signals from 27 infants: 20 full-term newborns and 7 late-preterm one month infants.

Time domain, frequency domain and non-linear methods (Phase rectified Signal Averaging) were employed to analyze the data.

Late-preterm were found to have higher HR and respiratory frequency, while presenting lower respiratory modulation.

Moreover, PRSA showed its usefulness as an investigation tool for possible cardiorespiratory distress.

These results back many recent studies suggesting that late-preterm, even if are often considered as fully developed, are still at higher risk for many complications, including respiratory distress.

***Keywords*— Cardio-respiratory control, Autonomic Nervous System, Prematurity, Non-linear Analysis**

I. INTRODUCTION

Preterm birth refers to baby born at less than 37 weeks of gestational age. This condition puts the newborn infant at risk for many medical complications, including neurological problem such as apnea, cerebral palsy, or issues related to cardio-respiratory control.

Another very subtle risk is related to Sudden Infant Death Syndrome, since infant's Autonomic Nervous System is still immature and thus baby is more vulnerable to external challenges [1], with possible control systems impairments.

SIDS highest incidence is not right after birth, but between the 2nd and the 4th months of life: in particular for premature infants this could be related to the fact that extra utero and in utero development are strongly different.

To investigate this issue, in this study we compare Heart Rate (HR) and Respiration parameters of full-term newborn and late-preterm one month infants, who are about the same gestational age.

Results show different degrees of development between the two populations, with a higher HR and respiratory frequency for preterm, who showed also a less prompt response in inspiration/expiration phases.

II. MATERIALS AND METHODS

A. Patients and data collection

We identified a total of 27 patients, 20 full-term newborns and 7 late-preterm one month infants. Average gestational age was respectively 39.4±0.8 and 35.8±1.5 weeks.

They were selected from a larger cohort of 308 healthy subjects, acquired at Columbia University Medical Center. The protocol was approved by the Board, and parental consent was obtained before each study.

Only signals when baby were in supine position and active sleep were analyzed, in order to limit confounding factors. States were coded with a scoring system developed in the lab [2]. ECG and Respiratory activity were recorded non-invasively, at a sampling rate of 500 Hz and 20 Hz respectively, by means of three leads on the chest and by a chest belt. Recording time was 3 minutes for each patient.

B. Cardio-respiratory analysis

Time domain analysis was applied on RR signal, calculating parameters from the adult and fetal HR analysis (mean RR, SDNN and RMSSD) given good results obtained in previous studies [3].

For the frequency domain analysis RR series and respiratory signals were resampled at 5 Hz by applying a cubic spline. Then Power Spectral Density (PSD) was estimated with Welch averaged modified periodogram method. Frequency bands chosen were: Low frequency (LF) 0.1-0.4 Hz, High Frequency (HF) 0.4-1.5 Hz. Parameters extracted from PSD were: LF, HF and total area, frequency of the highest peak of HF and LF.

Lastly nonlinear analysis was applied on both signals, using Phased Rectified Signal Analysis (PRSA) technique [4][5]. Briefly, this technique studies quasi-periodic oscillations and nonlinear effects in non-stationary signals.

The procedure starts by selecting anchor points (AP), points where signal values increase or decrease. In this study, increases or decreases in the signal are taken into account, as averages of a specific number of values, called T, of the time series. Afterwards, windows of length 2L are defined around each AP. The value of L is related to the longest period of the oscillation in analysis, and its size L was set to 30 samples. APs where no full surroundings of this length are available are excluded from the analysis. Since most of the APs are closer than 2L, most of the windows will overlap.

Lastly, the windows are aligned at the AP and the PRSA

curve is obtained by averaging the aligned windows.

The choice of T, the number of samples averaged to identify the anchor points, was optimized for each patient, depending on the frequency of interest, according to this empirical relationship T=1/(2.5*F). The frequency of interest in this case was the frequency of the HF peak of respiration PSD. Analysis was run both for increases and decreases.

The parameter extracted from the PRSA curved was the Acceleration/Deceleration Phase Rectified Slope (APRS, DPRS) proposed by Fanelli et al.[6].

C. Statistical analysis

Since some of the parameters were not normally distributed, a Mann Whitney test with 0.05 significance threshold was applied. Results are reported as median and Inter-Quantile Range (IQR). Outliers were excluded from the analysis using as thresholds Inter-Quantile1 - 1.5 IQR and Inter-Quantile3 + 1.5 IQR.

III. Results

Mean RR, HF central peak of respiration PSD and APRS for respiration provided significant results in differentiating the two populations analysed.

Preterm infants had on average higher HR (lower RR) and respiratory frequency, while they had lower values of APRS, as presented in Table I.

Figure 1 shows the boxplots for significant parameters.

Figure 2 presents the mean PRSA curves for respiration increase analysis.

TABLE I

MEAN AND IQR of significant parameters

Parameter	*Fullterm Newborn*	*Preterm One month*	*P-val*	*Effect size*
Mean RR (ms)	457±44	385±27	<0.01	2.7
RESP HF freq. Peak (Hz)	0.9±0.3	0.47±0.09	<0.01	2.36
RESP APRS	4.9±0.8	2.7±1.5	<0.5	1.62

IV. Discussion

High HR in preterm infants indicates sustained sympathetic activity and lower parasympathetic tone. Parasympathetic system develops late in pregnancy and an abrupt early birth may interrupt or slow down its normal developmental course

Moreover, high respiratory frequency can be a sign of underdeveloped pulmonary function. In addition, premature infants show lower APRS (Resp), indicating a slower and less pronounced respiratory modulation.

From a methodological perspective, PRSA proved to be a useful tool to capture alteration that were not otherwise noticeable with traditional time domain and frequency domain analysis.

These finding are also interesting from a clinical point of view, due to the growing relevance of respiratory control role in SIDS. As a matter of fact, some studies suggest that the fatal death occurs due to a failed coupling of cardio-respiratory response to adverse events, such as hyper-capnic environment [7].

In addition, late-preterm infants are often considered functionally mature with a consequent relative lack of attention to specific neonatal risks. Nonetheless, more and more studies are showing that late-preterm are more prone to delayed transition and overall immaturity, and should thus be treated differently than full term. In accordance with our findings, late preterm are more subject to delayed lung fluid clearance (transient tachypnea of the newborn), respiratory distress syndrome, pulmonary hypertension and apnea [8].

V. Conclusion

In this study we analyzed HR and respiration of full-term newborn and late-preterm on month. Results show clear difference in both mean HR and respiratory frequency suggesting an altered parasympathetic system development in ex-utero life.

In particular, PRSA candidates as a powerful tool of investigation of respiratory modulation.

This was a preliminary study, thus it presents limitations regarding the length of the recordings and the limited number of subjects, which will be addressed in future analysis.

VI. References

[1] W. G. Guntheroth and P. S. Spiers, “The triple risk hypotheses in sudden infant death syndrome.,” *Pediatrics*, vol. 110, no. 5, p. e64, 2002.

[2] M. Stefanski, K. Schulze, D. Bateman, R. Kairam, T. A. Pedley, J. Masterson, and J. L.S., “A scoring system for states of sleep and wakefulness in term and preterm infants,” *Pediatr Res.*, vol. 18, no. 1, pp. 58–62, 1984.

[3] M. Lucchini, M. G. Signorini, W. P. Fifer, R. Sahni, B. Deib, and P. Milano, “Novel heart rate parameters for the assessment of Autonomic Nervous System function in premature infants .,” *Physiol. Meas., in Press*.

[4] A. Bauer, J. W. Kantelhardt, A. Bunde, P. Barthel, R. Schneider, M. Malik, and G. Schmidt, “Phase-rectified signal averaging detects quasi-periodicities in non-stationary data,” *Phys. A Stat. Mech. its Appl.*, vol. 364, pp. 423–434, 2006.

[5] M. Lucchini, D. Widjaja, C. Varon, K. Jansen, and S. Van Huffel, “Phase-Rectified Signal Averaging to Evaluate ANS Development in Premature Infants,” in *BIOSIGNALS 2013- International Conference on Bio-inspired Systems and Signal Processing*, 2013, pp. 203–208.

[6] A. Fanelli, G. Magenes, M. Campanile, and M. G. Signorini, “Quantitative assessment of fetal well-being through ctg recordings: A new parameter based on phase-rectified signal average,” *IEEE J. Biomed. Heal. Informatics*, vol. 17, no. 5, pp. 959–966, 2013.

[7] A. J. Garcia, J. E. Koschnitzky, and J.-M. Ramirez, “The physiological determinants of sudden infant death syndrome.,” *Respir. Physiol. Neurobiol.*, vol. 189, no. 2, pp. 288–300, 2013.

[8] L. Jain, “Morbidity and Mortality in Late-Preterm Infants: More Than Just Transient Tachypnea!,” *J Pediatr.*, vol. 151, no. 5, pp. 445–446, 2007.

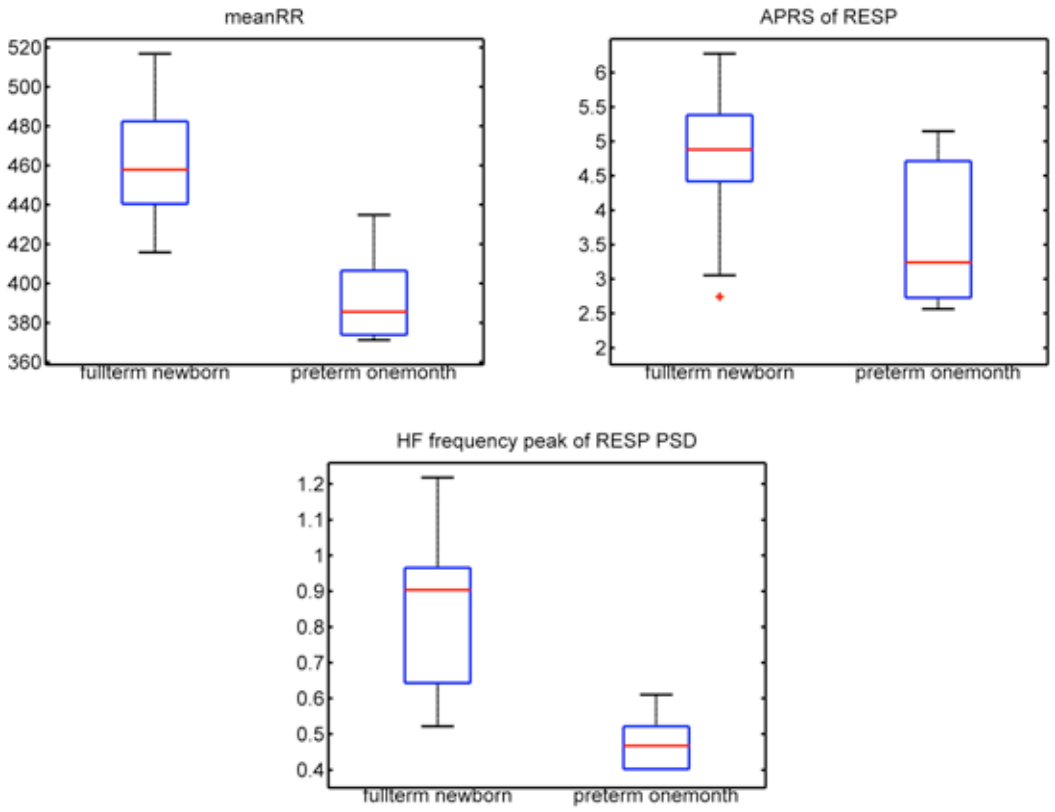

Fig. 1. Boxplot for significant parameters, meanRR, APRS(Resp) and HF central peak of respiration PSD.

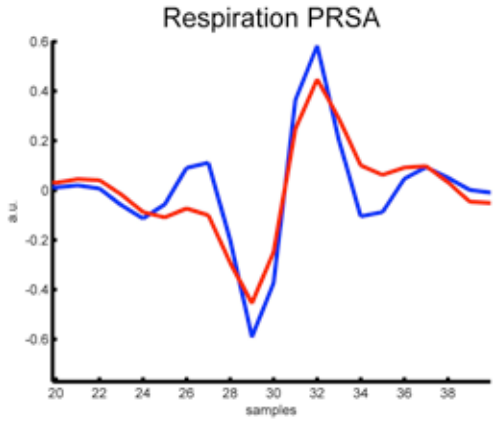

Fig. 2 Mean PRSA curves for respiration increase analysis, in red for one month premature and in blue for fullterm newborn. This figure is a zoom of the curve around the 10 samples before and after the AP, equivalent to 2 seconds before and after the AP.

Contactless video-based tracking of heart rate

Andrea Bandini[1,2], Silvia Orlandi[1], Alessandro Capo[1] and Claudia Manfredi[1]
[1]Dept. of Information Engineering, Università degli Studi di Firenze, Firenze, Italy
[2]Dept. of Electrical, Electronic and Information Engineering "Guglielmo Marconi", Università di Bologna, Bologna, Italy

***Abstract* — A video-based method is proposed to estimate heart rate (HR) through the changes in the reflected light coming from volumetric variations of blood vessels of the facial skin during the cardiac cycle. After suitable pre-processing of RGB video frames, the Independent Component Analysis (ICA) based on a robust algorithm is applied to detect the best source. Autoregressive Recursive Least Squares (AR RLS) is applied to estimate HR through the PSD and compared to a reference ECG and against a wavelet-based method giving the best results in tracking HR variations under a mild physical exercise. Being contact-less the method could be successfully applied to long-lasting monitoring of patients.**

***Keywords*—contactless HR estimation, video analysis, AR PSD, wavelets.**

I. Introduction

HEART rate (HR) estimation through contactless techniques recently gained great importance. Video-based methods exploit the volumetric variations due to the cardiac cycle that cause changes in blood vessels of the facial skin. They are similar to photo plethysmography (PPG) using ambient light as a source and digital cameras as sensors. RGB webcams [1], high speed and 5-channels colour cameras [2] are used. Most methods use a face tracking algorithm to track head and facial movements within a small region of interest (ROI) [1]. To filter out noise Blind Source Separation (BSS) techniques (in particular Independent Component Analysis - ICA) are applied [1]. To estimate the HR most methods are based on the highest peak of the Fast Fourier Transform (FFT) in the frequency range of interest (0.6-4 Hz) [2] or on the inter-beat interval by peak-picking in the selected source [1].

An issue raised by most of the ICA-based works is the choice of the source to be considered for HR estimation. Poh et al. [1] stated that the second component usually contains the strongest pulse signal. Monkaresi et al. [3] addressed this issue through machine learning techniques able to predict the best source for HR estimation within a temporal window. This method selects the source with the spectral content that minimizes the RMSE between the HR estimation and a reference value. All the first three components were found useful.

Following this approach we propose a recursive method for HR estimation whose accuracy is compared to the electrocardiographic data (ECG) and to the results obtained with a continuous wavelet transform (CWT). The method is applied on healthy subjects under mild physical exercise but it may find useful applications in the long-term monitoring of patients or for the study of emotional states.

II. Materials and Methods

To elicit a HR variation four healthy control subjects cycled on a cycling ergometer. The experiment duration was 450s, of which: 180s at rest, 90s during mild exercise (setting a power of 65 W and pedalling at 60-70 cycles per minute) and 180 s at rest. For a stable video recording of the face subjects avoided abrupt head movements. The reference ECG signal was recorded from the precordial leads V1 and V6 with a video-EEG system (EBNeuro Mizar-Sirius, 128 Hz sampling frequency). At the same time the subject's face was recorded with a Creative Senz3D webcam (resolution 1280x720 pixels at 30 frames per second (fps)). Colour frames were stored in 24-bit RGB images (8 bits per channel). Colour stream was recorded and stored in avi files through the OpenCV (v.2.4.9) libraries using a customized code written in C++ language.

A. Landmarks detection and ROI selection

The first step was the automated identification and location of facial landmarks (eyebrows, eyes, nose and mouth) in the video frames. The *Intraface* tracker algorithm [4] was used to locate two ROIs: one on the forehead and one in the central face region (including cheeks and nose), as shown in Fig.1. These ROIs were chosen as follows for their high skin blood perfusion, high visibility and uniform illumination.

- Forehead ROI: the two lower vertices are the central points of the eyebrows. Their horizontal distance defines the ROI width. From these points, the upper vertices were located at a vertical distance equal to 1/3 of the width. This value was selected in order to fit the ROI within the forehead avoiding hair regions.
- Cheeks ROI: the two upper vertices are the horizontal coordinate of the second external eyebrows points and the vertical coordinates between the two central nose points. The lower vertices were located at a vertical coordinate between nose tip and central nose base.

To make ROIs position integral with head movements, ROIs were normalized with respect to the head rotation angles.

B. ROI pre-processing

The R, G and B signals were extracted from the two ROIs by averaging pixels values on the 3 channels. This process was repeated for the whole video duration. Afterwards a detrend based on a smoothness priors approach [5] was applied to remove low frequencies. This method acts as a time-varying high pass FIR filter. The frequency response can be adjusted through a smoothing parameter λ that was set equal to 100 corresponding to a cut-off frequency of the filter of 0.66 Hz, thus filtering out events with frequency below 39 bpm. The detrended signals were normalized in amplitude subtracting their mean value and dividing by the standard deviation. Fig.2 shows the result of detrend and normalization.

C. ICA and filtering

The volumetric variations due to the cardiac cycle cause changes in blood vessels of the skin thus modifying the path length of the incident light. Haemoglobin absorption varies across the visible and near-infrared spectral range, with the highest peak in the green/yellow wavelength range (around 510-590 nm) [1]. However, video recordings performed with RGB colour cameras are a mixture of the reflected plethysmographic signal with other sources: skin colour variations due to the blood perfusion, light variations due to the sunlight or to the artificial illumination, flickering, noise, shadows due to the head movements, etc. To split these sources we applied the ICA based on the Joint Approximate Diagonalization of the Eigenmatrices (JADE) algorithm [6]. On the estimated sources a 5-point moving average window smoothing and a bandpass filtering between 0.6Hz and 3.5 Hz (36 and 210 bpm) with a 128-points Hamming window were applied. The filtered sources are shown in Fig. 3.

D. AR RLS and CWT

To track the HR variations an autoregressive (AR) model of order p=4 with recursive least squares (RLS) estimation was applied. The low order allowed smoothing the power spectral density (PSD) giving a single peak in the frequency range of interest (Fig.4). A forgetting factor λ=0.9889 was applied corresponding to 3s of the system memory.

Moreover the complex Morlet CWT was applied to the filtered sources. The frequency peak was computed as the weighted average of the peaks within the frequency range of interest (0.6-3.5 Hz), the weights being the peaks amplitudes. An example of the spectrogram obtained from the second independent component is shown in Fig.5.

The HR estimates obtained for both ROIs (forehead and cheeks) and with both estimation methods (AR RLS and CWT) were resampled at 128 Hz (sampling frequency of the EEG video) using a spline interpolation technique. The comparison with the reference HR values was made according to the root-mean-square error (RMSE) in bpm.

III. RESULTS

Source 3 extracted from the forehead gave the best results among the sources of both ROIs. For this signal the AR-RLS methods gave better results than the wavelet-based one, with mean RMSE around 9 bpm. Fig. 6 shows the results of both estimation methods as compared to the reference values.

Mean values and standard deviations of the RMSE for the two estimation methods are reported in Tab. 1. Both methods were compared with the reference ECG measures for the 3 independent sources (Source 1, Source 2 and Source 3 in Tab. 1) extracted from the two facial ROIs.

IV. CONCLUSION

In [1] the best source for HR estimation was the second one, related to the green channel of colour images where the highest plethysmographic content is present. Accuracy was 4.63 bpm in presence of motion artefacts. On the other hand Monkaresi et al. [3] demonstrated that useful information for HR estimation could be obtained from all the three estimated ICA sources. Performing a task similar to the one proposed here (indoor cycling) and combining ICA and k-NN the authors showed that the third source gave the best results with an error around 4 bpm. In our work, errors against the reference HR are higher than those proposed in [1, 3]. This could be due to motion artefacts during physical exercises.

Tab. 1: Mean value and standard deviation of RMSE for both estimation methods (AR-RLS and Wavelet-based methods) computed on the three independent sources extracted from the two facial ROIs (forehead and cheeks). These methods were compared with reference HR values extracted from an ECG. Values are in beats per minute (bpm).

ROI	Independent Source	AR-RLS	Wavelet
Cheeks	Source 1	14.42 ± 4.25	14.75 ± 3.59
	Source 2	16.44 ± 2.00	16.81 ± 1.84
	Source 3	11.10 ± 3.50	12.65 ± 2.64
Forehead	Source 1	12.48 ± 2.59	12.90 ± 2.60
	Source 2	14.79 ± 0.99	16.70 ± 2.34
	Source 3	9.58 ± 2.82	11.67 ± 2.25

Improvement could be given bya variable forgetting factor capable of decreasing the memory of the system during rapid HR variations and increasing it during steady state [7]. This would allow a better tracking of the varying dynamics of the system. Being totally non-invasive the method could be successfully applied to the study of emotional reactions in patients with neurological, psychological and psychiatric disorders. Its accuracy could be acceptable when applied to study the reactions after the administration of external stimuli of patients with disorders of consciousness (vegetative or minimally consciousness state), as these patients do not perform large movements of the head.

ACKNOWLEDGEMENT

The authors greatly acknowledge Casa di Cura Villa delle Terme, Impruneta, Firenze, that made available the bike and the ECG device and Ente Cassa di Rsparmio di Firenze for the financial support.

REFERENCES

[1] M-Z Poh, McDuff DJ, Picard RW. Advancements in noncontact, multiparameter physiological measurements using a webcam. IEEE Transaction on Biomedical Engineering. 2011; 58(1): 7-11.

[2] McDuff D, Gontarek S, Picard RW. Improvements in remote cardiopulmonary measurement using a five band digital camera. IEEE Transactions on Biomedical Engineering. 2014; 61(10): 2593-2601.

[3] [Monkaresi H, Calvo RA, Yan H. A machine learning approach to improve contactless heart rate monitoring using a webcam. IEEE Journal of Biomedical and Health Informatics. 2014; 18(4): 1153-1160.

[4] Xiong X, De la Torre F. Supervised descent method and its applications to face alignment. In: Proceedings of the IEEE Conference on Computer Vision and Pattern Recognition (CVPR), June 23–28, 2013, Portland, OR, USA. Los Alamitos, CA: IEEE Computer Society; 2013:532–539.

[5] Tarvainen MP, Ranta-Aho PO, Karjalainen PA. An advanced detrending method with application to HRV analysis. IEEE Transactions on Biomedical Engineering. 2002; 49(2): 172-175.

[6] Cardoso JF, Souloumiac A. Blind beamforming for non-Gaussian signals. Radar and Signal Processing, IEE Proceedings F. 1993; 140(6): 362-370

[7] Fort A, Manfredi C, Rocchi S. Recursive autoregressive spectral maps for ocular pathology detection. Ultrasound in Medicine & Biology. 1997; 23(3): 391-403.

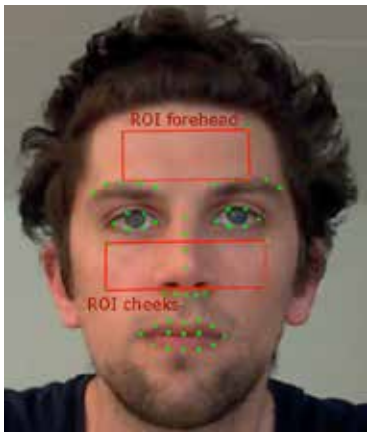

Fig. 1: ROIs selected from the *Intraface* landmarks.

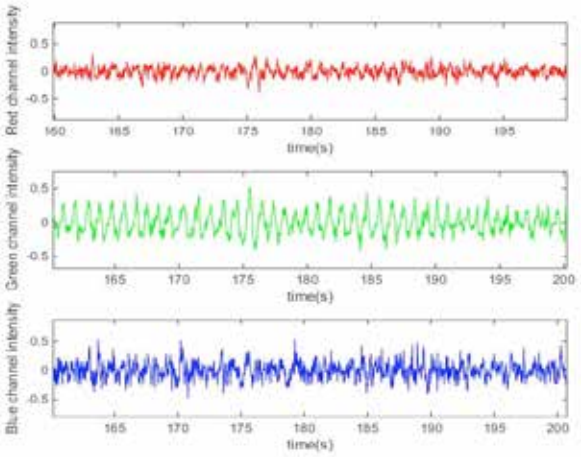

Fig. 2: mean R, G and B channel intensities after detrend and normalization. The highest oscillations in the green channel are consistent with the blood pulsations.

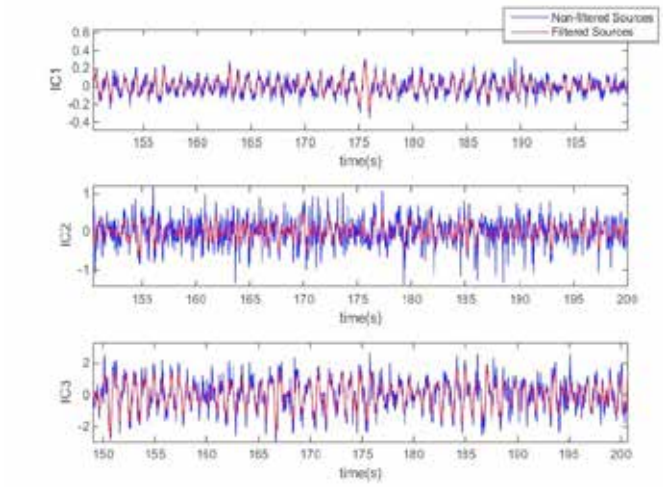

Fig. 3: Filtered sources after the ICA with the JADE algorithm

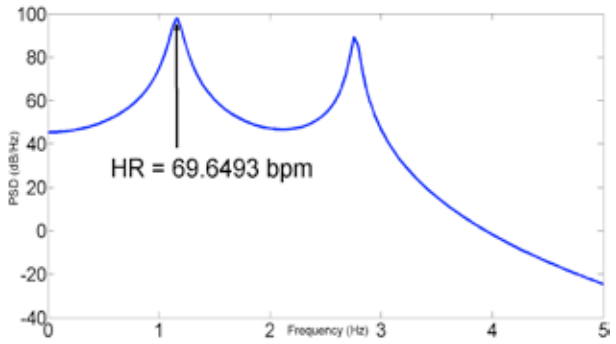

Fig. 4: AR Power Spectral Density (PSD) obtained by a RLS estimation of the parameters. The HR is given by the frequency value of the first peak converted to bpm

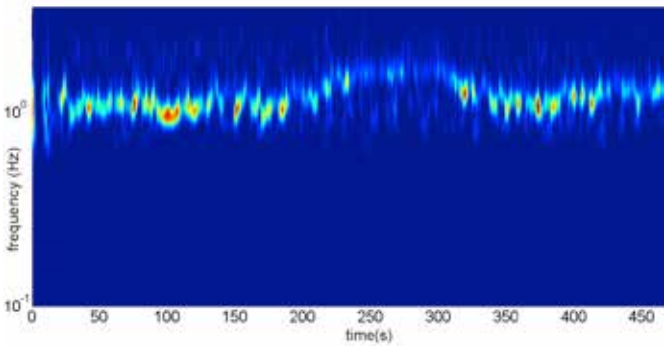

Fig. 5: Spectrogram of the second independent component. A high energy band (light colour) is shown in the frequency range of interest (0.6-3.5 Hz) and varies according to the HR variations due to the physical exercise (between 200 and 300 s).

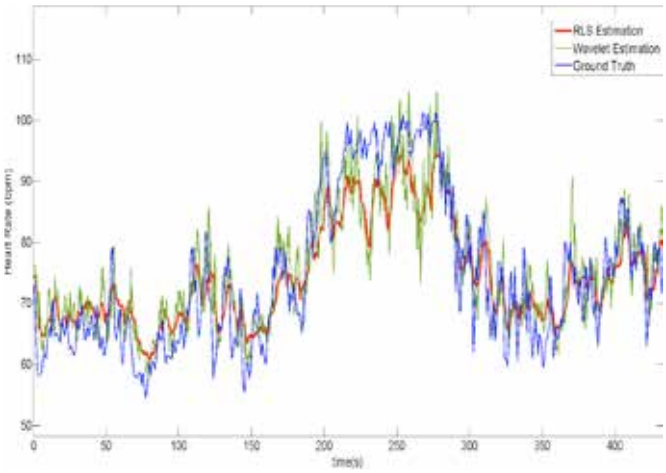

Fig.6: Comparison between the AR-RLS estimation (red line) wavelet estimation (green line) and ECG reference data (blue line).

Automatic Features selection in BCI-supported Motor Imagery practice for stroke Rehabilitation

F. Schettini[1,2], M.Martinoia[1,2], F. Pichiorri[1], E. Colamarino[1,2], D. Mattia[1], F.Cincotti[1,2]
[1] *Neuroelectrical Imaging and BCI Lab, Fondazione Santa Lucia IRCCS, Rome, Italy;*
[2] *DIAG, University of Rome "Sapienza", Rome, Italy;*

***Abstract*— Brain Computer Interfaces (BCIs) can support motor imagery practice during the neuromotor rehabilitation of post-stroke patients. The practical application of this approach in a clinical setting implies to simplify configuration procedures: the EEG activity to be employed in the BCI setting, and thus reinforced via the training, should be selected taking into account neurophysiological evidence and rehabilitation principles. In this study, we tested an automatic procedure to select the BCI control parameters (i.e. specific EEG signal's characteristics) based on neurophysiological and rehabilitation principles. To this aim, we compared the classification's performance of an algorithm for the automatic features selection (stepwise linear discriminant analysis) with a configuration procedures based on human choices. Preliminary results did not show significant differences of the proposed method with respect to the selection of features performed by highly skilled medical doctors and therapists.**

***Keywords*—Brain-Computer Interface, Motor Imagery, Stroke, Stepwise discriminant analysis**

I. Introduction

A Brain Computer Interface (BCI) system extracts specific features from EEG signal and converts them into an artificial output [1]. An important application of BCI technology regards the improvement of motor functions in stroke rehabilitation through motor imagery (MI) practice. Indeed MI can improve the recovery by stimulating neuroplasticity through repeated engagement of motor areas. The addition of a BCI allows the monitoring of Sensory Motor Rhythms (SMRs) modulation accompanying the imagination of a movement. SMRs are spontaneous EEG rhythms over the sensorimotor cortex in the Alfa and Beta frequency bands (7-30Hz); a BCI can detect this EEG modulation and provide a feedback to both therapist and patient [2] [3].

A recent work [4] demonstrated that the BCI-supported MI practice employed as an actual therapy could allow a better motor outcome. These results encouraged the diffusion of BCI technology from the research field to the clinical setting. This translation requires some expedients in order to make the set up *user-friendly*. The selection of control parameters is currently based on a semi-automatic procedure in which medical doctors and therapists manually select control features for BCI feedback (i.e. EEG channel and frequency) taking into account neurophysiological evidence and rehabilitation principles (e.g. MI related desynchronization on scalp electrodes relative to the affected hemisphere at sensorimotor relevant frequencies). With the aim to standardize this procedure in view of a wider employ of the BCI-based rehabilitation in stroke (e.g. for a multi-centric clinical trial), this study introduces a stepwise linear discriminant analysis (SWLDA) for the automatic selection of control parameters. The proposed procedure will be compared to the manual one using data of stroke patients.

II. Material and Methods

A. Study design and experimental intervention

We analysed the data of 16 patients who were a subset of the stroke patients involved in previous studies at IRCCS Fondazione Santa Lucia (see [2] [4] for an extended description of the experimental protocol). Briefly, in the training phase of the rehabilitation (i.e. the BCI-based therapy), the patient sat in a chair/wheelchair and his hands were covered by a white sheet on which a dedicated software projected a realistic visual representation of the patient's hands (Fig.1a). We asked the patients to imagine the movement (grasping and extension) of the affected hand, and they received a feedback when the trial was successful. The feedback consisted in the replication of the imagined movement by the virtual hand. Moreover, the therapist could monitor EEG activity and so encourage the patient during the session thanks to instant BCI feedback displayed on a screen.

B. Features selection: human choice vs SWLDA

During a previous screening session, the patients imagined or executed/attempted the movement without virtual hands. These data were used to identify the control features (i.e. power in a frequency bin on a channel) that drive the visual feedback to therapist and patient during the training by mean of an offline analysis. Currently, this selection is carried out by the therapists and the doctors of the NeuroImaging and BCI Laboratory of IRCCS Fondazione Santa Lucia. Particularly, they observe the R-square matrix (channel by frequency, Fig. 1b) obtained comparing task and rest related epochs. This is not an objective procedure and it is not suitable for ordinary therapists because it requires experience for visualizing patterns of desynchronization in the form of R-square matrices. In alternative, this study proposes the use of SWLDA as algorithm to automatically select control features. Indeed, it identifies an optimal subset of predictor variables (i.e. the features in this case) and assigns weights to them in order to build an effective regression model to evaluate the relationship between the predictors and the

dependent variable y (here equivalent to user's intention). During each iteration, the algorithm added or removed a feature from the classification model in order to obtain a combination of features ensuring a good classification performance. It is important to stress out that, in this specific application, BCI technology aims to assist MI in motor rehabilitation after stroke; therefore, good cursor control is not the only objective. Indeed ensuring the training of the "correct" sensorimotor activation is extremely important. In order to take into account these physiological components of the problem we defined some constraints (in terms of both topographic and spectral characteristics) on the initial set of features used as input for the SWLDA.

C. Analysis

In order to compare the classification performance achieved with both human selection and SWLDA, we assessed the AUC (Area under curve) of curve ROC (receiver operating characteristics). EEG signals from screening session were collected from 61 electrodes according to the 10–10 system with a 200 Hz frequency sampling; scalp signals were referenced to the linked-ear signal. Each run consisted of 15 trials related to motor imagery task and 15 trials of baseline rest (9s each). Trials were randomly presented within a run and, for each trial, we analyzed the 4 epochs corresponding to the 4 seconds during which the patient performed the MI's task. Data were preliminary spatially filtered by a common average reference (CAR). EEG spectral distribution was estimated using a Maximum Entropy Method analysis. After signal's elaboration, power spectrum values for all epochs have been limited to the features including the channels FC, C and CP (central and contralateral channel respect to the affected hemisphere) and we considered the frequencies into the range 7-29 Hz. Then we applied a SWLDA algorithm (Matlab® stepwisefit.m) in order to assess the classification model. We repeated this analysis three times considering different values of the maximum number of iterations (maxiter) of the algorithm: 2, 4 and 8 leading to a number of selected features less than or equal to 2, 4 and 8 respectively. The number 2 is coherent with the number of features manually selected by observing the R2 matrix. 4 is linked to the current montage during the training: 4 bipolar channels. Finally, we chose maxiter equal to 8 because a previous analysis showed that a greater number of iterations does not lead to better AUCs.

Regarding the human choice procedure, we considered the features and the weights that the medical doctors selected for each patient (two features with weights equal to -0,5 or three features with weights equal to -0,3). Then we used separately the outputs of the stepwise and the weights assigned by the therapists as input for a linear classification function in order to calculate the scores y:

$$y=\Sigma W*x+b,$$

where W were the weights, x the data (i.e. the features) and b was the intercept.

We compared the four cases (semi-automatic, SWLDA with maxiter equal to 2, 4 and 8) both in autovalidation and in crossvalidation condition. In the first condition we used as testing dataset the screening data previously exploited to obtain the parameters (W and b) with the stepwise and to plot the R-square matrix observed by the doctors in the manual case. In the crossvalidation condition, we tested the ability of the classifier to generalize by using the data from the first training session. Then we assessed the values of AUC for each patient for the 4 conditions and we applied a one-way ANOVA with features selection method as the factor and AUC values in the 4 conditions as dependent values.

III. RESULTS

Figure 2 shows the AUC values for both autovalidation and crossvalidation condition. For the autovalidation condition, a one-way ANOVA pointed out a significant difference ($F(3,60)=4.97$, $p<0.01$). According to the following Duncan's post hoc test, the SWLDA (maxiter 2,4 and 8) exhibited higher AUC values with respect to the manual selection (with $p<0.05$).

In the crossvalidation the average AUC values are numerically comparable and the one-way ANOVA did not point out significant differences for the analyzed sample ($F(3,60)=0.00570$, $p=0.99$).

IV. CONCLUSION

These preliminary results suggest that the SWLDA could be successfully applied as an automatic method for features selection to replace human selection in BCI-supported MI practice for stroke rehabilitation.

ACKNOWLEDGEMENT

This work was supported by the Promobilia Foundation (Foundation Ref N° 14214) and Sapienza Università di Roma, Progetti di Ateneo (C26A15N8LZ).

REFERENCES

[1] W Wolpaw E. J. (2012). "Brain-Computer Interfaces: Principles and Practice". USA: OUP

[2] F. Cincotti, F. Pichiorri, P. Aricò, F. Aloise, F. Leotta, F. de Vico Fallani, J. del R. Millán, M. Molinari, e D. Mattia, "EEG-based Brain-Computer Interface to support post-stroke motor rehabilitation of the upper limb", *Conf. Proc. Annu. Int. Conf. IEEE Eng. Med. Biol. Soc. IEEE Eng. Med. Biol. Soc. Annu. Conf.*, vol. 2012, pagg. 4112–4115, 2012.

[3] C. Sannelli, T. Dickhaus, S. Halder, E.-M. Hammer, K.-R. Müller, e B. Blankertz, "On optimal channel configurations for SMR-based brain-computer interfaces", *Brain Topogr.*, vol. 23, n. 2, pagg. 186–193, giu. 2010.

[4] F. Pichiorri, G. Morone, M. Petti, J. Toppi, I. Pisotta, M. Molinari, S. Paolucci, M. Inghilleri, L. Astolfi, F. Cincotti, e D. Mattia, "Brain-computer interface boosts motor imagery practice during stroke recovery", *Ann. Neurol.*, vol. 77, n. 5, pagg. 851–865, mag. 2015.

a)

b)

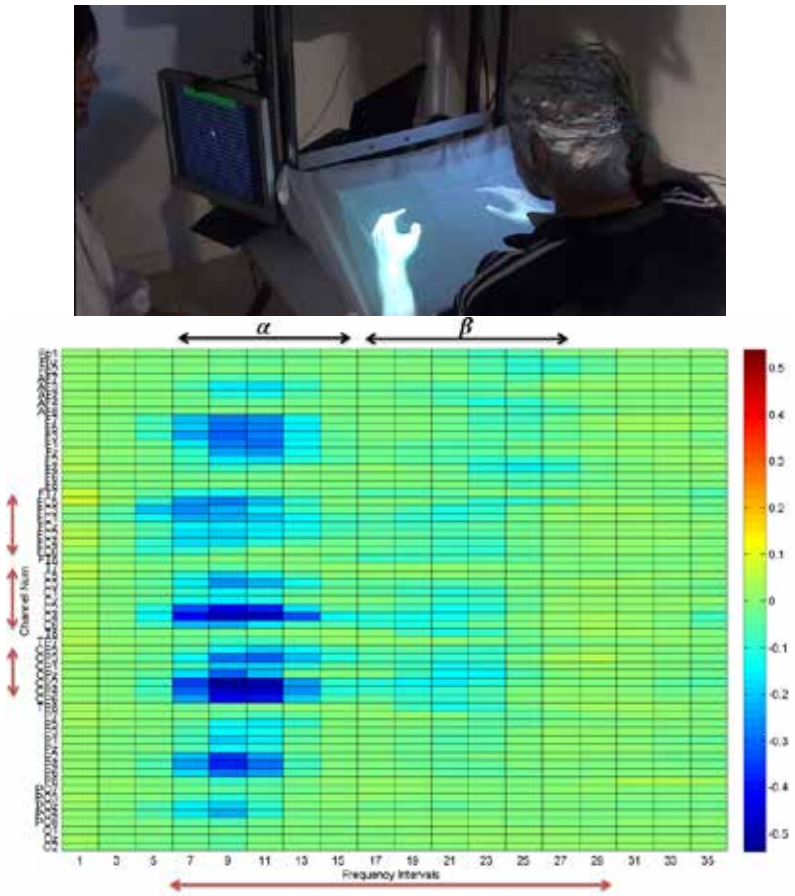

Fig. 1. a) Example of a channel-frequency R-square matrix related to task vs rest. The channels (FC, C, CP) and the frequencies (7-29 Hz) used as input for the SWLDA algorithm are highlighted together with Alfa and Beta frequency bands. b) Training session with the EEG-based BCI system for the rehabilitation after stroke through MI practice: the cursor's movement toward the target on the screen is the feedback to the therapist, whereas the virtual hands are the feedback for the patient.

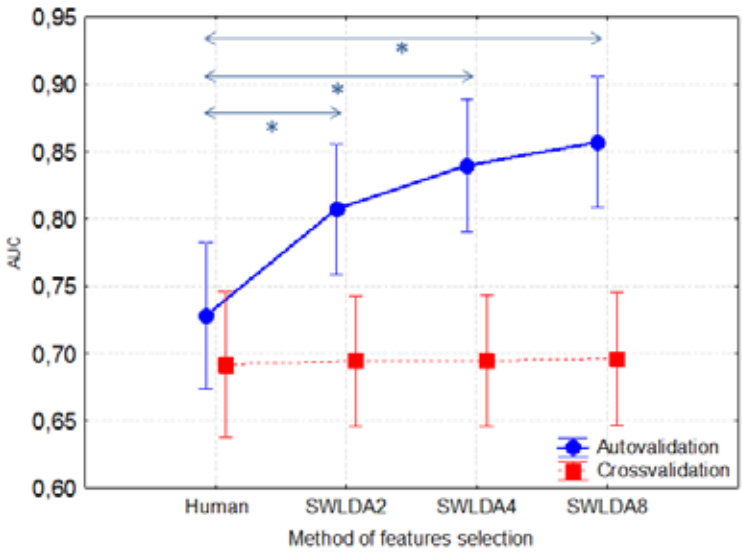

Fig. 2. Average AUC values for the autovalidation (blue) and crossvalidation (red) conditions. The symbol '*' shows the significant differences ($p<.05$) pointed out by the Duncan's post hoc test.

A semi-automatic image processing procedure for thermographic analysis

S. Matteoli[1], D. Coppini[1], and A. Corvi[1]
[1]*Bioengineering Laboratory, Department of Industrial Engineering, University of Florence, Florence, Italy*

***Abstract*— The semi-automatic imaging procedure shown in this paper is made to process thermographic images and, through a geometric transformation, to measure the Ocular Surface Temperature (OST) as well as visualizing the ocular areas in a fast, reliable and reproducible way. The strength of this method is that OSTs do not depend on the ocular geometry; hence it is possible to compare all ocular profile belonging to the same subject as well as from different populations. The procedure is applied to analyse the ocular temperature of two subjects and results are shown.**

***Keywords* — thermography, ocular disease, temperature, ocular profile.**

I. Introduction

Interest in the temperature of the eye spans almost 130 years [1,2], but accurate quantitative measurements of the profile of the ocular surface temperature (OST) has been possible only in the last few decades, thanks to the infrared thermography (IR) - a non-invasive, cheap and easy-to-use technique which allows measuring the OST with more accuracy, resolution, and speed than previously possible [2-4]. It is widely known that the ability to measure accurately the OST will increase the understanding of ocular physiology and should be a decisional support to the therapy integrated with classical diagnostic procedure. The use of ocular thermography offers great opportunities for monitoring the temperature of the anterior eye and analyzing the effects of some pathology in the OST [5-12]. The aim of the present study is to develop a semi-automatic imaging procedure that allows measuring the OST as well as visualizing the ocular areas from thermographic images in a fast, reliable and reproducible way. In this paper the procedure is applied for obtaining the OST and the thermal maps of two subjects' eyes: one affected with an ocular tumor and a healthy one.

II. Material and Methods

A. Experimental setting

From the acquired thermographic images, only the first frame corresponding to the eye opening was selected for further analysis, in order to avoid the influence of the tear-film evaporation [13].

B. Image processing

The image processing procedure was developed in Matlab (R2009, Mathworks, USA).

In order to study accurately the ocular thermal profiles, it was necessary to define the outline of the corneal surface by removing the unnecessary areas (i.e. eyebrows, eyelashes).

For doing that, a Matlab script applies a reversible geometric transformation to the corneal surface in order to adapt the subject's specific profile to a standard structure through a manual selection (by mouse) of eight points. Specifically, these points are placed on the contour of the eye: the first point is always placed on the left edge of the eye, regardless of whether it is in the nasal side or the temporal side, while the other seven points are chosen on the boundary moving in a clockwise direction. The third and the seventh points must be always positioned at the highest point of the upper arch, and the lowest point of the lower arch, respectively (Figure 1 (a)).

Afterwards, the script traces the outline of the corneal area through a 5-points interpolation through a Lagrange polynomial of fourth order. The interpolation is performed directly on the matrix of the image.

Once the coordinates of the points passing for the interpolating functions are known, the script traces the outline of the image by moving forward on the abscissa, and calculates cyclically (starting from the left of the image up to the right) the value of the corresponding ordinate obtained from the Lagrange interpolating function.

Before performing the geometric transformation, it was necessary to define the standard image used to normalize all ocular profiles. This standard image, built through another script, represents an ideal eye symmetrical both horizontally and vertically, and narrower in the area of the canti. Such geometry avoids falsifying the typical human eye shape during the imaging process.

The drawing of this new boundary was carried out using the same interpolating function described previously with the difference that the points from which the two curves pass are fixed and chosen to guarantee the symmetry of the image. The image thus obtained represents the "normalizing structure", which adapts all the ocular profiles.

All outline points (x,y) are saved in a vector that will be then used for the geometrical transformation.

Once the corneal area is delineated, the next step consists of adapting the number of columns of the subject-specific ocular profile, with highly variability in dimensions, to those of the standard image characterized by a predefined number of columns and rows. This procedure is made by resizing for a factor k, defined as the ratio between the number of columns in the standard image and the number of columns in investigated image. This resizing creates an image unfocused on the boundary and adapts the number of column of these two images. In order to define the outline of the resized image, the script searches, with a first control loop, points having the upper pixel in their column with a grey level of 255 - pure white - and the lower pixel with a grey level different from 255. In a second loop the script searches the points which having the upper pixel in their column the upper pixel with a grey level different from 255 and the lower pixel equal to 255. The geometrical transformation adapts the structure of the profile's outline to the standard image chosen previously. The algorithm considers a single column at a time

as a linear vector and applies a unidirectional scaling for a factor depending by the ratio of the first image column size and the size of the corresponding column of the standard image. Later this column is shifted upward or downward to create the standard image. At the end of the loop the image normalized respect to the standard image is obtained.

After applying the geometric transformation all ocular profiles belonging to the same subject as well as to different populations can be compared with each other because they are no more geometry-dependent. It is thus possible to subtract the masks of two profiles for highlighting the hottest and/or coldest areas of the eye that might indicate the presence of abnormalities.

From the normalized image of the eye it is then possible to calculate the OST. Thirty-one points are considered (Figure 1 (b)); these points are obtained as the intersection between a series of parallel vertical lines and a horizontal line passing for the middle of the image and two curves reproducing 1/3 and 2/3 scale version of the standard image. Points located in the two canti are not valuated as single points, but they represent the average temperature of both canti area. Figure 1 (c) shows the eye divided into five main areas that are the most used by oculists.

C. Subjects

The imaging procedure was applied for processing the thermographic images of two subjects: a healthy female (SAMA, 35 years old) with no ocular pathology and a female (MAFO, 55 years old) whose left eye has an active ocular tumour. The OST as well as the maps of the ocular temperature were obtained for both subjects.

III. Results

Table 1 shows the OST of the main ocular areas obtained for the two subjects under investigations. There is no significant difference between the right and left eye belonging to the healthy subject (P-value = 0.25), whereas MAFO's left eye is significantly warmer than the right one (P-value<0.0001).

Table 1 Ocular Surface Temperature of the main ocular areas

Area	Temperature (°C)			
	Sama Right eye	Sama Left eye	Mafo Right eye	Mafo Left eye
Central	34.19±0.19	34.20±0.11	34.76±0.06	36.30±0.08
Superior	34.38±0.17	34.40±0.08	35.19±0.06	36.40±0.14
Inferior	34.08±0.26	34.22±0.04	35.20±0.10	36.51±0.04
Nasal	34.86±0.23	34.65±0.22	35.41±0.26	36.72±0.10
Temporal	33.88±0.25	34.27±0.11	35.15±0.25	36.49±0.17

Figure 2 shows the thermal maps (in false colours) of the two subjects' eyes. Specifically, these maps indicate the difference in temperature between the two eyes of the same subject. MAFO's thermal map (Figure 2 (a)) shows an average temperature of about 1.5°C between the healthy and pathological eye, thus indicating that the left eye is warmer than the right one. SAMA's thermal map (Figure 2 (b)) shows instead a difference close to 0°C, thus indicating a no thermal difference between the two eyes.

IV. Discussion

The image processing procedure showed in this paper allows measuring the Ocular Surface Temperature (OST) and visualizing the thermal ocular maps in a fast (a few minutes for each subject), reliable and reproducible way. Furthermore, this method has the following features: 1) simplicity: there is no need of particular tools for making it work; 2) immediacy (results are easy to read); 3) modularity (all acquired variables are always transparent; therefore, they can be easily integrated with other programs); 4) generic (it can also be applied in other areas of the body by changing the shape of the standard image.

References

[1] A. Holmberg, "The temperature of the eye during the application of hot packs, and after milk injections". *Acta Ophthalmol*, vol. 30, pp. 347-364, 1952.

[2] C. Purslow, and J. S. Wolffsohn, "Ocular surface temperature: a review", *Eye & Contact Lens*, vol. 31, pp. 117-123, 2005.

[3] R. Mapstone, "Measurement of corneal temperature", *Exp Eye Res*, vol. 7, pp. 237-243, 1968.

[4] P. B. Morgan, M. P. Soh, N. Efron, and A. B. Tullo, "Potential applications of ocular thermography.", *Optom Vis Sci*, vol. 70, pp. 568–576, 1993.

[5] H. Fujishima, I. Toda, M. Yamada, N. Sato, and K. Tsubota, "Corneal temperature in patients with dry eye evaluated by infrared radiation thermometry", *Br J Ophthalmol*, vol. 80, pp. 29-32, 2006.

[6] A. Sodi, B. Giambene, G. Falaschi, R. Caputo, B. Innocenti, A. Corvi, and U. Menchini, "Ocular surface temperature in central retinal vein occlusion: preliminary data" *Eur J Ophthalmol*, vol. 17, pp. 755-759, 2007.

[7] D. Martin, and I. Fatt, "The presence of a contact lens induces a very small increase in the anterior corneal surface temperature." *Acta Ophthalmol (Copenh)*, vol. 64, pp. 512-518, 1986.

[8] S. Betney, P. B. Morgan, S. J. Doyle, and N. Efron, "Corneal temperature changes during photorefractive keratectomy", *Cornea*, vol. 16, pp. 158-161, 1997.

[9] A. Corvi, B. Innocenti, and R. Mencucci, "Thermography used for analysis and comparison of different cataract surgery procedures based on phacoemulsification", *Physiol Meas*, vol. 27, pp. 371-384, 2006.

[10] F. Vannetti, S. Matteoli, L. Finocchio, F. Lacarbonara, A. Sodi, U. Menchini, and A. Corvi, "Relationship between ocular surface temperature and peripheral vasoconstriction in healthy subjects: a thermographic study", *Proc Inst Mech Eng H*, vol. 228, pp. 297-302, 2014.

[11] S. Matteoli, L. Finocchio, I. Biagini, G. Giacomelli, A. Sodi, A. Corvi, G. Virgili, and S. Rizzo, "A thermographic study on eyes affected by Age-related Macular Degeneration: Comparison among various forms of the pathology and analysis of risk factors", *Infrared Physics & Technology,* Mar 2016.

[12] A. Sodi, S. Matteoli, G. Giacomelli, L. Finocchio, A. Corvi, and U. Menchini, "Ocular surface temperature in age-related macular degeneration", *J Ophthalmol*, vol. 2014, pp. 281010, 2014.

[13] P. B. Morgan, "Ocular thermography in health and disease", PhD Thesis University of Manchester, 1994.

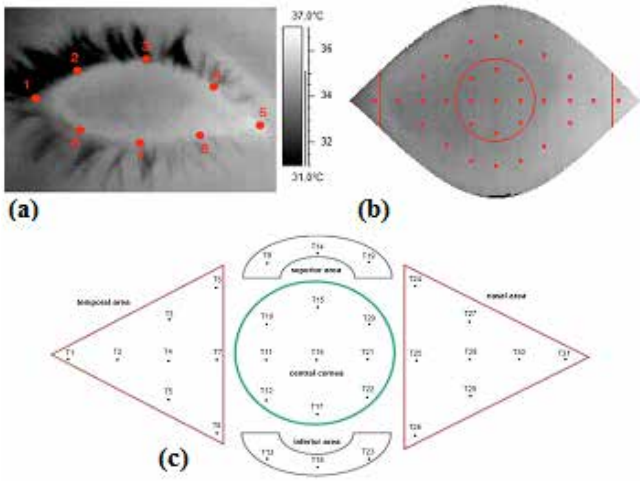

Figure 1 (a) typical thermographic image of an eye with the 8 points positioned on the contour; (b) normalized eye with the disposition of 31 temperature points; c) main areas of the eye

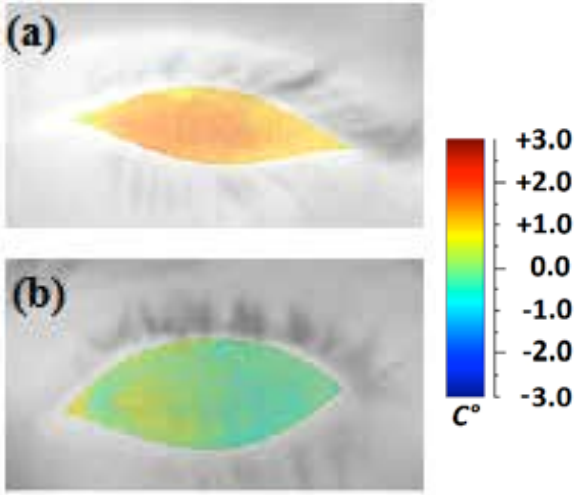

Figure 2 Thermal map of (a) MAFO's eye, (b) SAMA's eye

An adaptive BCI based on Motor Imagery

V. Mondini[1], A.L. Mangia[1], and A. Cappello[1]
[1] *Department of Electrical, Electronic and Information Engineering (DEI), University of Bologna, Cesena, Italy*

***Abstract*—In the present work, we developed an EEG-based Brain-Computer Interface which allows a subject to control the flexion-extension of a one degree of freedom (1DOF)-modelled arm through left- vs right-hand motor imagery. The presented system aimed to be a plug and play, fully automated device, which does not need the supervision of experts. In particular, an automated adaptive strategy, used to update the system's parameters in order to follow the subject's evolution, was developed. The system was online tested on 10 healthy subjects, seven of which gained control over the BCI in just three days.**

***Keywords*—BCI, EEG, adaptive system, CSP.**

I. Introduction

A Brain-Computer Interface (BCI) is a system creating a direct communication channel between the brain and the outside [1]. BCIs rely both on invasive and non-invasive techniques and, among the non-invasive ones, EEG-based BCIs are the most widespread [1]. One of the challenges of EEG-based BCIs is the non-stationary nature of EEG [2]. In particular, feedback training can modify the subject's EEG patterns with respect to the non-feedback data used to estimate the classifier, so an adaptation of the system's parameters might be useful.

In the present work, we developed an EEG-based BCI system, which allows a subject to control the flexion-extension of a 1DOF-modeled arm on the screen through left or right hand motor imagery (MI). The first aim of the work was to build up a system suitable for working like in real operating conditions: this means it should be completely automated, simple to use, flexible, plug and play, and it should not need the supervision of experts. Also, the system should be able to recognise a particular mental state whenever it occurs, instead of being optimized for a particular time-point. The second aim was to implement an adaptive strategy, able to deal with the feedback training-induced nonstationarities.

II. Methods

A. Signal acquisition and processing

The EEG signal was recorded from 11 electrodes (Fc5, Fc1, C3, Cp5, Cp1, Cz, Fc2, Fc6, C4, Cp2, Cp6), placed over the sensorimotor areas according to the international 10-20 system. Pre-processing steps included CAR re-referencing and temporal filtering in the 8-30Hz band. After pre-processing, the Common Spatial Pattern (CSP) [3] method was used for feature extraction. The CSP algorithm finds the matrix **W** which maps the recorded EEG multi-channel signals (**X**) in a new space, where the data show maximum difference in variance between the two classes (**Z**):

$$Z = W \cdot X \quad (1)$$

The log-transformed normalized variances of the time-series in the first and last two rows of **Z** were selected as features, and were later used to train a linear Support Vector Machine (SVM) classifier [4].

B. The online BCI system

The developed system, based on LabVIEW 2011, had a modular structure and was organised into three modules: *Training* (*T*), *Training&Updating* (*U*), *Classification* (*C*). The three modules were designed to be assembled together to set up a typical training session.

T module was designed to be run at the beginning of a training session, and it is necessary to make a first estimation of the **W** matrix and the SVM parameters. When *T* starts, an upward/downward pointing arrow appears on the screen over the modelled arm, and the subject is requested to imagine right/left hand movement depending on the direction of the arrow. Each arrow remains visible for 10s, during which sustained MI is requested. 2s-long EEG portions are extracted every 0.5s, and they are used for estimating **W** and training the classifier. Even though no feedback is given in this phase, *T* lasts for less than 3 minutes.

U module was designed to be run after *T* and reiterated several times. The main difference with respect to *T* is that feedback (i.e. the model's movement) is provided, permitting the subject to gain control over the BCI. At the end of each *U* repetition, the system automatically selects the "best" EEG portions depending on the given MI instruction and the classifier's output (class and distance from the separation hyperplane), and updates the system's parameters in order to follow the subject's evolution. In particular, after selecting the "best" portions (B) of the current *U* repetition, the system i) updates **W** using the B ii) remaps the old training set and B according to the new **W** iii) replaces the oldest elements of the training set with the ones in B and iv) retrains the SVM classifier. These steps are also summarized in Fig. 1.

At the end of each *U* repetition the classification accuracy, computed as the ratio between correctly classified EEG portions and the total number of processed ones, is evaluated.

In case average accuracy is too low (<40% in the last 3 *U* repetitions), *T* module is automatically repeated in order to reset the system's parameters (and to allow the subject to try a different imagination strategy). On the other hand, as soon as the subject proves to be skilled enough (>70% in the last 6 *U* repetitions), the system automatically switches to *C* module.

C module was designed to finally test the ability of the subject to control the system, through the reaching of some ball-shaped targets on the screen. In *C* module, the system's parameters are no longer updated.

C. Experimental setup

The system was online tested on ten healthy voluntary subjects (S01-S10). Only S01 and S04 had previous MI

experience. Each subject participated in 6 sessions of training (2 sessions per day). Each training session was composed by one initial *T* followed by a maximum of 16 *U* repetitions. As explained in the previous section, depending on the subject's performance, *T* could be repeated in the middle of a session, and *C* could be reached from 6 *U* repetitions on. In case *C* phase was reached, the session immediately concluded. Otherwise, the session was considered to be concluded after the 16 *U* repetitions.

D. System's evaluation

For each subject and session, besides the average accuracy we also evaluated chance level p_0 [5] and peak accuracy [6]. We compared each average accuracy with its p_0, evaluating the significance (α=0.05) of the difference via confidence intervals [5].

To evaluate the improvements in the subjects' performances, we tested the significance of the difference in both peak and average accuracy between their first and last session.

To finally evaluate the ability of the system to correctly classify the new data in every time-point and not specifically in a little temporal window, we computed the accuracy curves [6] over the trial period in the last session of each subject. We evaluated the grand average accuracy curve across subjects, and report here its mean and standard deviation.

III. Results and discussion

Seven out of ten subjects reached the criterion level of 70% (a commonly used threshold to consider adequate BCI control) with both peak and average accuracy, so they gained control over the BCI in just three days. Moreover, subjects S01-S03 reached peak accuracies over 90% in their last session. On the other hand, subjects S08-S10 did not reach the criterion level throughout the six sessions, but at least for S08 and S09 the average classification accuracy was most of the times significantly greater than chance (Fig. 2). The result is also in line with the well-known phenomenon of BCI illiteracy, which is that BCI control doesn't work for a non-negligible portion of users (15% to 30%) [7].

Despite the results of S08-S10, all the subjects increased their performance (both considering peak and average accuracy) between their first and last session, and the increase was statistically significant over the whole group ($p<0.01$).

As regards the ability of the system to evenly recognise every time-point of the trial, we obtained a grand average accuracy curve across subjects in their last session with a mean of 69.35% and a standard deviation of only 1.53%. The fact that the system is not optimized for any specific time-segment makes it suitable for recognizing a mental state whenever it occurs. The result is enhanced by the longer duration of our trial with respect to other studies [8].

The main qualities of the presented system concern, first of all, its automaticity: it does not need the supervision of experts, since it automatically regulates its parameters and switches between the modules depending on the subject's performances. Secondly, the system is not optimized for any specific time-segment, which makes it more suitable for working like in a real operating condition. Thirdly, thanks to its modular structure, the system is very flexible.

The main limitations of this system are i) that it isn't able to reduce BCI illiteracy respect to literature [7] and ii) that it doesn't assure a complete protection against artefacts. The problem of reducing BCI illiteracy has been previously investigated [9], but the cited system used an higher coverage setup (48 electrodes). Potentially, our system could represent a valiant portable alternative, once the "illiterate" subject has gained enough control with an higher coverage approach. As regards the second limitation, the inclusion of an online artefact detection algorithm, in order to exclude artefactual data when updating the system's parameters, could represent a possible extension.

IV. Conclusion

In the present study, we developed a fully automated, plug and play and adaptive BCI system to control a 1DOF-modeled arm using MI. The system was online tested on ten subjects, seven of which reached the criterion level of 70%, both with peak and average accuracy in three days. Despite these results, the system still presents the limitation of not being completely robust against EEG artefacts. The inclusion of an artefact recognition algorithm should improve the system's stability and the feedback quality.

References

[1] L. F. Nicolas-Alonso e J. Gomez-Gil, «Brain computer interfaces, a review», *Sensors*, vol. 12, n. 2, pagg. 1211–1279, 2012.

[2] A. Schlögl, C. Vidaurre, e K.-R. Müller, «Adaptive methods in bci research-an introductory tutorial», in *Brain-Computer Interfaces*, Springer, 2010, pagg. 331–355.

[3] Z. J. Koles, M. S. Lazar, e S. Z. Zhou, «Spatial patterns underlying population differences in the background EEG», *Brain Topography*, vol. 2, n. 4, pagg. 275–284, giu. 1990.

[4] C. J. C. Burges, «A Tutorial on Support Vector Machines for Pattern Recognition», *Data Mining and Knowledge Discovery*, vol. 2, n. 2, pagg. 121–167, giu. 1998.

[5] M. Billinger, I. Daly, V. Kaiser, J. Jin, B. Z. Allison, G. R. Müller-Putz, e C. Brunner, «Is it significant? Guidelines for reporting BCI performance», in *Towards Practical Brain-Computer Interfaces*, Springer, 2013, pagg. 333–354.

[6] J. Faller, T. Solis-Escalante, U. Costa, E. Opisso, J. Medina, R. Scherer, e G. R. Muller-Putz, «Online co-adaptive brain-computer interfacing: Preliminary results in individuals with spinal cord injury», in *Neural Engineering (NER), 2013 6th International IEEE/EMBS Conference on*, 2013, pagg. 977–980.

[7] T. Dickhaus, C. Sannelli, K.-R. Müller, G. Curio, e B. Blankertz, «Predicting BCI performance to study BCI illiteracy», *BMC Neuroscience*, vol. 10, n. Suppl 1, pag. P84, 2009.

[8] J. Faller, C. Vidaurre, T. Solis-Escalante, C. Neuper, e R. Scherer, «Autocalibration and recurrent adaptation: towards a plug and play online ERD-BCI», *Neural Systems and Rehabilitation Engineering, IEEE Transactions on*, vol. 20, n. 3, pagg. 313–319, 2012.

[9] C. Vidaurre e B. Blankertz, «Towards a cure for BCI illiteracy», *Brain topography*, vol. 23, n. 2, pagg. 194–198, 2010.

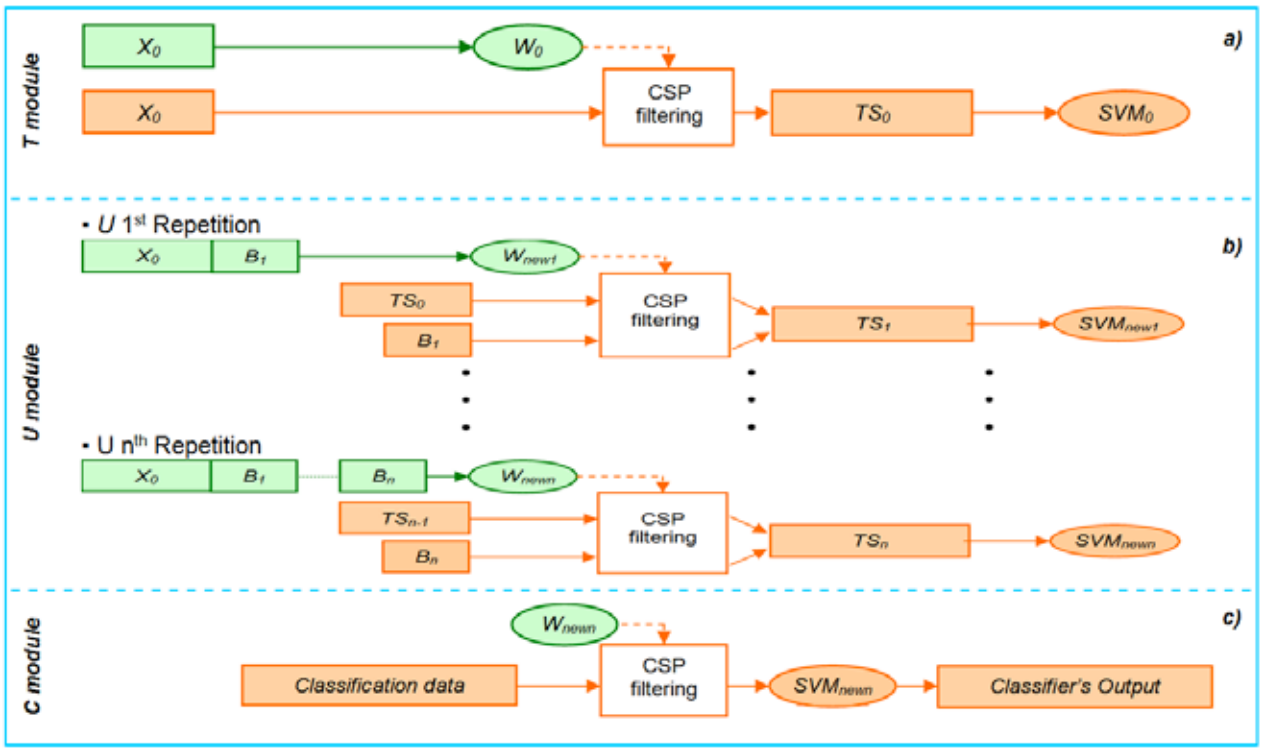

Fig. 1. A conceptual schema describes the evaluation/use of **W** matrix and SVM classifier in the three modules. In *a*) the first setting up of **W** and SVM, starting from the time-domain EEG signal (X_0), in *T* module is shown. In *b*) a diagram describes how **W** and SVM are updated in *U* modules, starting from the stored signal portions, the current B list and the previous training set. In *c*) the utilization of the definitive **W** and SVM in *C* module to classify the incoming signals and provide the feedback is shown.

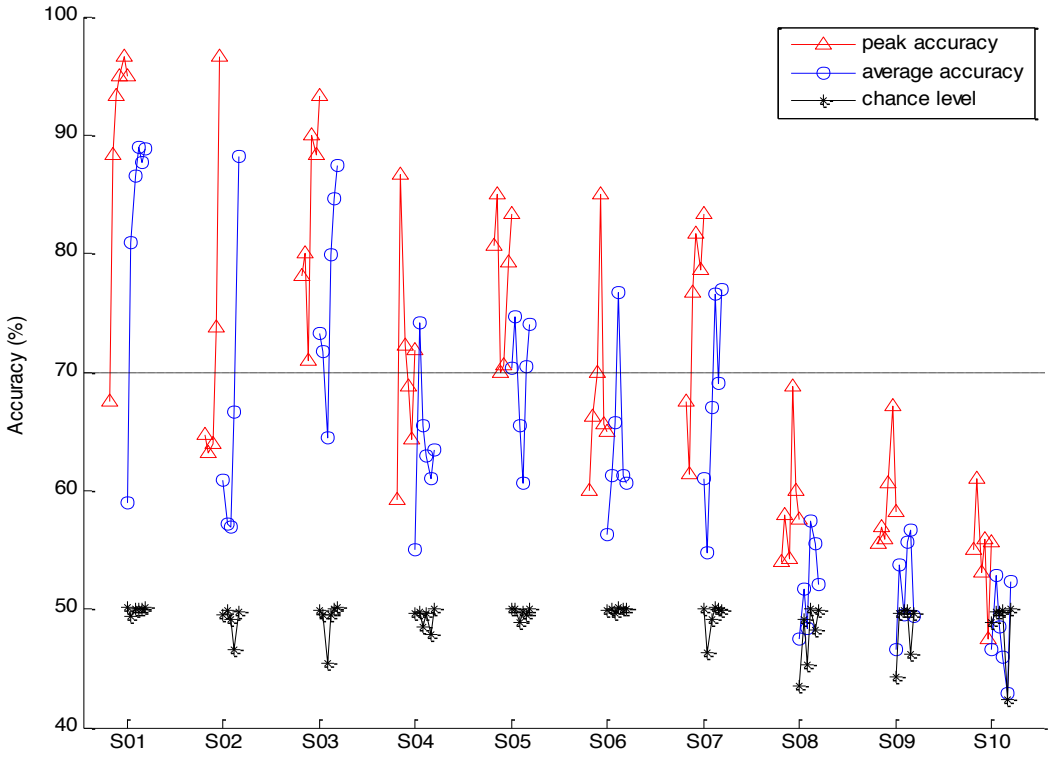

Fig. 2. The picture shows, for each subject, the trends over the six sessions for peak accuracy (red), average accuracy (blue) and chance level p0 (black) are shown. Since every average accuracy should be compared to the corresponding p0, the blue line of the former and the black line of the latter are aligned. A black, horizontal dashed lined indicating the criterion level of 70% is also added. For subject S02, session 6 was discarded because of artefacts in the EEG recordings.

Generic interactions between EEG global field power and end-tidal carbon dioxide to study brain-respiratory coupling

M.S. Morelli[1,2], G. Valenza[2,3], A. Greco[2,3], A. Giannoni[4], C. Passino[1,4], M. Emdin[1,4], E.P. Scilingo[2,3], L. Landini[3], N. Vanello[3]

[1] *Scuola Superiore Sant'Anna, Pisa*

[2] *Research Center "E. Piaggio", Faculty of Engineering, University of Pisa, Pisa*

[3] *Department of Information Engineering, University of Pisa, Pisa*

[4] *Fondazione Toscana Gabriele Monasterio, Pisa*

***Abstract*— To study brain-respiratory coupling the generic, i.e. linear and nonlinear, associations between electroencephalographic (EEG) global field power (GFP) in delta, theta, alpha and beta band and end tidal CO_2 ($P_{ET}CO_2$) were evaluated in healthy subjects during free breathing (FB) and breath hold (BH) tasks. The maximal information coefficient (MIC) index and the MIC-ρ^2 index (ρ is Pearson's correlation coefficient) were estimated as functions of the time lag (τ) between the two signals to evaluate the contribution of generic and "pure" nonlinear associations, respectively. The maximum MIC(τ_M) and corresponding MIC(τ_M)-$\rho(\tau_M)^2$ were compared. In delta and theta bands higher difference between the two indexes was found during BH task, while in alpha band the higher difference was found in FB task, suggesting that the contribution of linear and nonlinear interaction changes in different bands.**

***Keywords*—linear and nonlinear correlation, EEG, respiration.**

I. Introduction

Nonlinear interactions were largely studied in brain-heart coupling in physio-pathological conditions [1]. Another interesting area in which nonlinear interactions should be studied is the brain-respiratory coupling, specifically in the relationship between carbon dioxide (CO_2) variations and electroencephalographic (EEG) signals. In a recent work [2], correlational analysis between EEG global field power (GFP) in delta band and variations in end tidal CO_2 ($P_{ET}CO_2$) induced by 30 s of breath hold (BH) was performed. However, only a linear relationship between EEG and $P_{ET}CO_2$ was considered looking at the Pearson's correlation coefficient (ρ), completely neglecting nonlinear interactions.

In this work the generic interactions, i.e. linear and nonlinear, between GFP and $P_{ET}CO_2$ were studied through the maximal information coefficient (MIC) index. In particular a temporal correlation between the two signal was performed and the maximum value of MIC was considered. Moreover, the relative contribution of "pure" nonlinear effects to $P_{ET}CO_2$-GFP coupling was evaluated by studying the MIC-ρ^2 index .

II. Materials and Methods

A. Experimental protocol

Five healthy subjects (males, age 30± 6) lied down with their eyes closed, while EEG signals (64 channels Compumedics Neuroscan, SynAmps RT), exhaled CO_2 (Cosmoplus®; Novametrics) and oxygen saturation (Pulsox-7; Minolta) were recorded. The subjects performed two different tasks: a free breathing (FB) task (360 s of normal breath) and a BH task (30 s of normal breath and 30 s of BH for a total duration of 360 s). The experimental protocol was approved by the Institutional Ethical Committee.

B. EEG processing

The recorded EEG signals were analyzed using CURRY Neuroimaging Suite 7. Baseline correction and 1-30 Hz Hann band-pass filter were applied. Channels which showed poor signal-to-noise ratio and non-physiological trends were excluded from the analysis. Blink and cardiac artefacts were removed with principal component analysis. Time intervals with other kinds of irreducible artefacts were discharged. EEG global field power (GFP) in delta (1-4 Hz), theta (4-8 Hz), alpha (8-13 Hz) and beta (13-30Hz) bands was calculated using MATLAB (MathWorks, Natick, MA), as the mean EEG band power across all channels. GFP signal was then linearly detrended and resampled at 50 Hz.

C. Physiological Parameters

$P_{ET}CO_2$ was estimated from expired CO_2. During BH period $P_{ET}CO_2$ was obtained using a cubic spline model interpolation. $P_{ET}CO_2$ was linearly detrended and resampled at 50 Hz. Blood oxygen saturation level (SpO_2) was recorded to observe possible effects of the BH task.

D. Maximal Information Coefficient (MIC)

MIC [3] was calculated to quantify the generic relationship between GFP and $P_{ET}CO_2$. Specifically, MIC as functions of different time lags applied between GFP and $P_{ET}CO_2$ (MIC(τ)) was considered (see Appendix for details) shifting the $P_{ET}CO_2$ with respect to GFP between -30 and 30 s. Moreover, the MIC(τ)-$\rho(\tau)^2$ index was used to evaluate "pure" nonlinear interactions. At the time delay in which maximum MIC(τ) was found (τ_M), the comparison between MIC(τ_M) and corresponding MIC(τ_M)-$\rho(\tau_M)^2$ was performed in both task.

III. Results

A. Variation on physiological parameters induced by the tasks

No significant changes of SpO_2 were observed during FB and BH tasks. At a group-level, the observed maximum variations of CO_2 during FB was 6.5 ± 3.0 mmHg, while during the BH task was 11.7 ± 2.9 mmHg.

B. Evaluation of brain-respiratory coupling using MIC and MIC-ρ^2 indexes

MIC coefficients between EEG and $P_{ET}CO_2$ were found to be statistically significant ($p<0.05$) for all time lags. Table I and Table II show the results of the statistical comparisons between FB and BH sessions on MIC(τ_M) and MIC(τ_M)-$\rho(\tau_M)^2$ values, respectively. Values are reported for each subject and for each frequency band.

TABLE I
MAXIMUM MIC INDEX (MIC(τ_M))

Sub	*Delta Band*		*Theta Band*		*Alpha Band*		*Beta Band*	
	FB	*BH*	*FB*	*BH*	*FB*	*BH*	*FB*	*BH*
1	0.27	0.61	0.24	0.39	0.39	0.42	0.27	0.49
2	0.22	0.44	0.25	0.48	0.23	0.36	0.27	0.48
3	0.45	0.37	0.33	0.44	0.39	0.44	0.49	0.33
4	0.33	0.77	0.34	0.42	0.40	0.42	0.41	0.35
5	0.30	0.46	0.40	0.46	0.40	0.47	0.40	0.46

TABLE II
MIC(τ_M) -$\rho(\tau_M)^2$

Sub	*Delta Band*		*Theta Band*		*Alpha Band*		*Beta Band*	
	FB	*BH*	*FB*	*BH*	*FB*	*BH*	*FB*	*BH*
1	0.25	0.15	0.15	0.26	0.24	0.34	0.06	0.31
2	0.19	0.32	0.14	0.24	0.06	0.36	0.25	0.11
3	0.44	0.17	0.26	0.22	0.39	0.43	0.49	0.23
4	0.32	0.27	0.32	0.42	0.31	0.36	0.35	0.34
5	0.30	0.36	0.39	0.41	0.30	0.39	0.17	0.39

In Figures 1-4 the graphical representations of the results showed in Table I and Table II were reported for delta, theta, alpha and beta band in FB ((a) panel) and BH tasks ((b) panel). Moreover, to highlight the relevance of the linear contribution, the difference between MIC(τ_M) and MIC(τ_M)-$\rho(\tau_M)^2$ ((c) panel in all figures) was reported. No significant results in the differences between MIC(τ_M) and MIC(τ_M)-$\rho(\tau_M)^2$ were found, however, a possible trend of the coupling features can be observed. Specifically, in delta band (Fig. 1(c)) the difference between MIC(τ_M) and MIC(τ_M)-$\rho(\tau_M)^2$ is lower during FB task with respect to the BH task. In theta band (Fig. 2(c)), a similar trend was observed except for subject 4. On the other hand, in alpha band (Fig. 3(c)) the opposite behavior was observed, that is the higher difference between MIC(τ_M) and MIC(τ_M)-$\rho(\tau_M)^2$ is present during FB task respect to BH task. In beta band (Fig.4(c)) no particular trend was found.

IV. DISCUSSION AND CONCLUSION

In this work, the linear and nonlinear interactions between EEG-GFP in delta, theta, alpha and beta bands and $P_{ET}CO_2$ were studied in healthy subjects during a FB task and a BH task. To achieve this goal, MIC (a generic correlation index) and MIC-ρ^2 (a "pure" nonlinear correlation index) were estimated. MIC index could capture a wide range of nonlinear associations [3] and it was proven to be useful to show nonlinearity in a large number of study involving brain coupling [4][5][6]. The differences between MIC and MIC-ρ^2 in the two task were compared between the two tasks and statistical significance was calculated. The no significance of results can be justified considering the small number of subjects enrolled. In fact, the Wilcoxon test has a minimum reachable p-value of 0.062 when the number of paired samples is equal to 5, as in our case [7]. Nevertheless, some interesting points must be considered. Specifically, in delta band an higher difference between the two indexes was observe during BH task respect to FB task in all subjects, suggesting that during BH task an higher influence of the linear associations is present. The same behaviour was observed in theta band in 4 subjects on 5. In the alpha band the higher difference was shown during FB task suggesting that, differently from delta, the linear associations are more present during FB. All this results demonstrated, as expected, that brain-respiratory coupling is regulated both by linear and nonlinear interactions. We are conscious that these results are preliminary and limited by the low number of subjects, but we are convinced that they can provides important hints in the understanding of generic brain-respiratory coupling not only during BH task, but also during FB.

APPENDIX

A. MIC theory

Given two variable data x and y, the relationship between each other can be studied by partitioning the data scatter plot at different grid (G) sizes. If I_G is the mutual information of the probability distribution on a particular grid, m_{xy} represents the highest normalized mutual information corresponding to each x,y grid and can be derived as:

$$m_{x,y} = \max\{I_G\} / \log \min\{x, y\} \qquad (1)$$

Considering that samples size is n and B is a function of the sample size ($B=n^{0.6}$), MIC is defined as [3]

$$MIC = \max_{xy<B}(m_{x,y}) \qquad (2)$$

A MIC function (MIC(τ)) can be defined as the measure of similarity between two variables x and y as a function of the lag (τ) of one relative to the other and can be formally defined as:

$$MIC(\tau) = \max_{xy<B,\tau}(m_{x(\tau),y(t-\tau)}) \qquad (3)$$

REFERENCES

[1] G. Valenza, N. Toschi, and R. Barbieri, "Uncovering Brain-Heart Information through Advanced Signal and Image Processing," *Philos. Trans. R. Soc. A*, vol. 347, no. 2067, 2016.

[2] M. S. Morelli, N. Vanello, A. Giannoni, F. Frijia, V. Hartwig, M. Maestri, E. Bonanni, L. Carnicelli, V. Positano, C. Passino, M. Emdin, and L. Landini, "Correlational analysis of electroencephalographic and end-tidal carbon dioxide signals during breath-hold exercise," in *2015 37th Annual International Conference of the IEEE Engineering in Medicine and Biology Society (EMBC)*, 2015, pp. 6102–6105.

[3] D. N. Reshef, Y. A. Reshef, H. K. Finucane, S. R. Grossman, G. McVean, P. J. Turnbaugh, E. S. Lander, M. Mitzenmacher, and P. C. Sabeti, "Detecting novel associations in large data sets.," *Science*, vol. 334, no. 6062, pp. 1518–24, Dec. 2011.

[4] Z. Zhang, S. Sun, M. Yi, X. Wu, and Y. Ding, "MIC as an appropriate method to construct the brain functional network.," *Biomed Res. Int.*, vol. 2015, p. 825136, Jan. 2015.

[5] L. Dong, D. Gong, P. A. Valdes-Sosa, Y. Xia, C. Luo, P. Xu, and D. Yao, "Simultaneous EEG-fMRI: trial level spatio-temporal fusion for hierarchically reliable information discovery.," *Neuroimage*, vol. 99, pp. 28–41, Oct. 2014.

[6] G. Valenza, G. Alberto, C. Gentili, L. Antonio, L. Sebastiani, D. Menicucci, A. Gemignani, and E. P. Scilingo, "Combining EEG Activity and Instantaneous Heart Rate for Assessing Brain-Heart Dynamics during Visual Emotional Elicitation in Healthy Subjects," *Philos. Trans. R. Soc. A*, vol. In Press, 2016.

[7] T. Glover and K. Mitchell, *An Introduction to Biostatistics: Third Edition*. Waveland Press, 2015.

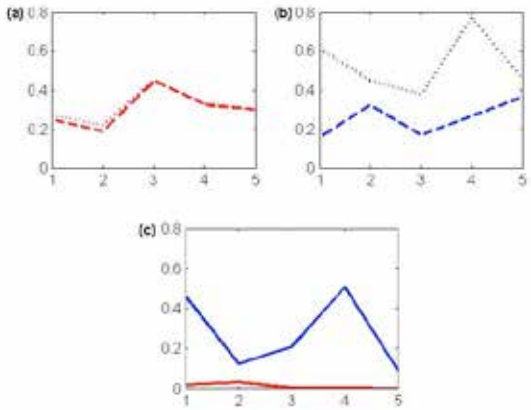

Fig. 1. MIC(τ_M), MIC(τ_M)-$\rho(\tau_M)^2$ and differences between the two index calculated in delta band during FB (red) and BH (blue). (a) Values of MIC(τ_M) (dotted line) and MIC(τ_M)-$\rho(\tau_M)^2$ (dashed line) during FB in five healthy subject; (b) Values of MIC(τ_M) (dotted line) and MIC(τ_M)-$\rho(\tau_M)^2$ (dashed line) during BH in five healthy subject; (c) Differences between MIC(τ_M)and MIC(τ_M)-$\rho(\tau_M)^2$in the two task (p-value=0.06).

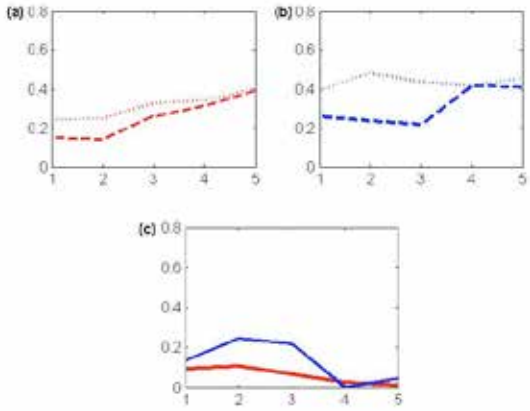

Fig. 2. MIC(τ_M), MIC(τ_M)-$\rho(\tau_M)^2$ and differences between the two index calculated in theta band during FB (red) and BH (blue). (a) Values of MIC(τ_M) (dotted line) and MIC(τ_M)-$\rho(\tau_M)^2$ (dashed line) during FB in five healthy subject; (b) Values of MIC(τ_M) (dotted line) and MIC(τ_M)-$\rho(\tau_M)^2$ (dashed line) during BH in five healthy subject; (c) Differences between MIC(τ_M)and MIC(τ_M)-$\rho(\tau_M)^2$in the two task (p-value=0.1).

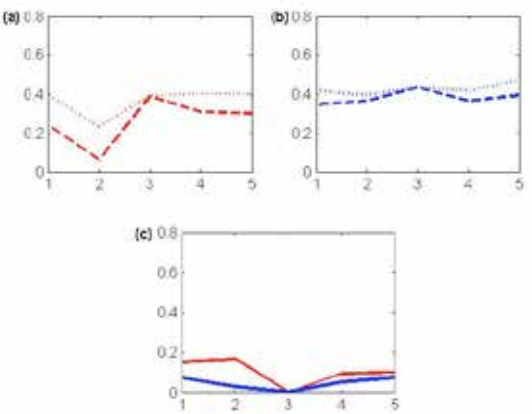

Fig. 3. MIC(τ_M), MIC(τ_M)-$\rho(\tau_M)^2$ and differences between the two index calculated in alpha band during FB (red) and BH (blue). (a) Values of MIC(τ_M) (dotted line) and MIC(τ_M)-$\rho(\tau_M)^2$ (dashed line) during FB in five healthy subject; (b) Values of MIC(τ_M) (dotted line) and MIC(τ_M)-$\rho(\tau_M)^2$ (dashed line) during BH in five healthy subject; (c) Differences between MIC(τ_M)and MIC(τ_M)-$\rho(\tau_M)^2$in the two task (p-value=0.06).

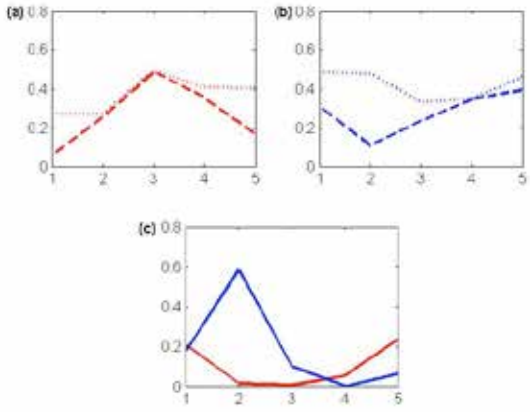

Fig. 4. MIC(τ_M), MIC(τ_M)-$\rho(\tau_M)^2$ and differences between the two index calculated in beta band during FB (red) and BH (blue). (a) Values of MIC(τ_M) (dotted line) and MIC(τ_M)-$\rho(\tau_M)^2$ (dashed line) during FB in five healthy subject; (b) Values of MIC(τ_M) (dotted line) and MIC(τ_M)-$\rho(\tau_M)^2$ (dashed line) during BH in five healthy subject; (c) Differences between MIC(τ_M)and MIC(τ_M)-$\rho(\tau_M)^2$in the two task (p-value=1).

Movement analysis of the upper limb during common daily actions in Multiple Sclerosis subjects

L. Pellegrino*[1], G. Stranieri*[1], G. Salis[1], A. Tacchino[2], G. Brichetto[2], M. Casadio[1]
[1] *Dept. Informatics, Bioengineering, Robotics and Systems Engineering, University of Genoa, Italy*
[2] *Italian Multiple Sclerosis Foundation (FISM), Genoa, Italy*
** Equal contribution*

***Abstract*—The goal of this study was to investigate the movement and muscle activity of the right dominant upper limb during common activities of daily life in people with Multiple Sclerosis (PwMS) with low or mild-moderate level of impairments. We found significant differences in the kinematic variables, e.g. smoothness and movement duration, in PwMS with mild-moderate impairment (PwHMS) compared to both PwMS with low impairment (PwLMS) and healthy subjects (HS) when holding and lifting objects such as bottles, cups and spoons. These differences increased if the objects were not empty and were correlated to abnormal activations of the trunk muscles.**

***Keywords*—Kinematic, EMG, Multiple Sclerosis.**

I. Introduction

Multiple sclerosis (MS) is a chronic progressive disease of the central nervous system, mainly diagnosed in young age (20-40 years old), and leading to cumulative heterogeneous disability over time. Motor impairments of the upper limbs occur in 66% of people with MS [1]. The level of arm and hand functionality defines the ability to perform activities of daily living (ADL), e.g. eating and/or dressing [2]. Simple tasks, like moving an object, are based on complex muscle activation patterns that can be compromised in subjects affected by MS. This pathology leads to a reduction in muscle strength, loss of coordination, tremor and fatigue. Studies on MS have been conducted mainly on the lower limbs probably because the disease affects them earlier than the upper limbs [3], and the existence of standard protocols of gait analysis makes relatively simple a comparison with healthy subjects (HS) [4].

In this study, we defined a simple protocol in order to investigate and characterize upper limb motor performance and muscle activity in subjects affected by MS while performing ADL.

II. METHODS

A. Subjects

Twenty-one subjects with clinically definite MS (15 Female (F) and 6 Male (M), age: 52±12 years) according to McDonald criteria, and twenty-one age and sex matched (15 F and 6 M, age: 52±12 years) HS participated in this study. All HS did not present any neurological or muscular disorders. The inclusion criteria were: (i) stable phase of the disease (no relapses in the last three months), (ii) Expanded Disability Status Scale (EDSS) $\leq$ 6, (iii) presence of neurological signs and symptoms at upper limbs, (iv) right manual dominance (as evaluated with the Edinburgh Handedness Inventory). The exclusion criteria were: (i) treatment with corticosteroids within the previous three months and (ii) difficulty to understand simple instructions (Symbol Digit Modality Test (SDMT) < 20). Clinical evaluation included Modified Fatigue Impact Scale (MFIS), ABILHAND, and Nine Hole Peg Test (9HPT), which measure respectively how fatigue affects the ADL, the perceived manual ability and the fine manual dexterity. Among all MS subjects, eleven subjects had a low level of impairment at the upper limb (PwLMS), while ten subjects had a moderate level of impairment (PwHMS).

B. Experimental set-up

The instrumental apparatus consisted of a stereophotogrammetric system with eight infrared cameras ("OptiTrack Flex 13M") used to record the trajectories of reflective markers applied to the skin of the subject. Eleven markers were used: seven placed on anatomical landmarks (right and left acromion, C7, sternum, elbow, wrist and metacarpus), one on the object and the remaining markers on three corners of the table; see Fig. 1. Muscle activity was recorded with surface electrodes for electromyography (EMG) using CometaWavePlus system. Each EMG sensor was equipped with a three axial accelerometer used to synchronize the EMG and the stereophotogrammetric system. Electrodes were placed according to guidelines of the Surface Electromyography for the Non-Invasive Assessment of Muscles European Community project (SENIAM). The activities of the following 16 muscles in the right dominant arm were recorded: triceps brachii long and lateral head, biceps brachii long and short head, brachialis, brachioradialis, infraspinatus, latissimus dorsi, upper trapezius, rhomboideus major, pectoralis major, anterior, medial and posterior deltoid, flexor and extensor carpi radialis.

C. Experimental protocol

Subjects were seated on a chair in front of a table with the left hand on the left thigh and the right hand on the right corner of the table, defined as the starting position. When the operator said "Go!", the subjects had to move the right hand and grasp an object placed in a fixed position in front of her/him on the table (phase 1), to bring it to the mouth (phase 2), to place the object back in its original place (phase 3), and to return with the hand in the starting position (phase 4). The objects used in this experiment were: (i) three bottles covered with black adhesive tape and filled with sand at different levels (weight 287 g, 408 g and 785 g); (ii) a plastic cup without a handle; and (iii) a spoon placed in an empty plate. Both (ii) and (iii) were used empty or filled with water. We asked the subjects to perform the task in the most natural way. The subjects grasped the same object 10 times, interlaced by a pause of 2-4 seconds. The experimental session lasted about 1 hour.

D. Data analysis

In all tasks we focused on the analysis of the kinematic parameters of the hand movements, in particular duration and smoothness considering the marker positioned on the

subject's wrist. The marker trajectories were filtered using a 4th order Savitzky-Golay filter with a cut-off frequency of 12 Hz. For each phase of the task, we estimated the movement onset as the instant when the hand's speed exceeds 10% of the peak speed and the movement termination as the instant when the speed went below the same threshold. The movement smoothness was evaluated using the Jerk index, the square root of the jerk normalized by duration and path length [5]. For each object, to quantify changes in the kinematic parameters, we ran a repeated measures ANOVA with two within-subjects' factors: phase (1 to 4) and objects weight (empty-full or empty-half-full); and one between-subjects factor: upper limb impairment level (0, low, moderate). We set $p<0.05$ as the threshold for significance.

The EMG signals were sampled at 2kHz and filtered, to remove motion artefacts and high frequency noise, using a Butterworth band pass FIR filter with cut-off frequencies of 30 and 550 Hz. Then, the filtered signals were rectified and low-pass filtered at 6 Hz (2nd order Butterworth filter) [6].

For each subject, the EMG signals were normalized by their median values computed over all tasks (every condition and object), since this normalization is more robust against high-amplitude spikes arising from noise [7]. For each phase we evaluated the root mean square of the signal and, to quantify changes in this parameter, we ran a repeated measures ANOVA with two within-subjects' factors: phase (1 to 4) and objects weight (empty-full or empty-half-full); and one between-subjects factor: upper limb impairment level (0, low, moderate). We set $p<0.05$ as the threshold for significance.

III. RESULTS

In the first and fourth phases, we observed similar performance for all PwMS subjects and their matched controls in terms of movement duration and smoothness despite of their impairment level (Fig. 2). However, during the phases 2 and 3, when subjects respectively lifted and repositioned the objects, the performance of the three populations was significantly different both in terms of jerk index (Bottle: $p=0.03$; Cup: $p=0.002$ and Spoon: $p=0.001$) and movement duration (Bottle: $p=0.017$; Cup: $p=0.005$ and Spoon: $p=0.010$). In fact movement smoothness and duration of the PwMS were smaller with respect to the one of healthy subjects.

Post hoc analysis highlighted not only a difference between controls and PwHMS (Fig. 2), but also between PwLMS and PwHMS (Fig. 2 panel B).

The duration of movement increased when the lifted object was full with respect to empty condition in all group during phase 2 (Fig. 2 panel A. Bottle: HS, $p=0.006$; PwLMS, $p=0.006$ and PwHMS, $p=0.025$; Cup: HS, $p<0.001$; PwLMS, $p<0.001$ and PwHMS, $p=0.001$; Spoon: HS, $p<0.001$; PwLMS, $p<0.001$ and PwHMS, $p=0.003$) and phase 3 (Bottle: HS, $p=0.049$; PwLMS, $p=0.03$ and PwHMS, $p<0.001$; Cup: HS, $p<0.001$; PwLMS, $p<0.001$ and PwHMS, $p<0.001$; Spoon: HS, $p<0.001$; PwLMS, $p<0.001$ and PwHMS, p=n.s.). The movement smoothness decreased when the lifted object was full both during phase 2 (Bottle: HS, $p=0.048$; PwLMS, $p=0.045$ and PwHMS, $p=0.048$; Cup: HS, p=n.s.; PwLMS, p=n.s. and PwHMS, $p=0.0028$; Spoon: HS, p=n.s.; PwLMS, $p=0.011$ and PwHMS, $p<0.001$) and phase 3 (Bottle: HS, $p=0.046$; PwLMS, $p=0.041$ and PwHMS, $p=0.02$; Cup: HS, p=n.s; PwLMS, $p=0.02$ and PwHMS, $p<0.001$; Spoon: HS, $p=0.002$; PwLMS, $p<0.001$ and PwHMS, $p=0.001$). These changes between full and empty objects were different across subject populations ("weight x impairment level"- Jerk index: Bottle $p=0.030$, Cup $p<0.001$, Spoon $p<0.001$; movement duration: Bottle $p=0.043$, Cup and Spoon p=n.s).

As regard the EMG signals, we observed significant differences among our subject populations in the trunk muscles. The RMS of the latissimus dorsi (LAT) and of infraspinatus (INFRA), indeed, in phase 2 and 3, for all groups increased between the empty and full conditions(LAT-Phase2: Bottle: $p=0.02$; Cup and Spoon: p=n.s.; Phase 3: Bottle: $p=0.02$; Cup: $p<0.001$ and Spoon: $p=0.045$; INFRA-Phase2: Bottle: $p<0.001$; Cup: p=n.s., Spoon: $p<0.001$; Phase 3: Bottle: $p<0.001$; Cup and Spoon: $p=0.045$); see Fig. 3 panel A, but the modulation of the muscle activations in phase 2 and 3 with respect to phase 1 and 4 (LAT: Bottle: $p=0.05$; Cup: $p=0.05$, Spoon: p=n.s.; INFRA: Bottle: p=n.s., Cup: $p=0.004$, Spoon: p=n.s.) was different in the PwHMS compared to the other two populations. Conversely, we found no significant difference among the subject populations for the arm muscles; see Fig. 3 panel B

IV. CONCLUSION

When interacting with objects more impaired PwMS had a significant reduction of smoothness and an increase of the duration of the movements compared with both HS and PwMS with low level of impairment. These differences increased when the objects were full and were correlated with abnormal muscular activation in the trunk muscles. This result can be correlated to the high level of impairment in the lower limbs of these subjects. This impairment may affect also the trunk muscles reducing the core stability and determining worse performance of the upper limb.

ACKNOWLEDGEMENT

The research was supported by the Italian Multiple Sclerosis Foundation (FISM, 2013- Cod. 2013/R/5) and Marie Curie Integration Grant FP7-PEOPLE-2012-CIG-334201 (REMAKE).

REFERENCES

[1] Spooren, A.I., A.A. Timmermans, and H.A. Seelen, *Motor training programs of arm and hand in patients with MS according to different levels of the ICF: a systematic review.* BMC Neurol, 2012. **12**: p.49.

[2] Yozbatiran, N., Baskurt F., Baskurt Z., Ozakbas S., Idiman E., *Motor assessment of upper extremity function and its relation with fatigue, cognitive function and quality of life in multiple sclerosis patients.*J Neurol Sci, 2006. **246**(1-2): p. 117-22.

[3] Benedetti, M.G., et al., *Gait abnormalities in minimally impaired multiple sclerosis patients.* Mult Scler, 1999. **5**(5): p. 363-8.

[4] Givon U., Zeilig G., and Achiron A., *Gait analysis in multiple sclerosis: characterization of temporal-spatial parameters using GAITRite functional ambulation system.* Gait Posture, 2009. **29**(1): p. 138-42.

[5] Teulings H.L., Contreras-Vidal J.L., Stelmach G.E., Adler C.H., *Parkinsonism reduces coordination of fingers, wrist, and arm in fine motor control.* Exp Neurol, 1997. **146**(1): p. 159-70.

[6] Kleissen, R. F. M., et al. *"Electromyography in the biomechanical analysis of human movement and its clinical application."* Gait & posture 8.2 (1998): 143-158.

[7] Cheung, V. C., Piron, L., Agostini, M., Silvoni, S., Turolla, A., & Bizzi, E. (2009). *Stability of muscle synergies for voluntary actions after cortical stroke in humans.* Proceedings of the National Academy of Sciences, *106*(46), 19563-19568.

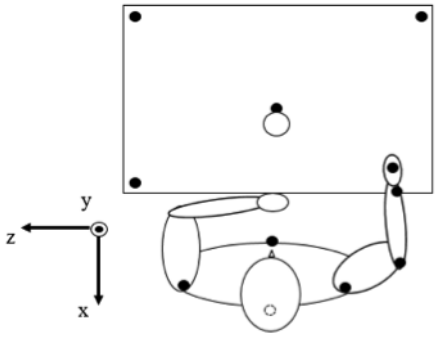

Fig. 1. Top view of the set-up with the XYZ coordinate system. The subject is represented with the arm in the initial position and the marker sites are shown as black dots.

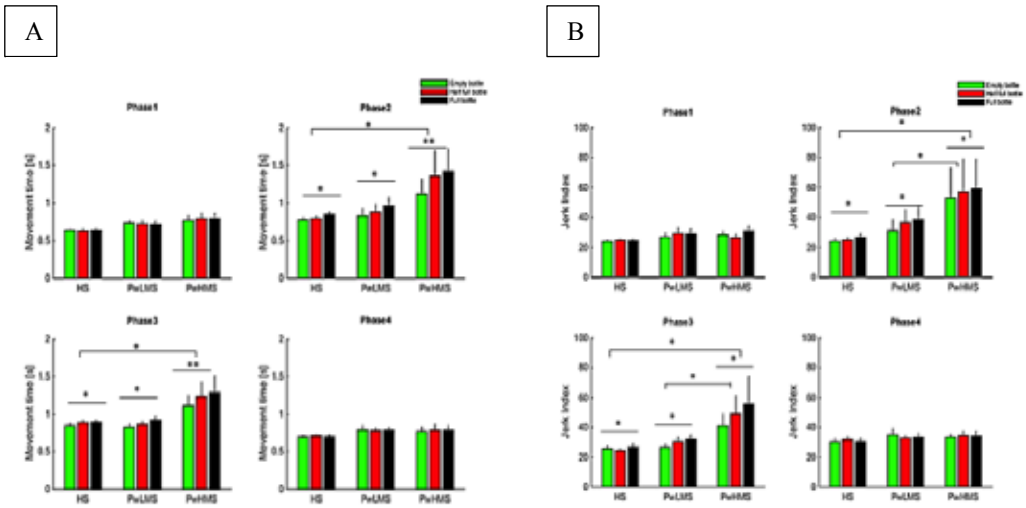

Fig. 2. Movement time (panel A) and Jerk index (panel B) in the 4 phases during the task with the bottle. Group subjects (HS: control subjects, PwLMS: person with a low level of impairment at the upper limb, PwHMS: person with a high level of impairment at the upper limb) are reported on the x-axis. Error bars denote the standard error. * indicates that the differences were statistically significative (post-hoc Fisher's LSD test).

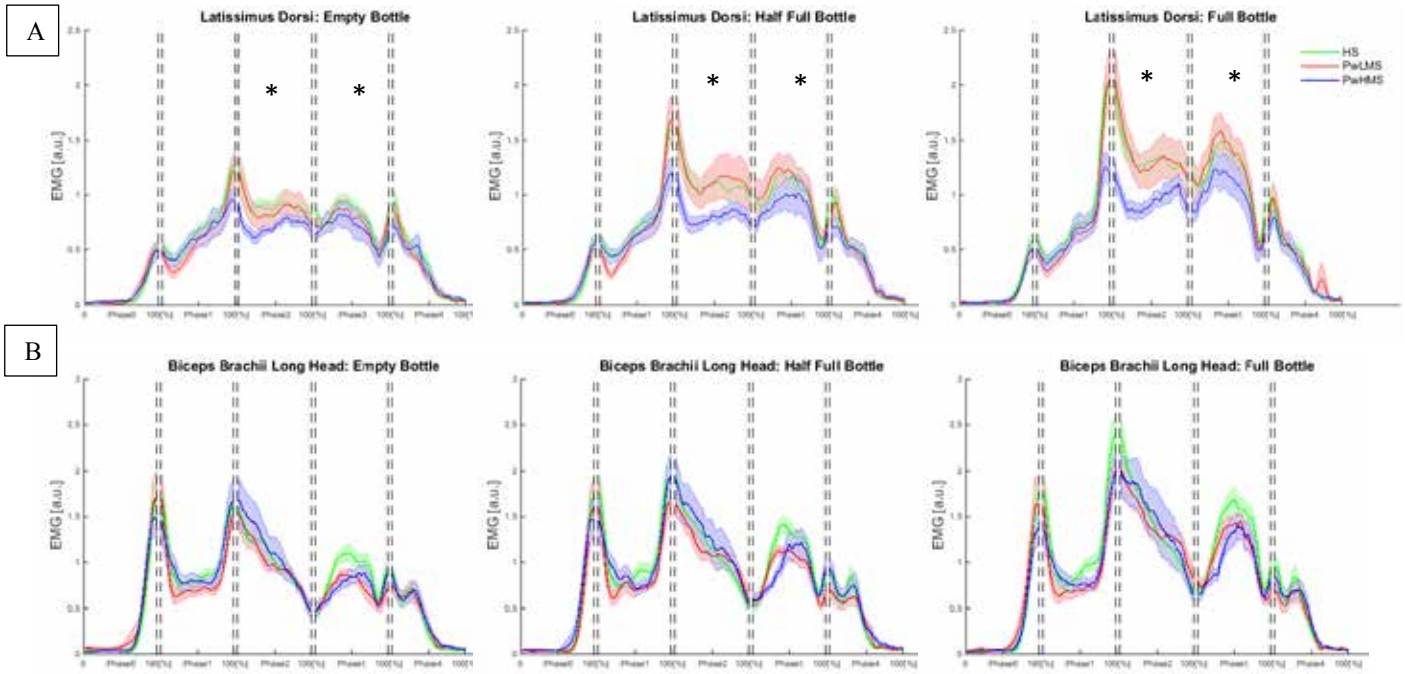

Fig. 3. EMG signals of latissimus dorsi (panel A) and biceps long head (panel B) during the task with the bottle. Green lines indicate HS, red lines PwLMS and blue lines PwHMS.

Statistical evaluation of changes in brain connectivity at the single subject level

M. Petti[1,2], J. Toppi[1,2], F. Pichiorri[2], F. Babiloni[2,3], F. Cincotti[1,2], D. Mattia[2] and L. Astolfi[1,2]
[1]Dept. of Computer, Control and Management Engineering, Sapienza University of Rome
[2] NEILab, IRCSS Fondazione Santa Lucia, Rome, Italy
[3] Dept. Molecular Medicine, Sapienza University of Rome

***Abstract*—Assessing changes in brain connectivity at the single subject level is a non-trivial question, with an impact in many applications. The aim of this study is to address the statistical validation of brain network changes at the single subject level, by means of a resampling approach exploiting a Jackknike procedure. Such approach was applied to multi-trials EEG datasets acquired from 12 stroke patients during the execution of a motor task before and after a 1-month training based on Motor Imagery with Brain Computer Interface support. Results confirmed that the proposed method allows to extract stable and reliable patterns of the network reinforced after the intervention, showing a significant correlation between graph measures of motor function network organization and the clinical outcome indicated by clinical scales.**

***Keywords*— Effective Connectivity, Partial Directed Coherence, EEG, Stroke.**

I. Introduction

In neuroscience, the concept of brain connectivity is crucial to understand how communication between cortical regions is organized. From EEG signals recorded on the scalp, *effective connectivity* [1] can be estimated by means of Partial Directed Coherence (PDC) [2]. Several studies proved that PDC technique is a powerful estimator of brain connectivity and it can be applied for the investigation of different cerebral functions in physiological and pathological conditions [3]. Usually, all the studies performed group analyses: when the aim of the study is to evaluate the effects of a treatment, and thus the possible recovery of a damaged brain function (*plasticity phenomena*), group analysis is a powerful method to assess the consistent effects of a therapy. On the other hand, the specificity of each patient's conditions leads to a difficulty in building homogeneous experimental groups, and specific effects at the single patient level may be hidden.

In this study we statistically evaluated at the single subject level the changes induced by a rehabilitative training on brain connectivity. To this purpose, we applied a resampling approach (jackknife, [4]) to multi-trials EEG data, generating a distribution of datasets in each single condition, to be then subjected to connectivity estimation to provide a distribution of the estimator in each condition. We used task-related EEG data recorded on subacute stroke patients in two recording sessions: one preceding and one following a rehabilitative intervention based on motor imagery with the support of Brain Computer Interfaces (BCI) [3]. In particular, for each patient, we compared the pattern underlying the attempted movement of the hand affected by the stroke before and after the intervention, with particular interest to the connectivity network that the subjects significantly reinforced after the training. Then we performed a correlation analysis to investigate the existence of a relationship between the organization of the reinforced pattern (measured by means of graph indices) and the functional outcome measures specific for the upper limb motor recovery.

II. Methods

A. Resampling approach: Jackknife

Given an EEG dataset characterized by a certain number of trials, Jackknife performs leave-*N*-out on trials, where *N* is a percentage of trials to be randomly excluded from the estimation. Repeating the procedure for *K* replications, we can obtain *K* datasets to be subjected to connectivity estimation. Here, we set the parameters to the following values: $K = 200$ replications, percentage of excluded trials $N = 50\%$.

B. Experimental design

EEG signals were acquired from 12 subacute stroke patients (mean age, 62.1 ± 9.9 years; 6 left/6 right affected hemisphere). All the patients underwent standard motor rehabilitation and a newly proposed add-on intervention based on a BCI-assisted upper limb motor imagery training [3]. Immediately before and after the training intervention, the patients were subjected to two screening sessions (PRE and POST) including clinical assessment and EEG recordings during the attempt of a simple movement by the hand affected by the motor deficit. The clinical assessment included the evaluation of the upper limb function by means of *Fugl-Meyer Assessment* (FMA, upper limb section).

C. Signal processing

After data preprocessing (down-sampling at 100 Hz, band pass filtering (1-45 Hz) and artifact rejection), we obtained for each patient and each condition (PRE and POST) an EEG dataset consisting of approximately 60 artifact-free trials related to the motor task. Then we applied the Jackknife method. Brain connectivity was estimated from 29 channels by means of PDC [2]. The achieved estimations were averaged within 5 frequency bands: theta (4-7 Hz), alpha (8-12 Hz), beta1 (13-21 Hz), beta2 (22-30 Hz) and gamma (31-45 Hz).

Once the patterns distributions were obtained for each patient, condition and frequency band, we performed the statistical comparison between PRE and POST conditions. In particular, to evaluate the effects of the rehabilitative intervention, we focused on the pattern that was significantly reinforced for each patient in the POST with respect to the PRE session (POST vs PRE). To perform this comparison,

we used a nonparametric test: the values in the POST pattern above the thresholds related to the percentile of 97.5% of the PRE distribution, were considered significantly reinforced. The PRE vs POST comparison (inverse condition) was also tested as control.

To summarize the properties of the reinforced networks we computed some binary graph indices able to evaluate the network organization [5].

Characteristic Path Length:

$$L = \frac{1}{n}\sum_{i\in N} L_i = \frac{1}{n}\sum_{i\in N}\frac{\sum_{j\in N, j\neq i} d_{ij}}{n-1} \quad (1)$$

where L_i is the average distance between node i and all other nodes and d_{ij} is the distance between node i and node j.

Clustering Coefficient. The binary directed version of Clustering Coefficient is defined as follows:

$$C = \frac{1}{n}\sum_{i\in N} C_i = \frac{1}{n}\sum_{i\in N}\frac{t_i}{(k_i^{out}+k_i^{in})(k_i^{out}+k_i^{in}-1)-2\sum_{j\in N} g_{ij}g_{ji}} \quad (2)$$

where t_i represents the number of triangles involving node i, k_i^{in} and k_i^{out} are the number of incoming and outcoming edges of nodes i respectively and g_{ij} is the entry ij of adjacency matrix.

Small-Worldness. A network G is defined as small-world network if $L_G > L_{rand}$ and $C_G >> C_{rand}$ where L_G and C_G represent the characteristic path length and the clustering coefficient of a generic graph and L_{rand} and C_{rand} represent the correspondent quantities for a random graph. On the basis of this definition, small-worldness can be defined as follows:

$$S = \frac{C_G / C_{rand}}{L_G / L_{rand}} \quad (3)$$

A network is said to be a small world network if S>1.

Correlation analysis

As a last step of the analysis, we performed Pearson's correlation (significance level 0.05) between the above defined neurophysiological indices extracted from the reinforced networks and the functional scale (FMA).

For the clinical measure, to account for the high inter-subject variability in terms of degree of the impairment, and for the consequent different level of recovery, we computed the parameter "effectiveness", defined as follows:

$$Eff_{FMA} = \frac{FMA_{POST} - FMA_{PRE}}{Score_{\max} - FMA_{PRE}} * 100 \quad (4)$$

where $Score_{max}$ is the maximum score that can be reached in FMA scale.

III. Results

Figure 1a shows the connectivity pattern reinforced at the end of the rehabilitative training obtained for a patient with a stroke in the left hemisphere: the pattern in the motor-related frequency band (beta1) shows a higher involvement of channels over the motor areas of the affected (left) hemisphere during the attempt to move the right hand.

Results of the Pearson correlation computed between graph indices extracted from the reinforced pattern and the clinical recovery are reported in Table I and in Fig. 1b and c.

TABLE I

Results of the Pearson correlation computed between graph indices extracted from the reinforced pattern of motor task and the clinical recovery measured in terms of Fugl-Meyer Assessment. Significances are highlighted in bold.

	THETA	ALPHA	BETA1	BETA2	GAMMA
	Smallworldness				
p	0,607	0,519	**0,001**	0,597	0,123
R	0,166	0,207	**0,822**	0,170	0,471
	Path Length				
p	0,468	0,653	**0,007**	0,764	0,151
R	-0,232	-0,145	**-0,735**	-0,097	-0,441
	Clustering				
p	0,390	0,368	**0,013**	0,350	0,093
R	0,274	0,286	**0,691**	0,296	0,507

Such results show that the properties of the functional network reinforced after the training are significantly correlated with the clinical outcome, and that his is specific for the frequency band related to motor function, which was trained during the intervention (beta1). In particular, the direct correlation between these neurophysiological measures and the clinical indices informs that the patients with higher clinical recovery show a better organization of the reinforced network related to the motor function (high clustering, low path length, high smallworldness). The PRE vs POST comparison performed as control returned no significant results.

IV. Conclusion

The results of this study provide some important points in support of the proposed approach. Indeed, they show the feasibility of the procedure in a study aimed at capturing intervention-related variations in the patients' physiological activity, i.e. in challenging conditions characterized by high individual variability. Furthermore, such results suggest that the proposed statistical evaluation at the single subject level is able to provide reliable and quantifiable neurophysiological measures of modifications in brain networks that reflect, in a significant way, the variations captured behaviorally by functional scales commonly used in the clinical practice.

Acknowledgement

Research partially supported by the University of Rome Sapienza: "Progetti di Ateneo per la Ricerca Scientifica anno 2014".

References

[1] K. J. Friston, C. D. Frith, and R. S. J. Frackowiak, "Time-dependent changes in effective connectivity measured with PET," *Hum. Brain Mapp.*, vol. 1, no. 1, pp. 69–79, Gennaio 1993.

[2] L. A. Baccalá and K. Sameshima, "Partial directed coherence: a new concept in neural structure determination," *Biol. Cybern.*, vol. 84, no. 6, pp. 463–474, May 2001.

[3] F. Pichiorri, G. Morone, M. Petti, J. Toppi, I. Pisotta, M. Molinari, S. Paolucci, M. Inghilleri, L. Astolfi, F. Cincotti, and D. Mattia, "Brain-computer interface boosts motor imagery practice during stroke recovery: BCI and Motor Imagery," *Ann. Neurol.*, vol. 77, no. 5, pp. 851–865, May 2015.

[4] J. W. Tukey, "Bias and confidence in not quite large samples," *Ann. Math. Stat.*, vol. 29, no. 2, pp. 614–623, Jun. 1958.

[5] M. Rubinov and O. Sporns, "Complex network measures of brain connectivity: Uses and interpretations," *NeuroImage*, vol. 52, no. 3, pp. 1059–1069, Settembre 2010.

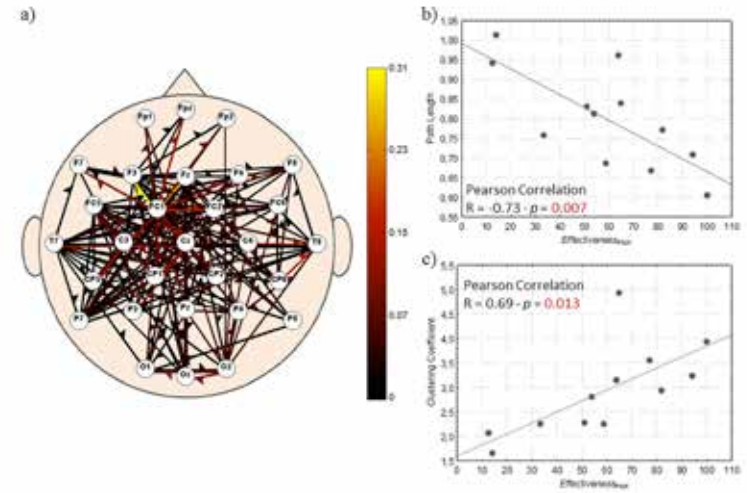

Fig. 1. a) Reinforced connectivity pattern obtained in beta1 band (typical of sensory-motor rhythms) for a representative patient with lesion in the left hemisphere. The scalp is seen from the above, with the nose pointing to the upper part of the page. Effective connections between the brain regions (29 channels: Fp1, Fpz, Fp2, F7, F3, Fz, F4, F8, FC5, FC1, FC2, FC6, T7, C3, Cz, C4, T8, CP5, CP1, CP2, CP6, P7, P3, Pz, P4, P8, O1, Oz, O2) are represented by arrows whose color and diameter code for the corresponding connectivity values estimated by means of PDC; b) scatter plot obtained between Path Length and the clinical recovery measured in terms of Fugl-Meyer Assessment in beta1 band; b) scatter plot obtained between Clustering and the clinical recovery measure in beta1 band.

Altered EEG microstate during induced hypoglycemia in type 1 diabetes

M. Rubega[1], G. Sparacino[1], A.S. Sejling[2], C.M. Michel[3], and M. Gschwind[3,4]
[1] *Department of Information Engineering, Università degli Studi di Padova, Padova, Italy*
[2] *Department of Cardiology, Nephrology and Endocrinology, Nordsjællands University Hospital, Hillerød, Denmark.*
[3] *Department of Neuroscience, Campus Biotech, University of Geneva, Geneva, Switzerland*
[4] *Department of Neurology, University Hospital Geneva, Geneva, Switzerland*

***Abstract*—The aim of this work is to capture topographical potential field changes (EEG microstates) during an insulin-induced hypoglycemia experiment in 19 patients with type 1 diabetes (T1D). Significant differences were found in the temporal dynamics of one microstate class in the theta band between euglycemia and hypoglycemia. These results encourage further quantitative investigation of brain network changes in hypoglycaemia, one of the final aims being the assessment of the possible use of the brain as noninvasive real-time biosensor to detect hypoglycaemia in T1D.**

***Keywords*—Type 1 diabetes, Hypoglycemia, EEG, Microstates.**

I. Introduction

In type 1 diabetic (T1D) patients, hypoglycaemia is a dangerous condition which may rapidly progress into coma, also without subject awareness, especially at night. Blood glucose (BG) monitoring through portable glucose electrochemical sensors is thus essential in the daily management of T1D. For such a scope, as complement to the use of BG sensors, the employment of the EEG signal has been investigated. Since the first studies in the 1950ies [1], several works, e.g. [2], have proven that power in the low theta ([4-8 Hz]) frequency EEG band increases during hypoglycemia [3]. Differences in terms of signal complexity have been also evidenced [4]. Recently, a research prototype portable device, measuring the EEG signal via subcutaneous electrodes and analysing it in real-time, has been proposed for the detection of hypoglycemic events [5]. Most of the published studies on EEG in hypoglycemia were led at single channel level. Multivariate analysis of EEG in hypoglycemia was, to the best of our knowledge, limited to the study of coherence reported in [6].

The aim of this work is to better understand the changes in brain network dynamics that lead to the theta power increase during hypoglycemia by performing topographical EEG analysis. By displaying the resting EEG electric potential amplitude of all channels as a topographic voltage map at each time point, it is possible to define a series of quasi-stable topographic configurations, which last several tens of milliseconds, termed "microstates" [7,8]. Different topographical configurations, i.e., different microstates, are thought to be related to different functional resting state networks as known from fMRI. In this work, we investigate if there are significant differences in the time-course of microstates in hypoglycemia (Hypo) compared to euglycemia (Eu) in the broadband, and in the theta frequency range.

II. Material and Methods

A. Database

The patient database is taken from a study approved by the local ethical committee, previously published by [9]. 19 patients with T1D (58% males; mean age, 55±2.4 years; diabetes duration, 28.5±2.6 years; glycated hemoglobin, 8.0±0.2%) participated in this study. Inclusion and exclusion criteria have previously been described in [9].

B. Experimental protocol

BG samples closely monitored during progressive induction of hypoglycemia using insulin, while the patients were sitting in a chair with eyes open and 19 EEG channels were simultaneously recorded by a digital EEG recorder using standard cap electrodes placed on the scalp according to the international 10/20 system. Offline, EEG was analogically low-pass filtered to avoid aliasing, then digitally acquired and finally down-sampled at 64 Hz. The dynamic range of the EEG was ±4620 μV with an amplitude resolution of 0.14 μ V. The internal noise level in the analogue data acquisition system was estimated to be 1.3 μV RMS.

C. Preprocessing

For each subject, a pre-analysis selected 5-min intervals in both Eu and Hypo conditions by visual inspection of the BG time-series (smoothed by a spline approximation of the samples), before and after it crossed the hypoglycemic threshold of 70 mg/dL. EEG data in Eu and Hypo were band-pass filtered between 1 and 40 Hz using a 3-order Butterworth filter; Independent Component Analysis was applied in order to remove cardiac and oculomotor artifacts (only components with clear eye blinks, saccades and cardiac artefacts were excluded). EEG signals were re-referenced to the common average-reference.

D. Frequency Analysis

Before applying microstates analysis, a frequency analysis was performed for each 5-min Eu and Hypo intervals, using a Welch's power spectral density (PSD) in theta band [4-8] Hz. Then, power in theta band was estimated from the averaged PSD. EEG data preprocessing and frequency analysis was realized with custom MATLAB® scripts (release 2014a, Mathworks Inc., Natick, Massachusetts, USA).

E. Microstates Analysis

Microstate analysis was performed with the freely available

CARTOOL software [10]. The analysis is based on a two-stage process to obtain the prototype topographies, which best explain most of the signal variance, in Eu and Hypo. The following analysis was performed in both data filtered in [1-40] Hz and in the theta band [4-8] Hz. First, for each patient, the time points of the maximum Global Field Power (GFP, i.e., the sum of the standard deviation of the field potentials at all electrodes of an average-reference map), were selected as the moments of high global neuronal synchronization, from Eu and Hypo. For each patient, the topographies of these time points were then clustered independently using a k-means clustering approach. The optimal number of clusters was selected based on the overall performance of multiple clustering validity criteria [11, 12]. In second step, the optimal clusters of each patient in Eu and Hypo were again clustered together to find the most common templates maps across the two glycemic conditions. Finally, these most common templates were fitted back to the original EEG in Eu and Hypo, and each time point *t* was labelled with the cluster maps based on Global Map Dissimilarity (GMD) measure

$$GMD(t) = \sqrt{\frac{1}{N}\sum_{i=1}^{N}\left(\frac{c_i(t)-\bar{c}(t)}{GFP_c(t)} - \frac{v_i(t)-\bar{v}(t)}{GFP_v(t)}\right)^2} \qquad (1)$$

where $c_i(t)$ is the voltage potential at the electrode *i* and $\bar{c}(t)$ is the average voltage potential of all electrodes at time *t* in the map *c* while $v_i(t)$ is the voltage potential at the electrode *i*, $\bar{v}$(t) is the average voltage potential of all electrodes at time *t* in the map *v* and *N=19* is the number of electrodes. The GMD is equivalent to the spatial Pearson's product-moment correlation coefficient between the potentials of the template map and the instant topography. This resulted in the microstates sequence. To compare the microstates sequences between Eu and Hypo, the following parameters were computed: the total time coverage (TTC) giving the percent of total time in the EEG recording, covered by each microstate class, the global explained variance (GEV) for each microstate class, calculated as the sum of the squared spatial correlation, weighted by the GFP at each time point, and giving a ratio of how well the template topography describe the whole data set [10], the occurrences/s describing the average number of appearances for the same microstate per second, and the microstate duration [13], given as median, geometric mean and geometric standard deviation [14] of the durations of each microstate in milliseconds. Wilcoxon signed-rank tests were used to assess whether or not the changes in the analyzed parameters were statistically significant comparing Eu with Hypo in an intra subject paradigm.

III. Results

In Fig 1, the difference between averaged EEG spectral power topography during insulin-induced Hypo and Eu in theta band is shown, confirming the expected higher amplitude of low-frequency EEG rhythms during Hypo with respect to Eu.

The 5 common template topographies obtained by the two-step k-means clustering from data filtered in [1-40] Hz range (Fig. 2) and the 6 common template topographies from data filtered in theta band (Fig. 3), look similar, indicating that low-frequency activity contribute to the EEG resting state network. Significant changes in the temporal dynamics of microstate class 6 was found in the [4-8] Hz filtered data, but not in the broad band data. Results of the comparison of the temporal parameters between Hypo and Eu are summarized in the boxplots in Fig. 4. All temporal parameters of map 6 increase during Hypo with respect to Eu ($p<0.05$).

IV. Conclusion

In this preliminary study, significant changes of the temporal dynamics of one specific microstate map was found during Hypo vs Eu in the theta-filtered data. This indicates that the well-known theta-power increase is specific to a unique large-scale brain network which spatial characteristics still remains to be elucidated using high-density EEG and electrical source imaging.

Acknowledgement

The authors thank Hyposafe A/S, Lynge, Denmark for assisting with providing the data.

References

[1] Ross IS, Loeser LH: Electroencephalographic findings in essential hypoglycemia. Electroencephalogr Clin Neurophysiol 1951, 3:141–148.

[2] Pramming S, Thorsteinsson B, Bendtson I and Binder C: The relationship between symptomatic and biomechanical hypoglycemia in insulin-dependent diabetic patients. J Intern Med 1990; 228:641–646.

[3] Tribl G, Howorka K, Heger G, Anderer P, Thoma H, et al.: EEG topography during insulin-induced hypoglycemia in patients with insulin- dependent diabetes mellitus. Eur Neurol 1996; 36:303–309.

[4] Fabris C, Sparacino G, Sejling AS, Goljahani A, Duun-Henriksen J, et al.: Hypoglycemia- related EEG changes assessed by multiscale entropy. Diabetes Technol Ther 2014; 16:688–694.

[5] Juhl CB, Hojlund K, Elsborg R, Poulsen MH, Selmar PE et al.: Automated detection of hypoglycemia-induced EEG changes recorded by subcutaneous electrodes in subjects with type 1 diabetes—the brain as a biosensor. Diabetes Res Clin Pract 2010; 88:22–28.

[6] Rubega M, Sparacino G, Sejling AS, Juhl CB, Cobelli C.: Hypoglycemia-Induced Decrease of EEG Coherence in Patients with Type 1 Diabetes. Diabetes Technol Ther. 2016; 18(3): 178-84.

[7] Lehmann D, Ozaki H, Pal I.: EEG alpha map series: brain micro-states by space-oriented adaptive segmentation. Electroencephalogr Clin Neurophysiol. 1987; 67(3): 271-88.

[8] Khanna A, Pascual-Leone A, Michel CM, Farzan F.: Microstates in resting-state EEG: current status and future directions. Neurosci Biobehav Rev 2015; 49, 105-113

[9] Sejling AS, Kjaer TW, Pedersen-Bjergaard U, Diemar SS, Frandsen CS, et al.: Hypoglycemia-associated changes in electroencephalogram in patients with type 1 diabetes and normal hypoglycemia awareness or unawareness. Diabetes 2014; 64:1760–1769.

[10] Brunet D, Murray MM, Michel CM.: Spatiotemporal analysis of multichannel EEG: CARTOOL. Comput Intell Neurosci 2011, 813870.

[11] Hartigan J.: Clustering Algorithms. New York USA Wiley 1975.

[12] Davies D and Bouldin D.: A cluster separation measure IEEE Transactions on Pattern Analysis and Machine Intelligence, 1979; (1): 224-227.

[13] Koenig T, Prichep L, Lehmann D, Sosa PV, Braeker E, et al.: Millisecond by millisecond, year by year: normative EEG microstates and developmental stages. Neuroimage. 2002; 16: 41-48.

[14] Limpert E and Stahel WA.: Problems with using the normal distribution-and ways to improve quality and efficiency of data analysis. PLoS One 6. 2011. e21403.

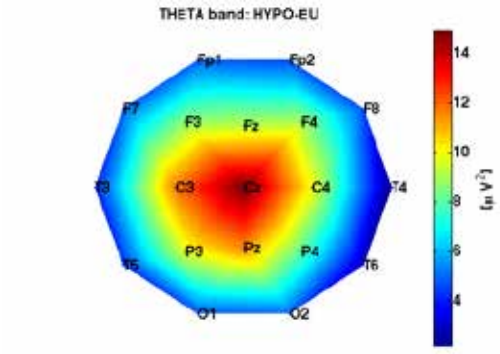

Fig. 1 Difference between averaged EEG spectral power topography in the theta band [4-8 Hz] of Hypo compared to Eu averaged across 19 T1D patients, confirming the preferential localization in the midparietal region.

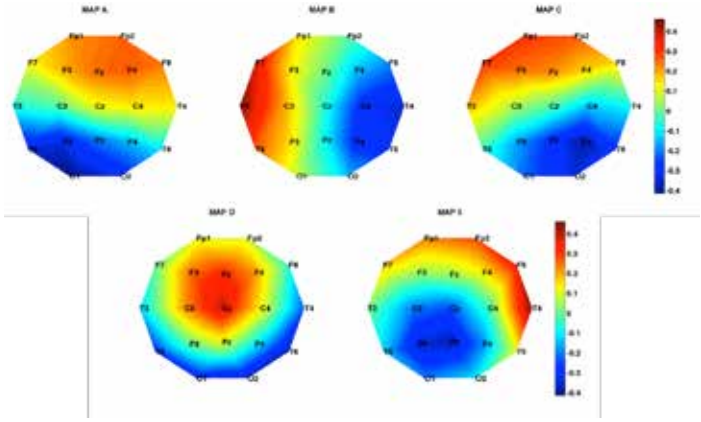

Fig. 2 Five most representative topographies for both glycemic conditions in all subjects from broadband data [1-40 Hz], named map A, B, C, D and 5, according to the microstate literature convention. Only the topography's relative configuration, but not its polarity is considered. These five template topographies are displayed per definition with red color towards the front.

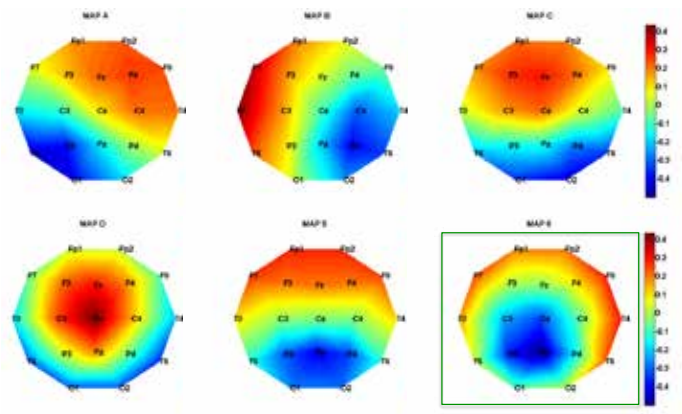

Fig. 3 Six most representative topographies for both glycemic conditions in all subjects from data filtered in theta band [4-8 Hz], named map A, B, C, D, 5 and 6. Map 6 is highlighted by the green square, indicating the significant difference of microstates parameters between Hypo and Eu for this map, as displayed by Fig. 4.

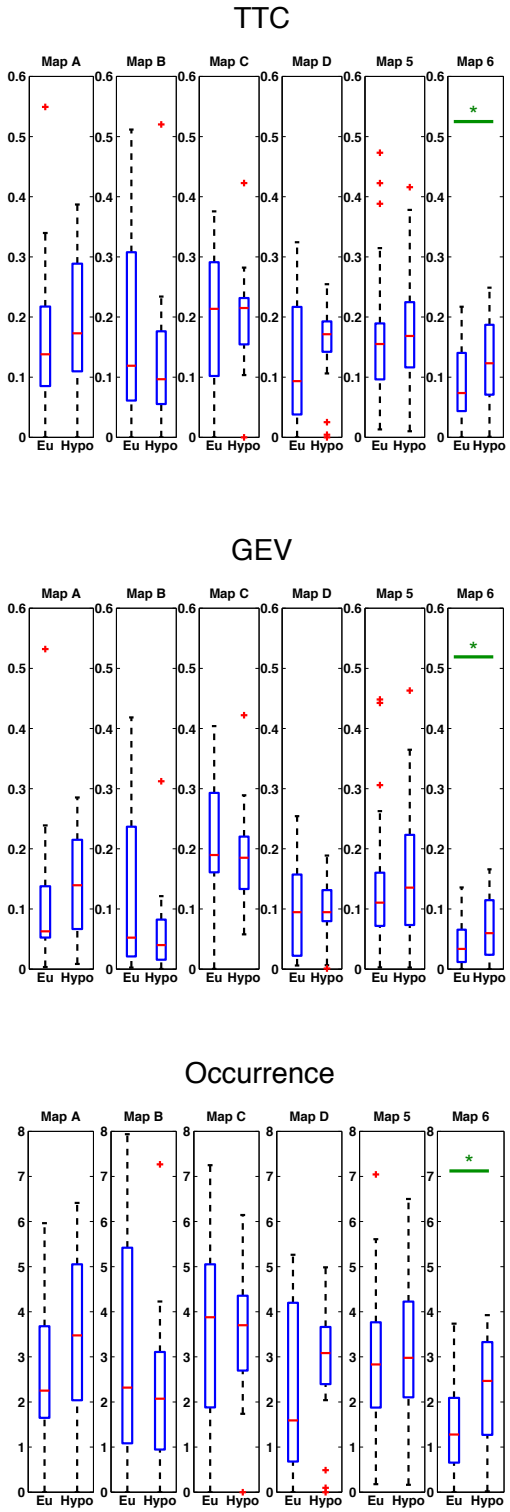

Fig. 4 Results of microstate temporal parameters of the theta-band filtered data, separated for each microstate class A, B, C, D, 5 and 6 during Eu and Hypo. During Hypo, there is a significant increase of all parameters: Total time coverage (TTC), Global Explained Variance (GEV) and Occurrence per second for microstate 6, as indicated by the green line with the asterisk ($p<0.05$).

Effectiveness of a consumer grade EEG amplifier for P300-based Brain Computer Interface Applications.

F. Schettini[1,2], V. Vulcano[1,2], A. Riccio[1], D. Mattia[1], F. Cincotti[1,2]
[1] *Neuroelectrical Imaging and BCI Lab, IRCCS Fondazione Santa Lucia, Rome, Italy;*
[2] *Dept. Computer, Control, and Management Engineering "Antonio Ruberti" University of Rome "Sapienza"*

***Abstract*— Brain Computer interface system demonstrated to be technology suitable to restore communication and interaction with the environment in people with severe motor disabilities. However, they still suffer from some usability and accessibility problems avoiding their diffusion as assistive technology. One limitation is related to the cost of the equipment. Recently several low cost electroencephalographic amplifiers are appearing on the market. In this work, we evaluated the effectiveness of the low cost amplifier Emotiv EPOC for a brain-computer interfaces application based on the P300 potential through a comparative study with a medical grade amplifier (gUSBamp - GTEC, Austria).**

We carried out the comparison in terms of BCI classification accuracy and in terms of latency and amplitude of the acquired potentials. Preliminary results pointed out that, with its current features, the consumer grade amplifier cannot ensure a performance level comparable to the medical grade amplifier one.

***Keywords*—BCI, consumer grade amplifier, assistive technology, P300-Speller.**

I. Introduction

A Brain Computer Interface (BCI) systems can provide an alternative communication channel for people with severe motor impairments. Indeed BCIs allow controlling external devices through direct brain activity recognition by a computer, bypassing neuromuscular-based systems [1].

At the state of the art, BCIs are mainly used in research laboratories and end users exploiting the BCIs as a means of replacement in their houses are still rare. The price of the electroencephalographic (EEG) amplifier is one of the main limitations for the dissemination of BCI technologies. In this study, we compared a low cost amplifier (Emotiv EPOC) with a device commonly used in research (g.tec, g.USBamp, Austria), in the context of a P300-based BCI application for communication.

P300 is an event-related potential that appears as a positive deflection in the EEG signal about 250-500 ms after the subject recognizes a relevant stimulus between a train of frequent stimuli [2]. Previous studies investigated the usability of different EEG headsets in within-subject experiments [3] without make uniform the EEG cap montage. In this study we used the same number of EEG channels at the same location for both considered devices in order to allows for a more direct comparison of system performance. The latter has been assessed in terms of potentials latency and amplitude and classification accuracy.

II. Material and Methods

A. Experimental Protocol and EEG data pre-processing

Nine healthy participants (3 male, mean age 25 ± 1) were involved in this study. The whole experiment was run with BCI2000 software [4]. We replicated the Emotiv declared montage on the gUSBamp cap to compare both amplifiers. So scalp EEG signals were recorded from 14 positions -AF3, F7, F3, FC5, T7, P7, O1, O2, P8, T8, FC6, F4, F8, AF4- with reference in P3 and ground in P4. Sampling rate was 128 Hz for both Emotiv and gUSBamp. The stimulation interface consisted in the 6 by 6 Farwell and Donchin's matrix Speller [5]. Each participant underwent 2 recording sessions, one with each amplifier, in the same day. We randomized the sessions order to avoid bias due to tiredness and training on the interface. A session consisted of 7 runs of 5 trials each. A trial corresponded to the selection of a single character and consisted of 10 random intensifications of the 12 stimulation classes (rows and columns). Subjects were asked to attend to the desired character and mentally count how many times it flashed. Each stimulus was intensified for 125ms and the inter stimulus interval (ISI) was set at 125ms.

Preliminarily, the EEG signal was band pass filtered (1-10Hz) and divided into 800ms Target and Non-Target epochs starting with the onset of each stimulus. Epochs were downsampled with a 6 as decimation factor. EEG epochs were subsequently reorganized into a three-dimensional array: each 2D matrix of the array represents a single epoch, where rows are epoch samples and columns acquisition channels.

B. Accuracy off-line Analysis

We did a 7-fold crossvalidation using a Stepwise Linear Discriminant Analysis classifier (SWLDA) [6] to detect whether a P300 was elicited in the brain.

We assessed off-line the effectiveness of the amplifiers as the offline classification accuracy, i.e. the percentage of characters accurately classified by the SWLDA classifier. We used the area under the ROC (Receiver Operating Characteristics) curve, abbreviated AUC, to compare classifier accuracy for both Emotiv and gUSBamp device and, since data were normally distributed, we applied a t-test dependent samples to investigate differences between the amplifiers.

C. N200 and P300 potentials Analysis

In order to assess amplitude and latency of N200 and P300 potentials we considered the RSquare values (statistical index

of separability between two classes [7]) related to target and non-target stimuli, for both Emotiv and gUSBamp. In particular, we used Signed RSquare to maintain the information on the sign of the values that form the two classes of data. In a first stage we identify N200 and P300 peaks in the subjects' Grand Average RSquare. Then, for each single subject, we looked for the for N200 and P300 peak considering 100 ms before and 100 ms after the Grand average peaks. We looked for the minimum potential values on P7, O1, O2, P8 channels for N200 and the maximum potential values on AF3, F7, F3, FC6, F4, F8, AF4 channels for P300. Finally, we applied a two-sample paired t-test to assess the differences in latencies and amplitudes of the potentials or a non-parametric Wilcoxon test whether the distributions were not normal.

III. Results and Discussion

A. Accuracy off-line Analysis

The Figure 1 illustrates the AUC mean values (across the runs) for each subjects for both Emotiv and gUSBamp. It shows that the Emotiv will always reach lower performance than those obtained using the gUSBamp, with a great variability between subjecs. A two-sample paired t-test showed significant differences ($p<0.005$) between the two distributions.

TABLE I

	P300 Amplitude (μV)		*P300 Latency (ms)*	
Channel	*Emotiv*	*gUSBamp*	*Emotiv*	*gUSBamp*
AF3	3.25±1.41	7.4±10.21	*395.8±53.8	316.8±69.6
F7	3.29±2.31	4.8±6.73	*394.1±62.5	319.4±73.1
F3	2.96±1.26	5.25±6.38	*401.9±55.9	314.2±68.2
FC5	2.38±1.18	2.89±3.25	*404.5±58.6	320.3±74
FC6	1.7±1.78	2.79±2.1	390.6±48.8	317.7±75.2
F4	2.89±0.89	4.42±4.37	*387.1±58.2	302.9±54.5
F8	3.05±1.64	3.35±2.73	396.7±52.5	331.6±82.8
AF4	*2.43±1.53	6.6±8.45	*408.8±50.2	316±71.5
	N200 Amplitude (μV)		*N200 Latency (ms)*	
P7	*-1.2±1.33	-2.52±1.25	*320.3±18.7	215.3±30
O1	-1.56±1.64	-2.4±1.38	*295.1±45	211.8±62.2
O2	*-1.31±1.56	-2.73±1.55	*288.2±43.4	191±61.3
P8	-1.73±2.25	-2.76±1.61	*293.4±42.3	191.8±40.6

The asterisk* indicates statistically significant differences between the two distributions.

B. N200 and P300 Analysis

Table I provides amplitude and latencies value assessed for both Emotiv and gUSBamp's in the interested channel. Emotiv latencies exhibit on average delay of 96.78 ± 9.52 ms for N200 and 80.08 ± 8.96 ms in P300: this difference was statistically significant ($p<0.05$) for each channel for N200 and for 6 channels out of 8 for P300. We did not find significant difference in terms of P300 amplitudes between Emotiv and gUSBamp (except for AF4, $p<0.05$). For N200 potentials, we detected an higher amplitude with the g.USBamp with respect to Emotiv's: we found on average a difference of 1.15 ± 0.26 μV and this difference was significant for 2 channels out of 4 ($p<0.05$).

C. Practical considerations

One main limitation of the Emotiv epoc is that the electrodes are fixed on a semi-rigid support so their positioning is dependent on the shape of subject head. This means that the Emotiv channels position not always match 10-20 standard position. Another factor that influences performance quality of the Emotiv, as well as the setup time, is the amount and the type of the user's hair. In fact, on a subject with curly hair it takes a longer time to mount the headset and to ensure a sufficiently low impedance value. Furthermore, the saline solution dries quickly leading to a decrease in performance during the use.

IV. Conclusion

These preliminary results suggest that, due to its current characteristics, Emotiv Epoc could not be recommended for critical applications where it is important to be fast and accurate, such as the use of P300-based BCI to restore communication and interaction with the environment in people with severe motor disabilities. However, a future improvement of design's flexibility and skin/electrode contact's stability could allow a more general use and therefore the application in clinical practice.

Acknowledgement

This work was supported by the Promobilia Foundation (Foundation Ref N° 14214).

References

[1] Wolpaw E. J. (2012). Brain-Computer Interfaces: Principles and Practice. USA: OUP, 3-11, 15- 39, 123-144, 147-162, 227-237, 351-360. *Neurophysiol.*, vol. 113, no. 6, pp. 767–791, Jun. 2002.

[2] J. Polich, "Updating P300: An integrative theory of P3a and P3b," *Clin. Neurophysiol.*, vol. 118, no. 10, pp. 2128–2148, Oct. 2007.

[3] Femke Nijboer, Bram van de Laar, Steven Gerritsen, Anton Nijholt and Mannes Poel, "Usability of Three Electroencephalogram Headsets for Brain–Computer Interfaces: A Within Subject Comparison" .

[4] G. Schalk, D. J. McFarland, T. Hinterberger, N. Birbaumer, and J. R. Wolpaw, "BCI2000: a general-purpose brain-computer interface (BCI) system," *IEEE Trans. Biomed. Eng.*, vol. 51, no. 6, pp. 1034–1043, Jun. 2004.

[5] L. A. Farwell and E. Donchin, "Talking off the top of your head: toward a mental prosthesis utilizing event-related brain potentials," *Electroencephalogr. Clin. Neurophysiol.*, vol. 70, no. 6, pp. 510–523, Dec. 1988.

[6] D. J. Krusienski, E. W. Sellers, F. Cabestaing, S. Bayoudh, D. J. McFarland, T. M. Vaughan, and J. R. Wolpaw, "A comparison of classification techniques for the P300 Speller," *J. Neural Eng.*, vol. 3, no. 4, pp. 299–305, Dec. 2006.

[7] A. C. Cameron and F. A. G. Windmeijer, "R-Squared Measures for Count Data Regression Models With Applications to Health-Care Utilization," *J. Bus. Econ. Stat.*, vol. 14, no. 2, pp. 209–220, Apr. 1996.

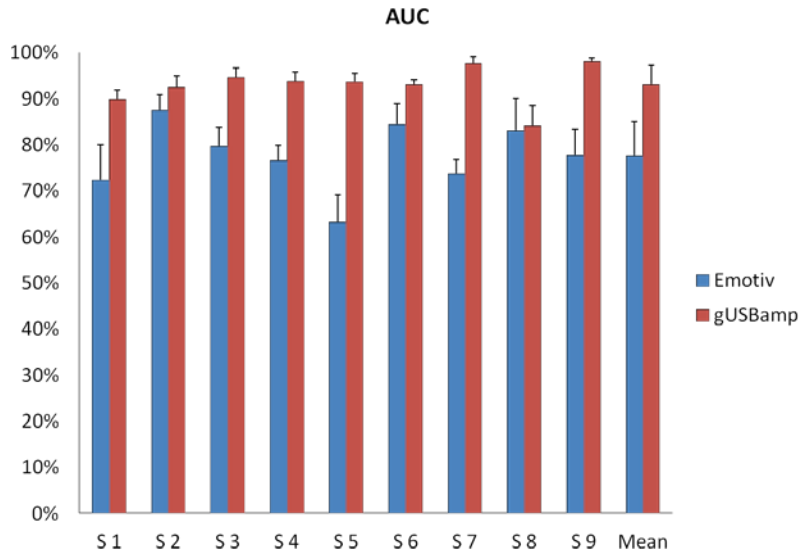

Fig.1: 7-fold crossvalidation results. Average AUC values for each subject for Emotiv and gUSBamp.

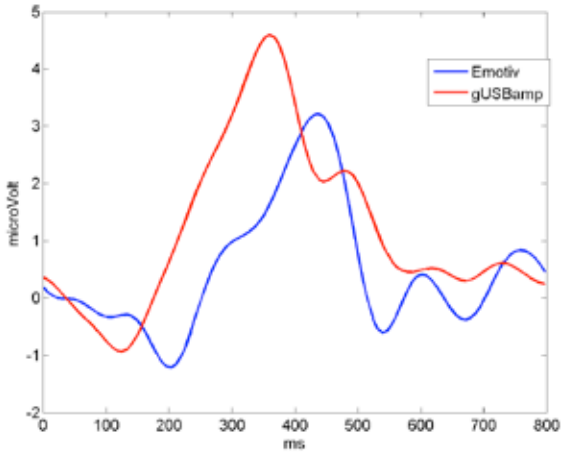

Fig.2: Grand Average (Target-Non Target) at the AF3 channel: for Emotiv, in blue, P300 latency and amplitude were 429.69 ms and 3.01 µV respectively; for gUSBamp, in red, P300 latency and amplitude were 359.38 ms and 4.6 µV respectively.

Objective assessment of the Manual Lymph Drainage technique in chronic leg ulceration

M. Sorelli[1], L. Cantasano[2], L. Rasero[2], L. Bocchi[1]
[1] *Dept. of Information Engineering, University of Florence*
[2] *Infectious and Tropical Diseases Unit and Department of health professions – Azienda Ospedaliera-Universitaria Careggi*

***Abstract*—Lymphostasis is a morbid condition frequently associated with limb ulceration. Manual Lymph Drainage (MLD) is a well-known massage technique for treatment of lymphedema. In this work, an objective method to assess the effectiveness of MLD is investigated. The dynamics of skin cooling after local heating at 43 °C has been compared before and after MLD, on the basis of a structural physiological model of the skin thermoregulation. Preliminary results, collected from a small sample of 7 patients, show a statistically significant increase ($p = 0.007$) of the ratio of the skin-subcutaneous tissue thermal conductance to the epidermis thermal capacitance, K_{ST}/C_S, after MLD. This finding encourages further experimentation on a wider group size.**

***Keywords*—lymphostasis, manual lymph drainage, microcirculation, thermoregulation.**

I. Introduction

LYMPHOSTASIS, secondary to the congestion of the lymphatic flow, is a condition often observed in patients with chronic leg ulcers [1]. At the early stages, lymphostasis of the lower limbs is associated with an intermittent, slight swelling of the affected leg, which frequently worsens as the days go by. If left untreated, the swollen areas stabilize over time, becoming more permanent; they do not subside overnight, and start to feel increasingly hard and solid. Manual Lymph Drainage (MLD) [2] appears to be a successful technique to treat these edematous conditions, as subjectively evaluated by patients and operators. Gentle circular and spiral shaped strokes are applied to the skin, so as to create the necessary pumping effect that assists lymph back-flow and aids the drainage of tissues. However, an objective method to assess the effectiveness of MLD is still lacking. Therefore, we aim at investigating the changes occurring in objective features of the edematous areas before and after a brief session of MLD (20min).

II. Materials and methods

A. Subjects

A group of 7 subjects with lower extremity lymphostatic edema was recruited to conduct a preliminary evaluation. All the subjects involved suffered from lower limb vascular ulceration. Participants agreed to be included in the study, after receiving complete information on the purpose of the research and the procedures involved.

B. Experimental setup

The experimental protocol included two measurement phases for each subject, respectively before and after the Manual Lymph Drainage (MLD) treatment. Skin temperature was recorded from the anterior area of the lower limb, with a PeriFlux 5020 Temperature Unit (Perimed, Stockholm, Sweden), that can provide controlled heating of the skin at the measurement site. The 5020 temperature unit is able to record the skin temperature with a maximum error of 0.1 °C, as reported by the instrument manufacturer. The temperature probe was secured to the underlying skin with medical tape, in order to prevent relative displacements that might induce artefacts in the temperature curve. Signals were acquired and digitized at a 1000 Hz sampling frequency with a dedicated NI-6009 USB digital board (National Instruments, Austin, U.S.), and stored on a laptop. Measurements were taken in a controlled ambient temperature, set at around 21 °C.

C. Thermal stimulation and data acquisition

Each temperature acquisition lasted around 8 minutes, and comprised three distinct phases:

1. Baseline (approximately 1 minute), in which no thermal stimulation was applied to the skin;
2. Heating (approximately 5 minutes), in which the skin was heated up at a stable temperature of 43 °C;
3. Cooling (approximately 2 minutes), in which the heat flow from the probe was stopped and the skin temperature gradually returned to its equilibrium.

The position where the thermal probe was originally placed for the pre-MLD acquisition was marked, so as to be able to take the post-MLD measurement exactly at the same spot, thus preventing the influence of spatial heterogeneities on the temperature signals. Since the thermal stimulation was manually initiated and disabled on the frontal panel of the PF 5020 unit, the duration of each phase might slightly vary among subjects. An example of a typical skin temperature curve, acquired with this procedure, is shown in Fig. 1.

D. Modeling

In order to quantitatively assess the effect of the MLD procedure on lymphostasis, a mathematical formalization of the structural ability of the skin to disperse heat was sought. A modified version of the physiological, compartmental model proposed in [3] has been adopted to this end. This structural model, shown in Fig. 2, includes four compartments representing, namely, the environment, the epidermis in contact with the thermal probe, the underlying subcutaneous tissue and the body core. According to this model, heat is exchanged between the environment and the skin surface via thermal conduction. This mechanism is also believed to dominate the heat transfer between the epidermis and the

subcutaneous tissue, as the epidermis does not have a direct blood supply. On the other hand, the body core exchanges thermal energy with the subcutaneous tissue mainly via the convective heat transport, mediated by the local blood flow. In this context, given the limited duration of the protocol, it was hypothesized that the amount of heat exchanged by the environment and the body core could not induce any significant temperature change to the respective compartments (i.e. the environment and core thermal capacitances are assumed to be theoretically infinite). The mathematical realization of the model, adopted to describe the skin temperature dynamics during the post-heating phase of the protocol, is given by the following system:

$$C_S \cdot \dot{T}_S = -(K_{ST} + K_{SE}) \cdot T_S + K_{ST} \cdot T_T + K_{SE} \cdot T_E \quad (1)$$

$$C_T \cdot \dot{T}_T = -(K_F \cdot F + K_{ST}) \cdot T_T + K_{ST} \cdot T_S + K_F \cdot F \cdot T_C \quad (2)$$

$$T_S(0) = 43\ ^\circ C \quad (3)$$

$$T_E = 21\ ^\circ C \quad (4)$$

$$T_C = 37\ ^\circ C \quad (5)$$

where T_S, T_T, T_E, T_C are, namely, the skin, tissue, ambient and body core temperatures ($[T_i] = °C$); C_S, C_T represent the skin and tissue thermal capacitances ($[C_i] = J \cdot °C^{-1}$); K_{ST} and K_{SE} respectively model the skin-tissue, skin-environment thermal conductances ($[K_{ii}] = W \cdot °C^{-1}$), while K_F symbolizes the heat exchanged by a ml of blood, per unit temperature difference ($[K_F] = J \cdot ml^{-1} \cdot °C^{-1}$), and F is the local blood flow ($ml \cdot s^{-1}$). It is straightforward to notice that the system above is non-linear, as F is in general not a constant term, being inherently related to the local temperature. The degree of local tissue perfusion is in fact modulated by a combination of control mechanisms, involving endothelial, adrenergic and sensory nerves [4], in response to local temperature changes. However, no high frequency perturbation nor slow fluctuation could be recognized in the skin temperature decay curve, due to the thermal inertia of the tissue. Therefore, the system above has been linearized, by assuming F to be constant throughout the entire duration of the post-heating phase of the protocol. Furthermore, since the measurement protocol makes only the skin temperature available, the basic structural parameters had to be combined in the following four unknown rate constants, so as to ensure the unique identifiability of the model:

$$a = K_F \cdot F / C_T \quad (s^{-1}) \quad (6)$$

$$b = K_{ST} / C_T \quad (s^{-1}) \quad (7)$$

$$c = K_{ST} / C_S \quad (s^{-1}) \quad (8)$$

$$d = K_{SE} / C_S \quad (s^{-1}) \quad (9)$$

Model identification has been carried out with the JSim simulation software [5]. The Simplex, bounded, non-linear steepest-descent, optimization algorithm, was chosen to fit the simulated $\check{T}_S$ model output to the experimental T_S data of the cooling phase. During data fitting, T_E and T_C were also allowed to vary around their hypothesized constant values, within a narrow interval (21-25 °C for T_E, 36-38 °C for T_C), in order to improve the optimizer performance. Nonetheless, the resulting average estimates well approximate the values which were originally hypothesized: $\check{T}_E = 21.10 \pm 0.06$ °C, $\check{T}_C = 37.04 \pm 0.13$ °C.

III. Results

The parameters derived from the original structural model, and identified by fitting the decay curve extracted from each temperature acquisition, have been compared using a paired t-test, to assess the presence of any significant change between the pre-MLD and post-MLD phases. A $p < 0.05$ was considered statistically significant; nevertheless, since the experimentation is still under progress, and data from a limited sample of only 7 subjects is currently available, the figures presented here have to be interpreted with a degree of caution. Preliminary results are summarized in Table 1, which reports the sample average and standard deviation of the aggregated parameters, before and after the MLD treatment. Among the five parameters, only K_{ST}/C_S exhibits a statistically significant increase after MLD, from 26.1 ± 5.4 1/ms to 30.2 ± 5.0 1/ms. A modest increase, though not significant, is also observed in $K_F \cdot F/C_T$ and K_{ST}/C_T. Widening the patients group size, the statistical analysis of the response to the MLD treatment will benefit from a larger power, allowing the reliable detection of narrower variations.

TABLE I
RESULTS OF THE FITTING PROCEDURE

Parameter		*Pre-MLD*	*Post-MLD*	*p*
$K_F \cdot F / C_T$	(1/ms)	13.6 ± 4.2	14.7 ± 3.2	0.480
K_{ST} / C_T	(1/ms)	12.9 ± 2.6	14.6 ± 3.0	0.214
K_{ST} / C_S	(1/ms)	26.1 ± 5.4	30.2 ± 5.0	0.007 †
K_{SE} / C_S	(1/ms)	5.2 ± 2.1	4.7 ± 1.6	0.211
K_{ST} / K_{SE}		6.2 ± 4.0	7.2 ± 3.8	0.072

† indicates a statistically significant difference

IV. Conclusion

A method to objectively assess the effect of the MLD treatment on lymphostasis, from the analysis of the skin temperature cooling curves, has been presented in this work. Preliminary results collected from 7 subjects with lymphostatic edema indicate a statistically significant increase in the K_{ST}/C_S rate constant. However, the small sample size currently available represents a major limitation of the present investigation. Further experimentation is under planning so as to elucidate the changes in the dynamics of the temperature decay curve after MLD with greater statistical significance.

References

[1] A. Szuba and S.G. Rockson, "Lymphedema: anatomy, physiology and pathogenesis", *Vascular Medicine*, vol. 2, pp.321-326, Nov. 1997.

[2] Lymphoedema Framework. "Lymphatic massage" in *Best practice for the management of lymphoedema. International consensus*. London: MEP Ltd, 2006, pp. 29-30.

[3] A. Bandini et al., "Effect of local blood flow in thermal regulation in diabetic patient", *Microvascular Research*, vol. 88, pp. 42-47, July 2013.

[4] J.M. Johnson and D.L. Kellogg, "Local thermal control of the human circulation", *J Appl Physiol*, vol. 109, pp. 1229-1238, October 2010.

[5] E. Butterworth, B.E Jardine and G.M. Raymond, "JSim, an open source modelling system for data analysis", F1000 Research 2014, **2**:288. Available: http://f1000research.com/articles/2-288/v3

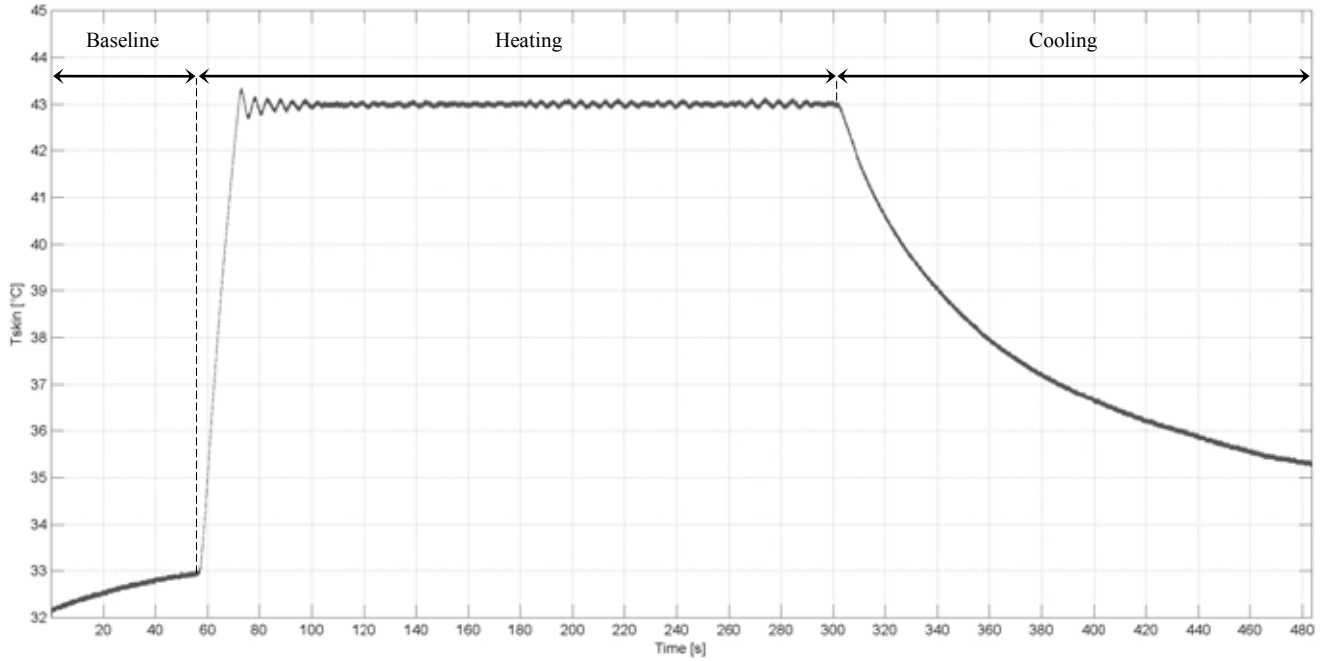

Fig. 1. Temperature signal acquired on the epidermis during a measurement session. The baseline, heating and cooling phases are clearly recognizable.

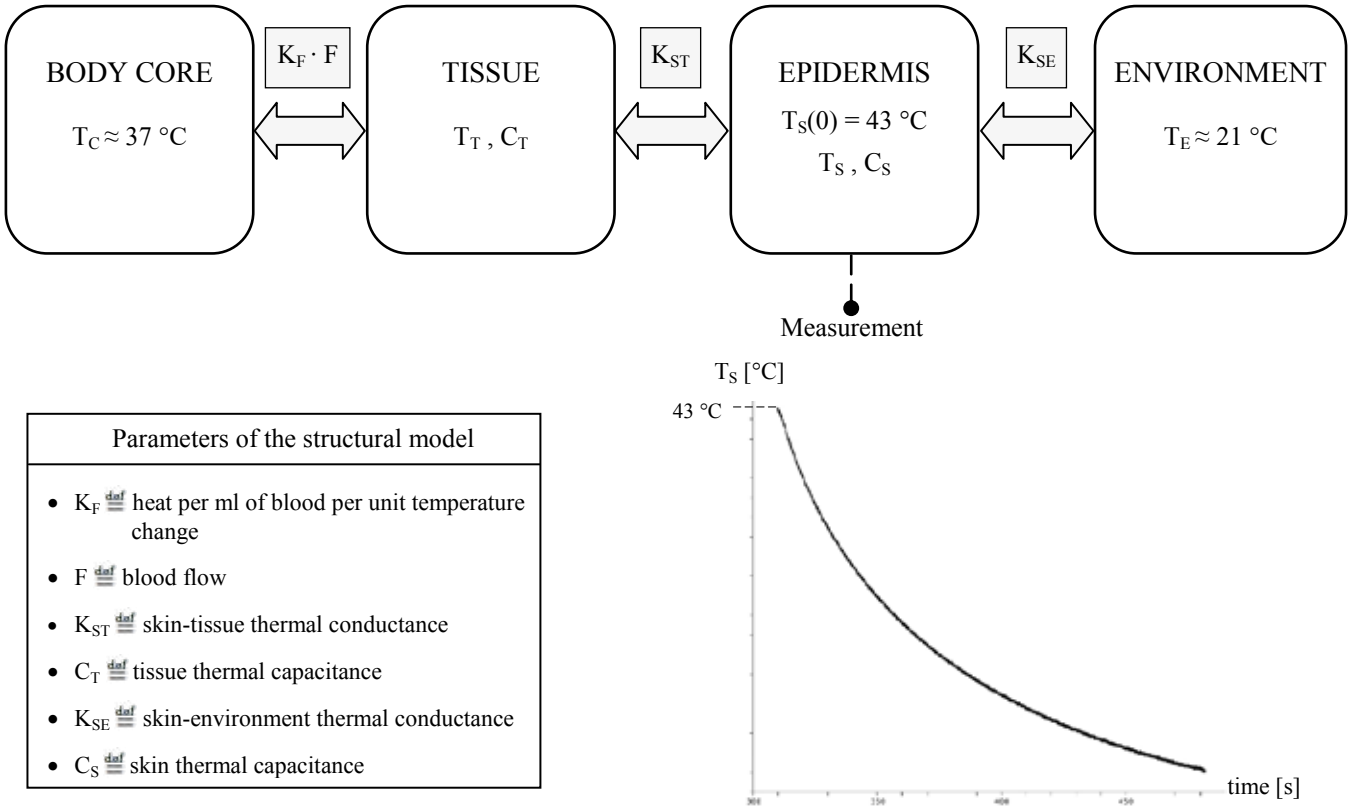

Parameters of the structural model

- K_F $\stackrel{def}{=}$ heat per ml of blood per unit temperature change
- F $\stackrel{def}{=}$ blood flow
- K_{ST} $\stackrel{def}{=}$ skin-tissue thermal conductance
- C_T $\stackrel{def}{=}$ tissue thermal capacitance
- K_{SE} $\stackrel{def}{=}$ skin-environment thermal conductance
- C_S $\stackrel{def}{=}$ skin thermal capacitance

Fig. 2. Block diagram of the thermal compartmental model adopted in this study. The definition of the structural parameters is summarized for clarity.

Towards Real Time Connectivity Estimation: a New Approach Based on Ridge Regression

J. Toppi[1,2], Y. Antonacci[1,2], D. Mattia[2] and L.Astolfi[1,2]
[1]Dept. of Computer, Control and Management Engineering, Sapienza University of Rome, Italy
[2]Neuroelectrical Imaging and BCI Lab, IRCCS Fondazione Santa Lucia, Rome, Italy

***Abstract*—Partial Directed Coherence is a spectral multivariate estimator of effective connectivity. It allows to provide accurate estimates of connectivity patterns, including all the sources simultaneously in the model and thus mitigating the hidden source problem. However, the accuracy of the multivariate approach is strongly limited by the amount of data used for the estimate. Such drawback limits the employment of PDC in the real time estimation of connectivity patterns, as alternative feature of a EEG-based Brain Computer Interface application. As for scarce amount of data, the estimation problem is under certain and thus the solutions are strictly correlated with each other (multi-collinearity). Ridge regression (RR) represents the theoretical solution to this issue. In this paper we defined and implemented a new algorithm based on RR for the connectivity estimation in the case of few data samples. We tested the algorithm on surrogate data for different lengths and number of nodes. Results demonstrated how the new algorithm shows higher performances with respect to the classical one in the case of few data samples and provided some guidelines for its employment in connectivity estimation.**

***Keywords*—Partial Directed Coherence, EEG, Multicollinearity, Ridge Regression, Real Time.**

I. Introduction

Effective Connectivity aims at describing the influence that one neural system exerts on another as a pattern holding the direction and the strength of the information flow between such systems [1]. It could be estimated by using different methods both in time as well as in frequency domain based on multivariate models (MVAR).

Among the multivariate spectral estimators, the Partial Directed Coherence (PDC) technique been demonstrated to be the most accurate [2], [3]. Being based on multivariate approach, PDC has the advantage to reconstruct the connectivity pattern including, simultaneously, all the sources (EEG signals) in the model. However, the accuracy of such multivariate estimate, based on ordinary least square (OLS) prediction, is strictly related to the amount of data available. The number of data points should be, in fact, at least, one order of magnitude higher than the number of MVAR parameters to be inferred in the estimation process. This led to limitations in the use of connectivity in real time applications involving EEG signals. As this is not the case, the estimation problem, modelled by MVAR, is ill-posed and under certain and provided estimates of MVAR parameters strictly correlated each other (multicollinearity) [4].

The ridge regression (RR) might represent a theoretical solution to multicollinearity issue since it reduces the solutions space dimension through a regularization approach [5]. For this reason, the aim of the present paper is to define, implement and test an algorithm for effective connectivity estimation, based on ridge regression, able to track brain networks with high accuracy in the case of scarce amount of data, as a first step towards the real time application. The accuracy and reliability of the new algorithm was tested under different conditions of data lengths and number of nodes.

A. Partial Directed Coherence

Supposing that the following MVAR process is an adequate description of the dataset *Y*:

$$\sum_{k=0}^{p} A(k)X(n-k) = E(n) \text{ with } A(0) = I \quad (1)$$

where *X(n)* is the data vector in time, $E(n) = [e_1(n),\ldots,e_n(n)]^T$ is a vector of multivariate zero-mean uncorrelated white noise processes, *A(1),A(2),…,A(p)* are the *NxN* matrices of model coefficients and *p* is the model order.

It is possible to define the PDC estimator as follows:

$$\pi_{ij}(f) = \frac{|A_{ij}(f)|^2}{\sum_{m=1}^{N}|A_{im}(f)|^2} \quad (2)$$

where $A_{ij}(f)$ represents the frequency version of *ij* coefficient of multivariate autoregressive (MVAR) model used for modeling the dataset under investigation [2].

B. Ordinary Least Square (OLS)

The OLS is the classical algorithm used to estimate MVAR coefficients and is based on the minimization of the MVAR residual *E* as follows:

$$\hat{A} = arg\ \min\ (\|Y - AX\|^2) \quad (3)$$

where *Y* is the vector of data at the actual samples and *AX* is the estimate of *Y* using the *p* data samples preceding the actual one (*X*).

C. Ridge Regression

Ridge Regression is like OLS prediction but shrinks the estimated coefficients towards zero as follows [5]:

$$\hat{A}^{ridge} = arg\ \min\ (\|Y - AX\|^2 + \lambda\|A\|^2) \quad (4)$$

where $\lambda \geq 0$ is a tuning parameter, which controls the strength of the penalty term. Note that, when $\lambda=0$, we get the linear regression estimate.

D. Simulation Study

The simulation study consisted of the following steps:

i. Generation of simulated EEG datasets, fitting predefined ground truth networks of 5, 10 and 15 nodes (factor NODES), under different conditions of data length (factor LENGTH: 100, 200, 300, 500).
ii. Estimation of the connectivity patterns through the classical OLS approach and the new proposed algorithm based on RR. The RR was applied for different values of

TABLE I
RESULTS OF ANOVA

Factors	Err_0	Err_1
NODES	315*	278.4*
LENGTH	2072*	395.8*
ALGORYTHM	1315*	650.9*
LENGTH x ALGORYTHM	1146*	526.4*
LENGTH x NODES	365*	254.4*
NODES x ALGORYTHM	768*	381,8*
LENGTH x ALGORYTHM x NODES	680*	342,3*

$p<0.01$

λ (factor LAMBDA: 0,1,3,5,10, the case λ=0 corresponds to OLS algorithm).

iii. Evaluation of the performances of the two algorithms through the null (Err_0) and non-null (Err_1) connections errors:

$$Err_0 = \frac{1}{n_{null} nF} \sum_{f \in N_f} \sum_{i \in N_{null}} (A(i,f) - \bar{A}(i)) \quad (5)$$

$$Err_1 = \frac{1}{n_{no-null} nF} \sum_{f \in N_f} \sum_{i \in N_{no-null}} \left(\frac{A(i,f) - \bar{A}(i)}{\bar{A}(i)} \right) \quad (6)$$

Where nF is the number of frequency samples used for the estimate, $\bar{A}$ is the ground-truth network used for generating surrogate data, N_{null} is the null connections set of dimension n_{null} and $N_{no-null}$ is the null connections set of dimension $n_{no-null}$.

To increase the robustness of the subsequent statistical analysis, the entire procedure was repeated 100 times. The two errors were subjected to a two-way repeated measures ANOVA considering as within main factors LENGTH and ALGORITHM and as between factor NODES.

II. RESULTS

The results of the ANOVA were reported in Tab.1. All the three factors and their interactions influenced the two error parameters.

In Fig.1 we reported a comparison for Err_1 (panels a-c) and Err_0 (panels b-d) between the two algorithms across different LENGTH and NODES. In Fig.1a we noticed how, in the case of short data length (100 samples) and 5 nodes, OLS showed a really higher Err_1 (higher than 100%) with respect to what achieved by RR in all cases out of λ=1. The increase of λ in RR reduced the error close to zero. However, high values of λ (above 7) led to an under-estimation of the parameters (negative values for Err_1). For longer data lengths (Fig.1c) RR continued to show the best performances even if the error is reduced also for OLS. As for 500 data samples, OLS and RR showed similar values. However high values of λ deteriorated RR performances. The situation became worse for higher number of nodes since the minimum data length needed for having a nice accuracy applying RR increased to 200 and 300 samples for 10 and 15 nodes, respectively.

In Fig.1b-d we noticed a similar trend for null-connections error. In the case of 100 data samples, OLS confirmed to have the worst performances with an error above 60% for all the considered nodes number. Such error reduced with the increase of λ values used in RR algorithm. OLS and RR showed similar performances for data lengths above 200 samples in 5 nodes case, above 300 for 10 nodes case and above 500 for 15 nodes case.

III. CONCLUSION

The algorithm defined and implemented for the purposes of this work provided valid and accurate results in the estimates performed on simulated data affected by multicollinearity. In such condition, the RR algorithm resulted as the best method to estimate MVAR parameters if compared with the classical OLS approach. The results provided also some guidelines for the employment of such algorithm for connectivity estimation. They highlight, in fact, λ=7 as optimal value for regularization parameters in the analyzed cases since higher values of λ led to under-estimates the MVAR parameters. Moreover they confirmed the inefficacy of the choice λ=1 in RR algorithm, as a case in which the multicollinearity is amplified because all the solutions converge towards a unique one [6].

However, the good performances of RR algorithm deteriorated with the increase of the number of nodes, as expected. The errors assumed acceptable values for MVAR models including until 10 nodes. In the case of 15 nodes, it is necessary to increase the data length until 500 samples to reduce the errors.

In conclusion, the results reported here demonstrated how the new proposed approach for connectivity estimation based on Ridge Regression is suitable for connectivity estimates in case of scarce amount of data, opening the way to its possible employment in real time applications.

ACKNOWLEDGEMENT

Research partially supported by the Italian Ministry of Education, Project FIRB 2013-RBFR136E24, by the University of Rome Sapienza: Progetti di Ateneo per la Ricerca Scientifica anno 2014 and Avvio alla Ricerca anno 2015.

REFERENCES

[1] K. Friston, R. Moran, and A. K. Seth, "Analysing connectivity with Granger causality and dynamic causal modelling," *Curr. Opin. Neurobiol.*, vol. 23, no. 2, pp. 172–178, Apr. 2013.

[2] L. A. Baccalá and K. Sameshima, "Partial directed coherence: a new concept in neural structure determination," *Biol. Cybern.*, vol. 84, pp. 463–474, May 2001.

[3] L. Astolfi, F. Cincotti, D. Mattia, M. G. Marciani, L. A. Baccala, F. de Vico Fallani, S. Salinari, M. Ursino, M. Zavaglia, L. Ding, J. C. Edgar, G. A. Miller, B. He, and F. Babiloni, "Comparison of different cortical connectivity estimators for high-resolution EEG recordings," *Hum Brain Mapp*, vol. 28, no. 2, pp. 143–157, Feb. 2007.

[4] D. E. Farrar and R. R. Glauber, "Multicollinearity in Regression Analysis: The Problem Revisited," *Rev. Econ. Stat.*, vol. 49, no. 1, pp. 92–107, 1967.

[5] A. E. Hoerl and R. W. Kennard, "Ridge Regression: Biased Estimation for Nonorthogonal Problems," *Technometrics*, vol. 12, no. 1, pp. 55–67, 1970.

[6] D. I. Gibbons and G. C. McDonald, "A Rational Interpretation of the Ridge Trace," *Technometrics*, vol. 26, no. 4, pp. 339–346, Nov. 1984.

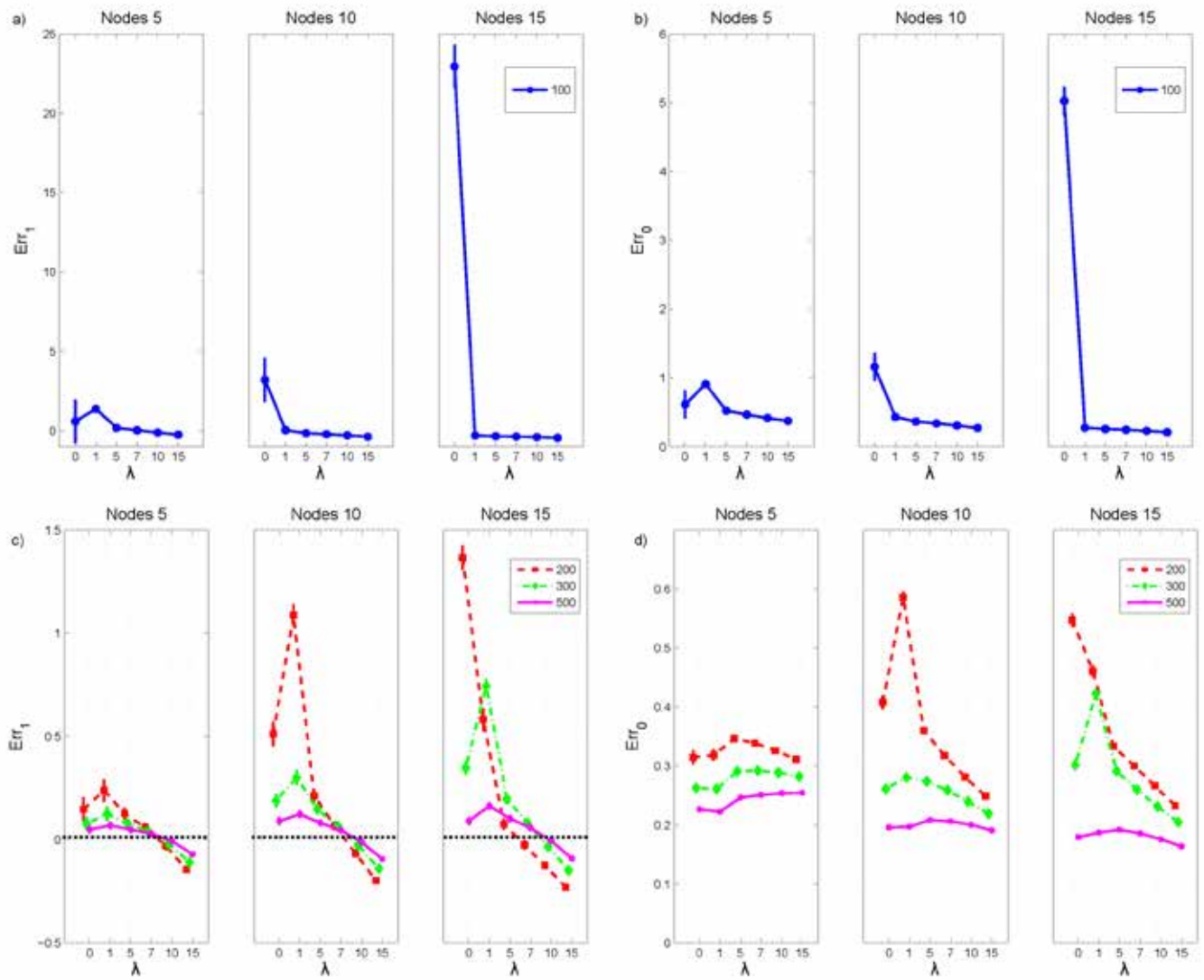

Fig.1 - Results of ANOVA on Err_1 (a) and Err_0 (b) achieved in PDC estimation process across different conditions of data lengths (factor LENGTH: 100 samples in panels a and b, 200-300-500 samples in panels c and d) and number of nodes (factor NODES). The trends were reported for different values of regularization parameter used in RR algorithm. The case λ=0 corresponds to OLS algorithm. The value of Err_1 and Err_0 achieved in the case of λ=0, 10 and 15 nodes and data length of 100 was too high to prevent the detailed observation of other cases. For this reason we decided to adjust the limits of y-axis without taking into account such values.

Assessing minimum continuous glucose monitoring sensor accuracy needed for non-adjunctive use

M. Vettoretti[1], A. Facchinetti[1], G. Sparacino[1] and C. Cobelli[1]
[1] *Department of Information Engineering, University of Padova, Padova, Italy*

***Abstract*—Continuous glucose monitoring (CGM) sensors, which measure glucose concentration in the subcutis almost continuously, can potentially improve glycemic control in type 1 diabetes (T1D). Despite becoming more and more accurate, CGM is still not approved to be used for insulin dosing non-adjunctively i.e. without requiring confirmatory measurements collected by fingerstick devices. Defining the minimum level of CGM accuracy required for its non-adjunctive use is currently matter of investigation in the literature. Current state-of-art methods present limitations that in this work we overcome by an approach based on the use of a recently proposed model of T1D patient decision-making. Some representative examples of results obtainable by the approach are then documented.**

***Keywords*—Glucose sensors, diabetes, simulation, modeling, measurement error.**

I. Introduction

Type 1 diabetes (T1D) is a chronic disease in which pancreas beta cells do not produce insulin, the hormone responsible for the control of blood glucose (BG) concentration. Conventional T1D therapy consists of exogenous insulin administrations tuned by self-monitoring of blood glucose (SMBG) measurements collected 3-4 times per day by fingerprick devices. Several clinical studies demonstrated that glucose control can be significantly improved by the use of continuous glucose monitoring (CGM) sensors [1], i.e. minimally-invasive sensors which measure interstitial glucose (IG) concentration every 1-5 minutes for up to 7 days. Indeed, CGM sensors can provide the patient in real-time with information about glucose trend and alerts in response to dangerous hyper/hypoglycemic events. Nevertheless, because it has suffered from accuracy problems, CGM is approved in the United States only to support conventional SMBG. Despite the recent improvements achieved in CGM sensors' performance, if CGM is accurate enough to be safely used non-adjunctively, i.e. without requiring confirmatory SMBG measurements before making therapeutic decision, is still an open question. Indeed, a minimum level of CGM sensor accuracy for non-adjunctive use has not been already defined.

Defining the minimum level of CGM accuracy required for non-adjunctive use is presently matter of investigation in the literature. In this contribution we demonstrate that the current state-of-art method to assess the minimum level of CGM accuracy needed for non-adjunctive use [2] has several critical aspects. To overcome its limits, we propose an alternative method based on the use of a recently proposed model of T1D patient decision-making [3]. The use of the new approach is demonstrated by some representative examples.

II. State of art and open issues

The current state-of-art method to assess the minimum level of CGM sensor accuracy for non-adjunctive use is due to Kovatchev et al. [2]. Simulations were performed by a retrospective method based on the net effect concept [4] that exploits a linear and time-invariant model of T1D patient physiology and consists in two steps. In the first step CGM and insulin pump data simultaneously recorded in a T1D patient are used to retrospectively estimate a signature of BG variability, called net effect, which is supposed to reflect a combination of components contributing to BG variability like oral carbohydrate intake, variation in insulin sensitivity and meal and exercise behaviours. In the second step, the estimated net effect signal is used as a forcing input in the patient model to predict the effect of a modified insulin therapy on glucose concentration.

Kovatchev et al. applied the simulation approach based on the net effect to assess the glycemic outcomes achieved by CGM-based therapies for different levels of CGM accuracy. CGM profiles were simulated randomly extracting error traces from a separate training set calculated as the difference between CGM and high-accuracy BG references. Sensor error traces were then modulated to simulate different levels of CGM accuracy that was quantified by the mean absolute relative difference (MARD) between CGM samples and BG references. Results allowed the authors to conclude that non-adjunctive use of CGM is feasible for sensors with MARD≤10%.

The method of Kovatchev et al. presents several critical aspects. First, it is based on a simplified model of patient physiology, which does not include inter- and intra-patient variability of physiology, since model parameters are set to population values constant over time. Moreover, the model is linearized about the basal state and thus it cannot properly describe the patient glucose-insulin dynamics when its state significantly moves from the basal, e.g. during meals.

Another issue concerns how CGM accuracy was simulated. Since CGM measures glucose concentration in the interstitial fluid while reference samples are collected in the blood, the CGM error traces include an error component introduced by the BG-to-IG kinetic, which is dependent on the BG profile [5]. Nevertheless, the authors improperly use the error traces extracted from the training dataset to simulate CGM error in the test dataset i.e. on different BG profiles, thus possibly generating not realistic CGM recordings.

Finally, CGM accuracy was assessed exclusively by MARD which is not sufficient to fully represent the sensor accuracy and its impact on glycemic outcomes. Indeed,

MARD is an index of the sensor average performance that results from the combination of several components contributing to the sensor error, described in section III.

III. The proposed method

The T1D patient decision-making model

An alternative strategy presently under development in our group is based on a T1D patient decision-making model [3], schematized in Fig. 1. The model includes four submodels:

- the UVa/Padova T1D simulator [6] (A), a non-linear model of patient physiology that allows to simulate BG dynamics of 300 T1D virtual patients for several days thanks to the description of inter-subject variability of model parameters and intra-subject variability of insulin sensitivity;
- models of SMBG [7] and CGM [8] errors (B);
- a model of the open-loop T1D therapy (C) i.e. the patient behaviour in tuning insulin and carbohydrate doses according to SMBG or CGM measurements;
- a model of insulin delivery via insulin pump (D).

CGM traces are simulated by the model of Facchinetti et al. [7], which explicitly takes into account the three main components of sensor error: BG-to-IG distortion, calibration error and measurement noise. As a result, CGM traces can be simulated starting from BG in three steps. First, the IG profile is obtained as the response to the BG profile of a first-order dynamic system with impulse response $h(t) = 1/\tau \cdot e^{-t/\tau}$ and time constant τ, equivalent to the two-compartment model published in [5]. Then, a first-order linear transformation with time-varying parameters is applied to IG to simulate the calibration error, thus obtaining IG_s:

$$IG_s = (a_0 + a_1 \cdot t) \cdot IG + b_0 + b_1 \cdot t \quad (1)$$

where a_0 and a_1 represent sensor multiplicative bias and drift, b_0 and b_1 represent sensor additive bias and drift. The final CGM trace is obtained adding to IG_s the sensor measurement noise which is simulated by a second-order autoregressive model with input noise variance λ^2. To sum up, the sensor error is described by 6 parameters: τ, a_0, a_1, b_0, b_1 and λ^2.

Defining minimum sensor accuracy for non-adjunctive use

The T1D patient decision-making model can be used for several applications involving the in silico testing of SMBG- and CGM-based T1D therapies. An interesting application is its use for the assessment of the minimum level of CGM sensor accuracy required for the non-adjunctive use. For such a purpose, a sensitivity analysis can be performed on CGM error parameters in order to assess how the components of the sensor error affect glycemic outcomes, such as the time spent in hyper/hypoglycemia. The final aim is to define the region in the space of sensor error parameters for which the non-adjunctive use of CGM is safe i.e. the glycemic outcomes obtained by the non-adjunctive use of CGM are comparable to those produced by the conventional SMBG. Since the parameters of the sensor error are not independent from each other, the sensitivity analysis must be performed taking into account the correlations between the sensor error parameters. For simplicity, in the following section we will present an example in which the T1D patient decision-making model is used to perform a sensitivity analysis on parameter a_0 assuming it independent from other sensor error parameters.

IV. Example

In the simulated example of Fig. 2, a sensitivity analysis is performed on multiplicative bias a_0. The red dash-dot line represents the BG profile obtained by the decision-making model when dinner insulin bolus is calculated by the true BG value, i.e. no error is simulated on glucose measurements. The black dash-dot line is the BG profile obtained when dinner bolus is calculated by the simulated CGM profile depicted in grey. In panels A, B, C and D, results are shown for different values of a_0 i.e. 1.100, 1.050, 1.025 and 1.000 respectively. While for a_0=1.100, 1.050, and 1.025, an overestimation of the insulin dose results in a nocturnal hypoglycemia with time spent below 70 mg/dl equal to 112, 72 and 40 min respectively, when a_0=1.000 hypoglycemia is prevented. Therefore, in this representative example the non-adjunct use of CGM is safe only for $a_0 \leq 1$. Importantly, this example points out how MARD is not appropriate to evaluate the impact of CGM accuracy on glycemic outcomes. Indeed, for all the tested values of a_0, CGM presents an MARD≤10% compared to BG (black dash-dot line), and thus it would be considered appropriate for non-adjunctive use according to the results of Kovatchev at al. [2].

V. Conclusion

A simulation approach to assess the minimum level of CGM sensor accuracy for non-adjunctive use was proposed based on a T1D patient decision-making model. Future works concern the extension of the sensitivity analysis to all the sensor error components, properly taking into account their correlation, and to the whole population of virtual subjects.

References

[1] J. E. Lane, J. P. Shivers and H. Zisser, "Continuous glucose monitors: current status and future developments", *Curr Opin Endocrinol Diabetes Obes*, vol. 20, no. 2, pp. 106-111, 2013.

[2] B.P. Kovatchev, S.D. Patek, E.A. Ortiz, and M. Breton, "Assessing sensor accuracy for non-adjunct use of continuous glucose monitoring," *Diabetes Technol Ther*, vol. 17, no.3, pp. 1-10, 2015.

[3] M. Vettoretti, A. Facchinetti, G. Sparacino, and C. Cobelli, "Patient decision-making of CGM sensor driven insulin therapies in type 1 diabetes: in silico assessment. *Conf Proc IEEE Eng Med Biol Soc*, pp. 2363-6, 2015.

[4] S.D. Patek, D. Lv, E.A. Ortiz, C. Hughes, S. Kulkarni et al., "Empirical representation of blood glucose in a compartmental model," in *Prediction Methods for Blood Glucose Concentration*, Springer International Publishing, 2016.

[5] K. Rebrin, G. M. Steil, W. P. Van Antwerp and J. J. Mastrototaro, "Subcutaneous glucose predicts plasma glucose independent of insulin: implication for continuous monitoring", *Am. J. Physiol.,* vol. 277, no. 3, pp. E561-571, 1999.

[6] C. Dalla Man, F. Micheletto, M. Breton, B.P. Kovatchev, and C. Cobelli, "The UVA/PADOVA Type I diabetes simulator: new features," *J Diabetes Sci Technol,* vol. 8, no.1, pp. 26-34, 2014.

[7] M. Vettoretti, A. Facchinetti, G. Sparacino, and C. Cobelli, "Accuracy of devices for self-monitoring of blood glucose: a stochastic error model," *Conf Proc IEEE Eng Med Biol Soc,* pp.2359-62, 2015.

[8] A. Facchinetti, S. Del Favero, G. Sparacino, and C. Cobelli, "Model of glucose sensor error components: identification and assessment for new Dexcom G4 generation devices," *Med Biol Eng Comput*, vol. 53, no.53, pp. 1259-69, 2015.

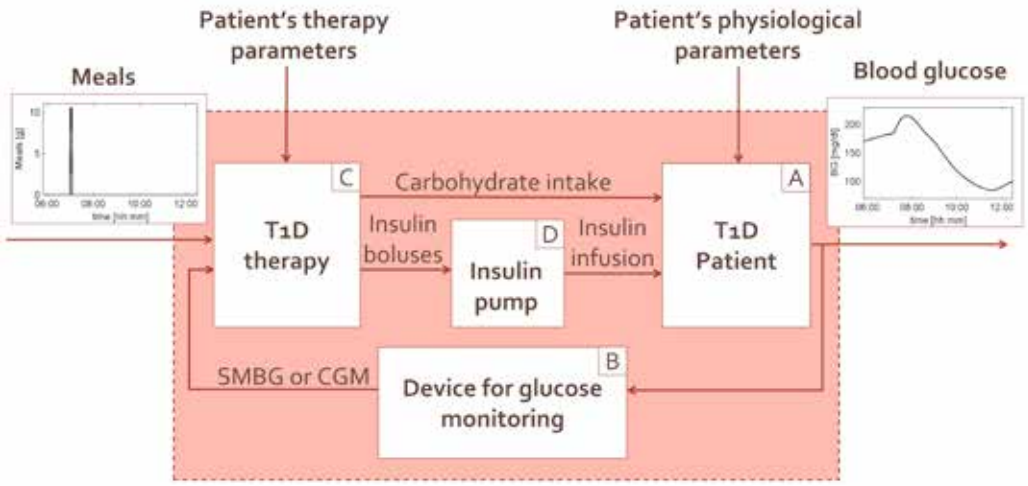

Fig. 1. Schematic representation of the T1D patient decision-making model. The model input are a sequence of meals and patient's therapy and physiological parameters, the model output is the resulting BG profile. The model is composed by four interconnected submodels: a model of the T1D patient physiology (A), models of SMBG or CGM device for glucose monitoring (B), a model of T1D therapy (C) and a model of insulin delivery via insulin pump (D).

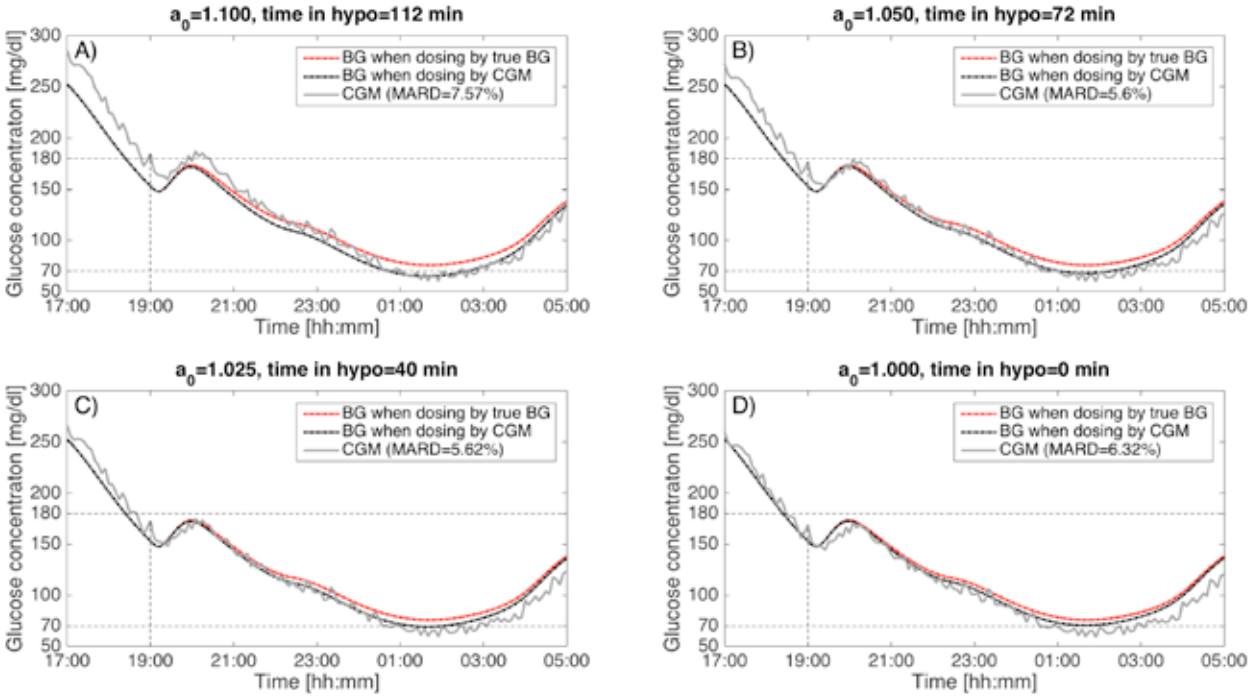

Fig. 2. Use of the T1D patient decision-making model to perform a sensitivity analysis on multiplicative bias a_0 in a representative subject. Panels A to D reports: the BG profile obtained when dinner insulin bolus is calculated by the true BG value (red dash-dot line); CGM profiles (grey line) simulated for different values of a_0, i.e. 1.100, 1.050, 1.025 and 1.000 respectively in panels A, B, C and D; the BG profile obtained when dinner bolus is calculated by the simulated CGM profile (black dash-dot line).

INFORMATICA MEDICA

Using MetaMap to extract medical concepts from unstructured clinical notes written in Italian

E. Chiaramello[1], A. Paglialonga[1], F. Pinciroli[1,2] and G. Tognola[1]
[1]CNR, Istituto di Elettronica e di Ingegneria dell'Informazione e delle Telecomunicazioni, Milano, Italy
[2]Retired Full Professor Politecnico di Milano, DEIB, e-HealthLAB, Milano, Italy

***Abstract*— We assessed the feasibility of using MetaMap to extract disorders, symptoms and findings from Italian clinical notes. We performed two experiments: in "Exp A" we used MetaMap and a knowledge source consisting of Italian UMLS sources to annotate Italian clinical notes, in "Exp B" we used MetaMap to analyze an English unsupervised translated version of the original Italian texts. Average recall, precision and F-measure were equal to 0.53, 0.98 and 0.69, in "Exp A", and to 0.75, 0.95 and 0.83, in "Exp B". For both experiments, MetaMap showed better performances for "Disorders" than for "Findings" and "Symptoms". In conclusion, MetaMap's performances with unstructured clinical notes written in Italian could be improved modifying MetaMap to allow generating Italian variants. MetaMap's performances with English translation the original Italian texts, performances were good enough to allow using MetaMap in clinical practice. Further improvements could be obtained using a supervised translation of medical terms.**

***Keywords*— Clinical information extraction, Unstructured clinical notes, Italian language, EHR data reuse.**

I. Introduction

NATURAL Language Processing (NLP) tools were developed to extract information from unstructured text and convert it to a structured form. NLP tools were adapted to analyze a wide range of texts, including clinical notes [1]. Clinical notes are widely used in clinical practice to report various types of information about patients. Information extraction from clinical notes has the potential to make a significant impact in many aspects of healthcare and biomedical research [1]. Nevertheless, it could be difficult, as clinical notes contain abbreviations, acronyms, misspellings, terms specific to the peculiar medical context, and are written by clinicians in their own languages [1]. Some efforts were recently done to develop new NLP tools for the extraction of medical concepts in texts written in languages different from English, e.g. for Spanish [2], French [3], and Swedish [4]. To the best of our knowledge, no previous study focused on the extraction of medical concepts from clinical notes written in Italian.

The goal of this study was to understand if it could be feasible to use a NLP tool developed to process English text to extract medical concepts from clinical notes written in Italian. Among all the well-established NLP tools, we chose to use MetaMap, a tool developed by the National Library of Medicine (NLM) [5]. MetaMap uses computational linguistic techniques to identify concept in free texts written in English and map them to the Unified Medical Language System (UMLS) [6]. Our need was to adapt the existing NLP tool to annotate Italian clinical notes and not to develop a new "Italian MetaMap". We performed two experiments: in "Exp A", we used MetaMap to annotate Italian clinical notes using a knowledge source consisting of Italian UMLS sources; in "Exp B", we translated clinical notes from Italian to English using Google Translator, and then we used MetaMap to annotate the translated texts.

II. Materials and Methods

A. Experimental Setup

Fig. 1 shows the workflow of the two experimental lines. We performed manual and MetaMap annotations on clinical notes written in Italian ("ITA-dataset") and on their unsupervised translation from Italian to English ("ENG-dataset"), using two knowledge sources, "ITA-Metathesaurus" containing Italian UMLS sources, and "ENG-Metathesaurus", containing English UMLS sources. We computed recall, precision and F-measure by comparing MetaMap's and manual annotations.

B. Dataset: normalization and ITA to ENG translation

Our dataset consists of 3462 unstructured sentences from clinical notes written in Italian, collected at the "Policlinico" hospital in Milan (Italy). We performed 'normalization', a text-preprocessing task aimed at removing acronyms, abbreviation and spelling errors. The normalized dataset was called "ITA-dataset". Clinical notes were then translated in English using Google Translator, obtaining "ENG-dataset".

C. Manual annotation

Two expert annotators manually identified medical conceps in "ITA-dataset" and "ENG-dataset", and assigned the corresponding Concept Unique Identifier (CUI) found in "ITA-Metathesaurus" and "ENG-Metathesaurus". The inter-annotator agreement was equal to 0.75. We extracted medical terms belonging to the semantic categories of "Disorders", "Findings", and "Symptoms".

D. MetaMap annotation

In addition to default processing options [6], we used the option "ignore_word_order" to allow MetaMap identifying those concepts in which words were not reported in the standard order.

E. Data analysis

Only cases in which manual and MetaMap annotations gave the same CUI were considered as exact matches. All the other cases, i.e. partial mapping, mapping to a CUI different from the one identified during the manual annotation, or missing identification of the noun phrase, were considered as failures. We computed recall, precision, and F-measures. As defined by [7], recall is the proportion of the target concepts

that MetaMap identified correctly, precision is the proportion of medical concepts mapped by MetaMap identified correctly and F-measure is the harmonic mean of precision and recall.

III. Results

Manual annotation of "ITA-dataset" and "ENG-dataset" led to a total number of 2077 medical concepts: for 99% of them (2056 concepts) we found a proper mapping in UMLS. More specifically, 77% of concepts were mapped as "Disorders", 11% as "Findings" and 12% as "Symptoms".

Fig. 2 shows MetaMap's performances. In "Exp A", on average, recall, precision and F-measure across the three semantic categories were equal to 0.53, 0.98 and 0.69. In "Exp B", on average, recall, precision and F-measure across the three semantic categories were equal to 0.75, 0.93 and 0.84. In both "Exp A" and "Exp B" "Disorders" had the highest recall among the three semantic categories, while "Findings" showed the lowest one. Precision had similar values for the three semantic categories, ranging from 0.98 to 1 ("Exp A") and from 0.90 to 0.94 ("Exp B").

IV. Discussion

A. Concepts coverage

In this study, we found that 99% of the concepts identified in the Italian clinical notes had a proper mapping in the Metathesaurus. Our findings are well in line with results found for texts originally written in English (see, e.g., [8]). Most of concepts were mapped as "Disorders": this is in line with previous findings that revealed that most medical terms in clinical notes belonged to the category of "Disorders" [9].

B. Recall and precision

In "Exp A", recall and precision were equal to 0.53 and 0.98. This means that, although MetaMap was developed to deal with texts written in English [6], it allowed identifying about half of the concepts in the originally written Italian texts. In "Exp B", recall and precision were equal to 0.75 and 0.95. Our results are in line with those obtained in previous studies, which applied MetaMap to medical texts originally written in English (see, e.g. [10]). In "Exp A", we obtained lower recall and higher precision than in "Exp B". This result was not surprising, as MetaMap processing was optimized for texts written in English, thus some of its processing steps do not work properly with texts written in Italian. In both experiments, we obtained better performances for the "Disorders" semantic category than for "Findings" and "Symptoms". This is in line with results described in [11], in which MetaMap was used with clinical discharge summaries originally written in English, achieving better performances for "Diseases" than for "Findings" and "Symptoms".

C. Variants, translations and slangs

We observed that MetaMap's failures occurred in "Exp A" were mainly due to the impossibility for MetaMap to generate variants for Italian noun phrases. As a matter of fact MetaMap's "variant generation" processing step is based on English linguistic sources [6] that do not apply with languages different from English. MetaMap's failures occurred in "Exp B" were mainly due to a bad ITA to ENG translation of medical terms and to the use of specific medical slang, a well-known feature of clinical notes [1].

D. Italian versus Spanish

The approach we used of combining unsupervised English translation and MetaMap is similar to the one described in [2], which assessed the feasibility of using MetaMap to extract concepts from unstructured texts written in Spanish. However, there were two main differences between our study and [2]: we used a different language (Italian vs Spanish in [2]) and we analyzed different types of texts (clinical notes vs articles from literature in [2]). Using a different language might affect both the accuracy of Google translation and the coverage of UMLS, while using clinical notes instead of biomedical literature could affect both the quality of Google translation and MetaMap's performance. It is interesting to compare our results and those reported by [2]: in "Exp B", we obtained an average recall equal to 0.75, which is slightly higher than mean similarity (a performance measure similar to recall) equal to 0.71 calculated across the experiments [2].

V. Conclusion

MetaMap's performances with English translation of Italian texts were good enough to allow using MetaMap in a wider investigation in clinical practice. Further improvements could be obtained using an affordable supervised translation of medical terms.

Acknowledgement

The activities come within the Scientific Agreement on "Progress in Clinical Informatics" [Polytechnic of Milan, Fondazione Ca' Granda Ospedale Maggiore Policlinico, and IEIIT CNR 2015-17].The authors gratefully acknowledge A. Bonalumi and A. Caroli from Osp Maggiore Policlinico, Milano, for their useful help in data collecting and management.

References

[1] S.M. Meystre, et al. "Extracting information from textual documents in the electronic health record: a review of recent research," *Yearb Med Inf,* vol. 35, pp. 128-144, 2008.

[2] F. Carrero, J.C. Cortizo, J.M. Gómez, "Building a Spanish MMTx by Using Automatic Translation and Biomedical Ontologies,", *Intelligent Data Engineering and Automated Learning*, pp. 346-353, 2008.

[3] L. Deléger, et al. "Extracting Medication Information from French Clinical Texts," *Stud Health Technol Inf,* vol. 160, pp. 949-53, 2010.

[4] M. Skeppstedt, et al, "Automatic recognition of disorders, findings, pharmaceuticals and body structures from clinical text: an annotation and machine learning study," *J. Biomed. Inf,* vol. 49, pp. 148-58, 2014.

[5] A.R. Aronson, "Effective mapping of biomedical text to the UMLS Metathesaurus: the MetaMap program", *Proceedings of the AMIA Symposium. AMIA*, 2001.

[6] O. Bodenreider, "The unified medical language system (UMLS): integrating biomedical terminology", *Nucleic acids research*, vol. 32(1), pp. 267-70, 2004.

[7] C.D. Manning, H. Schütze. Foundations of statistical natural language processing. MIT press, Cambridge, 1999.

[8] G. Divita, T. Tse, L. Roth, "Failure analysis of MetaMap transfer (MMTx)," *Stud. Health Technol. Inform*, vol. 107, pp. 763–67, 2004.

[9] S.T. Wu, et al, "Unified Medical Language System term occurrences in clinical notes: a large-scale corpus analysis," *JAMIA*, vol. 19, pp 149-56, 2012.

[10] S. Meystre, P.J. Haug, "Natural language processing to extract medical problems from electronic clinical documents: Performance evaluation," *J. Biomed. Inform*, vol. 39, pp. 589–599, 2006.

[11] T. Sibanda, T. He, P. Szolovits, and O. Uzuner "Syntactically-informed semantic category recognizer for discharge summaries." *AMIA annual symposium proceedings*, pp. 714–718, 2006.

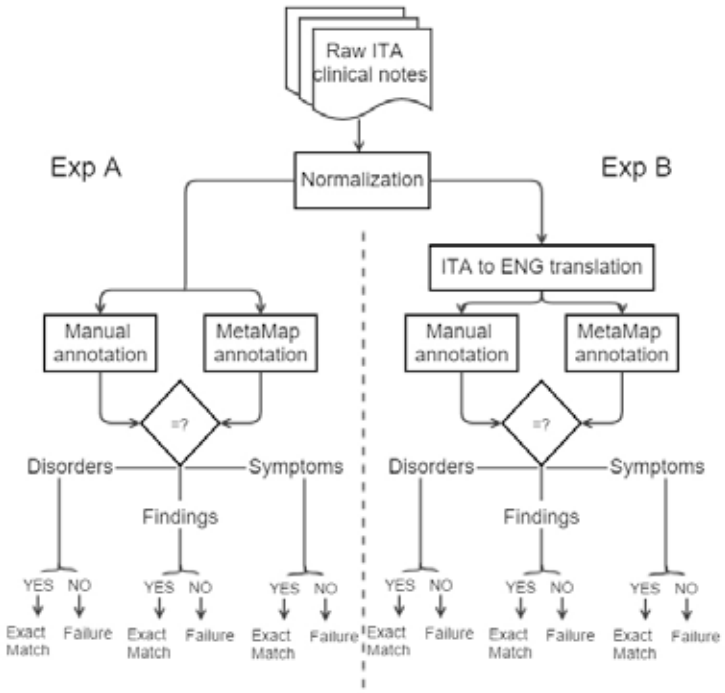

Fig. 1. Flowchart of "Exp A" and "Exp B".

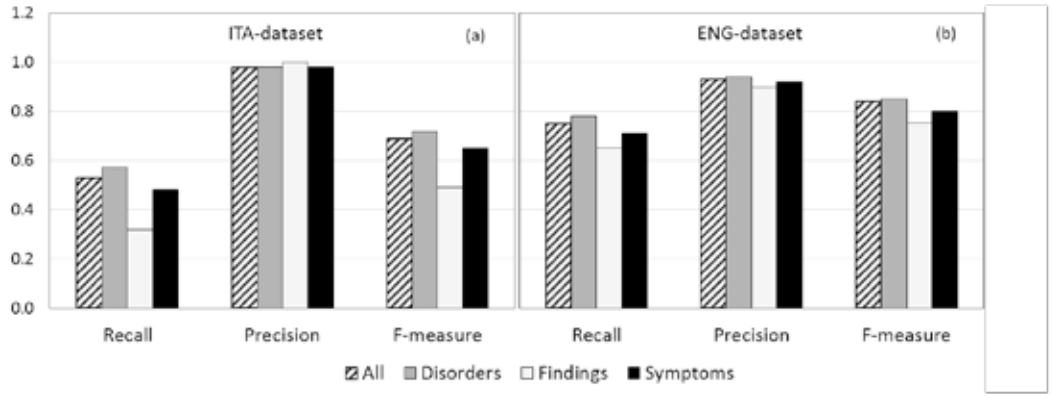

Fig. 2. Recall, precision, F-measure for (a) "ITA-dataset" ("Exp A") and (b) "ENG-dataset" ("Exp B")

Supporting utility coefficient elicitation in a shared-decision making context

E. Salvi[1], E. Parimbelli[1], S. Quaglini[1], and L. Sacchi[1]
[1]Department of Electrical, Computer and Biomedical Engineering, University of Pavia, Italy

***Abstract*— In shared decision making, the utility elicitation process involves the choice of one or more elicitation methods. This choice is not straightforward, especially for users who are not familiar with the theoretical framework, and decision support for this task is lacking. This paper presents the formalization and implementation of an evidence-based system meant to guide users in the choice and administration of a utility coefficients elicitation method.**

***Keywords*—shared-decision making, patient preferences, utility coefficients.**

I. INTRODUCTION

In a patient-centred care context, medical decisions are based both on clinical evidence and on patients' personal preferences. From the physician's perspective, involving patients in medical choices where a clinically superior alternative has not been proved means discussing with them all the available options and assessing their preferences discussing about possible outcomes, in a process known as *shared decision making* (SDM).

Decision trees (DT) [1] may be used to formally represent specific clinical decision problems. A DT is a graph representing the different options (e.g., two or more alternative drugs) and all their consequences in probabilistic terms. In those models, patients' preferences may be included as utility coefficients (UC), i.e. values that patients associate to the different health states they could experience after a therapeutic choice. The DT solution consists in finding the option that maximizes the expected utility. In order to elicit UCs, we developed UceWeb, a system that implements three well-known elicitation methods, namely time trade-off (TTO), standard gamble (SG), and rating scale (RS) [2]. UceWeb has already been tested on two sets of patients, affected by atrial fibrillation [2] and spinal cord injury [3] respectively, and during those experiences we detected some criticalities in the elicitation process, which will be illustrated in the next sections.

II. ANALYSIS OF THE PROBLEM

In a SDM scenario, given a decision problem modelled using a DT, the physician needs to elicit from the patient a utility coefficient for each health state included in the model. A physician who is not familiar with the underlying theoretical framework could assume that the different elicitation methods are equally applicable to every patient. On the contrary, elicited values may be biased due to specific characteristics of both patients and health states. For example, the standard TTO may be inappropriate when the elicitation concerns temporary health states, defined as non-chronic health states lasting less than one year [4]-[6]. In addition, it may not be suitable for patients whose life expectancy is lower than 5 years [7]-[8]. To our knowledge, no tools have been yet developed to guide the choice of the elicitation method, and this is detrimental for two main reasons. First, lack of support can impact on the physician's motivation to engage in SDM, because of the negative patients' feedback when unsuitable methods are used. Second, and more important, biased utility coefficients may lead to misjudging patients' preferences in the decision making process, ultimately leading to sub-optimal decisions. To bridge this gap, we propose a tool able to guide physicians in the choice of the utility elicitation method, which should be tailored both to the patient and to the actual health state. We embedded this tool in the UceWeb system.

III. PROPOSED SOLUTION

To properly implement the decision support tool, we first enhanced UceWeb by introducing two additional elicitation methods:

- a variant of the time trade-off method known as "daily time trade-off" (DTTO), which is characterized by a shorter time horizon than the original version [5],[9] .
- the "willingness to pay" method (WTP), which casts to a utility coefficient the patient's willingness to hypothetically trade an amount of resources in exchange for perfect health.

Moreover, we formalized twelve rules on the basis of the collected literature evidence (Table I). Each rule is made up of four components:

- *condition*: the patient's or the health state characteristic that triggers the rule
- *target*: the elicitation method the rule is referred to
- *action*: the type of recommendation the rule indicates about the target. Available actions are "suggest" (S), "advise against" (A) and "exclude" (E)
- *reliability score*: an integer value ranging from 1 to 5, assigned according to the significance of the supporting evidence (1 represents maximum reliability).

For example, the first rule in Table I means that in the literature there is highly reliable evidence that advises against the use of the TTO method when the elicitation concerns a temporary health state.

We implemented an engine that triggers rules by matching rule conditions with actual patient's and health state data, providing an overall recommendation for each elicitation method. That recommendation is presented as a traffic light, as shown in Figure 1. The traffic light colour represents the suggested action for the considered method. In case of no evidence, the colour is white. This information is

TABLE I
FORMALIZED RULES

Condition	*Action*	*Target*	*Reliability score*
Temporary health state (Non-chronic health state, lasting less than one year)	A	TTO	1
	S	DTTO	2
	A	SG	3
Patient unemployed (Patient who is not officially employed)	A	DTTO	4
Mild health state (Health state that is not highly impairing, whose utility coefficient is expected to be close to 1)	A	TTO	1
	S	DTTO	3
Short patient's life expectancy (Patient with life expectancy <5 years)	A	TTO	2
Patient is also a caregiver (Patient who feels responsible for young children or non autonomous adult family members)	A	TTO	3
	A	SG	4
Health state involving real-life risky decision (Impairing health state potentially curable with high-risk surgery)	S	SG	4
Zero-trader patient (Patient who refuses to trade/gamble in elicitation tasks independently from his/her perception of the examined health state)	E	Any method	1
Patient's life length expectation differs from the presented values (Patient who thinks his life expectancy is different from that presented during a TTO task)	A	TTO	3

Table I . The rules formalized in the decision support tool (A=advise against, S=suggest, E=exclude)

complemented with a legend showing the meaning of the colours, and with the detailed list of all the triggered rules, provided with the corresponding supporting evidence (Figure 2). It is also possible to retrieve the average rating scores assigned by the same patient and by the same physician in previous elicitations.

The complete UceWeb elicitation flow is summarized in Figure 3. As the decision support tool is activated, some recommendations are provided to the physician on the basis of patient's data and of the considered health state.

The physician can select the desired elicitation method according to the proposed recommendations. After this choice, the system might deliver further advices, which depend on the selected method and on the patient's attitude. For example, at the beginning of a standard TTO elicitation, the patient is presented with an estimate of his life expectancy. This value may differ from the patient's subjective expectation, and this difference may bias the resulting utility coefficient [10]-[11]. If such a divergence is detected, the physician receives a warning message in form of a yellow traffic light and can decide, after evaluating the available evidence, whether to proceed with the TTO elicitation. Testing the zero-trading condition is another key step in the flow. The majority of the elicitation tasks consist either in hypothetically trading time (TTO and DTTO) or resources (WTP) in exchange for perfect health, or in accepting a death risk in a hypothetical gamble for complete recovery (SG). In utility theory, patients are expected to be unwilling to trade/gamble only in case of perfect health. However, it has been shown that patients may behave as *zero-traders* due to factors that are independent from their perception of the examined health state [4],[12]. In case a patient is not willing to trade even if not judging a specific health state as perfect, the performed elicitation is not valid and the physician is asked to proceed with another method.

IV. CONCLUSION

The described decision support tool has currently been implemented and added to the Uceweb system. Future work will be focused on the validation of the tool during a real-world pilot study. The aim of the evaluation is to demonstrate that this system could help the physician to better understand the elicitation methods and promote shared decision making in clinical practice.

REFERENCES

[1] M. C. Weinstein and H. V. Fineberg, *Clinical Decision Analysis*. Saunders, 1980.

[2] E. Parimbelli, L. Sacchi, S. Rubrichi, A. Mazzanti, and S. Quaglini, 'UceWeb: a Web-based Collaborative Tool for Collecting and Sharing Quality of Life Data', *Methods Inf. Med.*, vol. 53, no. 6, Nov. 2014.

[3] E. Parimbelli, G. Fizzotti, C. Pistarini, C. Rognoni, and S. Quaglini, 'Quality of Life Measurements in Spinal Cord Injury Patients', *Stud. Health Technol. Inform.*, vol. 216, p. 998, 2015.

[4] K. S. Boye, L. S. Matza, D. H. Feeny, J. A. Johnston, L. Bowman, and J. B. Jordan, 'Challenges to time trade-off utility assessment methods: when should you consider alternative approaches?', *Expert Rev. Pharmacoecon. Outcomes Res.*, vol. 14, no. 3, pp. 437–450, May 2014.

[5] J. K. Buckingham, J. Birdsall, and J. G. Douglas, 'Comparing three versions of the time tradeoff: time for a change?', *Med. Decis. Mak. Int. J. Soc. Med. Decis. Mak.*, vol. 16, no. 4, pp. 335–347, Dec. 1996.

[6] D. R. Wright, E. Wittenberg, J. S. Swan, R. A. Miksad, and L. A. Prosser, 'Methods for Measuring Temporary Health States for Cost-Utility Analyses':, *PharmacoEconomics*, vol. 27, no. 9, pp. 713–723, Sep. 2009.

[7] J. N. Doctor, H. Bleichrodt, and H. J. Lin, 'Health Utility Bias: A Systematic Review and Meta-Analytic Evaluation', *Med. Decis. Making*, vol. 30, no. 1, pp. 58–67, Jan. 2010.

[8] B. J. McNeil, R. Weichselbaum, and S. G. Pauker, 'Speech and survival: tradeoffs between quality and quantity of life in laryngeal cancer', *N. Engl. J. Med.*, vol. 305, no. 17, pp. 982–987, Oct. 1981.

[9] R. Schiffner, S. Brunnberg, U. Hohenleutner, W. Stolz, and M. Landthaler, 'Willingness to pay and time trade-off: useful utility indicators for the assessment of quality of life and patient satisfaction in patients with port wine stains', *Br. J. Dermatol.*, vol. 146, no. 3, pp. 440–447, Mar. 2002.

[10] E. Heintz, M. Krol, and L.-Å. Levin, 'The Impact of Patients' Subjective Life Expectancy on Time Tradeoff Valuations', *Med. Decis. Making*, vol. 33, no. 2, pp. 261–270, Feb. 2013.

[11] F. van Nooten and W. Brouwer, 'The influence of subjective expectations about length and quality of life on time trade-off answers', *Health Econ.*, vol. 13, no. 8, pp. 819–823, Aug. 2004.

[12] L. A. Augestad, K. Rand-Hendriksen, K. Stavem, and I. S. Kristiansen, 'Time trade-off and attitudes toward euthanasia: implications of using "death" as an anchor in health state valuation', *Qual. Life Res.*, vol. 22, no. 4, pp. 705–714, May 2013.

Fig. 1. Example of recommendation for the DTTO method. The "Help" link shows the colour legend, "View details" shows the triggered rules summary, and "View rating" shows the rating scores obtained in previous elicitations.

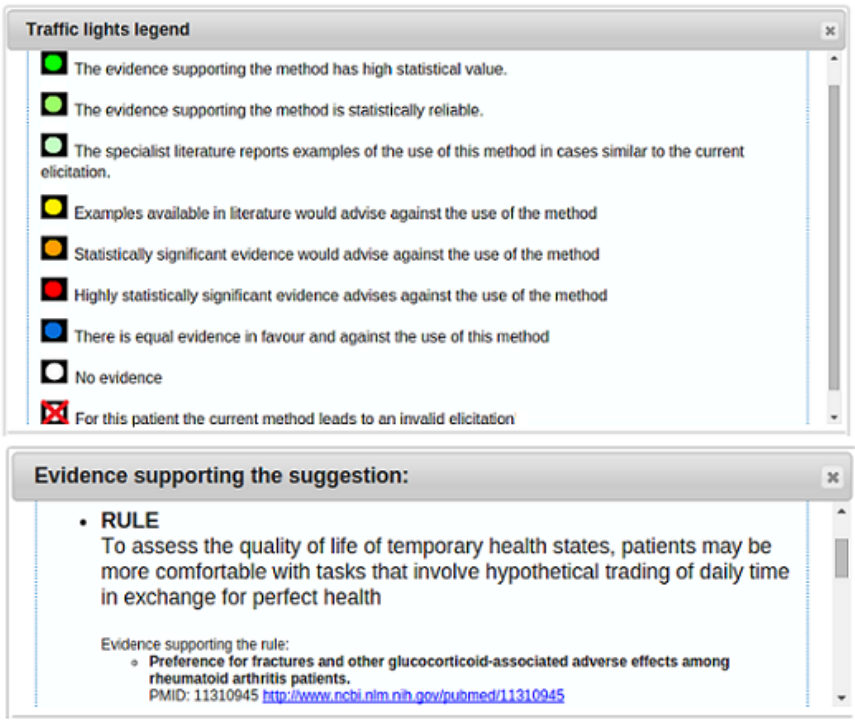

Fig. 2. Traffic light colors legend, available through the "Help" link, and summary of the triggered rules and related evidence, available through the "View details" link.

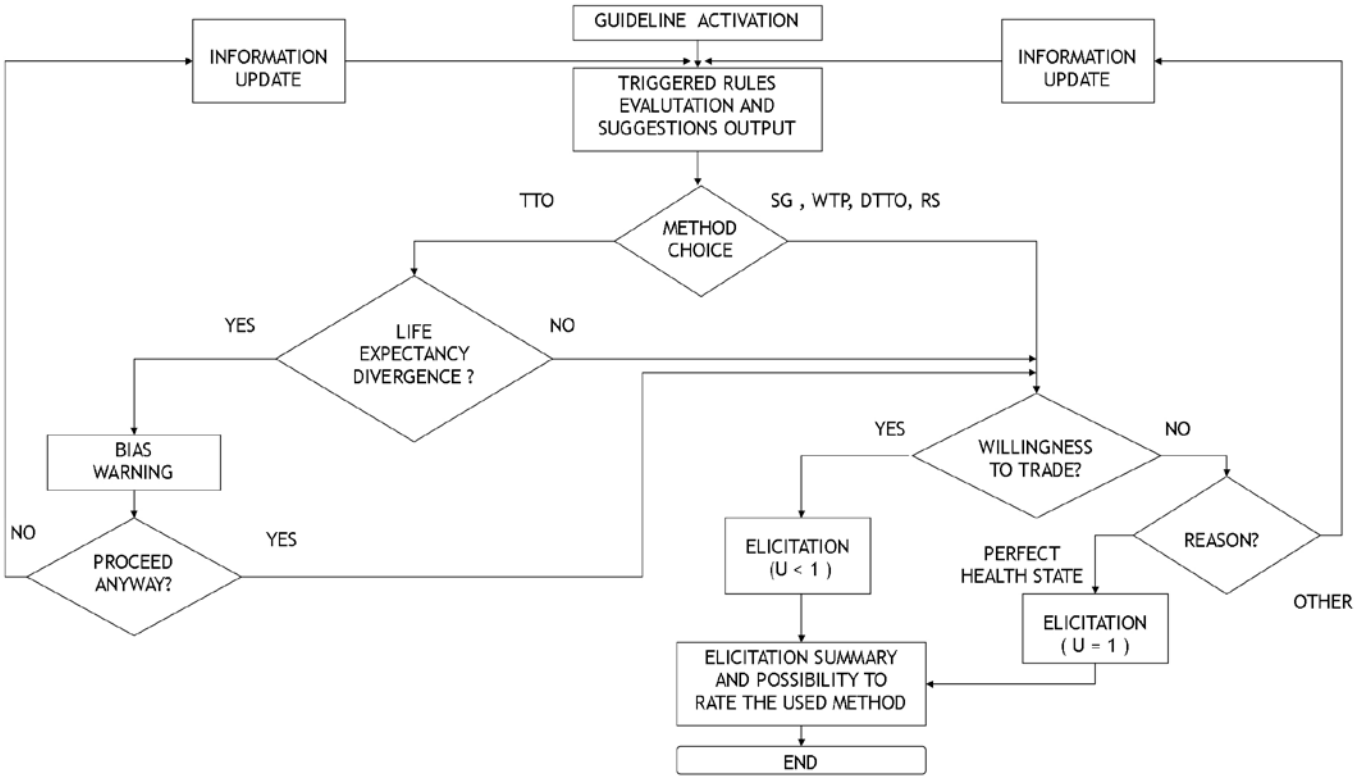

Fig. 3. Complete UceWeb elicitation flow (TTO = time trade-off, SG = standard gamble, WTP = willingness to pay, DTTO = daily time trade-off, RS = rating scale, U = utility coefficient).

Information Extraction from Italian medical reports: first steps towards clinical timelines development

N. Viani[1], V. Tibollo[2], C. Napolitano[2], S. G. Priori[2,3], R. Bellazzi[1], C. Larizza[1], and L. Sacchi[1]
[1] *Dipartimento di Ingegneria Industriale e dell'Informazione, Università di Pavia, Pavia*
[2] *IRCCS Fondazione Salvatore Maugeri, Pavia*
[3] *Dipartimento di Medicina Molecolare, Università di Pavia, Pavia*

***Abstract*—Clinical reports include valuable information in the form of unstructured text. In this work we present a rule-based, ontology-driven approach to mine clinical data from Italian reports belonging to patients with inherited or acquired heart diseases. The proposed approach is part of a Natural Language Processing pipeline that extracts both clinical and temporal information from free-form texts. Part of our pipeline has been validated on a set of medical reports provided by the Molecular Cardiology Laboratories of the Fondazione S. Maugeri hospital in Pavia, Italy.**

***Keywords*—natural language processing, text mining, knowledge representation, information extraction.**

I. Introduction

CLINICAL reports include a great amount of valuable information in the form of unstructured text. The need to extract such information to improve medical decisions on diagnosis, treatment and prognosis is well-known [1]. Given that many diseases require continuous monitoring over time, identifying clinically relevant events and eliciting temporal relations among them is crucial [2].

In the field of clinical Information Extraction (IE), many works have been published dealing with unstructured English texts [3]. However, the extent of the related research for other languages is considerably smaller. In the case of Italian, the essential lack of freely available annotated medical corpora makes it hard to develop supervised techniques to analyze unstructured texts. To overcome this problem, several strategies have been proposed, such as the annotation of Italian clinical texts and the adaptation of existing linguistic tools to the medical domain [4]. Unsupervised techniques for entity and relation extraction have been addressed, too [5]. A considerable amount of work for the automatic analysis of both English and non-English texts has involved unsupervised approaches. Among these, rule-based approaches play an important role. In the field of clinical IE, the development of rules has been also enhanced by using proper domain ontologies, containing information on the main clinical events and their attributes [6].

In this work we present a rule-based, ontology-driven approach to mine clinical data from unstructured Italian texts. The proposed approach is part of a NLP pipeline to extract both clinical and temporal information from a set of medical reports, with the final aim to automatically build a clinical timeline of the main events for each patient.

Part of our NLP pipeline has been validated on a set of medical reports provided by the Molecular Cardiology Laboratories of the Fondazione S. Maugeri hospital in Pavia, Italy. Medical reports belong to patients with inherited or acquired heart diseases (e.g. long QT and Brugada syndrome), and cover a time span of 5 years. Many of the relevant data included in the reports are currently manually stored in the TRIAD repository (http://triad.fsm.it/triadweb), a database for clinical and genetic variations in the field of inherited arrhythmogenic diseases.

II. Methods

In clinical reports, it is frequent to find occurrences of clinical events (e.g. instrumental tests, medications prescriptions, etc.) that are related to a set of attributes, which characterize the event itself. To explicitly represent this feature, we have defined an ontology, structured into Event and Attribute classes. Each Event is related to one or more Attributes, and the same attribute can be linked to more than one event. In the field of Cardiology, for example, an *ECG* test represents an event, while *heart rate*, *rhythm* and *QT length* represent some of its related attributes. All the concepts in the ontology are associated to a specific regular expression, which allows searching for their occurrence in free-form texts.

The IE pipeline that we implemented is based on Apache UIMA [7] and includes standard pre-processing steps, like sentence splitting, tokenization and part-of-speech tagging. To improve performances for those reports that are structured into specific sections, we included an optional configuration file where it is possible to specify this additional information, which will then be processed in the pipeline.

In our pipeline, clinical IE is performed in two steps. First, following the classification of medical concepts used in the 2010 i2b2 challenge on relation extraction [8], we identify mentions of medical problems, tests and treatments (the Events of the ontology). These *events* are extracted by relying on two external dictionaries: the Italian ICD9-CM dictionary, and the FederFarma Italian dictionary for drugs. For each identified event, we then look for its attributes using the developed ontology. Specifically, once the ontology is defined in Protegé-OWL, it is automatically translated into a configuration file used by an "Attribute-Value" UIMA Annotator. Negation detection is performed by relying on a basic implementation of the NegEx algorithm [9].

There are three main reasons why we opted for an ontology-driven approach. First, every time a concept has to

be added or modified, a simple ontology update is needed. Moreover, if the analysis of a new set of documents was needed, it would be only necessary to enrich the ontology with new domain-related information. Finally, to analyze a set of documents written in another language, it would be sufficient to modify the regular expressions associated to the concepts.

Given the lack of annotations in the analyzed corpus, to perform the evaluation of the proposed approach, we have considered the data stored in the TRIAD database. For a preliminary evaluation, we considered a subset of 4430 reports randomly chosen among the entire corpus (11000 reports).

III. Results

To evaluate our annotations, TEST, PROBLEM and TREATMENT events were considered. For events with class TEST, we selected those that are frequently performed in the Cardiology Unit: *ECG*, *Holter ECG* and *Effort Stress* tests. The identified attributes were mapped to the corresponding fields in the TRIAD system. For each identified event in the reports, only those attributes for which an entry was detected in the TRIAD system were considered, and annotations were marked as correct if both the attribute name and its value matched those included in the database. If the identified attribute was reported with a different value, the annotation was considered not correct.

The results obtained in this preliminary evaluation are displayed in Table 1. Dealing with TREATMENT events was not trivial: while reports often contain separate information on drug names, forms, and unit dosages, the TRIAD repository only stores drug names and daily doses. For this reason, the evaluation of TREATMENT annotations was performed both on drug names only, and on drug names with associated dosages (results marked with * in Table 1).

TABLE I
EVALUATION RESULTS

Event Name	*Attributes Annotated*	*Attributes in TRIAD*	*Correct Matches*	*Accuracy*
ECG	26669	22546	21352	94.7%
Holter	26767	21538	19058	88.5%
Effort Stress	9683	3978	2367	59.5%
Diagnosis	4202	4077	3607	88.5%
Prescribed Drug	8720 (8270*)	2436 (4584*)	2186 (2860*)	89.7% (62.4%*)

Evaluation results for TEST, PROBLEM and TREATMENT events. Evaluation of TREATMENT annotations was performed both on drug names only, and on drug names with associated dosages (*).

IV. Discussion

Diagnoses are identified with an accuracy of 88.5%, which indicates that, although many diagnoses are correctly identified, improvements are still possible. As regards TEST Events, while the annotation of *ECG* and *Holter* tests shows good performances (94.7% and 88.5%, respectively), accuracy drops when considering *Effort Stress* tests, probably because the results of such tests are described by physicians with sentences far more articulated than those used for electrocardiograms. As expected, the evaluation performed only on drug names led to a higher accuracy than the one obtained when considering both names and dosages.

Evaluating annotations against structured databases like TRIAD needs some caveats. First, the matching of the information written in the letter to the fields available in the database is a critical point. Moreover, it is not straightforward to recognize true annotation errors from database insertion mistakes. Finally, not all the data stored in the repository are reported in the medical text, which makes it hard to analyze missing data. To address these issues, efforts will be put into designing a more robust evaluation of automatic annotations.

V. Conclusion

The annotation procedure that we developed shows promising results. That said, improvements are still needed. As a first step, look-up dictionaries could be extended to include additional expressions used in reports. To this end, we plan to look for frequently used expressions denoting the occurrence of an event by studying text n-grams. Moreover, errors analysis on the results has shown that improvements of negation detection and misspelled words are needed.

By improving the pipeline steps, it would ultimately be possible to build a well performing system that automatically inserts data into the TRIAD system, saving a lot of manual work and improving data quality.

References

[1] C. Friedman, G. Hripcsak, "Natural language processing and its future in medicine," *Acad Med*, vol. 74 issue 8, pp. 890-5, Aug. 1999.

[2] L. Zhou, G. Hripcsak, "Temporal reasoning with medical data--a review with emphasis on medical natural language processing," *J Biomed Inform*, vol.40 issue 2, pp.183-202, Apr. 2007.

[3] S.M. Meystre, G.K. Savova, K.C. Kipper-Schuler, J.F. Hurdle, T.A. Pryor, R.M. Gardner, R.D. Clayton, H.R. Warner, "Extracting information from textual documents in the electronic health record: a review of recent research," *Yearb Med Inform*, pp. 128-44, 2008.

[4] G. Attardi, V. Cozza, D. Sartiano, "Annotation and Extraction of Relations from Italian Medical Records," in *2015 Proc. 6th Italian Information Retrieval Workshop*, Cagliari, Italy, May 2015.

[5] A. Alicante, A. Corazza, F. Isgrò, S. Silvestri, "Unsupervised information extraction from italian clinical records," *Stud Health Technol Inform*, vol. 207, pp.340-9, 2014.

[6] M. Toepfer, H. Corovic, G. Fette, P. Klügl, S. Störk S, F. Puppe, "Fine-grained information extraction from German transthoracic echocardiography reports," *BMC Med Inform Decis Mak*, vol.15, pp. 91, Nov. 12.

[7] D. Ferrucci, A. Lally, "UIMA: An Architectural Approach to Unstructured Information Processing in the Corporate Research Environment," *Nat Lang Eng*, vol. 10 issues 3-4, pp. 327–48, 2004.

[8] O. Uzuner, B. South, S. Shen, S. DuVall, "2010 i2b2/va challenge on concepts, assertions, and relations in clinical text," *J Am Med Inform Assoc*, vol. 18 issue 5, pp.552–6, 2011.

[9] W.W. Chapman, W. Bridewell, P. Hanbury, G.F. Cooper, B.G. Buchanan, "A simple algorithm for identifying negated findings and diseases in discharge summaries," *J Biomed Inform*, vol. 34 issue 5, pp.301-10, Oct. 2001.

be added or modified, a simple ontology update is needed. Moreover, if the analysis of a new set of documents was needed, it would be only necessary to enrich the ontology with new domain-related information. Finally, to analyze a set of documents written in another language, it would be sufficient to modify the regular expressions associated to the concepts.

Given the lack of annotations in the analyzed corpus, to perform the evaluation of the proposed approach, we have considered the data stored in the TRIAD database. For a preliminary evaluation, we considered a subset of 4430 reports randomly chosen among the entire corpus (11000 reports).

III. Results

To evaluate our annotations, TEST, PROBLEM and TREATMENT events were considered. For events with class TEST, we selected those that are frequently performed in the Cardiology Unit: *ECG*, *Holter ECG* and *Effort Stress* tests. The identified attributes were mapped to the corresponding fields in the TRIAD system. For each identified event in the reports, only those attributes for which an entry was detected in the TRIAD system were considered, and annotations were marked as correct if both the attribute name and its value matched those included in the database. If the identified attribute was reported with a different value, the annotation was considered not correct.

The results obtained in this preliminary evaluation are displayed in Table 1. Dealing with TREATMENT events was not trivial: while reports often contain separate information on drug names, forms, and unit dosages, the TRIAD repository only stores drug names and daily doses. For this reason, the evaluation of TREATMENT annotations was performed both on drug names only, and on drug names with associated dosages (results marked with * in Table 1).

TABLE I
EVALUATION RESULTS

Event Name	*Attributes Annotated*	*Attributes in TRIAD*	*Correct Matches*	*Accuracy*
ECG	26669	22546	21352	94.7%
Holter	26767	21538	19058	88.5%
Effort Stress	9683	3978	2367	59.5%
Diagnosis	4202	4077	3607	88.5%
Prescribed Drug	8720 (8270*)	2436 (4584*)	2186 (2860*)	89.7% (62.4%*)

Evaluation results for TEST, PROBLEM and TREATMENT events. Evaluation of TREATMENT annotations was performed both on drug names only, and on drug names with associated dosages (*).

IV. Discussion

Diagnoses are identified with an accuracy of 88.5%, which indicates that, although many diagnoses are correctly identified, improvements are still possible. As regards TEST Events, while the annotation of *ECG* and *Holter* tests shows good performances (94.7% and 88.5%, respectively), accuracy drops when considering *Effort Stress* tests, probably because the results of such tests are described by physicians with sentences far more articulated than those used for electrocardiograms. As expected, the evaluation performed only on drug names led to a higher accuracy than the one obtained when considering both names and dosages.

Evaluating annotations against structured databases like TRIAD needs some caveats. First, the matching of the information written in the letter to the fields available in the database is a critical point. Moreover, it is not straightforward to recognize true annotation errors from database insertion mistakes. Finally, not all the data stored in the repository are reported in the medical text, which makes it hard to analyze missing data. To address these issues, efforts will be put into designing a more robust evaluation of automatic annotations.

V. Conclusion

The annotation procedure that we developed shows promising results. That said, improvements are still needed. As a first step, look-up dictionaries could be extended to include additional expressions used in reports. To this end, we plan to look for frequently used expressions denoting the occurrence of an event by studying text n-grams. Moreover, errors analysis on the results has shown that improvements of negation detection and misspelled words are needed.

By improving the pipeline steps, it would ultimately be possible to build a well performing system that automatically inserts data into the TRIAD system, saving a lot of manual work and improving data quality.

References

[1] C. Friedman, G. Hripcsak, "Natural language processing and its future in medicine," *Acad Med*, vol. 74 issue 8, pp. 890-5, Aug. 1999.

[2] L. Zhou, G. Hripcsak, "Temporal reasoning with medical data--a review with emphasis on medical natural language processing," *J Biomed Inform*, vol.40 issue 2, pp.183-202, Apr. 2007.

[3] S.M. Meystre, G.K. Savova, K.C. Kipper-Schuler, J.F. Hurdle, T.A. Pryor, R.M. Gardner, R.D. Clayton, H.R. Warner, "Extracting information from textual documents in the electronic health record: a review of recent research," *Yearb Med Inform*, pp. 128-44, 2008.

[4] G. Attardi, V. Cozza, D. Sartiano, "Annotation and Extraction of Relations from Italian Medical Records," in *2015 Proc. 6th Italian Information Retrieval Workshop*, Cagliari, Italy, May 2015.

[5] A. Alicante, A. Corazza, F. Isgrò, S. Silvestri, "Unsupervised information extraction from italian clinical records," *Stud Health Technol Inform*, vol. 207, pp.340-9, 2014.

[6] M. Toepfer, H. Corovic, G. Fette, P. Klügl, S. Störk S, F. Puppe, "Fine-grained information extraction from German transthoracic echocardiography reports," *BMC Med Inform Decis Mak*, vol.15, pp. 91, Nov. 12.

[7] D. Ferrucci, A. Lally, "UIMA: An Architectural Approach to Unstructured Information Processing in the Corporate Research Environment," *Nat Lang Eng*, vol. 10 issues 3-4, pp. 327–48, 2004.

[8] O. Uzuner, B. South, S. Shen, S. DuVall, "2010 i2b2/va challenge on concepts, assertions, and relations in clinical text," *J Am Med Inform Assoc*, vol. 18 issue 5, pp.552–6, 2011.

[9] W.W. Chapman, W. Bridewell, P. Hanbury, G.F. Cooper, B.G. Buchanan, "A simple algorithm for identifying negated findings and diseases in discharge summaries," *J Biomed Inform*, vol. 34 issue 5, pp.301-10, Oct. 2001.

A decision support system for managing chemo-radiotherapy side effects in patients with head and neck cancer

E.M. Zini[1], G. Lanzola[1], P. Bossi[2], L. Licitra[2] and S. Quaglini[1]
[1] *Department of Electrical, Computer and Biomedical Engineering, University of Pavia, Italy*
[2] *Head and Neck Medical Oncology Department, IRCCS Foundation National Cancer Institute, Milan, Italy*

***Abstract*—Concurrent chemo-radiotherapy (CCRT) is a very efficient treatment for head and neck cancer but it can cause severe acute toxicity; therefore, home patients undergoing CCRT have to be tightly monitored. To this purpose, we already developed an app, addressed to patients or their home caregivers, whose configuration can be decided from time to time by the oncologists in order to meet specific patients' needs. The app regularly sends data to the hospital server for monitoring purposes. In this paper, we propose to improve this monitoring system with a guideline-based decision support system able to help doctors with the app configuration and, more in general, with prevention, diagnosis and treatment of CCRT side effects.**

***Keywords*—Telemedicine, m-health, decision support, patients' monitoring.**

I. Introduction

Concurrent chemo-radiotherapy (CCRT) is proved to be one of the most effective treatments for unresectable head and neck cancers (HNCs) in high risk patients [1]. Cetuximab added to radiotherapy is another effective option for locally advanced HNCs [2]. However, the benefits of these treatments may be compromised by their associated toxicity, which may lead to a severe impairment of the patient's quality of life or even to death. The occurrence of toxicity may require reducing the dose and treatment intensity, thus increasing the treatment duration and compromising the survival benefits of the integrated approach. In order to avoid an excessive worsening of the patients' quality of life, prevention and treatment of these toxicities become essential. To standardize the process of optimally adjusting the treatment for those patients, controlling the complications and reducing their management costs, the Italian Association of Medical Oncology (AIOM), the Italian Association of Oncologic Radiotherapy (AIRO) and the Italian Head and Neck Oncologic Society (IHNS) joined efforts to implement a comprehensive clinical practice guideline.

Within a collaboration with the IRCCS Foundation National Cancer Institute in Milan, the Laboratory for Biomedical Informatics "Mario Stefanelli" of the University of Pavia developed a mobile application called HeNeA (Head and Neck Application), to help the collection of patient-reported outcomes (PROs) [3]. Our organizational model envisages that HeNeA is configured by the physician when it is provided to the patient (e.g., at discharge or at a control visit). According to the guideline and depending on the therapy (radiotherapy alone or combined with systemic therapy), the oncologist defines which clinical parameters have to be collected (e.g., weight, temperature, blood pressure) and which questionnaires have to be filled in by the patient (e.g., MDADI for dysphagia, EuroQol for quality of life); the doctor also indicates the data collection frequency.

Data are automatically sent to the hospital server, through which the oncologists may oversee the patients' disease evolution in terms of temporal plots and aggregation charts (e.g., bar and pie charts). Moreover, HeNeA offers the possibility of keeping in touch with the health care staff or with "peer" patients. It supplies some educational material, to provide patients with all the information they might need about their disease and the possible side effects of the treatment.

Presently HeNeA is structured as a standalone monitoring system, implemented as a mobile application for the patient and a web application for the doctor, and lacks the dynamic integration of the guideline recommendations. In this work, we propose an extension to HeNeA, integrating two separate decision support systems (DSSs) within its workflow to simplify its adoption and make its use more straightforward for the physicians. The first DSS should help the doctors in properly configuring HeNeA with the most appropriate parameters and questionnaires for the actual patient, while the second one should support the doctor in optimizing the prevention, diagnosis and treatment of the CCRT side effects. This is accomplished by regularly inspecting risk factors and analyzing the PROs, in order to early identify the patients that require an intervention. We believe that integrating HeNeA with the guideline will improve both data collection, by a more correct personalization of the data input process, and PROs exploitation, by their timely integration with hospital data, which possibly will trigger new and more appropriate recommendations.

II. Methods

The clinical practice guideline is presently available in paper format, so it should be formalized and rendered into a computer-interpretable format to be integrated into HeNeA. An authoring tool would help in speeding up and simplifying this task. To this purpose, we chose Alium, by Deontics Ltd, which allows creating a care pathway using PRO*forma* to define processes, data, clinical logic and decisions.

PRO*forma* is a language representing clinical protocols and guidelines in a machine-executable format; it defines

processes as a set of PRO*forma* components [4]. The most frequently used components are tasks and data items. There are four classes of tasks: *Action*, which represents a procedure that needs to be executed in the external environment (e.g. a surgical procedure); *Enquiry*, which represents a point of information acquisition from an external person or system; *Decision*, which represents a point at which a choice has to be made; *Plan*, which is a collection of tasks grouped together [5].

An analysis of the guideline has shown that it can be subdivided into 7 areas: *Skin Care*, *Oral Cavity Care*, *Swallowing Care*, *Nutrition-Hydration*, *Septic Syndrome*, *Haematologic Toxicity Care* and *Pain*; each area includes different CCRT side effects. For each side effect, the guideline involves (i) risk factors assessment, (ii) evaluation of the patient's answers to a specific questionnaire and (iii) clinical evaluation. After this diagnostic assessment of the side effect, a set of actions for its prevention and/or treatment is suggested. The guideline provides separate recommendations concerning which data to collect (depending on the initial patient status) and how to interpret them. This translates into our proposal of two different decision support systems for the physician, one to customize HeNeA, that in turn will generate better recommendations and enquiries for the patient, and another one to obtain recommendations for the side effect management.

III. Results

The guideline workflow for HeNeA customization is shown in Figure 1: after a step of demographic data collection and assessment, general recommendations (i.e. valid for any patient) are chosen to be included in the app, in order to provide the patient with tips about the side effects prevention. Additional recommendations are then set based on the specific patient's data (e.g. recommendations for smokers). Finally, an evaluation for each side effect suggests which questionnaire the patient should fill-in and with which frequency.

Figure 2 shows the workflow for prevention, diagnosis and treatment of a generic side effect considered in the guideline (its PRO*forma* representation is shown in Figure 3). The first step is, again, the risk factors assessment, followed by a check of the presence of the side effect in the Electronic Health Record (EHR). If the side effect is already present, then it must be treated, otherwise it must be prevented. Since patients, while not hospitalized, access the radiotherapy service almost every day, the guideline is intended for them as well as for the healthcare personnel. Patients already receive recommendations, mostly related to prevention, through the app; the computerized guideline should provide doctors and nurses with recommendations about prevention and treatment of the side effects through the website interface. Figure 2 shows a general workflow that must be instantiated for every side effect, as each of them has specific recommendations for prevention and treatment.

Once a care pathway has been authored in Alium, an engine can execute the process description and show to the doctor decisions to be taken and actions to be performed (Figure 4). At the moment, data are entered by the doctor through an Alium-generated form, but the plan is to use in the future also data coming from an EHR. That being the case, we have defined an architecture to identify the points of integration of the proposed DSSs within HeNeA, as shown in Figure 5. The newly introduced elements in the HeNeA infrastructure are the two DSSs and the library of computer-interpretable guidelines, which are executed by the Alium engine upon doctor's request, providing support for the oncologist's decisions according to the patient's data extracted from the EHR and integrated with PROs coming from HeNeA.

IV. Conclusion

A decision support system could simplify the oncologist's work, supporting the doctor in decisions about the patient's monitoring and in the diagnosis or treatment of side effects. Moreover, collecting the patient's clinical data and answers to specific questionnaires through the mobile application could considerably reduce the overall time to prepare the visit, granting more time for the visit itself.

Finally, studies have proved that symptom monitoring during routine cancer care using PROs can enhance clinician awareness and improve symptom management. That being the case, tailoring the app setting for a specific patient could significantly improve the symptom monitoring. Conversely, when undetected in the absence of patient self-reporting, symptoms may continue to worsen and cause serious complications, lead to hospital visits, limit the ability to safely deliver chemotherapy and diminish outcomes [6].

Presently we are in the process of formalizing the guideline using Alium. The next step will consist in integrating the guideline into the HeNeA system: the PRO*forma Enquiries* should link directly to the EHR to fetch the data acquired through the mobile application. At the same time, the suggested recommendations should reach the oncologist through the same web application that presently shows the patients' data summaries by synchronising with HeNeA.

References

[1] J.P Pignon, A. Maître, E. Maillard, J. Bourhis, "Meta-analysis of chemotherapy in head and neck cancer (MACH-NC): an update on 93 randomised trials and 17,346 patients", *Radiother Oncol*, 2009 Jul; 92(1): 4–14.

[2] J.A. Bonner, P.M. Harari, J. Giralt, R.B. Cohen, C.U. Jones *et al.*, "Radiotherapy plus cetuximab for loco regionally advanced head and neck cancer: 5-year survival data from a phase 3 randomised trial, and relation between cetuximab-induced rash and survival", *Lancet Oncol*, 2010 Jan; 11(1): 21-8.

[3] S. Buzzacchino, G. Lanzola, P. Bossi, L. Licitra, S. Quaglini, "A mobile application supporting outpatient treatment and follow-up", Proceedings of MIE 2015

[4] D.R. Sutton, J. Fox, "The syntax and semantics of the PRO*forma* guideline modeling language", *J Am Med Inform Assoc*, 2003 Sep-Oct; 10(5): 433–443.

[5] D.R. Sutton, P. Taylor, K. Earle, "Evaluation of PRO*forma* as a language for implementing medical guidelines in a practical context", *BMC Med Inform Decis Mak*, 2006; 6: 20.

[6] E. Basch, A.M. Deal, M.G. Kris, H.I. Scher, C.A. Hudis *et al.*, "Symptom monitoring with Patient-Reported Outcomes during routine cancer treatment: a randomized controlled trial", *J Clin Oncol*, 2016 Feb 20; 34(6):557-565.

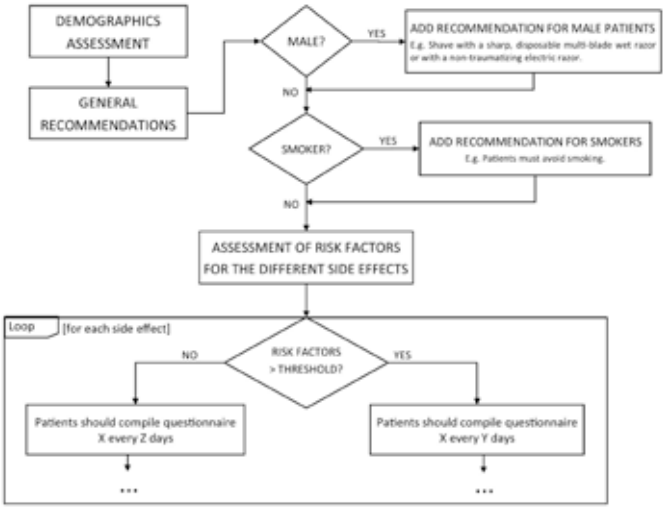

Fig. 1. A scratch of the workflow of decision support system for HeNeA customization.

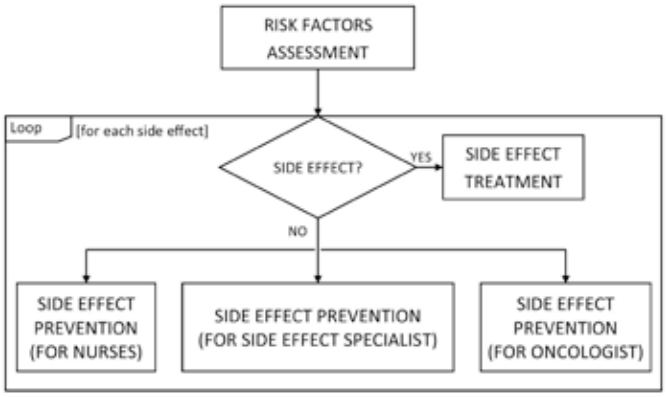

Fig. 2. The workflow of the DSS for side effect management.

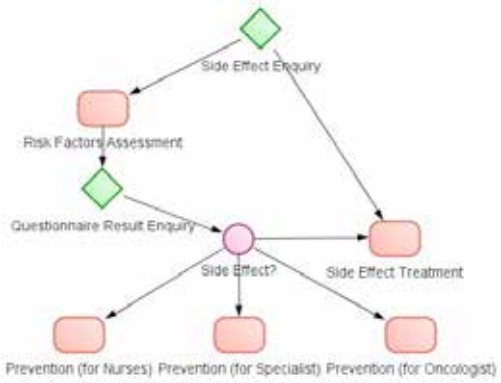

Fig. 3. PRO*forma* rendering of the workflow for side effect management shown in Figure 2.

Fig. 4. Alium rendering of a recommendation.

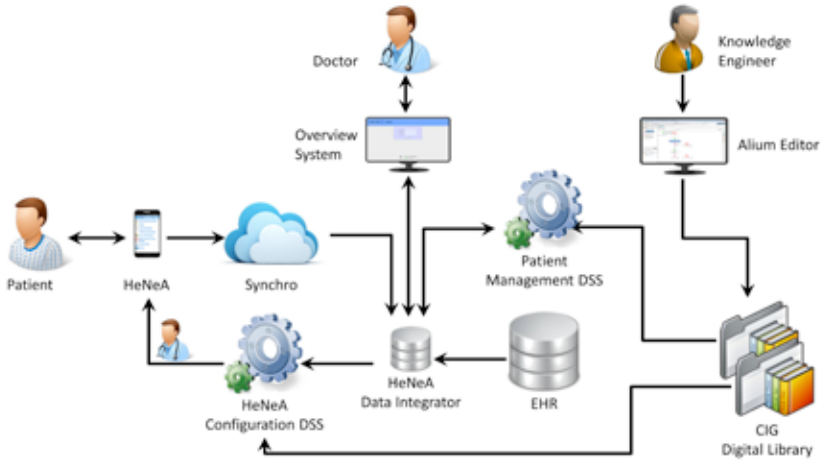

Fig. 5. The system architecture, showing in particular the two DSSs for HeNeA configuration and for side effect management.

INGEGNERIA CLINICA

The innovation in the ICT and new Models of distance e-learning in the Health Sciences

E. Campana[1], MR Giovagnoli[1], and D. Giansanti[2]
[1] *Universita' Sapienza, Roma*
[2] *Istituto Superiore di Sanità, Roma*

***Abstract*— E-learning is electronic learning, and typically, this means using a computer to deliver part, or all of a course whether it's in a school, part of your mandatory business training or a full distance learning course. Today Moodle has become a consolidated standard for the e-learning in many scenarios of e-learning in Italy focuses on Health Sciences. An example of this is the wide use of Moodle in Sapienza University (the largest university in Europe) and ISS (The Italian National Institute of Health). Facing Moodle for who has the ambition and general idea to rapidly design interfaces/modules/procedures could means:**

a) Facing the complexity of a standard system with both defined rules and defined steps.

b) To delay thus the design itself.

The purpose of the study, in order to overcome the two above listed problems, was to investigate the use of novel ICT technologies to construct new easy-to-design models of e-learning without recurring to adhere to the standard Moodle and compatible with the APP smartphone technology. We have proposed a new methodology of e-learning based both on the Google drive technology for the folder sharing and online surveys/online-modules easily designed using OneDrive and Excel Online. In particular three different modules for three different modalities of exams have been designed and tested at the minimal GSM supply.

***Keywords*— E-learning, Moodle, Digitalization, Smartphones, App, Survey**

I. INTRODUCTION

QUIte simply, e-learning is electronic learning, and typically this means using a computer to deliver part, or all of a course whether it's in a school, part of your mandatory business training or a full distance learning course.

In the early days it received a bad press, as many people thought bringing computers into the classroom would remove that human element that some learners need, but as time has progressed technology has developed, and now we embrace smartphones and tablets in the classroom and office, as well as using a wealth of interactive designs that makes distance learning not only engaging for the users, but valuable as a lesson delivery medium.

Building partnerships with quality training providers, and combining this with a dedicated experienced technical team and support staff. There are several benefits to e-learning whether you choose to use it on its own, or to enhance the existing in house training. It's cost effective and saves time is for example one of these.

By reducing the time taken away from the office, removing travel costs and doing away with printed materials, online learning helps you to save money and increase workplace productivity. It also means staff will be happier and focused. Many face to face courses only operate within normal office hours. By allowing staff to complete the course when and where they like you can make sure disruptions to your busy working schedule are minimized. This also means that staff will be happier because they don't need to travel to specific training centers, and if they have important work to catch up on mandatory training can be done outside of office hours in exchange for lieu time. Most of courses have an average learning time. E-learning is discreet, in fact not everybody feels comfortable learning in a large group, especially if they find something hard to understand that co-workers have no problem with. E-learning allows each individual to tackle the subject at their own pace, with interactive tasks being set in place to ensure a thorough understanding throughout each module.

B. Moodle in the field of Health Sciences Courses in Italy

In a study conducted during a Thesis focused in didactics furnished in Health Sciences in Italy we enlightened that Moodle [1-3] has becoming a "standard de-facto" both in:

1) University courses. The University "Sapienza", for example, the largest University in Europe, gives the chance to follow many course in e-learning modalities based in Moodle [4].

2) Institutional public entities. The Istituto Superiore di Sanità, the Italian Institute of Health *"*The Institute conducts scientific research in a wide variety of fields, from cutting-edge molecular and genetic research to population-based studies of risk factors for disease and disability. Research priorities are based on those set forth in the National Health Plan. The Institute is also involved in several major clinical trials, which are frequently conducted in cooperation with the Scientific Institutes for Research and Care "IRCCS" network and Hospitals and mostly important formation in Health Sciences*" plans e-learning courses in Moodle [5].

C. Vantages and disadvantages of using Moodle

As amply enlightened above, Moodle is in its different forms a standard. This means that for everyone which is going to face e-learning with the general idea and ambition to rapidly design interfaces/modules/procedures this could means:

a) To face the complexity of a standard system with both defined rules an defined steps
b) To delay the design itself

E. Purpose of the Study

The purpose of the study, in order to overcome the above listed problems, was to investigate the use of novel ICT technologies to design-and-test new easy to design models of e-learning without recurring to adhere to the standard Moodle and, very important, compatible with the APP in the smartphone technology.

II. METHODS

The methodological flow involved

- The investigation on a network drive methodology suitable to share "contents".
- The investigation of automatic tools suitable to design online forms capable to replace the most commonly furnished tests during the exams at University.

Both the two points should be smartphone-compliant.

A. Network drive technology

Sharing folders in Google Drive allows you to easily share multiple files also giving the possibility to decide the rights of modifying (or not) the files recalling the role of a system administrator, without charge. This is quite useful for the organization. In fact the Director of a Course and teacher could design a secure methodology to share-without "contents" relevant to the single courses.

B. The design of online forms.

Microsoft allows you to create online surveys (or modules) easily using OneDrive and Excel Online. The best part is that the participants are not required to sign in to OneDrive [6]. You can just generate a unique URL for the survey and distribute it.
Only the manager of the survey needs to have an account. To create your survey, open up your OneDrive account and from the Create menu dropdown, select the Excel Survey option.
We imagined there different scenarios for the design of these modules (Figure 1). The surveys in onedrive allows the design of questions with the following chances:

a) Text b) Paragraph Text c) Date d) Numerical
e) Time f) Yes or NO

Figure 2 Enlightens this in an "Italian menu"
The data captured by the survey or module are stored in a file based on Exel online.

III. RESULTS

We have designed the three different modules. One has been proposed for the course of Bioengineering at the Ital-ian Course at Sapienza University"Laurea Magistrale in Scienze delle Professioni Sanitarie Tecniche Diagnostiche. In this course the exam is based on:

- A monographic research (2/3 of the exam)
- A dissertation with the choice of one argument among three proposed.

The second module has been based on the exam of "informatics" in the same Course. This exam is based on several questions. Each questions has four possible chances; only one chance is correct. Figure 2 shows the configuration of questions. Figure 3 shows the module for exam in informatics. The third module is based on a general exam of Statistics as for example in Courses of the so called "Laurea Triennale". This module considers also numerical answers. The numerical answers from the sur-vey/module compiled by the student are as the other auto-matically stored in the Excel file also for automatically assign the assessment of the exam, as many teacher do. The module have been sent using the URL to destination. We have never assisted to failures in the delivery or in the compilation/submission. We have tested the methodology in critical conditions such as minimal GSM supply, during a trail with low GSM field of a train without WI-FI or in an uncomfortable territory (mounatins). We have never assisted to failures in the delivery or in the compilation/submission at the minimal GSM supply.

IV. CONCLUSION

A novel methodology for the e-learning has been investigated. The methodology was based both on the Google drive technology for the folder sharing and online surveys easily designed using OneDrive and Excel Online. Three different survey modules have been successfully designed for three different methodology of exams in e-learning modalities and successfully tested at the minimal GSM supply. Future activity will consider the inclusion of the methodology in the routine procedures in the Course at Sapienza University" Laurea Magistrale in Scienze delle Professioni Sanitarie Tecniche Diagnostiche, in particular will be focused to the twi following issues:

- The design modules for exams.
- The design of modules to collect the feedback of the students about considerations and problematics relevant to the didactics.

REFERENCES

[1] G Henrick and K. Holland "Moodel Administration Essentials" Book , Publisher Packt Publishing, 2015
[2] W. Rice "Moodle E-Learning Course Development" - Third Edition" Book , Publisher Packt Publishing
[3] Eva Heinrich, "Understanding Complex Information Technology Solutions: A Case Study on Moodle" Book, Publisher: Amazon Digital Services, Inc.
[4] https://elearning2.uniroma1.it/ (October 2015)
[5] http://vcms.iss.it/moodle19/ (October 2015)
[6] https://support.office.com/en-us/article/Surveys-in-Excel-hosted-online-5fafd054-19f8-474c-97ec-b606fcda0ff9 (October 2015)

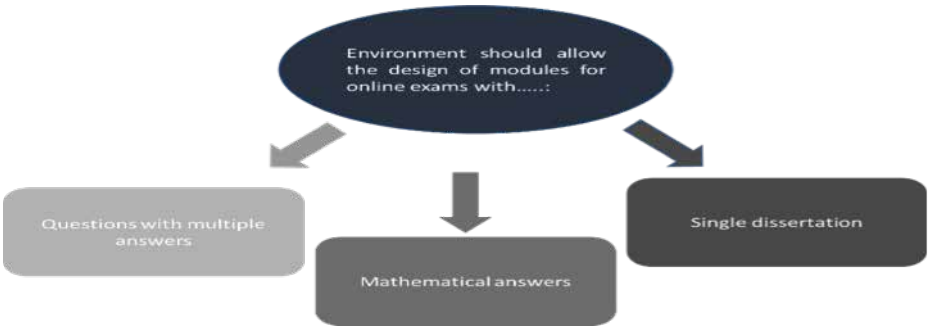

Fig. 1. The Requirements of the Environment for the design of the modules for the exam

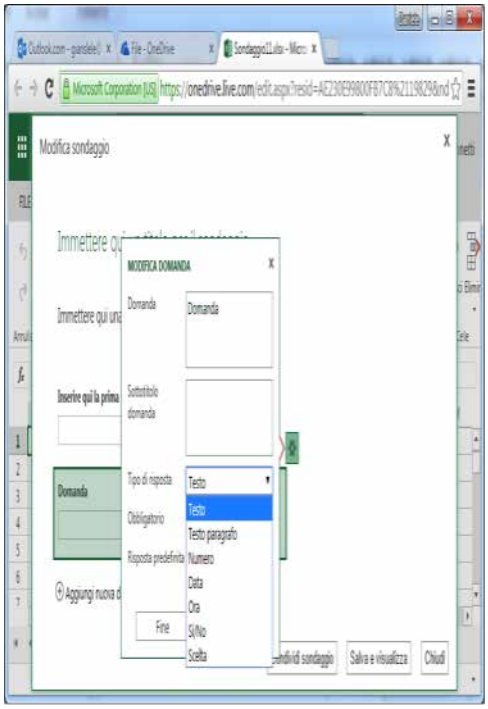

Fig. 2. Configuration of the Questions

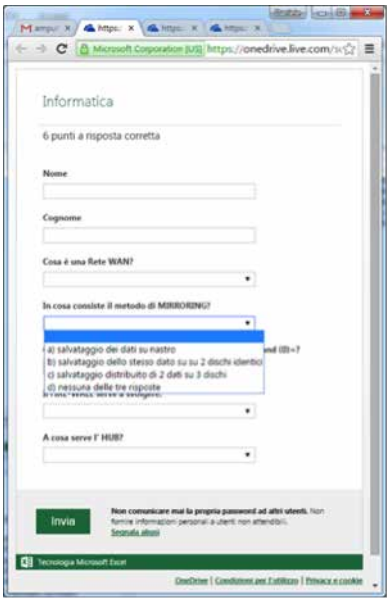

Fig. 3. Module for the exam in informatics

Towards the testing of Whatsapp for Digital Cytology Teleconsulting

A.M Palozzi[1], M.R Giovagnoli[1], and D. Giansanti[2]
[1] *Universita Sapienza, Roma*
[2] *Istituto Superiore di Sanità*

***Abstract*— WhatsApp Messenger is a proprietary cross-platform instant messaging client for smartphones. It uses the Internet to send text messages, multimedia files (images, video, audio), position to other users using standard cellular mobile numbers. Today, WhatsApp had a user base of up to one billion, making it the most globally popular messaging application.**

The image exchanging is a basic issue in digital-cytology in order to reach a correct diagnosis by means of the tele-consulting.

A study for the investigation of the use of Whatsapp in digital-cytology was designed.

Preliminary results are showing the usefulness of the methodology based on Whatsapp.

***Keywords*—Digital Cytology, Tele-consulting, Tele-pathology, Whatsapp messanger.**

I. INTRODUCTION

DIGItal cytology is a field of digital pathology that integrates medical knowledge and properly designed information and communication technologies to investigate the morphological alterations in different degrees of morbidity directly on a digital image called virtual glass (or e-slide)[1-3]. E-slides are the product of a digitalization workflow by means of a heterogeneous process that starts from the microscope slide. The core element of the digitalization process is the digital scanner whose degree of magnification depends on its scanning resolution. Until recently, e-slides were mainly exchanged using personal computers as clients, which rendered it possible to successfully set up effective networks for teleconsulting and e-learning[1,4,5]. In previous studies [6,7] we showed the importance of using health technology assessment (HTA) tools in telemedicine and e-health for the assessment of both the acceptance and performance of a telemedicine solution. In 2008, we successfully investigated the acceptance and performance of virtual microscopy using PC platforms with a dedicated HTA tool[8]. In recent years, further technological advances have opened up new directions of research for digital cytology, including integration with DICOM (www.dicom.com), integration with three-dimensional technologies and utilization of tablet technologies [9-14].

Today, tablets are replacing personal computers, especially in multimedia operations of medical images in telemedicine and e-health. Nevertheless, no one has so far investigated the implications of the introduction of tablets in the e-laboratory of cytology. The implications of the changes that tablets could introduce in the [15-16] e-laboratory are wide, which should be addressed by means of a proper HTA study.

In [22] we have investigated the introduction of the Tablet technologies in digital-cytology by means of a specific study of HTA.

The Tablets can be divided into three groups:
-Wearable Tablets (such as the smartphones).
-Portable Tablets (the ones large as an A4 or A4/2 foil).
-Not Portable (such as the Epson Xdesk).

New frontiers are today offered by the APPs for the smartphones for the exchange of the multimedia-files (images, video, audio) as for example in the case of the so called messengers. These APP are useful to send text messages, multimedia files (images, video, audio), position to other users using standard cellular mobile numbers. The investigation in telemedicine teleconsulting of new solutions based on these new APPs could introduce new opportunities for the remote diagnosis.

II. THE DESIGN OF THE SYSTEM FOR TELE-CONSULTING

The methodological flow involved the following steps:

1. Identification of the messenger
2. The choice of the medical images
3. Set up of the Work-group
4 Set up of an environment for the investigation of the Acceptance of the methodology

A. Identification of the messenger

WhatsApp Messenger is the most diffused and most convenient way of quickly sending messages on your mobile phone to any contact on your contacts list in the phone. Obviously the only requirement is that people involved in the Network must have the app installed on their own device. Currently, WhatsApp is compatible with just about all mobile operating systems on the market: Android, iOS, Symbian and Windows Phone. So this basically means you'll be able to use WhatsApp to communicate with any friend, regardless of what model of device they have. WhatsApp users can send text messages, voice messages, links and images to any other user. Automatic image compression makes transferring files very easy (although there is obviously some quality loss). This first characteristics makes Whatsapp useful for the remote-image exchanging

One of the most interesting and most used tools on WhatsApp is the one that lets you easily create and manage groups. Any user can enter any group, as long as they' ve

been invited by the group's creator, and they can leave it whenever they want.
This second characteristics makes Whatsapp useful for the creation of groups for tele-consulting in medical imaging such as in digital-cytology.

B. The set-up of a Work-group

A group has been settled up using the specific functionalities of Whatsapp.

A first LOGO has been defined.

At the moment a group of experts is under recruitment including subjects having worked in the previous investigations [1-15] and specialists in digital cytology.

Figure 1 enlightens the group of "Digital Cytology & Wapp"

C. The choice of the medical images

The e-slides scanned by means of the Aperio (Leica Microsystems, Inc., Buffalo Grove, IL, USA) scanner have been positioned in a server at http://www.diditalslide.it. All the e-slides have been investigated at Zoom level 1⁄4 40X. We used Image-scope which is compatible with the Windows OS platforms for the connection and extraction of the information. A total of 38 snapshots have been extracted from six e-slides relevant to cervico-vaginal [15]. For each one of them, three basic information have been furnished.

Figure 2 shows the image-exchanging in the environment of the WhatsApp. Figure 3 shows an image exchanged with the relevant magnification.

D. The set-up of an environment for the investigation of Acceptance the methodology

At the moment we are designing a specific environment for the assessment of the methodology based on the HTA methodology using the previous successful approach designed for the Digital Cytology. In order to speed the assessment we have planned to design the questionnaires for the data-collection in the HTA using the online-surveys based on "onedrive methodologies". This allows an easy collection of the feedback directly in *online excel* ready for the post processing elaboration and analysis (www.microsoft.com) .

III. CONCLUSION

This work from a global point of view shows how the so called multimedia-messangers mostly used for social networks could contribute in telemedicine-medical imaging. In particular the paper demonstrates that the use of Whatsapp for the tele-consulting is feasible. Even if the study is at an initial stage, preliminary results are indicating that the methodology could give a great contribution in the field of Telemedicine. The Output from the HTA study in fact is expected to give indications to stabilize and spread the methodology

ACKNOWLEDGEMENT

The author greatfully acknowledge the Staff of the Sapienza University "Facoltà di Medicina e Psicologia sede di Viterbo"

CONFLICT OF INTEREST

The authors declare that they have no competing interests

REFERENCES

[1] Giansanti D, Grigioni M, Giovagnoli MR. Virtual microscopy and digital cytology: Fact or fantasy? Preface. Ann Ist Super Sanita 2010;46:113–114.
[2] Giansanti D, Grigioni M, D'Avenio G, Morelli S, Maccioni G, Bondi A, Giovagnoli MR. Virtual microscopy and digital cytology: State of the art. Ann Ist Super Sanita 2010;46:115–122.
[3] Morelli S, Grigioni M, Giovagnoli MR, Balzano S, Giansanti D. Picture archiving and communication systems in digital cytology. Ann Ist Super Sanita 2010;46:130–137.
[4] Giansanti D, Castrichella L, Giovagnoli MR. Telepathology training in a master of cytology degree course. J Telemed Telecare 2008;14:338–341.
[5] Giansanti D, Castrichella L, Giovagnoli MR. New models of e-learning for healthcare professionals: A training course for biomedical laboratory technicians. J Telemed Telecare 2007;13:374–376.
[6] Giansanti D, Morelli S, Macellari V. Telemedicine technology assessment part II: Tools for a quality control system. Telemed J E Health 2007;13:130–140.
[7] Giansanti D, Morelli S, Macellari V. Telemedicine technology assessment part I: Setup and validation of a quality control system. Telemed J E Health 2007;13:118–129.
[8] Giansanti D, Castrichella L, Giovagnoli MR. The design of a health technology assessment system in telepathology. Telemed J E Health 2008;14:570–575.
[9] Giansanti D, Morelli S, Silvestri S, D'Avenio G, Grigioni M, Giovagnoli MR, Pochini M, Balzano S, Giarnieri E, Carico E. A look inside the future perspectives of the digital cytology. Presented in Computational Modelling of Objects Represented in Images III: Fundamentals, Methods and Applications, August 24, 2012 by CRC Editor(s): Paolo Di Giamberardino, Daniela Iacoviello, João Manuel R.S. Tavares, R.M. Natal Jorge Pag. 335-340
[10] Ash WM, Krzewina L, Kim MK. Quantitative imaging of cellular adhesion by total internal reflection holographic microscopy. Appl Opt 2009;48:144–152.
[11] Seet KY, Nieminen TA, Zvyagin AV. Refractometry of melanocyte cell nuclei using optical scatter images recorded by digital Fourier microscopy. J Biomed Op 2009;14:135–142.
[12] Cheong FC, Sun B, Dreyfus R, Amato-Grill J, Xiao K, Dixon L, Grier DG. Flow visualization and flow cytometry with holographic video microscopy. Opt Express 2009;17:1371–1379.
[13] Yu L, Mohanty S, Zhang J, Genc S, Kim MK, Berns MW, Chen Z. Digital holographic microscopy for quantitative cell dynamic evaluation during laser microsurgery. Opt Express 2009;17:12031–12038.
[14] Giovagnoli MR, et al. Towards digital cytology integration in the tablet technologies. Presented at the 5th International Congress on Virtual Microscopy, June 6–9, 2012, Venice, Italy
[15] Giansanti D, Boschetto A, Pochini M, Bottini L& Giovagnoli MR (2014):Design of a process for image improvement in digital cytology: a preliminary technology assessement, Computer Methods in Biomechanics and Biomedical Engineering: Imaging & Visualization, DOI: 10.1080/21681163.2014.883940
[16] Giansanti D, Pochini M, Giovagnoli NR. How tablet technology is going to change cooperative diagnosis in the cytology e-laboratory Telemed J E Health 2013;19:991–993.
[17] Giansanti D, Pochini M, Giarnieri E, Giovagnoli MR. Towards the integration of digital cytology in the tablet technologies. Diagnostic Pathol 2013;8(Suppl 1):S40.
[18] Huisman A, Looijen A, van den Brink SM, van Diest PJ. Creation of a fully digital pathology slide archive by high volume tissue slide scanning. Hum Pathol 2010;41:751–757.
[19] Demichelis F, Della Mea V, Forti S, Dalla Palma P, Feltrami CA. Digital storage of glass slides for quality assurance in histopathology and cytopathology. J Telemed Telecare 2002;8:138–142.
[20] Bondi A, Pierotti P, Crucitti P, Lega S. The virtual slide in the promotion of cytologic and hystologic quality in oncologic screenings. Ann Ist Super Sanita 2010;46:144–150.

[21] Giansanti D, Castrichella L, Giovagnoli MR. Telepathology requires specific training for the technician in the biomedical laboratory. Telemed J E Health 2008;14:801–807.
[22] Giansanti D. Pochini M. Giovagnoli MR Integration of tablet technologies in the e-laboratory of cytology: a health technology assessment. Telemed J E Health.2014 Oct;20(10):909-15

Fig. 1. The creation of the WorkGroup in the Environment of Whatsapp

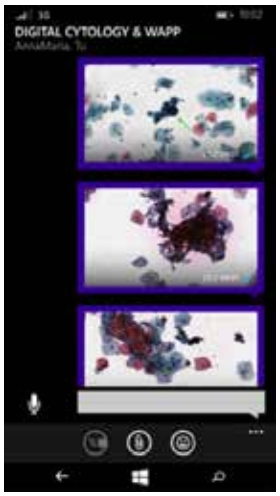

Fig. 2. The exchange of the images of digital Cytology in the Environment of Whatsapp

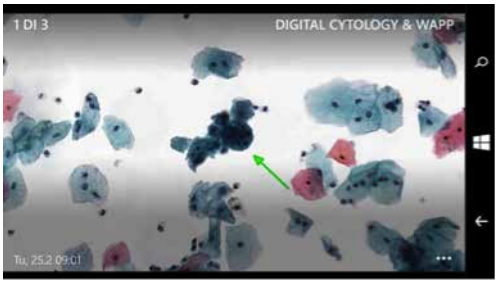

Fig. 3. A single image of digital-cytology in Whatsapp .

Telemedicine: from technological experiment to a new cultural model and for the Welfare State

Authors: Pasquale Raucci[1], Antonietta Perrone[1,2] and C.Authors: Giuseppe Fuschino[2], Alessandra Zannettone[2,1] , Dott. Mauro Feola[2,2], Aniello Leonardo Caracciolo[2,3]
[1] *Clinical engineering – Amos Scrl c/o ASL Cuneo1,* [1,2] *UOS Clinical Engineering – University Hospital Federico II of Naples*
[2] *UOS Clinical Engineering – University Hospital Federico II of Naples* [2,1] *UOS Clinical Engineering – University Hospital Federico II of Naples* [2,2]*Cardiac Rehabilitation decompensation unit – ASL CN1,* [2,3]*UOC Neurosurgery – AORN Sant'Anna and San Sebastiano of Caserta*

***Abstract*—The ASL CN1 with The Saint Anna and San Sebastiano of Caserta AORN, thanks to two groups of multidisciplinary professionals, supported by Partner companies that provide ICT services, have created two different projects, in two realities so culturally and geographically very different, in order to evaluate the effectiveness of telemedicine services in cancer prevention and monitoring of patients with chronic diseases, such as heart failure. The ultimate goal was to analyse the experimental data and evaluate using the MAST model (Model for the Assessment of Telemedicine) the impact of telemedicine on patients management as well as the effects in terms of re-engineering of processes and organizations.**

***Keywords*— Telemedicine, ICT technologies, networks, healthcare, MAST model, patients.**

I. INTRODUCTION

We live in an age in which the overall spending on the health sector is, on average, 9% of the gross domestic product of the European countries and chronic diseases affect only for 75% on the total health budgets. The number of European senior citizens and the incidence of chronic diseases are increasing.

While healthcare needs increase, the economic resources available diminish. This situation confers priority to an intervention of political rescheduling of the welfare planning, identifying and adopting new healthcare dispensing models. Now it is possible to encourage a healthy aging thanks to effective prevention from an early age and to the remarkable evolution of ICT technologies which are revolutionizing the prediction mode and disease treatment. The Observatory Netics, in its Telemedicine Market Overview 2015, has defined the year 2016 "that of telemedicine", the year that will see the take off telemedicine services, starting from those for home tele-assistance and tele-consultation that are constantly growing.

The Working Group that produced the projects presented below, believed in it since 2007, and the strategic guidelines of the National Health Service, as well as the penalty measures foreseen for inappropriate hospital admissions and delayed hospital discharges, predict that the year 2016 is "the turning point."

II. MATERIALS AND METHODS

The methodology chosen for the evaluation of the projects has been the MAST model (Model for the Assessment of Telemedicine) which is the gold standard in the HTA analysis indicating seven domains for accurate and cross-evaluation of telemedicine services.

The first experience concerned the prevention of breast cancer for women in Caserta. The service, originally designed and funded in 2007 as part of the POR Campania 2000-2006 Measure 4.11 was revised in 2013, with the adoption of cellular technologies that have enabled the transmission in mobility of medical images with a simultaneous reduction of the costs of connection. The prevention project, wanted by the hospital "Sant'Anna and "San Sebastiano", assisted by the Red Cross volunteers of the Caserta Provincial Committee, has allowed women living in rural areas of the province to undergo screening mammography free of charge and without having to go to the hospital of Caserta. Images sent with smartphone, through a secure network, arrived at the Operations Centre, located in the Hospital of Caserta, and there were consulted from the medical specialist for reporting. The second project involved the management of patients with chronic heart failure and residents in the te territories of competence of the ASL CN1. In this experience, unlike the usual care management, the project provided that the medical staff would go to the patient's home, detect the main clinical parameters using the "telemedicine kit", and then send the data to the Central, where the medical specialist takes care of reporting.

III. RESULTS

From the analysis of the experimental data has been clearly demonstrated that the approach to care by telemedicine has a profound social impact, it improves quality of life and it's not only economically sustainable but mostly capable of producing significant savings. Then in view of indentation of spending and improving the quality of life, information and communication technologies, and in particular the two telemedicine projects implemented, represented for the two regions a possible path to follow, able to offer delivery and management
models of alternative and more effective care, by transferring to the two territories, methods and skills currently available only in the hospitals.

IV. Conclusion and future developments

In conclusion, telemedicine can be a valuable and real tool to improve the Italian healthcare. Its affirmation, however, is limited by the absence of a legal regime governing the recognition by the National Health Service of the relative performance. Without an appropriate political, legislative and economic support, the modernization of our health care system it's impossible.

It is hoped, therefore, that in the near future, we can really talk about sustainable healthcare offer and in line with the needs of patients.

BIBLIOGRAPHY

- Ministero della Salute, "Telemedicina: Linee di indirizzo nazionali"
- Commissione permanente sull'Innovazione Tecnologica nelle Regioni e negli Enti Locali, "Tavolo di lavoro: Telemedicina" Giampiero Papi, Fabrizio L.Ricci, "La telemedicina"
- Giampiero Papi, Fabrizio L.Ricci, "La telemedicina"
- Giampiero Papi, Fabrizio L.Ricci, "La telemedicina"
- Ministero della Salute, "La telemedicina: linee di indirizzo nazionali"
- Abet F., Ricci F.L. , "La re-integrazione dei processi di cura"
- Ministero della Salute, "La telemedicina: linee di indirizzo nazionali"
- Ministero della Salute, "La telemedicina: linee di indirizzo nazionali"
- Corrado Jaccarino, Franco Servadei, Domenico Rossi, "L'emergenza neurochirurgica e la gestione delle immagini in rete"
- Ministero della Salute, "La telemedicina: linee di indirizzo nazionali"
- Ministero della Salute, "La telemedicina: linee di indirizzo nazionali"
- Giampiero Papi, Fabrizio L.Ricci, "La telemedicina"
- Ministero della Salute, "La telemedicina: linee di indirizzo nazionali"
- Giampiero Papi, Fabrizio L.Ricci, "La telemedicina"
- Giampiero Papi, Fabrizio L.Ricci, "La telemedicina"
- Garagnani, Arcuri "La telemedicina è uno strumento economicamente sostenibile nella collaborazione Ospedale-Territorio?"
- Corrado Jaccarino Franco Servadei, Domenico Rossi "L'emergenanza neurochirurgica e la gestione delle immagini in rete"
- Paolo Pari, Giampiero Vaschetto "Teleradiologia:rete metropolitana dei servizi radiodiagnostici di Pronto Soccorso"
- Marco Campari "L'impatto della e-health sulla telemedicina e sull'innovazione gestionale"
- Giovanni Mensa, Domenico Tangolo, Lorenzo Capussotti, Daniele Rege, Antonio Castellani "Progetto Ermes:discussione di casi clinici in teleconsulto" Cinzia Iannaccio, "Un dispositivo salvavita in caso di caduta degli anziani"
- Anna Rota, Francesca Santafede "La telemedicina Per pazienti BPCO e comorbilità"
- F.Fedele, S.Scalvini"modelli di telecardiologia attualmente in uso"
- Patrizio Bianchi,Laura Ramaciotti, "Pubblico e Privato per l'information communication technology della Sanità"
- Presidenza del consiglio dei Ministri, "Tavolo di lavoro:telemedicina"
- Antonio Leo Tarasco "La Telemedicina per lo sviluppo della sanità del Mezzogiorno:una introduzione giuridica"
- "Sanità ed E-Government:utilizzo dei sistemi informativi per una gestione della sanità più efficiente e trasparente"
- Presidenza del consiglio dei Ministri, "Tavolo di lavoro:telemedicina"
- Elio Borgonovi, "Conoscenze,tecnologie,politiche della salute"
- Mario Vannini "Introduzione:Lo sviluppo della telemedicina e telecardiologia:aspetti di politica sanitaria e strategie delle aziende territoriali e ospedaliere"
- Patrizio Bianchi,Laura Ramaciotti "Pubblico e Privato per l'information communication technology della sanità"
- Patrizio Bianche, Laura Ramaciotti "Pubblico e privato per l'information communication technology della sanità"
- Ministero della Salute, "Telemedicina, linee di indirizzo nazionali"
- Ministero della Salute, "Telemedicina, linee di indirizzo nazionali"
- Carla Collicelli "Innovazioni tecnologiche in sanità e contesto socio-politico"
- Ministero della Salute "Telemedicina, Linee di indirizzo nazionali"
- Carla Collicelli "Innovazioni tecnologiche in sanità e contesto socio-politico"
- Ministero della Salute "Telemedicina, Linee di indirizzo nazionali"
- Elio Borgonovi, "Conoscenze, tecnologie, politiche della salute"
- Ministero della Salute "Telemedicina, Linee di indirizzo nazionali"
- Ministero della Salute "Telemedicina, Linee di indirizzo nazionali"
- Antonio Leo Tarasco, "La telemedicina per lo sviluppo della sanità del Mezzogiorno:una introduzione giuridica"
- G.Cangelosi, "I servizi pubblici sanitari"
- Antonio Leo Tarasco, "La telemedicina per lo sviluppo della sanità del Mezzogiorno:una introduzione giuridica" 103
- Commissione Europea "Comunicazione al Parlamento Europeo, al Consiglio, al Comitato economico e sociale europeo e al Comitato delle regioni sulla telemedicina a beneficio dei pazienti, dei sistemi sanitari e della società"
- Cosiglio Europeo, "Sicurezza ed efficienza dell'assistenza sanitaria mediante sanità elettronica"
- Commissione europea, "Comunicazione al Parlamento Europeo, al Consiglio, al Comitato economico e sociale europeo e al Comitato delle regioni sulla telemedicina a beneficio dei pazienti, dei sistemi sanitari e della società"
- Comitato economico e sociale europeo(CESE) (51) Direttiva 2000/31/CE (52) Proposta di direttiva COM, 2008
- Tavolo permanente Sanità Elettronica delle Regioni e delle Province autonome, "Una politica per la sanità elettronica. Per un migliore e più efficiente sistema sanitario Nazionale attraverso l'innovazione digitale

Medical – IT Network: The design of incorporation of an innovative apparatus for Oncological Radiotherapy

Authors: Antonietta Perrone[1], Roberto Cuocolo[1,2] and C.Authors: Alessandra Zannettone[2], Giuseppe Fuschino[2,1] , Roberto Pacelli[2,2]
[1] *UOS Clinical Engineering – University Hospital Federico II of Naples* , [1,2] *UOC Medicina Nucleare*
[2] *UOS Clinical Engineering – University Hospital Federico II of Naples* [2,1] *UOS Clinical Engineering – University Hospital Federico II of Naples,* [2,2] *UOS Radiotherapy*

***Abstract*— The purpose of the standard IEC 80001-1 OF 2010 is to define roles and responsibilities for the management of the medical IT networks. At the University Hospital Federico II, we used the aforementioned standards to improve the planning and design of the incorporation in the IT network of the innovative LINAC TrueBeam.**

***Keywords*— Medical Device, network, data and system security, manufacturers, healthcare company, IT technologies.**

I. Introduction

The massive spread of Medical Devices (MD) equipped with a network interface (or capable of interacting with the computer infrastructure) has profoundly changed the scenario concerning not only the functions of the devices themselves, but even more their management, the interaction and interoperability with other elements making up the technological and information resources within healthcare companies. Since the manufacturer of the MD cannot decide the planning of the network or its operations, it is the healthcare company that must become the entity in charge of the risk management and hence the term of *responsible organization* .
The IT infrastructure of a healthcare company has at least two significant features:

1. Presence in the Network of MD that can also be electro-medical apparatus or MD software
2. Processing of sensitive data

These features imply a level of criticality in the MD management and IT infrastructure. These MD connected on the network, require not only the management of physical security (person, operator, environment), but also the data and system security. In addition you must also consider the privacy, since they handle sensitive data.
The standard IEC 80001-1 of 2010 specify on international level what has been said above.
The purpose of this standard is to define roles and responsibilities for the management of the medical IT networks (a data network that incorporates at least one medical device, in addition to all other hosts) to implement 3 key properties on which is based the measurement parameter of this standard that is: physical security, the effectiveness of networking, data security and systems.
This standard is directed to:
• Responsible Organisations;
• manufacturers of MD;
• to all providers of other IT technologies.

At the University Hospital Federico II, we used the aforementioned standards to improve the planning and design of the incorporation in the IT network of the innovative LINAC TrueBeam, for the technique IMRT, IGRT, VMAT; installed last December into the bunker of the department of integrated activities (DAI) of Morphological and Functional Diagnostics, Radiotherapy, Forensic Medicine of the university hospital.

II. Materials and methods

It was applied the principle of risk management before the LINAC was physically connected in the data network; this principle will be applied throughout the life cycle of medical device, in order to continuously assess the security of the whole MD and data network;
The Corporate Risk Manager has updated the virtual Medical IT Network Management files.
The action of risk management was made to grant:

- The physical safety of patients, operators, third parties, environment and property;
- the effectiveness or the ability to produce the expected outcome, determined by the connection of the new LINAC to the IT network;
- the data security, which as such are not yet information, and of systems, that is all that at the network level is able to make the data flow.

Safety:
• *risks related* to electrical safety. In the specific case, the manufacturer of the MD has predicted, in the documentation enclosed into the electromedical system, that the system could be put online during the use on the patient. The manufacturer then has already done its risk analysis via separation devices;

• risks arising from the malfunction of the MD:
- For failures or misconfigurations of interfaces;
- For unwanted interactions between the MD and the external IT world.

Efficacy:
They were assessed the aspects in terms of integration, interfacing and interoperability with the IT infrastructure (both systems engineering and above all operational) in order to implement, in an effective and safe way, the computerized data flow from MD (hardware and software) in the network.

This also contributes to the continuity of service and security of the data.
In regard to this it has been decided for the adoption of standards of communication (DICOM, HL7) and best practices.

Other tools used to guarantee the quality of information / data for clinical evaluation, were:
• Computer tools such as: 1) the digital signature 2) substitutive storage;
• Regulatory instruments such as the CE mark.

Data and system security:
Data and systems security has been ensured through the measures of confidentiality, integrity and availability of information.
Privacy (also called confidentiality) is the set of rules that restrict access to IT resources and information to authorized persons only. Confidentiality, complex to be pursued, it is not only applicative, but also of the network and of the system;
• integrity requires that the data is not modified or deleted, except through established procedures. In this regard it is important to use the electronic signature and the traceability of the action;
• availability or specific IT resources and information accessible with right modes and appropriate tools and therefore relevant to the purposes and not excessive.

Its 'clear that absolute security does not exist, unless infinite resources.
Ensuring availability, integrity, confidenziality of the data and of the systems (namely of information), we obtain safety and efficacy and therefore also physical security (not as regards the electrical safety, concept in itself, but for the physical safety related to possible erroneous interfacing and malfunction of the LINAC).

III. RESULTS

The design of the incorporation of the innovative LINAC TrueBeam into IT network has been performed:
a) complying with legal obligations;
b) in compliance with the principles of redundancy, resiliency, business continuity;
c) according to the centralization of services;
d) ensuring the training and continuous information of the operators on best and bad practices;

Finally, since a new medical device on the network may be the object of cyber attacks, but it can represent also the starting point, the MD manufacturers often represent an obstacle and often impose a number of limitations. Precisely for this reason, the IEC 80001 is addressed also to manufacturers of the MD.

IV. CONCLUSION AND FUTURE DEVELOPMENTS

In conclusion, the IEC 80001-1 standard does not define the acceptable level of risk that is up to the organizations in charge, according to its own characteristics, context and mission.
It's clear that, given the increasing convergence of medical devices and IT networks, it is essential to take an ever more active cooperation among professionals of the company management, the IT and Clinical Engineering Department.
The IT Department, which was worried only about the data and system security, and the clinical engineering departement, will need to work together in a unanimous manner, right from the planning stage of the IT medical network throughout the lifecycle of medical IT networks.
Technological advances have led to a vital interaction between the skills and professional process that until a few years ago were completely autonomous from different cultural skills, with obvious difficulties in integrating roles and responsibilities traditionally focused on issues and distinct approaches. That time is now essential.
Therefore we want to reiterate that the success of this scenario will depend not only on technology and skills but also and especially on the mutual cooperation and the mentoring of these two worlds who will converge in a new profession such as the "networks engineer".

BIBLIOGRAPHY

- Annibali A. Bellini, Fondamenti e strumenti dell'information technology, Giappichelli Editore, 2004
Axelrod W.C., Outsourcing Information Securit, Artech House Editore, 2004
- Bartolacci F., La gestione e il controllo dei processi di outsourcing, Giuffrè Editore, 2004
- Bedward D. Stredwick J., Managing Information. Core Management Butterworth-Heinemann Ltd Editore, 2003
- Bellinaso M. Hoffmann K., Asp.Net: sviluppo di applicazioni web. Dal design al deployment, Hoepli Editore, 2002
- Benyon P., E-Business, Palgrave Macmillan Editore, 2004
- Biagini C., Information technology ed automazione del progetto, Firenze University Press Editore, 2002
- Bisio C. Frigerio D., Business to consumer a misura di cliente. Una visione dell'
- Efectividad, seguridad y estimaciòn de costes del Sistema de radiochirugìa Ciberknife. (Nieves Calcerrada Dìaz-Santos, Ramòn Sabes Figuera - Novembre 2005).
- Documento dell'Associazione Italiana di Radioterapia Oncologia L'appropriatezza in radioterapia oncologica: indicazioni e considerazioni dell'Associazione Italiana di Radioterapia Oncologia (AIRO) versione 01.2012
- Manuale Linac
- Scheda Tecnica CyberKnife ® M6 ™ Series
- Scheda Tecnica The True Beam Systems Varian
- Scheda Tecnica The True Beam Systems Varian Built
- Advanced in Technology in radiation Oncology' (Mehemet Ufuk Abacioglu 'Eur Assoc Neuroncol Mag 2012; 2(1):11-4)
- TomoTherapy, Gamma Knife and CyberKnife Therapies for Patients with Tumors of the Lung, Central Nervous System, or Intra-Abdomen: A systematic Review of Clinical Effectiveness and Cost-Effectviveness. (Rhonda Buodreau, Michelle Clark, Emmanuel Nkansah - Settembre 2009)
- CyberKnife for Patients with Cancer of the Lung, Central Nervous System, or Intra-Abdomen: Clinical and Cost-Effectiveness DATE: 7 January 2010
- Aggiornamento del TomoTherapy, Gamma Knife and CyberKnife Therapies for Patients with Tumors of the Lung, Central Nervous System, or Intra-Abdomen: A systematic Review of Clinical Effectiveness and Cost-Effectviveness.

(Rhonda Buodreau, Michelle Clark, Emmanuel Nkansah - Settembre 2009) Cadth
- Stereotactic body radiotherapi (sbrt) for lung cancer – Report of the ASTRO Emerging Technology Committee
- Facts and fiction of Flattening Filter free (FF-FFF) X- ray Beams (J Ting, Melbourne Cancer center - AAPM 54th Annual Meeting)
- Corrente status and future perspective of flattening filter free photon beams (G. Dietmar et Al, Med. Phys. 38, 1289 - 2011).
- Feasibility and early clincial assessment of flattening filter free (FFF) based stereotactic body radiotherapy /SBRT) treatments. (Scorsetti et al., Radiation Oncology 2011 6:113).
- Systematic measurements of whole-body dose distributions for various treatment machines and delivery techniques in radiation therapy (Rogers A. Halg et Al, Medical Physics 39, 7662 – 2012
- Revision sistematica de la eficacia y seguridad del Ciberknife: indicaciones y resultados en el tratamiento de lesiones intra y extracraneales Informes de evaluacion de tecnologias saniitarias (UTES 2007/3) (M. José lopez - Pedraza Gomez, 2008)
.

Engineerization of DAP (Dose Area Product) Information for the Medical Record

N. Scotti[1], M. Pugliese[2],
F. Preziuso[3] andS. Casarella[3].

1. Dept. Electronic Engineering and Information Technology, University of Naples Federico II, Italy
2. Dept. Of Physics, University of Naples Federico II, Italy
3. A.O.R.N. "San Giuseppe Moscati" (Hospital) in Avellino, Italy.

***Keywords*— DAP, DICOM, PACS, Medical Record, Euratom directive 59/2013**

I. INTRODUCTION

In this paper we dealt with difficulties related to the radiation protection and to the informatization of the medical record, of the information related to the radio protection, regarding the health and the protection of patients that undergo to medical diagnosis through medical equipment which release ionizing radiations.

The goal of such a work is centered on the engineerization of the certification procedure of the DAP (Dose Area Product) information in favor of the AziendaOspedaliera di RilievoNazionale "San Giuseppe Moscati" in Avellino (Avellino Hospital).

The heart of this paper was the Euratom Directive 59/2013[4], which on chapter VI, paragraph 6.5, article 58, item b, prescribes that the DAP information, which is related to a specific practice of diagnosis, will have to be included in the patient's medical record.

Such a normative must be acknowledged in the legislature of all the State Members within February 6th, 2018.

II. MATERIALS

A. PACS

PACS (Picture Archiving and Communication System) consists of a hardware and software dedicated to the storage, transmission, display and printing of digital diagnostic images.

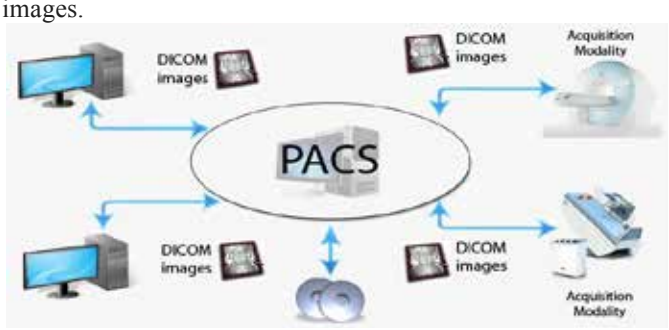

Fig.1: PACS System

The medical testis received and transmitted in the DICOM format, which also incorporate text and documents of various kinds.[1]

B. DICOM

The DICOM standard characterize a compression format for a digital image, but also describes the exchange processof medical data.

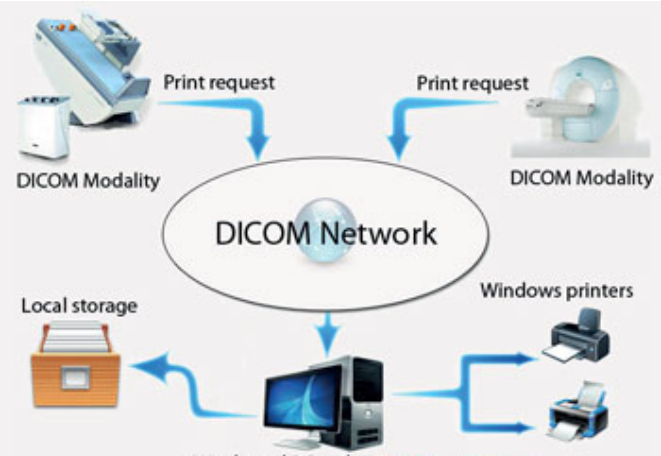

Fig.2: DICOM Network

DICOM structure is composed by:
- a header: containing the patient information, the procedure, time and data acquisition,etc.;

-an Image Data: containing the picture regarding the medical test.[2]

C. DAP

The DAP (Dose Area Product) is defined as the absorbed dose multiplied by the irradiated surface:

$$DAP = \text{Dose x detector surface area } [\text{ Gy cm}^2]$$

The DAP is one of the best indicators of biological risk due to ionizing radiation.

It is closely related to entrance dose and the size of the field, which depend on the total energy imparted to the patient, causing the biological risk.

The DAP provides a good estimate of the total energy of the radiation delivered to a patient during a procedure (diagnostic / surgical) and this is why it is the most practical quantities to be used for the monitoring of radiation given to the patient.

The DAP information is more practical because:

-all the examination is recorded;
-the patient's position with respect to the radiation beam is less important than it would be if it were used a TLD, so the measurement does not interfere with the patient's medical test;
-no need to disturb the patient to make measurements
-the DAP's information is not dependent from the measurement's point (from the x-ray source's distance).[3]

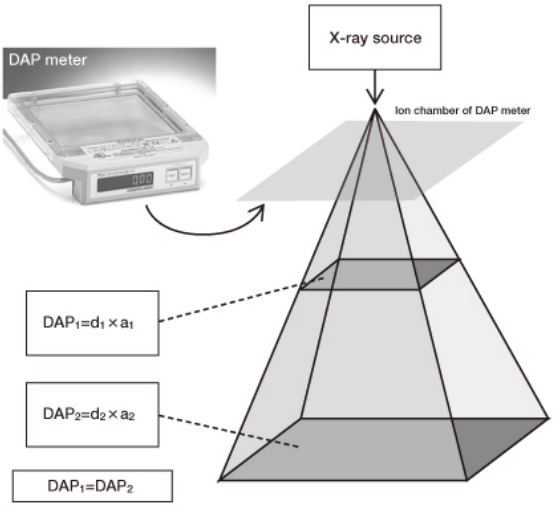

Fig.3: DAP'smeasurement

TABLE I
DAP REFERENCE DOSE

Medical Test	*Average DAP per radiograph [Gy cm²]*	*Weighted average value of DAP per repeat [Gy cm²]*
Upper limb	0.27	0.034
Lower limb	0.68	0.098
Skull	1.40	0.128
Lumbar spine	2.85	0.431
Pelvis	2.6	0.093
Chest	0.67	0.200
Plain abdomen	3.1	0.400
Intravenous urography (IVU)	10.51	0.234

Dose Area Product per repeat = 2.76 Gy cm^2).

III. METHODS

For this procedure two parallel works were used, one for the analogical equipment, the other for the digital equipment.

The digital equipment is already provided with the PACS connection, by the DICOM standard.

The DICOM standard offers various tags, which allow the transmission of patient's information, of the diagnosis, and of the relative medical conditions.

These tags also include the DAP tag, which allow the transmission related to the information of the dose given to the patient during the diagnosis test.

So, it was important updating the digital equipment to furnish them of such a DAP tag.

The analogical equipment is known to not possess the Integration Module DICOM, for the PACS transmission. Such machinery was equipped with the x-ray detector (Flat Panel), which is able to transmit both the diagnosis test and the DAP information.

IV. RESULTS AND CONCLUSIONS

By doing this, the information given by the analogical and digital equipment, were compared.

This has contributed to adding very important information in the patient's medical record.

Having this extra information in the medical record facilitate the protection of the patient that undergoes the medical diagnosis through ionizing radiation.

With such a product we have reached a great result.

Especially we are able to meet the deadline requirements of the Euratom directive 59/2013, earlier then the deadline.

Including such DAP information in the medical record is useful for prevention and protection of the biological risks due to ionizing radiation, and it will be also useful for researches and statistics always intended for the protection and health of the patient.

REFERENCES

[1] Lee F. Rogers, "*PACS: Radiology in the Digital World*", AJR:177, September 2001.
[2] Peter Mildenberger, Marco Eichelberg, Eric Martin, "*Introduction to the DICOM standard*", September 2001.
[3] J C Le Heron, "*Estimation of effective dose to the patient during medical X-ray examinations from measurements of the dose-area product*", Physics in Medicine and Biology, Volume 37, Number 2011.
[4] EURATOM directive 59, December 5Th 2013, [Online]. Available:http://eur-lex.europa.eu/legal-content/IT/TXT/?uri=CELEX%3A32013L0059

INGEGNERIA DELLA RIABILITAZIONE

Development of a wearable multi-channel sEMG acquisition system

Giacinto Luigi Cerone[1], Marco Gazzoni[1]

[1] *Laboratorio di Ingegneria del Sistema Neuromuscolare, Dipartimento di Elettronica e Telecomunicazioni, Politecnico di Torino, Italy*

***Abstract*—This work describes the development of a multichannel, wireless and compact EMG acquisition system managing up to 32 monopolar EMG signals sampled at 2 ksps with 16 bit resolution. The system can be connected to the receiver (PC, smartphone or tablet) either via a direct link (point-to-point connection) or through a router. The tests on the 32 channel analog front-end showed good performance in terms of 50Hz interference rejection. The characterization of the wireless link proved that it is possible to transfer up to 170 EMG channels sampled at 2ksps with 16 bit resolution and just 2ms of latency.**

***Keywords* — Surface EMG, Multi-channel sEMG, Biomedical Instrumentation, Wireless, Wearable.**

I. INTRODUCTION

In the last decade, mono- or bi-dimensional electrode arrays applied to the skin have remarkably improved surface EMG technique [1]. The use of mono or bi-dimensional electrode arrays for sEMG signal detection increase the reliability and the information content of sEMG and provide information not obtainable through traditional detection systems [2][3]. High Density EMG (HDEMG) provides indications of the peripheral muscle characteristics [4] as well as information about central control [5]. This work describes the development of a wearable multichannel sEMG acquisition system.

II. METHODS

The system architecture includes: (1) a transmitting unit managing up to 32 monopolar EMG signals sampled at 2 ksps with 16 bit resolution; (2) a mobile device (notebook, tablet or smartphone) that receives wirelessly the sampled signals. The transmitter and the receiver can be connected either via a direct link (point-to-point connection) or through a router. The latter type of connection can be useful in applications which need the connection of additional wireless modules (e.g. auxiliary channels) to the system or more modules in parallel.

A. Analog Front-end

The Intan RHD2132 front-end was chosen in order to minimize the size and encumbrance of the system. The RHD2132 chip is a low-power and ultra-compact (size 9x9 mm) bio-signal acquisition system, integrating 32 monopolar analog front-ends with fixed gain (192V/V) and programmable bandwidth, an analog multiplexer, a 16 bit resolution A/D converter and a SPI communication interface. Each analog front-end is AC coupled.

Considering the relatively low input impedance of the amplifier's reference pin (1.3GΩ at 10 Hz but only 13MΩ at 1kHz), 50Hz interference rejection has been verified using the Intan evaluation board and different hardware configurations listed in the following.

The reference electrode was connected in two different ways: (1) directly to the patient; (2) throw a low impedance virtual reference path.

The test has been performed in a known constant 50Hz field. Three levels of 50Hz field have been considered: field generator off, 20V/m, and 80V/m.

Each test was repeated powering the Intan Evaluation Board and the PC either from battery or power line.

These tests resulted in 24 different measures (*ref_el* (2) x *50Hz_Field* (3) x x *pc_power* (2) x *intan_power* (2)). For each configuration, 32 monopolar EMG signals have been acquired with an electrode matrix (1 cm i.e.d, circular electrodes; 4 mm in diameter) positioned on the Biceps Brachii muscle of one subject during rest.

Five-second long signals have been acquired and the Root Mean Square value (RMS (uV)) estimated on the whole signal for each channel.

B. Wireless MCU

The maximum data throughput achieved by the Wi-Fi link was obtained choosing a fixed TCP packet size of 1408 bytes, corresponding to 5.5ms of signal per channel (f_s=2ksps) and varying the number of simultaneously transmitted packets (data frame length) between a TCP socket open/close session. The packets were transmitted has soon has possible without any sampling task.

The generated Wi-Fi traffic has been analysed by means of a Wi-Fi packet sniffer. The throughput has been computed as in Eq. (1).

$$Throughput = \frac{t_{Tx}}{N_{Rx} * 1000} \qquad (1)$$

The throughput is expressed in kilo bits per seconds (kbps) while t_{Tx} and N_{Rx} are the acquisition time (s) and the number of bits received. Each recording session was five minutes long. The time latency due to the Wi-Fi link was estimated measuring the transmission time of a single data frame.

In order to achieve the high data throughput required for the 32 channel sEMG signal transmission (1 Mbps) and to connect the system to mobile devices without an ad-hoc receiver, the Texas Instruments CC3200 system on chip wireless MCU has been selected.

A real-time operating system was used and two different parallel tasks (sampling and transmission) were implemented.

The semaphores technique has been used in order to avoid conflicts between the two tasks.

C. sEMG acquisition software

The software for the acquisition and online visualization of the EMG signals was developed using the multi-platform Qt libraries (Android, Windows, Linux and MAC). Toghether with the acquisition system prototype, it has been used for preliminary sEMG acquisition tests. sEMG signals have been acquired from one subject during an isometric elbow flexion using a 32 electrodes linear array with 5mm inter-electrode distance positioned on the Biceps brachii.

III. RESULTS

A. Analog Front-end characterization

Fig. 1 shows the boxplots of the RMS value of the signals detected with a matrix of 32 electrodes with the subject at rest for different 50 Hz field intensities, REF electrode configurations, PC power supply modalities and Intan power supply modalities. It is possible to observe that the best configurations are the one with both PC and Intan evaluation board powered with a battery. The use of the circuit for the generation of low impedance virtual reference signal has a limited effect on 50Hz interference and it is indicated only in the case of power supply feeding.

Considering the aim of the project, it is possible to conclude that the relatively low input impedance of the Intan chip does not preclude the possibility to acquire sEMG signals with low 50Hz interference (RMS<10 uV) when the system is battery powered.

B. Wireless MCU tests

The maximum throughput reached by the CC3200 chip was 9 Mbps, allowing the transmission of up to 282 EMG signals sampled at 2ksps with 16 bit resolution. This result was obtained sending a data frame of 10000 packets corresponding to a 55s signal duration. Such data frame size is not compatible with the real time requirements of a wearable acquisition system.

Nevertheless, the resulting data throughput obtained sending only one fixed size data packet for each open/close socket session was 5.5 Mbps, allowing the transmission of up to 170 EMG signals sampled at 2ksps with 16 bit resolution. The measured latency was just 2ms. These results fit the goal of the project.

In order to characterize the robustness of the wireless link, the performance of the selected Wi-Fi module was tested also in terms of TCP packet losses through a virtual sinusoidal signal (f=80Hz, fs=2kHz) generated into the MCU, transmitted to the PC and multiplexed over 32 channels. This setup was necessary to precisely control, off-line, the correspondence between the transmitted and the received signal and, then, check for and count the number of lost data packets. No significant packet loss has been observed.

Fig. 2 shows EMG signals detected from the Biceps Brachii muscle during an isometric elbow flexion using a 32 electrode linear array with 5mm inter-electrode distance.

IV. CONCLUSION

This work describes the development and test of a 32 channels EMG acquisition system for wearable applications. The tests performed on the Intan RHD2132 single-chip analog front-end and the CC3200 wireless MCU satisfy the system requirements.

The integration of all system components into a miniaturized device is under development.

ACKNOWLEDGEMENT

This study was co-funded by the bank foundations Compagnia di San Paolo and Fondazione C.R.T.

REFERENCES

[1] R. Merletti, M. Aventaggiato, A. Botter, A. Holobar, H. Marateb, T. M. Vieira. Advances in surface EMG: recent progress in detection and processing techniques. Crit Rev Biomed Eng., pp. vol. 38, pp. 305-345, 2010

[2] M. J. Zwarts, B. G. Lapatki, B. U. Kleine, D. F. Stegeman. Surface EMG: how far can you go? Suppl Clin Neurophysiol, pp. vol. 57, pp.111-119, 2004

[3] G. Rau, E. Schulte, C. Disselhorst-Klug. From cell to movement: to what answers does EMG really contribute. J. Electromyogr. Kinesiol, pp. vol. 14, pp. 611–617, 2004,

[4] Merletti, R., Farina, D. & Gazzoni, M. The linear electrode array: a useful tool with many applications., Journal of Electromyography and Kinesiology, pp. 13: 37 - 47, 2003

[5] Holobar, D. Farina, M. Gazzoni, R. Merletti, D. Zazula "Estimating motor unit discharge patterns from high-density surface electromyogram"., Clin Neurophysiol, pp. vol. 120, pp. 551-562, 2009

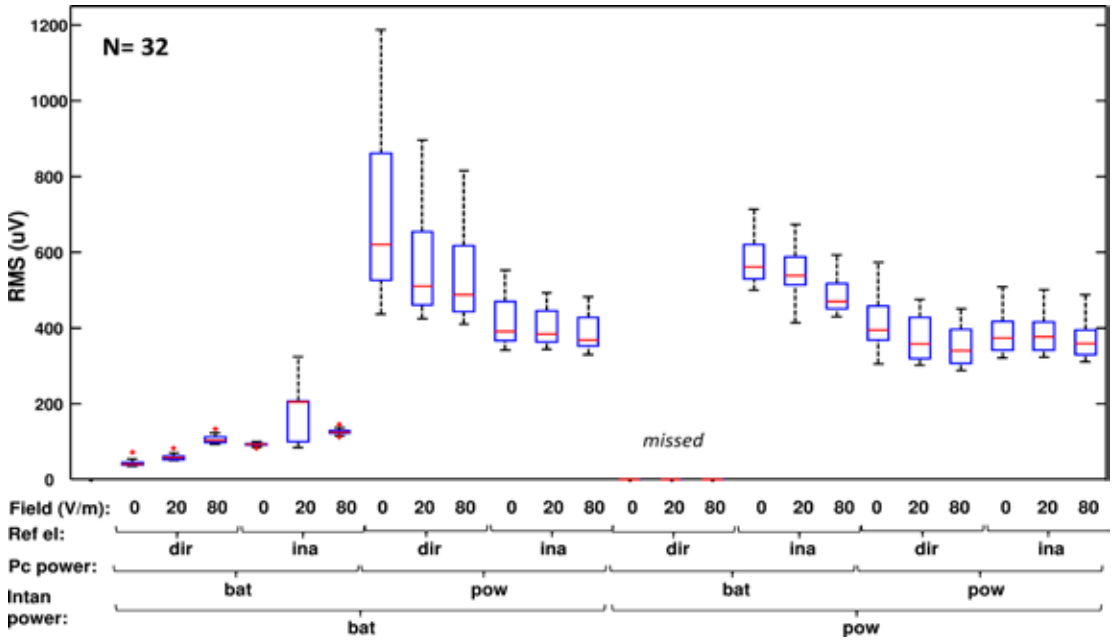

Fig. 1. Boxplots of the RMS value of the signals detected with a matrix of 32 electrodes with the subject at rest for different a) 50 Hz field intensities, b) REF electrode configurations (dir: reference electrode directly connected to the REF input of the Intan amplifier board; ina: reference electrode connected hrough a circuit intended to generate a low impedance virtual reference signal, c) PC power supply modalities (bat: battery; pow: power supply), and d) Intan power supply modalities. It is possible to observe that the best configurations are the ones with both PC and Imtan evaluation board powered with a battery. The higher effect in the reduction of 50Hz interference is obtained using a battery to power both the PC and the Intan amplifier board. The use of the circuit for the generation of low impedance virtual reference signal has a limited effect on 50Hz interference.

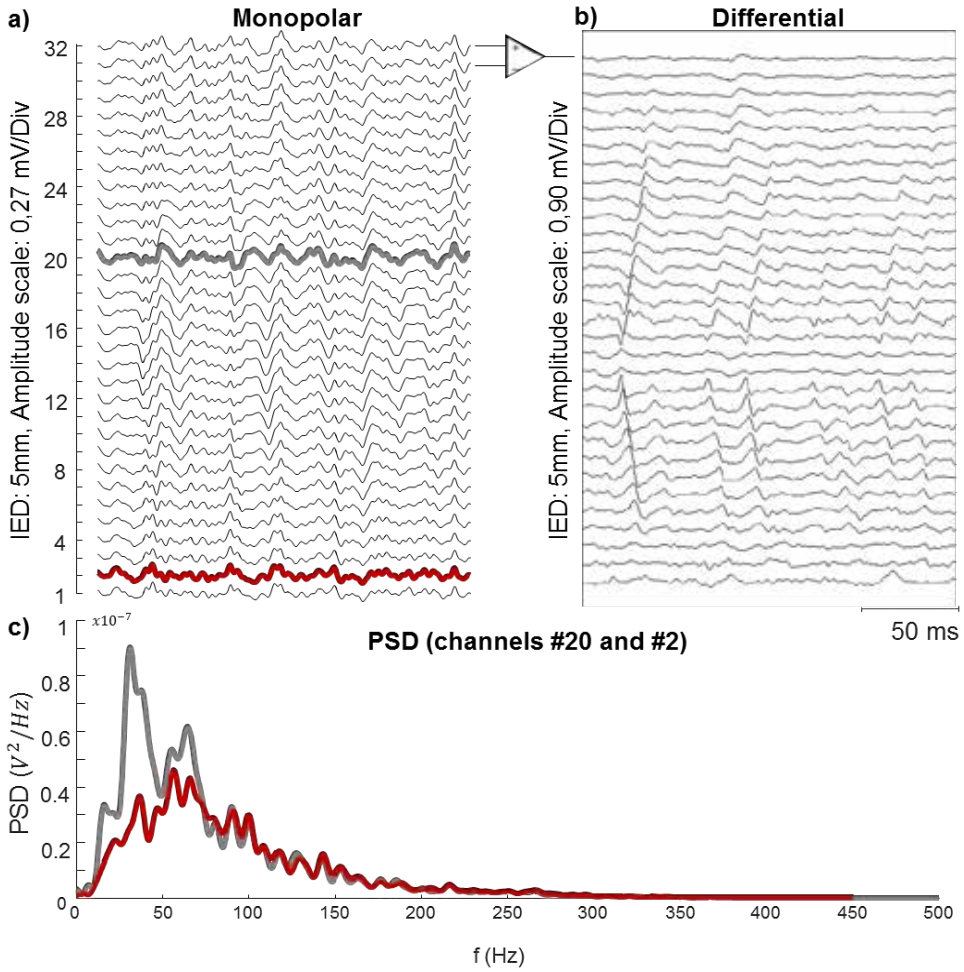

Fig. 2. Example of EMG recordings from the Biceps Brachii muscle obtained using a 32 electrodes linear array with 5mm inter-electrode distance. A) Monopolar and b) single differential EMG signals are shown. From the differential signals it is possible to identify the innervation zone (between channels 13 and 14) and the propagation of single MAUPs. c) PSD from monopolar channels 2 and 20. No spikes indicating 50Hz interference can be observed.

M-IMU and EMG signals for the control of trans-humeral prostheses

C. Lauretti[1], A. Davalli[2] , R. Sacchetti[2] and E. Guglielmelli[1] , L. Zollo[1]
[1] *Laboratory of Biomedical Robotics and Biomicrosystems, Università Campus Bio-Medico di Roma, IT*
[2] *INAIL centro protesi di Vigorso di Budrio (BO), IT*

***Abstract*— This paper introduces a novel control strategy for trans-humeral prostheses that, based on the coupled use of myoelectric and magneto-inertial sensors, allows managing simultaneous movements and more physiological reaching tasks with respect to the most adopted technique to control such prosthetic devices, i.e.\ conventional amplitude-based control . A comparative experimental analysis has been carried out on eight able-bodied individuals, in order to compare performance of the proposed control with the conventional one. The obtained results show that the proposed control can achieve higher performance than the commercially available EMG control strategies.**

***Keywords*—Upper-limb prosthesis, M-IMU, EMG electrodes.**

I. INTRODUCTION

THE incidence of upper-limb amputation is generally high worldwide [1]. Consequently, an increasing interest in the upper-limb prosthetics during the recent years is observed. The most adopted techniques to control such devices are based on surface EMG recordings.

In particular, most of the commercially available prosthetic systems are driven by a relatively simple control strategy, i.e. amplitude-based control [2], where the amplitude of EMG signals recorded from two antagonist muscles are compared to a predetermined threshold and used to actuate one of the motors embedded into the prosthesis. In order to manage multi-DoFs devices (such as trans-humeral prostheses), amplitude-based control uses a cyclic selection process to choose the joint to be driven, thus enabling only sequential movements. Co-contraction of the two target antagonist muscles (e.g. biceps and triceps) is used as trigger signal to select the joint to move; on the other hand, the isometric contraction of the two target muscles causes the movement (counterclockwise and clockwise, respectively) of the selected joint.

Pattern recognition applied to ElectroMyoGraphic (EMG) signals is another approach to control prosthetic devices that tries to address the issue of simultaneously control multiple joints [2]-[3]-[4]. It is not implemented in commercial devices, yet. Nevertheless machine learning methods could be efficiently applied to trans-humeral amputees and subjects with shoulder disarticulation that undergo a Targeted Muscle Reinnervation surgery (TMR) [5].

The purpose of this work is to propose a novel approach to EMG control of trans-humeral prostheses that allows simultaneously managing multiple DoFs in a more natural way than the commercially available amplitude based control, without resorting to pattern recognition.

It relies on the coupled use of magneto-inertial sensors and EMG; hence, it is named *combined M-IMU/EMG control*. A comparative analysis with the amplitude based control, named in the following traditional control, has been performed on eight healthy subjects. They have been asked to drive a virtual prosthesis with the two control strategies in activities of daily living..

II. COMBINED M-IMU/EMG CONTROL FOR TRANS-HUMERAL PROSTHESES

The proposed strategy is based on the coupled use of Magneto-Inertial Measurement Units (M-IMUs) and two EMG electrodes. The EMG electrodes are placed on two antagonist muscles, i.e. biceps and triceps, in order to record the target muscles myoelectric activity; on the other hand, the M-IMUs are placed on the user trunk and stump, respectively, in order to evaluate shoulder flexion-extension (F-E) and ab-adduction (AB-AD) angles. Using such an interface to drive the prosthesis , the user can choose between two states, explained in the following. If biceps and triceps are not co-contracted (first state), elbow and wrist joints will not move. In this state the user could control grasp and release of the hand by contracting biceps and triceps, respectively. On the other hand, if biceps and triceps are co-contracted (second state) the user can control elbow and wrist movements by exploiting the two shoulder DoFs monitored by means of the M-IMUs. In other words, the F-E movement of the user's shoulder causes the F-E of the prosthetic elbow. Instead, the AB-AD movement of the user's shoulder causes the prono-supination (P-S) of the prosthetic wrist. It is obvious that such a strategy allows the user to manage two prosthesis DoFs simultaneously, i.e. elbow F-E and wrist P-S.

III. EXPERIMENTAL VALIDATION AND RESULTS

A. Experimental setup

The experimental setup used to carry out the experimental trials includes the following components:

- Two double-differential EMG electrodes (Otto Bock 13E200=50 model) with an amplification gauge ranging in between 100 and 2000 have been used to acquire electromyographic activity of the target antagonist pair muscles.
- A National Instruments (NI) USB-6003 DAQ with a 16-bit ADC has been used for analog-to-digital conversion of the EMG signal.
- Two wireless M-IMUs (XSens MTw) have been used to detect shoulder flexion-extension and ab-adduction motion.
- An Awinda Station has been used to check the reception at 100 Hz of synchronised wireless data from the two wirelessly connected M-IMUs.
- A Virtual Reality (VR) purposely developed in Labview environment has been used to test the two control strategies on daily living tasks. The VR shows a virtual prosthesis closed to a table on which virtual objects, i.e. a bottle and a ball, are placed. The user can control the virtual prosthesis by means

of the IMUs and EMG electrodes previously applied onto his/her body, using the traditional myoelectric control and the combined MIMU/EMG control.

- Finally, a workstation is used to run the VR and perform sensor fusion.

B. Experimental protocol

Eight volunteer able-bodied individuals were recruited for this study. Before starting the test, they were trained to drive the virtual prosthesis by means of the traditional and the combined M-IMU/EMG control strategies, for a period of 1 second per control. After the training, they were asked to perform four different tasks in the VR with both controls. Each task was aimed to reach and grasp a virtual object properly placed in the VE (Fig. 1), i.e. a virtual bottle for tasks 1 and 3 and a virtual ball for tasks 2 and 4. Five trials for each task were performed, starting from the neutral position of the virtual prosthesis shown in Fig. 1a and 1d. Each task required to accomplish the following actions: shoulder F-E, shoulder AB-AD, elbow flexion, wrist P-S, hand closure . Visual feedback was provided by means of the VE: the virtual arm and the object turned green when the arm was around the target with a tolerance band of +/- 15° for each DoF. The task was completed when the subject held the virtual object with the virtual arm for 1 s.

C. Data analysis

The data acquired from the sensors were processed to extract quantitative indices capable of describing the subject's performance. They are: completion time, completion rate, and success rate.

- The completion time is the period of time that starts when the velocity grew up to the 10% of the peak value and ends when the velocity decrease to the 10% of the peak value.
- Completion rate is calculated for each joint as the ratio between the angle by which the joint rotates during the completion time, and the completion time.
- Success rate refers to the number of successful trials performed by a subject. For each task a maximum completion time of 20 seconds has been set. If the subject accomplished the task within this time, the task was considered successfully completed.

Mean value and standard deviation (STD) of completion time and completion rate, per task and per control strategy have been calculated. For each of these indices, in order to compare the results achieved for the two control strategies, a paired T-test was performed.

D. Experimental results

The plots of elbow F-E and wrist P-S for a representative subject are reported in Fig.2 for both the control strategies. For two tasks, mean value and standard deviation (STD) have been calculated on 5 trials. When the combined M-IMU/EMG control was adopted, the subject performed the tasks by simultaneously moving elbow and wrist. On the other hand, with the traditional EMG control the tasks were performed with sequential movements.

In Tab. 1 the values of the aforementioned performance indices, with mean and STD calculated on the eight subjects and p-VALUE, are reported for each control strategy. From these experimental results emerges that the savings in terms of completion time, when the novel control strategy is adopted, are significant: at worst, the duration of the task performing is reduced of 5 seconds. Likewise, it is interesting to note that completion rate increases, at least, of 0.09 [rad/s] for elbow F-E and of 0.12 [rad/s] for wrist P-S. Finally, it could be notice that the success rate improves of 10%, at worst.

IV. Conclusion and Future Works

In this work we have presented a novel control strategy for trans-humeral prostheses grounded on the combination of the data acquired by two M-IMUs and two EMG electrodes.

The findings of our study is that the novel control strategy allows performing simultaneous movements with better performance indices compared to the traditional strategy. Future efforts are mainly addressed to the development of an embedded version of the combined M-IMU/EMG and proceed with experimental tests with real prostheses on amputee subjects.

Acknowledgement

This work was supported by the Italian Institute for Labour Accidents (INAIL) with PPR 2 project (CUP:E58C13000990001) and by the European Project H2020/AIDE: Multimodal and Natural computer interaction Adaptive Multimodal Interfaces to Assist Disabled People in Daily Activities (CUP J42I15000030006).

References

[1] S. Adee, "The revolution will be prosthetized." Spectrum, IEEE 46.1 (2009): 44-48.W.-K. Chen, Linear Networks and Systems (Book style). Belmont, CA: Wadsworth, 1993, pp. 123–135.

[2] A. J. Young, L. H. Smith, E. J. Rouse and L. J. Hargrove, "A comparison of the real-time controllability of pattern recognition to conventional myoelectric control for discrete and simultaneous movements" , Journal of neuroengineering and rehabilitation, vol. 11, n. 1, p. 5, 2014, issn: 1743-0003. doi: 10 . 1186 / 1743 - 0003 - 11 - 5.

[3] A. J. Young, et al. "Classification of simultaneous movements using surface EMG pattern recognition." Biomedical Engineering, IEEE Transactions on 60.5 (2013): 1250-1258.

[4] A. J. Young, et al. "A comparison of the real-time controllability of pattern recognition to conventional myoelectric control for discrete and simultaneous movements." Journal of neuroengineering and rehabilitation 11.1 (2014): 1.

[5] J. J. Baker, et al. "Continuous detection and decoding of dexterous finger flexions with implantable myoelectric sensors." Neural Systems and Rehabilitation Engineering, IEEE Transactions (2010).

TABLE I

Condition	*Task*	*Completion Time [s]*	*P-VALUE*	*Completion rate EF-EE [rad/s]*	*P-VALUE*	*Completion rate WS-WP [rad/s]*	*P-VALUE*	*Success rate [%]*
Traditional	1	14±4	0.009	0.13±0.03	0.008	0.11±0.04	0.008	80
	2	14±4	0.007	0.13±0.03	0.021	0.13±0.03	0.07	72.5
	3	15±4	0.008	0.11±0.02	0.012	0.03±0.04	0.009	70
	4	16±4	0.007	0.09±0.04	0.022	0.03±0.03	0.006	77.5
Novel	1	9±5	0.009	0.22±0.08	0.008	0.23±0.08	0.008	95
	2	8±4	0.007	0.3±0.1	0.021	0.26±0.09	0.07	90
	3	9±4	0.008	0.2±0.1	0.012	0.21±0.05	0.009	97.5
	4	8±3	0.007	0.19±0.07	0.022	0.22±0.07	0.006	87.5

Values of performance indices for traditional EMG control and combined M-IMU/EMG

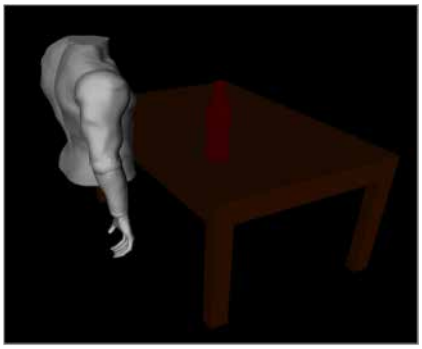

a) Task 1: Starting position.

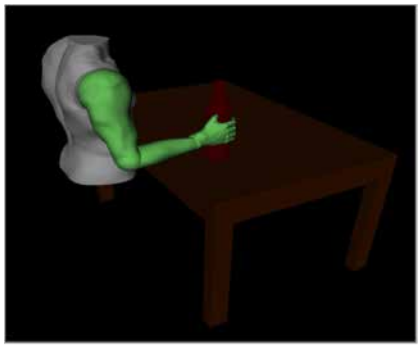

b) Task 1: Reaching the virtual object.

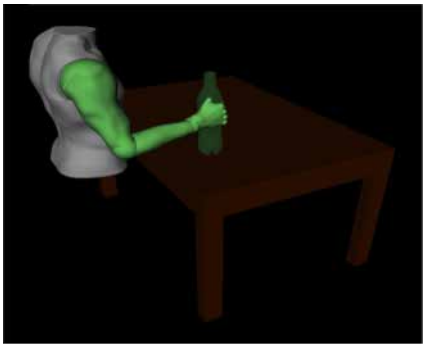

c) Task 1: Ending position.

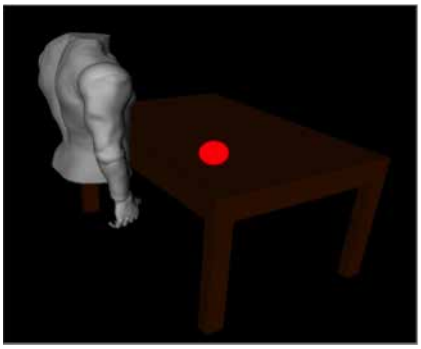

d) Task 2: Starting position.

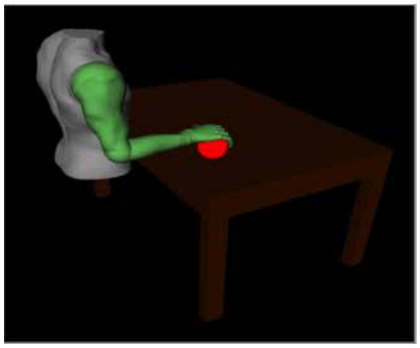

e) Task 2: Reaching the virtual object.

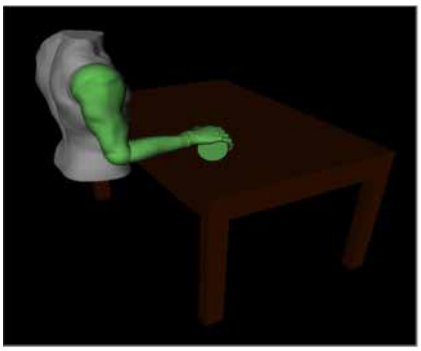

f) Task 2: Ending position.

Fig. 1. Virtual Reality developed in Labview environment

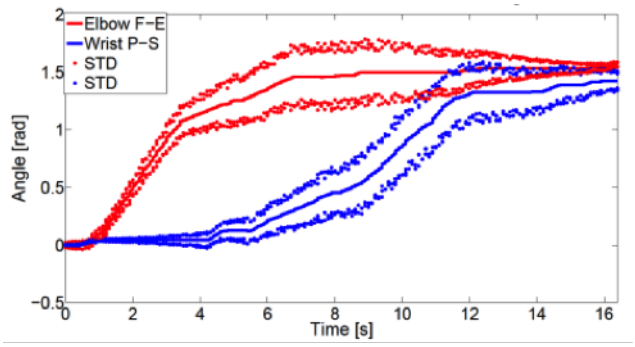

a) Traditional control: elbow F-E and wrist P-S (task 1).

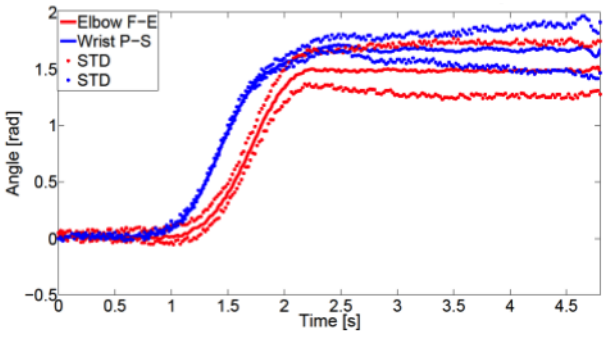

b) Combined M-IMU/EMG control: elbow F-E and wrist P-S (task 1)

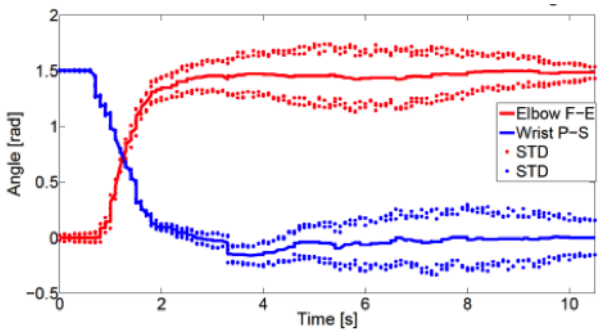

a) Traditional control: elbow F-E and wrist P-S (task 2).

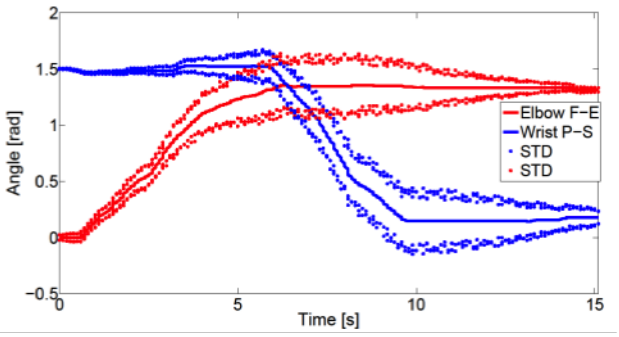

b) Combined M-IMU/EMG control: elbow F-E and wrist P-S (task 2)

Fig. 2. Experimental results for Elbow and Wrist angle achieved by a representative subject during tasks 1 and 2

A Modular Telerehabilitation Architecture for Upper-limb Robotic Therapy

D. Simonetti[1], L. Zollo[1], L. Vollero[2], G. Iannello[2] and E. Guglielmelli[1]
[1] *Laboratory of Biomedical Robotics and Biomicrosystems, Università Campus Bio-Medico di Roma, IT*
[2] *Laboratory of Computational Systems and Bioinformatics, Università Campus Bio-Medico di Roma, IT*

***Abstract*—This paper proposes the design and development of a modular architecture for upper limb robotic telerehabilitation. It is composed of four interacting subsystems, each with a specific role and its own functionalities. The architecture is designed to be modular and conceived to be tailored to different robotic devices in a realistic telerehabilitation scenario. The case study of a unilateral planar end-effector machine for upper-limb rehabilitation named CBM-Motus is presented. The experimental validation of the modular architecture is carried out on seven healthy subjects and preliminary results are finally reported and discussed.**

***Keywords*—Upper limb rehabilitation robotics, Stroke, Telemonitoring, Telecontrol.**

I. Introduction

The application of early supported discharge (ESD) [1] from hospitals with continued rehabilitation at home has promoted a growing interest in new technologies for telerehabilitation able to provide remote delivery and monitoring of rehabilitation services over telecommunication networks and internet. The systems for robotic telerehabilitation can be categorized into two different classes: systems in *unilateral* configuration and systems in *bilateral* configuration [2].

In unilateral configuration only the patient is connected to the robot while the therapist can remotely communicate with the robot and the patient [3]. Since the communication between patient and therapist is not required to be real-time, after a predefined time-lapse data are sent to the therapist interface in order to assess the therapy progress and, possibly, modify the treatment. In the bilateral configuration both the patient and therapist interact with a robot and communicate over the Internet through a shared virtual environment (SVE), normally using a client/server approach. The communication is real-time and enables the therapist to modify the current exercise or apply corrective actions during the tasks [4]. However, independently of the configuration type, robots for telerehabilitation have to address specific design requirements, system modularity and robust, reliable and safe communication are required since different modules and signals could be employed.

This work presents: i) the design and development of a modular architecture for upper limb robotic telerehabilitation, ii) the application of the proposed architecture to the CBM-Motus robotic machine [5], iii) the results of the experimental validation of modular architecture on seven healthy subjects and iv) the conclusions and future perspectives.

II. The modular telerehabilitation architecture and its application

A. Telerehabilitation architecture

The proposed general architecture is aimed to provide a flexible model exploitable in several rehabilitation scenarios. Our model assumes that three actors interact in the system: the patient, the therapist and the system manager[1]. The architecture is shown in Fig. 1 and it is composed of four subsystems that interact to supply different services (Fig. 2):

- The *Patient subsystem* is the component that physically interacts with the patient. It includes the robotic system and implements control and communication functionalities.
- The *Therapist subsystem* is the component that interacts directly with the therapist. It enables the remote monitoring and control of the patient.
- The *Manager subsystem* is the component that directly interacts with one of the system managers. It enables the control and the configuration of other entities, and the management of users.
- The *Communication HUB* is a component that provides different services. In particular, it implements all the functionalities required for recognizing the users and allowing them to communicate.

The architecture provides the following services:

- the *Authentication, Authorization and Accounting services* (AAA), that controls system access;
- the *Communication service*, that takes care of data transfer between subsystems;
- the *Exercise Execution service* (EE), that allows the patient to perform rehabilitation tasks with (patient-supervised) or without (patient-alone) the therapist supervision;
- *the Exercise Execution, Monitoring and Control service* (EEMC), that allows the therapist to monitor and control the execution of rehabilitation tasks. For instance, the therapist can adapt exercise execution by means of online parameters update. Finally,
- the *Exercise Execution, Logging and Analysis service* (EELA) is devoted to collect data generated during exercises. For instance, it makes them available for offline patient performance evaluation.

In our model, the A.A.A, the Communication and the EELA services are managed by the Communication HUB, whereas the EE and the EEMC are managed by the Patient and the Therapist subsystem, respectively. Each subsystem presented above has been implemented as a software component, with the Patient subsystem including the CBM-Motus machine as the robot for the upper-limb telerehabilitation.

B. The CBM-Motus

The CBM-Motus is a planar end-effector machine for upper-limb rehabilitation (Fig. 3) designed to have simple

[1] The system manager is the actor that manages all the components updating, for instance, modules and general parameters of the subsystems.

mechanical structure, lightness and compactness to enable portability [5]. The robot control belongs to the assist-as-needed paradigm thus providing the patient with the minimum level of assistance needed to execute the task, by monitoring the patient's condition using performance indicators.

An impedance control with adjustable parameters is implemented as follows

$$\tau = B(q)y + F_v\dot{q} + F_s sign(\dot{q}) \quad (1)$$

with

$$y = M_d{}^{-1}\left(M_d\ddot{q}_d + K_P\tilde{q} + K_D\dot{\tilde{q}}\right) \quad (2)$$

τ is the torque command, B is the inertia matrix (independent of robot configuration), $F_v\dot{q}$ and $F_s sign(\dot{q})$ are dynamic and static friction torques, which are not negligible in the CBM-Motus dynamics [5]. On the other hand, y represents the stabilizing action that makes the robot behave as a generalized mechanical impedance regulated by mass matrix M_d, stiffness matrix K_P and damping matrix K_D. The control is tailored on the subject's motion abilities by updating stiffness matrix K_P and time allotted for the task execution *t* during the therapy.

The two control parameters (i.e. K_P and *t*) are progressively updated, based on a weighted sum of following performance indicators: the *Aiming angle* (α), the area between the desired and the actual trajectory performed by the subject (*AREA)*, the normalized Mean Deviation from desired path (*nMD)*, the proportion of time (i.e. the percentage of samples) that movement speed exceeds the 10 % of the peak speed (*MAPR)*, the ratio between mean speed and peak speed (*SpeedMetric)* and the movement duration (*MD*). Finally, the complete architecture for telerehabilitation involving the CBM-Motus is presented in Fig. 4.

III. Experimental validation

A. Experimental setup

The patient-alone configuration of the Patient subsystem has been evaluated on seven healthy subjects who were asked to perform a typical point-to-point upper limb robotic exercise [7]. Each session consists of 160 point-to-point movements in 8 different directions rotated of 45°. They are grouped into 80 trials performed without assistance (K_P = 1 N/m, and *t* = 3000 ms), in order to measure subject performance and update control parameters by computing performance indicators on the Therapist side [6]-[8].

They have the twofold purpose of (i) evaluating the therapy progress and (ii) adapting the level of assistance to the patient's condition. Afterwards, control parameters K_P and t were sent to the Patient side and the block of 80 assisted point-to-point movements was performed again with a level of assistance tailored on the patient status. The session of 160 point-to-point movements was repeated in two different conditions, i.e. i) healthy behaviour and ii) simulated post-stroke behaviour. Finally, in order to assess the limits of the architecture in the *Internet* scenario, the computational time required to calculate performance indicators and the time required for transmitting data and commands between Patient and Therapist have been estimated.

B. Results

The Cartesian position and velocity during planar tasks for one subject are shown in Figs. 5-6 both for unassisted and assisted simulated post-stroke behaviour. As expected, after the adaptation of control parameters, the simulated post-stroke behaviour tends to the healthy one in terms of trajectories, velocity and smoothness (Fig. 6). Even though no clinical considerations can be extracted from these data, the indicators trend in Fig. 7 confirms the expected improvements between unassisted and assisted tasks, especially when the simulated post-stroke behaviour is observed. The performance evaluation of the Patient-Communication HUB-Therapist control loop led to results reported in Table 1. It can be shown that when coupled with typical communication latencies, they allow for a safe and reliable update of parameters, enabling a fine grained control (single trials update) in case of local networks, and a coarse grained control (update between groups of movements) in case of ADSL/LTE interconnections.

IV. Conclusion and future work

The paper has presented a novel modular architecture for telerehabilitation conceived to be as general as possible. The architecture applied to the CBM-Motus has demonstrated the modularity, functioning and reliability of the novel architecture able to be applicable to different unilateral robotic systems. Future studies on post-stroke subjects in-home tele-rehabilitation programs will be taken into account in order to enhance patients' independency and promote faster recovery from stroke.

Acknowledgement

This work was supported by the national project Industria 2015 - DAHMS (Distributed Architecture Home Modular Multifunctional Systems), CUP B85E10003020008 and by European Project H2020/AIDE: Multimodal and Natural computer interaction Adaptive Multimodal Interfaces to Assist Disabled People in Daily Activities, CUP J42I15000030006.

References

[1] Langhorne, Peter, and Lotta Widen-Holmqvist. "Early supported discharge after stroke." Journal of Rehabilitation Medicine 39.2 (2007): 103-108.

[2] Carignan, Craig R., and Hermano I. Krebs. "Telerehabilitation robotics: bright lights, big future?." Journal of rehabilitation research and development 43.5 (2006): 695.

[3] Butler, Andrew J., et al. "Expanding tele-rehabilitation of stroke through in-home robot-assisted therapy." International Journal of Physical Medicine & Rehabilitation 2014 (2014)..

[4] Basdogan, Cagatay, et al. "An experimental study on the role of touch in shared virtual environments." ACM Transactions on Computer-Human Interaction (TOCHI) 7.4 (2000): 443-460.

[5] Zollo, Loredana, et al. "Dynamic Characterization and Interaction Control of the CBM-Motus Robot for Upper-Limb Rehabilitation." International Journal of Advanced Robotic Systems 10 (2013).

[6] Zollo, Loredana, et al. "Multimodal Interfaces to Improve Therapeutic Outcomes in Robot-Assisted Rehabilitation." Gearing Up and Accelerating Cross-fertilization between Academic and Industrial Robotics Research in Europe:. Springer International Publishing, 2014. 321-343.

[7] Lo, Albert C., et al. "Robot-assisted therapy for long-term upper-limb impairment after stroke." New England Journal of Medicine 362.19 (2010): 1772-1783.

[8] Zollo, Loredana, et al. "Robotic technologies and rehabilitation: new tools for upper-limb therapy and assessment in chronic stroke." European journal of physical and rehabilitation medicine 47.2 (2011): 223-236.

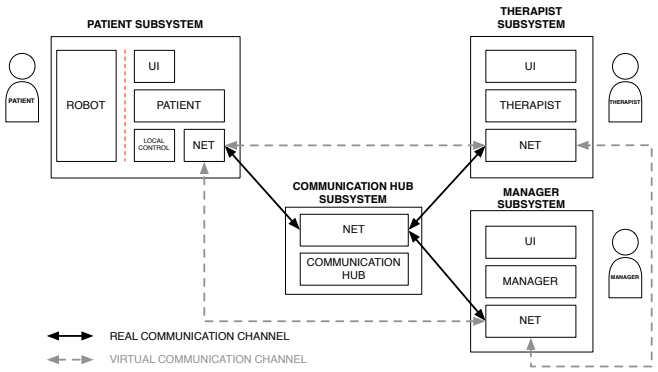

Figure 1. The proposed general architecture for telerehabilitation robotic systems.

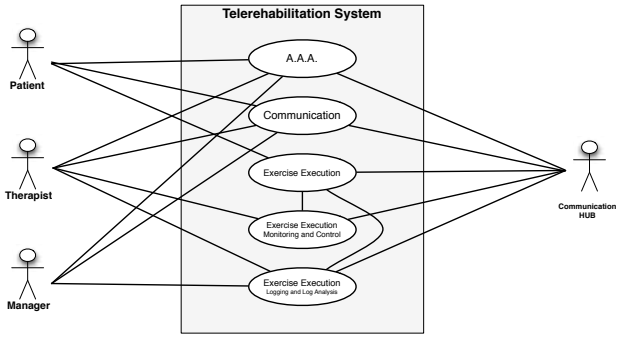

Figure 2. Telerehabilitation systems main services.

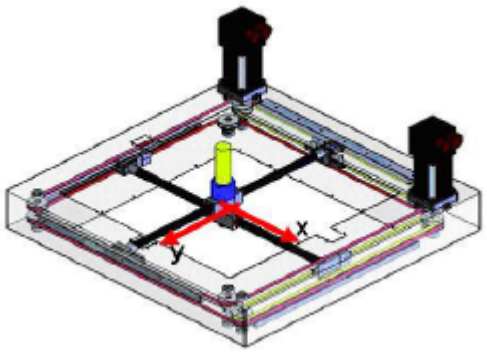

Figure 3. Overview of CBM-Motus with the modules composing kinematic structure.

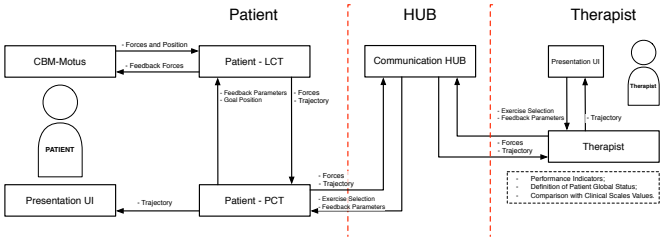

Figure 4. The modular architecture for telerehabilitation applied to the CBM-Motus rehabilitation robot. The patient side includes the robot and the patient-robot interaction modules; the therapist side includes evaluation and therapy modules, allowing therapy definition based on the evaluation of the patient thanks to quantitative performance indicators and clinical scales.

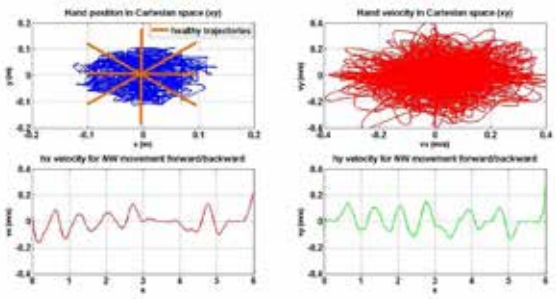

Figure 5. 80 repetitions of the clock game in unassisted simulated post-stroke condition: Cartesian position (upper left side), Cartesian velocity (right upper side), x component of hand velocity over time during NW forward/backward movement (lower left side), y component of hand velocity over time during NW forward/backward movement (lower right side).

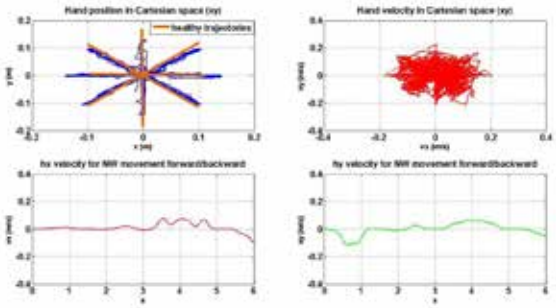

Figure 6. 80 repetitions of the clock game in assisted simulated post-stroke condition: Cartesian position (upper left side), Cartesian velocity (right upper side), x component of hand velocity over time during NW forward/backward movement (lower left side), y component of hand velocity over time during NW forward/backward movement (lower right side).

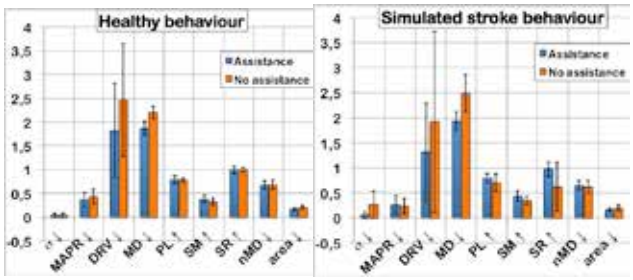

Figure 7. Values of performance indicators before and after updating control parameters. Mean values and standard deviations are reported both for healthy (left) and simulated post-stroke condition (right). The horizontal axis reports the selected performance indicators and the expected trend during motor recovery: α =Aiming angle, MAPR=Mean Arrest Period Ratio, DRV =Deviation from Ratio Between Velocities, MD=Movement Duration, PL=Path Length, SM=Speed Metric, SR=Success Rate, nMD=normalized Mean Deviation, area.

Table 1. Architecture validation: Computational time for updating control parameters (mean and standard deviation (SD)) and file size of the information exchanged throughout the architecture blocks

Trial	Time (mean)	SD	File size P→T	File size T→P
Single movements	0.23 s	0.01 s	8 B	K_p = 3B, t = 5B
16 movements	1.48 s	0.04 s	118 kB	K_p = 3B, t = 5B
80 movements	6.52 s	0.23 s	622 kB	K_p = 3B, t = 5B

INGEGNERIA TISSUTALE E MEDICINA RIGENERATIVA

3D tumor microtissues as testing platform for nanoparticles responsive to MMP-2 for on-demand release of anticancer drugs

V. Brancato[1], F.Gioiella[1], M.Profeta[2], G.Imparato[2], D.Guarnieri[2], F.Urciuolo[2] and P.A.Netti[1,2]
[1] *Interdisciplinary Research Centre on Biomaterials (CRIB), University of Naples Federico II, Naples, Italy*
[2] *Center for Advanced Biomaterials for HealthCare@CRIB, Istituto Italiano di Tecnologia, Naples, Italy*

***Abstract*— We fabricated 3D breast cancer microtissues and the healthy counterpart, both formed by fibroblasts and epithelial cells, to mimic the complexity of the tumor stroma microenvironment. We used these bioengineered tumor microtissues as testing platform to demonstrate the selectivity of stimuli responsive nanoparticles cleaved by metalloproteinases 2, a stroma remodelling enzyme, up-regulated in tumor microenvironment.**

***Keywords*— Bioengineered Microtissues, Nanoparticles, Drug delivery, 3D microenvironment.**

I. INTRODUCTION

Cancer development is a complex process regulated by interactions between epithelial cells, activated stromal cells, endothelial cells, interacting with soluble and insoluble components of the extracellular matrix (ECM). [1]–[2] So far, a variety of novel drug delivery systems have been developed to enhance the therapeutic performance of anticancer drugs. [3]–[4] Overcoming the many challenges of identifying a successful targeted drug delivery strategy requires a deeper understanding of events involving transport of drug or drug carrier to a target sites including the involvement of biological structures (namely extracellular matrix ECM) in the delivery. [5] Current cancer model system do not accurately recreate the tumor microenvironment, in fact only about 5% of cancer drug candidates that enter clinical trials will ever receive approval from the U.S. Food and Drug Administration. [6] Thus, there is an emerging need of novel 3D bioengineered microtissues for investigating and screening anticancer drug delivery systems. Moreover, the administered drugs accumulate not only in target tissues but also in healthy organs and, generating severe side effects that should be overcome [7]–[9]. So there is a striking need for more effective strategies to selectively release chemotherapeutic drugs within tumor sites. In this context, stimuli-responsive nanoparticles are able to achieve controlled drug delivery by exploiting the features of tumor microenvironment, like lowered interstitial pH or increased levels of enzymes as metalloproteinases (MMPs). [10]-[12] A novel nanocarrier has been developed to carry safely doxorubicin in tumor tissues and to respond to MMP-2 enzyme. The presence of the MMP-2 enzyme *in situ*, leads to the diffusion of doxorubicin only around the tumor tissue. [13]-[14] In the present work we tested MMP-2-stimuli-responsive nanoparticles in terms of DOX release in normal and tumoral 3D heterotypic breast microtissues (μTP). Indeed, normal and cancer associated fibroblast were cocultured, respectively, with normal and tumoral epithelial mammary cells in a 3D heterotypic μTP model, obtained slightly modifying a previous protocol. [15] Our breast cancer microtissues were more sensitive to doxorubicin in comparison to normal microtissues because they secreted a larger amount of MMP-2 in their microenvironment (fig.1). So the breast cancer model here presented could be a valuable candidate for the drug validation *in vitro*.

II. CONCLUSION

Previously published MMP-2 responsive nanoparticles were for the first time tested on 3D human breast cancer microtissues. 3D tumor microtissues could pave the way for efficient and valuable drug testing *in vitro*, offering a better tumor microenvironment replication.

ACKNOWLEDGEMENT

We are grateful for financial support provided by the following grants: FIRB project Newton (RBAP11BYNP_004) of the Italian Ministry of Education, University and Research (MIUR).

REFERENCES

[1] D. Huh, GA. Hamilton, DE. Ingber. “From 3D cell culture to organs-on-chips”, *Trends Cell Biol,* vol.21, pp.745e542 011.
[2] G. Imparato, F. Urciuolo, PA. Netti. “In vitro three-dimensional models in cancer research: a review” *Int Mat Rev,*vol.60, pp.297-311 2015.
[3] T.W. Hambley, W.N. Hait, “Is anticancer drug development heading in the rightdirection?” *Cancer Res.* Vol.69, pp.1259–1262, 2009.
[4] R.K. Jain, T. Stylianopoulos, “Delivering nanomedicine to solid tumors”, *Nat.Rev.Clin.Oncol.* vol.7, pp.653–664, 2010.
[5] SJ. Horning, DA. Haber, WKD. Selig, SP. Ivy, SA. Roberts, JD. Allen, EV. Sigal, CL. Sawyers. “Developing standards for breakthrough therapy designation in oncology”, *Clin Cancer Res,* vol. 15 pp.4297-304, 2013.
[6] IP. Witz, “The Tumor Microenvironment: The Making of a Paradigm” *Cancer Microenviron,* vol.2, pp.9-17. 2009
[7] C. Fischbach, R. Chen, T. Matsumoto, T. Schmelzle, JS. Brugge, Polverini PJ. “Engineering tumors with 3D scaffolds” *Nat Methods* vol.4 pp.855-860 2007.
[8] C. Ricci, L. Moroni, S. Danti, “Cancer tissue engineering-new perspectives in understanding the biology of solid tumours-a critical review” *OA Tissue Engineering*,vol.1 pp.1-4, 2013.
[9] LC. Kimlin, Casagrande G, Virador VM. “In vitro three-dimensional (3D) models in cancer research: an update”. *Mol Carcinog* vol.52, pp.167-82, 2013
[10] M. Ferrari, “Cancer nanotechnology: opportunities and challenges”, *Nat. Rev.Cancer* vol.5, pp.161–171, 2005.
[11] V.P. Chauhan, T. Stylianopoulos, Y. Boucher, R.K. Jain, “Delivery of molecularand nanoscale medicine to tumors: transport barriers and strategies”, *Ann.Rev. Chem. Biomol. Eng.* Vol.2, pp.281–298, 2011.
[12] Y.H. Bae, K. Park, “Targeted drug delivery to tumors: myths, reality and possibility”, *J. Control Release* vol.153, pp.198–205, 2011.
[13] D. Guarnieri, M. Biondi, H. Yu, V. Belli, A.P. Falanga, M. Cantisani, S. Galdiero,P.A. Netti, “Tumor-activated prodrug (TAP) - conjugated nanoparticles withcleavable domains for safe doxorubicin delivery”, *Biotechnol. Bioeng.* pp.601–611, 2014.

[14] M. Cantisani, D. Guarnieri, M. Biondi, V. Belli, M Profeta, L. Raiola, PA. Netti. "Biocompatible nanoparticles sensing the matrix metallo-proteinase 2 for the on-demand release of anticancer drugs in 3D tumor spheroids" *Colloids Surf B Biointerface,*. vol.135, pp.707-716. doi: 10.1016/j.colsurfb.2015.08.016.

[15] G. Imparato, F. Urciuolo, C. Casale, PA. Netti. "The role of microscaffold properties in controlling the collagen assembly in 3D dermis equivalent using modular tissue engineering" *Biomaterials* vol.34, pp.7851-7861, 2013

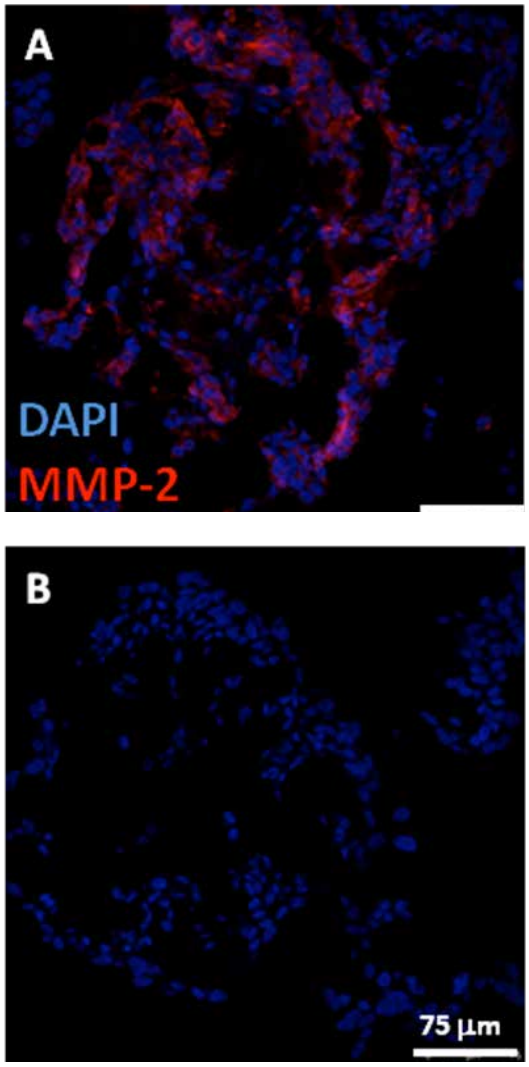

Fig.1 Matrix metalloproteinases 2 expression detected by immunofluorescence on formalin- fixed paraffin-embedded 7 µm slices of heterotypic cancer microtissues (A) and normal breast microtissues (B). Blue color indicated cell nuclei, red color stands for MMP-2 antibody. Images Scale bar is 75 µm.

Cellular Impedance Monitoring in a Bioreactor for Biological Barrier In-Vitro Models

L. Cacopardo[1], S. Giusti1[1,2], D. Barros[3], A.P Pego[3] and A. Ahluwalia[1]
[1] *Research Centre 'Enrico Piaggio', University of Pisa (Italy)*
[2] *IVTech S.r.l., Pisa (Italy)*
[3] *INEB–Instituto Nacional de Engenharia Biomédica, Universidade do Porto, Porto, Portugal*

***Abstract*—Biological Barriers are fundamental for regulating the passage or absorption of chemical substances in the human body, as well as for maintaining homeostasis. Thus the possibility to recreate physiologically relevant in-vitro barrier models can play a key role in the understanding of human pathophysiology and in drug design.**

Here, we present an advanced cell culture system able to mimic the dynamic environment of biological barriers while monitoring in real time cell behaviour through the inline measurement of cellular impedance.

***Keywords*—cellular impedance, TEER, bioreactors, biological barriers, in-vitro models.**

I. Introduction

In the human body, *physiological barriers* allow the separation between different compartments of the body or with the outer environment. These barriers have a fundamental role in the control of the absorption of external substances like nutrients and xenobiotics, as well as in the maintenance of the homeostasis of the different body compartments. Moreover, they act like the first level of defence against microorganisms, toxins and allergens. For these reasons, the study of biological barriers is crucial not only for a better understanding of their physiology and pathology, but also in drug testing and toxicology studies. The key point for regulating the passage of substances through all the different physiological barriers is the combination of cells and tight junctions, which control the paracellular and transcellular flux across the barrier and separate the apical and the basal compartment. Therefore, in vitro models are based on the culture of cell layers on permeable supports able to recreate these two compartments [1]. The first and simpler in-vitro model of physiological barriers is based on cells grown on *transwells*, maintained in static conditions within the traditional multiwell plates. However, several recent studies are focused on the implementation of more relevant models able to provide cells with an appropriate pattern of physical and chemical stimuli that better reproduce the physiological environment. Therefore, barrier-forming cells are often cultured in fluidic systems, generally defined as bioreactors, able to apply dynamic conditions [2].

The *integrity of the cellular barrier* is usually quantified by measuring the Trans Epithelial Electric Resistance (TEER), which evaluates the formation of tight junctions. This measurement is based on the application of a current and on the recording of the resultant voltage. The widely used TEER measuring system in cell culture is the EVOM (Epithelial VoltOhmMeter, WPI), furnished with a chopstick electrode for easily measuring the TEER in transwells. On the contrary, the possibility to perform TEER measurements inside a bioreactor during the experiment is still difficult and often requires the extraction of the cells from the device [3]. Moreover, the possibility to perform analysis such as the i*mpedance spectroscopy* can provide additional information on the cellular barrier. In particular, at low frequencies (f<5kHz), the current flows principally through paracellular pathway allowing TEER measurements, while at high frequencies (f>10kHz) it passes capacitively through the membrane, giving information on the cellular adhesion process, migration process and micro-motion [3].

In this context, we have developed a *new double-flow bioreactor which integrates a semipermeable membrane and four electrodes,* allowing the real time monitoring of the cell layer using both TEER measurements and impedance spectroscopy. The bioreactor can be interfaced directly with commercial measuring system, like the EVOM, for simple TEER measurement, or with a custom and stand-alone system for impedance measurements.

II. Material and Methods

A. The LB4 bioreactor

The *LiveBox4 bioreactor* (LB4) is the sensorized version of the LB2, a modular and transparent bioreactor with dual flow commercialized by IVTech S.r.l. This system is purposely designed for the culture of barrier forming cells, which are grown on a porous membrane placed in a holder between the two chambers.

The LB2 is the evolution of the Membrane Bioreactor (MB) [4], previously tested with Caco-2 cells as in-vitro model of intestinal epithelium. The main innovation of LB2 with respect to the MB is its transparency, which allow real time imaging using inverted microscopes.

The LB4 is made in PDMS (polidimethilsyloxane), a biocompatible polymer with good sealing properties. As shown in Figure 1.A, the LB4 has two different chambers (i.e. apical and basal), each one provided with four silicon tubes: two tubes represent the inlet and the outlet of the fluidic circuit (blue arrows), whereas the other two allow the integration of electrodes inside the chambers (red arrows). In order to maintain optimal fluidic characteristics for cells without affecting the hydraulic seal as well as the optical transparency, the position and the dimension of electrodes tubes was carefully evaluated. In order to select the electrode type, two solutions were compared: i) Ag electrodes for both voltage and current and ii) AgCl electrodes for voltage and Ag electrodes for current. The latter improved measurement stability.

In order to validate the bioreactor, it was interfaced with

the EVOM and tested with two different cellular models.

i) blood retinal barrier (BRB), using Human Umbilical Vein derived Endothelial Cells (HUVEC) seeded on porous polycarbonate membranes coated with 0.2% gelatin ($1.4x10^5$ cells/cm^2). After 24h, a flow was applied in the apical and basal circuit of the LB4 (50–50 µL/min, 100–100 µL/min) and maintained for up to 5 days.
ii) blood brain barrier (BBB), using immortalized mouse brain endothelial cells (bEnd3) seeded ($2x10^5$ cells/cm^2) on polycarbonate membranes coated with 0.1% (w/v) collagen. After 24h, flow (100–100 µL/min) was applied in the apical and basal circuit and maintained for up to 5 days.

In both cases, an independent control unit with a simple interface was used to acquire and store the TEER values at specific time points. :

B. Impedance spectroscopy with the AD5933

The cellular impedance measurement circuit is based on the AD5933 (Analog Devices Inc.) [5], an impedance spectrometer chip for measurements in range of 1 kΩ-10 MΩ, with frequency spectrum from 1 to 100kHz, using a bipolar electrode configuration, [5]. However, for cellular measurement, the impedances of interest are in the range of 10 Ω-1 kΩ and the frequency sweep should go from 20 Hz to 40 kHz.

Moreover, some precautions are necessary when employing the chip for biological measurement. First, the excitation signal output from the chip varies around a positive DC bias (VDD/2). This bias can lead to an electrochemical process at the interface between the metal electrodes and an aqueous solution that, if maintained for long time, may alter the medium where the cells grow. The amplitude voltage for the excitation signal from the AD5933, powered with a 5V supply, is 3 Vpp. This level is too high for impedance measurements at microscopic scales, as it can damage cells. Finally, the mayor limitation of the chip is the bipolar configuration, since the measured current can be affected by artefact impedances present at the electrode interface. These artefacts can be very high and comparable with the unknown impedance, especially at low frequencies [6].

In order to adapt the chip for cellular impedance measurements, an *analog front-end* was developed. The main modification regarded the passage from a two electrode to a four electrode (tetrapolar) approach, to avoid measurement artefact. In particular, the analog front-end can be divided in two parts (Fig. 2): an excitation stage, before the cell culture, and a receiving stage after it. The excitation stage is composed of a passive high pass filter, which remove the positive DC bias, an attenuator, which reduce the voltage amplitude, and a differential amplifier, which generates two symmetrical waves. On the other hand, the receiving stage presents an instrumentation amplifier with a very high common-mode rejection ratio and very high input impedances. Thanks to these features, the measured signal is not altered. In addition to the front end, an external circuit is necessary to reduce the output frequency of the AD5933. A *clock divider* [7] was realized with a 10 MHz oscillator and several flip flops, allowing measurement of frequencies lower that 1 kHz with sufficient resolution. The circuit is realized on a matrix board and controlled with *Arduino*. By accessing the program registers of the chip we can define the starting frequency, frequency step, the number of increments and to read the stored data, returning the magnitude and phase of the measured impedance.

The impedance spectroscope in the LB4 was evaluated using NaCl solutions at different concentration (0.001 M, 0.05 M, 0.01 M, 0.1 M, 1M). Both the chambers of the bioreactor were filled with the solution and impedance was measured between 0 and 41 kHz

III. . RESULTS

Cellular tests showed the ability of the LB4 bioreactor to support long term cell culture, providing an acceptable fluid dynamic environment for barrier forming cells. The online acquisition of TEER through the EVOM gave values comparable with the ones present in the literature both for HUVECs (Fig. 3a) and bEnd3 (Fig. 3b). In particular, for both cell models, TEER measurements show an increase in dynamic conditions, with respect to the static ones.

On the other side, the LB4 interfaced with the impedance-meter system resulted in reliable measurement (Fig. 3c, Fig. 3d), furnishing an increasing impedance with the inverse of the solution concentration (1/C). The developed circuit satisfy all the requirements for its use in cellular experiments.

IV. CONCLUSION

In this work, a bioreactor for advanced in-vitro models of biological barriers was presented. The LB4 is suitable for the dynamic cell cultures and online TEER measurements. Moreover, the LB4 can be interfaced with a customized impedance meter able to perform a frequency sweep useful for cellular impedance measurements. Measurements with NaCl solutions were correctly correlated with concentration, demonstrating that the chip is able to furnish reliable impedance measurements. Given transparency of the bioreactor and its compatibility with the microscope, in future studies cells will be monitored both optically and with impedance measurement.

REFERENCES

[1] Mullin J.M, Agostino N., Rendon-Huerta E. and Thornton J.J. 'Epithelial and endothelial barriers in human disease'. *Drug Discovery Today* Vol. 10, No. 6, March 2005.
[2] Martin I, Wendt D. and Heberer M. 'The role of bioreactors in tissue engineering'. *TRENDS in Biotechnology* Vol.22 No.2 February 2004.
[3] Benson K., Cramer S. and Galla H.J. 'Impedance-based cell monitoring'. *Fluids and Barriers of the CNS*. 2013, 10:5.
[4] Giusti S., Sbrana T., La Marca M., Di Patria V., Martinucci V., Tirella A., Domenici C., Ahluwalia A. 'A novel dual-flow bioreactor simulates increased fluorescein permeability in epithelial tissue barriers'. *Biotechnology Journal* 2014, 9, 1175–1184.
[5] AD5933 Datasheet, Analog Devices.
[6] Margo C., Katrib J., Nadi M. and Rouane A. 'A four-electrode low frequency impedance spectroscopy measurements system using the AD5933 measurement chip'. *Physiological Measurement* 34 (2013) 391–405.
[7] AN-843 Application Note, Analog Devices.

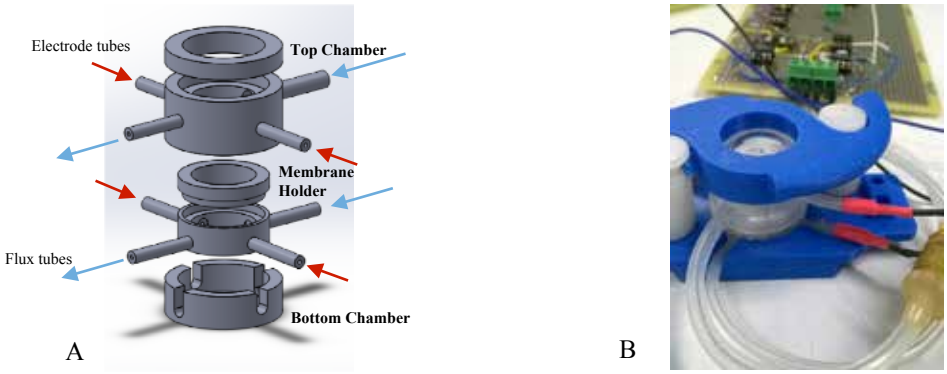

Fig. 1. LB4 Bioreactor: a) technical drawing; b) the bioreactor with its clamp system connected with the impedance-meter circuit.

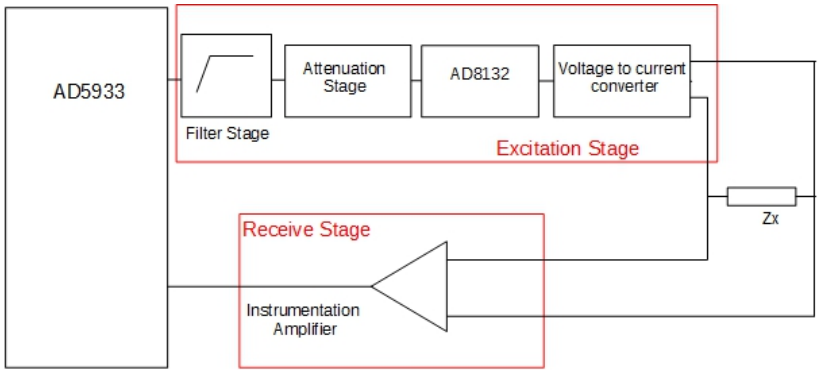

Fig. 2. Block scheme of the Analog Front End.

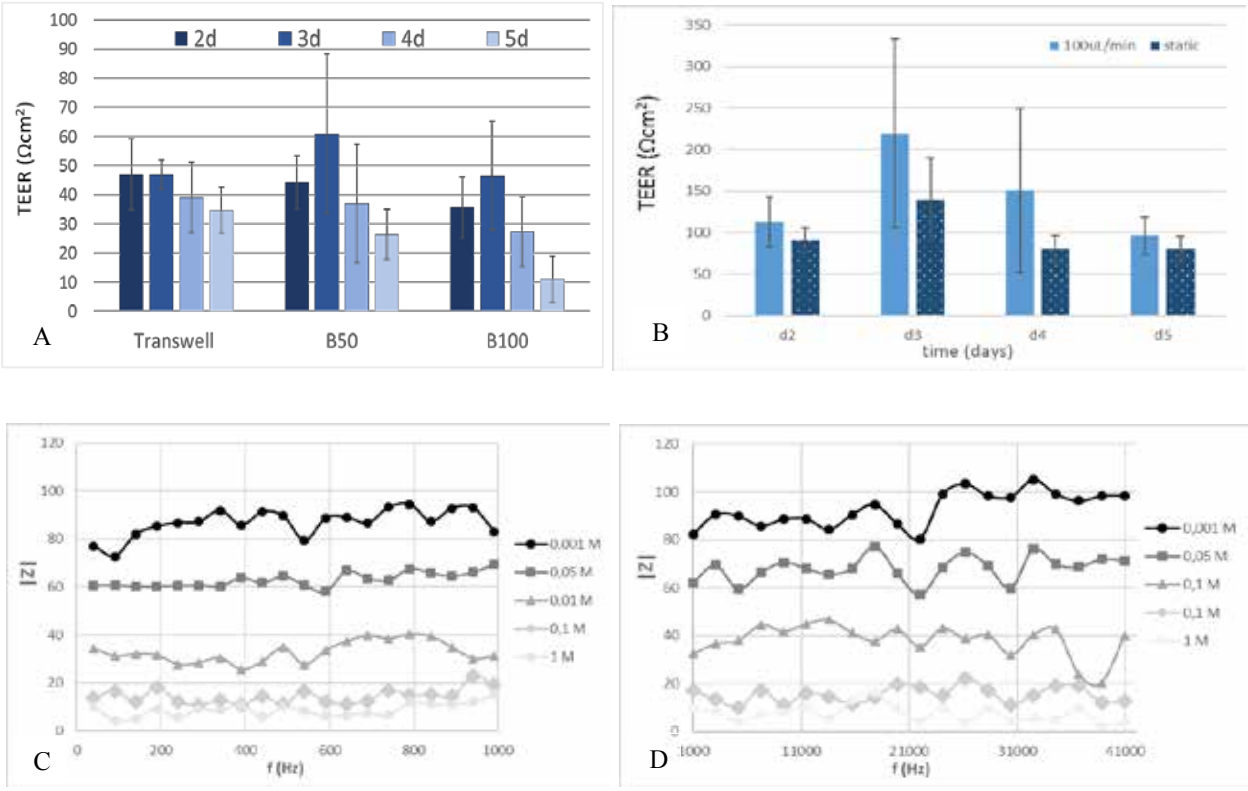

Fig. 3. Measurement in the LB4: a) with the EVOM and BRB model (d=day of culture, B50/B100= bioreactor with 50µL/min flow and 100µL/min); b) BBB model; c) with the impedance-meter and NaCl Solutions at low frequencies (40-1000 Hz); d) at high frequencies (1-40kHz).

Engineering of a novel organotypic model of the human intestinal mucosa

V. De Gregorio[1], G. Imparato[1], F. Urciuolo[1] and P.A. Netti[1,2,3]

[1] *Center for Advanced Biomaterials for HealthCare@CRIB, Istituto Italiano di Tecnologia, Largo Barsanti e Matteucci 53, 80125 Naples, Italy*

[2] *Interdisciplinary Research Centre on Biomaterials (CRIB), University of Naples Federico II P.le Tecchio 80, Naples, Italy*

[3] *Department of Chemical, Materials and Industrial Production (DICMAPI) University of Naples Federico II, P.le Tecchio 80; Naples, Italy*

Abstract- There is a growing need of developing organotypic intestinal models that are able to reproduce the physiological microenvironment and the complex functions of human intestinal epithelium *in vitro*. We propose an *in vitro* three-dimensional (3D) model of human intestinal mucosa which closely recapitulates the 3D tissue architecture of the small intestine. This model can be used as a valuable tool to testing platform or for use in pharmaceutical development applications.

***Keywords*-Organotypic culture, CaCo-2 cells, ECM, bottom-up approach.**

THE development of organotypic intestinal epithelial cultures was an essential milestone in tissue engineering that has provided researchers a more physiological model than two-dimensional culture to recapitulate the complex functions of human intestinal epithelium *in vitro*. In order to generate well-differentiated epithelial cell layers *in vitro*, it is necessary to reconstitute their natural microenvironment as closely as possible. Regarding to intestinal epithelium, this is traditionally achieved by culturing established cell lines, such as $CaCo_2$, on Transwell® fiters, which allow provision of different culture media and different culture conditions (submerged and emerged) to each side of the two-dimensional (2D) epithelial cell layer [1,2]. Another, recently developed approach is based on placing epithelial cells, in gels resembling the extracellular matrix, where they form self-organised three-dimensional (3D) cysts with internal lumina (i.e. organoids)[3,4]. However, since organoids are not easily suitable and more expensive, Caco-2 monolayer transwell assay, remain the norm as an *in vitro* model of human small intestinal mucosa's ability to absorb orally administered drugs. However, this culture system do not replicate all features of the *in vivo* microenvironment of intestinal epithelium due to the flat surface of the transwell insert and the lack of macrovilli structures. To overcome all these obstacles, a 3D macrometric intestinal stroma of endogenous nature, with defined compositions for expansion and delivery of intestinal epithelial cells is highly demanded [5]. As consequence, we propose an *in vitro* 3D model of human intestinal mucosa which mimics the physiology and the 3D tissue architecture of the small intestine for use in pharmaceutical development applications. At first we have achieved 3D intestinal stroma-like construct *in vitro* by using tissue precursors (μTPs) assembling strategy as previously described [6,7]. A microfabricated technique was used in order to realize a mold simulating the topography of intestinal crypts and villi. On such intestinal-stroma environment we succeeded in developing an intestinal epithelium by using CaCo-2 cells that show all the characteristic epithelial markers, resulting in an completely endogenous organotypic intestinal model. The possibility to have available such a complex model open the way for a variety of experimental investigations that include the study of intestinal physiology or intestinal diseases and pharmaceutical development applications.

REFERENCES

[1] J. Kowapradit, P. Opanasopit, T. Ngawhirunpat, A. Apirakaramwong, T. Rojanarata, U. Ruktanonchai, W. Sajomsang, In vitro permeability enhancement in intestinal epithelial cells (Caco-2) monolayer of water soluble quaternary ammonium chitosan derivatives. AAPS PharmSciTech. 2010;11(2):497-508

[2] V. Meunier, M. Bourrié,Y. Berger, G. Fabre, The human intestinal epithelial cell line Caco-2; pharmacological and pharmacokinetic applications. Cell Biol Toxicol. 1995;11(3-4):187-94.

[3] J.R. Spence,C.N. Mayhew, S.A. Rankin, M.F. Kuhar, J.E. Vallance, K. Tolle, E.E. Hoskins, V.V. Kalinichenko, S.I. Well, A.M. Zorn, N.F. Shroyer, J.M. Wells, Directed differentiation of human pluripotent stem cells into intestinal tissue in vitro. Nature. 2011;470:105-9

[4] A. Ootani, X. Li, E. Sangiorgi, Q.T. Ho, H. Ueno, S. Tod, H. Sugihara, K. Fujimoto, I.L. Weissman, M.R. Capecchi, C.J. Kuo. Sustained in vitro intestinal epithelial culture within a Wnt-dependent stem cell niche. Nat Med. 2009 Jun;15(6):701-6

[5] J. Yu, S. Peng, D. Luo, J.C. March. In vitro 3D human small intestinal villous model for drug permeability determination. Biotechnol Bioeng. 2012; 109(9):2173-8

[6]G. Imparato, F. Urciuolo, C. Casale, PA. Netti. The role of microscaffold properties in controlling the collagen assembly in 3D dermis equivalent using modular tissue engineering. Biomaterials 34 (2013) 7851-61

[7] F. Urciuolo, G. Imparato, C. Palmiero, A. Trilli and P. A. Netti, Effect of Process Conditions on the Growth of Three-Dimensional Dermal-Equivalent Tissue Obtained by Microtissue Precursor Assembly. Tissue Engineering 17 (2011) 155-64.

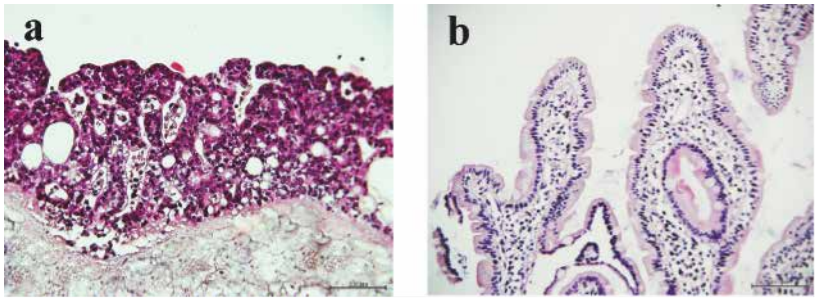

Fig. 1. Histological features of three dimensional organotypic intestine model. Microscopic H&E staining shows the architectural analogies between the complete organotypic intestinal model (a) and (b) intestine native tissue. Scale bar 100μm.

Characterization and biofabrication of a pH-sensible hydrogel

C De Maria[1], I Chiesa[1], S Angeli[1], A De Acutis[1], F Montemurro[1], G Mattei[1], AM Smith[2], A Saiani[2], G Vozzi[1,3]

[1] *Research Center E. Piaggio, University of Pisa, Italy.*

[2] *School of Materials & Manchester Institute of Biotechnology, The University of Manchester, UK.*

[3] *Department of Ingegneria dell'Informazione, University of Pisa, Italy*

***Abstract*— The combination of smart materials and biofabrication technologies offers new degrees of freedom in scaffold fabrication. In the present work, 3D scaffolds were produced by robotic dispensing of self-assembling hydrogels, whose rheological and mechanical properties can be controlled by varying the environmental pH.**

After the characterization of viscosity and elastic modulus at various pH, the fabrication parameters for 3D extrusion were analysed for determining the working window. In order to extend the fabrication capabilities, several extrusion media were tested as support material. Finite element models were used to explain experimental results and calculate biologically relevant parameters such as the shear stress during the extrusion process. A clinical relevant ear-shaped construct was fabricated as demonstrator.

***Keywords*—Biofabrication, Smart hydrogel, Material Characterisation, Finite Element Analysis**

I. Introduction

BIOPRINTING, one of the strategies of Biofabrication, is defined as application additive manufacturing processes for patterning and assembling living and non-living materials with a prescribed 2D or 3D organization to produce bioengineered structures serving in tissue engineering, regenerative medicine, pharmacokinetic and basic cell biology studies [1]. Among various techniques, robotic dispensing processes produce the most versatile hydrogel-based constructs with clinically relevant sizes, customized external shapes and reproducible internal microstructures, characterized by an engineered porosity and interconnectivity [2]. Ionic complementary peptide hydrogels represent an interesting building material: they combine biocompatibility with molecular self-assembly properties, and are tunable by varying external parameters such as pH [3].

Here we present the manufacturing process for fabrication of well-defined 3D construct using a phenylalanine-based nonapeptide, including its rheological and mechanical characterization, and the finite element (FE) model of the extrusion process.

II. Materials and Methods

A. Material preparation

The peptide FEFKFEFKK was synthesized via solid phase synthesis methods [4]. Phenylalanine (F), a non-charged amino acid with an isoelectric point (pI) 5.49, was combined with lysine (K) and glutamic acid (E), two charged peptides. Being their pI 9.8 and 3.15, they will carry a positive and a negative charge respectively at neutral pH.

B. Rheological and mechanical characterization

The shear rheology of FEFKFEFKK nonapeptide gel, at different concentrations and pH, was characterised using the Bohlin C-CVO rheometer.

The power law model of Ostwald and deWaele was used to interpret the rheological data [5]. The viscosity η [Pa] is linked to the shear rate $\dot{\gamma}$ [s^{-1}] according to (eq.1):

$$\eta = k\left(\dot{\gamma}\right)^{n-1} \qquad (1)$$

where k [$Pa \cdot s^n$] is the flow consistency factor, and n is the flow behaviour index, which is less than 1 for a pseudoplastic fluid. Data were logarithm transformed and a linear fitting was applied. The runs test was performed to verify the goodness of the fitting procedure.

Nano-indentation tests at constant strain rate ($\dot{\varepsilon}$ = 0.10 s^{-1}) were performed using a PIUMA Nanoindenter (Optics11, The Netherlands) equipped with a 61.5 μm spherical tip. Experimental load-indentation data were converted into stress-strain according to the nano-epsilon dot method [6]. Samples elastic moduli were derived as the stress-strain slope within 0.05 strain.

C. Bioprinting of smart hydrogels

The PAM^2 (Fig. 1A), a multiscale and multimaterial microfabrication system, was used to produce complex structures [7]. Both pressure- and piston-driven extruders were tested. The calibration procedure was performed by printing a serpentine structure varying the following parameters: gel concertation and pH, needle shape, extrusion pressure, extrusion flow, deposition plane velocity. Extrudability and shape retention were the two selection parameters: dimensions of stable structures were measured using an optical microscope (AX70, Olympus Italia, Milan), with a 4X and 10 X objective. Acquired pictures were analysed with the ImageJ software.

The creation of a complex required an extrusion media, as sacrificial material for supporting overhanging parts (bioplotting approach): alginate, polyvinyl alcohol (PVA) and polyvinylpirrolidone/PVA (PVP/PVA) hydrogel [8], at various concentrations, were tested as support material.

D. Finite element modelling

The FE model describes the fluid dynamics in the extrusion needle (both conical and cylindrical geometry) as a function of inner diameters, flow rate, pressure, concentration and pH.

Simulations were performed with Comsol Multiphysics®

(COMSOL, Inc.), using the stationary Navier-Stokes Non Newtonian application mode. Experimental data were introduced in the simulation using eq.1, supported by the software.

The model presents an axial-symmetric geometry was designed. In addition to axial-symmetry, the other boundary conditions are: no-slip over the needle wall, pressure equal to 0 [Pa] at the outlet; as the PAM^2 can work both in pressure and in position control, two cases were simulated by a determined pressure or a flow as boundary inlet condition.

III. Results and Discussion

The gels are shear thinning, with a viscosity from kPa·s to mPa·s across a shear rate range from 10^{-2} up to 10^3 s^{-1}. As the pH increases (from 3.7 up to slightly alkaline), the viscosity and stiffness of the gels increase: this behaviour allows the shape-retention during the printing procedure.

Both n and k parameters varies with pH and concentration ($R^2 > 0.7$); however, for a given concentration in the range 20-30 mg/ml, the sensitivity analysis demonstrated an higher importance of the k parameter, due to its variation of one order of magnitude.

The elastic modulus varies from 3.4 kPa to 6.9 kPa with a very high correlation with the k parameter ($R^2 > 0.9$).

Extrusion experiments for printer calibration were carried out using several needles from 0.34 mm up to 0.8 mm: the pseudoplastic behaviour determined a minimum extrusion flow rate (e.g. 0.4 µl/s for 0.34 mm diameter) due to the high pressure drop (> 10^6 Pa), as confirmed by FE model. Hydrogel strands extruded from smaller needles tend to swell up to a ratio 3:1 in respect to needle diameter.

A clinically-relevant ear-shaped 3D scaffolds were fabricated by printing hydrogels directly into the supporting material, and adjusting the pH values to values higher than 6.5 (Fig. 1B). The best supporting material was the PVA/PVP copolymer [8].

Simulations indicate a piston profile of the hydrogel flow inside the needle for more than 70% of the section, thus decreasing the "shear-zone" that deeply affects vitality in cell-laden hydrogel printing [9].

IV. Conclusion

This work has described the entire workflow for characterise and bioprinting hydrogel materials for 3D scaffold fabrication.

The bioprinting of 3D complex structures requires the accurate control of the flow rate, speed of the dispensing head, together with the appropriate choice of a suitable support material.

Amino acids can be combined in endless different ways leading to a vast number of building blocks with different physical properties, with potential uses as nanoactuators or drug delivery vehicles.

Starting from these considerations, bioprinting of smart hydrogel with tunable properties is still an incompletely explored field of research, which can offer higher versatility in tissue engineering and regenerative medicine applications.

Acknowledgement

AS and AMS are grateful to the EPSRC for their financial support (Fellowship grant nº: EP/K016210/1)

References

[1] J. Groll, T. Boland, T. Blunk, J.A. Burdick, D.W. Cho, P.D. Dalton, et al. Biofabrication: reappraising the definition of an evolving field. *Biofabrication*. 8(1):013001, 2016

[2] J. Malda, J. Visser, F.P. Melchels, T. Jüngst, W.E. Hennink, W.J. Dhert et al. 25th anniversary article: Engineering hydrogels for biofabrication. *Adv Mater* 25(36):5011-28, 2013

[3] S. Boothroyd, A.F. Miller, A. Saiani. From fibres to networks using self-assembling peptides. *Faraday Discuss*. 166, 195-207, 2013

[4] W. Chan, P. White, *Fmoc Solid Phase Peptide Synthesis: A Practical Approach*, Oxford University Press, 1999.

[5] W. Michaeli. *Extrusion dies for plastics and rubber* (3rd edition) Hanser Publishers, Munich, 1992

[6] G. Mattei, G. Gruca, N. Rijnveld, A. Ahluwalia, The nano-epsilon dot method for strain rate viscoelastic characterisation of soft biomaterials by spherical nano-indentation, *J. Mech. Behav. Biomed. Mater*. 50 150–159. doi:10.1016/j.jmbbm.2015.06.015, 2015

[7] A. Tirella, C. De Maria, G. Criscenti, G. Vozzi, A. Ahluwalia. The PAM^2 system: a multilevel approach for fabrication of complex three-dimensional microstructures. *Rapid Prototyping J.* 18 (4), 299-307, 2012.

[8] C. De Maria, A. De Acutis, M. Carrabba, G. Criscenti, G. Vozzi. Machine design for multimaterial processing, in *Nanobiomaterials in Soft Tissue Engineering - Applications of Nanobiomaterials* ISBN: 978-0-323-42865-1. Elsevier 2016

[9] Tirella A, Vozzi F, Vozzi G, Ahluwalia A. PAM2 (piston assisted microsyringe): a new rapid prototyping technique for biofabrication of cell incorporated scaffolds. *Tissue Eng Part C Methods*. Feb;17(2):229-37. doi: 10.1089/ten.TEC.2010.0195, 2011

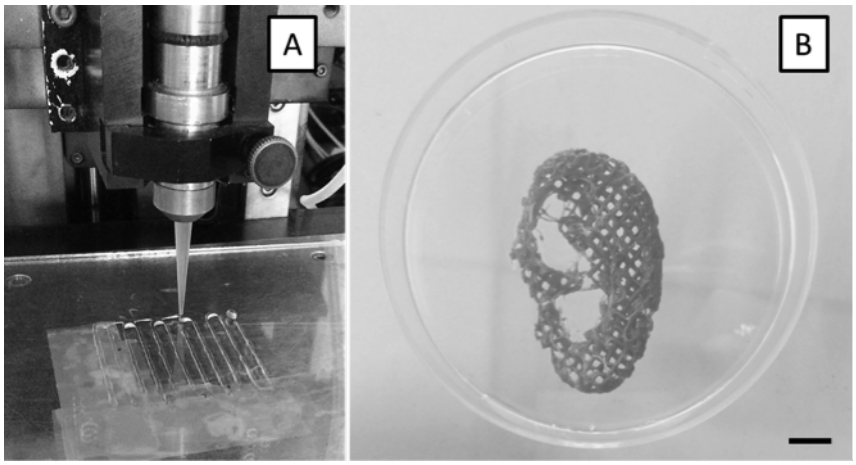

Fig. 1. Fabrication snapshot using pressure-driven extruder (A); auricle-shaped scaffold, as example of clinically relevant size construct (food coloring was mixed to the gel for visualization – scale bar 1cm) (B).

Investigating nonalcoholic fatty liver disease in a 3D liver-on-a-chip device

M. Gori[1], M.C. Simonelli[1], L. Businaro[2,3], M. Trombetta[1,3], A. Rainer[1,2,3]

[1]*Tissue Engineering Laboratory, Università Campus Bio-Medico di Roma, via Álvaro del Portillo 21, 00128 Rome, Italy*

[2]*National Research Council - Institute for Photonics and Nanotechnologies (CNR-IFN), via Cineto Romano 42, 00156 Rome, Italy*

[3]*UCBM-IFN Joint Laboratory for Nanotechnologies for the Life Sciences*

***Abstract* — Nonalcoholic fatty liver disease (NAFLD) is a chronic liver condition worldwide, although its underlying molecular mechanisms are still under investigation. So far, many *in vitro* studies on NAFLD have been hampered by the limitations of 2D culture systems, in which cells rapidly lose tissue-specific functions. The present liver-on-a-chip approach aims at filling the gap between conventional *in vitro* models, often scarcely predictive of *in vivo* conditions, and animal models, potentially biased by their xenogeneic nature, using a microfluidically perfused device under free fatty acid supplementation. This "NAFLD-on-a-chip" system represents the first *in vitro* model of human NAFLD developed within a microfluidic device in a sinusoid-like fashion.**

***Keywords* — microfluidics, liver-on-a-chip, NAFLD, high-content analysis**

I. Introduction

Conventional two-dimensional (2D) *in vitro* cell culture models still fail to provide accurate prediction of the *in vivo* pathophysiological behavior of tissues and organs. Hence, the development of three dimensional (3D) models with increased spatio-chemical complexity is being pursued, in order to better recreate cell-cell interactions within their microenvironment [1], [2] given that 2D culture systems have shown to lose most of the cell behaviors observed in native tissues [3], [4]. To date, however, the study of chronic pathophysiological states in clinically relevant models and timescales, remains the main challenge [5]. Organs-on-chip arise from this necessity, integrating biology and engineering on a single device, and taking advantage of microfluidic technology [6]. Microfluidic devices may also have a solid support from live cell microscopy and high-content analysis (HCA), which constitute powerful tools for cell analysis. Current research in the field aims to reproduce living systems on a chip [7], [8] without the presumption to totally replace animal testing, but certainly to reduce it and provide novel and more reliable disease models [9].

Also in the study of liver diseases, many efforts have been made to improve the physiological mimicry and diagnostic power of conventional *in vitro* models, and different liver-on-a-chip platforms have been fabricated for drug screening [10]-[13], but none of them for *in vitro* modeling of chronic liver diseases, such as nonalcoholic fatty liver disease (NAFLD).

NAFLD is the most common form of chronic liver disease worldwide, encompassing a broad spectrum of liver pathologies, ranging from simple steatosis to nonalcoholic steatohepatitis (NASH), fibrosis and cirrhosis, eventually leading to hepatocellular carcinoma [14]. However, the exact molecular mechanisms underlying NAFLD pathogenesis and progression are far from clear. So far, many *in vitro* studies on NAFLD have been hampered by the intrinsic limitations of 2D culture systems, in which cells rapidly lose tissue-specific functions. Our work addresses this issue for the first time, establishing a HCA methodology that successfully couples a microfluidically perfused liver sinusoid model with fluorescence-based functional assays, in order to characterize the pathogenesis of NAFLD in terms of: *i)* intracellular triglyceride accumulation, *ii)* cell viability/cytotoxicity, and *iii)* analysis of the cellular levels of reactive oxygen species (ROS).

II. Materials & Methods

A. Microfabrication

Microfluidic devices were fabricated as polydimethylsiloxane (PDMS, Sylgard 184, Dow Corning) replicas of a lithographically obtained SU-8 (Microchem) on silicon master. Chip design was derived and adapted from a previous work from Lee et al. [10]. Chip geometry is depicted in Fig. 1.

B. Cell culture

Human hepatoma HepG2/C3A cells (ATCC) were cultured in 3D under microfluidic perfusion through a set of microchannels that mimic the endothelial-parenchymal interface of a liver sinusoid, allowing the diffusion of nutrients and removal of waste products similarly to the hepatic microvasculature, and providing a neglectable shear stress to the cells [10]. A medium flow of 18 μL/day was provided through the mass transport channel, in agreement with the literature [10], [11]. Cells were maintained in culture until confluence before induction of steatosis.

C. Induction of steatosis

A combination of long-chain free fatty acids (FFAs), namely palmitic acid (PA) and oleic acid (OA) was dissolved in methanol (vehicle) and added to the medium [15], [16]. Steatosis was induced by modifying the method in [17]. Internal controls were represented by both liver-on-a-chip devices and 2D static cultures in medium with vehicle only.

D. High-content analysis of steatosis

Evaluation of intracellular triglyceride accumulation, cell viability/cytotoxicity, and oxidative stress was performed by HCA methodologies using fluorescence-based functional probes: AdipoRed assay, Live/Dead Viability/Cytotoxicity reagent, and carboxy-H_2DCFDA ROS detection reagent,

respectively (Thermo Fisher). Micrographs were acquired under an inverted epifluorescence microscope (Ti-E, Nikon) and analyzed using NIS Elements AR software (Nikon).

III. Results and discussion

A. Gradual and lower intracellular lipid accumulation in liver-on-a-chip devices compared to 2D static controls

Figure 2 shows the results of intracellular lipid accumulation measured through the AdipoRed assay. After 24h, the increase in intracellular triglyceride content of treated cells *vs.* internal controls was statistically significant only for 2D cultures. At 48h, a further increase in lipid content was measured for both chips and 2D cultures, with both groups showing statistical differences *vs.* their own internal controls. Furthermore, the difference between chip and plate was more pronounced.

B. Higher cell viability in on-chip cultures vs. 2D controls under conditions of hepatic steatosis

The cytotoxicity of the FFA treatment for both liver-on-a-chip devices and 2D cultures was investigated using the Live/Dead assay (Fig. 3). 2D cultures showed a marked decrease in cell viability following the FFA treatment, whereas high cell viability was maintained by on-chip cultures, in which the FFA overload appears to be much better tolerated. Importantly, after both 24h and 48h, on-chip cultures showed a significantly higher viability *vs.* 2D ones, for both the FFA-treated and control conditions. This outcome is in line with the different intracellular lipid accumulation, previously observed in Fig. 2, between plate and chip. Overall, under conditions of steatosis, the microfluidic model allows a higher hepatic cell viability than traditional 2D cultures.

C. Comparable levels of oxidative stress between on-chip and 2D cultures in the setting of steatosis

To investigate the oxidative stress caused by the exogenous lipid overload, we evaluated cellular ROS levels in both on-chip and 2D cultures after 24h and 48h (Fig. 4). ROS levels in FFA-treated cells, normalized to their internal controls, were very low after both 24h and 48h, and comparable between on-chip and 2D cultures The trend of ROS production, passing from 24h to 48h, was descendant, with a slightly lower level in chip compared to 2D culture, though the difference was not statistically significant. The reported low ROS production is in agreement with the literature [18].

IV. Conclusions

To our knowledge, this chip represents a more permissive tissue-like microenvironment for long-term culture of hepatic cells than conventional 2D static cultures. The developed model enables gradual and milder intracellular triglyceride accumulation, a higher hepatic cell viability, and minimal oxidative stress in prolonged dynamic cultures compared to 2D static cultures, thereby mimicking more closely the *in vivo* chronic condition of steatosis. In conclusion, this work may represent a starting point for the development of an on-chip model of NAFLD, which paves the way for a more detailed investigation to further dissect cellular, molecular and epigenetic mechanisms that orchestrate NAFLD development.

Acknowledgements

Manuele Gori is supported by a “Fondazione Umberto Veronesi" Fellowship. This work is partially supported by Università Campus Bio-Medico di Roma under the framework of the “Internal Grant Program”.

References

[1] M. W. Tibbit, K. S. Anseth, “Hydrogels as extracellular matrix mimics for 3D cell culture,” *Biotechnol Bioeng*, vol. 103(4), pp.655-663, July 2009.

[2] M. Verhulsel, M. Vignes, S. Descroix, L. Malaquin, D. M. Vignjevic, et al. “A review of microfabrication and hydrogel engineering for micro-organs on chips,” *Biomaterials*, vol. 35(6), pp.1816-1832, Feb 2014.

[3] D. Wirtz, K. Konstantopoulos, P. C. Searson, “The physics of cancer: the role of physical interactions and mechanical forces in metastasis,” *Nat Rev Cancer*, vol. 11(7), pp.512-522, Jun 2011.

[4] N. S. Hwang, M. S. Kim, S. Sampattavanich, J. H. Baek, Z. Zhang, et al. “Effects of three-dimensional culture and growth factors on the chondrogenic differentiation of murine embryonic stem cells,” *Stem Cells*, vol. 24(2), pp.284-291, Feb 2006.

[5] A. M. Ghaemmaghami, M. J. Hancock, H. Harrington, H. Kaji, A. Khademhosseini, “Biomimetic tissues on a chip for drug discovery,” *Drug Discov Today*, vol. 17(3-4), pp.173-181, Feb 2012.

[6] A. R. Perestrelo, A. C. Aguas, A. Rainer, G. Forte, “Microfluidic organ/body-on-a-chip devices at the convergence of biology and microengineering,” *Sensors (Basel)*, vol. 15(12), pp. 31142-31170, Dec 2015.

[7] C. Zhang, Z. Zhao, N. A. Abdul Rahim, D. van Noort, H. Yu, “Towards a human-on-chip: culturing multiple cell types on a chip with compartmentalized microenvironments,” *Lab Chip*, vol. 9(22), pp.3185-3192, Nov 2009.

[8] C. Luni, E. Serena, N. Elvassore, “Human-on-chip for therapy development and fundamental science,” *Curr Opin Biotechnol*, vol. 25, pp. 45-50, Feb 2014.

[9] K. H. Benam, S. Dauth, B. Hassell, A. Herland, A. Jain, et al. “Engineered in vitro disease models,” *Annu Rev Pathol,* vol. 10, pp.195-262, 2015.

[10] P. J. Lee, P. J. Hung, L. P. Lee, “An artificial liver sinusoid with a microfluidic endothelial-like barrier for primary hepatocyte culture,” *Biotechnol Bioeng,* vol. 97(5), pp. 1340-1346, Aug 2007.

[11] M. Y. Zhang, P. J. Lee, P. J. Hung, T. Johnson, L. P. Lee, et al. “Microfluidic environment for high density hepatocyte culture,” *Biomed Microdevices*, vol. 10(1), pp. 117-121, Feb 2008.

[12] J. Lee, S. H. Kim, Y. C. Kim, I. Choi, J. H. Sung, “Fabrication and characterization of microfluidic liver-on-a-chip using microsomal enzymes,” *Enzyme Microb Technol,* vol. 53(3), pp. 159-164, Aug 2013.

[13] M. B. Esch, J. M. Prot, Y. I. Wang, P. Miller, J. R. Llamas-Vidales, et al. “Multi-cellular 3D human primary liver cell culture elevates metabolic activity under fluidic flow,” *Lab Chip, vol.* 15(10), pp. 2269-2277, May 2015.

[14] B. Q. Starley, C. J. Calcagno, S. A. Harrison, “Nonalcoholic fatty liver disease and hepatocellular carcinoma: a weighty connection,” *Hepatology*, vol. 51(5), pp. 1820-1832, May 2010.

[15] A. Baylin, E. K. Kabagambe, X. Siles, H. Campos, “Adipose tissue biomarkers of fatty acid intake,” *Am J Clin Nutr,* vol. 76(4), pp. 750-757, Oct 2002.

[16] M. J. Gómez-Lechón, M. T. Donato, A. Martínez-Romero, N. Jiménez, J. V. Castell, et al. “A human hepatocellular in vitro model to investigate steatosis,” *Chem Biol Interact,* vol. 165(2), pp. 106-116, Jan 2007.

[17] M. Gori, B. Barbaro, M. Arciello, R. Maggio, C. Viscomi, et al. “Protective effect of the Y220C mutant p53 against steatosis: good news?” *J Cell Physiol,* vol. 229(9), pp.1182-1192, Sep 2014.

[18] N. C. Chavez-Tapia, N. Rosso, C. Tiribelli, “Effect of intracellular lipid accumulation in a new model of non-alcoholic fatty liver disease,” *BMC Gastroenterol*, vol.12, pp. 20, Mar 2012.

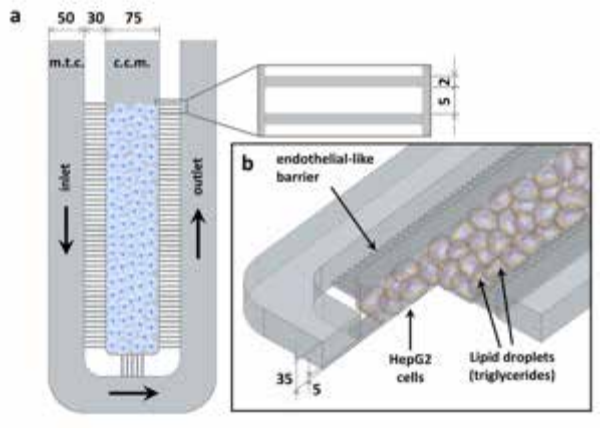

Fig. 1. Microarchitecture of the NAFLD-on-a-chip device. Top (a) and 3D (b) schematic view of the microfluidic device, showing the high-density culture of hepatic cells. Legend: m.t.c.: mass transport channel; c.c.m.: cell culture microchamber. Dimensions are in µm.

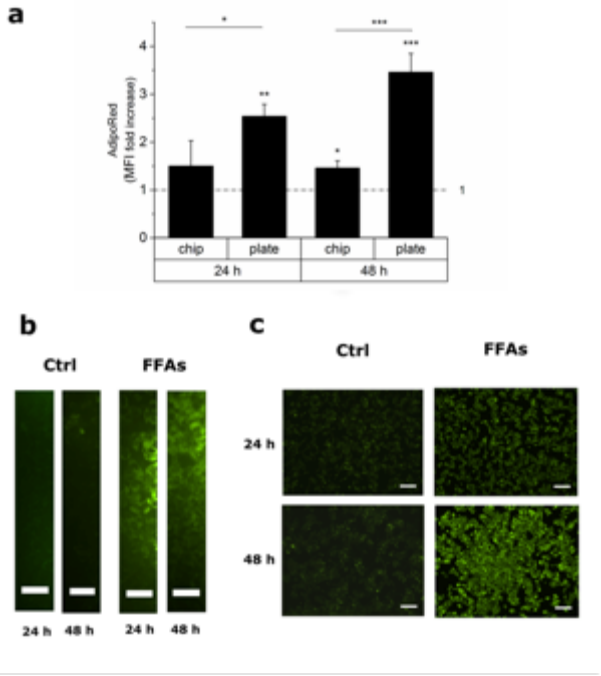

Fig. 2. AdipoRed assay for intracellular triglyceride accumulation. (a) Histogram showing the mean fluorescence intensity (MFI), expressed as the ratio between FFA-treated cells and internal controls, for on-chip and 2D cultures after 24h and 48h. * $p<0.05$, ** $p<0.01$, *** $p<0.001$. (b, c) Representative epifluorescence micrographs of the lipid overload (green cells) for on-chip (b) and 2D cultures (c). Scalebars: 50 µm in (b) and 200 µm in (c).

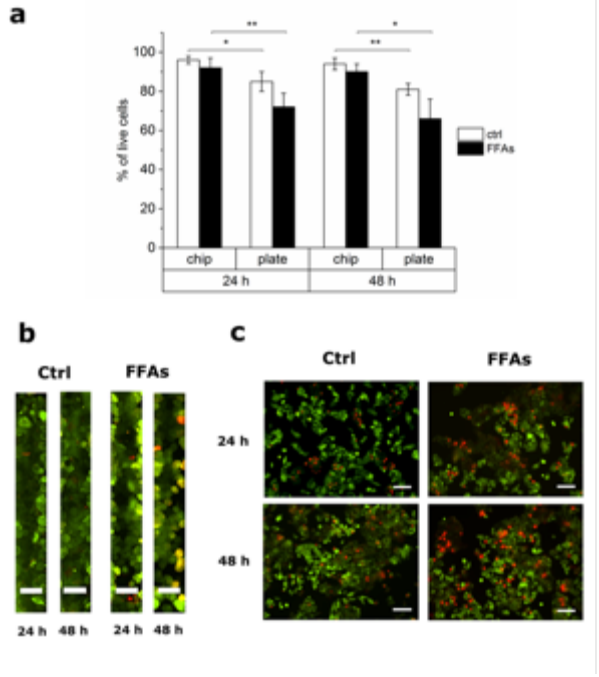

Fig. 3. Live/Dead assay for cell viability/cytotoxicity following the FFA treatment. (a) Histogram showing the percentage of living cells for control (white bars) and FFA-treated (black bars) groups in on-chip and 2D cultures after 24h and 48h. * $p<0.05$, ** $p\leq0.01$. (b, c) Representative epifluorescence micrographs of living cells (green) and dead cells (red) plotted in (a) within the chip (b) and the plate (c) after 24h and 48h. Images are at equal magnification (20x); scale bars represent 50 µm in (b) and 100 µm in (c).

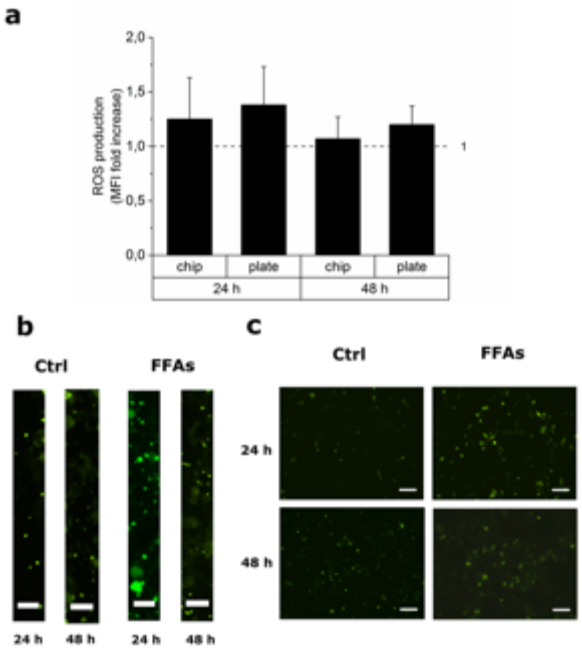

Fig 4. ROS detection assay for the analysis of oxidative stress levels, following the FFA treatment. (a) Plot showing the MFI for on-chip and 2D cultures after 24h and 48h. (b, c) Representative epifluorescence micrographs of intracellular ROS (green cells stained *via* carboxy-H_2DCFDA dye) for on-chip (b) and 2D cultures (c) after 24h and 48h. Scalebars: 50 µm in (b) and 100 µm in (c).

The effect of physical constraints on the function of cultured embryonic stem cells

M.M. Nava[1], A. Piuma[1,2], M. Figliuzzi[2], I. Cattaneo[2], B. Bonandrini[2], T. Zandrini[3], G. Cerullo[3], R. Osellame[3], A. Remuzzi and M.T. Raimondi[1]

[1] *Department of Chemistry, Materials and Chemical Engineering "Giulio Natta", Politecnico di Milano, Milano, Italy*
[2] *Istituto di Fotonica e Nanotecnologie (IFN)- CNR and Department of Physics, Politecnico di Milano, Milano, Italy*
[3] *IRCCS Istituto di Ricerche Farmacologiche "Mario Negri", Bergamo, Italy*

***Abstract*— Expansion of pluripotent stem cells in defined media devoid of animal-derived feeder cells and exogenous conditioning factors, such as the leukocyte inhibitory factor (LIF), would be advantageous for many regenerative, biological or disease-modelling studies. An increasing interest relies on the design and development of three-dimensional substrates to culture stem cells, in which the cues for pluripotency maintenance are provided by the architectural features of the substrate. Here we tested the possibility to use a substrate mimicking some geometric constraints of a three-dimensional native stem cell niche to maintain stem cell differentiation ability during in vitro expansion.**

***Keywords*—nanofabrication, embryonic stem cells, pluripotency, scaffold.**

I. Introduction

CELL-BASED therapy represents an important strategy to restore the function of injured cells, tissues and organs. However, the limited availability of desired cells hampers the success of this strategy. Recent advances in stem cell biology offer an opportunity to address this challenge. In particular, embryonic stem (ES) cells possess great potential because they can proliferate indefinitely without differentiation and, at the same time, retain the developing potential to generate cells of all three embryonic germ layers [1]. Different growth factors, cytokines and small molecules have been used to promote ES cells self-renewal. In particular, mouse ES cells (mESCs) have a requirement for IL6 family member cytokines such as leukemia inhibitory factor (LIF) to maintain self-renewal and pluripotency [2]. Such studies were mostly performed by means of two-dimensional (2D) culture systems. However, 2D culture substrates are considered limited to study the real situations in vivo [3], thereby, an increasing interest relies on the design and development of three-dimensional (3D) substrates to culture stem cell. Most of the currently available approaches for scaffold fabrication, based on self-assembly methods, do not allow for an accurate control of the geometrical structure of the substrate, which might play a crucial role in stem cell fate determination [4]. A novel technology which overcomes these limitations is laser two-photon polymerization (2PP) [5]. 2PP is a mask-less direct laser writing technique that allows manufacturing arbitrary microarchitectures with a spatial resolution down to 100 nm, thus better than the light diffraction limit. In 2PP, photopolymerization occurs by nonlinear two-photon absorption induced by femtosecond laser pulses in transparent materials. To investigate whether the 3D architecture is able to preserve pluripotency in mESCs, we designed and fabricated a new substrate with approximately 132 niche blocks (or "nichoids") per sample, covering the 70% of the available culture surface. This greatly improved layout allowed us to obtain a higher nichoid-cultured cell number per sample compared to our previous studies [6-8]. In this work, we report on the effect of the nichoid substrate on mESC pluripotency maintenance and differentiation during expansion in feeder-free conditions and in the absence of LIF via immunofluorescence image colocalization and quantification of specific pluripotency and differentiation markers.

II. Materials and Methods

A. Fabrication of the nichoid culture substrate by two-photon laser polymerization

The nichoids were directly two-photon polymerized in the SZ2080 photoresist [9] with 1% concentration of Irg photoinitiator. The laser used for 2PP was a cavity-dumped Yb:KYW system [10] producing pulses with 300-fs duration and 1-MHz repetition rate at 1030 nm wavelength, focused with a 1.4 numerical aperture (NA) oil immersion objective (Plan-APOCHROMAT,100×,Carl Zeiss, Germany). Optimum fabrication conditions were 1.5 mm/s writing speed, 12 mW average power (before the objective). Computer-controlled, 3 axis motion stages (ANT130, Aerotech, USA) were used to translate the sample relative to the laser to form the desired microarchitectures. Nichoids were laser written directly onto 12-mm diameter glass coverslips 150 μm-thick (Fig. 1A-C). To increase the niche surface to the flat glass ratio, a Poly-dimetylsiloxane (PDMS) ring (in gray in Fig. 1A) with 7-mm inner diameter was UV-bonded to the glass coverslips. Thus, we could cover the 70% of the available culture surface. Each nichoid was composed of 25 repetitive blocks 30 μm high and 90 μm × 90 μm in transverse dimensions and consisted of a lattice of interconnected lines, with a graded spacing between 10 and 30 μm transversely and a uniform spacing of 15 μm vertically (Fig. 1D). The overall size of each nichoid was 30 μm high and 450 μm × 450 μm in transverse dimensions (Fig.1E). The spacing between nichoids was set to 80 μm. Each repetitive unit (e.g. niche), as well as each block (e.g. nichoid) was surrounded by four outer confinement walls formed by horizontal lines spaced by 5 μm, resulting in gaps of 1 μm

B. Murine ESC culture, immunofluorescence staining and lineage commitments analysis

We expanded R1 mESCs for two weeks on the nichoid, flat glass and kidney extracellular matrix (ECM) culture substrate without using soluble conditioning factors. After 3, 7 and 14 days in culture, cells on different substrates were first imaged by phase contrast microscopy to assess colony size. In addition, cells were fixed in a 2% paraformaldehyde and 4% sucrose solution for 10 minutes at room temperature. Cells were then permeabilized in 0.1% Triton X-100 and treated with 3% BSA for 1 hour at room temperature. Immunofluorescence staining for the pluripotency marker octamer-binding transcription factor 4 (OCT4) was performed. While, to assess differentiation towards the endodermal and mesodermal germ layers, samples were stained for GATA binding protein 4 (GATA4) and α Smooth Muscle Actinin (α-SMA), respectively. Cell nuclei were counterstained with DAPI. Samples were finally mounted with a fluorescent mounting medium and imaged by laser confocal microscopy (LSM 510 Meta, Carl Zeiss, Germany). For nuclear markers (i.e. OCT4 and GATA4), we evaluated the occurrence of such markers within the nuclear region (i.e. DAPI), whereas for the cytoplasmic α-SMA, we measured the stained average area normalized by the overall field size. We used one-way ANOVA to assess statistical significance between groups. Discrepancies among groups were considered significant if the p value was < 0.05. The analysis was performed on 15 representative fields.

III. Results and Discussion

A. Mouse ESC colony size and morphology

To evaluate the geometrical constraint of the nichoid on mESCs, we first monitored the colony shape (Fig. 2A) and, then, assessed its characteristic size (i.e. diameter) (Fig. 2B). At 3 days of culture, we observed mESCs forming spherical aggregates on both nichoids and flat glass substrates having a comparable average diameter, 100-µm size in average. Interestingly, at 7 and 14 days of culture, the glass-cultured colonies dramatically increased their characteristic length spreading out, while mESC aggregates in the nichoids preserved their size and spherical shape (Fig. 2A). We addressed such distinct behavior to the physical and geometrical constraints provided by the 3D nichoid architecture. Indeed, cells cultured on flat substrates had not experience such confinement effect. Regarding renal ECM, mESCs rapidly underwent spreading and lost the tendency to form spherical embryonic bodies (Fig 2 A). Finally, to quantify the constraining effect of nichoids on mESCs, we measured the diameter of colonies that is an index of proliferation and pluripotency. With the exception of day 3, we found that the average colony diameter in nichoids was 20-30% lower in average compared to those cells cultured on flat glass, proving the containment effect provided by the 3D architecture of the nichoid samples. (Fig 2 B).

B. Mouse ESC pluripotency maintenance and differentiation

To evaluate the pluripotency maintenance on nichoid samples, we imaged and quantified the expression of OCT4 within DAPI-stained nuclei. We observed that mESCs expanded in the nichoids, the expression of OCT4 was almost 2-fold than the ones calculate in flat glass substrates and kidney ECM. Concerning the differentiation potential towards the endoderm and mesoderm germ layer, both GATA4 and α-SMA, respectively were significantly more expressed (i.e. 4-fold) in flat glass substrates compared to nichoids and renal ECM, suggesting a spontaneous commitment. Notably, GATA4 and α-SMA expression in nichoids and renal ECM was negligible (Fig. 3A, B).

IV. Conclusion

The nichoid was the only substrate, among those tested, allowing maintaining a pluripotency gene switched on and, simultaneously, two differentiation genes switched off in prolonged culture. These results demonstrate the ability of the nichoid substrate to promote maintenance of pluripotency of stem cells in expansion culture in the absence of a feeder layer and of exogenous soluble factors. Further studies are necessary to further understand which features of the physical microenvironment of the artificial niche microstructures are critical to function. The nichoid substrate may help elucidate mechanisms of pluripotency maintenance in vitro, while potentially cutting the costs and risks of feed-conditioning for industrial-scale expansion of stem cells.

Acknowledgement

Manuela Teresa Raimondi has received funding from the European Research Council (ERC) under the European Union's Horizon 2020 research and innovation programme (grant agreement No 646990 - NICHOID).

References

[1] A. M. Wobus, "Potential of embryonic stem cells" Mol Aspects Med, 2001, 22(3), pp.149-164.

[2] H.S. Zhou, J. Yong, X.M. Sun, C.Y. Wang, W.F. Yang, P. Zhang, J. Zhu, C. Shi and M. Ding, "A human endothelial cell feeder system that efficiently supports the undifferentiated growth of mouse embryonic stem cells." *Differentiation*, 2008, 76(9), pp. 923-930

[3] J. Wei, J. Han, Y. Zhao, Y. Cui, B. Wang, Z. Xiao, B. Chen, and J. Dai, "The importance of three-dimensional scaffold structure on stemness maintenance of mouse embryonic stem cells", *Biomaterials*, 2014, 35(27), pp. 7724-7733. doi: 10.1016/j.biomaterials.2014.05.060.

[4] M.M. Nava, M.T. Raimondi, and R. Pietrabissa, "Controlling self-renewal and differentiation of stem cells via mechanical cues", *J Biomed Biotechnol*, 2012, 2012, 797410, pp.1–12

[5] S. Maruo, and J. Fourkas, "Recent progress in multiphoton microfabrication". *Opt Lett*, 2008, 2(1–2), pp. 100–111

[6] M.T. Raimondi, S.M. Eaton, M. Laganà, V. Aprile, M.M. Nava, G. Cerullo, and R. Osellame. "3D structural niches engineered via two-photon laser polymerization promote stem cell homing", *Acta Biomater*, 2013, 9(1), pp. 4579–4584.

[7] M.T. Raimondi, M.M. Nava, S.M. Eaton, A. Bernasconi, K. Vishnubhatla, G. Cerullo, and R. Osellame, Optimization of femtosecond laser polymerized structural niches to control mesenchymal stromal cell fate in culture. *Micromachines*, 2014 5(2), pp. 341–358.

[8] M.M. Nava, N. Di Maggio, T. Zandrini, G. Cerullo, R. Osellame, I. Martin and M.T. Raimondi, "Synthetic niche substrates engineered via two-photon laser polymerization promote multipotency maintenance in the expansion of human mesenchymal stromal cells", *J Tissue Eng Regen Med*, Accepted for publication.

[9] A. Ovsianikov, J. Viertl, B. Chichkov, M. Oubaha, B. MacCraith, I. Sakellari, A. Giakoumaki, D. Gray, M. Vamvakaki, M. Farsari, , and C. Fotakis, Ultra-Low Shrinkage Hybrid Photosensitive Material for Two-

Photon Polymerization Microfabrication. *ACS Nano*, 2008 2(11), pp. 2257-2262

[10] A. Killi, A. Steinmann, J. Dörring, U. Morgner, M.J. Lederer, D. Kopf and C. Fallnich, High-peak-power pulses from a cavity-dumped Yb:$KY(WO_4)_2$ oscillator," *Opt. Lett*, 2005 30(14), pp.1891-1893

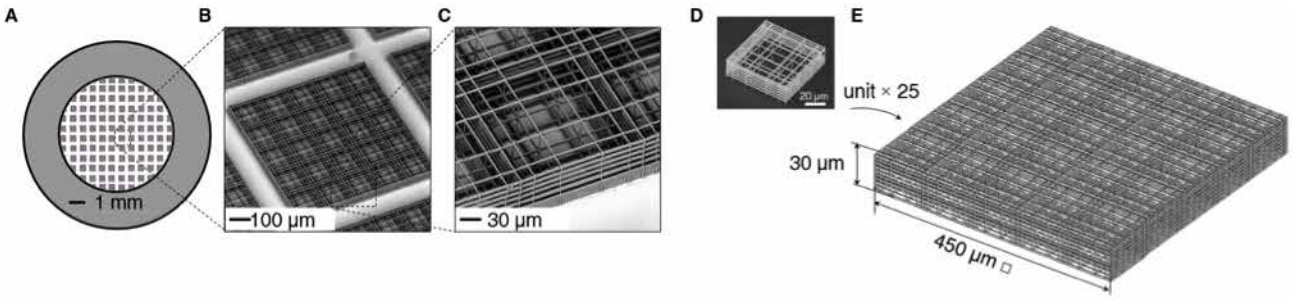

Fig. 1. The nichoid culture system fabricated by 2PP. (A) Top view of the nichoid culture system consisting of approximately 132 nichoids on a standard glass coverslip. To increase the niche surface to the flat glass ratio, a Poly-dimetylsiloxane (PDMS) ring (in gray) with 7-mm inner diameter was UV-bonded to the glass coverslips. (B) SEM pictures of the nichoid blocks and (C) Zoomed view. (D) SEM detail of the repetitive unit forming the nichoid culture substrate. (E) CAD of the nichoid block.

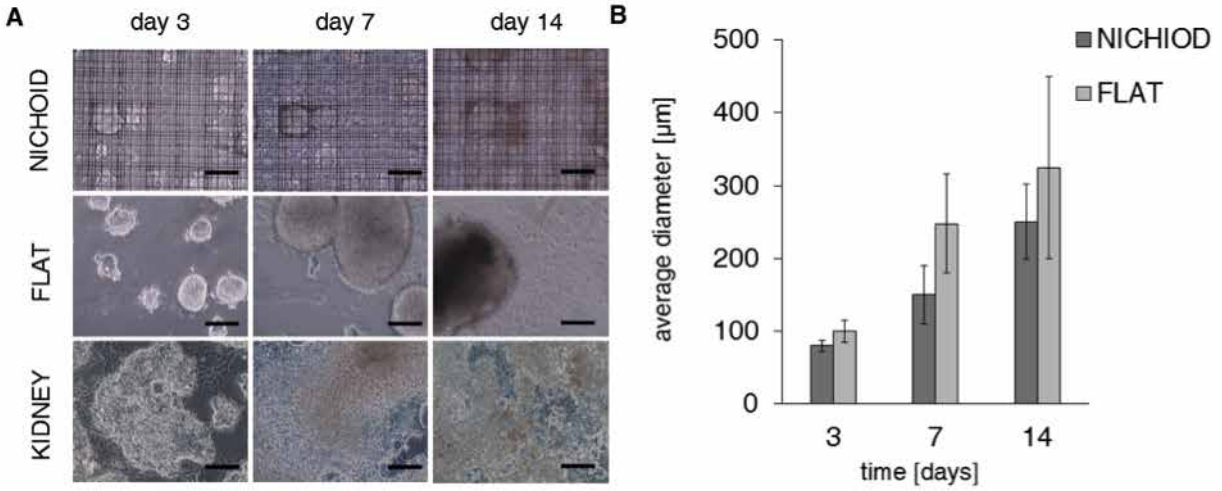

Fig. 2. Feeder-free maintenance and mESCs colony growth in the absence of a feeder-layer and of LIF. (A) Phase contrast images of mESCs colony growth on nichoid, flat glass and kidney matrix substrates at 3, 7 and 14 days of culture. Scale bar, 100 µm. (B) Colony diameter measured on nichoid and flat glass substrates.

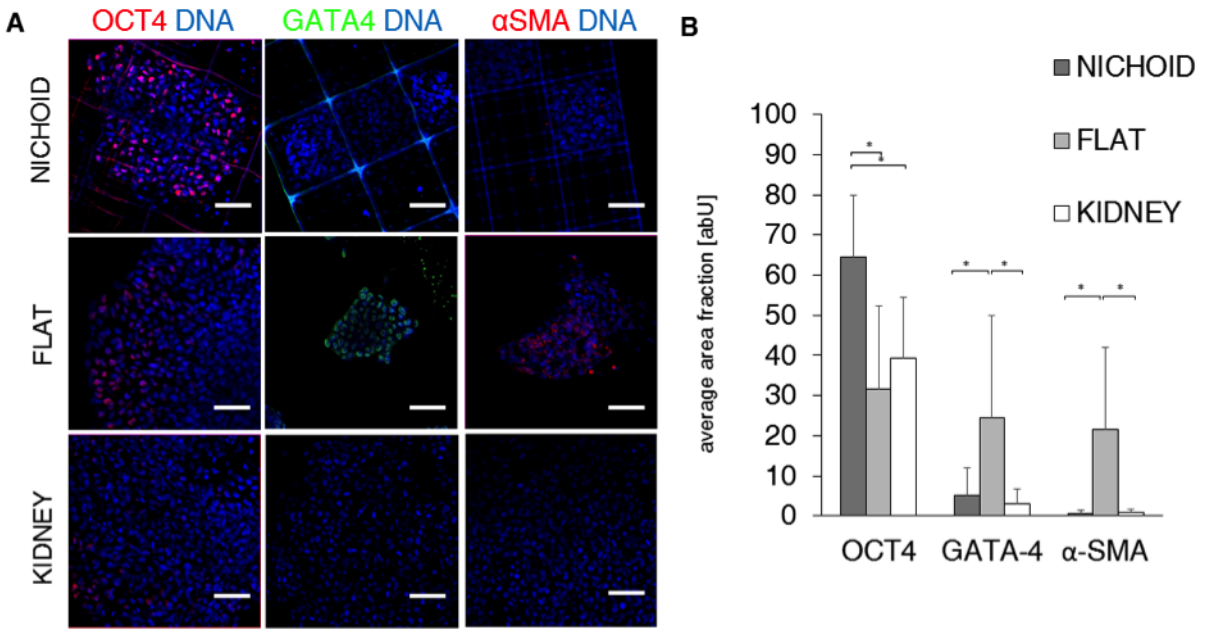

Fig. 3. Mouse embryonic stem cells expanded in the nichoid, flat glass and kidney ECM substrate in the absence of a feeder-layer and of LIF, at 7 culture days. (A) Immunofluorescence showing expression of the OCT4 pluripotency marker (red), the endoderm differentiation marker GATA4 (green) and the mesoderm differentiation marker αSMA (red). Nuclei are counterstained in DAPI (blue). Scale bar, 50 µm. B) Quantification of marker expression on immunofluorescence images; n=15, *p<0.01.

Effect of arginine and sodium tripolyphosphate on the stability of chitosan electrospun mats for soft tissue regeneration

P. Nitti[1], F. De Pascali[1], L. Natta[1], F. Scalera[1], F.Gervaso[1], A. Sannino[1]
[1]*Department of Engineering for Innovation, University of Salento, Via per Monteroni, Lecce*

***Abstract*— The soft tissues of the musculoskeletal system are characterized by a connective tissue composed of bundles of collagen fibers with preferential orientation. In order to induce the regeneration of such tissues, scaffolds with aligned fibers similar to those of native tissue are desirable since they are likely to allow cells to attach and proliferate along the optimal orientation. Aim of this study was the fabrication, of crosslinked chitosan/PEO mats by electrospinning, To improve the lifetime of chitosan mat two ionic crosslinkers were tested: Sodium Tripolyphosphate (TPP) and Arginine (Arg). The chitosan mats, before and after TPP and Arg stabilization, have been physical-chemically characterized by SEM, FT-IR, swelling measurements, in vitro stability test and tensile test.**

***Keywords*—Chitosan, electrospinning, Arginine, TPP.**

I. INTRODUCTION

THE soft tissues of musculoskeletal system (tendon, ligament, articular cartilage, intervertebral disc, meniscus) are characterized by an extracellular matrix (ECM) poorly vascularized, composed of bundles of collagen fibers with preferential orientations. To repair the injuries of soft tissue through a regenerative medicine approach, it is preferable to create tissue engineered constructs with aligned fibers similar to those of native tissue. Electrospinning is a quite simple technique that allows to realize tissue engineered constructs (i) made of nanometric fibrous structures, (ii) with preferred orientation, and (iii) that should enable cells to produce matrix along that optimal orientation [1]. To address this issue, in this study, a chitosan electrospun (ES) mat with oriented nanofibers was developed. Chitosan, a natural, biocompatible, biodegradable, antibacterial polymer was used in blend with polyethylene oxide (PEO). To prevent fiber dissolution in aqueous medium, two ionic nontoxic crosslinkers were tested and compared: sodium tripolyphosphate (TPP) [2] and Arginine (Arg).

.

II. EXPERIMENTAL METHODS

A Chitosan/PEO blend (70:30) was dissolved in 90% v/v acetic acid solution at a concentration of 4.5% w/v. The optimal spinning conditions were assessed and optimized. To generate fiber alignment, the spinneret was directed perpendicularly to a circular plate rotating from 300 to 1200 rpm (Fig. 1). The obtained chitosan mats have been cross-linked with TPP (4mM, pH 7) or Arg (0.2M, pH 11) and characterized by SEM and FT-IR [2, 3]. The swelling ratio in PBS and the mats stability in TRIS-HCl (pH 7.4, 37°C) till 30 days were also assessed. Finally, tensile test on the ES chitosan mats cross-linked with Arg were performed in order to evaluate the influence of fiber alignment on the mats mechanical properties.

III. RESULTS AND DISCUSSION

Firstly, different concentrations of chitosan and PEO and different ratios of blend were tested. The performed rheological tests showed a pseudoplastic behaviour of chitosan/PEO solutions and an increase of the viscous component increasing chitosan concentration on blends. The optimization of process parameters and collector geometry and the increase of collector speed allowed the obtainment of aligned beads-free nanofiber mats (Fig.2A). Architectural stability of nanofiber mat in aqueous medium was achieved by ionotropic crosslinking of chitosan by TPP ions and Arg. FT-IR analysis confirmed that both crosslinkers formed networks through the electrostatic interactions of the negatively charged groups with the positively charged groups of the chitosan chains. TPP crosslinking [2] was confirmed by the presence of antisymmetric stretching of P-O-P bridge (893 cm-1) a P=O stretching (1213 cm-1), while Arg crosslinking [3] showed a guanido group band (1630 cm-1) overlapping the chitosan band, symmetric bending CH2 (1467cm-1) and bending OH (1327cm-1). The morphologies of both crosslinked electrospun mats were examined by SEM (Fig. 2B, 2C). The fiber diameter distribution decreased increasing rotational speed of the collector from about 250 nm to 160 nm. Both TPP and Arg crosslinked mats had a maximum swelling degree in PBS after about 1h. Stability tests after 3, 7, 15, 30 days in TRIS-HCl (pH 7.4, 37°C) showed significant reduced weight loss for TPP mats after only 3 days, while Arg mats had only a small weight loss after 3 days and then remained unchanged. Therefore, Arg had a higher crosslinking action than TPP. The mechanical properties of hydrated Arg mats were determined in both parallel and perpendicular to fiber alignment directions. The elastic modulus in the fiber direction resulted higher than in the perpendicular direction (31.7MPa vs 7.2MPa), therefore in this strips the nanofibers made the material more extendable. FFT and MTT analyses are in progress to evaluate relative alignment value and to test biocompatibility of Arg mats, respectively.

IV. Conclusion

In the present work, ES chitosan mats with aligned nanofibers were successfully fabricated. The stability of ES mats in aqueous medium was improved by ionotropic cross-linking of chitosan by Arg ions. The Arg crosslinked chitosan/PEO mats may be considered as potential scaffold for soft tissue engineering

References

[1] B. Ma, J. Xie, "Rational design of nanofiber scaffolds for orthopedic tissue repair and regeneration", Nanomedicine (Lond), 8(9) (2013)

[2] S. D. Sarkar, B. L. Farrugia, "Physico-chemical/biological properties of tripolyphosphate cross-linked chitosan based nanofibers" , Materials Science and Engineering C 33 (2013) 1446–1454

[3] W.G Liu, J.R. Zhang, "A chitosan-arginine conjugate as novel anticoagulation biomaterial" Journal of material and science: materials in medicine, 15 (2004), 1199-1203.

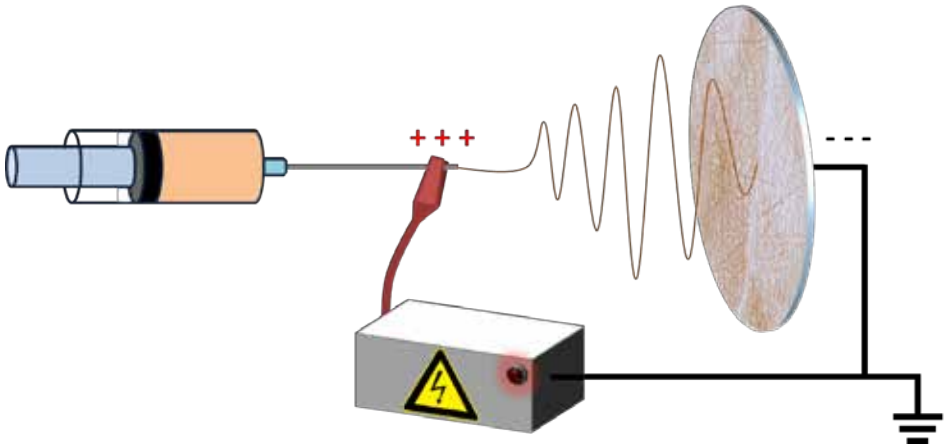

Fig.1 Electrospinning setup

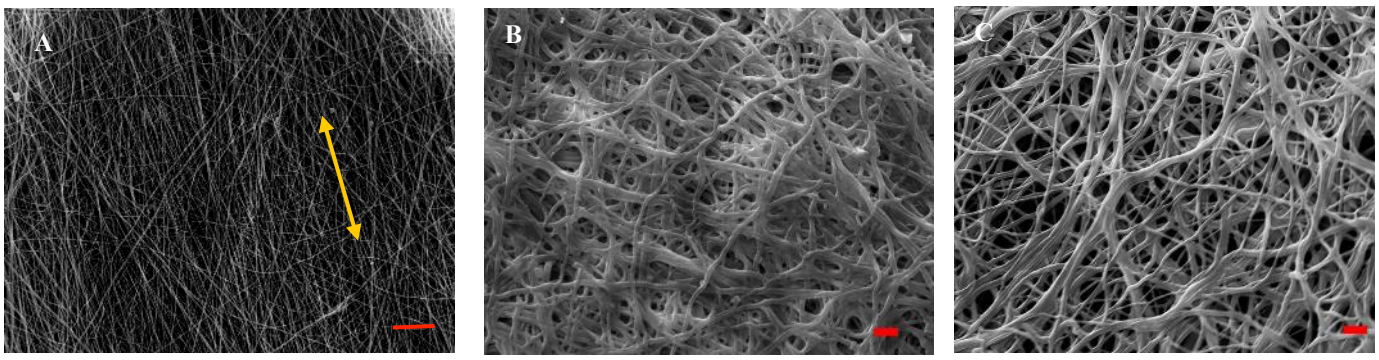

Fig.2 SEM micrographs of pure aligned chitosan/PEO, 8000X (A), crosslinked TPP (B) and Arg (C) 2000X.

Chitosan-based scaffolds exhibit modular features induced by magnetic nanoparticles and L-arginine amino acid

S.Scialla[1,*], R. Canoci[1], A. Barca[2], B. Palazzo[3], F. Scalera[1], T. Verri[2], A. Sannino[1] and F. Gervaso[1]
[1]*Department of Engineering for Innovation, University of Salento, Lecce - IT*
[2]*General Physiology Laboratories, Department of Biological and Environmental Sciences and Technologies, University of Salento, Lecce - IT*
[3]*Ghimas S.p.A., c/o Dhitech S.c.a.r.l., Campus Ecotekne, Lecce - IT*
*stefania.scialla@unisalento.it

***Abstract*— Large bone or osteochondral defects still need new approaches to ameliorate the regeneration process. The integration of magnetic nanoparticles into synthetic/natural scaffold formulations, could lead to obtain a suitable, responsive "*on demand*" tool able to guide the regeneration process. The aim of this work was the design and characterization of chitosan-based scaffolds containing dextran-grafted maghemite (DM) with modular mechano-structural and biomimetic properties implemented by the presence of a bioactive agent such the L-arginine amino acid. Both components can act as modulators of the scaffold features and, at the same time, the simultaneous presence of MNPs and L-Arg can be exploited to induce variations with respect to the cytocompatibility responses.**

***Keywords*—chitosan, magnetic nanoparticles, L-arginine, scaffold.**

I. INTRODUCTION

LARGE bone defects caused by degenerative diseases, prosthetic implant revisions, tumour excisions and traumas still represent a major challenge in the reconstructive orthopaedic field [1]. The difficulty of the regeneration process, when the size of the defect exceeds a critical value, depends on a variety of factors such as animal species, bone type, or healing failure [2]. In this context, the use of 3D biocompatible scaffolds exhibiting high levels of mimicry with natural tissues is a key feature for hard tissue regeneration. In order to improve scaffolds bio-mimicking, the need to integrate tissue-engineering approaches with nanotechnology emerges as a powerful strategy [3]. Particularly, magnetic nanoparticles (MNPs) are now being combined with biomaterials providing final magnetic scaffolds, with reinforced mechanical properties, which can be manipulated in situ by applying an external magnetic field, in order to guide the bone regeneration processes [4], [5]. This is leading to an emerging approached currently represented by the *magnetic-force based tissue engineering [6]*. Incorporated into synthetic/natural scaffold formulations, MNPs could be the suitable tool to guide "*on demand*" the regeneration process, by release of biomolecules, growth factors or therapeutic compounds involved in activation or triggering cell processes (e.g. proliferation and differentiation [7]) and physiological responses. Bearing this in mind, the aim of this work was the design and characterization of chitosan-based scaffolds containing dextran-grafted maghemite (DM) with modular mechano-structural and biomimetic properties implemented by the presence of a bioactive agent such the L-arginine amino acid.

II. MATERIALS AND METHODS

A. Chemicals

For DM nanoparticles synthesis iron (II) chloride tetrahydrate ($FeCl_2$•$4H_2O$, 99%), iron (III) chloride hexahydrate ($FeCl_3$•$6H_2O$, 98%) and dextran (MW = 6 kDa, synthesized by Leuconostoc mesenteroides) were used and purchased by Alfa Aesar. For scaffold preparation, chitosan (chitosan from shrimp shells; degree of deacetylation > 85%), glacial acetic acid and L-Arginine were used. All reagents used in this work were purchased from Sigma-Aldrich.

B. Cell-based assays

For *in vitro* cytocompatibility assays, the MG63 immortalized cell line was adopted (human osteosarcoma, ATCC n. CRL 1427), and the Dulbecco's Minimum Essential Medium (DMEM) was used for cell culture and treatments, supplemented with 10% (v/v) fetal bovine serum (FBS), 2mM L-glutamine, penicillin/streptomycin 100 µg/ml, phosphate-buffered saline (PBS); for the evaluation of cell proliferation, a standard protocol based on the metabolization of the 3-(4,5-dimethylthiazol-2-yl)-2,5- diphenyltetrazolium bromide (MTT) was used.

C. Scaffold synthesis

Magnetic chitosan-based scaffold were developed by using a freeze-drying technique. A colloidal suspension of DM nanoparticles, synthesized starting from a previous method published by Walsh et al. [8], was added to the chitosan slurry at different percentage (5-10-15% w/w with respect to the weight of chitosan used) before freezing. Stabilization of magnetic scaffolds with L-arginine was achieved by soaking freeze-dried scaffold in a 0,1 M L-Arg solution, under gentle agitation. Table I summarises scaffolds formulations. Scaffolds properties were evaluated by Scanning Electron Microscopy (SEM) and Energy Dispersive X-ray Spectrometry (EDX), compression test (Zwick), stability test in Tris-HCl at pH 7.4 and 37°C.

Material	*DM ($\%_{w/w}$)*	*Arg (M)*	*Nomenclature*

Chitosan (1,67% w/w)	-	-	Cs
	5	-	Cs/DM5
	10	-	Cs/DM10
	15	-	Cs/DM15
	-	L-Arg (0,1M)	Cs-Arg
	5		Cs/DM5-Arg
	10		Cs/DM10-Arg
	15		Cs/DM15-Arg

Table I: Summery of scaffold types synthesized

III. Results and Discussions

SEM micrographs have showed a homogeneous pores distribution, with a circular or elliptical shape (see Fig. 1), which gives to the scaffold a good interconnection degree. Particularly, the pores average diameter reduces in parallel to the DM content increase as shown in Table II, whereas, in the presence of L-Arg a greater reduction of the pores diameter has been detected (see Table III).

Samples	***Pore Diameter* (µm)**
Cs	185±32
Cs/DM5	164±38
Cs/DM10	167±42
Cs/DM15	152±45

Table II: Pores average diameter of the chitosan-based scaffolds in the presence of DM nanoparticles

Samples	***Pore Diameter* (µm)**
Cs-Arg	131±32
Cs/DM5-Arg	121±43
Cs/DM10-Arg	127±46
Cs/DM15-Arg	119±28

Table III: Pores average diameter of the chitosan-based scaffolds in the presence of DM nanoparticles and stabilized by L-Arg 0,1M

EDX analysis, showed in Fig. 2, have confirmed a "*bulk*" magnetization of scaffolds: it was verified that the DM are uniformly distributed along the whole diameter and the entire thickness of scaffold. Furthermore, the iron elemental content increases proportionally with the DM content.

Moreover, the compression tests results highlighted an increase of Young's modulus (E_{low}=kPa) by the increasing of DM percentage up to10% (Cs=1 ± 0,07 kPa; Cs/DM5=1,58 ± 0,24 kPa; Cs/DM10=1,62 ± 0,21 kPa) with the exception of Cs/DM15. In the presence of L-Arg, a considerable increase in the E_{low} has been shown with a same DM dose-dependence trend (Cs-Arg=8,38 ± 0,07 kPa; Cs/DM5-Arg=22,82 ± 1,90 kPa; Cs/DM10-Arg=20,01 ± 1,78 kPa). Interestingly, in both cases the 15% DM concentration induced a clear reduction of the E_{low} values (0,92 ± 0,14 kPa and 11,84 ± 0,80 kPa for Cs/DM15 and Cs/DM15-Arg, respectively). When the weight loss has been evaluated, arginine treatment resulted to improve scaffolds stability (30% weight loss for Cs/DM vs 15% weight loss for Cs/DM-Arg, up to 3 weeks in Tris-HCl pH 7.4).

Then, basic cytocompatibility of the synthesized scaffolds was assessed, by evaluating the metabolic activity, in terms of proliferation, of cells of the MG63 human osteoblast-like model, seeded directly onto the scaffold surface and grown for 24, 48 and 72 hours. By proliferation assays (showed in Fig. 3, left istogram) on cells grown into scaffolds, a minor cytocompatibility of Cs/DM5 was revealed at each time-point; on the other hand, Cs/DM10 and Cs/DM15 both showed optimal cytocompatibility after 72 h of growth, with a different behavior at short time possibly due to structural and/or mechanical differences in the 3D structure. When proliferation assays were performed with Cs/DM-Arg scaffolds (see Fig.3, istogram on the right), an evident dose-dependence related to concentration of DM particles was revealed in short times (24 h), with modular features and a more evident homogeneity of behavior at intermediate times, when compared to the Cs scaffolds without L-arginine.

For more, at each time analyzed, Cs/DM-Arg showed increased permissiveness to proliferation, even for the Cs/DM5-Arg compared to the Cs-Arg control, whereas the 5% of DM in the Cs scaffolds (without L-arginine) implied reduced proliferation.

IV. Conclusion

In conclusion, the present work has allowed the development of a protocol for synthesis of chitosan-based scaffolds with properties due to the presence of two molecular tools such as the MNPs and the L-arginine amino acid as a bioactive agent. Both components seem to act as modulators of the mechano-structural features; at the same time, the presence of MNPs and L-Arg can be used to induce variations with respect to the cytocompatibility responses. Overall, we give hints for a dual tool, represented the presence of DM and L-Arg, for acting on mechano-structural and biocompatible features of chitosan-based scaffolds, thus implementing the versatility of the polymer itself. This could represent an optimal starting point for design of scaffolds with "ad hoc" traits for the targeted bone or osteochondral defects.

V. References

[1] A. Oryan, A. Bigham-Sadegh, F. Abbasi-Teshnizi, "Effects of osteogenic medium on healing of the experimental critical bone defect in a rabbit model", *Bone*, 63, pp. 53-60, 2014.

[2] A.C. Allori, A.M. Sailon, S.M. Warren, "Biological basis of bone formation, remodeling and repair-part I: biochemical signaling molecules", *Tissue Eng Part B Rev*, 14,3, pp. 259-273, 2008.

[3] E.-S. Kim, E.H. Ahn, T. Dvir, and D.H. Kim, "Emerging Nanotechnology Approaches in Tissue Engineering and Regenerative Medicine." *International Journal of Nanomedicine 9*, Suppl 1, pp. 1-5, 2014.

[4] S. Gil, and J.F. Mano, "Magnetic composite biomaterials for tissue engineering", Biomaterials Science, 2, 6, pp. 812-818, 2014.

[5] A. Tautzenberger, A. Kovtun, A. Ignatius, "Nanoparticles and their potential for application in bone," *Int. J. Nanobiomed.*, 7, pp. 4545–4557, 2012.

[6] E. Castro, J.F. Mano, "Magnetic-Force-Based Tissue Engineering and Regenerative Medicine," *J. Biomedical Nanotechnology,* 9, 7, pp. 1129-1136, (8). 2013.

[7] J. M. Kanczler, H.S. Sura, J. Magnay, D. Green, R.O. Oreffo, J.P. Dobson, A.J. El Haj, "Controlled differentiation of human bone marrow
stromal cells using magnetic nanoparticle technology," *Tissue Eng. A*, 16, 10, pp. 3241–3250, 2010

[8] D. Walsh, S.R. Hall, A. Moir, S. C. Wimbush, and B. Palazzo, "Carbonated Water Mediated Preparation of Poly(N-isopropylacrylamide) Thermoresponsive Gels and Liquids," *Biomacromolecules*, 8, pp. 3800-3805, 2007.

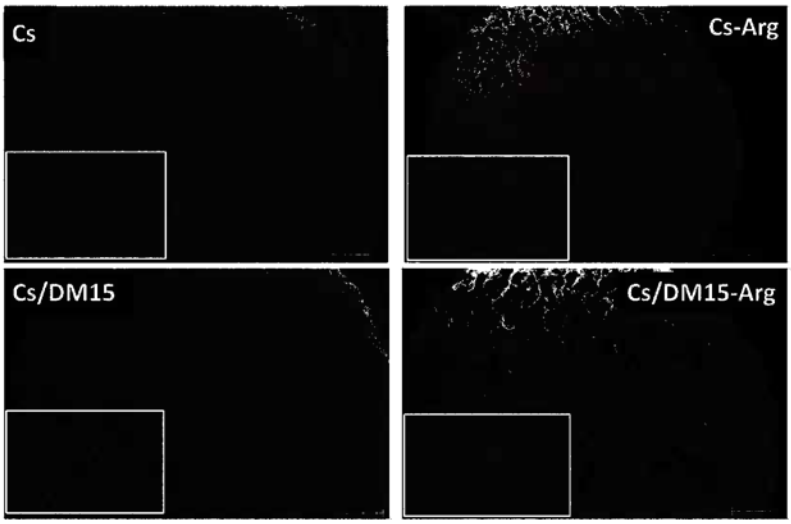

Fig. 1 SEM micrograph of cross section of the chitosan-based scaffolds functionalized with DM nanoparticles (on the left) and stabilized with L-Arg (on the right). For an easy comprehension, we have reported the controls (Cs and Cs-Arg) and the condition with the condition with the highest DM percentage (Cs/DM15 and Cs/DM15-Arg) (*Courtesy of D. Cannoletta, Department of Engineering for Innovation, University of Salento, Lecce*)

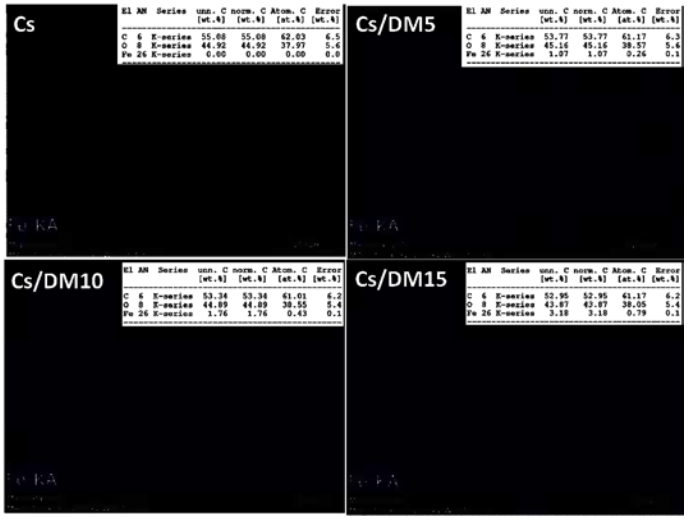

Fig. 2 Mapping of the Fe elemental content into the scaffolds in chitosan and chitosan functionalized by DM at different percentage; in detail, evaluation of atomic and ponderal percentages of chemical elements present (Fe, C, O)

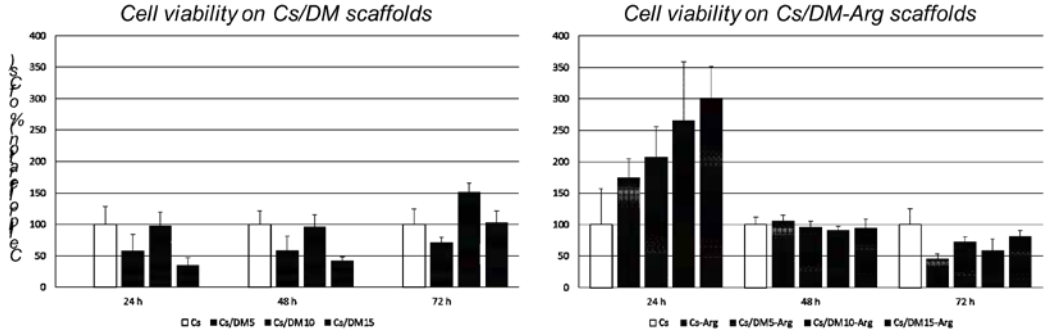

Fig. 3 MTT proliferation assay on MG63 cells at 24, 48 and 72 h after seeding in Cs/DM scaffolds (left) or Cs/DM-Arg scaffolds. Chitosan-based scaffold were obtained as cilinders with 6 mm diameter and 5 mm height, and were pre-hydrated in cell culture medium before being inserted in a 96-well plate for cell culture. Data are expressed as % proliferation with respect to control (Cs). For the Cs/DM scaffolds, reduced proliferation is shown with the Cs/DM5 composition, up to 48 h (istograms on the left). By adding L-Arg, dose-dependent increase of proliferation is shown at 24 h, and absence of significant variations respect to control (Cs) are indicated at extended time-points, probably due to time-dependent exhaustion of L-Arg as boosting metabolite for cell proliferation.

MODELLISTICA MATEMATICA

Simulation Framework to Optimize Parameters of Open-Loop Insulin Therapy in Type 1 Diabetes Patients

G. Cappon[1], M. Vettoretti[1], A. Facchinetti[1], G. Sparacino[1], C.Cobelli[1]
[1] *Department of Information Engineering, University of Padua, via Gradenigo 6/B, 35131 Padua, Italy*

***Abstract*— Type 1 diabetes therapy is based on multiple daily exogenous insulin administrations tuned according to blood-glucose (BG) measurements and some therapy parameters derived by physicians applying trial-and-error procedures. In this work a simulation framework is built to test algorithms for the automatic optimization of exogenous insulin administration based on the run-to-run (R2R) technique. Preliminary results show the R2R reduces time in hypoglycemia and BG variability, suggesting to further investigate this promising technique for the automatic calculation of the optimal insulin dosage.**

***Keywords*—Bolus Calculator, Insulin Dosing, Run-to-Run, Continuous Glucose Monitoring**

I. INTRODUCTION

TYPE 1 Diabetes (T1D) is an autoimmune disease characterized by the destruction of the pancreatic beta-cells responsible of insulin production. As a consequence of the lack of insulin, concentration of glucose in the blood (BG) can exceed the normal range (70-180 mg/dL). In order to avoid long-term complications due to hyperglycemia (BG>180 mg/dL), e.g. neuropathy, retinopathy and micro-macro-vascular heart diseases, or, in the case of hypoglycemia (BG<70 mg/dL), dangerous short-term episodes, like coma or even death, a therapy based on exogenous insulin administration is required.

The standard T1D therapy consists of multiple daily injections of insulin performed usually at meal time and tuned according to diet, physical activity and self monitoring blood glucose (SMBG) samples collected by patients using fingerstick devices 3-4 times a day. This therapy is uncomfortable and demanding for the patient, it greatly affects quality of life and can also result in a suboptimal control. In the last few years, several minimally-invasive technologies, such as pumps for continuous subcutaneous insulin infusion (CSII) and needle sensors for real-time continuous glucose monitoring (CGM), have been proposed to design new, more efficient, T1D therapies and improve quality of life of patients. CSII allows to avoid multiple injections, while CGM provides a BG measurement every 1-5 minutes, mitigating the need of repetitive use of SMBG. Numerous studies [1] have demonstrated how the use of CGM to treat T1D, even in an "open-loop" scenario, can help to control BG level reducing, for example, the time spent outside the optimal glucose range.

To get the best benefits from using CGM in an open-loop context, ad hoc rules to estimate the optimal amount of insulin to inject need to be devised. Simple rules for insulin dose calculation are used in the literature, which are based on two therapy parameters: the carbohydrate-to-insulin ratio (CR), i.e. the grams of carbohydrate (CHO) covered by one unit of insulin, and the correction factor (CF), i.e. the drop in BG concentration produced by one unit of insulin. These parameters are patient-specific and are usually tuned-up by physicians with empirical laws and trial-and-error procedures [2]. So far, to help the patient's in the insulin dosing, CSII systems embed insulin bolus calculators using CR and CF (with values inserted by the physician) to automate the insulin bolus calculation process and provide a decision support tool to patients. However, an automatic procedure for the calculation and tuning of the insulin amount would be desirable.

Attempts to improve the performance of such calculators have been carried out. In Herrero et al. [3], an approach to automatically adjust CR and CF using CGM measurements is presented. The method is based on a run-to-run (R2R) control technique i.e. and iterative procedure in which the values of CR and CF are updated daily according to a performance metric evaluating the distance between the minimum postprandial glucose concentration, which is measured by CGM, and the patient's target BG concentration. Clearly, the R2R assumes that the process to be controlled, in this case the BG profile, is strictly repetitive. Herrero et al. [3] preliminarly assessed the R2R performance on 20 virtual subjects by using a simulation framework in which inter- and intra-day variability of patient's physiology and behavior where artificially simulated by empirical suboptimal models, resulting in a non-realistic real-life scenario.

The aim of this work is to present an *in-silico* simulation framework that allows to test algorithms to optimize bolus calculator parameters, e.g. the R2R, in a realistic real-life scenario thanks to the inclusion of state-of-art models of variability of patient's physiology and behavior, and technology.

II. THE SIMULATION FRAMEWORK

The proposed simulation framework reproduces real-life situation and patient behaviours. It is based on the T1D Uva/Padova simulator [4], i.e. a model of glucose metabolism that was accepted by the Food and Drug Administration first in 2008 and then, in its revised version in 2013, to substitute preclinical trial for certain insulin treatments. To use the simulator for our scopes, models of CGM measurement error and patient errors in diabetes management such as miscalculations of meal carbohydrate content were incorporated. The framework is displayed in Fig. 1. Its inputs are the meal protocol, which contains the CHO content of each meal, and the patient-specific initial therapy parameters. The simulator output is the patient BG profile. The framework structure is composed by several

interconnected blocks described below.

A. Meal Management

The meal management block receives in input the meal protocol, which contains the information on time and amount of patient's meals, and measured CGM. The block gives in output the patient's estimate of meal CHO content that must be used for insulin bolus and CHO intake that includes both meals' CHO and 15-gram rescue CHO given every 15 min to treat hypoglycemia episodes i.e. when CGM<70 mg/dL. A scenario with realistic meal times and carbohydrate amounts has been generated (see Table I for further information).

TABLE I. MEAL PROTOCOL

	Breakfast	*Lunch*	*Dinner*
Time	[6 am, 8 am]	[12, 2 pm]	[8 pm, 10 pm]
CHO(g)	[30-50]	[40-70]	[30-60]

B. Insulin Bolus Calculator & Pump

The insulin bolus calculator & pump block simulates insulin doses calculation and infusion. Given the CHO count, the current BG concentration and the therapy parameters, it implements the standard insulin bolus calculator formula used to compute the insulin dose [5]:

$$B = \frac{CHO}{CR} + \frac{G_c - G_{sp}}{CF} - IOB \quad (1)$$

where B is the recommended dose of insulin (U), CHO is the estimated amount of CHO in the meal (g), CR is the insulin-to-carbohydrate-ratio (g/U), G_c is the current BG level (mg/dL), G_{sp} is target BG (mg/dL), CF is the insulin sensitivity factor (mg/dL/IU) and IOB is the insulin-on-board that describes how much insulin is still acting from the previous boluses computed as:

$$IOB = \sum_{i=1}^{n} B_i exp\frac{-(t - T_{B_i})}{\tau} \quad (2)$$

where B_i is the bolus administered at time T_{Bi} and τ a defined exponential decay constant.

C. Therapy Management

The therapy management block receives as input the meal protocol, the CGM measurements and initial therapy parameters and returns in output the optimized CR and CF values to be used for the glycemic control. To achieve this purpose, it implements the R2R approach as described in [3].

D. CGM Sensor

CGM sensor block receives in input the interstitial glucose concentration (IG) and returns in output the CGM recordings simulated according to the model of error described in [6].

E. T1D Patient

The T1D patient block simulate the BG and IG concentration in a T1D patient resulting from CHO intake and insulin pump infusion. The block implements the T1D UVa/Padova simulator [4] which describes physiological events related to BG dynamics (e.g. gastrointestinal CHO absorption and glucose, insulin and glucagon kinetics). The model has been extended to incorporate the inter- and intra-day variability of insulin sensitivity as described in [7]. The resulting model can be used to run multi-day simulations in a population of 100 adult virtual patients.

III. RESULTS

Simulations have been run in 10 virtual subjects for a 7-days period. Two different scenarios have been designed to perform a preliminary evaluation of R2R performance: in scenario A no therapy parameters optimization has been performed, while in scenario B it has been introduced the R2R approach to tune CR and CF values. Initial therapy parameters are set to suboptimal values to test the benefit of the R2R technique In Fig. 2 the results obtained for a representative subject are shown. It is easy to see how the BG profile relative to scenario B is better controlled than the one obtained for scenario A. Indeed, using R2R technique, the time spent in hypoglycemia is sensibly reduced as well as BG variability. This suggests that R2R is a promising technique to optimize bolus calculator parameters.

IV. CONCLUSION

A simulation framework to test *in silico* algorithms to optimize T1D open-loop therapy parameters has been proposed. The framework was used for a preliminary evaluation in 10 virtual subjects of the R2R algorithm, which was shown to be a promising technique to efficiently control BG concentration. The evaluation reported is, however, only preliminary. Indeed, since the method assumes that the BG profile is strictly repetitive, assumption that obviously is not true because several events like meal behaviors and physical exercise are not periodic and more heterogeneous real-life scenarios should be investigated (e.g. by simulated more complex 2-3 months scenarios). For this reasons, we are presently studying how to improve the entire approach by combining R2R with case-based reasoning (CBR), i.e. an artificial intelligence technique that try to solve new problems by applying solutions learned from solving similar problems in the past, to add flexibility to the optimization process as in [8].

REFERENCES

[1] Diabetes Control and Complications Trial (DCCT) Research Group, "The effect of intensive treatment of diabetes on the development and progression of long-term complications in insulin-dependent diabetes mellitus", in *N. Engl. J. Med*. vol. 329,1995, pp. 977–986.

[2] P. C. Davidson, H. R. Hebblewhite, R. D. Steed and B. W. Bode, "Analysis of Guidelines for Basal-Bolus Insulin Dosing: Basal Insulin, Correction Factor, and Carbohydrate-To-Insulin Ratio", in *Endocrine Practice* vol. 14 no. 9, 2008, pp. 1095-1101.

[3] P. Herrero et. al., "Method for automatic adjustment of an insulin bolus calculator: In silico robustness evaluation under intra-day variability", in *Computer Methods and Programs in Biomedicine* vol. 119, 2015, pp. 1–8.

[4] C. Dalla Man et al., "The UVA/PADOVA type 1 diabetes simulator: new features", in *J Diabetes Sci. Technol.* vol. 8 no. 1, 2014, pp. 26-34.

[5] S. Schmidt, K. Nørgaard, "Bolus calculators", in *J. Diabetes Sci. Technol.* vol. 8 no. 5, 2014, pp. 1035–1041.

[6] A. Facchinetti, S. Del Favero, G. Sparacino, C. Cobelli, "Model of glucose sensor error components: identification and assessment for new Dexcom G4 generation devices", in *Med. Biol. Eng. Comput.* vol. 53, 2015, pp. 1259–1269.

[7] R. Visentin et al., "Circadian variability of insulin sensitivity: Physiological input for in silico artificial pancreas", in *Diabetes Technol. Ther.* vol. 17 no. 1, 2015, pp. 1-7.

[8] P. Herrero, et. al., "Advanced insulin bolus advisor based on run-to-run control and case-based reasoning.", in *IEEE J. Biomed. Health Inf.* vol. 15 no. 3, 2015, pp. 1087-1096.

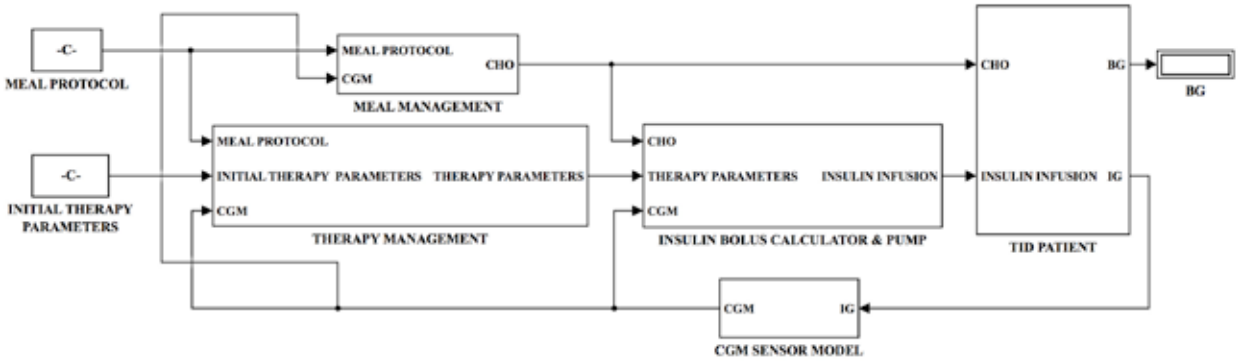

Fig. 1. Simulation Framework Scheme for T1D patient.

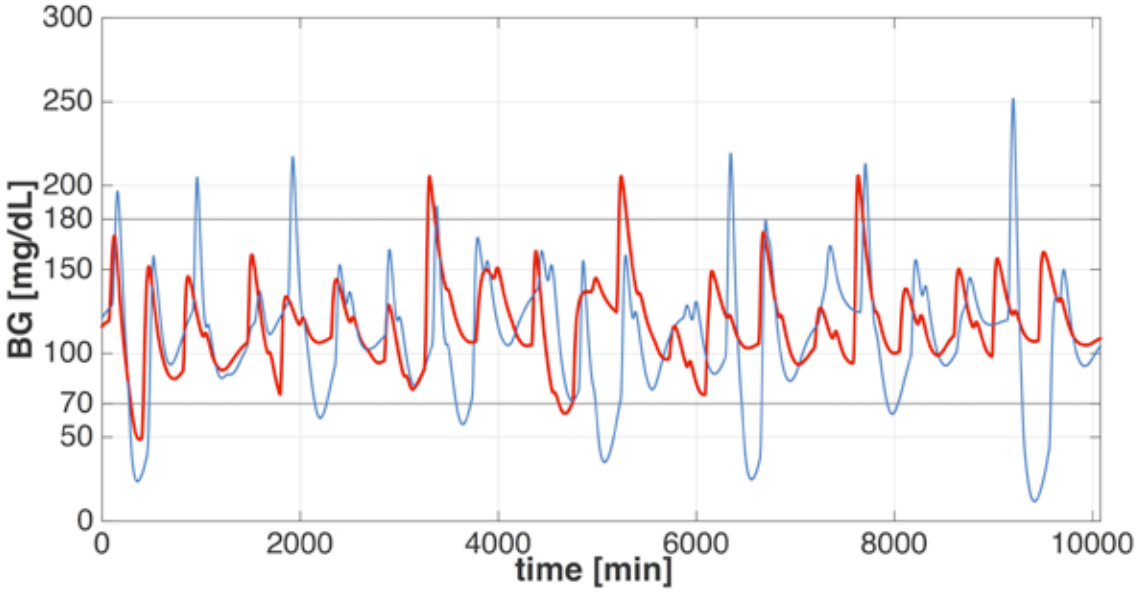

Fig. 2. Representative results of BG concentration profile of patient#6 for a 7-days period simulation. In blue, the BG profile obtained without optimizing the therapy parameters. In red, the same profile obtained with the R2R technique.

Viscoelasticity-assisted particle manipulation in microfluidics

M. De Corato[1], F. Del Giudice[2], M. Trofa[3], M.M. Villone[4], G. D'Avino[3], F. Greco[5], and P.L. Maffettone[3]

[1] *Imperial College London*
[2] *Okinawa Institute of Science and Technology*
[3] *Università degli Studi di Napoli "Federico II"*
[4] *Istituto Italiano di Tecnologia*
[5] *Consiglio Nazionale delle Ricerche*

***Abstract*— Manipulation of suspensions of particles of biological interest in microfluidic devices is required in counting, detecting, and sorting applications. Viscoelasticity of the suspending medium has proved to be an effective tool to control particle trajectories in devices with very simple geometries.**

***Keywords*—Microfluidics, Viscoelastic Focusing, Slippery Particles**

Manipulation of particles suspended in fluids flowing in microfluidic channels is required in a variety of biological, diagnostic and therapeutic applications. For instance, alignment of particles into a tight stream is a necessary step prior to counting, detecting, and sorting operations. Generally, this task is accomplished by using a Newtonian fluid as suspending medium and by properly fabricating a complex device aimed at displacing particle trajectories [1].

In the last years, however, the use of polymeric liquids in microfluidic processes has received a growing interest. Indeed, the addition of a small amount of a polymer in a Newtonian liquid flowing in a channel promotes the onset of elastic forces that can be exploited to manipulate the trajectories of suspended particles in simple devices, offering the possibility to align particles in simple straight microfluidic channels [2-5]. Experiments have been performed to investigate the effect of the channel length, flow rate, confinement ratio (i.e., the ratio between the particle and channel size) and fluid rheology on particle alignment [5-7].

Mofreover, particle alignment induced by fluid viscoelasticity can be combined with magnetophoresis to deflect magnetic beads in a H-shaped channel. High-efficiency separation of magnetic and non-magnetic beads is demonstrated [8].

All the aforementioned studies assume the validity of the *no-slip boundary condition* at all solid-fluid interfaces, i.e., the equality between the fluid velocity and the velocity of the solid surface immediately in contact with it. In some actual circumstances, however, such condition can be violated. This is indeed the case in many systems with at least one characteristic dimension of the order of microns, or smaller. In addition, elastic fluids, like polymer solutions, may show a relevant slip, that affects the migration of suspended particles [9].

REFERENCES

[1] N. Pamme, "Continuous flow separations in microfluidic devices", *Lab on a Chip*, 7, 1644-1659 (2007).

[2] M.M. Villone, G. D'Avino, M.A. Hulsen, F. Greco and P.L. Maffettone, "Simulations of viscoelasticity-induced focusing of particles in pressure-driven micro-slit flow", *Journal of Non-Newtonian Fluid Mechanics,* 166, 1396-1405 (2011).

[3] G. D'Avino, G. Romeo, M.M. Villone, F. Greco, P.A. Netti and P. L. Maffettone, "Single line particle focusing induced by viscoelasticity of the suspending liquid: theory, experiments and simulations to design a micropipe flow-focuser", *Lab on a Chip*, 12, 1638–1645 (2012)

[4] M.M. Villone, G. D'Avino, M.A. Hulsen, F. Greco and P.L. Maffettone, "Particle motion in square channel flow of a viscoelastic liquid: Migration vs secondary flows", *Journal of Non-Newtonian Fluid Mechanics,* 195, 1-8 (2013).

[5] G. Romeo, G. D'Avino, F. Greco, P.A. Netti and P. L. Maffettone, "Viscoelastic flow focusing in microchannels: scaling properties of the particle radial distributions", *Lab on a Chip*, 13, 2802-2807 (2013).

[6] F. Del Giudice, G. Romeo, G. D'Avino, F. Greco, P. A. Netti and P. L. Maffettone, "Particle alignment in a viscoelastic liquid flowing in a square-shaped microchannel", *Lab on a Chip*, 13, 4263-4271 (2013).

[7] F. Del Giudice, G. D'Avino, F. Greco, P. A. Netti and P. L. Maffettone, "Effect of fluid rheology on particle migration in a square-shaped microchannel", *Microfluidics and Nanofluidics,* 19*, 95-104* (2015).

[8] F. Del Giudice, H. Madadi, M. M. Villone, G. D'Avino, A. Cusano, R. Vecchione, M. Ventre, P. L. Maffettone and P. A. Netti, "Magnetophoresis 'meets' viscoelasticity: Deterministic separation of magnetic particles in a modular microfluidic device", *Lab on a Chip*, 15, 1912-1922 (2015).

[9] M. Trofa, G. D'Avino, M. A. Hulsen, F. Greco and P. L. Maffettone, "Numerical simulations of the dynamics of a slippery particle in Newtonian and viscoelastic fluids subjected to shear and Poiseuille flows", *Journal of Non-Newtonian Fluid Mechanics*, 228, 46-54 (2016).

Simulating the electromechanical response of a cardiac ventricular wedge affected from concentric hypertrophy: effects of growth and fibre dispersion

Fabrizio Del Bianco[1,2], Piero Colli Franzone[3], Simone Scacchi[4], and Lorenzo Fassina[1,2]
[1] *Department of Electrical, Computer and Biomedical Engineering, University of Pavia, Pavia, Italy*
[2] *Centre for Health Technologies (C.H.T.), University of Pavia, Pavia, Italy*
[3] *Department of Mathematics, University of Pavia, Pavia, Italy*
[4] *Department of Mathematics, University of Milano, Milano, Italy*

***Abstract*—We investigate qualitatively the epicardial electromechanical response of an *in silico* cardiac ventricular wedge under both healthy and concentric hypertrophic conditions. This is achieved by taking into account the growth of the wedge thickness and the fibre dispersion that may follow.**

***Keywords*—Electromechanical model, cardiac concentric hypertrophy, growth, fibre dispersion.**

I. Introduction

CARDIAC concentric hypertrophy is often a pathological remodelling caused by a long-term pressure overload inside ventricles [1]. This phenomenon leads to a progressive intracellular deposition of new sarcomere units in parallel to the preexistent ones and a possible increase in the angular dispersion of fibres. In this paper, we study how growth and fibre dispersion correlate with changes in the electromechanical response of a simulated ventricular wedge. To our knowledge, no previous *in silico* works have included both previous phenomena for mechanics (e.g. [2]-[4]) as we do instead. Moreover, electrophysiology is made dependent on growth and dispersion both at the cell and tissue scales.

II. Methods

A. The electrophysiological model

We employ the Bidomain model [5] coupled with the Faber-Rudy membrane model [6]. Considering a time interval of duration T, the complete model for a three-dimensional reference wedge Ω_0 is written as (simplified from [7])

$$\chi C_m \frac{\partial V}{\partial t} - J^{-1}\mathrm{Div}(J\mathbf{F}^{-1}\mathbf{D}_i\mathbf{F}^{-T}\mathbf{Grad}U_i) + \chi I_{ion}(V,\mathbf{w},\mathbf{c}) = 0 \quad \text{in } \Omega_0\times(0,T), \tag{1}$$

$$-\chi C_m \frac{\partial V}{\partial t} - J^{-1}\mathrm{Div}(J\mathbf{F}^{-1}\mathbf{D}_e\mathbf{F}^{-T}\mathbf{Grad}U_e) - \chi I_{ion}(V,\mathbf{w},\mathbf{c}) = i^e_{app} \quad \text{in } \Omega_0\times(0,T), \tag{2}$$

$$\frac{\partial \mathbf{w}}{\partial t} = \mathbf{R}_w(v,\mathbf{w}) \quad \text{in } \Omega\times(0,T), \tag{3}$$

$$\frac{\partial \mathbf{c}}{\partial t} = \mathbf{R}_c(v,\mathbf{w},\mathbf{c}) \quad \text{in } \Omega\times(0,T), \tag{4}$$

$$\mathbf{N}^T\mathbf{F}^{-1}\mathbf{D}_{i,e}\mathbf{F}^{-T}\mathbf{Grad}U_{i,e} = 0 \quad \text{in } \partial\Omega_0\times(0,T), \tag{5}$$

$$V(\mathbf{X},0) = V_0(\mathbf{X}) \quad \text{in } \Omega_0, \quad \mathbf{w}(\mathbf{x},0) = \mathbf{w_0}(\mathbf{x}), \quad \mathbf{c}(\mathbf{x},0) = \mathbf{c_0}(\mathbf{x}) \quad \text{in } \Omega, \tag{6}$$

where χ is the ratio of surface membrane area per tissue volume, C_m and I_{ion} are the capacitance and total ionic current per unit area of the surface membrane, i^e_{app} is the applied extracellular current stimulus per unit volume, U_i, U_e and V are the intracellular, extracellular and transmembrane potentials in Ω_0 (with $V=U_i-U_e$), v is the corresponding transmembrane potential in the current configuration $\Omega(t)$, **w** and **c** represent the gating variables or ionic intracellular concentrations from the Faber-Rudy model and $\mathbf{D_i}$ and $\mathbf{D_e}$ are the orthotropic intra- and extracellular conductivity tensors defined in $\Omega(t)$ and built upon the conductivity values taken from [7]. Moreover, J is the determinant of the deformation gradient tensor $\mathbf{F}=\mathbf{dx}/\mathbf{dX}$ (related to the deformation map $\Omega_0\rightarrow\Omega(t)$ with **X** and $\mathbf{x}=\mathbf{x}(\mathbf{X},t)$ the coordinates in Ω_0 and $\Omega(t)$ respectively) and Div and **Grad** stand for the operators divergence and gradient relative to **X**. At last, Equation (5) imposes the electrical insulation of the tissue boundary $\partial\Omega_0$.

B. The mechanical model

Growth is modelled by the multiplicative decomposition of the tensor **F** into an elastic part $\mathbf{F^e}$ and a growth part $\mathbf{F^g}$ [2][3]

$$\mathbf{F}=\mathbf{F^e}\mathbf{F^g}. \tag{7}$$

In particular, concentric growth is introduced by writing $\mathbf{F^g}$ as in [2]

$$\mathbf{F^g}=\mathbf{I}+(\theta_s-1)\mathbf{s_0}\otimes\mathbf{s_0}, \tag{8}$$

where $\mathbf{s_0}$ is the local sheet direction in Ω_0 and θ_s is a growth parameter.

Disregarding any volume forces and taking into account a quasi-static regime, equilibrium turns out to be [8]

$$\mathbf{Div(FS)} = \mathbf{0} \quad \text{in } \Omega_0\times(0,T), \tag{9}$$

where **S** is the second Piola-Kirchhoff stress tensor. **S** is computed from [2]

$$\mathbf{S}=(\mathbf{F^g})^{-1}\mathbf{S^e}(\mathbf{F^g})^{-T}, \tag{10}$$

where $\mathbf{S^e}$ is the elastic part of **S**. $\mathbf{S^e}$ includes both an active component $\mathbf{S^{e,act}}$, depending on the active tension T_a, and a passive component $\mathbf{S^{e,pas}}$ [4][7]

$$S^e_{MN}=S^{e,act}_{MN}+S^{e,pas}_{MN}=T_a\left(\frac{k_f}{1-2k_f}(C^e)^{-1}_{MN}+\frac{1-3k_f}{1-2k_f}\frac{1}{\mathbf{f_0}^T\mathbf{C^e}\mathbf{f_0}}f_{0,M}f_{0,N}\right)+\frac{1}{2}\left(\frac{\partial W}{\partial E^e_{MN}}+\frac{\partial W}{\partial E^e_{NM}}\right) \tag{11}$$

with M,N=1,2,3. $\mathbf{C^e}=(\mathbf{F^e})^T\mathbf{F^e}$ is the elastic part of the Cauchy-Green deformation tensor **C**, $\mathbf{E^e}=1/2(\mathbf{C^e}-\mathbf{I})$ is the elastic part

of the Lagrange-Green strain tensor $\mathbf{E}$, $\mathbf{f_0}$ is the local fibre direction in Ω_0 and k_f is a fibre dispersion parameter. The passive myocardium is modelled as an almost incompressible hyperelastic material. Hence, $\mathbf{S^{e,pas}}$ is derived from a strain-energy function W that includes a volumetric term. In particular, we adopt the orthotropic law proposed by Holzapfel [9] adding a quasi-incompressibility term [10]

$$W=\frac{a}{2b}\exp[b(I_1^e-3)]+\frac{a_f}{2b_f}(\exp[b_f(I_{4f}^e-1)^2]-1)+\frac{a_s}{2b_s}(\exp[b_s(I_{4s}^e-1)^2]-1)+ \\ +\frac{a_{fs}}{2b_{fs}}(\exp[b_{fs}(I_{8fs}^e)^2]-1)+c(\sqrt{\det(\mathbf{C}^e)}-1)^2, \quad (12)$$

where $I_1^e=\mathbf{C}^e:\mathbf{I}$, $I_{4f}^e=k_f I_1^e+(1-3k_f)\mathbf{f_0}(\mathbf{C}^e\mathbf{f_0})$, $I_{4s}^e=\mathbf{s_0}(\mathbf{C}^e\mathbf{s_0})$ and $I_{8fs}^e=\mathbf{f_0}(\mathbf{C}^e\mathbf{s_0})$ are the elastic invariants [4][8], $\det(\mathbf{C}^e)$ is the determinant of $\mathbf{C}^e$ and the values for the parameters a, b, a_f, b_f, a_s, b_s, a_{fs}, b_{fs} and c are taken from [11] and [10].

The stretch- and stretch-rate-dependent active tension $T_a=T_a(\lambda^e,d\lambda^e/dt)$ in (11) is computed from the Land et al. model [12] by following the observations in [3] about the use of the elastic fibre stretch $\lambda^e=\mathrm{sqrt}(\mathbf{f_0}^T\mathbf{C}^e\mathbf{f_0})$.

C. Hypertrophic alterations

Growth is introduced by choosing $\theta_s=2$ [2], whereas fibre dispersion is obtained by setting $k_f=0.0886$ [4]; the healthy values are 1 and 0 respectively. Moreover, we refer to the same value of θ_s to define the semi-major axis A along $\mathbf{s_0}$ of the resultant cell elliptical cross-section, i.e. $A=\theta_s R$, where R is the cell radius; the semi-minor axis B, instead, is kept equal to R. In this way, the plasma membrane area and the cell volumes are affected. This, in turn, alters the ratio χ, which is computed as $\chi=\mathrm{sqrt}(2(A^2+B^2))/(AB)+2/L$ (with L the cell length) for an elliptic cylindrical cell. However, we divide χ by 2 to obtain a physiological transmural conduction velocity of about 0.03 cm/ms in case of the healthy wedge.

D. The tissue geometry and meshes

We model our ventricular wedge as a slab with the reference configuration in Fig. 1. Then, $\theta_s=2$ means that the initial thickness of the hypertrophic wedge is twice bigger than the one of the healthy wedge. The endocardium is kept fixed to avoid any rigid motion and a cluster of nodes towards one of its corners is delivered a current stimulus with amplitude equal to 250 mA/cm^3 and duration 1 ms. Fibers rotate linearly from epicardium (-45^o) to endocardium (+45^o). Electrical and mechanical components are approximated, respectively, on a uniform mesh of 200 × 200 × 50 or 40 × 40 × 10 trilinear finite elements (yielding a mesh size of 0.1 or 0.5 mm) and using a time step of 0.05 or 1 ms. We refer the reader to [7] for other details about the numerical methods employed.

III. Results and Discussion

Fig. 2 displays the extracellular potentials U_e (or unipolar electrograms EGs) in nine nodes of a uniform 3 × 3 grid central to the mechanical mesh on the epicardium (see Fig. 1) for the healthy wedge and the hypertrophic ones with only growth or together with fibre dispersion. In the healthy wedge, the EGs located in the early excited and repolarized epicardial area show a deep Q wave in the local QRS complex followed by a positive T wave. When the epicardium is half excited and half repolarized, the EGs at sites on this boundary exhibit positive R and negative S waves with about the same amplitude followed by biphasic T waves. Finally, large R and negative T waves indicate a late excitation and repolarization. These EG morphologies are in agreement with those observed in measured and simulated EGs elicited by local stimulation in dogs (see [13]). When growth is incorporated, in the early excited and repolarized epicardial sites, the EGs display a local QRS complex with Q and S waves of the same amplitude and large R waves followed by multiphasic T waves. Conversely, in the late excited and repolarized sites, the EGs exhibit large R waves followed by negative T waves as in the healthy wedge. In those sites excited when the epicardium is half activated and half repolarized, the EGs show R and S waves with the same amplitude and biphasic T waves similarly to the healthy case again. The presence of fibre dispersion does not change further the morphology of EGs. However, the trajectories described by the nine nodes in the xy plane in Fig. 3 enlarge not only with growth but also with fibre dispersion. This means that the ventricular wedge requires more and more energy to beat and overcome its maladaptive remodelling.

References

[1] L. A. Taber, "Biomechanics of growth, remodeling, and morphogenesis," *Appl Mech Rev,* vol. 48, pp. 487–545, 1995.

[2] S. Göktepe, O. J. Abilez, K. K. Parker, and E. Kuhl, "A multiscale model for eccentric and concentric cardiac growth through sarcomerogenesis," *J Theor Biol,* vol. 265, pp. 433–442, 2010.

[3] L. C. Lee, J. Sundnes, M. Genet, J. W. Wenk, and S. T. Wall, "An integrated electromechanical-growth heart model for simulating cardiac therapies," *Biomech Model Mechanobiol*, in press.

[4] T. S. E. Eriksson, A. J. Prassl, G. Plank, and G. A. Holzapfel, "Modeling the dispersion in electromechanically coupled myocardium," *Int J Numer Method Biomed Eng*, vol. 29, pp. 1267–1284, 2013.

[5] P. Colli Franzone, L. F. Pavarino, and S. Scacchi, *Mathematical cardiac electrophysiology*. Cham: Springer, 2014.

[6] G. M. Faber, and Y. Rudy, "Action potential and contractility changes in $[Na^+]_i$ overloaded cardiac myocytes: a simulation study," *Biophys J*, vol. 78, pp. 2392–2404, 2000.

[7] P. Colli Franzone, L. F. Pavarino, and S. Scacchi, "Bioelectrical effects of mechanical feedbacks in a strongly coupled cardiac electro-mechanical model," *Math Mod Meth Appl S*, vol. 26, pp. 27-57, 2016.

[8] G. A. Holzapfel, *Nonlinear solid mechanics*. Chichester: John Wiley & Sons, 2000.

[9] G. A. Holzapfel and R. W. Ogden, "Constitutive modelling of passive myocardium: a structurally based framework for material characterization," *Philos Trans A Math Phys Eng Sci*, vol. 367, pp. 3445–3475, 2009.

[10] F. J. Vetter and A. D. McCulloch, "Three-dimensional stress and strain in passive rabbit left ventricle: a model study," *Ann Biomed Eng*, vol. 28, pp. 781–792, 2000.

[11] H. M. Wang et al., "Structure-based finite strain modelling of the human left ventricle in diastole," *Int J Numer Method Biomed Eng*, vol. 29, pp. 83–103, 2013.

[12] S. Land et al., "An analysis of deformation-dependent electromechanical coupling in the mouse heart," *J Physiol*, vol. 590, pp. 4553–4569, 2012.

[13] P. Colli Franzone, L. Guerri, M. Pennacchio, and B. Taccardi, "Anisotropic mechanisms for multiphasic unipolar electrograms: simulation studies and experimental recordings," *Ann Biomed Eng*, vol. 28, pp. 1326–1342, 2000.

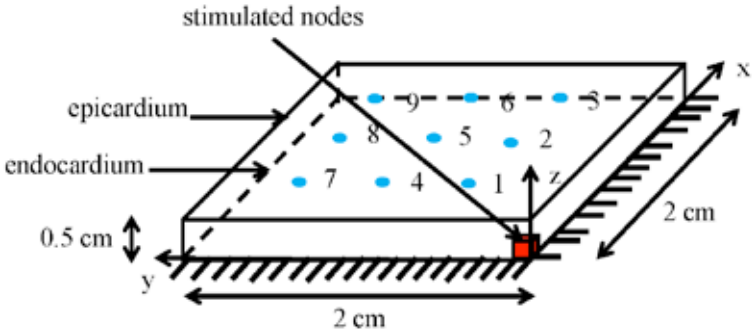

Fig. 1. Reference configuration for the ventricular wedge. A 2 cm × 2 cm × 0.5 cm slab with a fixed endocardium is adopted. The red cube of nodes is given the electrical stimulus. Nine points (denoted by numbered blue spots) belonging to a uniform 3 × 3 grid central to the mechanical mesh on the epicardium are chosen for showing results in Figs. 2 and 3.

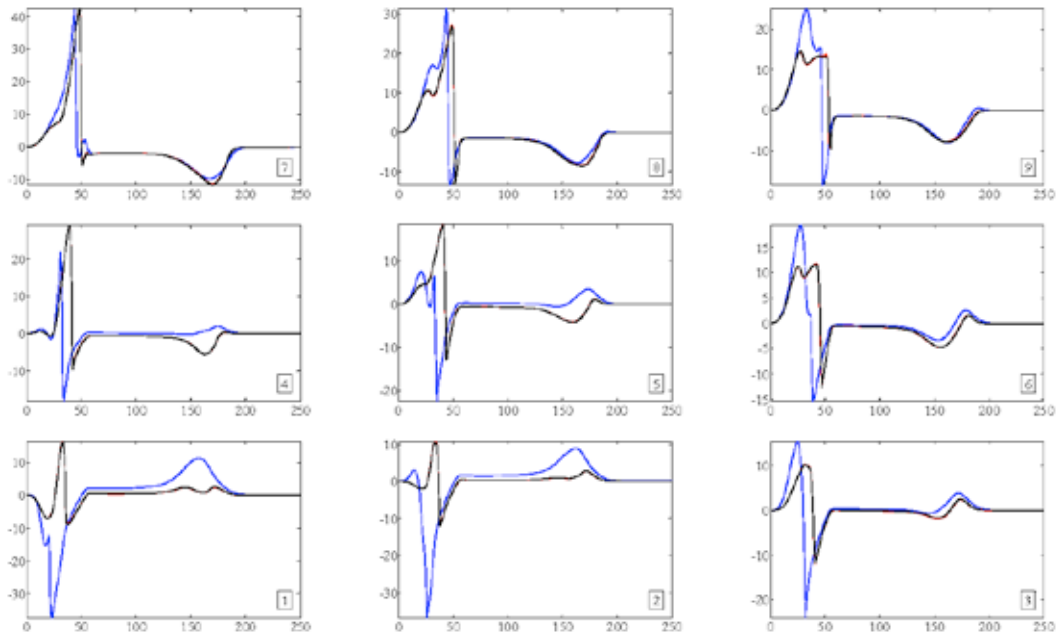

Fig. 2. Epicardial electrograms computed in the nine selected nodes of Fig. 1 for the healthy case (blue coloured), the hypertrophic one with only growth (red coloured) and the one with growth and fibre dispersion (black coloured); all values on the abscissa are in ms, whereas the ones on the ordinate are in mV.

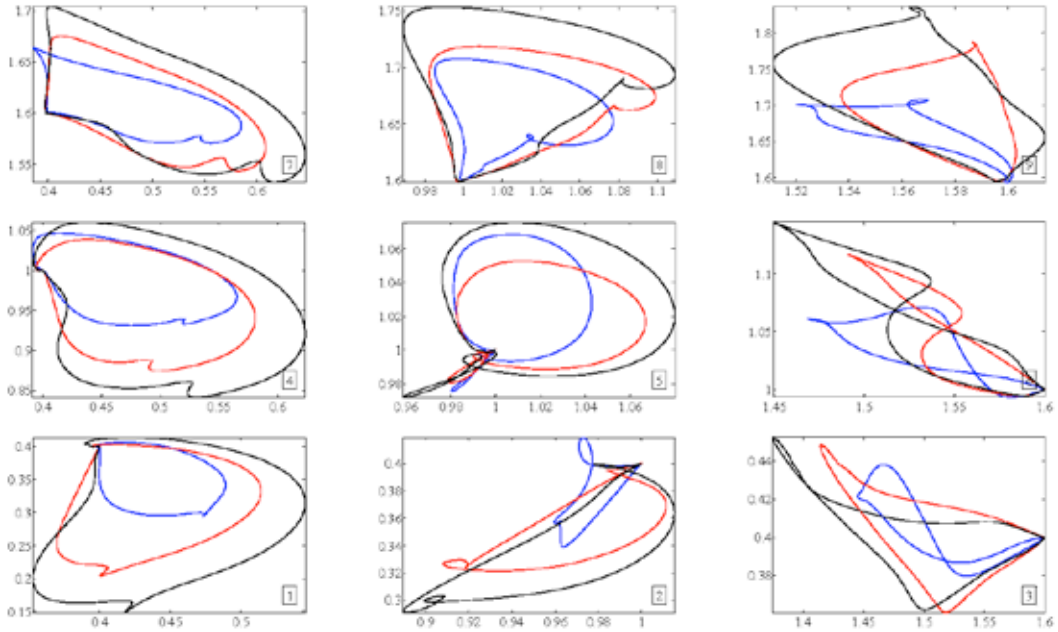

Fig. 3. Trajectories in the xy plane computed in the same nine selected nodes of Fig. 1 for the healthy case (blue coloured), the hypertrophic one with only growth (red coloured) and the one with growth and fibre dispersion (black coloured); all values are in cm.

Exploiting mathematical modelling to address the enigmas of glucagon secretion

Francesco Montefusco and Morten Gram Pedersen
Department of Information Engineering, University of Padova, Via Gradenigo 6/B, 35131 Padova

***Abstract*—The main mechanisms underlying glucagon secretion from pancreatic alpha-cells are still unclear and, when defective, are involved in the development of diabetes. Here we address this aim by developing a mathematical model that couples electrical activity and exocytosis to achieve a full picture of the role of the mechanisms underlying glucagon release. We devise a detailed model of Ca^{2+} dynamics by exploiting compartmental modelling of Ca^{2+} levels near open and closed high voltage-activated Ca^{2+} channels involved in exocytosis, in the sub-membrane Ca^{2+} compartment, in the bulk cytosol and in the endoplasmic reticulum. The model reproduces the effects of glucose, glucagon-like peptide 1 (GLP-1) and adrenaline, providing insight into the relative contributions of the various subcellular Ca^{2+} compartments in the control of glucagon secretion. Our results highlight that the number of open Ca^{2+} channels is a dominant factor in glucagon release, and clarify why cytosolic Ca^{2+} is a poor read-out of alpha-cell secretion.**

***Keywords*—Electrical activity, intracellular Ca^{2+} dynamics, exocytosis, computational model.**

I. Introduction

THE control of glucagon secretion from pancreatic alpha-cells, despite decades of investigations, is still unclear [1] and, when defective, is involved in the development of diabetes [2]. Hence, alpha-cells are being considered as a possible pharmacological target for the treatment of diabetes [3] and, for this reason, a better understanding of the regulation of glucagon exocytosis in response to glucose and other physiological factors is needed.

Glucose-induced inhibition of glucagon has been proposed to be due to a direct glucose effect on the alpha-cells, or alternatively, to paracrine factors released from neighbouring islet cells (such as insulin, zinc or GABA from beta-cells or somatostatin from delta-cells) that inhibit alpha-cells [1], [4]. However, two alternative theories have recently pointed out the important role for direct, intrinsic regulation of glucagon in physiological glucose range. One proposal suggests that glucose increase leads to a reduced conductivity of ATP-sensitive K^+ (KATP) channels resulting in a slight membrane depolarization, which prevents full action potential generation needed for complete activation of high voltage-activated (HVA) P/Q-type Ca^{2+} channels involved in exocytosis [4]-[5] (see Fig. 1, the purple lines in box A). The other proposal [6] claims that glucose stimulates calcium uptake into the endoplasmic reticulum (ER) (Fig. 1, box B), which terminates a store-operated current (SOC) leading to membrane hyperpolarization (Fig. 1, box A).

Further studies have shown that paracrine effects such as inhibition of glucagon secretion by glucagon-like peptide 1 (GLP-1) or stimulation of release by adrenaline involve cyclic adenosine monophosphate (cAMP)-mediated effects downstream of electrical activity [7] (Fig. 1, box C). On the one hand, GLP-1 causes a small increase in intracellular cAMP concentration that activates protein kinase A (PKA), leading to inactivation of the P/Q-type Ca^{2+} channels. On the other hand, adrenaline produces a large increase in intracellular cAMP concentration, leading not only to the inhibition of the P/Q type Ca^{2+} channels, as for GLP-1, but also to the activation of the low-affinity cAMP sensor Epac2, which mobilizes or primes granules at the HVA L-type Ca^{2+} channels and stimulates L-type Ca^{2+} currents.

In contrast to the long tradition of theoretical and computational investigations of electrical activity, exocytosis, and other aspects of beta-cell function [8], very little modelling has been performed for alpha-cells. Recent models have focused on the regulation of alpha-cell electrical activity as a result of glucose application [9]-[11], whereas glucagon exocytosis was mainly a read-out of electrical activity.

In this paper, to investigate theoretically the different aspects of alpha-cell function, such as electrical activity (Fig. 1, box A), calcium influx and diffusion (Fig. 1, box B) granule dynamics and exocytosis (Fig. 1, box C), we devise a model that characterizes in detail ion channels, the intracellular calcium dynamics and possible priming or recruitment of granules around the Ca^{2+} channels of various types. Our model allows us to reproduce different and independent experimental data, such as the effects of glucose and hormones (GLP-1 and adrenaline) on glucagon secretion, and to increase our understanding of the main control mechanisms operating in the alpha-cells.

II. Methods and results

The devised mathematical model of electrical activity and exocytosis in mouse alpha-cells is an updated version of previous models [9], [11], based on recent experimental data [5], [7]. Although alpha-cell electrical activity is well studied [9]-[11], coupling to exocytosis is not. Therefore, our model couples the electrical activity and exocytosis to give a unified picture of the main mechanisms that control glucagon secretion; we model exocytosis as depending on Ca^{2+} concentrations in the microdomains surrounding the P/Q- and L-type Ca^{2+} channels, $Ca_{P/Q}$ and Ca_L respectively, and the sub-membrane Ca^{2+} concentration, Ca_m. Moreover, we also consider the bulk cytosolic, Ca_c, and the endoplasmic-reticulum (ER), Ca_{er}, Ca^{2+} concentrations, in order to characterize the complete Ca^{2+} dynamics. The complete details of the model are given in [12]. Here, we show how the model is able to reproduce the effects of glucose increase as well as GLP-1 and adrenaline on glucagon exocytosis.

A. Effects of glucose increase on glucagon secretion

Fig. 2 shows the results of the devised model reproducing the effect of the glucose increase by decreasing the KATP-

channel conductance, g_{KATP}, [5], and increasing the leak conductance, g_L (see Eq. (1) in [12]). The model is able to reproduce electrical activity characterized by spikes with reduced amplitude due to the inhibitory effect of the glucose increase (Fig. 2A). The decrease of spike amplitude determines a significant reduction in glucagon secretion; in particular, the P/Q-type Ca^{2+} channel-dependent secretion, $GS_{P/Q}$ (defined by Eq. (15) in [12]) is significantly reduced (see the dashed-dotted plot in Fig. 2B showing the glucagon secretion rate from the P/Q-type microdomains, $GSR_{P/Q}$) because few P/Q-type Ca^{2+} channels are activated (Fig. 2E). Thus, it is the reduction of the number of open P/Q-type Ca^{2+} channels rather than a variation in local Ca^{2+} levels (Figs. 2C and 2G) or in cytosolic Ca^{2+} levels (Fig. 2H) that underlies the inhibition of glucagon release by glucose in the model. The L-type Ca^{2+} channels are not relevant for the glucagon secretion (Figs. 2B, 2D and 2F).

B. Effects of GLP-1 on glucagon secretion

Fig. 3 shows the results of the model reproducing the effect of GLP-1 by increasing the parameter $V_{mCaP/Q}$ of the steady state activation curve of the P/Q-type Ca^{2+} channels (see Eq. (2) in [12]), reflecting the GLP-1 mediated reduction of P/Q-type Ca^{2+} currents [7], and decreasing the leak conductance g_L (see Eq. (1) in [12]). The model reproduces the transient hyperpolarization of the cell and subsequently depolarization due to the simulated inhibitory effect of GLP-1, as observed experimentally [7] (Fig. 3A). The P/Q-type Ca^{2+} channel-dependent secretion, $GS_{P/Q}$, after the transient, is significantly reduced (see the dashed-dotted plot in Fig. 3B showing $GSR_{P/Q}$) due to the increase of $V_{mCaP/Q}$: the P/Q-type Ca^{2+} channels are closed (Fig. 3E). Thus, as above, it is the closing of the P/Q-type Ca^{2+} channels rather than a change in local Ca^{2+} levels (Figs. 3C and 3G) or in cytosolic Ca^{2+} levels (Fig. 3H) that underlies the inhibition of glucagon release by GLP-1 in the model. As for the previous case, the L-type Ca^{2+} channels are not relevant for the glucagon secretion (Figs. 3B, 3D and 3F).

C. Effects of adrenaline on glucagon secretion

Fig. 4 shows the results of the model reproducing the effect of adrenaline at low (1 mM) and at physiological (6 mM) glucose levels. The adrenaline effect is reproduced by increasing the L-type Ca^{2+} channel conductance, g_{CaL}, and decreasing the threshold value for exocytosis near L-type Ca^{2+} channels, K_L (se Eqs. (1), (16) and (17) in [12]), in order to reproduce the Epac2-mediated increase of the L-type Ca^{2+} currents and possible priming or recruitment of granules around the L-type Ca^{2+} channels [7], [13]. Moreover, we increase the leak conductance, g_L, and the parameter $V_{mCaP/Q}$ as for the simulated GLP-1 effect. At physiological glucose levels, we also decrease g_{KATP} as simulated for the glucose effects. At both glucose levels, in response to adrenaline, the simulated electrical activity exhibits reduced spike amplitude with an additional decrease at the higher glucose level (see Fig. 4A). The L-type Ca^{2+} channels mainly determine the glucagon secretion increase (see the dashed plot in Fig. 4B showing GSR_L) due to adrenaline: the microdomain Ca^{2+} concentration surrounding the open L-type Ca^{2+} channels (Fig. 4D) increases at both glucose levels and is much higher than the threshold value K_L, whose value is decreased considerable [12]. This effect compensates for the small decrease of the probability for the L-type Ca^{2+} channels to be opened (Fig. 4F). The P/Q-type Ca^{2+} channel-dependent secretion is significantly reduced, as shown for the simulated GLP-1 effect (Figs. 4C and 4E). The secretion depending on the sub-membrane Ca^{2+} concentration, GS_m (defined by Eq. (18) in [12]), decreases slightly (Figs. 4B and 4G), while the intracellular Ca^{2+} concentration shows a small increase (Fig. 4H).

III. CONCLUSION

The model reproduces the effects of glucose increase as well as GLP-1 and adrenaline on electrical activity and glucagon secretion, by simulating changes of ion channel characteristics (i.e. conductance, inactivation and activation functions), granule availability, and putative priming or recruitment of granules around the HVA Ca^{2+} channels. Most of the changes are experimentally supported, while others are speculative in order to reproduce the experimental data and could guide new experiments to validate our hypotheses.

REFERENCES

[1] J. Gromada, I. Franklin, and C. B. Wollheim, "Alpha-cells of the endocrine pancreas: 35 years of research but the enigma remains," *Endocr Rev*, vol. 28, no. 1, pp. 84–116, Feb. 2007.

[2] D. D'Alessio, "The role of dysregulated glucagon secretion in type 2 diabetes," *Diabetes Obes Metab*, vol. 13 Suppl 1, pp. 126–132, Oct. 2011.

[3] M. Christensen, J. I. Bagger, T. Vilsboll, and F. K. Knop, "The alpha-cell as target for type 2 diabetes therapy," *Rev Diabet Stud*, vol. 8, no. 3, pp. 369–381, 2011.

[4] J. N. Walker et al., "Regulation of glucagon secretion by glucose: paracrine, intrinsic or both?," *Diabetes Obes Metab*, vol. 13 Suppl 1, pp. 95–105, Oct. 2011.

[5] Q. Zhang et al., "Role of KATP channels in glucose-regulated glucagon secretion and impaired counterregulation in type 2 diabetes," *Cell Metab*, vol. 18, no. 6, pp. 871–882, Dec. 2013.

[6] Y.-J. Liu, E. Vieira, and E. Gylfe, "A store-operated mechanism determines the activity of the electrically excitable glucagon-secreting pancreatic alpha-cell," *Cell Calcium*, vol. 35, no. 4, pp. 357–365, Apr. 2004.

[7] Y. Z. De Marinis et al., "GLP-1 inhibits and adrenaline stimulates glucagon release by differential modulation of N- and L-type Ca2+ channel-dependent exocytosis," *Cell Metab*, vol. 11, no. 6, pp. 543–553, Jun. 2010.

[8] M. G. Pedersen, G. Cortese, and L. Eliasson, "Mathematical modeling and statistical analysis of calcium-regulated insulin granule exocytosis in β-cells from mice and humans," *Prog Biophys Mol Biol*, vol. 107, no. 2, pp. 257–264, Nov. 2011.

[9] P. M. Diderichsen and S. O. Göpel, "Modelling the electrical activity of pancreatic alpha-cells based on experimental data from intact mouse islets," *J Biol Phys*, vol. 32, no. 3–4, pp. 209–229, Oct. 2006.

[10] L. E. Fridlyand and L. H. Philipson, "A computational systems analysis of factors regulating α cell glucagon secretion," *Islets*, vol. 4, no. 4, pp. 262–283, 2012.

[11] M. Watts and A. Sherman, "Modeling the pancreatic α-cell: dual mechanisms of glucose suppression of glucagon secretion," *Biophys J*, vol. 106, no. 3, pp. 741–751, Feb. 2014.

[12] F. Montefusco and M. G. Pedersen, "Mathematical modelling of local calcium and regulated exocytosis during inhibition and stimulation of glucagon secretion from pancreatic alpha-cells", *J Physiol*, vol. 593, no. 20, pp. 4519–4530, Oct. 2015.

[13] J. Gromada et al., "Adrenaline stimulates glucagon secretion in pancreatic A-cells by increasing the Ca2+ current and the number of granules close to the L-type Ca2+ channels," *J Gen Physiol*, vol. 110, no. 3, pp. 217–228, Sep. 1997.

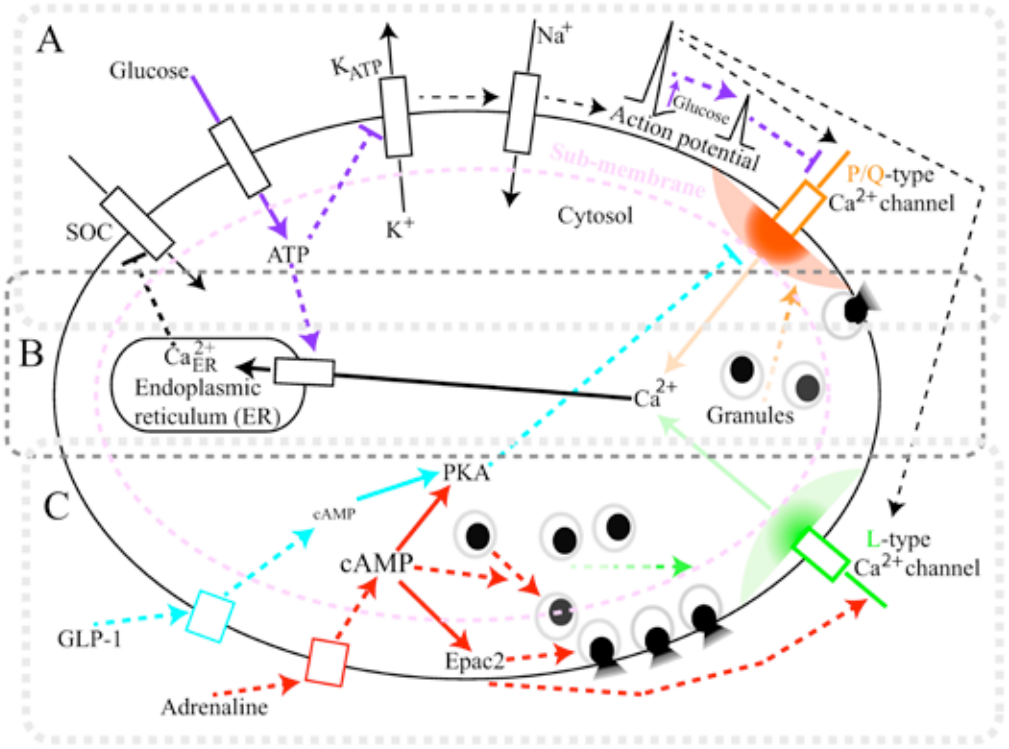

Fig. 1 Overview of the main mechanisms underlying glucagon secretion from alpha-cell in response to glucose and hormones. Box A: main channels determining alpha-cell electrical activity. Box B: calcium influx through HVA Ca^{2+} channels involved in exocytosis, Ca^{2+} diffusion and Ca^{2+} uptake from endoplasmic reticulum. Box C: inhibition of glucagon secretion by GLP-1 and stimulation of release by adrenaline.

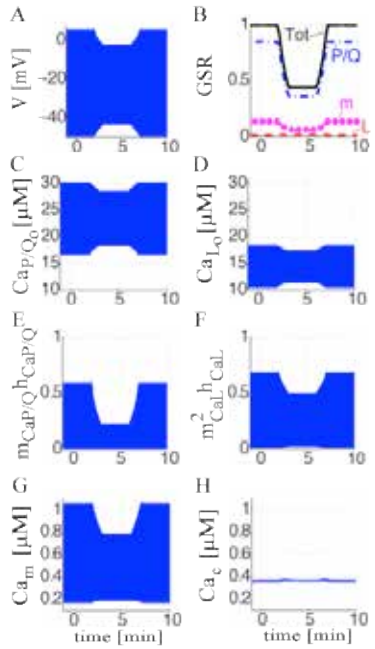

Fig. 2 Model results reproducing the effect of glucose increase between time t=2 min and t=6 min.

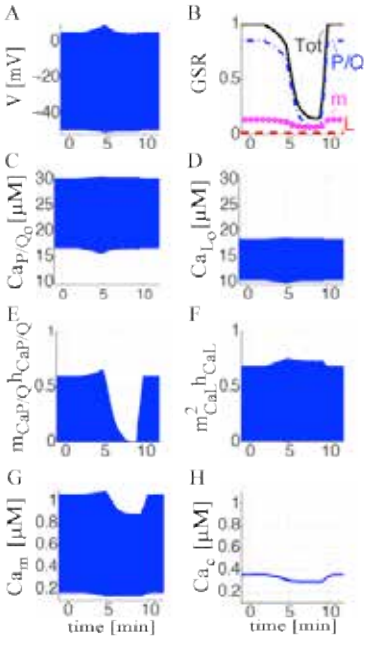

Fig. 3 Model results reproducing the effect of GLP-1 between time t=2 min and t=9 min.

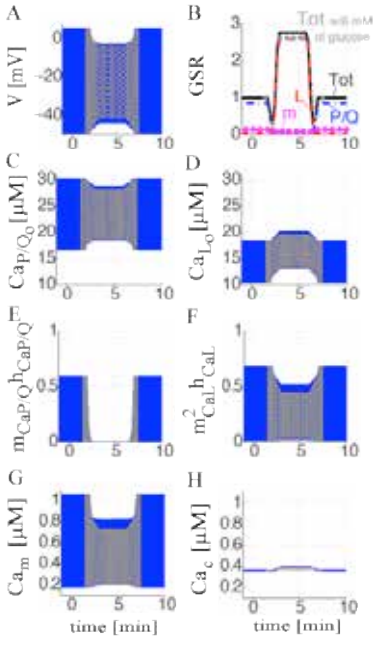

Fig. 4 Model results reproducing the effect of adrenaline between time t=2 min and t=6 min. Solid lines for the results at 1 mM of glucose, grey dotted lines for the results at 6 mM of glucose.

Simulated electrical activity (A) and the corresponding total glucagon secretion rate, GSR (solid plot in panel B), given by the sum of $GSR_{P/Q}$ (dashed-dotted), GSR_L (dashed), and GSR_m (dashed with circles). $GSR_{P/Q}$ is a function of the microdomains Ca^{2+} concentration surrounding the open P/Q-type Ca^{2+} channels, $Ca_{P/Qo}$ (C), the probability for the P/Q-type Ca^{2+} channels to be opened, $m_{CaP/Q}h_{CaP/Q}$ (E), its complement, and Ca_m (G) (see equations (15)-(16) in [12]). GSR_L is a function of the microdomains Ca^{2+} concentration surrounding the open L-type Ca^{2+} channels, Ca_{Lo} (D), the probability for the L-type Ca^{2+} channels to be opened, $m^2_{CaL}h_{CaL}$ (F), its complement, and Ca_m (G) (see equations (16)-(17) in [12]). GSR_m is a function of Ca_m (G) (see equation (18) in [12]). Cytosolic Ca^{2+} concentration, Ca_c, is reported in panel (H).

Evaluation of a tumor growth inhibition (TGI) model integrating dynamic energy budget (DEB) theory

E.M. Tosca[1], E. Borella[1], N. Terranova[2], M. Rocchetti and P. Magni[1]
[1] *Department of Electrical, Computer and Biomedical Engineering, University of Pavia, via Ferrata 5, Pavia, 27100, Italy*
[2] *Merck Institute for Pharmacometrics, Merck Serono S.A., Lausanne, Switzerland*

***Abstract*—Mathematical models for describing the tumor growth in animals often neglects the relationship between tumor and host organism. In this work we evaluate a new PK/PD DEB-based model able to describe the tumor-in-host growth kinetics under anticancer treatment and propose a comparative analysis between this tumor-in-host model and the Simeoni TGI model.**

***Keywords*—Tumor growth inhibition, DEB-based model, Cachexia, Drug development**

I. Introduction

CACHEXIA affects the majority of cancer patients and represents a common side effect of many types of chemotherapy. Hence, it is difficult to separate cancer cachexia from complications of anticancer therapy.

For this reason, in the preclinical studies the decrease in the net body weight is considered as a fundamental toxicological parameter to be evaluated. However, as the focus of these studies is to evaluate the anticancer activity, the impact of drug therapy on this important toxicity parameter is still obtained empirically by visual inspection of the animal body weight curves. In addition, mathematical models used to describe data on tumors growing in vivo often neglect the interactions between tumor and host organism.

To overcome this limitation, on the basis of the dynamic energy budget (DEB) theory [1], van Leeuwen et al. developed a tumor-in-host model able to describe the energetic interactions between tumor and host in rats [2].

Starting from this model and the Simeoni TGI model [3], a tumor-in-host DEB based model were defined to also include the pharmacological effect of anticancer treatments in xenograft mice [4]. The results is a model able to describe the pharmacological effect of a compound on the treated tumor as well as the side effects on the host nutrition on the basis of the energetic interactions.

Here a slightly revised model formulation and a new identification strategy are proposed. Moreover, a comparative study on the tumor growth in control groups between the DEB-TGI model and the widely used Simeoni TGI model is presented.

II. Theoretical: model presentation

A. Tumor-free and tumor-bearing individual model

The DEB theory [1] constitutes the general framework describing the host physiology; van Leeuwen et al. expanded this theory to include tumor growth, and showed its dependence on the host physiology as well as the effect of the tumor on its host [2]. The basic structure of the van Leeuwen model is illustrated in Fig 1.

B. Tumor-in-host DEB-based TGI model

The van Leeuwen model were modified in order to take into account the effect of an administered anticancer drug [4]. In particular, on the basis of the Simeoni TGI model the inhibition effect of an anticancer drug were modeled by assuming that a portion of proliferating cells becomes non-proliferating due to the anticancer treatment and goes to death through different stages of damage represented by a mortality chain. Furthermore, the drug side effect on the host body weight and a saturation phase in the tumor growth were introduced into the model. The resulted model is characterized by the equations reported in Fig. 2.

III. Methods

A. Dataset

Data for model validation refer to xenograft experiments conducted on Harlan Sprague Dawley mice. Average data of tumor and mice net body weight were considered for control and treated groups in several experiments involving six novel anticancer candidates and six drugs already available on the market. The PKs were derived from separated studies. The current example involves male mice treated with vehicle (arm a) and three groups treated with drug A following different schedules and doses (arms b, c and d).

B. Data analysis: fitting strategy

The PK/PD model were implemented in Monolix v. 4.3.3 and the experimental data were analysed adopting the following strategy. First, the physiological parameters of the tumor-free model were estimated on growth data of typical HSD mice or fixed to literature values; once identified the tumor-free individual model, obtained values were used to find the initial value for the energy reserve at the beginning of the experiment; finally, by fixing the tumor-free model parameters and the energy initial value, the tumor-related and the drug-related parameters were simultaneously estimated.

C. Comparative study: DEB-TGI and TGI Simeoni model

The similarity between the tumor growth profiles of the two TGI models were further investigated. In particular, a dynamic system analysis were accomplished to characterize

the phases of the tumor growth, then, model simulations were performed with Simulx to confirm the hypothesis emerged from the mathematical analysis.

IV. Results

A. Tumor-free model identification

The physiological parameters of the tumor-free model have been estimated on the growth data of male HSD mice. The obtained parameter values are reported in Tab. I.

TABLE I
PHYSIOLOGICAL PARAMETERS OF TUMOR-FREE MODEL

ξ	g	v	$V_{1\infty}$	m	e_0	w_0	ρ
-	-	*cm/week*	cm^3	*1/day*	-	g	-
0.2116	15	8.82	31.2	0.0267	0	1	1
-	6%	4%	3%	-	-	-	-

Physiological parameter values of the tumor-free model obtained from literature and data fitting (RSE are reported).

B. DEB-TGI model identification

By fixing the physiological parameters and the initial condition e_0 to the estimated values, the DEB-TGI model identification was performed against the control and the treated arms involving the same drug of several experiments. This allowed to estimate the same tumor-related and drug-related parameters in untreated and treated arms grouped by compound within experiment.

As an example, body weight and tumor growth profiles, obtained by simultaneously fitting of the control arm and the treated arms b and c, are shown in Fig. 3 together with the experimental data. The estimated parameters are reported in Tab.II. The goodness of the simultaneous fitting outlines the excellent model capabilities to describe experimental data coming from control and more groups treated with the same drugs by using a single set of parameters. Hence, the model drug-related parameters well characterize the drug potency independently from dose levels and schedules.

TABLE II
ESTIMATED PD PARAMETERS

μ_u	g_u	m_u	$\delta_{v_{max}}$	V_{u1_0}	W_0	ρ_b
-	-	*1/day*	-	cm^3	g	-
4.11	12.1	2.58e-4	0.131	0.0202	31.7	1
28%	26%	>100%	48%	30%	2%	-

K_1	K_2	C_{50}
1/day	*ml/mgday*	*mg/ml*
55.5	68.3	1.27e-4
>100%	14%	55%

Tumor-related and drug-related parameter estimates derived by simultaneously fitting of the control and single agent arms b and c (RSE are reported).

Model fitting results for the other analyzed experiments confirmed the model capability in well describing both body weight and tumor growth data from control and several treated groups. Of interest, tumor-related parameter were estimated to similar values in experiments involving the same tumor cell line.

C. DEB-TGI model predictive power

Since the proposed DEB-TGI model showed excellent fitting capabilities in all the considered experimental groups involving the control arm and different single arms, we decided to explore its predictive power. In particular, the tumor-related and drug-related parameters derived by fitting the control and the single agents arms b and c relative to drug A (Tab. II) were used to obtain the body weight and the tumor weight predictions for arm d involving drug A administered in a different schedule/dose. In Fig. 4, obtained prediction are shown together with the experimental data. Good predictive capabilities are indicated by the model predictions quite close to the experimental data. This suggests the potential use of the model for predicting new arms, by starting from parameter estimates obtained from arms involving the same compounds given in a different administration schedule/dose.

D. Comparative study: DEB-TGI and Simenoni TGI model

The mathematical analysis of the dynamic system showed that, as the Simeoni model, the DEB-TGI model predicts an exponential growth of the tumor in the early phases of its development. The exponential growth rate depends on several model parameters some of them related to the tumor cell lines and other to the host; its expression is reported below.

$$\hat{\lambda} = \frac{mg\mu_u}{g_u} - m_u.$$

Tumor weights of nine datasets were simulated with the DEB-TGI model using parameters obtained on the control groups of all the considered experiments. Then, the Simeoni model was identified on the simulated dataset, and parameter estimates were obtained: the two exponential growth rates have comparable values within each simulated control group. This result highlights that the parameter combination of the DEB-TGI model plays the same role within the dynamic system as the growth rate λ_0 in the Simeoni model. Further, it is worth to notice that the Simeoni switch between exponential and linear growth phases occurs always when the tumor slows down its growth, while the host degrades its structural biomass with a constant maximum rate, and the energy demand remains unfulfilled.

V. Conclusion

The tumor-in-host DEB-based model confirmed its good capability in describing tumor growth and host body growth even when an anticancer drug is administered. Moreover, from the comparative analysis a mechanistic meaning to the empirical unperturbed tumor growth function of the Simeoni model is provided by the new DEB-TGI model able to describe the energetic interaction between tumor and host.

Acknowledgement

This work was supported by the DDMoRe project (www.ddmore.eu).

References

[1] S. A. L. M. Kooijman, "Dynamic energy and mass budgets in biological systems," *Cambridge university press*, 2000.
[2] I. van Leeuwen, F. Kelpin, S. Kooijman, "A mathematical model that accounts for the effects of caloric restriction on body weight and longevity," *Biogerontology*, 3(6), 373–381, 2002.
[3] M. Simeoni, P. Magni, C. Cammia, G. De Nicolao G, V. Croci et al., "Predictive pharmacokinetic-pharmacodynamic modeling of tumor growth kinetics in xenograft models after administration of anticancer agents," *Cancer research*, 64(3), 1094-1101, 2004
[4] N. Terranova, F. Del Bene, M. Germani, M. Rocchetti, P. Magni, "An energy based model able to describe the effect of anticancer drugs on

tumor growth and host body weight," PAGE 23 Abstr 3176, 2014 .
Available: http://www.page-meeting.org/default.asp?abstract=3176

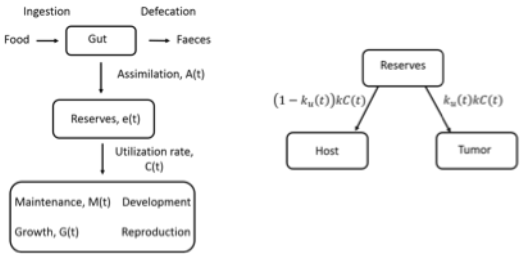

Fig. 1. Schematic representation of the DEB theory and van Leuween model concept; on the left energy fluxes in an individual organism, according to the DEB ; on the right energy-allocation rule in a tumor-bearing individual

$$\frac{dV(t)}{dt} \geq 0$$

$$\begin{cases} \frac{de(t)}{dt} = \frac{\nu}{V(t)^{1/3}}\left(\rho(t)\left(\frac{V_{1\infty}}{V_{u1}(t)+V(t)}\right)^{2/3} - e(t)\right) \\ \frac{dV(t)}{dt} = \frac{(1-k_u(t))\nu e(t)V(t)^{2/3} - gmV(t)}{(1-k_u(t))(e(t)+\omega g)} \\ \frac{dV_{u1}(t)}{dt} = \frac{(\nu V(t)^{2/3} + mV(t))gk_u(t)e(t)}{gg_u + (1-k_u(t))g_u e(t)} - m_u V_{u1}(t) - k_2 c(t) V_{u1}(t) \\ \frac{dV_{u2}(t)}{dt} = k_2 c(t) V_{u1}(t) - k_1 V_{u2}(t) \\ \frac{dV_{u3}(t)}{dt} = k_1 c(t) V_{u2}(t) - k_1 V_{u3}(t) \\ \frac{dV_{u4}(t)}{dt} = k_1 c(t) V_{u3}(t) - k_1 V_{u4}(t) \\ \rho(t) = \rho_b\left(1 - \frac{c(t)}{C_{50}+c(t)}\right) \\ W(t) = d_V(1+\xi e(t))V(t) \\ W_u(t) = d_{V_u}(V_{u1}(t) + V_{u2}(t) + V_{u3}(t) + V_{u4}(t)) \end{cases}$$

$$-\delta_{V_{max}} \leq \frac{dV(t)}{dt} < 0$$

$$\begin{cases} \frac{dV(t)}{dt} = \frac{(1-k_u(t))\nu e(t)V(t)^{2/3} - gmV(t)}{(1-k_u(t))(e(t)+\omega g)} \\ \frac{dV_{u1}(t)}{dt} = \left(\frac{mg\mu_u}{g_u} - m_u\right)V_{u1}(t) - k_2 c(t) V_{u1}(t) \end{cases}$$

$$\frac{dV(t)}{dt} < -\delta_{V_{max}}$$

$$\begin{cases} \frac{dV(t)}{dt} = -\delta_{V_{max}} \\ \frac{dV_{u1}(t)}{dt} = \frac{k_u(t)}{g_u}\left(e(t)\nu V(t)^{2/3} + \delta_{V_{max}} e(t) + \delta_{V_{max}}\omega g\right) - m_u V_{u1}(t) - k_2 c(t) V_{u1}(t) \end{cases}$$

Fig. 2. Equations of the DEB-TGI model; on the right the differential equations that change in the two cases different from dV/dt>0 are reported.

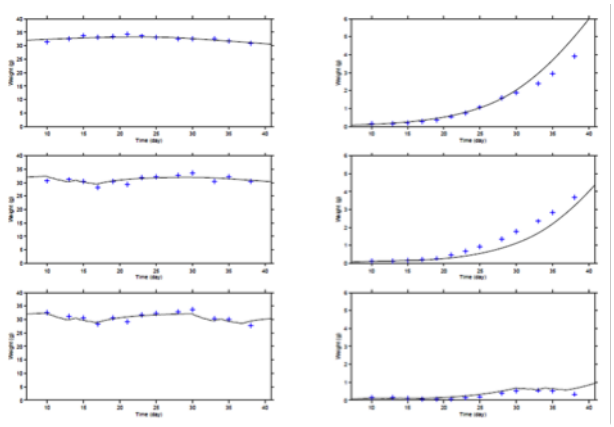

Fig. 3. Fitting results: on the top obtained body weight and tumor weight profiles together with experimental data are reported for the control group; below the corresponding profiles together with experimental data are shown for the treated arms b and c.

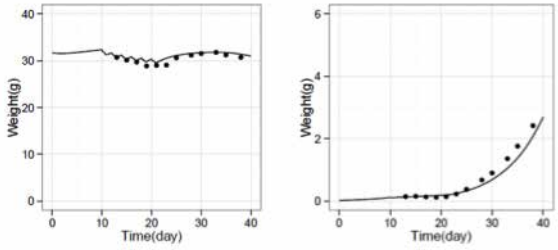

Fig. 4. Observed data and model predicted curves of the mice body weight (on the right) and the tumor growth (on the left) relative to arm d treated with Drug A.

Manipulation of soft particles in microfluidics

M. De Corato[1], F. Del Giudice[2], M. Trofa[3], M.M. Villone[4], G. D'Avino[3], F. Greco[5], and P.L. Maffettone[3]

[1] *Imperial College London*
[2] *Okinawa Institute of Science and Technology*
[3] *Università degli Studi di Napoli "Federico II"*
[4] *Istituto Italiano di Tecnologia*
[5] *Consiglio Nazionale delle Ricerche*

***Abstract*— Manipulation of suspensions of particles of biological interest in microfluidic devices is required in counting, detecting, and sorting applications. Viscoelasticity of the suspending medium has proved to be an effective tool to control particle trajectories in devices with very simple geometries.**

***Keywords*—Microfluidics, Viscoelastic Focusing, Slippery Particles**

A great variety of analytical and processing issues, such as separation, sorting, counting, and detection, require the capability of controlling the trajectories of particles suspended in fluids under continuous flow [1]. Several techniques suitable for this purpose are based on microfluidic flowcells, yielding specific particle patterns [2]. In particular, the ability to generate single-file particles (the so called "3D-focusing") is important in many applications.

A wide range of microfluidic particle focusing techniques are reported in the literature. Recently, it has been proposed to exploit the viscoelasticity of the suspending medium to induce the lateral motion of rigid particles. Experimental and numerical studies demonstrate that viscoelasticity-induced focusing is an effective method for particle alignment in a variety of geometries and flow conditions [3-8].

In applications of biological, biotechnological, and biomedical interest, the suspending fluids are often Newtonian, but the suspended particles, e.g., capsules, cells, can have a complex behavior due to their intrinsic deformability. Such feature promotes the onset of transversal motions that, in combination with particle deformation, can be exploited to manipulate the trajectories of the suspended particles, thus making it possible to focus or separate them [9-10].

REFERENCES

[1] M. Toner, D. Irimia, "Blood-on-a-chip", *Annu. Rev. Biomed. Eng*., 7, 77 (2005).
[2] G. M. Whitesides, "The origins and the future of microfluidics", *Nature*, 442, 368–373 (2006).
[3] M.M. Villone, G. D'Avino, M.A. Hulsen, F. Greco and P.L. Maffettone, "Simulations of viscoelasticity-induced focusing of particles in pressure-driven micro-slit flow", *Journal of Non-Newtonian Fluid Mechanics,* 166, 1396-1405 (2011).
[4] G. D'Avino, G. Romeo, M.M. Villone, F. Greco, P.A. Netti and P. L. Maffettone, "Single line particle focusing induced by viscoelasticity of the suspending liquid: theory, experiments and simulations to design a micropipe flow-focuser", *Lab on a Chip*, 12, 1638–1645 (2012)
[5] M.M. Villone, G. D'Avino, M.A. Hulsen, F. Greco and P.L. Maffettone, "Particle motion in square channel flow of a viscoelastic liquid: Migration vs secondary flows", *Journal of Non-Newtonian Fluid Mechanics,* 195, 1-8 (2013).
[6] G. Romeo, G. D'Avino, F. Greco, P.A. Netti and P. L. Maffettone, "Viscoelastic flow focusing in microchannels: scaling properties of the particle radial distributions", *Lab on a Chip*, 13, 2802-2807 (2013).
[7] F. Del Giudice, G. Romeo, G. D'Avino, F. Greco, P. A. Netti and P. L. Maffettone, "Particle alignment in a viscoelastic liquid flowing in a square-shaped microchannel", *Lab on a Chip*, 13, 4263-4271 (2013).
[8] F. Del Giudice, G. D'Avino, F. Greco, P. A. Netti and P. L. Maffettone, "Effect of fluid rheology on particle migration in a square-shaped microchannel", *Microfluidics and Nanofluidics,* 19*, 95-104* (2015).
[9] M. M. Villone, F. Greco, M. A. Hulsen and P. L. Maffettone, "Numerical simulations of deformable particle lateral migration in tube flow of Newtonian and viscoelastic media", *Journal of Non-Newtonian Fluid Mechanics*, 234, 105-113 (2016).
[10] M. Trofa, M. M. Villone, G. D'Avino, M. A. Hulsen, P. A. Netti and P. L. Maffettone, "Numerical simulations of the separation of elastic particles in a T-shaped bifurcation", *Journal of Non-Newtonian Fluid Mechanics*, (2016) in press

NEUROINFORMATICA

ToolConnect: A Functional Connectivity Toolbox for the Analysis of in vitro Neural Networks

V. P. Pastore, A. Godjoski, S. Martinoia, and P. Massobrio[1]

[1] *Neuroengineering and Bio-nano Technology Lab (NBT), Department of Informatics, Bioengineering, Robotics, System Engineering (DIBRIS), University of Genova, Genova – Italy.*

vito.paolo.pastore@edu.unige.it

***Abstract*—We developed a user-friendly toolbox to provide the researchers community with a powerful tool to perform functional connectivity analysis on in vitro neuronal networks coupled to standard and high-density MEAs. The toolbox has been designed to maximize efficiency (in terms of computational costs) while maintaining reliability and accuracy.**

***Keywords*—functional connectivity, neural networks, correlation algorithms, information theory algorithms.**

I. Introduction

One of the major goal of contemporary neuroscience is to study the relationship between network structure and functional dynamics. This can be undertaken by specifically addressing structural, functional and effective connectivity at different level of complexity and on different experimental models and extracting relevant parameters of network topology. Within the same framework of study, understanding how network dynamics arises from the properties of neurons and especially from their connectivity is extremely challenging. In most experimental models, the anatomical connectivity is only partially known and/or can be partially estimated-extracted. Therefore, functional connectivity techniques are often used to give a directed, dynamically changing assessment of network interaction [1]. The analysis of multiple neural spike train data recorded from experimental models has gained tremendous relevance with the widespread application of Micro-Electrode Arrays (MEAs) [2]. This analysis has been supported by a simultaneous advance in the quality of analytical methods that attempt to quantify the often highly complex interactions that are observed. To the best of our knowledge, there is no available dedicated software that collects and implements a set of different functional connectivity methods for spike trains acquired from in vitro neural networks. The purpose of this work was to develop a user-friendly toolbox [3] to provide the researchers community with a powerful tool to perform functional connectivity analysis on *in vitro* neuronal networks coupled to standard and high-density MEAs, guaranteeing efficiency and accuracy.

II. Materials and Methods

ToolConnect is a standalone windows Graphical User Interface (GUI) application written in C#, with a modular windows forms implementation using Microsoft Visual Studio with .NET framework 4.5 development environment. One of the major feature is the toolbox's independence from the acquisition system (e.g., Multi Channel Systems – Reutlingen, Germany, Qwane Biosciences - Lausanne, Switzerland, 3Brain – Wädenswil, Switzerland) and from the MEA layout (number of microelectrodes and spatial organization). The GUI provides the user with powerful tools to manipulate data and to perform functional connectivity analysis based on two correlation methods (cross-correlation and partial correlation) and two information theory based methods (transfer entropy and joint entropy). Some dedicated interfaces of the GUI allows the user to: i) plot the correlograms between each couple of the set of analyzed electrodes (for cross- and partial- correlation); ii) manage, thresh and plot the Connectivity Matrix (CM) and the connectivity graph; iii) extract the main topological features (degree, cluster coefficient, path length).

A. Cross-Correlation

Cross Correlation measures the frequency at which one particular neuron or electrode fires ("target") as a function of time, relative to the firing of an event in another network ("reference") [4]. Mathematically, CC reduces to a probability $Cxy(\tau)$ of observing an event in a train Y at time $(t+\tau)$, because of an event in another train X at time t (τ is the time shift or time lag). Connection strength among all possible pairs of neurons was evaluated on the basis of the peak value of the CC function.

B. Partial Correlation

Partial Correlation identifies the functional neural connectivity from simultaneously recorded neural spike trains. Partial Correlation analysis allows to distinguish between direct and indirect connections by removing the portion of the relationship between two neural spike trains that can be attributed to linear relationships with recorded spike trains from other neurons [5], [6]. We used the partialization analysis in the time domain, estimated by frequency domain and based on a scaled version of the partial covariance density. The scaled partial covariance density (SPCD) combines the advantages of the Cross Correlation histograms and the partialization analysis in the frequency domain. In particular, it can be interpreted in the same way as the Cross Correlation histograms with peaks indicating excitatory connections, while on the other hand it allows for the discrimination of direct and indirect connections and common inputs.

C. Transfer Entropy

Transfer Entropy (TE) is an information theoretic measure, which allows to extract causal relationships from time series, taking into account their past activity [7]. It shares some common properties with the Mutual Information (MI), and

takes into account the history and the dynamics of the peak trains. Differently from MI and CC, TE is not symmetric with respect to the exchange of the variables (time series) *X* and *Y*. Additionally, with respect to cross-correlation based methods, TE is sensitive to linear as well as nonlinear causal interactions.

D.Joint Entropy

Joint Entropy analyzes the cross Inter-Spike-Intervals (cISI): if two neurons are strongly connected the cISI histogram will show a peak and Joint Entropy will be close to zero, otherwise the cISI histogram will be almost flat, and the Joint Entropy will be high [8].

III. Results

We designed and developed TOOLCONNECT taking care to satisfy the user-friendliness requirement, while hiding the algorithms implementation specifics and software's design details. It is intuitive and straightforward to use and has a GUI, which permits also to inexperienced users to perform functional connectivity analysis (different methods can also run simultaneously), and to graphically represent the results. Figure 1 shows a screenshot of the last release of TOOLCONNECT's GUI. Figure 2 shows the connectivity graphs obtained from the analysis of cortical networks coupled to the MEA60 and the MEA2100 acquisition systems of Multi Channel Systems and the BioCam acquisition system of 3Brain Systems. To assess the performances of TOOLCONNECT in terms of computational efficiency and accuracy, we performed functional-connectivity analysis based on the cross-correlation method on hippocampal neuronal networks coupled to the MEA 60 from Multi-Channel Systems (MCS), during spontaneous and stimulus-evoked activity.

IV. Conclusion

To the best of our knowledge, TOOLCONNECT is the first functional connectivity toolbox providing a user-friendly and modular GUI, dedicated to the analysis of multiple spike trains recorded from in-vitro neural networks coupled to MEAs. It offers a complete set of connectivity methods and some powerful graphical tools of straightforward usage. The toolbox is developed taking care of the optimization of the resources usage (requested RAM) and the reduction of the computational time. We obtained acceptable performances with computational time lower than 2 minutes (for 10 minutes of recording sampled at 10 kHz). These performances make TOOLCONNECT compatible with high-density recording systems (e.g., the 4096 electrodes of the 3brain system). In this way, it will be possible to perform functional connectivity analysis on neural networks with dimensions of thousands of neurons preserving an acceptable spatial and temporal resolution, hence allowing to obtain realistic and complete information on the dynamics and the topology of such systems. TOOLCONNECT is available on INCF-Software center at the following web address: http://software.incf.org/software/toolconnect.

References

[1] A. A. Ioannides, "Dynamic functional connectivity," Current Opinion in Neurobiology 2007, 17:161-170.

[2] E. N. Brown, R. E. Kass, and P. P. Mitra, "Multiple neural spike train data analysis: state-of-the-art and future challenges," Nature Neuroscience 2004, vol. 7, no.5, pp. 456-461.

[3] V. P. Pastore, D. Poli, A. Godjoski, S. Martinoia, P. Massobrio, "ToolConnect: a functional connectivity toolbox for in-vitro cortical networks," 2016, Frontiers in Neuroinformatics [Online]. Available: http://dx.doi.org/10.3389/fninf.2016.00013

[4] E. Salinas, T. J. Sejnowski, "Correlated neuronal activity and the flow of neural information," 2001, Nature Reviews Neuroscience 2: 539–550.

[5] M. Eichler, R. Dahlhaus, J. Sandkühler, "Partial correlation analysis for the identification of synaptic connections. Biol Cybern", 2003 Oct.

[6] D. Poli, V. P. Pastore, S. Martinoia, P. Massobrio, "From functional to structural connectivity using partial correlation in neuronal assemblies," J Neural Eng. 2016 Feb 25;13.

[7] M. Lungarella, A. Pitti, Y. Kuniyoshi, "Information transfer at multiple scales," 2007, Physical Review E 76: 0561171–05611710.

[8] M. Garofalo, T. Nieus, P. Massobrio, S. Martinoia, "Evaluation of the performance of information theory-based methods and cross-correlation to estimatethe functional connectivity in cortical networks," PLoS One, 2009 Aug 4 [Online]. pp. 876—880. Available: http://www.halcyon.com/pub/journals/ 21ps03-vidmar

[9] G. O. Young, "Synthetic structure of industrial plastics (Book style with paper title and editor)," in *Plastics*, 2nd ed. vol. 3, J. Peters, Ed. New York: McGraw-Hill, 1964, pp. 15–64.

[10] Multi Channel Systems – Reutlingen, Germany [Website] : http://www.multichannelsystems.com

[11] Qwane Biosciences - Lausanne, Switzerland [Website]: http://www.qwane.com

[12] 3Brain – Wädenswil, Switzerland [Website]: http://www.3brain.com

Fig. 1. ToolConnect's GUI

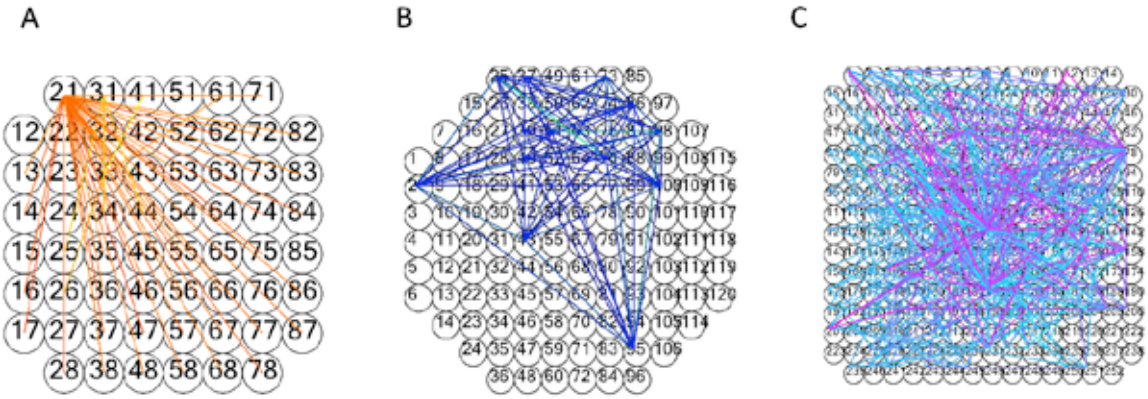

Fig. 2. Example of connectivity graphs obtained by ToolConnect's functional connectivity analysis applied to cortical networks coupled to different acquisition systems: (A) MEA60 (B) MEA 2100 (C) MEA256.

NEUROINGEGNERIA

A DTW-based Method for Detecting Electrically Evoked Auditory Brainstem Responses

M. Goffredo[1], C. Di Nardi[1], S. Giannantonio[2], A. Scorpecci[2], A. Ingrosso[2], P. Malerba[3], S. Conforto[1] and P. Marsella[2]

[1] *Department of Engineering, Roma Tre University, Rome, Italy*
[2] *Centro Impianti Cocleari, Ospedale Pediatrico "Bambino Gesù", Rome, Italy*
[3] *Cochlear Italia s.r.l. Bologna, Italy*

***Abstract*— A method for the analysis of Electrically Evoked Auditory Brainstem Responses (EABR) in subjects with cochlear implants is presented. The extraction of the III and V waves, which correspond to the cochlear nuclei and the inferior colliculi respectively, has been achieved with a template-based approach based on the Dynamic-Time-Warping algorithm. Experimental tests have been conducted on two young subjects who have been recently implanted. The obtained results have been compared with data manually annotated by clinicians and with literature. The outcomes confirmed that the proposed method automatically extracts the parameters typically used by clinicians for investigating the functioning of the auditory system in patients with cochlear implants. The performance of the algorithm is particularly encouraging for future applications to a wider population.**

***Keywords*— Electrically Evoked Auditory Brainstem Response, Dynamic Time Warping, Cochlear implant.**

I. Introduction

Cochlear implants have been widely applied in case of severe or total hearing loss [1] since they can effectively stimulate the auditory pathways with electrical pulses. In the last decade, electrophysiological assessments have been efficiently used for investigating the functioning of the auditory system and providing objective data for the management of patients with cochlear implants [2]. In particular, electrically evoked auditory brainstem response (EABR) has been used to study post-implant outcomes [3], and to predict neural survival [4]. EABR is analogous to the acoustic auditory brainstem response (ABR) since it is characterized by five electrically evoked waves, which are recorded within the first 10 ms of presentation of a stimulus [5]. However, since EABR is produced by an electrical pulse, the signal morphology is different from the ABR and it is characterised by the presence of a stimulation artefact within the first millisecond [2]. For these reasons, only electrically evoked III and V waves, which correspond to the cochlear nuclei and the inferior colliculi, are usually studied in EABR [6]. Typically, expert clinics and specialists perform the manual annotation of these waves via specific graphically oriented software (e.g. GSI Audera, SmartEP by Intelligent Hearing Systems). Although such procedure is widely recognised, it is time consuming and the outcomes could be compromised by the quality of the signal and the experience of the clinician. For these reasons, a method for the processing of EABR signal, which automatically extracts the relevant wave parameters, would be appealing.

While relatively few studies have investigated the possibility to automatically analyse ABR signals [7], [8], in our knowledge, scientific literature lacks of methods for the detection of the III and V waves in EABR.

The aim of this paper is to present a template-based approach for the analysis of EABR and for the automatic extraction on latencies and amplitudes of the waves that characterise the signal.

II. Materials and Methods

A. EABR analysis

The proposed method aims at detecting the III and V waves with a template-based approach founded on the Dynamic-Time-Warping (DTW) algorithm. The EABR signal is processes without considering the first millisecond, which is affected by the stimulation artefact.

A template $T(t)$ of a typical EABR has been built considering a mixture of K Gaussian distributions $T(t) = \sum_{k=1}^{K} \frac{w_k}{\sigma_k \sqrt{2\pi}} e^{-\frac{(t-\mu_k)}{2\sigma_k^2}}$ where w_k are the weights, with $\sum w_k = 1$, μ_k are the mean values and σ_k are the standard deviations of the Gaussians. The parameters used for building the template of EABR are: K=3; w_1= w_2=0.3; w_3=0.4; μ_1=2.46 s; μ_2=4.96 s; μ_3=6.35 s; σ_1=0.32 s; σ_2=0.52 s; σ_3=0.30 s. These figures have been chosen in accordance with literature on the characteristics of the III and V waves in EABR [2]. Fig. 1 shows the template $T(t)$, where the peaks of the III and the V waves are at 4.96 s and 6.35 s, respectively.

Given a EABR signal $S(t)$, the proposed method allows to align $S(t)$ with $T(t)$, and thus to extract the peaks of the III and the V waves in $S(t)$.

The DTW algorithm is a well-known technique to find an optimal alignment between two given (time-dependent) sequences under certain restrictions. Originally, DTW has been used in automatic speech recognition [9], but it has been applied in a wide range of signals which were characterised by time deformations [10], [11]. The algorithm is composed of two phases: the alignment phase; and the comparison phase. In order to find the similarity between time series, the DTW looks for the alignment that ensures the minimum distance between the aligned points (first phase); and then yields a distance measure between the two sequences (second phase). In this paper, only the alignment phase is applied in order to find the temporal matching between T and S and thus to extract the positions of the III and V waves.

Let T and S be the two discrete time series having different lengths, being $S=\{s_1, s_2,\ldots, s_N\}$ the input signal and $T=\{t_1, t_2,\ldots, t_M\}$ the reference signal. Let t_{III} and t_V be the samples of

T corresponding to the peaks of the III and the V waves respectively. The first step of the algorithm constructs a NxM matrix **d** in which every element represents the distance between the i^{th} element of the *S* and the j^{th} element of *T*: $\mathbf{d}(i,j) = |t_i - s_j|$. The algorithm looks for a DTW distance function between the two time series, by minimizing a cost function specifically calculated on the matrix **DTW**, obtained considering the cumulative distance from the adjacent cells:

$$\mathbf{DTW}(i,j) = \mathbf{d}(i,j) + \min[\mathbf{DTW}(i-1,j-1), \mathbf{DTW}(i,j-1), \mathbf{DTW}(i-1,j)]$$

The time series are then aligned through the generation of a warping path, W, which defines the correspondence of an element s_i to t_j with the condition that both the first and the last elements of *S* and *T* are aligned. This path is thus a sequence of points $W=\{w_1, w_2,\ldots, w_K\}$ with the generic element w_p associated with a specific position (i_p, j_p). The position of the III and the V waves in the input signal *S* will be given by looking at the samples that match t_{III} and t_V in W. Then, the amplitudes and latencies of the III and V waves of *S* are extracted.

B. Subjects

Two subjects with severe to profound sensory-neural hearing loss participated to the study. The first subject is a 16-year-old girl who was implanted in 2015 in one ear with Nucleus Cochlear CI512. The second subject is a 22-year-old girl who was implanted in 2014 in one ear with Nucleus Freedom CI24RE. A verbal uniform consent was obtained for participation and dissemination of the results. Subjects were lying comfortably in a bed in a quiet testing room. No sedation was used. Time of recording ranged between 35 and 45 min.

C. EABR recording and annotation

EABRs were recorded with the GSI Audera system. The active electrode was placed at the forehead (FPz) (International 10–20 System), reference electrode was placed on the contralateral mastoid, and the ground electrode was placed on the back of the neck.

Stimuli used to evoke the EABR were generated by a computer-controlled speech processor interface. A series of 25 l s/phase biphasic current pulses were presented to the patient at a rate of 21 Hz in a monopolar stimulation mode. Stimulus levels started from a threshold level obtained by the neural response telemetry [12] and up to the maximum comfortable level (increment steps of 5 units). Three stimulation electrodes were used: one located at the basal end of the implant electrode array (electrode 6), one in the middle (electrode 12) and one at the apical end (electrode 18).

A specialist annotated the III and V waves on the 42 recorded EABRs using the software GSI Audera.

III. RESULTS

The EABR waveforms have been analysed with the proposed algorithm and the peaks of the III and the V waves have been extracted. Fig. 2 shows an example of the detection.

Since the latency of the V wave is a very interesting parameter for the clinicians [6], the values obtained with the proposed method have been compared with data from literature [13]. Fig. 3 depicts these results in terms on mean values and standard deviations for the three electrodes which have been used for the electrical stimulation.

The accuracy of the detection has been expressed in terms of true positives (TP), false negatives (FN) and false positives (FP), calculated by comparing the obtained results with the annotated data (Fig. 4): TP when a peak is correctly detected; FN when it is missed; and FP when a noise spike is detected as peak.

IV. DISCUSSIONS AND CONCLUSIONS

A DTW-based method for the analysis of EABR has been presented. The results obtained from the processing of signals from subjects with cochlear implants, show a high accuracy in detecting the III and V waves (TP higher than 65%).

Moreover, the obtained latencies of the V waves are in agreement with published data [18], considering electrical stimuli placed at the basal end, middle and apical end of the implant electrode array.

Although these results have been obtained with a limited number of subjects, they are particularly encouraging, and foster future experiments on wider population of patients.

REFERENCES

[1] Middlebrooks, J. C., Bierer, J. A., & Snyder, R. L. (2005). Cochlear implants: The view from the brain. Current Opinion in Neurobiology, 15, 488–493.

[2] Cullington HT (2003) Cochlear Implants: Objective Measures. London:.

[3] Song, M. H., Bae, M. R., Kim, H. N., Lee, W. S., Yang, W. S., & Choi, J. Y. (2010). Value of intracochlear electrically evoked auditory brainstem response after cochlear implantation in patients with narrow internal auditory canal. The Laryngoscope, 120(8), 1625-1631.

[4] Kim, A. H., Kileny, P. R., Arts, H. A., El-Kashlan, H. K., Telian, S. A., & Zwolan, T. A. (2008). Role of electrically evoked auditory brainstem response in cochlear implantation of children with inner ear malformations. Otology & Neurotology, 29(5), 626-634.

[5] Deshpande, S. N., Houston, L., & Keith, R. W. (2013). Hearing testing, auditory brainstem response (ABR). In Encyclopedia of otolaryngology, head and neck surgery (pp. 1151-1158). Springer Berlin Heidelberg.

[6] Abbas, P. J., & Brown, C. J. (1991). Electrically evoked auditory brainstem response: growth of response with current level. Hearing research, 51(1), 123-137.

[7] Bradley, A. P., & Wilson, W. J. (2004). On wavelet analysis of auditory evoked potentials. Clinical neurophysiology, 115(5), 1114-1128.

[8] Picton, T., Hunt, M., Mowrey, R., Rodriguez, R., & Maru, J. (1988). Evaluation of brain-stem auditory evoked potentials using dynamic time warping. Electroencephalography and Clinical Neurophysiology/Evoked Potentials Section, 71(3), 212-225.

[9] Rabiner, L. R., Rosenberg, A. E., & Levinson, S. E. (1978). Considerations in dynamic time warping algorithms for discrete word recognition. The Journal of the Acoustical Society of America, 63(S1).

[10] Kovács-Vajna, Z. M. (2000). A fingerprint verification system based on triangular matching and dynamic time warping. Pattern Analysis and Machine Intelligence, IEEE Transactions on, 22(11), 1266-1276.

[11] Muscillo, R., Schmid, M., Conforto, S., & D'Alessio, T. (2011). Early recognition of upper limb motor tasks through accelerometers: real-time implementation of a DTW-based algorithm. Computers in biology and medicine, 41(3), 164-172.

[12] Di Nardo, W., Ippolito, S., Quaranta, N., Cadoni, G., & Galli, J. (2003). Correlation between NRT measurement and behavioural levels in patients with the Nucleus 24 cochlear implant. Acta otorhinolaryngologica italica, 23(5), 352-355.

[13] Zirn, S., Arndt, S., & Wesarg, T. (2015, April). Objective assessment of optimal group delays in cochlear implants. In Neural Engineering (NER), 2015 7th International IEEE/EMBS Conference on (pp. 683-686). IEEE.

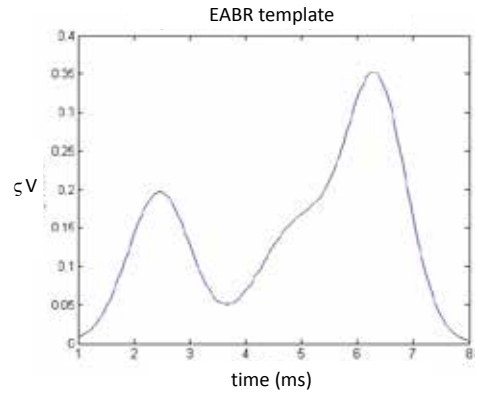

Fig. 1. EABR template composed of a mixture of three Gaussian distributions.

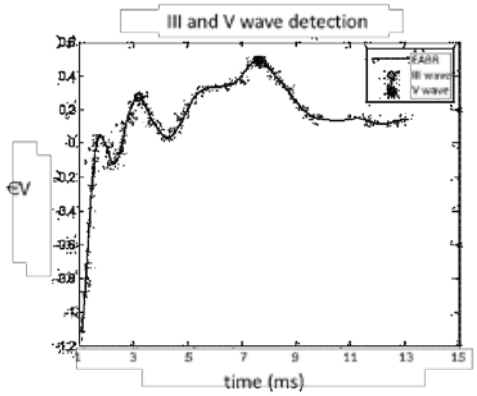

Fig. 2. Example of the detection of the peaks of III and V waves in a EABR signal (subject 2, electrode 12, +5 current level with respect to the neural response telemetry threshold).

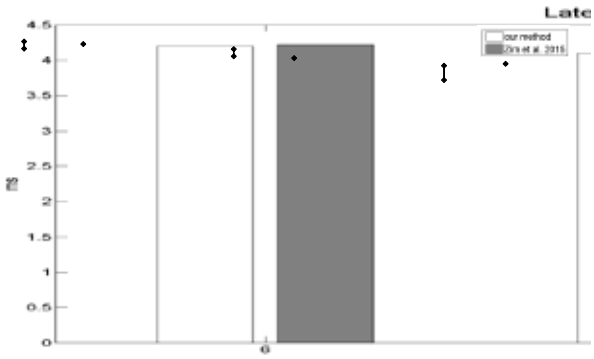

Fig. 3. Latencies of the V waves detected with the proposed method. Results are depicted as mean values and standard deviations and are compared with data by Zirn et al. [18].

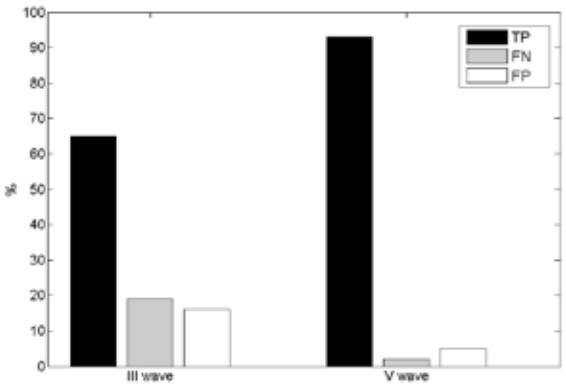

Fig. 4. Overall performance of the detection algorithm in terms of true positives (TP), false negatives (FN) and false positives (FP).

Evaluation of the Emotional Index elicited by the listening of Dante's Divine Comedy

E. Modica[1], G. Cartocci[3], D. Rossi[1], A.G. Maglione[3], P. Canettieri[2], M. Combi[2], R. Rea[2], L. Gatti[2], C.S. Perrotta[3], R. Verdirosa[3], R. Bernaudo[3], E. Lerose[3] and F. Babiloni[3, 4]

[1] *Dept. Anatomical, Histological, Forensic & Orthopedic Sciences, Sapienza University of Rome, Italy*

[2] *Dept. of European, America and Intercultural Studies of the University of Rome Sapienza, Rome, Italy.*

[3] *Department of Molecular Medicine, Sapienza University of Rome, Italy*

[4] *BrainSigns srl, via Sesto Celere 7/c, Rome, Italy*

***Abstract*—In this work, we describes the results of a pilot study that used the Emotional Index during the listening of a selected pieces of the "Divina Commedia" in a sample of 20 voluntary participants. Noteworthy, half of the participants had a literary formation in their studies (Humanist; they are students of literature at the University) while the other half of the sample are attending other university courses (Not Humanist). The study applied the gathering of the heart rate (HR) and galvanic skin response (GSR) variation during the listening of the excerpts. Results from the ANOVA showed as the Humanist group reported during the listening of the Divina Commedia higher values of EI indexes when compared to the values obtained in the Not Humanist sample. Such results are statistically significant.**

***Keywords*—Neuroaesthetics, EI.**

I. Introduction

NEUROAESTHETICS is an emerging disciplines investigating the biological underpinnings of aesthetic experiences, and since its formal birth in 90s by Semir Zeki [1] constitutes a field receiving growing interest by the scientific community Although traditional topic of neuroaesthetic investigation are visual art and music [2],[3], an enlargement in the horizon of artistic items to be investigated is beginning and literature and poetry are experiencing a renewed scientific interest from the neuroaesthetics perspective [4]. Two aspects of poetry may contribute to the emotional responses it may elicit: its lexical content and its structural features (i.e., poetic form). Meter and rhyme constitute the key features in poetry [5] additionally they have been found to be significant contributors to the aesthetic and emotional perception of poetry [6], but it is difficult to investigate the contribution of the content per se due to the needing to compare different kinds of pieces. The possibility to overcome this limitation is offered by the famous Italian XIV century poem the "Divine Comedy" by Dante Alighieri. The book is characterized by a repetitive and constant structure, as it is composed by three parts (canticas: Inferno -Hell-, Purgatorio –Purgatory- and Paradiso –Paradise-), each part is composed by thirty-three cantos of the same length. Studying the reaction to the exposure to stanzas belonging to each of the three canticas would enable to test the effect of the content of the pieces, maintaining the meter and the rhyme scheme constant. Furthermore, the comparison among different canticas would enable to assess the effect of a potentially differential previous knowledge of the peculiar cantica.

II. Methods

In the present study 20 healthy subjects(mean age Humanist 24.9 and Not Humanist 26.2 years old) have been enrolled on a voluntary base. The experiment was performed in accord to the principles outlined in the Declaration of Helsinki of 1975, as revised in 2000, and it was approved by the University ethical committee. Participants were sitting on a comfortable chair and instructed to listen to the auditory stimuli. The target stimuli belonged to the Divine Comedy by Dante Alighieri and each belonged to one of the three parts of the book: Inferno (Hell), Purgatorio (Purgatory) and Paradiso (Paradise). The three target stimuli randomly played among, so producing different trains. The train was preceded and followed by sentences belonging to a clinical standardized set (Audiometria Vocale. Cutugno, Prosser, Turrini), lasting 1 minute, that have been used as the baseline. At the end of the listening subjects underwent a short recognition test. At the end of the listening, subjects were asked whether they recognized the audio pieces and to say what they thought to have listened. These behavioral data were collected and analyzed.

A. HR and GSR recordings and signal processing

Electrodermal Activitity (EDA) and Heart Rate (HR) were recorded by means of a NeXus-10 (Mindmedia, The Netherlands) system with a sampling rate of 128 Hz. To obtain the HR signal the Pan-Tompkins algorithm [7] has been employed. Skin conductance was acquired by the constant voltage method (0.5 V). The electrodes were attached, on non-dominant hand, to the palmar side of the middle phalanges of the second and third fingers of the participant, following published procedures [8]. The tonic component of the skin conductance (Skin Conductance Level, SCL) was obtained using LEDAlab software [10]. In the attempt to match SCL and HR signals we referred to the circumplex model of affect plane [11], where the coordinates of a point in the space are defined by the HR (horizontal axis) to describe the valence and by the SCL (vertical axis) to describe the arousal phenomena [12]. In order to obtain a monodimensional variable, the emotional state of a subject has been described by the Emotional Index (EI), as defined in previous studies [13].The interpretation of the EI implies that the higher the value the more positive the emotion experienced by the subject and vice versa.

B. Statistical analysis

Statistical analysis has been performed on the biometric results obtained during the listening of the three poems by ANOVA repeated measures. Duncan's post hoc test has been used.

III. Results

A. Emotional Index

The Humanist group reported a higher average number of subjects who correctly recognized the different canticas. Approximately the 90% of the Humanist group verbally recognized the canticas in comparison to the 40% of the Not Humanists (Fisher's exact test p=0.06). The EI index (Fig. *1*) showed a statistical significant effect of the interaction between the background and the kind of cantica ($F=7.47$, $p<0.01$). Furthermore, a statistically significant effect was reported for the cantica ($F=17.38$, $p<0.01$), whilst the background effect did not show a statistical significance (0.84, p=0.37). Post hoc comparison showed a higher emotional reaction to Inferno and Paradiso canticas in comparison to the Purgatorio ($p<0.01$) in the Humanist group, while in the Not Humanist group the Inferno reported higher values in comparison to both Paradiso and Purgatorio ($p<0.01$, p=0.04 respectively). When the comparison of the Inferno cantica has been peformed between the two groups no statistical significant differences were shown (p=0.18). Conversely, statistical significant differences have been reported for Paradiso and Purgatorio comparisons between the groups ($p<0.01$ and p=0.01 respectively).

IV. discussion

Leader and colleagues [14] theorized a descriptive information-processing stage model for the aesthetic experience, consisting of 5 stages: perception, explicit classification, implicit classification, cognitive mastering and evaluation. The model differentiates between aesthetic emotion and aesthetic judgments as two types of output. This hypothesis is in accord with our data when considering results for the Emotional Index. In particular, the Humanist group showed a more selective emotional involvement for two of them: both Inferno and Paradiso in comparison to the Purgatorio. Additionally, except for the Inferno, there was a statistical significant difference in the EI for Paradiso and Purgatorio between the two experimental group. This result could be explained by the evidence that Inferno is the most studied cantica by Italian students (also in high schools) and the one that reported the highest percentage of recognition among all our experimental subjects.

V. Conclusion

In general, data suggest a difference on the base of the background in relation to the cantica. This result could be explained by the evidence that aesthetic experience is a function of previous knowledge [15]. In this framework, experts and non-experts rely on different cues to evaluate artworks in terms of liking and comprehension [16],[17]. The present results, obtained by a pilot study, need further investigation on an enlarged sample so to provide indications on the literature and poetry aesthetic experience in experts and non-experts.

Acknowledgement

Thanks to the Cinecittà Experimental Cinematografy Centre (Centro Sperimentale di Cinematografia di Cinecittà), to its director Adriano De Santis and to the actor Roberto Antonelli who gave voice to the Divine Comedy canticas.

References

[1] A. Chatterjee and O. Vartanian, "Neuroaesthetics," *Trends in Cognitive Sciences*, vol. 18, no. 7, pp. 370–375, Jul. 2014.

[2] T. Ishizu and S. Zeki, "Toward A Brain-Based Theory of Beauty," *PLoS One*, vol. 6, no. 7, Jul. 2011.

[3] R. J. Zatorre and V. N. Salimpoor, "From perception to pleasure: music and its neural substrates," *Proc. Natl. Acad. Sci. U.S.A.*, vol. 110 Suppl 2, pp. 10430–10437, Jun. 2013.

[4] A. M. Jacobs, "Neurocognitive poetics: methods and models for investigating the neuronal and cognitive-affective bases of literature reception," *Front Hum Neurosci*, vol. 9, Apr. 2015.

[5] R Jakobson, "Closing statement: Linguistics and poetics," *Style in language*, 1960, pp.350-377

[6] C. Obermeier, W. Menninghaus, M. von Koppenfels, T. Raettig, M. Schmidt-Kassow, S. Otterbein, and S. A. Kotz, "Aesthetic and Emotional Effects of Meter and Rhyme in Poetry," *Front Psychol*, vol. 4, Jan. 2013.

[7] J. Pan & W.J. Tompkins, "A real-time QRS detection algorithm". Biomedical Engineering, *IEEE Transactions on*, (3), 230-236, 1985.

[8] W. Boucsein, D. C. Fowles, S. Grimnes, G. Ben-Shakhar, W. T. roth, M. E. Dawson, D. L. Filion, and Society for Psychophysiological Research Ad Hoc Committee on Electrodermal Measures,

[9] "Publication recommendations for electrodermal measurements," *Psychophysiology*, vol. 49, no. 8, pp. 1017–1034, Aug. 2012.

[10] M. Benedek and C. Kaernbach, "A continuous measure of phasic electrodermal activity," *J Neurosci Methods*, vol. 190, no. 1–5, pp. 80–91, Jun. 2010.

[11] J. A. Russell and L. F. Barrett, "Core affect, prototypical emotional episodes, and other things called emotion: Dissecting the elephant," *Journal of Personality and Social Psychology*, vol. 76, no. 5, pp. 805–819, May 1999.

[12] I. B. Mauss and M. D. Robinson, "Measures of emotion: A review," *Cognition and Emotion*, vol. 23, no. 2, pp. 209–237, Feb. 2009.

[13] G. Vecchiato, A. G. Maglione, P. Cherubino, B. Wasikowska, A. Wawrzyniak, A. Latuszynska, M. Latuszynska, K. Nermend, I. Graziani, M. R. Leucci, A. Trettel, and F. Babiloni, "Neurophysiological Tools to Investigate Consumer's Gender Differences during the Observation of TV Commercials," *Comput Math Methods Med*, vol. 2014, 2014.

[14] H. Leder, B. Belke, A. Oeberst, and D. Augustin, "A model of aesthetic appreciation and aesthetic judgments," *Br J Psychol*, vol. 95, no. Pt 4, pp. 489–508, Nov. 2004.

[15] G. Consoli, "From beauty to knowledge: a new frame for the neuropsychological approach to aesthetics," *Front Hum Neurosci*, vol. 9, May 2015.

[16] I. C. Bohrn, U. Altmann, O. Lubrich, W. Menninghaus, and A. M. Jacobs, "When we like what we know – A parametric fMRI analysis of beauty and familiarity," *Brain and Language*, vol. 124, no. 1, pp. 1–8, Jan. 2013.

[17] H. Leder, G. Gerger, D. Brieber, and N. Schwarz, "What makes an art expert? Emotion and evaluation in art appreciation," *Cognition and Emotion*, vol. 28, no. 6, pp. 1137–1147, Aug. 2014.

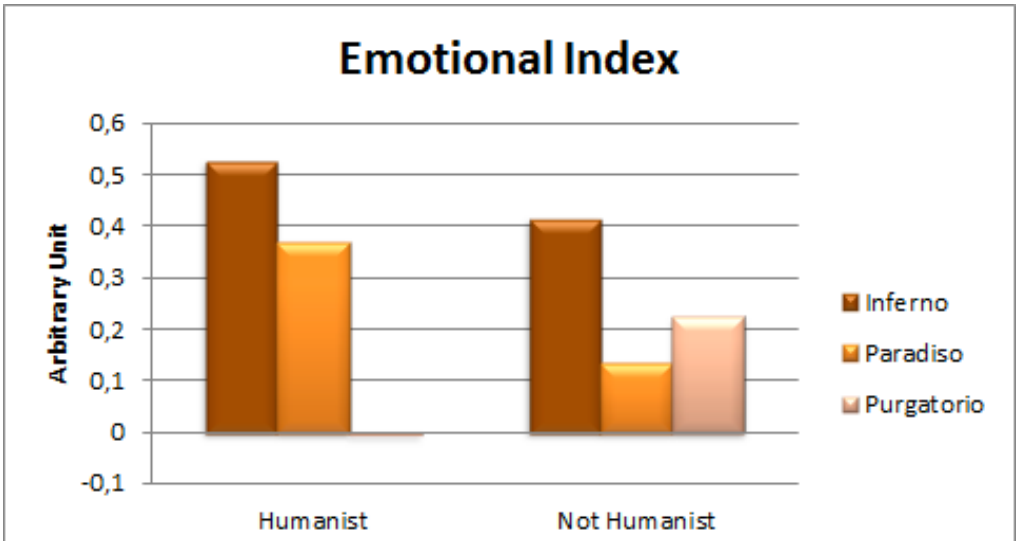

Figure 1. Emotional Index mean values for the Divine Comedy canticas in the Humanist and Not Humanist groups.

Nanotopographical Control of Neural Cells Assembly into Complex Networks

Valentina Onesto[1], Enzo Di Fabrizio[1,2], Mario Cesarelli[3], Maria Laura Coluccio[1], Natalia Malara[1], Francesco Amato[1], Francesco Gentile[3]

[1] *Department of Experimental and Clinical Medicine, University of Magna Graecia, 88100 Catanzaro, Italy*
[2] *King Abdullah University of Science and Technology, Thuwal, Saudi Arabia*
[3] *Department of Electrical Engineering and Information Technology, University Federico II, Naples, Italy*

***Abstract*— Devices with a controlled nano-topography for neural cells adhesion and organization were produced. The information content of a network of neural cells was correlated with the nano-geometry of the surface; the optimal roughness and nano-scale size of the substrate for which information in the network is maximized were found.**

I. Introduction

NEURONS are specialized cells which have the function to process and transmit information through electrical and chemical signals [1, 2]. There is an increasing interest in understanding the way neural cells assemble, and how the topology of the networks they form may influence, and perhaps improve, information transmission in those networks. In the body, the nanoscale structure of the extracellular matrix (ECM) provides a natural web of intricate nanofibers to support cells and present an instructive background to guide their behaviour [3]. ECM-cell interaction is mediated by transmembrane adhesion receptors, which form structures (Focal complexes and Focal adhesions) with a scale length comprised in the 30-100 nm dimensional range [4-6]. Nanotechnology may be used to produce controlled nano-scaled geometries to understand how the cellular sensory machinery interacts with extremely small cues to regulate cell behaviour. Different research groups demonstrated that topographic cues at the nano-scale may direct, control and, in some cases, improve neuronal adhesion [7], growth [8], differentiation [9], organization or self-organization into simple to complex networks [10], electrical signalling [11]. In this work, we produced nano-structured surfaces (Figure 1) to influence and guide the organization of neuronal cells into complex networks (Figure 2). We verified to which extent nano-topography influences the topology of networks that neurons form on a substrate. Using computer simulations and mathematical modelling based on an information theory approach, we provided an estimate of the information increase in clustered nerve cells.

II. Methods

A. Fabrication

Planar surfaces with a roughness in the 1-100 nm range were fabricated. Smooth silicon surfaces and standard glass substrates were used for comparison. Silicon wafers were etched in diluted KOH (potassium hydroxide) solutions at 70 °C to obtain corrugated profiles. Using different etching times, we produced surfaces with an average roughness R_a varying from 10 to 100 nm.

B. Sample characterization

Substrates for neural adhesion were verified using Atomic Force Microscopy (AFM). The AMF profiles of the samples were processed to derive the Power Spectrum density function, that delivers the information content of the substrates over multiple scales. From the power spectrum, we extracted the fractal dimension D_f which describes the topography of a substrate at an intimate level.

C. Biological preparation

Hippocampal cultures from dissociated primary central neurons were used. We used the methods described in [10] for culturing neurons on the substrates. Neurons were plated on either the nano-structured substrates and Poly-D-lysine coated plastic tissue culture dishes and smooth silicon substrates used as a control. Neurons on a substrate were imaged using confocal imaging and the methods described in [12].

D. Deriving the topological properties of neural networks

Confocal images of the cells cultured on the substrates were processed to extract the (i) average cluster coefficient and (ii) characteristic path length. The combination of these parameters gives an indication of the connectivity properties of the cells in a network. We implemented an algorithm described in details in [12], in which the core of the algorithm is constituted by the Waxman model. The Waxman model makes a decision on whether two nodes in a grid are connected.

E. Simulating Information in neural networks

We used a generalize leaky integrate and fire model to generate trains of signal in the grids. Resulting patterns of multiple spike trains in the grid were interpreted using an information theory based approach [13]. We take into account that the spike train of individual neurons, in response to a long sample of stimuli, may vary. A similar variability is described by the total entropy of the spike train, H. Similarly, the conditional or noise entropy N is the variability of the spike train in response to a sample of repeated stimuli. The information I that the spike train provides about the input is the difference between entropies, $I=H-N$. The Shannon entropy $H(S)$ of the distribution of probabilities P(s) for each stimulus is defined as

$$H(S) = -\sum_S P(S)\log_2 P(S) \quad (1)$$

III. Results

Using conventional wet etching procedures (see methods), we generated rough silicon substrates in which the average roughness of the substrates varies from $R_a^1 \sim 2\ nm$ (Figure 1a) to $R_a^4 \sim 50\ nm$ (Figure 1d), with intermediate values of roughness $R_a^2 \sim 15\ nm$ (Figure 1b) and $R_a^4 \sim 35\ nm$ (Figure 1c). The corresponding fractal dimensions were derived being $D_f^1 \sim 2.08$, $D_f^2 \sim 2.22$, $D_f^3 \sim 2.35$, $D_f^4 \sim 2.5$, and thus in this dimensional range fractal dimension is proportional to roughness. On culturing neural cells on the described surfaces, we observed that surface topography influences cells networking. While on planar, quasi smooth surfaces (R_a^1, Figure 2a-c), after 5 days from culture, cells are uniformly distributed on the surface, on rough substrates (R_a^3, Figure 2d-f) nerve cells show an increased ability to create patterns in which the nodes of the patterns form highly clustered groups, and the elements of the groups are connected by a finite, and generally low, number of steps.

Network analysis confirms that the clustering coefficient increases and the characteristic path length decreases with roughness for all the considered cases (Figure 3b). Networks with similar characteristics are named small world networks. Recently they attracted much attention because it is hypothesized that dynamical systems with a small world topology may feature enhanced signal propagation speed and computational capabilities [14]. Here, we used information theory based algorithms (see methods) to estimate the total information transmitted in a grid (Figure 3a) in which the elements of the grid are disposed as to reproduce cell topology measured on different substrates. On stimulating the system with an uncorrelated and correlated signal, we found that information in a grid increases with the small world attributes of the grid that, in turn, depend on the roughness of the substrates. In the considered scale range, increasing roughness enhances cell adhesion and cell networking: the major consequence of the augmented cell-cell interaction resides in an increase of information quantity in the network.

IV. Conclusion

We produced substrates with a controlled nano-topography for interaction with neural cells. We found that in a low $0 - 50\ nm$ dimensional range, increasing roughness promotes cells adhesion and networking. We estimated that the total information transmitted over networks of cells cultured over rough substrates may be increased from 3 to 4 folds compared to nominally flat substrates. This and other related studies are expected to have major impacts in (i) neural tissue engineering and regenerative medicine, (ii) the diagnosis and analysis of neurodegenerative disorders, (iii) bio-informatics and bio-computing.

References

[1] E. Kandel, J. Schwartz, and T. Jessell, Principles of Neural Science, 4/e ed. New York: McGraw-Hill, 2000.

[2] M.-H. Kim, M. Park, K. Kanga, and I. S. Choi, "Neurons on nanometric topographies: insights into neuronal behaviors in vitro," Biomaterials Science, vol. 2, pp. 148–155, 2014.

[3] M. M. Stevens and J. H. George, "Exploring and Engineering the Cell Surface Interface," Science, vol. 310, pp. 1135-1138, 2005.

[4] B. Geiger, A. Bershadsky, R. Pankov, and K. M. Yamada, "Transmembrane Extracellular Matrix–Cytoskeleton Crosstalk," Nature Reviews, Molecular Cell Biology, vol. 2, pp. 793-805, 2001.

[5] B. Geiger, J. P. Spatz, and A. D. Bershadsky, "Environmental sensing through focal adhesions," Nature Reviews, Molecular Cell Biology, vol. 10, pp. 21-33, 2009.

[6] P. Kanchanawong, G. Shtengel, A. M. Pasapera, E. B. Ramko, M. W. Davidson, H. F. Hess, et al., "Nanoscale architecture of integrin-based cell adhesions," Nature, vol. 468, pp. 580-586, 2010.

[7] C. Xie, L. Hanson, W. Xie, Z. Lin, B. Cui, and Y. Cui, "Noninvasive Neuron Pinning with Nanopillar Arrays," Nano Letters, vol. 10, pp. 4020–4024, 2010.

[8] K. Baranes, N. Chejanovsky, N. Alon, A. Sharoni, and O. Shefi, "Topographic Cues of Nano-Scale Height Direct Neuronal Growth Pattern," Biotechnology and Bioengineering, vol. 109, pp. 1791- 1797, 2012.

[9] A. A. K. Moe, M. Suryana, G. Marcy, S. K. Lim, S. Ankam, J. Z. W. Goh, et al., "Microarray with Micro- and Nano-topographies Enables Identification of the Optimal Topography for Directing the Differentiation of Primary Murine Neural Progenitor Cells," Small, vol. 8, pp. 3050–3061, 2012.

[10] T. Limongi, F. Cesca, F. Gentile, R. Marotta, R. Ruffilli, A. Barberis, et al., "Nanostructured Superhydrophobic Substrates Trigger the Development of 3D Neuronal Networks," Small, vol. 9, pp. 402–412, 2013.

[11] M. Tang, Q. Song, N. Li, Z. Jiang, R. Huang, and G. Cheng, "Enhancement of electrical signaling in neural networks on grapheme films," Biomaterials, vol. 34, pp. 6402-6411, 2013.

[12] G. Marinaro, R. La Rocca, A. Toma, M. Barberio, L. Cancedda, E. Di Fabrizio, et al., "Networks of Neuroblastoma Cells on Porous Silicon Substrates Reveal a Small World Topology," Integrative Biology, vol. 7, pp. 184-97, 2015.

[13] R. Q. Quiroga and S. Panzeri, "Extracting information from neuronal populations: information theory and decoding approaches," Nature Reviews Neuroscience, vol. 10, pp. 173-185, 2009.

[14] D. J. Watts and S. H. Strogatz, "Collective dynamics of 'small-world' networks," Nature, vol. 393, pp. 440-442, 1998.

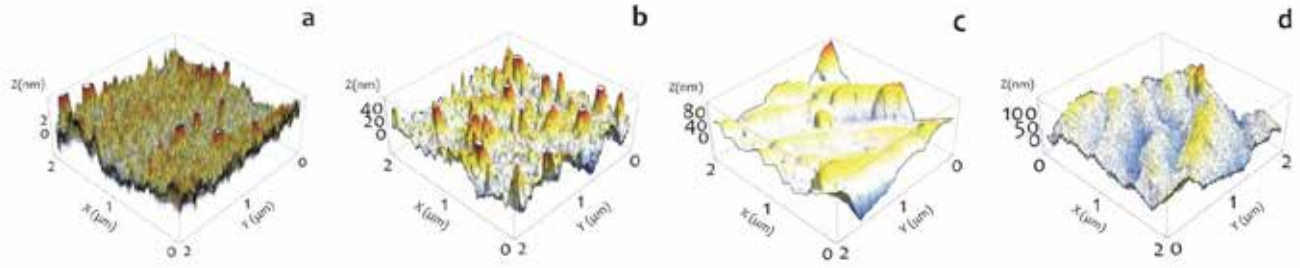

Fig. 1

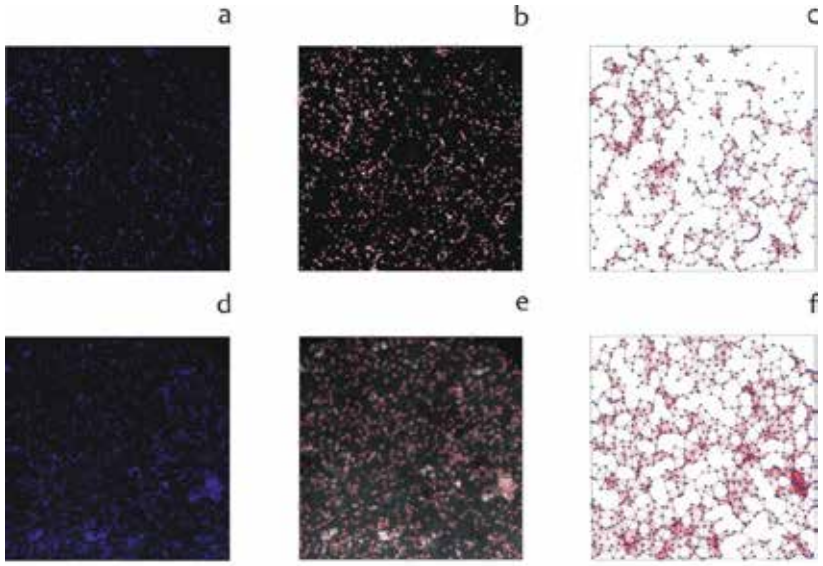

Fig. 2

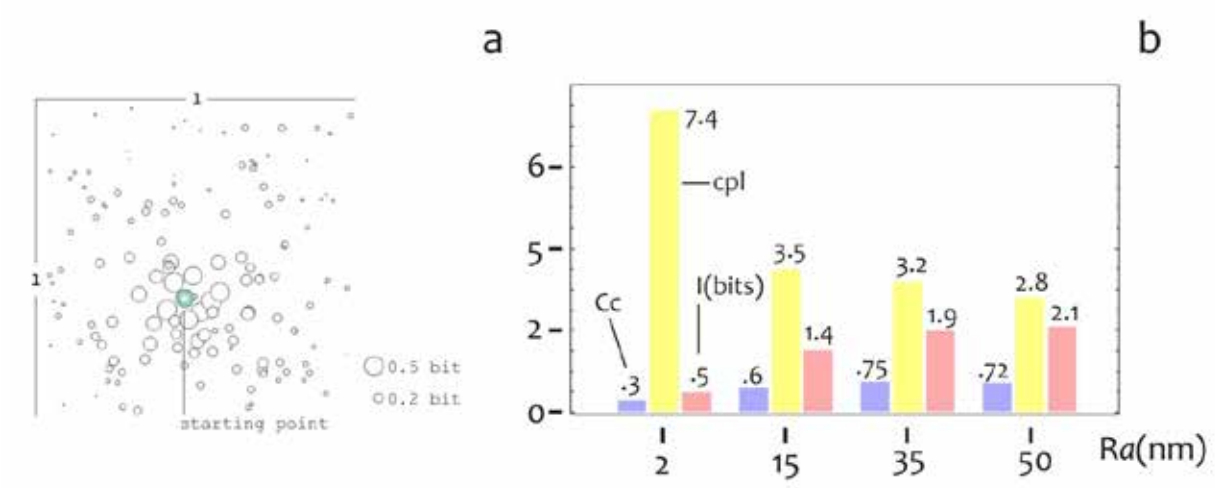

Fig. 3

Information in networks of nerve cells on nano-structured surfaces

Valentina Onesto[1], Enzo Di Fabrizio[1,2], Mario Cesarelli[3], Maria Laura Coluccio[1], Natalia Malara[1], Francesco Amato[1], Francesco Gentile[3]

[1] *Department of Experimental and Clinical Medicine, University of Magna Graecia, 88100 Catanzaro, Italy*

[2] *King Abdullah University of Science and Technology, Thuwal, Saudi Arabia*

[3] *Department of Electrical Engineering and Information Technology, University Federico II, Naples, Italy*

***Abstract*— Neural cells are the smallest building blocks of the central nervous system. Information in neural networks and cell-substrate interaction have been heretofore studied in isolation. Understanding how these fields correlate, and whether and to which extent surface nano-topography may induce nerve cells to cluster together into computational efficient networks, may provide new tools and criteria for tissue engineering and regenerative medicine. In this work, we used information theory approaches to study how information propagates in roughness induced neural cells networks. We found that information is maximized in small world architectures which, in turn, are generated over moderately rough substrates.**

I. Introduction

NEURONS are electrical active cells which process and transmit information through electrical and chemical signals [1, 2]. Understanding the way neural cells assemble, may provide new criteria for tissue engineering, regenerative medicine, the design of advanced lab-on-a-chips. Ultimately, it may explain the way human brain works and how it processes information. The complexity of human brain and behaviour may depend less on the specialization of individual nerve cells and more on the fact that a great many of these cells form complex networks. In complex systems interactions among large numbers of elements yield collective phenomena with improved abilities in contrast to isolated components of that system [3-5]. In cell-surface interaction, the cellular sensory machinery interacts with extremely small cues to regulate cell behaviour [6], therefore surfaces with random, rather than periodic, patterns at the nano-scale may control the organization of cells into clusters or networks with enhanced information speed. In [7], it was demonstrated that the adhesion and proliferation of neuroblastoma N2A cells is enhanced on silicon porous substrates with small average pore size and large fractal dimension: on similar substrates cells spontaneously assemble into clusters with a small world topology. Small world topology attracted recently much attention because it is hypothesized that dynamical systems with a small world topology may feature enhanced computational capabilities [5, 8]. Here, we used information theory based algorithms to simulate the total information transmitted in a grid in which the elements of the grid reproduce the topology of nerve cells cultured on nanostructured surfaces. Using variable such as the Shannon information rate, we provide an estimate of the quantity, quality and density of information exchanged in a grid of nerve cells. Moreover, we correlate the information in a grid with the topology of the grid.

II. Methods

A. Simulating Information in neural networks

We used a generalized leaky integrate and fire model to generate trains of signal in the grids. Resulting patterns of multiple spike trains in the grid were interpreted using an information theory based approach [9]. A way to study the activity of neuronal populations is to calculate the information about a given stimulus or behavior contained in the neuronal responses, using the formalism of Shannon information theory. The temporal sequence of pulses or spikes that propagates along the grid encodes the information transmitted over that grid, which can be represented through the sole Shannon information entropy. The spike train of individual neurons in response to a long sample of stimuli may vary. A similar variability is described by the total entropy of the spike train, *H*. Similarly, the conditional or noise entropy *N* represents the variability of the spike train in response to a sample of repeated stimuli. The information *I* that the spike train provides about the input is the difference between entropies, *I=H-N*. Suppose that a stimulus *s* belonging to a set *S* is presented with a probability *P(s)*. The Shannon entropy *H(S)* of the distribution of probabilities *P(s)* for each stimulus is defined as

$$H(S) = -\sum_{s} P(S) \log_2 P(S) \qquad (1)$$

The above formula quantifies the uncertainty about which stimulus is presented or, conversely, the average amount of information gained with each stimulus presentation. Entropy and information are both measured in bits if the logarithm is taken with base *2*. Operatively, to estimate the information transmitted in a specific network, we (i) stimulated the grid with an uncorrelated, random stimulus, from which we derived *H*; (ii) then, we stimulated the same grid with a periodic signal of time, from which we derived *N*; (iii) we derived the information *I* as *I=H-N*.

B. Deriving the topological properties of neural networks

Confocal images of the cells cultured on the substrates were processed to extract (i) the average cluster coefficient (*CC*) and (ii) the characteristic path length (*CPL*). The combination of these parameters gives an indication of the connectivity properties of the cells in a network. We implemented an algorithm described in detail in [10], whose core is constituted by the Waxman model. The Waxman model makes a decision on whether two nodes in a grid are

connected. It states that the probability of being a link between any two nodes exponentially decays with the Euclidean distance between them. Thus, for a given set of two nodes *u* and *v*, the link probability, *P(u, v)* is defined as:

$$P(u,v) = \alpha e^{-d(u,v)/\beta L} \quad (2)$$

where *d* is the Euclidean distance between nodes *u* and *v*, and *L* is the largest possible Euclidean distance between two nodes of the grid. In the equation, α and β are the Waxman model parameters and, upon tuning these, the graph may be more or less dense. The scalars α and β should be chosen between *0* and *1*, in a fashion that the network is sufficiently dense to reflect the topology of the system without loss of information. On the basis of *P*, one may derive the clustering coefficient

$$C_i = \frac{2E_i}{k(k-1)} \quad (3)$$

where *k* is the number of neighbors of a generic node *i*, E_i is the number of existing connections between those, *k(k- 1)/2* being the maximum number of connections, or combinations, that can exist among *k* nodes. The clustering coefficient C_i is defined locally, and a global value, *CC*, is derived upon averaging C_i over all the nodes that compose the graph. Similarly, the characteristic path length (*CPL*) is derived; *CPL* is calculated as the average minimum distance between any pair of nodes in the graph.

C. Fabrication

Planar surfaces with a roughness in the 1-100 nm range were fabricated following the methods reported in [11].

D. Sample Characterization

Substrates for neural adhesion were verified using Atomic Force Microscopy (AFM) [11].

E. Biological preparation

Hippocampal cultures from dissociated primary central neurons were be used. We used the methods described in [12] for culturing neurons on the substrates. Neurons on a substrate were imaged using confocal imaging and the methods described in [10].

III. Results

In isolated neurons, electric pulses excite the neuron until the response (potential) at the postsynaptic sites reaches and surpasses a limiting value (that is, a threshold), then, the target neuron produces an impulse (an action potential) that propagates in turn to another neuron; the time distribution of pulses encodes information. In considering an ensemble of neurons in a grid, the response of the grid is described by the superposition of individual responses, i. e. by a set of coupled differential equations. Using the algorithms described in the methods section, we extracted the cell centers and the cell to cell connections (Figure 1b-d) from confocal images of nerve cells cultured on nano-structured surfaces (Figure 1a), and the topology of the grid. We used these information to reproduce artificial networks in which the elements of the networks were excited with a variable function of time. Upon excitation, spikes propagate in cascade in the grid. Time spikes are grouped in sets of words, in which a word is an array of on (presence of a spike)/off (absence of a spike) events in a binary representation (Figure 2a). On sorting words in order of decreasing occurrence in the train, we obtained the associated entropy using equation (1) (Figure 2a). We repeated this procedure in response to an uncorrelated (Figure 2b) and time locked signal, and to a correlated (Figure 2c) signal of time. From the difference of entropies, we calculated the information transmitted over all the nodes of the grid (Figure 3a). We derived the information starting from cells cultured on either planar and rough silicon substrates and observed that information increases with surface roughness (Figure 3b). More important, information and topology of a grid are correlated, meaning that information in a network increases with the clustering coefficient and the inverse of the characteristic path length of that network (Figure 3c-d). These findings reinforce the view that networks with a small world architecture are computational efficient.

IV. Conclusions

We used information theory variables to simulate the information exchanged in neural networks. We found that information depends on the topology of the network over which it propagates: information increases moving from random to small world graphs. We demonstrated that cells on etched substrates may spontaneously assemble into clustered groups of cells, thus nano-topography can be used to control the organization of cells into computational efficient grids.

References

[1] [1] E. Kandel, J. Schwartz, and T. Jessell, Principles of Neural Science, 4/e ed. New York: McGraw-Hill, 2000.

[2] [2] M.-H. Kim, M. Park, K. Kanga, and I. S. Choi, "Neurons on nanometric topographies: insights into neuronal behaviors in vitro," Biomaterials Science, vol. 2, pp. 148–155, 2014.

[3] [3] J. P. Crutchfield, "Between order and chaos," Nature Physics, vol. 8, pp. 17-24, 2012.

[4] [4] J. J. Hopfield, "Neural networks and physical systems with emergent collective computational abilities," Proc. Nat. Acad. Sci. USA, vol. 79, pp. 2554-2558, 1982.

[5] [5] S. H. Strogatz, "Exploring complex networks," Nature, vol. 410, pp. 268-276, 2001.

[6] [6] P. Kanchanawong, G. Shtengel, A. M. Pasapera, E. B. Ramko, M. W. Davidson, H. F. Hess, et al., "Nanoscale architecture of integrin-based cell adhesions," Nature, vol. 468, pp. 580-586, 2010.

[7] [7] F. Gentile, R. L. Rocca, G. Marinaro, A. Nicastri, A. Toma, F. Paonessa, et al., "Differential Cell Adhesion on Mesoporous Silicon Substrates," ACS Applied Materials and Interfaces, vol. 4, pp. 2903–2911, 2012.

[8] [8] D. J. Watts and S. H. Strogatz, "Collective dynamics of 'small-world' networks," Nature, vol. 393, pp. 440-442, 1998.

[9] [9] R. Q. Quiroga and S. Panzeri, "Extracting information from neuronal populations: information theory and decoding approaches," Nature Reviews Neuroscience, vol. 10, pp. 173-185, 2009.

[10] [10] G. Marinaro, R. La Rocca, A. Toma, M. Barberio, L. Cancedda, E. Di Fabrizio, et al., "Networks of Neuroblastoma Cells on Porous Silicon Substrates Reveal a Small World Topology," Integrative Biology, vol. 7, pp. 184-97, 2015.

[11] [11] F. Gentile, L. Tirinato, E. Battista, F. Causa, C. Liberale, E. Di Fabrizio, et al., "Cells preferentially grow on rough substrates," Biomaterials, vol. 31, pp. 7205-12, 2010.

[12] [12] T. Limongi, F. Cesca, F. Gentile, R. Marotta, R. Ruffilli, A. Barberis, et al., "Nanostructured Superhydrophobic Substrates Trigger the Development of 3D Neuronal Networks," Small, vol. 9, pp. 402–412, 2013.

[13] [13] D. J. Watts, Small Worlds: The Dynamics of Networks between Order and Randomness. Woodstock: Princeton University Press, 2003.

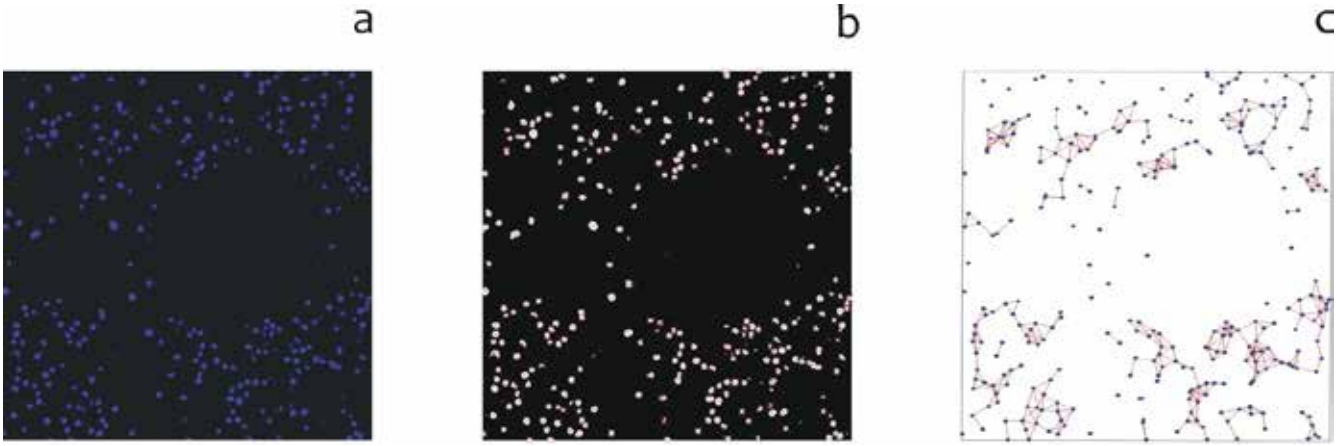

Figure 1

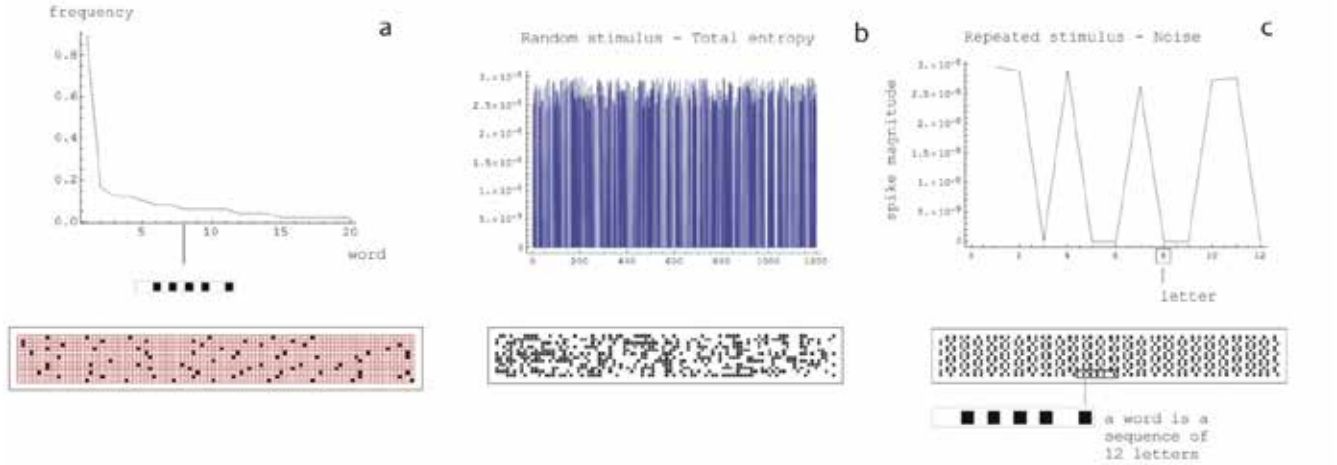

Figure 2

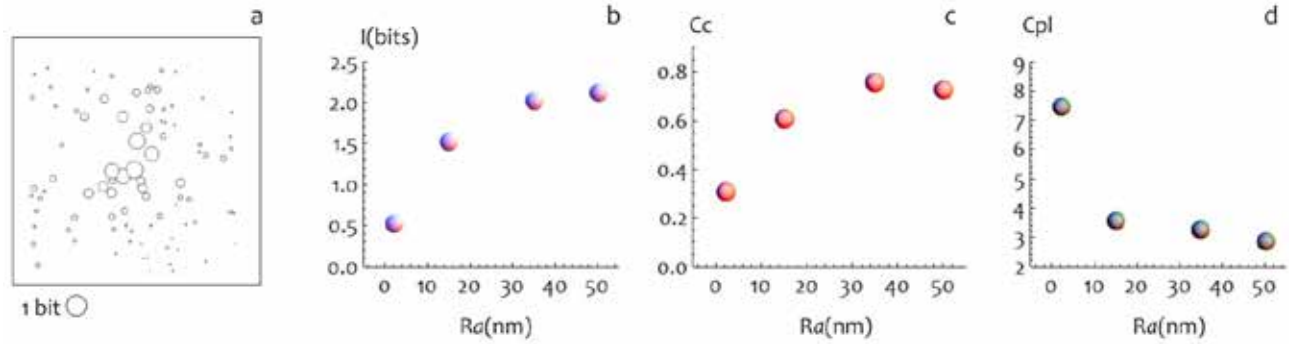

Figure 3

Development of chitosane derived scaffold for 3D engineered neuronal cultures

Pastorino Laura[1], Tedesco Mariateresa[1], Colistra Nicolò[1], Massobrio Paolo[1], Martinoia Sergio[1,2]
[1]*Neuroengineering and Bionanotechnology Lab (NBT), Department of Informatics, Bioengineering, Robotics and System Engineering (DIBRIS), University of Genova, Via All'Opera Pia 13, 16145 – Genova, Italy.*
[2]*Institute of Biophysics, CNR, Genova, Italy.*

***Abstract*—2D neuronal populations coupled to Micro-Electrode-Arrays (MEAs) constitute a well-established experimental in-vitro platform to study neurobiology, network electrophysiology, and basic injury-disease mechanisms. Besides clear advantages related of controllability and observability, such 2D neuronal model systems have major limitations, as they might be inherently unable to exhibit characteristics of in-vivo systems. Under this perspective the development of a 3D engineered in-vitro neuronal model can certainly be seen as a complementary-alternative and interesting tool for neurophysiological investigations. In this work, we propose a new approach for designing 3D engineered in-vitro neuronal cultures. To this aim, we have developed a 3D scaffold based on the assembly of chitosan microparticles in the view of mimicking the extracellular matrix environment.**

We show the procedure for fabricating the microbeads scaffold, for cell seeding and network formation and how we couple this 3D neuronal culture to standard MEAs. We present the spontaneous electrophysiological activity of such 3D neuronal networks and we compare the obtained dynamics from two types of chitosan-derived microbeads with standard 3D networks grown onto glass-microbeads and 2D nets.

***Keywords*—3D neural networks, network dynamics, chitosan, MEAs.**

I. Introduction

In the last years, new studies have been performed for developing in-vitro 3D neuronal systems [1]–[2]. The potential advantages of 3D engineered constructs are evident as they can be used as a more accurate investigational in-vitro platform than standard 2D network models [1]. Indeed, 3D networks coupled to Micro-Electrode Arrays (MEAs), represent a powerful in-vitro model capable of better emulating in-vivo physiology. In this work, we propose and compare different methods for the development of 3D in-vitro neuronal models with respect to a previous work, where the scaffold of 3D networks were realized by means of glass micro-beads [1]. Here, 3D neuronal constructs were developed and implemented by using assembled chitosan microparticles, ranging in diameters from 40 to 80 μm, depending on the preparation procedure [3].Chitosan is characterized by a greatest surface of amine content and, at the same time, by a lowest equilibrium of water content which contribute to the high viability of cells in culture [4]. Specifically, two protocols were adopted for the preparation of the micro-particles, one based on the use of a neutralizing solution as hardening medium and one based on the use of a cross-linking solution. Then, the micro-particles were assembled with neurons and the obtained 3D construct was coupled to a planar MEA to record the electrophysiological activity of the network. We analysed the dynamics of such 3D neuronal networks comparing their spontaneous activity with the ones of two specific control systems: (i) 3D hippocampal neuronal network grown onto glass microbeads and (ii) standard 2D networks, both coupled to MEAs [1].

II. Material and methods

A. Cell culture

Hippocampal neurons were dissociated from rats E18 Sprague Dawley. MEAs supports and all micrometric beads (made of neutralized and cross-linked chitosan) were sterilized and pre-coated with adhesion proteins (poly-lysine and laminin). The hippocampi were dissociated in a trypsin enzymatic solution and the cells were kept in a Neurobasal medium + B27 + Glutamax 1% and 1% Pen-Streptomycin. The cell suspension was added both to the preconditioned microparticle suspension at an high concentration of 3.10^6 cells\ml, and to the preconditioned MEA substrate at a lower concentration of 7.10^5 cells/ml. After few hours, the assembled neurons-microparticles suspension was transferred onto the top of the neuronal monolayer already attached to the MEA surface. Cultures were maintained in the incubator at 5% CO_2, 95% humidity and half of medium was changed weekly for a time around of 28 days.

B. Chitosan micro-beads

Chitosan neutralized micro-beads were formed by extruding 1% w/v chitosan solution through a 0.25 mm nozzle into a basic coagulation solution consisting of sodium hydroxide-ethanol-water (20:30:50 v/v). The cross-linked micro-beads were obtained based on ionic gelation of TPP with chitosan. Briefly, in this case the chitosan was extruded into a 1% w/v TPP solution at pH6. The micro-beads were removed from the neutralizing and cross-linking solutions by centrifugation followed by four washing steps in distilled water. The so obtained microspheres were finally sterilized in 70% ethanol for 3 hours.

C. Data and Statistical analysis

Data analysis was performed off-line by using a custom software package named SpyCode [5] developed in MATLAB (The Mathworks, Natick, MA, USA). We characterized the spontaneous activity by means of first-order statistics like mean firing rate, percentage of random spike, mean bursting rate, burst duration, network burst duration,

mean network bursting rate. Data were expressed as mean ± standard error of the mean. Statistical analysis was performed using MATLAB. Since data do not follow a normal distribution, we performed a non-parametric Mann-Whitney U-test.

D. MEA set-up

The electrophysiological activity of neuronal networks (18-21DIV) was recorded in all the performed experiments by means of planar TiN 60 channels MEAs, supplied by Multi Channel Systems (MCS, Reutlingen, Germany).

III. Results

The obtained chitosan microparticles were firstly characterized by optical microscopy. The obtained micro-particles showed a spherical shape for both protocols. The average diameter was found to be 70 ± 6µm for the neutralized microparticles and 40 ± 4µm for the cross-linked ones. The microstructure of the particles was then characterized by scanning electron microscopy (fig. 1a). The neutralized micro-particles showed a porous structure, while the cross-linked ones showed a more compact structure.

The microparticles based scaffold, put in contact with neurons showed to support quite well the development, over three to four weeks, of the hippocampal neuron culture. In fact, this polysaccharide is able to exert a positive effect on the cellular adhesion and to promote a quick neuritic growth. At the end of the electrophysiological sessions, the cultures were processed according to the methods of immunofluorescence (Fig. 1b). Confocal imaging was performed by using Leica TCS SP5 AOBS Tandem DM6000 upright microscope equipped with HCX APO 20x N.A. 0.50 WI objective.

We analysed the spontaneous electrophysiological activity of 3D neutralized chitosan hippocampal neuronal network and 3D cross-linked CS/TPP hippocampal neuronal network compared with the two gold-standard reference models (i.e., 2D and 3D with glass microbeads). We evaluated the percentage of random spikes and the mean firing rate in all (n =4) the performed experiments (Fig. 2). We observed that 2D networks exhibit a low percentage of random spikes (10.4 ± 3.8%) with a high frequency of firing (12.9 ± 7.1 spikes/s), differently the 3D networks show a higher level of random spikes with a lower firing rate. In particular, the 3D neutralized chitosan network presents a significant higher level of random spikes (40.7 ± 1.5%) but a very low frequency (2.3 ± 1 spikes/s). To quantify the bursting activity at the single channel level, the frequency and the duration of the bursts were evaluated in all the performed experiments. 2D networks present a strong synchronous bursting activity with a higher bursting rate (21.5 ± 9.8 burst/min) than the three 3D neural networks. In addition, we observed that 3D neutralized chitosan network exhibits a burst duration (311.7 ± 54.3 ms) higher than other cultures. Then, we computed the network mean bursting rate and duration evaluated over the entire dataset. In particular, the 3D neutralized chitosan network shows few network bursts (12.4 ± 5.2 NB/min) with a high duration (978.5 ± 310.5 ms).

IV. Conclusion

The new developed scaffolding procedure for realizing 3D neuronal networks can constitute an alternative 3D in-vitro neuronal model that can be used to investigate neurophysiological mechanisms and computational properties of neuronal networks in a controlled experimental setting. To further exploit the proposed 3D engineered neuronal networks and to study how the 3D neuronal network dynamics changes in different layers of the structure, 3D recording devices are needed. Finger like structure with embedded microelectrodes, sandwich-structure (i.e. standard MEA from the bottom side and a planar multi-channel recording structure on the upper side) or truly 3D-MEAs have to be developed to record the activity of the 3D neuronal network from different locations in the 3D space. A complete 3D-3D in-vitro system might open new prospects for manipulating, stimulating and recording the neuronal activity to elucidate neurophysiological mechanisms and to design bio-hybrid microsystems.

References

[1] M. Frega, M. Tedesco, P. Massobrio, M. Pesce, and S. Martinoia, “Network dynamics of 3D engineered neuronal cultures: a new experimental model for in-vitro electrophysiology”. Scientific Reports 4, Article number: 5489. June 2014.

[2] Tang-Schomer et al.” Bioengineered functional brain-like cortical tissue.” Proc.Natl. Acad Science 23;111(38) September 2014

[3] F. Croisier, C. Jérôme. “Chitosan-based biomaterials for tissue engineering”. European Polymer Journal, 49(4), 780-792. April 2013.

[4] V. Scanga, A. Goraltchouk, N. Nussaiba, M. Shoichet, and C. M. Morshead, “Biomaterials for neural-tissue engineering”. Can. J. Chem. Vol. 88. March 2010.

[5] L. L. Bologna, V. Pasquale, M. Garofalo, M. Gandolfo, P. L. Baljon, A. Maccione, S. Martinoia, and M. Chiappalone, “Investigating neuronal activity by SPYCODE multi-channel data analyzer”. Neural Net. 23, 685–697. May 2010.

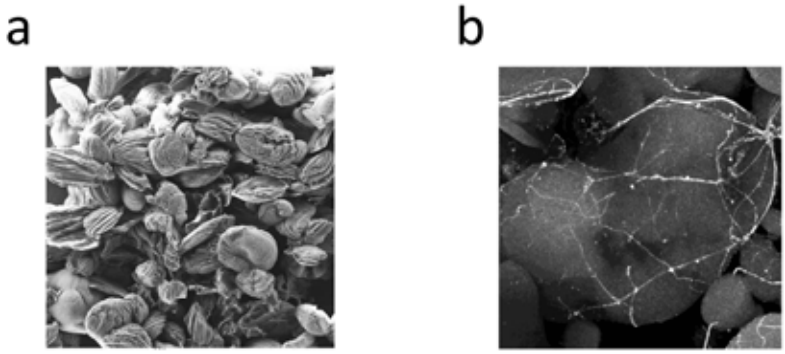

Fig. 1. (a). Scanning electron microscopy image of chitosan neutralized microparticles. (b). Confocal image (max projection, 213X213 µm) that shows rich neurite extension at DIV24 in-vitro of an hyppocampal culture, growth on neutralized chitosan microparticles immunolabeled with anti-tubulin ßIII-Alexa Fluor 546 conjugated.

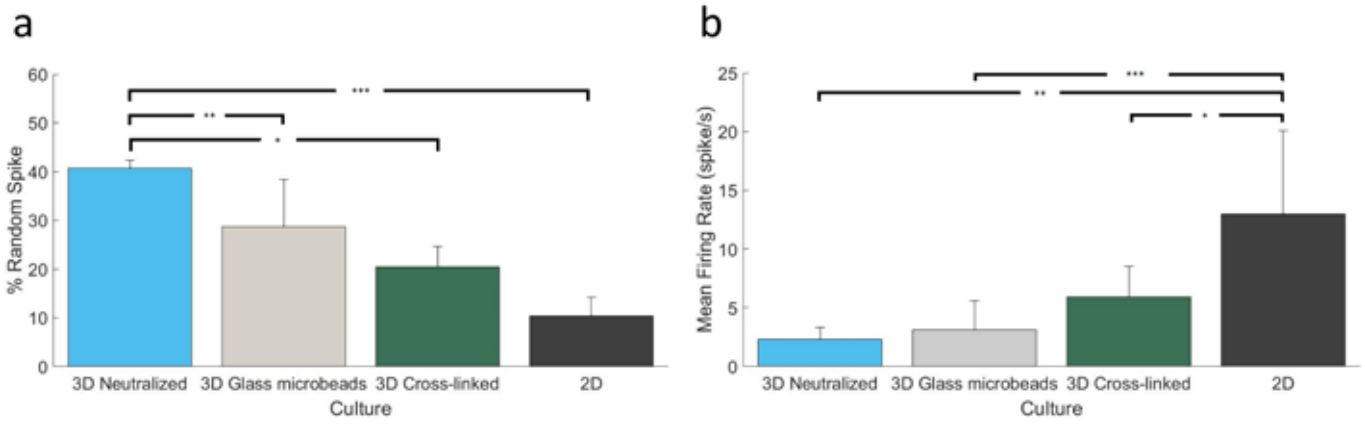

Fig. 2. (a). Percentage of random spikes ($* P_{value} = 2 * 10^{-7}$, $** P_{value} = 6 * 10^{-6}$, $*** P_{value} = 4 * 10^{-7}$, Mann-Whitney U-test). (b). Mean Firing Rate ($* P_{value} = 6 * 10^{-6}$, $** P_{value} = 6 * 10^{-8}$, $*** P_{value} = 6 * 10^{-10}$, Mann-Whitney U-test). Asterisks above the plots indicate statistically significant differences.

A novel sensitive and selective mechano-stimulation technology on genetically modified cells

C. Rojas[1], E. Defranchi[1], M. Fiore[2], M. Pusch[2], S. Shoam[3], and R. Raiteri[1,2]
[1] *Department of Informatics, Bioengineering, Robotics, and System Engineering, University of Genova, Genoa, Italy*
[2] *Istituto di Biofisica, Consiglio Nazionale delle Ricerche, Genoa, Italy*
[3] *Faculty of Biomedical Engineering, Technion-Israel Institute of Technology, Haifa 32000, Israel*

***Abstract*— We introduce an *in vitro* technique to modulate ion fluxes through cell membranes that over-express mechanically activated ion channels, namely Piezo channels, by the remote application of ultrasound.**

We propose this technique as a novel paradigm for noninvasively modulating the electrical activity of specific populations of neurons in the brain using acoustic waves: selected neurons are modified to sensitize them to mechanical stimuli, remotely generated acoustic waves can then provide a low intensity mechanical stimulus that excites/inhibits selectively and non-invasively the electrical activity of such neurons, without any risk of interfering or damaging the surrounding cells and tissues.

We present preliminary experimental results on the intracellular calcium response to the application of ultrasound on model cells transfected with Piezo1 channel as a proof of principle of the proposed strategy.

***Keywords*—mechano-receptors, acoustics, ultrasound stimulation, neuroengineering**

I. Introduction

OPTOGENETICS is widely considered as one of the major breakthrough technologies of the last decade [1-4]; one main critical aspect when *in vivo* therapeutic applications are foreseen is its invasive nature (light needs to be brought close to the modified neurons). Recently a procedure to manipulate the behaviour of *C. elegans* earthworms by ultrasound application has been proposed [5], presumably via stimulation of endogenous mechanosensitive ion channels. We propose to extend this strategy to vertebrates and, eventually, to humans: specific neuronal populations are sensitized to ultrasound stimulation by the targeted expression of mechanosensitive ion channels, thus providing selectivity as with optogenetics, yet in a much less invasive way.

Two proteins, Piezo1 and Piezo2, have been recently identified as the only directly mechano-gated mammalian membrane ion channels [6, 7]; both cation-selective channels are directly and rapidly (millisecond-timescale) activated by mechanical deformation of the plasma membrane; we hypothesize that modification of specific neuronal populations by the introduction of the Piezo channels will render the neurons sensitive to low intensity ultrasonic stimulation in a highly specific and predictable manner. To prove this hypothesis we conducted preliminary experiments on a model, easy to transfect, cell line named HEK293 and measured channel activation either as a direct current flow or as a flux of Ca^{2+} ions through the membrane.

II. Materials and Methods

A. Cell transfection

HEK293 cells were co-transfected with plasmid DNA encoding both human Piezo1 and a fluorescent label (Green Fluorescent Protein, GFP) using the Effectene reagent (Qiagen). GFP allows the identification of positively transfected cells in culture by fluorescence microscopy.

B. Patch clamp

Standard whole-cell patch clamp recordings were performed using the following solutions: extracellular: 140 mM NaCl, 6 mM $CaCl_2$, 2 mM KCl, 10 mH Hepes (pH 7.3); intracellular: 130 mM CsCl, 2 mM $MgCl_2$, 10 mM Hepes, 10 mM EGTA (pH 7.3). Cells were held at -60 mV and mechanically stimulated by indentation with a second blunt glass micropipette fixed to a computer-controlled piezoelectric actuator.

C. Ultrasound stimulation

We employed a commercial piezoelectric transducer (type BJC-4060T- 49HN PZT-8, Beijing Ultrasonic, China) driven by a custom built high frequency, high voltage power amplifier.

In order to optimize ultrasound transmission and generate a focused and uniform pressure field onto the cell culture area we designed and fabricated a coupling element consisting of a polymeric cone with an aperture of 5 mm in diameter, filled with degassed water. Figure 2A shows a schematic drawing (left) and a picture (right) of the set-up for ultrasound stimulation which was mounted onto an inverted microscope equipped for epi-fluorescence. The fine approach of the coupling cone toward the cell culture was controlled using a micrometer screw and the focusing capability of the inverted microscope in order to reproducibly reach a distance between the tip of the cone and the cell culture of 500 μm

The intensity and uniformity of the generated pressure field was mapped using a calibrated miniaturized hydrophone (Reson model TC4038-1) which was moved in front of the coupling cone using a micromanipulator.

D. Calcium imaging

The set-up for acoustic stimulation was mounted on top of an inverted microscope (Olympus IX70) equipped with a LED light sources (Rapp OptoElectronic) at 470 nm and 530 nm for fluorescence excitation and CMOS camera (ORCA-Flash4.0, Hamamatsu, Japan). Images were collected using Hamamatsu's proprietary software (HCImage) and post-processed using ImageJ software.

Intracellular Ca^{2+} was monitored non ratiometrically using the Ca^{2+} sensitive dye Rhod4, loaded into the cells at 10 μM as the AM-ester, with excitation at 530 nm and emission at 555 nm.

Normalized fluorescence intensity changes $\frac{\Delta F}{F}$ were calculated, as in Eq. (1).

$$\frac{\Delta F}{F} = \frac{(F-F_B)\cdot(F_0-F_B)}{F_0-F_B} \qquad (1)$$

Where F is the raw fluorescence signal, F_B is the background fluorescence, and F_0 is the average fluorescence signal in a time interval prior to the ultrasound stimulation (baseline).

III. Results and Discussion

Piezo1 DNA plasmids were amplified and co-transfected with a GFP expression marker into HEK293 cells. Piezo1 functionality in the transfected cells was first validated using patch clamp and direct mechanical stimulation, following the procedure described in [6]. Figure 1 shows an example of the current response to increasing indentations using a small glass pipette. Increase in the measured current after the pipette touches the cell is ascribed to the opening of membrane channels.

In parallel we preliminary verified the optical system's ability to reliably detect intracellular [Ca^{2+}] changes by adding the ionophore ionomycin to the culture medium (data not shown).

In a typical experiment we first loaded cultured Hek293 cells with the red fluorescent Ca^{2+} indicator Rhod4. We then imaged the cell culture in order to detect the green emission from GFP label as shown in figure 2B. From the image it is possible to identify transfected cells, that, we assume, express the Piezo1 channel. By phase contrast imaging we could select different cell areas (transfected and non transfected as a reference) where to monitor the fluoresce signal from the Ca^{2+} indicator during acoustic stimulation. We then applied a sequence of US pulses (30 ms duration, 100 ms interval between pulses, 16.6 kPa amplitude, 44kHz frequency) while monitoring the fluorescence intensities in the different regions of interest as shown in figure 2C. The graph in figure 2C shows an evident change fluorescence during the acoustic stimulation only for the two GFP-expressing cells. By repeating the experiment several times with different cell preparations we observed that the pulsed US train led to detectable stimulus–locked Ca^{2+} increases in a fraction of the GFP/Piezo1-expressing cells, but in none of the GFP/Piezo1-free cells, thus indicating an observed response specific to the presence of Piezo1.

Interestingly, the US parameters necessary for the observed channel activation (pressure of 10-20 kPa at low ultrasonic frequency of 44kHz) correspond to a Mechanical Index < 0.2, which is well below the upper limit of 1.9 set by FDA for diagnostic ultrasound scanners. At the same time, pressure levels found in extreme environmental conditions (e.g. in the air close to ultrasonic welders, where pressure waves of ~130dB=63.24 Pa at 22 kHz have been measured [8]) are unlikely to interfere with the proposed acoustic stimulation, because such values are three orders of magnitude lower than the local pressure necessary to obtain the observed cellular response, even without taking into account i) the almost complete reflection at the air/tissue interface due to the difference in acoustic impedance and ii) the skull attenuation. This makes the proposed stimulation strategy, at least in principle, compatible for *in vivo* chronic operation and, at the same time, seems to rule out the risk of interferences from the environment.

IV. Conclusion

We propose a new technique based on acoustic stimulation of cells overexpressing specific membrane receptors that is similar to optogenetics; yet, its non-invasive way of stimulation represents a major advantage when considering *in vivo* operation: while light needs to be brought close to the target cells in order to stimulate them, acoustic waves can be remotely focused virtually anywhere within the human central nervous system.

Our preliminary results provide a fundamental *in vitro* validation to the feasibility of the proposed approach. The long term goal is to develop a novel class of neuroprosthetic devices to induce compensatory neural activity in malfunctioning areas of the brain (e.g. in epilepsy, in hyper-excitability conditions after traumatic brain injury, or in other neuropathological situations).

Acknowledgement

Piezo1 DNA plasmids were kindly provided by P. Gottlieb (Buffalo Univ., NY). We would like to thank Michael Plaksin (Technion Israel Institute of Technology) for the helpful discussion regarding the US excitation set-up.

References

[1] Editors, "Method of the Year 2010". Nat Meth, vol. 8, pp. 1-1, 2011.
[2] N. K. Logothetis, "Bold claims for optogenetics". Nature, vol. 468, pp. E3-4; discussion E4-5, 2010.
[3] L. Fenno, O. Yizhar, and K. Deisseroth, "The development and application of optogenetics". Annu Rev Neurosci, vol. 34, pp. 389-412, 2011.
[4] M. Gross, "Shining new light on the brain". Curr Biol, vol. 21, pp. R831-3, 2011.
[5] S. Ibsen, A. Tong, C. Schutt, S. Esener, and S. H. Chalasani, "Sonogenetics is a non-invasive approach to activating neurons in Caenorhabditis elegans". Nat. Comm., vol. 6, 2015.
[6] B. Coste, J. Mathur, M. Schmidt, T. J. Earley, S. Ranade, M. J. Petrus, A. E. Dubin, and A. Patapoutian, "Piezo1 and Piezo2 are essential components of distinct mechanically activated cation channels". Science, vol. 330, pp. 55-60. , 2010.
[7] B. Coste, B. Xiao, J. S. Santos, R. Syeda, J. Grandl, K. S. Spencer, S. E. Kim, M. Schmidt, J. Mathur, A. E. Dubin, M. Montal, and A. Patapoutian, "Piezo proteins are pore-forming subunits of mechanically activated channels". Nature, vol. 483, pp. 176-81., 2012.
[8] B. Smagowska and M. Pawlaczyk-Luszczynska, "Effects of ultrasonic noise on the human body-a bibliographic review". Int J Occup Saf Ergon, vol. 19, pp. 195-202, 2013.

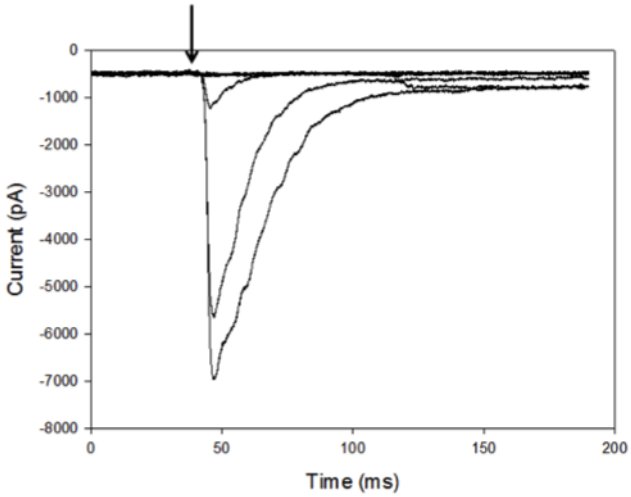

Fig. 1 *Current responses to mechanical stimulation from a HEK293 cell recorded in whole cell mode. Different plots correspond to increasing stimulation pipette indentation at the time point indicated by the arrow.*

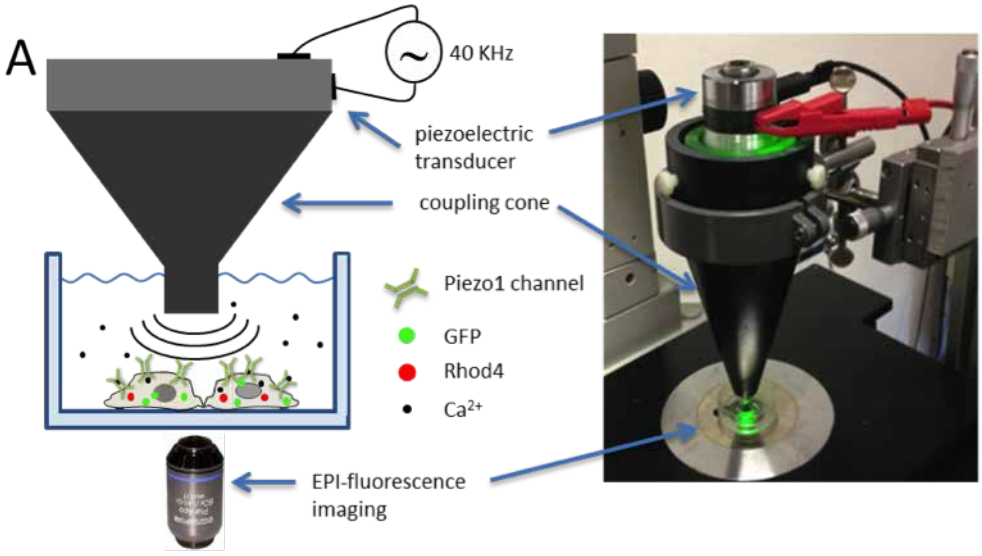

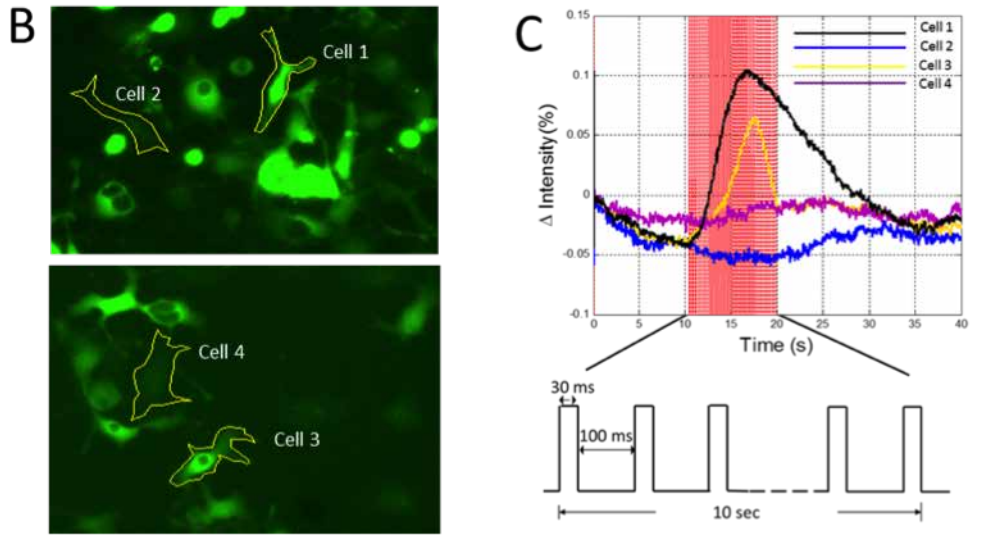

Fig.2 *(A) Schematic drawing and picture of the set-up set-up for acoustic stimulation and calcium imaging; (B) GFP fluorescence images of transfected HEK293 cells; (C) change in Rhod4 fluorescence intensity (calcium signal) calculated over the three cell areas indicated in (B), being cell 2 a reference cell not expressing GFP. The red bar in the graph indicates the 10 sec interval during which a train of 30 ms pulses of acoustic signal at 44 kHz was generated.*

Neurometric Evaluation of Effective and Ineffective Antismoking PSAs

D. Rossi[1], G. Cartocci[2], E. Modica[1], A.G. Maglione[2], I. Venuti[2], G. Rossi[2], E. Corsi[2] and F. Babiloni[2, 3]
[1] *Dept. Anatomical, Histological, Forensic & Orthopedic Sciences, Sapienza University of Rome, Italy*
[2] *Department of Molecular Medicine, Sapienza University of Rome, Italy*
[3] *BrainSigns srl, via Sesto Celere 7/c, Rome, Italy*

***Abstract*— Nowadays, public service announcements (PSAs) against smoke are considered "Effective" or "Ineffective" on the base of official reports concerning behavioral/attitudinal changes toward healthier patterns and health-related savings following the exposure to the PSA. In this pilot study, we described the results of the use of two neurometric indexes for the evaluation of the efficacy of a couple of antismoking PSAs in a reduced sample of voluntary participants. The neurometric indexes here employed are the Approach-Withdrawal (AW) and mental Effort (Efl).**

***Keywords*—Smoking, PSA, AW, Effort.**

I. Introduction

TOBACCO use is the leading cause of preventable death and smoking-related illness worldwide. Research has shown that antismoking Public Service Announcements may help reduce this tendency [1], [2]. In order to identify these PSAs as "Effective" or "Ineffective", not only by the official reports concerning behavioural/attitudinal changes, we studied the cognitive reaction to a couple of PSAs belonging to the two categories, according to key performance indicators (KPI) provided by independent health organizations.

EEG data has been gathered during the vision of these PSAs in a restricted group of voluntary participants: analysing the rhythm variation we were able to evaluate Approach-Withdrawal (AW) index [3] and Effort (Eff) [4].

Results are the comparison of these indexes related to the PSAs perception among the sample population.

II. Methods

A. Sample population

Seven healthy subjects (mean age 22,8, min 19 max 31 years old) have been enrolled on a voluntary base. Concerning smoking habits, 2 subjects were smokers and 3 ex-smokers, the remaining 2 subjects were not smokers. All subjects were given of detailed information about the study and signed an informed consent. The experiment was performed in accord to the principles outlined in the Declaration of Helsinki of 1975, as revised in 2000, and it was approved by the University ethical committee.

B. Stimuli presentation

Participants were sitting on a comfortable chair in front of a screen, where a series of TV advertisings were played. The two target stimuli, the Effective and the Ineffective TV advertisings were randomly interspersed among 8 distractors, so producing a 10 spots train, proceeded and followed by two parts of a documentary (60s each).

The two TV advertisings can be retrieved at the following links respectively:
https://www.youtube.com/watch?v=aHrdy6qcumg
https://www.youtube.com/watch?v=3B133Es-CKA .

C. EEG recording and signal processing

The EEG activity was recorded by means of a portable 24-channel system (BEmicro, EBneuro, Italy); 19 electrodes were used according to the 10-20 international system, with impedance below 10 kΩ, and a recording sampling rate of 256 Hz. In order to detect end remove eye movements, blinks and muscular artifacts from the EEG signal a notch filter (50 Hz), a lowpass filter (30 Hz) were applied as well as the Independent Component Analysis (ICA).

Individual Alpha Frequency (IAF) has been calculated for each subject in order to define the frequency bands as suggested in literature [5]. From the each frontal channel has been calculated the Global Field Power (GFP); several studies [3], [6], [7] suggest that the frontal cortex is an area of interest for the analysis of the Approach-Withdrawal attitude [3] and cerebral effort [5], [8] in response to a wide range of stimuli.

The AW index has been obtained as in Eq. (1).

$$AW = GFPa\_right - GFPa\_left \quad (1)$$

Where GFPa_right stands for the GFP calculated on frontal right electrodes (Fp2, F4 and F8) and GFPa_left on frontal left electrodes (FP1, F3 and F7), in alpha band, estimated for each second and then average for all the duration of the stimuli.

Then the AW index has been standardized to the baseline EEG activity acquired before and after the stimuli train, so that positive AW values mean an approach motivation toward the stimulus of the subject, while negative AW values a withdrawal tendency.

While for the evaluation of the cerebral effort GFP of frontal electrodes (Fp2, F4, F8, Fz, F7, F3and Fp1) of theta band has been calculated. Even in this case the effort index (Eff) has been standardized to the baseline EEG activity acquired before and after the stimuli train; in this way higher level of Eff imply higher level of task difficulty [4].

D. Statistical analysis

Paired t-test comparisons have been performed on the EEG estimated indexes.

III. RESULTS

A. Approach Withdrawal Index (AW)

The AW indexes estimated for the two evaluated PSAs reported a statistically significant higher value for the "Effective" PSA compared to the "Ineffective" PSA in the sample population ($t = 3.20$, $p = 0.02$), as reported in the Fig. 1. We can also note that the AW index is positive for the "Effective" PSA, but negative for the "Ineffective" PSA.

B. Effort Index (Eff)

Even for the estimated Effort Index, the values for the observation of the "Effective" PSA were higher when compared to the values of the "Ineffective" PSA, with a statistical significance ($t = 2.8$, $p = 0.03$), as shown in Fig. 2.

IV. DISCUSSION

The AW index values report a higher activity in the left frontal area and a reduced activity in the right frontal area [3] while observing the "Effective" PSA. This evidence is supported in literature [9] where is observed an increased deactivation in the right dorsal medial prefontal cortex and the parallel increased activation in the left frontal gyrus during the exposure to high quality and persuasive advertisement. The negative AW index values reported during the vision of the "Ineffective" PSA, suggesting a withdrawal motivation toward the spot, can be explained by the instinctive refuse of identification by the subjects, with the monkey that is the main feature of this ad.

Concerning the Eff values the higher level of effort shown for the "Effective" PSA can be explained, at the light of the AW results that supports a positive reaction toward this ad, by a higher level of cerebral involvement experienced by the subjects; on the contrary the "Ineffective" spot can be perceived as "too simple" by the subjects, explaining the low values of Effort index.

V. CONCLUSION

The neurometric approach applied in this pilot study to the evaluation of anti-smoking PSAs seems to be consistent with the classification of effectiveness based on behavioural and economic data, also it could be helpful in pre-evaluation of public health announcements to be aired.

Performing such studies on a realized PSA can be important in order to know in advance if a campaign can be successful or not and save, in this way, relevant economic support from the local Minister of Health. In the framework of a recently funded EU project, named "SmokeFreeBrain", the aim is to better characterize the successful antismoking PSAs, from the neurometric point of view and spread this knowledge among EU Minister of Health.

It must be noted that due to the small sample population and the limited number of PSAs analysed, further investigations must be conducted in term of enlarged stimuli sample and number of participants to extract the relevant features that characterize the realization of an effective anti-smoking PSAs.

ACKNOWLEDGEMENT

The present work was supported in part by the European Commission by Horizon 2020 project HCO-06-2015, "SmokeFreeBrain", GA n. 681120. Authors thank the students and the personnel of Residenza Universitaria Don Bosco of Rome for their availability.

REFERENCES

[1] M. M. Bala, L. Strzeszynski, R. Topor-Madry, and K. Cahill, "Mass media interventions for smoking cessation in adults," *in Cochrane Database of Systematic Reviews*, John Wiley & Sons, Ltd, 2013.

[2] M. Siegel and L. Biener, "The impact of an antismoking media campaign on progression to established smoking: results of a longitudinal youth study.," *Am J Public Health*, vol. 90, no. 3, pp. 380–386, Mar. 2000.

[3] R. J. Davidson, "What does the prefrontal cortex 'do' in affect: perspectives on frontal EEG asymmetry research," *Biological Psychology*, vol. 67, no. 1–2, pp. 219–234, Oct. 2004.

[4] M. G. Wisniewski, E. R. Thompson, N. Iyer, J. R. Estepp, M. N. Goder-Reiser, and S. C. Sullivan, "Frontal midline θ power as an index of listening effort," *Neuroreport*, vol. 26, no. 2, pp. 94–99, Jan. 2015.

[5] W. Klimesch, "EEG alpha and theta oscillations reflect cognitive and memory performance: a review and analysis," *Brain Research Reviews*, vol. 29, no. 2–3, pp. 169–195, Apr. 1999.

[6] G. Borghini, P. Arico, G. D. Flumeri, S. Salinari, A. Colosimo, S. Bonelli, L. Napoletano, A. Ferreira, and F. Babiloni, "Avionic technology testing by using a cognitive neurometric index: A study with professional helicopter pilots," in *2015 37th Annual International Conference of the IEEE Engineering in Medicine and Biology Society (EMBC)*, 2015, pp. 6182–6185

[7] A. G. Maglione, A. Scorpecci, P. Malerba, P. Marsella, S. Giannantonio, A. Colosimo, F. Babiloni, and G. Vecchiato, "Alpha EEG Frontal Asymmetries during Audiovisual Perception in Cochlear Implant Users. A Study with Bilateral and Unilateral Young Users," *Methods Inf Med*, vol. 54, no. 6, pp. 500–504, 2015.

[8] A. Gevins and M. E. Smith, "Neurophysiological measures of cognitive workload during human-computer interaction," *Theoretical Issues in Ergonomics Science*, vol. 4, no. 1–2, pp. 113–131, Jan. 2003.

[9] A.-L. Wang, K. Ruparel, J. W. Loughead, A. A. Strasser, S. J. Blady, K. G. Lynch, D. Romer, J. N. Cappella, C. Lerman, and D. D. Langleben, "Content matters: neuroimaging investigation of brain and behavioral impact of televised anti-tobacco public service announcements," *J Neurosci*, vol. 33, no. 17, pp. 7420–7427, Apr. 2013

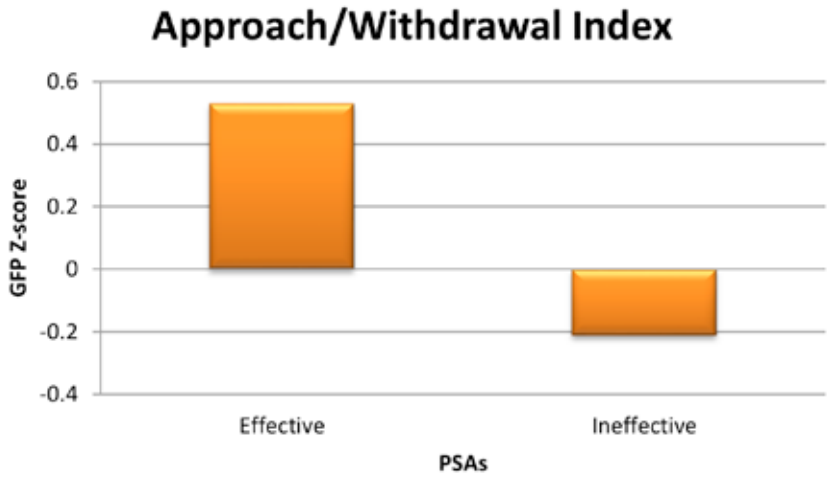

Fig. 1. Average values for the AW index for the "Effective" and "Ineffective" PSAs. The differences are statistically significant at p = 0.02.

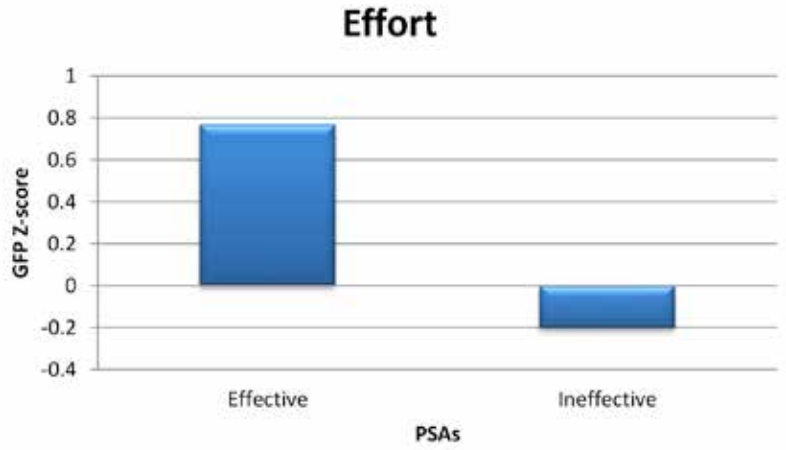

Fig. 2. Effort Index mean values for the "Effective" and the "Ineffective" PSAs. The differences are statistically significant at p = 0.03.

SYSTEM BIOLOGY

On a Zero-Retroactivity Subtraction Module for Embedded Molecular Feedback Controllers

M. Bilotta[1], C. Cosentino[1], A. Merola[1], M. Romano[1], and F. Amato[1]
[1]*Dipartimento di Medicina Sperimentale e Clinica, Università degli Studi Magna Graecia di Catanzaro*

Abstract— **The control of biochemical processes is a major goal in many fields, encompassing metabolic engineering and synthetic biology. Current approaches are based on ad-hoc designs, whereas a general and modular framework would be highly desirable, in order to exploit the well-assessed methods of control theory. A well-known problem when dealing with complex biosystems is represented by the retroactivity effect, which can significantly modify the dynamics of interconnected subsystems, with respect to the behaviour they exhibit when disconnected from each other. In the present work an implementation of a zero retroactivity Chemical Reaction Network Subtractor (CRNS) is proposed and its effectiveness is investigated through singular perturbations analysis. The proposed CRNS represents a first step towards the modular designing of embedded feedback biochemical controllers**.

***Keywords*—Retroactivity, synthetic biology, chemical reaction networks.**

I. Introduction

THE development of a general control theory for biomolecular processes would require the realization of a set of basic molecular circuits that can be assembled in a modular way. Unfortunately, in biological systems, modularity is generally compromised by *retroactivity*, which plays a role similar to impedance in electrical circuits, and consists of the effect of the reciprocal interactions arising from the interconnection of two modules [1].

Towards the realisation of modular embedded feedback controllers in synthetic biological systems, the availability of a well-characterised subtraction module is a key step. As illustrated in Fig. 1, a subtraction module is required to compare the desired set-point with the actual output of the process to be controlled. In particular, the theoretical analysis and the results obtained via numerical simulation show that the time-scale separation of the connected molecular subtractor can attenuate the retroactivity to the output effects [2].

The present work proposes a zero-retroactivity CRN-based subtraction module, which can be used as a basic component for designing feedback controllers for biochemical reaction networks. An implementation of a CRN feedback control system, using a CRN subtractor (CRNS) as a module for comparing the set-point and the process output, according to the scheme in Fig.1, is assumed.

II. Preliminaries

A. Chemical reaction network subtractors

Let us consider a reactor, containing a generic CRN C comprising four species. Let us assume that it is possible to inject from outside only species A and B into the reactor, and denote by $u_A(t)$ and $u_B(t)$ the number of molecules per unit volume injected per unit time, and by $y_C(t)$ the corresponding number of molecules per unit volume of a species C produced by the CRN in the same time interval.

The CRN

$$\emptyset \xrightarrow{u_A} \mathrm{A} \xrightarrow{k_1} \mathrm{C} \qquad \emptyset \xrightarrow{u_B} \mathrm{B}$$
$$\mathrm{A} + \mathrm{B} \xrightarrow{k_2} \mathrm{W} \tag{1}$$

produces an output flux $y_C = k_1 a$ that, as shown in Fig. 2, tends asymptotically to the difference of the input fluxes (if the changes over time of the input fluxes is sufficiently slow), therefore we will call it a CRNS [3].

Alternatively, let us consider another CRN (see Fig. 3), which involves a species B that can exist in two forms (e.g., a protein in phosphorylated or dephosphorylated form), which will be denoted by B° and B^*. We consider as input to this CRN the total flux of species B (in either one of the two forms), say u_B, and assume that such input flux is composed by a fraction λ of molecules of the form B°. Therefore, we have

$u_B = u_{B°} + u_{B*} = \lambda u_B + (1 - \lambda) u_B$ and the CRN reads

$$\emptyset \xrightarrow{u_A} \mathrm{A} \xrightarrow{k_1} \mathrm{C} \quad \emptyset \xrightarrow{\lambda u_B} \mathrm{B°}$$
$$\mathrm{A} + \mathrm{B°} \xrightarrow{k_2} \mathrm{B^*} \xleftarrow{(1-\lambda)u_B} \emptyset \tag{2}$$

B. Interconnected systems and retroactivity

Let us consider a generic system S with $\sigma \in D_u \subset \mathbb{R}_+^q$, $x \in D_x \subset \mathbb{R}_+^n$ and $v \in D_v \subset \mathbb{R}_+^p$ denoting concentrations of chemical species, such as proteins, enzymes, DNA sites, etc. Our aim is to investigate whether and to what extent the dynamics of system S change upon interconnection with other modules. Therefore, we consider the case in which the system S is connected to an upstream and a downstream module, as illustrated in Fig.4.

In the following, in place of a generic system S, we shall consider the two CRNSs (1) and (2). Moreover, in order to evaluate the retroactivity of the two subtractor realizations, we shall use the CRN

$$\emptyset \rightleftharpoons_{\delta_a}^{k_a} \mathrm{A} \qquad \emptyset \rightleftharpoons_{\delta_b}^{k_b} \mathrm{B} \tag{3}$$

as source module. As for the load module, we shall adopt the generic transcriptional mechanism,

$$\mathrm{C} + \mathrm{p} \rightleftharpoons_{k_{off}}^{k_{on}} \mathrm{D},$$

where p represents a promoter region, to which the species C can bind, and D denotes the complex C:p.

III. Main results

In what follows, we analyse the interconnected scheme described in the previous section, by applying an approach based on singular perturbations analysis [4]. The interconnected CRN (1) corresponds to the following reaction network

$$\emptyset \rightleftharpoons_{\delta_a}^{k_a} \mathrm{A} \overset{k_1}{\rightarrow} \mathrm{C} \qquad \emptyset \rightleftharpoons_{\delta_b}^{k_b} B \qquad (4a)$$

$$\mathrm{A} + \mathrm{B} \overset{k_2}{\rightarrow} \mathrm{W} \qquad \mathrm{C} + \mathrm{p} \rightleftharpoons_{k_{off}}^{k_{on}} \mathrm{D} \qquad (4b).$$

Let us assume mass-action kinetics and define the non-dimensional variables

$$\bar{k}_A := \frac{max_t k_a(t)}{\delta_a},\ \bar{k}_B := \frac{max_t k_b(t)}{\delta_b},$$
$$\sigma_A := \frac{a}{\bar{k}_A},\ \sigma_B := \frac{b}{\bar{k}_A},$$
$$x_1 := \frac{w}{\bar{k}_A},\ x_2 := \frac{c}{\bar{k}_A},\ \nu := \frac{d}{\bar{k}_A},$$
$$\tilde{k}_A(t) := \frac{k_a(t)}{\delta_A \bar{k}_A},\ \tilde{k}_B(t) := \frac{k_b(t)}{\delta_A \bar{k}_A}$$

and $\tau = \delta t$ (hence, $\dot{x}_i$ will denote $\frac{dx_i}{d\tau}$), and the timescale parameters

$$G_1 := \frac{k_1}{\delta_A},\quad G_2 := \frac{k_2 \bar{k}_A}{\delta_A},\quad G_3 := \frac{k_{off}}{\delta_a},$$

which weigh the relative velocity of dynamics, source, subtractor and load module, respectively. Then, the dynamics of the CRN (4) are described by

$$\dot{\sigma}_A = \tilde{k}_A(t) - \sigma_A - G_1\sigma_A - G_2\sigma_A\sigma_B \qquad (5a)$$
$$\dot{\sigma}_B = \tilde{k}_B(t) - \frac{\delta_b}{\delta_a}\sigma_B - G_2\sigma_A\sigma_B \qquad (5b)$$
$$\dot{x}_1 = G_2\sigma_A\sigma_B \qquad (5c)$$
$$\dot{x}_2 = G_1\sigma_A + G_3\left(\nu - \frac{x_2}{k_D}\left(p_{TOT} - \bar{k}_A\nu\right)\right) \qquad (5d)$$
$$\dot{\nu} = -G_3\left(\nu - \frac{x_2}{k_D}\left(p_{TOT} - \bar{k}_A\nu\right)\right) \qquad (5e),$$

where $k_D := \frac{k_{off}}{k_{on}}$ is the dissociation constant. We can identify the dynamics of the source module, that are

$$g_A(\sigma_A, t) = \tilde{k}_A(t) - \sigma_A\ ,\quad g_B(\sigma_B, t) = k_B(t) - \frac{\delta_b}{\delta_a}\sigma_B.$$

This means that, when the source module is not connected to the subtractor, the dynamics of the input species are given by $\dot{\sigma}_A = g_A(\sigma_A, t)$ and $\dot{\sigma}_B = g_B(\sigma_B, t)$.

Our goal is to evaluate how these dynamics are modified by the interconnection scheme, that is to quantify the retroactivity to the inputs of the subtractor.

In order to exploit singular perturbation analysis, we assume that the system dynamics can be separated into a slow and a fast subsystem, which is true if $G_3 >> G_2 >> G_1 >> 1$. Under the latter assumption, the standard singular perturbation form can be found by using the change of variables

$$z_1 = \sigma_A + x_1 + x_2 + \nu,$$
$$z_2 = \sigma_B + x_1,\ y_1 = x_1$$
$$y_2 = x_2 + \nu.$$

From this form it is easy to derive the solutions of the slow part for the dynamics of y_1 and y_2, which will be denoted by γ_{y1} and γ_{y2}, respectively. The solutions of the fast subsystems enable us to compute the modified dynamics, which read $\dot{\sigma}_A = g_A(\sigma_A, t) - \dot{\gamma}_{y1} - \dot{\gamma}_{y2}$ and $\dot{\sigma}_B = g_B(\sigma_B, t) - \dot{\gamma}_{y1}$. Finally, we get

$$\dot{\sigma}_A = \frac{g_A(\sigma_A,t)}{1+\mathcal{R}_A},\qquad \dot{\sigma}_B = \frac{g_B(\sigma_B,t)}{1+\mathcal{R}_B}, \qquad (6)$$

where $\mathcal{R}_A = \frac{d\gamma_{y1}}{d\sigma_A} + \frac{d\gamma_{y2}}{d\sigma_A}$ and $\mathcal{R}_B = \frac{d\gamma_{y1}}{d\sigma_B}$ represent a measure of the retroactivity to the first and to the second input, respectively.

Now, let us consider the second module, CRNS (2), to show that it exhibits zero-retroactivity to the input species B. The analysis performed above can be repeated for this CRNS, by substituting $b°$ for b and $b*$ for w. Note that the source can produce only the form B°, i. e. we are in the case $\lambda = 1$.

Differently from CRNS (1), in this case the (non-dimensional) dynamics of the input species B are given by $\dot{\sigma}_B = \dot{\sigma}_{B^\circ} + \dot{x}_1$. Therefore, the analysis of the reduced-order system, obtained through the singular perturbation analysis, yields

$$\dot{\sigma}_B = \dot{\sigma}_{B^\circ} + \dot{\gamma}_{y1} = g_B(\sigma_B, t),$$

which means that the dynamics of the input species B are not modified upon interconnection of the source and load modules with CRNS (2).

IV. Conclusions

One of the main goal in synthetic biology is the design of modular control systems for biochemical processes. A major obstacle toward this aim is represented by retroactivity of interconnected reaction networks. We have analysed the retroactivity of a CRN module that can be used as a subtractor in classical feedback control schemes. Using singular perturbations analysis, we have devised a special version of such module that exhibits zero-retroactivity to one of the inputs.

References

[1] D. Del Vecchio, A.J. Ninfa and E.D. Sontag. "Modular cell biology: retroactivity and insulation". *Molecular systems biology*, vol. 4(1), 2008.

[2] M. Bilotta, C. Cosentino, D.G. Bates, L. Salerno, and F. Amato. "Retroactivity analysis of a chemical reaction network module for the subtraction of molecular fluxes", in 2015 Proc. *Engineering in Medicine and Biology Society (EMBC), IEEE 37th Annual International Conference on*, pp. 941–944.

[3] C. Cosentino, R. Ambrosino, M. Ariola, M. Bilotta, A. Pironti, and F. Amato. "On the realization of an embedded subtractor module for the control of chemical reaction networks", *IEEE Transactions on Automatic Control*, 2016. In press.

[4] H.K. Khalil. *Nonlinear systems*. Prentice hall, New Jersey, 2002.

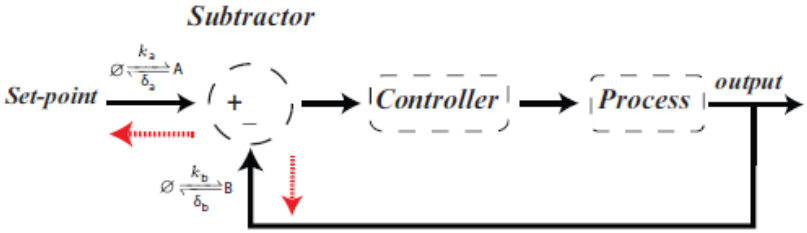

Fig. 1. A block diagram of the classical feedback control scheme is represented. The subtractor module allows the current output of the process being controlled to be compared with the desired value of the output (set-point), the difference between these two quantities computed by the subtractor then forms an error signal which constitutes the input to the controller. Retroactivity to the two inputs of the subtractor are shown as red arrows.

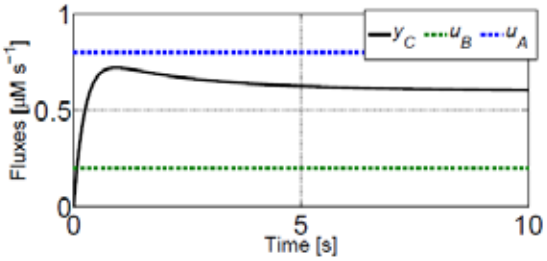

Fig. 2. Response of the isolated CRN subtraction module: The first input flux (species A) is $u_A = 0.8$ μM s^{-1}, the second input flux (species B) is $u_B = 0.2$ μM s^{-1}. The kinetic parameters in CRN (1) are set to $\kappa_1 = 4s^{-1}$ and $\kappa_2 = 3$ (μM s)$^{-1}$ therefore the output flux (solid line) of species C represents the difference between the two input fluxes (dashed lines).

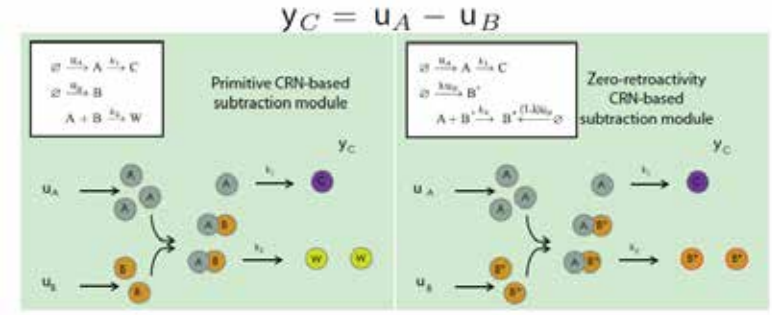

Fig. 3. Two alternative implementations of the CRN subtractor.

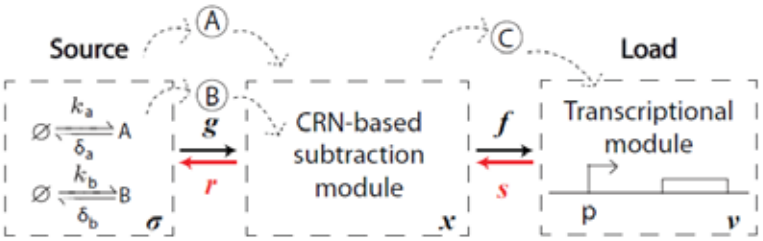

Fig. 4. The analysis of the retroactivity is realised by a modular interconnection of the CRN-based subtraction module. The CRN-based subtraction module takes as inputs the fluxes of species A and B generated from an upstream module. This source block is composed of reactions of formation and degradation for each input species. The output of the subtractor module is the flux of species C produced by the reactions of the CRNS. The transcription factor C binds to the promoter *p*, inducing the transcription and translation of a protein D. The red arrows denote retroactive fluxes arising upon interconnection of the CRNS with the source and load modules.

Mechanically-tuned alginate gels as new 3D breast cancer models

M. Cavo[1,2], M. Fato[1,2], F. Beltrame[1,2], and S. Scaglione[1]
[1] National Research Council (CNR) – IEIIT institute, 16100 Genoa (IT)
[2] University of Genoa – DIBRIS department, 16100 Genoa (IT)

***Abstract*—Three-dimensional (3D) cell cultures represent fundamental tools for the comprehension of cellular phenomena both in normal and in pathological conditions. When realizing 3D in vitro models, a proper design of chemical, physical and biological properties of the substrate has to be taken into account to positively influence cells activity. In particular, mechanical stimuli have a relevant role on cell fate, cancer onset and malignant progression. However, they can be difficulty tuned since they generally depend by a lot of variables.**

Here, we realized mechanically tuned alginate hydrogels for studying the role of substrate elasticity on breast adenocarcinoma cells (MCF-7) activity. The Elastic Modulus (E) was measured via Atomic Force Microscopy and a remarkable range (20–4000 kPa) was obtained. MCF-7 cells were encapsulated within the gels, on standard Petri and on alginate-coated dishes (as 2D controls). Cells showed dramatic morphological differences when cultured in 3D and in 2D, maintaining only in 3D a circular, cluster-organized conformation similar to the in vivo one. In 3D cultures, we observed a strict correlation between cells viability and substrate elasticity: MCF-7s constantly decreased in number with increasing hydrogel elasticity. The highest cellular proliferation rate, associated to formation of cell clusters, occurred in two weeks of culture only within the softest hydrogels (E=20-40 kPa), highlighting the need of adopting more realistic and *a priori* defined models.

***Keywords*—3D in vitro cancer models, breast cancer, hydrogels, stiffness.**

I. Introduction

A wide range of new 3D in vitro models is emerging to better mimic the physiological human context both in healthy and in pathological conditions, besides allowing reducing animal experiments. In the field of cancer disease, these clinically relevant in vitro models could help understanding tumor pathogenesis and cells chemo-resistance [1]. Significant potential exists with 3D Tissue Engineering (TE) based *in vitro* models, which can account for a number of advantages, such as reproducibility and tailorable complexities (e.g. cell types, substrate diffusion gradients, architecture and mechanical properties) [2]. These strategies aim to replicate the tissue/organ in culture, besides giving the ability to answer questions not amenable using traditional approaches [3]. To carry out experimental manipulation under physiological contexts, various 3D in vitro models have been proposed. Numerous scaffolds, ranging from ECM-derived materials to polymers in the form of foams or hydrogels are being investigated [2]. In particular, natural or synthetic hydrogels offer several advantages such as good biocompatibility and bioactivity, high water content as well as efficient transportation of oxygen and nutrients due to the reticulated structure of the cross-linked polymer chains. Specifically, hydrogels have been frequently used for probing the microenvironment influence on cell functions, as their properties can be finely tuned in space and time [4]. Among them, the seaweed-derived alginate is typically thought to be inert because it lacks the native ligands allowing interaction with mammalian cells [5]. For this reason, it would allow isolating substrate mechanical contribution on cells fate better than chemically bioactive materials, such as Matrigel, laminin-rich or collagen matrices, already adopted as 3D substrates for modeling cancer microenvironment [6]; moreover, alginate mechanical properties can be precisely tuned via calcium ions mediated cross-link.

In this study, we comparatively evaluated viability, proliferation, morphology and cluster organization in breast cancer cells (MCF-7) growing in mechanically tuned 3D alginate hydrogels. Among solid tumors, breast cancer has been chosen in this study, since satisfactory 3D in vitro models are not available yet, although it remains the second leading cause of cancer death among women [7].

The evaluation of the substrate stiffness effects on cells fate in a 3D environment puts the basis for the development of an in vitro breast cancer model directly mediated by substrate stiffness, exploiting the mechanotransduction principle.

II. Materials and Methods

A. Gels realization

3D alginate gels were realized as follows. Firstly, a 1% Agar solution containing calcium ions (solution A) was prepared by mixing Agar (DIFCO Laboratories) in physiological buffer enriched with $CaCl_2$ (J.T. Baker) at defined concentration (0.2 M, 0.5 M or 1 M). Solution A was brought to boiling point, poured into 6-well multi-well plates until obtaining 1 cm height and allowed to cool until complete solidification. 0.5 cm diameter molds were obtained by digging wells in the agar gel through a Pasteur glass. 0.5% w/v, 1% w/v or 2% w/v alginate solution (solution B) was prepared by mixing Alginate (Manugel GMB, FMC BioPolymer) in physiological buffer. A volume of 120 µm of solution B was put into each mold by a syringe. Gelation was allowed to take place at 37°C for 1 h, in order to ensure a complete diffusion of calcium ions from the agar mold to the alginate solution.

B. Atomic Force Microscopy (AFM) analysis

AFM was chosen for the mechanical characterization of 3D substrates, since it allows measuring substrates elasticity with a size-scale comparable to the cellular one, for a better

understanding of the cell-substrate stiffness interaction. We used an AFM microscope (Agilent Technologies 5500 ILM) mounted on an inverted optical microscope (Olympus IX70), equipped with triangular microcantilevers with nominal spring constant 0.06 N/m and pyramidal tips of a nominal radius of 10 nm. For each sample, 3 maps of 256 curves were taken over a regular grid in a 5×5 μm^2 area. The elastic modulus was calculated by considering the load–indentation curve.

C. Cell culture

MCF-7 (breast adenocarcinoma) cell line was expanded in Eagle's minimal essential medium (EMEM) enriched with 10% Fetal Bovine Serum (FBS), 1% L-glutamine and 1% pen/strept (all from Sigma Aldrich). Cell seeding within the gels was achieved by directly suspending cells in sterile alginate solution in order to obtain an amount of $0.8x10^5$ cells/sample. 2D cell cultures were carried out as control. Both 2D and 3D cell cultures were carried out up to 2 weeks in incubator at 37° C in an atmosphere of 5% CO_2 to allow gas exchange.

D. Cell viability: Live/dead staining

After 7 days, cellular viability was evaluated within the 3D gels. Gels were washed with phosphate-buffered saline (PBS) and incubated with a live/dead assay (Live/Dead Cell Double Staining Kit, Sigma Aldrich) at 37° C for 15 min. They were then imaged by using a microscope equipped with epifluorescence (Eclipse Ni-U, Nikon). The number of alive and dead cells per area were quantified using the open source image analysis software ImageJ (NIH).

E. Confocal fluorescence microscopy

To examine the spatial distribution and morphology of cells, both 2D and 3D samples were analyzed by optical confocal laser scanning microscopy. For all typologies, samples were fixed after 1 week with 4% paraformaldehyde. Nuclei were stained with DAPI dye (1 μg/ml), while actin filaments were stained with Alexa Fluor 488 phalloidin (100 μM), all by Sigma-Aldrich. Images were acquired by a confocal laser scanning microscope (Leica TCS SP5 AOBS).

F. Histology and immunohistochemistry

3D alginates were processed for histological analysis after 1 and 2 weeks of culture. Samples were fixed in 4% buffered formalin for 3 h and dehydrated in ethanol scale. Samples were paraffin embedded, cross-sectioned (7-μm thick) at different levels and stained with haematoxylin–eosin (H&E).

III. RESULTS

A. Gel mechanical characterization by AFM

A remarkable range of elasticities (20–4000 kPa) was obtained by varying alginate and cross-linker contents. In particular, a weaker cross-linker content (i.e. 0.2 M $CaCl_2$) didn't allow obtaining mechanical properties significantly different despite the increase of alginate percentage, resulting in overlapped elasticity ranges. Contrariwise, elastic moduli were significantly different among 0.5-1-2% alginate concentrations when gels were cross-linked with a higher $CaCl_2$ content (data not shown).

B. Cell viability

The quantitavive analysis of alive cells highlighted some differences among the gels: the amount of cells was significantly higher in gels characterized by an elastic modulus ranging between 20-40 kPa, where a significant cellular proliferation was observed. The total number of cells and the amount of alive cells was observed to strongly decrease with the progressive increase of stiffness.

C. Cell morphology: 2D versus 3D

The morphological observation showed alarming morphological and hence biochemical differences between cells in 2D and 3D. Cells embedded in the 3D gels were characterized by rounded shapes and a cluster organization. In contrast, cells showed a flat morphology and organized in a layer when seeded in Petri dish or in alginate-coated Petri dish (Fig. 1).

D. Cell cluster formation

The presence of cell clusters was confirmed also in the inlet parts of 3D gels by histological analysis. For this analysis, only alginates characterized by the best cellular viability results (20-40 kPa, 150-200 kPa and 500-1000 kPa) were analyzed. Interestingly, cell clusters greater than 100 μm and 300 μm were respectively found after 7 and 14 days in softest alginates (20-40 kPa), also corresponding to best Live/dead results (Fig. 2). In contrast, in stiffer gels clusters were composed only by few cells.

IV. CONCLUSIONS

3D mechanically-tuned alginate gels were successfully realized. MCF-7 breast cancer cells activity was investigated, carefully correlating cell fate to substrate mechanical properties. A deep difference among cell viability and proliferation capacity was observed by varying substrate elasticity. In particular, the best results appeared for substrate stiffness of 20-40 kPa, which promoted the formation of clusters up to 300 μm in two weeks. This organization was compared with 2D cultures, showing a greatly more representative structure of tumors than 2D cultures.

REFERENCES

1 D.W. Hutmacher et al., "Can tissue engineering concepts advance tumor biology research?," *Trends in biotechnology*, vol. 28(3), pp. 125-133, 2010.

2. C. Ricci., L. Moroni, and S. Danti, "Cancer tissue engineering: new perspectives in understanding the biology of solid tumors: A critical review." *OA Tissue Eng* vol. 1, p. 4, 2013.

3. C.M. Nelson, and M.J. Bissell, "Seminars in cancer biology". 342-352 (Elsevier).

4. M.W. Tibbitt, and K. S. Anseth, "Hydrogels as extracellular matrix mimics for 3D cell culture". Biotechnology and bioengineering vol. 103, pp. 655-663, 2009.

5. H. A. Awad, , M. Q. Wickham, H. A. Leddy, J. M. Gimble, and F. Guilak, "Chondrogenic differentiation of adipose-derived adult stem cells in agarose, alginate, and gelatin scaffolds,". Biomaterials vol. 25, pp. 3211-3222, 2004.

6. G. Y. Lee, P. A. Kenny, E. H. Lee, and M.J.Bissell, "Three-dimensional culture models of normal and malignant breast epithelial cells,". Nature methods vol. 4, pp. 359-365, 2007.

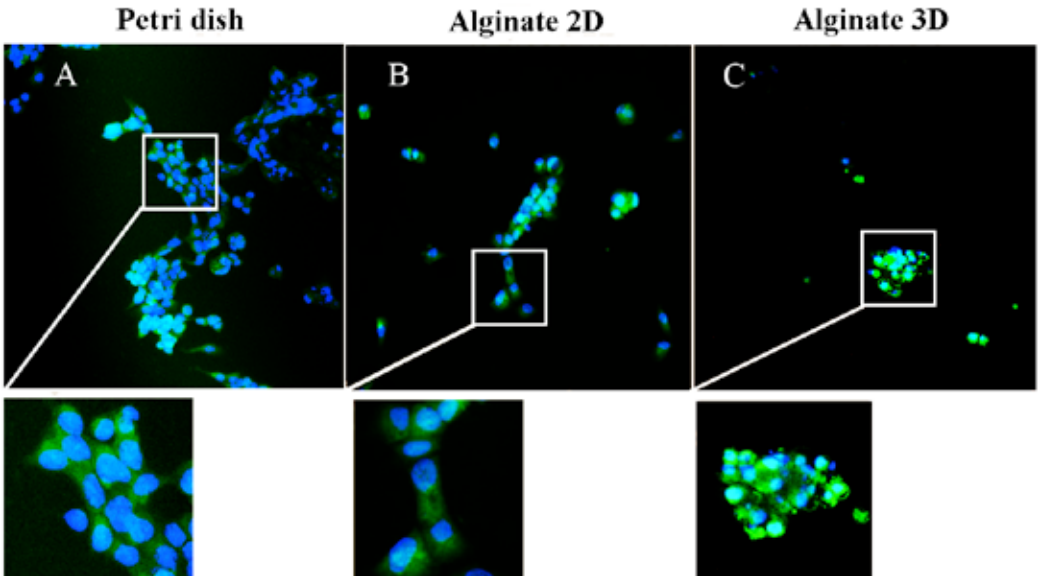

Fig. 1. Cells cultured on plastic (A), alginate thin layer (B) or embedded in 3D alginate hydrogel (C). Cells were stained with phalloidin for F-actin (green) and with DAPI for nuclei (blue).

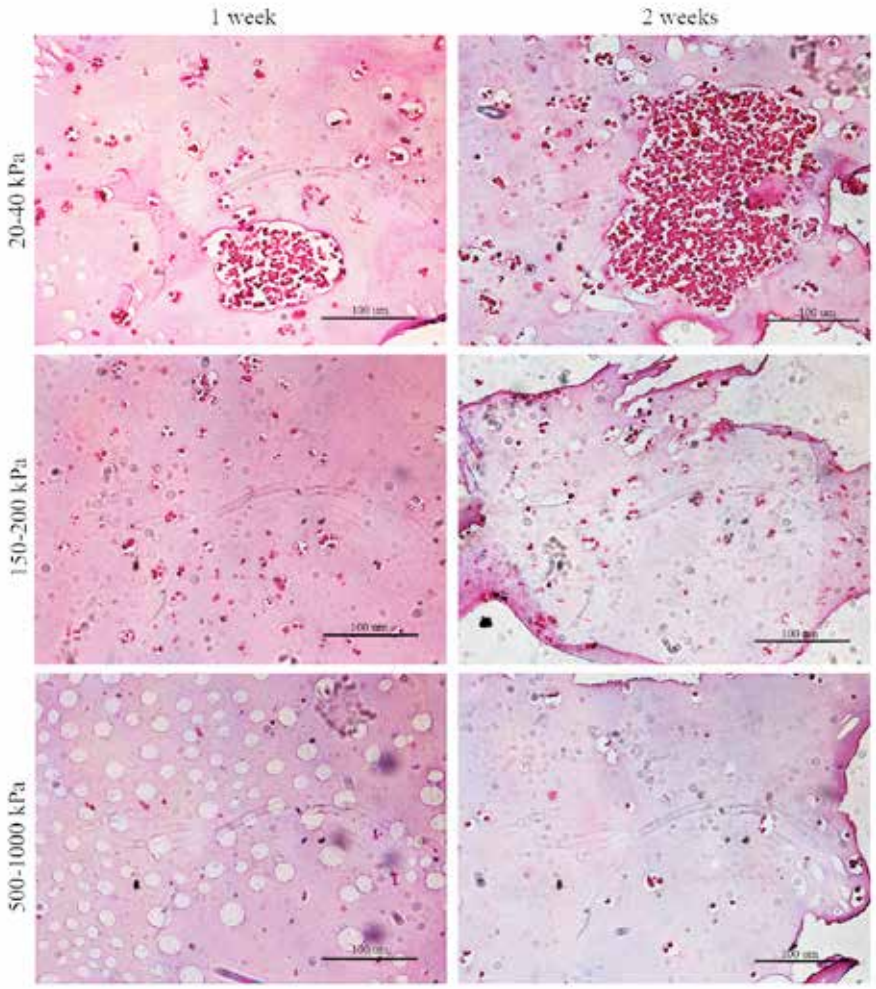

Fig. 2. H&E staining of alginate gel sections from 7 days (left) and 14 days (right) of cell culture.

Curcumin-biodistribution through biocompatible nanocapsules for oral release in intestinal epithelia in vitro

A. Langella[1,2], V. Calcagno[1,2], V. De Gregorio[1], G.Imparato[1], F.Urciuolo[1], R. Vecchione[1], PA. Netti.[1,2,3]
[1] Center for Advanced Biomaterials for HealthCare@CRIB,Istituto Italiano di Tecnologia Largo Barsanti e Matteucci 53, 80125 Naples Italy
[2] Department of Chemical,Materials and industrial Production (DICMAPI) University of Naples Federico II,P.le Tecchio 80, Naples Italy
[3]Interdisciplinary Research Centre on Biomaterials (CRIB), University of Naples Federico II, P.le Tecchio 80; Naples, Italy

***Abstract*—** The development of innovative nano-bio-encapsulation system continues to be an area of intense activity as new challenges demand the use of improved delivery systems. So an important aim is to carry out appropriate changes on this nano-systems-carrier able to satisfy the organ target features and appropriate in situ release.

Keywords: **CaCo2, Transwell cell culture, Drug delivery, Nanoemulsions, Curcumin**

INTRODUCTION

The use of molecules or food ingredients with positive effects on health, prevention and treatment of diseases is increasingly in demand. However, many nutraceuticals result unstable or poorly water soluble and their oral administration is limited. Developing suitable carrier systems remains a major challenge for biomedical scientists, since bioavailability is limited by the epithelial barriers of the gastrointestinal tract (GIT) [1]. Curcumin, a natural nutraceutical, was chosen as model drug because of its lipophilic nature, its poor stability and its poor oral administration. Furthermore, Curcumin is a major component of the Curcuma species, contains antioxidant and anti-inflammatory properties. Although it was found to induce apoptosis in cancer cells, the functional role of curcumin as well as its molecular mechanism in anti-inflammatory response, particularly in intestinal cells, has been less investigated. The intestine epithelial barrier is the first barrier and the most important location for the substrate coming from the lumen of the gut [1]. In this work an air liquid interface (ALI) of CaCo2 cells in Transwell was realized as an *in vitro* testing platform to evaluate the potential of an oral nano-delivery system (Figure 1) – i.e. an oil-in-water nanoemulsion [2] coated with an adhesive chitosan derivative. The presented testing platform allowed a comprehensive understanding on the route of the nano-system carrying the curcumin, its interaction with the intestinal mucosa and the antioxidant effects on cells. In this work an air liquid interface (ALI) of CaCo2 cells in Transwell was realized as an *in vitro* testing platform to evaluate the potential of an oral nano-delivery system, oil-in-water nanoemulsion coated with a thiolated glycol chitosan. Curcumin was chosen as model drug because of its lipophilic nature, its poor stability and its poor oral administration. The presented testing platform allowed a comprehensive understanding on the route of the nano-system carrying the curcumin, its interaction with the intestinal mucosa and the antioxidant effects on cells.[3] Results demonstrated that the in Transwell model, able to promote the polarization of the intestinal epithelium, is suitable to mimic as closely as possible the *in vivo* conditions.

METHODS

CaCo2 cell Monolayer were seed on polycarbonate Transwell insert and grown for 21 days. The Oil-in-Water nanoemulsion was chemically modified with GC, Rhodamine B and NAC to increase the mucoadhesion on intestinal mucosa.
The Delivey after 4h and 24h was assessed through confocal imaging and the Curcumin release was analysed by RP-HPLC.

RESULTS AND DISCUSSIONS

Nanoemulsion analysis.
Particles size of the starting nano-emulsion and of the nano-emulsion coated with glycol chitosan was characterized by DLS. – size increases of few nanometer (~105 nm) and PDI value remains below ~0.08. the final oil concentration is 2% (v/v) and only few milliliters are required for the tests. In addition to DLS analysis, confocal imaging of nanoemulsion coated with rhodamine B labelled chitosan and electron microscopy imaging of nanocapsules stained with OsO_4 vapors were performed (SEM micrograph in and TEM micrograph), thus clearly confirming the good size distribution and dimensions.

Cell cytotoxicity.
We tested the biosafety of the nano-emulsions by carrying out cytotoxicity tests on the system loaded with curcumin. As resulted from MTT test, cell viability was demonstrated, thus indicating the biosafety of the tested nanocarrier towards Caco-2 cells.
Effect on transwell cell culture.
Transepithelial electrical resistance (TEER), a widely accepted quantitative technique to measure the integrity of tight junctions in 2D cell culture models, was used to evaluate the transport of drugs or chemicals.

Transport of nanoemulsion.
Confocal analysis allowed to evaluate the presence, the localization and the transport of our nano-delivery system. In order to understand the transport of the nanoemulsion, glycol chitosan coating was covalently labelled with Rhodamine B. This labelling, together with the specific staining of the

biological sample, allowed to discriminate between the nanoemulsion (red channel), the nuclei (blue channel) and the cytoskeleton (green channel). (Figure 3).

CONCLUSIONS

Studies on polymeric nanoparticles used for drug delivery have led to innovative methods to develop 'functional foods' and found more application in treatment of many intestinal disease. Our major efforts was to confirm the curcumin benefic properties and to value the response in a *in vitro* model.

REFERENCES

[1] Artursson P, Palm K, Luthman K. Caco-2 monolayers in experimental andtheoretical predictions of drug transport. Adv Drug Deliv Rev. 2001 Mar1;46(1-3):27-43. Review. PubMed PMID: 11259831

[2] Vecchione R, Ciotola U, Sagliano A, Bianchini P, Diaspro A, Netti PA. Tunable stability of monodisperse secondary O/W nano-emulsions. Nanoscale. 2014 Aug7;6(15):9300-7. doi: 10.1039/c4nr02273d. PubMed PMID: 24988193.

[3] Cho JA, Park E. Curcumin utilizes the anti-inflammatory response pathway toprotect the intestine against bacterial invasion. Nutr Res Pract. 2015 Apr;9(2):117-22. doi: 10.4162/nrp.2015.9.2.117. Epub 2015Mar 6. PubMed PMID: 25861416; PubMed Central PMCID: PMC4388941.

FIGURES

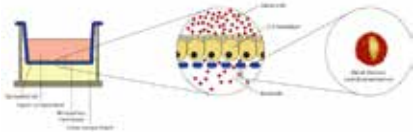

Figure 1. Schematic representation of air liquid interface of Caco-2 cells in Transwell system (on the left). In the central inset an enlarged view of the cell monolayer grown on the microporous membrane. On the left the oral nano-delivery system consisting of O/W nanoemulsion coated with a thiolated glycol chitosan.

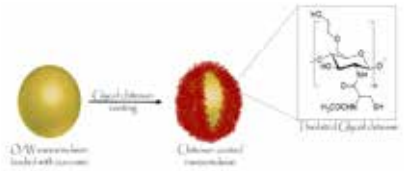

Figure 2. Schematic representation of the oral nano-delivery system proposed: an oil in water nanoemulsion loaded with the curcumin and coated with GC-NAC (glycol chitosan modified with N-acetyl-L-cysteine

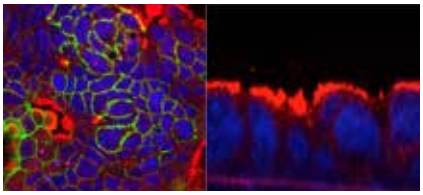

Figure 3 Confocal images of Caco-2 monolayer: Y-view matching on the left and Z-view matching on the right.

TECNOLOGIE NANO, MICRO E INDOSSABILI

Measurement of the inter-foot distance using a Time-of-Flight proximity sensor: preliminary evaluation during leg oscillation exercises

S. Bertuletti[1], A. Cereatti[1], M. Caldara[2] and U. Della Croce[1],
[1] *POLCOMING Department, University of Sassari, Sassari (SS), Italy, sbertuletti@uniss.it*
[2] *Department of Engineering and Applied Sciences, University of Bergamo, Dalmine (BG), Italy, michele.caldara@unibg.it*

***Abstract*—The distance between the feet during walking could be a key factor to better understand gait stability. The aim of this work was to investigate the application of an Infrared Time-of-Flight sensor in the inter-foot distance estimation during leg oscillation exercises. The results, compared to a stereo-photogrammetric system used as gold standard, showed a mean absolute error between 3.6 mm and 6.9 mm and a mean absolute percentage error in the range of 1.9% to 3.8%. An improvement of 50% (6 mm) in the inter-foot distance accuracy, compared to a wearable platform based on ultrasound and inertial sensors, was observed.**

***Keywords*—Inter-foot distance, wearable devices, Time-of-Flight, proximity sensor.**

I. Introduction

A simple and effective way to analyse human gait is through the estimate of the spatio-temporal parameters. Temporal parameters such as stride time, double support time, swing time and step time, allow the segmentation of the gait cycle into phases characterized by different body support and leg swing configurations. Spatial parameters are typically estimated by combining the temporal parameters estimates with foot kinematics information to obtain parameters such as stride length, velocity, step length, step width. Traditionally, spatio-temporal parameters during gait are determined in the laboratory setting using either an electronic walkway or stereo-photogrammetric (SP) systems [1]. These solutions can provide accurate estimates, but they are costly and their use is limited to the laboratory environment. To overcome these limitations, numerous studies employed wearable sensors to estimate many temporal and spatial gait parameters [2]. However, the step width represents an exception, even though it is considered a valuable parameter descriptive of the base of support during gait [3]. Wellar and colleagues found that decreased step width was closely correlated with fall frequency and dynamic instability, especially for elderly [4], [5]. The step width can be seen as the value of the inter-foot distance (IFD) during the double support phase of gait (i.e. both feet in contact with the ground). IFD is defined as the projection along the medio-lateral direction of the distance between corresponding points of the feet. Few studies have proposed the use of wearable technologies, such as ultrasounds and light intensity infrared sensors integrated into inertial measurement units, to estimate IFD during the mid-swing phase of gait as an alternative parameter to the step width (IFD_{sw}) [6], [7]. When using ultrasound technology, the distance between feet is determined by measuring the time required by an ultrasonic wave to travel from the transmitter to the receiver. Conversely, light intensity infrared sensors determine the distance by measuring the amount of the light reflected from the target. Light intensity infrared sensors have a faster response time than ultrasound, but their accuracy depends on many experimental factors, such as the color and the reflectance of the target surface [8]. Very recently, the Infrared Time-of-Flight technology (IR-ToF) has become popular for distance measurement thanks to the development of wearable and low-cost sensors. IR-ToF sensors measure the time an electromagnetic wave needs to travel a distance [9]. This technology has the advantage that it is more robust to the color of the target and the environmental conditions (such as ambient light) than light intensity infrared sensors. Moreover it provides a faster response than ultrasound due to the higher wave propagation speed.

The aim of this preliminary study was to investigate the feasibility of the use of IR-ToF sensor for IFD_{sw} estimates and to assess its accuracy in dynamic conditions similar to those encountered during gait.

II. Materials and Methods

A. IR-ToF proximity sensor characteristics

A development board (NUCLEO-F411RE) with a high-performance and low-power ARM Cortex-M4 microcontroller has been used in combination with the expansion card X-NUCLEO-6180XA1 of the IR-ToF proximity sensor VL6180X (measuring distance up to 0.6 m). This system prototype was connected to a personal computer via USB to acquire the measurements. Specifically, the present IR-ToF proximity sensor estimates the duration of the light travel to the nearest object and back to the sensor, by measuring the phase shift φ between the radiated *s(t)* and reflected *r(t)* IR waves (Fig. 1).

$$s(t) = \sin\left(2\pi f_m t\right) \tag{1}$$

$$r(t) = R \cdot \sin\left(2\pi f_m t - \varphi\right) = R \cdot \sin\left[2\pi f_m \left(t - \frac{2d}{c}\right)\right] \tag{2}$$

where R is a reflection coefficient. Once φ is measured (e.g. phase comparator circuit), the distance d between the position of the IR emitter and the target point can be easily calculated from Eq. (2) as follows:

$$d = \frac{c}{4\pi f_m} \cdot \varphi \tag{3}$$

where c is the speed of light ($3 \cdot 10^8$ m/s) and f_m is the modulation frequency of the radiated and reflected signals.

B. Experimental setup

Data from five healthy subjects (two females, three males; mean age 28.2 ± 3.9 years, mean height 1.74 ± 0.09 m) were acquired. The IR-ToF sensor expansion board was attached to a stationary wooden board perpendicular to the floor (height 80 mm) (Fig. 2a); the reflecting surface was a green flat cardboard (90 mm × 150 mm) firmly attached to the right shoe (Fig. 2b). The left foot was kept stationary, parallel to the right foot and out from the IR-ToF proximity sensor measuring cone. The green color for the reflecting surface

was chosen after a preliminary evaluation of different colors (red, blue, yellow, white and black). Three retro-reflective markers were placed on the right foot and three markers were attached to the IR-ToF sensor evaluation board. Markers positions recorded using a six-camera SP system (Vicon) were used as gold standard.

C. Experimental data acquisition

The following acquisitions were performed:
(1) Subject standing with parallel feet at a distance of 0.20 m ($Static_{20}$); (2) Subject standing with parallel feet at a distance of 0.30 m ($Static_{30}$); (3) Subject standing while oscillating the right leg five times (5 forward and 5 backward) at a distance of 0.20 at comfortable speed ($OscComfortable_{20}$); (4) Subject standing while oscillating the right leg five times at a distance of 0.20 m at slow speed ($OscSlow_{20}$); (5) Subject standing while oscillating the right leg five times at a distance of 0.30 m at comfortable speed ($OscComfortable_{30}$); (6) Subject standing while oscillating the right leg five times at a distance of 0.30 m at slow speed ($OscSlow_{30}$).

D. Data analysis

For each subject, a single value for the IFD_{sw} value was obtained in static trials and ten IFD_{sw} values (two times for each oscillation cycle) were obtained for the oscillation trials. The firmware of the IR-ToF proximity sensor was programmed to return a "0" value when no target point was in front of it. The sampling rate was set to 10 Hz, but, if required, it can be easily set up to a higher frequency by reprogramming the firmware. During static trials the IR-ToF based estimate of IFD_{sw} ($^{IR\text{-}ToF}IFD_{sw}$) was obtained as the mean of the estimated distances, while for the oscillation trials, it was obtained as the minimum of the readings (*point-to-point distance*) returned while the target point was in front of the IR-ToF sensor (Fig. 3). The IFD_{sw} estimated with the SP system ($^{SP}IFD_{sw}$) was obtained as the average value of the *point-to-plane distance* over the time interval during which the orthogonal projection of the IR-ToF sensor position fell within the reflective surface (Fig. 2b). For each measurement i, the error of the $^{IR\text{-}ToF}IFD_{sw}$ estimate was computed as the difference ($e_i = {}^{IR\text{-}ToF}IFD_{sw} - {}^{SP}IFD_{sw}$). Only for the dynamic trials, the mean error e over the 10 values measured during the five cycles of oscillation was calculated. Mean absolute error (mae_i) and mean percentage absolute error $\left(mae_{\%_i} = \frac{|e_i|}{{}^{SP}IFD_{sw}} \cdot 100 \right)$ were also computed. Finally, for each condition, the grand mean values E (standard deviation SD), MAE and $MAE_{\%}$ were computed over the subjects.

III. Results

The *mean* ± *sd* duration of a leg oscillation cycle was equal to 1.9 ± 0.4 s for comfortable speed trials and 3.2 ± 0.9 s for slow speed trials. An example of an oscillation cycle acquisition during $OscSlow_{20}$ trial is reported in Fig. 4. The values of E varied from 6.1 mm and 6.9 mm for static trials and from -1.3 mm and 3.3 mm for the dynamic trials. The MAE ($MAE_{\%}$) values varied between 6.1 mm (2.7%) and 6.9 mm (1.9%) in static trials, while for dynamic trials they varied between 3.6 mm (1.9%) and 5.2 mm (3.8%) (Table I).

IV. Discussion

The aim of the present study was to investigate the feasibility of the use of an IR-ToF sensor for estimating the IFD during the swing of gait. Since the board currently available is not wearable, we determined the accuracy of the IFD estimations during static trials and during the execution of leg oscillations evoking the leg swing during gait. The results showed a slight overestimation of the IFD in static trials. Instead, in dynamic trials, the probability to over/under estimate the IFD was very similar due to the closeness of E to zero. No noticeable variations of the accuracy were observed increasing the distance between the reflecting surface and the IR-ToF sensor and changing the characteristics of the oscillation. We found an increased accuracy by 50% (6 mm) with respect to that obtained in similar studies employing ultrasound technology [6]. The error mean values obtained in this study are similar to those obtained when IFD_{sw} was estimated with a light intensity sensor [7], while their standard deviation is lower. This is probably the result of the IR-ToF sensor signals being less noisy than those obtained from light intensity sensors.

TABLE I
E (SD), MAE AND $MAE_{\%}$ OF THE IFD FOR THE SIX CONDITIONS

Condition	E (SD) [mm]	MAE [mm]	$MAE_{\%}$ [%]
$Static_{20}$	6.1 (0.9)	6.1	2.7
$Static_{30}$	6.9 (2.6)	6.9	1.9
$OscComfortable_{20}$	1.7 (4.5)	3.7	3.8
$OscSlow_{20}$	3.3 (4.9)	4.6	3.8
$OscComfortable_{30}$	-0.5 (4.3)	3.6	1.9
$OscSlow_{30}$	-1.3 (5.8)	5.2	2.2

V. Conclusion

The findings of this study confirm that IR-ToF proximity sensors can be effectively used for the IFD estimation during leg swing with an average error up to 5.2 mm. The next step will be the integration of the IR-ToF sensor in a wearable inertial sensing platform for gait analysis in daily life.

References

[1] K. E. Webster, J. E. Wittwer, J. A. Feller, "*Validity of the GAITRite® walkway system for the measurement of averaged and individual step parameters of gait*", Gait Posture, 22(4):317–321, 2005.

[2] A. Muro-de-la-Herran, B. Garcia-Zapirain, A. Mendez-Zorrilla, "Gait Analysis Methods: An Overview of Wearable and Non-Wearable Systems, Highlighting Clinical Applications", Sensors 2014, 14, 3362-3394

[3] D.E. Krebs, D. Goldvasser, J.D. Lockert, L.G. Portney, K.M. Gill-Body, "*Is base of support greater in unsteady gait ?"*, Phys Ther, vol. 82, No. 2, 2002, pp. 138–47.

[4] C. Weller, C.J.A. O'Neill, A. Charlett, S.G. Bowes, A. Purkiss, P.W. Nicholson, R.J. Dobbs and S.M. Dobbs, "*Defining small differences in efficacy between anti-parkinsonian agents using gait analysis: a comparison of two controlled release formulations of levodopa/decarboxylase inhibitor*", British Journal of Clinical Pharmacology, 35: 379–385, 1993.

[5] A.V. Fried, J. Cwikel, H. Ring, D. Galinsky, "*ELGAM–extra laboratory gait assessment method: identification of risk factors for falls among the elderly at home*", Int Disabil Stud, 12:161–164, 1990.

[6] D. Weenk, D. Roetenberg, B.J.F. van Beijnum, H.J. Hermens, and P.H. Veltink, "*Ambulatory Estimation of Relative Foot Positions by Fusing Ultrasound and Inertial Sensor Data*", IEEE Transaction On Neural Systems And Rehabilitation Engineering, In press, 2014.

[7] D. Trojaniello, A. Cereatti, A.K. Bourke, K. Aminian, U. Della Croce, "*A wearable system for the measurement of the inter-foot distance during gait*", 20th IMEKO TC4 International Symposium and 18th International Workshop on ADC Modelling and Testing Research on Electric and Electronic Measurement for the Economic Upturn, September 2014, Benevento, Italy.

[8] M. Tarek, "*Using Ultrasonic and Infrared Sensors for Distance Measurement*", International Journal of Mechanical, Aerospace, Industrial, Mechatronic and Manufacturing Engineering Vol:3, No:3, 2009.

[9] *Time-of-Flight technology*, https://en.wikipedia.org/wiki/Time_of_flight.

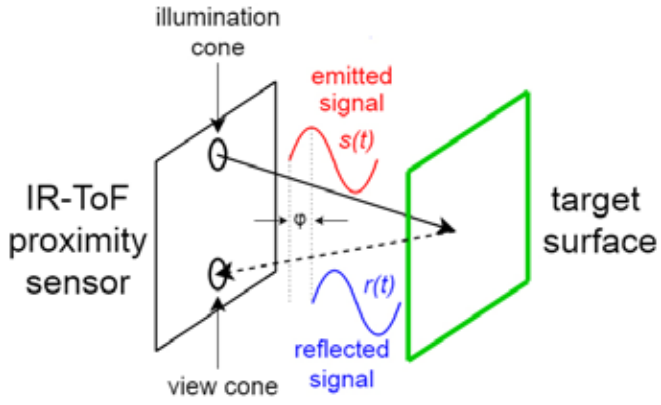

Fig. 1. The IR-ToF proximity sensor provides the distance estimate from the reflecting surface by measuring the phase shift φ between the emitted *s(t)* and the reflected *r(t)* signals.

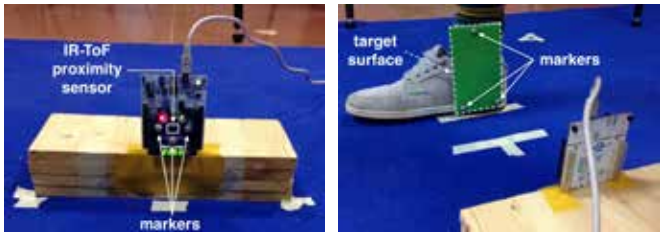

(a) Evaluation system *(b) Target*

Fig. 2. Experimental setup.

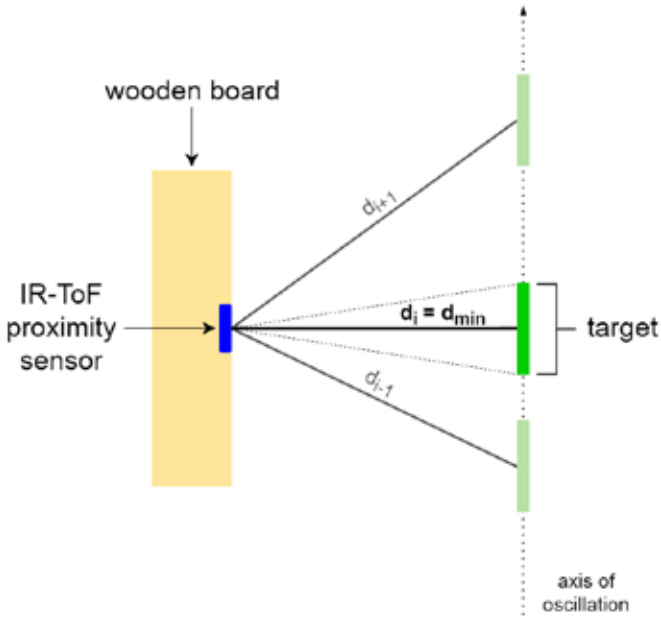

Fig. 3. The $^{IR\text{-}ToF}IFD_{sw}$ value was obtained as the minimum distance between the IR-ToF sensor and the reflecting surface. d_{i-1}, d_i and d_{i+1} were an example of the distance values obtained by the IR-ToF sensor during the oscillation exercise.

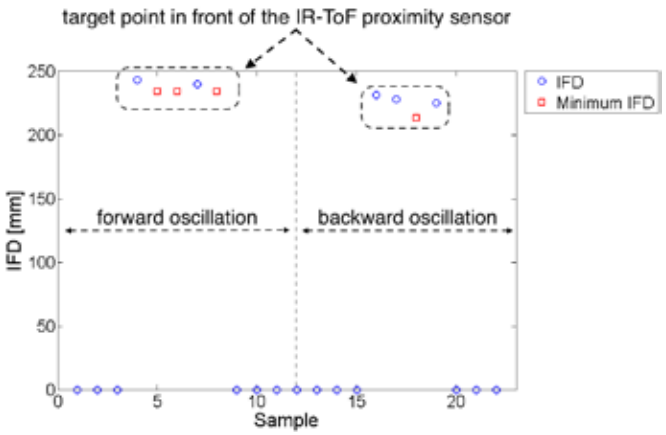

Fig. 4. An example of the readings from the IR-ToF sensor during a full leg oscillation ($OscSlow_{20}$), at a sampling rate equal to 10 Hz. The minimum IFD values are reported with a red square.

A miniaturized *in vitro* 3D model to assess the neuroprotective effect of mesenchymal stromal cell secretome on neuroblastoma cells exposed to oxidative stress

L. Boeri[1,2], M. Tunesi[1,3], C. Giordano[1,3], D. Albani[2], and M.T. Raimondi[1]
[1] *Department of Chemistry, Materials and Chemical Engineering "G. Natta", Politecnico di Milano, Milan, Italy*
[2] *IRCCS-Istituto di Ricerche Farmacologiche Mario Negri, Milan, Italy*
[3] *Unità di Ricerca Consorzio INSTM, Politecnico di Milano, Milan, Italy*

***Abstract*—To develop reliable and effective *in vitro* models for basic neuropathological research purposes, we have optimized a miniaturized microfluidic bioreactor. In this work we have adapted this 3D cell culturing concept to assess the effect of mesenchymal stromal cell (MSC) secretome on neuronal-like cells (SH-SY5Y) subjected to oxidative stress. MSC secretome has shown a significant neuroprotective effect, laying the groundwork for molecular studies searching for protective effect mediators.**

***Keywords*—Bioreactor, 3D cell culture, neuroprotection, mesenchymal stromal cell.**

I. Introduction

BECAUSE of the biological complexity of the mammalian brain, conventional 2D culture systems fail to provide topographical cues, enable cell differentiation into specific phenotype and fully reproduce *in vivo* cell behaviour [1]. Mimicking the 3D physical microenvironment of the multi-cellular cerebral architecture is thus crucial to study both neuropathological features and innovative therapeutic approaches.

We have recently developed a miniaturized bioreactor for the dynamic culturing of 3D cell constructs under perfused condition (Fig. 1A). It is also optically accessible, allowing the direct observation of cell constructs by viable staining and a standard fluorescence microscope (Fig. 2) [2].

In this work, we have optimized this 3D culture system to develop a reliable and effective *in vitro* model of Parkinson's disease to study the neuroprotective effect of mesenchymal stromal cell (MSC) secretome on SH-SY5Y neuroblastoma cells subjected to oxidative stress.

II. Materials and Methods

A. The miniaturized and optically accessible bioreactor

The dynamic culture system is characterized by three independent culture chambers, two of which may be eventually connected by a hydraulic bypass. Each chamber contains a 3D scaffold (6x3x0.4 mm, 3D Biotek, Fig. 1B). The scaffolds are made of poly(styrene) and they are obtained by fuse deposition modelling. They are composed of four layers of fibres (100 µm diameter, with a pore size of 300 µm) shifted of 150 µm with respect to the adjacent. The miniaturized bioreactor is optically accessible thanks to the optical transparency and low thickness of the components, allowing the direct observation of cell constructs while in culture, without the need of stopping the flow of culture medium [2].

B. Cell culture

SH-SY5Y human neuroblastoma cells (ATCC® CRL-2266™) were used as a model of dopaminergic neurons, while MSCs were extracted from rat bone marrow.

SH-SY5Y cells were cultured in Dulbecco's Modified Eagle medium, while MSCs were kept in alpha-Minimum Essential medium, both supplemented with 10% fetal bovine serum, 2 mM L-glutamine, 100 U/ml penicillin and 100 µg/ml streptomycin sulphate (Euroclone®).

Cell seeding in 3D scaffolds was optimized from a previous work [2]. The scaffolds were placed in an ultra-low attachment 24-well microplate (Corning® Costar®) and incubated overnight with 400 µl medium (under 5% CO_2 at 37 °C). The following day, they were covered with cell suspension (0.5 or $1 \cdot 10^6$ SH-SY5Y cells/400 µl; $0.25 \cdot 10^6$ MSCs/400 µl) and shaken by a 3D multifunction rotator (PS-M3D, VWR) for 3 h. The following day the samples were moved into clean wells and covered with 400 µl fresh medium.

To evaluate the number of SH-SY5Y cells in 3D scaffolds, cells were detached and lysed by repeated cycles of freezing (-80 °C) and thawing (37 °C on a orbital shaker). 2 µl lysate was assayed on a NanoQuat Plate™ (Infinite M200 PRO, Tecan) and DNA concentration was calculated by measuring the absorbance at 260 nm. Finally, the total number of cells in 3D scaffolds was estimated considering 6.4 pg DNA as the total amount of DNA in a human diploid cell [3]. Results were compared to those obtained after plating $0.5 \cdot 10^6$ SH-SY5Y cells in a standard 24-well microplate.

C. Oxidative damage

To produce oxidative and mitochondrial damage, SH-SY5Y cells were exposed to different concentrations (125 and 250 µM) of the neurotoxin 6-hydroxydopamine (6-OHDA, Sigma-Aldrich) in static or shaken conditions (by placing the samples on a multifunctional rotator). To assess the stability of the induced oxidative damage with time, cell metabolic activity was evaluated by Alamar Blue® assay (resazurin sodium salt, Sigma-Aldrich), at subsequent time points.

D. Conditioning assay

To assess the neuroprotective effect of MSC secretome on damaged SH-SY5Y cells, 3D scaffolds were assembled in the microfluidic bioreactor (Fig. 1A). A scaffold seeded with MSCs was placed in chamber 1, while chamber 2 hosted a scaffold seeded with SH-SY5Y cells previously damaged with 6-OHDA. We have connected chamber 1 and 2 by a bypass, so that MSC secretome could flow through the scaffold seeded with damaged SH-SY5Y cells. As a control, chamber 3 hosted a 3D scaffold seeded with damaged SH-SY5Y cells not conditioned by MSC secretome. After 3 days of conditioning, the bioreactor was disassembled and cell metabolic activity was evaluated by Alamar Blue® assay.

E. Alamar Blue® assay in dynamic conditions

Taking into consideration the possibility of assessing cell metabolic activity while in perfused culture, we have determined the conditions in which the results from Alamar Blue® assay in static conditions (incubation with 400 µl working solution for 3 h) are comparable to Alamar Blue® assay in dynamic conditions (perfusion with working solution at a flow rate of 5.0 µl/min for 3 h).

F. Western Blotting

To search for biochemical mediators of the neuroprotective effect of MSC secretome, 20 µg of the total protein extracts were assessed by Western Blotting and stained with antibodies specific to target proteins involved in neuroprotection against oxidative stress, such as Hsp70 and SIRT3 [4, 5]. We have quantified protein signals by densitometric analysis using ImageJ software.

G. Statistical analysis

Two-way analysis of variance (ANOVA) followed by Tukey's multiple comparison test was used for comparisons among the groups and time frames, while one-way ANOVA followed by Tukey's multiple comparison test was used for comparisons among the groups. The significance level was set at $p\text{-value} < 0.05$. All the results were reported as mean ± standard deviation (SD).

III. Results

A. Assessment of oxidative damage on SH-SY5Y cells

DNA measurements have indicated that the scaffolds seeded with $1 \cdot 10^{-6}$ SH-SY5Y cells contained a greater number of cells with respect to those seeded with $0.5 \cdot 10^{-6}$ SH-SY5Y cells and the 2D controls. However, morphological analysis has shown that scaffolds seeded with a greater cell density revealed pore occlusion due to cell clusters. On the contrary, scaffolds seeded with $0.5 \cdot 10^{-6}$ SH-SY5Y cells have shown a more homogeneous cell distribution in the fibres. For this reason, $0.5 \cdot 10^{-6}$ SH-SY5Y cells/scaffold was selected as seeding density.

The incubation with 6-OHDA reduced cell metabolic activity. In particular, we observed a reduction by 50% and 80% (mean value) for samples treated with 125 µM 6-OHDA or 250 µM 6-OHDA, respectively ($p\text{-value} < 0.0001$). Since a stable damage may be induced with a lower toxin concentrations, the incubation with 125 µM 6-OHDA may be preferred.

B. Neuroprotective effect of MSC secretome on SH-SY5Y cells

In the conditioning assay, SH-SY5Y cells conditioned with MSC secretome have shown a significant recovery from damage by up to 30% with respect to the untreated control. The protocol for Alamar Blue® assay adapted to perfused culture resulted in a reliable method to assess cell metabolic activity while in culture, avoiding the need to remove cell constructs from the bioreactor.

Currently we are searching for molecular basis of this neuroprotective effect. So far, we have identified Hsp70 and SIRT3 as possible candidates.

IV. Conclusion

Coherently with previous observations in static *in vitro* models and *in vivo* [6, 7], our advanced *in vitro* model was able to reproduce the neuroprotective effect of MSC secretome on damaged neuronal cells. In addition, thanks to the perfusion and optical accessibility of the bioreactor, our system offers the advantage of monitoring the effect of MSC conditioning non-destructively and for a longer culture period in comparison to standard 2D cultures, thus mimicking features of chronic neurodegeneration more realistically.

Acknowledgement

We acknowledge funding from European Commission (ERC grant No. 646990-NICHOID).

Disclosure

The authors have nothing to disclose.

References

[1] Y. Lai, K. Cheng, W. Kisaalita. *Three dimensional neuronal cell cultures more accurately model voltage gated calcium channel functionality in freshly dissected nerve tissue*. PLoS One. 2012; 7:e45074.

[2] M. Laganà, M. T. Raimondi. *A miniaturized, optically accessible bioreactor for systematic 3D tissue engineering research.* Biomed Microdevices. 2012 Feb; 14:225-34.

[3] J. Dolezel, J. Bartos, H. Voglmayr, J. Greilhuber. *Nuclear DNA content and genome size of trout and human.* Cytometry A. 2003 Feb; 51:127-8.

[4] M. Amadio, G. Scapagnini, U. Laforenza, M. Intrieri, L. Romeo, et al. *Post-transcriptional regulation of HSP70 expression following oxidative stress in SH-SY5Y cells: the potential involvement of the RNA-binding protein HuR*. Curr Pharm Des. 2008; 14:2651-8.

[5] S. H. Dai, T. Chen, Y. H. Wang, J. Zhu, P. Luo, et al. *Sirt3 protects cortical neurons against oxidative stress via regulating mitochondrial Ca2+ and mitochondrial biogenesis*. Int J Mol Sci. 2014 Aug 21;15:14591-609.

[6] Y. Yan, T. Ma, K. Gong, Q. Ao, X. Zhang, et al. *Adipose-derived mesenchymal stem cell transplantation promotes adult neurogenesis in the brains of Alzheimer's disease mice*. Neural Regen Res. 2014 Apr 15; 9:798-805.

[7] P. Hao, Z. Liang, H. Piao, X. Ji, Y. Wang, et al. *Conditioned medium of human adipose-derived mesenchymal stem cells mediates protection in neurons following glutamate excitotoxicity by regulating energy metabolism and GAP-43 expression.* Metab Brain Dis. 2014 Mar; 29:193-205.

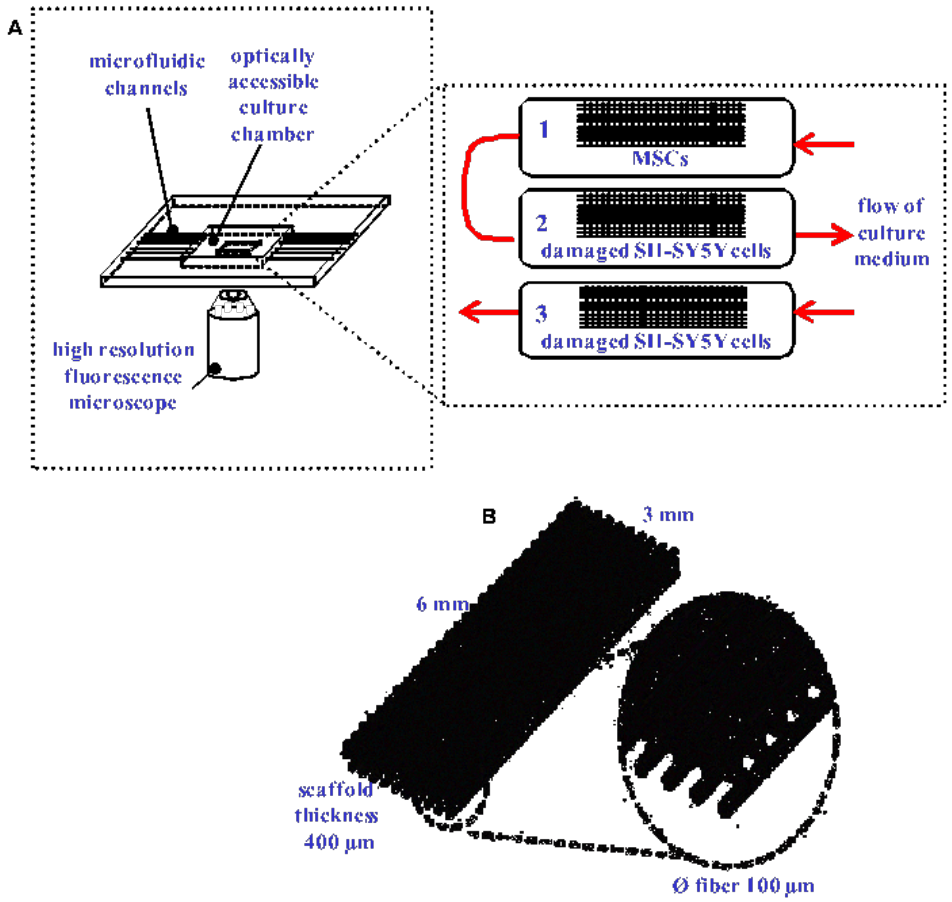

Fig. 1. (A) Scheme of experimental set-up. Culture medium is conveyed to the chambers by a syringe pump and microfluidic channels. The optical transparency and low thickness of the components allow the direct observation of cell constructs by a standard fluorescence microscope. Chambers 1 and 2 are connected by a hydraulic bypass. Chamber 1 contains a scaffold seeded with MSCs, chamber 2 hosts a scaffold seeded with damaged SH-SY5Y cells, while chamber 3 is independent and hosts a scaffold seeded with damaged SH-SY5Y cells. (B) 3D scaffold (6 mm×3 mm×0.4 mm).

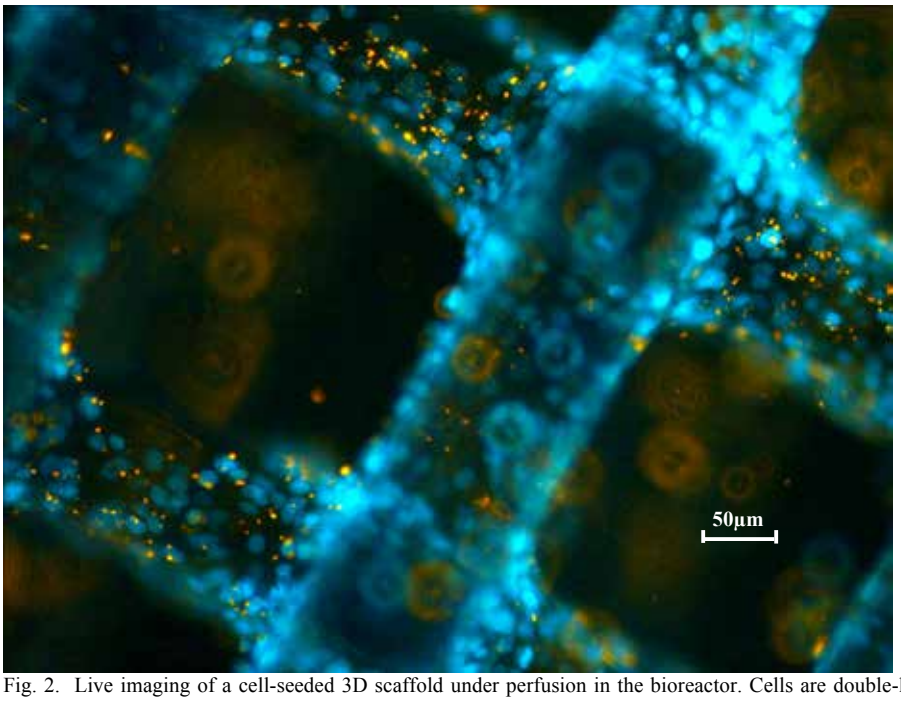

Fig. 2. Live imaging of a cell-seeded 3D scaffold under perfusion in the bioreactor. Cells are double-labelled with DAPI (nucleus, in blue) and quantum dots (cytoplasm, in orange).

Reconfigurable optical setup for solution concentration detection in rectangular capillary

G. Rigamonti[1], F.Carpignano[1]
[1]*University of Pavia,Pavia,Italy*

***Abstract*—We demonstrate an easily reconfigurable all-fiber setup for spectral and low coherence interferometric measurements of fluids collected in rectangular glass micro-capillaries, in view of their application as micro-opto-fluidic devices. Two broadband light sources emitting in the near infrared region (1.2-1.7 µm) were used, allowing optical readout in a spectral range that is minimally invasive for biological materials. We here report the results obtained on glass micro-capillaries with channel depth of 50-µm and 20-µm, and compare the applied measuring techniques in terms of detection limits and detection range.**

***Keywords*—Low-coherence interferometry, spectral reflectivity measurements, glass rectangular micro-capillaries, infrared radiation.**

I. INTRODUCTION

In recent years, great interest has been paid to the development of label-free sensors, since label-free detection methods are safer, less invasive, and potentially realizable at lower cost [1], [2]. Among these sensors, increasing attention is devoted to optical label-free devices that measure volumetric changes of the refractive index of homogeneous solutions [3]. A glass micro-capillary can be view as an optical device composed by two borosilicate glass walls separated by the inner gap [5]. In this perspective, glass micro-capillaries with rectangular cross-section are good candidates to be the core elements of micro-opto-fluidic devices. In fact they are commercially available at low cost and allow to work with ultra-low quantities of materials, important factor for example in biochemical and biological analysis, since the refractive index (RI) of a solution scales with its bulk concentration, instead of the total number of molecules [3]. Moreover, rectangular micro-capillaries are well suited for optical analysis since optical distortions and scattering caused by the wall curvature of round cross-section capillary are strongly reduced [4]. In this work we propose an all-fiber setup that can be easily reconfigured for low-coherence interferometric measurements or for spectral reflectivity measurements. Both techniques are suitable for characterization and readout of rectangular glass micro-capillaries in view of their application as micro-opto-fluidic devices for RI detection. We have tested two kinds of capillaries, with inner channel size of 50 µm x 500 µm and 20 µm x 200 µm, and wall thicknesses of the order of the channel minor dimension (nominal values). We have applied our setup for detection of glucose concentration in water solutions and we here compare the results obtained with both measuring techniques.

II. INSTRUMENTAL CONFIGURATION

Fig. 1 shows the block diagram of the experimental setup used for spectral and low-coherence interferometric measurements. In both cases a broadband light source emitting in the near infrared region (1.2 µm to 1.7 µm) was used, namely a Tungsten lamp for interferometric measurements and a diode-pumped Erbium-doped fiber source (EBS) for spectral measurements. The Tungsten lamp emitted a power spectral density of about −60 dBm/10 nm in the wavelength range from 1.2 µm to 1.7 µm, while the EBS provided an optical power with spectral density of around -10 dBm/0.1 nm on a 45 nm bandwidth, with central wavelength $\lambda_c \approx 1.55$ µm. The emitted light is fiber coupled and it is divided along two different arms: the measuring path, ending toward the device under test, and the reference path, both ending with a pigtail style focuser with aspheric lens (by OzOptics). The lens on the measuring arm shines a 50 µm diameter beam orthogonally to the capillary under test placed at a working distance of 23.5 mm. Mirror and device under test are mounted on a x-y-z micro-positioner. In case of spectral measurement, the reference path is ended with an angled connector to avoid back-reflection. The light reflected back from the device (and from the reference mirror in case of interferometric measurements) is coupled back into the optical fiber path and redirected to the photodetector. As it can be noticed, several components are common to both experimental configurations, namely the light source, the fiber paths, the readout lens and the beam-splitter, allowing a rapid exchange between configurations.

III. EXPERIMENTAL RESULTS

We applied low-coherence interferometry and spectral reflectometry for optical detection of the concentration of aqueous solutions inside of borosilicate glass rectangular cross-section micro-capillaries (Vitrotubes™, VitroCom, New Jersey, USA). We used capillaries with channel depth d = 50 µm and glass wall thicknesses t_f e t_b of the same size and flat side w = 500 µm, as well as capillaries with $d = t_f = t_b$ = 20 µm and w = 200 µm, as reported in Fig.1. All capillaries were 50 mm long. Standard tolerances are equal to ± 10 % for channel depth and width and ± 20 % for walls thicknesses. We applied the proposed detection methods to fluids of biological interest, i.e., glucose solutions in water at different concentrations. Solutions filled the capillaries just by capillary action.

Interferometric Measurements

The signals were acquired in the time domain and then converted in the Optical Path (*OP*) domain thanks to the relation $OP = v * t$, where v = 5 µm is the speed of the reference mirror. Fig. 2 shows the interferometric signals collected on a 50-µm capillary. Each group of fringes corresponds to an in-depth interface of the device (i.e., air-glass interface). Each trace is normalized with respect to the peak value and a digital filter improved the signal-to-noise ratio. Since in the case of broadband radiation and dispersive

media the optical path is also defined as $OP = n_g * d$, where n_g is the group refractive index of the crossed medium and d its geometrical thickness, when a liquid is inserted into the gap, the relative *OP* increases proportionally [6]. This causes a lengthening of the optical path OP_{gap} relative the capillary channel, as can be noticed by the black trace in Fig. 2. As expected, being the refractive index of glucose higher than that of air, we detected a longer OP_{gap} when the capillary was filled with this fluid. We repeated the experiment with solutions at different concentrations of glucose in water, from 0 to 30%. For each acquired signal we extracted the optical paths relative to walls and channel and plotted them as a function of the concentration of glucose in water. Reported values and standard deviations were calculated on at least three different measurements. As an example, in Fig. 3 are reported the optical paths relative to the channel and to one of the walls as a function of the concentration of glucose in water. As expected a linear increase of the OP_{gap} was found as the glucose concentration increased, while no concentration dependent change in the OP_{wall} was observed. A sensitivity value, defined as $S = dOP_{gap}/dC$, equal to 0.065 μm/C [%] was found. Another important parameter is the limit of detection (*LOD*), defined as [7] $LOD = 3\sigma/S$ where σ is the standard deviation of data, that gives the minimum change of concentration of the solute in solution that can be detected. In our experiment we calculated a best *LOD* of 2.6 C [%].

Spectral Measurements

Shining a broadband light source orthogonally to the flat long side of the capillary and coupling the back-reflected light to an optical spectrum analyzer, it is possible to observe that the spectrum exhibits different deep reflectivity notches separated by intervals were the reflectivity is high [8]. Since resonances usually correspond to spectral reflectivity minima, a change in the RI of the tested fluid sample is easily recognized from a shift of the wavelength position where the resonance occurs [9]. Specifically, a shift toward longer wavelengths is observed when fluids with increasing RI values are inserted in the capillary. Fig. 4 shows a subset of four reflectivity spectra collected on a 50-µm capillary filled with solutions with different concentrations of glucose in water. As expected, a shift of the spectra toward longer wavelengths as the glucose concentration is increased can be clearly noticed. The *FSR (*Free Spectral Range) highlighted in the picture is the distance between two consecutive minima (or maxima) of the same spectrum, and gives the maximum interval of wavelength in which the spectrum shift can be detected without ambiguity. The *FSR* highlighted in picture is equal to 6 nm. This gives a limit to the maximum change of concentration (and consequently of RI) that can be investigated. Fig. 5 shows the mean value of the wavelength positions of minima as a function of the concentration of glucose. All reported values and standard deviations were calculated at least on three values. For this experiment we obtained a maximum sensitivity $S = 0.00051$ µm/C [%] for the minimum starting at $\lambda_{min} = 1.56$ µm and *LOD* of the order of 10^{-2} C [%]. We then repeated the same experiment on a 20-μm capillary. Being the *FSR* of a cavity inversely proportional to its depth, we were able to investigate fluids with a wider RI change. We used Glucose solutions in water with concentration up to 25 % and all shifts were maintained within a *FSR*. The calibration curve is reported in Fig. 6. Sensitivities of the same order of magnitude and *LOD* of the order of 10^{-1} were obtained.

IV. Conclusion

In this work, we demonstrated an easily reconfigurable setup for spectral and low-coherent interferometric measurements combined with rectangular glass micro-capillaries in view of their application as micro-opto-fluidic sensors of fluid refractive index. Good results in term of sensitivity and ability to discriminate between different fluids were obtained. In particular, interferometric measurements allowed to reach high sensitivity values, while lower values were obtained for spectral reflectivity measurements. Moreover, spectral reflectivity is affected by a maximum change that can be detected without ambiguity, depending on the *FSR* of the monitored structure, and consequently on its dimensions. On the other hand, spectral measurements exhibited a better *LOD*, in the range of 10^{-2} – 10^{-1} C [%], compared to *LOD* of the order of 10^{1} obtained with the interferometric technique. In conclusion, low-coherence interferometry allows to investigate big leaps of RI but has not the ability to detect very small changes. On the other hand, spectral reflectivity has a better resolution but with a limit in the range of variation that can be monitored without ambiguity. So, investigating the same capillary with the two techniques it is possible to overcome the limitations of each measurement.

Acknowledgement

The authors wish to thank Prof. S. Merlo for fruitful discussions and revisions. FC is currently located at Plasmore srl, Pavia, Italia.

References

[1] N. M. M. Pires, T. Dong, U. Hanke, and N. Hoivik, "Recent developments in optical detection technologies in lab-on-a-chip devices for biosensing applications," *Sensors*, vol. 14, no. 8, pp. 15458–79, Jan. 2014.

[2] H. K. Hunt and A. M. Armani, "Label-free biological and chemical sensors," *Nanoscale*, vol. 2, no. 9, pp. 1544–59, Sep. 2010.

[3] X. Fan and I. M. White, "Optofluidic microsystems for chemical and biological analysis," *Nat. Photonics*, vol. 5, no. 10, pp. 591–597, Sep. 2011.

[4] T. Tsuda, J. V. Sweedler, and R. N. Zare, "Rectangular capillaries for capillary zone electrophoresis," *Anal. Chem.*, vol. 62, no. 19, pp. 2149–2152, Oct. 1990.

[5] S. J. Orfanidis, *Proc. Electromagn. Waves Antennas.,* 2014, pp. 186-234

[6] F. Carpignano, G. Rigamonti, and S. Merlo, "Characterization of rectangular glass microcapillaries by low-coherence reflectometry," *IEEE Photonics Technol. Lett.*, vol. 27, no. 10, pp. 1064–1067, Feb. 2015.

[7] I. M. White and X. Fan, "On the performance quantification of resonant refractive index sensors," *Opt. Express*, no. 1–2, pp. 117–127, Jan. 2008.

[8] F. Carpignano, G. Rigamonti, T. Migliazza, and S. Merlo, "Refractive Index Sensing in Rectangular Glass Micro-Capillaries by Spectral Reflectivity Measurments," J. Sel. Topics Quantum Electron., vol. 22, no. 3, pp. 1–9, Aug. 2015.

[9] G. Barillaro, S. Merlo, S. Surdo, L. M. Strambini, and F. Carpignano, "Integrated optofluidic microsystem based on vertical high-order one-dimensional silicon photonic crystals," *Microfluid. Nanofluidics*, vol. 12, no. 1–4, pp. 545–552, Nov. 2012.

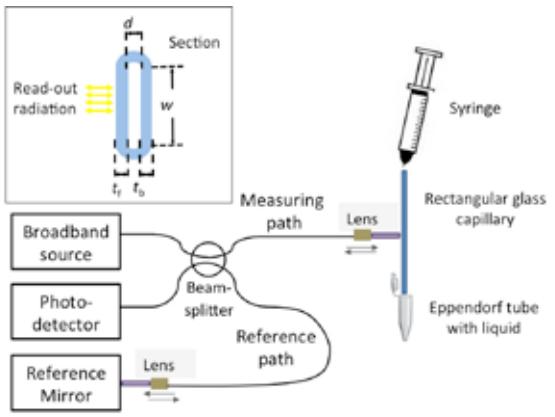

Fig. 1. Reconfigurable instrumental configuration. Inset: schema of capillary section t_f, tb: thickness of the front and back glass wall. d: depth of the inner channel. w: width of the flat side of the capillary.

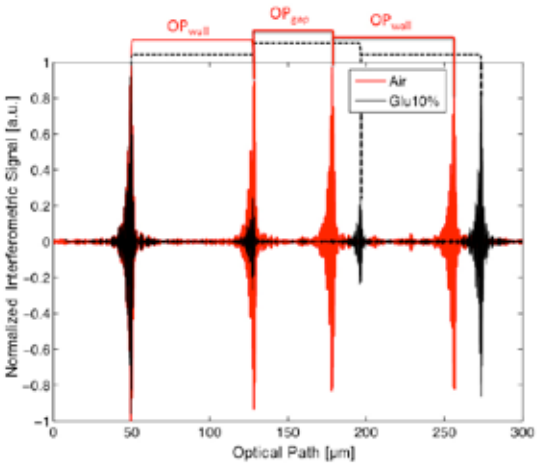

Fig. 2. Normalized interferometric signal as a function of the optical path obtained on a 50-μm capillary. Red trace: empty capillary; black trace: capillary filled with glucose solution at 10% concentration.

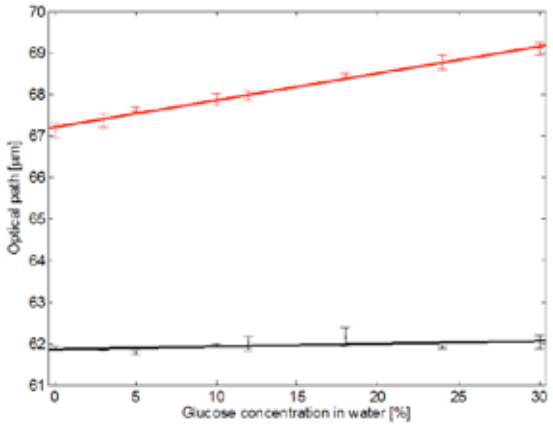

Fig. 3. Optical paths (OP) relative to the inner channel (red) and to one wall (black) of a 50-μm capillary as a function of the glucose concentration in water expressed in %.

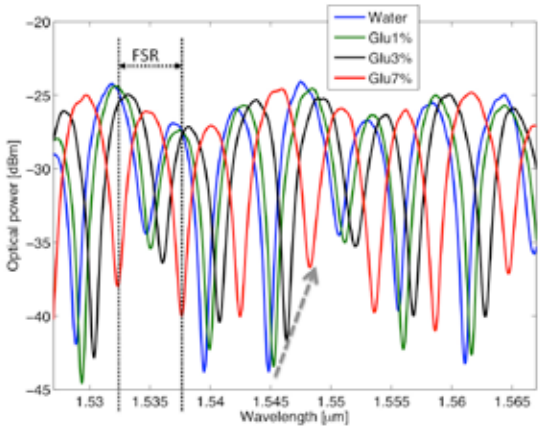

Fig. 4. Optical power spectra relative to 50-μm capillary considering glucose solutions in water at 0% (blue trace), 1% (green trace), 3% (black trace), and 7% (red trace) concentrations as filling fluid. As an example, the grey arrow indicates the shift of one spectrum minimum at the increase of the refractive index of the solution. FSR= Free spectral range.

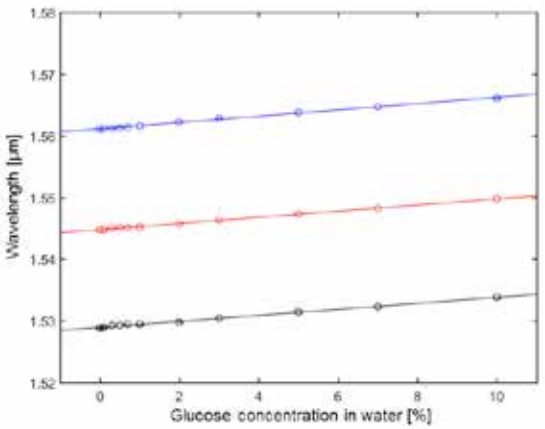

Fig. 5. Calibration curves of a 50-μm capillary as solution concentration sensor. Mean values with error bars of the wavelength position (as an example) of some detected experimental minima as a function of the concentration of the tested glucose solutions. Glucose solutions in water in a range concentration of 0-10% were used for the experiment. Linear fitting provides the sensitivity.

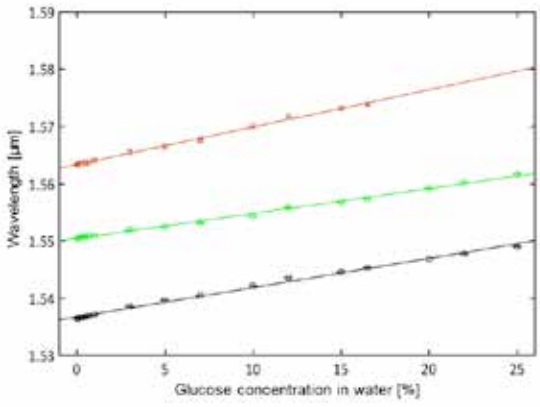

Fig. 6. Calibration curves of a 20-μm capillary as solution concentration sensor. Mean values with error bars of the wavelength position of all detected experimental minima as a function of the concentration of the tested Glucose solutions. Data reported in the image are relative to the wavelengths within a Free Spectral Range. Glucose solutions in water at concentration of 0%, 0.1%, 0.3%, 0.5%, 0.7%, 1%, 3%, 5%, 7%, 10%, 12%, 15%, 16.5%, 20%, 22%, and 25% were used for the experiment. Linear fitting provides the sensitivity.

TELEMEDICINA

Continuous glucose monitoring improves euglycemic range in preterm infants vs. conventional sparse sampling: necessity of a glucose telemonitoring service in neonatal intensive care units

E. Losiouk[1], G. Lanzola[1], A. Galderisi[2], D. Trevisanuto[2], G. Steil[3], A. Facchinetti[4], and C. Cobelli[4]
[1]*Dept. of Electrical, Computer and Biomedical Engineering, University of Pavia, Pavia, Italy*
[2]*Neonatal Intensive Care Unit, Department of Woman and Child's Health, University of Padova, Padova, Italy*
[3]*Boston Children's Hospital, Harvard Medical School, Boston, MA, USA*
[4]*Department of Information Engineering, University of Padova, Padova, Italy*

***Abstract*—Hypo and hyperglycaemic oscillations in preterm newborns during the first days of life are associated with increased mortality and neurological impairments. Recently, real-time continuous glucose monitoring systems proved to be superior in maintaining glucose within the safety range in neonatal intensive care unit with respect to standard sparse heel pricks. However, one major limitation is that glucose concentration values are available only on the portable sensor receiver. We improved the system with a telemonitoring service for the transmission of data, acquired through the Dexcom G4 PLATINUM with Share, from hospitalized preterm new-borns to a remote server. This allows clinicians and health-care staff to better oversee the situation and enforce standard care practices.**

***Keywords*— glycaemia sensor, Bluetooth low energy, remote monitoring, preterm newborns.**

I. Introduction

HYPERGLYCAEMIA (HYPER) and hypoglycaemia (HYPO) represent dangerous conditions for very low birth weight infants (VLBWI). HYPER proved to be associated with increased mortality and morbidity [1], [2], while HYPO episodes could lead to neurological impairments [3].

Current techniques for glucose monitoring applied on VLBWI include arterial sampling or heel prick performed several times during the day. Due to the fragility of those patients, the frequency of samples is less than the one adopted in adults and precludes the detection of all HYPER and HYPO possibly occurring between sampling times. The introduction of a continuous glucose monitoring (CGM) system yields a better control of glycaemia values, reducing, in the meanwhile, the pain suffered by the patient during heel prick measurements. Despite their effectiveness, there is some controversy about the adoption of CGM systems in intensive care, especially considering HYPO events detection [4], [5]. However, "the clinical advantages of the use of CGM systems in the intensive care setting would not be to diagnose hypoglycaemia, but to provide continuous information regarding trends in glucose levels" [6].

In preterm infants, preliminary results showed that a continuous blood glucose control using a Dexcom G4 PLATINUM with Share (DEXG4) sensor with a suitable algorithm regulating glucose infusion rates and HYPO alarms, increased the time spent in normal glycemic range when compared to standard glycemic monitoring. [7]. However, one of the major limitations was that the CGM signal and its processing output were available only on the DEXG4 portable receiver and could not be remotely monitored outside of the Neonatal Intensive Care Unit (NICU).

In this paper, we describe the remote monitoring (RM) system we developed for acquiring data from DEXG4. That system is presently being used experimentally at the Padova NICU for accessing and visualizing data remotely by the physicians (trial approved by the Ethical Committee of University-Hospital of Padova; 3440/AO/15).

II. Methods

The design of the overall architecture, shown in Figure 1, was influenced both by previous experiences accomplished by some of the authors in acquiring and transferring medical data [8], [9], and by the specific requirements of this case study.

Data acquisition starts from the DEXG4 system, comprising a sensor and a portable receiver. The sensor is applied on the preterm infant's thigh and continuously acquires blood glucose levels. The portable receiver collects glycaemia values and makes them available over the Bluetooth Low Energy (BTLE) protocol. Then an Android smartphone receives the data from the DEXG4 and securely relays those to a server. The smartphones may be located on the cradles next to the DEXG4s or be positioned in a common shelf in the NICU room. A WiFi or 3G connection is used to send data by the smartphone over the network, while a Web application at monitoring stations allows to visualize data.

Additional specific requirements were the following ones:

- Real-time operation: data acquisition and visualization replicating the DEXG4 operation, to monitor the preterm newborn health status with minimal delay;
- Flexibility: visualization of the latest and historical CGM values using charts and textual interfaces including the possibility of downloading data;

- Alarms: signaling dangerous events such as HYPO and HYPER;
- Annotations: possibility of manually adding annotations about significant events through the web interface.

III. RESULTS

Two different components were developed in order to implement the RM service: an Android mobile application, called *Neokid*, and a web application. In the main screen of Neokid, shown in Figure 2, the user sees the identifier of the patient associated to the mobile device, the most recent glycaemia value-time pair and the last sensor calibration value-time pair. In addition, two icons in the upper part of the interface give visual feedback about connection status of the mobile device with DEXG4 device and with the remote server. Those links and other useful parameters can be configured before starting the session through three screens provided by Neokid. Finally, Neokid is equipped with a buffering feature that, in case of network connectivity problems, temporarily saves any data on a local data storage on the mobile app until the connection towards the remote server is resumed.

The second component is the web application, which comprises two separate screens. The first one provides a summary overview of all the patients currently being monitored. In fact, the web app was designed to streamline the activities of the physicians, that need a general overview of all their patients' health statuses in order to promptly undertake corrective actions if needed. Figure 3 shows the web application summary panel, where information about the last glycaemia value, hypo- and hyper- risk and global blood glucose tendency are reported. In case of missing data or dangerous glycaemia values, the panel border of that patient is highlighted in red, and an optional beeping sound along with a message is provided to the user depending on the alarm severity.

The second main feature of the web application is provided by the real-time monitoring chart, visible in Figure 4. The orange vertical line corresponds to the current date time, while glycaemia values are drawn as consecutive red circles, interspersed by blue squares used for marking sensor calibration events. The interface refreshes automatically, according to the chosen frequency, and shows data with a delay between 5 and 10 minutes that recalls the delay with which data become available on the DEXG4 portable receiver. On the left of the graph, information about the last glycaemia value is shown. Finally the user can manually insert some remarkable events in order to possibly detect correlations between those and glycaemia trend.

IV. CONCLUSION

The overall system has been tested on twelve VLBWI, each one enrolled into a seven-day trial. During that test no technological limits were noticed. Accessing all VLBWI data from a central location that also signalled alarms, reduced the daily workload of physicians that did not have to consult anymore every single receiver's display nor to hear the alarms coming from those. Moreover, the general supervision was improved considering that both physicians on ward at the NICU and those outside it could see blood glucose values in real-time, and have the opportunity to react in case of HYPO events.

The web component has turned out to be modular enough to be used in different contexts concerning the RM of patients' health status [10], [11], [12]. The mobile application, instead, is very specific due to the unique communication protocol used by DEXG4 receiver.

Future developments may include the integration of glycaemia trend together with other signals, already displayed on single monitors located near the cradles in the NICU, in order to simplify the task of overseeing all VLBWI.

ACKNOWLEDGEMENT

We would like to thank Dexcom Inc, CA, USA, for kindly providing materials, especially Stefania Guerra and Apurv Kamath.

REFERENCES

[1] S. P. Hays, E. O. Smith, A. L. Sunehag. "Hyperglycemia is a risk factor for early death and morbidity in extremely low birth-weight infants", *Pediatrics,* 2006, vol. 118, pp. 1811–1818.

[2] G. Alexandrou, B. Skiöld, J. Karlén, M. K. Tessma, M. Norman, et al., "Early hyperglycemia is a risk factor for death and white matter reduction in preterm infants", *Pediatrics,* 2010, vol. 125, pp. 584–591.

[3] C. J. D. McKinlay, J. M. Alsweiler, J. M. Ansell, N. S. Anstice, J. G. Chase, et al., "Neonatal glycemia and neurodevelopmental outcomes at 2 years", *The New England Journal of Medicine*, 2015, vol. 373, pp. 1507-1518.

[4] B. C. Bridges, C. M. Preissig, K. O. Maher, M. R. Rigby, "Continuous glucose monitors prove highly accurate in critically ill children", *Critical Care*, 2010, vol. 14, R176.

[5] J. J. M. Ligtenberg, M. E. de Plaa, J. G. Zijlstra, "Continuous subcutaneous glucose monitoring: good enough to use in glucose regulation protocols?", *Critical Care*, 2011, vol. 15, pp. 403.

[6] K. Beardsall, S. Vanhaesebrouck, A. L. Ogilvy-Stuart, C. Vanhole, M. VanWeissenbruch, et al., "Validation of the continuous glucose monitoring sensor in preterm infants", *Archives of disease in childhood. Fetal and neonatal edition*, 2013, vol. 98, pp. 136-140.

[7] A. Galderisi, A. Facchinetti, G. Steil, P. P. Ortiz-Rubio, C. Cobelli, et al., "Neonatal hypoglycemia continuous glucose monitoring: a randomized controlled trial in preterm infants", in *2016 Proc. ATTD Conf.*

[8] D. Capozzi, G. Lanzola, "A generic telemedicine infrastructure for monitoring an artificial pancreas trial", *Computer Methods and Programs in Biomedicine*, 2013, vol. 110, pp. 343-353.

[9] G. Lanzola, S. Scarpellini, F. Di Palma, C. Toffanin, S. Del Favero, et al., "Monitoring artificial pancreas trials through agent-based technologies a case report", *Journal of diabetes science and technology,* 2014, vol. 8, pp. 216-224.

[10] J. Kropff, S. Del Favero, J. Place, C. Toffanin, R. Visentin, et al., "2 month evening and night closed-loop glucose control in patients with type 1 diabetes under free-living conditions: a randomised crossover trial", *The Lancet Diabetes & Endocrinology*, 2015, vol. 3, pp. 939-947.

[11] G. Lanzola, I. Secci, S. Scarpellini, A. Fanelli, G. Magenes, et al., "A mobile remote monitoring service for measuring fetal heart rate", in *2013 Proc. MEDICON Conf.*, pp. 1435-1438.

[12] E. Losiouk, G. Lanzola, R. Bonfanti, D. Iafusco, I. Rabbone, et al., "Perceived utility of a remote monitoring system for pediatric subjects affected by type 1 diabetes in PEDarPAN (PEDiatrics artificial PANcreas) summer camp", in *2016 Proc. ATTD Conf.*

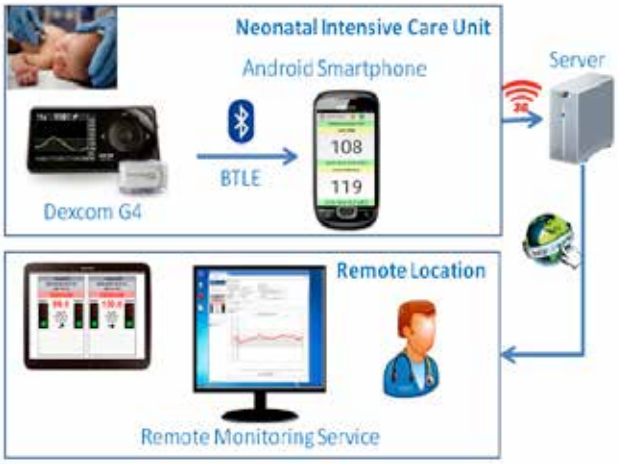

Fig. 1. The remote monitoring system architecture.

Fig. 2. The mobile application main screen.

Fig. 3. Running patients' overview in the web application showing glycaemia last values and trends.

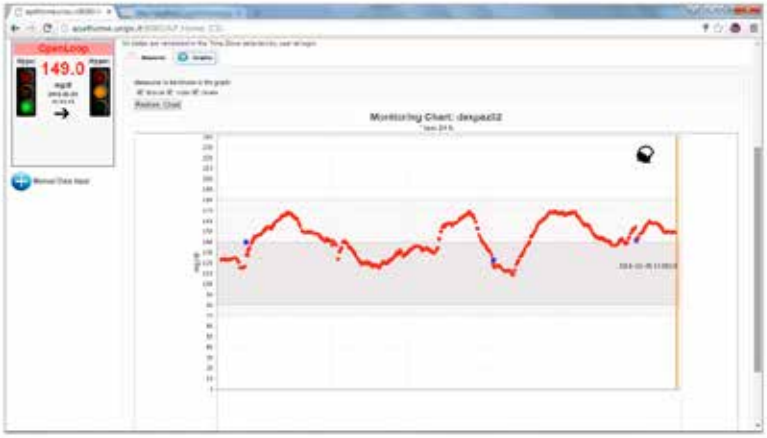

Fig. 4. The chart illustrating the patient's glycaemia evolution in the web application.

An ICT platform for independent living and remote health monitoring

S. Macis, D. Pani, D. Loi, A. Ulgheri and L. Raffo
Department of Electrical and Electronic Engineering, University of Cagliari - Italy

***Abstract*—Active ageing and tele-health platforms are, nowadays, the most sought-after means to overcome the rising problem of population ageing. Helping older adults live autonomously in their homes through ICT solutions could be a way to relieve the burden on the Healthcare Systems. This paper presents a novel ICT platform designed specifically for the elderly and aimed to improve their independent living and their health status, exploiting remote health monitoring features. Preliminary studies on usability allowed to improve the system in preparation for the field trials in three European countries.**

***Keywords*—Active ageing, telemonitoring, ICT.**

I. Introduction

THE modern society is dealing with a progressive ageing of the population. The disproportion between new-borns and elderly will lead to a drastic change in the age population structure. This will have many consequences for the society, including an increase in the health expenditure [1]. In this scenario, the development of services for independent living is of paramount importance to enable the elderly to live autonomously in their homes as long as possible. Such services often include health telemonitoring features, aimed at supporting vital signs monitoring from remote. Nowadays, telehealth is one of the most sought-after approach for chronic patients' management, allowing to provide hitherto unavailable monitoring features at an affordable cost. From a technological viewpoint, digital divide hampers the widespread adoption of these platforms [2]. User-centred design is the key to pursue usability and acceptability of ICT systems targeted to the elderly.

This paper presents the architecture of a novel ICT platform with tele-health features, designed to support older adults' independent living. The platform, developed within the European project HEREiAM, aims to overcome the digital divide problem by exploiting the TV as interaction mean and paradigm, since previous studies [3] demonstrated this is the most familiar technological instruments for the elderly. Preliminary results of usability tests conducted both with elderly users and general practitioners are presented.

II. Materials and Methods

A. HEREiAM global architecture

HEREiAM provides several independent living services, such as remote-care services (tele-health), participation services (video-call and social apps), shopping services (shopping app), some support services (agenda and message apps) and a security service (activities detection app). To provide them, the system architecture is organized in three levels:

- the platform level (the server side of the system) managing the HEREiAM registered users
- the third party level
- the home level, including all the hardware and software present in the users' homes.

1) Platform level

In order to support tele-health along with other less critic services, the platform level includes features enabling the secure exchange of medical data with a remote server, according to the current regulations. It follows a Service Oriented Architecture (SOA) and a documental approach, i.e. it is based on the production, exchange and sharing of documents. It is an innovative evolution of the commercial product X1.V1 (Dedalus S.p.A.). Natively implemented in compliance with the Integrating Healthcare Enterprise (IHE) standards, it conforms to several standards [4]. To enable sharing measurements with other systems (such as Electronic Health Record ones), the medical data and all the other data exchanged through the platform comply with an XML schema derived from the Clinical Document Architecture (CDA), an HL7 draft standard for trial use document format.

2) Third party level

The third party level includes external service providers, caregivers or relatives of the users that, through a web portal developed for them, will have access to some data and will be able to communicate with the users at home. In order to facilitate third parties to join the platform and offer their services, being able to customize the system to the different regional uses and needs, we decided to exploit Android as operating system at home level, developing the services as Apps. Taking into account the target of users and the user interaction paradigm, third parties can offer services only if their (approved) App follows precise guidelines developed in the framework of the project. This ensures that appearance, user interaction paradigm, symbols, colours, fonts, etc. all respect precise usability criteria.

3) The home level

All the services are developed as Android Apps and the elderly are able to use them through a TV and remote control. The core of the system is an Android TV-box connected to the Internet, and to the TV via the HDMI port (Fig. 2). It can be controlled through a custom remote control developed exploiting the experience gained in several usability tests carried out during the project. Additionally, a webcam enables video-call functionalities whereas Bluetooth support and a ZigBee dongle provide wireless connectivity to medical devices and home sensors. User authentication is provided by a personal smart card.

B. The health telemonitoring service

This service exploits an asynchronous store-and-forward paradigm. The platform level provides secure transmission and storing of data. At third party level, a general

practitioner's web front-end (hereafter called Health Portal) provides access to the medical data, in a simple and secure way, for monitoring purposes. From this service's viewpoint, the home level represents a front-end for the medical devices in charge of performing the vital signs acquisition.

From the Health App (Fig. 3), the users can select the medical device (sphygmomanometer, weight scale and glucometer). The data is sent from the medical device to the app, which displays it and, after the user approval, formats it as an XML document to be sent through a secure connection.

Bluetooth allows wireless connection of the medical devices to the system. To enable the use of different medical devices, HEREiAM supports both Serial Port Profile (SPP, still featured by several medical devices) and the newest Health Device profile (HDP). The former requires to know the low-level proprietary protocol details to interpret the acquired data whereas the latter not, being it part of the standard. Details on this aspect can be found in [4].

Finally, the Health Portal is a web interface, designed to be simple and intuitive, with only the important information highlighted. After the login, general practitioners or caregivers can view the list of their patients, select one of them, select the type of measurement and the time range. A line chart (

Fig. *4*) allows analysing the trends of records over time, whereas a table contains the details of each point. A messaging service allows sending feedback to the patient, who will be notified through the Message App included in HEREiAM.

C. Platform evaluation

To perform a preliminary validation of the telehealth framework, some usability tests have been carried out.

For the usability tests with the elderly, 28 older adults (14M and 14F, aged 79±6) were recruited in a general practitioner facility. Three of them had a primary school certificate, 22 had a high school diploma and the remaining 3 had a university degree. The test consisted in a brief presentation of the system by the experimenter, and a set of tasks to be performed with the app and the medical devices. No sensible data has been gathered during the tests. After trying the application, all participants filled in two usability questionnaires, the System Usability Scale (SUS) [5] and the Post-Study System Usability Questionnaire (PSSUQ) [6].

For the evaluation of the Health Portal usability, seven general practitioners (3M and 4F, aged 41±13), selected by convenience sampling, were asked to autonomously use the website, populated with real data taken from one of the researchers. Then, they were asked to fill in the Website Quality (WQ) [7] and the WebQual 2.0 questionnaire [8].

III. Results

All the results are encouraging. The elderly rated the system 85.8±13, over 100, with the SUS, whereas the four different results generated by the PSSUQ questionnaire are shown in

Fig. *5* (the lower, the better). Notably, the system usefulness marked the lowest score, since the interviewed elderly where not chronic patients requiring daily monitoring of such parameters.

The general practitioners' evaluations are reported in Table I and II. All four aspects evaluated by the WQ questionnaire marked a high score (maximum is 7). The specific content scored the lowest result, since the Health Portal is very simple and essential and it does not include many contents, except the required ones.

The three aspects evaluated in the WebQual 2.0 marked a high score, as the overall satisfaction. The results are very similar to those obtained with the WQ questionnaire, as expected.

TABLE I
WEBSITE QUALITY RESULTS

	Mean	*Stdv*
Technical adequacy	6.063	0.312
Content quality	6.167	0.167
Specific content	5.762	0.218
Appearance	6.086	0.167

TABLE II
WEBQUAL 2.0 RESULTS

	Mean	*Stdv*
Usability	6.063	0.312
Information quality	6.167	0.167
Service interaction	5.762	0.218
Overall	6.086	0.167

IV. Conclusion

In this paper, the architecture of a novel ICT system, based on the TV, for independent living and remote health monitoring has been presented. The system aims at providing different kind of services to support elderly daily activities, including a vital signs Telemonitoring one. Results obtained from preliminary usability tests performed on the telemonitoring framework were encouraging. In the next months, three field trials will take place, in Italy, the Netherlands and Belgium, where 75 users will test the system with all its services and data gathered will help evaluate the real usability of the platform.

Acknowledgement

This work is part of a project financed by the AAL Programme (Ref. AAL-2012-5-064). The authors would like to thank all the partners involved in the project for their contribution.

References

[1] World Health Organization, Global Health Expenditure Database. Available: http://apps.who.int/nha/database

[2] B. Reginatto, "Understanding barriers to wider telehealth adoption in the home environment of older people: An exploratory study in the irish context", *International Journal on Advances in Life Sciences*, vol. 4(3-4), pp. 63-76, 2012.

[3] S. Macis et al., "Towards an integrated TV-based system for active ageing and tele-care", *Atti Quarto Congresso Nazionale di Bioingegneria (GNB 2014)*, Pavia, 2014.

[4] S. Macis et al., "Home Telemonitoring of Vital Signs Through a TV-based Application for Elderly Patients", *IEEE International Symposium on Medical Measurements and Applications (MeMeA),* Turin, 2015.

[5] J. Brooks, "A quick and dirty usability scale", 1996.

[6] J.R. Lewis, “IBM computer usability satisfaction questionnaires: psychometric evaluation and instructions for use”, *International Journal of Human-Computer Interaction*, vol. 7(1), pp. 57–58, 1995.
[7] A.M. Aladwani and P.C. Palvia, “Developing and Validating an instrument for measuring user-perceived web quality”, *Information & Management*, vol. 39(6), pp. 467–476, 2002.
[8] S.J. Barnes and R. Vidgen, “An integrative approach to the assessment of e-commerce quality”, Journal of Electronic Commerce Research, vol. 3, pp. 114–127, 2002.

Fig. 1. Overview of the main user interface and remote control

Fig. 2. Home level hardware

Fig. 3. Health App main screen

Reading Time	Systolic [mmHg]	Diastolic [mmHg]	Pulse rate [bpm]
01/06/15 10:44	99	78	80
03/06/15 10:51	104	80	71
05/06/15 11:18	104	72	67
06/06/15 11:35	107	81	64
06/06/15 11:39	114	84	66
07/06/15 16:25	123	98	76
10/06/15 16:41	146	99	79
12/06/15 16:52	104	78	71
18/06/15 17:33	118	89	83

Fig. 4. The Health portal data visualization interface

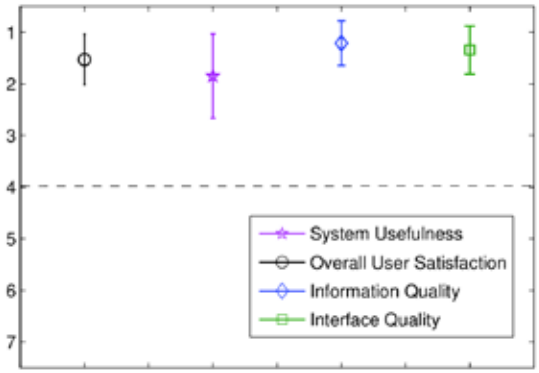

Fig. 5. PSSUQ scores

ABSTRACT
ESB

Numerical comparison of fatigue criteria for NiTi cardiovascular devices

D. Allegretti[1], L. Petrini[2], W. Wu[1], F. Miliavacca[1] and G. Pennati[1]
[1] *Laboratory of Biological Structure Mechanics, Dept. CMIC 'Giulio Natta', Politecnico di Milano, Italy*
[2] *Department of Civil and Environmental Engineering, Politecnico di Milano, Italy*

***Abstract*—NiTi devices are widely used in biomedical fields due to the material flexibility and ability to recovery high strains. However the fatigue behaviour of these devices is still undermined by failure. The particular biomechanical operating environment is characterized by multi-axial cyclic loading transferred to the implanted device. The computational finite elements analysis is a power tool to investigate the state of load imposed from point to point in the devices, but the numerical results have to be correctly analyzed. In this work the fatigue performance of different geometries have been numerically studied and analyzed with different fatigue criteria. The comparison of the results allowed to highlight similarities and differences of the studied approaches and to get some hints for the selection of the most suitable criteria for NiTi cardiovascular devices.**

***Keywords*— Nitinol, stent, peripheral, fatigue.**

I. Introduction

Nickel-Titanium alloys (NiTi) are widely used in biomedical fields. In particular, several cardiovascular minimally-invasive devices exploit NiTi pseudo-elastic behavior. Notwithstanding the high performance of NiTi peripheral stents or cardiovascular valves, due to the material flexibility and ability of recovery high strains, the fatigue behavior is still an open issue[1]. Stents and valve implantation foresees a first step of device crimping, then a partial recovery of the original shape during self-expansion in the site to be treated and finally cyclic loading due to leg or heart movements that may induce multi-axial solicitations [2]. During these three phases, the material response greatly varies from point to point due to the complex geometry of the devices [3]. Accordingly, the material is subjected to elastic cycles in austenitic phase in some zones, while it is partially transformed in martensite in other zones where it may cycle elastically from the lower plateau to the upper one or vice versa. Finally plasticization of martensitic phase may be reached in other areas. Considering also that the interaction of mean and alternate strains on the NiTi fatigue life does not follow the Goodman relation and it is strongly dependent from the specimen production process, it is clear that the prediction of cardiovascular device fatigue resistance is not an easy task. In this work, we numerically analyzed the fatigue performance of two geometries under multiaxial loads using different fatigue criteria.

II. Materials and Methods

Physiological loads acting on NiTi stents may induce axial, bending and torsional cyclic solicitations. Accordingly, fatigue analysis requires criteria able to take into account multiaxial load conditions. In order to compare failure prediction of few multiaxial criteria proposed in the literature, two different geometries and different loading conditions were considered by finite element analyses. A V-shape geometry, resembling the basic element constituting a stent, was used to have a quick and useful view on the performance of the different criteria. Moreover, a stent geometries composed by 6 rings, reproducing a commercial stent (Maris Plus), was analysed to capture in more detail the influence of the complexity of the device geometry on the fatigue behaviour. Maximum and minimum displacement (L) and angle (A) were applied to get the load ratio R = $L_{min}/L_{max}=A_{min}/A_{max}$ equal to 0, -1 and >0 (Fig.1). The corresponding alterante and mean component $\Delta L/A_a = \frac{L/A_{max}-L/A_{min}}{2}; \Delta L/A_m = \frac{L/A_{max}+L/A_{min}}{2}$ considered are reported in Table 1 for the two geometries.

TABLE I
Loading applied in the analysis

	mm | Degree	*V-Shape*	*Stent*
R=0	ΔL_m	10	15
	ΔL_a	10	15
	ΔA_m	/	30°
	ΔA_a	/	30°
R=-1	ΔL_m	0	0
	ΔL_a	15	2,5
	ΔA_m	/	0°
	ΔA_a	/	15°
R>0	ΔL_m	17.5	25
	ΔL_a	2.5	5
	ΔA_m	/	45°
	ΔA_a	/	15°

Different loading conditions imposed in the analysis. The displacement [ΔL] is given in mm, the angle [ΔA] in degree.

In this work 5 different fatigue criteria have been compared: Coffin-Manson (Δε1), Tresca strain (Tresca), Smith-Watson-Trooper (SWT), Brown Miller (BM), Fatemi-Socie (FS).

For each analysis, the results obtained through the different criteria have been compared in terms of the location of the critical nodes in the geometry and the critical nodes damage parameter values.

III. Results

A. V-shape geometry

The results of the different analyses performed on the V-shape geometry indicate that the most critical zone is the peak of the V. The difference between criteria results is in the position of the most critical nodes of the inner zone of the

peak. An example of the results for the load ratio R>0 are reported in figure 2. For each criterion the 5 most critical nodes have been considered: they are reported in Table 2 by the node number and distinguishing the location with respect to the geometry by colour, point positioned at the left of the peak are in black, at the center are in green and the right side are in red.

TABLE II
V-Shape – R>0

Tresca	*BM*	*FS*	*SWT*	Δε1
23093	*23202*	*24510*	24619	23202
24728	*24619*	*24401*	24510	24619
23202	*23093*	*24506*	24401	23093
24619	*24728*	*24619*	24728	24728
22984	*23311*	*24292*	24292	23311

Most critical nodes for each fatigue criteria used in the analysis of the V-shape geometry.

B. Stent geometry

The results of the different analysis performed on the stent geometry have been studied with the 5 different fatigue criteria. An example of the results for the load ratio R>0 are reported in the table 3 and in figure 3. The critical nodes are grouped in five main critical zones. For each criterion the 5 most critical nodes have been considered (Fig.3): they are reported in Table 3 by the node number and distinguishing the critical zones with respect to the geometry by colour.

TABLE II
Stent – R>0

Tresca	*BM*	*FS*	*SWT*	Δε1
111171	*113547*	*111171*	112359	113547
111172	*111172*	*111163*	112360	111172
111163	*113548*	*111172*	112351	113548
107275	*111171*	*111164*	107275	111171
107276	*113539*	*111170*	112362	113539

Most critical nodes for each fatigue criteria used in the analysis of the stent geometry.

IV. Conclusion

The comparison of the results allowed to highlight similarities and differences of the studied approaches and to get some hints for the selection of the most suitable criteria for NiTi cardiovascular devices. Finally, the influence of plasticity on the fatigue response was numerically investigated.

These analyses represent a preliminary study and a future development is the comparison of the presented results with planned ad-hoc experimental fatigue tests to validate the predictions.

References

[1] Scheinert, D., S. Scheinert, J. Sax, C. Piorkowski, S. Braunlich, M. Ulrich, G. Biamino and A. Schmidt. Prevalence and clinical impact of stent fractures after femoropopliteal stenting. J. Am. Coll. Cardiol. 45(2):312-315, 2005.

[2] Ansari, F., L. Pack, S. Brooks and T. Morrison. Design considerations for studies of the biomechanical environment of the femoropopliteal arteries. J. Vasc. Surg. 58:804-813, 2013.

[3] Meoli, A., E. Dordoni, L. Petrini, F. Migliavacca, G. Dubini and G. Pennati. Computational study of axial fatigue for peripheral Nitinol stens. J. Mater. Eng. Perform. 23:2606-2613, 2014.

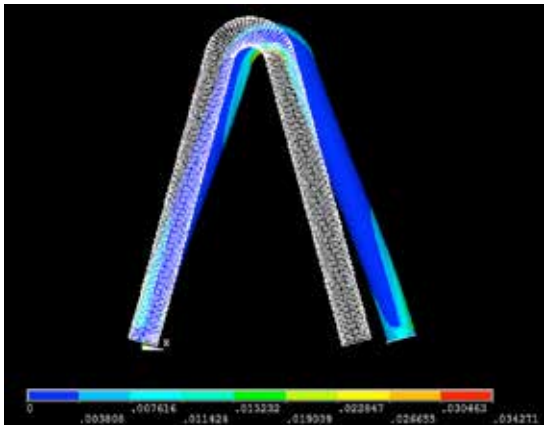

Fig. 1. Example of displacement applied to the V-shape geometry. The deformed (colour map image) and the underformed shapes (dashed image) are reported.

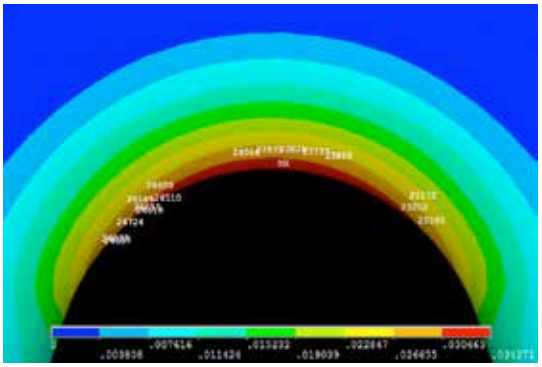

Fig. 2. Results of the V-shape geometry for the load ratio R>0. The inner zone of the peak are highlighted. The most critical nodes resulted by the analysis done with the different fatigue criteria are reported.

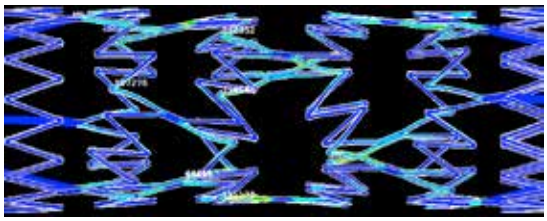

Fig. 3. Results of the stent geometry for the load ratio R>0. The most critical nodes resulted with the different fatigue criteria are highlighted.

Comparison of mechanical properties of neat, decellularized and coated thacheal tissues

S. Montesanto, O. Fici, M. Cammarata, V. Brucato, V. La Carrubba, G. Baratta, and M. Zingales
[1] *Department of Civil, Environmental, Aerospace, Materials Engineering (DICAM)- University of Palermo, Viale delle Scienze Ed. 8, 90128 Palermo, Italy*

***Abstract*— Tracheal tissue is a complex multi-layer structure. Accurate information on its mechanical properties are essential for a reliable prediction of tracheal deformation, which has a significant clinic relevance. The use of a decellularized trachea does not ensure stable mechanical properties of the construct. A coating process with a porous synthetic membrane based on PLLA allowed a precise control of the mechanical proprieties.**

***Keywords*—Decellularization, mechanical proprieties, hybrid tissues, tracheal tissue.**

I. Introduction

Decellularized tissues and organs have been successfully used in a variety of tissue engineering/regenerative medicine applications, and the decellularization methods used vary as widely as the tissues and organs of interest [1]. The efficiency of cell removal from a tissue is dependent on the origin of the tissue and the specific physical, chemical, and enzymatic methods that are used. Each of these treatments affect the biochemical composition, tissue ultrastructure, and mechanical behaviour of the remaining extracellular matrix (ECM) scaffold, which in turn, affect the host response to the material [2]. Tracheal tissue is a multi-layer structure composed of cartilage, trachealis muscle, mucosa, submucosa membrane and adventitial membrane. An accurate knowledge of its mechanical properties is essential for a reliable prediction of tracheal deformation, which has a significant clinic relevance [3, 4].

The use of a decellularized trachea (natural scaffold), as a matter of fact, dose not ensure stable mechanical properties of the construct, does not guarantee a reproducibility of the internal and external structure and, eventually, does not allow a precise control of its biodegradation kinetics.

In this work, a coating process with a porous synthetic membrane via a combination of Dip-coating and Diffusion Induced Phase Separation (DIPS) was designed and carried out. Experimental results show that coating with the synthetic material helps to recover the mechanical properties lost, owing to decellularization of porcine trachea rings [5].

II. Materials and Methods

The porcine trachea used in this study were supplied from Villabate slaughterhouse.

A. Decellularization methods

Sodium Dodecyl Sulfate (SDS) was used as detergent for the decellularization. The porcine trachea was soaked into SDS bath for 24 h at room temperature. THereafter, the sample was maintained in a box containing PBS 1X at 4°C until it was analysed.

B. Tracheal tissue coating

Dip coating consists in the immersion of a biological tissue in a PLLA-dioxane viscous solution (with 8% wt/wt of dioxane) with subsequent extraction at a controlled constant rate. Via this technique it is possible to control the thickness of the coating layer by varying tissue extraction rate, solution temperature and polymer concentration (see fig. 1).

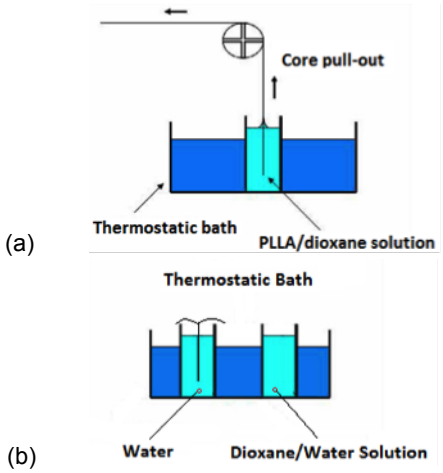

Fig. 1. Schematic of the Dip-coating (a) and DIPS (b) processes.

The subsequent pool immersion of the tissue, covered by a continuous layer of a viscous polymer solution, into a coagulation bath, represents the Diffusion Induced Phase Separation (DIPS) step.

The bath contains pure water. Via DIPS, the simultaneous solvent (dioxane) diffusion out of the polymeric film and counterdiffusion of the nonsolvent (water) from the coagulation bath towards the polymeric film will induce the phase separation process. Fig. 1 reports a schematic of the two processes. In this study, extraction rate, polymer solution concentration and process temperature were taken constant in all experiments: the extraction velocity was set to 3cm/min, the polymer solution concentration to 8 wt% PLLA and the temperature to 30 °C [6].

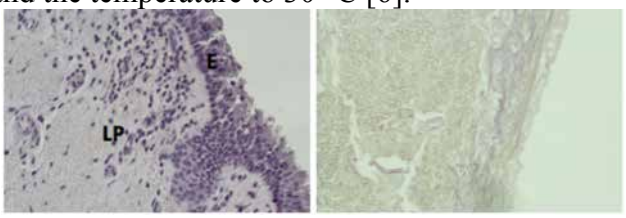

Fig. 2. Comparison between a native tissue (right side) and a decellularized tissue (lef side).

C. Mechanical characterization

Tensile tests were performed to investigate the mechanical behaviour of trachea rings obtained using porcine tracheas. A force speed of 0.1 g/s was set, while the temperature was taken constant at the value of 30°C. Bose biaxial instrument was utilized in uniaxial mode to determine the stress/strain behaviour.

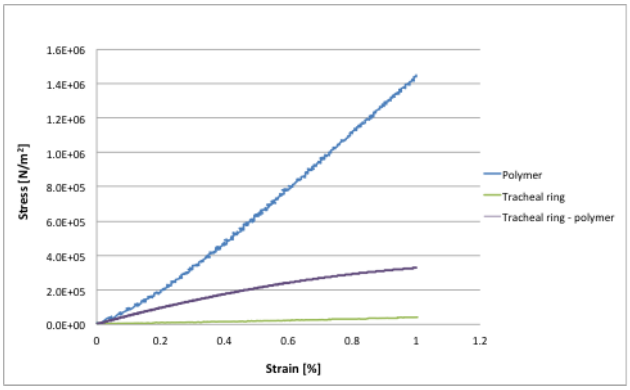

Fig. 3. Comparison of tensile mechanical properties of polymer, hybrid tissue and tracheal ring.

III. Results and Discussion

A. Tissue decellularizzation

SDS is very effective in removal of cellular components from tissue (see figure 2). On the other hand, however, it tends to disrupt the native tissue structure, and it causes a partial loss of tissue integrity. However, it does not appear that SDS severely removes collagen and/or cartilage from the tissue.

B. Tensile behaviour

By coupling dip coating and DIPS it is possible to produce a 3D biohybrid synthetic/natural scaffold able to guarantee enhancement of the mechanical properties lost during decellularization of the native tissue.

Mechanical tensile tests on the native trachea, ofn the neat polymeric film and on the bioengineered (hybrid) tissue are reported in fig. 3, to show the recovery of the mechanical properties attained via coating with PLLA. The improvement of the mechanical performance is evident up to strains as high as 1%, comparable with the physiological deformations of the examined tissue.

IV. Conclusions

A biohybrid material has been prepared via coating of a decellularization tracheal tissue with a PLLA membrane. Mechanical preliminary tests show that the biohybrid material exhibit performances similar to those of native tracheal tissue, thus allowing one to recover the property loss due to the decellurarization protocol.

Acknowledgement

This study has been supported by the Italian Ministry of University and Research (PRIN 2010–2011 - prot. 20109PLMH2_008). The experimental facility at the BNM2- LAB of the CHAB Center of Palermo University is gratefully appreciated.

References

[1] T.W. Gilbert, T.L. Sellaro, S.F. Badylak, “Decellularization of tissues and organs,” *Biomaterials*, vol.27, pp.3675-3683, 2006.

[2] R.W. Grauss, M.G. Hazekamp, F. Oppenhuizen, C.J. van Munsteren, A.C. Gittenbergerde Groot, M.C. DeRuiter, “Histological evaluation of decellularised porcine aortic valves: matrix changes due to different decellularisation methods”, *Eur J Cardiothorac Surg*, vol. 27, pp. 566-571, 2005.

[3] R.B. Hirschi, R. Tooley, A. Parent, K. Johnson, R.H. Bartlett, “Evaluation of gas exchange, pulmonary compliance, and lung injury during total and partial liquid ventilation in the acute respiratory distress syndrome”, *Crit. Care Med*., vol. 24 pp. 1001-1008, 1996.

[4] O. Trabelsi, A.P. del Palomar, J.L. Lopez-Villalobos, A. Ginel, M. Doblare, “Experimental characterization and constitutive modeling of the mechanical behavior of the human trachea”, *Medical Engineering and Physics*, vol. 32 pp.76–82, 2010.

[5] Patent Application No. 102016000033555 filed 01/04/2016

[6] S. Montesanto, G.A. Mannella, F. Carfì Pavia, V. La Carrubba, V. Brucato, “Coagulation bath composition and desiccation environments tuning parameters to prepare skinless membranes via diffusion induced phase separation,“ *J. Appl. Polym. Sci.,* vol. 132, 2015.

Multiscale computational modeling of aortic mechanics via a patient-specific strategy

D. Bianchi[1], M. Marino[2], and G. Vairo[1]
[1] University of Rome "Tor Vergata"- Department of Civil Engineering & Computer Science (DICII), Via del Politecnico 1, 00133 Rome - Italy, e-mail: d.bianchi@ing.uniroma2.it, vairo@ing.uniroma2.it ;
[2] Leibniz Universität Hannover - Institut für Kontinuumsmechanik, Appelstr. 11, 30167 Hannover - Germany, e-mail: marino@ikm.uni-hannover.de

***Abstract*—A novel computational approach for analysing the mechanical response of aortic segments accounting for patient-specific data is proposed. A parametric tool, suitable for parametric biomechanical analyses, is developed by integrating: (i) segmentation techniques to define the geometry from aortic patient-specific CT images; (ii) multiscale homogenization techniques to describe the non-linear mechanics of biological tissues, as depending on micro- and nano-structural parameters obtained from histological and biochemical data; (iii) a non-linear finite-element formulation of the equilibrium problem. The proposed model has been applied for reproducing an inflation test on aortic segments. Moreover, the influence on aortic macroscale response of a localized defect affecting the crimp of collagen fibers is analyzed, proving that the adopted multiscale structural approach is able to investigate the etiology of cardiovascular diseases and physio-pathological remodelling mechanisms.**

***Keywords*—Aortic mechanics, patient-specific computational models, Multiscale tissue modelling, Non-linear finite element formulation, Cardiovascular diseases.**

I. Introduction

Cardiovascular diseases (CVDs) are the leading cause of death worldwide but their etiology is debated and the therapeutic approaches are still based on the definition of risk parameters mainly evaluated on the own experience of clinicians. In this framework, computational models have recently provided novel insights into aortic biomechanics, in both health and disease scenario [1],[2]. Although several reliable methods exist for reconstructing the geometry of computational domains from patient-based CT (computed tomography) images, a key aspect for accurate analyses is represented by the constitutive description of the tissue, characterized by anisotropic and non-linear mechanical response. Many constitutive formulations are available in literature [3],[4], but they generally have weak relation with histological/biochemical parameters. On the other hand, a multiscale structurally-motivated approach for tissue constitutive description has been recently proposed by some of the authors and has been proved, referring to simple study cases only, to be effective to reproduce tissue behaviour, by introducing parameters that straight describe histological and biochemical properties [5]-[9]. In order to allow the use of this refined constitutive description, that has never been employed in numerical simulations reproducing complex patient-specific geometries, a fully-personalized clinical application integrating a computational strategy for non-linear finite-element (FE) analyses of aortic segments is herein presented. In detail, patient-specific geometrical modeling is coupled with the aforementioned multiscale structural constitutive formulation, resulting in an overall 3D macroscale description explicitly depending on dominant micro- and nano-scale personalized features. The preliminary case study of a thoracic aortic segment undergoing an inflation test is numerically addressed, comparing different constitutive strategies and proving the capability of the proposed integrated computational approach to analyze the influence of possible localized tissue defects on aortic biomechanics.

II. Materials and Methods

A general methodology for developing 3D-FE models of blood vessels incorporating patient-specific geometry from computer tomography (CT) images and histological, biochemical and biophysical data is herein described. The corresponding schematic is represented in Fig. 1.

A. Constitutive description

In the framework of a multiscale strategy and referring to the tunica media only, the multi-layered histologic structure of the aortic tissue, constituted by the occurrence of media lamellar units (MLUs), is modelled as a layered structure comprising N perfectly-bonded layers characterized by the same thickness. Each MLU is composed by an elastin layer (EL) of thickness h_{EL} and an interlamellar substance (IL) of thickness h_{IL}. In turn, the interlamellar substance has a multi-layered sub-structure made up of concentrically fiber-reinforced sub-layers, comprising elastin, muscle cells, and crimped collagenous fibers whose main direction is helically arranged around the vessel axis. The orientation of collagen fibers with respect to the vessel axis is described by the wrapping angle ϑ_F, varying along the vessel thickness. Each IL sub-layer is here modelled as a composite material made up of crimped collagen fibers, taken aligned in the same direction, embedded in a linearly elastic isotropic matrix, describing both the elastin network and the muscle cells, having comparable stiffness [10]. Collagen fibres in soft tissues are bundles of densely packed tilted fibrils, laterally linked by means of proteoglycans. In turn, collagen fibrils are made up of staggered arrays of tropocollagen molecules, mutually interconnected by intermolecular covalent cross-links. Both micro-scale and nano-scale features of collagen fibers are accounted for, via a multiscale homogenization process [5]-[9].

B. Vessel geometry

The reference vessel configuration Γ_o is reconstructed from 3D contrast-enhanced CT images (Fig. 1). Such images

describe, with a sub-millimetric resolution, the anatomy of blood vessels through 3D arrays of grayscale intensities, and they contain body projection over coronal, sagittal and axial planes. By employing a region- based model which involves the Geodesic Active Contours algorithm [11], an image segmentation process is applied, providing a description of the aortic geometry via a surface mesh. Segmentation errors, due to possible coarse resolution of medical devices and/or involuntary patient movements, are reduced by applying a Taubin smoothing algorithm [12]. Finally, curves resulting from the intersection of the smoothed surface mesh with a family of planes orthogonal to the mean vessel axis are employed for generating the loft surface Γ_o used for FE simulations.

C. Numerical model

The surface of the aortic segment, resulting from the geometric reconstruction, is treated as a Mindlin-Reissner shell. In order to avoid locking phenomena related with both shell formulation and tissue incompressibility, a mixed displacement-pressure finite-element formulation is employed, by considering a MITC shell element [13]. In detail, shell surface is discretized by means of iso-parametric 6-nodes 2D-triangular elements with quadratic (resp., linear) shape functions for displacements and rotations (resp., for pressure). In agreement with a computational homogenization strategy, a material map is computed on the basis of the homogenization procedure previously recalled. By employing an updated-Lagrangian strategy, both geometric and material non-linearities are treated via an incremental approach, by solving a series of incremental linearly-elastic sub-problems, and thereby allowing for a step-by-step updating of: (i) geometry; (ii) reference coordinate system; (iii) material properties. Figure 2 gives a schematic representation of the implemented solution algorithm.

III. Results

As a case study, a thoracic aortic segment subjected to an inflation test up to 180 mmHg is numerically addressed. Numerical results are obtained by adopting the above introduced multiscale homogenization procedure and by describing histochemical properties as referred to a homogeneous distribution into the aortic domain (homogeneous non-linear model, HNM) and to a localized defect (defect non-linear model, DNM). In the latter case, values of model parameters coincide with the HNM's ones with the exception of an higher initial collagen fiber amplitude in a region located below the middle section of the aortic segment (Fig. 1). Figure 3 shows that the localized defect of collagen fiber crimp in the DNM case induces significant differences in the macroscopic strain field of the overall aortic domain with respect to the HNM case.

IV. Conclusions

The mechanical response of aortic segments has been addressed by proposing a novel integrated computational approach able to describe, in a general patient-specific framework, both aortic geometry and material properties. A geometric reconstruction procedure from 3D computer-tomography images has been coupled with a multiscale non-linear constitutive description, accounting for highly-personalized histological and biochemical features. In detail, a multi-step homogenization approach based on a bottom-up strategy (from the nano-up to the macroscale) has been employed for describing the non-linear and anisotropic response of aortic tissues. Dominant nano- and micro scale mechanisms have been consistently up-scaled following a structurally-motivated multiscale strategy, which allows to couple in a non-phenomenological scheme the tissue macroscale mechanics with both histological subscale arrangement and biochemical environment.

Acknowledgement

Present research study was partially supported by Italian Minister of University and Research, MIUR (PRIN, Grant number F11J12000210001). M. Marino gratefully acknowledges a post-doctoral fellowship from the Alexander von Humboldt Foundation.

References

[1] F. Auricchio, M. Conti, S. Morganti, A. Reali, 2013, Patient-specific finite element analysis of carotid artery stenting: a focus on vessel modeling. *Int. J. Numer. Methods Biomed. Eng.* 29, p.p. 645–664

[2] D.Roy, G. Holzapfel, C. Kauffmann, G. Soulez, 2014, Finite element analysis of abdominal aortic aneurysms: geometrical and structural reconstruction with application of an anisotropic material model. *IMA J. Appl. Math*. 79, p.p. 1011–1026.

[3] G. Holzapfel, T. Gasser, R. Ogden, 2000, A new constitutive framework for arterial wall mechanics and a comparative study of material models. *J. Elast.*, 61, p.p. 1–48.

[4] F. Auricchio, A. Ferrara, S. Morganti, 2012, Comparison and critical analysis of invariant-based models with respect to their ability in fitting human aortic valve data. *Ann. Solids Struct. Mech.*, 4, p.p. 1–14.

[5] F. Maceri, M. Marino, and G. Vairo, 2010, A unified multiscale mechanical model for soft collagenous tissues with regular fiber arrangement, *J. Biomech.*, 43 pp. 355-363,.

[6] F. Maceri, M. Marino, and G. Vairo, 2012, Elasto-damage modeling of biopolymer molecules response, *Comput. Model. Eng. Sci.*, 87, pp. 461-481.

[7] F. Maceri, M. Marino, and G. Vairo, 2013, Age-Dependent Arterial Mechanics via a Multiscale Elastic Approach, *Int. J. Comput. Methods Eng. Sci. Mech.*, 14, p.p. 141-151.

[8] M. Marino, and G. Vairo, 2014, Stress and strain localization in stretched collagenous tissues via a multiscale modelling approach, *Comput. Methods Biomech. Biomed. Engin.*, 17, p.p. 11-30.

[9] M. Marino, G., Vairo, 2013,Multiscale elastic models of collagen bio-structures: from cross-linked molecules to soft tissues. A., Gefen (Ed.), *Studies in Mechanobiology, Tissue Engineering and Biomaterials*, vol.14, Springer, Berlin, Germany, p.p. 73–102.

[10] M.A. Zulliger, A. Rachev, N. Stergiopulos, 2004, A constitutive formulation of arterial mechanics including vascular smooth muscle tone, *Am. J. Physiol. Heart Circ. Physiol.*, 287, p.p. 1335-1343.

[11] V. Caselles, F. Catte, T. Colle and F. Dibos, 1993, A geometric model for active contour , *Numer. Math.*, 66, p.p. 1-31.

[12] G. Taubin, 1994,Curve and surface smoothing without shrinkage, Technical Report, RC-19563, IBM-Research.

[13] D. Chapelle and K.J. Bathe, 2003, *The Finite Element Analysis of Shells Fundamentals.* Springer Berlin Heidelberg, (2003).

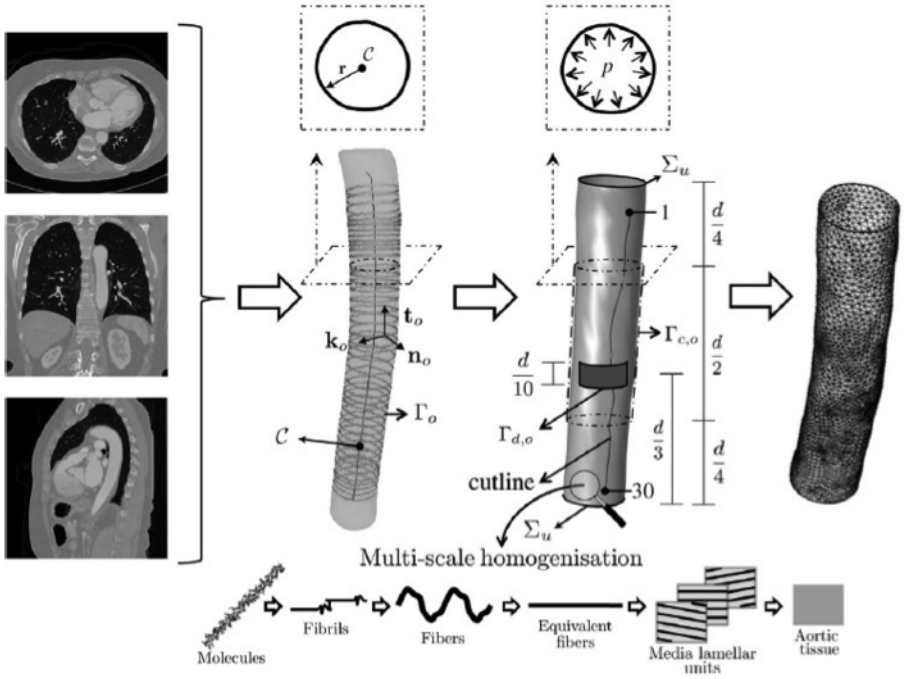

Fig. 1 Patient-specific aortic models. From left to right: CT images; geometric reconstruction; numerical model integrated with a multiscale homogenization approach to describe the tissue mechanical behavior; computational mesh.

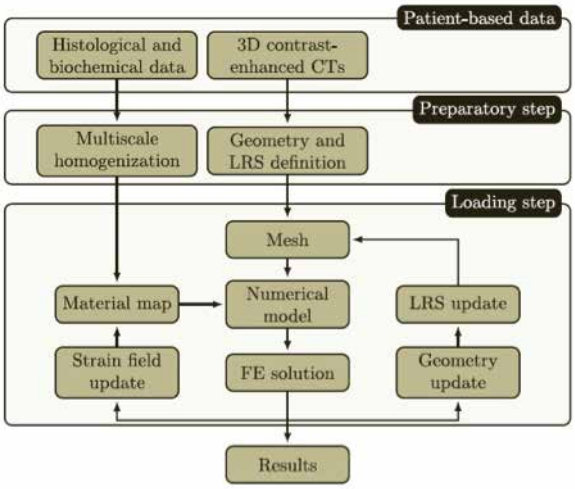

Fig. 2 Flowchart of the implemented solution algorithm. CT: computer tomography; LRS: local reference system; FE: finite element.

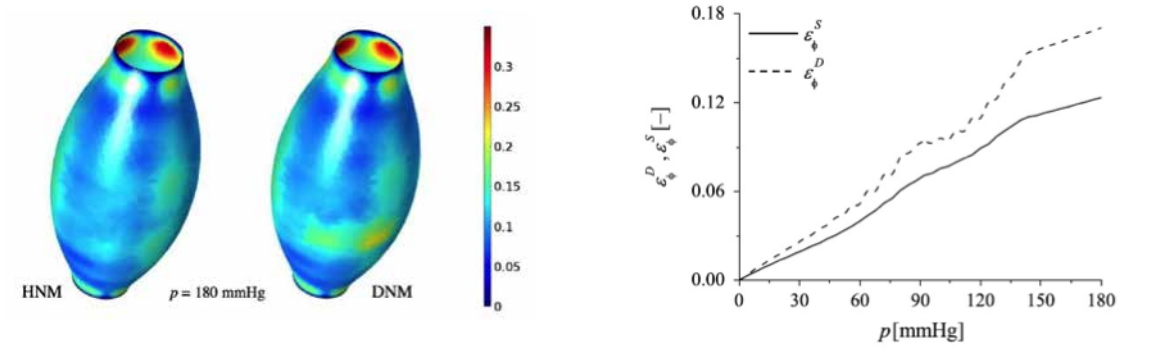

Fig. 3 (left) Distribution of the circumferential strain ε_ϕ at p = 180 [mmHg] in HNM and DNM cases. (right) Average circumferential strain vs. the pressure p in the defect zone $\left(\varepsilon_\phi^D\right)$ and in the surrounding tissue $\left(\varepsilon_\phi^S\right)$ for the DNM case.

Enzymatically Stiffenable Gelatin Hydrogels for Engineering Pathophysiological Organ Models

L. Cacopardo[1], G. Mattei[1] and A. Ahluwalia[1]
[1] *Research Centre 'Enrico Piaggio', University of Pisa (Italy)*

***Abstract*—Developing cell culture substrates that mimic the mechanical properties of the native cellular micro-environment is critical to engineer physiologically relevant in-vitro organ models. Moreover, considering that tissue ageing and fibrotic processes are generally associated with an extracellular matrix (ECM) stiffening, cell culture substrates capable of reproducing this healthy-to-aged/fibrotic transition in-vitro are fundamental for the realization of pathophysiologically relevant organ models. Here, we present transglutaminase-gelatin hydrogels with stiffenable properties as cell culture substrates for engineering tissue ageing or fibrotic models in-vitro.**

***Keywords*—nano-indentation, gelatin, transglutaminase, hydrogels, fibrotic models, in-vitro organ models.**

I. Introduction

The classical tissue engineering approach based on the successful interaction between cell, scaffold and bioreactor, represents an attractive strategy for the development of in-vitro organ models [1]. An ideal scaffold should mimic most of the properties of the native extracellular matrix (ECM) to provide cells with an appropriate microenvironment promoting their growth, differentiation and function. Among the ECM cues, biomechanical properties play a critical role in regulating pathophysiological cell behaviour and directing the development of tissue fibrosis, which is generally associated with an enzyme-mediated ECM hardening [2]. Tissue ageing is also associated with ECM hardening. For example, ageing in the cardiovascular system is characterized by an enhanced collagen and calcium deposition in the ECM and an increased protein cross-linking [3], while fibrosis may be observed in hepatic or pulmonary tissue affected by hepatitis [4] or lung disorders [5], respectively.

Based on the hypothesis that tissue stiffness increases as ageing/fibrosis progresses, dynamic scaffolds that mimic the elasticity of healthy and aged/diseased tissue ECM in-vitro need to be engineered to temporally manipulate their mechanical properties on demand [6].

Gelatin (a commercially available biomaterial derived from collagen) is often used as the organic component of scaffolds because of its biocompatibility [7]. However, due to its rapid degradation in typical cell culture environments (T = 37 °C), gelatin-based scaffolds are often covalently crosslinked using various chemical reagents (e.g. glutaraldehyde, formaldehyde [7]) or enzymes (e.g. transglutaminase [8]) to improve their stability and enhance the mechanical properties. In particular, transglutaminase is a calcium-independent enzyme that catalyses the formation of covalent cross-links between glutamine and lysine residues in proteins. Since it is commonly used in food manufacturing processes approved for human consumption by the U.S. Food and Drug Administration, this enzyme seems to be a promising cross-linking agent with respect to glutaraldehyde and formaldehyde, that may reduce gelatin biocompatibility if not completely washed out prior to cell seeding, and cannot be used in presence of cells.

Here we present the use of microbial transglutaminase (mTG) as a biocompatible second step enzymatic crosslinker for gelatin hydrogels to engineer pathophysiological in-vitro models that can be dynamically stiffened during cell culture from healthy towards aged/fibrotic environments at a user-defined time.

II. Materials and Method

A. Hydrogel Preparation

Since we are interested in characterizing mTG-mediated hardening at 37 °C (physiological temperature), gelatin hydrogels need to be stabilized via pre-crosslinking. Two series of pre-crosslinked mTG-gelatin samples were obtained adding 1 and 10 units of mTG (Activa WM, kindly gifted by Ajinomoto) per gram of gelatin to 5% w/v Type A gelatine solution (G2500, Sigma-Aldrich). The latter was then cast into custom cylindrical moulds (13 mm diameter – 8 mm height) and incubated at 37 °C (Day -1), obtaining 1 and 10 unit/gram (U/g) mTG-gelatin samples, respectively.

After 24h (Day 0), the hydrogels were carefully removed from the moulds and each sample was placed in different wells of a 12-well plate. Here, the hydrogels were submerged in 5 mL of mTG solutions at different concentrations (prepared in 1x phosphate buffered saline, PBS) to exogenously provide 10 and 100 units of mTG per gram of gelatin to crosslink (U/g). Finally, samples were incubated at 37 °C to be stiffened towards aged/fibrotic models. Samples immersed in 1x PBS (i.e. provided with no exogenous mTG or 0 U/g mTG) were used as controls.

B. Mechanical Testing

Nano-indentation tests were performed using a PIUMA Nanoindenter (Optics11) with a 61.5 μm spherical tip. Each hydrogel was glued on a Petri dish using cyanoacrylate (Attack, Loctite) and submerged with deionized water before testing. At least 10 indentations were performed on different surface points of each sample, using a constant strain rate of $\dot{\varepsilon} = 0.05\ s^{-1}$. Hydrogels were tested at day 1 and 7 after incubation in mTG solution. Experimental data were analysed with the nanoepsilon dot method, deriving elastic moduli as the stress-strain slope within 0.10 strain [9].

C. Statistical Analysis

Statistical analyses were performed with GraphPad Prism (Graph Pad Software Inc.). Data obtained for 1 and 10 U/g mTG-gelatin hydrogels were analysed separately with a 2-way ANOVA to investigate the effect of both exogenous mTG concentration and incubation time on the elastic modulus of each group of samples. Multiple comparisons were performed with Sidak test, in order to investigate either the effect of incubation time on resultant E for each exogenous mTG concentration or the effect of mTG concentration at the same time point. Statistical significance was set to $p < 0.05$.

III. Results

Figure 1A shows mTG-gelatin hydrogels removed from the moulds (day 0): 10 U/g hydrogels appear opaque and more stiff with respect to 1 U/g ones that are transparent and soft.

After 24 h of incubation in mTG, the elastic modulus (E) of 1 U/g gels significantly increases with exogenous mTG concentration (Fig. 2). Although higher in controls with no mTG (0 U/g), as expected, at 24 h the modulus of 10 U/g samples immersed in mTG solution is generally lower than that of 1 U/g gels and reaches a plateau at 10 U/g mTG.

The differences measured via nanoindentation are also appreciable in Fig. 1. At day 1 (Fig. 1B), control samples appear softer with respect to day 0 (Fig. 1A), while the other gels tend to shrink and become more opaque with increasing exogenous mTG concentration. On the contrary, differences are less evident in 10 U/g gels, except for the control that seems to be less shrunk and opaque than those exposed to 10 and 100 U/g exogenous mTG.

After 7 days of incubation, the E continues to increase significantly for both 1 and 10 U/g samples immersed in both 10 and 100 U/g mTG solutions with respect to 24 h (Fig. 3A-B), while it decreases in case of controls ($p < 0.05$ only in case of 10 U/g gels), suggesting that hydrolysis prevails over the enzymatic crosslinking.

The interaction between the two factors (i.e. exogenous mTG and incubation time) was significant for both 1 and 10 U/g pre-crosslinked samples, with incubation time effect depending on the level of mTG concentration. In particular, the elastic modulus increases with time only in presence of mTG, while it decreases between day 1 and day 7 in absence of the enzyme (Fig. 3A-B). Moreover, the E increases increasing the exogenous mTG concentration ($p < 0.05$ only in the case of 10 U/g gels at day 7, between 10U/g and 100U/g exogenous concentrations).

IV. Conclusion

Pathophysiological in-vitro models are important to understand the processes underneath aging and several diseases, such as fibrosis. Given the critical role of the biomechanical environment in regulating cell behaviour and directing the development of tissue fibrosis, mTG-gelatin hydrogels were designed to reproduce the typical stiffness of healthy soft tissues and to subsequently be stiffenable via enzymatic activity to recreate aged or fibrotic environments, in an in-vivo like manner.

We demonstrate that mTG can be used as a second step crosslinker to increase the elastic modulus of gelatin substrates, thus reproducing the transition from healthy to aged/fibrotic environments in-vitro. Microbial transglutaminase is an attractive biocompatible agent [8] for altering the mechanical properties of amino-containing scaffolds during cell culture to engineer fibrotic/aged organ models in-vitro.

Thanks to exogenous mTG administration, the elastic modulus of 1 U/g samples can be varied from about 4 to70 kPa. These values cover the range of typical pathophysiological elastic moduli of soft tissues [10].

References

[1] Mattei G., Giusti S., Ahluwalia A., 'Design Criteria for Generating Physiologically Relevant In Vitro Models in Bioreactors'. *Processes* 2:548-69, 2014.

[2] Frantz C., Stewart KM and Weaver VM. 'The extracellular matrix at a glance'. *Journal of Cell Science*, 123:4195-200, 2010.

[3] Wu M., Fannin J., Rice K. M., Wang B. and Blough E. R. 'Effect of aging on cellular mechanotransduction'. *Ageing Research Reviews* 10, 1–15, 2011.

[4] Yeh, W., Li P., Jeng Y., Hsu H., et all. 'Elastic Modulus Measurements of human liver'. *Ultrasound Medicine in Medicine and Biology* 28, 4467–474, 2002.

[5] Booth, A. J., Hadley R., Cornett A., Dreffs A., et al. 'Acellular Normal and Fibrotic Human Lung Matrices as a Culture System for In Vitro Investigation'. *American Journal of Respiratory and Critical Care Medicine* Vol 186, 2012, doi:10.1164/rccm.201204-0754OC.

[6] Guvendiren M. and Burdicj J. 'Stiffening Hydrogels to probe short- and long-term cellular response to dynamic mechanics'. *Nature Communication*, 3:792, 2012.

[7] Mattei G., Ferretti C., Tirella A., Ahluwalia A. and Mattioli-Belmonte M. 'Decoupling the role of stiffness from other hydroxyapatite signalling cues in periosteal derived stem cell differentiation'. *Scientific Reports* 5:10778, 2015.

[8] Broderick E., Halloran D., Rochev Y., Griffin M., Collighan R. and Pandit A. Set al, 'Enzymatic Stabilization of Gelatin-Based Scaffolds' JBMR B, 72:37-42, 2005.

[9] Mattei G, Gruca G., Rijnveld N. Ahluwalia A. 'The nano-epsilon dot method for strain rate viscoelastic characterisation of soft biomaterials by spherical nano-indentation'. *Journal of the Mechanical Behavior of Biomedical Materials*, 50:150-9, 2015.

[10] Wells R. 'Tissue mechanics and fibrosis'. *Biochimica et Biophysica Acta-Molecular Basis of Disease* 1832: 884–890, 2013.

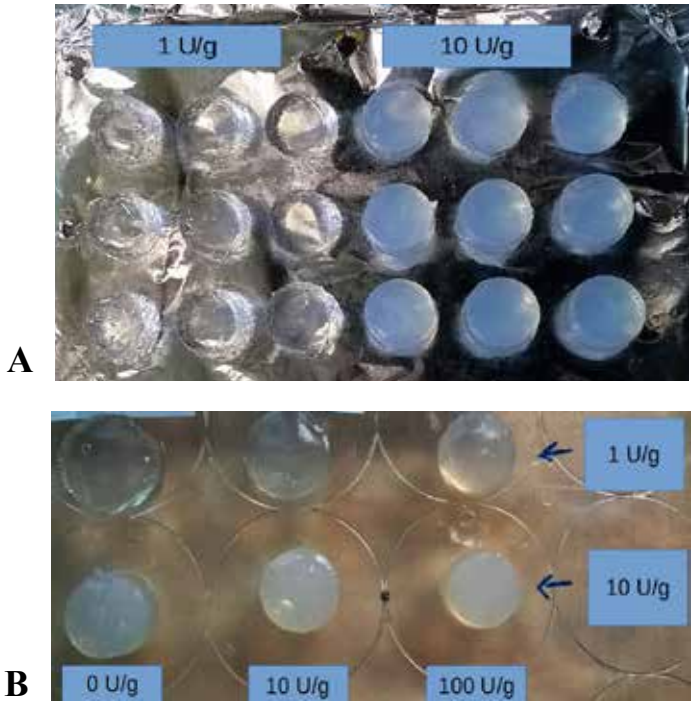

Fig. 1. mTG-gelatin hydrogels: a) day 0 (1 U/g and 10 U/g represent the internal concentrations of mTG); b) day 1 (U/g values on the rows represent mTG internal concentrations, while U/g values on the columns are the exogenous mTG concentrations administered to mTG-gelatin samples).

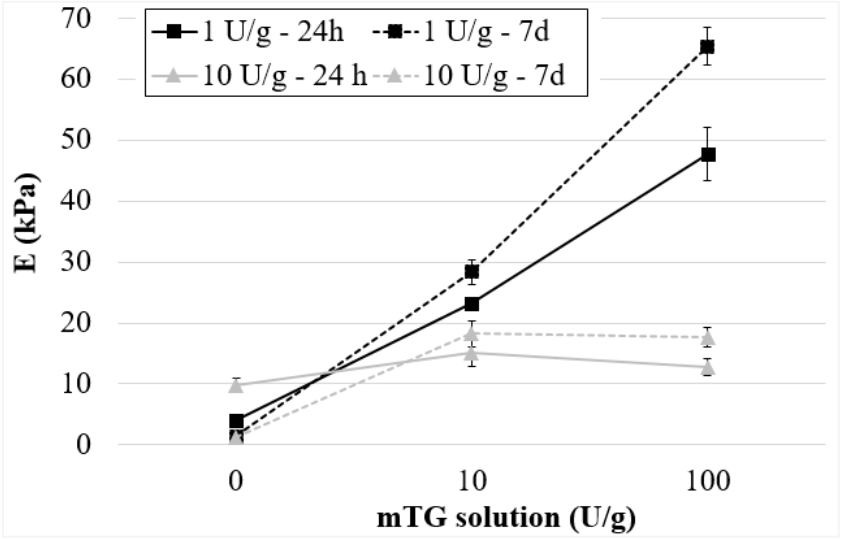

Fig. 2. Elastic moduli of 1 and 10 U/g mTG-gelatin samples immersed in mTG solutions after 1 and 7 days.

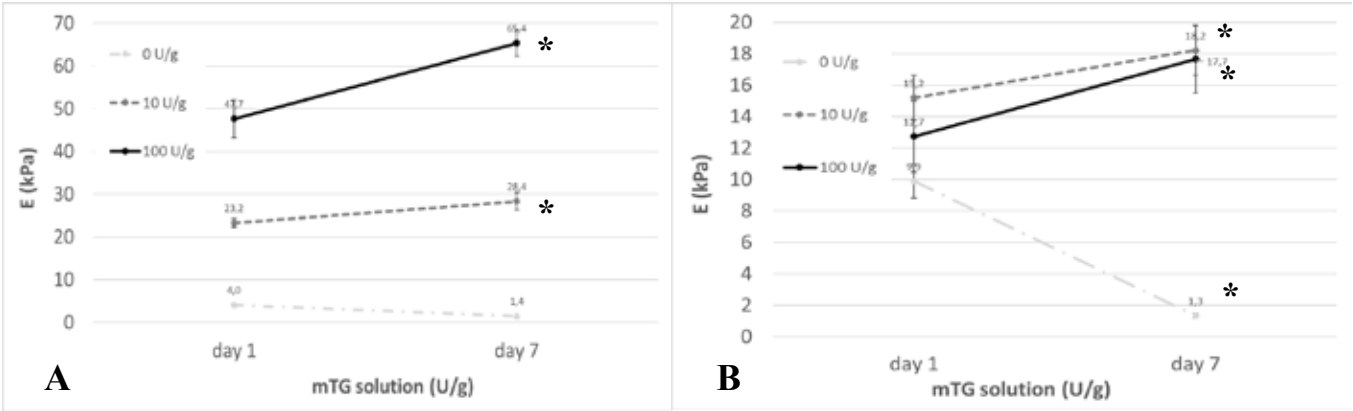

Fig. 3. ANOVA interaction plot of a) 1 U/g and b) 10 U/g mTG-gelatin samples. For each exogenous mTG concentration, significant differences between E at day 1 and 7 are denoted with an asterisk ($p < 0.001$).

Biomechanical evaluation of skin lesions: a combined approach

E. Cutrì[1], F. Crippa[1], G. Franzetti[1], E. Mortin[2], G. Spadola[3], A. Testori[3], L. Mainardi[2], and G. Pennati[1]
[1] *LaBS-Depart. of Chemistry, Materials and Chemical Engineering, 'Giulio Natta', Politecnico di Milano, Milan, Italy.*
[2] *Depart. of Electronics, Information and Bioengineering, Politecnico di Milano, Milan, Italy.*
[3] *Dermatoncological Surgery Division, Istituto Europeo di Oncologia, Milan, Italy.*

***Abstract*—Malignant melanoma is a highly aggressive skin cancer whose rate of mortality dramatically decreases if detected in the initial phases of its development. For this reason, early recognition of melanoma is of upmost importance. Enhancement in the imaging technique such as confocal laser scanning microscopy (CLSM) enabled the obtainment of high-resolution images but up to date, a definitive diagnosis can be achieved only after excisional biopsy and subsequent histological analysis. Literature studies assessed alteration in the mechanical properties of the biological tissue when a pathological condition occur. In this context, we propose a combined approach comprising an experimental analysis and a computational modelling. The latter will be devoted to the obtainment of transverse displacement from CLSM images while the former will be devoted to the development of a multiscale approach to fully characterize the skin and skin lesion. Such a combined approach will allow further understanding on biomechanical changes that occur in presence of skin lesions.**

***Keywords*—skin lesion, multiscale, skin biomechanics**

I. Introduction

MALIGNANT melanoma is a highly aggressive skin tumour whose incidence has dramatically risen in the last decades causing the 75% of skin cancer-related deaths [1]. The 5-years survival rate ranges from 15% if lately detected to 99% if early detected [2]. For these reasons, the early recognition of melanoma is of upmost importance. Currently, the diagnosis is performed using the so-called ABCDE rule, which is based on the visual evaluation of dermatoscopic features (Asymmetry of the lesion, Border irregularity, Color variegation, Diameter dimension and Evolution). Suspicious melanoma undergo to excisional biopsy and subsequent histological analysis. Improvements in diagnostic imaging technique allowed the obtainment of higher resolution with respect to classical dermatoscopy analysis. Confocal laser scanning microscopy (CLSM) is able to provide the visualization of the upper layers of the skin layers with a cellular resolution. Nevertheless, biopsy and histological analyses are mandatory to provide a final diagnosis. In this context, exploring new methodologies to investigate the changes occurring when such a pathological conditions initiate could suggest new clinical pathways. Starting from these considerations, our study aims at evaluating if mechanical alterations that occur when the pathology develops can be used to help the clinical decision. Several literature study in fact assessed a modification of the mechanical properties of biological tissues during the development of the metastasis of cancers such as carcinoma [3], [4] or melanoma [5]-[7].

In this view, a combined approach including an experimental analysis and a computational study is proposed to characterize the mechanical properties of the superficial layers of the skin and skin lesion . In the latter CLSM images of the skin and skin lesions are obtained before and after the application of a mechanical stimulus. The depth-dependent behaviour of the skin layers is investigated by calculating the transverse displacement after the stimulus. The former is aimed at reproducing the experimental condition to identify the different layers material parameters for skin and skin lesions that allow reproducing the transverse displacement experimentally obtained.

II. Material and Methods

To fully characterize the skin and skin lesions, a combined approach is proposed comprising an experimental and a computational analysis. The former is devoted at the evaluation of the response of the skin and skin lesion when a displacement field is applied. The latter is aimed at the assessment of the different mechanical properties of the skin layers and to establish if the skin and skin lesions exhibit a different behaviour.

A. Experimental set up

The experimental set up consisted of a CLSM Vivascope® 1500 (MAVIG VivaScope Systems, Munich, Germany), a tissue ring, an adhesive plastic window, an adhesive tape (Opsite Flexigrid, Smith & Nephew, London, UK) and a (pliers) support. The schematic of the experimental set up is illustrated in figure 1. The CLSM probe is coupled to the tissue ring on which a disposable adhesive plastic window is glued. This plastic window adheres to the skin. In this way, a displacement is applied to the CSLM probe, which in turn transmits it to the skin. In vivo CLSM images were acquired on the dorsal forearm of healthy Caucasian volunteers. Image stacks (500 x 500 μm, depth 152 μm) were acquired in undeformed and deformed (i.e., the CLSM probe is submitted to a displacement of 250 μm along the X direction) configurations (Fig. 1). For both configurations, the stacks were reconstructed and the displacement field was computed through a registration strategy, which estimated the best alignment of the deformed and undeformed images [8]. The depth-dependent displacement was computed to evaluate if different behaviors are evident in the different layers for the skin and skin lesion.

B. Computational model

To obtain the mechanical information of the different skin layers, a multi-scale approach was adopted ranging from macroscale, microscale up to cellular scale. The schematic of the multi-scale approach is illustrated in figure 2.

Starting from CLSM subject specific model of the skin and skin lesions have been created.

1. Tissue macroscale model

The subject specific 3D FE tissue macroscale models were developed using Abaqus 6.13 ® (SIMULIA, Dessault Systèmes, France). Each layer was modelled as an isotropic hyperelastic material using the Neo-Hooke constitutive equation and incompressibility was assumed. For each layer the thickness is measured from CLSM images and assumed constant. A displacement type boundary condition is applied in correspondence of the area of the adhesive plastic window, a shear stress is applied to simulate the effect of the fluid under the same plastic window. The model is complemented with appropriate boundary conditions to simulate the effect of surrounding tissue. The material parameters of the different layers are initially set according to literature data and then iteratively varied until the numerical transverse displacement matches the experimental one.

2. Tissue microscale model

Once the material parameters in the tissue macroscale models are obtained, the corresponding subject specific 3D FE tissue microscale models accounting for the upper layers of the skin (i.e., stratum corneum, epidermis, basal membrane and dermis) are set up. These models were developed using Abaqus 6.13 ® and the material behaviour of each layer is describe as an incompressible isotropic hyperelastic material as in the tissue macroscale models. At this level, the peculiar morphology of the basal membrane is taken into account. The geometry of the basal membrane is reconstructed from CLSM images using Rhinoceros (Seattle, WA, USA). To obtain the material parameter of the membrane a traction test in numerically performed on a specimen comprising the subject specific basal membrane the epidermis and the dermis. This information is then added to the tissue microscale models. Each subject specific model is then complemented with displacement boundary conditions obtained from the corresponding tissue macroscale model.

3. Cellular model

The cellular scale model was developed using Chaste (Cancer, Heart And Soft Tissue Environment, University of Oxford), an open source code which allows the modelling of the interactions among different types of cells. The aim of the model is to reproduce the cellular composition of different regions of interest modifying the ratio of melanocytes- and keratinocytes. Two families of cells have been defined, the leukocytes and melanocytes each with a cellular dimension of 8 µm. The cellular interaction are set according to literature indications. A displacement boundary condition is applied.

C. Results

For the sake of brevity, we report the comparison of the transverse displacement computed for skin and skin lesion from the CLSM registration and that numerical simulated using the tissue macroscale model (Fig. 3). A good agreement has been achieved between the experimental (dots) and the computational (line) for both the skin lesion (a) and the skin (b). In addition, it worth noting that while in the case of skin the slope of the displacement show only a variation from the stratum corneum to the lower layers, in the skin lesion the changes in the slope are observed in the epidermis, the DEJ and the dermis. These changes depend on the variation of the mechanical properties: the estimated Young's modulus in case of skin lesion at the derma-epidermal junction the is five-fold greater than case of normal skin. The analysis of the deformation field for skin (c-d) and skin lesions (e-f) also showed a higher gradient of the deformation in the skin lesion in correspondence of the DEJ.

III. Conclusion

The combined approach here proposed allowed to obtain the experimental transverse displacement in skin and skin lesions of healthy volunteer. The multiscale model provided important information on the modification of the mechanical properties in the skin lesion with respect to the normal skin. Such a methodology represents an interesting and suitable tool to be applied in the investigation of the melanoma to obtain further understanding of such pathology as well as indications to support clinical diagnosis.

Acknowledgement

This project was supported by Fondazione Ieo, Milan, Italy.

References

[1] A.V. Giblin, J.M. Thomas. (2007). "Incidence, mortality and survival in cutaneous melanoma" *J Plast Reconstr Aesthet Surg*, vol 60, pp. 32-40. http://dx.doi.org/ 10.1016/j.bjps.2006.05.008

[2] Skin Cancer Foundation. Skin Cancer Facts. 2012. Available from: http://www.skincancer.org/Skin-Cancer-Facts.

[3] M. J. Paszek, N. Zahir, K. R. Johnson, J. N. Lakins, G. I. Rozenberg, A. Gefen, C. A. Reinhart-King, S. S. Margulies, M. Dembo, D. Boettiger, D. A. Hammer, V. M. Weaver. (2005) "Tensional homeostasis and the malignant phenotype" *Cancer Cell,* vol. 8 (3), pp. 241-54. http://dx.doi.org/ 10.1016/j.ccr.2005.08.010

[4] M. Plodinec , M. Loparic , C.A. Monnier, E. C. Obermann, R. Zanetti Dallenbach , P. Oertle , J. T. Hyotyla, U. Aebi, M. Bentires-Alj, R.Y. Lim and C. A. Schoenenberger. (2012). "The nanomechanical signature of breast cancer" *Nat Nanotechnol,* vol. 7 (11), pp. 757-65. http://dx.doi.org/ 10.1038/nnano.2012.167

[5] M. I. Miga, M. P. Rothney and J. J. Ou. (2005). "Modality independent elastography (MIE): potential applications in dermoscopy" *Med Phys,* vol. 32 (5), pp. 1308-20. http://dx.doi.org/ 10.1118/1.1895795

[6] S. J. Kirkpatrick, R. K. Wang, D. D. Duncan, M .Kulesz-Martin and K., Lee. (2006). "Imaging the mechanical stiffness of skin lesions by in vivo acousto-optical elastography," *Optics express,* vol. 14 (21), pp. 9770-9. http://dx.doi.org/ 10.1364/OE.14.009770

[7] G .Weder, M. C. Hendriks-Balk, R. Smajda, D. Rimoldi, M. Liley, H. Heinzelmann, A. Meister, and A. Mariotti. (2014). "Increased plasticity of the stiffness of melanoma cells correlates with their acquisition of metastatic properties" *Nanomedicine: Nanotechnology, Biology, and Medicine*, vol. 10, pp. 141:148. http://dx.doi.org/ 10.1016/ j.nano.2013.07.007

[8] E. Montin, E. Cutrì, G. Spadola, A. Testori, G. Pennati, L. Mainardi. (2015, November.) "Tuning of a deformable image registration procedure for skin component mechanical properties assessment" *Proceedings of the Annual International Conference of the IEEE Engineering in Medicine and Biology Society, EMBS,* pp. 6305-6308. http://dx.doi.org/ 10.1109/EMBC.2015.7319834.

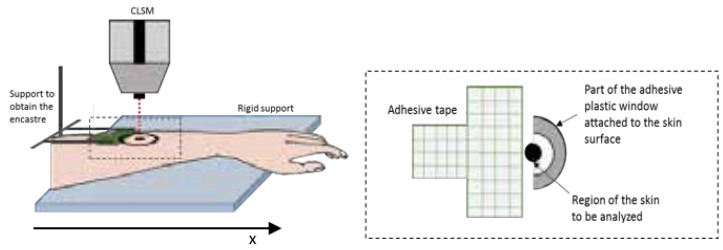

Fig. 1. Schematic of the experimental set up. The CLSM probe is attached to the skin through a tissue ring and an adhesive plastic window (*left*). The adhesive plastic window was cut so that only half was attached to the skin surface and on the opposite side, an adhesive tape was attached onto the skin surface and held through a support to obtain an encastre (*right*).

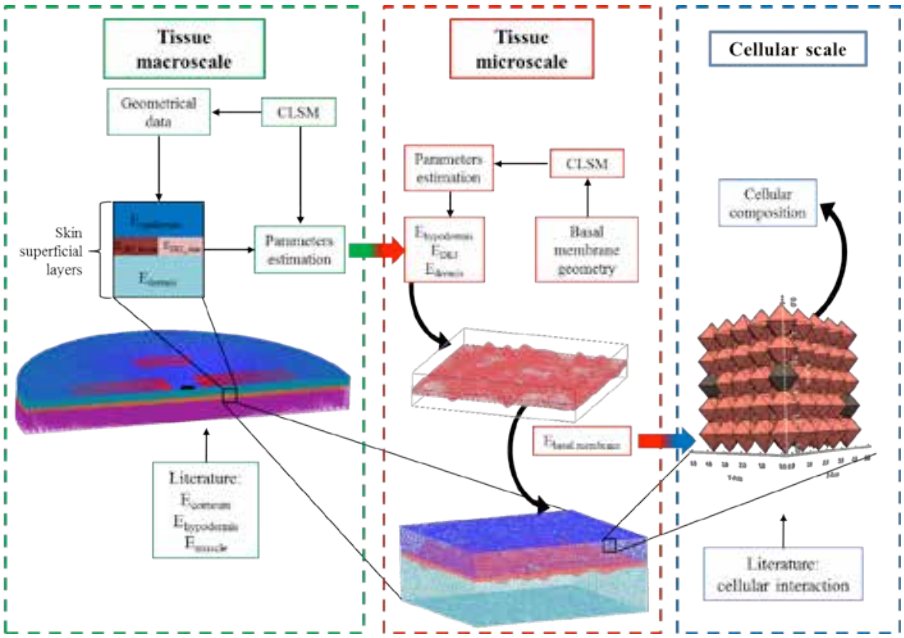

Fig. 2. Schematic of the multiscale model. From the left to the right: tissue macroscale (*green*), tissue microscale (*red*) and cellular scale model (*blue*).Geometrical data from CLSM and data from literature are integrated in the models. The figure underlines the communications of parameters between the three models.

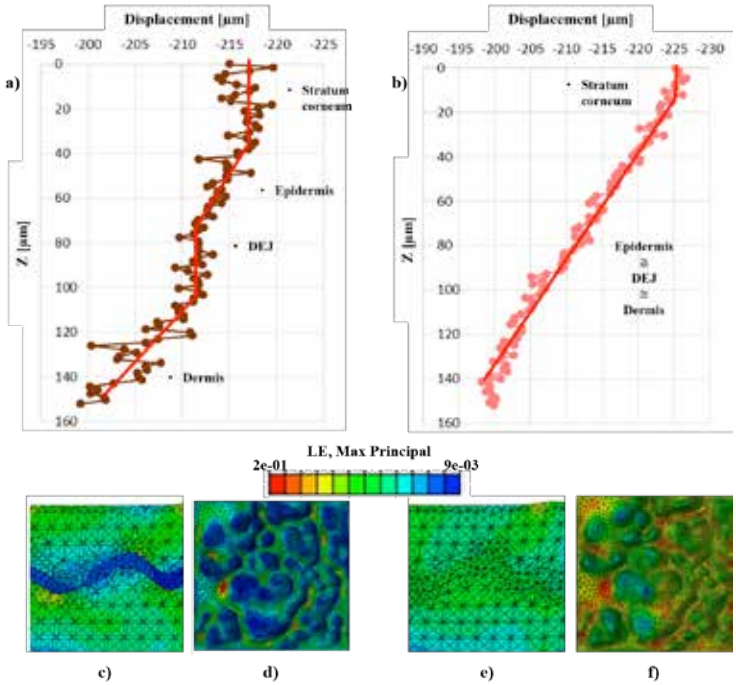

Fig. 3. Results of the computational model. *Top*: comparison of the transverse displacement for the skin (a) and skin lesion (b) obtained from the CLSM images (dots) and from simulation (line). *Bottom:* maps of the deformation for the skin (c-d) and the skin lesion (e-f).

First application of digital volume correlation to study the efficacy of prophylactic augmentation

V. Danesi[1], G. Tozzi[2], and L. Cristofolini[2]
[1] *Department of Industrial Engineering, Alma Mater Studiorum – University of Bologna, Italy*
[2] *School of Engineering, University of Portsmouth, UK*

***Abstract*—The aim of this study was to measure, for the first time, the full-field three-dimensional strain distribution inside prophylactic-augmented vertebrae in the elastic regime and to failure. Eight porcine vertebrae were prophylactically augmented using two different cements. They were micro-CT scanned (40 micrometer voxel) in the unloaded state and at 5%, 10% and 15% compression. Internal strains were computed using digital volume correlation (DVC). For both cement types, the highest strains were measured in the regions adjacent to the injected cement mass, whereas the cement-interdigitated-bone was less strained. While this was already visible in the elastic regime (5%), it was a predictor of the localization of failure, which became visible at higher degrees of compression (10% and 15%) when failure propagated across the trabecular bone, sometimes reaching the cortex. Localization of the high strains and failure was consistent between specimens, but different between the two cement types: for one cement (having a lower young modulus) this was located at mid-height, at the same level as the cement mass; for the other one (having a higher young modulus) strain concentration and failure were cranial or caudal to the cement mass. This study demonstrated the potential of DVC in measuring the internal strain (elastic regime) and failure in prophylactic-augmented vertebrae. While the cement-interdigitated region becomes stronger (less strained), the adjacent non-augmented trabecular bone is affected by the stress concentration induced by the cement mass, and tends to fail. This approach can help establishing better criteria to improve the vertebroplasty and augmentation.**

***Keywords*— Prophylactic vertebral augmentation, Digital volume correlation, Bone fracture, Full-field three-dimensional strain measurement.**

I. Introduction

THERE are cases in which vertebrae are at high risk of fracture, such as in with low bone mineral density or metastatic lesion. One prophylactic strategy that has recently been proposed to reduce fracture risk in weak vertebrae is the mechanical reinforcement of the vertebral body by injection of a foreign augmentation material. Past studies only investigated structural failure [1-3] and the surface strain distribution [4]. To elucidate the failure mechanism of the augmented vertebral body, information is needed about the internal distribution of strains. With the recent and rapid progress of high-resolution micro-CT imaging in conjunction with *in situ* mechanical testing, digital volume correlation (DVC) emerged as a novel tool for the measurement of 3D deformation fields throughout entire bone volumes [5]. The aim of this study was to improve the understanding of the failure mechanism inside prophylactic-augmented vertebral bodies under compression. DVC was used for the first time to measure the full-field internal strain distribution inside the vertebral body, in the injected cement, and in the cement-bone interdigitated region of vertebrae that were prophylactic-augmented with two different cements, including both the elastic regime (axial components of strain), and the internal micro-failure mechanism.

II. Materials and Methods

Eight single thoracic porcine vertebrae were divided in two groups:

- Augmentation with Cal-CEMEX Spine (Tecres, Italy) was performed on 4 intact vertebrae.
- Augmentation with Mendec Spine (Tecres, Italy) was performed on 4 intact vertebrae.

Destructive tests were performed with a step-wise axial compression (0%, 5%, 10% and 15% compression). MicroCT images were acquired at each step (typically 40 micron resolution). DVC analysis (LaVision, UK) was performed on the microCT-reconstructed volumes to obtain the full-field displacement and strain distribution, in order to identify the onset and progression of bone-biomaterial failure in the natural and prophylactic augmented vertebral body.

III. Results

In all of the augmented specimens, the micro-CT images (Fig. 1) showed a main micro-damage, at 15%. For both cement types, the cement region appeared to be undamaged, even at the final loading stage (15%); failure tended to initiate in the trabecular bone adjacent to the cement-bone interdigitated region. In the majority of the Mendec specimens (3 out of 4, Fig. 1) the main micro-

damage was localized in the trabecular bone at mid-height, at the same level of the cement mass. Such a collapse seemed to initiate from the cement-bone interface, then gradually spread across the trabecular bone anteriorly and finally in the transverse plane reaching the cortical bone. Only for specimen Mendec-4 collapse initiated at the two extremities (Fig. 1, 15%), which ended with a trabecular crushing in most of the cranial and caudal region, far away from the augmented region. The specimens augmented with Cal-CEMEX showed a main micro-damage localized in the trabecular region just cranial or caudal to the cement mass (Fig. 1, 15%). Only in Cal-CEMEX-3 the micro-damage was at the same height of the cement mass, towards anterior (Fig. 1, 15%). Similar to the Mendec specimens, such a collapse initiated from the cement-bone interface, and gradually developed across the trabecular anteriorly or posteriorly in the transverse plane, in some cases affecting the cortical bone (Cal-CEMEX-2 and Cal-CEMEX-3).

At the first compression step (5%) the localization of high-strain regions varied between specimens (Fig. 3-4). Conversely in the final loading step (15%) the cement regions seemed to be less strained in all specimens, and the largest strains were generally observed adjacent to the cement-bone interdigitated region. In the Mendec specimens, the highest strains observed at 10% and 15% compression were at mid-height, at the same level of the cement mass (Fig. 2). Conversely, in the Cal-CEMEX specimens the largest strains were just cranial and caudal of the cement mass (Fig. 3). The highest strain was localized in a single region within the augmented vertebral body for most specimens; the only exceptions were Mendec-3 and Cal-CEMEX-4, where two distinct strain peaks were observed, adjacent to the cement mass. For the specimens augmented with both cement types, the regions of high strain seemed to match very well the localization of micro-damage visualized in the micro-CT images (Fig. 1). Strains were markedly lower away from the most stressed regions where damage initiated. The strain distribution in the augmented vertebrae in the elastic regime (5%) seemed to predict the location of the micro-damage initiation before it actually became identifiable (at 10% and 15%) in the most of the specimens (Fig. 2 and 3). Only the specimen Mendec-1 showed a relocation of the highest axial strain from the posterior (5%, Fig. 2) to the anterior region (15%).

IV. Conclusion

Both the micro-CT images, and the DVC strain analysis highlighted that: the cement mass was less strained than any other regions in the vertebra and was never the point of failure initiation. This can be explained with the additional stiffening and reinforcement associated with the infiltration of the cement inside the trabecular bone. The highest strains and failure were localized in the bone adjacent to the cement-bone interdigitated region. This can be explained by the stress concentration between two regions: the cement-interdigitated bone, which has become stiffer and stronger, and the adjacent non-augmented trabecular bone (where some trabeculae might also have been damaged by the injection process). The specimens augmented with the two cement types seemed to have different failure mechanisms: this could be possibly associated with the different stiffness of the two cements. In conclusion, this study has demonstrated the potential of digital volume correlation in measuring the internal strain (elastic regime) and failure in prophylactic-augmented vertebrae. It has been shown that failure starts inside the augmented vertebral body, next to the injected cement mass. This can help establishing better criteria (in terms of localization of the cement mass) to improve the clinical protocols for vertebroplasty and augmentation.

Acknowledgement

The authors with to thank: Tecres for donating the bone cements and providing the injection kits. Funding was provided by the Royal Society (RG130831), the University of Portsmouth and the European Society of Biomechanics (ESB mobility award 2014).

References

[1] M. Kinzl, "The effect of standard and low-modulus cement augmentation on the stiffness, strength, and endplate pressure distribution in vertebroplasty," *Eur Spine J*, vol.21,pp.920-9,2012.

[2] N. Furtado, "A Biomechanical Investigation of Vertebroplasty in Osteoporotic Compression Fractures and in Prophylactic Vertebral Reinforcement," *Spine*, vol.32, 2007.

[3] P.F.Heini, "Augmentation of mechanical properties in osteoporotic vertebral bones a biomechanical investigation of vertebroplasty efficacy with different bone cements," Eur Spine J, vol.10, pp.164-71, 2001.

[4] L. Cristofolini, "A preliminary in vitro biomechanical evaluation of prophylactic cement augmentation of the thoracolumbar vertebrae ", JMMB *in press*

[5] B. C. Roberts, "Application of the digital volume correlation technique for the measurement of displacement and strain fields in bone: a literature review", *J Biomech,* vol.47, pp.923-34, 2014

On the impact of modeling assumptions in subject-specific hemodynamic simulations of low-density lipoproteins transport in aorta

G. De Nisco[1], P. Zhang[2], D. Gallo[1], X. Liu[2], X. Deng[2], R. Ponzini[3], G. Rizzo[4], and U. Morbiducci[1]
[1] *Department of Mechanical and Aerospace Engineering, Politecnico di Torino, Turin, Italy*
[2] *School of Biological Science and Medical Engineering, Beihang University, Beijing, China*
[3] *CINECA, Milan, Italy*
[4] *IBFM, Research National Council, Milan, Italy*

***Abstract*—In this study we use an image-based hemodynamic model of human aorta to investigate the influence of different strategies of applying boundary conditions (BCs) on low-density lipoproteins (LDL) transport and wall transfer. Findings from simulations clearly show that the imposition of idealized, rather than PC-MRI measured velocity profile as inflow BCs in subject-specific computational models of mass transport could largely affect the location and extension of regions of LDL polarization at the luminal surface of the aorta.**

***Keywords*— Low-density lipoproteins transport, arterial mass transport, computational hemodynamics, atherosclerosis.**

I. Introduction

THE complex hemodynamics observed in the human aorta make this district a site of election for an in depth investigation of the relationship between fluid structures, transport and patho-physiology. In fact, it is well known that hemodynamics play an important role in the mass transport of blood specimen, and in turn, in their transfer to the vascular wall and ultimately in the localization of vascular disease in areas of complex arterial flow. In particular, the accumulation of lipoproteins in the arterial intima is a hallmark of atherosclerosis. Low-density lipoproteins (LDL) are the most abundant atherogenic lipoproteins in plasma and high plasma levels of LDL are causally related to the development of atherosclerosis [1].

In the last decade the coupling of medical imaging and computational fluid dynamics (CFD) has contributed to enhance the comprehension of the aortic hemodynamics, with the possibility to obtain highly resolved blood flow patterns in anatomically realistic arterial models. In particular, in the context of a subject-specific oriented approach, PC-MRI has emerged as able to provide the anatomical and hemodynamic inputs to even more realistic, fully personalized flow simulations [2]. Moreover, personalized computational modeling of mass transfer has been proposed as a powerful way of addressing abnormalities in mass transfer patterns, which could be in themselves atherogenic [3]. In this regard, a recent study investigated the effects of geometric features of human aorta on the flow pattern and the luminal surface LDL concentration. More in detail, it was investigated the role played by aortic torsion, branching, taper, and curvature on LDL transport and luminal surface distribution in four aortic models with different geometry [4].

In this study we analyze the influence of different possible strategies of applying PC-MRI measured data as inflow boundary conditions (BCs) to confidently model LDL transport and transfer in image-based hemodynamic models of human aorta. In detail, the influence on LDL transport of assumptions regarding the velocity profile at the inlet section of the ascending aorta. We impose PC-MRI measured 3D velocity profiles (i.e. locations-dependent direction and magnitude of velocity vectors at the inlet section) at the inlet of the computational model and compare the obtained results, in terms of low-density lipoproteins transport, to the results of two equivalent computational models with the same instantaneous flow rate prescribed as measured 1D velocity profiles (i.e. magnitude of velocity vectors normal to the inlet surface) and flat velocity profile inlet BCs. Technically, steady-state flow simulations were carried out at three representative phases of the cardiac cycle for the three inlet velocity profiles considered. The LDL distribution at the aortic luminal surface was computed and the results were compared.

The study here presented would contribute to clarify which is the impact of the conditions applied at inflow boundaries on aortic LDL transport. In particular, the comparison of LDL transport at the aortic luminal surface as obtained prescribing idealized *vs* measured velocity profiles as inflow BCs, will contribute to clarify which is the level of detail obtained from measured phase velocity, sufficient to satisfactorily simulate mass transport/transfer in personalized computational hemodynamics models of human aorta.

II. Methods

The geometry of an ostensibly healthy human aorta was reconstructed from 4D PC-MRI images. PC-MRI slices were used to generate the model of aorta into the Vascular Modeling Toolkit environment by applying a multiple step procedure for the extraction of the surface mesh of the thoracic aorta from PC-MRI data [5]. The finite volume method was applied to perform numerical simulations under steady flow conditions. The general purpose CFD code Fluent (ANSYS Inc., USA) was used on computational mesh-grids with high quality prismatic cells near the wall at the inlet surface and structured tetrahedral elsewhere, semi-automatically generated using ICEM (ANSYS Inc., USA). The domain was equipped with straight flow extensions at the outlet faces and divided into about $4 \cdot 10^6$ cells. Blood was modeled as an isotropic, incompressible, homogeneous, Newtonian viscous fluid with density equal to 1060 kg/m^3 and dynamic viscosity equal to 3.5 cP. The LDL diffusion coefficient in blood was set to $5.94 \cdot 10^{-9}$ m^2/s. Arterial walls

were assumed to be rigid with no-slip condition at the wall. At the outlet sections of the model measured flow rate ratios were imposed as outflow BCs, as detailed in [5].

Steady state LDL transport in flowing blood can be described by the convective-diffusion equation for the LDL concentration C:

$$u \cdot \nabla C - D_L \nabla^2 C = 0 \qquad (1)$$

where u is the velocity vector and D_L is the diffusivity of LDL in flowing blood, set to $4.8 \cdot 10^{-12}$ m^2/s [4].

Flow simulations were carried by applying conditions at boundaries as measured at three different phases of the cardiac cycle (i.e. acceleration phase, systolic peak and deceleration phase, Figure 1), for a total number of nine simulations. According to a previous strategy [2], the following BC strategies were applied at the inlet section of the ascending aorta. The first strategy consists in the application of the measured PC MRI velocity profiles at the inlet section. Technically, at the inlet section of the model the measured three components of the velocity were extracted from the phase images. Using phase-contrast flow data, two different inflow conditions were generated, by imposing at the inlet of the ascending aorta: (1) PC-MRI measured 3D velocity profile at systolic peak, and at two phases of the cardiac cycle, one along the acceleration phase and the other along the deceleration phase; (2) PC-MRI measured 1D velocity profile at the same phases of cardiac cycle, obtained considering the measured velocity component orthogonal to the inlet section of the anatomic model (i.e., the axial velocity component). The second strategy is a widely applied approach and consists in the application of the measured velocity waveform at the inlet surface in terms of idealized flat velocity profile, where the velocity magnitude of flat profile was obtained by averaging 1D velocity profile, at each one of the three considered phases of cardiac cycle.

The equation (1), governing mass transport, was solved coupled to the Navier-Stokes equations by imposing the following BCs:

$$\text{BC } inlet: \quad C = C_0 \qquad (2)$$

$$\text{BC } outlet: \quad C = \frac{\partial C}{\partial n} \qquad (3)$$

$$\text{BC } wall: \quad D_L \left(\frac{\partial C}{\partial n}\right) = v_w C_w \qquad (4)$$

where C_0 is the LDL concentration in the bulk flow (set equal to $2.86 \cdot 10^{-9}$ mol/m^3 [4]), C_w is the concentration of LDLs at the luminal surface of the artery, v_w is the filtration velocity of fluid across the vessel wall (set equal to $4 \cdot 10^{-8}$ m/s [4]), and suffice n indicates the direction normal to the boundary.

LDL transport was computed for the three inflow conditions cases and the impact of the choice of idealized rather than measured velocity profiles as inflow BCs was investigated focusing on LDL transfer to the aortic luminal surface.

III. Results

As main finding of the study the uptake of LDL at the aortic wall (normalized with respect to the initial LDL concentration C_0 at the aortic inlet section) is reported. In detail Figure 1 presents the LDL accumulation profiles at the luminal surface obtained by imposing in silico (FLAT panel) and in vivo (1D and 3D panels) velocity profiles as inflow BCs for the three simulated phases of the cardiac cycle. Notably, differences in LDL patterns at the luminal surface are present, depending on the applied velocity profile at the inflow. In detail, the surface area subjected to elevated LDL accumulation is markedly wider than the 3D and 1D cases, when flat velocity profile is prescribed at the aortic inflow section. The FLAT case presents three luminal regions at the aortic arch subjected to severe polarization of LDL, more evident during the acceleration phase of the cardiac cycle (inner lateral edge of the brachiocephalic artery, intrados of the ascending aorta and inner wall of the descending aorta). The same regions were identified in [4], as interested by elevated LDL accumulation. LDL polarization at these luminal regions sensibly decreases in 1D and 3D simulation cases. Results obtained for 3D and 1D cases show a more uniform LDL distribution at the wall along the aortic arch, with a weak increase in LDL polarization at the inner wall of the descending aorta. In general, Figure 1 confirms that light or negligible differences can be appreciated in LDL transport between 1D and 3D cases at the three cardiac phases here investigated.

IV. Conclusion

The findings of this study show that the imposition of idealized velocity profile as inlet BCs in subject-specific computational hemodynamics models of mass transport in the human aorta could largely affect the location and extension of regions of LDL polarization at the luminal surface. We conclude that the plausibility of the assumption of idealized velocity profiles as inlet BCs in personalized model of the aortic hemodynamics could not, or could loosely, hold true. This finding needs further investigation, because of the fact that it is derived from steady-state flow analysis. The same analysis will be extended to unsteady-state simulations, applying the same scheme as proposed in previous works [2]. Ultimately, the approach here proposed is intended to be applied to elucidate the role played by the aortic helical flow in mass transport [6], in particular in testing the hypothesis that the promoted-by-helicity mixing of blood could be beneficial in suppressing severe LDL polarization at peculiar aortic regions, thus being part of the physiologic atheroprotective mechanism.

References

[1] J.M. Tarbell, "Mass transport in arteries and the localization of atherosclerosis", *Ann Rev Biomed Eng*, vol. 5, pp. 79-118, Aug. 2003.

[2] U. Morbiducci, R. Ponzini, D. Gallo, C. Bignardi, G. Rizzo, "Inflow boundary conditions for image-based computational hemodynamics: Impact of idealized versus measured velocity profiles in the human aorta", *J Biomech*, vol. 46, pp. 102–109, Jan. 2013.

[3] C.R. Ethier, "Computational modeling of mass transfer and links to atherosclerosis", *Ann Biomed Eng*, vol. 30, pp. 461-471, Apr. 2002

[4] X. Liu, F. Pu, Y. Fan, X. Deng, D. Li, S. Li, "A numerical study on the flow of blood and the transport of LDL in the human aorta: the physiological significance of the helical flow in the aortic arch", *Am J Phys Heart Circ Phys*, vol. 297, pp. H163–H170, 2009.

[5] D. Gallo, G. De Santis, F. Negri, D. Tresoldi, R. Ponzini et al., "On the use of in vivo measured flow rates as boundary conditions for image-based hemodynamic models of the human aorta: implications for indicators of abnormal flow", *Ann Biomed Eng*, vol. 40, pp. 729-741, March 2012.

[6] U. Morbiducci, R. Ponzini, G. Rizzo, M. Cadioli, A. Esposito et al., "Mechanistic insight into the physiological relevance of helical blood flow in the human aorta: an in vivo study", *Biomech and Modeling in Mechanobiology*, vol. 10, pp. 339-355, June 2011.

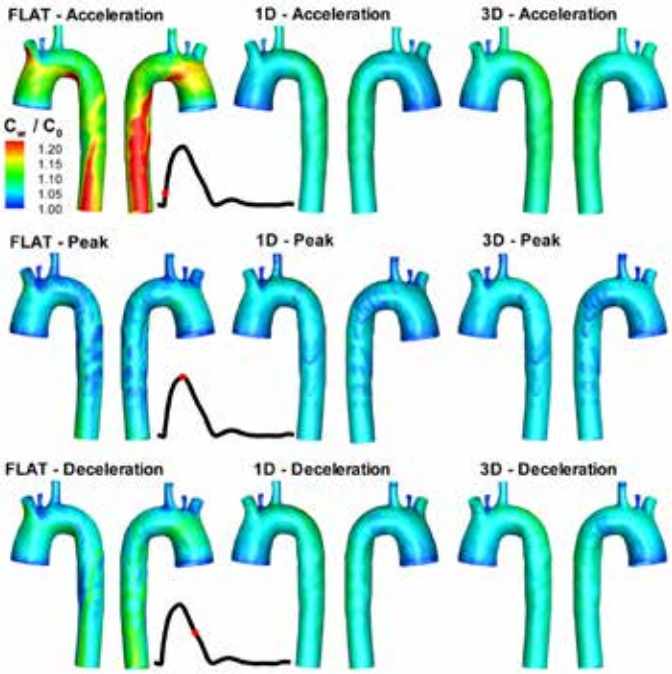

Fig. 1. Comparison of the normalized LDLs concentrations at the luminal surface for the simulated inflow boundary conditions.

Tendon tissue engineering: decellularization protocol for equine-derived tendon matrix

M. Ferroni[1*], A.F. Pellegata[2*], M. Bottagisio[2], M. Moretti[2], A.B. Lovati[2] and F. Boschetti[1]
[1] *Department of Chemistry, Materials and Chemical Engineering Giulio Natta, Politecnico di Milano, Milan, Italy*
[2] *Cell and Tissue Engineering Laboratory, IRCCS Galeazzi Orthopaedic Institute, Milan, Italy*
** These authors contributed equally to this work*

***Abstract*—Tendon ruptures remain a clinical challenge and require the replacement of the damaged tissue. The current use of autografts is an established approach but related to a low biocompatibility and biomechanical properties. This study aimed to identify a novel decellularization protocol for equine tendons to obtain a suitable substitute for the regeneration of injured tendons. Samples were analyzed by biochemical and biomechanical tests. 1% TBP+3% PAA was identified as the proper decellularization protocol, then tested for cell viability.**

***Keywords*—xenograft, biomaterials, decellularization, equine tendon biomechanics.**

I. Introduction

TRAUMATIC tendon ruptures or losses require a surgical replacement of the damaged tissue. Currently, tendon autografts are the common choice to reconstruct the tendon integrity but with several limitations [1], [2]. In the recent years, tissue engineering widely investigated the use of scaffolds that might be seeded with host cells to promote tissue and functional integration [3]. Several decellularization techniques of xenografts by using chemico-physical agents have been studied, since bioengineered graft with biochemical and biomechanical properties similar to the native tendon should be compatible with the receiving host [2]. In this context, equine species is the most suitable source in terms of tissue supply, whereas the tri(n-butyl) phosphate (TBP) and peracetic acid (PAA) are the most efficient agents to optimize cell removal, maintaining all functional requirements. Our study wants to identify a proper decellularization protocol to obtain an extracellular matrix as suitable substitute able to deliver reseeded cells for the regeneration of injured tendons. The main goal was to remove intrinsic cells from equine superficial digital flexor tendons (SDFT) by means of the 1% TBP associated or not to low concentrations of PAA. Thus, we evaluated the biochemical and biomechanical properties of decellularized tendons and we compared them to fresh-stored SDFT to determine any effect of the treatments on the tissue. Finally, we tested the best decellularization protocol in supporting the attachment and growth of the NIH-3T3 murine fibroblasts.

II. Materials and Methods

A. Preparation of equine SDFT

Equine SDFT were harvested from adult horses and 10 cm length portions were excised, washed in phosphate-buffered saline (PBS) and dry-stored at -80 °C. Then, specimens were thawed at room temperature (RT) in saline solution, sectioned into slices and frozen until processing.

B. Decellularization methods

Tendon slices of each donor were treated by one of the following protocols starting from 1% TBP: (1) 0% PAA, (2) 1% PAA, (3) 3% PAA and (4) 5% PAA. An untreated slice of each donor was used as control (native tendon, NT). Slices to treat were immersed in PBS, then decellularized in 1% TBP buffered in 1M Tris-HCl (pH=7.8) under agitation. Following, slices were rinsed and stored to remove residual detergents. After this passage, specimens were immersed in 0.0025 % DNAse-I in PBS under agitation and later washed in ddH2O and PBS. The last step was a different incubation in 0%, 1%, 3% or 5% aqueous solution of PAA. Finally, slices were rinsed in ddH2O and PBS, then stored in PBS or dry-stored for several analyses.

C. Biochemical characterization

DNA assay allowed to measure DNA content and post-decellularization cellular component by means of a cell proliferation assay (CyQuant® kit–LifeTechnologies, Monza, Italy) and fluorescence spectroscopy (Perkin Elmer Victor X3 microplate reader). The quantification of sGAG was performed on decellularized and native tendons using the 1,9-dimethylmethylene blue dye-binding assay (Sigma-Aldrich, Milan, Italy). The sGAG concentration was determined by reading the absorbance at 500 nm (Perkin Elmer Victor X3 microplate reader). In order to quantify the collagen content, we firstly removed proteoglycans and prepared the supernatant obtained from the collagen residue. The optical densities, obtained from the supernatant by absorption spectroscopy, were interpolated in a curve of absorbance, using collagen type I from rat-tail soluble in acetic acid. Data obtained were expressed as total acid-soluble collagen.

D. Biomechanics

Biomechanical testing was performed starting from rectangular specimens obtained from the decellularized and native tendons, using an electromagnetic testing machine (MTS Synergie, Eden Prairie, MN, USA), equipped with a load cell of 1 kN. The mean dimensions of the samples were 39±8 mm length, 14±2 mm width and 2.4±0.6 mm thickness. Tension protocol consisted of multi-ramp stress-relaxation tests, followed by the strain-controlled tension up to failure at 1%/s strain rate. For stepwise stress relaxation tests, three tension steps up to 2% strain were applied, at 1%/s strain rate, followed by 1000s of stress relaxation. The pure elastic response (Er) was calculated from the equilibrium data of the stress relaxation tests. The tendon hyperelastic response, the elastic modulus at high strains (EM) and the failure stress and

strain were derived from the failure tests. Experimental data were fit to a viscoelastic model by means of a Prony series to evaluate the first four relaxation time constants.

E. Repopulation of the decellularized matrix

Tendons decellularized by means of TBP + 3% PAA were sterilized into 70% ethanol, washed in PBS and left unseeded as negative control or seeded with NIH-3T3 murine fibroblasts and cultured in complete medium. 150 μL of the cell suspension was deposed onto the surface to seed the tendon. Then, the medium was added and both the unseeded and seeded tendon matrices were statically cultured for 7 days. The cell viability of seeded fibroblasts was evaluated performing a Live&Dead Viability/Cytotoxicity test (Life Technologies, Monza, Italy).

III. Results

A. Biochemical analysis

The DNA content data, measured to analyze the capability of the decellularization protocols on cell removal, show that all treated samples reduce the DNA content if compared to the NT, supporting previous histological cell count. Moreover, an important decrease in DNA content was found in the groups treated with TBP + 3% PAA and TBP + 5% PAA (cell removal of 98% and 99%, respectively) and it responds to the minimal criteria (50ng/mg dry weight in Fig. 1A) to satisfy the purpose of tissue decellularization [2]. Figure 1B shows a significant decrease of sGAG content in tendon treated with TBP + 5% PAA but no significant differences were detected in the samples decellularized with TBP + 1% PAA, TBP + 3% PAA and TBP, with respect to NT. Figure 1C reports a significant decrease of the collagen content in tendon treated with all the protocols with respect to NT but a higher collagen content for the TBP group compared to the other protocols.

B. Biomechanical tests

The results of stress-relaxation tests conducted on native and decellularized samples with TBP + 1% PAA, TBP + 3% PAA, TBP + 5% PAA and TBP are reported in figure 2.A. The results of the failure tests report a hyperelastic response, particularly figure 2.B shows the EM at high strains. The tendons treated with all the decellularization protocols did not show significant changes in EM compared to the NT but only a significant difference was found between TBP + 1% PAA and TBP + 5% PAA, indicating a stiffer behavior of tendons treated with TBP + 1% PAA. The EM value for NT was 181±78 MPa. According to this, there was not a significant difference in failure stress and strain values measured after the decellularization with respect to the NT (one-way ANOVA coupled with Bonferroni's post hoc test). The average values of the relaxation constants at 2% of strain are shown in figure 3 and were not dependent on the decellularization protocol.

C. Cell colonization of the decellularized matrix

Accordingly to biochemical and biomechanical results, TBP + 3% PAA was considered the best decellularization protocol and used to reseed the equine tendons with NIH-3T3 fibroblasts. After 7 days of culture, the Live&Dead assay demonstrated a preserved viability of the seeded cells (Fig. 4), with a percentage of living cells of 80±9 %. This analysis, in addition to the collagen content in reseeded matrix, showed metabolic activity, NIH-3T3 viability and well distribution on the surface of the construct.

IV. Discussion and Conclusion

The present study wants to identify a proper decellularization protocol for large equine tendons by means of specific combination of TBP and PAA, biochemical and biomechanical tools. The results of the current study indicated that the TBP + 3% PAA and TBP + 5% PAA treatments reduced the resident cell amount by obtaining DNA values lower than the minimal criteria for clinical use [3]. The percentage of cell removal obtained by these two treatments was the most effective data obtained until now in the field of tendon decellularization protocols, to the best of our knowledge. These data strictly correlated with the sGAG analysis, in which well-preserved sGAG content was found in tendons treated with TBP + 3% PAA without any significant difference compared to the NT. Total collagen content was lower in all the tested decellularization protocols, since the exposure to PAA could affect the collagen content. All the tested decellularization protocols produced acellular scaffolds with mechanical properties similar to the NT for EM, failure stress and strains. High concentrations of PAA affected the pure elastic response of the tendon as evaluated by the stress-relaxation tests. Nevertheless, the tendons treated with TBP + 1% PAA demonstrated a greater stiffness in the whole viscoelastic behavior, whereas higher concentrations of PAA restored the viscoelastic response of the NT behavior. The maintenance of proper biomechanical features is mandatory either for the tissue engineering approaches to develop a tendon substitute. In terms of cell viability, our results demonstrated a good fibroblast cytocompatibility of the decellularized matrix with TBP + 3% PAA. According to the results of the current study, the TBP + 3% PAA seems to be the most suitable decellularization protocol for large tendon grafts, being highly effective in cell removal, matrix structure and cell reseeding. Our protocol led to the generation of biocompatible, acellular tendon scaffolds that will be suitable as substitutes for tendon tissue engineering.

Acknowledgement

This study was funded by the Italian Ministry of Health (RF- GR-2011-02348899). The NIH-3T3 murine fibroblasts were kindly provided by Dr S. Previdi (Institute for Pharmacological Research Mario Negri, Milan, Italy).

References

[1] L. W. Yao, et al. (2015). Patellar tendon autograft versus patellar tendon allograft in anterior cruciate ligament reconstruction: a systematic review and meta-analysis. *Eur. J. Orthop. Surg. Traumatol. 25(2)*. pp. 355-365. doi: 10.1007/s00590-014-1481-5.

[2] C. W. Cheng, L. D. Solorio, and E. Alsberg (2014). Decellularized tissue and cell-derived extracellular matrices as scaffolds for orthopaedic tissue engineering. *Biotechnol. Adv. 32(2).* pp. 462-484. doi:10.1016/j.biotechadv.2013.12.012.

[3] P. M. Crapo, T. W. Gilbert, and S. F. Badylak (2011). An overview of tissue and whole organ decellularization processes. *Biomaterials. 32(12)*. pp. 3233-3243. doi:10.1016/j.biomaterials.2011.01.057.

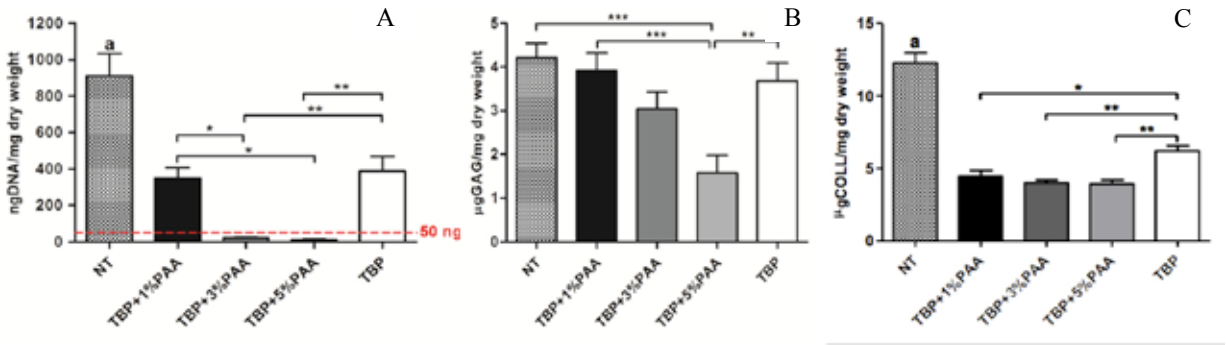

Fig. 1. Effects of the decellularization protocols on DNA (A), sGAG (B) and collagen content (C). Comparisons among groups were analyzed with one-way analysis of variance (ANOVA) coupled with Bonferroni's post hoc test (* $p<0.05$, ** $p<0.01$; a, *** $p<0.001$).

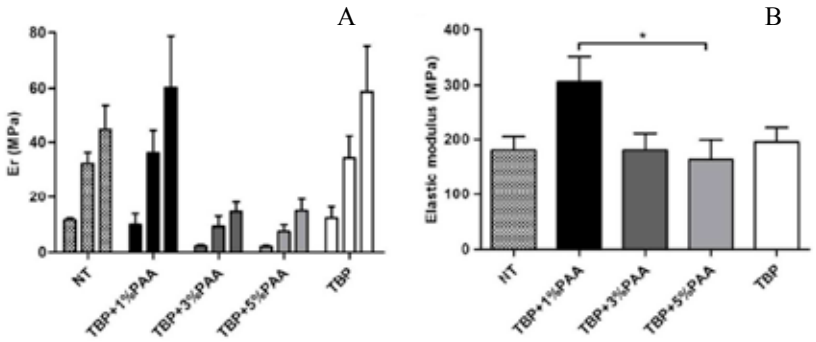

Fig. 2. Histogram of the relaxation moduli for the three ramps (A) and elastic modulus (B) comparing NT and the decellularization protocols. Comparisons among groups were analyzed with one-way analysis of variance (ANOVA) coupled with Bonferroni's post hoc test (*$p<0.05$).

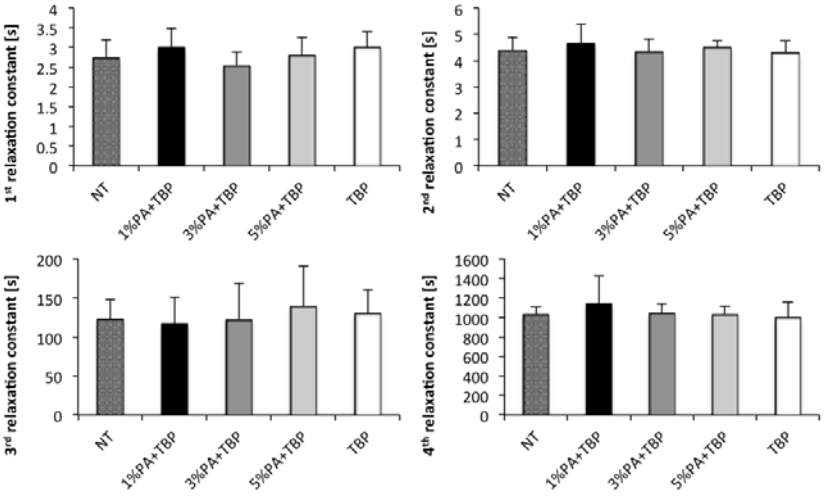

Fig. 3. Relaxation time constant values of the first four terms of Prony series for each decellularization protocols.

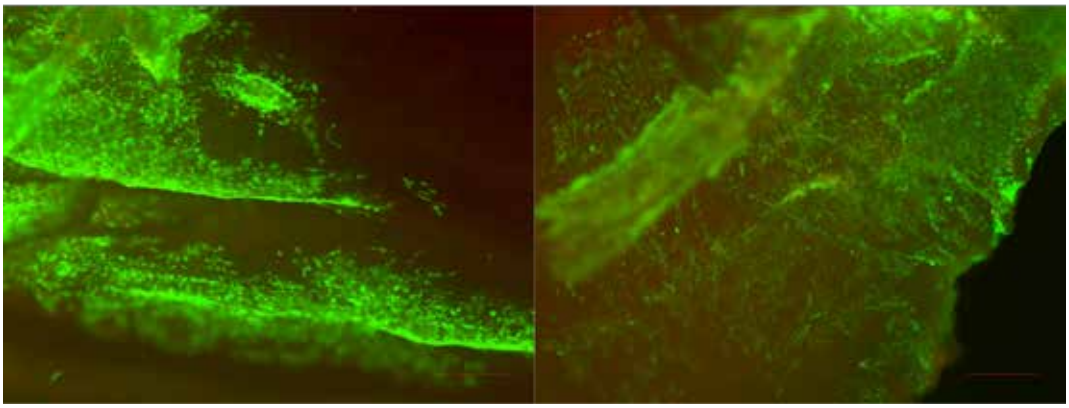

Fig. 4. Two representative panels of the Live&Dead of the reseeded matrix, with a percentage of living cells of 80±9 % and dead cells of 20±9 % (scale bars 200 µm).

Numerical model of ocular posterior chamber: fluid-dynamics for intravitreal drug delivery

M. Ferroni[1], A. Moioli[1], E. C. Sganzerla[1], M. G. Cereda[2], and F. Boschetti[1]
[1] *Department of Chemistry, Materials and Chemical Engineering Giulio Natta, Politecnico di Milano, Milan, Italy*
[2] *Eye Clinic, Department of Biomedical and clinical science Luigi Sacco, Sacco Hospital, University of Milan, Milan Italy*

***Abstract*—Nowadays, intravitreal injections are one of the most common techniques for the treatment of ocular diseases. To predict the transport mechanism of the injected drug, the fluid-dynamics inside the posterior chamber has to be known. This study aims at implementing a full CFD modeling of the vitreous domain. The main novelty of this work is the optimization of the boundary conditions. Results of the full CFD model suggest that effects of the physiological environment and the saccade must be taken into account.**

***Keywords*—computational fluid-dynamics, ocular drug delivery, vitreous, saccade.**

I. Introduction

MANY ocular diseases can be treated by means of specific drugs, delivered by several clinical methods. One of the possible drug delivery method consists in the intravitreal injection, which overcomes the limits of topical and intravenous drug delivery techniques but can lead to other ocular complications. The vitreous humor is a gel-like structure that acts as delivery medium in the posterior chamber of the eye. Several studies showed a liquefaction process after the age of 50 years, inducing an increase of the liquid volume [1]. Numerical models are powerful tools able to study the intravitreal fluid-dynamics, which is fundamental to predict the drug delivery mechanism. To the best of our knowledge, few literature studies have been devoted to the evaluation of the ocular fluid-dynamics. One study defines the flow of aqueous humor inside the vitreous and reports that the drug distribution is strictly related to the diffusion coefficients and the size of molecules [2]. By contrast, other works consider the effect of saccadic movements on the drug distribution injected intravitreally and report that convection transport is dominant for different diffusivities and injection locations [3], [4]. The goal of our study is to implement a novel CFD model able to compute the overall ocular fluid-dynamics, accounting for both the physiological environment and the ocular saccadic movement due to the extraocular muscles. In our opinion, this approach will allow us to define a powerful tool to predict the fluid-dynamics and the consequent drug delivery in case of ocular diseases.

II. Materials and Methods

A. Geometrical model

The model geometry represents the effective anatomy and shape of the human posterior chamber, which is bounded by the hyaloid membrane, the lens and the retina-choroid-sclera (RCS) membrane (Figure 1.A). The values of the radii of curvature of the retina and lens are equal to 0.85 cm and 0.55 cm, respectively. The retina and lens have two centers of curvature with respect to the hyaloid membrane, the posterior one of 0.61 cm, and the anterior one of 0.24 cm.

B. Governing equations

The fluid-dynamics of the vitreous is modelled by means of the Navier-Stokes and the continuity equations for a 3D unsteady incompressible Newtonian flow:

$$\rho \nabla \cdot \boldsymbol{u} = 0 \quad (1)$$

$$\rho \frac{\partial \boldsymbol{u}}{\partial t} + \rho(\boldsymbol{u} \cdot \nabla)\boldsymbol{u} = \nabla \cdot [-pI + \mu(\nabla \boldsymbol{u} + (\nabla \boldsymbol{u})^T)] \quad (2)$$

where ρ is the fluid density, $\boldsymbol{u}$ the fluid velocity vector, p the hydraulic pressure and μ the fluid viscosity. The vitreal density and viscosity are equal to 995.32 kg/m^3 and $7.3164 \cdot 10^{-4}$ Pa·s respectively, because we considered the high liquefaction for age-related diseases and the specific ocular temperature (T=34°C) [5].

C. Boundary conditions

We identified two kinds of boundary conditions, one related to the physiological surrounding around the posterior chamber and the other connected to the ocular saccadic movements. In particular, we imposed i) no aqueous permeation through the lens, ii) pressure at the posterior hyaloid surface equal to the physiological intraocular pressure

(IOP) and iii) normal velocity across the porous RCS membrane and defined as follows:

$$n \cdot v = Kp(p - Pv) \quad (3)$$

where Kp is the hydraulic conductivity ($5 \cdot 10^{-10}$ cm/Pa·s) [2] and Pv (1200 Pa) is the venous pressure downstream. Then, we implemented the real saccadic movement to all the external boundaries, connected to the rotation imposed by the extraocular muscles (Figure 2). This eye angular displacement relation consists in a fifth polynomial function with 50° of saccade amplitudes, the maximum angular displacement that a human eye can reach [3].

D. Mesh and computer code

Structured meshes (Figure 1.B), used to discretize the computational domains, and all the simulations were performed using the commercial software Comsol Multiphysics 5.2 (COMSOL Inc., Burlington, MA, USA).

III. Results

A. Effects of the physiological environment

We firstly simulated the effect of the physiological environment without considering the saccadic rotation. The results report an internal pressure equal to 2000 Pa in the entire posterior chamber and a steady permeating flow across the SCR membrane, with a mean velocity magnitude at the retinal surface and inside the vitreous chamber are $4 \cdot 10^{-7}$ cm/s and $1.08 \cdot 10^{-6}$ cm/s, respectively. The total volumetric flow through the retinal surface is 0.18312 µL/min. These results match with the data proposed by Stay *et al*.

B. Effects of the saccadic movements

In a second model, we considered only the ocular saccadic movement due to the extraocular muscles stimuli. The overall fluid-dynamics is quite different if compared to the previous one, particularly the mean velocity magnitude at the retinal surface and inside the vitreous chamber are definitely higher (3.705 cm/s and 0.612 cm/s, respectively). Figure 3.A-B shows the velocity distribution on the equatorial plane at specific time steps (the acceleration time t_P and the saccade duration D). Figure 4.A-B underlines the changes in wall shear stress distribution on the vitreous chamber wall. Shear stress values increase when the velocity of the movement is maximum ($t=t_P$) and decrease when the angular velocity tends to zero, due to the change in the angular motion direction (t=D). The maximum values of shear stress and velocity and the overall distribution are in accordance with previous studies [3].

C. Full CFD model

The full CFD model aimed at the description of the overall fluid-dynamics, considering the boundary conditions imposed in the previous models at the same time. The velocity distribution on the equatorial plane does not show huge differences if compared to the previous simulation (Figure 3.C-D), confirmed by the mean velocity magnitude at the retinal surface and inside the chamber (3.667 cm/s and 0.608 cm/s, respectively). Even if we do not report significant changes in wall shear stress on the lens and retinal surface (Figure 4.C-D), a higher volumetric flow rate (3.7 µL/min) due to the simultaneous presence of IOP, ocular saccadic rotation and Darcy's flow across the retina is noticed. Streamline analysis for the averaged flow field shows two main stagnant regions on the equatorial plane (Figure 5).

IV. Conclusion

The present study aims at implementing a fully CFD model of the posterior chamber of the eye. It overcomes the limitations of literature works and represents a generalized tool to predict the ocular fluid-dynamics. Our approach will be useful to study the transport mechanisms after intravitreal injections of drugs and the changes in fluid-dynamics due to specific diseases (e.g. glaucoma, age-related macular degeneration) and surgery (e.g. vitrectomy), by tuning the model parameters.

References

[1] B. Lee, M. Litt, and G. Buchsbaum. (1992). Rheology of the vitreous body. Part I: Viscoelasticity of human vitreous. *Biorheology 29(5-6)*. pp.521-533.

[2] M. S. Stay, J. Xu, T. W. Randolph, and V. H. Barocas. (2003). Computer simulation of convective and diffusive transport of controlled-release drugs in the vitreous humor. *Pharm Res*. *20(1)*. pp. 96–102. doi: 10.1023/A:1022207026982.

[3] O. Abouali, A. Modareszadeh, A. Ghaffariyeh, and J. Tu. (2011). Numerical simulation of fluid dynamic in vitreous chamber due to saccadic eye movement. *Med Eng Phys*. *34(6)*. pp. 681-692. doi: 10.1016/j.medengphy.2011.09.011.

[4] A. Modareszadeh, O. Abouali, A. Ghaffarieh, and G. Ahmadi. (2013). Saccade movements effect on the intravitreal drug delivery in vitreous substitutes: a numerical study. *Biomech Model Mechanobiol*. *12(2)*. pp. 281–290. doi: 10.1007/s10237-012-0398-3.

[5] M. R. Romano, J. L. Vallejo-Garcia, V. Romano, M. Angi, P. Vinciguerra, and C. Costagliola. (2013). *Thermodynamics of vitreoretinal surgery.*, *Current Eye Research*, *38(3)*, pp. 371-374. doi: 10.3109/02713683.2012.745160.

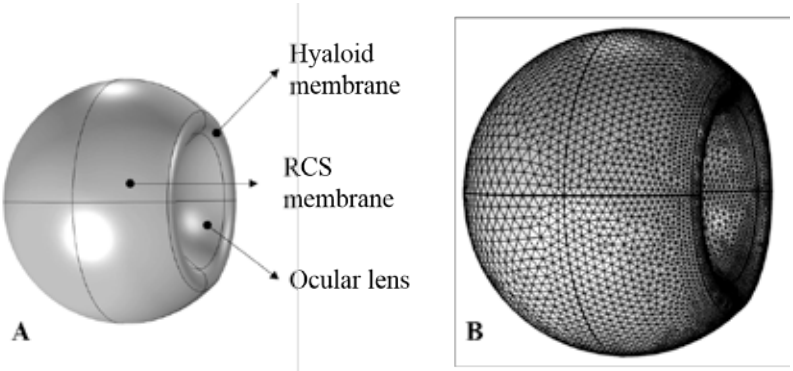

Fig. 1. Geometrical simplification of the ocular posterior chamber (A). Structured mesh used to discretize the whole CFD domain (B).

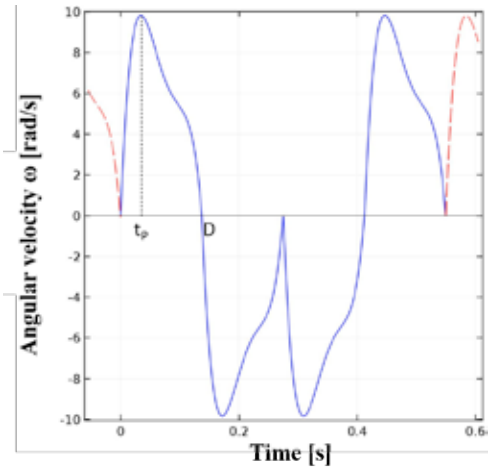

Fig. 2. The time law of the real saccadic rotation consists in four successive motions for each period, where a saccade to the left is followed by a return to the starting position and continues to the right at the same

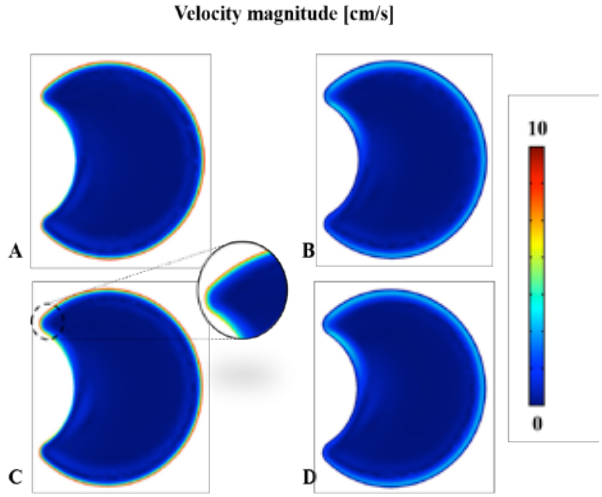

Fig. 3. Effects of the 50° saccadic movements in terms of velocity magnitude on the equatorial plane of the vitreous chamber at time t_P (A) and D (B). The full CFD model does not show significant changes (C, $t = t_P$ - D, t = D).

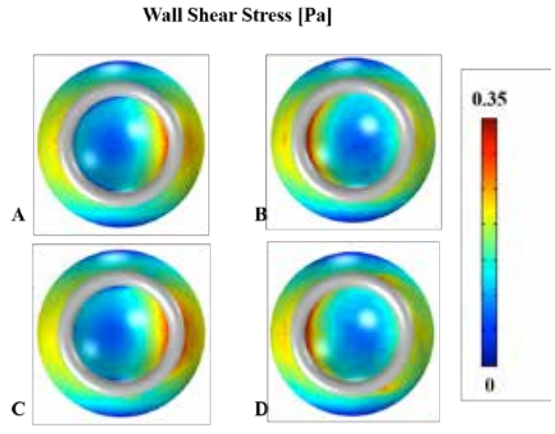

Fig. 4. Comparison of the wall shear stresses in presence of only the 50° saccadic movements (A, $t = t_P$ – B, t = D) and those obtained by the full CFD model (C, $t = t_P$ – D, t = D).

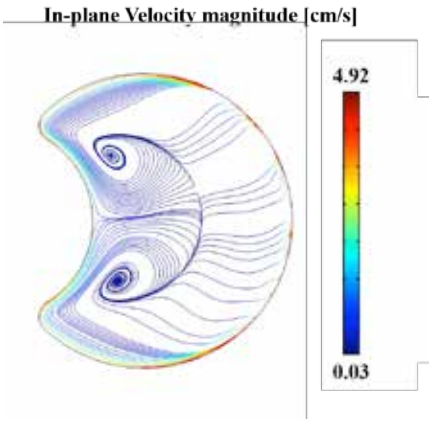

Fig. 5. Streamlines of averaged flow in equatorial plane of vitreous chamber computed by the full CFD model.

A novel pipeline for the analysis of the Multilayer Flow Modulator stent

A. Finotello[1], E. Faggiano[2], M. Conti[2], S. Morganti[2], G. Spinella[3], B. Pane[3], D. Palombo[3] and F. Auricchio[2]

[1] *University of Genova, Department of Experimental Medicine, Genova*
[2] *University of Pavia, Department of Civil Engineering and Architecture, Pavia*
[3] *Vascular and Endovascular Surgery Unit, University Hospital IRCCS San Martino-IST, Genova*

***Abstract*—The purpose of this work is to define a full framework for the analysis of the Multilayer Flow Modulator (Cardiatis, Isnes, Belgium) device in the repair of thoraco-abdominal aneurysms that provides reliable and accurate results to the surgeons. The framework includes an in-vitro study, a geometrical analysis and an in-silico investigation. In this work, the focus is given on the geometrical analysis. Therefore, geometrical indices to measure anatomical changes of the lumen and the aneurysm sac before and after the intervention are introduced. Results of the study for four patients with a two years follow-up are presented.**

***Keywords*—medical image processing, geometric analysis, TAA aneurysms, multilayer flow modulator.**

I. Introduction

Open surgery of thoraco-abdominal aortic aneurysm (TAAA) is the gold standard approach for treating such pathology but, endovascular aortic implantation can be considered a valuable alternative for patients who are not eligible for such an invasive procedure. The multilayer flow modulator (MFM) is an uncovered, self-expanding mesh of braided cobalt alloy representing a new paradigm to treat aortic aneurysms. Its main feature is to change the blood flow within the aneurysm, modifying turbulent to laminar flow and supporting the formation of organized, stable thrombus inside the aneurysm sac. As a consequence, the wall shear stress (WSS) is reduced protecting against the rupture. Thanks to device porosity, another important feature consists in the ability of maintaining perfused the side branches [1].

Clinical articles containing the firsts follow-up data of patients with Cardiatis can be found [2]. Engineering studies of the same subject are not in literature. In this context, a full engineering framework for the analysis of the MFM device represents an innovation. The study is intended to help clinicians understanding the feasibility of the intervention in TAAA using this novel device and interpreting the post-operative (short and long term) outcomes.

The overall project is divided into three tasks: in-vivo analysis, in-vitro experiments and numerical simulations. In detail, in vivo-analysis puts forth the aim of reconstructing aneurysms geometry and analyzing its changes in time, after the implantation of the MFM stent. In-vitro experiments aim at analyzing the performance of the stent in terms of porosity measuring the pressure drop through the surface of the stent. In-silico analyses integrate the previously mentioned studies simulating the hemodynamics around the stent for the quantification of WSS and flow behavior. In this paper main focus is given on the preliminary results of the in-vivo geometric procedure.

II. Methods

Through bioimaging techniques and geometrical analysis, starting from Computed Tomography (CT) images, we define a pipeline for the analysis of the geometric and morphological changes of the aneurysmatic lumen and thrombus induced by the implanted MFM device. The dataset is composed by CT images of four patients undergoing endovascular treatment at IRCCS AOU San Martino-IST, Genova. For each patient one pre-operative CT (*Pre*) and three post-operative CTs in the firsts two years of follow-up, at established times, were collected: immediately after intervention (*Post*), after 1 year (*1y*) and after 2 years (*2y*). International Review Broad approval was obtained for the conduct of this study, and the board waived the need for patient consent.

A. Segmentation and surface registration

Different segmentation processes are employed in order to extract the lumen, the MFM and the aneurysm region. A semi-automatic gradient-based level set method [3] is used to extract the lumen. A threshold technique (Hounsfield units >1000) is employed to recognize the stent region. A semi-manual technique is chosen to discern the aneurysm external wall. In particular, the manual contour of a reduced number of slices is extracted; then a 3D surface interpolation using radial basis functions is performed [4]. Later, the Iterative Closest Point algorithm [5] is used to register the follow-up surfaces to the pre-operative reference one.

B. Geometric analysis

Once segmented, we distinguish between the aneurysm, the total flow in the aneurysm sac and the residual blood flow, i.e. the blood that still flows outside the implanted stent. For each patient under study, we aim at verifying the presence or absence of blood flowing inside the aneurysm and the growth and the morphological changes of the aneurysm sac. To this end, geometric measurements on sections and volumetric indices are evaluated. Once observed that side branches remain perfused, they are eliminated from the reconstructed anatomical surface and only the principal lumen is considered [6]. Then, centerline of the vessel is computed and sections are generated, at given distances, perpendicular to this centerline. We remark that, thanks to the surface registration step, the sections are extracted at the same positions in all the pre-operative and post-operative surfaces allowing a direct comparison between different time instants. For each section we evaluate area, maximum and minimum diameter and a shape index that ranges from 0 to 1 where 1 signify a completely circular shape [7]. These

measurements are taken both for the lumen and for the total aneurysm sac.

We also evaluate some volumetric indices. First of all, we consider the total aneurysm volume (v_{tot}) and the percentage of aneurysm growth in comparison with the pre-operative configuration ($v_{tot\%}$). Residual flow volume (v_{rf}) and the percentage of total flow growth in comparison with the pre-operative blood-flow configuration ($v_{l\%}$) are also estimated. Finally, we have introduced the *RTR* ratio (see Eq. (1)), which is a 3D size index related to the percentage of intraluminal thrombus in the aneurysm sac.

$$RTR = \left(1 - \frac{v_{rf}}{v_{tot} - v_{fi}}\right) \cdot 100 \qquad (1)$$

where v_{fi} is the volume of blood inside the MFM. A value of 100 % indicates a complete thrombization of the aneurysm.

III. Results

In Fig. 1 the geometric 3D reconstructions of the four patients are reported. We take the configuration *Post* as an example. Red color refers to the circulating flow, yellow to the MFM and green to the intraluminal thrombotic zone. In Fig. 2 the results obtained from the analysis on sections are presented. Considering the lumen section area, for Patient 1 we observe that after 1 year the blood flows completely inside the stent while after 2 years there is a new increment.

TABLE I
VOLUMETRIC INDICES

		v_{tot} (10^5 mm^3)	$v_{tot\%}$	v_{rf} (10^5 mm^3)	$v_{l\%}$	*RTR*
Patient 1	*Pre*	2.8				
	Post	3.9	38 %	0.5	17 %	77 %
	1y	3.8	37 %	0.1	-14 %	94 %
	2y	5.2	79 %	1.0	42 %	71 %
Patient 2	*Pre*	1.1				
	Post	1.1	11 %	0.4	-12 %	61 %
	1y	1.6	47 %	0.5	24 %	58 %
	2y	2.1	94 %	0.8	53 %	58 %
Patient 3	*Pre*	3.8				
	Post	3.9	3.2 %	1.4	40 %	48 %
	1y	4.3	13 %	0.95	17 %	69 %
	2y	4.8	26 %	1.0	24 %	70 %
Patient 4	*Pre*	2.1				
	Post	2.1	0.1 %	0.2	-10.8 %	87 %
	1y	1.95	-6.7 %	0.185	-11.7 %	88 %
	2y	1.9	-9.5 %	0.135	-12.9 %	90 %

Volumetric indices for all patients in pre-operative and post-operative configurations are calculated.

The total aneurysm remains stable until 2 years when a sudden growth is detected. Patient 2 is characterized by a gradual increase in time of both lumen and aneurysm area sections. For the Patient 3 after 1 year, the lumen areas have decreased in the proximal region but increased in the distal one. Aneurysm important growth is observed only after 2 years. Trend reversal is observed for Patient 4: both the lumen section areas and the aneurysm section areas decreased.

In Table I results of the volumetric indices are reported. Considering the aneurysm sac, for the first and the second patient, a nearly linear growth is observed. Patient 3 has a little growth of the aneurysm while for Patient 4 a volume reduction is detected. After 1 year, *RTR* index of Patient 1 has increased until 94 % indicating a nearly full thrombosed sac. For Patient 2 and Patient 4 *RTR* index does not change in time, but the latter is fixed at a higher value (≈90 %). In Patient 3 an important thrombization process is observed in the first year (*RTR* from 48 % to 69 %) followed by a stabilization.

In Fig. 3 a signed distance computed between the *Pre* and the *2y* configuration is presented to graphically illustrate the aneurysm zones where the maximum volumetric changes occurred.

IV. Conclusions and Future Developments

We have defined a new pipeline for the geometric analysis of aneurysms treated with the MFM device. The dataset is composed of four patients affected by TAAA of different geometrical shape. They are also characterized by an extremely different behaviour in terms of MFM implantation response. Therefore, our pipeline has been proved and is able to provide multiple and accurate results for any aneurysm shape and for any morphological change in time.

This is a first step within a larger project for the study of MFM feasibility.

References

[1] M. Henry, A. Polydorou, N. Frid, P. Gruffaz, A. Cavet, I. Henry et al., "Treatment of renal artery aneurysm with the Multilayer stent" in *J. Endovasc. Ther.* 2008

[2] M. Henry, A. Benjelloun and I. Henry, "The Multilayer Flow Modulator stent for the treatment of arterial aneurysms concept-Indications-contraindications", in *Journal of Indian College of Cardiology.* 2015.

[3] L. Antiga, M. Piccinelli, L. Botti, B. Ene-Iordache, A. Remuzzi, and D.A. Steinman, "An image-based modeling framework for patient-specific computational hemodynamics." in *Medical & biological engineering & computing*, 46(11), 1097-1112. 2008

[4] A. Fetzer, S. Zelzer, T. Schroeder, H.P. Meinzer and M. Nolden, "An interactive 3D segmentation for the Medical Imaging Interaction Toolkit (MITK) ", Conference: MICCAI, At Harvard Medical School, Boston, MA, United States, Volume: Proc MICCAI IMIC (Interactive Medical Image Computing). 2014.

[5] P.J. Besl and N.D. McKay, "A Method for registration of 3-D shapes" in *Proceedings of Spie- The International Society for Optical Engineering,* 14(3):239-256. 1992

[6] L. Antiga and D.A. Steinman, "Robust and objective decomposition and mapping of bifurcating vessels." in *IEEE Trans Med Imaging.* 2004

[7] M. Piccinelli, D.A. Steinman, Y. Hoi, F. Tong, A. Veneziani, and L. Antiga, "Automatic neck plane detection and 3D geometric characterization of aneurysmal sacs" in *Annals of Biomedical Engineering,* Vol. 40, No.10, pp.2188-2211. 2012

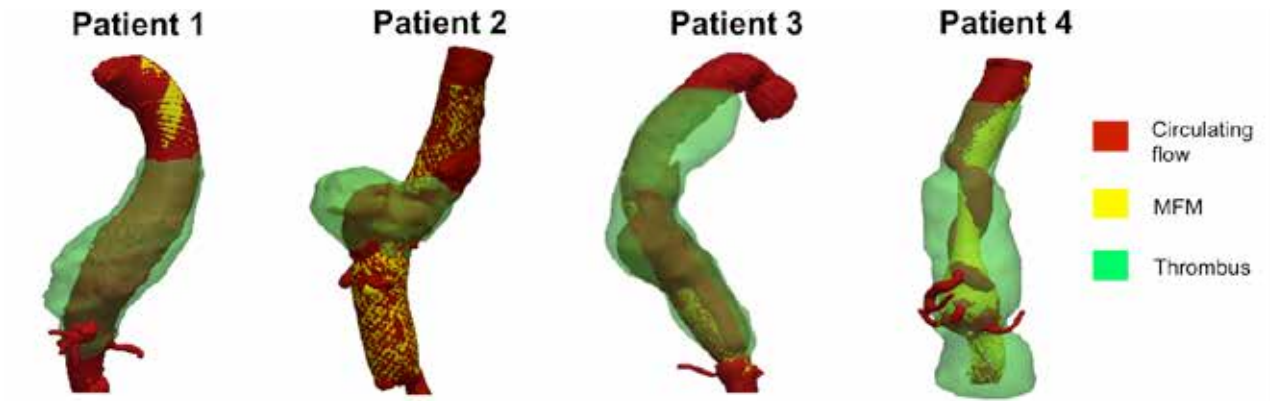

Fig. 1. 3D reconstructions concerning the configuration *Post* are depicted.

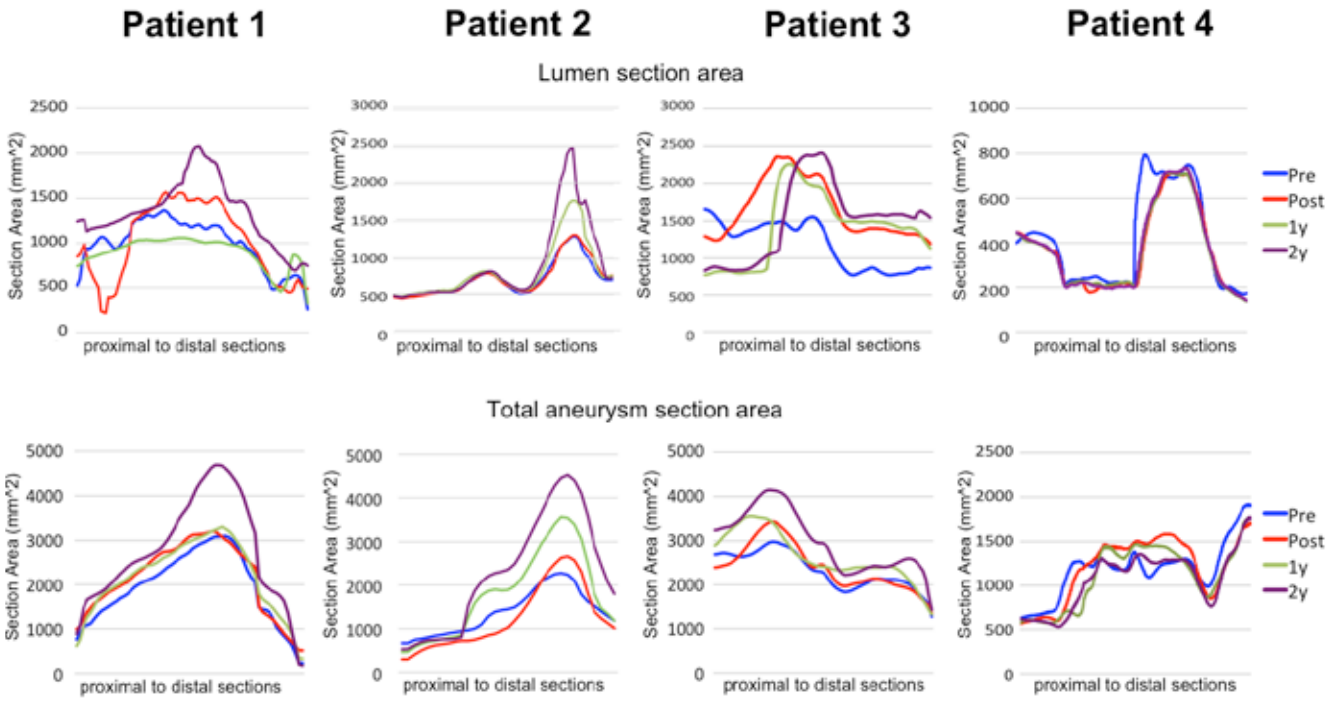

Fig. 2. Geometric indices on sections: total lumen area and total aneurysm area, for the four patients in all time configurations are considered.

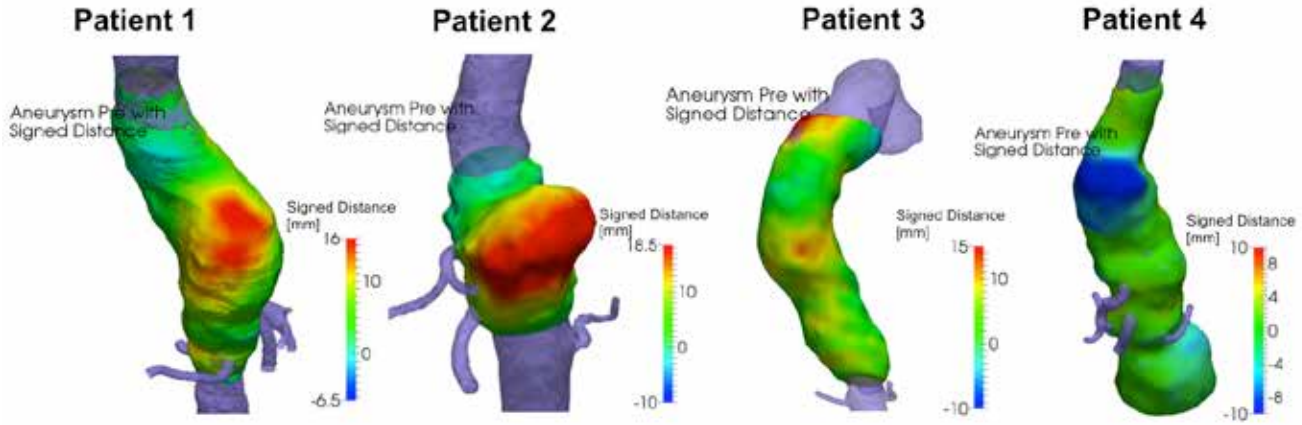

Fig. 3. For all patient signed distance between the pre-operative and the last (2y) configuration is depicted.

Experimental/computational approach of the nuclear pore complex mechanics

A García[1], R Marotta[3], M Tunesi[1], MM Nava[1], R Fedele[2], E Jacchetti[1], JF Rodríguez Matas[1] and MT Raimondi[1]

[1] *Department of Chemistry, Materials, and Chemical Engineering Giulio Natta Politecnico di Milano, Italy.*
[2] *Department of Civil and Environmental Engineering (DICA) Politecnico di Milano, Italy.*
[3] *Electron microscopy lab, Nanochemistry Department Istituto Italiano di Tecnologia, Genoa, Italy*

***Abstract*—Recent findings have shown that nuclear distortions may alter the import flux of transcription factors toward the nucleus and control the expression of genes and the protein synthesis. A possible mechanism of such a mechanosensory system resides in the nuclear pore complex (NPC). NPCs are generally considered sites of active transcription. Here we hypothesized that cell-stretching forces can mechanically activate the pore, thus allowing faster diffusivity of molecules. To this purpose, we recreated the two extreme nuclear deformation conditions (spread and round). Cell nuclei were imaged by confocal microscopy and by scanning transmission electron tomography (STEM) to asses nuclear and pore features. We also developed a multyphysics model accounting for the change in permeability in response to deformation. We found an increase in the nuclear envelope (NE) surface by up to 50% in deformed cells. Non-significant differences in both shape and size of the reinforcement ring of single NPCs with NE deformation. The computational simulations show that NE-NPC structure predominates compared to the NPC structure.**

***Keywords*—Nuclear Pore Complex, Nuclear Envelope, Diffusion, Permeability.**

I. Introduction

A basic recent understanding in stem cell differentiation is that the cell is able to translate its shape (e.g. roundish or deformed) into a fate decision. However, the mechanisms by which phenotype expression is regulated by cell shape are complex and poorly understood. Our hypothesis is that cell deformation induces nuclear deformation, which in turn causes strains in the nuclear envelope (NE). This induces a change in porosity and in permeability of the NE that affects the flux of transcription factors involved in stem cell differentiation [1]. To demonstrate this hypothesis, we set-up a numerical model of the interaction between the nuclear pore complex (NPC) and the NE.

II. Material and methods

Firstly, we recreated the two extreme deformation conditions for the NE. We isolated mesenchymal stromal cells (MSC) from the bone marrow of adult rats. To recreate the deformed configuration, we processed the cells for microscopical analysis when they were in adhesion to a flat culture substrate. On the contrary, to recreate the roundish configuration, we fixed and processed the cells in suspension. In both configurations, we acquired images of the whole nuclei by scanning confocal microscopy, to measure the NE deformation. In addition, we reconstructed 3D portions of the NE by scanning transmission electron tomography (STEM), see Fig. 1 and Fig. 2, to measure geometrical parameters of the NPC size/shape.

Secondly, in order to couple a change in permeability of the NE at the microscale with a change in configuration of a single NPC at the nanoscale (in response to the deformation applied to the NE), we fed the measured data into a computational model of the NPC-NE mechanical interaction.

III. Results

Our preliminary results show an increase in the NE surface by up to 50% together with a significant change of the local NE curvature in deformed cells, compared to roundish ones. However, we found non-significant differences in both shape and size of the reinforcement ring of single NPCs with NE deformation.

IV. Conclusion

The computational simulations show that the highly different mechanical response of the NE structure, compared to the NPC structure, predominates in determining the change in porosity of the NE in response to the applied strains. This result is consistent with experimental published evidences showing a dramatic change in NPC density and shape in cells lacking lamin, an essential nuclear protein anchoring the NPCs to the NE [2].

Acknowledgement

Manuela Teresa Raimondi has received funding from the European Research Council (ERC) under the European Union's Horizon 2020 research and innovation programme (grant agreement No 646990 - NICHOID).

References

[1] Nava et al. "*Computational prediction of strain-dependent diffusion of transcription factors through the cell nucleus,*" Biomech Model Mechanobiol, 2015, pp 1-11.

[2] Giacomini et al. "*Lamin B1 protein is required for dendrite development in primary mouse cortical neurons,*" (2015) Mol Biol Cell, doi:10.1091/mbc.E15-05-0307

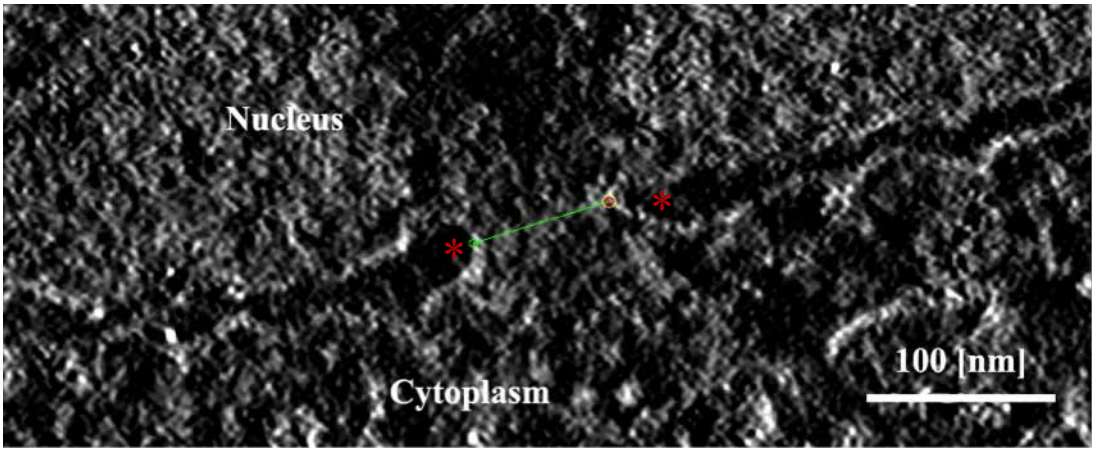

Fig. 1. Single tomographic slice through the nuclear envelope of a MSC cell grown in suspension. The highlighted distance (green) in the nuclear envelope (asterisks) corresponds to a nuclear pore complex.

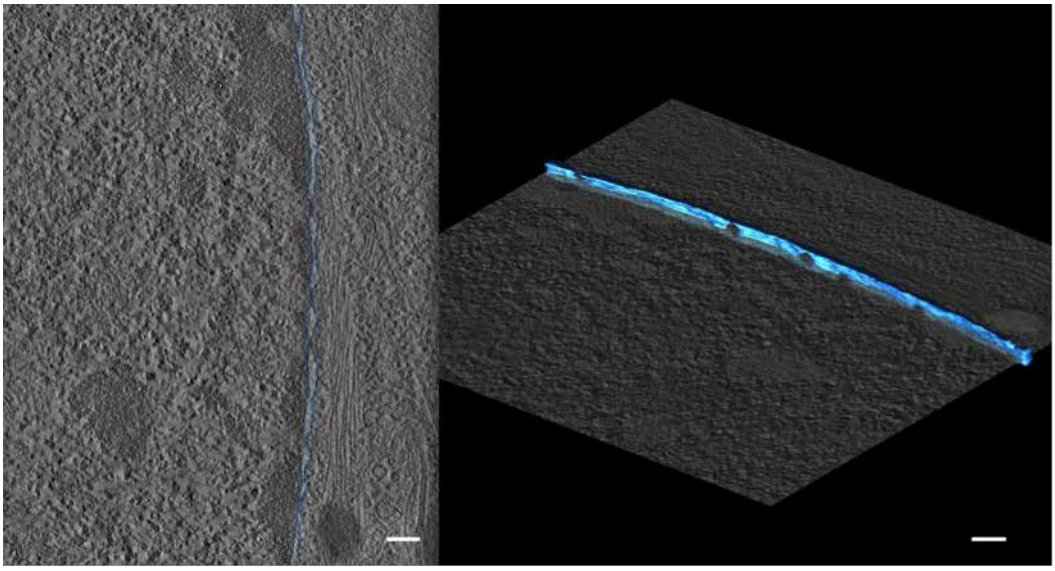

Fig. 2. Slice segmentation (blue-left image) and corresponding 3D reconstruction (blue-right image) of the nuclear envelope of a MSC. In the images it is possible to properly differentiate the location of four Nuclear Pore Complexes. The scale bar in both images corresponds to 150 [nm].

A microfluidic stretchable device for generation of multiaxial deformation patterns

S.M. Giannitelli[1,2], A. Gizzi[1,2], C. Cherubini[1], L. Businaro[2,3], M. Trombetta[1,2], and A. Rainer[1,2]
[1] *Department of Engineering, Università Campus Bio-Medico di Roma, Rome, Italy*
[2] *UCBM-CNR Joint Lab for Nanotechnologies for the Life Sciences (nano4life), Rome 00128, Italy*
[3] *Institute of Photonics and Nanotechnology-CNR, Rome 00156, Italy*

***Abstract*—We present a novel microfluidic device for the induction of complex multiaxial deformation patterns onto a stretchable porous elastic membrane. Here we report mathematically informed design, fabrication and validation of the device, which is currently under investigation for prospective application as a (co-)culture platform for excitable cells.**

***Keywords*—Microfabrication, Multiaxial cell stretching, Biomechanical optimization, Multiphysics *in silico* modelling.**

I. Introduction

In vitro cell/organ-on-a-chip models of biological microenvironments represent an emerging tool to study complex biological systems mimicking *in vivo* conditions [1]. This approach, coupling co-culture protocols, biomechanical engineering optimization and microfluidic technologies, allows to provide a high degree of control over the experimental parameters exploiting the power of modern microscopy tools, often not applicable in *in vivo* experiments [2].

Although microfluidic stretchable devices have been already developed and successfully used to study cell response under different mechanical stimuli [3], [4], a multiaxial dynamic control of cell strain is still under exploitation. In this perspective, a novel multiaxial microfluidic stretchable device is presented, which has been designed and fabricated by soft-lithographic techniques.

Realistic three-dimensional simulations of the device have been conducted via dedicated numerical modeling. The synergistic use of advanced theoretical modeling of cells and tissue electro-mechanics, microfabrication technologies and actuated 3D multilayer cultures allow for a better control of the microenvironment and represent an advanced tool for in *in vitro* research studies.

II. Materials and Methods

A. Chip design

The device consisted of two superimposed 3 x 3 mm^2 chambers separated by a porous membrane. Vacuum-driven actuators were purposely designed for multiaxial stretching of the porous membrane. Chip design also included microfluidic channels for selective perfusion of the upper and lower chambers.

B. Theoretical modelling and numerical simulation

Design optimization was performed by Finite Elements Analysis. Accurate solution of micro-features (up to 10 μm) was ensured via mesh sensitivity analysis performed over three discretization levels. The finest mesh level consisted of $\sim 4 \cdot 10^5$ tetrahedral quadratic elements and $\sim 1.5 \cdot 10^6$ degrees of freedom. The numerical solution was obtained by using Comsol Multiphysics 5.2 (COMSOL Inc., Burlington, MA) on a HP Z-800 multiprocessor workstation (192 GB RAM). The computational time was ~15 min using ~30 GB RAM.

C. Device fabrication

The device was fabricated by replica molding of polydimethylsiloxane (PDMS) starting from a silicon master with the desired relief pattern. Master molds were fabricated with SU8-2075 negative photoresist (Microchem, Newton, MA) following a standard photolithographic process according to the manufacturer's instructions. The two halves of the chip (representing the upper and lower microchannel layers) were individually prepared by casting PDMS (10:1 v/v pre-polymer to curing agent ratio) on the microfabricated mold, followed by thermal curing.

The porous membrane was prepared by a soft-lithographic technique casting PDMS (15:1 v/v ratio) onto a photo-lithographically obtained silicon master containing arrays of circular pillars.

The two chip halves with interposed porous membrane were accurately aligned and bond together by oxygen plasma activation.

D. Device actuation

Actuation of the device was performed by applying controlled vacuum levels (in the 0-600 mbar range at 50 mbar steps) at each actuator inlet using a multichannel programmable pressure controller (Elveflow OB-1 controller).

Membrane stretching was observed under a fully motorized inverted optical microscope (Nikon Ti-E) equipped with a high speed camera (Andor NEO 5.5) and control software (NIS-Elements AR).

Displacement field was calculated by particle tracking algorithm that was applied to the micrograph sequences using membrane pores as an interpolating mesh.

Equibiaxial loading patterns were studied and compared with the results of *in silico* analysis.

III. Results and Discussion

A. Device performance

Figure 1 shows the optimized geometry resulted from in silico analysis (Fig. 1A) and the corresponding microfabricated device (Fig. 1B). Thickness of the porous

membrane (10 μm) and geometry of vacuum actuators were designed as a result of in silico optimization.

Figure 2 reports a representative example of design validation. Figure 2A shows the results of numerical simulations for an applied vacuum level of 600 mbar, while Figure 2B illustrates the experimentally calculated displacement field derived from particle tracking applied to micrograph datasets. Good agreement (less than 5% error) between experimental and in silico data was reported.

The strain field (calculated from displacement datasets) gave a central circular region of ca. 1 mm diameter characterized by a relatively constant strain level (ca. 7%), in agreement with the in silico model.

IV. Conclusion

A novel microfluidic stretchable devise has been designed and successfully fabricated on the base of *in silico* optimization analysis. Good agreement between experimental and finite element analysis results has been achieved in the case of equibiaxial loading patterns.

Acknowledgement

This work is supported by Università Campus Bio-Medico di Roma (Internal Grant Program).

References

[1] A.R. Perestrelo, A.C. Águas, A. Rainer, and G. Forte, " Microfluidic Organ/Body-on-a-Chip Devices at the Convergence of Biology and Microengineering," *Sensors*, vol. 15, pp. 31142-31170, 2015.

[2] S.N. Bhatia, and D.E. Ingber, "Microfluidic organs-on-chips," *Nature biotechnology*, vol. 32, pp. 760-772, 2014.

[3] H.J. Kim, D. Huh, G. Hamilton, and D.E. Ingber, "Human gut-on-a-chip inhabited by microbial flora that experiences intestinal peristalsis-like motions and flow," *Lab on a Chip*, vol. 12, pp. 2165-2174, 2012.

[4] D. Tremblay, S. Chagnon-Lessard, M. Mirzaei, A.E. Pelling, and M. Godin, "A microscale anisotropic biaxial cell stretching device for applications in mechanobiology," *Biotechnology letters*, vol. 36, pp. 657-665, 2014.

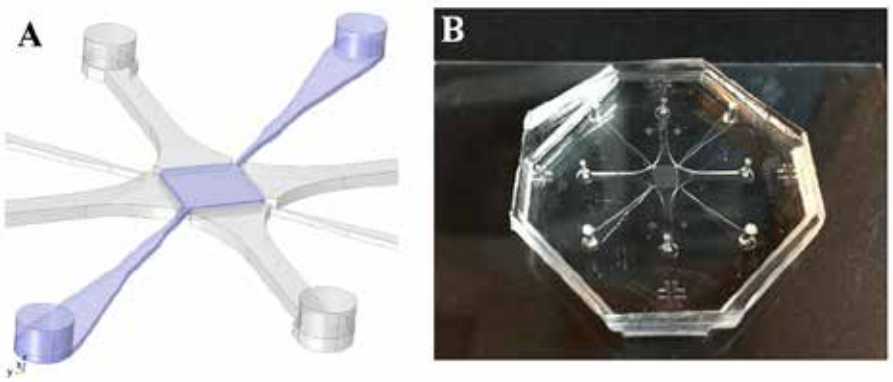

Fig. 1. 3D schematization of chip geometry obtained by in silico optimization (A) and microfabricated PDMS microfluidic devise (B).

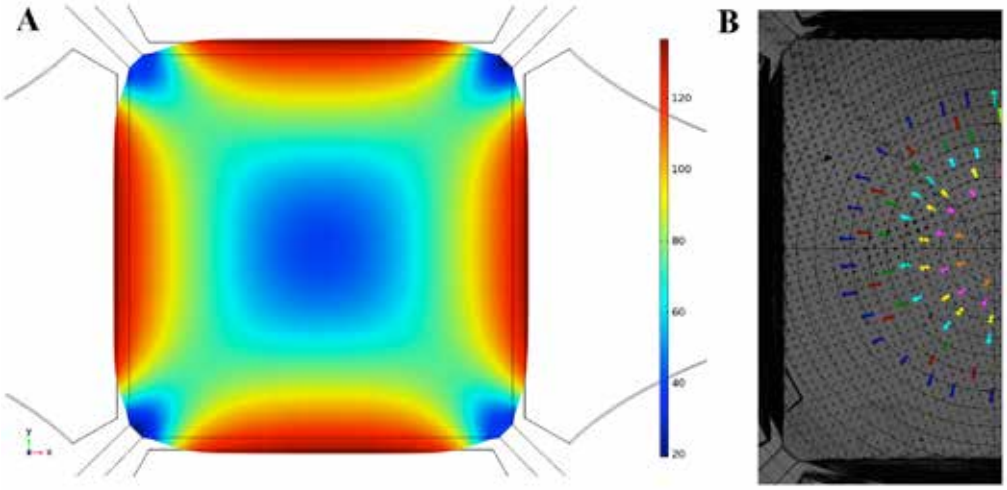

Fig. 2. Color map of membrane displacement for an applied vacuum level of 600 mbar: (A) finite element simulation and (B) experimental results. Displacements are expressed in μm.

Comparison of standard and minimally invasive decompression techniques for lumbar spinal stenosis

C. Ottardi[1], F. Costa[2], A. Ortolina[2], T. Bassani[3], D. Volkheimer[4], H-J.Wilke[4], F. Galbusera[3], T. Villa[1,3]
[1] *LaBS, Department of Chemistry, Materials and Chemical Engineering "G. Natta", Politecnico di Milano, Italy*
[2] *Department of Neurosurgery, Humanitas Clinical and Research Center, Rozzano, Italy*
[3] *IRCCS Istituto Ortopedico Galeazzi, Milano*
[4] *Institute of Orthopedic Research and Biomechanics, Ulm University, Ulm, Germany*

***Abstract* — Lumbar spinal stenosis can be surgically treated with traditional or minimally invasive decompression techniques. This study was focused on the comparison between different techniques, by means of in vitro testing on human spinal specimens. A spine tester was used to apply pure moments along three axis. The range of motion (ROM) and the neutral zone of the intact and decompressed specimens (after each resection step) was calculated. The unilateral laminotomy exhibited only small variations with respect to the intact spine. Also the minimally invasive laminectomy caused only minor changes of the flexibility. Two levels decompression caused greater differences on the ROM and the spinal instrumentation was always effective for the stabilization.**

Both minimally invasive and standard decompression techniques caused minor destabilization at the treated level.

***Keywords* — Spine biomechanics, Lumbar spinal stenosis, laminotomy, flexibility tests.**

I. INTRODUCTION

LUMBAR spinal stenosis (LSS) is usually described as a reduction of the spinal canal volume, which can also trap the nerve roots causing pain and radicular symptoms [Aebi et al. 2008]. This pathology is often caused by disc degenerations and protrusion, osteophytes formation or hypertrophy of the flaval ligament. The clinical options are conservative treatments followed by decompressive techniques when the first strategy fails. Several surgical techniques can be employed (depending on the type of stenosis) in order to enlarge the spinal canal allowing the decompression of the nerve roots.

-Laminectomy: is the traditional technique used to cut the whole lamina, the spinous process and the involved ligament (usually flaval, supraspinous and interspinous);

-Laminotomy: is a minimally invasive technique that consists in the removal of part of the lamina, preserving the supraspinous and interspinous. The flaval ligament normally is removed;

-Facetectomy: this technique is the partial or total removal of the facets.

All the techniques can be performed monolaterally or bilaterally. Even if the rate of success of the surgical procedure is high, clinical studies identified a risk of instability suggesting the instrumentation with spinal fixators problems [Aebi et al. 2008].

The goal of this study was to perform an in vitro characterization of the spine, following minimally invasive or traditional surgical decompression techniques. The flexibility of the intact, destabilized and subsequently instrumented spine was calculated.

II. MATERIAL AND METHODS

Six human specimens of healthy lumbar spines were tested. The study was performed using a spine tester, able to reproduce pure unconstrained moments along three axis in order to simulate flexion-extension, lateral bending and axial rotation. Therefore, 7.5 Nm were applied in all the directions of movement without preload. A motion capture system was used to acquire the movement of each motion segment and consequently calculate range of motion (ROM) and neutral zone (NZ) of each specimen.

Several decompression techniques were reproduced, using an incremental damage approach (Fig. 1). After the two steps, equally performed on all the specimens the samples were divided in two groups:

1- Intact specimen (n=6);
2- Unilateral laminotomy for bilateral decompression at L3-L4 (UNI-1L, n=6);
3a- Minimally invasive laminectomy at L3-L4 (BI-1L, n=3) and spinal fixation at L3-L4;
3b- Unilateral laminotomy for bilateral decompression at L4-L5 (UNI-2L, n=3);
4b- Minimally invasive laminectomy at L4-L5 (BI-2L, n=3) and spinal fixation at L3-L4.

A neurosurgical drill was used to create the decompressions and flexibility tests were performed after each resection.

A statistical analysis was conducted on the steps having 6 samples.

III. RESULTS

Unilateral laminotomy for bilateral decompression (UNI-1L) at L3-L4 had only a slight influence on the ROM, for all the typical movements of the spine (Fig. 2). The statistical analysis showed a not significant 8% increase of the ROM in flexion-extension. Conversely, the variation of the NZ resulted significant, with an increase of about 30%. In addition, the lateral bending showed significant differences

for both ROM and NZ. The axial rotation revealed a significant variation of ROM and NZ only on the left side.
Performing a minimally invasive laminectomy at the same level (BI-1L) did not cause significant changes.
The surgical techniques performed on two level led to higher variations.
The posterior instrumentation with spinal fixators greatly stabilized the spine, increasing the stiffness of the construct.

IV. DISCUSSION

This biomechanical study supported the finding that decompression techniques are able to preserve the physiological stability of the treated levels, considering either ROM or NZ. The limited number of samples did not allow a statistical analysis of all the surgical techniques. However, various interesting clinical findings can be drawn. First, the bilateral decompression obtained following unilateral laminotomy resulted slightly relevant thus, its role in inducing iatrogenic instability is negligible. The minimally invasive laminectomy did not produce a substantial instability. Also in literature the effect of minimally invasive decompressions was judged marginal [Ivanov et al 2007].
Extending the decompressions on the second level (L4-L5) induced higher changes, probably due to the higher flexibility of the lower lumbar segment. Therefore, a decompression performed at this motion segment may be more critical increasing the risk of destabilization.

V. CONCLUSION

The results of the biomechanical testing showed that the unilateral laminotomy for bilateral decompression caused only minor destabilization at the treated level, considering ROM and NZ. Also the minimally invasive technique had a small effect on the biomechanics. Thus, it can be stated that both techniques are safe and equally effective from a biomechanical perspective.

VI. ACKNOWLEDGEMENTS

The work has been funded by the Italian Ministry of Health (project GR-2011-02351464). Pedicle screws and rods have been provided for free by Sintea Plustek Srl (Assago, Italy). The microdrill has been loaned by Tekmed Instruments Spa (Rozzano, Italy).

REFERENCES

[1] M. Aebi, N. Boos and I. Zintel. “Spinal Disorders. Fundamentals of Diagnosis and Treatment”, *Springer*, 2008, pp. 513-533.
[2] A. Ivanov, A. Faizan, K. Sairyo, N. Ebraheim, A. Biyani, VK. Goel, “Minimally invasive decompression for lumbar spinal canal stenosis in younger age patients could lead to higher stresses in the remaining neural arch - a finite element investigation”, *Minim Invasive Neurosurg,* 2007, 50(1):18-22.

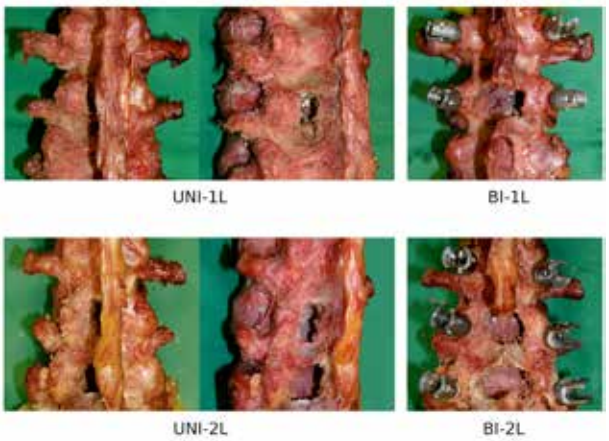

Fig. 1 Decompression and stabilization procedures performed on the specimens: unilateral laminotomy at L3-L4 ("UNI-1L", n=6 specimens); bilateral laminotomy at L3-L4 ("BI-1L", n=3); unilateral laminotomy at L3-L5 ("UNI-2L", n=3); bilateral laminotomy at L3-L5 ("BI-2L", n=3).

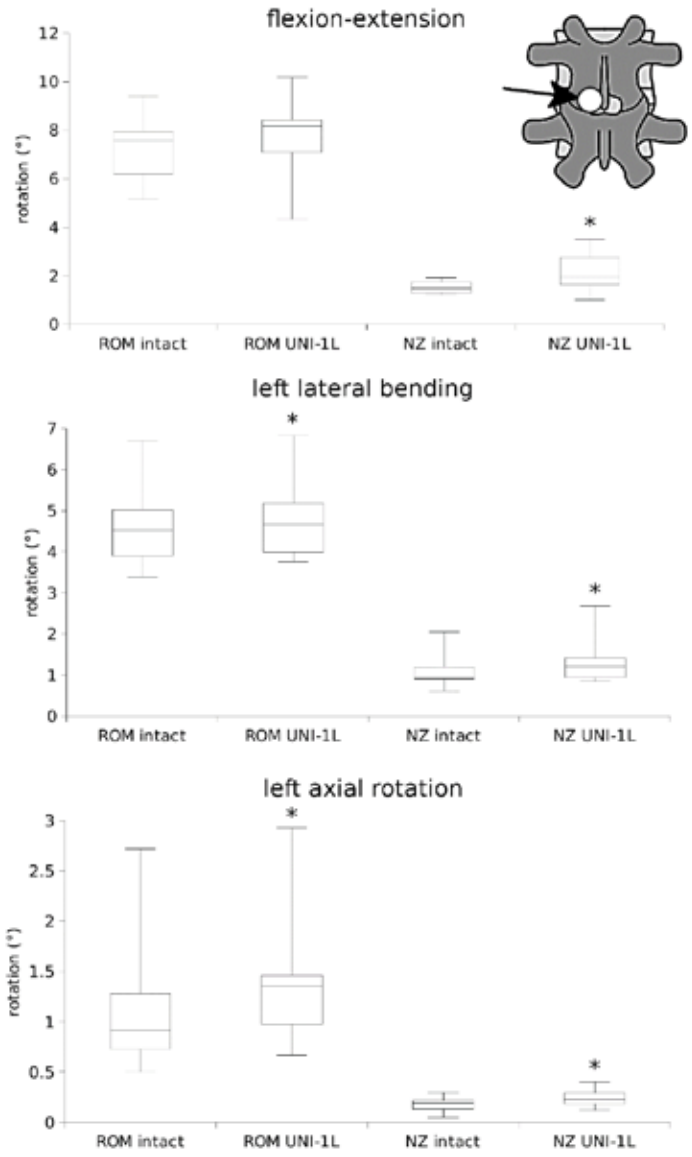

Fig. 2 Statistical comparison of the range of motion (ROM) and of the neutral zone (NZ) between the intact specimens and those subjected to unilateral laminotomy at L3-L4 ("UNI-1L"), in flexion-extension, left lateral bending and left axial rotation. "*" indicates a statistically significant difference ($p<0.05$) between the intact and the decompressed condition (n=6).

The evaluation of strain on spine segments in a contactless way and full-field view

M. Palanca[1], M. Marco[1, 2], K. Ożóg[1, 3], and L. Cristofolini[1]
[1] School of Engineering and Architecture, Alma Mater Studiorum – Università di Bologna, Italy
[2] Department of Mechanical Engineering, University Carlos III of Madrid, Spain
[3] Dept. of Biomedical Eng. Mechatronic and Theory of Mechanisms, Wroclaw Univ. of Technology, Poland

***Abstract*—The strain distribution was never studied in spine segments (vertebrae and intervertebral discs) due to its complex geometry and structure. DIC allowed measuring the displacements and strains on the surface of a specimen in a contactless way and providing full-field view. After a validation to estimate the DIC measurement uncertainties, a speckle pattern was prepared on porcine spine segments and then the spines were tested in a loading machine until failure. DIC measured displacement and strain, simultaneously, on the surface of vertebrae and intervertebral discs. Failure strain on vertebrae around 10000 microstrain and on intervertebral discs around 70000 microstrain, proved the measurement reliability and a new way to test spines and increase the present knowledge.**

***Keywords*—Spine, experimental tests, imaging, Digital Image Correlation**

I. Introduction

SPINE is one of the most complex and vital structure in the human skeletal apparatus [1]. Diseases related to spine could involve in pain and immobility, with a series of complications that reduces the life quality [2]. Due to these reasons, knowing the biomechanics of spine is really important in a society that increases the longevity year after year. Until now, the combination of soft tissues (intervertebral discs) and hard tissues (vertebrae), that composes the spine, made impossible the evaluation of displacements and strains under physiological loading conditions with traditional measurement techniques (e.g. strain gauges). In the last years Digital Image Correlation (DIC) changed the scenario of the traditional measurement techniques in biomechanics [3] allowing the computation of displacements, and through differentiation, strains in a contact-less way and providing a full-field view of the examined surface.

This work want to explain a protocol of validation of DIC system, in order to define the measurement uncertainties, and a strain measurements procedure on multi-vertebrae segment, in a contactless way and full-field view, using DIC.

II. Material and methods

A. The validation and optimization of DIC

A commercial 3D-DIC system (Q400, Dantec Dynamics, Denmark), with two 5Mpix cameras and 35mm lens, was used to measure the strain. Before starting to use DIC as a reliable tool, an estimation of the strain uncertainties was performed. A flat aluminium beam was covered with optimized speckle pattern [4] to allow a univocal identification of the surface. Two images of the beam (resolution of 30 μm/pixel) were acquired by the system in a zero-displacement and zero-strain condition (fixed and unloaded). A region-of-interest (ROI) similar to the frontal projection of a three-multi-vertebrae segments was defined on the beam, in order to have the spatial condition as similar as the spine test. A three-parameters factorial design was implemented to investigate the effect of the key parameters of DIC (facet size, grid spacing and filtering on displacement field) on the strain measurements; in terms of systematic and random error, respectively, the average and standard deviation of the measurement point over ROI, and so as to minimize the strain measurement uncertainties.

B. The preparation of specimens

Segments of three/four vertebrae were extracted from porcine lumbar spines. All the soft tissues and spinal processes of external vertebrae were removed with surgical tools and without damage the specimen. In order to create a speckle pattern in the best way possible on soft (intervertebral discs)[5] and hard (vertebrae) tissues the specimens were stained with methylene-blue-saturated water solution for 6 times every 15 minutes, to prepare the dark background. Instead, the white speckle pattern was created through an airbrush airgun [4, 6] using a water-based paint, to minimize interactions, which could damage the bone tissue (Fig. 1). Finally, to enable mechanical testing in loading machine parallel basis were prepared potting external vertebrae in poly-methyl-methacrylate till half of their height.

C. In vitro loading tests

The spine segments were tested in pure axial loading and in isostatic conditions. In order to avoid transmission of any additional load a homemade setup was built using low-friction linear bearings and ball joint. The load was applied through a loading machine in position control, using a monotonic ramp, running at 1mm/s, until failure. Images of specimens under loading were recorded at 6.8 Hz. Using the optimized parameters setup, the displacements and strains were evaluated on the entire frontal surface of the specimens.

III. Results

A. The optimized DIC parameters

The better compromise between measurement uncertainties and spatial resolution was obtained with a facet size of 33 pixels, a grid spacing of 19 pixels and a filter of displacement over a 5x5 data grid. The resultant systematic and random

errors were, respectively, of 10 microstrain and under 100 microstrain. The above-mentioned key parameters will be used for the strain measurement on spine as well, obtaining an equivalent measurement surface for each measurement point, similar to the one of strain gauge.

B. The results of loading tests

Displacement and strain were evaluated on the entire frontal surface of the multi-vertebrae specimen, in both the tissue (intervertebral discs and vertebra) up to failure. The axial strain (Fig. 2) in the vertebrae, prior to failure, was under 10000 microstrain; while in the intervertebral discs, where started the failure, the strain exceeded 70000 microstrain.

IV. DISCUSSION

The evaluation of the measurement uncertainties guaranteed the setting of the best parameters setup and to know the reliability of the measurement tool before starting to use it on complex specimens, such as biological ones. Strains were evaluated on the entire ROI without any loss of information, showing the suitability of the speckle pattern prepared in a non-conventional way [3]. Moreover, no variations, in terms of measurement uncertainties, were reported respect the traditional speckle pattern [4]. The evaluated failure strains were in agreement with the literature [7, 8] but, according to the authors' best knowledge, no-one performed this kind of measures, strain on soft and hard tissue simultaneously, before.

V. CONCLUSION

This study showed the capability of DIC in strain measurement on complex specimens, in term of material properties and geometry, to study and examine in depth the biomechanics of spine. The assertion of these potentialities could open the way to further application of DIC to study the behaviour of human spines.

ACKNOWLEDGEMENT

The authors wish to thank Remo Antelli for donating the porcine spines.

REFERENCES

1. Fung, Y.C., *Bone and cartilage*, in *Biomechanics - Mechanical properties of living tissues*. 1980, Springer Verlag: New York. p. 383-415.
2. Brandolini, N., L. Cristofolini, and M. Viceconti, *Experimental Method for the Biomechanical Investigation of Human Spine: a Review* Journal Of Mechanics in Medicine and Biology, 2014. **14**(01): p. 1430002.
3. Palanca, M., G. Tozzi, and L. Cristofolini, *The Use Of Digital Image Correlation In The BIomechanical Field: A Review.* Inter Biomech, 2016. **3**(1): p. 1-21.
4. Palanca, M., T.M. Brugo, and L. Cristofolini, *Use of Digital Image Correlation to Understand the Biomechanics of the Vertebra.* Journal Of Mechanics in Medicine and Biology, 2015. **15**(2): p. 1540004-1/1540004-10.
5. Lionello, G., C. Sirieix, and M. Baleani, *An effective procedure to create a speckle pattern on biological soft tissue for digital image correlation measurements.* J Mech Behav Biomed Mater, 2014. **39**: p. 1-8.
6. Lionello, G. and L. Cristofolini, *A practical approach to optimizing the preparation of speckle patterns for digital-image correlation.* Measurement Science and Technology, 2014. **25**(10): p. 107001.
7. Bayraktar, H.H., et al., *Comparison of the elastic and yield properties of human femoral trabecular and cortical bone tissue.* J Biomech, 2004. **37**(1): p. 27-35.
8. Spera, D., K. Genovese, and A. Voloshin, *Application of Stereo-Digital Image Correlation to Full-Field 3-D Deformation Measurement of Intervertebral Disc.* Strain, 2011. **47**: p. e572-e587.

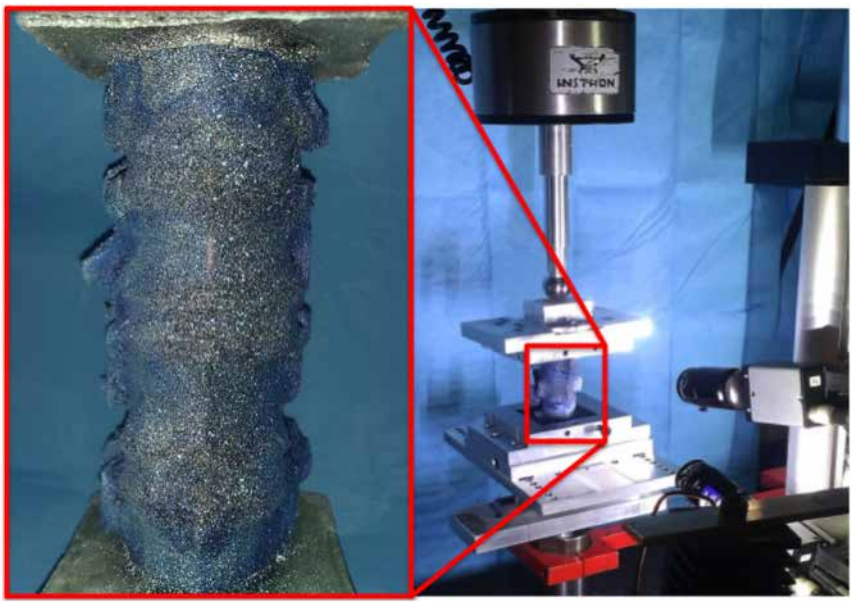

Fig. 1. Left, a three-vertebrae segment spine with white-on-black speckle pattern. Right, overview of the testing setup.

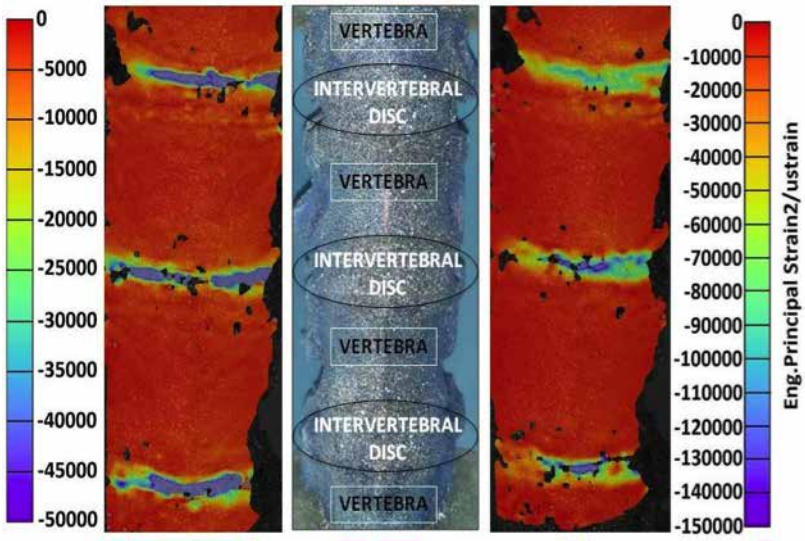

Fig. 2. Axial strain distribution in vertebrae and intervertebral discs. On the left the strain under a load of 1522N and on the right the strain under a load at 3418N, just prior to failure.

Modelling Right Heart Failure in Patients with Pulmonary Hypertension

F. Scardulla[1], P. Mercadante[1], S. Pasta[2,3], D. Bellavia[3] and C. Scardulla[3]
[1] DICGIM, Universitá di Palermo, Palermo, 90128, Italy
[2] Fondazione Ri.MED, Via Bandiera n.11, 90133, Palermo, Italy
[3] IRCCS ISMETT, Via Tricomi n.5, 90128, Palermo, Italy

***Abstract*—Standard of care in precapillary (group I) pulmonary hypertension (PH) includes serial right ventricular (RV) catheterizations in order to monitor RV performance and pulmonary bed pressures, unfortunately with associated costs and side effects related to invasive procedures. Our aim was two-fold: 1) to develop a biventricular finite-element model coupled to a lumped-parameter circulatory system of PH; 2) to assess accuracy of proposed computational model in predicting hemodynamic impairment due to PH and abnormal motion of interventricular septum.**

***Keywords*—finite-element method, lumped-parameter model, pulmonary hypertension.**

I. Introduction

Pulmonary hypertension (PH) is a pathological condition in which the mean pulmonary artery pressure is higher than the normal condition [1]. Specifically, PH is defined when right ventricular (RV) pressure exceeds 25 mmHg at rest [2]. This condition may ultimately lead to right ventricle failure (RVF). Conceptualized hemodynamically, RVF occurs at the point at which cardiac output (CO) and blood pressure drop despite an increased RV end-diastolic pressure (Ref). Although PH can be seen at echocardiography [3], pressure measurements by Swan-Ganz catheterization of right side represent the gold standard for the diagnosis of PH and to assess disease severity [4, 5].

II. Methods

Patient Study Group

We retrospectively identified 10 patients with Group I PH underwent right-sided cardiac catheterization to monitor the progress of pulmonary disease. Standard echocardiography and delayed enhanced (DE) CMR were performed within 2 weeks from RV catheterization in order to collect hemodynamic and morphological data. Specifically, left ventricular (LV), ejection fraction, cardiac output (CO), cardiac index (CI) and pulmonary capillary wedge pressure (PCWP) were collected from standard 2D or Doppler echocardiography. While, RV end-diastolic and end-systolic volume, RV stroke volume, RV cardiac output, RV ejection fraction were measured from DE-CMR.

Lumped-Parameter Modelling of PH

To simulate the hemodynamic impairment due to PH, we used the CircAdapt open-source cardiovascular tool (www.circadapt.org/) as a lumped-parameter model of heart and circulation. The CircAdapt is configured as a network composed of several module types representing myocardial walls, cardiac valves, large blood vessels, and peripheral vasculature to enable real-time simulation of hemodynamic under normal and pathological conditions

Both RV and LV end-diastolic and end-systolic volumes as collected by DE-CMR were used as input parameters in the lumped-parameter model. We interactively adjusted the pulmonary vascular resistance (PVR) and myocardial contractility parameters (i.e. passive stiffness and active contraction) to match both LV and RV ventricular volumes.

For each patient, the model output consisted in the RV and LV pressure-volume loops, which were used as boundary conditions for the biventricular finite-element model. Additionally, standard hemodynamic parameters such as the CO were computed with CircAdapt and then compared to those derived by RV catheterization.

Finite Element (FE) analysis

Numerical simulations were performed according to our previously described biventricular model [6, 7]. The substantial difference with this model was the use of the Holzapfel's constitutive formulation and a thermal-mechanical analog approach to describe active myocardial contraction [8]. This allowed us to avoid numerical issues that are often observed with the Fung's law. LV and RV geometries were obtained *via* parameterized geometric surfaces initialized by morphological measurements collected by DE-CMR. The biventricular model represented the end-systolic ventricular-chamber configuration and then meshed with brick elements in ABAQUS FE code (Simulia, Inc., Providence, RI). Cardiac myofiber angles at epicardium and endocardium were 60° with respect to the circumferential direction of LV wall. We fully constrained the displacement of the ventricular basal line because the mitral valve annulus and aortic valve annulus are much stiffer than the myocardium.

For each patient, RV and LV pressure loading profiles computed with the lumped-parameter simulation of PH were applied to the endocardium using the hydrostatic fluid cavity modeling capabilities of ABAQUS/Standard. Thus, the passive heart behavior was calibrated by iteratively adjusting the material parameters *C* of Holzapfel's law in order to match the measured values of RV and LV end-diastolic volumes. Similarly, the active heart behavior was tuned by scaling the fictitious temperature field. Septal motion was compared to that observed in 4 healthy patients investigated previously [6, 7].

III. Results and Discussion

Linear regression analysis was used to assess associations between catheter- and lumped-derived parameters (see Table 1). Primary dependent (i.e. predicted) variables were CI and PCWP. Hemodynamic parameters predicted by lumped-parameter modeling were comparable to those actually measured in cath-lab ($p<0.05$ for all). Specifically, the lumped-parameter model was able to predict cardiac index with high accuracy (R^2=0.82, p<0.001), although prediction of PCWP was just moderate. It is worthy of consideration that CI is considered as a prognostic indicator to assess the severity of PH [1]. Although a large cohort is needed, the lumped-parameter modeling appears promising to distinguish the less from the most "malignant" PH. Additionally, this tools is based on non-invasive measures as compared to that achieved by catheterization.

TABLE I: Descriptive Statistics of Collected Measurements

Variables	Lumped Model	Outcome: CI (Cath)	Outcome: PCWP (Cath)
Stroke Volume (mL)	54.2±15.2	0.68 (0.01)	0.03 (0.7)
Cardiac Output (Lit./min)	4.1±1.1	0.74 (<0.001)	0.02 (0.72)
Cardiac Index (Lit/min/m^2)	2.4±0.6	0.82 (<0.001)	0.02 (0.72)
RV Systolic Pressure (mmHg)	64.2±12.9	0.01 (0.97)	0.14 (0.36)
Systolic Pulmonary Artery Press. (mmHg)	62.5±12.8	0.01 (0.79)	0.03 (0.71)
Diastolic Pulmonary Artery Pressure (mmHg)	37.1±10.1	0.12 (0.37)	0.52 (0.04)

Numerical simulations revealed that RV experiences severe myocardial stress during cardiac beating (see Figure 1). Specifically, end-systolic myocardial stress was as high as 221 kPa at apex. This pronounced stress is caused by the fact that the RV volumes were markedly high (180.4± 60.1ml) since the increase of intraventricular pressure due to the pulmonary disease leads to an adverse remodeling characterized by ventricular dilatation. Indeed, RV is a compliance chamber that is not able to adequately contrast the high pressure demand. This mechanism ultimately leads to failure of RV chamber. In healthy patients, the mean value of RV end-systolic myocardial stress was 24.3±6 9.7kPa, and this is significantly lower than that shown by patients with PH. Using a similar biventricular finite-element model, Wenk and collaborators [9] found that RV end-systolic myocardial stress in patients with dilated cardiomyopathy was 58.5 kPa, although RV volume was reported as morphologically normal. Similarly, end-diastolic RV myocardial stress in PH was found higher than that showed by healthy patients (150 kPa for PH compared to 13 kPa for normal hearts).

Most importantly the interventricular septum exhibited an abnormal motion throughout cardiac beating. As PH became more severe, the pattern of septal motion was characterized by a normal left-ward shift towards RV during diastolic filling followed by an abnormal right-ward shift towards LV during ejection and isovolumic relaxation phases. This was likely caused by the time courses of simulated ventricular pressures. In simulation of PH, RV pressure exceeded LV pressure during systole, with pressure decay delayed with respect to that of LV. This time course was not observed for healthy patients where interventricular septum did not move over LV. A similar mechanism of abnormal motion for the interventricular septum can be seen clinically in PH [2] and corroborated by Lumens and collaborators [10].

IV. Conclusion

In this study, an approach for modeling the interaction between the heart and the circulatory system was developed by coupling a patient-specific biventricular finite-element model to that of a lumped-parameter that represents the systemic and pulmonic circulatory system. Thus, this approach was adopted to study the mechanism of PH by comparing hemodynamic data to those derived by right side catheterization and by assessing cardiac mechanics. Results showed a good agreement between lumped- and catheter-related hemodynamic measures and the ability of our biventricular model to capture the systolic abnormal motion of interventricular septum observed clinically. This may allow less invasive clinical procedure and rapid computational prediction for the diagnosis of PH. Further studies on large patient cohort are warranted to refine model and confirm results.

Acknowledgement

Mr. F. Scardulla thanks the Italian Ministry of Education, University and Research for supporting his research. The Departments of Radiology at ISMETT have given their support providing clinical cases and offering medical knowledge. This support is gratefully acknowledged.

References

[1] Bourji, K.I. and P.M. Hassoun, *Right ventricle dysfunction in pulmonary hypertension: mechanisms and modes of detection.* Curr Opin Pulm Med, 2015. **21**(5): p. 446-53.

[2] Saggar, R. and O. Sitbon, *Hemodynamics in pulmonary arterial hypertension: current and future perspectives.* Am J Cardiol, 2012. **110**(6 Suppl): p. 9S-15S.

[3] Forfia, P.R. and J.L. Vachiery, *Echocardiography in pulmonary arterial hypertension.* Am J Cardiol, 2012. **110**(6 Suppl): p. 16S-24S.

[4] Kholdani, C.A. and W.H. Fares, *Management of Right Heart Failure in the Intensive Care Unit.* Clin Chest Med, 2015. **36**(3): p. 511-20.

[5] Harjola, V.P., et al., *Contemporary management of acute right ventricular failure: a statement from the Heart Failure Association and the Working Group on Pulmonary Circulation and Right Ventricular Function of the European Society of Cardiology.* Eur J Heart Fail, 2016. **18**(3): p. 226-41.

[6] Scardulla, F., et al., *Mechanics of pericardial effusion: a simulation study.* Proc Inst Mech Eng H, 2015. **229**(3): p. 205-14.

[7] Scardulla, F., et al., *Evaluation of ventricular wall stress and cardiac function in patients with dilated cardiomyopathy.* Proc Inst Mech Eng H, 2016. **230**(1): p. 71-4.

[8] Bagnoli, P., et al., *Computational finite element model of cardiac torsion.* Int J Artif Organs, 2011. **34**(1): p. 44-53.

[9] Wenk, J.F., et al., *A coupled biventricular finite element and lumped-parameter circulatory system model of heart failure.* Comput Methods Biomech Biomed Engin, 2013. **16**(8): p. 807-18.

[10] Lumens, J. and T. Delhaas, *Cardiovascular modeling in pulmonary arterial hypertension: focus on mechanisms and treatment of right heart failure using the CircAdapt model.* Am J Cardiol, 2012. **110**(6 Suppl): p. 39S-48S.

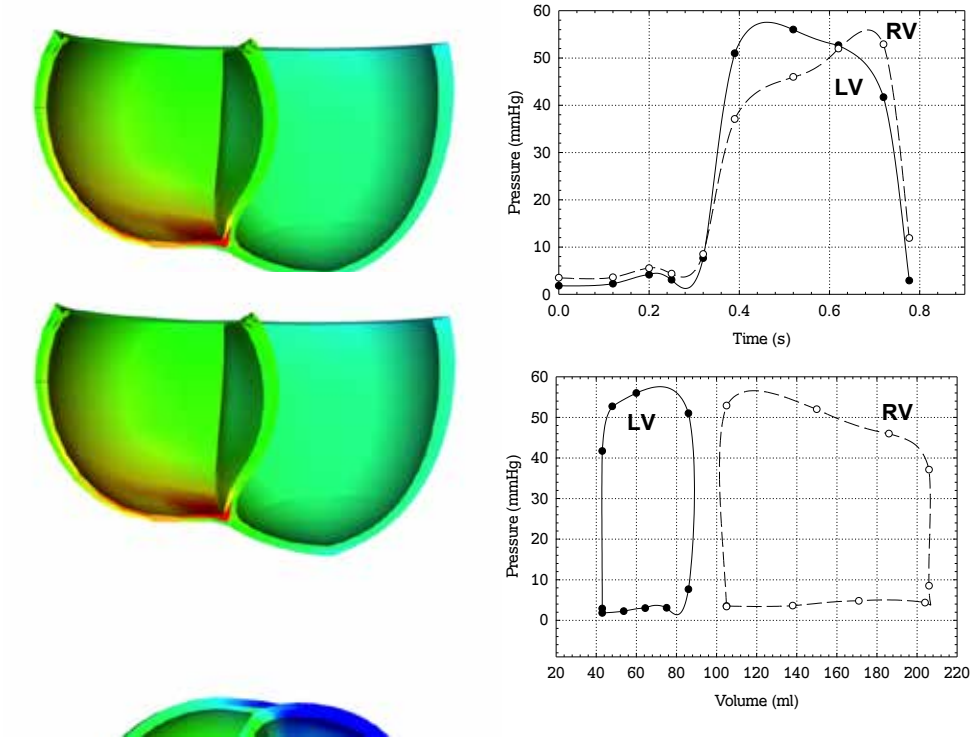

Fig. 1. End-systolic myocardial wall stress showing abnormal motion of interventricular septum (left); pressure-time and pressure-volume loop obtained by the lumped-parameter model (right).

Mechanical characterization of polymeric microspheres through micro-compression testing

G. Serino[1], V. Crognale[2], C. Del Gaudio[2], U. Morbiducci[1], and A. Audenino[1]
[1] *Department of Mechanical and Aerospace Engineering Politecnico di Torino Turin, Italy*
[2] *Department of Enterprise Engineering University of Rome "Tor Vergata"*

***Abstract*— Usage of polymeric microspheres in biomedical applications is dramatically increasing in the last years. Their massive use is promoted by the maturation of methodologies for their preparation, that allow the control of their shape and size. Here we present a study were a test bench is proposed for the characterization of the mechanical properties of polymeric microspheres. In detail, compression tests are performed on three types of gelatine microspheres characterized by three different values of concentration of genipin (0.1%, 0.5%, 1%). Microspheres mechanical properties are evaluated by using nanoindentation and applying the Hertz model, assuming microspheres incompressibility and a Poisson's coefficient equal to 0.5. The values of Young's modulus obtained for the three types of microspheres are 2.56 ±0.95 GPa (0.1% of genipin), 1.87 ±0.91 GPa (0.5% of genipin), and 3.44 ±0.66 GPa (1% of genipin), respectively, confirming that their mechanical behavior depends upon the concentration of the genipin used for their preparation. The obtained results, obtained by applying the Hertz theory, satisfactorily agree with the experimental data, indicating that the Hertz model is adequate to describe the mechanical properties of the investigated microspheres.**

***Keywords*—Nanoindentation, micro-compression, microspheres.**

I. Introduction

POLYMERIC microspheres are largely adopted in biomedical applications as, e.g., embolic agents to treat hyper-vascular tumors [1], or in tissue engineering [2]. The class of polymeric microspheres used for biomedical applications are mainly composed by hydrophilic polymers, because of their biocompatibility. In particular, the injection of gelatin microspheres is very promising, because of their poor antigenic properties and higher absorbability, when compared with other biocompatible polymers as collagen [3].

In this study the mechanical properties of a new design of polymeric microspheres to be used as carriers for local release of drugs and grow factors, are investigated. The rationale of the study is that, since the microspheres have to be injected into the target tissue, the rheological behavior of suspensions or dispersions of such microspheres, and their effectiveness in properly delivering drugs, will depend upon their mechanical properties [3][4]. Technically, nanoindentation is applied on microspheres of size in the range 30-70 μm. To measured load-displacement data, the Hertz model is applied to estimate the Young's modulus. Once fully validated, the protocol here proposed for the mechanical characterization of polymeric microspheres used for drug delivery will allow: (1) to support their design phase and (2) to improve their effectiveness in targeting the release of drugs.

II. Material and methods

The water-in-oil emulsion method was applied to gelatin type A derived from the porcine skin to produce three types of microspheres characterized by a different percentage of genipin (Figure 1), and with an average radius equal to (mean ± SD) 44.12±11.12 μm for group 1, 51.78±10.45 μm for group 2 and 50.88±9.30 μm for group 3. Genipin in three different values of concentration (w/v) %: 0.1% (group 1) ,0.5% (group 2), and 1% (group 3), was used as natural cross-linker (the presence of genipin affects the structural characteristics of the polymer and the degradation kinetics as well).

Nanoindentation combined with the Hertz model was applied to estimate the mechanical properties of the microspheres. In nanoindentation, when the contact between the specimen and the indenter tip is detected, its displacement is measured as the load is applied. From the measured load-displacement curve (Figure 2) it is possible the estimation of the Young's modulus of the specimen.

In detail, the Nanoindenter XP (Agilent/MTS company), characterized by a theoretical force resolution of 50 nN and a theoretical displacement resolution lower than 0.01 nm, was adopted and a specific protocol was developed for characterize the microspheres through a micro-compression test. In detail, here a flat end punch with a diameter of 500 μm was selected for indentation. The compression test is characterized by three steps: loading, hold and unloading. During the loading and unloading phases the velocity of the indenter punch was set at a constant value of 10 nm s^{-1}. The hold phase consisted of a stabilization period along which the maximum value of the load was maintained for a period of 5 s. The maximum value of the load was obtained in correspondence of an indentation depth equal to the 5% of the initial radius of the microsphere. The initial radius of each microsphere was evaluated before the beginning of the test, using the optical system embedded in the Nanoindenter XP. Load and displacement signals were acquired at a sampling rate of 5 Hz.

On measured load-displacement curves as obtained from the compression tests, the Hertz model [5] was applied and the Young's modulus was estimated according to:

$$F = \frac{4\sqrt{R}}{3}\frac{E}{1-\upsilon^2}\sqrt{\left(\frac{H}{2}\right)^3} = \frac{4\sqrt{R}}{3}E^*\sqrt{\left(\frac{H}{2}\right)^3} \quad (1)$$

where F is the load, H is the displacement, E is the Young's modulus, υ is the Poisson's ratio and R is the radius of the microsphere. The value of the Poisson's ratio was assumed to be equal to 0.5 [2][6]. The linear least squares method has been applied to estimate the value of E on the experimental data. By applying the Hertz contact model we implicitly

made the assumptions that: (1) microspheres are spherically shaped; (2) deformation is symmetric; (3) microspheres are made of a purely elastic and isotropic polymer; (4) only small deformations affect indented microspheres.

III. RESULTS

Typical compression load-displacement curves as obtained from nanoindentation are presented in Figure 2. The curves is characterized by an hysteresis loop typically characterizing viscous-elastic materials.

For each group of polymeric microsphere 40 tests were carried out. Outliers have been excluded by applying the modified Thompson's Tau method.

The Young's modulus was estimated by using the Hertz contact model, applied to the linearized experimental data measured along the loading phase. We obtained three average values of Young's modulus equal to 2.56 ±0.95 GPa, 1.87 ±0.91 GPa, and 3.44 ±0.66 GPa (mean ± SD) for group 1, 2 and 3 respectively.

The percentage of genipin influences the mechanical properties of the microspheres. Indeed the analysis of variance (ANOVA) applied to the tests carried out on microspheres shows a correlation ($p<0.05$) between their mechanical properties and the percentage of genipin used during the production of the microspheres. The progressive increase in the percentage of genipin in microspheres composition is not related to a linear increase of the Young's modulus. Load-displacement curves obtained for microspheres belonging to group 1 show a mean peak load value higher than group 2 (Figure 3), indeed the experimental curves obtained for the group 1 are characterized by an higher slope respect the curve belonging to group 2.

Since the level of (imposed) deformation is the same in all the experiments, the estimated Young's Modulus of microspheres of group 2 is lower than group 1.

Individual Young's modulus from single microspheres were used as input variable in the Hertz model and theoretical results were compared with experimental data relative to the sole loading phase of the curve. The explanatory results displayed in **Errore. L'origine riferimento non è stata trovata.** are representative of all the nanoindentation tests performed on single microspheres and indicate that there is a satisfactory agreement between the Hertz model for contact and the experimental data.

IV. DISCUSSION

Application of polymeric microspheres in medicine has increased in the past years thanks to the development of novel methods for their preparation that allow a fine control of their size and shape. The degradation rate of the gelatin microspheres, that regulates the rate of drug delivery, depends strongly on their mechanical properties. Usually, this kind of microspheres are injected in the target tissues by using a solution or an appropriate gel in which they are in suspension. The rheological property of such suspensions of microspheres are affected by the mechanical properties of these microspheres. Hence, from the characterization of the mechanical behavior of polymeric microspheres it is possible to obtain knowledge which is fundamental for improving microspheres design and, ultimately, drug delivery.

As for the analysis here presented, for the three preparations of microspheres the average values of the standard error (and of R^2) with respect to the load-displacement curves estimated by applying the Hertz contact model are equal to 1.55 mN (R^2= 0.98), 1.59 mN (R^2= 0.99), and 2.10 mN (R^2= 0.99) , for group 1 group 2 and group 3, respectively. These data confirm that the selected Hertz model satisfactorily fits the experimental data as obtained from the application of a nanoindentation strategy, making the estimated mechanical properties reliable.

The estimation of a Young's modulus value for microspheres belonging to group 2 lower than group 1 can be explained in terms of the procedure applied for microspheres fabrication. Since it is expected an higher value for the Young's modulus, by increasing the percentage of genipin in fabricated microspheres, the counter-intuitive here presented results could be ascribed to fabrication parameters setting which could influence the ultimate mechanical features of microspheres. In particular, two of this parameters could markedly influence the crosslinking phase of the fabrication process, i.e., the stirring speed and the crosslinking time, because they determine size distribution, independent and individual growth of the microspheres, and the degree of crosslinking. We conjecture that the setting adopted for these parameters in the fabrication of microspheres belonging to group 2 has lead to an impairment of the mechanical properties for this group, also in the presence of an higher percentage of genipin, with respect to group 1. Several limitations could weaken the findings of this study. In particular, the defined deformation at 5% of the initial diameter, which limits the validity of these results only for small deformation. Moreover, nanoindentation tests were carried out in dry condition, while the physiological environment is an aqueous environment. Further analysis is needed to clarify if dry tests can be representative of the in vivo behavior of the microspheres.

In conclusion, the preliminary findings presented here confirm the potential (1) of using nanoindentation and (2) of applying the Hertz model for a mechanical characterization of gelatin microspheres. The presented approach could be easily extended to characterize the mechanical behavior of microspheres obtained using, e.g., chitosan, or blends of gelatin and chitosan.

REFERENCES

[1] K. Hidaka,M. Nakamura, K. Osuga, H. Miyazaki, S. Wada, "Elastic cherecteristics of microspherical embolicagents used for vascular interventional radiology", *J of the Mechanical Behavior of Biomedical Materials,* 3:497-503, 2010.

[2] C. X. Wang, C. Cowen, Z.Zhang, C.R. Thomas, "High-speed compression of single alginate microspheres", *Chimical Engineering Science*, 60:6649-6657, 2005.

[3] W.J.E.M. Habraken, L.T. de Jonge, J.G.C. Wolke, L. Yubao, A.G. Mikos, J.A. Jansen, "Introduction of gelatin microspheres into an injectable calcium phosphate cement", *J Biomed Mater Res,* 87A:643-655, 2008.

[4] Y. Yan, Z. Zhan, J.R. Stokes, Q. Zhou, G. Ma, et al, "Mechanical characterization of agarose micro-particles with a narrow size distribution" *Powder Technology,* 192:122-130, 2009.

[5] H. Hertz, *On the contact of elastic solids,* 318, 1896.

[6] K Hidaka, L.Moine, G.Collin,D. Labare, J.L. Grossiord, et al,"Elasticity and viscoelasticity of embolization microspheres", *J of the Mechanical Behavior of Biomedical Materials,* 4:2161-2167, 2011.

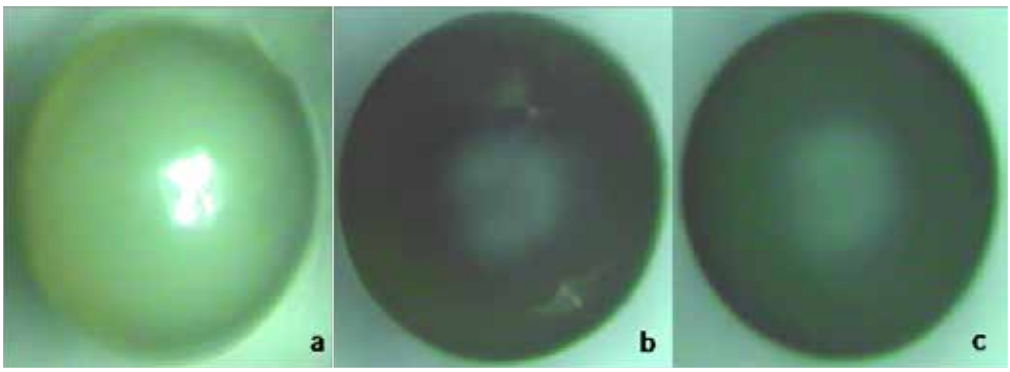

Figure 1: Representative images of group 1 (a) group 2 (b) and group 3 (c), taken by the optical microscope built in the Nanoindenter XP. (Resolution: 0.2 µm/pixel).

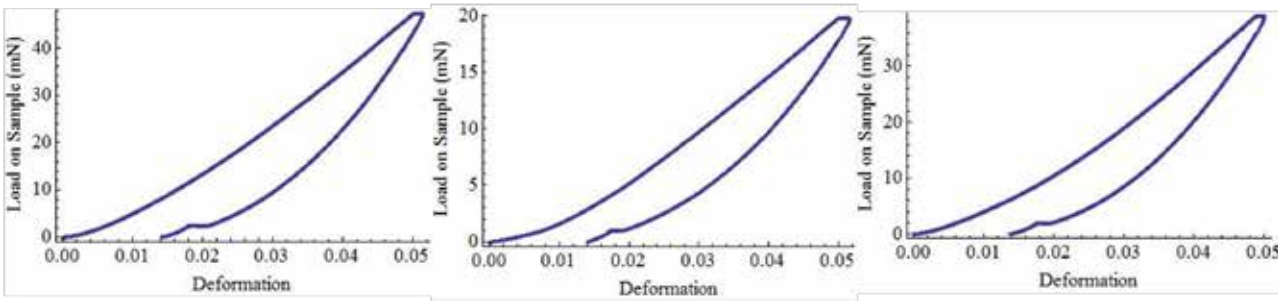

Figure 2: Typical Load-Displacement curve as obtained from nanoindentation tests on gel microspheres of group 1 (a), group 2 (b) and group 3 (c).

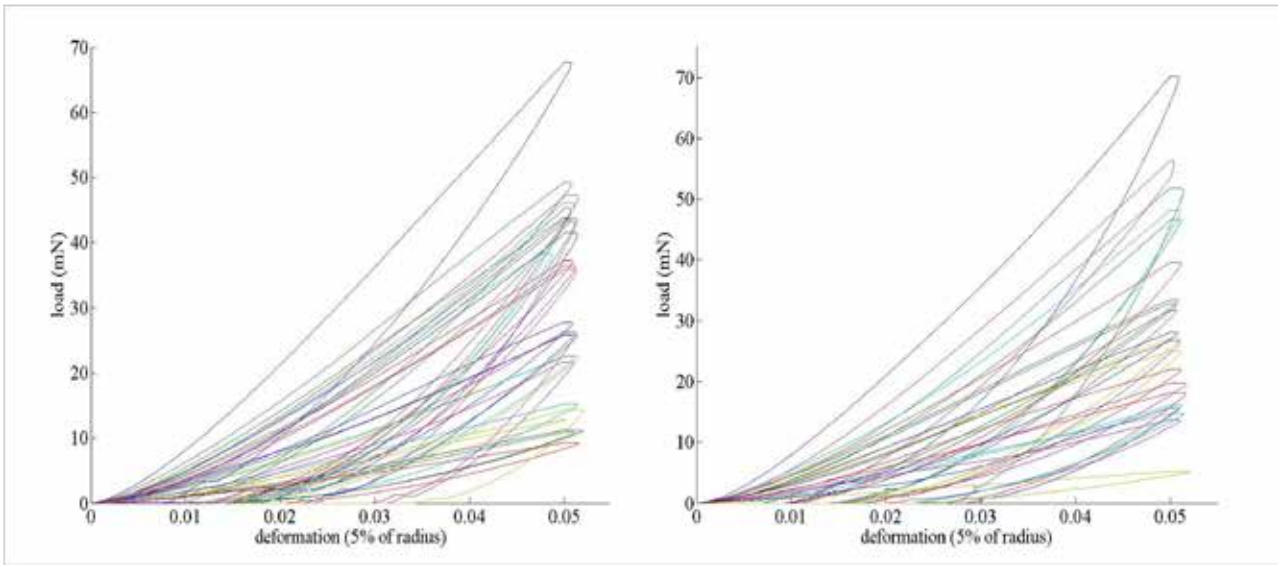

Figure 3: Experimental curves obtained by the microindentation tests. On the left curves obtained for microspheres with 0.1% of genipin. On the right curves obtained for microspheres with 0.5% of genipin

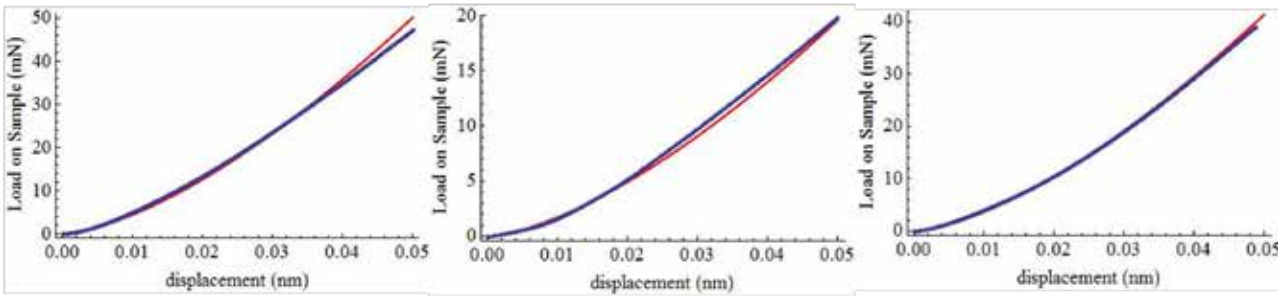

Figure 4: Comparison of the loading phase as obtained from the experimental data (blue curve) and from the Hertz model (red curve), for group 1 (a), group 2 (b), group 3 (c).

Titanium craniofacial prostheses manufacturing using non-conventional forming processes

T. Villa[1], M. V. Caruso[2,3], G. Ambrogio[2], L. De Napoli[2], L. La Barbera[1], G. Palumbo[4], D. Sorgente[4], A. Piccininni[4], P. Guglielmi[4], G. Fragomeni[3]

[1] *Department of Chemistry, Materials and Chemical Engineering, Politecnico di Milano*
[2] *Department of Mechanical, Energetic and Management Engineering (DIMEG), University of Calabria*
[3] *Department of Medical and Surgical Science, University of Catanzaro*
[4] *Department of Mechianics, Mathematics and Management (DMMM), Politecnico di Bari*

***Abstract*—In particular situations, such as in presence of congenital malformations, pathologies or traumas, skull can present bone defects or empties, which can be characterized by complex geometries that vary from case to case. For repairing these defects/empties, patients must undergo cranioplasty procedures, during which a proper prosthesis is anchored to the skull, replacing the missing bone parts. Nowadays, starting from diagnostic images, patient-specific prostheses can be manufactured, made of biocompatible materials. Among metallic materials, titanium alloys are the most suitable for this application.**

The aim of this study is to present a methodology to manufacture craniofacial prostheses in titanium alloy using non-conventional forming processes. In details, the complete procedure starts from the design of both the prosthesis and the anchoring system, choosing the optimal material and the best manufacturing process according to the geometry of the defect, the available time and the cost.

In order to demonstrate the potency of this approach, two case studies were reported.

***Keywords*—craniofacial titanium prostheses, non-conventional forming processes, realization procedure.**

I. Introduction

THE skull is one of the most complex bones and it plays a key role because it protects the brain, the organ that makes us human, and has a strong aesthetic impact [1]. So, it sums both functional and aesthetic aspects. Unfortunately, because of congenital malformations, pathologies or traumas, the skull can present defects or empties, which are repaired with cranioplasty interventions [2]. In particular, during this surgical procedure, a prosthesis made with biocompatible material [2], such as titanium and its alloys [1],[3], is anchored to the skull. Moreover, titanium is chosen as it has excellent mechanical properties [3] and favours osseointegration with the host bone [4].

In order to fulfil the evident aesthetic requirements, such prostheses must be patient customized. In particular, these prostheses can be manufactured using computer-aided-design/computer-aided manufacturing (CAD/CAM) technique [5]: CAD/CAM titanium implants show the lowest rate of complications and have reasonable costs [6]. Regarding the manufacturing different processes, such as the milling [7] or the additive manufacturing [8], can be used even if the optimal one has not yet been established.

The aim of this study was to present a complete procedure for the manufacturing of such titanium prostheses based on the use of non-conventional forming processes.

II. Procedure

The necessary steps to manufacture craniofacial prostheses in titanium by means of the non-conventional processes are illustrated in Figure 1 and described below.

A. Medical scan and DICOM images

Thanks to the research and technological development in imagining techniques, nowadays morphological aspects can be evaluated by means of the computer tomography (CT) and magnetic resonance imaging (MRI), which provide 2D multiplanar images or slices in the DICOM format [9]. So, a 3D visualization is available.

B. Virtual modelling

Starting from diagnostic images of the defected skull, a virtual model can be obtained by means the segmentation process, using different software [10]. For this work, the open source software Invesalius was chosen for the 3D/volumetric reconstruction [11]. Since it provides a STL file, in order to obtain a 3D solid model of skull bone, reverse engineering [12] was used. After that, the prosthesis was designed considering the defect morphology and trying to get an appearance of the resulting treated skull as close as possible to a normal one.

C. Design of anchoring system

In case of titanium customized craniofacial prostheses made with forming processes, they have a greater area and a larger perimeter with respect to the defect [13], but no information regarding the overlap length is available. Furthermore, titanium and skull bone have different elastic modules, reported in [14] and [15] respectively. For these two reasons, a detailed design of the anchoring system is necessary.

To realize it, a hybrid approach was developed (Figure 2). In details, an optimization procedure, based on the ANOVA analysis and the response surface methodology -RSM- [16], was implemented in order to identify the optimal values for the overlap length and the screw shank diameter for a specific defect area, considering the worst accidental compressive load. In this case, the bone that adheres to the prosthesis must resist, so the maximum stress must be evaluated to establish the best anchoring system. Different simulations were carried out using finite-element modeling (FEM) and considering five factors (screw shank diameter, overlap length, load

intensity and its tilt angle and the damaged area) and their values range. Moreover, the stress numerical results were used as input data for the optimization process. Regarding the FEM analyses, they were carried out using Comsol Multiphysics 5.2 (COMSOL Inc, Stockholm, Sweden), whereas for the optimization procedure, Design Expert Software (Stat-Ease, Inc., Minneapolis, USA - trial version) was used.

D. Prosthesis manufacturing

As reported before, in this study non-conventional forming processes were considered to manufacture the prostheses. In details, superplastic forming (SPF) and single-point incremental forming (SPIF) were chosen.

In case of SPF, a sheet is deformed with high temperatures under the action of an in-pressure inert gas, instead, during the SPIF, a rotating tool/punch deforms the sheet with high speeds. Both processes used the CAD/CAM approach, employing an electro-hydraulic machine in the SPF and a 3axis CNC machine in the SPIF. A sketch of the two methodologies are reported in Figure 3. Both technologies allow to create prostheses with very low thicknesses and high mechanical strength. Furthermore, the advantage of SPF is that it can be used to obtain prostheses with complex geometry, whereas the benefit of the SPIF is that prostheses can be made in low times, without employ moulds.

E. Biocompatibility check

The most important property of the bone substitutive materials is the biocompatibility. Even if the titanium alloys normally show this feature, the manufacturing process could have been altered this property, and, consequently, biocompatibility of the final prosthesis must be verified through citotoxicity tests.

III. VALIDATION

To demonstrate the procedure feasibility and to validate it, two different defects were considered and the relative prostheses were made applying the methodology (Figure 4).

In details, the prosthesis relative to the frontal damage was made with the SPF because of the complex geometry, whereas the prosthesis relative to the lateral defect was realized using the SPIF in order to obtain it in very low times. Regarding the SPF manufacturing, the undeformed sheet was heated up to 850°C and then subjected to argon in pressure. Instead, in the SPIF, a hemispheric punch (diameter of 15 mm) deformed the sheet with a continuous movement (constant tool depth step of 0.1 mm and a tool feed rate of about 2000 mm/min), following the trajectory generated by the CAD/CAM program. Nano-indentation tests were also performed in order to measure hardness and elastic modulus variation deriving from the manufacturing process. Results highlighted that no significant changes are generated by the processes. The two realized prostheses are reported in Fig. 4.

IV. CONCLUSION

This work presented a procedure to realize craniofacial prostheses in titanium with non-conventional forming processes, the superplastic forming and the single-point incremental forming. Both these two technologies have proved to be suitable for this application, with the advantage of obtaining both extremely thin and, at the same time, resistant prostheses. The necessary aesthetic and biocompatibility requirements have also been demonstrated that can be fulfilled by the usage of the two technologies.

ACKNOWLEDGEMENT

This research is funded by the Italian Ministry of University and Research within the project PRIN "Bioforming".

REFERENCES

[1] M. C. Goiato, R. B.Anchieta,, M. S. Pita, D. M. dos Santos, "Reconstruction of skull defects: currently available materials", *Journal of Craniofacial Surgery*, vol. 20(5), pp.1512-1518, 2009.

[2] P. Solaro, E. Pierangeli, C. Pizzoni, P. Boffi and G. Scalese, "From computerized tomography data processing to rapid manufacturing of custom-made prostheses for cranioplasty", *Journal of neurosurgical sciences*, vol. 52(4), pp.113, 2008.

[3] M. A. H Gepreel, M. Niinomi, "Biocompatibility of Ti-alloys for long-term implantation", *Journal of the mechanical behavior of biomedical materials*, vol. 20, pp. 407-415, 2013.

[4] T. Albrektsson, P. I., Brånemark, H. A. Hansson, J. Lindström, "Osseointegrated titanium implants: requirements for ensuring a long-lasting, direct bone-to-implant anchorage in man", *Acta Orthopaedica*, vol. 52(2), pp. 155-170, 1981.

[5] L. C. Hieu, E. Bohez, J. Vander Sloten, H. N.Phien, E.Vatcharaporn, P. H Binh, ... P. Oris, "Design for medical rapid prototyping of cranioplasty implants", *Rapid Prototyping Journal*, vol. 9(3), pp.175-186, 2003.

[6] M. Cabraja, M. Klein, T. N Lehmann, "Long-term results following titanium cranioplasty of large skull defects", *Neurosurgical focus*, vol. 26(6), pp. E10, June 2009.

[7] M.Wehmöller, S.Weihe, C. Rasche, P. Scherer, H. Eufinger, "CAD/CAM-prefabricated titanium implants for large skull defects-clinical experience with 166 patients from 1994 to 2000", In *International Congress Series*, vol. 1268, pp. 667-672, June 2004.

[8] A. L. Jardini, M. A. Larosa, C. A. de Carvalho Zavaglia, L. F. Bernardes, C. S. Lambert, P. Kharmandayan ... R. Maciel Filho, "Customised titanium implant fabricated in additive manufacturing for craniomaxillofacial surgery: This paper discusses the design and fabrication of a metallic implant for the reconstruction of a large cranial defect", *Virtual and Physical Prototyping*, vol. 9(2), pp. 115-125, 2014.

[9] P. Mildenberger, M. Eichelberg, E. Martin, "Introduction to the DICOM standard", *European radiology*, vol. 12(4), pp. 920-927, 2002

[10] G. L. Presti, M. Carbone, D. Ciriaci, D. Aramini, M. Ferrari, V. Ferrari, "Assessment of DICOM viewers capable of loading patient-specific 3D models obtained by different segmentation platforms in the operating room", *Journal of digital imaging*, vol. 28(5), pp. 518-527, 2015

[11] T.F. de Moraes, P.H. Amorim, F.S. Azevedo, J.V. da Silva, "InVesalius-An open-source imaging application. Computational Vision and Medical Image Processing", in *VipIMAGE 2011*, vol. 405. 2011.

[12] E. Maravelakis, K. David, A. Antoniadis, A. Manios, N. Bilalis, Y. Papaharilaou, "Reverse engineering techniques for cranioplasty: a case study", *Journal of medical engineering & technology*, vol. 32(2), pp. 115-121, 2008

[13] B. Lu, D.K. Xu, R.Z Liu., H. Ou, H. Long, J. Chen, "Cranial reconstruction using double side incremental forming". *Key Engineering Materials*, vol. 639, pp. 535-542, 2015.

[14] M. Vosough, F. Schultheiss, M. Agmell, J.E. Stahl,"A method for identification of geometrical tool changes during machining of titanium alloy Ti6Al4V", *The International Journal of Advanced Manufacturing Technology*, vol. 67(1-4), pp. 339-348, 2013

[15] J.S. Raul, D. Baumgartner, R. Willinger, B. Ludes, "Finite element modelling of human head injuries caused by a fall". *International Journal of Legal Medicine*, vol. 120(4), pp. 212-218, 2006.

[16] İ. Asiltürk, S. Neşeli, M. A. İnce, "Optimisation of parameters affecting surface roughness of Co28Cr6Mo medical material during CNC lathe machining by using the Taguchi and RSM methods". *Measurement*, vol. 78, pp. 120-128, 2016

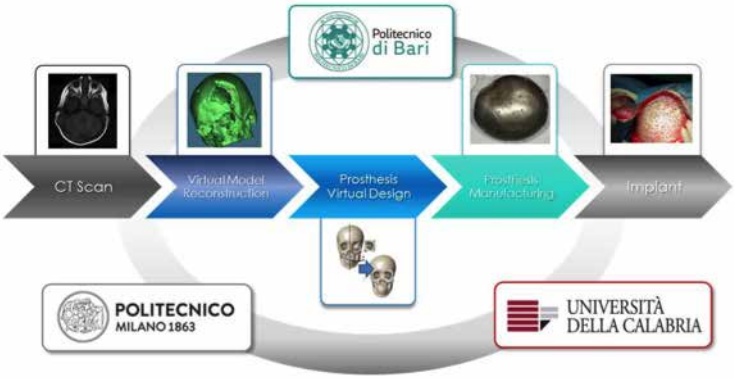

Fig. 1. Steps of presented procedure for the realization of craniofacial prostheses in titanium by means of non-conventional processes

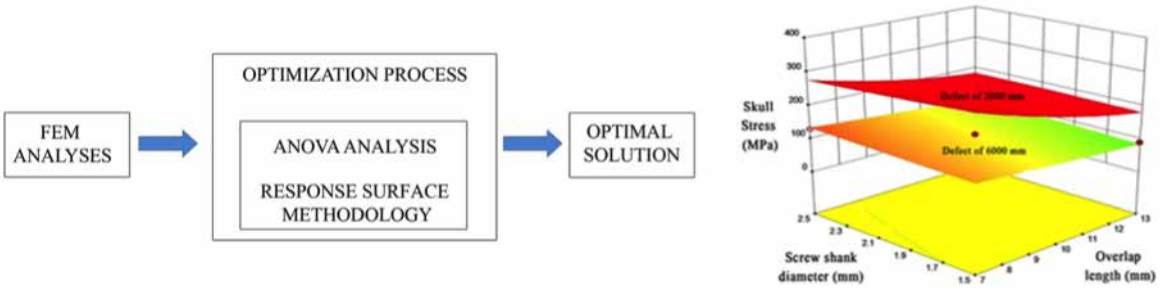

Fig. 2. Steps of the procedure used to design the optimal anchoring system (left) and results of the optimization of (right)

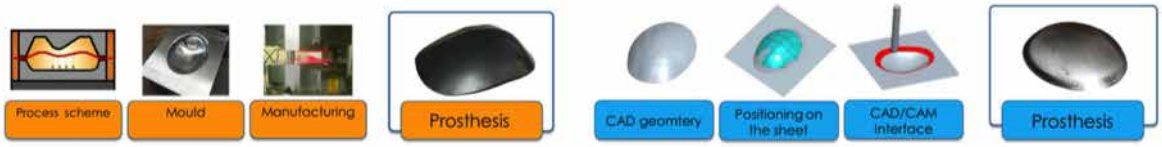

Fig. 3. Non-conventional forming procedures: superplastic forming (SPF, left) and single-point incremental forming (SPIF, right)

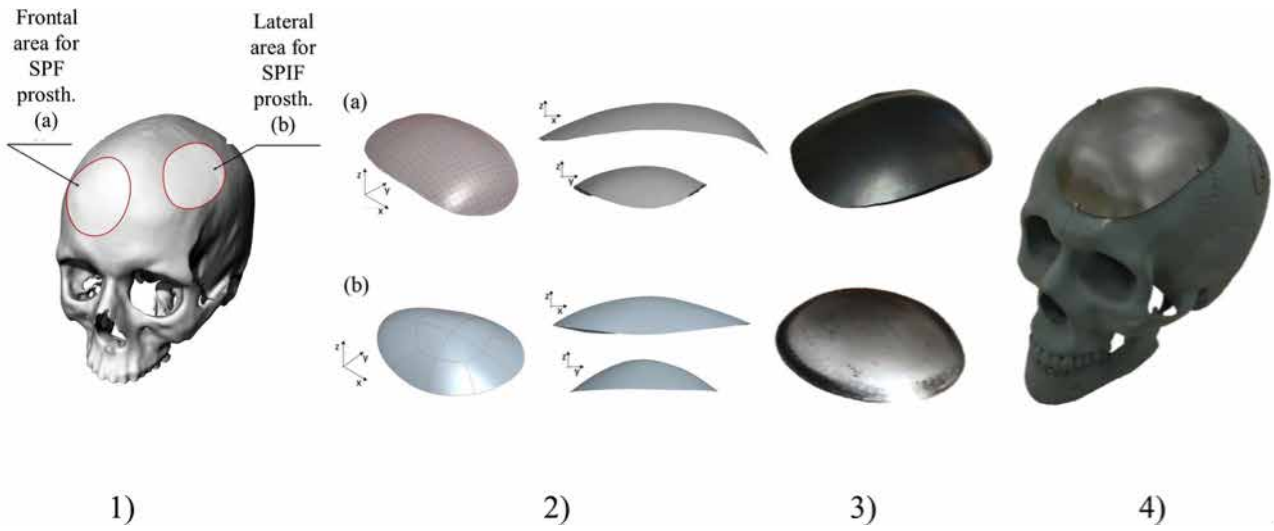

Fig. 4. (1) Skull defects areas (2) relative CAD models of the prostheses (3) manufactured prostheses (4) SPF prosthesis mounted on the skull model

INDICE AUTORI

A

B

C

D

E

F

G

I

J

K

L

M

N

O

P

Q

R

S

T

U

V

W

Y

Z

ORGANIZING SECRETARIAT
YES MEET
Via S. Nicola, 4
80067 – Sorrento (NA), Italy
Tel. +39 0818770604
Fax + 39 0818770258
info@yesmeet.it

PUBLISHER
EDIZIONI ZIINO – Italy
www.stampacongressi.com
info@stampacongressi.com

ISBN
978-88-941906-0-1